THE MECHANICAL BEHAVIOR OF SALT

Understanding of THMC Processes in Salt

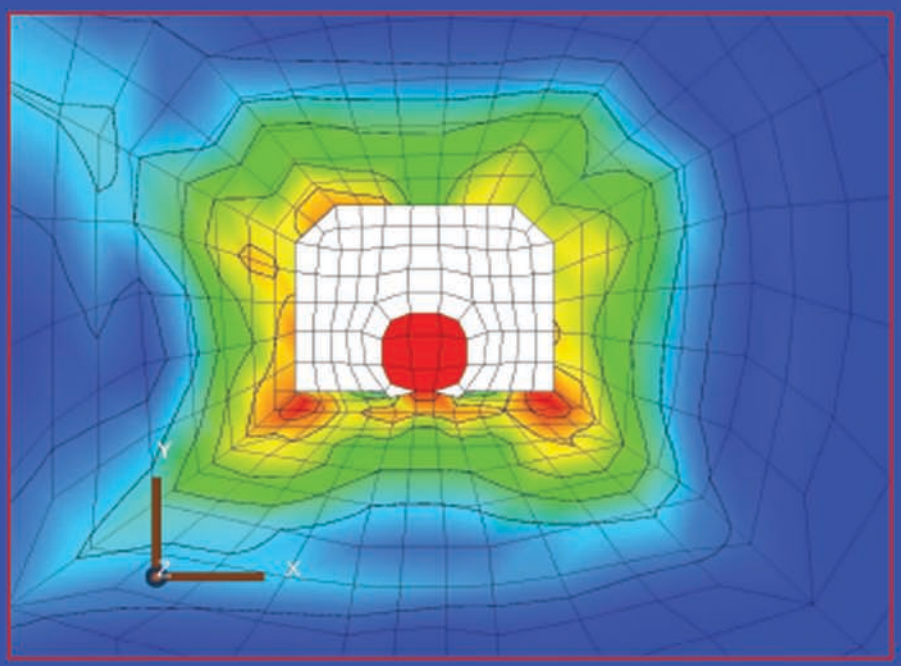

Manfred Wallner
Karl-Heinz Lux
Wolfgang Minkley
H. Reginal Hardy, Jr.
EDITORS

Taylor & Francis
Taylor & Francis Group

THE MECHANICAL BEHAVIOR OF SALT – UNDERSTANDING OF THMC PROCESSES IN SALT

BALKEMA – Proceedings and Monographs
in Engineering, Water and Earth Sciences

PROCEEDINGS OF THE 6th CONFERENCE ON THE MECHANICAL BEHAVIOR OF SALT 'SALTMECH6', HANNOVER, GERMANY, 22–25 MAY 2007

The Mechanical Behavior of Salt – Understanding of THMC Processes in Salt

Editors

Manfred Wallner
Federal Institute for Geosciences and Natural Resources (BGR), Germany

Karl-Heinz Lux
Clausthal University of Technology (TUC), Germany

Wolfgang Minkley
Institute for Rock Mechanics GmbH Leipzig (IfG), Germany

H. Reginald Hardy, Jr.
Pennsylvania State University (PSU), USA

Taylor & Francis
Taylor & Francis Group
LONDON / LEIDEN / NEW YORK / PHILADELPHIA / SINGAPORE

Cover illustration:
Results of a three-dimensional numerical model including the coupling of thermomechanical and hydromechanical properties: Permeability in the excavation damaged zone (EDZ) around a drift in rock salt backfilled with crushed salt. In the drift a heat source represents the thermal load of a high-level radioactive waste canister. Situation ten years after start of heating.
Project BAMBUS, code JIFE (courtesy of Ulrich Heemann, BGR).

All papers published in this volume were refereed before publication. Original papers and papers dealing with particular and important case histories were accepted. The Organizing Committee is not responsible for the statements made or for the opinions expressed in this volume.

Taylor & Francis is an imprint of the Taylor & Francis Group, an informa business

© 2007 Taylor & Francis Group, London, UK

Typeset by Charon Tec Ltd (A Macmillan Company), Chennai, India
Printed and bound in Great Britain by Bath Press Ltd (A CPI-group company), Bath

All rights reserved. No part of this publication or the information contained herein may be reproduced, stored in a retrieval system, or transmitted in any form or by any means, electronic, mechanical, by photocopying, recording or otherwise, without written prior permission from the publishers.

Although all care is taken to ensure integrity and the quality of this publication and the information herein, no responsibility is assumed by the publishers nor the author for any damage to the property or persons as a result of operation or use of this publication and/or the information contained herein.

Published by: Taylor & Francis/Balkema
P.O. Box 447, 2300 AK Leiden, The Netherlands
e-mail: Pub.NL@tandf.co.uk
www.balkema.nl, www.taylorandfrancis.co.uk, www.crcpress.com

ISBN 13: 978-0-415-44398-2

The Mechanical Behavior of Salt – Understanding of THMC Processes in Salt –
Wallner, Lux, Minkley & Hardy, Jr. (eds)
© 2007 Taylor & Francis Group, London, ISBN 978-0-415-44398-2

Table of contents

Foreword IX

Acknowledgements XI

Conference organization XIII

Part 1. THM-processes in salt rocks – observations at laboratory and in-situ scales

Geomechanical investigations on the integrity of geological barriers with special regard to laboratory tests 3
U. Düsterloh & K.-H. Lux

Lode angle effects on the creep of salt 9
K.D. Mellegard, K.L. DeVries & G.D. Callahan

Gas transport in dry rock salt – implications from laboratory investigations and field studies 17
T. Popp, M. Wiedemann, A. Kansy & G. Pusch

Excavation damaged zones in rock salt formations 27
N. Jockwer & K. Wieczorek

Investigations on damage and healing of rock salt 33
O. Schulze

The influence of humidity on microcrack processes in rock salt 45
J. Hesser & T. Spies

Petrophysical and rock-mechanical characterization of the excavation-disturbed zone in tachyhydrite-bearing carnallitic salt rocks 53
T. Popp, K. Salzer, M. Wiedemann, T. Wilsnack & H.-D. Voigt

Deformation of a halite-anhydrite sequence under bulk constriction: Preliminary results from thermomechanical experiments 63
G. Zulauf, J. Zulauf & O. Bornemann

Experimental research on deformation and failure characteristics of laminated salt rock 69
Y.P. Li, C.H. Yang, Q.H. Qian, D.H. Wei & D.A. Qu

Part 2. Constitutive models for the mechanical behavior of rock salt

Comparison of advanced constitutive models for the mechanical behavior of rock salt – results from a joint research project – I. Modeling of deformation processes and benchmark calculations 77
O. Schulze, U. Heemann, F. Zetsche, A. Hampel, A. Pudewills, R.-M. Günther, W. Minkley, K. Salzer, Z. Hou, R. Wolters, R. Rokahr & D. Zapf

Comparison of advanced constitutive models for the mechanical behavior of rock salt – results from a joint research project – II. Numerical modeling of two in situ case studies and comparison 89
Z. Hou, R. Wolters, R. Rokahr, D. Zapf, K. Salzer, R.-M. Günther, W. Minkley, A. Pudewills, U. Heemann, O. Schulze, F. Zetsche & A. Hampel

The Composite Dilatancy Model: A constitutive model for the mechanical behavior of rock salt 99
A. Hampel & O. Schulze

A model for rock salt, describing transient, stationary, and accelerated creep and dilatancy 109
R.-M. Günther & K. Salzer

Constitutive models to describe the mechanical behavior of salt rocks and the imbedded weakness planes 119
W. Minkley & J. Mühlbauer

Fundamentals and first application of a new healing model for rock salt 129
K.-H. Lux & S. Eberth

Crack-initiation and propagation in rock salt under hydromechanical interaction 139
U. Heemann, W. Sarfeld, C. Hillmann & B. Faust

Part 3. Deformation processes at very large temporal and spatial scales – geological systems

The effect of grain boundary water on deformation mechanisms and rheology of rocksalt during long-term deformation 149
J.L. Urai & C.J. Spiers

Stress relaxation experiments on compacted granular salt: effects of water 159
X. Zhang, C.J. Peach, J. Grupa & C.J. Spiers

Deformation mechanisms and rheology of Pre-cambrian rocksalt from the South Oman Salt Basin 167
J. Schoenherr, Z. Schléder, J.L. Urai, P.A. Fokker & O. Schulze

Evolution of a young salt giant: The example of the Messinian evaporites in the Levantine Basin 175
C. Hübscher & G.L. Netzeband

Part 4. THM-processes in crushed salt backfill of final repositories – observations at laboratory and in-situ scales, modeling

Thermomechanical modelling of the behaviour of drifts in rock salt 185
S. Olivella & A. Gens

Modeling of hydro-mechanical behavior of rock salt in the near field of repository excavations 195
A. Pudewills

Simulation of long term thermal, hydraulic and mechanical interaction between buffer and salt host rock 201
W.Q. Wang, R. Walsh, H. Shao, M.L. Xie & O. Kolditz

Post-tests on thermo-mechanically compacted salt backfill 209
C.-L. Zhang, T. Rothfuchs & J. Droste

In-situ measurements and 3-D model calculations of backfill compaction and EDZ development in waste disposal drifts in salt rock 215
S. Heusermann & U. Heemann

Long-term laboratory investigation on backfill 223
D. Stührenberg

Microstructural study of reconsolidated salt 231
G.M. Pennock, X. Zhang, C.J. Peach & C.J. Spiers

Mechanical and permeability properties of highly pre-compacted granular salt bricks 239
K. Salzer, T. Popp & H. Böhnel

Part 5. THMC-processes in backfill materials – laboratory observations and modeling

The mechanical behavior of building materials based on the hydration of evaporite minerals 251
Th. Leusmann & H.-J. Engelhardt

Self sealing backfill (SVV) – A salt based material for constructing seals in salt mines 259
H.-J. Herbert

Coupled modelling of the C: HM behaviour of self healing salt based backfill 269
F. Werunsky, Z. Hou & H.C. Moog

Reactive transport modelling in salt material based on Gibbs energy minimization 277
M.L. Xie, H.C. Moog, W.Q. Wang, H.-J. Herbert, H. Shao & O. Kolditz

Coupled modelling of physical/chemical retardation and transport of CO_2/CH_4 for a backfilled salt rock repository 285
H. Alkan & W. Müller

Part 6. Studies of mining and mine abandonment

Dynamic processes in salt rocks – a general approach for softening processes within the rock matrix and along bedding planes 295
W. Minkley, J. Mühlbauer & G. Storch

Performance of a mining panel over tachyhydrite in Taquari-Vassouras potash mine 305
L. Rothenburg, A.L.P. Carvalho Jr. & M.B. Dusseault

Monitoring of roof stability in salt mines 315
J.-P. Schleinig & V. Lukas

Determination of mechanical homogeneous areas in the rock salt mass using creep properties for a classification scheme 321
I. Plischke

Modeling of strain softening and dilatancy in the mining system of the southern flank of the Asse II salt mine 327
P. Kamlot, R.-M. Günther, N. Stockmann & G. Gärtner

Three-dimensional geomechanical modelling of old mining rooms in the central part of the Bartensleben salt mine 337
S. Fahland, S. Heusermann, R. Eickemeier, H.-K. Nipp & J. Preuss

Geotechnical control of critical construction elements during the backfilling activities of the ERAM – Experience gained in using the observation method 345
R. Mauke, B. Stielow & M. Mohlfeld

Part 7. Cavern design for gas storage and solution mining

Effects of cavern shapes on cavern and well integrity for the strategic petroleum reserve 353
S.R. Sobolik & B.L. Ehgartner

Influence of effective stress on strain rate around the gas storing cavern 363
J. Ślizowski & K.M. Urbańczyk

Pillar deformation-induced surface subsidence in the Hengelo brine field, the Netherlands 369
R.F. Bekendam & J.L. Urai

Execution and analysis of sonar surveys to support rock-mechanical evaluations 377
A. Reitze, H. von Tryller & F. Hasselkus

Some aspects of the transient behavior of salt caverns 383
M. Karimi-Jafari, P. Bérest & B. Brouard

THMC numerical simulation and a solution mining method for thin salt deposits 391
W.G. Liang, Y.S. Zhao, C.H. Yang & M.B. Dusseault

Usability evaluation of the existing solution-mined caverns for gas storage 399
C.H. Yang, Y.P. Li, Q.H. Qian, D.H. Wei, F. Chen & X.Y. Yin

The engineering thermal analysis for natural gas storage in deep salt formation 401
J.W. Chen, C.H. Yang, Y.P. Li & X.Y. Yin

Investigation on the long-term stability of gas storage in Jintan Salt Mine 407
X.Y. Yin, C.H. Yang, Y.P. Li & J.W. Chen

Part 8. Abandonment of caverns

The Bernburg test cavern – in situ investigations and model studies on cavern abandonment 417
D. Brückner, A. Lindert & M. Wiedemann

Deep salt cavern abandonment: A pilot experiment 427
G. Hévin, C. Caligaris, J.G. Durup, O. Pichayrou & C. Rolin

Long-term behaviour of sealed brine-filled cavities in rock salt mass – A new approach for physical modelling and numerical simulation 435
K.-H. Lux

Deep salt-cavern abandonment 445
B. Brouard, P. Bérest & M. Karimi-Jafari

Author index 453

The Mechanical Behavior of Salt – Understanding of THMC Processes in Salt –
Wallner, Lux, Minkley & Hardy, Jr. (eds)
© 2007 Taylor & Francis Group, London, ISBN 978-0-415-44398-2

Foreword

The Sixth Conference on the Mechanical Behavior of Salt continues a long-lasting tradition. The series started at the Pennsylvania State University, USA in 1981, the second conference was held at the Federal Institute of Geosciences and Natural Resources, Hannover, Germany in 1981, the third conference at the École Polytechnique, Palaiseau, France in 1993, the fourth conference at the École Polytechnique National, Montreal, Canada in 1996 and the fifth conference at the University of Bucharest, Romania in 1999.

The conference is jointly organized by the Federal Institute of Geosciences and Natural Resources (BGR), the Institute for Rock Mechanics GmbH Leipzig (IfG) and the Clausthal University of Technology (TUC), Germany.

Like the previous conferences various aspects of rock salt behavior are covered. However, a special focus is directed on the understanding of thermal, mechanical, hydraulic and chemical coupled processes (THMC) which are of particular interest regarding advanced problems in waste disposal, storage and mining. The conference is held at the Federal Institute for Geosciences and Natural Resources Hannover, Germany, and brings together colleagues from many disciplines.
The main topics of the conference are:

- laboratory and in-situ investigations,
- modeling, e.g. derivation of constitutive equations,
- numerical computations and prediction of long-term behavior,
- THMC processes in mining projects, storage and permanent disposal,
- case studies: geology, various mining and storage applications and abandonment.

They are grouped in eight thematic parts of this volume. We are very pleased to issue the conference proceedings in direct relationship to the conference. Thus, the published information will obviously find an immediate distribution.

We cordially thank all the authors, the reviewers and last but not least Taylor and Francis, as publishers for their excellent efforts in due time.

Manfred Wallner – Federal Institute for Geosciences and Natural Resources (BGR), D
Karl-Heinz Lux – Clausthal University of Technology (TUC), D
Wolfgang Minkley – Institute for Rock Mechanics GmbH Leipzig (IfG), D
Henry Reginald Hardy, Jr. – Pennsylvania State University (PSU), USA

Taylor & Francis
Taylor & Francis Group
http://taylorandfrancis.com

The Mechanical Behavior of Salt – Understanding of THMC Processes in Salt –
Wallner, Lux, Minkley & Hardy, Jr. (eds)
© 2007 Taylor & Francis Group, London, ISBN 978-0-415-44398-2

Acknowledgements

For the generous financial support special thanks go to the sponsors of the conference 'SaltMech6'

- **Akzo Nobel Base Chemicals**
- **DBE TECHNOLOGY GmbH**
- **DEEP Underground Engineering GmbH**
- **esco – european salt company GmbH & Co. KG**
- **GSF – Forschungszentrum für Umwelt und Gesundheit, GmbH**
- **GTS – Grube Teutschenthal Sicherungs-GmbH und Co. KG**
- **Gesteinslabor Dr. Eberhard Jahns e.K.**
- **K + S Aktiengesellschaft**
- **KBB Underground Technologies GmbH**
- **SOCON Sonar Control – Kavernenvermessung GmbH**
- **VNG – Verbundnetz Gas AG**

We thank the members of the International Scientific Board as well as the following colleagues for carefully reviewing the manuscripts of this proceedings volume: Hans-Joachim Alheid, Dieter Brückner, Ralf Eickemeier, Dieter Eisenburger, Ralf-Michael Günther, Ulrich Heemann, Jürgen Hesser, Peter Kamlot, Hartmut Kern, Gerhard Mingerzahn, Jan Mühlbauer, Klaus Salzer, Hajo Schnier, Michael Schramm, Hans-Dieter Voigt and Ralf Wolters.

We thank Katrin Zaton and Petra Mehlhorn for collection and formal proof of the manuscripts and extensive communication with the authors.

Taylor & Francis
Taylor & Francis Group
http://taylorandfrancis.com

The Mechanical Behavior of Salt – Understanding of THMC Processes in Salt –
Wallner, Lux, Minkley & Hardy, Jr. (eds)
© 2007 Taylor & Francis Group, London, ISBN 978-0-415-44398-2

Conference organization

Advisory Board
Manfred Wallner, BGR (D)
Karl-Heinz Lux, TUC (D)
Wolfgang Minkley, IfG (D)
H. Reginald Hardy, Jr., Penn State Univ. (USA)

International Scientific Board
Pierre Bérest, École Polytechnique (F)
Otto Bornemann, BGR (D)
Nicolaie Cristescu, Univ. of Florida (USA)
Fritz Crotogino, KBB UT GmbH (D)
Gérard Durup, Gaz de France (F)
Maurice Dusseault, Univ. of Waterloo (CA)
Peter A. Fokker, Shell Research (NL)
Antonio Gens, Univ. of Catalunya (E)
Mehdi Ghoreychi, INERIS (F)
Frank D. Hansen, SANDIA (USA)
Stefan Heusermann, BGR (D)
Udo Hunsche, BGR (D)
Nina Müller-Hoeppe, DBE TEC GmbH (D)
Tom Pfeifle, SANDIA (USA)
Horst Pitterich, FZK (D)
Alexandra Pudewills, FZK (D)
Henry Rauche, ERCOSPLAN (D)
Reinhard B. Rokahr, Univ. of Hannover (D)
Tilmann Rothfuchs, GRS (D)
Chris Spiers, Univ. of Utrecht (NL)
Jacek Tejchman, Univ. of Gdansk (P)
Janos Urai, RWTH Aachen (D)
Leo van Sambeek, RESPEC (USA)
Wolfgang Voigt, BA Freiberg (D)

Organizing Committee
Uwe Düsterloh, TUC (D)
Bettina Landsmann, BGR (D)
Till Popp, IfG (D)
Otto Schulze, BGR (D)
Thomas Spies, BGR (D)

Taylor & Francis
Taylor & Francis Group
http://taylorandfrancis.com

Part 1. THM-processes in salt rocks – observations at laboratory and in-situ scales

Taylor & Francis
Taylor & Francis Group
http://taylorandfrancis.com

The Mechanical Behavior of Salt – Understanding of THMC Processes in Salt –
Wallner, Lux, Minkley & Hardy, Jr. (eds)
© 2007 Taylor & Francis Group, London, ISBN 978-0-415-44398-2

Geomechanical investigations on the integrity of geological barriers with special regard to laboratory tests

U. Düsterloh & K.-H. Lux
Professorship for Waste Disposal and Geomechanics, Clausthal University of Technology, Clausthal-Zellerfeld, Germany

ABSTRACT: Two criteria are currently used for verifying integrity of geological barriers. We shall describe them as mechanical criterion and hydraulic criterion. The mechanical criterion states that the integrity of the geological barrier is deemed to be proven if the state of stress which is computed in a model calculation is unsuitable for creating dilatancy deformations in the surrounding rock. The hydraulic criterion is fulfilled if the minimal principal stress in a model calculation is higher than the respective, depth-dependent hydraulic pressure of brine. There is currently no scientific consensus whether the proof of barrier integrity must only fulfil one of the two criteria or whether the criteria are mutually independent and must be seen as complementing each other. New tests on large rock salt cores on which a hydraulic fluid pressure is imposed in addition to the triaxial mechanical stress will be presented. As a result of the tests, it can be demonstrated that the aforesaid criteria must be considered as mutually independent.

1 INTRODUCTION

Two criteria – a mechanical criterion and a hydraulic criterion – are currently used for verifying integrity of geological barriers. The mechanical criterion states that the integrity of the geological barrier is considered to be proven if the state of stress computed in a model calculation is unsuitable for creating dilatant deformations in the surrounding rock. This statement is synonymous with furnishing proof that the damaged zone induced in the contour area of underground pit constructions (zone of dilatant rock resulting from excavation) does not propagate into the water-bearing cover rock or adjacent rock. Thus a migration or flow pathway with increased permeability between the biosphere and the repository horizon does not occur.

The hydraulic criterion states that the integrity of the geological barrier is considered to be proven if the minimum principal stress in a model calculation model is greater than the hydraulic pressure of a brine column calculated in each case as a function of the depth. The above statement is fulfilled physically if the mechanical compressive stresses on the grain boundaries of the rock particles are greater than a fluid pressure of a fluid column estimated as a function of depth. If the aforesaid boundary condition is fulfilled for an adequately thick area of the geological barrier, there is no possibility of migration of potentially inflowing water from the salt level to the repository. That is, the rock mass has to be free of discontinuity surfaces and has to be impermeable in the undisturbed state.

The extent to which only one of the aforesaid criteria needs to be fulfilled for furnishing proof of the barrier integrity or whether the criteria must be considered as mutually independent and mutually complementary are still the subject of scientific discussion. The authors assume that both aforesaid criteria must be fulfilled equally for furnishing proof of the barrier integrity since the hydraulic criterion is associated with proof against active hydraulic fractures with the creation of microfissures/macrofissures and the mechanical criterion is associated with proof against gradual microfissure formation as the result of rheologically related damage processes. Fabric damage can thus be attributed to hydrostatic pressure of the applied groundwater and a resultant infiltration accompanied by microcracks on the one hand but can also be attributed to mechanical deconsolidation processes on the other and the reasons are thus fundamentally different.

2 FUNDAMENTAL REQUIREMENTS FOR GEOLOGICAL BARRIERS

The criteria compiled by AkEnd (2002) for the selection procedure of a repository site for furnishing proof of a "favourable geological overall situation", can be used as the fundamental requirements concerning the geological barriers or the spatially more confined inclusion rock zone (part of the geological barrier which must ensure inclusion of the waste in the case of

normal development of the repository for the isolation period in interaction with technical and geotechnical barriers). The following minimum requirements are stated:

The isolation rock zone must consist of rock types which can be assigned to a rock permeability category lower than 10^{-10} m/s.
The isolation rock zone must have a thickness of at least 100 m.
The depth of the surface of the required isolation rock zone must be at least 300 m.
The repository mine may not be deeper than 1500 m.
The spatial extent of the isolation rock zone must allow implementation of a repository ($\approx$3 km^2 in salt, $\approx$10 km^2 in clay and granite, resulting from volume of waste produced in Germany, single-repository concept).
The isolation rock zone or the host rock may not be subject to the risk of rock burst.

There may be no findings or data which would put in doubt compliance with the geoscientific minimum requirements for rock permeability, thickness and extent of the isolattion rock zone over a period in the order of magnitude of 1 million years.

Over and above the aforesaid minimum requirements, AkEnd initially stated 10 verbally argumentative requirements for assumption of a "favourable geological overall situation". These are as follows:

- No transport or slow transport by groundwater at the repository level
- Favourable configuration of host rock and isolation rock zone
- Good spatial characterisability
- Good predictability of the long-term conditions
- Favourable rock-mechanic conditions
- Low tendency of the formation of permeable pathways for water
- Good gas compatibility
- Good temperature compatibility
- High radionuclide retention capacity if the rock
- Favourable hydrochemical conditions

The aforesaid fundamental requirements were underpinned with criteria and numerical values (indicators) by AkEnd, defining what geoscientific characteristics a suitable geological barrier must feature resp. which indicators characterise a "favourable", "conditionally favourable" or "less favourable" geological overall situation. We shall not reiterate these criteria at this point and we refer the reader to the concluding report of AkEnd (2002).

Thus, together with the exclusion criteria

- large-area uplifts exceeding 1 mm on average per annum,
- existence of active fault zones in the repository area,
- expected seismic activities exceeding earthquake zone 1 in accordance with DIN 4149,
- quaternary or expected future volcanism in the repository region and
- no young groundwater (containing tritium and/or ^{14}C) in the isolation rock zone,

there exists a very extensive catalogue of the geoscientific characteristics which a geological barrier must feature from the point of view of safe long-term final storage of radioactive wastes in deep geological formations.

The requirements, criteria and indicators listed are relevant for the decision whether a location is suitable for the construction of a repository. One aspect which differs fundamentally from this is the question how and with which instruments proof should be furnished that there is no risk to man and the environment, at no point in time within the required verification period. From this, we are necessarily faced by the requirement in respect of concepts, verification criteria and limit values suitable for quantitatively mapping and assessing the technogenic and geogenic action to which the geological barriers are subjected during operation and after sealing of the repository and the resultant action on the repository system. The overriding aim in this case is furnishing proof of maintenance of the primarily existing barrier integrity (integrity, i.e. intactness of barrier system).

3 QUESTIONS RELATING TO HYDRAULIC INTEGRITY

Despite the very unequivocal formulation of the criterion, a detailed consideration of specific tasks throws up certain questions which are not answered by the above criterion. Such questions include

- By which amount (absolute or relative) must the hydraulic pressure, including a safety margin, be less than the minimum stress?
- What is the minimum thickness of the rock zone in which the hydraulic criterion is met?
- Do partial transgressions of the hydraulic criterion directly lead to a macrofracture or to any other failure of the geological barrier ?
- Can the findings on the fracture failure of the rock, taken from repository cavern construction, be applied to the boundary conditions of constant pressure obtained in repository construction?
- What consequences does a partial violation of the hydraulic criterion have in respect of spatial and time-specific integrity?
- How do the load-bearing behaviour and the healing behaviour of rock zones change, in which the hydraulic criterion is violated and for which fluid infiltration must be assumed?

- At what infiltration rate does a fluid penetrate into the geological barrier in the event of a violation of the hydraulic criterion and to what extent are the infiltration rate and the infiltration quantity dependent on the pressure difference between minimum rock stress and fluid pressure, on stratification of the rock and on orientation of the principal stresses for instance?

Basically, the above-listed questions have not been answered definitively to date but, in contrast, the majority of the questions must be assigned to the area of current scientific research. Below, we shall present some of these initial investigation results so as to convey an impression of which concepts and instruments are currently used to elaborate answers to the above-formulated questions on the one hand and to develop computer models with which a coupled simulation of mechanical and hydraulic processes can be performed within the framework of furnishing proof on the other.

4 LABORATORY INVESTIGATIONS TO EVALUATE THE HYDRAULIC INTEGRITY OF GEOLOGICAL BARRIERS

Figures 1 and 2 show the testing equipment used for laboratory analysis of the boundary conditions leading to infiltration of a fluid phase into the rock salt.

A photographic view of the sample preparation is given in Figure 3. The subject of the investigation relates to cylindrical salt test specimens whose upper end faces have a borehole for the admission of the triaxially stressed specimens with a tracer fluid.

A bore with a diameter of approx. 3 mm is made down to a depth of approx. 120 mm into the test specimen at the centre. To avoid damage in the close-up range of the bore hole induced by drilling, the bore hole creation is done stepwise by a center hole, a pilot hole and a final hole as shown in Figure 3.

Finally the hole was sealed by fitting and jamming an infiltration bolt. The bolt avoids lateral infiltration in the area of fluid admission. To avoid contact between rock salt at sample end face and tracer fluid, the upper end of the bolt is connected to a steel-plate. Taken into account the above mentioned sample preparation, wetting of rock salt with fluid is limited to the rock salt area at the bottom of the hole. Subsequent to the installation of the delivery of the fluid, the samples are coated with an impermeable rubber jacket to protect the rock salt against infiltration of hydraulic oil from the confining pressure. To build up the coupled hydro-mechanical loading three hydraulic cycles are available. Beside two hydraulic cycles to generate the axial and confining stresses an independent third cycle was used to control the fluid pressure and the fluid inflow.

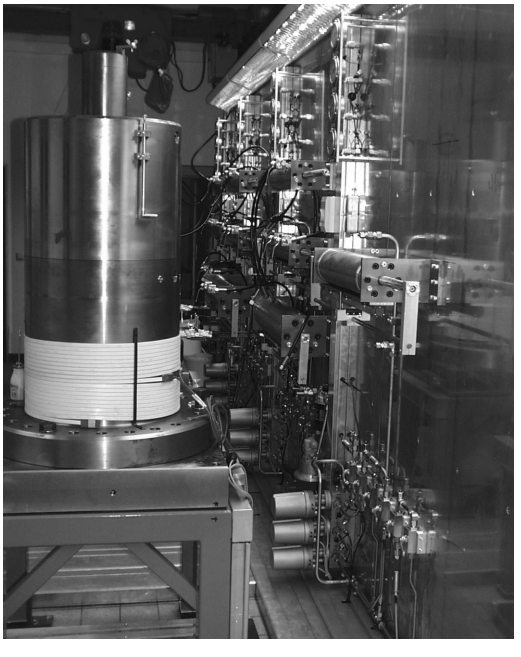

Figure 1. Test installation for analysis of the pressure-driven infiltration – lateral view.

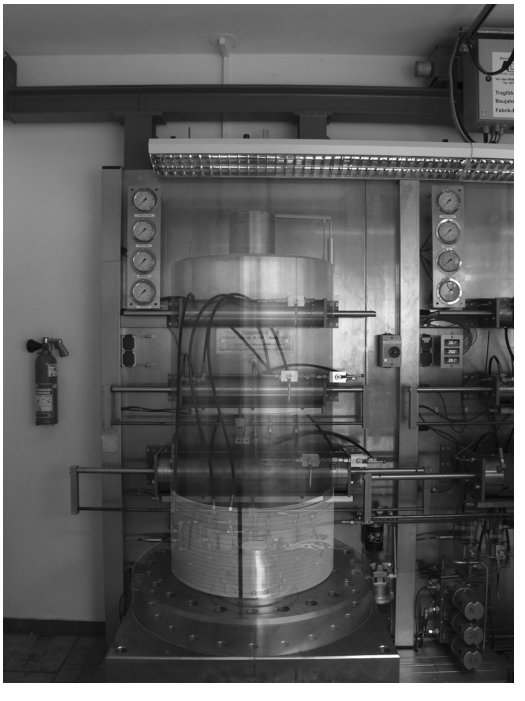

Figure 2. Test installation for analysis of the pressure-driven infiltration – front view.

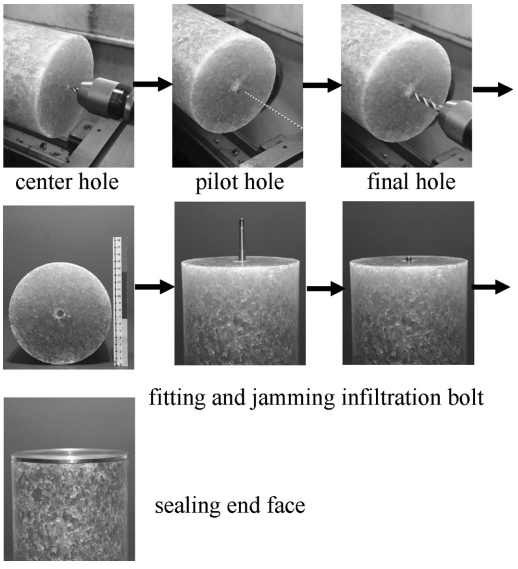

Figure 3. Sample preparation for infiltration tests.

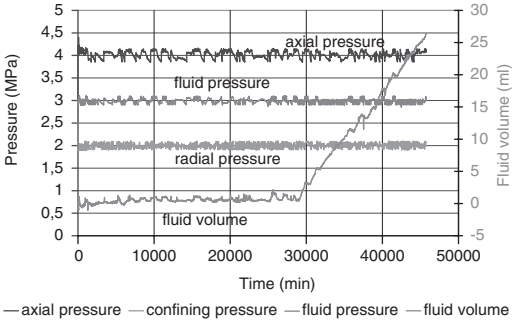

Figure 4. Measurement results of infiltration test.

Measurement of fluid inflow is done with a high accuracy by detecting the translation of a cylinder.

In order to derive the boundary conditions under which a fluid can penetrate into the rock salt matrix, the test specimen is subjected axially and radially to mechanical stresses which approximately correspond to the level of the present state of stress in the rock of the geological barrier. In addition to these mechanical stresses, a pressurised tracer fluid is admitted via the bore hole at the end-face. Finally, for varied pressure differences $p_{fl}-\sigma_{min}$ (fluid pressure – minimum stress), an analysis is conducted in order to establish under what boundary conditions the tracer medium penetrates into the rock salt test specimen, which infiltration rate is observed and which infiltration is quantitatively observed.

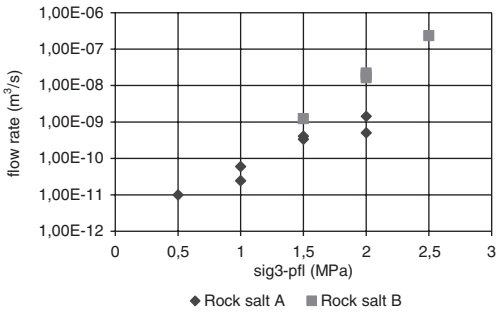

Figure 5. Steady state flow rate (m^3/s) as a function of the pressure difference (minimal principle stress – fluid pressure) after break through.

The principally measured parameters are shown in Figure 4. The continuous monitoring of the mechanical and hydraulic pressures with a high-resolution recording of the infiltrated tracer fluid quantities over the test period allows the sound evaluation of the material behavior.

The measured results of an infiltration test plotted by way of the example in Figure 4 document that no direct fracture results in the case of transgression of the minimum principal stress by the fluid pressure under constant pressure boundary conditions as can be characteristic of the area of geological barriers. Rather, a distinction can be made between two characteristic phases of fluid infiltration. The first phase (so-called infiltration phase) is characterised by continuous resaturation of the test specimen at a comparatively low rate, accompanied by the creation of microfissures. The second phase of infiltration, the so-called flow phase, is characterised by an approximately stationary seepage flow at a far higher rate, corresponding to *Darcy's* flow model. This flow phase starts with a downstream infiltration by the tracer fluid.

Infiltration rate and, after break-through, the flow rate do depend on the pressure difference between minimum principal stress and fluid pressure (cf. Figure 5 and Figure 6).

As a measure for the rate of extension of the infiltration front the mean infiltration rate is used, Figure 7. It is determined as a quotient of the distance the fluid covered (in the direction of the maximum principal stress) and the corresponding time of the test. The determination is performed using the elapsed time until the downstream infiltration occurs and the distance between the final depth of the infiltration borehole and the end surface of the specimen (compression test, TC). Respectively, the determination is performed by the distance between the final depth of the infiltration borehole and the shell of the specimen (in cas of extension test, TE). Finally the determination is performed

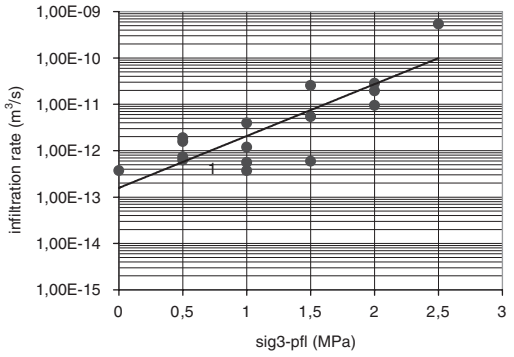

Figure 6. Infiltration rate (m^3/s) as a function of the pressure difference (minimal principle stress – fluid pressure) before break through.

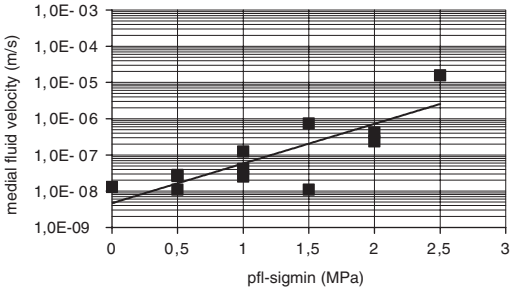

Figure 7. Mean infiltration rate (m/s) as a function of the pressure difference (fluid pressure – minimal principle stress).

by the testing time of premature finished tests and the measured depth of the infiltration zone.

In order to do this the samples are removed from the autoclave, sawn open and the distance between infiltration front and initial drilling is measured before downstream infiltration occurs.

The stress geometry (TC, TE), the stratification of the salt rock and the crystallinity influence the direction of infiltration and thus, the location and instant of the transition between infiltration phase and flow phase. The trend, shown in the series of tests on infiltration which have not yet been completed, is that the direction of infiltration follows the direction of the maximum principal stress but, however, it is superimposed by the alignment of the crystal grains.

This effect especially occurs if the tracer fluid encounters the contact planes of macro-crystals (cf Figure 8).

In such cases, the infiltration front mainly propagates parallel to the grain surface. In addition, from the investigation results available to date, it can also be deduced that a macrofracture can be observed only if the fluid overpressure exceeding the value of the minimum stress is applied at a comparatively high rate.

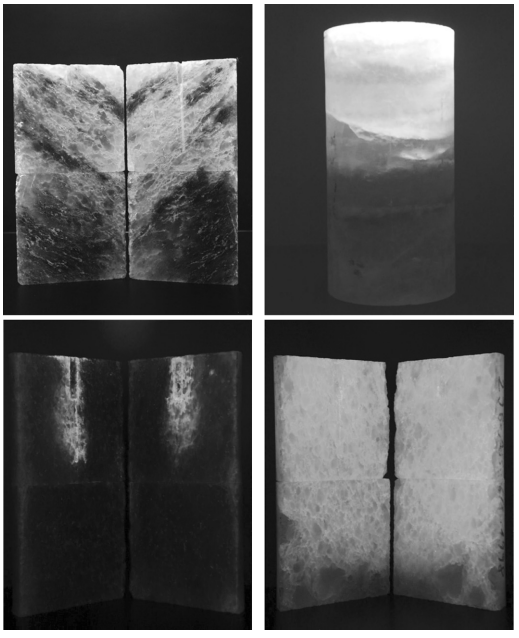

Figure 8. Influence of stratification and cristallinity on the direction of fluid spread.

No formation of macroscopic fracture cracks but the above-described continuous infiltration occurs under the rather constant fluid pressures obtaining in the area of geological barriers.

To summarise what has been said above, it can be stated, in respect of furnishing proof of hydraulic barrier integrity, that laboratory instruments are available for quantification of the boundary conditions and dependences under which infiltration of fluidic phases into the rock salt rock formation occurs. However, extensive tests are still required for corroboration of the findings available to date.

Ultimately, the dependences between pressure difference, stress geometry, infiltration rate, infiltration quantity, stratification and crystallinity, deduced from laboratory tests, can be applied to computing algorithms for arithmetic verification. Initial approaches have been developed at the Professorship of Disposal Technology and Geomechanics (Lux, 2005, 2006). However, results relating to computational simulation of the infiltration process and subsequent seepage flow process in geological barriers can be reported only after conclusion of the work.

As regards the current practice of verification, we can directly deduce, from what has been said above, that arithmetic verification of the hydraulic integrity can currently proven only if

- the calculated, depth-related hydraulic pressure is lower than the minimum principal stress,

- the rock zone in which the criterion is fulfilled features an adequate thickness,
- the rock zone is not damaged by dilatancy deformation and
- the barrier contains no masked discontinuity surfaces.

If, by contrast, the fluid pressure and the minimum principal stress have approximately the same level or if the fluid pressure is greater than the minimum principal stress, numerical verification can be performed only if the pressure-driven infiltration is simulated space-specifically and time-specifically on the basis of the investigations outlined above.

5 CONCLUSIONS

The precondition for safe operation and decommissioning of underground dumps and repositories require geotechnical, safety-related verifications on an computable basis. A part of the geotechnical safety-related verification is furnishing proof of the integrity of the geological and geotechnical barriers, i.e. furnishing proof that there are no risks, either of ingress of potentially inflowing water from the cover rock and adjacent rock into the repository or escape of contaminated solutions from the repository into the biosphere. Currently, two criteria are stated for verification of barrier integrity: a mechanical criterion and an hydraulic criterion. The mechanical criterion is fulfilled if the stresses obtaining in the calculation model are not suitable for producing dilatant deformation at the adjoining rocks. The hydraulic criterion is fulfilled if the minimum principal stresses obtaining in the computational model are lower than the hydrostatic pressure calculated depth-specifically in each case.

What has been said demonstrates that the work of AkEnd has produced a very broad characterisation of the geoscientific characteristics which a geological barrier must feature from the point of view of long-term, safe final storage of radioactive wastes in deep geological formations. One question which must basically be distinguished from this is the question how and with which instruments proof is to be furnished that there is no risk to man and the environment resulting from harmful ionising radiation e at any time within the required verification period. There are still scientific deficits in this aspect, particularly in the sector of laboratory and computed mapping of geomechanically-geohydraulical coupled processes. Presentation of a new type of test technique has indicated one option for in-depth analysis of the questions to be answered within the framework of furnishing proof of hydraulic integrity. Using the new testing technique it is possible to analyse the space and time dependent process of fluid infiltration into the rock mass taken into account geomechanically-geohydraulical coupled loadings. A fundamental result of the presented testing technique is the potential to quantify the propagation of the infiltration zone in space and time and therefore to calculate the integrity of the barrier in a numerical manner.

REFERENCES

AkEnd – Arbeitskreis Auswahlverfahren Endlagerstandorte (2002): Empfehlungen des AkEnd, W&S Druck GmbH, Köln.

Düsterloh, U. & Lux, K.-H. 2003. Geologische und geotechnische Barrieren – Gedanken zur Nachweisführung in: Schriftenreihe der Professur für Deponietechnik und Geomechanik, Heft 13, Clausthal.Düsterloh, U. & Lux, K.-H. 2004. Geomechanical investigations into the hydraulic integrity of geological barriers: Int. J. Rock Mechanics and Mining Sciences 41 (410).

Lux, K.H. 2005. Zum langfristigen Tragverhalten von verschlossenen Salzkavernen – ein neuer Ansatz zu physikalischer Modellierung und numerischer Simulation:

Theoretische und laborative Grundlagen: Erdöl, Erdgas, Kohle, Jg. 121, 2005, H. 11, S.414-421.

Rechnerische Analysen und grundlegende Erkenntnisse: Erdöl, Erdgas, Kohle, Jg. 122, 2006, H. 4, S.150-158.

Validation am Beispiel eines Feldversuchs und ergänzende hydromechanische Analysen im Hinblick auf die Stillegungsplanung: Erdöl, Erdgas, Kohle, Jg. 122, 2006, H. 11, S.420-428.

The Mechanical Behavior of Salt – Understanding of THMC Processes in Salt –
Wallner, Lux, Minkley & Hardy, Jr. (eds)
© 2007 Taylor & Francis Group, London, ISBN 978-0-415-44398-2

Lode angle effects on the creep of salt

K.D. Mellegard, K.L. DeVries & G.D. Callahan
RESPEC, Rapid City, South Dakota, USA

ABSTRACT: The steady-state creep rate of salt is typically described using only the maximum and minimum principal stresses and is generally considered to be independent of the intermediate principal stress; thus, the steady-state creep rate of salt is expected to be the same under both compressive and extensile states of stress. However, little experimental evidence has been obtained regarding the transient nature of salt under alternating states of stress between triaxial compression and triaxial extension; i.e. alternating Lode angles. Multistage creep tests were performed to investigate the time-dependent behavior of salt at two Lode angles. The data show that Lode angle does not affect the steady-state strain rate of salt; however, each time the Lode angle was changed, a significant transient response was observed. This transient response to changes in Lode angle is not predicted by constitutive models commonly used to evaluate natural gas storage caverns.

1 INTRODUCTION

1.1 *Background*

Cavern stability is a crucial consideration for the design and development of storage caverns in salt formations. Acceptable operating pressures for a salt cavern are determined from a geomechanics evaluation based on the requirement that the cavern response satisfy various design constraints related to the deformation characteristics of the salt. Even with complete knowledge of the salt characteristics, problems may still arise because the state-of-the-art in salt mechanics has not advanced to the point of establishing a full understanding of salt response at all possible states of stress. This is important for salt storage caverns because varying states of stress exist around the caverns, and they can continue to change over time as operating conditions change and the salt deforms (creeps). The state of stress generally varies between triaxial extension and compression, so the creep behavior of salt must be well defined under similar stress conditions.

1.2 *Technical approach*

The prevailing engineering application view of natural rock salt generally considers salt to be an isotropic material and the state of stress can be represented by three invariant quantities. These invariant quantities are often the principal stresses. For this paper, the state of stress is represented by the invariants, I_1 (representing mean stress), J_2 (representing shear stress), and ψ (the Lode angle which is a convenient alternative to J_3). A detailed explanation of triaxial stress states is given in the appendix.

The Lode angle invariant changes from $-30°$ to $+30°$ as the intermediate principal stress value changes from the maximum principal stress to the minimum principal stress (tension is positive). The general assumption is that salt behavior is independent of ψ, which means that the intermediate principal stress does not play a role in the material response and adequate characterization of the salt behavior can be based on the invariants J_2 and I_1.

Previous researchers (Hunsche et al. 1994, Mellegard et al. 1992, Wawersik et al. 1979) have examined the role of the intermediate principal stress in the creep of salt. This paper extends that research by reporting the results of a series of triaxial compression and extension laboratory creep tests on salt specimens from a bedded salt formation near Cayuta, New York, USA (DeVries et al. 2005). This testing provides experimental evidence that demonstrates how changes in the Lode angle could influence the development of constitutive models.

2 TRIAXIAL STRESS STATES

Typically, laboratory test data are collected from triaxial compression tests as illustrated in Figure 1. In a triaxial compression test, the magnitude of the compressive confining pressure is less than the magnitude of the compressive axial stress. Figure 1 also illustrates

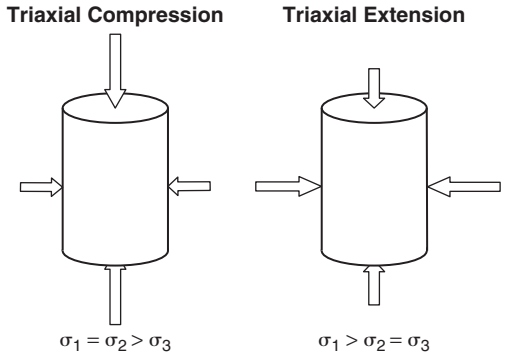

Figure 1. Illustration of triaxial compression and triaxial extension tests performed on circular cylindrical specimens.

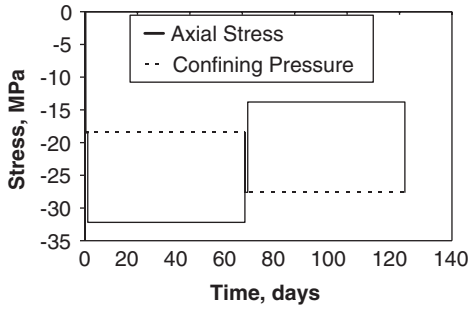

Figure 2. Typical test system load path for a creep test.

the triaxial extension test where the magnitude of the compressive confining pressure is greater than the magnitude of the compressive axial stress.

While these two types of tests do not look substantially different, the results can be dramatically different if the behavior of the material being tested depends on the intermediate principal stress. When solid, cylindrical specimens are being tested, two of the principal stresses are always equal to the confining pressure, so the only Lode angles that can be investigated are $-30°$ (extension) and $+30°$ (compression). The laboratory tests presented in this paper were performed using solid, cylindrical specimens, so only the results for these two specific Lode angles are reported.

3 LABORATORY CREEP TESTS

Constant stress creep tests typically maintain constant mean and deviatoric stresses throughout the test and measure changes in deformation. Figure 2 shows an example of the axial stress and confining pressure load paths used to complete the creep tests. The specimens are initially hydrostatically loaded to the confining pressure level specified for the test; then the stress difference is applied to the specimen. For a test performed at a triaxial compression state of stress, the axial stress is increased while holding the confining pressure constant. For a test performed at a triaxial extension state of stress, the axial stress is decreased while the confining pressure is held constant. During the test, the current specimen dimensions are continually updated so the axial force can be adjusted to obtain the desired axial stress.

Because two of the principal stresses are equal to the confining pressure, isovolumetric deformation requires that the lateral strain be half the axial strain and of opposite sign. This has been shown to be true for natural rock salt at moderate confining pressures for literally hundreds of different test specimens. For triaxial compression, the axial strain is negative, while for triaxial extension, the axial strain is positive.

Table 1 presents the test conditions and results for six creep tests performed at 40°C or 55°C. The specimens tested had nominal diameters of 10 cm and lengths of 20 cm. Each test was performed on a unique specimen and had multiple stages. The test conditions given in the table are presented in two formats: (1) in terms of confining pressure, σ_{conf}, and axial stress, σ_{axial}, and (2) in terms of the stress invariants I_1, $\sqrt{J_2}$, and ψ. Also given are the duration of each test stage and the steady-state axial strain rate observed in each stage. The steady-state strain rate was estimated from the data collected at the end of each stage.

The data from each individual test are shown graphically in Figures 3 through 8. Each figure plots the specimen response in terms of total axial strain (includes elastic and inelastic components) as a function of time. Also shown on each figure are the test loading conditions (axial stress and confining pressure) plotted as a function of time. In some cases, the first stage was initiated under a triaxial compression state of stress and, in other cases, the first stage was initiated using triaxial extension. This approach was taken to check the possibility that the test results might depend upon the order in which the stages were completed. In general, the ordering of the applied stress states (compression followed by extension or extension followed by compression) had no effect on the test results.

The data in Table 1 show that Lode angle does not affect the steady-state strain rate of Cayuta salt, at least for the stresses and temperatures investigated. This is evident because the steady-state strain rates at different Lode angles for any single test have nearly identical magnitudes and only the sign changes. The strain rate variation among the tests is attributed to specimen-to-specimen variation.

The fact that Lode angle has no effect on the steady-state strain rate does not necessarily mean that Lode angle does not affect other aspects of the salt behavior.

Table 1. Summary of creep tests.

Specimen I.D. (Temperature)	Stage	σ_{conf} (MPa)	σ_{axial} (MPa)	I_1 (MPa)	$\sqrt{J_2}$ (MPa)	ψ^* (deg)	Duration (days)	Axial steady-state strain rate ($\times 10^{-9}$ s^{-1})
BAL1/48/4	1	−27.6	−13.8	−69	8	−30	64	0.19
(40°C)	2	−18.4	−32.2	−69	8	+30	70	−0.15
	3	−27.6	−13.8	−69	8	−30	68	0.15
	4	A series of short duration compression/extension cycles						
BAL1/125/1	1	−27.6	−48.3	−103.5	12	+30	61	−0.72
(40°C)	2	−27.6	−6.9	−62.1	12	−30	63	0.96
	3	−34.5	−13.8	−82.8	12	−30	57	0.65
BAL1/179/1	1	−27.6	−13.8	−69	8	−30	67	1.0
(55°C)	2	−18.4	−32.2	−69	8	+30	80	−0.9
	3	A series of short duration compression/extension cycles						
BAL1/180/2	1	−18.4	−32.2	−69	8	+30	37	−2.0
(55°C)	2	−27.6	−13.8	−69	8	−30	45	2.1
	3	−18.4	−32.2	−69	8	+30	44	−2.1
	4	−27.6	−13.8	−69	8	−30	63	2.2
BAL1/179/2	1	−17.2	−34.6	−69	10	+30	71	−2.3
(55°C)	2	−28.7	−11.6	−69	10	−30	76	2.9
	3	A series of short duration compression/extension cycles						
BAL1/179/4	1	−28.7	−11.6	−69	10	−30	72	2.2
(55°C)	2	−17.2	−34.6	−69	10	+30	53	−2.1
	3	A series of short duration compression/extension cycles						

* +30° = triaxial compression, −30° = triaxial extension.

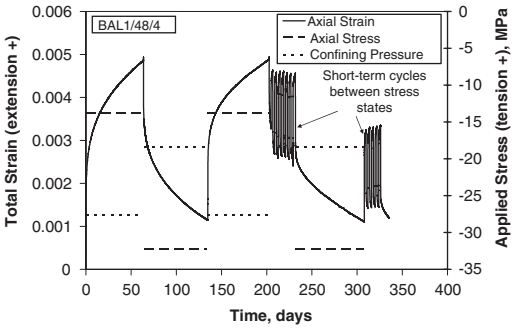

Figure 3. Creep test on BAL1/48/4.

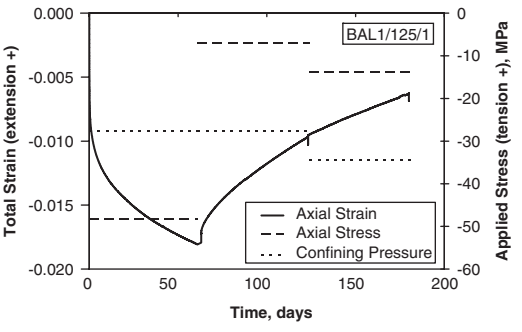

Figure 4. Creep test on BAL1/125/1.

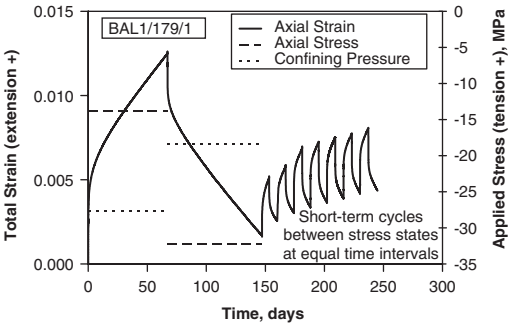

Figure 5. Creep test on BAL1/179/1.

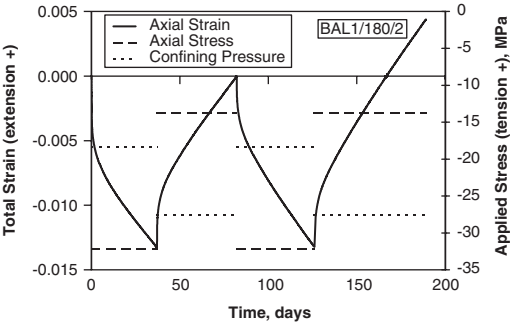

Figure 6. Creep test on BAL1/180/2.

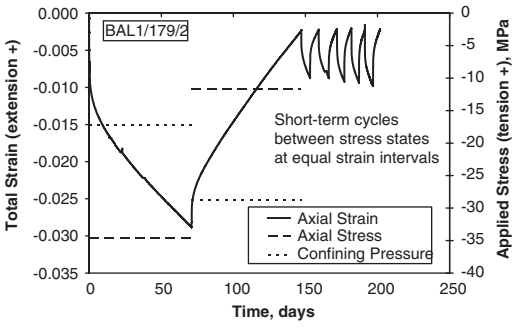

Figure 7. Creep test on BAL1/179/2.

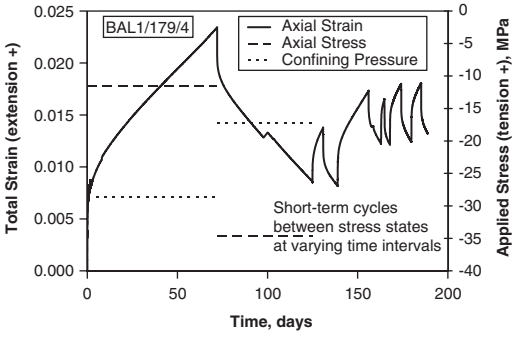

Figure 8. Creep test on BAL1/179/4.

For example, the initial strain rate observed in a creep test is very high and gradually decreases to the steady-state value as the specimen hardens. The specimen hardening is often considered to be isotropic, which means hardening should reach a static value at steady-state conditions for a given combination of I_1 and J_2. If the hardening is isotropic, then a change in Lode angle should not cause additional transient behavior, but rather, the strain rate should simply change sign and deformation should continue at the magnitude of the previously established steady-state rate.

The actual hardening behavior of salt can be observed in Figures 3 through 8. Within each test, all stages were completed at the same mean stress (except for BAL1/125/1) and stress difference magnitude with only the Lode angle changing between stages. The test on BAL1/125/1 included a change in mean stress and demonstrated that the creep of salt does not display large mean stress dependence.

For the other five tests presented, if only isotropic hardening were exhibited by the salt specimens, there should have been no transient response when the Lode angle changed between compression and extension (a change in the intermediate principal stress). However, a distinct transient response was seen each time the Lode angle was changed, indicating that hardening is not isotropic, but instead, the deformation induces an anisotropic hardened state. As shown in Figures 3 through 8, some of the tests included a final stage wherein multiple cyclic changes in Lode angle were performed relatively quickly. A transient response continues to reappear within each short cycle, indicating that the hardening must continually go through a transient phase to accommodate a change in Lode angle. These data indicate that the average transient strain rate might be slightly higher in extension than compression, but the difference was not large and the cyclic loading was not continued for a very long period of time.

4 NUMERICAL SIMULATIONS

Numerical modeling of natural gas storage caverns has been performed using several different constitutive models to describe the creep behavior of salt. A few of the widely used creep laws include: Norton Power law (Norton 1929), the Munson-Dawson law (Munson et al. 1989), and the Lubby2 law (e.g. Lux & Heusermann 1983). The Norton Power law only takes steady-state constitutive behavior into account while the other material laws incorporate transient behavior. Whereas the Norton Power law would not be expected to capture the transient responses observed for the creep tests presented here, the capability of the other widely used creep laws, that include transient rheological behavior, is questioned for the conditions applied during the laboratory tests.

To demonstrate this issue, simulations of the first two stages of the creep tests using specimens BAL1/179/2 and BAL1/179/4 were performed using the Norton Power, Munson-Dawson, and the Lubby2 laws. Parameter values chosen for these models were not considered relevant for this demonstration; thus, accurate prediction of the strain-versus-time data is not expected. Undoubtedly, parameter values could be determined that match the first stage of these tests with great precision; however, the predicted response of the models during the second stage is of primary interest. Specifically, the result of greatest interest is the strain rate and general trend of the strain-versus-time results predicted by the models following the Lode angle change.

Figure 9 illustrates the predicted axial strain results for the first two stages of the tests. The total measured axial strains for the two tests are provided in this figure for comparative purposes. The creep laws do not predict the observed transient response following a Lode angle change. For each of the creep laws, the magnitude of the predicted strain rate immediately following the simulated change in Lode angle is identical to that

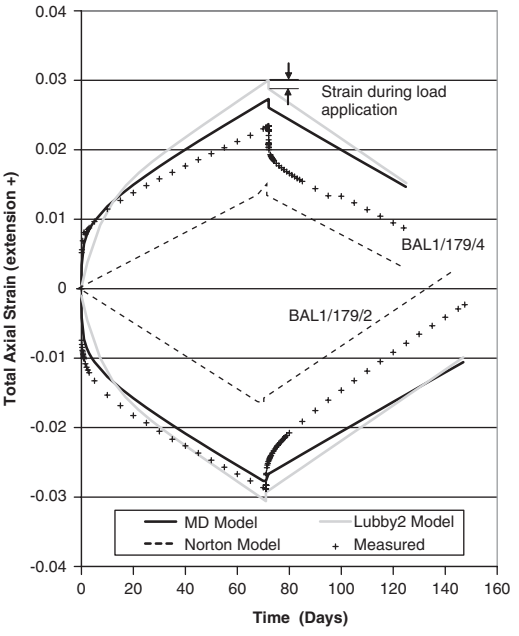

Figure 9. Creep law simulations of constant deviatoric stress tests with a change in Lode angle.

immediately preceding the change in the Lode angle, only with a change in the sign (direction of strain).

The strains predicted as a result of applying the different confining pressures and axial stresses between the first and second stages of the tests are apparent in Figure 9, as illustrated by the abrupt change in strain between the two stages. The predicted strain that accumulated between the end of the first stage and the beginning of the second stage is predominately elastic because of the very short time required to apply the new load condition. This strain is relatively small compared to the total strain recorded during each stage of the test.

The results of the numerical simulations of the creep tests demonstrate that three of the widely used creep laws for evaluating natural gas storage do not have the capability to reproduce the transient behavior of salt exhibited by the laboratory creep tests performed to assess the influence of intermediate principal stress on the creep behavior. Although not investigated, it is expected that few, if any, of the constitutive models developed for salt have this capability. Obviously, those models that only incorporate isotropic hardening do not have the capability to reproduce these test results. Constitutive models that incorporate a tensor formulation for back-stress have the potential for predicting the observed transient responses. However, any model formulated must comply with the isovolumetric creep of salt at moderate and high confining pressures (i.e. at stress states that suppress the formation of microcracks and associated dilatancy).

5 CONCLUSIONS

The value of the intermediate principal stress (represented here by the Lode angle) does not have a significant effect on the steady-state strain rates exhibited by salt. However, a change in the Lode angle does affect the transient behavior of salt. The test results presented here provide insight into the role of the intermediate principal stress as it relates to the creep and hardening of salt. Creep constitutive model development or review should be considered to assess the best way of incorporating Lode angle effects into those models.

The numerical simulations and laboratory tests presented here provide a thought-provoking topic and further illustrate the complex behavior of salt. Additional experimental and microstructural studies are likely to provide the key to explain the intriguing behavior exhibited by these laboratory tests. An area where accurate prediction of this uncharacterized behavior of salt could have an impact is geomechanical modeling of natural gas storage caverns. Previous cavern evaluations have shown that the state of stress in the salt changes from triaxial compression to triaxial extension, depending on the pressure in the cavern (DeVries et al. 2005). The significance of this behavior is a topic for future research.

ACKNOWLEDGEMENTS

The authors acknowledge the sponsor for this work, the US Department of Energy's National Energy Technology Laboratory (NETL) in Pittsburgh, Pennsylvania. This work was funded under Contract No. DE-FG26-02NT41651 and was directed by Mr. Gary Sames.

REFERENCES

Chen, W.F. & Hahn, D.J. 1988. *Plasticity for structural engineers*. New York: Springer-Verlag.

DeVries, K.L., Mellegard, K.D., Callahan, G.D. & Goodman, W.M., 2005. *Cavern roof stability for natural gas storage in bedded salt*. RSI-1829. prepared by RESPEC, Rapid City, SD, for U.S. Department of Energy, National Energy Technology Laboratory, Morgantown, WV.

Hunsche, U., Schulze, O., & M. Langer, 1994. Creep and failure behavior of rock salt around underground cavities. *Proceedings of the 16th World Mining Congress,* Sofia, Bulgaria. Vol. 5: 211–213.

Lux, K.H. & Heusermann, S. 1983. Creep tests on rock salt with changing load as a basis for the verification of theoretical material laws. *Proceedings, 6th International Symposium on Salt*, Toronto, Ontario, Canada, May 24–28, Alexandria, VA: The Salt Institute. 417–135.

Mellegard, K.D., Callahan G.D., & Senseny, P.E. 1992. *Multiaxial creep of natural rock salt*. SAND91-7052. Albuquerque, NM: Sandia National Laboratories.

Munson, D.E., Fossum, A.F., & Senseny, P.E. 1989. Advances in resolution of discrepancies between predicted and measured in situ WIPP room closures. SAND88-2948. Albuquerque, NM: Sandia National Laboratories.

Nayak, G.C. & Zienkiewicz, O.C. 1972. A convenient form of invariants and its application in plasticity. *Journal of the Structural Division.* ASCE. Vol. 98: 949–954.

Norton, F.H. 1929. *Creep of steel at high temperatures*. New York, NY: McGraw-Hill Book Company.

Wawersik, W.R., Hannum, D.W. & Lauson, H.S. 1979. *Compression and extension data for dome salt from West Hackberry, Louisiana.* SAND79-0668. Albuquerque, NM: Sandia National Laboratories.

APPENDIX

The representation of two states of stress (triaxial compression and triaxial extension) in principal-stress space is considered to help facilitate the discussion of states of stress around underground openings and as a means to visualize those states of stress. Consider the state of stress at a point (Q) in a body represented by the principal stresses σ_i ($i = 1, 2, 3$), as shown in Figure A1. If the principal stresses are taken as the Cartesian coordinates in a three-dimensional space, an isotropic potential (or yield) surface may be mapped in the coordinate system.

A vivid two-dimensional illustration of the bounding states of stress is achieved by projecting these stresses into the π-plane or Haigh-Westergaard stress space (e.g. Chen & Hahn 1988). The π-plane is a plane perpendicular to the hydrostatic axis where the mean stress is zero, and Haigh-Westergaard stress space is similar to the π-plane but includes those planes where the mean stress is a nonzero constant. For simplicity, these representations will be referred to as the π-plane recognizing the shortcomings in nomenclature as stated above.

Local two-dimensional Cartesian and polar coordinate systems embedded in the π-plane are convenient for representing yield or potential surfaces. This fact exists because a unique state of stress can also be uniquely defined by three stress invariants. Of particular interest are the invariants of the deviatoric stress tensor, S_{ij} ($S_{ij} = \sigma_{ij} - \sigma_m \delta_{ij}$), which are:

$$J_1 = 0$$

$$J_2 = \frac{1}{2} S_{ij} S_{ji} \qquad \text{(A-1)}$$

$$J_3 = \frac{1}{3} S_{ij} S_{jk} S_{ki}.$$

Now consider the principal stress space of Figure A2. Figure A2 is a view looking directly down the hydrostatic axis. In this orientation, the principal stress coordinate axes appear to be 120° apart. Cartesian coordinates x and y are defined as shown in Figure 3 (the choice is arbitrary). The x and y axes selected originate at point O on the hydrostatic axis. The x-axis is located 30° counter-clockwise from the σ_1-axis, and the y-axis lies along (but not parallel to) the σ_1-axis. In terms of the principal stresses, the coordinates are:

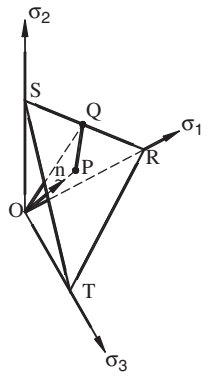

Figure A1. Stress points in principal stress space.

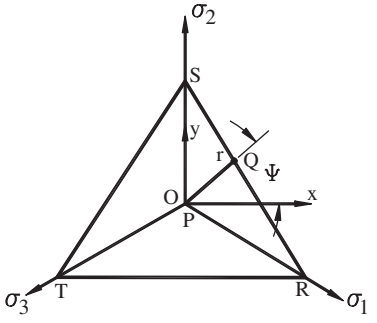

Figure A2. Stress points in principal stress space viewed down the hydrostatic axis.

$$x = \frac{\sigma_1 - \sigma_3}{\sqrt{2}} \qquad \text{(A-2)}$$

$$y = \frac{2\sigma_2 - \sigma_1 - \sigma_3}{\sqrt{6}}. \qquad \text{(A-3)}$$

Equations 2 and 3 may be used to obtain a polar coordinate (r, ψ) system, *viz*:

$$r = \sqrt{x^2 + y^2} = \frac{1}{\sqrt{3}} \sqrt{(\sigma_1 - \sigma_2)^2 + (\sigma_2 - \sigma_3)^2 + (\sigma_3 - \sigma_1)^2} \qquad \text{(A-4)}$$

$$\psi = \tan^{-1}\left(\frac{y}{x}\right) = \tan^{-1} \frac{1}{\sqrt{3}} \left[\frac{2\sigma_2 - \sigma_1 - \sigma_3}{\sigma_1 - \sigma_3}\right]. \qquad \text{(A-5)}$$

The angle ψ is referred to as the Lode angle. The Lode angle may be expressed in terms of the invariants J_2 and J_3 as (Nayak and Zienkiewicz 1972):

$$\psi = \frac{1}{3}\sin^{-1}\left[\frac{-3\sqrt{3}J_3}{2J_2^{3/2}}\right]. \tag{A-6}$$

However, when the Lode angle is defined in this manner, it is restricted to $-30° \leq \psi \leq 30°$. This restriction requires symmetry of the yield condition in all 60° sextants in the π-plane. When J_2 is expressed in terms of the principal stresses, it becomes:

$$J_2 = \frac{1}{6}\left\{(\sigma_1 - \sigma_2)^2 + (\sigma_2 - \sigma_3)^2 + (\sigma_1 - \sigma_3)^2\right\} \tag{A-7}$$

From Equations 4 and 7, one readily sees that the distance from the hydrostatic axes to a stress point is equivalent to $\sqrt{2J_2}$ when lying in the π-plane.

Taylor & Francis
Taylor & Francis Group
http://taylorandfrancis.com

The Mechanical Behavior of Salt – Understanding of THMC Processes in Salt –
Wallner, Lux, Minkley & Hardy, Jr. (eds)
© 2007 Taylor & Francis Group, London, ISBN 978-0-415-44398-2

Gas transport in dry rock salt – implications from laboratory investigations and field studies

T. Popp & M. Wiedemann
Institut für Gebirgsmechanik GmbH, Leipzig, Germany

A. Kansy & G. Pusch
TU Clausthal – Institut für Erdöl- und Erdgastechnik, Clausthal, Germany

ABSTRACT: Gas transport properties are key issues in the long term assessment of storage of high level radioactive or toxic waste in salt formations. Whereas extensive knowledge exists regarding the initial and dilatant rock salt properties, little is known about consequences due to the long term gas generation in a radioactive waste repository. Because rock salt is attributed to be impermeable for gases and fluids gas pressures will be built up with time until a level that may exceed the fracturing pressure of the rock (generally discussed as gasfrac-scenario). For an assessment of the provable impact of increasing gas pressures on the integrity of rock salt we present preliminary results from a long-term field test with progressive gas injection in a gas-tight sealed borehole. To detect micro-cracking a highly sensitive micro-seismic network was installed. Remarkably, in the multi-stage injection tests the gas-breakthrough was obtained at a gas pressure of 140 bar slightly above the primary stress state inducing a pressure build-up in two neighbored control bore holes. Due to the associated permeability increase of 3 orders (up to $10^{-20}\,m^2$) transient pressure decay occurs coevally in the pressurized injection-borehole. Reaching equilibrium at around 100 bar the primary gas-integrity is partly restored in the order of $10^{-22}\,m^2$. Most important, no pressure induced micro-seismic activity was observed during the gas-breakthrough which clearly contradicts the gas-frac-scenario. For comparison, we performed additional laboratory investigations highlighting the impact of increasing pore pressures on permeability whereby the effect of the gas-breakthrough could be attributed to pressure induced opening of grain boundaries. In addition, special account is taken to the effect of anhydrite bearing intercalations which may canalize the spatial gas migration in salt.

1 INTRODUCTION

Besides other host rocks salt formations are considered for the long term storage of radioactive waste to exclude a threat to actual and future generations. This means that the host rock's integrity has to be guaranteed during construction, operation and in the post-closure phase of a repository. Consequently, the contribution of the geological barrier to the safety of a repository has to be assessed by study of its natural characteristics and the main processes influencing radionuclide transport, i.e. the impacts of disturbance induced by the excavation of the underground facilities and long term effects, e.g. gas generation. Since the gas transport properties of rock salt are responsible for the required integrity, knowledge about the relationship between the developments of stress respectively gas pressure induced damage and permeability is of utmost importance.

The objectives of our investigations are:

(1) to summarize the state of knowledge about gas transport in undisturbed and dilated rock salt, i.e. domal salt.
(2) to investigate pressure dependent gas-migration in salt in a field test, particularly, the course of the breakthrough when achieving the minimal stress.
(3) to perform additional laboratory tests as a prove of the observed phenomena and an identification of possible pathways of the gas-breakthrough.

2 CURRENT UNDERSTANDING OF GAS TRANSPORT

2.1 *Undisturbed state and EDZ*

Rock salt in undisturbed state is characterized by low porosity («0.5%), low permeability (typically «$10^{-20}\,m^2$), and extremely low water content. In domal

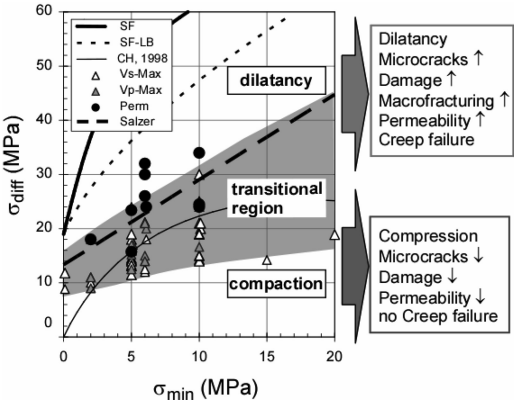

Figure 1. The modified dilatancy concept for rock salt. Experimental results from deformation tests are indicated where various micro-cracking sensitive physical parameters (Vp, Vs and permeability) were measured (Popp et al., 2001). Short-term failure strength (compression) for rock salt (origin: BGR): SF respectively SF-LB (lower bound). Dilatancy boundaries: CH, 1998 – Cristescu & Hunsche, 1998; Salzer – Salzer et al., 2002.

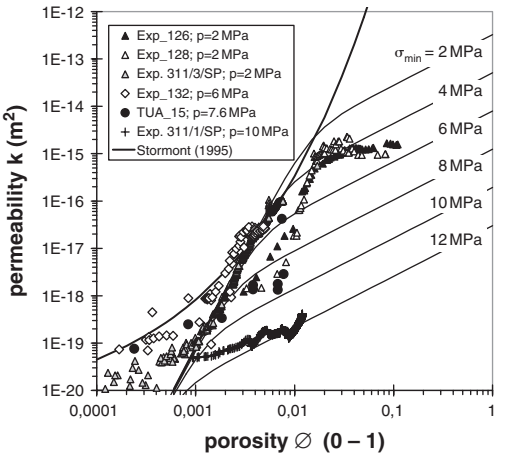

Figure 2. Measured and calculated permeability/porosity relationships depending on the minimal stress. For modeling the modified approach of Heemann & Heusermann (2004) as represented by isolines is used in comparison to the function given by Stormont (1995).

salt (e.g. older rock salt, z2HS, Asse salt mine (D)) the inter-granular absorbed water was determined in the order of ≤0.05 wt.-%. (Gies et al., 1994). Higher results of up to 0.2 wt.-% were attributed to hydrous minerals, e.g. polyhalite. Because rock salt shows a marked plasticity, no open fractures or fissures are present causing low gas flow in the initial state.

During and after excavation of an underground facility, the surrounding rock expands into the cavity due to stress release, initiating of a so-called excavation disturbed zone (EDZ). An overview about the current understanding of EDZ nature and properties in rock salt was recently given by Rothfuchs et al. (2003).

The occurrence of the EDZ, and thus, the development of potential hydraulic pathways is closely related to stress dependent property changes as it was demonstrated through permeability measurements in field tests (e.g. Stormont et al., 1991; Wieczorek, 2003) and under laboratory conditions (e.g. Stormont & Daemon, 1992; Popp et al., 2001).

Referring to the relevant in situ-stress conditions the so-called "dilatancy concept" has been evaluated as a reliable basis for a prognosis of the EDZ (Cristescu & Hunsche, 1998). As shown in Figure 1 the stress space below the failure boundary is separated by the dilatancy boundary in the two domains, compaction and dilatancy. However, it has to be mentioned, that this boundary is more a transitional field than a distinct line, because the detection of onset of micro-cracking depends obviously on the sensitivity of the measured parameter, as shown in Figure 1.

High-resolution ultrasonic velocity measurements (e.g. Schulze et al., 2001) give clear hints of local onset of micro-cracking at lower stresses, whereby in axial compression tests Vs decreases sooner than Vp (the reverse is true under extensional conditions). Because a nice agreement with the onset of humidity-induced creep acceleration was observed (Hunsche & Schulze, 2003) this stress level has to be understood as the "lower damage boundary" which corresponds roughly to the older formula given by Cristescu & Hunsche (1998).

Measurements of the volume change during deformation proved opening of micro-cracks (respectively onset of dilatancy, primary at significant higher stress levels resulting in a dilatancy boundary as described for instance by Salzer et al. (2002). Importantly, only at onset of dilatancy coevally an increase of permeability is observed (see Figure 1).

Short term deformation experiments on natural rock salt (e.g. Popp et al., 2001) and synthetic salt (e.g. Peach & Spiers, 1996) show a drastic rise of permeability (up to 5 orders of magnitude). Generally, the permeability (k) increase during dilatant deformation is a function of dilatancy respectively porosity (ϕ):

$$k = k_0 \cdot \phi^n \quad (1)$$

However, as can be seen from Figure 2, a unique permeability-porosity relationship as proposed by some authors (e.g. Stormont, 1995) gives not an adequate approximation of the observed experimental permeability evolution. Although there is a significant data scatter (compare discussion in chapter 2.2) two parts of permeability evolution have to be distinguished: (1) an initial steep increase

Table 1. Parameters for describing permeability as function of porosity depending on the minimal stress σ_{min} (after Heemann & Heusermann (2004).

Parameter	Value	Parameter	Value
a_k	4.27E-14 m^2	a_ϕ	0.0263
b_k	1.26 MPa^{-1}	b_ϕ	0.3093 MPa^{-1}
n_1	4	n_2	1.07

due to progressive development of micro-cracks, and (2) beyond a certain threshold boundary a saturation state with moderate increase due to widening of created pathways.

Additionally, as firstly mentioned by Popp (2002), the threshold until reaching the saturation level in region (2) is obviously a function of σ_{min} (Fig. 2). Based on his original description Heemann & Heusermann (2004) developed a modified equation for an approximation of the experimentally data sets (note the various model curves in figure 2):

$$k = \frac{k_{tp}}{\left(\left(\frac{\phi}{\phi_{tp}}\right)^{-n_1} + \left(\frac{\phi}{\phi_{tp}}\right)^{-n_2}\right)} \quad (2)$$

n_1 and n_2 are constant inclination values according to the two relevant porosity/permeability slopes in the double logarithmic diagram. The other parameters are depending on the minimal principal stress σ_{min} (for parameters of the constitutive equations see Table 1):

$$k_{tp} = a_k \cdot \exp(-b_k \cdot \sigma_{min}) \quad (3)$$

$$\phi_{tp} = a_\phi \cdot \exp(-b_\phi \cdot \sigma_{min}) \quad (4)$$

Although the modeled permeability data seems to be slightly overestimated in region 2 the new concept of stress and porosity dependent permeability evolution has been successfully proved by the latter authors in the BAMBUS-project.

Under non-dilatant conditions, i.e. below the dilatancy boundary any increase of porosity and permeability even with time is impossible instead but crack-sealing or in the long-term healing is induced. However, it has to be mentioned, that the permeability/porosity relationships for rock salt undergoing dilatant deformation and the reverse, i.e. compaction of pre-dilated or granular salt, are different. A compilation of permeability/porosity data sets for granular salt is given by Müller-Lyda et al. (1999).

2.2 *Lithological aspects of gas-transport*

With respect to the reliability of the performed modeling, as included in Figure 2, everybody has to be taken account considerable deviation of individual permeability tests due to anisotropy and lithological effects. As already demonstrated by Popp et al. (2001) stress-induced crack evolution is strongly anisotropic depending on the acting stress field also resulting in anisotropic gas transport.

In addition, the general permeability-porosity-relationships are found to be overlapped by lithological effects which can result in deviations of more than one order of magnitude of permeability for a desired stress level. Impurities in rock salt are usually present, e.g. anhydrite and detrial argillaceous clay materials besides other minor constituents (e.g. polyhalite, dolomite, magnesite and hematite). Popp et al. (2001) have shown for a stratigraphical sequence of the Staßfurt rock salt (Na2) that depending on the content and distribution of anhydrite impurities the permeability systematically varies.

To illustrate localized gas transport phenomena in anhydritic rock salt portions we performed special flooding experiments with diiodine-methane (CH_2I_2) along axially deformed salt cores from the Bernburg site (Saxony Anhalt, D). This rock salt is characterized by distinct anhydrite intercalations. Diiodine-methane has a high absorption for x-rays which allows therefore visualization of pores or cracks filled with CH_2I_2 during transmission. The flooding experiments were performed in the X-ray computer tomography lab of the Tech. Univ. Clausthal (D).

Exemplarily it can be seen in Figure 3 that flow is pronounced along border regions of anhydritic rock portions which are probably acting as local stress concentrations thus initiating preferred micro-crack accumulation. In consequence, gas flow parallel anhydrite beddings may be favored whereas intact and persistent anhydrite layers may act as barriers, thus resulting in canalized gas flow.

2.3 *Long-term gas-pressure build up*

In the long-term when waste is disposed of in a salt repository, although there is only a small availability of water, significant quantities of gas are expected to be produced by various processes (e.g. corrosion and microbial degradation, and, in addition, in the case of radioactive waste radiolysis), which need to escape from the repository area (IAEA, 2001). Otherwise, in closed parts of the repository, pressures may build up that may exceed the fracturing pressure of the rock, opening up new paths through the barriers and creating new transport channels both for toxic gases and for contaminated solutions impeding the integrity of underground waste disposal facilities.

Therefore, the influence of pore pressures on the mechanical and transport properties must be known for an assessment of the long-term integrity of the rock surrounding a repository. In particular, permeability of the salt as a function of increasing gas pressure

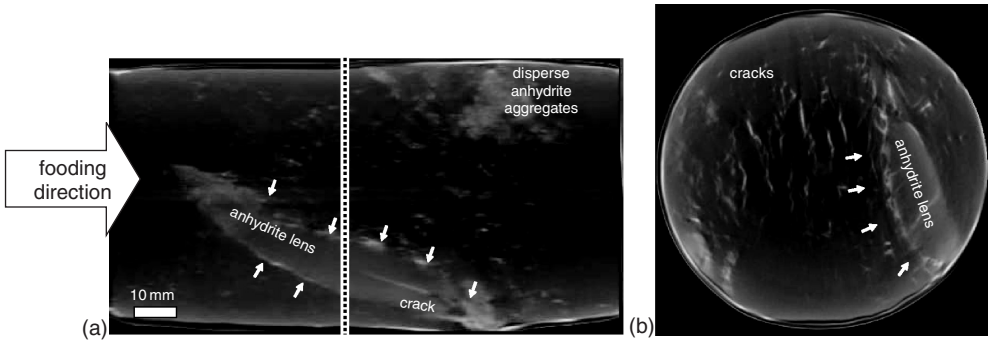

Figure 3. X-ray tomography of an axially deformed salt core after axial core flooding with CH_2I_2. (a) left: axial profile; (b) right: radial profile. Primary, diiodine-methane filled pores and subordinately anhydrite intercalations are light-colored due to higher absorption than salt. Diffuse distributed and preferably axial oriented cracks are visible. Note that particularly the borders of the anhydrite lens show local disturbances (indicated by arrows).

is an important parameter for evaluating the risk of pneumatic fracturing the salt barrier.

3 THE FIELD TEST AT THE BERNBURG SITE

3.1 *Geological situation and test design*

With respect to current problems of gas-pressure build up in salt two field tests are underway in the Bernburg salt mine since 2004 in two different lithological units: (1) the older rock salt (Na2, Staßfurt rocksalt) where the geological situation corresponds to domal conditions and (2) the younger rock salt (Na3, Leine salt) where a bedded salt formation exists. In addition to observations of gas transport features, both test sites are equipped with a very sensitive micro-seismic monitoring systems (operated by GMuG Obermörlen) to detect gas-pressure induced rock disturbances or, at least, a potential gas-frac. Because the first test has now a duration of more than 500 d including gas-breakthrough, re-frac and healing phases we want to focus on these results.

The test area is situated in a level of about −455 m NN (respectively 520 m depth) within in a very homogenous part of the older rock salt (Stassfurt-salt Z2: overall maximal thickness of up to 400 m) near the so called Grönaer shaft anticline (Fig. 4). The rock salt is free of potash and is typically characterized by alternating layers of medium to coarse grained rock salt from white into grey indicating primary sedimentary bedding with intercalated anhydrite dominated salt beds (portion of about 5% anhydrite) up to 5 cm thickness and 30–50 cm distance. But due to the tectonically induced stresses the sulphate layers are not interconnecting. Because the test site is close to the safety pillar of the shaft no significant mining activities were performed which warrants undisturbed conditions in deeper wall portions.

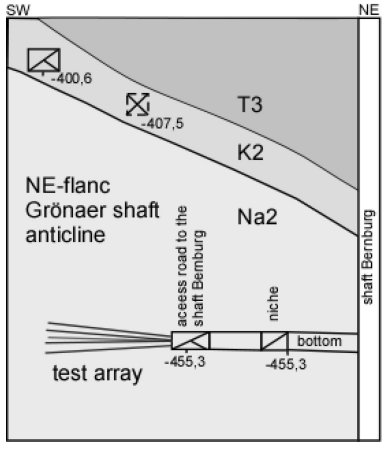

Figure 4. Geological situation of the borehole test in the NE-flanc of Grönaer shaft anticline. Note the schematic depicted bore hole array.

An array of 9 boreholes, each 25 m long, was installed in the access drift to the shaft Bernburg in SW-direction. It consists of the nearly horizontal central injection borehole (Ø = 60 mm) and four surrounding control boreholes (Ø = 42 mm), parallel drilled in distances of 1 respectively 2 m to detect gas-breakthrough. In addition, a micro-seismic monitoring array was installed in four funnel-shape oriented bore holes (Ø = 101 mm), each equipped with two seismic sensors, in the near field of the test (approx. 2 to 4 m distance).

The measuring holes were sealed using a hydro-mechanical packer system positioned in around 10 m depth, i.e. behind the dilated contour as was proved by hydro-frac measurements (see below). Because the quality of the test results strongly depends on the reliability of the borehole sealing, especially in the

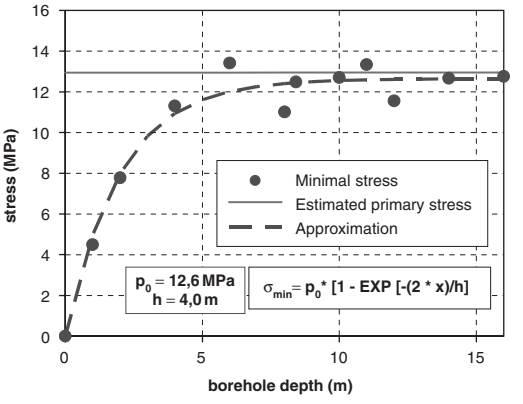

Figure 5. Variation of the minimal stress as determined by hydro-frac tests in the horizontal level of the test site. The data scattering is referred to local leakiness along anhydrite portions complicating the determination of the static pressure.

injection hole, a new double-packer system with a total length of 1 m was developed. In contrast to common straddle packer systems, it consists of two elastomer elements, each compressed by a hydraulic cylinder. The main advantage is the control of the time depended packer settlement due to the visco-plastic behaviour of both, the surrounding salt and the elastomer material by measuring the oil pressure decay in the hydraulic loading system. After ensuring stable packer conditions a first tightness test was performed showing a gas pressure increase in the control space between the two packers. Because this effect was attributed to local leak along the first packer due to the drilling induced EDZ around the borehole, it was decided to inject viscous oil into the central part of the double-packer system which successfully prevented further leakage.

The total volume sealed in the injection borehole is 0.046 m^3. The injection and the 4 control boreholes were completed with gas-tight fittings and valves (Hy-Lok 105 Series) and equipped with pressure transducers.

Because the knowledge about the primary stress field and the mechanical behaviour of the surrounding salt rock is a prerequisite for each further evaluation of the observed pressure behaviour long term extensometer and hydro-frac measurements (vertical and horizontal in the test drift) were performed.

As shown in Figure 5 the minimal stresses in the contour increases with progressive borehole depth until reaching a saturation state in a depth of around 7 m. The measured value of an undisturbed stress state of 12.6 MPa corresponds fairly well with the average value of 13.0 MPa calculated with an average pressure gradient of 0.024 MPa/m which is typical for the Bernburg location.

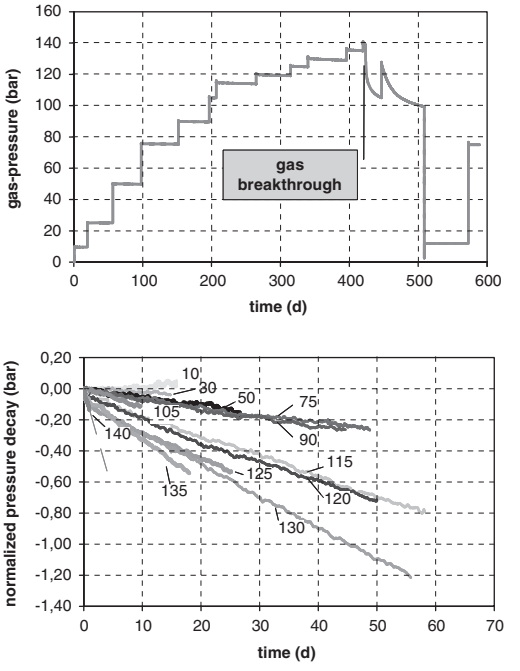

Figure 6. Multi-stage gas-pressure injection test. (a) above: complete test duration. (b) below: normalized pressure decay (referred to the initial pressure: $\Delta p = p_{f(t)} - p_i$) curves for the various steps. At each curve the initial pressure level is indicated (p_i (bar)).

3.2 *Test results*

After realizing stable packer conditions (after several days), the injection tests started in February 2005 with stepwise pressurization, using dry N_2. The complete course of gas injection cycles is depicted in Figure 6.

The so performed pulse tests show very limited pressure decay in the various steps, between nearly zero and 1 bar/50 days, which required test durations for each step of between 20 and 50 days. Because the shape of pressure decay corresponds roughly to straight lines, nearly-stationary gas flow is expected in the injection tests until 135 bar.

The evaluation of the pressure decay rates as a function of pressure shows a progressive increase which can sufficiently approximated by a quadratic relationship as included in Figure 8. Thus, the observed pressure dependence of pressure decay rates corresponds nicely to Darcy-flow of compressible media.

As can be seen from the Figures 6b and 8 the pressure discharge accelerates when the injection pressure is increased to 135 bar which is slightly above the estimated primary stress state of 13 MPa. Further pressure increase up to 140 bar results in a more pronounced pressure decay (in the order of −0.15 bar/d)

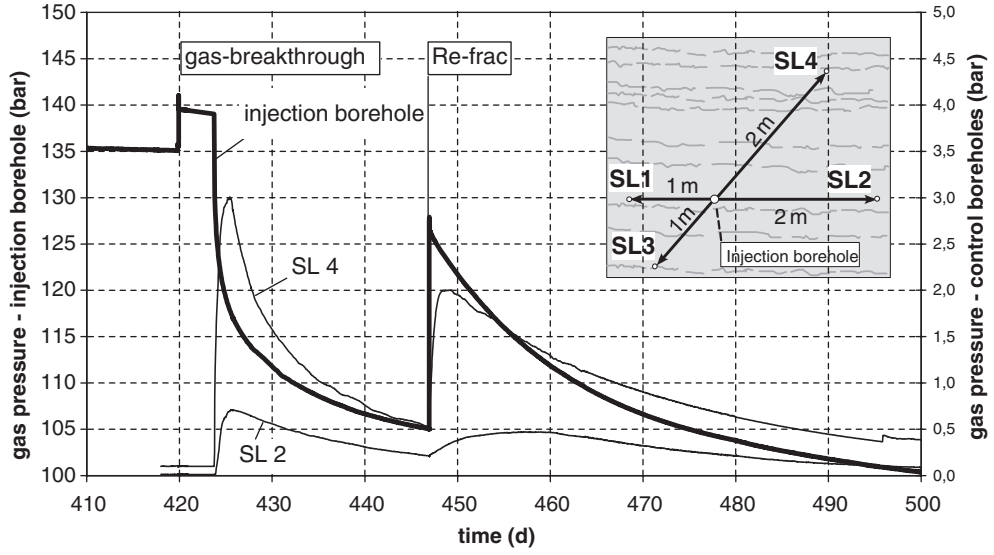

Figure 7. Gas-breakthrough in the pulse test at nominal 140 bars. The inset shows the arrangement of the injection borehole (in the center) and the four surrounding control bore holes. The visible bedding consisting of non connecting anhydrite-portions is nearly horizontal.

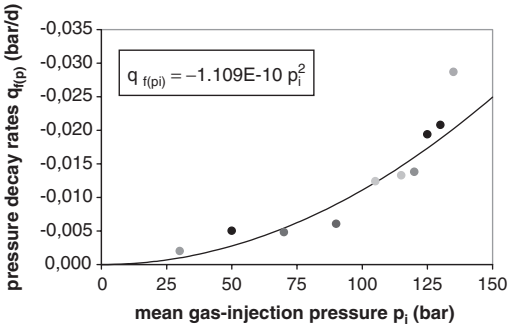

Figure 8. Gas-pressure decay rates from pulse tests vs. mean gas pressure.

which was nearly 5 times higher than before. In addition, after 4 days in the transient phase of the pulse test a dramatic gas-pressure drop occurred accompanied by the gas-breakthrough into two of the four control boreholes (compare detail section in Figure 7).

Amazingly, the pressure build-up occurred in the two more distant boreholes (d = 2 m), arranged diagonal above (SL4: $\uparrow p_p = 3.2$ bar) respectively parallel (SL2: $\uparrow p_p = 0.7$ bar) to the central injection borehole.

Remarkably, the rapid pressure decay during the break-through is characterized by transitional behavior aspiring an extrapolated equilibrium state at around 100 bar, which would reached after approx. 50 d. Restoring the injection pressure to around 128 bar replicates nearly the same pressure decay.

With respect to the potential gas-frac scenario, it is important to note that the highly sensitive micro-seismic monitoring gives no hints for a pressure induced change in the micro-seismic activity during the whole pressurization cycle, in particular also not during the gas-breakthrough phase (not shown here). However, during the test period discontinuous appearance of seismic events were observed but they are mostly related to EDZ phenomena in the drift contour.

In the next step, to investigate the healing capacity of the salt, the gas pressure was lowered to 10 bars resulting in a very low pressure decay (of only −0.0006 bar/d) over a period of more than 50 days. Increasing the pressure up to 75 bar yields nearly the same result which was generally attributed to existing gas pressure loading in the borehole contour.

3.3 *Preliminary evaluation of the permeability data*

The evaluation of test results primary depends on the main process governing the flow properties of rock salt (e.g. Ehgartner & Tidwell, 2000). Generally, for simplification, the hydraulic system in salt rocks is usually described on the base of Darcy-flow, whereby coupled non-linear gas/brine flow properties are neglected. This approach is also of concern here for the following reasons:

(1) Although the depositional environment of salt is generally wet, it can be assumed that in domal salt most of the primary fluids have been squeezed

and kneeded out during diagenesis and later halokinetic events, respectively accumulated in intra-crystalline fluid inclusions due to dynamic recrystallisation (Roedder, 1984). Therefore it is hypothesized that the grain boundaries at the Bernburg site contain mainly interstitial gas with pore pressures significantly less than lithostatic pressures, which is in contrast to bedded salt formations (i.e. at the WIPP-site, e.g. Beauheim & Roberts, 2002).

(2) A correlation between capillary gas-threshold pressures and permeability as proposed by Davies (1991) suggests extremely high gas injection pressures for intact rock salt which would inhibit gas-intrusion into the salt. Our gas injection tests, as can be seen in Figure 8, clearly document that the gas migration rates rises up directly depending on injection pressure. In addition, no discontinuous pressure behavior is observed in the pressure cycle up to 135 bar which contradicts two-phase flow.

Consequently, we used two approaches, both basing on pure gas phase flow for estimating permeability: (1) an analytical solution according to a simple radial gas flow model with stationary flow consisting of the borehole with given dimensions and a cylindrical flow area whose radius depends on filling up a given porosity of 0.5% with a mean pore pressure; (2) the computer code of the so called r-z-model which comprises a numerical simulator for spatial flow around a borehole with an automatic inverse modeling capability of the measured pressure decay curves as developed by the working group of Prof. Häfner, TU Freiberg). The tool for evaluating pulse-tests was successfully applied in numerous projects (e.g. Voigt et al., 2001).

The permeability results obtained for the various injection steps are summarized in Figure 9, which shows the permeability evolution as a function of nominal gas pressure in the injection borehole. Remarkably, both approaches are sufficiently in agreement confirming a very low permeability of $<10^{-23}$ m^2 at injection pressures below the undisturbed stress state of around 13.0 MPa.

At pressures $\geq$120 bar a slight increase of permeability is observed until the gas-breakthrough occurs at 140 bar resulting in a rise of three orders of magnitude to approx. 10^{-20} m^2. With the coeval transient pressure decay the permeability decreases until preserving stable flow conditions at around 100 bar, respectively at 10^{-22} m^2. The permeability drop is replicated in the re-frac cycle when the injection pressure is increased to around 128 bar (Figure 7).

The application of the r-z-model offers an estimate of gas-pressure distribution during the gas-breakthrough corresponding to a permeability increase up to 10^{-20} m^2. As depicted in Figure 10 the extent of the pressurized zone at the gas breakthrough as can be seen from the pressure isoline of 3 bar, is in the order of around 1 m. However, during the breakthrough an pressure rise up to 3 bar was observed only in the more distant control boreholes which implies that the pressure distribution in the test site is not homogenous.

This infers that the reliability of the performed modeling is restricted to isotropic salt conditions. In consequence, the here presented permeability results are in a preliminary state, because the lithological random conditions are up to now not well understood, and need to be supplemented by a more adequate modeling.

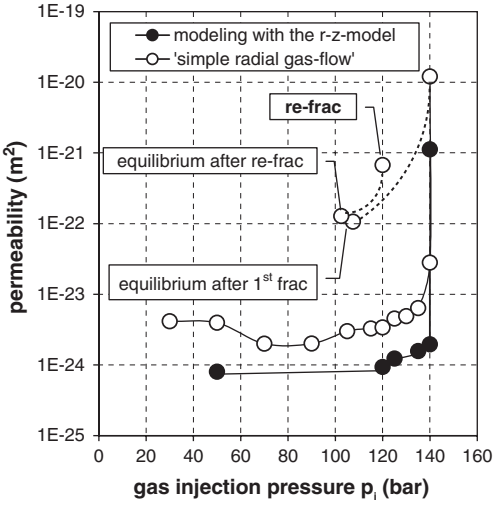

Figure 9. Gas-permeability evolution during stepwise gas-injection. Note, that at the pressure step of 140 bar two permeability values were estimated, before and during gas-breakthrough.

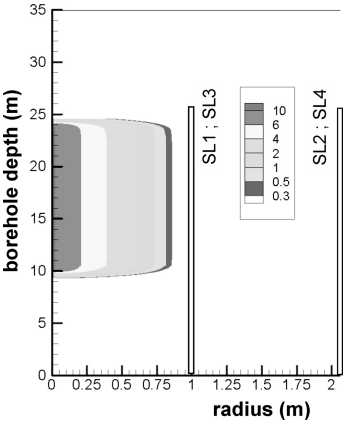

Figure 10. Extent of the pressurized zone around the injection bore during gas-breakthrough.

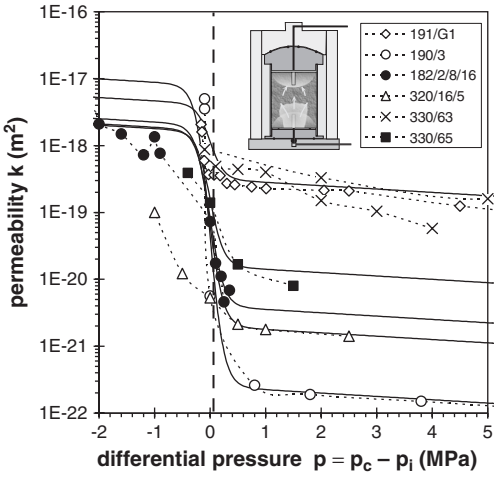

Figure 11. Permeability vs. differential pressure. Summary of gas-injection tests performed at 10 MPa quasi-hydrostatic pressures. Additionally, model curves based on hyperbolic tangent function are included. The inset shows the scheme of the cell.

4 LABORATORY INVESTIGATIONS

In the course of the project an extensive laboratory program on gas transport in rock salt (taken from various locations) has been performed under realization of a wide spectrum of experimental conditions (e.g. dilated and pre-compacted core samples). Some of the results are already published in Kansy & Popp (2006). Here, we want to focus on the results on gas-breakthrough experiments.

The sample arrangement, as schematically depicted in Figure 11, consists of the standard arrangement for measuring gas-permeability in the triaxial cell. A cylindrical sample is hydrostatically loaded and subjected to stepwise pressurization the lower end. Measuring the axial gas outflow facilitates the calculation of the gas permeability.

The permeability evolution of various injection tests is summarized in Figure 11 as a function of differential gas pressure which is simply the difference between the confining ($p_c = \sigma_{min}$) and the gas injection pressure (p_i). Generally, three pressure regions have to be discriminated:

Region 1 – beginning at low gas pressures (p_i «σ_{min}) the initial measured permeability continuously increases slightly during stepwise pressurization independently from the initial permeability state

Region 2 – when p_i approaches σ_{min} the gas breakthrough occurred resulting in a steep increase of permeability (up to 5 orders, whereby the lower the initial permeability the higher the rise).

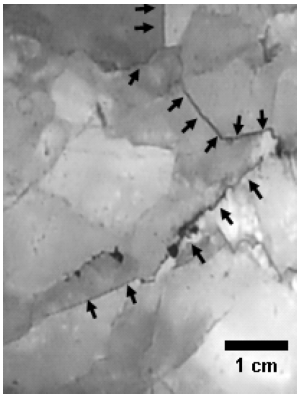

Figure 12. Dilated grain boundaries after the gas breakthrough (indicated by arrows). For better visualization the sample has been flooded with a colored solution ("Prüfrot") impregnating opened pore space.

Region 3 – at pressures $p_i > \sigma_{min}$ a plateau of permeability at $k > 10^{-18}$ m^2 is reached. However, the permeability evolution in this region was not sufficiently identified due to technical reasons (i.e. inflating of the sample tube).

In summary, the observed results confirm fairly well the observations made in the field test, in particular, reversibility of the permeability course (not shown here). However, the permeability rise at the threshold is significantly more pronounced which we attribute to scale effects due to the limited sample size. Visual inspection of the gas pressurized samples clearly reveals dilated grain boundaries acting as flow paths.

5 SUMMARY AND CONCLUSIONS

In the last decade the knowledge regarding transport properties in salt, particularly in the dilatant stage, has been noticeable improved. The general "dilatancy concept" developed by Cristescu & Hunsche (1998) has been confirmed as state of the art to describe stress induced damage or healing respectively sealing in rock salt (Hunsche & Schulze, 2003). However, a unique quantitative specification regarding the stress dependent onset of dilatancy seems to be unlikely due to overlapping lithological effects. In addition, detection of onset of micro-cracking depends on the sensitivity of the used technique inferring that local damage occurs already at lower stresses than measured by the volumetric strain resp. indicated by the coeval permeability rise. Nevertheless, for the description of the permeability-porosity relationship reliable functions are available with consideration of the minimal stress.

Referring to the long term properties some uncertainties remain, e.g. quantification of healing. However, dilatant regions in rock salt will disappear with

time because of its crystal plasticity and humidity assisted compaction resulting in a very low permeability. In consequence, in the long-term gas pressure build-up will occur if the gas generation rates are sufficient high enough. With respect to the possible gas migration scenario, our results from in-situ tests at the Bernburg site are a valuable base for assessment of property changes in rock salt during gas-pressure build-up, although they are not finished yet:

(1) the initial permeability of undisturbed salt was estimated to be in the order of «10^{-23} m^2, slightly increasing during pressure build-up at pressure $p_i \geq 120$ bar. The pressure related stepwise rise of nearly-stationary gas-migration rates indicates true advective (Darcian) gas flow.
(2) Exceeding the primary stress (respectively σ_{min}) at $p_i = 140$ bar results in a discontinuous acceleration of gas intrusion to the salt until slightly time-delayed the gas-breakthrough occurred. Due to the associated permeability increase of 3 orders (up to 10^{-20} m^2) a pressure drop coevally occurs in the pressurized gas-reservoir until reaching equilibrium at around 100 bar. At that stage the primary gas-integrity is partly restored in the order of 10^{-22} m^2.
(3) Repeating the gas injection at a level of around 130 bar results in the same transient pressure behavior comprising the partial integrity recovery (respectively permeability drop) at lowered pressure.

Evaluation of the observed pressure decay during breakthrough suggests an increase of permeability in the order of three magnitudes which does not support the feared pneumatic frac-scenario. In addition, no pressure induced micro-seismic activity was observed during the gas-breakthrough which also clearly contradicts the gasfrac-scenario.

As inferred from microstructural observations we believe that only local widening of bottle-necks or linking-up of pre-existing pathways such as grain boundaries causes the observed increase of permeability (generally described as "secondary permeability", e.g. Stormont, 2001) which is not accompanied with a measurable increase in porosity. The coeval pore pressure drop leads to a quasi-elastic closure of the prior opened path ways and thus to a recovery of hydraulic integrity. Because the observed permeability reversibility can be understood as "self healing" this process may act as a "safety valve" if a gas-pressure increase in salt occurs.

The extent of gas migration depends on the internal storage capacity of the salt as given by its porosity and the mean pore pressure. However, controlled by the amount of gas produced in the repository the permeation zone affected by gas-intrusion will evolve with time during each breakthrough cycle as should be tested by appropriate model calculations.

ACKNOWLEDGEMENTS

The studies presented in this paper were funded by the German Federal Ministry of Research and Education under contract 02C 0952 and the Federal Office for Radiation Protection (BfS) within the UFO-Plan project SR 2470 "Untersuchungen zur Barriereintegrität im Hinblick auf das Ein-Endlager-Konzept", respectively. As project officers, H. Pitterich (FZK), M. Beushausen and G. Stier-Friedland (both BfS) attended with benevolent interest.

We thank the "european salt company" (esco) for facilitating the installation and operation of the test-site over the aspired test duration of around four years in the active salt mine Bernburg. The research benefited from the fruitful cooperation and discussions with many colleagues from various institutions (e.g. BfS, BGR, GRS and TU Clausthal). In particular, O. Schulze (BGR) and V. Meyn (TU Clausthal) provided continuously valuable contributions. G. Manthei (GMuG) performed the micro-seismic monitoring. H.-D. Voigt (TU Bergakademie Freiberg) gave important hints for handling the r-z-program for evaluating the pulse-tests. In addition, he kindly reviewed a preliminary version of the paper.

REFERENCES

Beauheim, R.L & Roberts, R.M., 2002. Hydrology and hydraulic properties of a bedded evaporite formation, *J. Hydrology*, 259 (1), 66–88.

Cristescu, N. & Hunsche, U., 1998. *Time effects in Rock Mechanics.* Wiley & Sons, Chichester.

Davies, P.B., 1991. Evaluation of the role of threshold pressure in controlling flow of waste-generated gas into bedded salt at the Waste Isolation Pilot Plant (WIPP). Sandia Rep. SAND 90-3246.

Ehgartner, B. & Tidwell, V., 2000. Multiphase flow and cavern abandonment. *Proc. SMRI Fall Meeting*, San Antonio, 73–86.

Gies, H, Gresner, H., Herbert, H.-J., Jockwer, N., Mittelstädt, R., Mönig, J. & Nadler, F., 1994. Das HAW-Projekt Versuchseinlagerung hochradioaktiver Strahlenquellen im Salzbergwerk Asse: Stoffbestand und Petrophysik des Steinsalzes im HAW-Feld (Asse, 800-m-Sohle), *GSF-Bericht*; 94,16.

Voigt, H.-D., Häfner, F., Sitz, P. & Wilsnack, T., 2002. Bestimmung geringer Durchlässigkeiten im Gebirge. "*Bergbau*" – *Zeitschrift für Rohstoffgewinnung, Energie und Umwelt*. Nr. 12, Essen, S. 537–539.

Heemann, U. & Heusermann, S., 2004. Theoretical and experimental investigation on stresses and permeability in the BAMBUS project. *DisTec 2004, International Conference on Radioactive Waste Disposal*, April 26–28, 2004, Berlin.

Hunsche, U. & Schulze, O., 2003. The dilatancy concept – a basis for the modelling of coupled T-M-H-processes in rock salt.- *Proceedings of a European Commission Cluster Conference*, Luxembourg, Nov 2003. Eds: C. Davis & F. Bernier. p. 102–109.

IAEA. 2001. The use of scientific and technical results from underground research laboratory investigations for the geological disposal of radioactive waste. *International Atomic Energy Agency*, IAEA-TECDOC-1243.

Kansy, A. & Popp, T., 2006. Modellentwicklung zur Gaspermeation aus unterirdischen Hohlräumen im Salzgebirge (02C0952). *7. Projektstatusgespräch des Projektträgers Forschungszentrum Karlsruhe Wassertechn. und Entsorgung*, 3./4. Mai 2006, Karlsruhe (ISSN 140-6751), 69–86.

Müller-Lyda, I., Birthler, H & Fein, E., 1999. Ableitung von Permeabilitäts-Porositäts-Relationen für Salzgrus. *GRS-Bericht 148*, Braunschweig, Germany

Peach, C.J. & Spiers, C.J., 1996. Influence of crystal plastic deformation on dilatancy and permeability development in synthetic salt rock, *Tectonophysics*, 256, 101–128.

Popp, T., 2002. Transporteigenschaften von Steinsalz. *Meyniana*. 54, 113–129.

Popp, T., Kern, H. & Schulze O. 2001. The evolution of dilatancy and permeability in rock salt during hydrostatic compaction and triaxial deformation. *J. Geophys. Res.* 106, No. B3, 4061–4078.

Roedder, E., 1984. *The fluids in salt.* Am. Mineral., 69, 413–439.

Rothfuchs, T., Wieczorek, K., Olivella, S. & Gens, A., 2003. Lessons Learned in Salt, Impact of the Excavation Disturbed or Damaged Zone (EDZ) on the performance of radioactive waste geological repositories. *European Commission CLUSTER Conference on the Impact of EDZ on the Performance of Radioactive Waste Geological Repositories*. 3–5 November 2003, Luxembourg.

Salzer, K., Schreiner, W. & Günther; R.-M., 2002. Creep law to decribe the transient, stationary and accelerating phases. In: *The Mechanical Behavior of Salt V;* Proc. of the Fifth Conf., (MECASALT V), Editors: N.D. Cristescu, H.R. Hardy, Jr., R.O. Simionescu, Bucharest 1999, Balkema, Lisse, 177–190.

Schulze, O., Popp, T. & Kern, H., 2001. Development of damage and permeability in rock salt undergoing deformation. In. Proceedings of the EUG 10 – Conference, 28th March – 1st April 1999, Strasbourg, France, Symposium J3 – Radioactive Waste Disposal, M. Langer et al. (Eds.). – *Engineering Geology*, 61, 163–180.

Stormont, J.C., Howard, C.L., & Daemen, J.J.K., 1991. In Situ Measurements of Rock Salt Permeability Changes Due to Nearby Excavation, *Sandia National Laboratories, SAND90-3134*, Albuquerque.

Stormont, J.C. & Daemen, J.J.K. 1992. Laboratory study of gas permeability changes in rock salt during deformation, *Int. J. Rock Mech. Min. Sci. Geomech. Abstr.,* 29, 325–342.

Stormont, J.C., 1995. The influence of rock salt disturbance on Sealing. *Second North American Rock Mechanics Symposium,* Montreal, Quebec.

Stormont, C., 2001. Evaluation of Salt Permeability Tests, *Research Project Report No. 2001-2-SMRI,* Solution Mining Research Institute, 3336 Lone Hill Lane Encinitas, California, USA.

Wieczorek, K., 2003. EDZ in Rock Salt: Testing Methods and Interpretation. *European Commission CLUSTER Conference on the Impact of EDZ on the Performance of Radioactive Waste Geological Repositories*. 3–5 November 2003, Luxembourg.

The Mechanical Behavior of Salt – Understanding of THMC Processes in Salt –
Wallner, Lux, Minkley & Hardy, Jr. (eds)
© 2007 Taylor & Francis Group, London, ISBN 978-0-415-44398-2

Excavation damaged zones in rock salt formations

Norbert Jockwer & Klaus Wieczorek
Gesellschaft für Anlagen- und Reaktorsicherheit (GRS) mbH, Braunschweig, Germany

ABSTRACT: During an ongoing project which succeeds previous investigations of the excavation damaged zone (EDZ) performed in the Stassfurt halite of the Asse salt mine, the EDZ evolution, especially after cutting off the contour zone, is investigated. Three test locations have been prepared in the floor of an almost 20 year old gallery on the 800-m level of the Asse mine: (1) the drift floor as existing, (2) the new drift floor shortly after removing of a layer of about 1 m thickness of the floor with a continuous miner, (3) the new drift floor 2 years after cutting off the 1-m layer. Subject of investigation are the diffusive and advective gas transport and the advective brine transport very close to the opening. Spreading of the brine is tracked by geoelectric monitoring in order to gain information about permeability anisotropy. Results obtained up to now show that EDZ cut-off is a useful method to improve sealing effectiveness when constructing technical barriers.

1 INTRODUCTION

Salt formations are considered as potential host rocks for nuclear waste disposal. After the operational phase of a repository the openings, e.g., boreholes, galleries, and chambers have to be sealed in order to avoid the release of radionuclides into the biosphere. For optimising the sealing techniques knowledge about the excavation damaged zones (EDZ) around these openings is essential. Excavation disturbed zones in rock salt develop in the vicinity of openings during and after excavation, changing the original properties of the rock salt which is characterised by a very low porosity, low permeability and low water content. The highly inhomogeneous stress state around an opening leads to dilatancy, i.e., increase of porosity by microfracturing, and thus to a potential increase in permeability by several orders of magnitude.

For long term safety aspects of a repository and especially for the design and construction of sealing elements the knowledge of the gas and water migration in the excavation disturbed zone, its size and its development with time is essential. Furthermore it is of importance to investigate technical methods for reducing the EDZ.

At the Asse salt mine in the Stassfurt halite on the 800-m level the EDZ is investigated in the frame of an ongoing project with the objective to investigate the diffusive and advective gas transport and the advective brine transport very close to the opening. Spreading of the brine is tracked by geoelectric monitoring in order to gain information about permeability anisotropy and porosity.

Three test locations on the floor of an 20 years old gallery have been prepared:

1. the drift floor as existing
2. the new drift floor shortly after removing of a layer of about 1 m thickness of the floor with a continuous miner
3. the new drift floor 2 years after cutting off the 1-m layer

2 LAYOUT OF THE TEST FIELD

Usually in-situ measurements on gas and water permeability are performed in boreholes which are sealed with packer systems. For investigations close to the opening the boreholes and packers have to be very short and sealing to the surface is not granted. During injection tests a significant portion of the injected fluid will migrate directly though the EDZ into the opening above the borehole, so that the rock portion affected by injection may be too small for representative results. A new method was therefore developed and tested for the first time in the frame of the BAMBUS II project (Bechthold et al. 2004).

A square plastic sheet with a side length of 1.8 m was embedded into a fresh layer of salt concrete and secured by screws. When the salt concrete was cured, a tight sealing of the surface was achieved. After installation of the sheet and curing of the salt concrete, five boreholes (BRL1–BRL5) were drilled into the salt below the sheet (see Figure 1). Each of the five boreholes is equipped with a plug at the borehole bottom which provides a 60-mm long test interval. The top

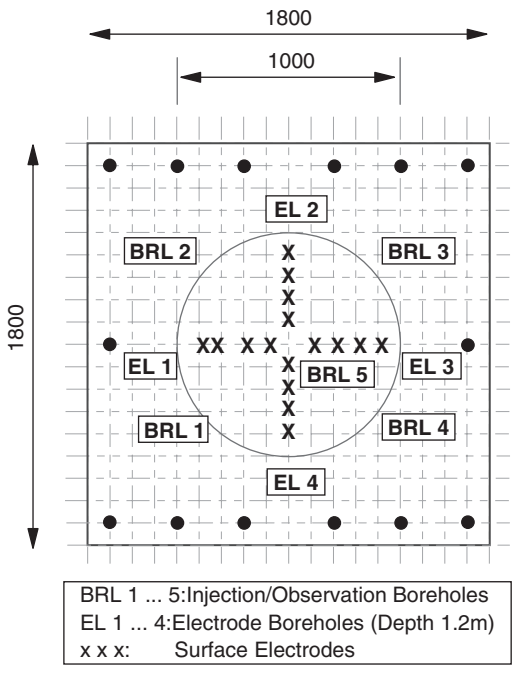

Figure 1. Plastic sheet embedded in salt concrete on the drift floor with the boreholes for gas or brine injection (BRL1–BRL5), the boreholes for the electrode chains (EL1–EL4), and the surface electrodes.

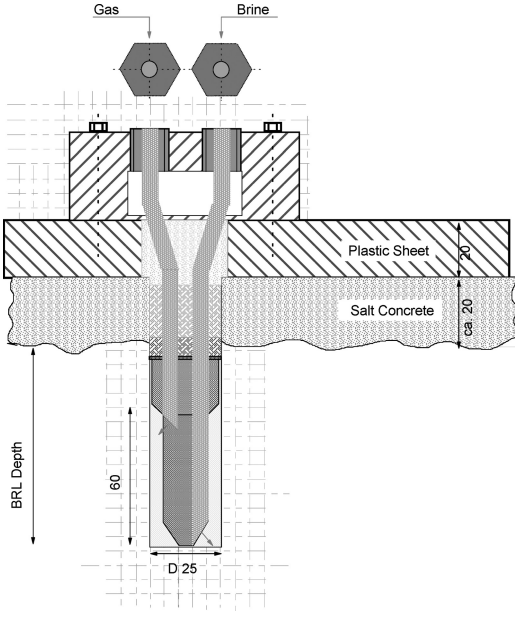

Figure 2. Cross section through a measurement borehole (dimensions in mm).

of the different test intervals is 40 to 900 mm below the surface of the salt floor, respectively. Two injection/ventilation tubes run from the open gallery into this interval. The borehole void above the plug is sealed with resin. Four additional boreholes (EL1–EL4) for installation of electrode chains were drilled and instrumented with 13 electrodes each. 16 surface electrodes were installed between the salt and the salt concrete layer to complete the geoelectric array. Electrode spacing is 0.1 m.

Each of the three test locations was equipped with one of these systems. The borehole and electrode arrangement is shown in Figure 1, and Figure 2 shows a cross section through a measurement borehole.

3 INVESTIGATION METHODS

The investigations performed comprise measurements of gas diffusivity and gas permeability as well as brine injection tests with geoelectric tracking of the brine.

3.1 *Gas diffusivity*

Right after installation of the test location the residual volume of each boreholes is purged and flooded at atmospheric pressure with a gas mixture of 2 vol% of helium, neon, krypton, iso-butane, and sulphur hexafluoride each (tracer gases) within the matrix of 90 vol% nitrogen. After about 10 days the gas in the residual volume is extracted and the composition with regard to the tracer components is determined by a gas chromatograph. Additionally, oxygen is determined in order get information about the tightness of the system. After the first extraction the residual volume is purged and flooded with the gas mixture again, but the second extraction and analysis is performed after about 50 days. The whole procedure is repeated with the third extraction and analysis after about 150 days.

With the results of the concentration of the tracer components the diffusivity is calculated using the finite element code ANSYS.

3.2 *Gas permeability*

Gas injection testing is performed in each of the five boreholes BRL1–BRL5 of the different test locations. Nitrogen is injected at a rate of 200 ml/min up to a maximum overpressure of 1 MPa, or to a steady stress state if this is reached at a lower borehole pressure. The pressure development in all boreholes is recorded during the injection and the subsequent shut-in phase.

The gas injection system comprises a PC-based data acquisition system with pressure transducers and a programmable flow controller/flowmeter. The pressure transducers are connected to the injection/observation boreholes; each one of the boreholes can

function as injection borehole by connecting a nitrogen tank via the flow controller/flowmeter. Injection rates of 20 ml/min up to 2000 ml/min and pressures up to 5 MPa are possible.

The recorded data are evaluated in terms of permeability using the computer code Weltest 200. It provides means to calculate the analytic solution to the diffusion equation or to numerically model pressure distribution in one- or two-dimensional models, and to iteratively minimize the deviation between the measured and calculated pressure data. For measurements with gas, the real pressure has to be transformed into the so-called pseudo-pressure $m(p)$ due to the highly pressure-dependent material properties of gas:

$$m(p) = 2\int_{p_i}^{p} \frac{p}{\mu(p)z(p)}\,dp$$

with the initial pressure p_i, the viscosity $\mu(p)$, and the z-factor $z(p)$.

The parameters affecting the calculated pressure development are the rock permeability, the rock porosity, the wellbore storage coefficient, and the skin factor. The skin factor accounts for an increased or decreased permeability of a zone close to the borehole wall, which can be due to the drilling procedure. No hints to such effects have been found in the relatively small permeability boreholes during earlier measurements; moreover, the whole rock close to the excavation is disturbed, so that no additional disturbance by drilling is regarded.

The calculated pressure curves are rather insensitive to changes in porosity. Therefore, the porosity is held constant at 0.2%. This is a likely value for the deeper boreholes, while the porosity around the boreholes very close to the drift surface will be higher, but increasing the porosity by a factor of ten has no significant influence on the best fit permeability. Wellbore storage is important during the injection phase and controls the peak pressure reached during injection. The pressure curve form, especially during the shut-in phase, is controlled by the permeability.

Gas injection tests are performed at different times before and after the diffusivity measurements, but prior to brine injection testing.

3.3 *Liquid injection testing*

For brine injection only the central borehole of each test arrangement is used. During a first injection campaign saturated brine is injected to saturate the pore space near the injection hole. A second injection is then evaluated in terms of permeability to brine, which can be done in a similar way as the gas injection tests. The brine used for injection is a saturated IP9 solution in order to minimize chemical interaction with the rock salt.

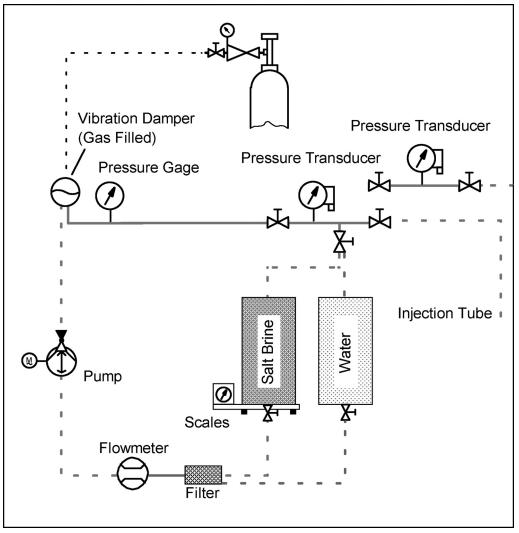

Figure 3. Liquid injection system.

The liquid injection system was developed and successfully used in the frame of an earlier project (Wieczorek & Zimmer 1998). A sketch is shown in Figure 3. Brine can be pumped into the test interval of the injection borehole via a filter and a flowmeter. Both the injection and the return tube are equipped with pressure transducers. The return tube is needed to let the gas out of the test interval. The amount of brine injected is measured by the flowmeter; additionally, the brine tank is put on scales providing backup information. The pump and flowmeter are laid out for injection rates between 200 and 1800 ml/min; the maximum injection pressure is 10 MPa. A water tank can be connected instead of the brine tank in order to be able to rinse the system.

3.4 *Geoelectric tomography*

The electric conductivity of porous rocks is determined by the pore liquid. Thus, geoelectric measurements for determination of electric resistivity and its changes are adequate for monitoring changes in the water content of such rocks. For rock salt, a broad database on the relation between resistivity and water content is available (Kulenkampf & Yaramanci 1993, Yaramanci 1994).

The geoelectric measurements are performed as dipole-dipole measurements: Two electrodes are used for injecting a low-frequency alternating current into the formation, while the resulting potential difference between pairs of other electrodes is measured, giving an apparent resistivity for each single measurement. The injection and measurement dipoles are located in the same or in different boreholes and on the surface

profiles. By varying both the injection dipole and the measurement dipole, a large number of single measurements is obtained.

The resulting data of the two vertical planes including the central liquid injection borehole (i.e., the plane including EL1, EL3, and BRL5 and the suface electrodes in between as well as the plane including EL2, EL4, and BRL5 and the corresponding surface electrodes; see Figure 1) are used as input for inverse finite element modelling using the computer code SensInv2D (Fechner 2001). From the vector of apparent resistivities the resistivity distribution in the considered plane is calculated as best fit between measured data and calculated response. The optimization method applied is the MSIRT (multiplicative simultaneous iterative reconstruction technique, Kemna 1995).

The measuring system is a automatic geoelectric apparatus for direct-current measurement which is capable of controlling up to 240 electrodes.

4 RESULTS

As the whole project is still running the results are preliminary. First results are available on gas diffusivity and permeability. Liquid injection tests are currently prepared in the test field, therefore, only the results of an earlier test with a similar borehole arrangement performed in the frame of the BAMBUS II project can be presented. Until the symposium the measurements will almost be finished and final results can then be presented.

4.1 *Gas diffusivity*

The gas diffusivity in the 20 years old floor close to the surface is in the range of 10^{-8} m^2 s^{-1} and decreases to the range of 10^{-9} m^2 s^{-1} at a distance of 70 cm to the surface. The drift floor after removal of a layer of 1 m thickness shows a gas diffusivity in the range of 10^{-9} m^2 s^{-1} close to the surface and decrease to the range of 10^{-10} m^2 s^{-1} at a distance of 70 cm.

Results of measurements on the drift floor two years after removal of a layer of 1 m thickness are not available yet.

4.2 *Gas permeability*

Gas injection tests in the 20 years old floor yield permeabilities up to the range of 10^{-15} m^2 a few centimetres below the surface, which decreases to about 10^{-17} m^2 at a depth of 0.7 m. This is in agreement with earlier measurements in the frame of the BAMBUS II project.

In contrast to these relatively high permeabilities found below the original floor, the measurements at the location where 1 m of salt below the floor had been removed yields permeability values of 10^{-18} m^2 directly below the mine floor, which decreases below 10^{-19} m^2 already at 0.3 m depth. This result agrees again with earlier BAMBUS II measurements, but with packer tests performed at depths of 1 m and more below the floor.

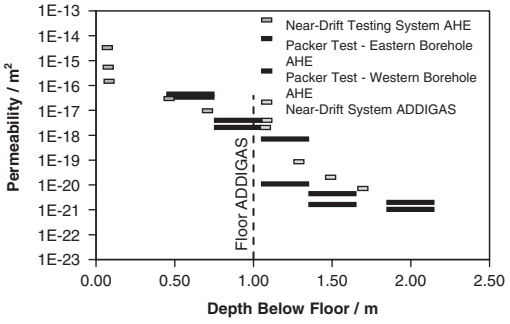

Figure 4. Permeability results obtained with the near drift testing system and packer tests below the original drift floor (AHE) and below the drift floor after removal of 1 m of salt (ADDIGAS).

Figure 4 illustrates these results. After removal of the EDZ, namely a package of 1 m below the drift floor, the original permeability is more or less kept.

The measurements at this location were performed first two months after EDZ removal. Repeating the measurements 14 months later showed no significant changes in permeability. This shows that EDZ removal is an effective method to improve seal performance.

4.3 *Liquid injection*

A liquid injection test performed in the frame of BAMBUS II (Bechthold et al. 2004) showed that all the brine (in total 8.8 l) injected into the central borehole of 10 cm depth remained in the upper 30 cm layer below the floor. This is illustrated by the Figures 5 and 6 which show the resistivity distribution in the rock before and after the brine injection: The geoelectric measurement performed prior to brine injection, Figure 5) shows a very smooth tomogram with resistivities of 10000 to 60000 Ωm and higher resistivities towards the sides and the lower border of the investigation area as effects of the model borders. The values are in the range of typical rock salt. After the brine injection a pronounced decrease of resistivity can be detected (Figure 6), but it is restricted to the uppermost 30 cm below the floor.

The resistivity of the moist zone ranges down to 200 Ωm which corresponds to a water content around 1 vol.%. Assuming a radial spread of the brine in a layer of 30 cm and a uniform water content of 1 vol.%, the radius of the moist zone would be 1 m, which is, again,

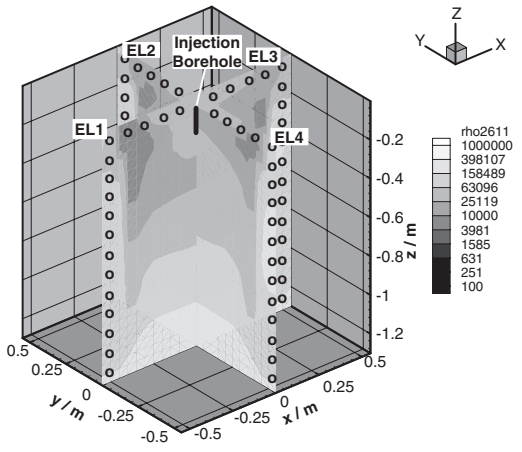

Figure 5. Resistivity tomograms of the near-surface testing arrangement obtained before a brine injection campaign (scale in Ωm).

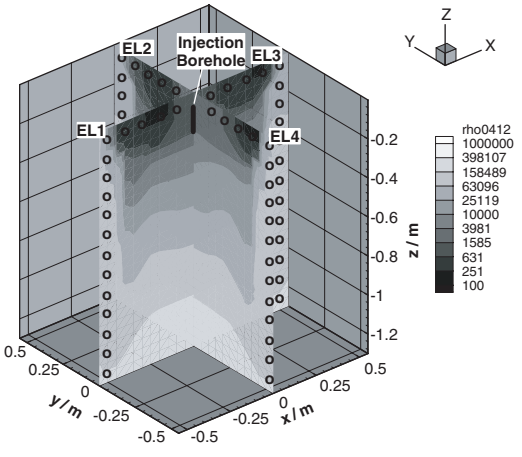

Figure 6. Resistivity tomograms of the near-surface testing arrangement obtained before after the brine injection campaign (scale in Ωm).

in good agreement with observations during injection (the side length of the sheet is 1.8 m, and the first centimetres of salt beyond the sheet became wet).

Since only partial saturation was reached during the brine injection test, the porosity of the uppermost decimetres of the salt has to be considerably higher than 1%.

5 CONCLUSIONS

From the results of the ongoing investigations of the advective flow and diffusion of the rock salt below the 20 years old drift floor and below the floor after removal of the EDZ the following preliminary conclusions can be drawn:

1. Both the permeability and the diffusivity of the salt below the floor are considerably higher if the EDZ is not removed.
2. After removal of the EDZ the hydraulic properties of the salt below do not change significantly within months, meaning EDZ removal is effective for improving seal performance.
3. EDZ permeability is highly anisotropic. Future brine injection tests will yield more information on this topic.
4. The employed methods of gas and brine injection and geoelectric tomography are suitable for obtaining relevant EDZ data.

ACKNOWLEDGEMENTS

The presented work was founded by the German Bundesministerium für Wirtschaft und Arbeit (BMWi) under the contract No. 02 E 9824 (ADDIGAS). The work performed in the frame of the BAMBUS II project was co-funded by the German Bundesministerium für Wirtschaft und Arbeit (BMWA) under contract No. 02E9118 and by the Commission of the European Communities (CEC) under contract No. FIKW-CT-2000-00051.

The authors would like to thank for this support.

REFERENCES

Bechthold, W., Smailos, E., Heusermann, S., Bollingerfehr, W., Bazargan Sabet, B., Rothfuchs, T., Kamlot, P., Grupa, J., Olivella, S., Hansen, F.D. 2004. *Backfilling and Sealing of Underground Repositories for Radioactive Waste in Salt (BAMBUS-II Project)*, EUR 20621, Commission of the European Communities.

Fechner, T. 2001. *SensInv2D-Manual*. Neuwied: Geotomographie.

Kemna, A. 1995. *Tomographische Inversion des spezifischen Widerstandes in der Geoelektrik.* Master Thesis, University Cologn.

Kulenkampf, J. & Yaramanci, U. 1993. Frequency dependent complex resistivity of rock samples and related petrophysical parameters. *Geophysical prospecting* Vol. 41, p 995–1008.

Wieczorek, K. & Zimmer, U. 1998. *Untersuchungen zur Auflockerungszone um Hohlraeume im Steinsalzgebirge.* Final Report, GRS-A-2651, Braunschweig: Gesellschaft fuer Anlagen- und Reaktorsicherheit (GRS) mbH.

Yaramanci, U. 1994. Relation of in situ resistivity to water content in salt rocks. *Geophysical Prospecting* Vol. 41, p 229–239.

Taylor & Francis
Taylor & Francis Group
http://taylorandfrancis.com

The Mechanical Behavior of Salt – Understanding of THMC Processes in Salt –
Wallner, Lux, Minkley & Hardy, Jr. (eds)
© 2007 Taylor & Francis Group, London, ISBN 978-0-415-44398-2

Investigations on damage and healing of rock salt

Otto Schulze
Federal Institute for Geosciences and Natural Resources (BGR), Hannover (FRG)

ABSTRACT: The dilatancy concept provides the criterion to decide whether creep deformation without volume increase or dilatant deformation with propagating damage will occur. Different observation methods are commonly used to detect dilatancy related effects. Since the different effects seem to suggest different dilatancy boundaries, the equations for the dilatancy boundary can be very different. We present our recent results and a comment on the various methods to detect dilatancy. The evolution of damage is discussed on the basis of the volumetric strain, and the energy to produce the irreversible volumetric strain yields a measure for the occurrence of failure. First results from our laboratory work on the compaction behavior of heavily damaged rock salt like that one in the EDZ are presented. Based on these results, the compaction and permanent healing are described by the evolution of the permeability during a transition from the dilatant into the non-dilatant stress domain.

1 INTRODUCTION

The deformation behavior of rock salt depends on different micro-mechanical processes. For the modeling of these processes by constitutive equations and for the prediction of the long-term behavior it is very important to distinguish between processes without dilatancy and those which are coupled with the evolution of dilatancy and damage, Figure 1.

The domain with no dilatancy, where compaction may occur, and the domain with dilatancy related effects are separated by the so-called dilatancy boundary. Of special concern are the processes like creep without dilatancy, softening by humidity induced creep and weakening by propagating damage, failure, and the recovery of damage by compaction and healing. The contribution of each of these processes to the deformation behavior is depending very sensitively on the stress state with respect to the boundary where dilatancy starts to occur.

In this context, the understanding of the competing processes of damage respectively compaction and healing is of vital importance for the performance of long-term safety analyses, where the evaluation of constitutive equations for the relevant processes and their integration into numerical models require consistent experimental data sets. The purpose of this paper is, to illustrate the progress of experimental work performed in the last decade in the BGR focusing on this item. After introducing the knowledge state of the dilatancy concept, the recent results of well documented experiments concerning creep and damage will be briefly discussed. The main part deals with our investigations on compaction and healing, where the term compaction is preferably used. The term healing should be reserved for the permanent compaction. Both terms are discussed on the basis of the

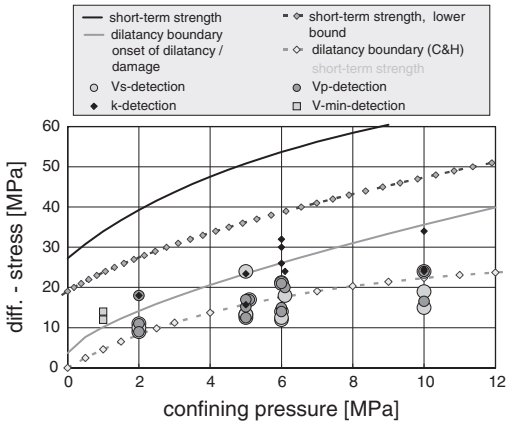

Figure 1. Short-term failure strength and the dilatancy boundary of rock salt derived from experimental investigations at BGR. For comparison the dilatancy boundary (C & H) of Cristescu & Hunsche (1998) is included. Generally, the dilatancy boundary separates the domain with dilatancy related processes from those related with compaction. The determination of the dilatancy boundary can be performed by the application of different detection methods: decrease of ultrasonic wave velocity Vs and Vp, onset of permeability k (Popp et al. 2001); minimum of volumetric strain V-min $= \varepsilon_{\mathrm{vol,min}}$.

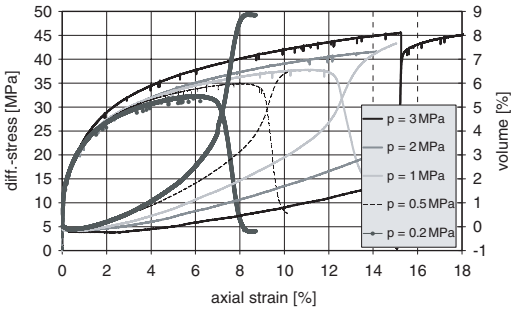

Figure 2. Evolution of diff.-stress and volumetric strain in dependence on the confining pressure during short-term strength testing (axial strain rate 1.0E-05 1/s; temperature $T = 30°C$) on rock salt of type "Speisesalz" from the Asse salt mine.

permeability and porosity measurements during the isostatic loading of pre-damaged rock salt.

2 THE DILATANCY BOUNDARY

The determination of the dilatancy boundary is generally based on short-term tests. During a common strength test on a cylindrical specimen in the loading geometry "compression", where the axial strain rate $\dot{\varepsilon}_1$, the confining pressure p_c, and the temperature T are kept constant and where the increase of the deviatoric stress $\Delta\sigma = \sigma_1 - p_c$, $\sigma_1 > p_c$, and of the volumetric strain ε_{vol} are measured to record the deformation behavior, the evolution of dilatancy is obvious. It develops very soon after the start of such a test. A set of results is given in Figure 2. The investigated rock salt is the so-called Speisesalz from the Asse salt mine. This rock salt consists of rather clean halite maintaining a good reproducibility of the test results. Nevertheless, the determination of the onset of dilatancy is a difficult task.

An example is given in Figure 3. The specimen is pre-compacted for two days at the isostatic pressure $p_{iso} = 20$ MPa. Then, the testing is performed at $T = 30°C$, $p_c = 1$ MPa, and at the strain rate 1.0E-05 1/s. After subtracting elastic compaction ($E = 36$ GPa; $\nu = 0.27$), the minimum of volumetric strain is defined as the point where the dilatancy starts to propagate.

The value $\Delta\sigma_{dil}(p_c = 1\ \text{MPa}) = 14$ MPa shows as an example the determination of the dilatancy boundary $\Delta\sigma_{dil}(p_c)$, see Figure 1, which includes a further test result with $\Delta\sigma_{dil}(p_c = 1\ \text{MPa}) = 12$ MPa at 1.0E–06 1/s.

To avoid the uncertainty in the determination of the minimum of the volumetric strain in these short-term strength tests and to check if the strain rate may affect the results, a set of stress controlled strength

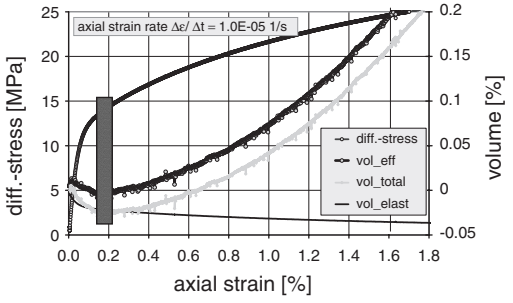

Figure 3. Determination of the dilatancy boundary by detecting the minimum of the volumetric strain (confining pressure $p_c = 1$ MPa; axial strain rate 1.0E-05 1/s; $T = 30°C$.

tests was performed where the deviatoric stress is increased step-wise from the non-dilatant into the dilatant domain. During these creep test intervals, the onset of dilatancy is just determined at the stress, where the volumetric strain starts to increase. The results are compiled in Figure 1 (see straight line, dilatancy boundary), resulting all together in the lines 'dilatancy boundary' and 'dilatancy boundary (C & H)'.

In this $\Delta\sigma$–p_c – diagram (loading geometry "compression"), the plotted lines represent the transformed equations of the short-term failure strength $\tau_{o,f}$

$$\tau_{o,f} = (-0.0201 \cdot \sigma_o^2 + 2.12 \cdot \sigma_o + 4.6562) / \sqrt{3} \qquad (1)$$

where

$$\tau_o = 1/3 \cdot [(\sigma_1 - \sigma_2)^2 + (\sigma_2 - \sigma_3)^2 + (\sigma_3 - \sigma_1)^2]^{1/2} \qquad (2)$$

$$\sigma_o = 1/3 \cdot (\sigma_1 + \sigma_2 + \sigma_3) \qquad (3)$$

the dilatancy boundary as derived by Cristescu & Hunsche (1998)

$$\tau_{o,\,D\text{-}CH} = 0.8996 \cdot \sigma_o - 0.01697 \cdot \sigma_o^2 \qquad (4)$$

and the dilatancy boundary as derived by the application of the technique with creep test intervals

$$\tau_{o,\,D} = b \cdot \sigma_o^{\,c} \qquad (5)$$

with $b = 2.61248/\sqrt{3}$ and $c = 0.78093$.
τ_o is the octahedral shear stress and σ_o the mean stress (Schulze et al. 2001).

In addition, the data point from Figure 3 is plotted and many data points from the work of Popp et al. (2001) who have used ultrasonic wave velocities (transversal Vs and longitudinal Vp) and the damage related increase of permeability to determine the dilatancy boundary. The results do not really match with the plotted lines for the dilatancy boundary. As stated in several contributions to the Luxembourg conference (Davies & Bernier 2005), the dilatancy boundary

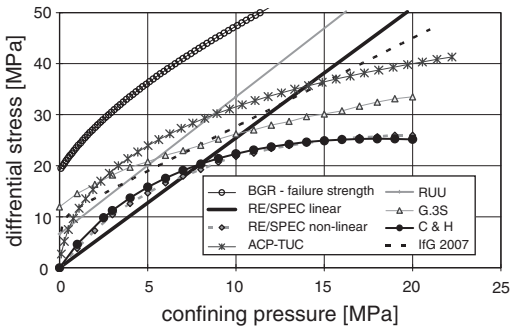

Figure 4. Compilation of the dilatancy of different working groups (extended after Hunsche 1998): RUU-Spiers et al. (1989); RE/SPEC-Van Sambeek et al. (1993); G.3S-Thorel & Ghoreychi (1996), C & H-Cristescu & Hunsche (1998); ACP-TUC-Alkan et al. (2007); IfG 2007-Günther & Salzer (2007).

is more a band than a distinct line. The different experimental techniques which are used to deform a specimen and to detect the onset of dilatancy as well as the specific behavior of different rock salt types may cause the broad band of uncertainty. In model calculations, this uncertainty may remain without a consequence, because the damage related evolution of strength and strain remain moderate as long as the state of stresses remains in the vicinity of the broad dilatancy boundary. But this point has to be investigated in more detail to receive reliable long-term predictions.

Hunsche & Schulze (2000) report that the dilatancy boundary can be modeled only as a function of stresses, the influence of other parameters (e.g. stress geometry, loading rate, type of rock salt) would be negligible. This would hold also for the equations published by other groups. The author is not aware of investigations with contradicting results.

A comprehensive compilation of the dilatancy boundaries from different working groups is given in Figure 4 (Hunsche 1998). For comparison the short-term failure strength, lower bound, is plotted (compare Figure 1). Figure 4 makes it obvious that more and high quality experimental work is needed to derive a stronger and more reliable criterion for the detection of the onset of dilatancy and the modeling of dilatancy related processes. In our present work we use Equation (5). But, for long-term safety analyses of a repository and underground structures which may depend more sensitively on dilatancy, Equation (4) is the more "conservative" one. As can be seen in Figure 1, this equation has some sound evidence.

3 CREEP

In our work, the deformation behavior of rock salt is described by the Composite Dilatancy Model (CDM) which was developed by Hampel et al. (2002) in close cooperation with BGR. At present, the CDM can describe the creep processes in the non-dilatant stress domain as well as damage, failure and the post-failure behavior of rock salt. But the further improvement and development has to include also the processes of compaction and healing.

For creep without volume change the Orowan equation is used to relate the macroscopic deformation rate to the dominant micro-mechanical processes

$$\varepsilon_{cr} \sim b \cdot \rho \cdot v \qquad (6)$$

where $\dot{\varepsilon}_{cr}$ is the macroscopic strain rate, b the Burgers vector of a gliding dislocation, $\rho = 1/r^2$ the density of gliding dislocations with mean distance r, and v their mean velocity. The velocity v itself depends on stress, temperature and the parameters of the microsubstructure, Q is the activation energy for dislocations, M the Taylor-factor for cubic crystal symmetry (fcc), Δ a the activation area for moving dislocations and σ^* the effective stress acting on these dislocations:

$$\varepsilon_{cr} = \frac{b}{M}\frac{1}{r^2} v_0 \exp\left(-\frac{Q}{RT}\right) \sinh\left(\frac{b\,\Delta a\,\sigma^*}{M\,k_B\,T}\right) \qquad (7)$$

In detail, Hampel et al. (2002) and Hampel & Schulze (2007) derive a set of formulas which describe the creep controlling micro-mechanical processes and the evolution of the affected parameters of the microstructure on basis of Orowan's equation.

4 DAMAGE

The deformation of rock salt in the dilatant stress domain generates damage. The evolution of damage is strongly coupled with the stress concentration at dislocation pile-ups. This causality is generally accepted (e.g. Munson et al. 1999). Therefore, in the CDM the evolution of damage is modeled as a function of the creep deformation. Since rock salt exhibits no brittle failure behavior, but even a ductile post-failure behavior, also this process is modeled as a function of the creep rate. Incorporating humidity induced creep, which takes place only in dilated rock salt, the total strain rate $\dot{\varepsilon}_{tot}$ is expressed by the creep rate $\dot{\varepsilon}_{cr}$ where the impact of the humidity induced creep on ductility is denoted by F_h, that of the damage (i.e. damage induced weakening/softening) by δ_{dam}, and that of the post-failure behavior by P_F

$$\dot{\varepsilon}_{tot} \sim P_F \cdot \delta_{dam} \cdot F_h \cdot \dot{\varepsilon}_{cr} \qquad (8)$$

In case of the deformation in the non-dilatant stress domain, these additional impact factors have the value of unity. The functions F_h and P_F are not discussed further in this paper. Details are outlined by Hampel & Schulze (2007).

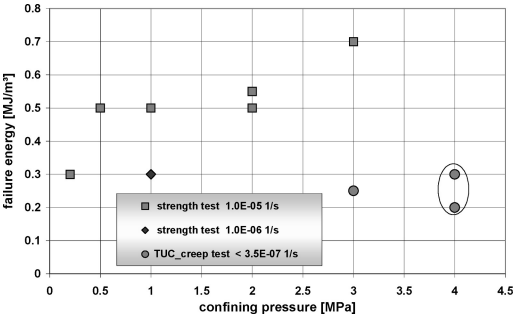

Figure 5. Damage energy at failure $d_{dam,f} = \int \sigma_o \cdot d\varepsilon_{vol}$ in dependence of the confining pressure (i.e. minimal principle stress) and the strain rate derived from short-term strength tests and two creep tests (Düsterloh, TUC). At the constant strain rate 1.0E-05 1/s the failure energy increases as the confining pressure is increased. On the other hand, reduction of deformation rate causes a reduced failure energy.

The damage function δ_{dam} depends on the irreversible volume change energy d_{dam} (briefly: damage energy) which evolves during the deformation under the conditions of the dilatant stress domain

$$\delta_{dam}\,(d_{dam}, \sigma_{min}) = \exp\,[\delta_1 \cdot (d_{dam}/\sigma_u)^{\delta_2 \cdot \sigma_{min}}] \quad . \qquad (9)$$

The parameters δ_1 and δ_2 are derived by adjusting the CDM to the results of the short-term failure strength tests, $\sigma_u = 1$ MPa.

Continuous damage causes failure. To model and predict failure, we use the post-failure function P_F which contains the parameter ε_F to denote the onset of failure. The parameter ε_F is empirically determined by the evaluation of the mentioned set of short-term failure tests. In addition to this empirical parameter ε_F Hunsche (1998) suggests to analyze the damage energy at failure. He postulates that failure will occur at a certain limit of the damage energy,

$$d_{dam,f} = \int \sigma_o \cdot d\varepsilon_{vol} \qquad (10)$$

where $d_{dam,f}$ is defined as a function of the mean stress σ_o, see Equation (3), and the volumetric strain

$$\varepsilon_{vol} = (V - Vo)/Vo = \Delta V/Vo. \qquad (11)$$

The initial volume of an undamaged or consolidated specimen is Vo and $\Delta V/Vo$ its relative volume change. Hunsche (1998) reports that the failure energy $d_{dam,f}$ ranges between 0.4 to 0.8 MJ/m^3, where the mean value, $d_{dam,f} = 0.7$ MJ/m^3, was found to depend not significantly on the type of the investigated rock salt or on other parameters like loading geometry, minimal principle stress, and loading rate.

To confirm these results and to improve the data basis for the further development of the CDM, the short-term tests in Figure 2 are used. In Figure 5, the determined failure energies are plotted in dependence on the confining pressure (i.e. minimal principle stress). The results of two creep tests are included (differential stress $\Delta\sigma \approx 40$ MPa; confining pressure $p_c \leq 4$ MPa; strain rates are 2.9E-07 1/s and 3.5E-07 1/s; temperature $T = 30°C$). The two creep tests are performed by U. Düsterloh, TU Clausthal (TUC). The new results exhibit a broader range, than Hunsche (1998) has reported. Therefore, the question arises whether the failure energy may depend on further parameters than just the mean stress σ_o and the accumulated volumetric strain ε_{vol}. The strength tests which are performed at 10^{-5} 1/s exhibit a clear trend, the failure energy increases as the confining pressure is increased. But it becomes also obvious that the failure energy decreases if the deformation rate is reduced, see the test result at 10^{-6} 1/s. In addition, this trend is confirmed by the results of the two TUC-creep tests where the failure energy is determined just before tertiary creep starts, i.e. at 3.5E-07 1/s and at 2.9E-07 1/s. Unfortunately, at present we can not measure the volumetric strain and therefore not determine the evolution of the damage energy at lower strain rates. This restriction results from the limits of resolution which, for instance, are caused by systematic errors resulting from unavoidable leakage in the device for the volume measurement during long-term testing (see Chapter 5.1).

Nevertheless, the reported range of the damage energy at failure $d_{dam,f}$ is nearly confirmed (Hunsche 1998). But the failure energy obviously has no constant value. In the investigated range of rather small confining pressures ($p_c \leq 4$ MPa), which is relevant for the evolution of damage in the excavation disturbed zone (EDZ), and at a constant deformation rate the failure energy $d_{dam,f}$ increases as p_c increases. On the other hand, $d_{dam,f}$ decreases if the applied deformation rate is reduced. With respect to these competing trends it has to be stressed that the damage energy at failure may not be a "conservative" measure for the prediction of the damage affected long-term creep failure, as long as this energy is derived from short-term strength testing at rather high minimal principle stresses and high deformation rates. However, for technical reasons, this is often the case in laboratory work.

The interrelation between the evolution of the damage energy d_{dam} and the occurrence of failure at ε_F (the parameter which denotes the onset of failure in the CDM so far) becomes evident by results like those plotted in Figure 6. During common short-term strength testing ($\dot{\varepsilon}_1 = 1.E\text{-}05$ 1/s; $T = 30°C$; $p_c = 1$ MPa) the flow stress $\Delta\sigma = \sigma_1 - p_c$ and the volumetric strain develop in the well-known manner. The evolution of $d_{dam} = \Sigma(\sigma_o \cdot d\varepsilon_{vol})$ is also plotted (not to scale). In all the analyzed strength tests, the determination of the rate of the damage evolution $\Delta d_{dam}/\Delta\varepsilon_1$ exhibits a rather constant slope, where the

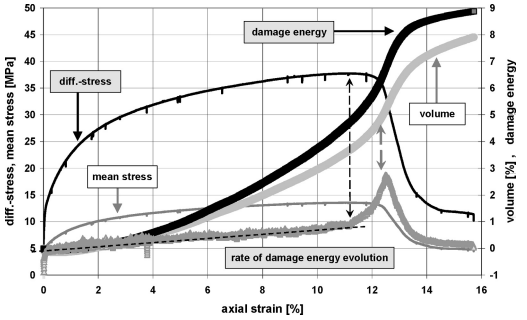

Figure 6. Evolution of flow stress (diff.-stress $\Delta\sigma = \sigma_1 - p_c$), mean stress σ_o, volumetric strain ε_{vol}, irreversible volume change energy $d_{dam} = \Sigma(\sigma_o \cdot d\varepsilon_{vol})$, and the rate of the damage energy evolution $\Delta d_{dam}/\Delta\varepsilon_1 = \Delta[\Sigma(\sigma_o \cdot d\varepsilon_{vol})]/\Delta\varepsilon_1$– the last two are not to scale. Peak strength is found to coincide with the end of the linear range of damage evolution rate, whereas its maximum occurs at the point of inflection of the strength curve in the post-failure range.

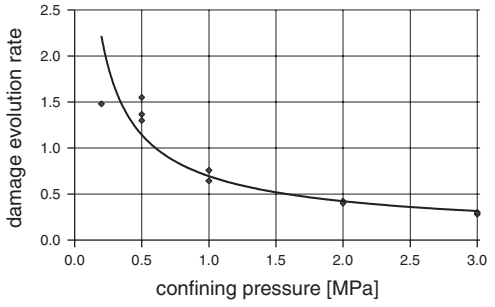

Figure 7. Rate of the damage evolution $\Delta d_{dam}/\Delta\varepsilon_1$ (arbitrary units) in the pre-failure range in dependence on the confining pressure p_c derived from short-term strength tests on rock salt (Asse – Speisesalz) at the strain rate 1.0E-05 1/s; T = 30°C.

deviation from this constant slope coincides with the peak strength at failure. In addition, we find that the slope of the damage evolution rate in this pre-failure range depends on the confining pressure (see Figure 7). These correlations may deliver a more reliable measure for the prediction of failure and the consecutive post-failure behavior than the empirical parameter ε_F. However, one has to keep in mind that the rate $\Delta d_{dam}/\Delta\varepsilon_1$ has its maximum when the post-failure range is already reached.

These results and the consequences for the prediction of the failure behavior need further investigations and improvements.

5 COMPACTION AND HEALING

After the end of excavation and back-filling the shear stress in the rock salt is continuously decreasing by creep until the isostatic state of stress is reached. Therefore, the state of stresses in the EDZ will consequently move from the dilatant into the non-dilatant domain. At last, this causes the re-compaction and the related decrease of the permeability in the rock salt of the EDZ.

It has to be stated that in this work the term "compaction" is generally used to describe the overall decrease of porosity and permeability. This term does not distinguish mechanically induced crack closure from true healing (due to mass transfer by chemical processes like solution and re-precipitation, recrystallization etc.). The latter will accomplish a recovery of the cohesion between crack planes. With respect to this definition we want to elaborate results for the evolution of the temporal compaction and the permanent healing of rock salt with long-term tests which should deliver a data base for the further and appropriate development of the CDM-system. To analyze the involved processes, we perform, for instance, isostatic compression tests on pre-damaged rock salt specimens where the temporal and permanent decrease of the volume (bulk porosity) and the evolution of the permeability are monitored.

5.1 *Experimental*

The pre-damage is normally produced during short-term strength tests like those in Figure 2. In our testing device, the volume increase is monitored continuously by a balance calculation on the oil volume in the Kármán cell (i.e. a triaxial pressure cell for a cylindrical specimen). So we can directly see which amount of dilatancy is reached and may be appropriate for the investigation of the compaction behavior. At the end of a test the dimensions of a specimen and the bulk density ρ are determined with high accuracy. Thus, the continuous volume measurement in the pressure cell is calibrated, i.e. it makes the indirect measure for the bulk porosity possible, where the porosity is defined by $\Phi = \varepsilon_{vol} = (V - Vo)/Vo = (\rho_o - \rho)/\rho$.

In addition, the evolution of porosity is calculated from the gas pressure in the pore system of a specimen, which decreases as the pore volume increases during the reduction of the isostatic pressure on the specimen and vice versa. This method for the calibration of the porosity measurements works properly only if the porosity related contribution to the bulk volume change (i.e. the bulk volume change minus the calculated elastic compaction of undamaged rock salt) is equal to the change in the gas accessible pore volume. In the following this is anticipated (Stormont & Daemen 1992). From these different calibrations we receive an uncertainty of $\Delta\Phi \leq 0.1\%$.

The permeability is measured by the gas pulse technique with dry nitrogen gas, where the method of Peach (1991) is used for the evaluation of the permeability.

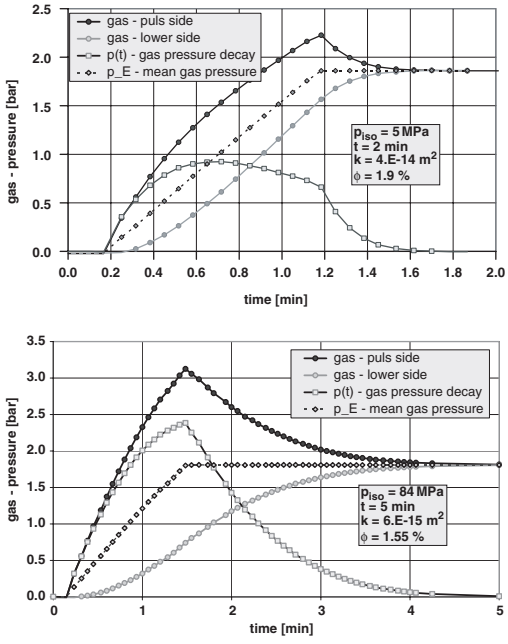

Figure 8. Gas pulse testing on pre-damaged rock salt during two steps of isostatic compaction. The examples demonstrate the decay of permeability k in dependence on the isostatic compaction pressure p_{iso}. Note, that the porosity Φ has also decreased during the isostatic loading on the rock salt specimen.

As an example, the determination of the permeability during an isostatic compaction test with two different testing sections is shown in Figure 8. A permeability only lower than $k = 1.E\text{-}13\,m^2$ can be measured with this technique, because at a higher permeability the gas pressure equilibrates through the specimen already during the pressure build-up in the top and bottom gas reservoirs V_1 and V_2. The complete course of the tests is depicted in Figure 11.

One has to keep in mind that the initial porosity of the pre-damaged specimen $\Phi_o(p_{iso} = 0) = 2.63\%$. It only decreases to $\Phi_{70}(p_{iso} = 0) = 2.36\%$ during the nearly 70 days of compaction testing. Thus, the permanent reduction at the end of the test at again $p_{iso} = 0$ MPa is just $\Delta\Phi(p_{iso} = 0) \approx 0.3\%$. In the last compaction step with $p_{iso} = 12$ MPa, the porosity has its minimum, Φ ($p_{iso} = 12$ MPa) = 1.36%. These changes can be measured quite well, but it becomes obvious that an improvement of the devices for the measurement of the porosity and of the continuous evolution of porosity during a stepped long-term compaction test is needed.

The Klinkenberg effect, i.e. the dependence of the permeability on the gas pressure, is studied in detail at the section with $p_{iso} = 10$ MPa. The results are

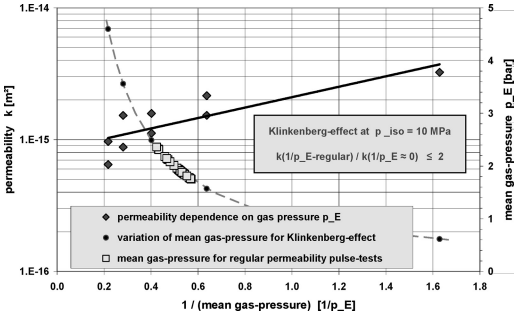

Figure 9. Dependence of the permeability k on the mean gas pressure p_E which is measured during an isostatic compaction test at $p_{iso} = 10$ MPa. The regular permeability tests are per-formed at a mean gas pressure of $p_E \approx 2$ MPa. Then, the correction with respect to the Klinkenberg-effect is negligible. Additionally, the range of the so-called mean gas pressure is indicated which is regularly applied during the performed long term compaction test.

plotted in Figure 9. Thus, this effect is nearly negligible: $k(1/p_E) = 0.9905 \cdot (1/p_E) + \ln(8.2E\text{-}16)$.

To avoid additional uncertainty, the gas pulse tests are performed with nearly always the same "mean gas pressure for regular permeability pulse tests", i.e. $p_E \approx 0.2$ MPa, see Figure 9, which makes a Klinkenberg correction unnecessary.

$$p_E = (p_1 \cdot V_1 + p_2 \cdot V_2) / (V_1 + V_2). \quad (12)$$

5.2 *Results*

The behavior of damaged rock salt during recompaction is investigated in detail with that specimen which already has a volumetric pre-damage of $\varepsilon_{vol} = (\rho_o - \rho)/\rho = \Phi_o(t = 0, p_{iso} = 0) = 2.63\%$. This dilation was produced during a long-term uniaxial strength test (constant strain rate 1.0E-08 1/s; $T = 22°C$; $\sigma_{1,max} = 26$ MPa; $\varepsilon_1(\sigma_{1,max}) = 10\%$; testing time about 110 days). The uniaxial compression is performed at a relative humidity of 20% r.h. and the interim storage of the tested specimen at a humidity of less than 40% r.h., i.e. at a rather dry condition. The damage energy is $d_{dam} \leq 0.2$ MJ/m³.

The compaction is performed at $T = 30°C$ by the application of an isostatic pressure which is increased stepwise up to $p_{iso} = 12$ MPa and then decreased in steps again (whole testing time: ~ 70 d). Isostatic loading of the dilated specimen results in a spontaneous but rather small decrease of permeability respectively porosity, as can be seen in Figure 10 and Figure 11. During constant loading sections, the porosity and the permeability are further decreasing, where a short transient behavior with a more rapid decrease in the first stage of a section is detected until a more or less stationary decrease is obtained. The time dependence is plotted in Figure 11.

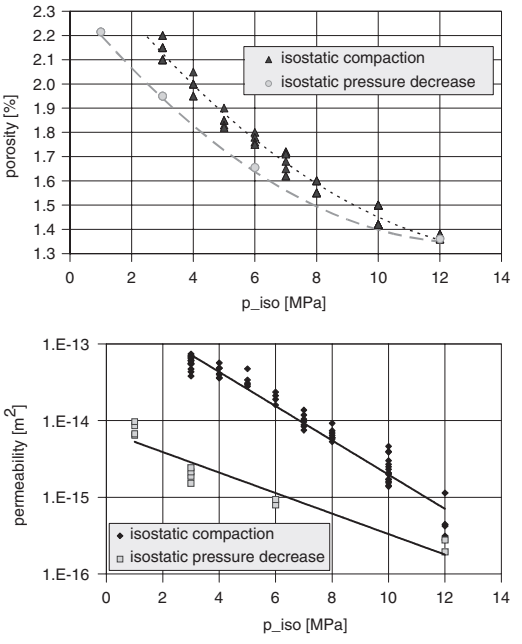

Figure 10. Evolution of the general trends of the porosity (upper part) and the permeability (lower part) in dependence on the stepped isostatic pressure, where the time dependence is dominant (Figure 11). Permanent decrease of porosity and of permeability (i.e. healing) is obvious.

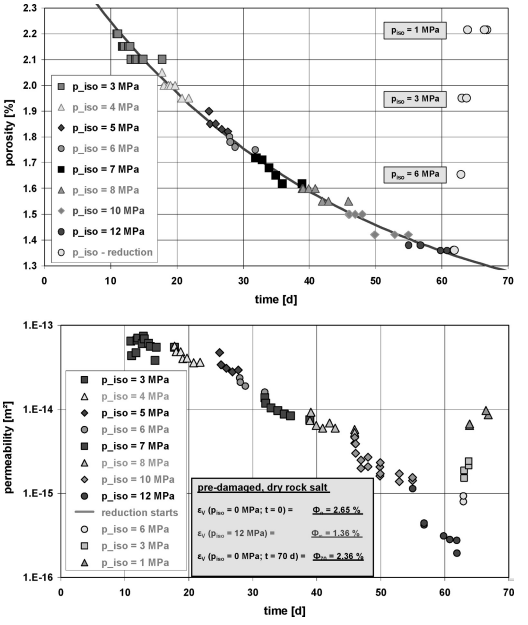

Figure 11. Evolution of porosity (upper part) and permeability (lower part) in dependence on time during stepped isostatic loading with a time dependent transient compaction and decrease of the permeability, but a spontaneous decompaction and permeability increase after 61 days of compaction.

However, stepwise unloading of the sample results in a spontaneous increase of both, permeability and porosity, which partially restores the initial state of dilatancy.

Therefore, Figure 10 and Figure 11 clearly demonstrate that the permanent volume decrease (i.e. real healing) remains small, which is directly confirmed by the measurement of the specimen's volume after this compaction test, $\Delta\Phi = 2.63\%–2.3\% \approx 0.3\%$. In between, the porosity decreases to $\Phi(p_{iso} = 12\,\text{MPa}) = 1.3\%$. The permanent decrease in permeability achieves one order of magnitude, but decreases in between about three orders of magnitude during the stepwise increased isostatic pressure.

The variation of the consecutive measured porosity and permeability during the compaction respectively de-compaction cycle is compiled in Figure 12. In the double-logarithmic plot the relation between permeability k and porosity Φ follows straight lines, in accordance to a power law $k = A \cdot \Phi^n$ (Stormont & Daemen 1992). But the slopes are rather different with $n(+) \approx 10$ in case of the stepwise increase of the isostatic pressure up to $p_{iso} = 10\,\text{MPa}$ (dark solid line) and $n(-) \approx 7.4$ in case of the stepwise reduction of the isostatic pressure (light solid line). In the testing section $p_{iso} = 12\,\text{MPa}$ the slope in the $k = A \cdot \Phi^n$ – relation is much steeper (dashed line). In a first attempt, the hysteresis between the k-Φ-trend lines is attributed to permanent compaction (i.e. healing).

For comparison, the permeability-porosity relation of Popp (2002) is plotted which is mainly derived from the k-Φ-data of strain rate controlled strength tests. As already recommended by Stormont & Daemen (1992), an appropriate k-Φ-relation has to comprehend two processes. The basic idea is as follows. During loading in the dilatant stress domain micro-cracks are generated, which will progressively interconnect, causing a steep increase in the k-Φ-relation. Afterwards, the micro-cracks of the interconnected net-work can widen, but for reasons of geometry this process has a minor influence on the slope in the permeability-porosity relation.

Popp (2002) and Heemann & Heusermann (2004) have accordingly developed a model which separates the two branches by the determination of a transition point (tp) which depends on the minimal principal stress (i.e. the confining pressure p_c). Therefore, their modeling cares for the dependence of the permeability-porosity relation on the confining pressure p_c during the loading in the dilatant stress domain:

$$k = k_{tp} / [(\Phi/\Phi_{tp})^{-n_1} + (\Phi/\Phi_{tp})^{-n_2}] \qquad (13)$$

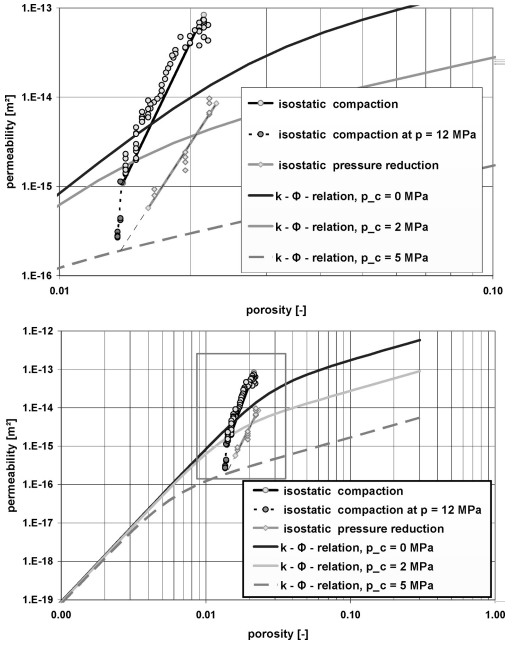

Figure 12. Evolution of permeability in dependence on porosity during isostatic compaction. Dark solid line represents measurements during the stepwise increase of the isostatic pressure $p_{iso} \leq 10$ MPa, dark dashed line those during the section with $p_{iso} = 12$ MPa, and light solid line those during the reverse cycle, i.e. the stepwise reduction of p_{iso}. For comparison, the evolution of permeability and porosity during loading in the dilatant stress domain is plotted (Popp 2002, Heemann & Heusermann 2004), where the modeling of the k-Φ-relation cares for the dependence on the confining pressure p_c.

with the exponents n_1 and n_2 for the first and second part of the k-Φ-relation, $k_{tp} = a_k \cdot \exp(b_k \cdot p_c)$ and $\Phi_{tp} = a_\Phi \cdot \exp(b_\Phi \cdot p_c)$ define the transition points of permeability and of porosity, a_k, b_k, a_Φ, b_Φ are parameters of the transition point.

In case of a progressive loading in the dilatant stress domain, the sensitivity of the permeability on the propagating porosity results in $n_1 = 4$ at the beginning of damage and converges down to $n_2 = 1$ after passing the transition point, in contrast to the slope of $n(+) \approx 10$ during the isostatic compaction or $n(-) \approx 7.4$ during the pressure reduction. Therefore, the evolution of the permeability during progressive damage and its dependence on the consecutive increase of volume and porosity is obviously different from the one during the isostatic compaction or the pressure reduction in the non-dilatant stress domain.

5.3 *Discussion*

During deviatoric loading in the dilatant stress domain, where the dilatancy and the permeability are increasing, the evolution of the permeability is often described as a function of the volumetric strain (i.e. porosity), but also by more sophisticated models concerning the evolution of the crack geometry and crack topology as well as their impact on transport properties (e.g. Peach 1991; Stormont & Daemen 1992; Alkan & Pusch 2003).

Anyway, a prerequisite for a reliable permeability-porosity relation, like that of Equation (13), is the knowledge about the evolution of the volumetric strain. In the ductile rock salt, the porosity is increasing if deformation takes place under the conditions of the dilatant stress domain. As already mentioned (chapter 4), the evolution of damage is strongly coupled with dislocation controlled deformation processes. Based on the results of Hunsche & Schulze (2000) the stress-dependent function $r_v(\tau_o, \sigma_o)$ is determined which relates the volumetric strain rate $\dot{\varepsilon}_{vol}$ to the rate of pure dislocation creep $\dot{\varepsilon}_{cr}$

$$\dot{\varepsilon}_{vol} \sim r_v(\tau_o, \sigma_o) \cdot \dot{\varepsilon}_{cr} \tag{14}$$

Thus, using a constitutive law for the creep behavior of rock salt, as defined in Equation (6) (Hampel & Schulze 2007), the evolution of the porosity during loading in the dilatant stress domain can be calculated and the coupled evolution of the permeability is predictable by the application of a reliable k-Φ-relation like that one of Equation (13).

But, concerning the reported compaction behavior of pre-damaged dry rock salt, the results make obvious that other processes are responsible for the development of the porosity and the permeability than creep performed by dislocations. This process is the basis for Equation (14). The main difference results from the fact that the porosity and the permeability already decrease during loading with the application of an isostatic pressure. The application of a deviatoric stress in the non-dilatant stress domain and therefore dislocation processes may have an additional influence on the compaction behavior, but this is not investigated in this work.

Peach (1991) performed a similar compaction experiment on dry rock salt. Pre-damage is $\varepsilon_{vol} = 1.3\%$ which is produced during a short-term triaxial strength test (strain rate 4.5E-05 1/s; room temperature; $p_c = 5.1$ MPa; $\Delta\sigma_{max} = 45$ MPa; $\varepsilon_1(\Delta\sigma_{max}) = 10\%$; testing time approx. 40 min). On basis of his results (reported in Fig. 3.23, Fig. 3.27, and Fig. 3.28, for instance) the author states that the decrease in permeability can be described by an elastic closure model like that of Walsh (1981)

$$(k/k_o)^{1/3} \sim \log(p/p_o) \tag{15}$$

k_o is the initial permeability, p_o the initial isostatic pressure.

Indeed, in that work the permeability decreases spontaneously as soon as the isostatic pressure is increased. On the other hand, Peach (1991) also reports that his measurements on the permeability behavior exhibit a time dependent decrease of the permeability during a testing section where the isostatic pressure is kept constant (reported in Fig. 3.25 and Fig. 3.26).

The comparison of these results with those of Figure 10 and Figure 11 shows in a preliminary conclusion that in this work no significant dependence on the stepped isostatic pressure increase can be detected – neither for the porosity nor for the permeability. Instead, the porosity as well as the permeability are smoothly decreasing with time, although the observation period is limited to just some months. In Figure 10 the porosity and the permeability do decrease during compaction in a section where the isostatic pressure is kept constant, but there is no stepwise decrease when the next step in the isostatic loading program is started. Thus, the time dependence seems to be dominant for the compaction behavior. In this work, this is valid for the decrease of the porosity and the permeability.

It has to be stressed that in both investigations the clean rock salt from the Asse mine, Speisesalz horizon, is used. One reason for the observed differences with respect to a poro-elastic behavior (Equation 15) can result from the rather different deformation rates during the preceding damage treatments by strength testing in the dilatant stress domain, i.e.:

$\Delta\varepsilon_1/\Delta t = 4.5\text{E-}05$ 1/s; $\Delta\sigma_{max} = 45$ MPa; $\varepsilon_{1,max} = 10\%$; $p_c = 5.1$ MPa; Peach (1991)
$\Delta\varepsilon_1/\Delta t = 1.0\text{E-}08$ 1/s; $\Delta\sigma_{max} = 26$ MPa; $\varepsilon_{1,max} = 10\%$; uniaxial testing; this work.

But the properties of the micro-crack network and the influence of different crack patterns on the compaction behavior in relation to time and pressure are not investigated in this work.

In a preliminary attempt the measured compaction behavior is analyzed more in detail. For this purpose, the normalized permeability k/k_o is plotted versus the time $(t-t_o)$ for each section, where the isostatic pressure is kept constant, see Figure 13. The permeability k_o is that at the start of a section at time t_o.

In the section with $p_{iso} = 3$ MPa, the interpolation line shows that only a moderate decrease of the permeability is detected. But in this first testing section, a transient settlement of the devices may cause this result. From a technical point of view, the sections with $p_{iso} = 4$ MPa to $p_{iso} = 10$ MPa are the more reliable. Here, the resulting behavior does not allow to deduce a pressure dependent evolution. Within the limits of uncertainty, the time constant A in the $\ln(k/k_o) = A \cdot (t-t_o)$ – relation, which is the basis for the lines in Figure 13, remains always the same. Whereas in the section with $p_{iso} = 12$ MPa, the influence of the pressure becomes significant. This

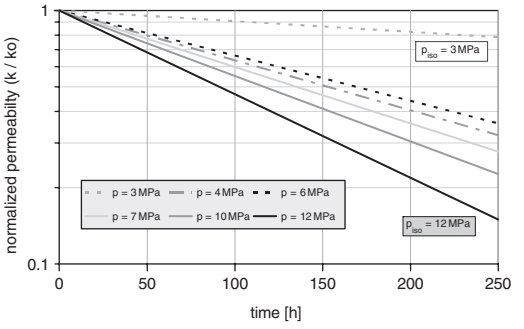

Figure 13. Evolution of normalized permeability $\ln(k/k_o) = A \cdot (t-t_o)$ in dependence on time $(t-t_o)$ during different testing sections with constant isostatic pressure p_{iso} where k_o is the permeability at the beginning of a section at time t_o.

deviation from the preceding compaction behavior becomes also obvious in Figure 12, there the slope of the k-Φ-relation is much steeper in the section with $p_{iso} = 12$ MPa than in the sections with the lower pressures. Peach (1991) argues that additional processes like creep assisted crack closure may significantly contribute to the compaction, when the isostatic pressure is increased to a certain limit. Nevertheless, a poro-elastic Walsh-model is not applicable for the ductile rock salt.

One has to keep in mind that in the rock salt of the EDZ the initial state of stresses will be in the dilatant stress domain and will slowly move into the non-dilatant stress domain. This process depends on the convergence of the underground openings and the stress redistribution in the EDZ, both are controlled by long-term creep. Therefore, the compaction behavior at low isostatic pressures should be of special interest. If a sensitivity parameter n in accordance to $k \sim \Phi^n$, which is determined in the steeper branch, i.e. at a relative high isostatic pressure, is used for the long-term prediction, the impact of compaction on the permeability decrease may be seriously overestimated.

Instead of Equation (14), which allows to describe the development of damage and volume increase in the dilatant stress domain, an equation has to be applied which depends on the asymptotically decreasing porosity itself. For the interpolation of the porosity data, which are plotted in Figure 11, Equation (16) is used

$$\dot{\varepsilon}_{vol} = -B \cdot (\varepsilon_{vol} - \varepsilon^*_{vol})$$
$$\varepsilon_{vol}(t) = (\varepsilon_{vol,\,t=0} - \varepsilon^*_{vol}) \cdot \exp[-B \cdot (t - t_o)] + \varepsilon^*_{vol} \qquad (16)$$

where B is the time constant for the compaction rate $\dot{\varepsilon}_{vol}$; ε^*_{vol} the residual porosity at infinite time and $\varepsilon_{vol,t=0}$ the porosity at the start of the compaction. This equation yields a basis for the further investigation and

interpretation of the compaction behavior of damaged rock salt.

The interpretation of the behavior of porosity and permeability in case of a reduction of the pressure remains an open question. A unique poro-elastic modeling can't predict the measured permanent decrease of the porosity as well as of the permeability (i.e. permanent healing which develops even in dry rock salt). But in general, the state of in-situ stresses will not move backwards into the direction of the dilatant stress domain. Therefore, our future work will be concentrated on the improvement of the experimental technique to monitor the evolution of damage at rather low deformation rates and on the compaction behavior of the damaged rock salt at rather low stresses which are of relevance for the in-situ conditions. These items seem to be most important for the improvement of the constitutive equations which are needed for the prediction of the restoration of the barrier function in the EDZ.

6 CONCLUSIONS

The prerequisite for the prediction of damage and healing of rock salt is the knowledge of the dilatancy boundary which yields the criterion whether dilatation or compaction is dominating.

The processes, which are active in the dilatant stress domain and which produce damage, are described by the CDM-system. This constitutive model is based on micro-mechanical deformation processes which are controlled by dislocation mechanisms.

The investigation on the compaction and healing behavior of pre-damaged dry rock salt shows that the decrease of the porosity and the permeability is primarily time dependent. The isostatic pressure has a minor influence.

The relation between permeability and porosity can be described by a power law $k \sim \Phi^n$. The sensitivity (i.e. the exponent n) during compaction in the non-dilatant stress domain is much greater than in case of progressing damage during loading in the dilatant stress domain.

The principal challenges remaining for the understanding of the coupled processes of damage and compaction respectively healing in rock salt are:

- Further long-term compaction tests at moderate stresses are needed with the consecutive measurement of permeability and porosity. The testing duration has to be much longer than several month, otherwise the empirical equations for the extrapolation of the compaction behavior cannot be checked.
- Development of generally agreed constitutive models for the compaction of dilated rock salt.
- Implementation in numerical codes, which facilitate reliably extrapolations to in-situ conditions.
- Understanding of physical processes which control the efficiency of healing in dilated rock salt with respect to humidity effects.
- The impact of a pore-pressure (gas respectively salt solutions), i.e. chemical and hydraulic interaction.

ACKNOWLEDGEMENT

The author is indebted to Andreas Hampel and Till Popp for fruitful discussions.

REFERENCES

Alkan, C., Y. Cinar & G. Pusch 2007. Rock salt dilatancy boundary from combined acoustic emission and triaxial compression tests. *Int. J. Rock Mech. & Min. Sci.* 44: 108–119.

Alkan, H. & G. Pusch 2005. Percolation Model of the Excavation Damaged Zone in Rock Salt. In C. Davies & F. Bernier (eds.), *Impact of the excavation disturbed or damaged zone (EDZ) on the performance of radioactive waste geological repositories, Proc. of a European Commission Cluster conference and workshop, Luxembourg, 3 to 5 November 2003*: 245–249. EUR 21028 EN.

Cristescu, N. & U. Hunsche 1998. *Time effects in rock mechanics.* Series*: Materials, modelling and computation*. Chichester (UK): John Wiley & Sons.

Davies, C. & F. Bernier (eds.) 2005. *Impact of the excavation disturbed or damaged zone (EDZ) on the performance of radioactive waste geological repositories. Proc. of a European Commission Cluster conference and workshop, Luxembourg, 3 to 5 November 2003*. EUR 21028 EN.

Günther, R.-M. & K. Salzer 2007. A model for rock salt, describing transient, stationary, and accelerated creep and dilatancy. In K.-H. Lux, W. Minkley, M. Wallner, & H.R. Hardy, Jr. (eds.), *Basic and Applied Salt Mechanics; Proc. of the Sixth Conf. on the Mech. Behavior of Salt. Hannover* 2007. Lisse: Francis & Taylor (Balkema). (this issue).

Hampel, A. & O. Schulze 2007. The Composite Dilatancy Model: A constitutive model for the mechanical behavior of rock salt. In K.-H. Lux, W. Minkley, M. Wallner, & H.R. Hardy, Jr. (eds.), *Basic and Applied Salt Mechanics; Proc. of the Sixth Conf. on the Mech. Behavior of Salt. Hannover* 2007. Lisse: Francis & Taylor (Balkema). (this issue).

Hampel, A. & U. Hunsche 2002. Extrapolation of creep of rock salt with the composite model. – In N.D. Cristescu, H.R. Hardy, Jr., R.O. Simionescu (eds.), *Basic and Applied Salt Mechanics; Proc. of the Fifth Conf. on the Mech. Behavior of Salt, Bucharest* 1999: 193–207. Lisse: Balkema.

Heemann, U. & S. Heusermann 2004. Theoretical and experimental investigation on stresses and permeability in the BAMBUS project. In *DISTEC 2004, Disposal Technologies and Concepts, International Conference on Radioactive Waste Disposal, April 26–28, 2004 Berlin*: 481–488. Conference Proceedings.

Hunsche, U. & O. Schulze 2000. Measurement and Calculation of the Evolution of Dilatancy and Permeability in Rock Salt. – In O. Kolditz et al. (eds.), *Proc. 3. Workshop Kluft-Aquifere "Gekoppelte Prozesse in Geosystemen", Hannover, Nov. 2000,* 60/2000: 107–113; Inst. f. Strömungsmechanik u. Elektr. Rechnen im Bauwesen der Uni. Hannover.

Hunsche, U. 1998. Determination of the dilatancy boundary and damage up to failure for four types of rock salt at different stress geometries. In M. Aubertin & H.R. Hardy, Jr. (eds.), *The Mechanical Behavior of Salt IV; Proc. of the Fourth Conf., Montreal* 1996: 163–174. Clausthal: Trans Tech Publications.

Munson, D.E., K.S. Chan & A.F. Fossum 1999. Fracture and healing of rock salt related to salt caverns. *SMRI-Meeting paper, April 14–16, 1999, Las Vegas (NV).* Solution Mining Research Institute.

Peach, C. 1991. *Influence of deformation on the fluid transport properties of salt rocks.* Geologica Ultraiectina No.77. Rijksuniversiteit Utrecht.

Popp, T. 2002. Transporteigenschaften von Steinsalz. *Meyniana* 54: 113–129.

Popp, T., H. Kern & O. Schulze 2001. The evolution of dilatancy and permeability in rock salt during hydrostatic compaction and triaxial deformation. *J. Geophys. Res. – Solid Earth* 106, No B2: 4061–4078.

Schulze, O., T. Popp & H. Kern 2001. Development of damage and permeability in deforming rock salt. In Ch. Talbot & M. Langer (eds.) *Special Issue on Geosciences and Nuclear Waste Disposal. Engineering Geology* 61: 163–180. Amsterdam: Elsevier.

Spiers, C.J., C.J. Peach, R.H. Brzesowsky, P.M. Schutjens, J.L. Liezenberg & H.J. Zwart 1989. Long-term rheological and transport properties of dry and wet salt rocks. *Final Report, Nuclear Science and Technology, Commission of the European Communities*. EUR 11848 EN.

Stormont, J.C. & J.J.K. Daemen 1992. Laboratory study of gas permeability changes in rock salt during deformation. *Int. J. Rock Mech. Min. Sci. & Geomech. Abst.* 29: 325–342.

Thorel, L. & M. Ghoreychi (1996). Rock salt damage – experimental results and interpretation. In: M. Ghoreychi, P. Bérest, H.R. Hardy, Jr. & M. Langer (eds.), *The mechanical behaviour of salt. Proc. of the Third Conf., Palaiseau (France)* 1993:175-189. Clausthal: Trans Tech Publications.

Van Sambeek, L., A. Fossum, G. Callahan & J. Ratigan 1993. Salt mechanics: Empirical and theoretical developments. In H. Kalihana, H.R. Hardy, Jr, T. Hoshi & K. Toyokura (eds.), *Proc. Seventh Symp. on Salt, Kyoto (Japan)* 1992(1): 127–134. Amsterdam: Elsevier.

Walsh, J.B. 1981. Effect of pore pressure and confining pressure on fracture permeability. *Int. J. Rock Mech. Min. Sci. & Geomech. Abstr.* 18: 429–435.

Taylor & Francis
Taylor & Francis Group
http://taylorandfrancis.com

The Mechanical Behavior of Salt – Understanding of THMC Processes in Salt –
Wallner, Lux, Minkley & Hardy, Jr. (eds)
© 2007 Taylor & Francis Group, London, ISBN 978-0-415-44398-2

The influence of humidity on microcrack processes in rock salt

Jürgen Hesser & Thomas Spies
Federal Institute for Geosciences and Natural Resources (BGR), Hanover, Germany

ABSTRACT: Field measurements of acoustic emission in salt mines indicate significant influence of humidity of the mine air on the microcrack activity in the rock mass, e.g. as mild seasonal variations in long-term measurements and as strong variations during the backfilling of large rooms with salt concrete. Laboratory tests were performed to gain more knowledge about this humidity induced microcrack processes in rock salt. Results of mechanical and ultrasonic measurements in the tests are presented and interpreted. The decrease of the flow stress and the rising activity of the acoustic emissions as a consequence of rising humidity in the experiments were caused by the reduction of the cohesion of the rock salt sample due to penetration of moisture into open microcracks and pores of the dilated sample.

1 INTRODUCTION

Underground cavities are mined for mineral extraction, the purpose of infrastructure, the storage of fluids and for the disposal of toxic or radioactive waste, for instance. In any of these cases the safe construction and operation of the cavities are necessary as well as the long-term safety after the closure of disposal mines. Therefore geomechanical investigations have to be performed with the aim to predict the state of stresses and the deformation with regard to the mechanical stability and hydraulic integrity of the rock mass. Under these aspects, especially the detection and monitoring of zones with the generation and development of microcracks or macrofractures are very important tasks in geomechanics (Heusermann 2001).

There were many investigations on the thermomechanical behaviour of rock salt in the last decades with the result that the physical mechanisms are very well-known which control the distinct nonlinear behaviour of rock salt. They are already described in different constitutive models (Menzel & Schreiner 1977, Hunsche & Schulze 1994, Cristescu & Hunsche 1993, Hou 1997) with application in different numerical codes. The influence of humidity on the creep deformation of rock salt was included in the constitutive model of Schulze (Hunsche & Schulze 2001). On this basis reliable predictions of the deformation and stress behaviour in the long-term are possible.

But there is still the question left of understanding the influence of humidity on the evolution of the damage of the micro- and macrostructure. This requires specific laboratory testing and field experiments as well as continuous measurements of deformation and stresses in existing mines. In this context acoustic emission measurements and active ultrasonic measurements are very useful methods as they provide results on damage of the rock with high sensitivity and resolution (Budzinski et al. 2004, Spies 2001).

Observations in salt mines including acoustic emission measurements, presented in this paper, show that variations of the relative humidity of the mine air seem to have an influence on the micro-crack activity in rock salt. To understand the fundamental processes in the rock mass which might be initiated by the humidity, special laboratory investigations were performed. The combined interpretation of field and laboratory results provide a basis for the understanding of the humidity induced processes in rock salt with special regard to microcrack generation and strength.

2 EVIDENCE FROM FIELD MEASUREMENTS

Since 1994 acoustic emission measurements are used for the long-term monitoring of the rock mass in the repository for radioactive waste in Morsleben (ERAM), Germany (Spies et al. 2004). These measurements are performed in different mine sections and the results are used as a contribution for the evaluation of integrity and stability.

In one of the observed mine sections, the results of the measurement show a clear seasonal variation of the acoustic emission activity (see figure 1 with time period from January 1998 to December 2002).

In the months of summer the acoustic activity was always on a high level while in winter and spring

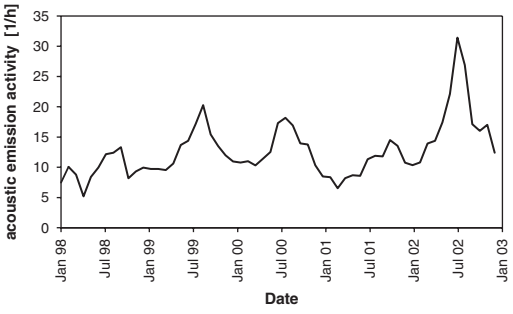

Figure 1. Seasonal variations of the acoustic emission activity in a mine section far away from the shafts.

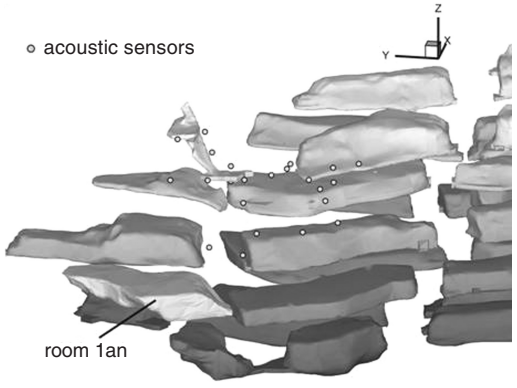

Figure 2. Cavities in the mine section with locations of the acoustic sensors.

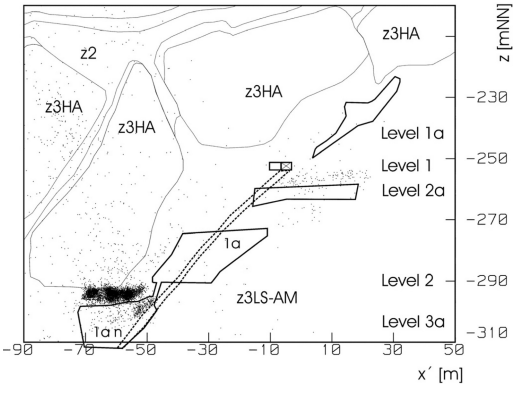

Figure 3. Locations of the acoustic emissions during one week while backfilling the room 1an at level 3a with salt concrete.

there was a low acoustic emission activity. A detailed evaluation of the measurement data shows that the additional events in summer are located in pillars and in the contour zones of the cavities.

Because there was no mining activity in this mine section during the observation time, climatic conditions were assumed to influence the acoustic emission activity. Based on information from the staff at the repository, we know that temperature changes by only about ±2°C during the whole year in the mine section. But the relative humidity amounts to about 20% in winter and increases up to 60% in summer. This oscillation of the relative humidity correlates very well with the oscillation of the acoustic emission activity. Therefore significant influence of humidity due to seasonal variations on acoustic emission activity is expected. Similar observations from long-term acoustic emission measurements in the Asse salt mine are reported by Spies et al. (1997).

Currently the mine is prepared for its sealing and closure, and so several rooms in the ERAM are backfilled with salt concrete since September 2003. An intensive observation have been done to get knowledge and experience about the deformation processes and load redistribution in the rock mass effected by changes of temperature and humidity due to the filling of cavities with salt concrete. One of the large rooms, called room 1an, was backfilled from September 2003 till March 2004. It is located at Level 3a. Especially in this case the measurement of acoustic emission was performed which, for technical reasons, can monitor the roof of the cavity but not the floor and the walls as all sensors are located above the cavity. The situation in this mine section with the location of the acoustic sensors is displayed in figure 2.

The rooms are situated in rock salt (z3LS-AM) and in the hanging roof there are big blocks of anhydrite (z3HA). This situation can bee seen in figure 3.

In the years before backfilling no significant acoustic activity was observed in the vicinity of room 1an. But during the backfilling of Room 1an the activity of the acoustic emissions was increasing extremely. Two month after the backfilling was started, a new strong acoustic emission activity was observed and there was a significant concentration of the acoustic emissions in the roof of Room 1an as it can be seen in figure 3.

Because there were no other changes of the conditions in the near field of this cavity, it is obvious that this increase of the acoustic emission activity is a result of the backfilling with salt concrete.

More information about the microcrack processes shows figure 4. In this figure the evolution of acoustic emission rates are displayed together with the development of the temperature and the humidity in the open gap beneath the roof of the room.

A general increase of the acoustic emission rate can be stated, which correlates very well with the general increase of the temperature measured in the backfilled room. The causes and effects of the temperature changes in regard to acoustic emission activity are already described in Fahland et al. (2005). Based

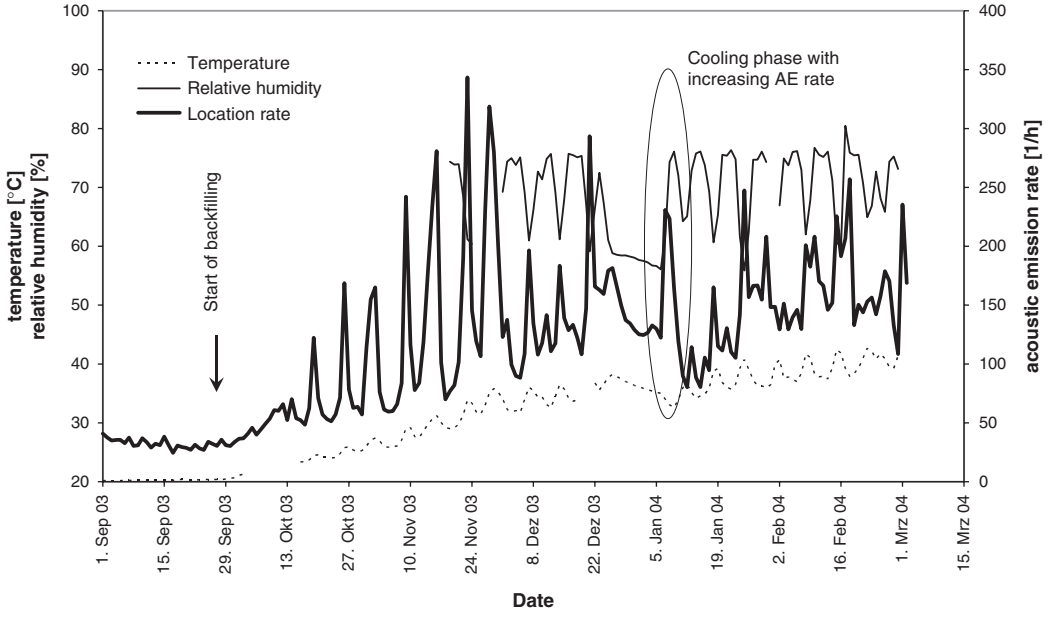

Figure 4. Acoustic emission rate, temperature and humidity in room lan during sequential backfilling.

on this result it seems that heating initiates thermal induced microcrack generation and in connection to this irreversible dilatant deformation of the rock mass.

Although there is a cooling period after a short break during the turn of the year and after restarting the backfilling on January 6th the detected acoustic emission rate is increasing. Hence there must be other influences on the microcrack generation in this case.

If we look at the relative humidity in Room 1an in figure 4 there is a reversed curve shape in relation to the development of the temperature and acoustic emission activity. The changes of the humidity are a result of the very wet salt concrete that is filled into the room. A part of the water in the salt concrete mixture is evaporating so that the humidity in the room is increasing. At the weekend when no salt concrete is filled into the cavity no (additional free) water is available to evaporate and humidity decreases while temperature is increasing. Logically there is an oscillation of the measured humidity with a relative high and constant level in the working days at 75% relative humidity and with minimum values down to about 60% when backfilling is interrupted at the weekends.

A zoomed look at figure 5 shows an increase of the acoustic emission rate and the relative humidity after the break of backfilling at the turn of the year while temperature is decreasing.

This observation shows very clearly that not only changes of temperature with coupled changes of the state of stresses results in variations of the acoustic emission activity. It has to be stated that also

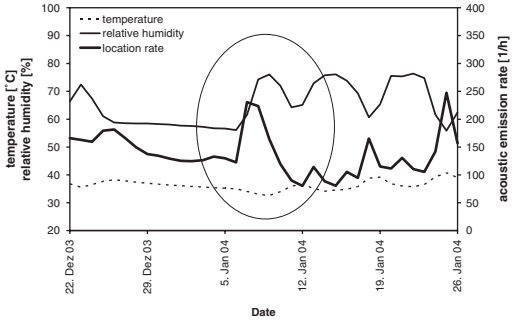

Figure 5. Zoomed view on acoustic emission rate, temperature and humidity in room 1an during sequential backfilling.

relative humidity has a significant influence on the micro-crack activity in the rock mass. And of course both – temperature and humidity – are affecting the micro-crack processes in the rock mass.

It's easy to demonstrate that rising temperature in the rock mass leads to additional loads or load redistribution causing microcrack generation if the total load exceeds the dilatancy boundary of rock salt. But what are the special effects in the case of humidity changes? Can this observed microcrack generation be traced back to humidity induced processes in the structure of the rock salt accompanied by the increase of ductility (Le Cleac'h et al. 1996) or by a local reduction of the cohesion (Brodzky & Munson 1991)?

3 LABORATORY INVESTIGATION

To gain more knowledge about humidity induced processes which are initiating acoustic emissions by microcrack generation in rock salt a specific laboratory investigation was performed. This lab test was planned following the humidity conditions similar to the observed conditions in the backfilled cavity.

3.1 *Experiment*

Because of the fundamental character of this investigation a specimen of pure rock salt with a mid grain size was used to avoid unexpected effects. With respect to former lab tests it is necessary to have stress states above the dilatancy boundary. This is an essential, thus moisture in from of brine films can penetrate into the structure of the rock salt specimen especially into cracks or pores. Another ambition was to measure the reaction due to the moisture in the cracks or pores as long as possible. Considering these items a deformation controlled uniaxial compression test was performed with a constant axial compression rate of $1 \cdot 10^{-8}\ s^{-1}$.

To warranty defined test conditions due to temperature and humidity the rock salt specimen was situated in a box with air conditioning. During the whole duration of the lab test a constant temperature was applied. In the first phase of the experiment the relative humidity in the climatic chamber was hold constant at about 45% relative humidity until an axial compression of 1.8% was reached – after test duration of about 21 days with the constant compression rate mentioned above. From our experience we knew that cracks were generated in a sufficient amount and moisture could penetrate into the structure of the rock salt sample. In the second phase of this experiment the relative humidity was raised to a value of 70% relative humidity. This condition was held constant for about 4 weeks. At the end of this phase an axial sample compression of 4.1% was obtained. After that the humidity was reduced again to a value of 45% for duration of about 3 days.

To qualify the humidity induced damage of the rock salt specimen during the whole experiment the acoustic emissions were counted and the ultrasonic travel times were measured in different directions between twelve sensors spatially distributed on the surface of the sample.

3.2 *Testing results*

Figure 6 shows the axial load of the specimen, the temperature and the relative humidity in the climatic exposure test cabinet – each as a function of time – together with the number of acoustic emissions recorded during the lab test.

The 6th day shows a data loss caused by a stop of the control unit. In this time interval the deformation was kept constant, so it was possible to restart the test at the same point without any difficulties.

In the first 21 days with a constant relative humidity of 45% a typical hardening curve was recorded with an increase of the axial stress. A theoretical extrapolation of the curve shape shows, that the maximum was not reached in this first test phase (uniaxial strength $\beta^D \approx 25$ MPa). Although the axial compression was rising with a constant rate, the development of the number of acoustic emissions was increasing in this time interval as the flow stress did.

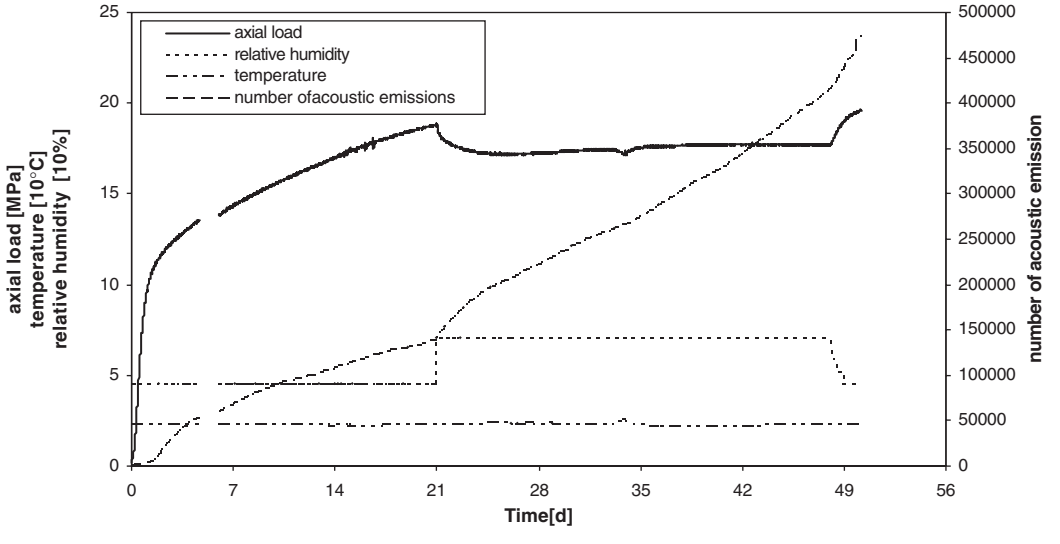

Figure 6. Axial load, temperature, relative humidity and number of acoustic emissions as functions of time.

The humidity was changed from 45% to 70% at day 21. A significant reduction of the axial stress from 18.5 MPa to 17 MPa was determined although the axial compression rate was constant the whole time. After the humidity induced stress relaxations had ended the axial load was increasing again, but very slightly in comparison to the first three weeks. The maximum load in the second test phase with a relative humidity of 70% amounts to 17.7 MPa and the load remained constant during a test interval of about 4 weeks.

The number of acoustic emission was rising immediately after the relative humidity was increased. Except of the steep transient phase between the 21st and 25th day the number of acoustic emissions was increasing nearly linearly till day 37. From the 6th week of the lab test the acoustic emission curve was rising progressively.

After the 48th day the relative humidity was reduced again to a value of 45%. In figure 6 it can be seen that the axial stress is increasing immediately. Also the number of acoustic emissions is rising significantly.

3.3 *Interpretation*

In the first test phase with a constant relative humidity of 45% a typical hardening curve of the axial stress and an increase of the number of acoustic emission was observed. These acoustic emissions were caused by microcracks generated at weak locations in the structure of the rock salt sample and by the opening of grain boundaries. Of course these cracks are preferred locations in the structure of the rock salt specimen where moisture can intrude. This generation of the microcracks and the opening of the grain boundaries lead to an irreversible volume increase called dilatancy. At the same time the deformation produces strain hardening which causes stress concentrations especially at the tips of the microcracks.

The increasing of the relative humidity to 70% led to a significant reduction of the axial stress first. Afterwards the axial stress was increasing again but in a very slight way and reached a maximum value on a comparative low level which remained constant for several weeks. With the change of the relative humidity the number of acoustic emission increased without delay.

This behaviour is caused by the moisture that was penetrating into the microcracks and pores in the structure of the rock salt specimen. At the tip of the cracks and at the grain boundaries the humidity gets in contact with the rock salt, so softening processes can occur. As a consequence of these softening processes ionic bonds at these locations may weaken. From the mechanical point of view this effect results in the reduction of cohesion. This result is also described in Brodzky & Munson (1991) and gives an explanation why the axial load is decreasing immediately when the relative humidity in the climatic chamber was heightened. But in addition to the spontaneous weakening after the increase of humidity, which is correlated with the steep increase of acoustic emission, the flow stress is reduced by humidity assisted recovery of the deformation hardening from nearly 20 MPa to 17 MPa.

A further result is the change in the succeeding hardening behaviour, although the axial strain was kept constant all the time.

Nevertheless, the acoustic emission activity remained high in the testing section with 70% relative humidity. Thus, microcracks are produced continuously by the reduction of cohesion at crack tips. They will finally grow together which leads to macro fractures in the rock salt specimen and early failure. This is concluded from the number of acoustic emission, where the acoustic emission rate is slightly increasing, after the 37th day of testing.

At the end of the lab test, the reduction of the relative humidity led instantaneously to a significant increase of the axial stress and the number of acoustic emission.

On the one hand, this very sensitive reaction of flow stress on the reduction of the relative humidity confirms the interpretation mentioned above, namely that the increase of the humidity causes a reduction of the cohesion and strength – and therefore an increase of the acoustic activity by microcrack generation and crack propagation. On the other hand, the reduction of the humidity lets the cohesion rise again.

But in contrast to the beginning of the lab test, now after nearly 7 weeks and an axial compression of 4.1% the rock salt specimen is damaged in a way, that the re-established hardening deformation causes progressive damage in the still existing solid material bridges in the rock salt specimen. Coalescence of the microcracks occurs resulting in macro fractures and finally in the failure of the sample.

The very sensitive reactions of the stress and the acoustic emission activity to the changes of relative humidity show that the influence of the humidity on the strength behaviour and microcrack processes in rock salt can be switched on and off without a real retardation. This instantaneous reaction depends on the availability of moisture due to the solution processes at the tips of microcracks and pores.

Only in the case when moisture is available this humidity induced processes can take place. This significant sensitivity of the strength and acoustic emission rate of rock salt on the present humidity can be seen in the results of the laboratory test of course and in the data of the field measurements.

4 CHARACTERIZATION OF DAMAGE

Regarding the humidity induced damage of the rock salt specimen ultrasonic travel times of longitudinal

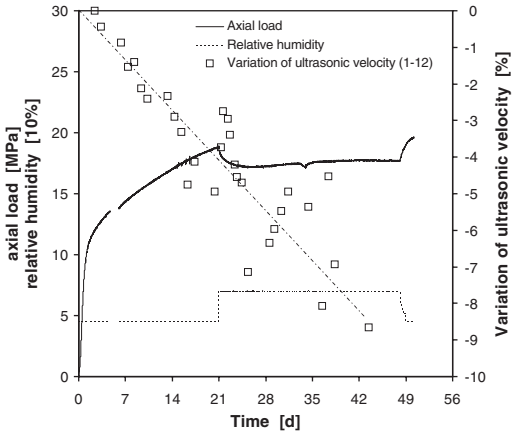

Figure 7. Axial load, relative humidity and variation of the ultrasonic velocity in vertical direction.

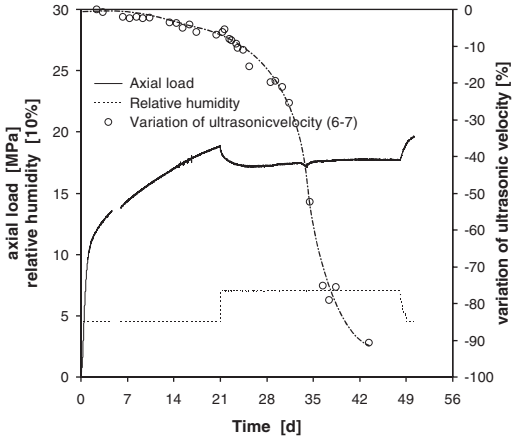

Figure 8. Axial load, relative humidity and variation of the ultrasonic velocity in horizontal direction in the middle of the specimen.

p-waves were determined in different directions through the rock salt specimen once or twice every day. For each distance between transmitter and receiver the ultrasonic velocities v_P were calculated. In relation to the ultrasonic velocity at the beginning of the lab test, the velocity changes were determined as a function of time (or axial compression) to characterize the progress of the damage. This variation of the ultrasonic velocities was calculated with the following equation:

$$\Delta v_{P,rel} = \frac{v_P - v_{P0}}{v_{P0}} \cdot 100\% \qquad (1)$$

with $\Delta v_{P,rel}$ = variation of ultrasonic velocity in relation to the velocity at the beginning of the lab test in %
v_P = current ultrasonic velocity in m/s
v_{P0} = ultrasonic velocity at the beginning of the lab test in m/s

Figure 7 shows the axial load of the specimen, the relative humidity in the climatic chamber and the variation of the ultrasonic velocity in the vertical direction (parallel to the load).

The reaction of the flow stress during the strength test with a deformation rate of $1 \cdot 10^{-8}\,s^{-1}$ on the changes of relative humidity is already described in the previous chapter. Looking at the results of the ultrasonic velocity variations with time in the first test phase there is a very low dispersion of the results. But in the second test phase after increasing the relative humidity in the climatic chamber the variations of the ultrasonic velocities spread out in a wide range. From the beginning to the end of the lab test the ultrasonic velocities v_P in the axial direction were decreasing by 9%.

The trial to fit a curve to this results leads to a straight line from the beginning to the end of the measurements. This seems to be a good regression. But in figure 6 it can be seen that the number of acoustic emissions was increasing when the relative humidity was heightened. This should be seen in the development of the ultrasonic velocity variations as well – at least in different gradients of two straight lines before and after the change of humidity. But there is no change of the slope for the ultrasonic velocity with time in the vertical direction, see figure 7. The comparison with the acoustic emission activity shows, that regarding solely the velocity changes in the direction parallel to the axial load would induce a false interpretation of the mechanical behaviour of the rock salt specimen due to damage, whether it is humidity induced or not.

With this background it is necessary to look at the variation of ultrasonic velocities in the radial directions (perpendicular to the axial load), too. Figure 8 shows the results of velocity changes in the middle of the rock salt specimen.

First of all, there is a much lower dispersion of the results displayed in figure 8 than in figure 7. Further, it can be seen that in the first test phase the ultrasonic velocity was reduced continuously up to −8%. After the humidity was increased the ultrasonic velocity decreased dramatically nearly to −90% in relation to the ultrasonic velocity at the beginning.

This result is in accordance with the observed trend of the activity of the acoustic emissions. The increasing microcrack generation and propagation caused by the humidity induced reduction of the cohesion leads to an increase of the damage of the rock salt sample.

With respect to the determined values of the velocity changes perpendicular to the axial load the damage seems to be strong and the density of the microcracks should be very high.

But why is there such a difference between the results of the measurements in vertical and horizontal

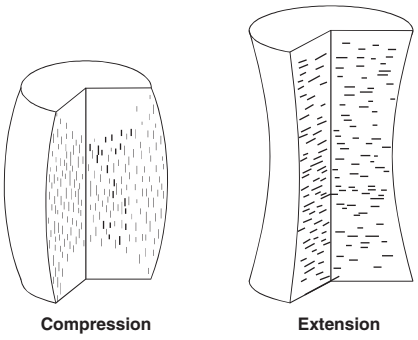

Figure 9. Orientation of the microcracks in dependence on the load geometry.

direction? The important fact to answer this question is the orientation of the microcracks in relation to the load direction as described in Schulze & Popp (2002). If an axial compression load is applied then the microcracks are oriented in the axial direction. Thus, an axial extension load leads to microcracks in the horizontal direction. A sketch of that can be seen in figure 9.

This means that the orientation of the micro- cracks is always parallel to the direction of the maximum principal stress and of course only ultrasonic velocities v_P measured in the direction more or less perpendicular to the direction of the maximum principal stress can be used to characterize the damage of the rock salt specimen in the right way. And of course these observed microcrack processes which are depending on direction of the maximum principal stress lead to anisotropic material properties even when the rock mass has isotropic material properties in its original state.

5 CONCLUSION

In the final repository for nuclear waste in Morsleben (ERAM) observations in different mine sections show an obvious influence of the relative humidity on the acoustic emission activity and thus on the generation of microcracks in the rock mass.

For the understanding of these humidity induced processes in the rock mass – the microcrack generation and the damage in particular – a laboratory test was performed with humidity conditions similar to the conditions observed in situ.

This test showed a very sensitive reduction of the flow stress and a significant acoustic emission activity after increasing the relative humidity from 45% to 70%. Both – the decrease of the flow stress and the rising activity of the acoustic emissions – were mainly caused by the reduction of the cohesion of the dilated rock salt sample as a result of the moisture penetration into open microcracks and pores forming brine films. Reducing the relative humidity again from 70% to 45% at the end of the test led immediately to an increase of the flow stress and near the failure also to an increase of the acoustic emission activity.

Additionally, the damage of the rock salt specimen was characterized by determining ultrasonic velocities of longitudinal waves v_P in different directions. The obtained results point to the formation of anisotropic material properties because the orientation of the microcracks is always more or less parallel to the direction of the maximum principal stress. With respect to this correlation, the evolution of acoustic emission activity and the ultrasonic velocity v_P delivers measures for the monitoring of the damage progress. Furthermore the influence of thermal und humidity variations can be separated where in case of increasing humidity the rock salt seems to weaken by the reduction of cohesion in the range of stresses near the strength.

ACKNOWLEDGEMENT

We cordially thank Otto Schulze for jointly discussing the results of this study and for extensive revision of the paper.

REFERENCES

Brodzky, N.S. & Munson, D.E. 1991. The effect of brine on the creep of WIPP salt in laboratory tests. *Proc. 32nd US Symp. On Rock Mechanics:* 703–712, University of Oklahoma.

Budzinski, D.; Spies, T.; Alheid, H.-J.; Weber, J.R.; Eisenblätter, J. 2004. Detailed characterization of fractures in the rock mass using engineering geology methods, ultrasonic and permeability measurements. In Schubert (ed.), *Rock Engineering – Theory and Practice; Proc. EUROCK 2004 & 53rd Geomechanics Colloquy, Salzburg: 421–424.* Verlag Glückauf Essen, ISBN 3-7739-5995-8.

Cristescu, N. & Hunsche, U. 1993. A comprehensive constitutive equation for rock salt: determination and application. *3rd Conf. on the Mechanical Behavior of Rock Salt, Ecole Polytechnique:* 177–191.

Fahland, S.; Eickemeier, R. & Spies, T. 2005: Bewertung von Gebirgsbeanspruchungen bei Verfüllmaßnahmen im ERAM; In Busch, Maas, Meier, Sroka, Löbel, Klapperich & Tondera (ed), *5. Altbergbaukollloquium vom 3. bis 5. November 2005*, TU Clausthal, Verlag Glückauf GmbH, Essen, ISBN 3-7739-6010-7.

Heusermann, S. 2001. Beurteilung der geomechanischen Stabilität und Integrität von Endlagerbergwerken im Salzgebirge auf der Grundlage geologischer und ingenieurgeologischer Untersuchungen. *Geologische Beiträge Hannover* 2:159–174.

Hou, Z. 1997. Untersuchungen zum Nachweis der Standsicherheit für Untertagedeponien im Salzgebirge. Dissertation, TU Clausthal, ISBN 3-89720-099-6.

Hunsche, U. & Schulze, O. 1994. Das Kriechverhalten von Steinsalz. *Kali- und Steinsalz*, Band 11, Heft 8/9: 238–255.

Hunsche, U. & Schulze, O. 2001. Humidity induced creep and its relation to the dilatancy boundary. Basic and Applied Salt Mechanics. In Cristescu, Hardy & Simionescu (ed.), *Proc. of the Fifth Conf. on the Mech. Behavior of Salt (MECASALT V), Bucharest 1999*: 73–87. Lisse: Balkema.

Le Cleac'h, J.M.; Ghazali, A.; Deveughele, M. & Bruhlet, J. 1996. Experimental study of the role of humidity on the thermomechanical behaviour of various halitic rocks. *The Mechanical Behaviour of Salt, Proc. 3rd Conference, Palaiseau (France)*; Trans Tech Publications, Clausthal.

Menzel, W. & Schreiner, W. 1977. Zum geomechanischen Verhalten von Steinsalz verschiedener Lagerstätten der DDR. Teil 2: Das Verformungsverhalten. *N.B.*, 7. Jg. Heft 8: 565–571.

Schulze, O. & Popp, T. 2002. Untersuchungen zum Dilatanzkriterium und zum Laugendruckkriterium für die Beurteilung der Integrität eines Endlagerbergwerkes in einer Steinsalzformation. *Zeitschrift für Angewandte Geologie* (2/2202): 16–22.

Spies, T. 2001. Comprehensive study of microfracturing in salt rock. *Proc. V International Symposium on Rockbursts and Seismicity in Mines (RaSiM5), Magaliesberg, Südafrika, Symposium Series 27:* 167–172. The South African Institute of Mining and Metallurgy Johannesburg.

Spies, T.; Hesser, J.; Eisenblätter, J.; Eilers, G. 2004: Monitoring of the rock mass in the final repository Morsleben: experiences with acoustic emission measurements and conclusions. – *Proceedings of DisTec 2004*, 303–311, Berlin.

Spies, T.; Meister, D.; Eisenblätter, J. 1997. Acoustic emission measurements as a contribution for the evaluation of stability in salt rock. In Gibowicz & Lasocki (ed.), *Proc. IV. Intern. Symp. on Rockbursts and Seismicity in Mines, Krakau, April 11–14*: 135–139, Rotterdam : Balkema.

The Mechanical Behavior of Salt – Understanding of THMC Processes in Salt –
Wallner, Lux, Minkley & Hardy, Jr. (eds)
© 2007 Taylor & Francis Group, London, ISBN 978-0-415-44398-2

Petrophysical and rock-mechanical characterization of the excavation-disturbed zone in tachyhydrite-bearing carnallitic salt rocks

T. Popp, K. Salzer & M. Wiedemann
Institute for Rock Mechanics GmbH (IfG), Leipzig, Germany

T. Wilsnack
Consulting for Mining, Water and Waste Disposal Engineering (IBeWa), Freiberg, Germany

H.-D. Voigt
Freiberg University of Mining and Technology, Institute of Drilling Engineering and Fluid Mining, Germany

ABSTRACT: Drift sealing systems requiring long-term stability are important components in technical barrier concepts for hazardous-material disposal sites in salt formations. In contrast to rock salt, special problems for sealing systems in potash formations arise because of the ease of dissolving minerals such as carnallite and tachyhydrite-kieserite mineral. Therefore, besides the geo-chemical and technical aspects (e.g. development of an appropriate dam building material) the main emphasis of current investigations is to understand the excavation-disturbed zone (EDZ) because of its importance as a potential "short circuit" pathway around the sealing structure. Results of numerous geophysical in-situ investigations (e.g. permeability and electrical-resistance measurements) in the abandoned potash mine Teutschenthal (D) are presented in this paper. These investigations identified local geological and hydraulic problem areas which may affect the sealing efficiency of the dam building. Additionally rock-mechanical laboratory tests on the carnallitic host rock prove to be a prerequisite for characterizing near-field properties in potash mines.

1 INTRODUCTION

In developing the barrier concepts for final abandonment of salt mines used for the final storage of toxic waste materials (of conventional or radioactive type), drift sealing systems with long-time stability represent an important component. The principal feasibility of drift dams in monophase rock salt has already been proven (e.g. by in-situ tests in the Sondershausen mine; see Sitz et al., 2003). In contrast for the readily soluble salt rocks as found in potash formations, a sealing system with proven long-term stability was just recently developed (Sitz et al., 2005).

Usually, potash zones are interbedded (sandwich) strata within a larger evaporite sequences composed mostly of rock salt (e.g. Jeremic, 1994). Important potassium (potash) minerals are carnallite ($KCl \cdot MgCl_2 \cdot 6H_2O$), sylvite (KCl), kainite ($MgSO_4 \cdot KCl \cdot 3H_2O$) and polyhalite ($K_2SO_4 \cdot 2CaSO_4 \cdot 2H_2O$). These potash minerals are often found in association with kieserite ($MgSO_4 \cdot H_2O$) and tachyhydrite ($CaCl_2 \cdot 2MgCl_2 \cdot 12H_2O$). The potash facies are complex and often depend on local post-depositional tectonic deformation and secondary mineral reactions from brine migration.

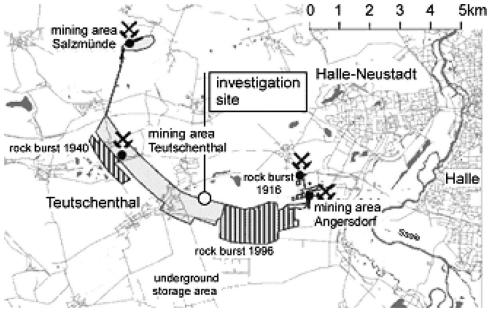

Figure 1. Teutschenthal region (after Minkley & Menzel, 1999).

We investigated the rock-mechanical and geo-hydraulic characterization at the abandoned potash mine Teutschenthal, situated in Saxony-Anhalt located about 2 to 10 kilometres west from the town of Halle (Figure 1).

The Teutschenthal mine consists of several interconnected mining fields. From 1908 until 1982

predominantly carnallitite and rock salt were mined. During this period, two rock bursts occurred (one in 1916 and the other in 1940). Years after the mine was abandoned, a third rock burst happened in 1996 resulting in a 2.5 km^2 collapse of the eastern mining field. This 1996 rock burst had a magnitude of $M_L = 4.8$ (Minkley & Menzel, 1999).

To help preserve the still remaining open cavities of the mine, back-filling operations are carried out using mainly filter ashes. To warrant that this type of backfill (waste material) provides long-term safety, the individual mining fields must be separated by sealing constructions within the carnallite-rich formations. Design and planning for sealing structures required investigating the near-field properties of the surrounding carnallitite – in addition to technical problems (e.g. construction materials which have the required long-term stability – see Sitz et al., 2005) and geo-chemical problems (e.g. dissolution reactions and thermal stability of the host rock – see Freyer et al., 2006).

The Teutschenthal mine is in a bedded carnallitite together with kieserite and tachyhydrite which when in contact with humidity tends to immediately weather. Therefore, the excavation-disturbed zone, which is primary induced by rock stresses, is superposed by a weathering zone, which is induced by chemical solution processes.

Because the potash situation seems to be more complex than for rock-salt, comprehensive understanding of the in-situ conditions and of the mechanical properties of materials is required for assessing the long term integrity of the sealing system. Our investigative approach was based on:

1) Quantifying the range of the EDZ by integrating different methods of in-situ investigation, i.e., permeability, geo-electrical and rock-mechanical measurements.
2) Determining site-specific rock-mechanical parameters with laboratory tests, i.e., triaxial compression strength and shear tests.

Because the potash seam is in a very heterogeneous state, the geologic and stratigraphic situation of the Teutschenthal carnallitite deposit must first be explained. The emphasis of the petrophysical in-situ studies is presented on a seam section for the upper part of the deposit. This seam section was exposed by a circular gallery, the so-called 3a-horizon. In the early 1960s, this gallery was driven by a full-face cutting machine. At this site the rock massif has an increased content of tachyhydrite and, thus, is probably quite unfavourable for construction of a dam.

2 LITHOLOGICAL CONDITIONS

The mining fields of the Teutschenthal mine were driven at exploitation depths between 600 m and 900 m

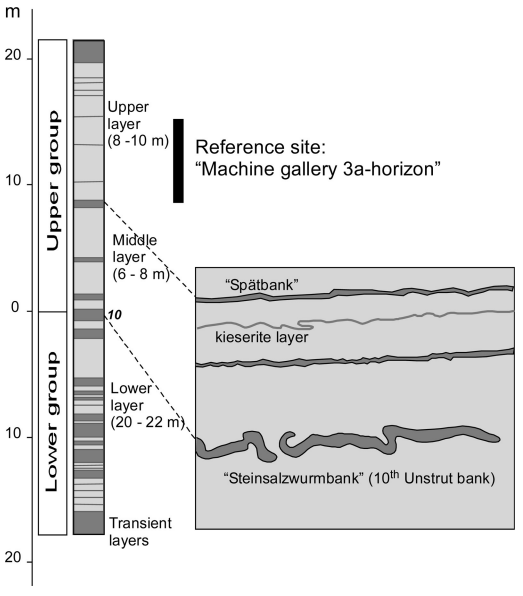

Figure 2. Lithostratigraphy and average thickness of the carnallitic seam in the Teutschenthal area. Carnallitite is light-grey and prominent rock salt layers are indicated by dark-grey. The schematic profile indicates the stratigraphical position of the reference site "Machine gallery 3a-horizon". The magnified profile section corresponds to the mined strata.

along the NE flank of the Teutschenthal anticline, which strikes from NW to SE and is situated at the SE edge of the Mansfield syncline. Below the overlying Quaternary, Tertiary, and Triassic beds; the Permian follows along with the Zechstein. Apart from local tectonics causing fluctuations in its thickness, the Zechstein is deposited normally, and has a slope varying between 2° and 10° towards NNE.

Mainly potash salt was mined with some secondary rock salt production. Up to a 15-m thickness of potash salts were worked from the carnallitic potash seam in the upper beds of the 40 to 45 m thick K2 sequence. The general bedding of the carnallitite near the Teutschenthal arch is spatially continuous and with consistency of the layered sequences. The basic sequence is for a carnallitite, then a kieserite and followed by a halite stratum (partly divided with a fine basal stratum of clay). The thickness of the individual members varies from several decimetres down to microscopic dimensions. Depending on local tectonic deformation, the potash seam is either predominantly a bedded carnallitite or a fragmented carnallitite conglomerate and can be subdivided into several types as shown in Figure 2.

The lowest part of the deposit consists of fragmental carnallitite conglomerate which is predominantly of red colour and is structured by numerous rock salt banks and kieserite banks. Above all, the rock salt

banks, the so-called Unstrut banks, serve as datum horizons.

The middle part of the deposit consists of a plurality of carnallitite strata which are mainly of grey colour but may also be of red, white or yellow colour. The carnallitites alternate with thin layers of rock salt, kieserite, tachyhydrite, and clay. In a subordinate manner bischofite ($KCl \cdot MgCl_2 \cdot 6H_2O$) is also found.

The top portion of the deposit is formed by the so-called Spätbank above which a more red-colored carnallitite is found. At the same time, the tachyhydrite contents increases from less than 3% in the middle part of the deposit below the Spätbank up to values from 8.5 to 40% above the Spätbank. This increase is linked with a change from a subordinate tachyhydrite distribution in the matrix to coarsely developed local lenses or layers of tachyhydrite.

Both because the rock salt proportion increases and the carnallitite decreases toward the roof and the tachyhydrite content increases in the roof causing the rock massif to become less mechanically stable, a potash-rich slice of approximately 15-m thickness was mined from between the Spätbank in the roof and the 5th Unstrut bank as the floor boundary (see extract in Figure 2).

In the Stassfurt potash seam, the investigated zone (profiled region) extends normal to the stratification from approximately 4–5-m above to approximately 1-m below the so-called Spätbank, i.e. it has a total thickness of approximately 6.5 m (see Figure 3). This profiled region is accessible by the opening-up in the gallery and by upward boreholes at the test site in the machine gallery on the 3a-horizon in the Teutschenthal mining field.

The formation of the tachyhydrite in general and its specific but frequent occurrence in the Teutschenthal area in association with kieserite have not been well understood until now. On the basis of isothermal equilibrium studies d'Ans (1961) has debated several possibilities how tachyhydrite might have been formed. Accordingly, the physico-chemical prerequisites are quite lucid. The general question of its occurrence in the Teutschenthal area revolves around its association with kieserite even though the $CaCl_2$-enriched solutions, which are required for tachyhydrite should exclude the presence of $MgSO_4$ (thus, kieserite). According to Rösler & Koch (1968) the formation of tachyhydrite with decreasing halite is conceivable, as "primary segregation" in the carnallite and bischofite region of oceanic salt deposits. The known German deposits might have been formed in a metamorphous manner by the decomposition of carnallite or from high-temperature $CaCl_2$-enriched metamorphous solutions. Thus, it is possible to explain the common occurrence of tachyhydrite together with carnallite, halite, kieserite and partially sylvinite without any formation of anhydrite seams.

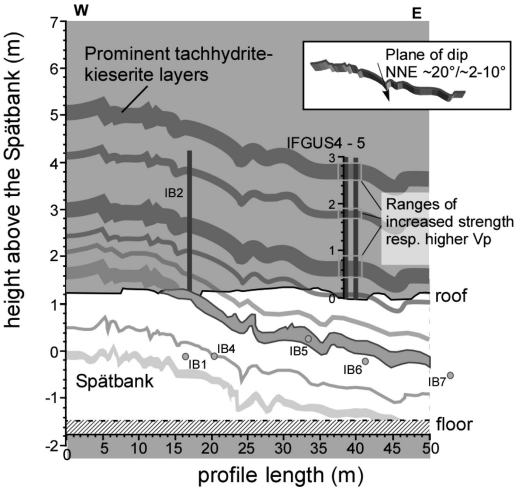

Figure 3. Generalized geological W-E-profile of the reference site "machine gallery 3a-horizon" at the mining area Teutschenthal (N-wall). Prominent kieserite-tachyhydrite layers are schematically shown as well as the position of the Spätbank which marks the onset of the top layer region of the potash seam. Additionally, the positions are indicated of the various drill holes in the roof and the wall which were used for permeability measurements (IB, IB2, IB4 – 7) and ultrasonic transmission measurements (IfGUS 4–5).

3 OCCURRENCE OF THE EDZ

3.1 *Petrophysical and geotechnical measurements*

The EDZ around a mined opening results primarily from the induced effective stress field and the strength properties of the rock massif. A secondary EDZ influence occurs because of the additional cavities on the mined opening caused by dissolution of the readily soluble and hygroscopic minerals tachyhydrite and (minor) carnallite. Kieserite-tachyhydrite strata are exceptionally susceptible. Therefore, gaping fissures in the walls with transversal dimensions up to several centimetres are found extending up to several decimetres into the rock massif.

At the experimental site, the slope of the stratum towards NNE means that stratigraphically different massif units are locally exposed by the machine gallery, which runs horizontally in eastern direction (see Figure 3). Crossing of the bedding and the clay strata means that weathering is more distinct in the walls than in the roof. Sporadically, small-tectonic discontinuities occur which are characterized by intensive weathering due to humidity anomalies in fold structures but are locally restricted to dimensions of metres.

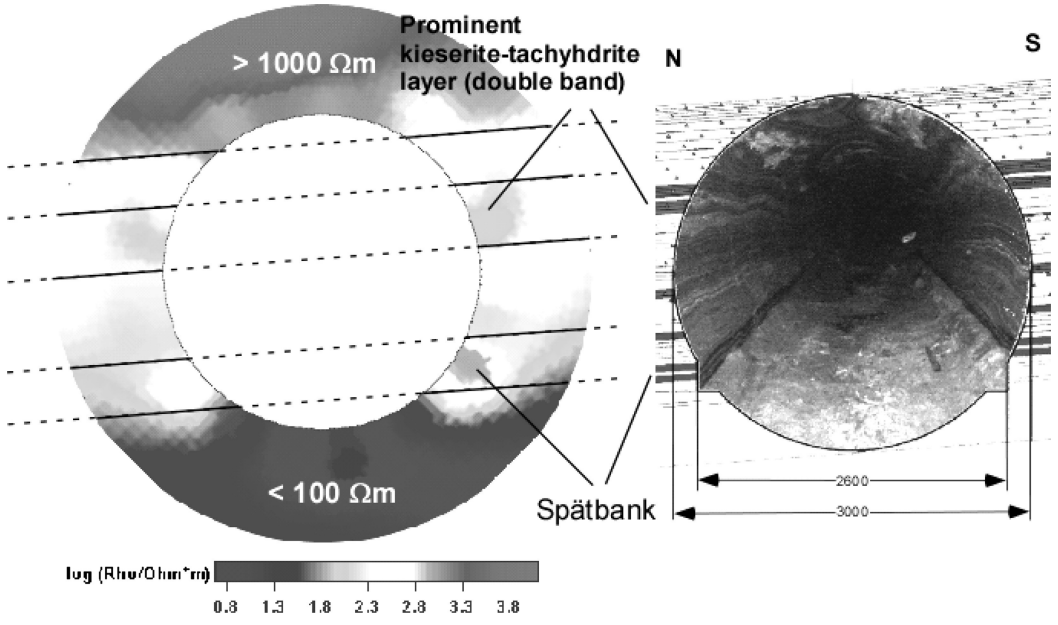

Figure 4. Geo-electrical ring profile at 34.5 m in the experimental drift (investigator: A. Just, Geophys. Inst., Univ Leipzig). (Left side) Resistivity distribution in the ring space (up to 1 m); (right side) Looking into the gallery at the reference location with a schematic geologic profile superimposed (according to Landsmann, personal communication).

In order to determine the spatial extent and properties of the EDZ at the experiment site, a comprehensive programme of in-situ tests was carried out:

1) Measurements of gas permeability made in the wall and roof by IBeWA. Because of the slope (see Figure 3), alternating salt beds are intercepted by horizontal boreholes in the experimental gallery: Determination of flow parameters in boreholes ($Ø = 70$ mm) were made using pulse tests and a 4-fold packer arrangement. Evaluation of the pressure drop curves were made using the specifically developed evaluation model described by Belohlavek et al., 1999.
2) Determination of the minimum stress distribution by hydrofrac measurements in two, 15-m long, boreholes drilled horizontally and vertically.
3) Evaluation of stress-induced core disking during drilling.
4) Geo-electrical measurements (performed by the Institute of Geophysics, Univ. of Leipzig (D)) using ring profiles perpendicular to the gallery axis and longitudinal profiles along the roof and the walls. These electrical measurements were made in a dipol-dipol arrangement in a multi-electrode measurement array (32 measurement electrodes at separation distances between 30 cm and 1 m depending on the type of the profile. RESECS's DC geo-electric apparatus (GeoServe Kiel, D) was used. Measurements were initially evaluated as pseudo-sections using specifically adapted technique described by Just et al. (2004). Subsequently, for inversion, the 2D programme DC2DSIRT was used (Kampke, 1996).
5) Ultrasonic cross hole measurements: P-wave velocities were measured in intervals of about 10 cm along two parallel bore holes (distance 1 m) using a Krautkrämer Branson USD10NF Ultrasonic Digital Receiver and two longitudinal acoustic transducers (build by GMuG, Obermörlen, D). The transducers have an eigen-frequency of around 100 kHz. The velocity was calculated by dividing the average transducer distance by the travel time. Layer-induced velocity anisotropy was tested by measuring borehole sets both in the walls and roof of the drift.
5) Geo-radar: Along linear profiles in the wall and the roof of the drift K-UTEC (Sonderhausen, D) performed Geo-radar measurements using a high-frequency antenna (900 MHz), which provides high resolution and a penetration depth of several meters, to detect fissures with widths as small as 1 mm.

The geo-electric ring profile (Figure 4) along with knowledge of stratum-specific resistivities confirmed the three-dimensional vertical structure of the different strata within the massif and the associated stratum-specific and direction-dependent weathering. The greatest resistivity values (up to 10.000 Ωm)

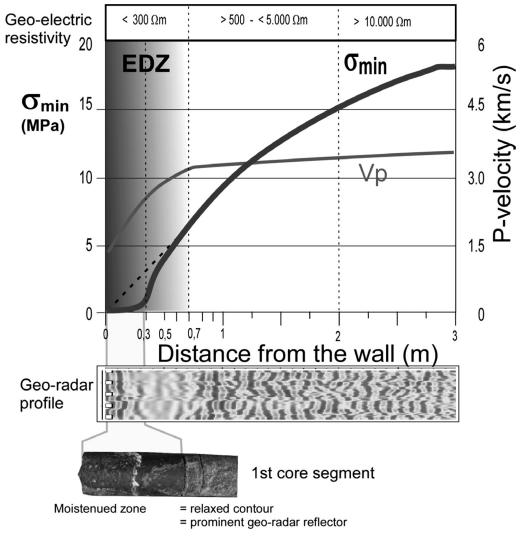

Figure 5. Synthesis referring to the determination of the depth of the EDZ in the wall by various measuring procedures and in-situ observations.

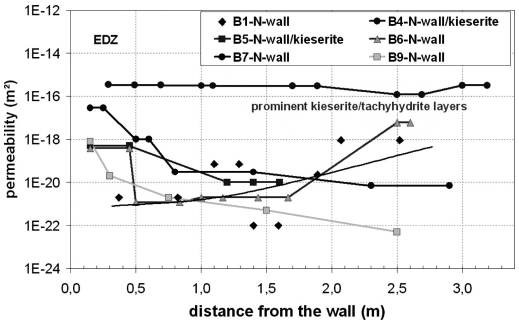

Figure 6. Depth variation of permeability measured along the exploration drift. Individual positions of each borehole along the investigation drift are shown in Figure 3 and the lithological reference profile is given in Figure 7.

were measured in the roof. In the walls the resistivity level was significantly lower (between 100 and 1000 Ωm), which indicates the deep penetration of moisture. At the exposed kieserite-tachyhydrite layer (double band), the resistivity is significantly increased, suggesting humidity penetration parallel to the strata as part of the weathering effect. Within the horizon extremely low resistivity values were also measured (from <100 Ωm to 5–10 Ωm) that result from residual brines from piled up backfill.

In Figure 5 the results of the different methods for determining the range of the EDZ depth are schematically shown as parameter variation with increasing distance from the wall. The EDZ depth is indicated by a discontinuity in the depth-dependent variation of the measured parameter.

Depending on the resolution of the method, a the two-part EDZ is observed. The shallowest is a relatively compact and de-stressed marginal zone (to approximately 0.3 m) that has moisture penetration and forms the "intact shell" of the gallery contour. Beyond this zone is a loosened-up zone with less moisture penetration. The transition between these zones is observed in the geo-radar measurements as a distinct discontinuity and in the geo-electric measurements significantly different electrical resistances. Areas with kieserite and tachyhydrite show generally lower resistivity values compared to the more tight-bedded carnallitite. The transition to the undisturbed massif, i.e. the maximum range of the EDZ, lies at a depth of approx. 0.7 m from the wall.

The velocity into the wall is characterized by rapid velocity increase up to a more or less constant value at a depth of about 0.7 m. These quasi intrinsic velocities vary locally between 3.0 and 3.5 km/s, and obviously depend on total kieserite content because of its greater density compared to carnallite, tachyhydrite, and halite, respectively.

The stress distribution was found to be nearly equal in the wall and in the roof of the circular drift, and nearly unaffected by the neighbouring room-pillar system of salt mining. The stress gradient is characterized by an initial low-stress zone of about 30 cm thickness followed by a steep increase until reaching a plateau of about 18.3 MPa, which is similar in magnitude to the lithostatic stress. The distribution of high stresses qualitatively corresponds to the location of core disking. Slices of several centimetres thickness were usually observed in cores recovered from nearly horizontal holes drilled into the wall. Core disking indicates high-stress regimes in the brittle carnallitite; however the first core segment of around 30-cm length remains nearly intact, which suggests stress relaxation perhaps induced by humidity effects.

3.2 *Identification of potential local pathways*

The vertically heterogeneous deposit with discrete strata or packs of strata having a different lithology makes it necessary to study the permeability both parallel and perpendicular to the strata, as well as within the sequence of strata. As is shown in Figure 3 the boreholes for permeability measurements were distributed along the gallery. In Figure 7 the boreholes are projected into a vertical reference profile (at profile metre 28) so permeability results can be discussed according to their position with respect to the strata sequence.

Our results as depicted in Figure 6 differ from the experience gathered in rock salt – usually a general trend of decreasing permeability with increasing

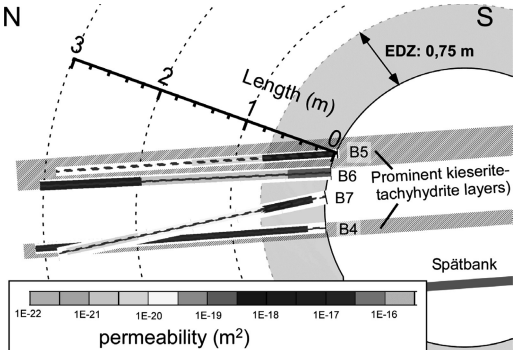

Figure 7. Interpretation of permeability measurements performed in various bore holes (B4–B7) along the experimental drift (projection into a schematic geologic vertical cross-section at 28 m). The measured permeability values are indicated by grey scales.

measurement depth beyond the opening. We attribute our difference to bedding effects.

In carnallitite varieties which have distant bands or which is more compact than the "normal," a decreasing permeability from 10^{-16} m^2 to 10^{-20} m^2 is observed when the EDZ is exceeded. This holds true for all measurements in boreholes B7 and B9, and the shallower sections (until 2 m depth) in boreholes B1, B5 and B6 (Figure 6). In addition, as already discussed earlier, transition zone with pronounced permeability decrease extends to approx. 0.7 m (compare Figure 5).

In contrast, for stratified areas with significant intercalary beds of clay or single prominent kieserite and tachyhydrite bands, a comparatively greater permeability (10^{-16}–10^{-17} m^2) was measured that seems to be independent of depth (compare Figure 6: for the total length of B4 to the deeper sections of the borehole B6).

Although only some of the permeability measurements are presented here, even these partial results makes clear that measurements made in different boreholes must consider possible geological differences. In principle, the inhomogeneity in the strata sequence in the vertical direction has a dominating effect resulting in a distinct difference in the weathering behavior parallel to the stratification, i.e., into the wall, and perpendicular to the stratification, i.e., into the roof. The permeability measurements made in the wall had greatest permeability results (between 10^{-17} m^2 and 10^{-15} m^2) in those carnallitic areas that also contain closely situated bands with high contents of kieserite and tachyhydrite and intercalary beds of clay. Since – in the scale of the experimental site – the areas of greater permeability must be considered potential penetration pathways along side a sealing structure and, thus, represent problematic zones for the barrier system.

4 ROCK-MECHANICAL INVESTIGATIONS

4.1 *Strength and dilatancy behavior*

Since the rock mechanical properties of tachyhydrite bearing carnallitite are not well known, a special laboratory testing program was performed. Because of the core-disking, conventionally drilled core samples were not suitable for the intended rock-mechanical studies, and the test samples were prepared from a big rock block taken from the massif.

The longitudinal velocities measured in the core samples had a remarkable scattering depending on the type of core sample and the direction (transversal or along the axis of the sample). The axial-direction velocities varied between 2.9 and 3.6 km/s with most at 3.1 km/s. On average, the transversal-direction velocities (radial direction – parallel to the foliation) were generally 10% lower (the vertical velocity anisotropy with respect to the strata was approximately 15%).

On average, the density is 1.75 ± 0.03 g/cm^3 which means that the density is clearly lower than that of a carnallitite with around 60% carnallite (C_{60}) having a density of 1.85 g/cm^3 (mainly carnallite and rock salt, without kieserite). The reason of lower density is the high volumetric portion of tachyhydrite ($\rho \approx 1.6$ g/cm^3) in the order of 10–15%.

The specific stress-strain behavior of the carnallitite from the experimental site was measured with a servo-hydraulic testing machine of the IfG. They represent the basis for evaluating the strength and dilatancy as a function of the deformation. The test samples were well dried before the tests. The tests were carried out by applying a confinement in the range of $0 \leq \sigma_3 \leq 15$ MPa. The uniaxial and triaxial compression tests were carried out with the constant deformation rate of $\dot{\varepsilon} = 2.5 \cdot 10^{-5}$ s^{-1}.

Figure 8 showing the stress-strain curves illustrates the dependency of the load bearing capacity and the dilatancy on the deformation at different confining pressures (σ_3) for different samples.

Additionally, in Figure 9 the dependencies of strength and dilatancy on the confining pressure are compared to earlier test results on carnallitic material from a slightly lower stratigraphical position. The failure stress and load bearing capacity in the post-failure region increase with rising confining pressure for both types of test specimens. The measured volumetric strain curves (depicted in Figure 8) reveal that in the beginning of axial compression the sample is subject first to an elastic volume reduction before its volume increases due to the strain-dependent increase in the crack density when the dilatancy threshold is exceeded.

Since, in contrast to rock salt, the mineral carnallite has no crystallographic glide planes, the inelastic deformation of carnallitite results mainly from rupture deformation, i.e. mechanical twinning,

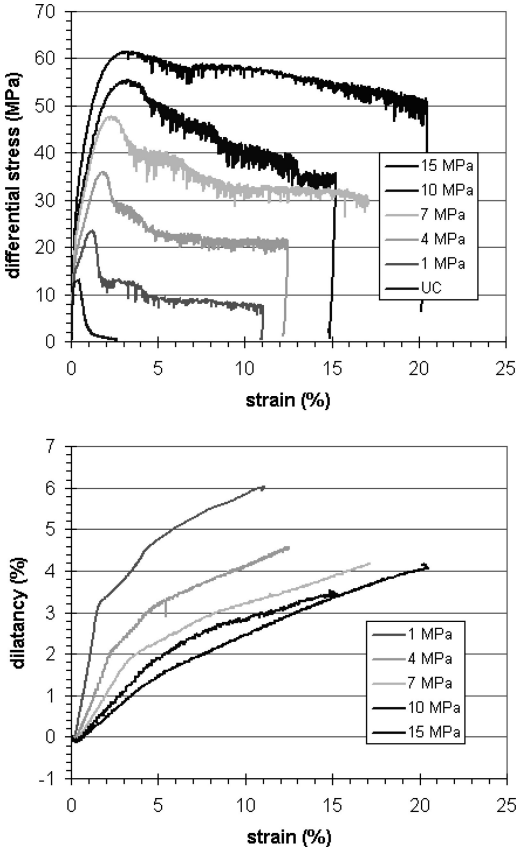

Figure 8. Summary of triaxial strength tests on carnallitic samples at 23°C. (top) stress–strain curves, (bottom) dilatancy as a function of axial strain. Labor Nr. 304: Teutschenthal experimental site 3a-horizon.

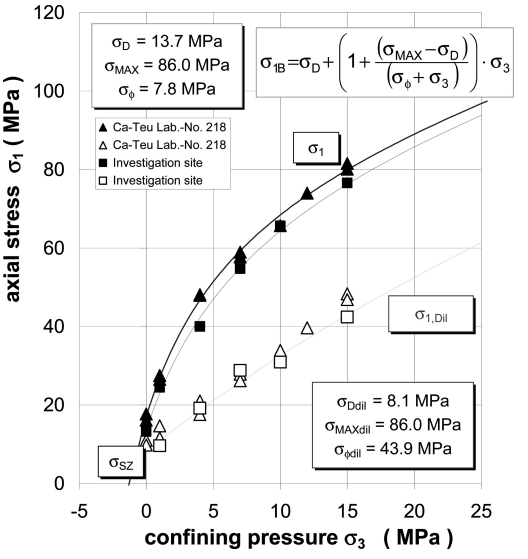

Figure 9. Triaxial failure strength and dilatancy boundaries as a function of confining pressure (σ_1 vs. σ_3) of carnallitite from two locations at Teutschenthal: Lab. No. 304 – reference site 3a-horizon; Lab. No. 218 – recovered from approx. 1 m below the Spätbank. – solid symbols – strength data; open symbols – dilatancy.

crack formation and displacement on shear planes as revealed by the increase of dilatancy with increasing axial deformation.

4.2 *Material parameters to describe the strength and weakening behavior*

The elasto-plastic constitutive relationship developed by Minkley et al. (2001) was used to describe the strength and softening behavior of carnallitite. In this relationship, the strength is determined not only at either the failure point or at the minimum of the dilatancy curve but also as a set of characteristic strength curves as a function of the plastic deformation ε^P. In an analogue way, the dilatancy behavior is determined from volumetric deformation values (after first meeting the strength and dilatancy thresholds when $\varepsilon^P = 0$) in discrete deformation steps for $\Delta\varepsilon_1 = 0.1\%$.

As a result of this test sequence, a number of curves are obtained which depend on the investigated states of plastic deformation. These curves allow a detailed characterization of different deformation states. For the determination of the required parameters, the values of tan ß were determined as the slope of dilatancy vs. axial deformation in the dilatancy region and are represented as a function of the confining pressure. The material parameters of the investigated carnallitite 304 are listed in Table 1.

4.3 *Shear strength of stratified carnallitite*

The properties of potential weakness zones are important for performing a stability analysis of underground cavities and for forecasting the behavior of the rock massif. The carnallitite under investigation is stratified with beds of different mineralogical composition. These lithologic inhomogeneities can be activated as rock-mechanical interfaces in a manner that reduces the strength properties of the solid rock.

The MTS shear test system of the IfG makes it possible to align the layer faces or interfaces of a test specimen such that the action line of the shearing force lies immediately in this plane and the action line of the normal force is perpendicular to it, respectively, so that the effective shear stress is equal to the total shear stress (for details see Minkley & Mühlbauer, this volume).

The shear test results were obtained from two series of samples: pre-damaged core material from core holes and intact specimens from the sample block.

Table 1. Strength (a) and dilatancy parameters (b) of the carnallitite from the reference site 3a-horizon (dried samples).

ε_p (%)	0.0	0.2	0.5	1.0	3.0	5.0	10.0
(a)							
$\sigma_D(\varepsilon_p)$ (MPa)	13.6	10.9	5.3	5.6	0.9	0.0	0.0
$\sigma_\phi(\varepsilon_p)$ (MPa)	7.7	7.9	7.8	8.2	9.5	9.8	16.8
$\sigma_{MAX}(\varepsilon_p)$ (MPa)	86.0	86.0	86.0	0.86	0.86	0.86	0.86
(b)							
$\sigma_\psi(\varepsilon_p)$ (MPa)	5.9	7.6	5.6	11.4	12.8	42.0	
$\tan\beta\,(\varepsilon_p)$ (−)	0.22	0.81	2.95	4.5	7.4	4.5	

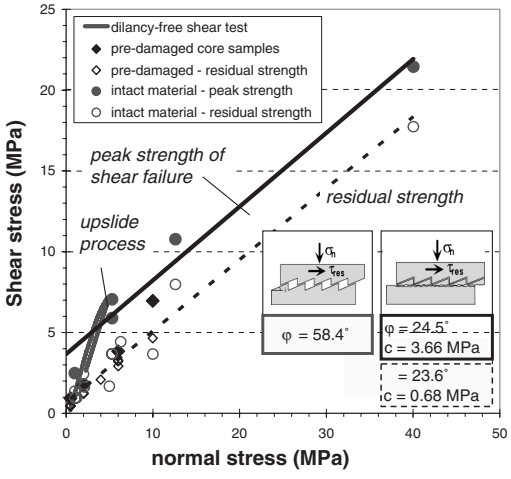

Figure 10. Shear strength of foliated carnallitite with interbedded kieserite-tachyhydrite aggregates. The insets show schematically the various processes of shear failure on a weakness plane together with the various Coulomb-parameters.

The test program comprises 9 conventional shear tests at a constant shear displacement rate of 0.002 mm/s under constant nominal loading of $\sigma_n = 0.2$ to 40 MPa until the peak shear strength is reached. After reaching each level of residual strength, the normal loading was varied in up to three steps and the residual strength was again determined.

Exemplarily, a so-called dilatancy-free shear test was carried out. To prevent shear dilatancy (upsliding), the normal stress was continuously increased until the rupture of the sample occurred (for details see Blümel, 2000).

The individual data of all tests are shown in Figure 10. These data have been derived as maximum (peak) and residual strength values obtained from the curves of the shear tests.

Depending on the applied normal stress, a two-phase course for the shear strength appears. For the dilatancy-free shear test and the shear test at $\sigma_n = 1$ MPa and on samples taken from the big block at $\sigma_n \approx 5$ MPa and following the initial upslide and shear processes (upslide process with $\varphi =$ ca. 58°), a nearly linear trend of strength values appears with a quite narrow scattering considering the variety of samples. The related residual strength values show a comparable friction angle with low cohesion. The strength values determined on the pre-damaged core was generally of the same level as the residual strength and, thus, do not represent the unaffected rock massif.

By means of a regression analysis from the individual values the upslide angle and friction angle, respectively, the Mohr-Coulomb strength and residual strength parameters of the interface were determined. The corresponding values of the internal friction angle φ and the cohesion c are as follows:

$\varphi_G = 24.5°$ $\quad c_G = 3.66$ MPa

and for the residual shear strength

$\varphi_{residual} = 23.6°$ $\quad c_{residual} = 0.68$ MPa

5 SUMMARY AND CONCLUSIONS

The investigation presented here illustrates the complexity of the EDZ in potash salt rock which contains readily soluble minerals. The EDZ that develops around an opening depends primarily on the rock-mechanical properties of the salt rock and the induced stress states. After excavating a gallery, a deep-reaching weathering of the readily soluble salt components (parallel to the strata) is superimposed on the EDZ in a stratum-specific manner. When hygroscopic salt minerals like tachyhydrite and kieserite undergo dissolution processes, related moisture penetration pathways will develop.

The extent and the order of magnitude of the EDZ as is superimposed by weathering processes result from the volumetric portion and from the degree of aggregation of these minerals as a function of the time and intensity of exposure. The weathering effect is different for the vertically heterogeneous sequence of strata

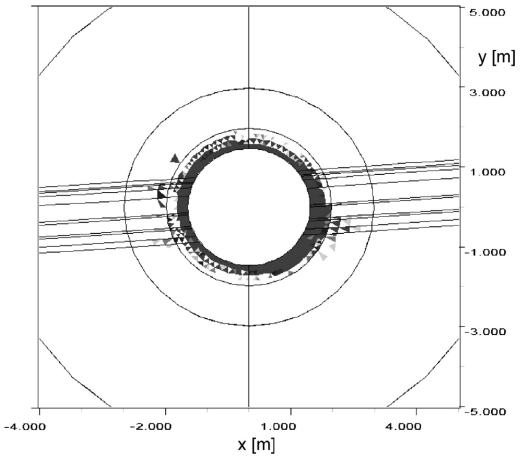

Figure 11. Numerical modelling of the spatial extent of the EDZ around the 3a-drift as indicated by signatures with various shades of grey corresponding to the state of damage – Vertical cross section.

than along (parallel) to particular stratum. However, the exact causes of this different material behavior are not yet known.

As a whole, the lithologic heterogeneity around the gallery makes it clear that a specific site characterisation is required before erecting any sealing construction. Irrespective of the above, the interdisciplinary approach as documented herein allowed us to examine general principles about the development of the EDZ in these readily soluble potash rocks.

Moreover, the rock mechanical investigations as described before form the basis for an essential computational modelling of a sealing structure using site-specific host rock properties and construction materials. Preliminary modelling was performed using UDEC simulating the temporal evolution of the convergence processes in the 3a drift since the beginning of the sixties when the machine gallery was installed. As damage parameter we used the residual strength according to the Minkley-model. It can be seen in Figure 11 that highly damaged rock portions are restricted to a zone of around 60 cm which corresponds fairly well to the in situ observations.

Based on the various studies performed in the context of this research, a fundamental sealing concept has been developed for solving the technical and geological problems resulting from this complex situation (Sitz et al., 2005). The concept is mainly based on a special concrete as building material, composed of MgO and silicatic granular components prepared with a saturated $MgCl_2$–$CaCl_2$ solution. In addition, technical measures are foreseen to minimize weathering effects and to qualify problems zones by injection.

Nevertheless, the complex spatial geometry of potential pathways as given by the rock structure requires a complex 3D-model. In addition, the mechanical and hydraulical integrity of the complete sealing construction will strongly depend on the interaction between the building material and the rock at the opening surface. For describing these properties, i.e. shear and tensional strength respectively, discrete permeability measurements of the rock/concrete interface and further rock mechanical investigations are still needed.

ACKNOWLEDGEMENTS

The studies presented in this paper were funded by the German Federal Ministry of Research and Education under contract 02C0942 and the Landesamt für Altlastenfreistellung Sachsen-Anhalt (D). We also thank the "Grube Teutschenthal Sicherungs GmbH & Co. KG" (GTS) for technical and financial support.

As project manager, P. Knoll (GTS) efficiently organized the joint project of the various involved companies, i.e. GTS, IBEWA, IfG, K-UTEC (Sonderhausen) and TU Bergakademie Freiberg (BAF). Most of the work has been done in close cooperation with the partners, i.e. D. Freyer, M. Gruner, W. Kudla, P. Sitz and W. Voigt (all BAF); T. Fliss (K-UTEC). V. Böttge (Landesamt für Geologie und Bergwesen, Sachsen-Anhalt) is thanked for fruitful discussions and comments. M. Schmidt (GTS) was responsible for co-ordinating the in-situ-work.

The geo-electrical measurements were performed by the team of Prof. F. Jacobs (Univ. Leipzig), i.e. A. Just, Y. Krause and W. Schönfelder.

We also appreciate the thorough review made by Leo van Sambeek and his valuable input to improve the English during preparing the final version of the paper.

REFERENCES

Belohlavek, K-U., Behr, A., Foerster, S. & Haefner, F., 1999. In-Situ Determination of Geohydraulic parameters of natural Salt Rocks for Gas Loosening Zones Around Drifts (Cavities). *SMRI Spring Meeting*, April 11–14, Las Vegas.

Blümel, M., 2000. Neue Laborversuchstechniken für felsmechanische Versuche (Improved Procedures for Laboratory Testing) – DGGT (ed.): *Proceedings of the EUROCK 2000 Symposium,* Aachen, 27.–31. März 2000, 573–578, Essen (Glückauf).

D'Ans, J., 1961. Über die Bildungsmöglichkeiten des Tachyhydrits in Kalisalzlagerstätten. – *Kali u. Steinsalz*, 3, 119–125.

Freyer, D., Voigt, W. & Böttge, V., 2006. Zur thermischen Stabilität von Tachhydrit und Carnallit. *Kali und Steinsalz*, 1, 28–37.

Jeremic, M.L., 1994. *Rock Mechanics in Salt Mining*. Rotterdam: Balkema.

Just, A., Krause, Y. & Jacobs, F., 2003. Möglichkeiten und Grenzen untertägiger Geoelektrikmessungen im Salz.

Proc. 20. In: *Kolloquium Elektromagnetische Tiefenforschung*, Eds.: A. Hördt & K. Spitzer, Königstein, 29.9.–3.10.2003. Deutsche Geophysikalische Gesellschaft.

Kampke, A., 1996. *Modellierung und Inversion von Daten der induzierten Polarisation für zweidimensionale Verteilungen der elektrischen Leitfähigkeit*. Diplomarbeit. Institut für Geophysik und Meteorologie, Technische Universität Braunschweig.

Minkley, W., Menzel, W., Konietzky, H. & te Kamp, L., 2001. A Visco-Elasto-Plastic Softening Model and Its Application for Solving Static and Dynamic Stability Problems in Potash Mining, in *FLAC and Numerical Modeling in Geomechanics* – 2001 (Proceedings of the 2nd International FLAC Conference, Lyon, France, October 2001), D. Billaux et al., Eds. Lisse: Balkema. 21–27.

Minkley, W. & Menzel, W., 1999. Vorausberechnung des Kollapses eines Grubenfeldes Gebirgsschlag Teutschenthal 11. Sept. 1996. *Proc. 9*th *Int. Congress on Rock Mechanics*, Paris, Vol. 2, 1115–1118.

Rösler, H.J. & Koch, K., 1968. *Salzmikroskopie* – Manuskript Bergakademie Freiberg.

Sitz, P., Gruner, M. & Rumphorst, K., 2003. Bentonitdichtelemente für langzeitsichere Schachtverschlüsse im Salinar. *Kali und Steinsalz*, 3, 6–13.

Sitz, P., Gruner, M. & Knoll, P., 2005. Streckenverschlüsse im Carnallitit. *Kali und Steinsalz*, 2, 16–25.

The Mechanical Behavior of Salt – Understanding of THMC Processes in Salt –
Wallner, Lux, Minkley & Hardy, Jr. (eds)
© 2007 Taylor & Francis Group, London, ISBN 978-0-415-44398-2

Deformation of a halite-anhydrite sequence under bulk constriction: Preliminary results from thermomechanical experiments

G. Zulauf & J. Zulauf
Institut für Geowissenschaften, Universität Frankfurt a.M., Altenhöferallee 1, Frankfurt a.M., Germany

O. Bornemann
Bundesanstalt für Geowissenschaften und Rohstoffe, Stilleweg 2, Hannover, Germany

ABSTRACT: A new deformation apparatus has been used to model the internal kinematics of salt diapirs. We deformed layers of Gorleben anhydrite, embedded in Asse halite, under bulk constriction with the layers being oriented parallel to the major stretching axis, X, of the finite strain ellipsoid. Further deformation conditions were as follows: $T = 345°C$, $\sigma_{max} = 4.59$ MPa, $d\varepsilon/dt = 10^{-7}\ s^{-1}$, $e_{X(max)} = 122\%$. 3D-images, based on computer tomography, suggest a strong interaction between folds and boudins, both of which affecting the anhydrite layer. D_1-folds, with axes subparallel to X, are hardly developed. D_2-folds, with axes subperpendicular to the layer, affect the boudins resulting in oblique orientation of the latter. With increasing layer thickness the length of boudins increases. However, the geometric data are not in line with results of analytical solutions derived for power-law material and with geometric data of folds and boudins produced by analogue experiments.

1 INTRODUCTION

The internal parts of salt diapirs are largely characterized by steeply plunging linear (L > S) fabrics. Examples of such fabrics are present in the salt diapirs of northern Germany, Texas and Louisiana (Lotze 1957, Balk 1949, 1953, Hoy et al. 1962). Near the core of the Upheaval Dome in Utah, radial shortening produced constrictional bulk strain, forming an inward verging thrust duplex and tight to isoclinal, circumferentially trending folds (Jackson et al. 1998).

The 3D-geometry, flow lines and distribution of finite strain within an idealized axisymmetrical salt diapir have been illustrated by Talbot and Jackson (1987). All the stream tubes in the lower half of the stem converge upward. The strain near the central axis is characterized by pure constriction supporting prolate fabrics and related L-tectonites.

There may be several generations of folds within a salt diapir. The youngest folds recognized in stems of salt diapirs are known from German Zechstein salt as curtain folds (Kulissen- or Vorhangfalten, Hartwig 1925, Lotze 1957, Trusheim 1960) because the steeply inclined bedding planes define steeply plunging cylindrical folds. In a horizontal section of a salt diapir the axial planes of curtain folds are generally radial and the envelope is more or less concentric. The grain-shape lineation tends to parallel the hinge lines of curtain folds (Talbot and Jackson, 1987).

The modeling results of Ramberg (1981) suggest constrictional flow in the basal parts of axisymmetric diapirs. Thus, only curtain folds with steep hinges, aligned parallel to the subvertical X-axis of the finite strain ellipsoid, are likely to be generated in the basal parts of diapiric stems. Older folds, such as recumbent sheath folds, which were generated in the source layer, will steepen and rotate into the constrictional flow regime at the base of the stem where they are refolded by curtain folds (Talbot and Jackson 1987). In cases of rheological stratification (e.g. stiff anhydrite or shale layers embedded in a weaker halite matrix), the curtain folds should be associated with boudins, the latter resulting from vertical extension parallel to the steep axes of the curtain folds. Examples of folded and boudinaged anhydrite layers, embedded in a steep prolate halite matrix, have been described from Miocene salt diapirs of Yemen (Davison et al. 1996a,b).

In the present study we present first results of thermomechanical experiments which have been carried out to model the kinematics of stems of salt diapirs. We deformed layers of anhydrite embedded in a halite matrix under bulk constriction and elevated temperature. The geometry of the folded and boudinaged anhydrite layer is compared with geometrical data

obtained from analogue modeling and from analytical solutions.

2 EXPERIMENTAL SETUP

We carried out four experiments with halite-anhydrite samples using a new deformation rig.

Samples of Asse Speisesalz Na2SP (northern Germany), which are largely free from a grain-shape fabric, show the lowest degree of mechanical anisotropy under constriction and thus have been used for the experiments. The grain size varies from 2–12 mm. According to microscopic and XRD analyses, the samples used in the present study consist of almost pure halite, with anhydrite and polyhalite as impurity phases. The total water content of other Asse Na2SP samples is 0.05 wt% (Urai et al. 1987). The microfabrics of Asse halite suggest that natural deformation was accommodated by dislocation and dissolution-reprecipitation creep (Urai et al. 1987).

The anhydrite samples used for our experiments have been collected from the Gorleben deep borehole 1004. XRD analyses revealed impurities of halite, polyhalite and magnesite. The grain size varies considerably from $<100\,\mu$m to 10 mm. Most of these grains have a dirty habitus, the latter resulting from numerous fluid inclusions and opaque phases. Rosette shaped aggregates of anhydrite are frequently present on almost all scales. The anhydrite rosettes are partly truncated by highly lobate seams which are rich in opaque phases. These seams reflect localized dissolution-reprecipitation creep. Evidence for moderate crystal plastic deformation is given by twinning on the {101} planes and weak bending of long-prismatic crystals. In contrast to these features, there are few anhydrite crystals which are almost clean and free from deformation fabrics. These crystals grew late within small veins or in open pore space.

The initial model dimensions (halite matrix + anhydrite layer) were $48 \times 60 \times 60$ mm along the X-, Y- and Z-axis of the finite strain ellipsoid, respectively. The thickness of the anhydrite layer, H_i, was changed from run to run ($H_i = 1.1$ mm, 1.5 mm, 2.0 mm, 2.5 mm). The uncertainty of layer thickness is 0.1 mm. The experiments were carried out under bulk constriction with the stiff layer oriented parallel to the X-axis of the finite strain ellipsoid. Deformation conditions during the constrictional runs were as follows: termperature, $T = 345°$C, strain rate, $\dot{e} = 2 - 4 \times 10^{-7}\,s^{-1}$, finite strain, $e_{Y=Z}$, $= -33\%$ and $e_X = 122\%$, maximum stress difference, $\sigma_{max} = 4.9$ MPa. Only in that run where H_i was set at 2.5 mm, the deformation of the sample was limited to a finite strain $e_{Y=Z} = -17\%$ and $e_X = 44\%$, respectively, because the pre-scribed stress limit of the machine was exceeded.

The new deformation apparatus was built at the Technische Fakultät, Universität Erlangen-Nürnberg. The basic concept of the new machine is similar to that of the apparatus described in Zulauf et al. (2003). It is supporting the full range of three-dimensional coaxial deformation. However, in contrast to the old machine, the new one is able to work at higher temperature and pressure.

The deformation rig consists of a stable frame made of steel in which four principal aluminum plates have been orthogonally assembled. The sample is sandwiched between the four plates which are driven by two separate step motors. In cases of pure constrictional strain (Flinn parameter $k = \infty$) the number of revolutions of both motors is the same, meaning that two of the plates are moving with the same velocity. To increase the temperature of the plates, the latter are subdivided into 3 zones, each of which contains 4 heating cartridges. The temperature of each plate is measured by 7 thermocouples. At pre-scribed time intervals the temperature values are recorded by the control unit and adjusted to the target value. The heating cartridges support a maximum deformation temperature of 375°C with an uncertainty of less than 0.1°C.

Measurements of in-situ stresses allow constraining in-situ viscosities in the direction of the principal strain axes. There are two single-point load cells to determine the horizontal and vertical stress during deformation. During an experimental run, the temperature, stress and strain data are recorded for every twelve seconds.

The deformed samples have been investigated using computer tomography (CT) and conventional cuts along YZ- and $XY = XZ$-sections (for details, see Zulauf et al. 2003). The CT-studies were performed at the clinic of Frankfurt University in the Neuroradiologie Department using a multislice spiral CT-scanner (Phillips CT Brilliance with 6 lines). Geometrical parameters of folds and boudins have been determined from CT-images using the software *Smoooth* which is produced and distributed by M. Peinl (Frankfurt a.M.). Smoooth supports the production, visualisation and analyses of DICOM volumetric data.

The initial wavelength of folds (W_i sensu Ramsay and Huber 1987, p. 383) has been determined by measuring the average fold arc lengths (Sherwin and Chapple 1968). The normalized initial wavelength W_d is calculated by dividing the initial wavelength through the finite layer thickness H_f. Because of strong boundary effects, geometrical parameters have not been determined from folds and boudins of the marginal parts of the deformed samples.

3 RESULTS

The stress-strain plots of the four runs show striking differences with increasing layer thickness. Most of

these differences can be explained by the fact that the stamp of the horizontal load cell, which records the stress parallel to the layer, was placed on the anhydrite layer, whereas the stamp of the second load cell, which records the vertical stress perpendicular to the layer, was placed on the halite matrix.

If H_i was set at 1.1 mm, the paths of both flow curves are closest to each other, meaning that the stiff anhydrite layer did not significantly affect the bulk mechanics of the sample. The plot shows non-linear flow curves with an initial linear increase of stress and strain until plastic yielding is achieved at $e_{Y=Z} = -3$ and -7%, respectively. Both flow curves do not indicate steady-state behaviour, but strain hardening. The latter is particularly strong at advanced finite strain. There is a striking increase in horizontal and vertical stress at $e_{Y=Z} =$ ca. -25%. After attaining this strain state, both flow curves show the same steep path, the latter reflecting significant strain hardening.

If H_i was set at 1.5 mm, the flow curves are similar to those described from the previous run. This holds particularly for the striking increase in horizontal and vertical stress at advanced finite strain ($e_{Y=Z} =$ ca. -25–-28%). However, plastic yielding along the horizontal direction (parallel to the anhydrite layer) was achieved much later ($e_{Y=Z} =$ ca. -7%) than the yielding along the vertical direction ($e_{Y=Z} =$ ca. -3%). The later onset of plastic yielding in the direction parallel to the anhydrite layer is also given in those runs where the layer thickness was still higher, meaning that the layer is mechanically active at low finite strain if $H_i >>$ ca. 1 mm.

At $H_i = 2.2$ mm the horizontal and vertical flow curves are almost parallel at advanced finite strain magnitudes. However, the curves do not show the same path particularly during the final part of the run. The stress parallel to the layer is ca. 0.5 MPa higher than the stress perpendicular to the layer. Thus, the anhydrite layer was mechanically active not only at low finite strain but throughout the entire run.

The difference between horizontal and vertical stress was still higher (ca. 2 MPa) if the layer thickness was set at 2.5 mm. Because of increased mechanical significance of the anhydrite layer, the pre-scribed stress limit (4.59 MPa) was reached in the horizontal direction (along the layer) already at $e_{Y=Z} = -17$%. Thus, the experiment had to be stopped much earlier than in the other runs described above.

In all of the deformed samples there is striking boudinage of the stiff anhydrite layer in sections cut parallel to the X-axis of the finite strain ellipsoid and perpendicular to the layer ($XY = XZ$ sections; Fig. 1). The boudin patterns are particularly obvious from CT images which are oriented subparallel to the layer (Fig. 2a). Most of the boudins are not penetrative and are trending oblique to the principal strain axes.

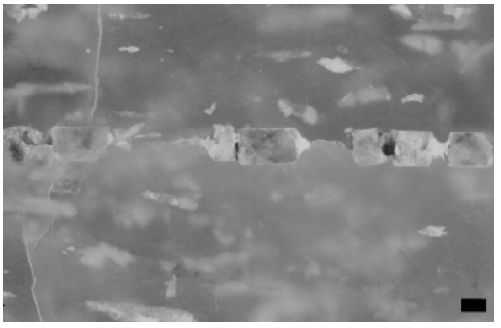

Figure 1. Close-up view ($XY = XZ$ section) of deformed sample showing anhydrite boudins embedded in foliated halite matrix. Initial thicknes (H_i) of anhydrite layer = 1.5 mm. Necks between the anhydrite boudins are different in composition. Some are entirely filled with halite. Other necks show open space or are filled with a white mineral which could be grinding powder. Note slightly folded healed fracture at the left-hand side of the photograph which cuts only through halite. Scale bar = 1 mm.

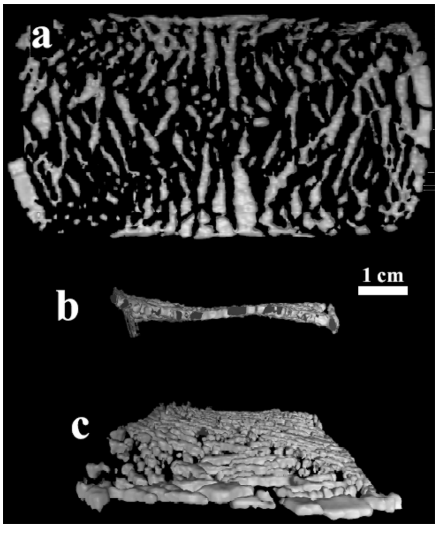

Figure 2. CT-images of deformed anhydrite layer (matrix of deformed halite not shown). Initial thickness (H_i) of anhydrite layer = 1.5 mm. (a) View perpendicular to the layer showing boudins which are partly affected by weak D_2-folding. (b) View parallel to the major stretching axis, X, showing weak D_1-folding. Dark areas denote dissected parts of the anhydrite layer. (c) View slightly oblique to the layer subparallel to X.

Some boudins show open folding with the fold axis being oriented perpendicular to the layer (Fig. 2a). This holds particularly for cases where the layer is initially thin ($H_i < 2.0$ mm). This type of folds is referred to as D_2-folds (Zulauf & Zulauf 2005). The latter post-date

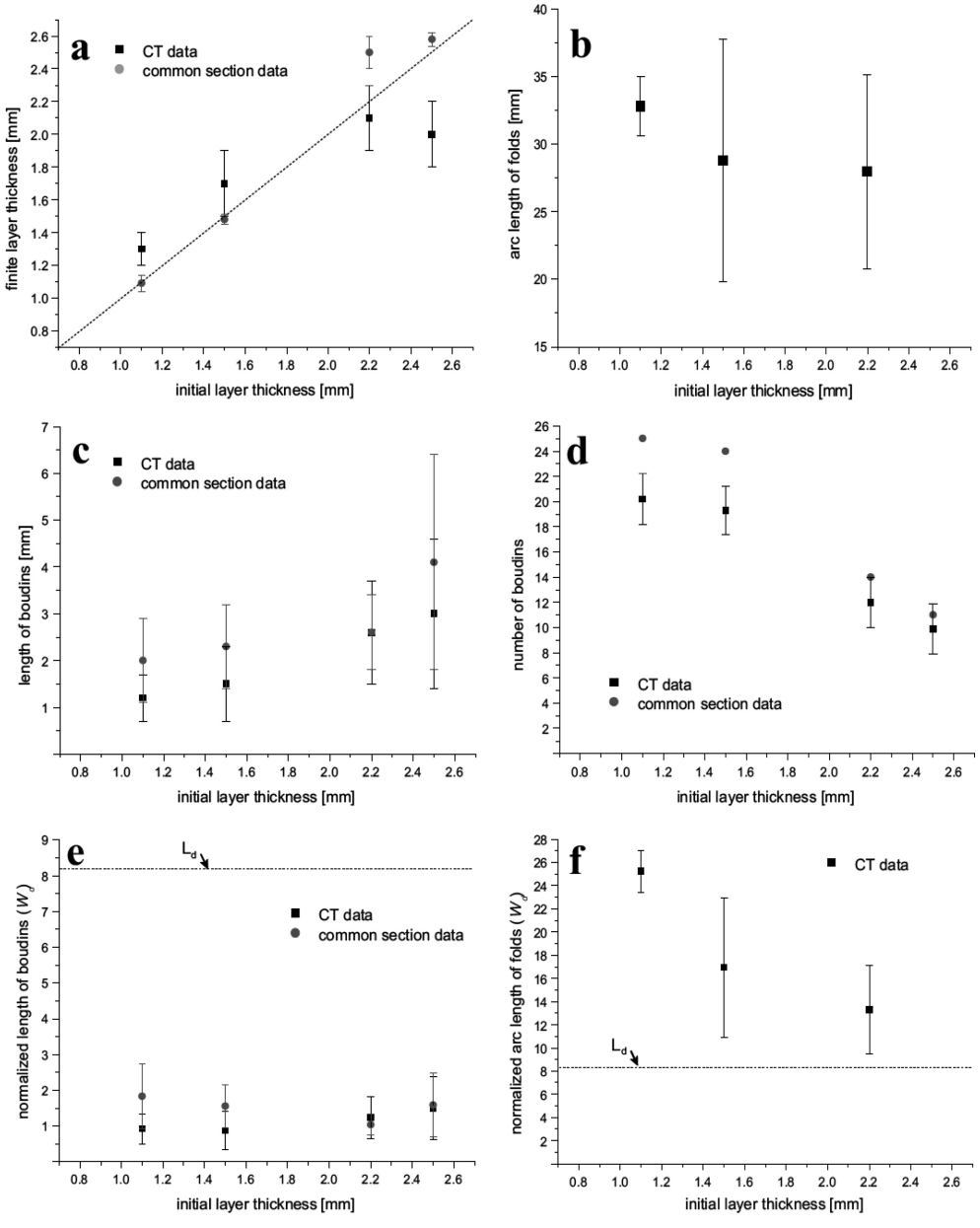

Figure 3. Geometric data of anhydrite layer embedded in halite matrix deformed under bulk constriction with the layer parallel to X. Deformation temperature, T, $=345°C$. $e_{Y=Z} = 2 - 4 * 10^{-7}$ s^{-1}. Geometric parameters are plotted vs. initial layer thickness (H_i). Data shown have been obtained by Computer Tomography (CT) and by analysis of common sections cut parallel to X and perpendicular to the layer (c, d, e) and perpendicular to X and perpendicular to the layer (a, b, f). $L_d =$ normalized initial wavelength calculated after equation (1). Finite strain ($e_{Y=Z}$) $= -32\%$ for initial layer thicknesses 1.1, 1.5, and 2.2 mm. Finite strain ($e_{Y=Z}$) $= -17\%$ for initial layer thickness of 2.5 mm.

D_1-folds which are sometimes visible in sections cut perpendicular to the X-axis (see below).

Statistic analyses of both conventional cuts ($XY =$ XZ sections) and CT images show a clear increase in the length of boudins with layer thickness (Fig. 3c), whereas the number of boudins decreases (Fig. 3d).

Close-up views of $XY = XZ$ sections show the layer to be affected by fracture boudinage consistent with

brittle-ductile behaviour of anhydrite. Most of the fractures are aligned subperpendicular to the layer. In a few cases, however, there are fractures which are oriented oblique to the layer. The boudins are in a few cases asymmetric with respect to the X-axis suggesting local non-coaxial deformation. The necks between the boudins are in most cases entirely filled with halite. However, in a few cases halite was not able to fill the neck completely (Fig. 1). A further feature of $XY = XZ$ sections is a striking fabric in the deformed halite matrix (Fig. 1).

In YZ-sections cut perpendicular to the X-axis, the anhydrite layer shows weak D_1-folding (sensu Zulauf and Zulauf, 2005) and significant drag at both ends due to friction along the boundaries between sample and plate of the machine (Fig. 2b). The low number of folds results in a large uncertainty of geometric data. Consequently, a clear relation between H_i and arc length of folds is not supported by the data obtained (Fig. 3b). In contrast to $XY = XZ$ sections, there is no striking fabric in the halite matrix in YZ sections.

The thickness of the anhydrite layer did not significantly change during constriction (Fig. 3a). There is a peculiar behaviour of thickness data obtained by conventional cuts and by CT data. In cases where the layer was initially thin, the CT images yielded higher values for the thickness. If the layer was initially thick, the thickness derived from CT images is strikingly below the data obtained from conventional sections. The reason for this peculiar contradiction is currently under investigation.

4 DISCUSSION AND CONCLUSIONS

The different grain-shape fabrics in YZ- and $XY = XZ$-sections suggest a strongly prolate fabric of the deformed halite consistent with bulk pure constriction. According to first microfabric analyses this L-fabric results from the shape-preferred orientation of halite and anhydrite crystals. The long axes of both are oriented subparallel to the X-axis.

The experiments have further shown that bulk constriction results in coeval folding and boudinage of the anhydrite layer. The length of boudins increases with layer thickness, whereas the thickness of the layer itself does not significantly change. These features are largely in line with results of previous constrictional experiments, the latter carried out with rheologically stratified plasticine as analogue material (Kobberger & Zulauf 1995, Zulauf et al. 2003, Zulauf & Zulauf 2005). However, the geometry of the anhydrite instabilites differs significantly from that produced with plasticine. This holds particularly for constrictional D_1-folds which show much higher growth rates in plasticine (Zulauf et al. 2003, Zulauf & Zulauf 2005) than in anhydrite of the present study, although the viscosity ratio between layer and matrix was lower in plasticine samples than the viscosity ratio between anhydrite and halite. Constrictional D_1 folds, with axes subparallel to X, initiate at $e_{Y=Z} = -10\%$ and are distinct at $e_{Y=Z} = -20\%$ (Zulauf & Zulauf, 2005). Thus, the weak folding or even the lack of folding of the anhydrite layers cannot be explained by the lower magnitude of finite strain of anhydrite-halite samples ($e_{Y=Z} = -33\%$) compared to plasticine samples, the latter with maximum finite strain of $e_{Y=Z} = -50\%$.

The higher strain magnitude of the plasticine samples, on the other hand, explains the higher degree of both D_2-folding and rotation of D_1-boudins towards the X-axis, as compared to deformed halite-anhydrite samples. This observation is compatible with incremental deformation studies which have shown that D_2-folding and D_2-boudinage is significant under bulk constriction at $e_{Y=Z} > -30\%$ (Zulauf & Zulauf 2005).

Theories of buckle folding in non-linear materials suggest the initial wavelength of buckle folds and boudins to be the same. The geometrical and rheological parameters of these instabilities are related by the following equation (Fletcher 1974, Smith 1977, 1979),

$$L_d \approx 3.46\ (n_2^{1/6}/\ n_1^{1/3})(\eta_1/\eta_2)^{1/3} \qquad (1)$$

where L_d is the theoretical wavelength/thickness ratio (normalized initial wavelength), and n_1, η_1 and n_2, η_2 are the stress exponents and the effective viscosities in the flow laws for layer and matrix, respectively.

Under the deformation conditions of the present study, dry halite should be deformed by climb-controlled dislocation creep (subgrain rotation recrystallization) with strain hardening resulting in an apparent viscosity of ca. 3×10^{13} Pa s (Fransen 1994). Anhydrite, on the other hand, should be deformed in the brittle-plastic regime that is characterized by twinning, kinking and microfracturing (Müller et al. 1981, Ross et al. 1987). The corresponding viscosity is ca. 8×10^{14} Pa s. Thus, for the present experiments the viscosity ratio, m, between anhydrite layer and halite matrix is estimated at ca. 27. At $T = 250$–$450°C$ and $\dot{e} = 10^{-3} - 10^{-7}\ s^{-1}$, the stress exponent of dry halite has been determined at ca. 6 (Fransen 1994). The stress exponent of anhydrite is ca. 5 at $T = 400$–$800°C$ and $\oplus = 10^{-3} - 10^{-6}\ s^{-1}$ (Dell'Angelo & Olgaard 1995).

Inserting these rheological data into equation (1) results in a normalized initial wavelength, L_d, for folds and boudins of 8.1, where L_d = arc length of folds, or length of boudins, divided by finite layer thickness. The actual value of the normalized length of the anhydrite boudins, ($W_{d(Boudin)}$), is much below the L_d value (Fig. 3e). The normalized arc length of folds ($W_{d(Fold)}$), on the other hand, is much higher than L_d (Fig. 3f). A significant difference between $W_{d(Boudin)}$ and $W_{d(Fold)}$ is compatible with our observation that the growth rate of boudins is much higher than the growth rate of D_1-folds.

The behavior of plasticine approximates the results of analytical solutions much more than the behavior of anhydrite-halite. Given that plasticine is deformed at low strain rates ($6 * 10^{-5}$ s^{-1}), the values of $W_{d(boudin)}$ and L_d are similar within uncertainties (Zulauf & Zulauf 2005).

There are several reasons which might explain the geometrical incompatibilities between halite-anhydrite and plasticine samples mentioned above: (1) the size of samples is larger and the finite strain is higher in cases of plasticine samples, (2) deformation of anhydrite-halite samples was affected by moderate volume gain as is indicated by some of the necks which are partly forming open space, whereas deformation of plasticine samples was constant in volume, (3) anhydrite was deformed in the brittle-viscous regime as is indicated by distinct fracture boudinage, whereas the stiff plasticine layers were deformed more viscously, (4) under the deformation conditions used in the present study ($T = 345°C$, $\dot{e} = 2 - 4 * 10^{-7}$ s^{-1}) halite (+anhydrite) did not flow in steady state but showed strain hardening. Thus, the stress exponents published in the literature may deviate from the actual values. This difference in rheological parameters might further explain why the geometric data of the anhydrite instabilities deviate significantly from geometrical data of analytical solutions, the latter assuming steady-state viscous flow.

The open questions addressed above require further investigations concerning the microfabrics and deformation mechanisms of the experimentally deformed halite and anhydrite.

ACKNOWLEDGEMENTS

We thank A. Kiehm (Instiut für Neuroradiologie, Universität Frankfurt a.M.) and M. Peinl (Institut für Geowissenschaften, Universität Frankfurt a.M.) for help with the CT images. Thanks also to R. König, H. Miller and the staff of the workshop of the Technische Fakultät, Universität Erlangen-Nürnberg for building the new deformation apparatus. Financial support by Deutsche Forschungsgemeinschaft is acknowledged (grant Zu 73/13-1).

REFERENCES

Balk, R. 1949. Structure of Gand Saline dome, Van Zandt County, Texas. *AAPG Bulletin* 33: 1791–1829.

Balk, R. 1953. Salt structure of Jefferson Island salt dome, Iberia and Vermilion Parishes, Lousiana. *AAPG Bulletin* 37: 2455–2474.

Davison, I., Alsop, G.I. & Blundell, D.J. 1996a. *Salt tectonics: some aspects of deformation mechanism*. In: Alsop, G.I., Blundell, D.J. & Davison, I., Salt Tectonics, *Geological Soc. Spec. Publ.* 100: 1–10.

Davison, I., Bosence, D., Alsop, G.I. & Al-Aawah, M.H. 1996b. *Deformation and sedimentation around active Miocene salt diapirs on the Tihama Plain, northwest Yemen*. In: Alsop, G.I., Blundell, D.J. & Davison, I., Salt Tectonics, *Geological Soc. Spec. Publ*. 100: 23–39.

Dell'Angelo, L.N. & Olgaard, D.L. 1995. Experimental deformation of fine-grained anhydrite: evidence for dislocation and diffusion creep. *J. Geophys. Res*. 100B: 15425–15440.

Fletcher, R.C. 1974. Wavelength selection in the folding of a single layer with power-law rheology. *American Journal of Science* 274: 1029–1043.

Fransen, R.C.M.W. 1994. The rheology of synthetic rocksalt in uniaxial compression. Tectonophysics, 233, 1–40.

Hartwig, G. 1925. Praktisch-geologische Beschreibung des Kalisalzbergwerkes 'Rössing-Barnten' bei Hildesheim. *Jber. niedersächs. geol. Ver*. 17: 1–74.

Hoy, R.B., Foose, R.M. & O'Neill, B.J. 1962. Structure of Winnfield salt dome, Winn Parish, Louisiana. *AAPG Bulletin* 46: 1444–1459.

Jackson, M.P.A., Schultz-Ela, D.D., Hudec, M.R., Watson, I.A. & Porter, M.L. 1998. Structure and evolution of Upheaval Dome: A pinched-off salt diapir. *GSA Bulletin* 110: 1547–1573.

Kobberger, G. & Zulauf, G. 1995. Experimental folding and boudinage under pure constrictional conditions. *Journal of Structural Geology*, 17: 1055–1063.

Lotze, F. 1957. *Steinsalz und Kalisalze I*. Gebrüder Borntträger, Berlin, 465 p.

Müller, W.H., Schmid, S.M. & Briegel, U. 1981. Deformation experiments on anhydrite rocks of different grain sizes: Rheology and microfabric. *Tectonophysics* 78: 527–543.

Ramberg, H. 1981. *Gravity, deformation and the Earth's crust* (2nd ed.), London, Academic Press, 452 p.

Ramsay, J.G. & Huber, I.H. 1987. *The techniques of modern structural geology, Volume 2: Folds and fractures*: London, Academic Press. 700 pp.

Ross, J.V., Bauer, S.J. & Hansen, F.D. 1987. Textural evolution of synthetic anhydrite-halite mylonites. *Tectonophysics* 140: 307–326.

Sherwin, J.-A. & Chapple, W.M., 1968, Wavelengths of single layer folds: A comparison between theory and observation. *American Journal of Science* 266: 167–178.

Smith, R.B. 1977. Formation of folds, boudinage, and mullions in non-Newtonian materials. *GSA Bulletin* 88: 312–320.

Smith, R.B. 1979. The folding of a strongly non-Newtonian layer. *American Journal of Science* 279: 272–287.

Talbot, C.J. & Jackson, M.P.A. 1987. Internal kinematics of salt diapirs. *AAPG Bull*. 71: 1086–1093.

Trusheim, F. 1960. Mechanism of salt migration in northern Germany. Bull. *Am. Assoc. of Petrol. Geol*. 44: 1519–1540.

Urai, J.L., Spiers, C.J., Peach, C.J., Franssen, R.C.M.W. & Liezenberg, J.L. 1987. Deformation mechanisms operating in naturally deformed halite rocks as deduced from microstructural investigations. *Geol. Mijnbouw* 66: 165–176.

Zulauf, G., Zulauf, J., Hastreiter, P. & Tomandl, B. 2003. A deformation apparatus for three-dimensional coaxial deformation and its application to rheologically stratified analogue material. *J. Struct. Geol*. 25: 469–480.

Zulauf, J. & Zulauf, G. 2005. Coeval folding and boudinage in four dimensions. *J. Struct. Geol*. 27: 1061–1068.

The Mechanical Behavior of Salt – Understanding of THMC Processes in Salt –
Wallner, Lux, Minkley & Hardy, Jr. (eds)
© 2007 Taylor & Francis Group, London, ISBN 978-0-415-44398-2

Experimental research on deformation and failure characteristics of laminated salt rock

Y.P. Li & C.H. Yang
Institute of Rock & Soil Mechanics, Chinese Academy of Sciences, Wuhan, P.R. China

Q.H. Qian
Engineering Institute of Engineering Corps, PLA University of Science & Technology, Nanjing, P.R. China

D.H. Wei & D.A. Qu
West-east Pipeline Company, PetroChina Company Limited, Beijing, P.R. China

ABSTRACT: For investigation of the mechanical and failure characteristics of the laminated salt rock, a series of conventional test were carried out. Three types of samples, pure salt rock samples, pure interlayer (mud rock) samples and salt rock samples with interlayer, were prepared in this study. Uniaxial and triaxial compression experiments showed that the presence of mud rock interlayers in salt rocks affects the mechanical properties and failure pattern of the salt rock significantly. The presence of hard mud rocks in salt rock formations enhances the stiffness and strength of the composite rocks. An interesting 'stress drop' phenomenon was observed and then was interpreted by using the Cosserat medium model. The present results may be expected to provide useful reference for the site selection and design of oil/gas storage cavern in bedded salt rock formations.

1 INTRODUCTION

Salt rocks are commonly utilized as the geologic host rocks for storage of gas and crude oil, and are also being considered for the disposal of radioactive waste. Different from the salt rock dam in other countries, the salt rock formations in China are usually laminated with many salt rock layers and mud rock layers alternately. The laminated salt rocks can exhibit considerable different mechanical properties from the pure salt rocks due to the presence of mud interlayers, therefore, founding an appropriate constitutive theory and the failure criterion for the composite rocks becomes a kernel theoretical problem.

The laminated salt rocks are defined here as a composite rocks with a series of parallel alternate rock layers, for example, the salt rocks with minor mud rock interlayers. The Cosserat medium theory has been employed successfully to analyze the elastic-plastic deformation of the jointed rocks (Muehlhaus & Vardoulakis 1986, Dowson & Cundall 1995, Iordache et al. 1998, Bai & Pollard 2000, Forest et al. 2000, Forest et al. 2001). Xian & Tan (1989), Zhang et al. (2000) and He et al. (2003) also carried out researches on deformation and failure characteristics of laminated rocks. Recently, an expanding Cosserat medium constitutive theory (Yang & Li 2005, Li & Yang 2006, Yang et al. 2006) was proposed for the stability analysis of structures, e.g. salt caverns, in bedded salt rock formation.

To investigate the strength and failure characteristics of laminated salt rocks, a series conventional compression experiments and also creep experiments were carried out on three types of samples, namely, pure salt rock samples, pure mud rock interlayer samples and laminated salt rock samples with mud rock interlayer. The results of compression experiments are presented in this paper.

2 COMPRESSION EXPERIMENTS ON THREE TYPES OF SALT ROCK SAMPLES

2.1 *Experiment equipment and samples*

In the present tests, the XTR01 Electric-fluid Serving Compression Machine (shown in Figure 1) of the Rock and Soil Mechanics Institute, CAS, was employed to study the deformation and failure characteristics of laminated salt rocks. A series of compression experiments at different confining pressures, 0 MPa (uniaxial

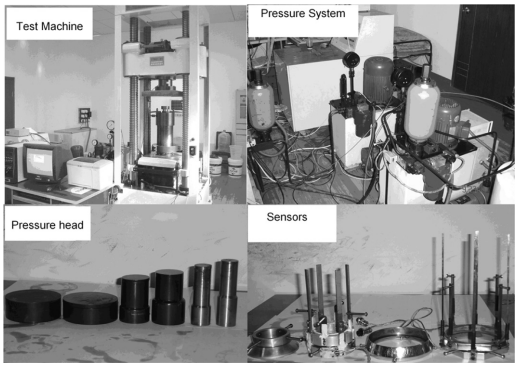

Figure 1. XTR01 electric-fluid serving compression machine.

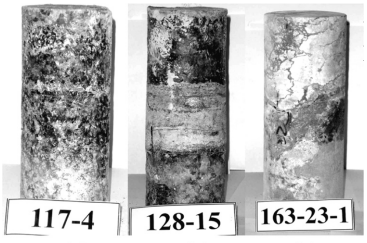

Figure 2. The photos of three typical rock core samples: (a) salt rock, (b) salt rock with mud interlayer, and (c) mud rock.

compression), 5 MPa, 10 MPa, and 15 MPa, respectively, were carried out on three types of samples. The loading process was controlled by the strain ratio. The given strain ratio in present tests was 1×10^{-4}/s.

The rock samples were from Yingcheng Salt Mine, Hubei province, China. The three typical core samples were shown in Figure 2.

2.2 *Experiment results*

The experimental results under uniaxial compression were listed in Table 1. The results indicated that, among there kinds of samples, the uniaxial compression strength, Young's modulus and elastic limit axial pressure of mud rocks were the highest, that of the pure salt rocks are the lowest while that of the salt rocks containing mud are the medium. The uniaxial compression strength of the composite rocks increased with the increase of the volume fraction of mud rock.

The results of triaxial compression were shown in Table 2. The tests were performed under three different confining pressures, 5, 10 and 15 MPa respectively. From Table 2, one knew that the ultimate compression strength of the three kinds of samples all increase with the increase of the confining pressures.

2.3 *Stress–strain curves and 'stress drop' phenomenon*

Under uniaxial compression, the elastic modulus and ultimate strength of the mud rock were the highest among the three types of rocks and that of the salt rock are the lowest while that of the composite rock of salt rock and mud rock are in-between. It was also observed that the ultimate compression strength of the composite rock increased with the increase of the volume fraction of the mud rock.

The stress–strain collection curves (including axial stress difference vs. axial strain curve and axial stress difference vs. radial strain curve) at different confining pressures, 0 MPa (uniaxial case), 5 MPa, 10 MPa and 15 MPa, respectively, were shown in Figure 3.

For the uniaxial case shown in Figure 3a, as the axial stress reaches the peak value, the axial strain of salt rocks was the largest among three kinds of rock samples while that of the composite rock was between the other two. This indicated that the presence of mud interlayers affected the failure characteristics and deformation capability obviously. From Figures 3b, 3c and 3d, one knew that, at high confining pressures, the salt rocks and the composite rocks transformed to be ductile materials from brittle ones. At the same confining pressure, the corresponding axial strains of the composite rocks were between the other two while the axial stress differences reached peak value. In addition, the salt rock exhibited obvious strain-hardening property.

From Figure 3, one could find a special 'stress drop' phenomenon of the stress–strain curves. For the composite rock at uniaxial case, there was an approximate 4 MPa of stress drop before the axial stress difference reaching peak value. This indicated that the hard-brittle interlayer was suffering fracture while the salt rock kept still intact state. The stress recovered immediately after dropping, and the materials then underwent a strain-softening process until whole collapse. For low confining pressure case, the stress drop phenomenon was also observed. As shown in Figure 3b, there were two times of this phenomenon though the drop values (about 2 MPa) were smaller than that of the uniaxial case. For the high confining pressure case, the special phenomenon was suppressed.

2.4 *Failure patterns of three kinds of rock samples*

Shown in Figure 4 were the typical failure patterns of the three kinds of rock samples under uniaxial compression. They were all split along one or more tensile cleavage planes along the axial direction. However, the failure of the composite rock was remarkable different from the other two. The intrinsic uniaxial compression strength of the mud rock is higher than that of the salt rock, but it was surprising that the interlayer phase was split first. The cracks then extended to the interface of

Table 1. Results of uniaxial compression tests.

	Sample number	Volume fraction of interlayer (%)	Ultimate strength (MPa)	Young's modulus (GPa)	Poisson ratio	Elastic limit stress (MPa)
Mud rock	163-23-1	100	23.72	20.91	0.195	18.5
	163-23-2	100	24.11	22.65	0.269	19.2
Average value			23.92	21.78	0.232	18.9
Salt rock	128-15	32.1	23.29	7.65	0.158	14.7
containing	140-21-1	18.5	19.29	5.32	0.304	13.4
mud rock	169-7-2	25.2	22.54	16.15	0.313	14.2
	169-7-1	34.8	24.64	11.21	0.293	12.8
Average value			22.54	10.08	0.267	13.8
Salt rock	117-4	0	17.06	5.91	0.311	10.6
	116-24	0	20.26	4.39	0.313	10.8
Average value			18.66	5.15	0.312	10.7

Table 2. Results of triaxial compression tests.

	Sample number	Confining pressure (MPa)	Ultimate strength (MPa)	Young's modulus (GPa)
Mud rock	171-26-2	5	59.83	27.63
	171-26-3	10	67.04	30.89
	169-12	15	73.51	32.72
Salt rock containing	107-5	5	51.54	15.65
mud rock	121-18-1	10	66.03	28.72
	128-21	15	81.39	34.48
Salt rock	115-25	5	43.09	15.47
	129-10	10	63.40	20.75
	110-31	15	71.62	21.69

two materials and resulted in the cleavage of salt rocks as shown in Figure 4b.

The failure patterns of these rocks at triaxial compression were demonstrated in Figure 5. They were apparent different. The mud rock sample fractured along an oblique shearing plane while the salt rock sample exhibit obvious plastic failure characteristics. The failure of the composite rock sample was rather complex. The mud phase fractured by shear first and then the cracks propagated to the salt phase.

One can infer reasonably that the stress drop phenomenon was corresponding to the hard interlayer fracturing first, which will result in a local transient unloading.

3 THEORETICAL ANALYSIS ON STRESS DROP PHENOMENON

3.1 *Expanded Cosserat constitutive model for layered rocks*

Considering the characteristics of layered rocks, Yang et al. (2006) proposed an expanded Cosserat constitutive model, in which the influence of bending is taken into account. In this model, a new unit cell, containing two alternate layers, was employed to simulate the compatibility of the meso-displacement between two layers with mismatch mechanical properties. This model provides a new way for the analysis of layered salt rock. Having the Cosserat stresses, namely the macro-average ones, determined, the conventional stresses of the different layers in a unit cell can be obtained in sequence. Then the conventional stresses can be utilized through a routine way for the strength and failure analysis. Here only a brief summary is given out.

The representative unit shown in Figure 6 is the composite of materials A and B. The 3-dimensional expanded Cosserat medium constitutive relationship was deduced based on the classical continuum theory, assuming that:

- Two different isotropic materials are bonded perfectly without sliding, opening or imbedding;
- The four side surfaces keep planar when the material suffers tensile or bending deformation; and
- The deformation is small.

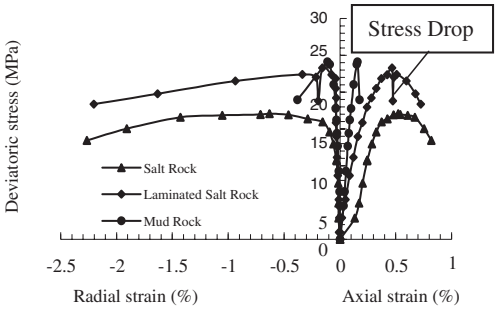

(a) Confining pressure: 0 MPa

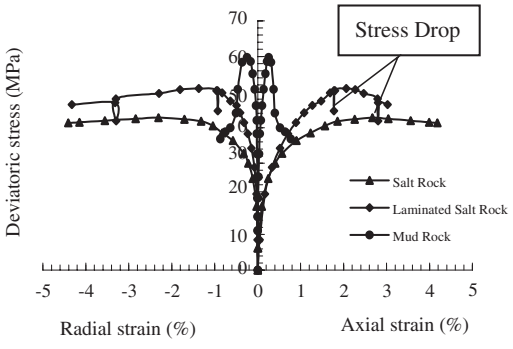

(b) Confining pressure: 5 MPa

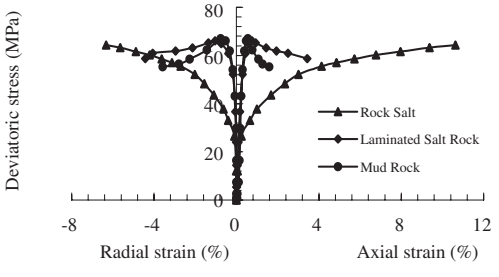

(c) Confining pressure: 10 MPa

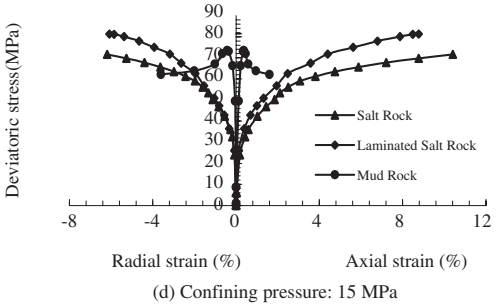

(d) Confining pressure: 15 MPa

Figure 3. Typical stress–strain curves of three kinds of rock samples at different confining pressures.

(a) salt rock (b) laminated salt rock (c) mud rock

Figure 4. Failure patterns of rock samples under uniaxial compression.

(a) salt rock (b) laminated salt rock (c) mud rock

Figure 5. Failure patterns of rock samples under triaxial compression.

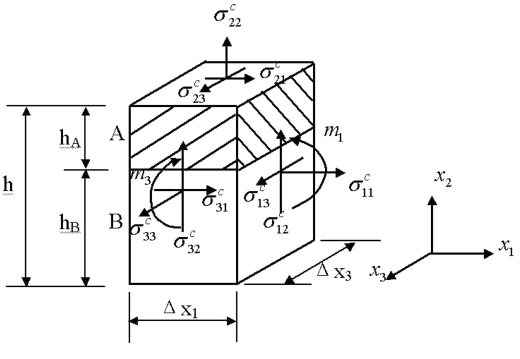

Figure 6. Material point of the Cosserat medium for layered rockmass.

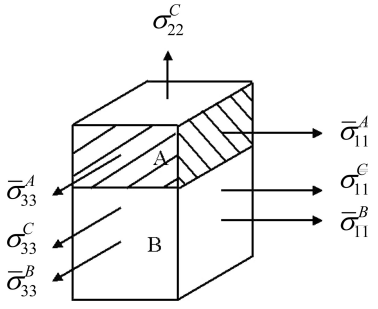

Figure 7. The normal stresses in a unit.

The global Cosserat constitutive relationship for the composite material was

$$\begin{Bmatrix} \varepsilon_{11}^c \\ \varepsilon_{22}^c \\ \varepsilon_{33}^c \\ \varepsilon_{12}^c \\ \varepsilon_{21}^c \\ \varepsilon_{32}^c \\ \varepsilon_{23}^c \\ \varepsilon_{13}^c \\ \kappa_1 \\ \kappa_3 \end{Bmatrix} = \begin{bmatrix} D_{11} & D_{12} & D_{13} & 0 & 0 & 0 & 0 & 0 & 0 & 0 \\ & D_{22} & D_{23} & 0 & 0 & 0 & 0 & 0 & 0 & 0 \\ & & D_{33} & 0 & 0 & 0 & 0 & 0 & 0 & 0 \\ & & & D_{44} & D_{45} & 0 & 0 & 0 & 0 & 0 \\ & & & & D_{55} & 0 & 0 & 0 & 0 & 0 \\ & & & & & D_{44} & D_{45} & 0 & 0 & 0 \\ & & & Sym & & & D_{55} & 0 & 0 & 0 \\ & & & & & & & D_{66} & 0 & 0 \\ & & & & & & & & D_{77} & 0 \\ & & & & & & & & & D_{88} \end{bmatrix} \begin{Bmatrix} \sigma_{11}^c \\ \sigma_{22}^c \\ \sigma_{33}^c \\ \sigma_{12}^c \\ \sigma_{21}^c \\ \sigma_{32}^c \\ \sigma_{23}^c \\ \sigma_{13}^c \\ m_1 \\ m_3 \end{Bmatrix} \tag{1}$$

where $\sigma_{ij}^c (i,j=1,2,3)$ are the Cosserat stresses, $\varepsilon_{ij}^c (i,j=1,2,3)$ are the corresponding Cosserat strains, $\kappa_i (i=1,3)$ are the independent curvatures and $m_i (i=1,3)$ are the corresponding couple-stresses. The eight independent nonzero elements in the flexibility tensor can be defined completely in terms of the elastic moduli and the volume fractions of two layers. The expressions for these factors were presented in (Yang et al. 2006).

3.2 *Stress drop phenomenon explanation*

The expanded Cosserat medium constitutive model was adopted here to analyze the experimental phenomena above.

Shown in Figure 7 is a unit of Cosserat medium, on which the normal Cosserat stresses $\sigma_{22}^c, \sigma_{11}^c$ and σ_{33}^c are acting. For the quasi-triaxial loading case, σ_{22}^c is the axial stress while σ_{11}^c or σ_{33}^c is the confining pressure. One has

$$\begin{aligned} \sigma_{11}^c &= \sigma_{33}^c \\ \bar{\sigma}_{11}^A &= \bar{\sigma}_{33}^A \\ \bar{\sigma}_{11}^B &= \bar{\sigma}_{33}^B \end{aligned} \tag{2}$$

where $\bar{\sigma}_{11}^A, \bar{\sigma}_{33}^A, \bar{\sigma}_{11}^B$ and $\bar{\sigma}_{33}^B$ are the average side normal stresses of layer A and layer B respectively. Due to the mismatch of elastic properties of two layers, the average stresses $\bar{\sigma}_{11}^A$ and $\bar{\sigma}_{11}^B$ are not necessary equal to maintain equal side normal strains. The average components can be readily deduced (Yang et al. 2006).

$$\begin{aligned} \bar{\sigma}_{11}^A = \bar{\sigma}_{33}^A &= \frac{E_A D_{12} + \mu_A}{1-\mu_A}\sigma_{22}^c + \frac{E_A (D_{11}+D_{13})}{1-\mu_A}\sigma_{11}^c \\ \bar{\sigma}_{11}^B = \bar{\sigma}_{33}^B &= \frac{E_B D_{12} + \mu_B}{1-\mu_B}\sigma_{22}^c + \frac{E_B (D_{11}+D_{13})}{1-\mu_B}\sigma_{11}^c \end{aligned} \tag{3}$$

where E_A, E_B, μ_A and μ_B are Young's modulii and Poisson ratios of two layers respectively, and D_{11}, D_{12} and D_{13} are the components of the flexibility matrix[6].

$$\begin{aligned} D_{12} &= -\left(\frac{\alpha_A \mu_A}{1-\mu_A} + \frac{\alpha_B \mu_B}{1-\mu_B}\right)\left(\frac{\alpha_A E_A}{1-\mu_A} + \frac{\alpha_B E_B}{1-\mu_B}\right)^{-1} \\ D_{11} + D_{13} &= \left(\frac{\alpha_A E_A}{1-\mu_A} + \frac{\alpha_B E_B}{1-\mu_B}\right)^{-1} \end{aligned} \tag{4}$$

where α_A and α_B are the volume fractions of salt and mud rock layers.

Substituting experimental results: $E_B = 5.15$ GPa, $\mu_B = 0.31$ and $\alpha_B = 0.7$ for salt rock and $E_A = 21.78$ GPa, $\mu_A = 0.23$ and $\alpha_A = 0.3$ for mud rock, to Equation 2 and 3, one gets

$$\begin{aligned} \bar{\sigma}_{11}^A = \bar{\sigma}_{33}^A &= \sigma_{11}^c + \sigma_*^A \\ \bar{\sigma}_{11}^B = \bar{\sigma}_{33}^B &= \sigma_{11}^c + \sigma_*^B \end{aligned} \tag{5}$$

where the additional equivalent side normal stresses:

$$\begin{aligned} \sigma_*^A &= 1.062\sigma_{11}^c - 0.533\sigma_{22}^c \\ \sigma_*^{\mathrm{B}} &= -0.456\sigma_{11}^c + 0.230\sigma_{22}^c \end{aligned} \tag{6}$$

Let consider two cases: for uniaxial compression: $\sigma_{22}^c = -10$ MPa and $\sigma_{11}^c = 0$ MPa, one obtains $\sigma_*^A = 5.33$ MPa and $\sigma_*^B = -2.30$ MPa; and for triaxial compression: $\sigma_{22}^c = -15$ MPa and $\sigma_{11}^c = -5$ MPa, one knows $\sigma_*^A = 2.65$ MPa and $\sigma_*^B = -1.17$ MPa. It can be concluded that, due to the mismatch of elastic properties of salt and mud rocks, the additional equivalent tensile stress applied on the mud rock (stiff one) weakens its strength, while the additional equivalent compression stress applied on the salt rock (soft one) enhances its strength on the contrary. This could interpret well why the mud rock layers fracture prior to the salt rock layers and thus the stress drop phenomenon. As soon as the mud rock layer splitting occurs, the interactional restriction between two adjacent layers is released partially, resulting in a sudden drop of compression modulus of the samples. The transitory softening process presents the stress drop phenomenon observed above. While the loading increases continually, the two layers reach a new displacement

coordination state, and the stress recover fast until it reaches the peak value.

By calculating the effective stresses considering Equation 6, one knows the tension limit of the hard mud rock layer should be reached theoretically sooner. However the stress drop phenomenon demonstrated above which is interpreted as fracture process in the hard mud rock layer occurred under very high loadings. This is because the stress boundary conditions of the experimental samples are not wholly the same as the displacement boundary conditions of the theoretical model, in which it is assumed that the four side surfaces of the unit keep planar. This assumption is reasonable while considering a meso-unit in an infinite body, but it would somewhat overestimate the interactional displacement restriction between two adjacent layers.

The deformation and failure characteristics of laminated salt rocks are important for the study on the stability of oil/gas storages in bedded salt rocks formation. The theoretical analysis in this paper is restricted in elastic state, so, the experimental and theoretical researches on elasto-plastic and rheological constitutive model of layered salt rocks should be carried out further.

4 SUMMARY

For investigation of the mechanical and failure characteristics of the laminated salt rock, a series of conventional tests were carried out. The compression experiments indicated that the presence of mud rock interlayers in salt rocks affects the mechanical properties and failure pattern of the salt rock significantly. The presence of hard mud rocks in salt rock formations enhances the stiffness and strength of the composite rocks. What's more, the hard mud rock interlayers may fracture prior to the salt rock and then results in the final collapse though the inherent strength of the former is higher than that of the later. This point and its consequent result 'stress drop' phenomenon were analyzed theoretically by using the expanding Cosserat medium model.

ACKNOWLEDGMENTS

The authors acknowledge the financial support from National Natural Science Foundation of China (50434050, 50374064) and the Project of National Basic Research Program of China (2002CB412704).

REFERENCES

Forest, S., Pradel, F. & Sab, K. 2001. Asymptotic analysis of heterogeneous Cosserat media. *Int J Solids Structures* 38: 4585–4608.

Dawson, E.M. & Cundall, P.A. 1995. Cosserat plasticity for modeling layered rock. In Myer, Cook & Goodman (ed.), *Proceedings of the Conference on Fractured and Jointed Rock Masses.* Netherlands: A.A. Balkema.

Forest, S., Barbe, F., & Cailletaud, G. 2000. Cosserat modelling of size effects in the mechanical behaviour of polycrystals and multi-phase materials. *Int J Solids Structures* 37: 7105–7126.

Bai, T. & Pollard, D.D. 2000. Fracture spacing in layered rocks: a new explanation based on the stress transition. *J Structural Geology* 22: 43–57.

Iordache, M.M. & Willamb, K. 1998. Localized failure analysis in elastoplastic Cosserat continua. *Comput Methods Appl Mech Engrg* 151: 559–586.

Muehlhaus, H.B. & Vardoulakis, I. 1986. Axially symmetric buckling of a laminated half space with bending stiffness. *Mechanics of Materials* 5: 109–120.

He, P.T. & Huang, Z.P. 2003. Studies of strength and deformation characteristics for stratified rock. *Chinese Rock and Soil Mechanics* 24(Suppl 1): 1–5.

Zhang, D.L., Wang, Y.H. & Qu, T.Z. 2000. Influence analysis of interband on stability of stratified rockmass. *Chinese Journal of Rock Mechanics and Engineering* 19(2): 140–144.

Xian, X.F. & Tan, X.S. 1989. *Failure Mechanism of Stratified Rock Mass.* ChongQing: ChongQing University Press.

Yang, C.H & Li, Y.P. 2005. The expanded Cosserat medium constitutive model for laminated salt rock. *Chinese Journal of Rock Mechanics and Engineering* 24(23): 4226–4232.

Li, Y.P & Yang, C.H. 2006. The three-dimensional expanded cosserat medium constitutive model for laminated salt rock. *Chinese Rock and Soil Mechanics* 27(4): 509–513.

Yang, C.H., Li Y.P., Yin, X.Y., Chen, F. & Zhang C. 2006. Cosserat Medium Constitutive Model for Laminated Salt Rock and Numerical Analysis of Cavern Stability in Deep Bedded Salt Rock Formations. *Proceedings of the 41st U.S. Rock Mechanics Symposium & 50th Anniversary*. Golden, Colorado, USA.

Part 2. Constitutive models for the mechanical behavior of rock salt

Taylor & Francis
Taylor & Francis Group
http://taylorandfrancis.com

The Mechanical Behavior of Salt – Understanding of THMC Processes in Salt –
Wallner, Lux, Minkley & Hardy, Jr. (eds)
© 2007 Taylor & Francis Group, London, ISBN 978-0-415-44398-2

Comparison of advanced constitutive models for the mechanical behavior of rock salt – results from a joint research project – I. Modeling of deformation processes and benchmark calculations

O. Schulze[2)], U. Heemann[2)], F. Zetsche[2)], A. Hampel[1)], A. Pudewills[3)], R.-M. Günther[4)], W. Minkley[4)], K. Salzer[4)], Z. Hou[5,*)], R. Wolters[5)], R. Rokahr[6)] & D. Zapf[6)]

1) Consultant, Essenheim, Germany
2) Federal Institute for Geosciences and Natural Resources (BGR), Stilleweg, Hannover
3) Forschungszentrum Karlsruhe GmbH, Institut für Nukl. Entsorgung (INE), Karlsruhe
4) Institut für Gebirgsmechanik GmbH (IfG), Friederikenstr, Leipzig
5) Clausthal University of Technology, Professorship for Disposal Technology and Geomechanics (TUC), Erzstraße, Clausthal-Zellerfeld
**) now with: Clausthal University of Technology, Institute of Petroleum Engineering*
6) Leibniz Universität Hannover, Institut für Unterirdisches Bauen (IUB), Welfengarten, Hannover

ABSTRACT: In this first part of the joint project, the partners document their constitutive models and the results of their recently performed comparative model calculations. An elaborated database is used for the reliable determination of salt-type specific parameter values of the respective models. Individual back-calculations of different types of laboratory tests allow to examine and to compare the features of the models in detail. The results demonstrate that the models have reached a high standard in describing various important deformation processes like creep, dilatancy, damage, failure, and post-failure behavior under different influences. It can be concluded that the partners do have appropriate tools for model calculations. Furthermore, the comparisons show, how the models and the numerical codes can be developed and improved further.

1 INTRODUCTION

For the prediction of the mechanical behavior of rock salt, all those processes have to be taken into account which contribute substantially to the time-dependent and spatial evolution of stress and strain in the material. In the past, several constitutive models were developed by different groups to describe the phenomena observed during mechanical loading and deformation. Of main concern is the modeling of the processes which cause transient creep including recovery, steady-state creep, dilatancy and propagation of damage, humidity induced processes, failure, and post-failure strength. Only with appropriate models, the long-term prediction of the mechanical behavior will be reliable, as it is required for the assessment and approval of an underground repository, for instance. Such models should be physically based taking into account as far as possible the knowledge about the dominant micro-mechanical processes.

The partners of this joint project (the authors of this paper) decided to document their constitutive models and the results of the recently performed comparative model calculations in two contributions. In this first part, the features and the capacity of the individual constitutive models, the determination of the respective salt-type dependent model parameters and the related model calculations of specific laboratory tests will be presented. The second part (Hou et al. 2007) deals with the comparative numerical modeling of two in-situ case studies within this project.

2 DATA BASIS

Constitutive models should take into account as far as possible all the relevant processes that are active during the loading and the deformation of rock salt. For the prediction of the material behavior, especially in the context of long-term safety analyses, these processes are modeled by constitutive equations which are implemented in appropriate numerical codes. In any model, specific parameter values are needed which represent the properties of each type of rock salt under investigation.

The parameter determination is a big challenge, because not all of the deformation processes can be measured individually and, thus, not all parameters can

be determined independently. Therefore, they have to be deduced from a bundle of reproducible and reliable deformation experiments. In addition, a distinct type of rock salt requires a unique set of parameter values for the modeling of its deformation behavior under different and changing influences in various possible underground situations – without further (more or less arbitrary) adaptations.

In general, the parameter values of the respective models are determined by back-calculations of laboratory experiments. For this purpose, the experimental database should result from tests which are performed under well-defined conditions. For the separation and the identification of the different processes and the consecutive determination of the parameters, qualified experiments are needed which cover all the processes, i.e. the spectrum of mechanisms requires different and well adapted types of mechanical tests. Therefore, the short-term strain rate controlled strength tests as well as the long-term creep tests from laboratory work are preferred which offer the advantage of precisely defined and well-controlled testing conditions.

Data from in-situ observations and in-situ measurements are also very useful, especially in the case of low stresses and low deformation rates beyond the limits of resolution in the laboratory. However, one has to keep in mind that in-situ the boundary conditions are often not sufficiently known and several influences may be indistinguishably active at the same time.

In this project, the so-called Speisesalz from the Asse mine is selected as a reference material. This type of rock salt consists of rather clean halite maintaining a good reproducibility of the test results that yield the basis for the parameter evaluation. The same methods are applied to determine the parameter values for the numerical simulations of an in-situ situation in the Staßfurt rock salt horizon of the Sondershausen formation (older halite), and for the numerical simulation of a room-and-pillar model, both are described in part II of this contribution (Hou et al. 2007).

2.1 *Long-term creep*

Among the relevant processes, first of all the deformation behavior during loading of rock salt in the non-dilatant stress domain is examined, i.e. creep without weakening by damage and volume creep (i.e. dilatancy). For this purpose, the well established creep testing technique is used, where the stress difference $\Delta\sigma = (\sigma_1 - \sigma_3)$ is increased and subsequently held constant to receive data for the transient creep behavior and for the stress sensitivity of the steady-state creep rate. σ_1 is the axial stress, σ_3 is the confining pressure p_c. All the experiments are performed on cylindrical specimens under the load geometry 'compression'. Thus, σ_3 stands for the minimal principle stress. The testing is generally performed at or near ambient temperature (22°C or 30°C) which is representative for most of the in-situ situations, except from the case of HAW-disposal. Nevertheless, even at ambient conditions the temperature has to be kept as constant and stable as possible during the long-term creep tests to avoid additional uncertainties in the determination of the values of the model parameters.

A special challenge is the modeling and proper computation of the creep behavior in course of stepwise increased and reduced stresses, where progressive deformation hardening and recovery are present. Only if the rate-controlling mechanisms are properly modeled the long-term stress redistribution near an underground opening will be predicted reliably.

2.2 *Dilatancy affected deformation*

Of particular importance is the dependence of the material behavior on the state of stresses with respect to the dilatancy boundary. This boundary separates the stress domain without damage affected deformation processes from the domain where the stress-strain behavior is superimposed by micro-cracking, weakening and at last failure. In this domain, the so-called tertiary creep comes into account. All these phenomena have to be included into a complex constitutive model.

For the determination of the model parameters at stresses and strain rates, where dilatancy related processes will dominate the material behavior, strain rate-controlled short-term strength tests complete the required experimental database. In such experiments the deformation hardening, the onset of dilatancy, the progression of damage and volumetric strain, the failure strength, and the post-failure behavior are the main processes in the material. The modeling of this behavior is an ambitious task, because all the mentioned mechanisms can contribute to the overall deformation behavior at the same time.

Some of the strength tests are stopped just before the peak strength is reached. Careful measurement of the dimensions and the density of the already heavily deformed specimens yield data for the recalibration of the volume-measuring device, whose accuracy is found to be satisfying, and for the calibration of the numerical models with respect to the prediction of volume increase until failure during the deformation in the dilatant stress domain. These tests are indispensable to check the comparability of the results and to achieve sound confidence.

It should be mentioned that humidity induced creep may be also of concern in stress situations near and above the dilatancy boundary. Zones of a rock salt formation exhibit evidently the influence of the seasonal variation in humidity of the air during the weathering of a mine – for instance in a room-and-pillar system, where the EDZ has spread out up to a relevant portion around underground openings. But this impact is generally not modeled and implemented in the numerical

codes up to date (However, one of the considered models, the CDM, already does, see chapter 3).

In this context, the mechanisms of pressure solution creep or fluid assisted diffusional transport, the so-called FADT-creep should briefly be mentioned (Urai et al. 1986, Spiers & Schutjens 1990, Spiers et al. 1989). These mechanisms can substantially contribute to the overall strain and stress redistribution during long-term creep at rather low stresses, because they do linearly depend on stress and, therefore, their contribution to the strain rate reduces only linearly with decreasing stress. However, one has to keep in mind, that the presence of more or less continuous films of brine on the grain boundaries and other intercrystalline surfaces is the prerequisite. Therefore, this class of mechanisms may have importance in case of the compaction of crushed salt used as a backfill material. For technical reasons, the backfill may have higher water content than the principally dry rock salt. In this work, fluid assisted processes are not taken into account.

3 CONSTITUTIVE MODELS

In this joint project the modeling of deformation processes is concentrated on non-dilatant creep as well as on dilatancy and damage affected deformation processes. The dependence on temperature and the consequences of the dilatant deformation on the evolution of permeability and pore pressure effects, which may become of concern for the material behavior if the permeation of a pressurized fluid into the damaged salt takes place, are not considered in this project.

In general, a phenomenon (i.e. a single deformation process) is described by one or by a set of appropriate equations. Then, the combination of these modules reflects the overall coupling of the involved deformation processes. In the following, the models of the partners are presented. The elastic deformation is generally modeled by applying Hooke's law, in the following, this is only mentioned if elasticity depends explicitly on the evolution of damage.

3.1 *The CDM model system*

The partners Hampel and BGR use the modules of the CDM (Composite Dilatancy Model; Hampel & Schulze 2007, Hampel & Hunsche 2002) which describes the total inelastic strain rate $d\varepsilon_{tot}/dt$ as a product of different functions which are responsible for different processes.

$$d\varepsilon_{tot}/dt = d\varepsilon_{cr}/dt \cdot F_h \cdot \delta_{dam} \cdot P_F \quad (1)$$

The CDM consists of a term $d\varepsilon_{cr}/dt$ which refers to the dependence of the total strain rate on the deformation rate of non-dilatant creep

$$d\varepsilon_{cr}/dt \sim \rho \cdot b \cdot v(T, \Delta\sigma, S) \quad (2)$$

This Orowan-type creep rate combines the micromechanical dislocation mechanisms with the macroscopic creep rate $d\varepsilon_{cr}/dt$, where $\rho = 1/r^2$ is the dislocation density with r as the mean distance between dislocations, b is the absolute value of the Burgers vector, and v(T, $\Delta\sigma$, S) is the mean dislocation velocity. The latter depends on the temperature T, the stress difference $\Delta\sigma$, and the relevant parameters which characterize the deformation microstructure S (i.e. subgrain size, dislocation distance, thickness of subgrain walls). The dependence on temperature is described by an Arrhenius term and the stress dependence by a hyperbolic sine term. The parameters of the microstructure develop in dependence of the creep rate reflecting the close correlation between changes in the microstructure and the evolution of transient creep to steady-state creep

$$dS/dt = [(S_\infty - S) / k_S] \cdot d\varepsilon_{cr}/dt \quad (3)$$

where S_∞ denotes the steady-state values of the microstructural parameters which are determined from experimental investigations. The parameter k_S represents the evolution constants in the different functions S(t) for the micro-structural changes.

The second term in Equation (1), the function F_h, refers to the dependence on the relative humidity Φ at the free surfaces and in the pore system of dilated rock salt

$$F_h = f(\Phi, \sigma_{min}, \tau_o) \quad (4)$$

where σ_{min} is the minimal principle stress and τ_o the octahedral shear stress.

The third term in Equation (1), δ_{dam}, refers to the dependence of the total strain rate on the evolving damage.

$$\delta_{dam} = f(d_{dam}, \sigma_{min}) \quad (5)$$

The damage influence function δ_{dam}, which causes weakening and at last failure, is expressed by the dependence on the minimal principle stress σ_{min} and the damage evolution function d_{dam} which depends on the mean stress σ_o and the volumetric strain rate $d\varepsilon_{vol}/dt$

$$d(d_{dam})/dt = \sigma_o \cdot d\varepsilon_{vol}/dt \quad (6)$$

The equation for the volumetric strain rate expresses the experimentally found dependence on the rate of dislocation creep $d\varepsilon_{cr}/dt$

$$d\varepsilon_{vol}/dt = r_V(\tau_o, \sigma_o) \cdot d\varepsilon_{cr}/dt \quad (7)$$

The empirical function $r_V(\tau_o, \sigma_o)$ depends on the octahedral shear stress τ_o and the mean stress σ_o. At the dilatancy boundary, r_V becomes zero. The volumetric strain is generally: $\varepsilon_{vol} = \varepsilon_1 + \varepsilon_2 + \varepsilon_3$.

The last term in Equation (1), the function P_F refers to the dependence of ε_{tot} on the post-failure deformation behavior

$$P_F = f[(\tau_o - \tau_D), \sigma_{min}, (\varepsilon_{tot} - \varepsilon_F)] \quad (8)$$

where $\tau_D = f(\sigma_o)$ is the octahedral shear stress at the dilatancy boundary and the expression $(\varepsilon_{tot} - \varepsilon_F)$ is the strain in the post-failure range. The strain at failure ε_F is determined empirically. All the dilatancy related terms in Equation (1) converge to unity in case of a non-dilatant creep deformation below the dilatancy boundary. For further details see Hampel & Schulze (2007).

3.2 *The IfG-G&S model*

The partner IfG uses two different models, a strain-hardening model (IfG-G&S) and an elasto- visco-plastic model (IfG-M).

In the IfG-G&S model, the total inelastic strain rate $d\varepsilon_{tot}/dt$ is expressed by

$$d\varepsilon_{tot}/dt = A_p \cdot \sigma^{n_p} / (\varepsilon^V + \varepsilon^V{}_o)^{\mu} \quad (9)$$

where the pre-factor A_p refers to the individual behavior of a distinct type of rock salt, the stress exponent n_p reflects the stress sensitivity of the strain rate, and ε^V is the effective hardening component of the strain and ε_o^V its initial part. $(\varepsilon^V + \varepsilon_o^V)$ influences the total strain rate non-linearly by the exponent μ.

The evolution of the effective strain hardening ε^V is described by

$$d\varepsilon^V/dt = d\varepsilon_{tot}/dt - d\varepsilon^E/dt - d\varepsilon^S/dt \quad (10)$$

where the general progress in hardening $d\varepsilon^V/dt \sim d_{tot}/dt$ is reduced by the recovery creep rate $d\varepsilon^E/dt$ and the damage evolution $d\varepsilon^S/dt$.

The recovery creep rate

$$d\varepsilon^E/dt = \varepsilon^V / t_o \quad (11)$$

is depending on the present hardening component of the strain ε^V and a recovery time t_o which is determined experimentally and depends on the distinct characteristics of a certain type of rock salt.

The damage evolution rate $d\varepsilon^S/dt$, that is the last term in Equation (10), is found to be equal to the volumetric strain rate $d\varepsilon_{vol}/dt$

$$d\varepsilon^S/dt = d\varepsilon_{vol}/dt = f(\sigma_{min}, U_{Dil}) \quad (12)$$

The complex parameter U_{Dil} describes the progress of damage, where U_{Dil} is a function of the total strain times the present shear stress minus the shear stress of the dilatancy boundary, which is experimentally determined and found to be a non-linear function of the minimal principle stress. Therefore, U_{Dil} is the deformation energy performing during deformation in the dilatant stress domain.

During testing at a constant stress, the effective hardening rate $d\varepsilon^V/dt$ of Equation (10) is positive in the transient creep domain and converges to zero in case of steady-state creep. If damage is super-imposing the deformation, the effective strain hardening rate $d\varepsilon^V/dt$ decreases, converges to zero at failure, and becomes progressively negative in the post-failure range causing accelerating tertiary creep.

It has to be mentioned that the stress sensitivity parameter n_p is not a constant like in a standard "power creep law". Instead, this parameter is modeled in dependence on the damage evolution

$$n_p = f(\sigma_{min}, \varepsilon_{vol}) \quad (13)$$

In the IfG-G&S, also the elastic parameters are expressed in dependence on the damage evolution, i.e. on the volumetric strain ε_{vol}. For further details see Günther & Salzer (2007).

3.3 *The IfG-M model*

In the IfG-M model, the stress-strain relation is described by an extended Burgers-model which consists of a Kelvin-element to reflect the transient creep ε^K and a Maxwell-element to reflect the steady-state creep ε^M. In addition, the IfG-M model consists of a damage module, which describes the evolution of damage, failure, and the post-failure behavior by the contribution of the plastic strain ε^p which is modeled on basis of the plastic flow theory.

Thus, the total inelastic strain ε^{inel} consists of the viscous strain ε^v and the plastic strain ε^p

$$\varepsilon^{inel} = \varepsilon^v + \varepsilon^p \quad (14)$$

with $\varepsilon^v = \varepsilon^K + \varepsilon^M$

In the simplified one-dimensional notation, the transient creep rate $d\varepsilon^K/dt$ is defined as a function of the shear stress σ, the viscosity of the Kelvin-element η_K, and of the shear modulus G_K

$$d\varepsilon^K/dt = (1/\eta_K) \cdot \sigma - (G_K/\eta_K) \cdot \varepsilon^K \quad (15)$$

The extended Burgers model takes into account the deformation history. The state variable that records history is ε^K, for which an additional evolution equation is utilized.

The steady-state creep rate $d\varepsilon^M/dt$ is defined as a function of the shear stress σ, the viscosity of the Maxwell-element η_M, and of the shear modulus G_M

$$d\varepsilon^M/dt \sim (d\sigma/dt) / G_M + \sigma / \eta_M \quad (16)$$

where the viscosity η_M of the Maxwell-element is modeled as a non-linear function of the effective stress σ_{eff}

$$\eta_M \sim \eta^*_M \cdot \exp(-m_M \cdot \sigma_{eff}) \quad (17)$$

The parameter m_M is determined from experimental results.

The second term of Equation (14), that is the plastic strain ε^p, results from the sum of strain increments $\Delta\varepsilon^p$ which depend on the evolution of the plastic potential g_s during loading and deformation in the dilatant stress domain and the so-called multiplyer λ_s

$$\Delta\varepsilon^p = \lambda_s \cdot \partial g_s/\partial\sigma \quad (18)$$

where the plastic potential g_s is derived from a modified non-linear Mohr-Coulomb criterion representing the stress and strain dependent dilatancy boundary. Of course, Equation (18) is valid only if the dependence of the plastic strain increments on the plastic potential and the components of the three-dimensional stress field is taken into account.

The multiplyer λ_s is a rather complex function. It namely depends on the state of stresses with respect to the strength at failure and the strength at the dilatancy boundary, that is the stress limit for plastic flow. But in the IfG-M model the commonly used Equation (18) is extended, it includes the calculation of the strain hardening in case of a state of stresses beyond the dilatancy boundary and the strain softening if the stress reaches the failure boundary.

In the model, the new deviatoric stress state is computed, assuming stress redistribution by visco-elastic strain increments. If the yield function

$$f_S = \sigma_1 - \sigma_3 + \sigma_D - \frac{\sigma_{MAX} - \sigma_D}{\sigma_\phi - \sigma_3} \cdot \sigma_3 \quad (19)$$

results in $f_s < 0$, plastic flow is taking place, and the stresses must be corrected by the impact of an incremental plastic strain before their value is assigned to the new state of stresses. On basis of this procedure, the evolution of the yield function is updated. The hardening or softening lags one time step behind the corresponding plastic deformation. In an explicit code, this error is small, because the steps are small.

In the yield function of Equation (19) the denoted stresses have the following meaning: σ_3 minimal principal stress; σ_1 maximal principal stress; $\sigma_D(\varepsilon^p)$ uniaxial strength; $\sigma_{MAX}(\varepsilon^p)$ maximum of effective strength; $\sigma_\phi(\varepsilon^p)$ curvature parameter for the strength surface.

In case of a continuous, damage affected deformation in the dilatant stress domain, the softening of the strength will converge to the present state of stresses which will lead to the failure and post-failure deformation behavior, where the flow stress in the post-failure domain is primarily depending on the minimal principle stress.

Again, the elastic moduli are expressed in dependence on the damage evolution, i.e. on the progress in the volumetric strain: $K(\varepsilon^p_{vol})$, $G(\varepsilon^p_{vol})$, where the volumetric strain ε_{vol} is modeled in dependence on the dilatancy function (which depends on the flow potential g_s) times the plastic flow ε^p. For further details we have to refer to Minkley & Mühlbauer (2007).

3.4 *The TUC model*

The partner TUC uses the constitutive model Hou/Lux (Hou 1997, 2002 & 2003, Hou & Lux 2000). In this model, the total strain rate $d\varepsilon_{ij}/dt$ is the result of the additive superposition of the elastic part $d\varepsilon^{el}_{ij}/dt$, of the visco-plastic part at constant volume $d\varepsilon^{vp}_{ij}/dt$, of the damage-induced dilatancy part $d\varepsilon^{d}_{ij}/dt$ and of the healing-induced compaction part $d\varepsilon^{h}_{ij}/dt$. The latter is not mentioned in this work, for details see Hou (2002, 2003).

In the simplified one-dimensional form it follows that the total creep rate $d\varepsilon/dt$ consists of

$$\begin{aligned} d\varepsilon/dt &= d\varepsilon^e/dt + d\varepsilon^{ie}/dt \\ &= d\varepsilon^e/dt + d\varepsilon^{vp}/dt + d\varepsilon^d/dt + d\varepsilon^h/dt \end{aligned} \quad (20)$$

Similar to the expression for the Kelvin-element (Equation (15)) the term for the transient creep rate $d\varepsilon^{tr}/dt$ in the expression for viscous creep $d\varepsilon^{vp}/dt = d\varepsilon^{tr}/dt + d\varepsilon^{ss}/dt$ consists of two terms

$$\begin{aligned} d\varepsilon^{tr}/dt \sim\ & (1/\eta_K) \cdot \sigma/(1\text{-}D) \\ & - [\varepsilon^{tr}/(\eta_K \cdot \varepsilon^{tr}_\infty)] \cdot \sigma/(1\text{-}D) \end{aligned} \quad (21)$$

This time, the damage parameter D affects the transient creep rate directly, i.e. increasing damage reduces the strength, whereby the efficiency of the stress as well as the transient creep rate do increase. The parameter ε^{tr}_∞ reflects the fact that the transient creep will end at a certain value. This parameter is determined from experimental results, where it is found that this strain limit depends on the effective shear stress (von Mises stress) σ_{eff} and also on the damage parameter D

$$\varepsilon^{tr}_\infty \sim 1/G_K \cdot \sigma_{eff}/(1\text{-}D) \quad (22)$$

In addition, similar to the Equation (17) the viscosity of the Kelvin-element is already a non-linear function of the damage affected von Mises stress

$$\eta_K \sim \eta^*_K \cdot \exp[-m_K \cdot \sigma_{eff}/(1\text{-}D)] \quad (23)$$

Finally, the shear modulus G_K is expressed in dependence on the damage parameter

$$G_K \sim G_K^* \cdot \exp(-m_G \cdot \sigma_{eff}/(1\text{-}D)] \quad (24)$$

The second term of the visco-plastic strain rate $d\varepsilon^{vp}/dt = d\varepsilon^{tr}/dt + d\varepsilon^{ss}/dt$ results from the additive

steady-state creep rate $d\varepsilon^{ss}/dt$ which basically consists of a Maxwell-element.

$$d\varepsilon^{ss}/dt \sim \sigma_{eff} / (\eta_M) \cdot 1/(1\text{-}D) \quad (25)$$

Again, the viscosity term is expressed as a function of the damage affected shear stress, similar to Equation (23).

The damage-induced strain rate $d\varepsilon^{d}/dt$ in Equation (20) contains two terms: $d\varepsilon^{ds}/dt$ is resulting from the shear-induced damage and $d\varepsilon^{dz}/dt$ is resulting from damage under a tensile stress. Both terms are expressed on basis of the plasticity theory, i.e. by the derivatives of the plastic potential with respect to the stress components. The Hou/Lux-model has no specific function for the evolution of the volumetric strain rate $d\varepsilon_{vol}/dt$, because this is the result of the additive superposition of the three normal strain rates that result from shear- and tensile-induced damage ($d\varepsilon^{ds}/dt$ and $d\varepsilon^{dz}/dt$, respectively).

As in the non-associated IfG-M model, the damage evolution depends on the evolution of the flow function, which is derived from the stress exceeding the dilatancy boundary – or from the tensile stress. In general, the tensile strength is set to zero.

The damage parameter D is classically defined in dependence on Young's modulus E, which can be determined experimentally in accordance to Equation (26).

$$D = (Eo - E) / Eo = 1 - [1/(1 - \varepsilon_{vol})] \cdot (Vp/Vp_o)^2 \quad (26)$$

The calculated damage parameter D should be checked experimentally by the measured volumetric strain ε_{vol} and the measured longitudinal ultrasonic wave velocity Vp, where Eo and Vp_o are the values in the primary state.

Based on experimental results and the experience from the application of the Hou/Lux-model, the degree of damage in a sample or in the EDZ can be classified as failed ($D > 0.4$), as strongly damaged ($0.4 \geq D > 0.1$), as damage affected provoking tertiary creep ($0.1 \geq D > 0.015$), as slightly damaged without tertiary creep ($0.015 \geq D > 0.0001$), as marginally damaged, but still impermeable ($D \leq 0.0001$), and as an intact rock mass ($D = 0$).

3.5 *The FZK-INE model*

The partner FZK-INE applies an elasto-visco-plastic concept to describe the deformation rate

$$d\varepsilon^{tot}/dt = d\varepsilon^{elast}/dt + d\varepsilon^{vp}/dt \quad (27)$$

The visco-plastic strain rate $d\varepsilon^{vp}/dt$ consists of two terms, the non-dilatant deformation rate $d\varepsilon^{vp,c}/dt$ describing visco-plastic flow without volume change and the deformation rate $d\varepsilon^{vp,d}/dt$ due to damage describing the volume change (dilatancy or compaction) of the rock salt. It has to be mentioned that the term concerning the non-dilatant creep $d\varepsilon^{vp,c}/dt$ consists of a module for the steady state creep behavior and of a module which describes the transient creep rate, where the transient strain limit is modeled by a time constant reflecting a time dependent hardening behavior.

Both, the term for the non-dilatant creep rate $d\varepsilon^{vp,c}/dt$ and the one for the volume deformation rate $d\varepsilon^{vp,d}/dt$ use an associated flow rule (i.e. the visco-plastic potential function Q is the same as the yield function Φ_F) and follow the general form

$$d\varepsilon^{vp,c\text{-}d}/dt \sim \gamma(T) \cdot \Phi_F^{c\text{-}d} \cdot \partial Q/\partial\sigma \quad (28)$$

where $\gamma(T)$ denotes the dependence on temperature maintained by an Arrhenius equation, Φ_F^{c-d} is the flow function for non-dilatant creep or volumetric creep, respectively, $\partial Q/\partial\sigma$ represents the dependence of the deformation on the flow potential Q.

In case of non-dilatant creep, the flow function Φ_F^c yields a common power creep law

$$\Phi_F^c \sim (q)^{2m} \quad (29)$$

but becomes more complicated as a part of the equation for the volumetric strain rate

$$\Phi_F^d \sim (n_1 \cdot p^2 + n_2 \cdot q^2)^m \quad (30)$$

where p denotes the mean stress and q the deviatoric stress.

The material functions n_1 and n_2 are depending on the state of stresses and the volumetric strain. In addition, they contain the parameters c_1, c_2 and c_3, which reflect the individual behavior of a certain type of rock salt.

$$n_1 = c_1 \cdot (q^2/p^2 - c_2 \cdot (\varepsilon_{vol,o} + \varepsilon_{vol}) / (1 + \varepsilon_{vol})) \quad (31)$$

$$n_2 = 1 - c_3 \cdot n_1 \cdot p^2 / q^2 \quad (32)$$

The initial porosity of rock salt $\varepsilon_{vol,o}$ may be different from zero. For further details we have to refer to Pudewills (2007).

3.6 *The IUB-MDCF model*

The partner IUB uses its modification of the former MDCF model, which was originally developed by Munson & Dawson (1984). The recent improvements of the IUB-MDCF model (MDCF: Multimechanism Deformation Coupled Fracture) are described by Hauck (2001) and Rokahr et al. (2004). The total inelastic strain rate $d\varepsilon^{inel}/dt$ consists of the modules $d\varepsilon^{cr}/dt$ for non-dilatant creep, $d\varepsilon^{\omega-sh}/dt$ for damage by shear and $d\varepsilon^{\omega-te}/dt$ for damage by tensile deformation.

In addition, the term $d\varepsilon^{\omega-h}/dt$ represents the modeling of long-term healing processes.

$$d\varepsilon^{inel}/dt = f(\sigma^{cr}) \cdot d\varepsilon^{cr}/dt + f(\sigma^{\omega\text{-}sh}) \cdot d\varepsilon^{\omega\text{-}sh}/dt + f(\sigma^{\omega\text{-}te}) \cdot d\varepsilon^{\omega\text{-}te}/dt + f(\sigma^{\omega\text{-}h}) \cdot d\varepsilon^{\omega\text{-}h}/dt \quad (33)$$

The specific flow function $f(\sigma^{xx}) \sim \partial\sigma^{xx}/\partial\sigma_i$, i.e. the derivative of the effective stress with respect to the stress components, and the individual strain rates $d\varepsilon^{xx}/dt$ reflect the contribution of a single process to the total deformation. In this paper, the contribution by tensile deformation and of healing are not discussed. For details see Hauck (2001). The term concerning the non-dilatant creep $d\varepsilon^{cr}/dt$ consist of the sum of the three different steady state creep rates $d\varepsilon^{cr}_{ss,1-3}/dt$. They represent three individual dislocation creep mechanisms corresponding to the deformation-mechanisms maps as discussed by Munson & Dawson (1984).

$$d\varepsilon^{cr}_{ss,1\text{-}3}/dt \sim A_{1\text{-}3} \cdot \exp(-Q_{1\text{-}3}/(R\cdot T)) \cdot [\sigma^{cr}/(G\cdot(1\text{-}\omega))]^{n_{1\text{-}3}} \quad (34)$$

The pre-factor A_{1-3}, the activation energy Q_{1-3}, and the stress sensitivity parameter n_{1-3} reflect the individual contribution to steady-state creep by each mechanism. It is important to note that the steady creep rates, which itself do not contribute to the evolution of damage and volumetric strain, are affected by the evolution of damage, if the damage related modules of Equation (34) have become active during loading in the dilatant stress domain. This is ex-pressed by $\sigma^{cr}/(G \cdot (1-\omega))$. Therefore, the stress σ^{cr} which is required to maintain a constant strain rate will decrease as the damage affected shear modulus $G \cdot (1-\omega)$ decreases. The evolution of the damage function ω is primarily depending on the state of stresses.

Furthermore, the transient creep behavior has to be modeled. This is done by the function F which distinguishes between transient hardening creep (hardening parameter Δ) and transient recovery creep (recovery parameter δ), where the hardening and the recovery parameters can be rather different to model the well-known different hardening and recovery behavior of rock salt.

$$d\varepsilon^{cr}/dt = F[\Delta((\varepsilon_{tr\text{-}max} - \zeta)/\varepsilon_{tr\text{-}max} > 0)] \cdot \Sigma(\varepsilon^{cr}_{ss,1\text{-}3}/dt)$$
$$d\varepsilon^{cr}/dt = F[\delta((\varepsilon_{tr\text{-}max} - \zeta)/\varepsilon_{tr\text{-}max} < 0)] \cdot \Sigma(\varepsilon^{cr}_{ss,1\text{-}3}/dt) \quad (35)$$

The transient creep phase ends, as soon as the internal state variable ζ converges to the transient strain limit ε_{tr-max}. Then, $F = 1$, otherwise $F > 1$ causes the transient creep behavior during strain hardening or $F < 1$ causes the transient creep behavior during the recovery of the preceding strain hardening, for instance after a stress reduction. The complex function $d\zeta/dt$ which describes the evolution of the internal state variable ζ depends on the difference $(\varepsilon_{tr-max} - \zeta)$, the sum of the steady state creep rates, and the hardening and recovery parameters. It has to be noted that the transient creep limit is not a constant, but is depending on $\sigma^{cr}/(G \cdot (1-\omega))$. This way, the coupling between non-dilatant viscous flow and damage related softening is established.

Again, the onset of damage is described in dependence on the state of stresses. This concept is applied by all partners. IUB uses, in dependence of the type of the rock salt, a value of approximately 30% of the short-term failure strength $\sigma_{Dil}(\sigma_{min}) = 0.3 \cdot \sigma_{max}(\sigma_{min})$, which is found to be adequate for the prediction of the long-term strength and the modeling of the damage evolution. Thus, in Equation (33) the term for the shear-depending strain rate $f(\sigma^{\omega-sh}) \cdot d\varepsilon^{\omega-sh}/dt$ truly contributes to the overall inelastic strain rate, but only its part where the stress $\Delta\sigma^{\omega-sh} = (\sigma^{cr} - \sigma_{Dil})$ gives rise for the progress of damage. The shear strain rate $d\varepsilon^{\omega-sh}/dt$ is depending on the function $F^{\omega-sh}$, which describes the transient behavior of the shear strain rate in accordance to the concept of Equation (35), times the steady state shear strain rate $d\varepsilon^{\omega-sh}_{ss}/dt$, which is a complex function of parameters concerning the type of rock salt, the dilatancy boundary, and the damage affected shear modulus $G \cdot (1-\omega)$. Finally, this portion of the shear strain rate yields the volumetric strain rate, where the derived equation is depending on the dilatancy boundary and the present mean stress.

4 MODEL CALCULATIONS

On basis of the individual constitutive models, each partner has performed his back-calculations of laboratory experiments. In general, one set of parameters should be used for the modeling of all types of experiments with one salt type, i.e. for the selected long-term tests as well as for the short-term tests.

In Figure 1 the results of three uniaxial long-term creep tests are plotted. Although the test conditions are always the same, i.e. stress $\sigma_1 = 14$ MPa, temperature $T = 22°C$, testing duration 1250 days, at the end of the test, the steady-state strain rates $\Delta\varepsilon/\Delta t$ differ between 2.5E-06 l/d and 5.0E-06 l/d. This is an example for the unavoidable natural scatter of the material behavior. Therefore, parameters, which are found to be suitable for the adjustment of a certain model to laboratory data, will definitely depend on the selection of experiments (see the example 'IUB-modeling' in Figure 1). Thus, a sufficient number and a careful selection and evaluation of laboratory tests is essential for a reliable parameter determination. In order to reduce the remaining ambiguity of parameter determination based on laboratory tests, additional

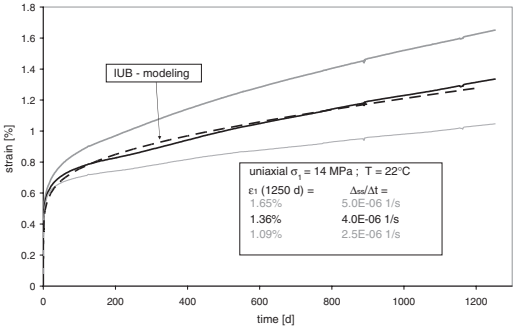

Figure 1. Three creep curves, uniaxial testing, $\sigma_1 = 14$ MPa, temperature T = 22°C. Dashed line: IUB-modeling.

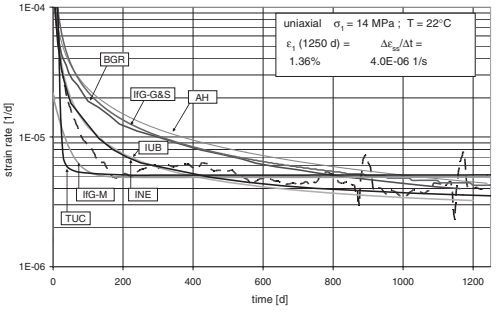

Figure 2. Strain rate of one of the selected creep tests (uniaxial test with $\sigma_1 = 14$ MPa, temperature T = 22°C, dashed line) and the results of the back-calculations of the partners.

information from in-situ measurements is often used or even required.

However, individual laboratory test curves or in-situ data might be adjusted with different accuracy by different partners, depending on the significance the respective partner has given to a certain test curve among the variety of available or selected data.

In addition, even if a constitutive model would generally comprehend all the processes of relevance and if the chosen equations would be well adapted to perform calculations, each modeler may put special emphasis on different items of the material behavior and the modeling of the controlling deformation processes. Therefore, also the equations of the constitutive models will be different, as has been made obvious in the preceding chapter 3 "Constitutive models". Consequently, the different features of the constitutive models of the different groups will yield an additional reason for systematic differences between the results of model calculations.

Therefore, the aim of this comparison of the advanced constitutive models for the mechanical behavior of rock salt is not to find the best adaptation to individual test curves by tuning the parameters, but to find out if the models and the representative parameters for a certain type of rock salt are suitable to predict all the different aspects of material behavior.

In Figure 2 the consequence of this concept is shown. All the analytic or semi-analytic model calculations predict the steady-state creep rate at the end of testing in the right order of magnitude, for comparison see the dashed experimental curve. However, it has to be stressed that the results of the modeling exhibit rather different characteristics concerning the transient creep behavior. Consequently, the predicted strains vary between 1.2% to 1.9% at the end of this long-term uniaxial creep test (1250 days). Nevertheless, the long-term creep behavior is quite well predicted, because one has to keep in mind that this calculation is performed without a special optimization of the parameters to fit this single experiment.

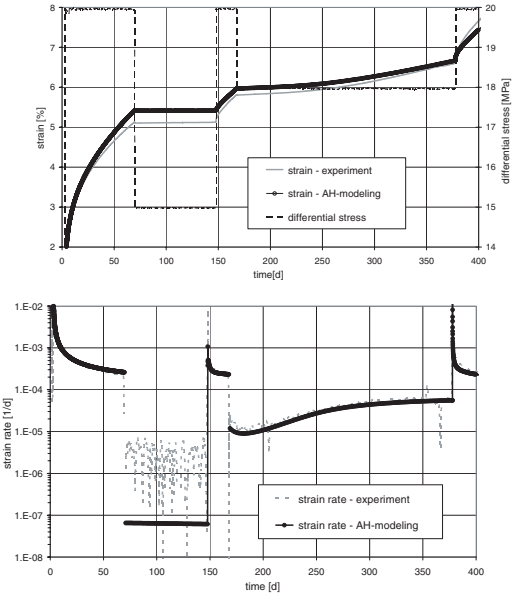

Figure 3. Multi-stage triaxial creep test, temperature T = 50°C, confining pressure $p_c = 20$ MPa, differential stress $\Delta\sigma$: 20 MPa, 15 MPa, 20 MPa, 18 MPa, and 20 MPa. For comparison, the modeling of Hampel (AH-CDM) is plotted (dark lines).

The next task concerns the modeling of a stress drop experiment and of the related recovery creep, which is a really ambitious job. The concept of this test is illustrated in Figure 3. The creep test is performed at constant temperature (50°C) and constant confining pressure ($p_c = 20$ MPa). After about 70 days of testing, the differential stress $\Delta\sigma = (\sigma_1 - p_c) = 20$ MPa is dropped to $\Delta\sigma = 15$ MPa. At this point, the creep rate slows down to almost zero, i.e. to the limit of resolution without a detectable macroscopic recovery creep. After additional 80 days of testing, the differential stress is set back to $\Delta\sigma = 20$ MPa,

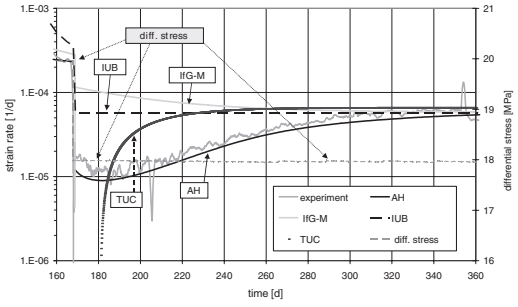

Figure 4. Multi-stage triaxial creep test, temperature $T = 50°C$, confining pressure $p_c = 20$ MPa; test section with differential stress $\Delta\sigma$: 20 MPa and 18 MPa. For comparison, four of the model calculations are plotted (AH-CDM, IfG-M, IUB, TUC).

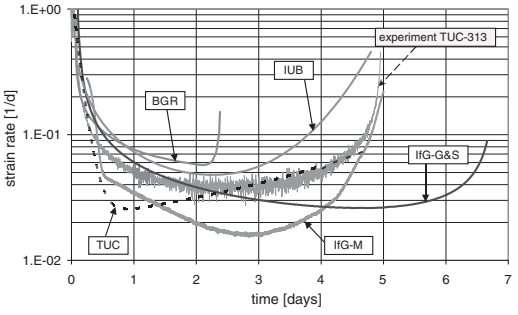

Figure 5. Triaxial creep failure test, temperature $T = 30°C$, confining pressure $p_c = 3$ MPa, differential stress $\Delta\sigma = 38$ MPa. Experiment (TUC-313, light grey line) and five of the model calculations (BGR-CDM, IfG-G&S, IfG-M, IUB, TUC).

causing a new transient creep behavior after the pre-hardening had partially recovered during the testing section at $\Delta\sigma = 15$ MPa. After 20 more days of testing at $\Delta\sigma = 20$ MPa, steady-state creep behavior re-establishes. Now, the stress is reduced to only $\Delta\sigma = 18$ MPa. This time, a larger recovery creep behavior is observed and recorded. Finally, after about 380 days of testing, the stress is set back to $\Delta\sigma = 20$ MPa. Again, steady-state creep behavior is reached after a short phase of transient creep.

In Figure 3, also the result of the modeling of Hampel (AH) with the CDM is plotted. In the CDM, special emphasis is put on the modeling of the evolution of the microstructure during hardening and recovery in dependence on stress and strain. Therefore, the CDM can model the different sections of this creep test almost perfectly.

For comparison, results from the application of some of the other models are plotted in Figure 4. For clarity, only the test section after the stress drop from $\Delta\sigma = 20$ MPa to $\Delta\sigma = 18$ MPa is shown. First of all, it has to be stressed that each model does predict the steady-state creep rate in the right order of magnitude. However, in the transient creep section the different graphs elucidate the different tendencies predicted by the models. The course of the TUC-modeling results from a strong hardening during the preceding test section at $\Delta\sigma = 20$ MPa. Then, this hardening recovers within a short time, thus steady-state creep behavior is following quite soon.

On the other hand, the IfG-M modeling exhibits an expanded transient creep phase, where the deviation from the steady-state rate and, therefore, the decay in the transient creep behavior are rather small. Thus, the order of magnitude of the steady-state creep rate is already met soon after the stress drop.

In contrast to these results, the IUB-modeling shows a steady-state behavior right after the stress drop. Although the IUB-MDCF model consists of a rather sophisticated term for the transient hardening and recovery creep, the modeling yields no reaction in this section. However, in the test section after the stress drop from $\Delta\sigma = 20$ MPa to $\Delta\sigma = 15$ MPa, the IUB-MDCF exhibits a pronounced transient recovery creep behavior (not shown in this work).

Concerning the transient creep behavior, we have to state that the modeling requires improvements (see examples of Figure 2 and Figure 4). Of course, in some cases the time-dependent and spatial changes in the overall stress field can already be predicted by the application of the terms describing the steady-state creep behavior in the far-field, where the long-term evolution of stress and strain may be dominated by steady-state creep. However, the stress redistribution and evolution of strain in the vicinity of underground constructions are sensitively depending on transient creep.

The next example for the comparison of the constitutive models deals with damage affected creep. The creep test is performed at constant temperature (30°C), constant confining pressure ($p_c = 3$ MPa), and a differential stress of $\Delta\sigma = 38$ MPa. At these conditions and for this type of rock salt, the onset of dilatancy is expected to be at $\Delta\sigma_{Dil}(\sigma_3 = 3\text{ MPa}) \approx 20$ MPa and the short-term failure strength at 45 MPa to 48 MPa. These test conditions yield tertiary creep and creep failure. The measured creep rates and some results of the modeling are shown in Figure 5. The order of magnitude of the minimal creep rate is met quite well without individual adaptations of the model parameters to this test. The prediction of the tertiary creep behavior is also qualitatively correct, however, the onset of the acceleration of the creep rate and the strain at creep failure are predicted within a certain bandwidth corresponding to a factor of ± 2 of the experimentally determined failure strain.

The last group of experiments, which is mentioned in this contribution, are strain rate controlled

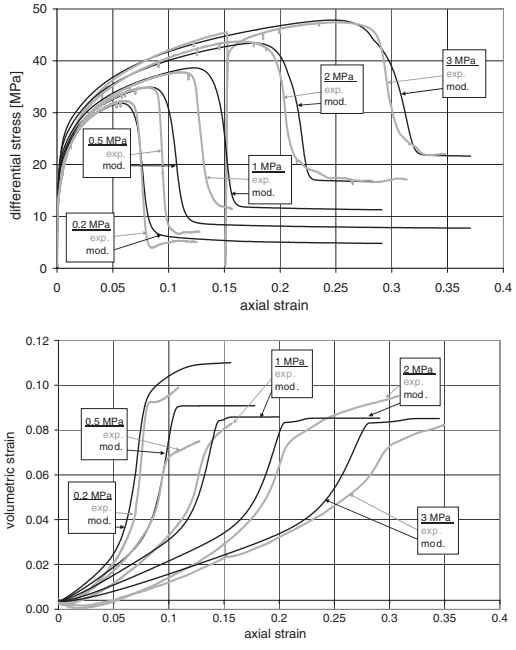

Figure 6. Triaxial rate-controlled short-term strength test, $\Delta\varepsilon/\Delta t = 1.0E\text{-}05$ 1/s, temperature $T = 30°C$, various confining pressures as indicated. Experiments (light grey lines) and exemplary model calculations with IfG-G&S. Upper part: diff. stress vs. axial strain; lower part: volumetric strain vs. axial strain.

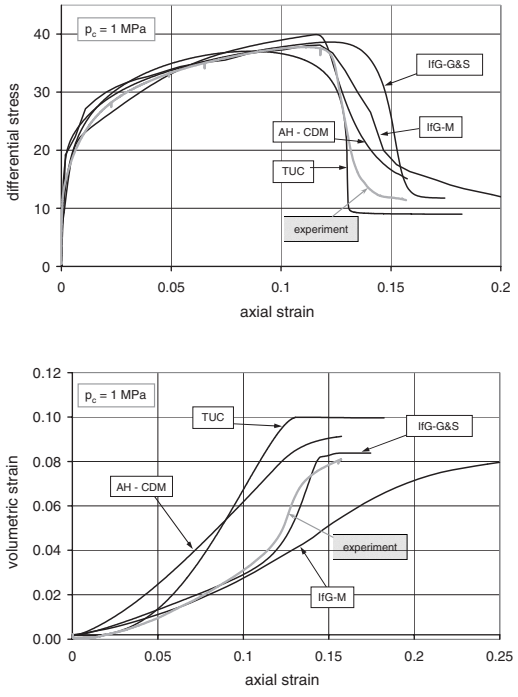

Figure 7. Triaxial rate controlled short-term strength test, $\Delta\varepsilon/\Delta t = 1.0E\text{-}05$ 1/s, temperature $T = 30°C$, confining pressures $p_c = 1$ MPa. Experiment (light grey line) and exemplary model calculations of four partners (AH-CDM, IfG-G&S, IfG-M, TUC). Upper part: diff. stress vs. axial strain; lower part: volumetric strain vs. axial strain.

short-term strength tests ($\Delta\varepsilon/\Delta t = 1.E\text{-}05$ 1/s = const.). They are performed at constant temperature ($T = 30°C$) and at different confining pressures in order to investigate the evolution of dilatancy, damage, short-term failure strength, and the post-failure behavior. Nearly all models are suitable to predict the hardening and the increase of the flow stress quite satisfactory, as well as the progressive weakening by damage processes, which cause failure, and, in dependence on the confining pressure, the drop down to the level of the residual strength. As an example, in Figure 6 the results from the application of the IfG-G&S model are shown. For comparison, some modeling results of the other groups are documented in Figure 7 concerning a strength test at $p_c = 1$ MPa ($T = 30°C$; $\Delta\varepsilon/\Delta t = 1.0E\text{-}05$ 1/s). In conclusion, we can state that the experimental graphs of the flow stress (i.e. the differential stress $\Delta\sigma = (\sigma_1 - p_c)$ versus axial compressive strain) as well as the graphs of the volumetric strain evolution are met. Of course, it depends on the demands for precision and reliability if the quality of these results is acceptable or if further model improvements are required.

The post-failure behavior is a point of special interest. Most of the models predict a constant residual strength, where also the volumetric strain remains constant during the further deformation. This is a consequence of the concept to correlate the residual strength with the dilatancy boundary, i.e. the damaged and failed material cannot suffer stresses beyond the dilatancy boundary anymore. The dilatancy boundary is generally expressed as a function of the state of stresses, but a unique equation does obviously not exist. Each model predicts a (slightly) different dilatancy boundary and, thus, residual strength.

The reason for different equations for the dilatancy boundary originates from the uncertainty in its determination. At low stresses and strains, i.e. at the start of a strength test, the measure of the volumetric strain and its evolution remains rather small. In addition to the scatter caused by the individual behavior of specimens, the limited resolution and reproducibility of the volume measurement devices seems to be insufficient in this range for technical reasons.

Unfortunately, the minimum of the volumetric strain appears just in this range, whereat in most of the models the minimum is used as the key parameter for the determination of the dilatancy boundary. In addition, the determination of the minimum in the

curve of volumetric strain versus axial strain is uncertain because of its flatness (Figure 7 bottom, close to the beginning of the curve). Therefore, it is not really surprising that different groups derive different equations for the dilatancy boundary and, as a consequence, differences in the residual strength (Figure 7 top).

Although the various selected laboratory tests could generally be modeled quite well, especially the modeling of creep failure (Fig. 5) and the evolution of dilatancy (Fig. 7 bottom) require further improvements for a reliable transfer of short-term (laboratory) results to long-term predictions, see also part II of this contribution (Hou et al. 2007).

5 SUMMARY

In this paper concerning the first part of the joint project, the constitutive models of the partners and the results of some of the comparative model calculations are presented. With the back-calculations of different types of laboratory experiments, the features and capabilities of the constitutive models of the partners were checked in detail. The results of this work demonstrate that the partners do have appropriate tools for reliable model calculations, i.e. to predict the time-dependent and spatial evolution of stress, strain, dilatancy, and strength around underground cavities and structures in rock salt.

We want to stress, that model calculations as required for long-term prediction, safety analysis, and confidence building concerning the construction and operation of underground repositories should only be performed with tools, which are suitable to model all the processes of relevance with one representative set of parameters for a certain type of rock salt without further adaptations.

In rock salt, the rate controlling microscopic deformation mechanisms are generally always the same. Nevertheless, different types of rock salt may exhibit a different mechanical behavior. The main reason results from the so-called impurities (i.e. second phase particles) in the grains of the halite (e.g. Hunsche et al 1996). Thus, the parameter values of the fundamental equations can be different for different types of rock salt.

In case of the Sondershausen rock salt, which is subject of the model calculations of underground structures in the second part of this project (Hou et al. 2007), the material is investigated and characterized by laboratory tests similar to the procedure for the selected rock salt from the Asse mine, reported in this part. Those experiments yield very similar results and the applied model calculations consequently quite similar parameters, confirming the suitability of the constitutive models for the description of the mechanical behavior of different types of rock salt.

Although the results of this comparative study are quite satisfactory, we see that the evolution of dilatancy affected processes and the prediction of creep failure have to be investigated further in more detail. This is not only of importance for the improved determination of the volumetric strain and damage evolution to predict more precisely the strength and strain at failure, for instance. In addition, the correlation and coupling of permeability with the volumetric strain (i.e. porosity) must be known better to receive more reliable permeability-porosity relations for the prediction of the barrier function and sealing capacity of rock salt in the EDZ during damage evolution or compaction after reconsolidation.

ACKNOWLEDGEMENT

Financial support by the Federal Ministry of Research and Technology (BMBF) and advisory support by the Project Management Agency Forschungszentrum Karlsruhe (PTKA-WTE) is gratefully acknowledged.

REFERENCES

Günther, R.-M. & K. Salzer 2007. A model for rock salt, describing transient, stationary, and accelerated creep and dilatancy. In K.-H. Lux, W. Minkley, M. Wallner, & H.R. Hardy, Jr. (eds.), *Basic and Applied Salt Mechanics; Proc. of the Sixth Conf. on the Mech. Behavior of Salt. Hannover* 2007. Lisse: Francis & Taylor (Balkema). (this issue).

Hampel, A. & O. Schulze 2007. The Composite Dilatancy Model: A constitutive model for the mechanical behavior of rock salt. In K.-H. Lux, W. Minkley, M. Wallner, & H.R. Hardy, Jr. (eds.), *Basic and Applied Salt Mechanics; Proc. of the Sixth Conf. on the Mech. Behavior of Salt. Hannover* 2007. Lisse: Francis & Taylor (Balkema). (this issue).

Hampel, A. & U. Hunsche 2002. Extrapolation of creep of rock salt with the composite model. In N.D. Cristescu, H.R. Hardy, Jr. & R.O. Simionescu (eds.), Basic and Applied Salt Mechanics, Proc. 5th Conference on the Mechanical Behavior of Salt (MECASALT 5), Bucharest, 1999: 193–207. Lisse: Swets & Zeitlinger (A.A. Balkema Publishers).

Hauck, R. 2001: Tragverhalten tiefliegender Salzkavernen bei atmosphärischem Innendruck. Dissertation an der Universität Hannover.

Hou, Z., R. Wolters, R. Rokahr, D. Zapf, K. Salzer, R.-M. Günther, W. Minkley, A. Pudewills, U. Heemann, O. Schulze, F. Zetsche & A. Hampel 2007. Comparison of advanced constitutive models for the mechanical behavior of rock salt – results from a joint research project. II. Numerical modeling of two in situ case studies and comparison. In K.-H. Lux, W. Minkley, M. Wallner, & H.R. Hardy, Jr. (eds.), *Basic and Applied Salt Mechanics; Proc. of the Sixth Conf. on the Mech. Behavior of Salt. Hannover* 2007. Lisse: Francis & Taylor (Balkema). (this issue).

Hou, Z. 2003. Mechanical and hydraulic behaviour of salt in the excavation disturbed zone around underground

facilities. *Int. J. of Rock Mechanics and Mining Sciences*, 40 (5): 725–738.

Hou, Z. 2002. Geomechanische Planungskonzepte für untertägige Tragwerke mit besonderer Berücksichtigung von Gefügeschädigung, Verheilung und hydromechanischer Kopplung. *Habilitationsschrift an der TU Clausthal.* Clausthal – Zellerfeld: Papierflieger Verlag.

Hou, Z. 1997. Untersuchungen zum Nachweis der Standsicherheit für Untertagedeponien im Salzgebirge. *Dissertation an der TU Clausthal.* Clausthal-Zellerfeld: Papierflieger Verlag.

Hou, Z. & K.-H. Lux 2000. Ein Schädigungsmodell mit Kriechbruchkriterium für duktile Salzgesteine auf der Grundlage der Continuum-Damage-Mechanik. *Bauingenieur*, 75 (13).

Hunsche, U., G. Mingerzahn & O. Schulze 1996. The influence of textural parameters and mineralogycal composition on the creep behavior of rock salt. In M. Ghoreychi, P. Bérest, H. Hardy, Jr. & M. Langer (eds*), The Mechanical Behavior of Salt; Proc. Third Conf*., Palaiseau (France), 14–16 September, pp. 143–151. Clausthal: Trans Tech Publications.

Minkley, W. & J. Mühlbauer 2007. Constitutive models to describe the mechanical behavior of salt rocks and the imbedded weakness planes. In K.-H. Lux, W. Minkley, M. Wallner, & H.R. Hardy, Jr. (eds.), *Basic and Applied Salt Mechanics; Proc. of the Sixth Conf. on the Mech. Behavior of Salt. Hannover* 2007. Lisse: Francis & Taylor (Balkema). (this issue).

Munson, D.E. & P.R. Dawson 1984. Salt constitutive model using mechanism maps. In H.R. Hardy, Jr. & M. Langer (eds.) The mechanical behavior of salt. *Proc. 1st Conf. on Salt*: 673–680. Clausthal-Zellerfeld: Trans Tech Publ.

Peach, C. 1991. *Influence of deformation on the fluid transport properties of salt rocks.* Geologica Ultraiectina No.77. Rijksuniversiteit Utrecht.

Pudewills, A. 2007. Modeling of hydro-mechanical behavior of rock salt in the near field of repository excavations. In K.-H. Lux, W. Minkley, M. Wallner, & H.R. Hardy, Jr. (eds.), *Basic and Applied Salt Mechanics; Proc. of the Sixth Conf. on the Mech. Behavior of Salt. Hannover* 2007. Lisse: Francis & Taylor (Balkema). (this issue).

Rokahr, R., K. Staudtmeister & D. Zander-Schiebenhöfer 2004. Application of a continuum damage model for cavern design. Case study: Atmospheric pressure. *SMRI-Meeting paper, April 18–21, 2004, Wichita (Kan), USA.*. Solution Mining Research Institute.

Spiers, C.J. & P.M.T.M. Schutjens 1990. Densification of crystalline aggregates by fluid-phase diffusional creep. In D.J. Barber & P.G. Meredith (eds.) *Deformation Processes in Minerals, Ceramics and Rocks*: 334–353. London: Unwin Hyman.

Spiers, C.J., C.J. Peach, R.H. Brzesowsky, P.M. Schutjens, J.L. Liezenberg & H.J. Zwart 1989. Long-term rheological and transport0 properties of dry and wet salt rocks. *Final Report, Nuclear Science and Technology, Commission of the European Communities*. EUR 11848 EN.

Urai, J.L., C.J. Spiers, H.J. Swart & G.S. Lister 1986. Weakening of rock salt by water during long-term creep. *Nature* 324: 554–557.

The Mechanical Behavior of Salt – Understanding of THMC Processes in Salt –
Wallner, Lux, Minkley & Hardy, Jr. (eds)
© 2007 Taylor & Francis Group, London, ISBN 978-0-415-44398-2

Comparison of advanced constitutive models for the mechanical behavior of rock salt – results from a joint research project – II. Numerical modeling of two in situ case studies and comparison

Z. Hou[5,*)], R. Wolters[5)], R. Rokahr[6)], D. Zapf[6)], K. Salzer[4)], R.-M. Günther[4)], W. Minkley[4)], A. Pudewills[3)], U. Heemann[2)], O. Schulze[2)], F. Zetsche[2)], A. Hampel[1)]

[1)] *Consultant, Am Fasanenweg Essenheim, Germany*
[2)] *Federal Institute for Geosciences and Natural Resources (BGR), Stilleweg, Hannover*
[3)] *Forschungszentrum Karlsruhe GmbH, Inst. f. Nukl. Entsorgung (INE), Karlsruhe*
[4)] *Institut für Gebirgsmechanik GmbH (IfG), Friederikenstr, Leipzig*
[5)] *Clausthal University of Technology, Professorship for Disposal Technology and Geomechanics (TUC), Erzstr, Clausthal-Zellerfeld*
[*)] *now with: Clausthal University of Technology, Institute of Petroleum Engineering, Germany*
[6)] *Universität Hannover, Institut für Unterirdisches Bauen (IUB), Welfengarten Hannover*

ABSTRACT: In the second part of the joint research project, the partners performed model calculations on two different underground structures in order to check, demonstrate and compare the abilities of their constitutive models and calculation tools. The first structure was a 35-year-old horizontal drift in 720 m depth in the salt mine "Sondershausen", the second consisted of a room-and-pillar model bearing system with a pillar slenderness of $\alpha = 1$ under three different loads. The results from the benchmark calculations of the project partners are discussed in comparison with each other and, in case of the horizontal drift, also with in-situ measurements. Except for two calculations of the slender pillar under very high loads, all partners got comparable results with a good agreement between the measured and the calculated minimum stresses, deformation rates as well as the permeability profiles of the 35-year-old drift in the Sondershausen salt mine.

1 INTRODUCTION

For the prediction of the mechanical behavior of rock salt, all processes which contribute substantially to the time-dependent and spatial evolution of stress and strain in the material have to be taken into account. In the past, several constitutive models were developed by different groups to describe the phenomena observed during mechanical loading and deformation processes. Of main concern is the modeling of the dominant processes which cause transient creep including recovery, steady-state creep, evolution of dilatancy and propagation of damage, humidity induced processes, failure, and post-failure strength. Only with appropriate models, the long-term prediction of the mechanical behavior that is e.g. required for the construction and assessment of underground repositories for toxic wastes, will be reliable.

In this joint project, the partners document the principles of their recent constitutive models and perform comparative calculations. In the first part of this benchmark project, the parameters of the respective models for rock salt in the Asse mine and in the salt mine Sondershausen were determined based on the results of short-term strength tests and long-term creep tests from the laboratory. Furthermore, the modeling of the various important deformation processes with the respective constitutive models was checked in detail by calculations of specific laboratory tests. The calculation results, the constitutive models, and the determined parameter values are reported in the first paper (Schulze et al. 2007).

In the second part of this project, the partners performed model calculations on two different underground structures using the same parameter values determined in the first part. The results of these two benchmark calculations and their comparisons are shown and discussed in the following.

The project partners, their constitutive models and used codes are shown in Table 1.

Table 1. Used constitutive models and numerical codes of all project partners (Schulze et al. 2007).

Partner	Constitutive model	Code
Hampel	CDM	FLAC (FDM)
BGR	CDM	JIFE (FEM)
IfG	Minkley	FLAC (FDM), UDEC (DE)
IfG	Günther/ Salzer	FLAC (FDM), UDEC (DE)
INE	FZK model	ADINA, MAUS (FEM)
TUC	Hou/Lux	MISES3 (FEM), FLAC (FDM)
IUB	MDCF-IUB	UT2D (FEM)

2 BENCHMARK I: THE HORIZONTAL DRIFT "EU1" AT THE SONDERSHAUSEN MINE

2.1 *In-situ conditions and measurements*

The first in-situ structure used for the benchmark calculations was the horizontal drift "EU1" at the Sondershausen salt mine. It was excavated in 1963 using a full-face tunneling machine at a depth of approximately 720 m in the lower part of the Staßfurt rock salt. It was selected as an example for the calculations because of the following factors:

- This site is documented quite well.
- Results of laboratory tests on the rock salt from this drift were available. These data were used to determine the values of the model parameters for this type of rock salt.
- Since the former mining fields lay at a minimum distance of about 800 m from this drift, no mining influences can be assumed (Fig. 1). Thus, in view of these circumstances, the peripheral conditions support the use of a plain strain model.
- The temperature $T = 303$ K in the drift EU1 is almost constant, so that the temperature effect on the creep behavior of rock salt was not to be considered.
- The geometrical model is very simple because of the circular cross-section of the drift EU1. Furthermore, the drift is located in an area where nearly no further mining activity is disturbing the in-situ stress field (Fig. 1). Therefore, the boundary conditions of the simulation calculations were well defined. Thus possible differences in the computational results of the project partners should be attributed to the constitutive models and not to different geometrical models or boundary conditions.

In 1998, i.e. 35 years after the excavation, a research project concerning an experimental drift sealing construction was started. Before the beginning of setting up the sealing system (Fig. 1), the permeability and the minimal principal stress were determined in the rock salt around this drift (Häfner et al. 2001, Salzer et al. 2000). In addition, the deformation rate was monitored for about 150 days (from December 1998 to May 1999). Therefore, the deformation rate in the stationary phase and the spatial distribution of the in situ stresses as well as the permeability are known quite well.

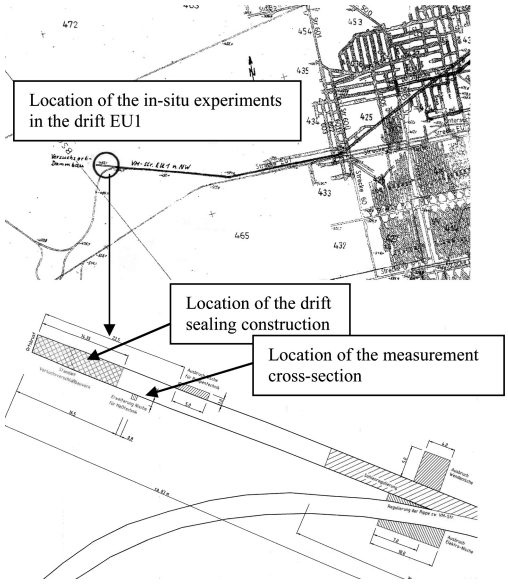

Figure 1. Location of the in-situ measurements in the machines drift EU1 in the Sondershausen salt mine.

2.2 *Calculation model and boundary condition*

As mentioned above, the in-situ measurement area in the drift EU1 to be modeled is a typical plain strain situation. The symmetrical calculation model with a height of 200 m and a width of 100 m is shown in Figure 2. The drift EU1 has a diameter of 3 m. The primary stresses in the rock salt mass are usually assumed to be isotropic.

On the upper model boundary a load of 15.7 MPa is applied, while the horizontal displacements on both model outsides and the vertical displacements at the model bottom are restrained. The specific weight of compact rock salt is $\gamma = 0.022\,\mathrm{MN/m^3}$. Therefore, the estimated values of the primary stresses amount to $\sigma_0 = 17.9$ MPa in the level of the drift EU1 and $\sigma_0 = 21.1$ MPa at the model bottom. For comparisons of the results among the partners and with the in-situ measurements, the points a to e in the calculation model in Figure 2 were chosen to display the evolution of stresses and displacements. The in-situ extensometers for deformation measurements were 5 m long and located between the points d and e in the wall and between b and f in the roof, see Figure 2. The

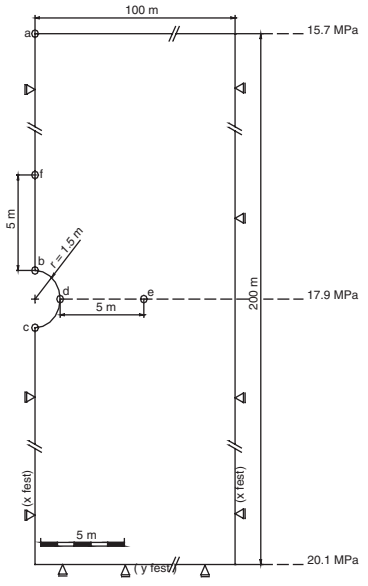

Figure 2. Calculation model of the drift EU1 in Sondershausen.

measured deformation rates in the wall and in the roof are relative values at d with respect to e, and at b with respect to f.

Model calculations were carried out by each partner using the respective constitutive models and codes (Tab. 1) in order to determine the creep deformation, the excavation damaged zone (EDZ) and dilatancy, and the convergence and stress rearrangements caused by creep and damage in the 35 years after the excavation of the drift EU1.

2.3 *Comparison of calculated stress distributions with measurements*

Figure 3 illustrates how well the measured and calculated minimum principal stress distributions agree on an horizontal path from the drift EU1 into the salt 35 years after the excavation. The agreement between the results of the partners is not self-evident, because each partner used its own constitutive model and the individual parameter values for this salt type were determined from the results of laboratory experiments which had lasted only 200 days in case of creep tests and a few hours in case of strength tests.

The temporal development of the von Mises stresses around the drift EU1 is shown in Figure 4. The stress maximum is reduced during creep. It is not located directly at the drift contour, but deeper inside the rock mass because of the strain softening in the EDZ around the drift.

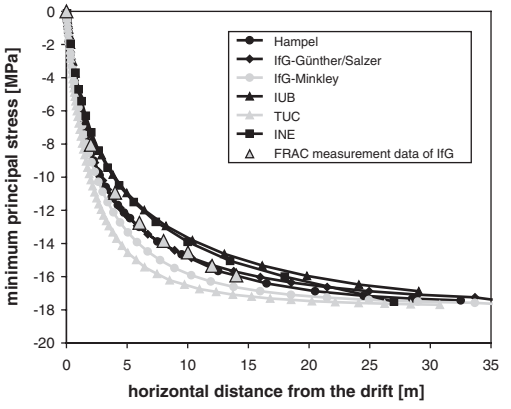

Figure 3. Calculated and measured minimum principal stress distributions around the drift EU1 35 year after the excavation.

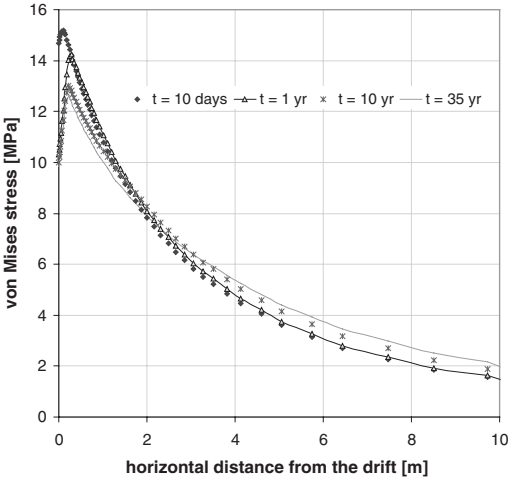

Figure 4. Von Mises stress distributions around the drift EU1 at different times, calculated by TUC using the *Hou/Lux* model and the FEM code *MISES3.*

2.4 *Comparison of calculated deformation rates with measurements*

The time dependent deformation rates were recorded in the wall and in the roof of the drift with 5 m long extensometers. Unfortunately, the measurements began only 35 years after the excavation and lasted only 150 days. Figure 5 shows the calculated results of the project partners. About 10 years after the excavation of the drift, creep is almost stationary. All calculated results agree within less than a factor of three with the in-situ data which have an order of magnitude of about 1 mm/yr. The simulation of Hampel was calculated with the parameter values which were not re-adjusted

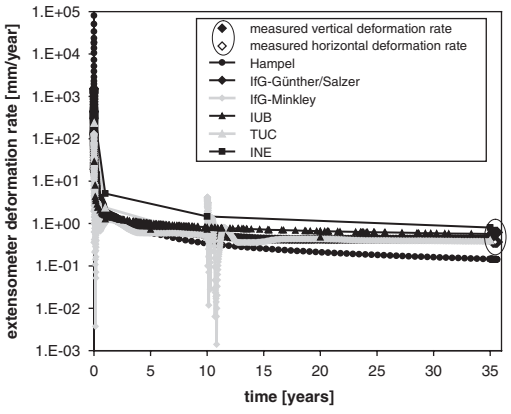

Figure 5. Calculated and measured deformation rates in the wall and in the roof (measurements only in the last 150 days).

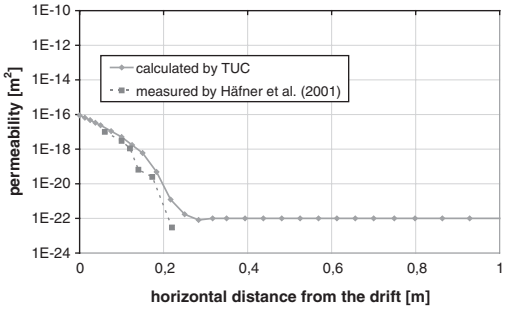

Figure 6. Calculated and measured permeability distributions on a horizontal path from drift EU1 into the salt 35 years after excavation.

to the in-situ data, but determined only from a good approximation of the laboratory test results.

2.5 *Comparison of calculated EDZ with measurements*

The calculation of permeability was not part of this joint research project. The EDZ could be determined from the dilatancy distribution. However, two project partners (TUC and INE) have calculated the permeability based on the dilatancy. Figure 6 compares the measured permeability with the permeability calculated by TUC using the permeability model originally proposed by Hou (2002). As a result of the EDZ, the permeability has a maximum value of $K = 10^{-16}\,m^2$ at the drift contour. This is much larger than the primary permeability of $K_{min} = 10^{-22}\,m^2$. Consequently, K decreases with an increasing distance from the drift. Looking at a specific example, the measured range of permeability in the EDZ results in a magnitude of radial extension r_a from 0.2 to approximately 0.6 m,

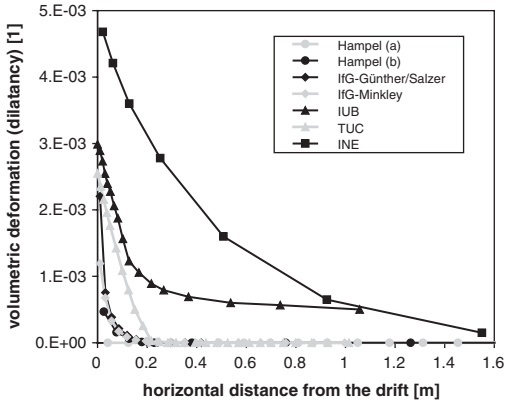

Figure 7. Calculated dilatancy distributions around drift EU1 35 years after the excavation.

depending upon the exact position of the measuring points, Häfner et al. (2001).

The radial extension of the EDZ of $r_a \approx 0.27$ m, calculated by TUC, is well within these ranges.

The EDZ based on the calculated dilatancy distributions in Figure 7 has an extension of 0.2 m to about 1.5 m among the project partners, while the maximum dilatancy at the drift contour is in the range of 0.05% to 0.48%. In the FZK model of INE no dilatancy boundary is used, dilatancy begins at the onset of deformation. Therefore, a bigger dilatancy as well as a larger EDZ is calculated by INE. For the dilatancy boundary in the MDCF-IUB model of IUB values of 30% of the short-term strength of rock salt are assumed. Thus, especially at higher minimum principal stresses the IUB dilatancy boundary is much lower than those of the project partners TUC, Hampel or IfG. Therefore, a much larger EDZ with a dilatancy of 0,07% is calculated by IUB.

In addition, the calculated deformation rates in Figure 5 show the same tendency like the calculated dilatancy in Figure 7: Partners, who calculate a higher deformation rate, get a larger EDZ as well as a bigger dilatancy because of dilatancy induced creep deformations.

Furthermore, the rate at which the EDZ extends is time-dependent and continuously decreasing. Thus, after about 35 years the EDZ will either change only slowly yet or already not alter anymore.

It can be concluded that the agreements between measured and calculated minimum stresses, deformation rates and permeabilities confirm the general suitability of the used constitutive models for such analyses. The differences in the extension and values of dilatancy are generated mainly by the different dilatancy boundaries used by the partners: In Figure 7 e.g. simulation Hampel (a) was calculated with a BGR dilatancy boundary and shows now dilatancy, while

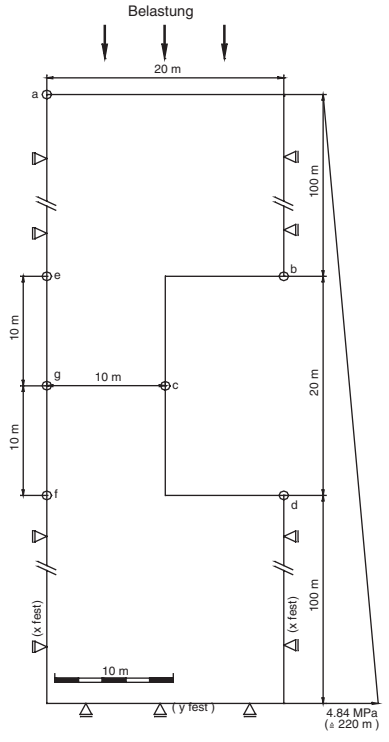

Figure 8. Calculation model of the pillar-and-room system.

simulation Hampel (b) with the lower Cristescu-Hunsche dilatancy boundary reveals an EDZ.

3 BENCHMARK II: A MODEL PILLAR-ROOM-SYSTEM

3.1 *Calculation model and boundary condition*

In the second example, a more complicated model room-and-pillar bearing system was calculated. For three different locations with respect to depth (i.e. 320 m, 550 m, and 770 m below surface) the behavior of a slender pillar (slenderness = height/width = 1) was modeled under the corresponding pillar loads of $p_p = 18.4$, 28.4 and 38.4 MPa (simulation case A, B and C) by applying the parameter values for the salt type around drift "EU1" from Sondershausen.

In order to simplify the simulation, a long pillar and, therefore, a plane strain model were chosen by all partners. Thus the form factor (width/length ratio) is zero. The calculation model with a height of 220 m and a width of 20 m is shown in Figure 8. The pillar has a height and a width of 20 m, while the room width is also 20 m. Because of symmetry, only a half pillar and a half room must be simulated.

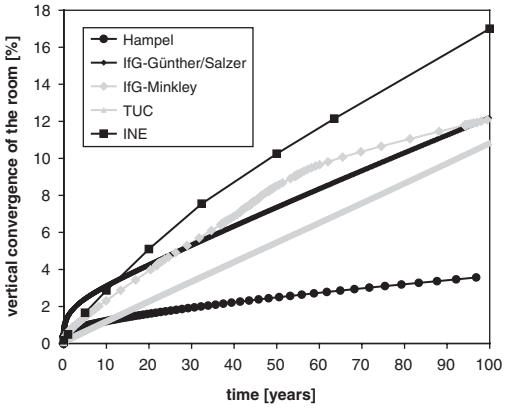

Figure 9. Calculated vertical convergence in the middle of the room (case A: slender pillar at 320 m depth).

At the upper model boundary, three loads 7, 12 and 17 MPa are applied corresponding to the simulation cases A, B and C, respectively. The horizontal displacements at both model outsides and the vertical displacements at the lower model boundary are restrained. The primary stresses in the rock salt mass are usually assumed to be isotropic. The density of the rock salt mass is $\gamma = 0.022\ \mathrm{MN/m^3}$. The temporal developments of stresses and displacements which were calculated by the partners, were compared at the points a to g in the calculation model in Figure 8.

In contrast to the first benchmark example, the deformation in the slender pillar was expected to be dominated by damage related processes, especially under the higher pillar loads in cases B and C. The goal of the three calculations was to simulate damage and dilatancy dominated creep processes as well as creep-failure, post-failure behavior, and the time until pillar rupture (time-to-rupture). After the excavation of the room, creep calculations were carried out for 100 years or until pillar rupture.

3.2 *Case A: pillar load $p_p = 18.4$ MPa*

Figures 9 to 13 show some calculated results of 4 project partners. All results depict no pillar failure until the end of calculation at t = 100 years. That means, the time-to-rupture of this room-and-pillar bearing system is expected to be much longer than 100 years under the pillar load of $p_p = 18.4$ MPa. The vertical convergences in the middle of the room at t = 100 years lie in the range of 4 to 17%. Like in the simulation of "EU1" (Fig. 5), INE calculated the largest vertical convergence, Hampel the smallest, while the partners IfG and TUC got similar results of about 11 to 12% (Fig. 9). The result differences among the partners are larger than in benchmark I ("EU1") because of a much longer simulation time (100 instead of 35 years),

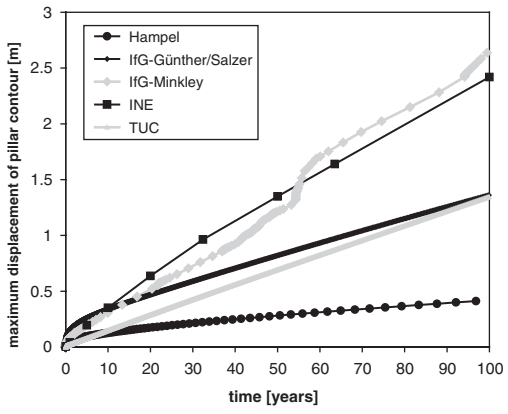

Figure 10. Calculated horizontal displacement of the pillar contour at half pillar height (case A).

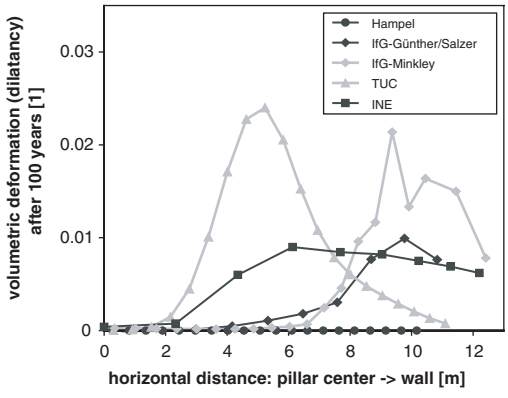

Figure 11. Calculated dilatancy distributions on a horizontal path at half pillar height (case A, at t = 100 years).

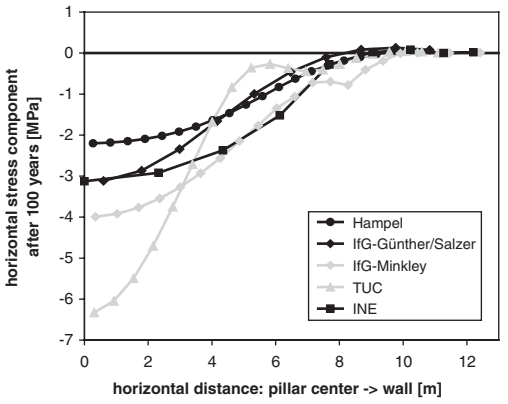

Figure 12. Calculated horizontal stress distributions in the modeled half of the pillar (case A, at t = 100 years).

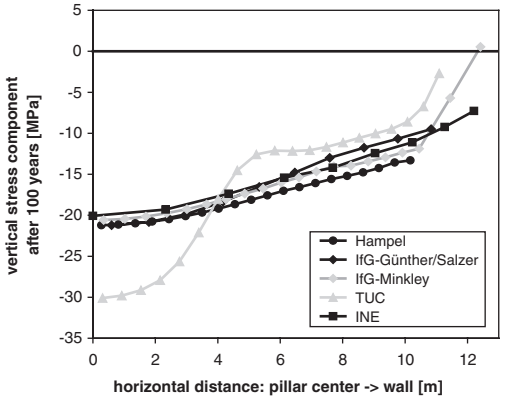

Figure 13. Calculated vertical stress distributions in the modeled half of the pillar (case A, at t = 100 years).

a much higher dilatancy and thus a more extended EDZ. The small deformation values of Hampel are explained as follows: They were calculated with the original CDM which describes the creep behavior of rock salt very well for creep rates measurable in the laboratory, i.e. at von Mises stresses bigger than 10 MPa at room temperature. However, it underestimated creep deformation at very low creep rates (in-situ loads $\ll$10 MPa). Meanwhile, Hampel modified the CDM, used it already to simulate drift "EU1" again, and got more realistic deformation rates, see Figure 5.

Except with the IfG-Minkley model, the above tendency is found also for the calculated horizontal displacements. Compared to INE, Minkley calculated a smaller vertical convergence and a bigger horizontal displacement. This means that with IfG-Minkley a much larger dilatancy especially in the near field of the EDZ is simulated than with the FZK model of INE, see Figure 11.

Apart from Hampel (see above), the calculated maximum dilatancy and the extension of the EDZ are comparable among the partners even 100 years after the excavation of the room, as shown in Figure 11, while the positions of maximum dilatancy are quite different. However, all of the calculated maxima lie inside, not at the pillar's surface. TUC and INE got the maximal dilatancy at 1/4 pillar width about 5 to 6 m from the pillar wall, much deeper than Günter & Salzer and Minkley of IfG. This difference and much more the different shape of dilatancy curves in Figure 11 are connected to different distributions of horizontal and vertical stresses shown in Figures 12 and 13. The shape of the stress and dilatancy distributions calculated by TUC and IfG-Minkley are quit similar, but the strain softening in the EDZ and the stress rearrangement from the EDZ into the pillar center area calculated by TUC are much stronger than by IfG-Minkley (Figs 12–13).

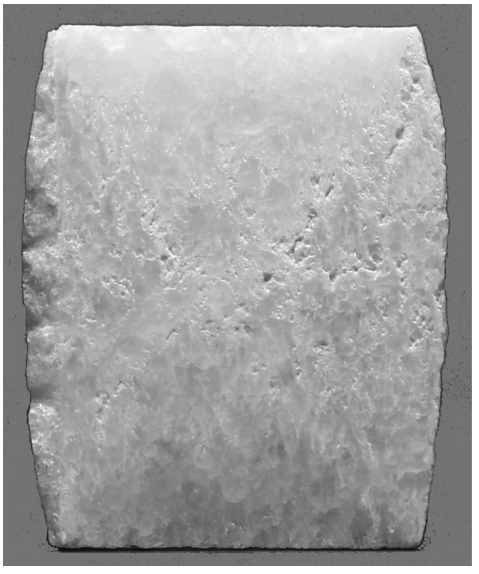

Figure 14. The damage and pore distribution in a vertical section of a rock salt sample (with slenderness 0.5) after a triaxial test.

Figure 14 shows the damage and pore distribution in a vertical section of a rock salt sample (with a slenderness of 0.5) after a triaxial test. An x-shaped damage zone is clearly formed, so that the maximal dilatancy in the upper half must be in the middle of the sample with a slenderness of 0.5. It is to be assumed that the more slender a pillar is, the closer the maximal dilatancy must lie to the pillar wall.

The horizontal stresses close to the pillar wall (up to 3 m) are approximately zero (Fig. 12), so that a uniaxial stress state is dominating in this zone. The higher horizontal stresses as well as triaxial stress states are firstly built into the pillar center area.

3.3 *Case B: pillar load $p_p = 28.4$ MPa*

The higher pillar load of $p_p = 28.4$ MPa causes a pillar contour rupture at time $t = 22$ years after IfG-Günter/Salzer. However, in TUC a break in the numeric simulation occurred at time $t = 4.56$ years, in INE at $t = 50$ years, as shown in Figures 15 and 16.

Contrary to case A and as shown in Figure 17a, the dilatancy boundary is exceeded even in the center of the pillar immediately after the excavation. As a consequence, an x-shaped EDZ through the center of the pillar is developed and becomes bigger and especially weaker, so that a contour rupture happens at time $t = 22$ years after IfG-Günter/Salzer.

For pillar stability it is not directly crucial how large the EDZ becomes. This is particularly and impressively confirmed by the results of Günter and

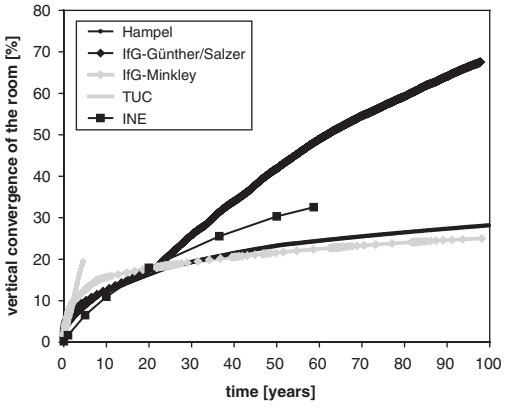

Figure 15. Calculated vertical convergence in the middle of the room (case B: slender pillar at 550 m depth).

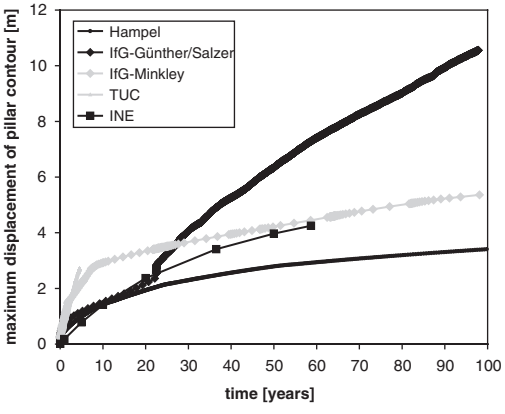

Figure 16. Calculated horizontal displacement of the pillar contour at half pillar height (case B).

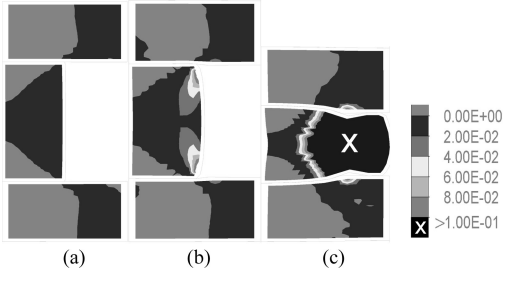

Figure 17. Dilatancy distributions calculated by IfG-Günter/ Salzer for case B (a: $t = 10$ d, b: $t = 10$ years, c: $t = 100$ years).

Salzer in Figures 16–17. Their curve in Figure 16 shows a contour break after 22 years, after which creep, dilatancy and damage continue to increase further. After the sudden contour rupture, the contour is

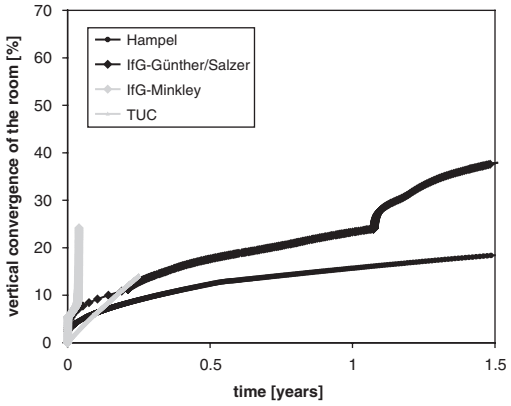

Figure 18. Calculated vertical convergence in the middle of the room (case C: slender pillar at 770 m depth).

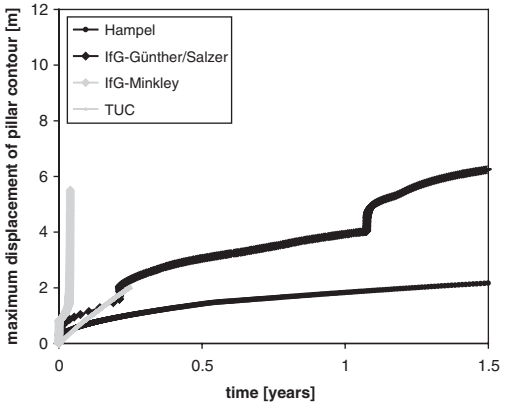

Figure 19. Calculated horizontal displacement of the pillar contour at half pillar height (case C).

strongly loosened up (Fig. 17, marked by "x") and does not have any considerable load-bearing capacity anymore. The pillar does not fail nevertheless, because the x-shaped center with the highest effective loads still exhibits nearly no dilatancy (and thus hardly damage). After the contour rupture, Günter and Salzer left the strongly damaged zone in the model during the further numerical calculation. Therefore, in their FLAC simulation this leads to a so called self-backfill (Fig. 17c).

The computation of such procedures does not only make high demands on the constitutive models, but also on the numerical treatment of the simulation and on a careful examination of the plausibility of the results. The examples shown here demonstrate the efficiency and high standard of modern constitutive models for salt rocks.

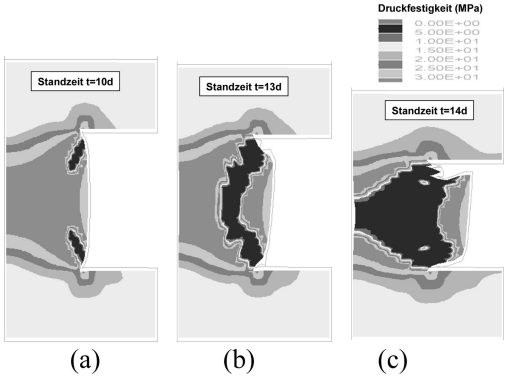

Figure 20. Development of a failure zone with a considerable strength reduction due to an immediate strain softening, calculated by IfG-Minkley for case C (a: t = 10 d, b: t = 13 d, c: t = 14 d).

3.4 *Case C: pillar load $p_p = 38.4$ MPa*

Because the uniaxial compression strength of about 33 MPa is smaller than the pillar load of $p_p = 38.4$ MPa in case C, the pillar is overloaded immediately after the room excavation. Therefore, it takes only a short time until the first pillar contour rupture can be determined in Figures 18–20.

The successive failure progress from the contour area to the pillar center is impressively shown by the development of strength drops calculated by IfG-Minkley in Figures 20a–20c. The strain softening sets in firstly at the corners between pillar and roof as well as pillar and floor (Fig. 20a). Already after 13 days, a continuous broad shear zone has been developed in the pillar as the strength strongly has dropped almost to zero (Fig. 20b). After redistributions of stresses from the pillar contour area into the pillar center, this center area is also overloaded. After 14 days the destabilization governs the whole pillar, even the pillar center area (Fig. 20c).

3.5 *Analytical calculation of the time-to-rupture of the room-and-pillar system after the Hou/Lux method and its comparison with numerical results*

In contrast to the first example, the horizontal drift, the deformation in the slender pillar is dominated by damage related processes. Although all the model calculations qualitatively show the same trends in the evolution of strain, stress, volumetric deformation and damage, some differences e.g. with respect to the stress in the center of a pillar, the progress of dilatancy with time and especially the time-to-rupture of this room-and-pillar system are clearly observed. In order to get a base for comparison, the analytical method

Table 2. Time-dependent load bearing capacity (in MPa) of long pillars according to the Hou/Lux method.

Time-to-rupture yr	Load bearing capacity of long pillars (MPa)				
	$\alpha = 1$	$\alpha = 2$	$\alpha = 3$	$\alpha = 4$	$\alpha = 5$
0	51.7	75.7	93.1	109.9	126.4
0.5	**38.5**	66.0	86.7	105.1	122.6
10	**28.5**	57.2	79.4	98.5	116.4
100	23.6	51.0	74.1	93.7	111.9
1000	19.5	42.4	65.9	86.1	104.6
4000	**18.4**	40.8	64.2	84.5	103.1
10,000	16.9	38.1	60.9	81.4	100.2

Table 3. Comparison of the calculated time-to-rupture of the long pillar with a slenderness of $\alpha = 1$.

Partner	Case A: $p_p = 18.4$ MPa	Case B: $p_p = 28.4$ MPa	Case C: $p_p = 38.4$ MPa
TUC (Analytical)	4000 yr	10 yr	0.5 yr
TUC (Numerical)	>100 yr	>4.5 yr*	>0.25 yr*
IfG-Minkley	>100 yr	>100 yr	12 days
IfG-Günter/ Salzer	>100 yr	22 yr	0.2 yr

* The calculations were broken off automatically due to numerical problems, e.g. a too big creep rate or damage.

after *Hou/Lux* is used to determine the short-term and time-dependent load bearing capacity of pillars (Hou 1997 and Hou & Lux 1999), which is a further development based on the model-mechanical method of Uhlenbecker (1968) and the analytical method of Menzel (1972).

For the estimation of the short-term load bearing capacity of pillars, the analytical method by *Hou/Lux* takes account of the continuity of the *Mohr* failure hypothesis, the post-failure behavior and the successive failure process from the pillar contour to the center of the pillar. The time-dependent load bearing capacity of pillars is calculated by using the *Hou/Lux* constitutive model, the dilatancy boundary, the creep rupture criterion and the time-dependent strength of rock salt as well as a successive creep rupture progress from the pillar contour to the pillar center.

The analytical results for long pillars with a slenderness of $\alpha = 1$ to 5 are shown in Table 2, while in Table 3 the analytical time-to-rupture of the long pillar with $\alpha = 1$ in three cases is compared with the numerical results.

The time-dependent pillar load bearing capacity is increased with the slenderness and decreased with the time-to-rupture. The larger the slenderness of a long pillar is or/and the larger the time-to-rupture becomes, the slower the pillar load bearing capacity is decreased with time.

The analytically calculated time-to-rupture of the long pillar with a slenderness of $\alpha = 1$ in load cases A, B and C is t = 4000, 10 and 0.5 years, respectively, and agrees well with the numerical results of some partners as shown in Table 3.

4 CONCLUSION

7 partners listed in Table 1 had joined this research project and worked very well together in the last nearly 3 years. The benchmark calculations on two different underground structures and comparisons of the numerical results among the project partners, in case of the 35-year-old horizontal drift EU1 additionally with data from in-situ measurements, allow the following conclusions:

- The good correlations between the measured and the calculated minimum stresses, deformation rates and permeabilities in the 35-year-old horizontal drift EU1 confirm the general suitability of the used constitutive models for such analyses, where the deformation is dominated by transient and stationary creep processes. An EDZ with an extension between 0.2 to 1.5 m and a very small maximal dilatancy of 0.25 to 0.45% in the EDZ are determined by the project partners. Furthermore, the speed at which the EDZ extends is time-dependent and continuously decreasing. Thus after about 35 years, the EDZ will either barely change or not alter at all.
- Differences of the extension and values of dilatancy around the drift EU1 between the partners come mainly from different dilatancy boundaries used in the different constitutive models.
- In contrast to the horizontal drift EU1, the deformation in the slender pillar is dominated by damage related processes, especially at the higher pillar loads.
- In case A, the pillar is loaded with a pillar load of $p_p = 18.4$ MPa. The maximum dilatancy at the end of the calculations of the partners keeps at a relatively low level of 1 to 2%, so that damage could not have much influence on the deformation process. Till the end of calculation (t = 100 years), there is no pillar rupture or contour rupture calculated by any partner. Therefore, the time-to-rupture of this room-and-pillar bearing system must be much longer than 100 years in this load case. Furthermore, almost all partners get comparable results in this case. However, differences of the results of the partners are larger in comparison with the simulations of the drift EU1 because of a larger dilatancy and a more extended EDZ.

- Contrary to case A, in case B under a pillar load $p_p = 28.4$ MPa, the dilatancy boundary is exceeded immediately after the excavation, even in the center of the pillar. As a consequence, an x-shaped EDZ through the center of the pillar is developed and gets bigger and especially weaker, so that a contour rupture happens at the time $t = 22$ years according to IfG-Günter/Salzer. Differences of calculation results of the project partners are larger, because the maximum dilatancy is very high ($>10\%$) in this case.
- In case C, the pillar load of $p_p = 38.4$ MPa is bigger than the uniaxial compression strength of 33 MPa. Therefore, the pillar is overloaded immediately after the room excavation. A short time later, the pillar rupture is calculated by a few project partners. The successive failure progress from the contour area to the pillar center is impressively shown by the development of strength drops calculated by IfG-Minkley. In this case, the most different results among the partners in all three cases are calculated because of the largest dilatancy and damage.
- In order to get a base for comparisons, the analytical method after *How/Lux* is used to estimate the short-term and time-dependent load bearing capacity of pillars. The time-dependent pillar load bearing capacity is increased with the slenderness and decreased with the time-to-rupture. The larger the slenderness of a long pillar is or/and the longer the time-to-rupture becomes, the slower the pillar load bearing capacity is decreased with time.
- The analytically calculated time-to-rupture of the long pillar with a slenderness of $\alpha = 1$ in load cases A, B and C is $t = 4000$, 10 and 0.5 years, respectively, and agrees well with the numerical results calculated by some partners.
- All partners were able to simulate all the considered relevant processes with their constitutive models, like transient, stationary and tertiary creep, strain softening, dilatancy, even creep rupture. The computation of such processes like dilatancy does not only make substantial requirements on the constitutive models, but also on the numerical treatment of the simulations, and a careful examination to plausibility of the results. The examples shown here demonstrate the efficiency and high standard of modern constitutive models for rock salt.
- The lower the dilatancy and the smaller the EDZ is, the better the calculated results of the project partners agree with each other. The damage-related processes and the damage induced deformations can not be described comparably by all partners. This point, the damage-porosity-permeability relationship and more complicated in-situ bearing systems should be investigated in a further joint research project.

REFERENCES

Häfner, F et al. 2001. *Abschlussbericht zum BMBF-Forschungsvorhaben "In-situ-Ermittlung von Strömungskennwerten natürlicher Salzgesteine in Auflockerungszonen gegenüber Gas und Salzlösungen unter den gegebenen Spannungsbedingungen im Gebirge"*. Freiberg: IfBF der TU Bergakademie Freiberg.

Hou, Z. 1997. *Untersuchungen zum Nachweis der Standsicherheit für Untertagedeponien im Salzgebirge, Dissertation an der TU Clausthal.* Clausthal-Zellerfeld: Papierflieger Verlag.

Hou, Z. 2002. *Geomechanische Planungskonzepte für untertägige Tragwerke mit besonderer Berücksichtigung von Gefügeschädigung, Verheilung und hydrome¬chanischer Kopplung. Habilitationsschrift an der TU Clausthal.* Clausthal – Zellerfeld: Papierflieger Verlag.

Hou, Z. & Lux, K.-H. 1999. Some new developments in the design of pillars in salt mining. In Vouille & Berest (ed.), *Proceedings of 9th international congress on rock mechanics (volume 1), Paris, September 1999*. Rotterdam: Balkema.

Menzel, W. 1972. Beitrag zur Dimensionierung von Kammerpfeilern im Salzbergbau. *Neue Bergbautechnologie*, 2. Jg., Heft 5: 345–353.

Salzer, K.; Menzel, W. & Günter, R.-M. 2000. Prognose der Auflockerungszone am Beispiel der EU1 (Standort Versuchsverschlussbauwerk). *Vortrag 2. Fachgespräch „Stoßnahe Auflockerungszonen: Detektion, Quantifizierung und Modellierung ihrer mechanischen und hydraulischen Eigenschaften.* FZK Karlsruhe, Mai 2000. Karlsruhe: FZK.

Schulze, O. et al. 2007. Comparison of advanced constitutive models for the mechanical behavior of rock salt – results from a joint research project: I. Modeling of deformation processes and benchmark calculations. In Hardly et al. (ed.), *Understanding of THMC processes in salt rocks; Proceedings of 6th conference on mechanical behaviour of salt, Hannover, 22–24 May 2007*. Rotterdam: Balkema.

Uhlenbecker, F.W. 1968. *Verformungsmessungen in der Grube und ergänzende Laboruntersuchungen auf dem Kaliwerk Hattorf im Hinblick auf eine optimale Festlegung des Abbauverlustes bei größtmöglicher Sicherung der Grubenbau.* Dissertation an der TU Clausthal.

The Mechanical Behavior of Salt – Understanding of THMC Processes in Salt –
Wallner, Lux, Minkley & Hardy, Jr. (eds)
© 2007 Taylor & Francis Group, London, ISBN 978-0-415-44398-2

The Composite Dilatancy Model: A constitutive model for the mechanical behavior of rock salt

A. Hampel
Consultant, Am Fasanenweg 4, Essenheim, Germany

O. Schulze
Federal Institute for Geosciences and Natural Resources (BGR), Stilleweg, Hannover, Germany

ABSTRACT: The Composite Dilatancy Model (CDM) describes transient and steady-state creep, the evolution of dilatancy and damage, failure, and the post-failure behavior of different types of rock salt under different loading conditions and temperatures. Creep is modeled by constitutive equations for the velocity of mobile dislocations and their interactions with other dislocations, particles of salt minerals and with the changing subgrain microstructure of the material. Above the dilatancy boundary the CDM takes into account the increasing influences of damage and humidity on deformation which result in a higher deformation rate and inelastic volumetric strains. After failure, the CDM describes the considerable reduction of the load-bearing capacity of rock salt and its approach to a residual strength which corresponds to a stress level near the dilatancy boundary. In this contribution the current stage of development of the CDM, its various features, and an example for its application are presented.

1 THE PHYSICAL BASIS OF THE CDM

The basic idea of the Composite Dilatancy Model (CDM) is to describe macroscopic creep of compact undamaged rock salt by means of the microscopic mechanisms that control the movement of dislocations under various influences (Hampel & Hunsche 2002). Therefore, transient and steady-state creep are not modeled as two individual processes. Like in nature, transient creep develops gradually towards steady-state creep, until hardening and softening of the material have reached a dynamic equilibrium.

Transient and steady-state creep are linked to the deformation microstructure and changes of it. An important influence has the subgrain structure that is already found as a grown-in structure in natural rock salt before a deformation in the laboratory (Hampel & Hunsche 1998, 2002, Hunsche & Hampel 1999). Subgrains are formed inside a grain by a heterogeneous distribution of dislocations. These were generated during a previous deformation and arranged themselves in chains in order to minimize potential energy. Therefore, it is a relatively stable structure that effects the stress level within the subgrains and, thus, the velocity of dislocations moving there.

When the stress difference exceeds the dilatancy boundary, further deformation processes like an inelastic volume change (dilatancy) and damage gradually set in. While creep is still the dominating mechanism, the evolution of dilatancy and damage are physically linked to it and are modeled with the CDM this way. An example for this link is the piling up of moving dislocations which results in the hardening of the material (−> creep). The evolution of stress concentrations in front of the pile-ups can eventually generate microcracks (−> damage) that elongate and widen up (−> dilatancy) during a further deformation above the dilatancy boundary.

In dilatant salt, humidity from the environment or from inclusions in the salt matrix can spread out through opened pathways. Numerous laboratory experiments (Hunsche & Schulze 1996, 2002) as well as in situ measurements (Plischke & Hunsche 1989) have shown that humidity has a significant influence on the deformation of rock salt, and have led to the modeling of this effect with the CDM.

Propagating damage results in an increased deformation rate and, in terms of stresses, a reduction of the load-bearing capacity of the material (softening by damage). Finally, short-term failure (during rapid loading) or creep rupture will occur when microcracks merge to a localized macroscopic crack. Then, in compression tests with a constant applied strain rate (failure tests), a maximum in the stress difference is observed.

The post-failure behavior is modeled by a rapid stress- and strain-dependent increase of the deformation rate that results in the observed rapid stress reduction. However, the heavily damaged and cracked rock salt is still able to carry a (reduced) load, the residual strength, which corresponds to a stress level near the dilatancy boundary.

In the following section the current mathematical formulation of the CDM is introduced which reflects these physical processes mentioned above.

2 THE MATHEMATICAL FORMULATION OF THE CDM

2.1 *Transient and steady-state creep*

The basic equation of the CDM is Orowan's relation that combines the macroscopic shear rate $d\gamma/dt$ with the average microscopic velocity v and density ρ of mobile dislocations, b is the magnitude of the Burgers vector of dislocations in NaCl (Frost & Ashby 1982):

$$\frac{d\gamma}{dt} = b\,\rho\,v \tag{1}$$

For numerical reasons, in the CDM the dislocation spacing r is used instead of ρ:

$$\rho = \frac{1}{r^2} \tag{2}$$

In the expression for the dislocation velocity, an Arrhenius term takes into account that creep is a thermally activated process with a (constant) activation energy Q. However, the effective temperature dependence of creep is salt type-dependent. This is expressed through a hyperbolic sine function that reflects the competition of hardening and softening processes. The Taylor factor M takes into account that natural rock salt is a polycrystalline material. Then, Equation (1) yields the following basic differential equation for the creep strain ε_{cr}:

$$\frac{d\varepsilon_{cr}}{dt} = \frac{b}{M}\frac{1}{r^2}\,v_0\,\exp\left(-\frac{Q}{R\,T}\right)\sinh\left(\frac{b\,\Delta a\,\sigma^*}{M\,k_B\,T}\right) \tag{3}$$

v_0 is a velocity constant and used as a model parameter, T = temperature, R = universal gas constant, k_B = Boltzmann constant. The activation area Δa and the effective internal stress σ^* are important quantities and are explained later in detail.

In addition to Equation (3), five more differential equations of the following type form the basic set of the CDM and reflect the link between macroscopic creep and the evolution of the microstructure:

$$\frac{dS}{dt} = \frac{dS}{d\varepsilon_{cr}}\cdot\frac{d\varepsilon_{cr}}{dt} = \frac{S_{ss}-S}{k_S}\cdot\frac{d\varepsilon_{cr}}{dt} \tag{4}$$

S stands for 1) the sizes (average diameters) w_1, w_2 and w_3 of three different fractions of the total number of subgrains that evolve with a different rate during deformation, 2) for the average dislocation spacing r, and 3) for the width a of "subgrain walls" (more precisely: regions around subgrain walls with an increased local stress level). The evolution rates of these five quantities are characterized by the rate constants (model parameters) $k_S = k_{w,1}$, $k_{w,2}$, $k_{w,3}$, k_r and k_a. The index "ss" denotes the equilibrium value of the structure variable S during steady-state creep.

The mean subgrain size w is calculated from the portions $c_{w,i}$ of the individual fractions:

$$w = c_{w,1}\,w_1 + c_{w,2}\,w_2 + c_{w,3}\,w_3 \tag{5}$$

In general, these portions are stress- and temperature-dependent functions in order to reflect the stress and temperature dependence of transient creep. Currently, only a simple dependency on the stress difference $\Delta\sigma$ is used:

$$c_{w,1}(\Delta\sigma) = \max(0,\,1-c_1\,\Delta\sigma) \tag{6}$$

$$\begin{aligned} c_{w,3}(\Delta\sigma) &= [c_3\cdot(\Delta\sigma-c_2)]^{c_4} \quad \text{for } \Delta\sigma > c_2 \\ c_{w,3}(\Delta\sigma) &= 0 \quad \text{otherwise} \end{aligned} \tag{7}$$

$$c_{w,2}(\Delta\sigma) = 1-c_{w,1}(\Delta\sigma)-c_{w,3}(\Delta\sigma) \tag{8}$$

The c_i (i = 1 to 4) are model parameters and determined with laboratory creep tests at different $\Delta\sigma$.

The physical origin of differences in the mechanical behavior of different salt types are modeled through the activation area Δa:

$$\Delta a = \frac{b}{\frac{1}{d_p}+\frac{1}{r}} \tag{9}$$

The parameter d_p denotes the spacing of (small) particles of salt minerals inside the salt matrix that act as dislocation obstacles. Laboratory investigations have shown that the distribution of such particles, which is a consequence of local geological processes, determines these differences rather than their overall chemical content (Hunsche et al. 1996). The "r" in Equation (9) takes into account that interacting dislocations form dislocation jogs which are also obstacles against the dislocation motion.

As mentioned above, the subgrain structure influences the effective internal stress σ^* inside the subgrains that drives the mobile dislocations (σ^* must not be mixed up with the overall effective stress σ_{eff}!). This is described by the following equation:

$$\sigma^* = \begin{cases} \dfrac{4\,\sigma_s^{\,3}}{27\,\sigma_{G,r}^{\,2}} & \text{for} \quad \Delta\sigma < \dfrac{3\,\sigma_{G,r}}{2\,k_s} \\ \sigma_s - \sigma_{G,r} & \text{otherwise} \end{cases} \tag{10}$$

The lower case in Equation (10) describes that a moving dislocation feels the local stress level σ_s inside the subgrains, reduced by the back stress $\sigma_{G,r}$ from the other dislocations. The upper case in Equation (10) reflects the observation that rock salt has no visible yield strength ($\sigma^* -> 0$ for $\Delta\sigma -> 0$).

σ_s is calculated as follows:

$$\sigma_s = k_s \, \Delta\sigma \tag{11}$$

$$k_s = \frac{1 - f_h \, k_h}{1 - f_h} \tag{12}$$

The factors k_s and k_h describe the local stress decrease inside the subgrains (s = soft regions) and increase in the "subgrain walls" (see above, h = hard regions), respectively. The volume fraction f_h of the hard regions can be estimated as follows (Hampel & Hunsche 2002, Weidinger et al. 1997):

$$f_h = \frac{2\,a}{w} \tag{13}$$

The back stress depends on the sign of the current or previous stress change:

$$\sigma_{G,r} = \begin{cases} \dfrac{k_{G,r}}{r} \text{ at and after } d(\Delta\sigma)/dt > 0 \\ \dfrac{k_{G,r}}{r_{ss}} \text{ at and after } d(\Delta\sigma)/dt < 0 \end{cases} \tag{14}$$

$$k_{G,r} = k_{G,r}(T) = \alpha \, M \, G(T) \, b \tag{15}$$

$\alpha = 0.17$ is the dislocation interaction constant, and G is the shear modulus, for which Frost & Ashby (1982) gave the temperature dependence:

$$G(T) = 15{,}000 \text{ MPa} \left(1 - 0.73 \cdot \frac{T[K] - 300\,K}{1070\,K} \right) \tag{16}$$

Finally, the steady-state (index "ss") and the initial (index "0") values of the evolution of the microstructure variables w, r and a are known from laboratory investigations (Hampel & Hunsche 2002, Hunsche & Hampel 1999, Weidinger et al. 1997):

$$w_{ss} = w_{ss}(T, \Delta\sigma) = \min\left(33 \frac{G(T)\,b}{\Delta\sigma}, d_K \right) \tag{17}$$

$$r_{ss} = r_{ss}(T, \Delta\sigma) = \min\left(\frac{G(T)\,b}{k_{s,ss}\,\Delta\sigma}, d_K \right) \tag{18}$$

$$a_{ss} = a_{ss}(T, \Delta\sigma) = \frac{1}{2} f_{h,ss} \, w_{ss}(T, \Delta\sigma) \tag{19}$$

$$w_0 = c_{w,1} \, w_{1,0} + c_{w,2} \, w_{2,0} + c_{w,3} \, w_{3,0} \tag{20}$$

$$r_0 = r_{ss}(T_{nat}, \Delta\sigma_{nat}) \tag{21}$$

$$a_0 = \frac{1}{2} f_{h,ss} \, w_0 \tag{22}$$

For numerical reasons, w_{ss} and r_{ss} are limited to the grain size d_K for $\Delta\sigma -> 0$. $w_{1,0}$, $w_{2,0}$ and $w_{3,0}$ are model parameters, T_{nat} and $\Delta\sigma_{nat}$ denote the natural in situ temperature and stress difference at the underground location of the rock salt and can be roughly estimated (e.g. $T_{nat} = 300$ K) or calculated ($\Delta\sigma_{nat}$, using w_0 for w_{ss} in Equation (17) assuming a steady-state grown-in microstructure).

2.2 *Dilatancy, damage, post-failure behavior and their influence on deformation*

In the stress space, the dilatancy boundary separates the region of compressibility (below it) from that one of dilatancy and damage (above it). Currently, in the CDM the BGR dilatancy boundary is used as follows (Hunsche et al. 2003), expressed in octahedral stresses, see Figure 5:

$$\tau_D(\sigma_{okt}) = \frac{b_D}{\sqrt{3}} \cdot \left(\frac{\sigma_{okt}}{\sigma_u} \right)^{c_D} \tag{23}$$

with $b_D = 2.61248$ MPa, $c_D = 0.78093$, $\sigma_u = 1$ MPa.

However, although the formula defines a precise stress condition, the dilatancy boundary should rather be interpreted as a fuzzy band, where dilatancy, damage and related effects like the influence of humidity gradually set in.

As mentioned in section 1, creep is very important also above the dilatancy boundary, not only as a deformation process itself, but also as the underlying process for the evolution of dilatancy and damage that are linked to it. In the CDM, this is modeled by the following equation for the total deformation rate:

$$\frac{d\varepsilon_{tot}}{dt} = P_F \cdot \delta_{dam} \cdot F_h \cdot \frac{d\varepsilon_{cr}}{dt} \tag{24}$$

Various factors take into account that the different influences of humidity (F_h), damage (δ_{dam}), and the post-failure behavior (P_F) increase the strain rate of pure creep in the dilatant stress region.

The humidity influence is modeled as follows (Hunsche & Schulze 1996, 2002):

$$F_h(\Phi, \sigma_3, \tau_{okt}) = 1 + f_\Phi(\Phi) \, f_c(\sigma_3, \tau_{okt}) \tag{25}$$

A relative humidity Φ can only increase the deformation rate, if the minimum principle stress σ_3 and the octahedral shear stress τ_{okt} ensure that the stress is close to or above the dilatancy boundary:

$$f_\Phi(\Phi) = c_{\Phi 1} \cdot \sinh(c_{\Phi 2} \cdot \Phi) \tag{26}$$

$$f_c(\sigma_3,\tau_{okt}) = \left[1+\left(\frac{\sigma_3}{\sigma_u}\right)^{ex1}\right]^{ex2} \quad \text{for } \sigma_3 \geq 0$$

$$f_c(\sigma_3,\tau_{okt}) = 1 \qquad \text{otherwise} \tag{27}$$

$$\text{with} \quad ex1 = c_{fc1}\,\tau_{okt}\,, \quad ex2 = -\left(\frac{c_{fc2}}{1+\tau_{okt}/\sigma_u}\right)^2$$

and $c_{\Phi 1} = 0.1$, $c_{\Phi 2} = 0.1$, $c_{fc1} = 0.08$ 1/MPa, $c_{fc2} = 18$ and $\sigma_u = 1$ MPa (independent of the salt type).

As mentioned above, the evolution of inelastic volumetric strains ε_{vol} (dilatancy) and damage is physically linked to the creep process. This is reflected in the CDM by a stress-dependent function r_v that was determined in laboratory tests (Hunsche et al. 2003):

$$\frac{d\varepsilon_{vol}}{dt} = \sqrt{\frac{3}{2}} \cdot r_v(\sigma_{okt},\tau_{okt}) \cdot F_h(\Phi,\sigma_3,\tau_{okt}) \cdot \frac{d\varepsilon_{cr}}{dt} \tag{28}$$

$$r_v(\sigma_{okt},\tau_{okt}) = 3 \cdot \left[\frac{\tau_{okt} - \tau_D(\sigma_{okt})}{\sigma_{okt}}\right]^2 \quad \text{for } \tau_{okt} > \tau_D \tag{29}$$

$$r_v(\sigma_{okt},\tau_{okt}) = 0 \quad \text{otherwise}$$

For modeling the damage evolution, a "BGR damage parameter" d_{dam} is introduced that corresponds to the volume change energy:

$$\frac{d\,(d_{dam})}{dt} = \sigma_{okt} \cdot \frac{d\varepsilon_{vol}}{dt} \tag{30}$$

The influence of damage on deformation is currently described with an empirical function:

$$\delta_{dam}\,(d_{dam},\sigma_3) = \exp\left\{\delta_1 \cdot \left(\frac{d_{dam}}{\sigma_u}\right)^{\delta_2\,\sigma_3}\right\} \tag{31}$$

with δ_1 and δ_2 as model parameters determined by adjusting the CDM to failure test results.

Finally, the increase of deformation rate and rapid decrease of stress in the post-failure region is modeled by means of the function P_F which is dependent on the stress difference to the dilatancy boundary $\Delta\tau_D$ and the strain difference to the failure strain ε_F:

$$\frac{dP_F}{d\varepsilon_{tot}} = c_{PF} \cdot \frac{\Delta\tau_D}{1 + |\Delta\tau_D|} \cdot \Delta\varepsilon_F{}^{n_{PF}} \quad \text{for } \Delta\varepsilon_F > 0$$

$$P_F = 1 \quad \text{otherwise}$$

$$\text{with} \quad \Delta\tau_D(\sigma_{okt},\tau_{okt}) = \tau_{okt} - \tau_D(\sigma_{okt}) \tag{32}$$

$$\Delta\varepsilon_F(\varepsilon_{tot}) = \varepsilon_{tot} - \varepsilon_F$$

$$c_{PF}\,(\sigma_3) = c_{PF1} \cdot \exp\{c_{PF2} \cdot \sigma_3\}$$

c_{PF1}, c_{PF2}, and n_{PF} are model parameters. The calculation of ε_F with the CDM is currently being improved, so far it has been determined empirically.

For simulations of underground structures in rock salt, the CDM is transformed to a three dimensional formulation by applying the Levy-Mises theory:

$$de_{kl}^{(pl)} = \frac{3}{2} \cdot \frac{d\varepsilon_{eff}}{\sigma_{eff}}\, s_{kl} \tag{33}$$

The components of the plastic deviatoric strain increments $de_{kl}^{(pl)}$ are connected to the deviatoric stress components s_{kl} through the effective strain increment $d\varepsilon_{eff}$ and effective stress σ_{eff} which correspond to quantities used or calculated in the CDM:

$$d\varepsilon_{eff} = F_h(\Phi,\sigma_3,\tau_{okt}) \cdot d\varepsilon_{cr}$$
$$\sigma_{eff} = \Delta\sigma \tag{34}$$

3 CALCULATIONS OF CREEP AND FAILURE TESTS WITH THE CDM

The various features of the CDM described in Sections 1 and 2, can be illustrated in detail best with calculations of laboratory creep and failure tests. In underground structures the various deformation processes are superimposed under locally different and changing conditions. Therefore, it is the aim to model all the different processes, influences and conditions with the CDM using a single uniform set of model parameter values for each salt type.

In Figure 1 six creep tests from the BGR laboratory are shown in comparison with their CDM simulations. The tests were performed with salt type Asse-Speisesalz near room temperature with different stress differences and confining stresses. The model curves in this figure as well as in Figures 2–4 and 6 were all calculated with the same uniform set of model parameter values which was determined for Asse-Speisesalz.

While this set characterizes the average mechanical behavior of this salt type, individual specimens of same type and from the same location show a natural scattering of test results because of individual differences in the microstructure, e.g. the local distribution of salt minerals. This explains why small deviations of some model curves from the experimental data have to occur. Of course, each test curve in Figures 1–4 and 6 could be adjusted almost exactly with an individual choice of model parameter values, but to model all tests of one salt type with the same set of parameter values is a much bigger challenge.

Except for the two uniaxial tests in Figure 1, where a small influence of humidity cannot be excluded because their stress states lie above the dilatancy

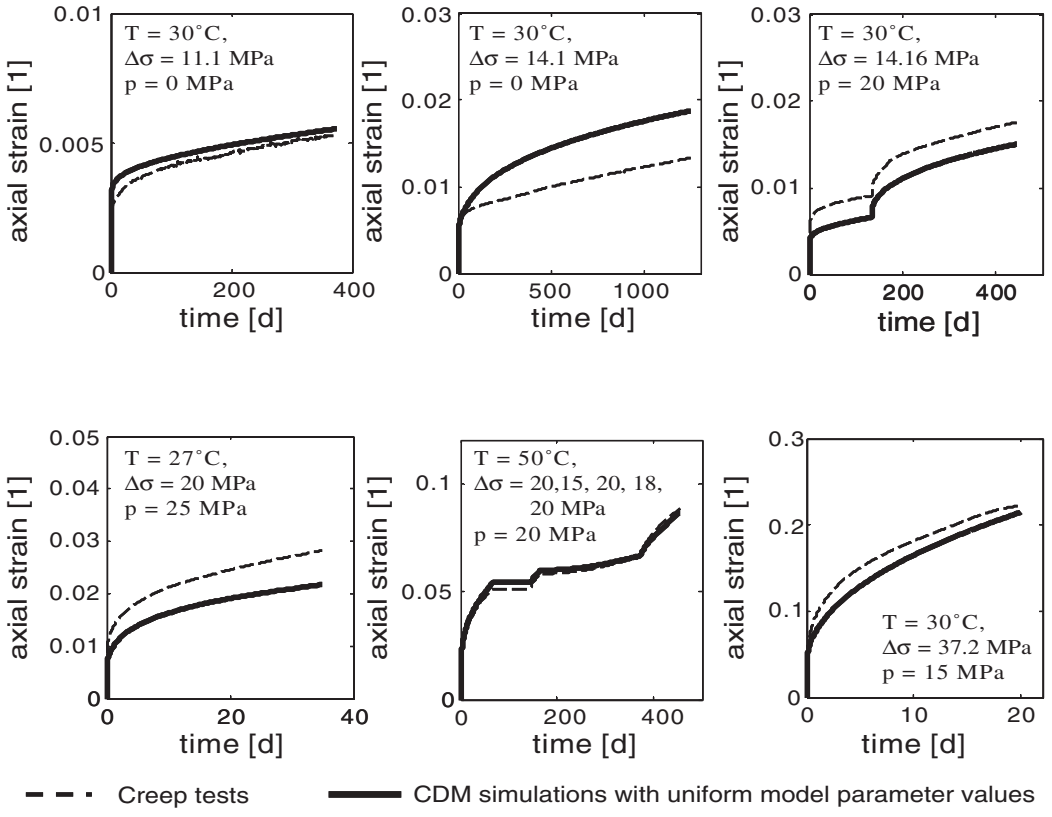

Figure 1. Six one- or multistage laboratory creep tests with salt type Asse-Speisesalz (test temperatures T, stress differences $\Delta\sigma$, and confining stresses p as indicated) were simulated with the CDM using the same model parameter values. This demonstrates that the stress and temperature dependence of creep is described correctly with the CDM. While the model describes the average mechanical behavior of the salt type under different test conditions and influences, individual specimens reveal a natural scattering of test results because of an individual geological history. Therefore, some model curves deviate slightly from the respective experimental data.

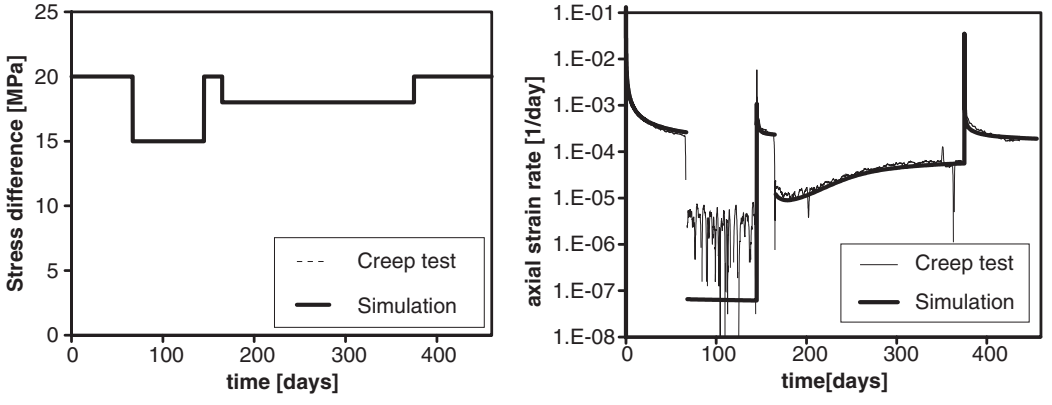

Figure 2. Multistage creep test with two stress reductions (same test as in the middle diagram of the bottom row of Figure 1). The CDM simulation describes the recovery creep after a small stress reduction from 20 to 18 MPa, but no recovery (in the given time period of 78 days) after a reduction to 15 MPa, both in good agreement with the measured creep curve (right).

boundary, the confining stresses have no influence on deformation in the other tests (i.e. below the dilatancy boundary). Therefore, the differences in transient and steady-state creep of the six tests were caused mainly by the individual stress differences. This is taken into account with Equations 6–8.

In Figure 2 the five-stage creep test from Figure 1 is shown again in detail. In the strain rate vs. time plot, the modeled recovery creep after the stress reduction from 20 to 18 MPa agrees exactly with the test data.

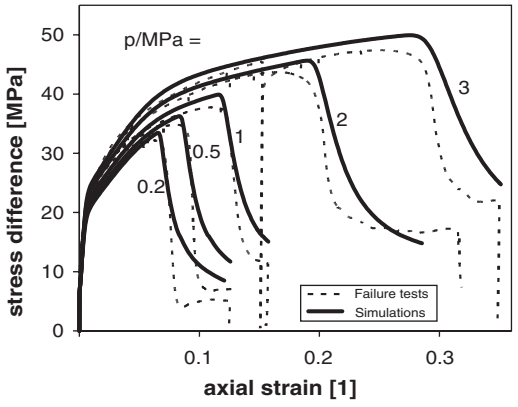

Figure 3. Five laboratory failure tests with Asse-Speisesalz at T = 303 K with a constant applied axial strain rate of 1E−5 1/s and various confining stresses p as indicated. The CDM simulations were performed with the same model parameter values as those in Figures 1 and 2. The evolution of the stress difference is modeled up to the post-failure region (failure = stress maximum). The CDM describes the influence of the confining stress p mainly through the modeled humidity and damage influences on the creep rate above the dilatancy boundary.

After the previous larger reduction to 15 MPa no recovery was observed within the given period of 78 days. This is also modeled correctly.

With the adjustments of the CDM to the creep tests, the values of the model parameters characterizing the creep of Asse-Speisesalz were determined: v_0, d_p for steady-state creep, and $w_{1-3,0}$, $k_{w,1-3}$, k_r, c_{1-4} for transient creep (k_a is always $1 \cdot 10^{-4}$). Using these values, the characteristic values of the model parameters for the deformation processes above the dilatancy boundary δ_1 and δ_2 (damage influence), c_{PF1}, c_{PF2}, and n_{PF} (post-failure behavior) were determined in simulations of failure tests. For the modeling of the humidity influence no salt type-dependent parameter values are used, see Equations (26) and (27).

In Figures 3 and 4 the resulting model curves are compared with the experimental data. They show that the mechanical behavior above the dilatancy boundary up to the residual strength is also modeled correctly with the CDM and the uniform set of constant parameter values. This comprises the influence of the confining stress p (in general: minimum principle stress σ_3) and of the strain rate as well as the volume increase after passing the dilatancy boundary.

The contributions of the individual deformation processes creep, dilatancy (humidity) and damage influence, and post-failure behavior to the total deformation ε_{tot} can be demonstrated with calculations of a creep test that was performed at a stress state close to the short-term failure boundary, see test TUC-313 in Figures 5 and 6.

In Figure 6a this test is compared with creep test 95008 which has a similar stress difference and, thus, a similar octahedral shear stress, see Figure 5. Because of a much higher confining stress p, test 95008 lies below the dilatancy boundary and, therefore,

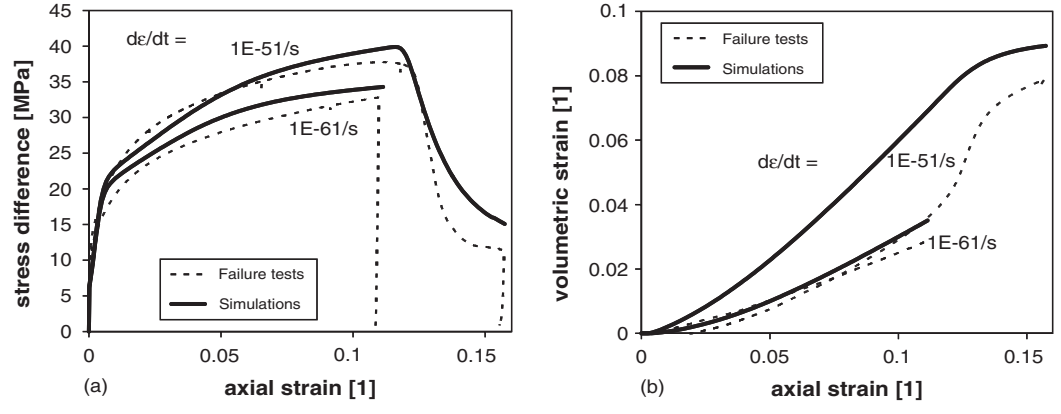

Figure 4. (a) Two failure tests with Asse-Speisesalz at room temperature with confining stress p = 1 MPa and different axial strain rates as indicated, were calculated also with the same characteristic set of model parameter values for this salt type. (b) In the CDM the evolution of the volumetric strain is modeled in dependence of the calculated creep strain. This dependence was confirmed by several experimental results (Hunsche et al. 2003).

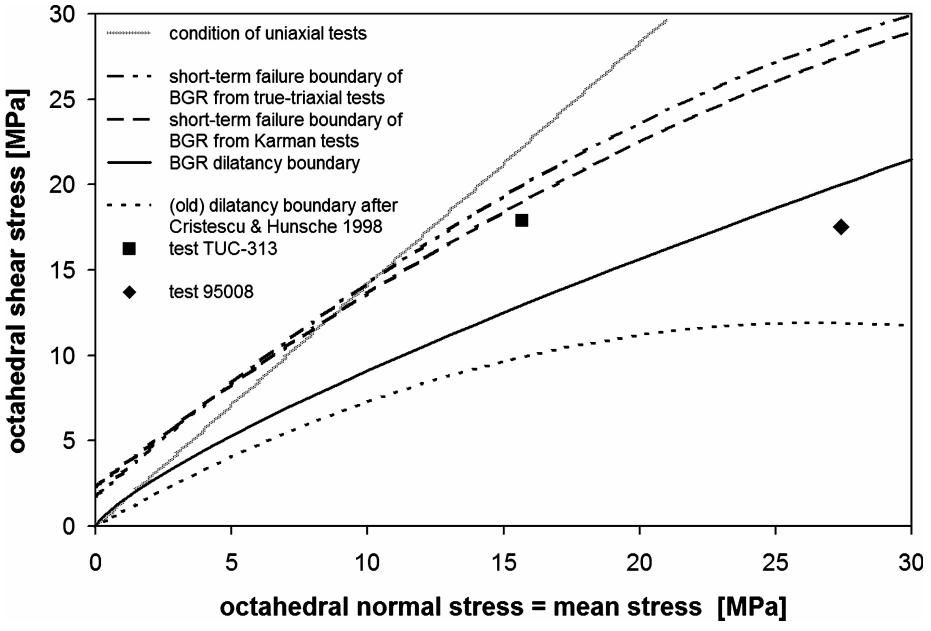

Figure 5. Octahedral stress diagram with two dilatancy boundaries, two short-term failure boundaries and the stress conditions of uniaxial tests and of two individual creep tests: test TUC-313 with T = 303 K, $\Delta\sigma$ = 38 MPa, p = 3 MPa and test 95008 with T = 303 K, $\Delta\sigma$ = 37.2 MPa, p = 15 MPa, see Figure 6.

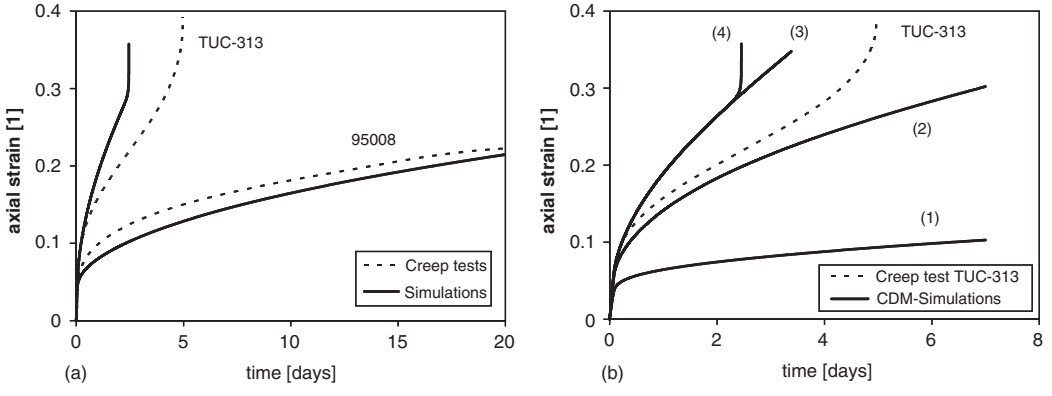

Figure 6. (a) Comparison of two creep tests and their CDM simulations with the uniform set of model parameter values. The tests were performed with a similar stress difference but different confining stresses, see Figure 5. The CDM describes the difference of the two curves by larger dilatancy (humidity) and damage influences on deformation in test TUC-313. The increasing damage finally leads to creep rupture. With a higher confining stress in test 95008, below the dilatancy boundary these influences are almost totally suppressed. (b) Test TUC-313 was simulated several times by successively taking into account (1) only creep, (2) creep and humidity influence, (3) creep, humidity and damage influence, and (4) creep, humidity and damage influence and post-failure behavior. The resulting model curve (4) lies a little higher than the experimental curve because the simulations were performed with the uniform set of model parameter values for Asse-Speisesalz and not with an individual adjustment of the CDM to this test.

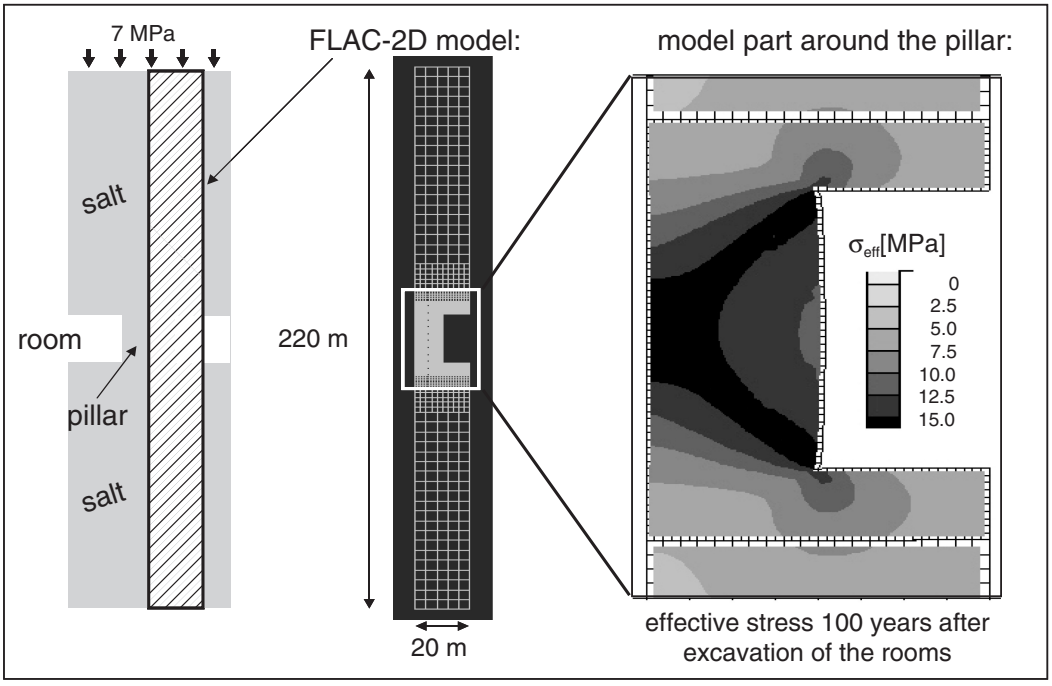

Figure 7. Example for the applicability of the CDM in calculations of underground structures in rock salt. The sketch (left) and the FLAC^{2D} model (center) show a vertical cut through a slender pillar (height/width = 20 m/20 m = 1) that was simulated with the CDM under an applied stress of 7 MPa at the model's upper end (corresponding to a depth of the pillar of about 430 m). The contour plot (right) shows the distribution of the effective stress 100 years after the excavation of the rooms.

shows mainly pure creep (because of its proximity to the dilatancy boundary, there is already a humidity influence). Both tests were calculated with the same model parameter values. Therefore, the difference between the two curves is modeled correctly by means of the (larger) humidity and damage influences, and the post-failure behavior above the dilatancy boundary in test TUC-313.

By setting in Equation (24) the factors P_F, δ_{dam} and F_h successively to one, the respective contribution of the different processes can be studied, see Figure 6b. This is an advantage of the modular structure of the CDM.

Finally, in Figure 7 an example demonstrates the applicability of the CDM in calculations of underground structures in rock salt. The model of a vertical cut through a slender pillar was calculated with the CDM and the finite difference code FLAC^{2D} (Itasca Inc.) for a period of 100 years after the excavation of the adjacent rooms (for symmetry reasons only one half of the pillar was calculated). The contour plot of the effective stress in the magnified model section around the pillar shows the concentration of the stress to an x-shaped region inside the pillar after 100 years. The slight bowing-out of the pillar's side face(s) is visible, too.

4 SUMMARY

The Composite Dilatancy Model (CDM) has been developed in order to describe transient and steady-state creep, the evolution of dilatancy and damage, their influences on deformation, failure, and the post-failure behavior of different types of rock salt under different loading conditions and temperatures.

Pure creep below the dilatancy boundary is modeled on the basis of a description of the underlying microscopic mechanisms of dislocation motion under various influences of the microstructure.

Therefore, transient creep is the consequence of a changing subgrain structure which is a stable heterogeneous dislocation distribution, and a changing dislocation spacing. Thus, hardening and softening of the material occur naturally after an increase or decrease of the stress difference, respectively, without further adjustments of the model. Furthermore, steady-state creep arises automatically as deformation continues under a constant stress difference.

All processes above the dilatancy boundary are modeled through their physical link to the creep process. In dilatant salt the influence of humidity on deformation, that was investigated in the BGR laboratory and is observed in situ, is taken into account.

The increase of the deformation rate caused by dilatancy, humidity, and damage as well as the post-failure behavior are modeled through process-related functions. They result in the damage softening of the material (stress reduction due to damage).

In this paper, the various features of the CDM were demonstrated with calculations of stress-controlled creep tests and strain-controlled failure tests that were performed with salt type Asse-Speisesalz near room temperature with different stress differences, confining stresses (i.e. minimum principle stresses), and strain rates.

All model curves were calculated with the same uniform set of model parameter values. Nevertheless, they show a good agreement with the experimental data. It should be emphasized that it is a special challenge to a constitutive model to describe with the same model parameter values stress-controlled creep tests with a duration of up to 1300 days as well as strain-controlled failure tests with a duration of only hours and a continuously changing stress difference between 0 and 50 MPa. This verifies that the processes and influences are modeled correctly with the CDM.

A further advantage of the modular structure of the CDM is that the respective contribution of the different deformation processes can be studied.

Finally, one result from a simulation of a slender pillar in rock salt about 430 m below surface is shown to demonstrate the applicability of the CDM in calculations of underground structures in rock salt.

5 OUTLOOK

Some formulations of the CDM are currently being improved further in order to be able to predict the dilatancy and damage evolution and their influence on deformation with higher precision. This will improve the predictions of the processes in the excavated disturbed rock zone (EDZ). Since these processes are linked to the porosity and, thus, to the permeability of damaged rock salt, the calculation of this important process with the CDM will also be possible in the near future.

REFERENCES

Cristescu, N. & Hunsche, U. 1998. *Time effects in Rock Mechanics.* Series: *Materials, Modelling and Computation*. Chichester: John Wiley and Sons.

Frost, H.J. & Ashby, M.F. 1982. *Deformation-mechanism maps*. Oxford: Pergamon Press.

Hampel, A. & Hunsche, U. 1998. Die Beschreibung der rißfreien transienten und stationären Verformung von Steinsalz mit dem Verbundmodell. *Geotechnik* 21: 264–267.

Hampel, A. & Hunsche, U. 2002. Extrapolation of creep of rock salt with the composite model. In N.D. Cristescu, H.R. Hardy Jr. & R.O. Simionescu (eds.), *Basic and Applied Salt Mechanics, Proc. 5th Conference on the Mechanical Behavior of Salt (MECASALT 5), Bucharest, 1999*: 193–207. Lisse: Swets & Zeitlinger (A.A. Balkema Publishers).

Hunsche, U. & Hampel, A. 1999. Rock salt – the mechanical properties of the host rock material for a radioactive waste repository. *Engineering Geology* 52: 271–291. Amsterdam: Elsevier Science Publishers.

Hunsche, U., Mingerzahn, G. & Schulze, O. 1996. The influence of textural parameters and mineralogical composition on the creep behaviour of rock salt. In M. Ghoreychi, P. Berest, H.R. Hardy Jr. & M. Langer (eds.), *The Mechanical Behavior of Salt*; *Proc. 3rd Conference, Palaiseau, 1993*: 143–151. Clausthal-Zellerfeld: Trans Tech Publications.

Hunsche, U. & Schulze, O. 1996. Effect of humidity and confining pressure on creep of rock salt. In M. Ghoreychi, P. Berest, H.R. Hardy Jr. & M. Langer (eds.), *The Mechanical Behavior of Salt*; *Proc. 3rd Conference, Palaiseau, 1993*: 237–248. Clausthal-Zellerfeld: Trans Tech Publications.

Hunsche, U. & Schulze, O. 2002. Humidity induced creep and its relation to the dilatancy boundary. In N.D. Cristescu, H.R. Hardy Jr. & R.O. Simionescu (eds.), *Basic and Applied Salt Mechanics, Proc. 5th Conference on the Mechanical Behavior of Salt (MECASALT 5), Bucharest, 1999*: 73–87. Lisse: Swets & Zeitlinger (A.A. Balkema Publishers).

Hunsche, U., Schulze, O., Walter, F. & Plischke, I. 2003. Projekt Gorleben 9G2138110000 – Thermomechanisches Verhalten von Salzgestein. Abschlussbericht. Hannover: Bundesanstalt für Geowissenschaften und Rohstoffe.

Plischke, I. & Hunsche, U. 1989. In-situ-Kriechversuche unter kontrollierten Spannungsbedingungen an großen Steinsalzpfeilern. In V. Maury & D. Fourmaintraux (eds.), *Rock at Great Depth, Proc. intern. symp., Pau (France) 1989*: 101–108. Rotterdam: Balkema.

Weidinger, P., Hampel, A., Blum, W. & Hunsche, U. 1997. Creep behaviour of natural rock salt and its description with the composite model. *Materials Science and Engineering A*234–236: 646–648.

Taylor & Francis
Taylor & Francis Group
http://taylorandfrancis.com

The Mechanical Behavior of Salt – Understanding of THMC Processes in Salt –
Wallner, Lux, Minkley & Hardy, Jr. (eds)
© 2007 Taylor & Francis Group, London, ISBN 978-0-415-44398-2

A model for rock salt, describing transient, stationary, and accelerated creep and dilatancy

R.-M. Günther & K. Salzer
Institute for Rock Mechanics GmbH, Leipzig, Germany

ABSTRACT: In the scope of a unified approach to describe the creep behavior the constitutive model as presented here describes comprehensively the mechanical behavior of rock salt in a good approximation. In this model, hardening is used as an inner variable of state. This model has been verified by the results which were obtained when recalculating a plurality of different laboratory tests. Evidently, hardening is governed by the processes of deformation and recovery on the one hand and by those of damage on the other one, i. e. the formulation of the constitutive laws is based just on those processes of crystal physics which are the origin of the mechanical behavior of salt rock. These considerations have allowed to demonstrate that the hardening-reducing effect of damage can be put on the same level as the dilatancy, the latter being a function both of deformation work performed above the dilatancy boundary (damage work) and minimum stress which has to be determined from triaxial tests. The paper contains a complete set of equations, which are used in model calculations.

1 INTRODUCTION

It is well known that salt rock responses to loading by elastic and viscoplastic deformation. The stress-deformation behavior which is characterized by time-dependent ductile deformation without any visible macroscopic fracture is denoted as creep. Creep tests under constant stress conditions reveal that creep is subdivided into the following three phases:

1 primary creep – also denoted as transient or non-stationary creep,
2 secondary or stationary creep, and
3 tertiary creep or creep failure.

These three phases of the creep are in a close relation to each other and develop in the result of intracrystalline deformation. Primary creep is characterized by high deformation rates. Decisive causes for primary creep are the dislocations which are present within the lattice structure and which start to move when stress increases. With growing deformation, the motion capacity of the present dislocations diminishes. If deformation continues, new dislocations will be produced within the lattice. Thus, the dislocation density rises, and this process will cause an increasing resistance against deformation itself so that for maintaining a constant deformation rate an increasingly higher force is necessary or the deformation rate will decrease even when load is kept constant. This material hardening which increases with increasing deformation is counteracted by the recovery of dislocations. Out of this process, stationary creep develops by the fact that formation rate and recovery rate of the dislocations tend to approach equal values. In this phase of creep the density of dislocations, the deformation resistance and consequently also the creep rates evolve to constants (Blum 2004). When damage processes and the softening processes which are linked to them and which start in the stress space above the dilatancy boundary (Hunsche et al. 2003) achieve a critical value, creep will pass into its tertiary phase so that we can observe creep failure.

In the last decades numerous approaches have been developed for establishing the constitutive behavior of rock salt mainly motivated by the possible use of excavated openings in rock salt formations as repositories for nuclear waste. A comprehensive overview is given in the contribution Hampel et al. (this volume). Here, a more detailed description of the newly developed constitutive Günther-Salzer-model is presented which is based on these physical processes and which describes all three creep phases in the scope of a creep model. It represents the actual state of developing work performed by the authors in the recent years (e.g. Salzer, 1993; Salzer et al., 1998 and 2002).

With respect to the new constitutive law, the theoretical considerations are illustrated together with the derivation of the corresponding parameters of the constitutive law for a Staßfurt rock salt variety taken from the Sondershausen mine and with the recalculation of the respective laboratory tests. The calculations as required for this aim have been carried out using

the calculation programme FLAC (Itasca 2000) into which said constitutive model has been implemented as DLL file.

2 DAMAGE-FREE CREEP

According to the strain-hardening theory (Odqvist & Hult 1962), which is the base of the constitutive model, the tensor of the deformation rate is described by the equation:

$$\dot{\varepsilon}_{ij} = \dot{\varepsilon}^{el}_{ij} + \dot{\varepsilon}^{cr}_{ij} \ , \tag{1a}$$

$\dot{\varepsilon}^{el}_{ij}$ being the elastic part and $\dot{\varepsilon}^{cr}_{ij}$ being the creep part of the deformation tensor and

$$\dot{\varepsilon}^{el}_{ij} = -\nu/E\,\dot{\sigma}_{kk}\,\delta_{ij} + (1+\nu)/E\,\dot{\sigma}_{kk}$$

$$\dot{\varepsilon}^{cr}_{ij} = 3/2\,\dot{\varepsilon}^{cr}_{eff}\,S_{ij}/\sigma_{eff} \tag{1b}$$

where ε_{eff} is the effective deformation and σ_{eff} is the effective stress.

$$\varepsilon_{eff} = \sqrt{3/2 \sum_{ij} \varepsilon^2_{ij}}$$
$$\sigma_{eff} = \sqrt{2/3 \sum_{ij} \sigma^2_{ij}}\,, \quad S_{ij} = \sigma_{ij} - 1/3\,\sigma_{kk}\,\delta_{ij} \tag{1c}$$

In this connection, creep is described by using the following approach for strain-hardening:

$$\dot{\varepsilon}^{cr}_{eff} = A_p \frac{\sigma^{n_p}_{eff}}{(\varepsilon^{V,0}_{eff} + \varepsilon^{cr}_{eff})^{\mu}} \tag{2}$$

where A_p, n_p, and μ are material parameters. In the beginning of loading, deformation is dominated by the migration of those dislocations which are already present in the crystal (initial hardening $\varepsilon^{V,0}_{eff}$). With progressing deformation, new dislocations are generated which cause an increase in hardening. Equation (2) means that the part of the deformation which increases hardening and the total creep deformation ε^{cr}_{eff} are identical. With growing deformation ε^{cr}_{eff}, the dislocation density increases and the creep rate diminishes (Fig. 11a).

For determining these creep parameters, creep tests have been required which were to be carried out in the laboratory over a long period without any dilatancy effect. With test periods of few months, recovery processes play no yet an important role. This allows to describe quite well the creep behavior using the strain-hardening approach as has been shown by comparing the calculated and the measured values of the creep deformation of the Staßfurt rock salt taken from the Sondershausen mine (Fig. 1). For this rock salt variety, the following creep parameters have been determined:

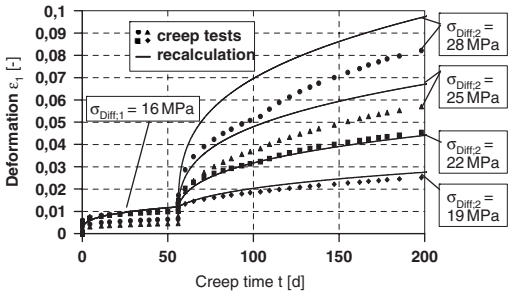

Figure 1. Creep tests carried out on Staßfurt-rock salt, Sondershausen mine, and recalculation.

$$A_p = 2.7 \cdot 10^{-24}\,[d^{-1}], \quad n_p = 11.88, \quad \mu = 2.6$$

This strain-hardening approach has been implemented in the FEM code MKEN and utilized for solving diverse rock mechanical problems (Salzer & Schreiner 1991).

Those processes which result in a reduction of the number of present dislocations are denoted as recovery. They counteract the advancing material hardening. It is well known that recovery is a mainly thermal activated process which is more efficient at higher temperatures. With growing dislocation density, or hardening, also the recovery rate increases. That part of the deformation which has hardening effect ε^{V}_{eff}, does not grow any more adequatly with the total deformation ε^{cr}_{eff}, but tends to approach a saturation value. Here, creep passes into its secondary (stationary) phase. Thus, when considering recovery in the creep approach, according to equation (3) the total creep rate $\dot{\varepsilon}^{cr}_{eff}$ is obtained from the part $\dot{\varepsilon}^{V}_{eff}$ which has hardening effect, and another part $\dot{\varepsilon}^{E}_{eff}$ which describes recovery.

$$\dot{\varepsilon}^{cr}_{eff} = \dot{\varepsilon}^{V}_{eff} + \dot{\varepsilon}^{E}_{eff}$$

and

$$\dot{\varepsilon}^{V}_{eff} = \dot{\varepsilon}^{cr}_{eff} - \dot{\varepsilon}^{E}_{eff} \tag{3}$$

For the recovery rate will be assumed:

$$\dot{\varepsilon}^{E}_{eff} = \frac{\varepsilon^{V}_{eff}}{t_0} \tag{4}$$

where t_0 = recovery time

At present, due to the diverse effects the recovery time t_0 cannot be derived from theoretical considerations. However, since recovery time has an essential effect on the stationary creep rate it is useful to determine the value of t_0 by way of recalculation of the

results which have been obtained from in-situ measurements or from creep tests lasting over long periods. Regarding the laws of crystal physics which describe recovery in a first approximation it is appropriate to use the Arrhenius approach for the temperature dependency of recovery time t_0 (Salzer et al. 1999).

$$t_0 = t_C \cdot e^{\frac{Q}{R \cdot T}} \tag{5}$$

where Q denotes the activation energy for the recovery process and t_C is a time constant. For room temperature the recovery time t_0 is in the range of several dozens of years.When substituting in the creep approach of eq. (2) the total deformation ε_{eff}^{cr} by the accumulated hardening ε_{eff}^{V} then in the strain-hardening approach the recovery can be taken into consideration. The result is

$$\begin{aligned} \dot{\varepsilon}_{eff}^{cr} &= A_p \frac{\sigma_{eff}^{n_p}}{(\varepsilon_{eff}^{V,0} + \varepsilon_{eff}^{V})^{\mu}} \\ \dot{\varepsilon}_{eff}^{V} &= A_p \frac{\sigma_{eff}^{n_p}}{(\varepsilon_{eff}^{V,0} + \varepsilon_{eff}^{V})^{\mu}} - \frac{\varepsilon_{eff}^{V}}{t_0} \end{aligned} \tag{6}$$

In case of high values of hardening ε_{eff}^{V} recovery and hardening are in a dynamic equilibrium, i. e. the stationary creep phase is reached (Fig. 11b).

In a good approximation the pre-hardening $\varepsilon_{eff}^{V,0}$ can set to zero. For the hardening rate in the stationary state the expression $\dot{\varepsilon}_{eff,S}^{V} = 0$ applies which results in:

$$\begin{aligned} \dot{\varepsilon}_{eff,S}^{cr} = \dot{\varepsilon}_{eff,S}^{E} \quad &\Rightarrow \quad A_p \frac{\sigma_{eff}^{n_p}}{(\varepsilon_{eff,S}^{V})^{\mu}} = \frac{\varepsilon_{eff,S}^{V}}{t_0} \\ \left(A_p \cdot t_0 \cdot \sigma_{eff}^{n_p}\right)^{\frac{1}{1+\mu}} &= \varepsilon_{eff,S}^{V} \end{aligned} \tag{7a}$$

By substituting eq. (7a) into eq. (2) the pre-factor A_s and the stress exponent n_s for stationary creep (power law) are obtained as

$$\begin{aligned} \dot{\varepsilon}_{eff,S}^{cr} &= A_s \cdot \sigma_{eff}^{n_s} \\ A_s &= A_p \left(\frac{1}{A_p \cdot t_0}\right)^{\frac{\mu}{1+\mu}} \\ n_s &= \frac{n_p}{1+\mu} \end{aligned} \tag{7b}$$

When the temperature dependent recovery time t_0 according to eq. (5) is taken into consideration the temperature dependency for creep is calculated as follows:

$$A_s = A_p \left(\frac{1}{A_p \cdot t_0}\right)^{\frac{\mu}{1+\mu}} \cdot e^{-\frac{Q(1+\mu)}{\mu \cdot R \cdot T}} \tag{7c}$$

For the first time this creep approach has been described by Salzer (1993) and a summarizing presentation of the application of this approach has been given by Salzer et al. (1998).

3 CONSIDERATION OF DAMAGE

In triaxial compression tests the specimen is compressed under a constant deformation rate. For this purpose, load is increased permanently until fracture occurs (Fig. 6). Focusing on the relevant deformation processes, in the crystalline structure the movement of present dislocations and the generation of more and more dislocations are activated, which, due to the growing dislocation density, causes an increase of hardening and consequently of the strength too. Because of the short test periods the recovery of dislocations does not play any substantial role, especially at room temperature conditions. At the same time more and more pile-ups of dislocations develop, which counteract increasingly the deformation. Consequently, locally increased stresses will develop at loads beyond the dilatancy boundary resulting in the formation of microcracks and in progressive damage. In laboratory tests, the progressive damage can be measured as an increase in volume (dilatancy) (Fig. 7). The term dilatancy boundary corresponds to that stress level at which an increase of the specimen volume is measured first.

In this connection, the damage process counteracts the growing hardening. As a result, the material becomes more and more ductile. Under consideration that deformation part ε_{eff}^{S}, which characterizes the damage process and strain softening, resp., (in the following briefly denoted as damage) eq. (3) yields:

$$\begin{aligned} &\dot{\varepsilon}_{eff}^{V} = \dot{\varepsilon}_{eff}^{cr} - \dot{\varepsilon}_{eff}^{E} - \dot{\varepsilon}_{eff}^{S} \\ &\text{and} \\ &\dot{\varepsilon}_{eff}^{V} = \dot{\varepsilon}_{eff}^{cr} - \dot{\varepsilon}_{eff}^{S} \qquad \text{for } \dot{\varepsilon}_{eff}^{E} \to 0 \end{aligned} \tag{8}$$

Here, in the case of triaxial compressive short-term tests, the recovery can be neglected at room temperature. That means, if damage rate and creep rate are equal, then hardening and strength respectively, become constant. The generation of dislocations and the evolution of damage and microcracks resp. are in equilibrium with regard to their effects. At this state the material is on the yielding point with ideally plastical behavior. Consequently, the peak strength is obtained if the salt is no longer subject to deformation hardening, i.e. when the effective hardening rate $\dot{\varepsilon}_{eff}^{V}$ is equal to zero. A classical strength criterion (yield function) is not required anymore.

$$\dot{\varepsilon}_{eff}^{V} = \dot{\varepsilon}_{eff}^{cr} - \dot{\varepsilon}_{eff}^{S} = 0 \quad \Rightarrow \quad \sigma_{eff} = \sigma_{eff,Max} \tag{9}$$

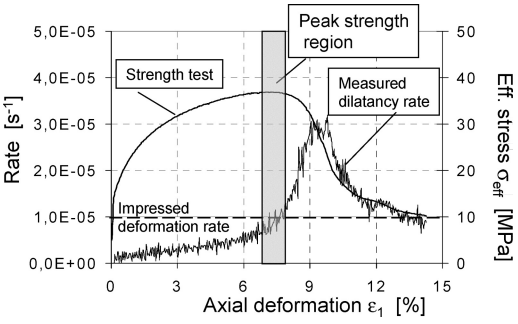

Figure 2. Triaxial test, measured deformation rate and dilatancy rate.

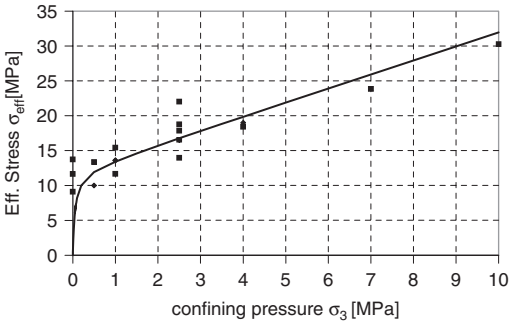

Figure 3. Dilatancy boundary for the Staßfurt rock salt from the Sondershausen mine (compression test).

When the damage rate $\dot{\varepsilon}^{S}_{eff}$ exceeds the creep rate $\dot{\varepsilon}^{cr}_{eff}$ then the effective hardening rate $\dot{\varepsilon}^{V}_{eff}$ becomes negative and the material softens. The strength is now in the post-failure region.

In Fig. 2 the trace of the dilatancy rate $\dot{\varepsilon}_{Vol}$ as measured in the triaxial test has been plotted versus the axial deformation ε_1. For comparison, the externally impressed deformation rate of the triaxial test (with $\dot{\varepsilon}_1 = 1 \cdot 10^{-5}\,s^{-1}$) has been plotted as a black line, for better orientation, and the measured trace of strength too. It can be seen, that in the pre-failure region the dilatancy rate $\dot{\varepsilon}_{Vol}$ is significantly below the deformation rate and rises in a comparatively uniform manner along with the deformation. In the region of peak strength the dilatancy rate $\dot{\varepsilon}_{Vol}$ reaches the value of the deformation rate and begins to rise in an over-proportionate manner. This acceleration is linked with the phenomenon of coalescence of microcracks to macrocracks. In the first third of the post-failure region this process is terminated by the fact that the dilatancy rate reaches its maximum value.

In principle, the effects as represented in Fig. 2 can be observed in all triaxial tests which have been investigated. In the constitutive model, this behavior is taken into consideration in that way that the effective hardening rate $\dot{\varepsilon}^{V}_{eff}$ is lowered by the dilatancy rate $\dot{\varepsilon}_{Vol}$. Therefore, the damage rate $\dot{\varepsilon}^{S}_{eff}$ in eq. (8) is replaced by the dilatancy rate $\dot{\varepsilon}_{Vol}$.

$$\dot{\varepsilon}^{V}_{eff} = \dot{\varepsilon}^{cr}_{eff} - \dot{\varepsilon}^{E}_{eff} - \dot{\varepsilon}_{Vol} \tag{10}$$

The material strength is the measurable resistance which a material opposes to plastic deformation resp. failure. In the constitutive model this causal relationship is described by the current effective hardening ε^{V}_{eff} as an internal state variable, which determines the visco-plastic behavior. Therefore, a formulation of the strength by a failure criterion is not required. It is replaced by the description of the dilatancy behavior.

4 DILATANCY AS FUNCTION OF DAMAGE WORK AND MINIMUM STRESS

In the constitutive model dilatancy is described as a function of minimum stress σ_3 and the specific deformation work above the dilatancy boundary $\dot{\varepsilon}_{Vol} = f(\sigma_3, U_{Dil})$. Here, the specific deformation work above the dilatancy boundary U_{Dil} (in the following briefly denoted as damage work) is defined as follows:

$$\begin{aligned} \Delta U_{Dil} &= (\sigma_{eff} - \sigma^{Dil}_{eff}) \cdot \Delta\varepsilon_{eff} \\ U_{Dil} &= \int (\sigma_{eff} - \sigma^{Dil}_{eff}) \cdot d\varepsilon_{eff} \end{aligned} \tag{11}$$

Many tests have shown that dilatancy boundary and residual strength can approximately be equated one to the other. This allows to describe the damage work according to eq. (11) in a simple manner and to ensure that the calculated final value of softening tends towards the value of the residual strength. In the constitutive model the dilatancy boundary is described as follows (Fig. 3):

$$\sigma^{Dil}_{eff}(\sigma_3) = \sigma_3 \cdot \left[\frac{D_1}{D_2 + \sigma_3} + D_3 \right] \tag{12}$$

wherein for the Staßfurt rock salt of the Sondershausen mine the following parameters have been determined: $D_1 = 12$ MPa, $D_2 = 0.05$ MPa, and $D_3 = 2$ MPa.

When plotting the measured dilatancy ε_{Vol} in dependency of the damage work U_{Dil} in a diagram (Fig. 4), the following functional relationship between these two quantities appears:

$$\varepsilon_{Vol}(U_{Dil}) = A_1 \cdot U_{Dil} + \frac{A_2}{A_3} \cdot \exp\left[A_3 \cdot U_{Dil}\right] \tag{13}$$

Depending on the confining pressure σ_3 different curve parameters A_1, A_2, and A_3 (Fig. 4) will be obtained which, in a good approximation, will be described as

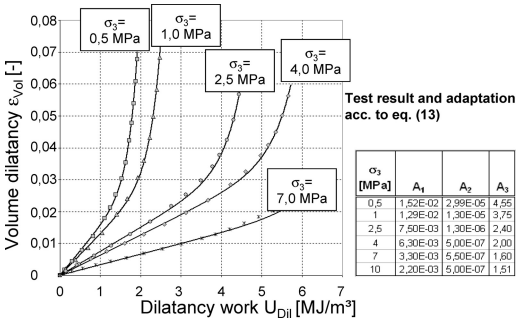

σ3 [MPa]	A1	A2	A3
0,5	1,52E-02	2,99E-05	4,55
1	1,29E-02	1,30E-05	3,75
2,5	7,50E-03	1,30E-06	2,40
4	6,30E-03	5,00E-07	2,00
7	3,30E-03	5,50E-07	1,60
10	2,20E-03	5,00E-07	1,51

Figure 4. Relationship between dilatancy ε_{Vol} and damage work U_{Dil}, adaptation to tests (A_i, $i = 1, 2, 3$ $[MPa]^{-1}$).

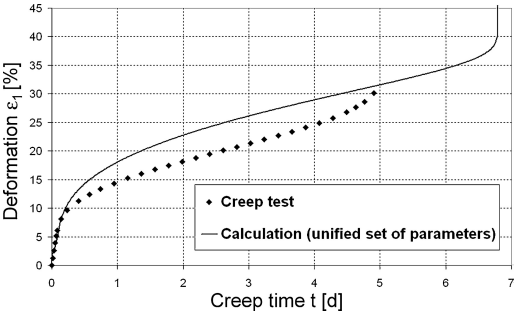

Figure 5. Creep failure of Asse "Speisesalz" and its recalculation ($\sigma_1 = 41$ MPa, $\sigma_3 = 3$ MPa).

exponential functions of σ_3 given below. In this case, for the Staßfurt rock salt from the Sondershausen mine the following parameters have been derived:

$$\begin{aligned} A_1 &= a_1 + a_2 \cdot \exp[a_3 \cdot \sigma_3] \\ A_2 &= a_4 + a_5 \cdot \exp[a_6 \cdot \sigma_3] \\ A_3 &= a_7 + a_8 \cdot \exp[a_9 \cdot \sigma_3], \quad a_i, i = 1...9\ [MPa]^{-1} \end{aligned} \tag{14}$$

with

$$\begin{aligned} a_1 &= 2.1 \cdot 10^{-3} & a_2 &= 0.016 & a_3 &= -0.39 \\ a_4 &= 5 \cdot 10^{-7} & a_5 &= 8 \cdot 10^{-5} & a_6 &= -2 \\ a_7 &= 1.5 & a_8 &= 4.15 & a_9 &= -0.6 \end{aligned}$$

After substituting eq. (14) into eq. (13) also the dependency on the minimum principal stress σ_3 is obtained:

$$\varepsilon_{Vol}(U_{Dil}, \sigma_3) = A_1 \cdot U_{Dil} + \frac{A_2}{A_3} \cdot \exp[A_3 \cdot U_{Dil}] \tag{15}$$

By differentiating eq. (15) with respect to U_{Dil} the increase of dilatancy as a function of the performed damage work is calculated as:

$$\varepsilon_{Vol} = A_1 + A_2 \cdot \exp[A_3 \cdot U_{Dil}] \cdot U_{Dil} \tag{16a}$$

In the numerical implementation the change in dilatancy in finite time steps corresponds to the increase multiplied by the change of work in the respective time step:

$$\frac{\Delta \varepsilon_{Vol}}{\Delta t} = \dot{\varepsilon}_{vol} = [A_1 + A_2 \cdot \exp[A_3 \cdot U_{Dil}]] \cdot \frac{\Delta U_{Dil}}{\Delta t} \tag{16b}$$

In creep tests at constant deviatoric stress conditions above the dilatancy boundary the described procedure results in the phenomenon that, with growing creep time, the effective hardening ε_{eff}^{V} is permanently reduced as a function of the work performed above the dilatancy boundary until the material passes into the tertiary phase of creep.

Since for the Staßfurt rock salt from the Sondershausen mine no creep test results are available which cover the accelerated creep phase, here the recalculation of a creep failure of the Asse "Speisesalz" will be presented where said recalculation has been performed using this constitutive model (Fig. 5).

5 MODIFIED STRESS EXPONENT IN THE DILATANCY REGION

From recalculation of the triaxial tests with constant deformation rate we conclude that the stress exponent n_p above the dilatancy boundary depends on both the minimum stress and the dilatancy in the following form:

$$\begin{aligned} n_p &= g(\sigma_3, \varepsilon_{Vol}) \\ n_p &= \frac{n_{\varepsilon_{Vol;0}} + n_1 \cdot \exp[n_2 \cdot \sigma_3] \cdot [1 - \exp(-n_3 \cdot \varepsilon_{Vol})]}{(1 - \varepsilon_{Vol})^{n_4}} \end{aligned} \tag{17}$$

where $n_{\varepsilon_{Vol;0}}$ denotes the stress exponent for the non-damaged material. This exponent can be derived from creep tests carried out in the stress space below the dilatancy boundary. The other material parameters must be determined by way of stepwise calibration to approximate to the test results of the triaxial compression tests. In eq. (17) the effect of the minimum stress with increasing material damage and dilatancy, resp., is taken into consideration. In this case, for the Staßfurt rock salt the following values have been determined: $n_{\varepsilon_{Vol;0}} = 11.88$, $n_1 = 0.55$, $n_2 = -0.18$, $n_3 = 2000$, and $n_4 = 0.5$. A recent recalculation of the triaxial tests (Fig. 6) provides evidence that by means of the indicated dependency of the stress exponent n_p on both the minimum stress σ_3 and the dilatancy ε_{Vol} according to eq. (17) the strength and deformation behavior of ductile salt rock can be represented in a very good

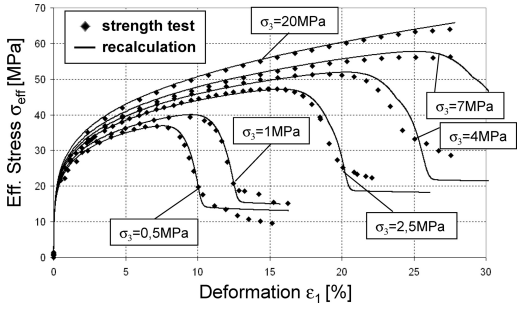

Figure 6. Comparison between calculated and measured strength behavior (constant deformation rate $\dot{\varepsilon} = 1 \cdot 10^{-5}$ 1/s).

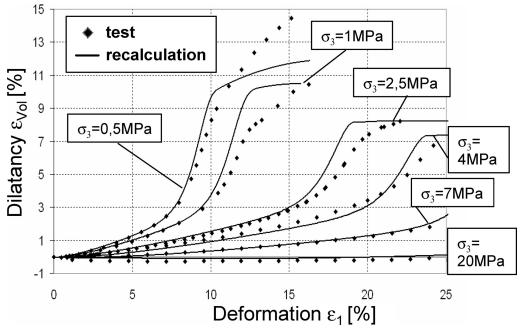

Figure 7. Comparison between calculated and measured dilatancy behavior (constant deformation rate $\dot{\varepsilon} = 1 \cdot 10^{-5}$ 1/s).

approximation. The same can be stated with respect to the description of the behavior of dilatancy (Fig. 7).

In the constitutive model the strength and dilatancy behavior is determined by the accumulated damage work U_{Dil}. Under low deformation rates the part of the total deformation without damage is growing whereas under fast deformation the part of damage is quite high. Therefore, in the constitutive model the ratio between the deformation parts which are induced by damage and those free of damage depends on the deformation rate too. Since hardening is determining the strength, the concept of the accumulated damage work U_{Dil} results in a strength and dilatancy behavior which depends on the deformation rate so that the short-time strength as determined in the fast triaxial test as well as the lower long-time strength can be calculated.

Fig. 8 demonstrates a comparison between the measured strength behavior and that which has been calculated on the basis of the constitutive model at different deformation rates. In Fig. 9 the respective dilatancy behavior is represented. The comparison shows that at different deformation rates the constitutive model allows to simulate the measured strength and dilatancy behavior quite well.

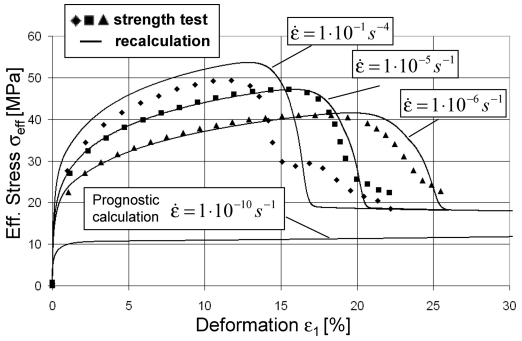

Figure 8. Comparison between calculated and measured strength behavior at different deformation rates (confining pressure $\sigma_3 = 2.5$ MPa).

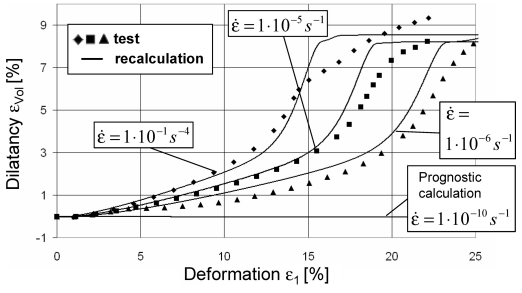

Figure 9. Comparison between calculated and measured dilatancy behavior at different deformation rates (confining pressure $\sigma_3 = 2.5$ MPa).

To illustrate an important consequence which can be drawn from the presented relationships, in addition a prognostic calculation has been carried out using a deformation rate of $\dot{\varepsilon} = 1 \cdot 10^{-10} \mathrm{s}^{-1}$ which is typical of the conditions found in situ (extra curve in Fig. 8). Due to this low deformation rate in the predicted test ($\sigma_3 = 2.5$ MPa) no stresses develop which exceed the dilatancy boundary ($\sigma_{\mathrm{eff}}^{\mathrm{Dil}}(\sigma_3 = 2.5\,\mathrm{MPa}) = 17\,\mathrm{MPa}$). Therefore, at this rate and at the given confining pressure the deformation is free of damage, i. e. remains without any dilatancy. (Fig. 9).

6 ELASTIC CONSTANTS UNDER DILATANCY AND STRESS CORRECTION

As a result of the dilatant loosening-up also the elastic behavior of the rock body alters so that with increasing damage its compressibility increases and the Poisson's ratio ν tends towards the value of 0.5. In non-damaged and non-loosened rock elements the well known relationships with respect to E and ν

apply for the compression modulus and for the shear modulus.

$$K = \frac{E}{3 \cdot (1 - 2\nu)}$$
$$G = \frac{E}{2 \cdot (1 + \nu)} \quad (18)$$

To describe the elastic parameters in dependence of the dilatancy the following relationships provide a practical phenomenological description:

$$K(\varepsilon_{Vol}) = \frac{K_0 - K_R}{(1 + \varepsilon_{Vol})^{\alpha}} + K_R$$
$$\nu(\varepsilon_{Vol}) = \frac{\nu_0 - \nu_R}{(1 + \varepsilon_{Vol})^{\alpha}} + \nu_R \quad (19)$$

where K_0 – compression modulus for non-damaged salt = 16.6 GPa, K_R – compression modulus in the region of residual strength = 0.1 GPa, ν_0 – Poisson's ratio for non-damaged salt = 0.25, ν_R – Poisson's ratio in the region of residual strength and α – parameter of curvature = 18 for the Staßfurt rock salt under investigation.

These equations (18 and 19) allow to calculate the dilatancy-depending shear modulus:

$$G(\varepsilon_{Vol}) = \frac{3}{2} K(\varepsilon_{Vol}) \cdot \frac{1 - 2 \cdot \nu(\varepsilon_{Vol})}{1 + \nu(\varepsilon_{Vol})} \quad (20)$$

In the calculation the elastic volume change results from the change of the octahedral normal stress $\Delta\sigma_0$.

$$\Delta\sigma_0 = K \cdot \Delta\varepsilon^{e}_{Vol} \quad (21)$$

Under the influence of the dilatancy the compression modulus changes according to eq. (19). In addition, the damage-induced volume increase $\Delta\varepsilon_{Vol}$ as calculated according to eq. (16b) counteracts the elastic volumetric compaction $\Delta\varepsilon^{e}_{Vol}$. Both, the dilatancy-depending compression modulus $K(\varepsilon_{Vol})$ and the damage-induced volume increase $\Delta\varepsilon_{Vol}$ in eq. (21), need to be taken into account in correcting the octahedral normal stress by alteration of the stress state. As a result of both, the accumulated (ε_{Vol}) and incremental ($\Delta\varepsilon_{Vol}$) volume increase, the correction is obtained according to the following equation:

$$\Delta\sigma_0 = K(\varepsilon_{Vol}) \cdot (\Delta\varepsilon^{e}_{Vol} - \Delta\varepsilon_{Vol}) \quad (22)$$

7 IN SITU CASE STUDIES

In the frame of a joint benchmark project, model calculations were performed on two different underground structures to check, demonstrate and compare the abilities of the constitutive models and calculation tools(Hampel et al. 2007).

In the first example, a horizontal drift in the salt mine "Sondershausen" which was excavated in 1963, was used as reference site, because the local conditions regarding stress state and convergence are documented quite well, and because results of laboratory tests on the Staßfurt rock salt samples from this drift were available (Hampel et al. 2007). These data were used to determine the values for the model parameters for this type of rock salt (compare chapters 2–6).

Recently, 35 years after excavation, the convergence rate in the drift (1 mm/a) was monitored over a period of 150 days. In addition, the results of hydraulic fracturing are available allowing an estimate of the spatial distribution of the in situ stresses, i.e. the minimal stress component. Permeability measurements indicate a small EDZ around the gallery contour in the order of 10–20 cm. It is important to note that the drift is situated in an area where nearly no further mining activity is disturbing the in-situ-stress-field. Therefore, the boundary conditions of simulation calculations were well defined. This simulation calculations were used to calibrate the recovery time $t_0 = 7000$ d. The results of the model calculations agree well with in-situ data for the stress, the convergence rate and the distribution of the EDZ.

In the second example, a more complicated artificial room-and-pillar situation was calculated. For three different cases with respect to pillar load (i.e. $\sigma_{Pill} = 18.4$ MPa – model A, 28.4 MPa – model B, and 38.4 MPa – model C) the behavior of a rather slender pillar (width/height = 20 m/20 m) was modelled by applying the parameter values for the Staßfurt rock salt from the "Sondershausen" mine.

Without showing the results in detail it has to be stated that the modelling results agree well with observations made in-situ on pillar behavior in various rock salt mines, especially concerning the order of pillar deformation rate and the shape of contour failure. It is important to note that the constitutive model was able to reproduce in detail a sudden contour collapse too (Fig. 10). Unfortunately in-situ measurement data for such pillars are not available, so at present a quantitatively comparison with the calculated behavior is not possible.

8 CONCLUSION

The presented constitutive model describes the mechanical behavior of rock salt in a good approximation comprehensively within the scope of a unified creep approach where the hardening has been implemented as an interior state variable. Hereby, hardening is determined by the processes of migration and generation of dislocations and their recovery on one hand

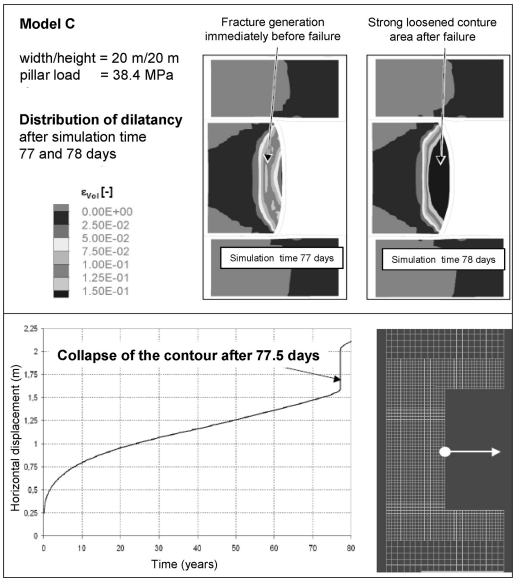

Figure 10. Simulation of a contour collapse for the pillar model with the highest load. Top: Calculated distribution of volumetric deformation (dilatancy). Bottom: Calculated development of horizontal displacement.

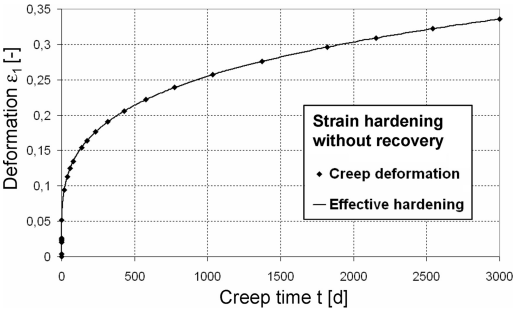

Figure 11a. Modelling of creep deformation – exemplary behavior (only strain-hardening without recovery and damage/dilatancy).

and by those of damage on the other one. These crystal-physical processes that are governing the mechanical behavior of the salt rocks form the thoretical base for the formulation of the constitutive model.

In the following, the individual contribution of the various effects which have been integrated into the constitutive model is demonstrated in synoptic figures referring exemplarily to a hypothetic creep test.

In the region of low deformation, i.e. in the region of primary creep below the dilatancy boundary, the hardening matches the effective deformation (Fig. 11a).

Over longer periods of time and for higher temperatures the recovery acts in a hardening-reducing

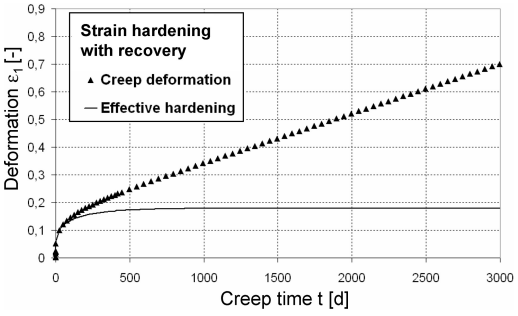

Figure 11b. Modelling of creep deformation – exemplary behavior (strain-hardening with recovery but without damage/dilatancy).

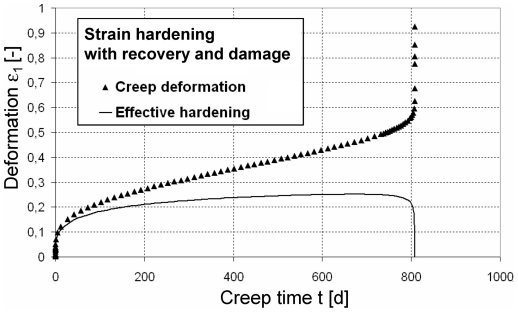

Figure 11c. Modelling of creep deformation – exemplary behavior (strain-hardening with recovery and damage/dilatancy).

manner so that finally a dynamic equilibrium between hardening and recovery establishes, i.e. the phase of stationary creep is reached (Fig. 11b).

If creep occurs in the stress space above the dilatancy boundary micro cracking evolves, whereby the progressive damage leads to a reduction of the hardening. Our studies have demonstrated that the hardening-reducing effect of damage can be equated to the dilatancy. The latter can be described as a function of both, the deformation work performed above the dilatancy boundary (damage work) and the minimum stress. Both influence parameters have to be determined by means of triaxial tests. Finally, in creep tests the reduction of the hardening along with growing damage and dilatancy, resp., results in an accelerated creep and in creep failure, resp. (Fig. 11c).

In conclusion, the new constitutive law was proven as a usefull tool for describing not only short-term but also long-term behavior of rock salt undergoing deformation.

Within the scope of the joint benchmark project the presented constitutive model and its application to real underground structures has been compared with other constitutive models. About this comparison will be reported in detail by Hou et al. (2007).

ACKNOWLEDGEMENT

The presented work was granted by the Federal Ministry of Research and Technology under the contract 02 C 1024 in the frame of a joint research project (BMBF-Verbundvorhaben “Die Modellierung des mechanischen Verhaltens von Steinsalz – Vergleich aktueller Stoffgesetze und Vorgehensweisen”).

REFERENCES

Blum, W. 2004. *Mechanische Eigenschaften*. Erlangen: Institute for Material Sciences, University of Erlangen (unpubl.).

Hampel, A. Heemann, U., Schulze, O., Zetsche, F., Pudewills, A., Günther, R., Minkley, W., Hou, Z., Wolters, R., Düsterloh, U., Rokahr, R., Zapf., D. 2007. Comparison of advanced constitutiv models for the mechanical behavior of rock salt – results from a joint research project. I. Modeling of deformation processes and benchmark calculations. *Proceedings of the 6th Conference on Mechanical Behavior of Salt, Hannover, 22–25.05. 2007*.

Hou, Z. Hampel, A., Heemann, U., Schulze, O., Zetsche, F., Pudewills, A., Günther, R., Minkley, W., Wolters, R., Düsterloh, U., Rokahr, R., Zapf., D. 2007. Comparison of advanced constitutiv models for the mechanical behavior of rock salt – results from a joint research project. II. Numerical modelling of two in situ case studies and comparison. *Proceedings of the 6th Conference on Mechanical Behavior of Salt, Hannover, 22–25.05. 2007*.

Hunsche, U., Schulze O., Walter, F., Plischke, I. 2003. *Thermomechanisches Verhalten von Salzgestein. Abschlussbericht Projekt Gorleben.* Hannover: Bundesanstalt für Geowissenschaften und Rohstoffe (unpubl.).

ITASCA. 2000. FLAC 4.0 *Fast Lagrangian Analysis of Continua Version 4.0 – User's Manual.* Minneapolis: ITASCA Consulting Group Inc.

Odqvist, F. K. G. & Hult, H. 1962. *Kriechfestigkeit metallischer Werkstoffe*. Berlin: Springer Verlag.

Salzer, K & Schreiner, W. 1991. Der Rechencode MKEN zur Ermittlung der Zeitabhängigkeit des Spannungs-Verformungszustandes um Hohlräume im Salzgebirge. *Kali und Steinsalz, Band 10, Heft 12.*

Salzer, K 1993. *Ableitung eines kombinierten Kriechgesetzes unter Berücksichtigung der Erholung. Teilbericht zum BMFT Vorhaben 02 C 00 628.* Leipzig: Institut für Gebirgsmechanik (unpubl.).

Salzer, K., Konietzky, H., Günther, R.-M. 1998. A new creep law to describe the transient and secondary creep phase. In Annamaria Cividini (ed.), *Application of Numerical Methods to Geotechnical Problems: Proceedings of the Fourth European Conference on Numerical Methods in Geotechnical Engineering (NUMGE98)*, *Udine, 14.-16.10.98: 377–387.* Wien: Springer Wien New-York.

Salzer; K., Schreiner, W., Günther, R.-M. 1999: Creep law to decribe the transient, stationary and accelerating phases. In N. D. Cistescu, H. R. Hardy, R. O. Siminonescu (ed.), *Basic and Applied Salt Mechanics: Proceedings of the 5th Conference on Mechanical Behavior of Salt, Bucharest, 9-11.08. 1999: 177–190.* Lisse: Balkema.

Taylor & Francis
Taylor & Francis Group
http://taylorandfrancis.com

The Mechanical Behavior of Salt – Understanding of THMC Processes in Salt –
Wallner, Lux, Minkley & Hardy, Jr. (eds)
© 2007 Taylor & Francis Group, London, ISBN 978-0-415-44398-2

Constitutive models to describe the mechanical behavior of salt rocks and the imbedded weakness planes

W. Minkley & J. Mühlbauer
Institut für Gebirgsmechanik GmbH, Leipzig, Germany

ABSTRACT: Up to now salt rock mass has been predominantly regarded as a continuum and the mechanical effect of the present discontinuities and bedding planes have been neglected to a great extent. However, for a complete understanding of a couple of geomechanical phenomena this approach proves to be insufficient. When solving numerous practical problems in potash and rock salt mining it clearly turned out that a treatment without taking the existing bedding planes and discontinuities into account will not provide a satisfying explanation of the observed rock mechanical processes. Therefore, for a mechanical description of the complex properties of the salt rock mass a visco-elasto-plastic constitutive model is presented, which comprises the hardening/softening behavior and dilatancy effects for salt rocks, as well as a specific friction model, which comprises displacement- and velocity-dependent shear strength softening for salt bearing bedding planes.

1 INTRODUCTION

Generally, when rock mechanical problems are studied, the salt rock mass is regarded as a continuum and a special emphasis is given to its visco-plastic behavior. However, it does not prove possible to describe comprehensively the stability behavior of mine cavities in salt rocks solely on the basis of the viscous properties and, for instance, time-dependent softening effects.

When investigating the in situ observed fracture and dilatancy processes in chamber horizons, it turned out that the observed significant floor heave movements are linked with mechanically activated weakness surfaces and bedding planes in the mining floor. Such intensive floor lift phenomena have been observed in numerous cases, e.g. before the heavy rock burst in a trona (a water-bearing sodium carbonate compound) salt mine in Wyoming, which happened in 1995 (Swanson & Boler 1995), and before the rock burst with a similar magnitude in 1996, which destroyed the eastern mining field of the Teutschenthal salt mine in the central area of Germany.

The mechanisms of floor lifts and the development of relevant failure processes in the working floor are closely connected with the softening and dilatancy properties of the solid salt rocks and with the existing bedding planes which can act as sliding faces. They are just those weakness planes at a short distance to the mined cavity which actually allow a significant softening process (Fig. 1). If fracture processes happen inside the working floor, shear displacements occur on the bedding planes within this zone. The extent of the heave movement essentially depends on the distance between the bottom of the cavity and the present bedding planes or discontinuity surfaces, respectively. It further depends on the chamber width, on the age of the working panel, and on the mechanical properties of the solid salt rock and the imbedded weakness planes.

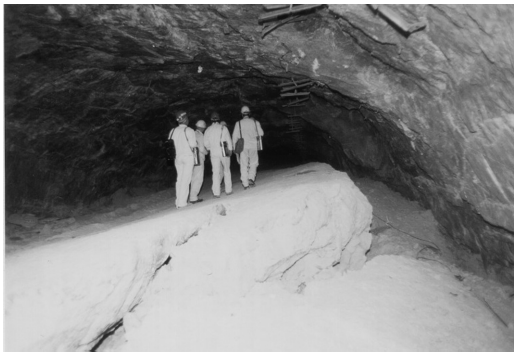

Figure 1. Extreme floor lifts caused by numerous bedding planes in the floor.

On existing discontinuities between viscous salt rock and such layers which are not able to creep like high-strength anhydrite rock beds, high shear stressses can occur as well as rupture processes of considerable magnitude. This way, when in 1975 above the former Neustassfurt potash mine a large sinkhole developed as

Figure 2. Softening phenomena within the rock and on horizontal bedding planes of a hard salt pillar.

a result of a progressive caving to the surface, slide processes have played a decisive role (Salzer et al. 2004). These slide processes occurred between the Stassfurt potash seam in steep stratification and the so-called main anhydrite which is found in the roof. By means of micro-seismic monitoring such shear movements and separation processes, respectively, between rock salt and the subjacent main anhydrite can be detected by measurements of acoustic emission (Spies et al. 2004).

In potash mining the contact properties of the bedding planes to the hanging and underlying salt bedrock affect the load bearing behavior of pillars to a considerable extent. The triaxial constraint of the pillars and, thus, their maximum bearing capacity are transmitted via the mechanical contact conditions at the transition to the surrounding rock masses. Depending on the properties of the solid salt rocks and the existent bedding planes, shear displacements on the contact zones can occur either slowly or abruptly, in connection with contour failure processes or even a pillar collapse.

For assessing the safety and the stability of mine openings in salt rocks the mechanical behavior of bedding planes is of high practical importance. However, on this behavior very little research work has been done up to now. In cases where the roof or floor is stratified, the contour stability of cavities is essentially determined by the mechanical properties of the bedding planes. This way, the observed collapse of compact pillars in potash mining can only be understood, when a loss in cohesion and of adhesive friction on the contact to the surrounding salt rock mass is taken into consideration.

Particularly, under dynamic loading conditions just those mechanical properties of the salt rock mass get decisive significance which represent its discontinuum-mechanical attributes. These properties have been induced already during the saline sedimentation or later by tectonic processes. Therefore, for a comprehensive treatment of corresponding rock mechanical problems it is required to describe the softening behavior of both, the salt rocks and the imbedded weakness planes (Fig. 2).

Therefore, in the following, first of all a visco-elasto-plastic constitutive model for salt rocks is presented which has been developed in the Institute for Rock Mechanics, Leipzig. This constitutive model implies both hardening/softening behavior and dilatancy. Subsequently, a shear model including displacement- and velocity-dependent softening for the application in salt formation with bedding planes is presented.

2 VISCO-ELASTO-PLASTIC CONSTITUTIVE MODEL FOR SALT ROCKS

A constitutive model for salt rocks must comprise the following deformation properties (Döring et al. 1964):

- reversible time-independent deformation components (elasticity);
- reversible time-dependent deformation components (persistence);
- irreversible permanent deformation components (viscosity, plasticity).

Whereas plasticity is predominantly an attribute of polycrystalline rocks, viscosity is more a characteristical feature of non-crystalline structures.

Moreover, salt rocks – like other rock materials too – exhibit softening phenomena. Softening in this context stands for the decrease of strength of the rock material, when deformation is increasing (strain softening). Under this aspect, in dependence on the rock properties and the loading conditions, different features in their behavior appear. When an abrupt softening occurs, the phenomenon is called brittle fracture, whereas if gradual softening occurs the material presents yield failure behavior. So, perfect plastic yield is interpreted as deformation without any softening.

In the physical sense, softening is caused by the generation and accumulation of microcracks and defects within the rock material which progressively develop to macrocracks. During this process, the strength drops to a certain residual level. This residual strength is mainly due to friction processes which run on the formed macroscopic fracture surfaces. Thus, this residual strength is regarded as the lower yield limit of the rock material in the post-failure state.

In the developed constitutive model the plastic behavior implying the softening of the polycrystalline salt rocks is described by a modified non-linear Mohr-Coulomb yield or failure criterion using a non-associated flow rule. The Mohr-Coulomb fracture hypothesis in which the yield point and failure limit depend on the minimal principal stress σ_3 is generally accepted for rock materials.

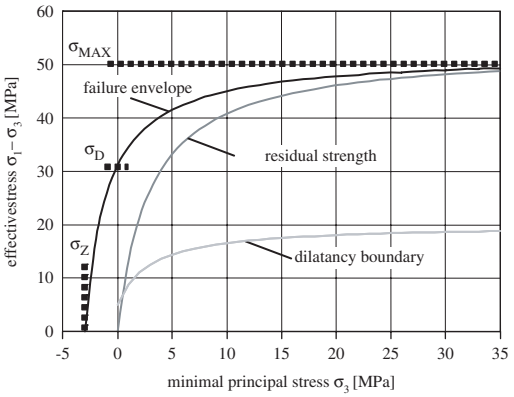

Figure 3. Yield points in the visco-elasto-plastic constitutive model.

A failure criterion which satisfies the above mentioned demands on the basis of a modification of the Mohr-Coulomb model has been developed by Minkley (1997):

$$\sigma_{1,B} = \sigma_D + N_\phi \cdot \sigma_3 \tag{1}$$

with the function for friction:

$$N_\phi = 1 + \frac{\sigma_{MAX} - \sigma_D}{\sigma_\phi + \sigma_3} \tag{2}$$

respectively,

$$\sigma_{eff,B} = \sigma_D + \frac{\sigma_{MAX} - \sigma_D}{\sigma_\phi + \sigma_3} \cdot \sigma_3 \tag{3}$$

where $\sigma_3 =$ minimum principal stress; $\sigma_{1,B} =$ maximum principal stress at failure; $\sigma_{eff,B} = \sigma_{1,B} - \sigma_3 =$ maximum effective stress at failure; $\sigma_D(\varepsilon^p) =$ uniaxial strength; $\sigma_{MAX}(\varepsilon^p) =$ maximum effective strength; $\sigma_\phi(\varepsilon^p) =$ curvature parameter for strength surface; and $\varepsilon^p =$ plastic shear deformation.

For clarification of the function of the respective parameters compare Figure 3 where the failure criterion is plotted as $\sigma_1 - \sigma_3 = f(\sigma_3)$. σ_{MAX} is the maximum effective stress the rock can carry and to which the failure criterion moves towards with increasing minimum principal stress σ_3. For salt rocks under mining conditions the non-linearity of the failure envelope can not be ignored. The non-linear failure criterion describes both compression and tension. More precisely, the tensile strength is given by:

$$\sigma_Z = \sqrt{\frac{1}{4}\left(\sigma_\phi + \sigma_{MAX}\right)^2 - \sigma_D \cdot \sigma_\phi} - \frac{1}{2} \cdot \left(\sigma_\phi + \sigma_{MAX}\right) \tag{4}$$

From the modified non-linear Mohr-Coulomb failure criterion (Eq. 3), the flow rule for plastic flow can be deduced (pressure with negative sign):

$$f_S = \sigma_1 - \sigma_3 + \sigma_D - \frac{\sigma_{MAX} - \sigma_D}{\sigma_\phi - \sigma_3} \cdot \sigma_3 \tag{5}$$

The plastic potential for non-associated flow is given by:

$$g_S = \sigma_1 - \sigma_3 - \frac{\sigma_{MAX,\psi} - \sigma_D}{\sigma_\psi - \sigma_3} \cdot \sigma_3 \tag{6}$$

where $\sigma_{MAX,\psi}(\varepsilon^p) =$ maximum effective strength at the dilatancy boundary; and $\sigma_\psi(\varepsilon^p) =$ curvature parameter of the dilatancy function.

If the failure envelope is reached, plastic deformations occur in addition to the elastic deformations. Using the flow rule, the plastic incremental deformation part can be determined:

$$\Delta\varepsilon_i^p = \lambda_S^* \cdot \frac{\partial g_S}{\partial \sigma_i} \qquad i = 1,3 \tag{7}$$

Besides the elasto-plastic characteristic, most salt rocks show viscous behavior. Therefore, the elasto-plastic softening model is already combined with the Burgers creep model. The incremental form of the Burgers model is given in the *FLAC* manuals (Itasca 1998). The determination of the multiplier λ^*_S in Equation (7) is obtained for $f_S = 0$:

$$\lambda_S^* = \frac{\sqrt{C_4^*} - C_2^*}{2 \cdot C_1^*} \tag{8}$$

$$C_1^* = -\frac{1}{\sigma_\phi}\left(\alpha_2 - \alpha_1 \cdot N_\psi\right) \cdot \left[\left(\alpha_2 - \alpha_1 \cdot N_\psi\right) - \left(\alpha_1 - \alpha_2 \cdot N_\psi\right)\right]$$

$$C_2^* = -\frac{1}{\sigma_\phi}\left(\alpha_2 - \alpha_1 \cdot N_\psi\right) \cdot \left(\sigma_1 - 2 \cdot \sigma_3 + \sigma_{MAX} + \sigma_\phi\right) + \left(\alpha_1 - \alpha_2 \cdot N_\psi\right) \cdot \left(1 - \frac{\sigma_3}{\sigma_\phi}\right)$$

$$C_3^* = \frac{\sigma_3}{\sigma_\phi} \cdot \left(\sigma_1 - \sigma_3 + \sigma_{MAX}\right) - \left(\sigma_1 - \sigma_3 + \sigma_D\right)$$

$$C_4^* = C_2^{*2} - 4 \cdot C_1^* \cdot C_3^*$$

$$\alpha_1 = K + \frac{2}{3 \cdot a} \qquad \alpha_2 = K - \frac{1}{3 \cdot a}$$

$$a = \frac{1}{2 \cdot G^M} + \frac{\Delta t}{4} \cdot \left(\frac{1}{\eta^M} + \frac{1}{A^* \cdot \eta^K}\right)$$

$$A^{*} = 1 + \frac{G^{K} \cdot \Delta t}{2 \cdot \eta^{K}}$$

$N_\psi =$ is the dilatancy function:

$$N_{\psi} = 1 + \frac{\sigma_{\psi}^{2}}{\left(\sigma_{\psi} - \sigma_{3}\right)^{2}} \cdot \tan\beta_{0} \tag{9}$$

where $\tan \beta_0$ and σ_ψ depend on the plastic deformation ε^p.

For volume increase (dilation) is valid:

$$\frac{\Delta V}{V_0} = \varepsilon_{Vol}^{p} = \left(N_{\psi} - 1\right) \cdot \varepsilon^{p} \tag{10}$$

The parameters which describe the dilatancy are: $\beta_0(\varepsilon^p) =$ ascent angle of the dilatancy curve; $\varepsilon^p_{Vol} = f(\varepsilon^p)$ at uniaxial loading ($\sigma_3 = 0$); and $\sigma_\psi(\varepsilon^p)$ = curvature parameter of the dilatancy function.

The model allows to describe the creep behavior including creep rupture. The primary creep phase is modelled by the Kelvin model with Kelvin shear modulus G^K and Kelvin viscosity η^K. The secondary creep phase is controlled by the Maxwell viscosity η^M. The tertiary creep phase is governed by a dilation softening mechanism. Under the assumption that $\eta^K \rightarrow \infty$ and $\eta^M \rightarrow \infty$ (i.e. no viscous deformation) the equations in (8) yield

$$a = \frac{1}{2 \cdot G^{M}}$$

and the material behavior coincides with the time-independent elasto-plastic model section. Within the visco-elasto-plastic material model, the stress dependency of the creep rate is governed by the exponential dependency of the Maxwell viscosity η^M on the deviatoric stress σ_V (Lux 1984):

$$\eta^{M} = \eta_{0}^{M} \cdot e^{-m \cdot \sigma_{V}} \tag{11}$$

In the constitutive model the short-time and the long-time strengths are taken into consideration by a yield limit which depends on the deformation rate.

The rock mechanical quantities which determine this limit are the compressive strength σ_D at $\sigma_3 = 0$ and the maximum effective strength σ_{MAX} at $\sigma_3 \rightarrow \infty$ (Fig. 3). Both quantities depend on the deformation rate $\dot{\varepsilon}$. On the basis of results obtained in experimental tests on different salt rocks the following relationships have been introduced for this purpose:

$$\sigma_{D}(\varepsilon) = \sigma_{D}\left(1 + a_{M} \cdot \left(f(\varepsilon) - 1\right)\right)$$

$$\sigma_{MAX}(\varepsilon) = \sigma_{MAX}\left(1 + a_{M} \cdot \left(f(\varepsilon) - 1\right)\right) \tag{12}$$

with

$$f(\dot{\varepsilon}) = \frac{1}{2}\left(1 + \tanh\left(b_{M} \cdot \log\frac{\dot{\varepsilon}}{\dot{\varepsilon}_{W}}\right)\right)$$

The parameters used here have following meaning: $a_M =$ reduction factor short-time strength $\rightarrow$ long-time strength; b_M = velocity factor; and $\dot{\varepsilon}_W =$ deformation velocity at the inflection point.

In the modified non-linear Mohr-Coulomb plasticity model both the dilatancy boundary and the failure limit are described by the yield function (Equation 3). Here, the dilatancy boundary or damage limit, resp., is regarded as the lower yield envelope in the pre-failure state, whereas the residual strength is regarded as the lower yield limit in the post-failure region. The dependence of the yield limit on both the minimum principal stress σ_3 and on the deformation velocity $\dot{\varepsilon}$ is described in a functional manner while the dependence on the plastic deformation ε^p is given in tables. This procedure allows a universal adaptation to the pronounced non-linear deformation behavior of the salt rocks.

In Figure 4 the concept of the model is illustrated. This model distinguishes between 4 different deformation components, the sum provides the total magnitude of deformation ε.

Below the dilatancy boundary the deformation is composed of the following components:

$$\varepsilon = \varepsilon^{e} + \varepsilon^{en} + \varepsilon^{v} \tag{13}$$

Above the dilatancy limit the total deformation is given by:

$$\varepsilon = \varepsilon^{e} + \varepsilon^{en} + \varepsilon^{v} + \varepsilon^{p} \tag{14}$$

Both the elastic deformation component ε^e and the component of the elastic persistence ε^{en} are reversible quantities whereas both the viscous (ε^v) and the plastic portions of deformation ε^p are irreversible quantities.

Furthermore, in the model it is assumed that volume expansion is only provided by the elastic and the plastic volumetric deformation components:

$$\varepsilon_{Vol} = \varepsilon_{Vol}^{e} + \varepsilon_{Vol}^{p} \tag{15}$$

Then, in the case of compression, volume compaction occurs below the dilatancy limit ($\varepsilon^e{}_{Vol} < 0$), whereas plastic volume dilatation due to damaging processes will occur, when the dilatancy limit is exceeded, $\varepsilon^p{}_{Vol} > 0$. At the dilatancy boundary applies:

$$\frac{d\varepsilon_{Vol}}{d\varepsilon} = 0$$

Salt rocks possess elastic as well as plastic and viscous properties which are superimposing each other. The presented concept (Fig. 4) of the visco-elasto-plastic constitutive model is based on the well accepted

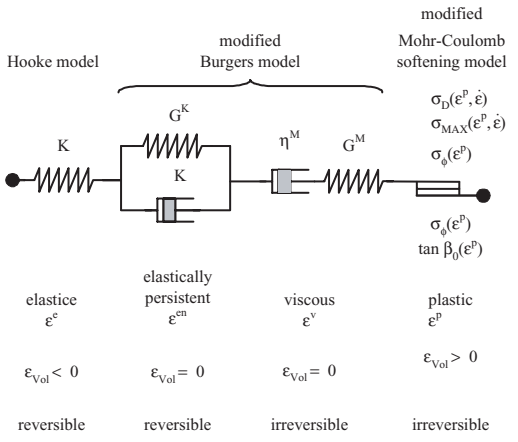

Figure 4. Visco-elasto-plastic model concept.

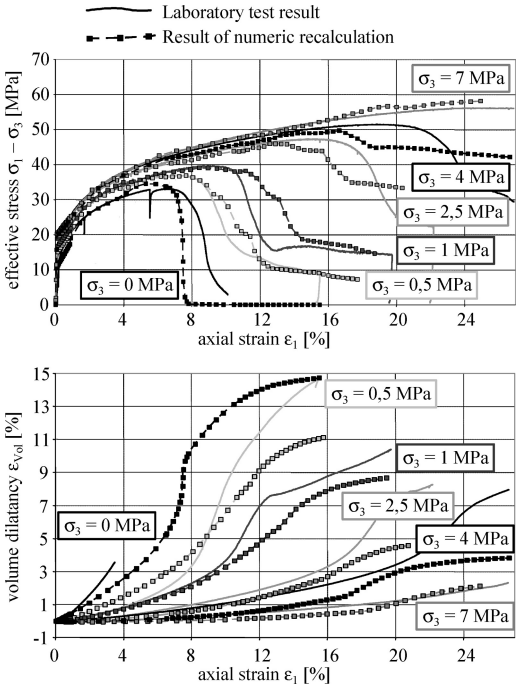

Figure 5. Recalculation of strength tests carried out on rock salt. Upper part: stress-strain curves; lower part: dilatancy curves.

standard models of mechanics. This concept is applicable in a universal manner to both, salt rocks and non-saline rock materials too. The explained constitutive model is suitable for the description of the time-dependent mechanical behavior of salt rocks presenting both ductile and brittle material behavior.

In Figure 5 a comparison is shown between the stress-strain curves, which are obtained in laboratory

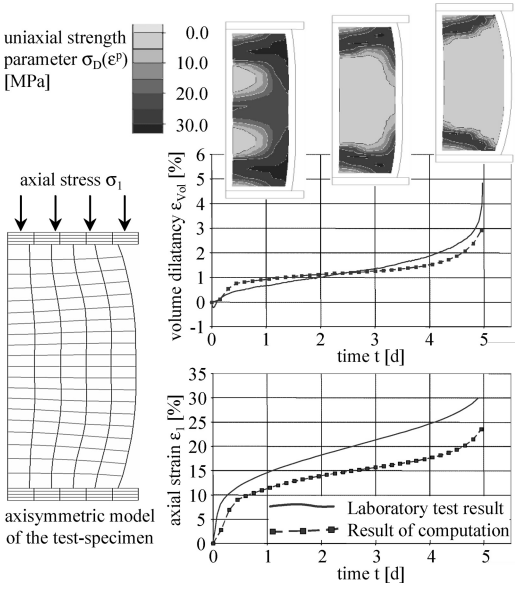

Figure 6. Recalculation of a creep test on a rock salt specimen: axial stress $\sigma_1 = 41$ MPa and confining pressure $\sigma_3 = 3$ MPa. Time-dependent development of the uniaxial strength parameter σ_D (compare equation 3) within the specimen.

tests on several rock salt specimens under uniaxial and triaxial loading conditions, and the results of the corresponding numerical recalculations. It is quite evident, that the strain-hardening behavior rises with increased confining pressure σ until the peak strength is reached, and the level of the post-failure stress drop reduces. At higher confining pressures, the dilatancy (Fig. 5, lower part) is heavily depressed. Laboratory test results and numeric recalculations are obviously in a good agreement.

As noted already, the constitutive model also describes the viscous behavior of salt rocks until creep failure. The recalculation of a creep test carried out on a rock salt specimen is shown in Figure 6.

3 SHEAR MODEL FOR BEDDING PLANES

For the understanding of the instability, which is observed in fault zones, on crack surfaces, and bedding planes in the rock mass, it is necessary to describe the softening processes occurring on present mechanical weakness planes. For this purpose, two model concepts are commonly used in geomechanics (Brady 1990):

– velocity-dependent softening (velocity weakening)
– displacement-dependent softening (displacement weakening)

The dependence of friction on the shear rate is known for a long time. As a result, instable sliding

on natural rock joints has been accepted. It has to be noted that the conception, that the dynamic friction coefficient is smaller than the static coefficient, was the starting point for the interpretation of seismic instability (Brace & Byerlee 1966).

Dietrich (1978) has introduced a velocity-depending formulation by means of friction phenomena with respect to the change in the shear resistance or an equivalent friction coefficient: Thus, he can explain the dynamic instability, which is observed in the case of earthquakes, for instance. This formulation has been refined, among others, by Rice (1983) and Ruina (1983). From their analytical solutions it follows that the friction coefficient increases instantaneously, when the sliding rate rises abruptly. But afterwards, the effective friction coefficient drops to a lower level. That means that a velocity-dependent shear softening process becomes active which provokes an unstable sliding.

Displacement-dependent softening models describe the drop of shear strength by assuming the progressive damaging of the unevenness of the joint planes at increasing shear displacement (Cundall & Hart 1984, Indraratna & Haque 2000).

In contrast to most joints in other types of rock, the properties connected with cohesion and adhesive bonds on discontinuities and bedding planes in salt rocks are of special importance – besides the friction itself (Fig. 8). In contrast to rocks like silicatic rock, already under quite normal loading conditions, as they are generally found in a mine, the salt rocks exhibit to a great extent the capability to reactivate adhesive and cohesive forces on reclosed parting planes (Minkley 1989).

A further particularity of the shear behavior on bedding planes in salt rocks, is the evident dependence on the velocity. The developed shear model (IfG 2005), which implies the displacement-dependent and the velocity-dependent strength softening, is based on the concept of Cundell & Lemos (1990). The essential features of the shear model for bedding planes in salt rocks are:

- Dependence of the adhesive friction coefficient on the displacement rate of the shear process
- The shear stress versus shear displacement curve approaches a "target" shear strength of the bedding plane
- The "target" shear strength remains constant until the softening region is reached, then it decreases with the progressing shear displacement.

In the incremental formulation, the shear model can be described as follows. For the relationship between normal loading and normal displacement we use:

$$\Delta\sigma_N = k_N \cdot \Delta u_n \tag{16}$$

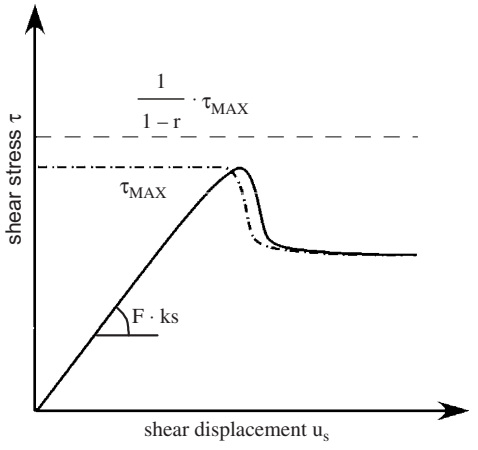

Figure 7. Shear model with strength softening.

where k_N is the normal stiffness and Δu_n is the normal displacement between the joint surfaces.

The model responds to the shear loading with an irreversible non-linear behavior. The shear stress increment is calculated as follows:

$$\Delta\tau = F \cdot k_S \cdot \Delta u_s \tag{17}$$

Here, k_S is the shear stiffness and Δu_s is the shear displacement parallel to the shear plane (Fig. 7).

The factor F which reduces the slope is a function of the distance between the current shear stress τ and the peak shear strength τ_{MAX}:

$$F = 1 - \frac{\tau}{\tau_{MAX}} \tag{18}$$

When taking into account the adhesive friction which is of essential importance for the bedding planes in salt rocks, the shear strength is found to be:

$$\tau_{MAX} = \mu \cdot \sigma_N + c \tag{19}$$

with the friction coefficient:

$$\mu = \mu_K (1 + \Delta\mu)$$

which is consists of the coefficient of the kinetic friction:

$$\mu_K = \tan\left(\phi_R + i_0 \cdot e^{-K2\frac{\sigma_N}{\sigma_K}}\right) \tag{20}$$

and the coefficient of the adhesive friction:

$$\Delta\mu = \Delta\mu_{vel} \cdot e^{-K1\frac{\sigma_N}{\sigma_K}} \tag{21}$$

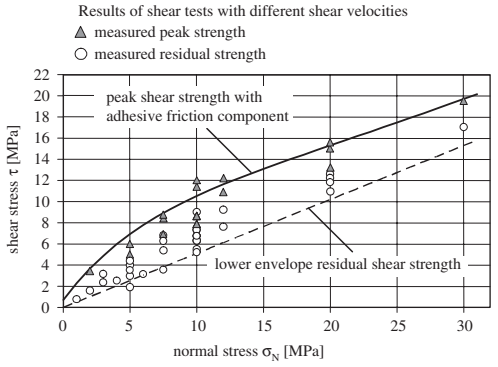

Figure 8. Laboratory test results to determine peak and residual shear strengths on the bedding plane carnallitite/ rock salt.

Here are: c = cohesion; ϕ_R = angle of residual friction; i_0 = upslide angle; σ_K = compressive strength in the contact area; and K1, K2 = curvature parameters.

The effects of the kinetic and the adhesive friction components are proportional to the normal loading σ_N on the bedding plane. The cohesion diminishes only during very quick slide processes, whereas during a quite slow shear process the cohesive forces are maintained due to the specific characteristics of the salt which are covered by the rules of the physics of interfaces.

The dependence of the friction on the velocity v of the active shear process is represented by the following function:

$$f_{vel}(v) = \frac{1}{2}\left(1 + \tanh\left(b_S \cdot \log\frac{v}{v_K}\right)\right) \qquad (22)$$

Accordingly, the velocity-dependent extent inside the adhesive friction coefficient can be expressed by:

$$\Delta\mu_{vel} = \frac{\mu - \mu_K}{\mu_K} = \Delta\mu_{MAX} \cdot f_{vel} \qquad (23)$$

In the physical interpretation, this means that in the case of a dynamical slide process at high shear velocities ($f_{vel} \approx 1$) an adhesive friction resistance must be overcome before a loss of strength appears. Under such conditions a significant drop in shear stress occurs (Fig. 9, upper diagram).

In contrast to that, in slow shear processes ($f_{vel} \approx 0$) no additional resistance of adhesive friction develops as in the case of a quick movement and, thus, cohesion is maintained. Such slide processes on the bedding planes run practically without any drop in shear stress (Fig. 9, lower diagram).

Besides the velocity-dependent shear behavior also a strength softening that depends on the passed shear

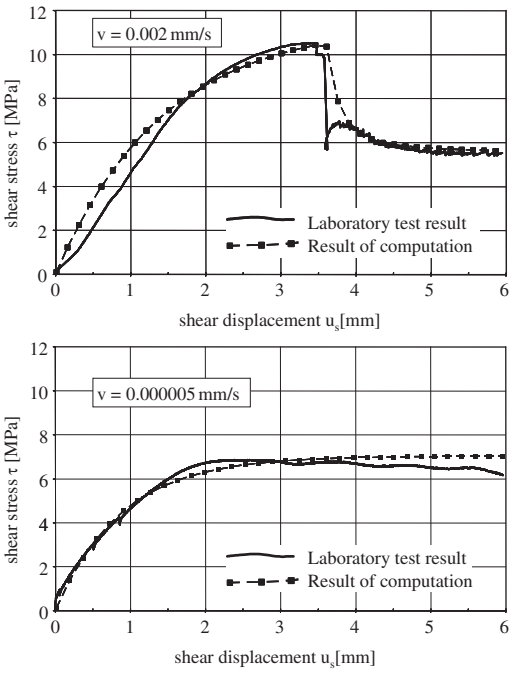

Figure 9. Recalculation of direct shear tests with different shear velocities v on the bedding plane carnallitite/rock salt; Normal loading $\sigma_N = 10$ MPa.

displacement has been taken into consideration, in the developed shear model. As soon as the peak shear strength is approached, a reduction of the adhesive friction component occurs which depends on the plastic shear displacement. When the maximum shear strength τ_{MAX} has been approached up to a certain level r which must be preset, shear softening occurs if the following relationship is valid:

$$\tau \geq (1 - r) \cdot \tau_{MAX} \qquad \text{or} \quad F \leq r \qquad (24)$$

The reduction of the adhesive friction along the shear displacement in incremental formulation follows the relationship:

$$\Delta\mu_S^p = -\Delta\mu_{vel} \cdot \frac{\Delta u_s^p}{L1} \qquad (25)$$

where the increment of plastic shear displacement is defined by:

$$\Delta u_s^p = (1 - F)\Delta u_s \qquad (26)$$

The shear parameter L1 determines the steepness of the shear stress drop in the post-failure region. With increasing shear displacement the peak shear strength will be passed, furthermore, the upslide angle i_0 is

Table 1. Shear model parameters for bedding planes carnallitite/rock salt.

Parameter	Symbol	Value	Unit
Residual friction angle	ϕ_R	29	deg
Upslide angle	i_0	5	deg
Compressive strength contact area	σ_K	10	MPa
Curvature parameter 1	K1	1.0	
Curvature parameter 2	K2	0.4	
Cohesion	c	0.7	MPa
Maximum adhesive friction coefficient	$\Delta\mu_{MAX}$	1.5	
Softening distance 1	L1	0.003	m
Softening distance 2	L2	0.08	m
Distance parameter	r	0.08	
Velocity factor	b_S	1.2	
Critical shear velocity	v_K	0.00001	mm/s
Shear stiffness	k_S	8	GPa/m
Normal stiffness	k_N	10	GPa/m

lowered to reproduce the abrasion process resulting in a reduction of the unevenness between the joint faces and, additionally, mylonitisation. The difference between the present shear strain and the shear strain to reach the residual shear strength plateau of smoothed shear planes by abrasion is described by the parameter L2. For the reduction of the upslide angle in incremental form applies:

$$\Delta i = -i_0 \cdot \frac{\Delta u_s^p}{L2} \tag{27}$$

The incremental Equations (25) and (27) correspond to an exponential reduction of the adhesive friction component and the upslide angle during proceeding shear displacements on the bedding plane in the post-failure state.

The effective dilatancy angle i is calculated as follows:

$$i = \arctan\frac{\tau}{\sigma_N} - \arctan\mu_K \tag{28}$$

The parameters as required for the shear model are summarised in Table 1. The given quantities have been determined in several direct shear tests which were carried out on bedding planes between carnallitite and rock salt (Fig. 8). For the presented recalculation of some shear tests the *3DEC*-model as shown in Figure 10 has been used.

4 IMPLEMENTATION AND APPLICATION IN PRACTICE

The visco-elasto-plastic constitutive model implying hardening/softening behavior has been programmed

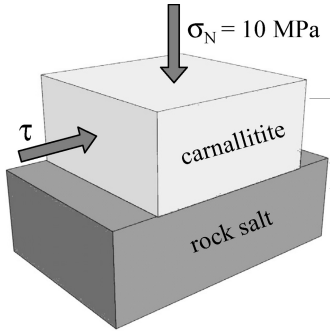

Figure 10. *3DEC*-simulation of shear tests carried out on the bedding plane between carnallitite and rock salt.

in C++ and is available as a DLL-file (Dynamic Linked Libraries) for high-performance calculation programs in the domains of continuum mechanics and discontinuum mechanics on the basis of:

- finite differences: *FLAC^{2D}, FLAC^{3D}*
- distinct elements: *UDEC, 3DEC*

These programs use an explicit time-step algorithm (Cundall & Board 1988) which is specifically suited for the modelling of non-linear processes and instability problems.

The developed shear model for bedding planes can be implemented as a user-defined joint constitutive model into the computation codes *UDEC* and *3DEC* in the domain of discontinuum mechanics.

Examples of the verification and practical application of the introduced constitutive models will be presented in another paper in this volume (Minkley et al. 2007). The usage of these constitutive models allows to describe the mechanical behaviour of the salt rock mass from the aspects of continuum mechanics as well as discontinuum mechanics.

ACKNOWLEDGEMENTS

The studies presented in this paper were funded by the German Federal Ministry of Research and Education under contracts 02C0264, 02C0639/3 and 02C0892.

We also appreciate the thorough review made by Otto Schulze (BGR) which helped to prepare the final version of the paper.

REFERENCES

Brace, W.F. & Byerlee, J.D. 1966. Stick-slip as a mechanism for earthquakes. *Science* 153: 990–992.

Brady, B.H.G. 1990. Keynote lecture: Rock stress, structure and mine design. In C. Fairhurst (ed.), *Proc. 2nd Int. Symp. on Rockbursts and Seismicity in Mines, Minneapolis, 8–10 June 1990*: 311–321. Rotterdam: Balkema.

Cundall, P.A. & Hart, R.D. 1984. *Analysis of block test no. 1 inelastic rock mass behavior: phase 2 – a characterization of joint behavior (final report)*. Itasca Consulting Group Report, Rockwell Hanford Operations, Subcontract SA-957.

Cundall, P.A. & Board, M. 1988. A Microcomputer Program for Modelling Large-Strain-Plasticity Problems. In G. Swoboda (ed.), *Proc. 6th Int. Conference on* Numerical Methods in Geomechanics, *Innsbruck, 14–17 April 1988*: 2101–2108. Rotterdam: Balkema.

Cundall, P.A. & Lemos, J.V. 1990. Numerical simulation of fault instabilities with a continuously-yield joint model. In C. Fairhurst (ed.), *Proc. 2nd Int. Symp. on Rockbursts and Seismicity in Mines, Minneapolis, 8–10 June 1990*: 147–152. Rotterdam: Balkema.

Dietrich, J.H. 1978. Time-dependent friction and the mechanics of stick-slip. *Pure and Applied Geophysics* Vol. 116: 790–806.

Döring, T., Heinrich, F., Pforr, H. 1964. Zur Frage des Verformungs- und Festigkeitsverhaltens statistisch isotroper und homogener Gesteine mit inelastischen Verformungseigenschaften. In G. Bilkenroth & K.H. Höfer (eds), *Proc. 6th Int. Meeting of the Int. Bureau of Rock Mechanics, Leipzig, 3–7 November 1964*: 68–80. Berlin: Akademie.

IfG 2005. *Prognose der dynamischen Langzeitstabilität von Grubengebäuden im Salinar unter Berücksichtigung von Diskontinuitäts- und Schichtflächen*. Final report for Forschungszentrum Karlsruhe, FKZ 02C0892. Leipzig: Institut für Gebirgsmechanik.

Indraratna, B. & Haque, A. 2000. *Shear Behaviour of Rock Joints.* Rotterdam: Balkema.

Itasca 2005. *FLAC – Fast Lagrangian Analysis of Continua, Vers. 5.0*. Minneapolis: Itasca Consulting Group Inc.

Lux, K.H. 1984. *Gebirgsmechanischer Entwurf und Felderfahrungen im Salzkavernenbau.* Stuttgart: Enke.

Minkley, W. 1989. Festigkeitsverhalten von Sedimentgesteinen im post-failure-Bereich und Gebirgsschlagerscheinungen. In V. Maury & D. Fourmaintraux (eds), *Proc. Int. Symp. Rock at Great Depth, Pau, 28–31 August 1989, Vol. 1*: 59–65. Rotterdam: Balkema.

Minkley, W. 1997. Sprödbruchverhalten von Carnallitit und seine Auswirkungen auf die Langzeitsicherheit von Untertagedeponien. *Scientific reports 5*: 249–275. Karlsruhe: Forschungszentrum Karlsruhe.

Minkley, W., Mühlbauer, J., Storch, G. 2007. Dynamic processes in salt rocks – a general approach for softening processes within the rock matrix and along bedding planes. *In Proc. 6th Conference on the Mechanical Behaviour of Salt, Hannover, 22–25 May 2007*, in press. Rotterdam: Balkema.

Rice, J.R. 1983. Constitutive relations for fault slip and earthquake instabilities. *Pure and Applied Geophysics* Vol. 121: 443–475.

Ruina, A. 1983. Slip instability and state variable friction laws. *J. Geophys. Res.* 88: 10359–10370.

Salzer, K., Minkley, W., Popp, T. 2004. Safety assessment for the land surface in the vicinity of the potash shaft Neustassfurt VI. In H. Konietzky (ed.), *Proc. 1st Int. UDEC/3DEC Symposium, Bochum, 09/29-10/01 2004*: 113–119. Rotterdam: Balkema.

Spies, T., Hesser, J., Eisenblätter, J., Eilers, G. 2004. Monitoring of the rock mass in the final repository Morsleben: experiences with acoustic emission measurements and conclusions. In S. Jakusz (ed.), *Proc. Int. Conf. on Radioactive Waste Disposal, Berlin*, *26–28 April,* publ. on CD-ROM: 303–311. Hamburg: Kontec.

Swanson, P.L. & Boler, F.M. 1995. *The magnitude 5.3 seismic event and collapse of the Solvay Trona Mine: Analysis of pillar/floor failure stability.* U.S. Bureau of Mines, Open File Rept.: 86–95.

Taylor & Francis
Taylor & Francis Group
http://taylorandfrancis.com

The Mechanical Behavior of Salt – Understanding of THMC Processes in Salt –
Wallner, Lux, Minkley & Hardy, Jr. (eds)
© 2007 Taylor & Francis Group, London, ISBN 978-0-415-44398-2

Fundamentals and first application of a new healing model for rock salt

K.-H. Lux
Professorship for Waste Disposal and Geomechanics, Clausthal University of Technology, Clausthal-Zellerfeld, Germany

S. Eberth
DBE TECHNOLOGY GmbH, Peine, Germany

ABSTRACT: A new phenomenological model for the description of healing of damage and dilatancy in rock salt has been implemented in the *Hou/Lux* constitutive model *(Hou, Lux, 1998)*. It was tested in laboratory tests and applied to an in-situ project in rock salt. Based on the laboratory results, three phases to describe decrease of damage and dilatancy could be identified. A change in the applied load, i.e. a decrease of deviatoric stress and simultaneous increase of isotropic stress, creates a stress state that provides good healing conditions, so that in the first phase of the healing process (micro-)cracks are degenerated and closed to a large extend. This first phase is called the fissure closing phase. In the following second phase, which is called fissure sealing phase, cracks are closed as well, but not as fast as in the fissure closing phase as it is time-dependent contrary to the load-dependent fissure closing phase. When both, the fissure closing phase and the fissure sealing phase are concluded, the third and actual healing phase begins. It is assumed that in this phase, the mineral structure of nearly closed cracks in the rock texture and thus its mechanical properties are restored by rearranging grain boundaries, forming sub-grain structures and new grains via mass transport effects. The new healing model was validated by means of numerical simulations of a lab test, one in-situ situation, and of one hypothetical situation.

1 INTRODUCTION

In the final disposal of radioactive waste in deep geologic formations rock salt as a host and barrier rock plays the most important role for establishing long-term safety.

For reliable and meaningful numerical analysis to prove the barrier integrity the dilatancy boundary as well as the healing boundary of rock salt must be identified. Both, the dilatancy boundary and the healing boundary, in combination with the damage and healing process must be integrated into the constitutive models. Without this step, the description of dilatancy when the dilatancy boundary is exceeded or the description of compaction and healing when the healing boundary is not met, is not possible.

The primary permeability of undisturbed rock salt is low. However, due to changes in the state of stress caused by the excavation of drifts dilatant deformation occurs, which causes a change in the mechanical and hydraulic properties. The increased permeability of the excavation damage zone (EDZ) surrounding cavities and of damaged barriers can be improved by reducing the secondary permeability. Convergence of the host rock leads to a contact pressure onto seals and dams which are built in cavities. Thus, the deviatoric stresses decrease and the isotropic stresses increase, leading to a reduction in damage and moreover to a decrease in the induced secondary permeability. In analyses which focus on long-term safety, integration of damage reduction, crack closing, sealing and healing is essential.

In this paper, the aspects of damage reduction through the three phases fissure closing, fissure sealing and fissure healing which were identified in lab test are described and analysed by means of numerical examples.

2 BASICS OF THE HEALING PROCESS

In the context of this paper, the word *healing* will be used for both, the overall process of damage decrease as well as for the third phase, the true healing phase. In lab tests with pre-damaged core samples the reduction of dilatancy (given by the volumetric strain) was measured online. The damage reduction was calculated and plotted based on the velocity measurements of ultrasonic waves (p-waves). For the numerical treatment of the measured reduction of damage and dilatancy

in lab tests a boundary function is necessary to prove whether the requirements for healing are met. The flux function F^h (for healing) describes this requirement, *Hou (2002):*

$$F^h = \frac{2}{3}\sigma_3 + \frac{2}{3\,a_5}\ln\left(\frac{a_6 - \sigma_v}{a_6}\right) \tag{1}$$

with
σ_3 : min. principal stress, MPa
a_5: parameter, 1/MPa
a_6: parameter, MPa
σ_v effective stress, MPa

In the development of damage and healing in a structural area three different states can be identified:

1 $F^h < 0$: The rock/rock mass is damaged, but healing is not possible.
2 $F^h > 0, D > 0$: In a damaged area of rock/ rock mass the damage decreases.
3 $F^h < 0$, $F^d < 0$: In the observed structural area neither damage increase nor healing occur.

Note: compressive stresses are positive and tensile stresses are negative. D describes the actual damage and F^d represents the flux function of the damage increase. Healing only occurs, if the flux function F^h has positive values.

2.1 *Identification and description of the phases of healing and deduction of the basic terms*

2.1.1 *Laboratory tests*

Figure 1 shows the different phases identified in the lab tests to determine healing behaviour. For the physical modelling the dilatancy-graph is divided into three phases which can be characterized as follows:

1 Fissure closing phase: Compared to the other two phases of the healing process the (mostly) secondary pore spaces (integral = dilatancy) close fast due to the increase of the minimum principal stress. The speed of fissure closing is directly related to the increase of the minimum principal stress. This phase is abbreviated *fc* for *fissure closing*.
2 Fissure sealing phase: Under unchanging stress, remaining open pores close more slowly than in the previous phase. This phase is called *fissure sealing (fs)*.
3 Healing phase: The third phase is considered to be the actual healing phase because changes in the mineral structure and recristallisation occur. The reduction rate of damage and dilatancy decrease is relatively low. This phase is called *fissure healing (fh)*.

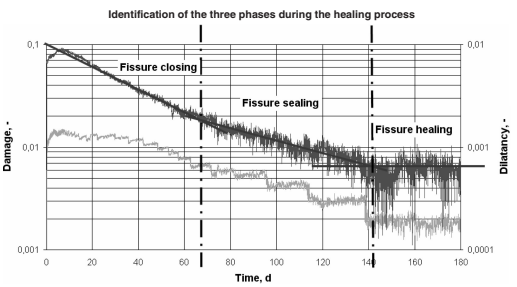

Figure 1. Damage (light grey measured curve) and dilatancy (dark grey measured curve) reduction in semi-logarithmic diagram and identification of the three phases of the healing process. On the left the scale for the damage is shown, on the right the scale for the dilatancy.

The physical model has to take into account these three phases and has to describe the decrease of damage and dilatancy depending on the relevant parameters.

2.1.2 *Deduction of the basic terms of dilatancy and damage reduction*

To describe the rate of dilatancy and damage reduction the following model which takes into account the three mentioned phases *fissure closing (fc), fissure sealing (fs)* and *fissure healing (fh)* is proposed:

$$\dot{\varepsilon}^h_{Vol} = \dot{\varepsilon}^{fc}_{Vol} + \dot{\varepsilon}^{fs}_{Vol} + \dot{\varepsilon}^{fh}_{Vol} = \left(\dot{\varepsilon}^{fc}_x + \dot{\varepsilon}^{fc}_y + \dot{\varepsilon}^{fc}_z\right) + \left(\dot{\varepsilon}^{fs}_x + \dot{\varepsilon}^{fs}_y + \dot{\varepsilon}^{fs}_z\right) + \left(\dot{\varepsilon}^{fh}_x + \dot{\varepsilon}^{fh}_y + \dot{\varepsilon}^{fh}_z\right)$$
$$\Rightarrow \dot{\varepsilon}^h_{vol} = -\varepsilon^+_{vol} \cdot \left(\frac{1}{fc1} \cdot \dot{F}^h + \frac{I_1}{fs1} + \frac{1}{fh}\right) \cdot \left(1 - \frac{gh}{3}\right) \tag{2}$$

with
ε^+_{vol} dilatancy at the beginning of fissure closing, –
fc1 parameter for fissure closing, MPa
fs1 parameter for fissure sealing, MPa · d
fh time of fissure healing, d
gh ratio of axial to radial strains during the healing process,
$\dot{F}^h$ control variable for the intensity of fissure closing
I_1 first stress invariant, MPa

The three phases can be described independently with one single equation using different parameters. The transition from fissure closing to fissure sealing occurs at $\dot{F}^h = 0$, i.e. when the state of stress remains constant. The transition from fissure sealing to healing starts when the remaining dilatancy ε_{vol} drops below $\varepsilon_{vol,healing}$, a value determined in lab tests. $\dot{F}^h$ is considered to be a "control function" for the fissure closing phase:

$$\dot{F}^h = \frac{\Delta F^h}{\Delta t} \tag{3}$$

with
$\dot{F}^h$ numerical value of the control function of the healing process
Δt time increment
Thus, $\dot{F}^h$ decelerates or accelerates the closing process in the fissure closing phase.

Figure 1 shows that in phases 1 and 2 the progress of the damage reduction curve is different than the

Table 1. Description of the parameters of the phs-model.

Parameter	Description and unit
phs-model	Physical healing in salt, constitutive model to quantify the healing process in rock salt
fc1: fissure closing 1	The parameter fc1 quantifies the rate of fissure closing in the first phase. Parameter fc1 can be interpreted as a sort of compression-modulus: the smaller fc1, the faster the fissures close under identical stress states. A possible name could be fissure-closing-modulus. The unit is: MPa
fc2: fissure closing 2	The correction parameter fc2 describes the rate of damage reduction in the fissure closing phase which is lower than the dilatancy reduction. The unit is: –
fs1: fissure sealing 1	The parameter fs1 quantifies the rate of fissure sealing in the second phase. The fissures close by time-dependent stress rearrangements by viscous deformations in the fissure zones. It is assumed that when the fissure closing phase is concluded the fissure flanks align more or less accurately. So, in the fissure sealing phase pores and open gaps at the end of fissures close through viscoplastic deformations under the stress state represented by I_1. Unit: MPa · d
fs2: fissure sealing 2	The correction parameter fs2 describes the rate of damage reduction in the fissure sealing phase which is lower than the dilatancy reduction. The unit is: –
fh: fissure healing	The parameter fh quantifies the rate of healing due to recristallisation and rearrangements of grains in the mineral structure in the third phase. Unit: d
gh: geometrical healing	This parameter describes the axial to radial strains ratio in the healing process. Unit: –

progress of the dilatancy reduction curve. Hence, it is necessary to introduce two additional parameters. In the healing phase, the damage reduction curve and the dilatancy reduction curve run almost in parallel so that the introduction of an additional parameter for this phase is not necessary.

To describe the damage reduction in the three phases the following model is proposed:

$$\dot{D} = -D \cdot \left(\frac{\dot{F}^{h}}{fc1 \cdot fc2} + \frac{I_1}{fs1 \cdot fs2} + \frac{1}{fh} \right) \qquad (4)$$

Parameter fc2 describes the reduction of the damage decrease in the fissure closing phase. Analogous to this, fs2 describes the reduction of damage in the fissure sealing phase.

2.1.3 *Summarised description of the healing model*
The healing model is described with the equations for the reduction of dilatancy (2) and damage (4). It is called phs-model. The abbreviation ***phs*** stands for ***p****hysical* ***h****ealing in* ***s****alt*.

3 FIRST APPLICATION OF THE PHS-MODEL BY NUMERICAL SIMULATION OF A LAB TEST

As a first application of the derived material parameters the numerical simulation of lab test number 307 was planned. See fig. 3 for the measured curves of the lab test, fig. 4 for the comparison of the calculated to the measured curves and section 3.1. for the lab test conditions. If the material parameters are correct and the phs-model adequate, the numerical simulation and the measurement results of the lab test depicted as curves of damage and dilatancy reduction in figure 3 should correlate. For the numerical simulation, the FEM-code *MISES3* is used.

3.1 *Lab test conditions and parameters*

For the determination of relevant material parameters lab tests were performed with rock salt core samples from the Asse mine *(Düsterloh 2003, 2004, 2005)* with a height to width ratio of l/d = 300/150 mm. Steel plates were mounted at both ends of the core samples and both, salt and steel were covered with a rubber liner. In the test apparatus, the axial stress was applied to the bottom steel plate while the top steel plate was rigidly mounted. Radial stress was applied to the sample via the rubber liner by means of oil pressure. In order to reduce open pores and cracks in the sample that were due to mining and handling in the lab, the core sample was pre-compacted by means of an isotropic stress which was kept constant for a certain time. Afterwards, the volume of the specimen was measured. Accompanying the lab test, axial compression ε_1^-, dilatancy ε_{vol}^+ and the velocities of ultrasonic waves v_p and v_s were measured. From the velocities of the ultrasonic waves the damage *D* can be calculated.

For the numerical simulation of the lab test a rotationally symmetric model of the core specimen with steel plates was generated using 680 isoparametric 8-nodal-elements. The constraints and directions of the loads are shown in figure 2. Table 2 shows the material parameters used, a_0 to a_{17} being parameters for the *Hou/Lux* constitutive model and the columns to the left side containing parameters for the viscoplastic deformation model (creep parameters). For the analysis of the results over time, three representative elements (301, 305 and 310) were selected, see fig. 2. Due to their location in the middle of the core sample their results are not influenced by the constraints of the steel plates.

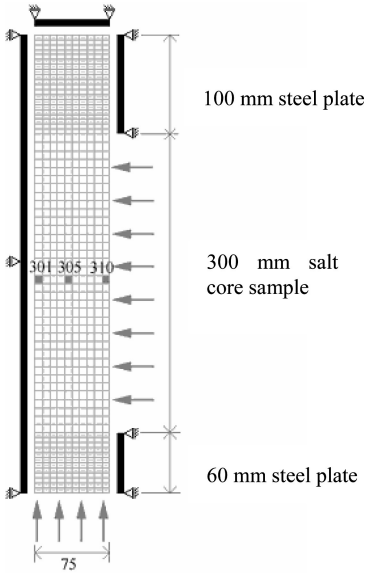

Figure 2. Rotationally symmetric semi-model of the core sample with steel plates (from top to bottom: 100 mm steel plate, 300 mm salt core sample, 60 mm steel plate), constraints and middle axis. The three representative elements 301, 305 and 310 for the examination of the calculated values are marked.

Table 2. Material parameters for the viscoplastic deformation, the *Hou/Lux* constitutive model (for damage and dilatancy) and for the phs-model.

Material parameters from Düsterloh (2005)					
Viscoplastic deformation			Damage and healing		
$\bar{G}_k^*$	MPa · d	$3{,}0 \cdot 10^4$	a_0	–	0,35
$\bar{\eta}_k^*$	MPa · d	$1{,}5 \cdot 10^5$	a_1	–	6,0
$\bar{\eta}_m^*$	MPa · d	$1{,}5 \cdot 10^7$	a_2	–	4,0
k_1	1/MPa	−0,191	a_3	1/d	$1{,}0 \cdot 10^{-07}$
k_2	1/MPa	−0,168	a_4	–	0,9
m	1/MPa	−0,247	a_5	1/MPa	0,15
l	1/K	0	a_6	MPa	53,0
T	K	295	a_7	MPa	27,6
			a_8	1/MPa	0,30
$\bar{G}_{kE}^*$	MPa · d	$3{,}05 \cdot 10^4$	a_9	–	1,0
k_{1E}	1/MPa	−0,191	a_{10}	1/MPa	0,25
l_{1E}	1/K	–	fc1	MPa	13,0
			fc2	–	4,0
			fs1	MPa · d	4221,0
			fs2	–	1,5
			fh	d	3200
			gh	–	1,04
			a_{15}	1/d	$1{,}67 \cdot 10^{-7}$
			a_{16}	–	6,0
			a_{17}	–	5,5

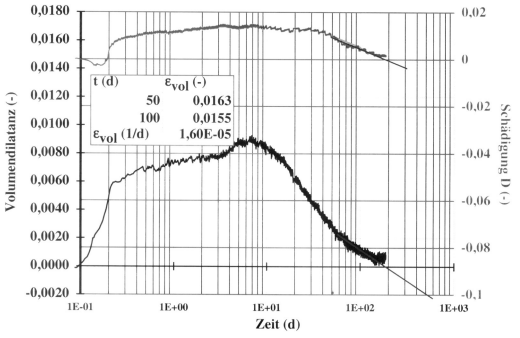

Figure 3. Measured curves of dilatancy (dark grey measured curve, bottom) and damage reduction (grey measured curve, on top) of a 180 day lab test over time; time scale is logarithmic. The left scale is for the dilatancy, the right scale is for the damage.

Corresponding to the four different load cases, the lab test can be divided into four different phases:

1 Load application phase: The axial/radial stress of $\sigma_1/\sigma_{2,3} = 30/29.5$ MPa at the beginning of the test is decreased with a rate of $\dot{\sigma}_{2,3} = 1$ MPa/10 min to an axial/ radial stress of $\sigma_1/\sigma_{2,3} = 30/4$ MPa ($\rightarrow$ $\sigma_v = 0.5$ MPa up to $\uparrow$ $\sigma_v = 26$ MPa).
2 Damage phase: The axial/radial stress of $\sigma_1/\sigma_{2,3} = 30/4$ MPa remains constant over a period of $\Delta t = 9360$ min (equivalent to $\Delta t = 6.5$ d, $\rightarrow$ $\sigma_v = 26$ MPa).
3 Load reduction phase: The radial load is increased with a rate of $\dot{\sigma}_{2,3} = 0.5$ MPa/d until after $\Delta t = 73440$ min ($\Delta t = 51$ d) the axial/ radial load reaches $\sigma_1/\sigma_{2,3} = 30/29.5$ MPa ($\rightarrow$ $\sigma_v = 26$ MPa down to $\downarrow$ $\sigma_v = 0.5$ MPa). The fissure closing phase starts when the axial/ radial load reaches $\sigma_1/\sigma_{2,3} = 30/6$–7 MPa, i.e. after t = 8 d.
4 Healing phase: The axial/ radial stress of $\sigma_1/\sigma_{2,3} = 30/29.5$ MPa remains constant until the end of the test at t = 196 d ($\rightarrow$ $\sigma_v = 0.5$ MPa).

The most important results, i.e. the curves of dilatancy and damage reduction over time, are presented in figure 3 with a logarithmic time scale.

The axial strain was measured during the lab test as well. The measurement results can be compared to the calculated axial distortion. Thus, the axial strain is an additional control parameter for the results of the numerical calculation.

3.2 *Results of the numerical simulation*

Figure 4 compares the measurement results of dilatancy (both grey curves) and damage reduction (black and light grey curves) to the calculated results over time.

To facilitate comparison both results are combined in one diagram. In the lab test, damage and dilatancy

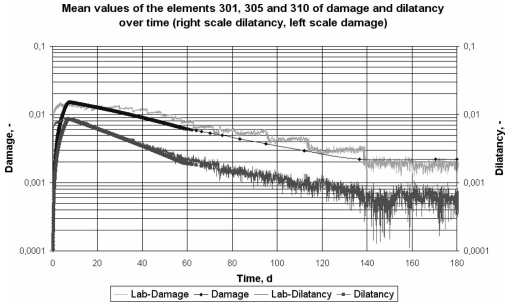

Figure 4. Calculated damage and dilatancy reduction compared to the measurement values of the lab test, plotted semi-logarithmically. The mean value of the elements 301, 305 and 310 is presented. The black and light grey curves show the calculated against the measured damage values with the scale on the left; both grey curves show the calculated against the measured dilatancy values with the scale on the right.

Table 3. Comparison of the results of the numerical simulation and the results of the lab test.

	301	305	310	Mean value 301,305,310	Lab test
Damage, max., %	1.45	1.5	1.55	1.5	1.5
Damage,t = 60d, %	0.6	0.61	0.64	0.62	0.7
Damage,t = end of test, %	0.2	0.2	0.2	0.2	0.2
Dilatancy, max., %	0.8	0.85	0.9	0.85	0.9
Dilatancy, t = 60d, %	0.18	0.18	0.19	0.185	0.2
Dilatancy, t = end of test, %	0.08	0.08	0.08	0.08	0.08

were measured integrally. For this reason, the diagram shows the mean values of dilatancy and damage calculated from the three elements 301, 305 and 310 (figure 2). In figure 4, both, the shape of the curve and the numeric values, show a good fit of the mean calculated values and the measurement values of the lab test.

The measurement data of the lab test were used to calculate the axial compression. The logarithmically corrected axial distortion after damage was about $\varepsilon = 8.9\%$. The sample had a height of $l = 300$ mm so the measured axial distortion of $\varepsilon = 8.9\%$ means a shortening by 2.67 mm. The calculated deformation from the numerical analysis was 2.56 mm which agrees well with the value derived from the test measurement. Both, the measured values as well as the calculated results are not shown in figures.

In table 3, the results of the lab test and the numerical simulation for the dilatancy and damage reduction of the three representative elements 301, 305 and 310 are compared.

Another application of the new healing model is the numeric simulation of in-situ underground cavities.

4 APPLICATION OF THE HEALING MODEL TO UNDERGROUND STRUCTURES

Due to good documentation in the literature, a drift reinforced by a cast iron bulkhead in the Asse mine and a dam constructed in the Sondershausen salt mine were used for a further application of the healing model. For both numerical calculations the FEM-code *MISES3* is used.

The aim of the cross-analysis of the reinforced drift in the Asse mine was the comparison of measured and calculated permeabilities. Due to the stress conditions in the reinforced drift, at least fissure closing or sealing should have occurred, leading to a reduction of damage and dilatancy. In combination with a modified porosity-permeability-model (poro-perm-model) according to *Hou (2002)*, the phs-model should have been suitable to simulate the measured permeability.

The aim of the numerical simulation of the dam in the Sondershausen mine was to predict the evolution of the permeability in the EDZ in the contact zone of the dam, in the contact zone above the crushed rock salt seal and in the crushed rock salt itself. This example was to demonstrate the functionality of the phs-model in combination with two poro-perm-models (according to *Hou (2002)* and *GRS (2001))* and the compaction term *(Korthaus, 1998; Hein 1991)* for complex numerical simulations.

4.1 *Application of the healing model to simulate the drift reinforced by cast iron bulkhead in the Asse mine – cross-analysis*

4.1.1 *Subsurface situation and measurement values*

The drift considered in the Asse mine (depth z = 700 m) was excavated in 1911; in 1914 it was reinforced over a length of 25 m with a cast iron bulkhead for testing purposes. The space between the cast iron bulkhead and the drift wall was filled with concrete.

Due to the rigid bulkhead and concrete backfilling it was assumed that after several decades, damage and dilatancy in the former drift contour would be healed. To prove this assumption, *GRS (2001)* performed permeability measurements in boreholes of 7 m depth during the ALOHA2 project. One borehole was drilled into the floor of the open drift. In the reinforced section, three boreholes were drilled: the first horizontally into the side wall, the second into the side wall at an angle of 45° and the third vertically into the floor. Figure 5 shows the results of the permeability measurements.

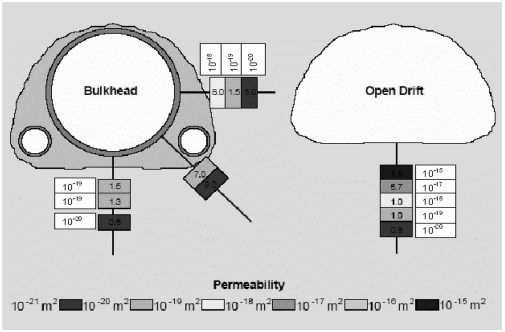

Figure 5. Asse drift with boreholes and measured permeability. Left: Reinforced drift, right: open drift. Numbers in white boxes show the exponent of the permeability.

Table 4. Parameters for the elastic constitutive model for concrete, rock salt and cast iron

	Concrete	Rock salt	Cast iron
Young's Modulus, MPa	10000	25000	100000
Poisson ratio ν, -	0.18	0.27	0.3

Table 5. Parameters for the *Hou/Lux* constitutive model and the phs-healing model.

Parameters for Asse Rock Salt					
$\bar{G}^*_k$	MPa · d	$5.08 \cdot 10^4$	a_0	–	0.08
$\bar{n}^*_k$	MPa · d	$8.94 \cdot 10^4$	a_1	–	6.0
$\bar{n}^*_m$	MPa · d	$4.06 \cdot 10^7$	a_2	–	4.0
k_1	1/MPa	−0.191	a_3	1/d	$2.0 \cdot 10^{-10}$
k_2	1/MPa	−0.168	a_4	–	0.855
m	1/MPa	−0.247	a_5	1/MPa	0.04
l	1/K	0	a_6	MPa	53.0
T	K	295	a_7	MPa	27.6
			a_8	1/MPa	0.25
$\bar{G}^*_{kE}$	MPa · d	$5.08 \cdot 10^4$	a_9	–	1.0
k_{1E}	1/MPa	−0.191	a_{10}	1/MPa	0.25
l_{1E}	1/K	–	fc1	MPa	13.0
			fc2	–	4.0
			fs1	MPa · d	12263
			fs2	–	1.5
			fh	D	100000
			gh	–	1.04
			a_{15}	1/d	$1.12 \cdot 10^{-9}$
			a_{16}	–	5.0
			a_{17}	–	5.5

4.1.2 *Geomechanical parameters and FEM-model*

For the cross-analysis the following assumptions were made:

– The primary stress is isotropic and is p = 15 MPa corresponding to the depth of z = 700 m.

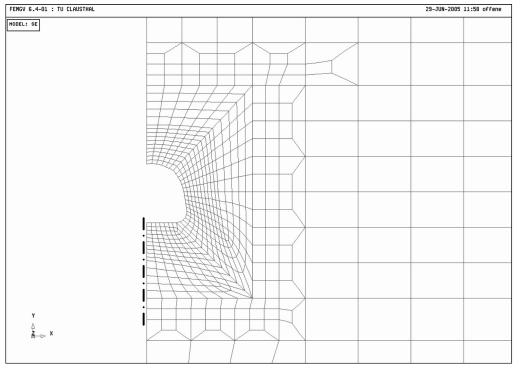

Figure 6. FEM-model of the open drift, the dashed line indicating the vertical borehole.

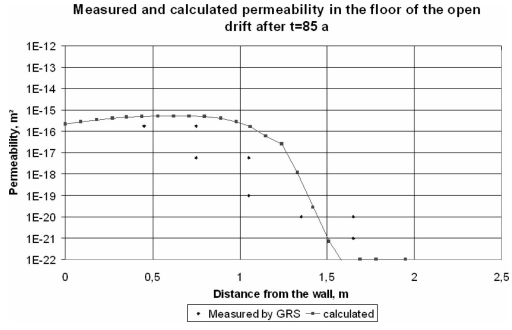

Figure 7. Permeability in the floor over the distance and comparison of the calculated values (line with dots) with the measured values (dots) at t = 85 a.

– For the *Hou/Lux* constitutive model the parameters shown in table 5 were used.

The numerical simulations were performed taking into account the mentioned geomechanical conditions. Assuming symmetry, each of the two FEM-models was generated as a semi-model. The symmetry plane as well as the right boundary are vertically fixed. The lower boundary is vertically fixed while the upper boundary is free in all directions.

The FEM-model for the open drift was generated using 1278 isoparametric 8-nodal-elements and is shown in figure 6. The height of the open drift is about 3 m and the width is about 4 m.

Figure 8 shows the FEM-model of the reinforced drift for the numerical simulation as well as the intersection line for the boreholes of the permeability measurements. The FEM-model of the reinforced drift contains additional elements for the cast iron bulkhead and the concrete backfill. The inner diameter of the bulkhead is about 2.3 m. It was generated using 1464 isoparametric 8-nodal-elements.

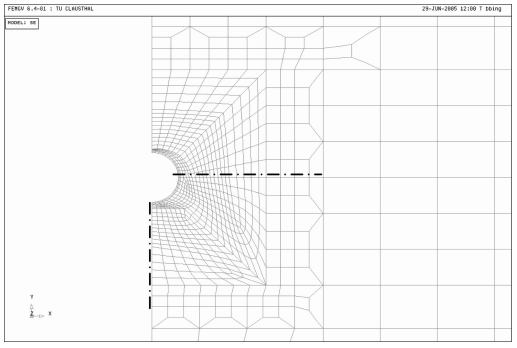

Figure 8. FEM-model with intersection lines for the horizontal and vertical boreholes.

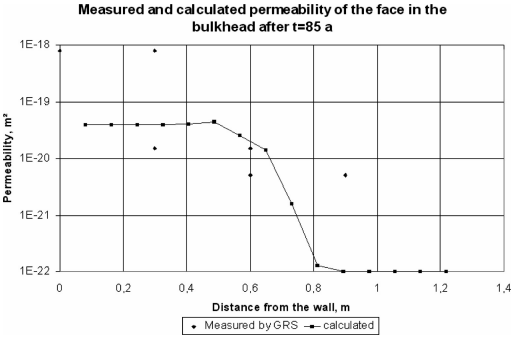

Figure 9. Permeability after t = 85 a ($\Delta t = 82$ a reinforced drift) over the distance from the face. Comparison between measured permeability (dots) and calculated permeability (line with dots) in the face.

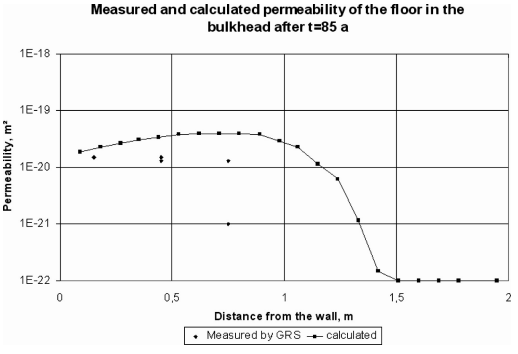

Figure 10. Permeability after t = 85 a ($\Delta t = 82$ a reinforced drift) Comparison between measured permeability (dots) and calculated permeability (line with dots) in the floor.

4.1.3 *Results of the simulation of the open drift*

Figure 7 shows the results of the comparison between the measurements performed by the *GRS (2001)* and the numerical simulation. The obvious decrease of measured permeability, starting at a distance of about 1 m from the drift contour, indicates the transition from the disturbed zone to the intact rock mass. The intensity of permeability reduction from the contour to the rock mass is slightly overestimated in the calculations while the depth of the disturbed zone corresponds well with the measured values.

4.1.4 *Results of the simulation of the reinforced drift*

The most important result of the numerical simulation is the comparison between the measured and the calculated permeability. It was assumed that the drift had remained open for three years after excavation before the cast iron bulkhead was installed. During this period, structural changes occurred so that an area of increased secondary permeability was created. It was further assumed that the damage as well as the increased permeability could be reduced, at least to a certain degree, by the convergence of the rock mass on the bulkhead. The convergence itself causes an increase of contact pressure and thus, the reduction of the deviatoric stresses.

Figures 9 and 10 each show a comparison of the measured and the calculated permeability in the horizontal intersection of the wall, respectively in the vertical intersection of the floor of the drift. The width of the zone of increased permeability is calculated satisfactorily, the values are calculated fairly well.

4.1.5 *Summary and conclusion*

Assuming that the measured decrease in permeability in the disturbed zone around the drift is caused by a reduction of dilatancy and of damage, the calculated results can be considered to confirm the applicability of the implemented phs-model.

4.2 *Application of the phs-model to simulate a dam in the Sondershausen salt mine*

The phs-model was used to simulate a dam with an assumed sealing of crushed rock salt in the drift on the right side of the dam. The actual drift is not sealed, thus there are no measurements for the porosity or permeability in the seal available to compare the calculated results.

4.2.1 *Subsurface situation and measurement values*

The structure and the dimensions of the dam in the Sondershausen salt mine is shown in figure 11 *(Sitz, 1999)*.

A rotationally symmetric FEM-model according to the Sondershausen dam was created. It was modelled with a bentonite sealing plug and salt briquette brickwork.

For the calculation with a drift sealing of crushed salt, the drift on the right side of the dam was sealed as shown in figure 12. It was assumed that sealing was performed after the drift had remained open for

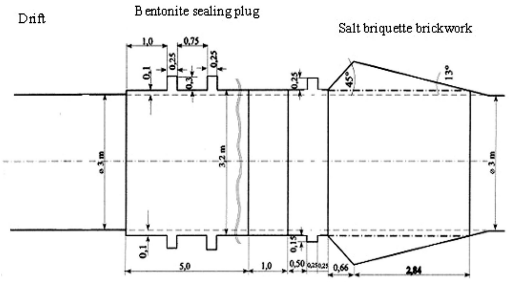

Figure 11. Structure of the dam in the Sondershausen mine.

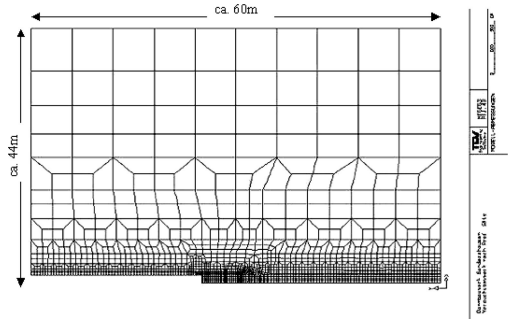

Figure 12. FEM-model based on the dam in the Sondershausen salt mine.

30 years and that the drift had not been pre-treated in the area of the sealing with crushed rock salt. Thus, the situation is comparable to a sealed drift which is additionally sealed against brine inflow by a dam. By sealing the drift it is possible to simulate both, the reduction of damage and dilatancy in the excavation damaged zone as well as the compaction of the crushed rock salt and the resulting reduction of permeability. For both processes, the healing in the EDZ and the compaction of the crushed rock salt, suitable constitutive models to describe the evolution of the permeability are available. For the description of permeability reduction in the seal, a further poro-perm-relation was used *(GRS, 1999)*. For the compaction of the crushed salt a suitable relation was used *(Korthaus, 1998; Hein, 1991)*.

4.2.2 *Geomechanical parameters and FEM-modelling*

For the numerical simulation, the following assumptions were made:

- Isotropic primary stress $p = 16$ MPa
- Density of salt briquettes $\rho = 2000$ kg/m^3
- Density of bentonite bricks $\rho = 1600$–1700 kg/m^3
- The poro-perm-relation of the *GRS (1999)* was used, with $K = 6.237 \cdot 10^{-10} \cdot n^{4.497}$ for $n > 0.3\%$

Table 6. Parameters for the material of the dam, values in brackets are estimates; *(IfG, 1999)*.

	Data	E, GPa	ν, -	φ,°	*c, MPa*
Salt briquettes	Lab test	20	0.15	46	8.6
Salt briquette-brickwork	Lab test	4	0.03	20	0
Bentonite bricks	Lab test	5	(0.22)	20–23	2–3
Bentonite brickwork	(esti-mated)	(10)	(0.03)	(10)	(0)

Table 7. Material parameters for rock salt.

Rock salt					
$\bar{G}^*_k$	MPa · d	$1.5 \cdot 10^4$	a_0	–	0.08
$\bar{\eta}^*_k$	MPa · d	$1.19 \cdot 10^5$	a_1	–	6.0
$\bar{\eta}^*_m$	MPa · d	$2.0 \cdot 10^8$	a_2	–	4.0
k_1	1/MPa	-0.121	a_3	1/d	$2.0 \cdot 10^{-10}$
k_2	1/MPa	-0.148	a_4	–	0.65
M	1/MPa	-0.200	a_5	1/MPa	0.08
L	1/K	0	a_6	MPa	58.0
T	K	295	a_7	MPa	30.0
			a_8	1/MPa	0.30
$\bar{G}^*_{kE}$	MPa · d	$1.5 \cdot 10^4$	a_9	–	1.0
k_{1E}	1/MPa	-0.121	a_{10}	1/MPa	0.25
l_{1E}	1/K	–	fc1	MPa	13
			fs1	MPa · d	12263
			fc2	–	4
			fs2	–	1.5
			fh	D	100000
			gh	–	1,04
			a_{15}	1/d	$1.67 \cdot 10^{-9}$
			a_{16}	–	5.0
			a_{17}	–	5.5

- For the compaction term *Korthaus/Hein (1998),* the relevant parameters were taken from literature: Activation energy $Q = 154.21$ kJ/mol; $A = 1.9 \cdot 10^{-6}$ 1/sMPa^5; initial porosity in the seal (crushed rock salt) $n_0 = 0.31$; universal gas constant $R = 8.3143 \cdot 10^{-03}$ kJ/(K · mol); $a = 0.01648$, $b = 0.9$; $c = 0.1$; $d = 0.0003$
- Permeability of the salt briquettes $K = 1 \cdot 10^{-16}$ m^2
- Permeability of bentonite bricks $K = 2 \cdot 10^{-18}$ m^2 *(Sitz, 1999)*

For the numerical simulation, the original time scale was used as follows:

- Excavation and time of usage until $t = 30$ a.
- Treatment of the drift contour in the dam area and instantaneous backfilling at $t = 30$ a.
- Duration of the dam installation according to *Sitz (1999)* $t = 303$ d; i.e. the dam is finished in the drift at $t = 30$ a + 303 d.

The Table 6 shows the relevant material parameters for the numerical simulation.

Table 8. Comparison of permeability to porosity evolution.

Time after dam installation, a	*Permeability EDZ/ dam, m^2*	*Permeability EDZ/seal, m^2*	*permeability in the EDZ/ seal plug, m^2*	*Porosity in the seal, -*
5	10^{-19}	10^{-17}	10^{-12}	0.307
25	10^{-19}	10^{-17}	10^{-12}	0.27
100	10^{-19}	10^{-17}	10^{-12}	0.24
250	10^{-19}	10^{-18}	10^{-13}	0.21
500	10^{-20}	10^{-19}	$10^{-14.}$	0.15
1000	10^{-20}	10^{-20}	10^{-16}	0.06

Table 7 shows the material parameters for the rock salt. The parameters for viscoplastic deformation and the parameters for the strength were derived from lab tests. The parameters for the evolution of damage and dilatancy as well as for healing were taken from lab tests made with core samples of a different location because tests with Sondershausen rock salt do not yet exist.

The FEM-model is rotationally symmetric, the drift axis being the symmetry axis so that the primary stress is constant throughout the whole model. It was generated using 2003 isoparametric 8-nodal-elements, 420 of which model the seal. Figure 12 shows the complete model with its dimensions. The right and the left model boundaries are horizontally fixed and the lower boundary under the dam and the seal is vertically fixed.

4.2.3 *Results of the numerical simulation*

The evolution of porosity and permeability of the seal and the evolution of permeability of the EDZ are the most important results; they are compared in table 8. The evolution of the permeability is extremely important because it shows the degree of healing in the EDZ. The permeability evolution in the EDZ is directly coupled via a poro-perm model to the reduction of dilatancy which, beside damage reduction, is an important characteristic of the phs-model. Furthermore, the permeability is a criterion to assess the capability of the seal to act as a barrier against brine inflow. The permeability evolution of the seal is coupled by the compaction-term *(Korthaus, 1998; Hein, 1991)* to the poro-perm term by *GRS (2001)*.

4.2.4 *Summary and conclusion*

The numerical simulation of the dam in the Sondershausen salt mine has shown that the phs-model in combination with the *Korthaus/Hein* compaction term for crushed rock salt and the poro-perm model coupled with the EDZ and the poro-perm model for the seal *(GRS, 2001)* is a powerful tool for the simultaneous calculation of the permeability evolution in the EDZ as well as in the seal. Considering that the effectiveness of a geotechnical barrier like a dam may be limited in time, the permeability evolution in the EDZ and in the seal is a measure for the functionality requirements on the barrier. The barrier is redundant when the EDZ and backfill are compacted to such a degree that they can act as permanent barriers against brine inflow. The healing of the EDZ and thus the reduction of secondary permeability can be described by the numerical simulation.

5 SUMMARY AND CONCLUSIONS

For proving the long-term safety of a final repository for radioactive waste, an understanding of the behaviour and evolution of geological and geotechnical barriers is of utmost importance. In particular, an understanding of damage and healing processes in the mineral structure is crucial. In recent years, a phenomenological constitutive model has been developed which integrally includes fissure closing, fissure sealing and healing.

In a lab test, these three phases mentioned above could be identified. Each phase is characterized by different parameters which are implemented in the healing model for numerical simulation. After a long-term lab test, a first set of parameters was developed. This set of parameters was used for a numerical simulation of this test and showed good agreement with the measured parameters. A first validation of the healing model by means of the numerical simulation of two well documented in-situ mine constructions was performed. First, the reinforced drift in the Asse mine was cross-analysed, then, a model of the dam in the Sondershausen mine was examined. Based on several control measurements and a good agreement of the calculated with the measured values it can be said that the newly implemented phs-model proved its suitability for such analyses.

REFERENCES

Düsterloh, U. 2003, 2004, 2005. *Durchführung und Auswertung von Laborversuchen zur Verheilung im Salzgestein und Parameterbestimmung.* TU Clausthal, Professur für Deponietechnik und Geomechanik, unveröffentlicht.

GRS 1999. *Ableitung einer Permeabilitäts-Porositätsbeziehung für Salzgrus*. Gesellschaft für Reaktorsicherheit, Braunschweig, GRS-Heft 148.

GRS 2001. *Untersuchungen zur hydraulisch wirksamen Auflockerungszone um Endlagerbereiche im Salinar in Abhängigkeit vom Hohlraumabstand und Spannungszustand (ALOHA2).* Abschlussbericht des Forschungsvorhabens 02 E 9118.

Hein, H.-J. 1991. *Ein Stoffgesetz zur Beschreibung des thermomechanischen Verhaltens von Salzgranulat*. Dissertation an der RWTH Aachen.

Hou, Z. 2002. *Geomechanische Planungskonzepte für untertägige Tragwerke mit besonderer Berücksichtigung*

von Gefügeschädigung, Verheilung und hydromechanischer Kopplung. Habilitationsschrift an der Professur für Deponietechnik und Geomechanik der TU Clausthal.

Hou, Z. & Lux, K.-H. 1998. Ein neues Stoffmodell für duktile Salzgesteine mit Einbeziehung von Gefügeschädigung und tertiärem Kriechen auf der Grundlage der Continuum-Damage-Mechanik. *Geotechnik 21 (1998) Nr. 3*.

IfG Leipzig. 1999. Wissenschaftliche Berichte *FZKA-PTE Nr. 6, Untertägige Entsorgung, 4. Statusgespräch, 1999*, Clausthal-Zellerfeld.

IfG Leipzig.1999. *Bestimmung gesteinsmechanischer Parameter am Steinsalz der Blindstrecke im Bereich der Maschinenstrecke EU1 in der Grube Sondershausen*. Institut für Gebirgsmechanik, Leipzig.

Korthaus, E. 1998. *Experiments on Crushed Salt Consolidation with True Triaxial Testing Device as a Contribution to an EC-Benchmark Exercise* (FZKA 6181), Forschungszentrum Karlsruhe.

Sitz, P. 1999. *Untertägige Entsorgung, 4. Statusgespräch zu FuE Vorhaben, 1999,* Clausthal-Zellerfeld.

The Mechanical Behavior of Salt – Understanding of THMC Processes in Salt –
Wallner, Lux, Minkley & Hardy, Jr. (eds)
© 2007 Taylor & Francis Group, London, ISBN 978-0-415-44398-2

Crack-initiation and propagation in rock salt under hydromechanical interaction

U. Heemann
Federal Institute for Geosciences and Natural Resources (BGR), Hannover, Germany

W. Sarfeld & C. Hillmann
Scientific Research and Development (SRD), Berlin, Germany

B. Faust
Ingenieurbüro Faust & Fritsche (IFF), Berlin, Germany

ABSTRACT: For the finite-element modelling of macroscopic cracks in geomechanics a "smeared crack"-element has been developed. When tensile strength has been exceeded, it opens in direction of maximum tensile stress till tension is reduced to zero. Opening of the elements is strictly modelled sequentially – element by element – in order to simulate consistent growth of a macroscopic crack. The cracked elements are able to close again taking account of friction and sliding. In case of rock salt this fracture property has to work also under the action of creep and dilatancy. Last, but not least, opening and closure can be modelled under the further influence of fluid pressure.

1 INTRODUCTION

In geomechanics, macroscopic cracks may happen to appear where no one has expected them or where neither the exact location, orientation, dimension nor the time of creation is known. Thus, in order to model such cracks, there is need for finite elements which detect by themselves when a critical state of stress is reached. They must be able not only to calculate the orientation of the crack but also to simulate its growth over several elements to reach macroscopic dimensions. For rock salt Norton creep as well as dilatancy (Cristescu, Hunsche 1998) are very important material properties which have to be modelled as well. In case of long-term safety assessment, the interaction of the crack and the hydraulic pressure of a fluid have also to be taken into account.

In literature there are already some attempts to model this phenomenon by different techniques, e.g. – beyond element debonding, embedded elements, meshfree methods, and others – the technique of smeared cracks (Jirásek, Zimmermann 1998). Those other models are developed usually for the simulation of reinforced concrete with decreasing stiffness as a function of crack opening (de Borst 1997). Here for the macrocrack the stiffness vertical to the crack is assumed to be zero while reduction of stiffness (in rock salt) principally is attributed to dilatancy due to microcracking. Furthermore the element is capable of creep and hydro-mechanic coupling. The development of this model has been done independently. The crack model discussed here has been implemented into the JIFE (Java Interactive Finite Element code) code.

2 TECHNIQUE OF "SMEARED CRACK"

2.1 *Method of cracking*

In every finite element and in every time increment the current mean values of stress are determined at the centre of the element. If the tensile strength is exceeded, the element is signed as a possible candidate for cracking. But only that element, that exceeds tensile strength first, really changes to status "cracked". The direction of the local maximum tensile stress is noticed and works as the normal of the crack.

In the coordinate system of the crack plane (local system) those strain equations defining vertical node movement as well as shear movement of the crack are taken out of the equation system. The justification or even mathematical necessity for that is given by the fact that the crack strains can not be calculated as functions of the current state of stress, temperature, or the increment of time. Crack opening is totally determined by the surrounding system, not by internal

quantity. That is different to all other strains (elastic, creep, thermal, …). Due to that, those components of the total strain

$$\varepsilon_{ij}^{tot} = \varepsilon_{ij}^{elast} + \varepsilon_{ij}^{creep} + \varepsilon_{ij}^{therm} + \cdots + \varepsilon_{ij}^{crack} \tag{1}$$

that are influenced by the crack can not be calculated and the displacements neither. That information has to be found later by means of material law iteration. Taking out these equations, the description of the finite element matrix gets the same form as in case of plane stress. So node displacement vertical to the crack plane (crack opening) as well as displacement "in plane" (crack shear) will lead to no response and is free. Thus, in principle, arbitrarily large crack opening or shear can happen within one increment without any numerical problem for the element.

After having changed the status of the element and thus its matrix, the calculation of the total system is redone. In the following material law iteration, the stresses on the crack plane are assumed to be zero. So the remaining stress components and resulting elastic and inelastic strains can be calculated iteratively. The crack strains result as the difference of total and all other calculated strains.

$$\varepsilon_{ij}^{crack} = \varepsilon_{ij}^{tot} - \left(\varepsilon_{ij}^{elast} + \varepsilon_{ij}^{creep} + \varepsilon_{ij}^{therm} + \cdots\right) \tag{2}$$

After having got a consistent stress-strain-system so far, it is checked whether another element will change its status and which one will be the next. So this procedure of changing the element matrix and recalculation is repeated so long till no element with overcritical tensile stresses is left and the calculation of that time increment is closed.

There can be as much as three orthogonal cracks within one element.

2.2 *Closing of cracks and shear*

Though crack strain does not affect the stress of the element directly – it's still zero on all crack planes usually – it is important for the detection of closure. If the corresponding component on the trace of the local crack strain tensor gets negative at the end of the increment, the crack must have closed in between (new status "closed"). Thus the element has to be treated similar to an uncracked one again. But, making use of the difference between crack strain at start and end of the time increment, the point of time for closure can be calculated and the amount of crack shear strain having reached so far. The shear strain is treated like a given plastic deformation while the opening part of crack strain is set to zero. Recalculating the model, it has to be checked whether the maximum shear stress resulting from Coulomb's law of friction is exceeded on the still existing crack plane. If so, the element status is changed to status "sliding".

Similar to the situation in case of crack strain, the amount of slide shear is unknown and taken out of the local system of equations while maximum shear stress following Coulomb's law is assumed to be valid. This shear mode of deformation is thus controlled only by the total system. But, after having solved the total equation system again, in material law iteration the friction shear as well as all stresses can be determined. Total system calculation and material law iteration are repeated till no relevant changes evolve.

Of course, sliding elements can change back their status to simple "closed" and closed elements can reopen again (status "open") in case of any tensile stress vertical to the crack plane.

2.3 *Hydro-mechanical coupling*

As far as the mechanical system is regarded, the action of a hydraulic pressure can be included simply by setting the stress component vertically to the crack plane to the (negative) value of the pressure instead of zero. On the other hand, the flow process needs permeability and porosity. The porosity results as the trace of the crack strain tensor. Permeability k can be calculated from the crack opening h and element volume V using

$$h_i = {}_{elem}V\ \varepsilon_{ii}^{crack} \tag{3}$$

thus getting a "smeared out" permeability

$$k^{crack} = c^{geom}\ \frac{{}_{elem}V^{2/3}}{12}\left(\varepsilon_{ii}^{crack}\right)^3. \tag{4}$$

c^{geom} is just a geometric constant near 1 accounting for the influence of roughness or complex fracture planes.

The monolithic matrix for the hydro-mechanical coupling already existed in JIFE and had to be modified only by some iterative algorithms.

2.4 *Basic performances*

As a demonstration of the principles of the smeared crack, in a first example three simple cubes of edge length 1 are elongated in three different directions, parallel to one main axis (1 1 1), in an "arbitrary" direction (1 1 2) and along the body diagonal (1 1 1) (s. Fig. 1). All three cracks generated are perpendicular to the direction of tension irrespective of the orientation of the element.

In the next example a single element (s. Fig. 2, step 0) with an elastic modulus of $E = 10^4$ MPa, a Poisson ratio $\nu = 0.25$, tensile strength $f_t = 1.0$ MPa and a coefficient of friction $\mu = 0.3$ has been elongated in vertical direction by means of a displacement pattern such that it would have been twice as long as it had

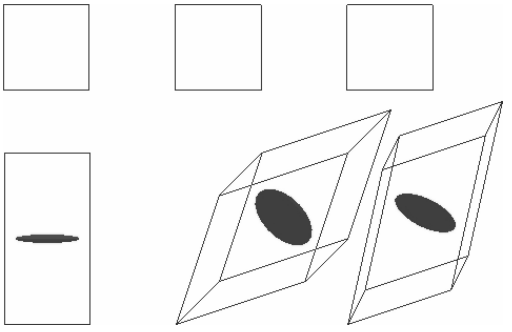

Figure 1. Three cubes (upper row, here the XY-faces are shown) have been torn along one main axis (0 0 1), in an "arbitrary" direction (1 1 2) and along the body diagonal (1 1 1). The cracks, here represented by ellipsoids, are always perpendicular to the direction of tension.

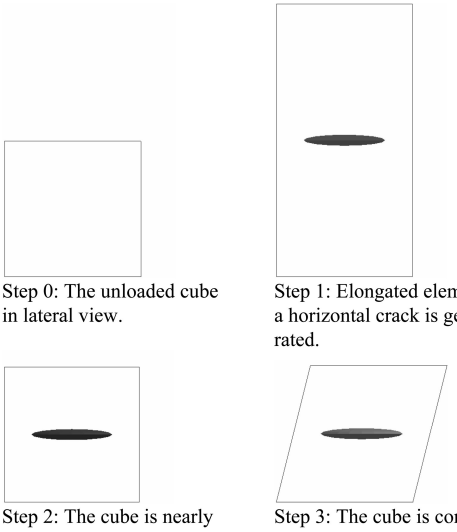

Step 0: The unloaded cube in lateral view.

Step 1: Elongated element, a horizontal crack is generated.

Step 2: The cube is nearly closed except for a narrow opening of 0.001.

Step 3: The cube is compressed and sheared at the same time. The crack shows strong friction gliding.

Figure 2. Crack generation and closure with frictional sliding.

been before. In a first step this elongation is calculated, but the algorithms notice that tensile strength has been exceeded. Thus, its status has changed to "cracked" and recalculated (s. Fig. 2, step 1). Now a horizontal crack is assumed and the vertical stress results as zero.

In step 2 the crack is nearly closed again (crack opening of 0.001). In step 3 it gets a further vertical compression of -0.002 and simultaneously a shear of 0.25. The vertical pressure is 10 MPa while the shear stress results as 7.5 MPa as Flicks law requires. The

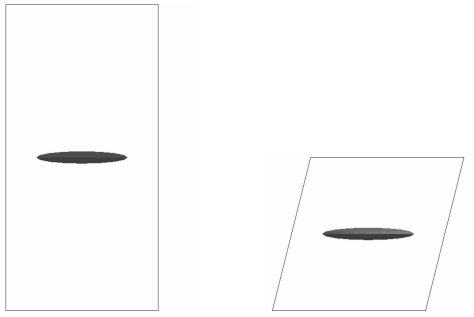

Step 1: The same situation as in Fig. 2, step 1.

Step 2: Steep closure of the crack the small resulting shear stress doesn't allow sliding.

Figure 3. Crack generation and closure without frictional sliding.

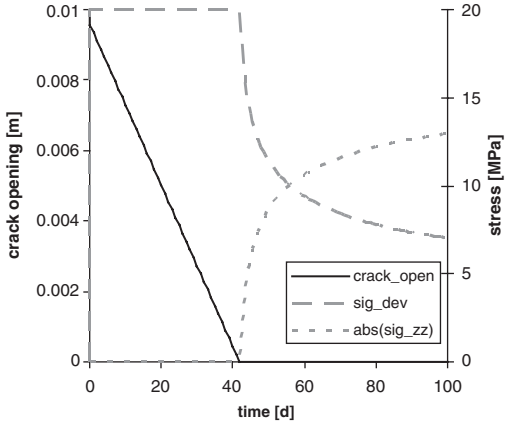

Figure 4. Closure of a crack due to creep induced, by lateral stress. The vertical stress is zero till crack closes and then quickly raises thus reducing deviatoric stress and creep rate.

mayor part of the shear strain has happened due to frictional sliding.

If in step 2 a compression of -1.001 and shear of 0.25 is imposed simultaneously onto the element (s. Fig. 3), most part of the movement including shear has happened without contact and so only a very small elastic shear of $\sim$2.5E-4 results with a frictional shear stress of $\sim$2.5 MPa. That is lower than Flicks law demands and so full cohesion is modelled without sliding.

In the following example an element made of salt has been cracked such that a small crack opening of 0.01 results. Then the faces of the element parallel to the crack have been fixed such that it can be compressed parallel to the crack but not perpendicularly. Giving a compressive load of 20 MPa parallel to the crack plane, due to lateral elastic expansion the

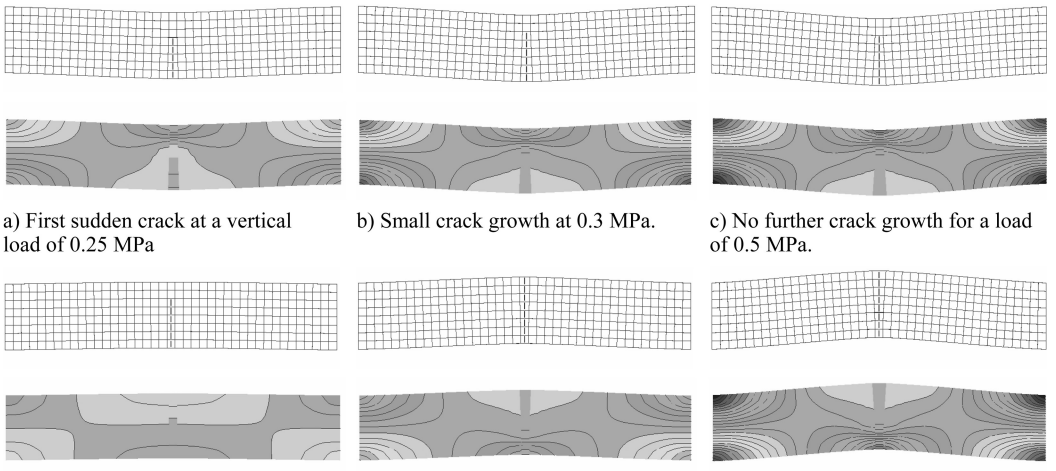

a) First sudden crack at a vertical load of 0.25 MPa

b) Small crack growth at 0.3 MPa.

c) No further crack growth for a load of 0.5 MPa.

d) Closure of lower elements at an upward load of 0.125 MPa, reopening of upper two cracked elements.

e) Cracking of the last two elements at a load of 0.3 MPa.

f) No change of open crack length for a load of 0.5 MPa, symmetric situation compared to Fig. 5c).

Figure 5. Crack generation in a beam due to bending, showing instable and stable growth, closure and reopening of the cracks.

crack is closed by 4.32E-4 instantaneously (s. Fig. 4). Due to the creep rate of ~2.28E-4 d^{-1}, resulting from the deviatoric load, the remaining crack opening is reduced to zero within 41.97 d. Then the axial stress is rising and the deviatoric load is getting reduced.

2.5 *Complex models*

A bar of elastic material is fixed at both ends (s. Fig. 5). It is loaded stepwise with a vertical load of up to 0.5 MPa on top of its ridge. For the purpose of demonstration, cracking has only been allowed in the middle of the bar.

Due to the horizontal tension, resulting from vertical load, a crack instantaneously divides more than half of the bar after the critical stress has been reached (s. Fig. 5a). For the given load the crack finds a new state of equilibrium. For slowly increasing load the crack stops for a while and then grows only for one further element (s. Fig. 5b) till it finally stops due to the pressure ahead of the crack (s. Fig. 5c). The vertical load is then replaced by a similar upward load from below. For a small load the lower cracked elements are closed and take over pressure while two upper elements keep open with a small gap (s. Fig. 5d). With increasing load the remaining elements ahead of the crack open so that the bar is totally divided (s. Fig. 5e). With a full load of 0.5 MPa the stress field as well as the opening of the elements get the principally same form as before (s. Fig. 5f).

In a small two dimensional model a chamber with an incoming edge has been excavated (s. Fig. 6a). The overall hydrostatic stress before excavation is 20 MPa. The excavation here is simulated by slowly reducing the pressure on the faces of the chamber. Without cracking, tensile stresses develop in that edge due to partial expansion by stress release (s. Fig. 6b). The tensile strength of the rock is set to 1 MPa. With reduction of inner pressure two first cracks appear at the vertical and horizontal edges with highest tensile stress, but small spatial extension. After further reduction of inner pressure a macroscopic crack starts to grow (s. Fig. 6c) till it nearly totally separates a big part of the rock (s. Fig. 6d). Then calculation is stopped because of numerical problems evolving. If the rock has enough time to reduce the deviatoric and thus tensile stresses due to creep (here Norton) no macrocracks appear.

A further two-dimensional model has been set up with two kinds of rock salt differing in the ability to creep by a factor of 8 (s. Fig. 7a). Under the action of a lateral stress of 15 MPa the stiffer core material gets a vertical tensile stresses caused by the embracing softer material which is trying to elongate vertically with a higher rate.

The first crack appearing near to the neck of the inner structure reduces the vertical stress in its neighbourhood thus prohibiting the generation of very near other macrocracks (s. Fig. 7b).

So, further macrocracks are spaced more or less equidistantly throughout the inner core (s. Fig. 7c, d). Some cracks even grow a little bit into the outer material in accordance with physical expectation. But also in an area below the stiff core the softer salt is getting vertical tension thus leading to further fracturing in the

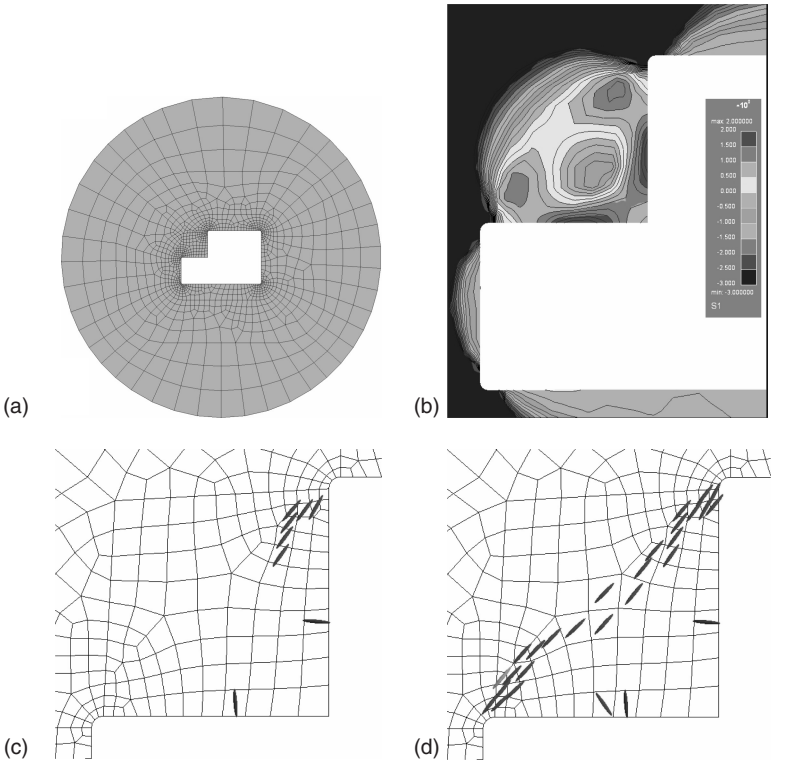

Figure 6. a) Geometry of model for a chamber in rock. b) Tensile stresses (maxim. tens. eigenstress) in the section of the incoming edge when no cracks are allowed. c) Two first cracks at the faces of the rock, then after further stress reduction a macroscopic crack is starting from an inner area of tensile stress. d) The macroscopic crack is growing from one corner to the other nearly separating a big part of the rock.

soft material. The very small cracks along the border of the two materials (s. Fig. 7d) are in agreement with stress evolution but may be avoided in future by getting a better description of the competing dilatancy in the regime of low tensile stresses. The vertical stresses are released to zero in most parts of the model (s. Fig. 7e). It can be seen that in some cases (s. e.g. Fig. 7b) the macroscopic fracture orientation does not correspond very well with that of the local orientation of individual element cracks. But in general that is no problem (s. also Fig. 6d).

The hydro-mechanical interaction of the crack is demonstrated by means of a two-dimensional model of a back filled bore hole in rock salt (s. Fig. 8) under hydraulic pressure. The rock stress as well as the hydraulic pressure of the liquid inside rock and backfill are taken to be 12 MPa initially. The stiffness of the backfill is regarded as being very small while its porosity and permeability are very high. In fact, it is needed only as a carrier of the liquid inside and doesn't have any physical meaning at all.

Then a small mechanical load of 2 MPa has been added in horizontal direction in order to get a slightly anisotropic stress field. Inside the backfill further liquid is filled in with a rather high rate in order to simulate the technical performance of a hydraulic pressure test. After having reached a critical state of stress, a sudden crack is evolving on both sides of the borehole (s. Fig. 8). Because of the rather high permeability of the crack (s. Eq. 3) the liquid flows out of the bore hole and the hydraulic pressure can't grow anymore – it is even reduced again a little bit. Effectively, the growth of crack length and volume is controlled by the limited rate of "liquid production". The hydraulic pressure results as identical to the minimal stress of 12 MPa as expected.

3 SUMMARY AND OUTLOOK

The calculations have shown that the "smeared crack" model is a rather powerful tool for the calculation of macroscopic crack growth in rock salt, capable also of hydro-mechanical interaction with a liquid inside the crack. The interaction with thermally induced stresses has not been shown here but can be taken into account

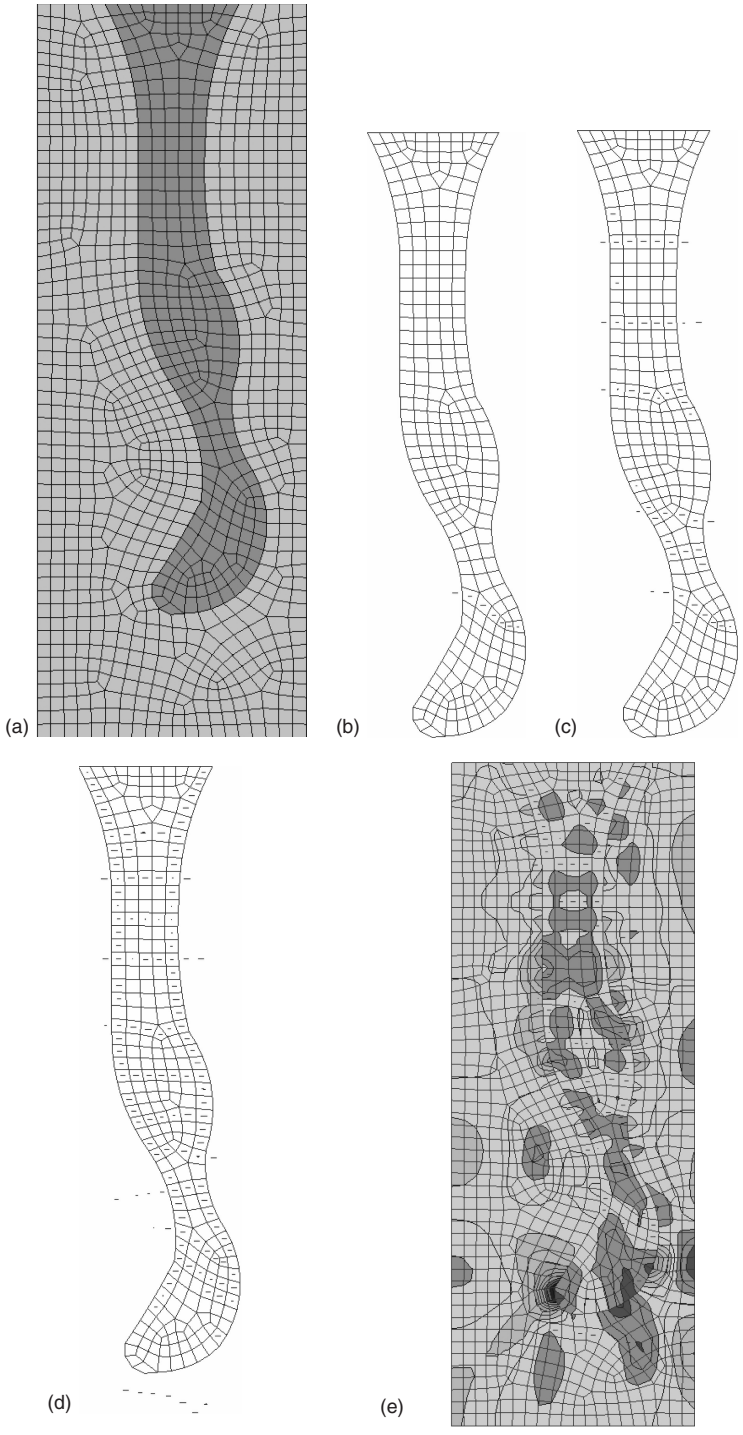

Figure 7. a) Two kinds of rock salt are horizontally squeezed. The inner rock salt has a lower creep ability than the outer one. b) Due to different creep near to the narrow part of the core material the highest tension appears and after 3 d a macro crack is generated. c) After 5 d further macrocracks have been generated. d) After 10 d the macrocracks are rather dense and small cracks appear at the border of the two materials. e) The vertical stress is released to zero in almost all parts of the model.

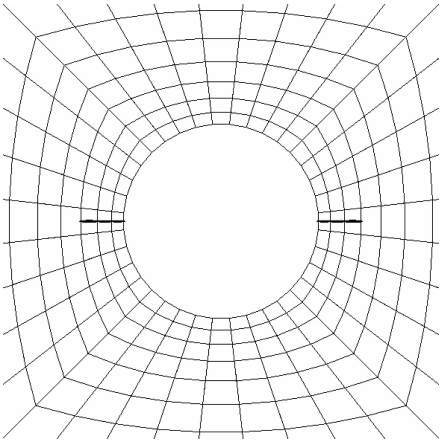

Figure 8. As a consequence of constant inflow of a liquid inside the bore hole and resulting pressure, a crack on two sides is originated and keeps growing in correlation to the increase of liquid volume.

as well. Further work will have to be done on the extension of the model onto more complex models for the mechanical behaviour of rock salt as, e.g. the CDM (Composite Damage Model) model (Hampel, Schulze 2007) as well as the combination with all other THMC processes implemented in JIFE. Another item is given by an improved algorithm to get a better agreement of local and macroscopic crack orientation for any arbitrary mesh.

REFERENCES

Cristescu, N. & Hunsche, U. 1998. Time Effects in Rock Mechanics, John Wiley & Sons, Chichester.

de Borst, R. 1997. Some recent developments in computational modeling of concrete fracture. *International Journal of Fracture.* 86, p. 5–36.

Hampel, A. & Schulze, O. 2007. The composite model: A constitutive model for the mechanical behavior of rock salt. – In: M. Wallner, W. Minkley, K.-H. Lux & H.R. Hardy Jr. (Eds.): *The Mechanical Behavior of Salt. Proceedings of the 6th Conference*, Hanover, 2007, A.A. Balkema Publishers.

Jirásek, M. & Zimmermann, T. 1998. Analysis of rotating crack model. *Journal of Engineering Mechanics ASCE,* 124, p. 842–851.

Taylor & Francis
Taylor & Francis Group
http://taylorandfrancis.com

Part 3. Deformation processes at very large temporal and spatial scales – geological systems

Taylor & Francis
Taylor & Francis Group
http://taylorandfrancis.com

The Mechanical Behavior of Salt – Understanding of THMC Processes in Salt –
Wallner, Lux, Minkley & Hardy, Jr. (eds)
© 2007 Taylor & Francis Group, London, ISBN 978-0-415-44398-2

The effect of grain boundary water on deformation mechanisms and rheology of rocksalt during long-term deformation

J.L. Urai[1] & C.J. Spiers[2]
[1] *Endogene Dynamik, Faculty of Geo-Resources and Materials Technology, RWTH Aachen University, Germany*
[2] *HPT Laboratory, Faculty of Geosciences, Utrecht University, The Netherlands*

ABSTRACT: Reliable modeling of the deformation of rocksalt under the very low strain rates characterizing long term engineering conditions or natural halokinesis requires extrapolation of experimentally-derived flow laws to rates much lower than those attainable in the laboratory. This extrapolation must be based on an understanding of the microscale deformation mechanisms operating under these conditions, from studies of natural laboratories. The engineering creep laws generally used in the salt mining industry are based on dislocation creep processes quantified in laboratory experiments of necessarily limited duration. However, a large body of evidence clearly demonstrates that under conditions of long-term deformation, grain boundary dissolution-precipitation processes, such as solution-precipitation creep (or "pressure solution") and dynamic recrystallization, play a significant role. In this contribution, we briefly review the microphysics of grain boundary water related, solution-precipitation processes in halite, together with the flow behaviour associated with these processes, and we discuss the contribution of these mechanisms to the strain rate during long-term creep.

1 DEFORMATION MECHANISMS AND RHEOLOGY OF HALITE IN EXPERIMENTS

1.1 *Deformation mechanisms*

Polycrystalline halite rocks (rocksalt) consist of grains of halite (NaCl), with a diameter between 0.01 mm and several dm, containing impurities in solid solution, secondary mineral phases and fluids trapped in inclusions, grain boundaries or in pores. Under deviatoric stress, rocksalt can deform by a range of processes.

The deformation mechanisms known to operate at temperatures relevant for engineering and natural halokinetic conditions (20–200°C) are summarized in Fig. 1.

At very low effective confining pressures (less than a few MPa) and high deviatoric stresses, inter- and intragranular microcracking, grain rotation and intergranular slip are important strain accumulating processes alongside crystal plasticity, and the mechanical properties and dilatational behaviour are dependent on the effective mean stress or effective confining pressure (Cristescu & Hunsche 1998, Peach & Spiers 1996, Cristescu 1998, Peach et al. 2001). At high enough deviatoric stress, the material fails in a (semi)brittle manner, with failure described by a pressure (effective mean stress) dependent failure envelope.

With increasing effective mean stress, microcracking and dilatancy are suppressed and crystal plastic processes dominate.

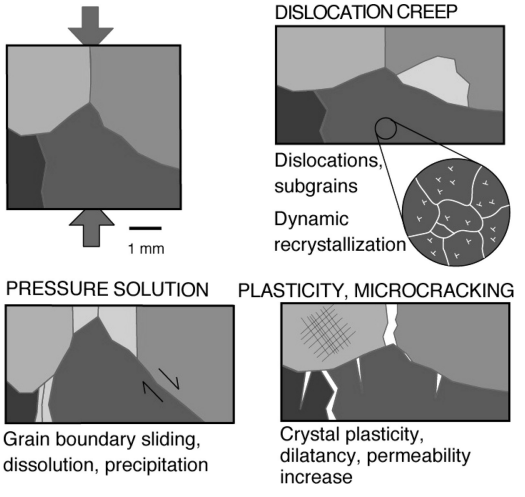

Figure 1. Schematic drawing of the microstructural processes that can operate during deformation of rocksalt at temperatures in the range 20–200°C. Different shades of green represent crystals with different orientation. See text for explanation.

At temperatures in the range 100–200°C, dislocation creep is important in laboratory experiments, and polycrystalline halite can deform to large strains by this mechanism (Fig. 2), even at confining pressures

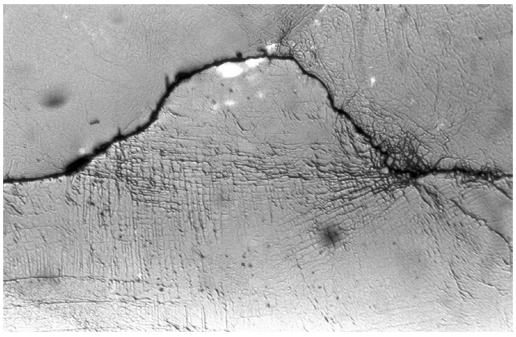

Figure 2. Reflected light optical micrograph of experimentally deformed rock salt (Asse Speisesalz, 150 °C, 50 MPa, 3×10^{-5} s^{-1}), showing dislocation slip lines, incipient subgrains and minor grain boundary microcracking. Image is approximately 1 mm wide.

as low as 10 MPa. During this process subgrains are formed in the halite grains, and the diameter of the subgrains is correlated with the deviatoric stress (Carter et al. 1993, see Fig. 9). If the polycrystal contains small but significant amounts of water in the form of saturated brine inclusions or grain boundary films, as is generally the case for both natural and synthetic samples, fluid assisted grain boundary migration is an efficient process of reducing dislocation density and hence removing the stored energy of dislocations, even at room temperature (Schenk & Urai 2004, Schenk et al. 2006 – see Fig. 3).

While dislocation creep processes take place in the crystal lattice of the halite grains, solution-precipitation creep, or "pressure solution", is a process, which occurs in the grain boundaries. Here, in the presence of a small amount of saturated grain boundary brine, grains dissolve at highly stressed boundaries, and after diffusion of the material through the grain boundary fluid, the material crystallizes at interfaces under low normal stress (Schutjens & Spiers 1999, Spiers et al. 2004 – Fig. 4). This process is accompanied by intergranular sliding and rotation (grain rearrangement), and can lead to compaction of porous salt or to deviatoric strain of non-porous aggregates (Spiers et al. 1999).

This recrystallization process involves grain boundary migration by solution-precipitation transfer across grain boundary water/brine films (Fig. 3b), and is driven by chemical potential differences across grain boundaries related to the dislocation density differences between old deformed grains and newly growing grains (Peach et al. 2001). In strongly deformed, wet rock salt, the migration process is very rapid, reaching rates up to 10 nm/s at room temperature (Schenk et al. 2006).

Solution-precipitation creep is an important deformation mechanism in most rocks in the Earth's

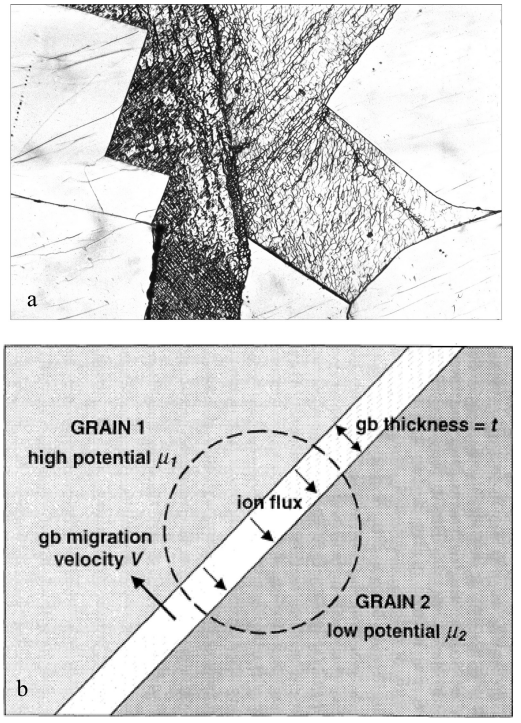

Figure 3. a) Reflected light micrograph of experimentally deformed rocksalt, showing deformed grains replaced by new, strain free grains (Asse Speisesalz, 150°C, 100 MPa, 3×10^{-5} s^{-1} followed by stress relaxation). The grain boundary migration is assisted by the presence of thin fluid films on the grain boundaries, and can take place at significant rates at room temperature. b) Diagram illustrates the principle of grain boundary migration by solution-precipitation transfer across fluid-filled grain boundaries.

crust (Renard & Dysthe 2003), but is especially rapid in rocksalt. Early reports, theoretical treatments and reviews are given by Durney (1976), Rutter (1976), Sprunt & Nur (1977), Rutter (1983) and Tada & Siever (1996). Recent theoretical treatments of the process are given by Lehner (1990) and Kruzhanov & Stöckhert (1998). In brief, the differences in chemical potential μ between points in the solid at grain boundaries under high stress and those under lower stress provide the driving force for dissolution, transport by diffusion in the intergranular fluid, and precipitation (Fig. 4). Additional driving force (chemical potential drop) both along and across grain boundaries can be provided by internal plastic deformation of the grains, giving rise to combined grain boundary migration and solution-precipitation creep.

The above processes have been documented in laboratory experiments and in naturally deformed salt from a wide range of settings (Urai et al. 1987, Spiers & Carter 1998, Trimby et al. 2000, Ter Heege

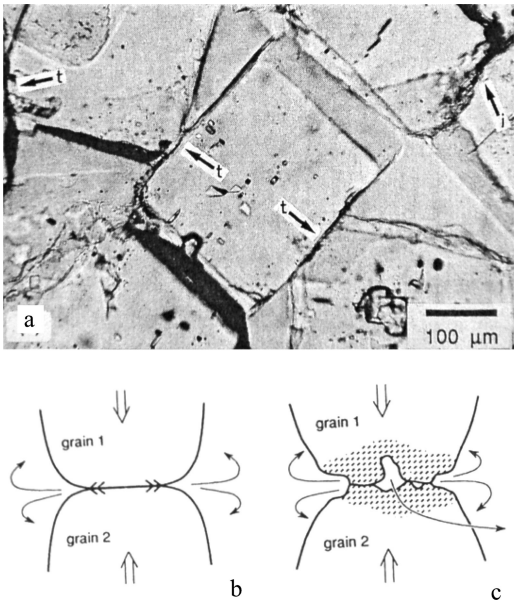

Figure 4. (a) Typical microstructure of solution-precipitation deformation in a porous halite polycrystal containing saturated brine (after Spiers et al. 1990). Diagram shows the mechanisms of solution-precipitation creep without plasticity of the crystals (b), via a thin fluid-filled grain boundary, and (c) combined operation of solution-precipitation creep and crystal plasticity (after Spiers & Brzesowsky 1993).

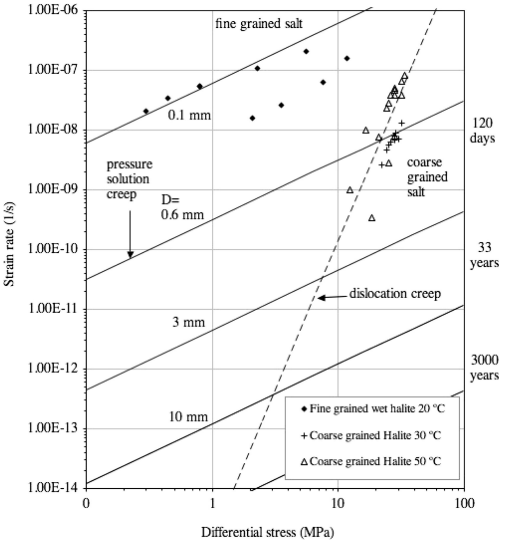

Figure 5. Differential stress–strain rate diagram summarizing low temperature laboratory data for a wide range of salts, from experiments by Sandia, BGR, Utrecht University and other Laboratories. Application of these data to conditions of long-term creep requires extrapolation. Broken line is extrapolation of the (grain size insensitive) dislocation creep law, taking $n = 5$ (BGR creep law). Solid line is the room temperature solution-precipitation creep law for different grain sizes. It can be seen that for a grain size of 3 mm the two mechanisms contribute equally to the deformation at a strain rate around 10^{-11} s^{-1}. Time to reach 10% strain at different strainrates is shown on the right side of the graph (after Schleder & Urai 2005).

et al. 2005, Schléder & Urai (in press); Schleder et al. (subm). The relative importance of each process depends strongly on variables such as temperature, confining pressure, grain size, solid solution impurities and second phase content, and, importantly, on the presence of sufficient water in grain boundaries to enable solution-precipitation phenomena (Fig. 5).

Fluid assisted grain boundary migration and solution-precipitation processes do not operate in dry salt, i.e. synthetic samples made of carefully dried material (<5 ppm water, ter Heege et al. 2005) or natural samples deformed under dilatant conditions which allow intergranular water to evaporate (Peach et al. 2001). The fields in which different deformation mechanisms are dominant can be represented in deformation mechanism maps (Fossum & Fredrich 2002, Ter Heege et al. 2005 – Fig. 6).

Published deformation mechanism maps tend to differ in the mechanisms included, depending of the time scales of interest.

1.2 *Rheological behaviour*

The rheology of a given crystalline material depends on the dominant deformation mechanism, which in turn depends on the time scale and hence deformation rate of interest. For rocksalt, summaries of behaviour observed in experiments have been published by, for example, Urai et al. (1986), Cristescu & Hunsche (1998), Hunsche & Hampel (1999), Fossum & Fredrich (2002) and Ter Heege et al. (2005).

Considering steady state, non-dilatant deformation, the main classes of equations for the creep strain rate of rocksalt are written

$$\dot{\varepsilon}_{DC} = A \exp\left(\frac{-Q_{DC}}{RT}\right)(\sigma_1 - \sigma_3)^n \qquad (1)$$

for dislocation creep, and

$$\dot{\varepsilon}_{PS} = B \exp\left(\frac{-Q_{PS}}{RT}\right)\left(\frac{\sigma_1 - \sigma_3}{TD^m}\right) \qquad (2)$$

for solution-precipitation creep, with the total strain rate being the sum of the two

$$\dot{\varepsilon} = \dot{\varepsilon}_{DC} + \dot{\varepsilon}_{PS} \qquad (3)$$

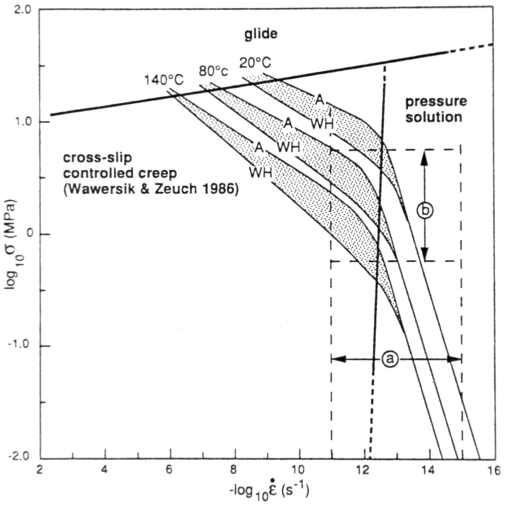

Figure 6. Deformation mechanism map for dense rocksalt, incorporating solution-precipitation creep for a grain size $D = 10$ mm. It can be seen that at low temperature and slow strain rates deformation is in the transition between dislocation creep and solution- precipitation creep (after Spiers et al. 1990).

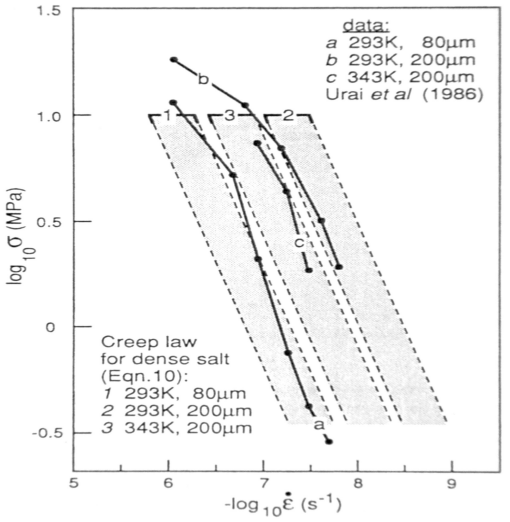

Figure 7. Steady state strain rate data of fine-grained wet rocksalt samples deforming by solution-precipitation processes, showing a stress exponent n close to 1. Gray bands represent the theoretical flow law for this process (from Spiers et al. 1990).

In these equations, written in a form appropriate for axially symmetric compressive deformation, A and B are material parameters, Q_{DC} and Q_{PS} represent (apparent) activation energies for dislocation and pressure solution creep, R is the gas constant, T is absolute temperature, σ_1 and σ_3 are the maximum and minimum principle compressive stresses, D is grain size, and n and m are the exponents of stress and grain size respectively. Two important differences between equations (1) and (2) are firstly the dependence of strain rate on stress ($n = 1$ for solution-precipitation creep or pressure solution while $n > 1$ for DC creep – see Fig. 7) and secondly the dependence of strain rate on grain size. Note that for dislocation creep deformation is grain size independent, while the exponent $m = 3$ makes pressure solution creep strongly grain size dependent.

At differential stresses below 15–20 MPa and strain rates below 10^{-6} s^{-1}, both uniaxial and triaxial experiments on natural and synthetic rocksalt show power law dislocation creep behaviour with a stress exponent n of 5–6 at the higher stresses and 3.5–4.5 at lower stresses (Wawersik & Zeuch 1986, Carter et al. 1993, Spiers & Carter 1998, Hunsche & Hampel 1999). The apparent activation energy for creep is unusually low, taking values of 50–70 kJ mol^{-1}. Intragranular microstructural signatures including wavy deformation band (slip/sub-boundary) structures indicate that cross-slip of screw dislocations may be the rate controlling process at differential stresses ($\sigma_1 - \sigma_3$) above 10–15 MPa ($n = 5$–6), while well formed equiaxed subgrains indicate that climb-controlled recovery becomes dominant at lower stresses ($n = 3$–4). A large amount of published data on natural rocksalt deformed in the laboratory indicates that for a given differential stress, the rate of dislocation creep can vary by approximately three orders of magnitude, caused by differences in concentration of impurities in solid solution, amount and distribution of secondary mineral phases, grainsize, subgrain size, dislocation density and fluids in grain boundaries (Hunsche et al. 1996).

Deformation experiments, performed in the dislocation creep field at confining pressures high enough to suppress dilatancy (>10–20 MPa), have shown that "wet" samples containing more than 10–20 ppm of water (brine) at grain boundaries undergo rapid dynamic recrystallization by fluid assisted grain boundary migration, alongside dislocation creep. Compared with dry rocksalt samples (<10 ppm water), this recrystallization process leads to a reduction in average dislocation density, an associated reduction of flow strength by 25–50% and power law flow behaviour with an n-value of about 4.5 (Peach et al. 2001, ter Heege et al. 2005). In addition, during dynamic recrystallization of wet salt (>10–20 ppm), the grain size evolves such that a systematic relation between flow stress and grain size is established, with deformation occurring close to the boundary between the dislocation and solution-precipitation or pressure solution creep fields (ter Heege et al. 2005, Fig. 8).

Solution-precipitation creep has been widely recorded in laboratory experiments on wet, fine

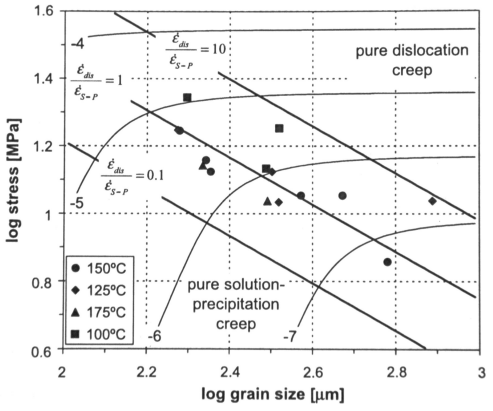

Figure 8. Dynamically recrystallized grain size versus stress data for synthetic rocksalt samples, superposed on a deformation mechanism map, showing that these samples deform in the transition region between dislocation creep and solution-precipitation creep (from ter Heege et al. 2005).

grained (<500 μm) polycrystalline halite at temperatures in the range 20–200°C, leading to quite rapid linear viscous deformation of dense salt (equation 2) and compaction of porous material (e.g. Urai et al. 1986, Spiers et al. 1990, Spiers & Brzesowsky 1993, Renard et al. 2002, 2004). The process has also been observed at individual halite grain contacts under stress (e.g. Gratier 1993, Schutjens & Spiers 1999, De Meer et al. 2005) and in salt aggregates containing second phases (Renard et al. 2001, Zoubtsov et al. 2004). Possible evidence for pressure solution has also been reported by Berest et al. (2005) in low stress creep experiments on coarse, natural rocksalt, in which much faster rates of deformation were observed than expected by extrapolating conventional dislocation creep laws obtained at higher stresses and strain rates (cf. Fig. 5). In addition, rapid long-term deformation of pillars and galleries in potash mines has been attributed to solution-precipitation creep in rocksalt (Campos de Orellana 1998, Lee and de Souza 1998), though such *in-situ* experiments have not yet been sufficiently documented to allow full quantification of the processes operating (Bekendam and Urai, this volume).

However, because of the strong grain size dependence and limited duration of laboratory tests, solution-precipitation creep is rarely seen in experiments on natural rocksalt (grain size typically 1 cm), and it is therefore not usually included in engineering descriptions of salt rheology (Cristescu & Hunsche 1998, Hunsche & Hampel 1999, Fossum & Fredrich 2002). Nonetheless, predictions made using equation (2) suggest that provided the salt contains sufficient water (>10–20 ppm, as most natural salts do), pressure solution creep should become important at strain rates below those reached in experiments (see Figs 5 and 6).

As indicated above, at low confining pressures and high deviatoric stresses, flow of rocksalt is accompanied by dilatant grain boundary microcracking and rapid permeability increase (Cristescu & Hunsche 1998, Peach & Spiers 1996). The mechanical conditions under which this occurs have been accurately delineated by Cristescu and Hunsche 1998 and Cristescu 1998 (see also Schulze et al., this volume). While the onset of microcracking has a minor direct effect on creep behaviour, it is important to note that it can strongly influence the effects of water on creep. In salt containing small quantities of water, microcracking disrupts grain boundary films and inhibits both grain boundary migration and pressure solution, particularly if the water can escape from the sample (Peach et al. 2001). On the other hand, under conditions where microcracking allows free brine or water vapour access to the interior of a creeping salt sample, then both recrystallization and solution-precipitation creep effects can be strongly enhanced.

Note that despite the large amount of data now available on solution-precipitation creep in salt, details of the microphysics of the process are incompletely understood. This is at least partly due to the difficulties of imaging the fine-scale (1–100 nm) structure of wetted grain boundaries during deformation. Approaches applied here include in-situ infrared and electrical resistivity measurements, interference microscopy, and electron microscopy of frozen boundaries using cryo-SEM (Hickman & Evans 1995, Watanabe & Peach 2002, Spiers et al. 2004, De Meer et al. 2005, Schenk et al. 2006).

2 NATURAL LABORATORIES

Studies of rocksalt deformation in nature are essential for reliable extrapolation of laboratory data to describe the flow of salt during slow, human-induced or natural flow, because such studies provide a detailed understanding of the deformation mechanisms and microstructural processes that operate at strain rates well below those accessible in laboratory experiments. In recent years, major advances in this field have been reported, based on developments in microstructural and textural/orientation analysis using electron backscatter diffraction (EBSD), microstructure decoration by gamma-irradiation, Cryo-SEM and other methods. Samples from a wide range subsurface and surface locations have been studied (e.g. Schleder & Urai 2005, in press, Schleder et al., submitted).

In addition there has recently been much progress in measuring the surface displacement field in areas of active salt tectonics, in salt mining districts, on

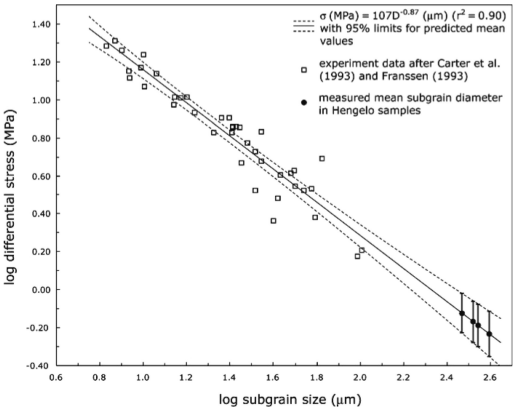

Figure 9. Subgrain-size versus differential stress data from experimentally deformed rocksalt, providing the basis for measurement of in-situ differential stress in core samples. Solid dots with error bars are the application of this technique to Hengelo Rocksalt (after Schleder & Urai 2005).

sediment rafts above mobile salt, on emerging salt diapirs, and in areas where removal of ice sheets has led to a change of overburden load. These data can be inverted using non-linear finite element techniques, to obtain constitutive equations for salt flow during slow natural deformation (Weinberger et al. 2006, Urai & Kenis, unpublished data). Insight into the in-situ rheology of salt on the time scale of years has also been gained by simply adjusting the flow laws used in numerical models of mining-related subsidence to obtain a match with surface displacement evolution. Studies of this type, conducted in relation to deep solution mining operations at Barradeel in the Netherlands (2–3 km depth), suggest salt flow behaviour involving dislocation creep (n value of 3–4) combined with a linear viscous flow law comparable to that expected for solution-precipitation creep (Breunese et al. 2003).

Microstructural studies of naturally deformed salt show that low temperature dislocation glide and dislocation creep processes, solution-precipitation creep and water-assisted dynamic recrystallization are all of major importance (Urai et al. 1987, Spiers & Carter 1998, Schleder & Urai 2005, in press). The relative importance of these processes varies strongly, as a function of grain size, impurity content, stress path and fluid chemistry. Differential stress, as measured using laboratory-calibrated subgrain-size piezometry (Fig. 9), is usually less than 2 MPa in rocksalt deforming in nature, in agreement with in-situ stress measurements and geologic flow rates (Spiers & Carter 1998, Schleder & Urai 2005). Higher stresses, up to 5 MPa are recorded in the near-surface parts of diapir stems where salt is extruded to the surface (Schleder & Urai, in press).

Microstructural studies also show, in agreement with recent experiments, that during fluid-assisted dynamic recrystallization of salt in nature (water content >10 ppm), the grain size adjusts itself so that the material deforms close to the boundary between the dislocation and pressure solution creep fields. Power law flow, as measured in recrystallizing samples (ter Heege et al. 2005), with an n-value of about 4.5 is therefore proposed to be a good representation of this behavior. In samples which are sufficiently fine grained, solution-precipitation creep (equation 2), is found to be dominant both in salt glaciers recrystallized after extrusion to the surface, and in very fine grained primary rocksalt in the subsurface (Schleder & Urai 2005, in press). At geologic strain rates, such salt will be orders of magnitude weaker than would be predicted from extrapolation of short-term experiments on coarse-grained rocksalt (see Fig. 5).

The rather high variability of flow strength in layers of rocksalt in nature is in good agreement with the small-scale folding ubiquitously observed in layers of naturally deformed salt. This has not yet been incorporated in numerical models of salt tectonics, which typically assume much more homogeneous material properties and accordingly produce much less heterogeneous strain fields.

It is an interesting and as yet unexplained microstructural observation that despite the high rate of fluid-assisted grain boundary migration observed in experiments, most naturally deformed rocksalt is not completely recrystallized and preserves subgrains. The most likely explanation for this is that below some critical difference in driving force for cross-boundary solution-precipitation transfer, surface energy driving forces cause necking of grain boundary fluid films to form isolated fluid inclusions (or possibly some other structural change), thus rendering the boundaries immobile.

In the following, we consider a number of recent examples of how microstructural studies of natural salt can elucidate operative deformation processes and rheology in nature.

2.1 *Evidence for dilatancy and fluid flow in rocksalt in the deep subsurface*

Intact rocksalt has an extremely low permeability ($<10^{-21}$ m^2), which imparts excellent sealing capacity. However, we know from experiments that at sufficiently low effective mean stress, dilatancy and extensional (Mode I) fracture can occur in deforming salt, producing significant permeability (Peach & Spiers 1996). If this occurs in nature, fluid flow will be possible. Evidence for fluid flow, in the form of saturated brines of different chemical composition, and of hydrocarbons is frequently found in naturally deformed salt (Schleder et al., submitted, Schönherr

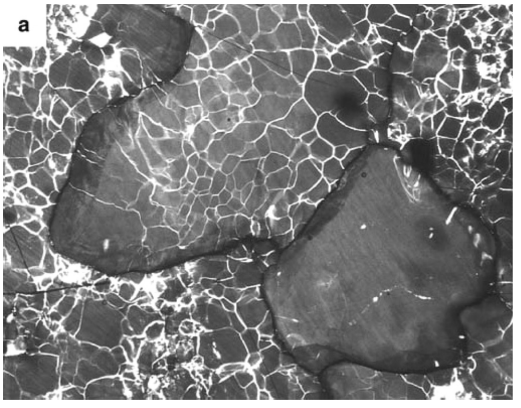

Figure 10. Typical micrograph of Hengelo Rocksalt, decorated to show the microstructure, with subgrains (white lines), grain boundaries (dark bands), showing clear evidence for "overgrowth" due to solution-precipitation processes such as pressure solution and and grain boundary migration. Mean grainsize in Hengelo samples is between 5 and 25 mm. Width of image is 7 mm (from Schleder & Urai 2005).

et al. submitted). Microstructural evidence suggests that both diffuse dilatancy and Mode I fracturing can occur at very low effective stress conditions, i.e. at near-lithostatic fluid pressures and differential stress of a few MPa, in the deep subsurface, followed by crack healing through precipitation form supersaturated solutions.

2.2 *Deformation mechanisms in the Hengelo Salt*

As an example of a study of deformation mechanisms in natural salt, we briefly review the work done recently by Schleder & Urai (2005) on the bedded salt mined by AKZO at Hengelo in the Netherlands. Deformation of the Hengelo rocksalt in the geologic past has taken place probably during Cretaceous tectonic inversion in the area.

The microstructure of core samples from the subhorizontal, bedded Main Röt Evaporite Member (AKZO well 382, depth interval of 420–460 m) was studied by transmitted and reflected light microscopy of gamma-irradiation decorated samples. Primary microstructures compares favourably with those found in recent ephemeral salt pans. In addition, in all layers the grains are rich in deformation-related substructures such as slip bands and subgrains indicating strains of a few percent (Fig. 10). The study of gamma-irradiation decorated thin sections showed that the main recrystallization mechanism was grain boundary migration (Fig 10). This process removes primary fluid inclusions and produces clear, strain-free (subgrain- and slip band free) new grains. Differential stresses as determined by subgrain size piezometry (Fig. 9) were 0.45–0.97 MPa.

The corresponding deformation mechanisms are inferred to be a combination of dislocation creep, dynamic recrystallization and solution-precipitation processes. Solution-precipitation processes are activated by the small amount of brine present in grain boundaries. Inserting the above differential stress values determined from subgrain size into published flow laws for dislocation creep and for pressure solution (Carter et al. 1993, Spiers & Carter 1998) yields transitional strain rates between 10^{-12} and 10^{-13} s^{-1}. The data provide a view of very slow deformation of the Hengelo Rocksalt, up to strains of about 10%, with a significant role played by solution-precipitation processes in controlling rheology.

2.3 *Salt glaciers*

Microstructural processes in mylonitic shear zones from extrusions of Eocene-Oligocene rocksalts from the Garmsar hills and Eyvanekey plateau (central Iran) were recently were studied by Schleder & Urai (in press), using transmitted light microscopy of gamma-irradiated thin sections, subgrain size palaeopiezometry of polished and chemically etched samples and texture measurements by EBSD.

The less deformed "protomylonites" found in the stem region of the emerging diapirs? comprise 2–6 mm sized grains, occasionally rich in primary fluid inclusions indicative of their primary non-recrystallized state. Abundant, well-developed subgrains suggest that the protomylonite deformed mainly by dislocation processes. Elongated subgrains at grain edges point to recrystallization by fluid-assisted grain boundary migration. Recrystallized, strain-free grains are common. The material in the highly deformed mylonitic zones found in the salt glaciers is extremely fine-grained (∼0.6 mm). Microstructures such as oriented fibrous overgrowths and growth banding (observed in gamma-irradiated sections, Fig. 11) suggest that the principal deformation mechanism was solution-precipitation creep accompanied by grain boundary migration and grain boundary sliding.

Crystal fabrics measured by EBSD show only a weak crystallographic preferred orientation consistent with solution-precipitation accommodated grain boundary sliding. Using published flow laws for this mechanism (Spiers et al. 1990), plus slope-based estimates of the gravitational shear stress driving glacier flow, the strain rate in the fine-grained mylonites was estimated to be about 10^{-10} s^{-1}.

3 DISCUSSION AND CONCLUSIONS

Through integration of all available data, it is now possible to provide a rather complete model of the deformation mechanisms and microstructural evolution of rocksalt under a wide range of conditions,

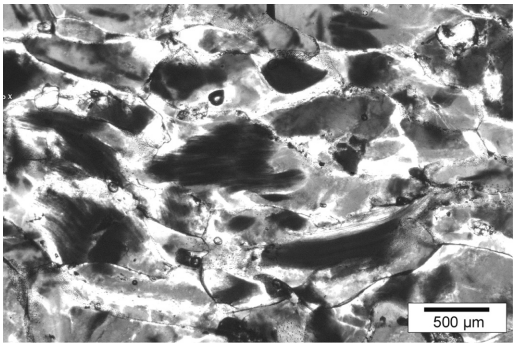

Figure 11. Typical microstructure of solution-precipitation deformation in glacier salt from Iran, as observed in gamma-irradiated sections (after Schleder & Urai, in press). Microstructures such as oriented fibrous overgrowths on both sides of a grain boundary, growth banding and the absence of slip lines or subgrains suggest that the principal deformation mechanism was solution-precipitation creep accompanied by grain boundary migration and grain boundary sliding. Crystal fabrics measured by EBSD in these samples show only a weak crystallographic preferred orientation consistent with solution-precipitation accommodated grain boundary sliding.

including strain rates well below those reached in laboratory experiments (equations 1–3).

At these low rates, microstructural studies of natural salts and extrapolation, long term in-situ and subsidence measurements, and extrapolation of experimental data for fine grained samples indicate that solution-precipitation creep and fluid assisted dynamic recrystallization are important processes, significantly contributing to the total strain rate.

The available data provide a reasonable basis for modeling the mechanical behaviour of salt under geotechnical and natural conditions. However, in many current studies the effects of water-activated grain boundary processes are often neglected, and this omission must lead to errors in prediction of displacement rates, especially over long periods.

Geo-mechanical modeling efforts can thus be significantly improved by making full use of the data available on the effects of water, and some of the discrepancies seen in experimental data on different salts can probably also be explained in terms of these effects.

Additional improvements can be made by obtaining a more detailed understanding of the mechanism of both transient and steady state dislocation creep, and by improving microphysical models for the effects of solution-precipitation creep, recrystallization and surface energy driven grain boundary and crack healing on flow and transport properties.

Further work is also needed on deformation mechanisms in naturally deformed rocksalt from a wider range of geological settings, and in comparing constitutive equations obtained in the laboratory with those obtained from inverting surface displacement data obtained above salt mining sites and salt extrusions.

REFERENCES

Berest, P., Blum, P.A., Charpentier, J.P., Gharbi, H. and Vales, F. (2005). Very slow creep tests on rock samples. International Journal of Rock Mechanics and Mining Sciences, 42, 569–576.

Breunese, J.N., Eijs, R.M.H.E. van, Meer, S. de, Kroon, I.C. (2003) Observation and prediction of the relation between salt creep and land subsidence in solution mining – The Barradeel case. SMRI conference, Chester, UK.

Campos de Orellana A.J. (1998) Non-associated pressure solution creep in salt rock mines. In: Mechanical behavior of salt, vol. 22, pp. 429–444, Trans Tech Publications, Series on Rock and Soil mechanics, Clausthal-Zellerfeld.

Carter, N.L., Horseman, S.T., Russell, J.E. and Handin, J. (1993). Rheology of rocksalt. *J. Struct. Geol.*, *15*, 1257–1271.

Cristescu N.D. (1998). Evolution of damage in rocksalt. In: Mechanical behavior of salt, vol. 22, 131–142, Trans Tech Publications, Series on Rock and Soil mechanics, Clausthal-Zellerfeld.

Cristescu N.D. and Hunsche, U. (1998). Time Effects in Rock Mechanics. John Wiley & Sons, 342 p., ISBN 0-471-95517-5.

De Meer, S., Spiers, C.J. and Nakashima, S. (1995) Structure and diffusive properties of fluid-filled grain boundaries: An in-situ study using infrared (micro) spectroscopy. Earth Planet. Sci. Lett., 232 (3–4), 403–414.

Durney D.W. (1976) Pressure-Solution and Crystallization Deformation Philosophical Transactions of the Royal Society of London. Series A, Mathematical and Physical Sciences, Vol. 283, No. 1312, pp. 229–240.

Fossum A.F. and Fredrich J.T. (2002) Salt Mechanics Primer for Near-Salt and Sub-Salt Deepwater Gulf of Mexico Field Developments SANDIA REPORT SAND2002–2063

Gratier, J-P. (1993) Experimental pressure solution of Halite by an indenter technique Geophysical Research Letters vol. 20, no. 15, p. 1647–1650.

Hickman, S.H., Evans, B. (1995) Kinetics of pressure solution at Halite-silica interfaces and intergranular clay films. Journal of Geophysical Research, Volume 100, p. 13113–1313.

Hunsche U. Hampel A. (1999) Rocksalt – the mechanical properties of the host rock material for a radioactive waste repository. Engineering Geology, Volume 52, Number 3 pp. 271–291.

Hunsche, U. Mingerzahn G., Schulze O. (1996): The influence of textural parameters and mineralogical composition on the creep behavior of rock salt.- In: The Mechanical Behavior of Salt III; Proc. Third Conf., Palaiseau (France) 1993; Editors: M. Ghoreychi, P. Berest, H. Hardy, Jr. & M. Langer; p. 143–151. Trans Tech Publications, Clausthal.

Kruzhanov, V. Stöckhert B. (1998) On the Kinetics of Elementary Processes of Pressure Solution. Pure and Applied Geophysics Volume 152 p. 667–683.

Lee R. and de Souza E. (1998) The effect of brine on the creep behaviour and dissolution chemistry of evaporites Can. Geotech. J./Rev. can. geotech. 35(5): 720–729.

Lehner, F.K. (1990) Thermodynamics of rock deformation by pressure solution. In: *Deformation Processes in Minerals, Ceramics and Rocks*, Eds D.J. Barber, and P.D. Meredith, 296–333, Unwin Hyman, London.

Peach, C.J. and Spiers, C.J. (1996). Influence of crystal plastic deformation on dilatancy and permeability development in synthetic salt rock. *Tectonophysics*, Vol. 256, 101–128.

Peach, C.J., Spiers, C.J. and Trimby, P.W. (2001) Effect of confining pressure on dilatation, recrystallization and flow of rocksalt at 150°C. J. Geophys. Res., 106, B7, 13, 315–13,328.

Renard F., Dysthe, D., Feder, J., and Jamtveit, B. (2002). Healing of fluid-filled microcracks, In: "Poromechanics II", Ed. by J.-L. Auriault et al., Proceedings of the second Biot Conference on poromechanics, A. A. Balkema Publishers, pp. 925–931.

Renard, F. Dysthe, D., Feder, J., Bjørlykke, K. and Jamtveit, B. (2001) Enhanced pressure solution creep rates induced by clay particles: Experimental evidence in salt aggregates. Geophysical Research Letters, 28, 1295–1298.

Renard, F., and Dysthe, D. (2003). Pressure Solution, In Encyclopedia of Sediments and Sedimentary Rocks, edited by G. V. Middleton, Kluwer Academic Publishers, ISBN 1-4020-0872-4.

Renard, F., Bernard, D., Thibault, X., and Boller, E. (2004) Synchrotron 3D microtomography of Halite aggregates during experimental pressure solution creep and evolution of the permeability, Geophysical Research Letters, 31, L07607, doi:10.1029/2004GL019605.

Rutter E.H. (1983) Pressure solution in nature, theory and experiment Journal of the Geological Society, Volume 140, Number 5, 1983, pp. 725–740.

Rutter, E.H. (1976). The Kinetics of Rock Deformation by Pressure solution Philosophical Transactions of the Royal Society of London. Series A, Mathematical and Physical Sciences, Vol. 283, pp. 203–219.

Schenk, O. and Urai, J.L., 2004. Microstructural evolution and grain boundary structure during static recrystallization in synthetic polycrystals of sodium chloride containing saturated brine. Contributions to Mineralogy and Petrology, 146: 671–682.

Schenk, O., Urai, J.L. and Piazolo, S., 2006. Structure of grain boundaries in wet, synthetic polycrystalline, statically recrystallizing Halite – evidence from cryo-SEM observations. Geofluids, 6(1): 93–104.

Schléder, Z. and Urai, J.L., (2005). Microstructural evolution of deformation- modified primary Halite from Hengelo, the Netherlands. International Journal of Earth Sciences, 94(5–6): 941–956.

Schléder, Z. and Urai, J.L., (in press) Deformation and recrystallization mechanisms in mylonitic shear zones in naturally deformed extrusive Eocene-Oligocene rocksalt from Eyvanekey plateau and Garmsar hills (central Iran). Journal of Structural Geology.

Schléder, Z., Urai, J.L., Nollet, S. and Hilgers, C., submitted. Deformation and recrystallization mechanisms and fluid flow properties of rocksalt as evidenced by microstructures – a case study on Zechstein (Z1) rocksalt from Neuhof salt mine (Germany). SPP 1134 Special Volume of IJES.

Schoenherr, J. Urai, J.L. Kukla, P.A. Littke, R. Schléder, Z. Larroque, J-M. Newall, M.J. Al-Abry, N. Al-Siyabi, H.A. Rawahi, Z. (in press) Limits to the sealing capacity of halite: A case study of the Infra-Cambrian Ara Salt from the South Oman Salt Basin. AAPG Bulletin.

Schutjens, P.M.T.M. and Spiers, C.J. (1999) Intergranular pressure solution in NaCl: Grain-to-grain contact experiments under the optical microscope. Oil & Gas Science and Technology - Rev. IFP, 54,(6), 729–750, 1999.

Spiers, C.J. and Carter, N.L. (1998) Microphysics of rocksalt flow in nature. In: Aubertin, M., and Hardy, H.R. (eds.): The mechanical behavior of salt, proceedings of the 4th conference, Trans Tech. Publ. Series on Rock and Soil Mechanics, 22, 115–128.

Spiers, C.J., and Brzesowsky, R.H. (1993) Densification behaviour of wet granular salt: theory versus experiment. In: Kakihana, H., Hardy, H.R. Jr., Hoshi, T. and Toyokura, K. (eds.), Seventh Symposium on Salt , vol. 1. Elsevier Science, Amsterdam, 83–92.

Spiers, C.J., de Meer, S. Niemeijer, A., Zhang, X. (2004) Kinetics of rock deformation by pressure solution and the role of thin aqueous fims. in: Nakashima. A. (ed) Proceedings of the international symposium on "Physiochemistry of water and dynamics of materials and the earth – Sructures and behaviours of the thin film water", September 2003. Frontier Science Series no. 44, Universal Academy Press, Tokyo.

Spiers, C.J., Schutjens P.M.T.M. Brzesowsky, R.H. Peach C.J. Liezenberg J.L. Zwart H.J. (1990) Experimental determination of the constitutive parameters governing creep of rocksalt by pressure solution. In: Knipe, R.J. Rutter E.H. (eds) Deformation Mechanisms, Rheology and Tectonics. Geological Society special Publication 54: 215–227.

Sprunt, E.S., Nur, A. (1977) Experimental study of the effects of stress on solution rate Journal of Geophysical Research, Volume 82, Issue B20, p. 3013–3022.

Tada, R., Siever, R. (1996) Experimental knife-edge pressure solution of Halite. Geochimica et Cosmochimica Acta, vol. 50, Issue 1, pp.29–36.

Ter Heege, J.H., De Bresser, J.H.P. and Spiers, C.J. (2005) Rheological behaviour of synthetic rocksalt: The interplay between water, dynamic recrystallization and deformation mechanisms. J. Struct. Geol., 27, 948–963.

Ter Heege, J.H.P., De Bresser, J.H.P. and Spiers, C.J. (2005) Dynamic recrystallization of wet synthetic polycrystalline Halite: Dependence of grain size distribution on flow stress, temperature and strain. Tectonophysics, 396, 35–57.

Trimby, P.W., Drury, M.R. and Spiers, C.J. (2000) Recognising the crystallographic signature of recrystallisation processes in deformed rocks: a study of experimentally deformed rocksalt. J. Struct. Geol., 22, 1609–1620.

Urai J.L. Spiers C.J. Peach C.J. Franssen R.C.M.W. Liezenberg J.L. (1987) Deformation mechanisms operating in naturally deformed Halite rocks as deduced from microstructural investigations. Geologie en Mijnbouw 66: 165–176.

Urai J.L. Spiers C.J. Zwart H.J. Lister G.S. (1986) Weakening of rocksalt by water during long term creep. Nature 324: 554–557.

Watanabe, T. and Peach, C.J. (2002) Electrical impedance of plastically deforming Halite rocks at 125°C and 50 MPa. J. Geophys. Res. – Solid Earth, 107, B1, 10.1029/2001JB000204.

Wawersik, W.R. and Zeuch, D.H. (1986). Modelling and mechanistic interpretation of creep of rocksalt below 200°C. Tectonophysics 121, 125–152.

Weinberger, R., Lyakhovsky, V., Baer, G., and Begin, Z. B. (2006). Mechanical modeling and InSAR measurements of Mount Sedom uplift, Dead Sea Basin: Implications for rock-salt properties and diapir emplacement mechanism. Geochem. Geophys. Geosyst., 7, Q05014.

Zoubtsov, S., Renard, F., Gratier, JP, Guiguet, R., Dysthe, D. K., and Traskine V. (2004) Experimental pressure solution creep of polymineralic aggregates, Tectonophysics, 385, 45–57.

The Mechanical Behavior of Salt – Understanding of THMC Processes in Salt –
Wallner, Lux, Minkley & Hardy, Jr. (eds)
© 2007 Taylor & Francis Group, London, ISBN 978-0-415-44398-2

Stress relaxation experiments on compacted granular salt: effects of water

X. Zhang, C.J. Peach, J. Grupa & C.J. Spiers
Faculty of Geosciences, Utrecht University, Utrecht, The Netherlands

ABSTRACT: Stress relaxation experiments were carried out in 1-D compaction mode on granular salt with various pore fluid phases at room temperature. Merck salt (99.5% pure NaCl), sieved into different grain size fractions, was used as starting material. Samples were first compacted rapidly to a fixed porosity in the range 30–0.3% and the applied stress was then allowed to relax at fixed crosshead displacement. The effects of water content, applied stress, grain size, and porosity were systematically investigated. In fully dry, argon-flushed samples, the measured relaxation creep rates were insensitive to grain size but very sensitive to applied stress with an apparent power law stress exponent (n) of around 20. However, if the samples were exposed to lab air, the stress exponent dropped sharply ($n = 5.1$) compared to the dry samples, showing significant weakening by moisture. In samples flooded with NaCl saturated solution, the stress exponent was found to be almost exactly 1 at the lower stresses investigated (<20–15 MPa). The creep rate of samples flooded with brine was sensitive to grain size. The mechanical results together with microstructural analysis showed that the dominant deformation mechanism in the dry, argon-flushed samples was probably dislocation glide whereas it was pressure solution in the brine-flooded samples at stresses <20–15 MPa. However, the relaxation behaviour seen in samples tested with lab air ($n = 5.1$) is less easily explained. The dominant process is certainly not pure dislocation creep or glide, since it is activated by the access of lab air (moisture). Extensive recrystallization by grain boundary migration is observed in these samples and it must play a role in controlling relaxation and apparent n-value, possibly with a contribution from pressure solution and/or plasticity coupled solution transfer.

1 INTRODUCTION

The deformation of rocksalt is of interest to geoscientists for two reasons. First, understanding the rheological properties is key for many important engineering operations in salt formations, namely, salt mining, radioactive waste disposal, and storage of oil and gas (Urai et al., 1986; Carter et al., 1993; Bechthold et al., 2004). Second, the deformation microstructures characteristic of rocksalt, which can be easily reproduced in the lab, clearly reveal many of the fundamental mechanisms operating in geomaterails. Among them are pressure solution creep (Spiers et al., 1990; Spiers & Brzesowky, 1993), dynamic recrystallization by grain boundary migration (Guillopé & Poirier, 1979; Urai, 1983; Urai et al., 1987; Peach et al., 2001) and competition between dislocation and grain size sensitive diffusion processes (De Bresser et al., 2001). These processes are too slow in most other minerals to be reproduced and quantified in lab experiments. Salt thus provides a model material for the study of these processes.

Among the many factors influencing the rheological properties of rocksalt, such as stress, temperature grain size, porosity and impurities, the effects of small quantities of water play a major role in controlling the active deformation mechanisms (Drury & Urai, 1990; Peach et al., 2001; Hunsche & Schulze, 1996, 2002). Many discrepancies between different experimental studies are probably caused by neglect of these effects, which occur even when only trace amounts of water are present (Ter Heege et al., 2005).

In this study, we aim to investigate the effects of water on the dominant deformation mechanisms in granular salt at room temperature, in order to gain insight into salt backfill behaviour at porosities in the range 10 to 0.1%. We apply the stress relaxation technique to pre-compacted, porous polycrystalline salt to obtain rheological data for 1-D compaction at near-constant porosity values.

2 EXPERIMENTS

Analytical grade sodium chloride (Merck, 99.5% pure) powder, sieved into grain size fractions of <50, 70 ± 20, 137 ± 12, 280 ± 20, 412 ± 12 and $560 \pm 20\,\mu m$, was used in this study. Most of the samples were oven-dried at 50°C for several days before use. Very dry samples were dried in-situ, i.e. within

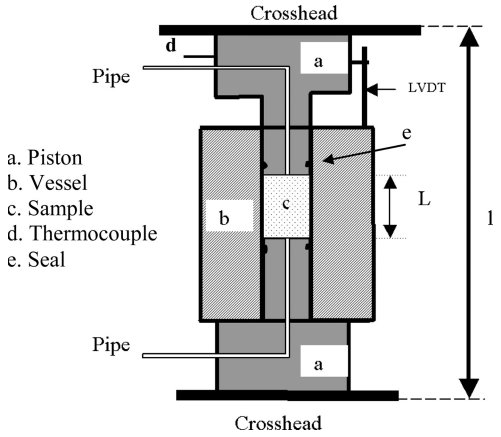

Figure 1. Schematic diagram of 1-D compaction vessel used for compaction/relaxation experiments.

the vessel used for compaction, at temperatures of 100–150°C. These samples were immediately flushed with dry argon after heating, and were continuously flushed throughout compaction and relaxation testing. Lab air was allowed to enter selected samples by exposing them to air during preparation and testing. Decane or saturated solution were vacuum-injected into other samples. The pore fluid pressure was maintained at ~0.1 MPa (1 atmosphere) in all cases.

The compaction/stress-relaxation experiments were carried out in an Instron 8562 materials testing machine and oedometer of diameter about 20 mm (Figure 1). The applied stress and the relative positions of the crossheads can be measured by the Instron machine. An additional LVDT was placed between the top piston and top of the vessel. A K type thermal couple was placed in the top piston to measure the apparatus/sample temperature. The testing machine was covered with a thermal insulation box, keeping the temperature variation within ±0.1°C.

To reduce the friction between the sample and the vessel wall, a thin layer of Boron Nitride was sprayed in the inner wall of the vessel. All experiments were carried out at room temperature (21°C). In a standard relaxation test, the sample was first compacted to a porosity of 25% at approximately constant strain rate (10^{-5}–10^{-4} s^{-1}), with the pores filled with lab air. Pore fluid was then introduced. The sample was then compacted to the desired porosity for relaxation testing, its compliance was measured by rapid cyclic loading, and relaxation was initiated. Signals for stress, piston displacement and temperature were logged as a function of time. After the experiments, the samples were thin sectioned for microstructural studies.

The stress relaxation method is commonly used in rock deformation experiments to obtain creep data at low strain rates within practical measuring times (Rutter & Mainprice, 1978). The technique involves interruption of a conventional compression or compaction test by actively maintaining a fixed position of the loading piston and then measuring the stress relaxation in the sample. The stress relaxation behaviour is due to creep in the sample, as the elastic strains in the sample plus apparatus are converted into permanent (plastic) deformation of the sample. To determine the plastic strain rate in the sample ($\dot{\varepsilon}_p$), and its relation to the rate of axial stress change ($d\sigma/dt$), the elastic compliance of the testing machine has to be taken into account, using the equation (Spiers et al., 1986)

$$\dot{\varepsilon}_p = \left[\frac{A}{L}S_a + S_s\right]\frac{d\sigma}{dt} \qquad (1)$$

where A is the cross section area of the sample, L is its length, S_a is the elastic compliance of the testing machine (expressed in m/N), and S_s is the elastic compliance of the sample (Pa^{-1}), which in a compaction test depends on sample porosity.

Equation (1) can accordingly be solved for $\dot{\varepsilon}$ at all points along a stress relaxation curve, yielding a σ–$\dot{\varepsilon}$ relation. The elastic compliance of the machine was tested in a dummy run before each experiment. The sample compliances are dependent on the porosity and were measured just before and after each relaxation test.

The great advantage of the relaxation method is that one can experimentally determine a relationship between the flow stress and flow rate of the sample, thus obtaining a flow law for the material in a single test. In the case of porous samples, the mechanical behaviour depends much on porosity. During a stress relaxation test, the porosity is (practically) constant, so that the effect of changing pore structure is effectively eliminated. Moreover, at low porosity, the compaction rate usually becomes so slow ($<10^{-8}$ s^{-1}) that ongoing displacement is difficult to measure with sufficient precision using traditional constant load compaction. By contrast, in adopting the stress relaxation technique, the stress drop (relaxation) can be very precisely and easily measured during the creep of the sample.

However, a disadvantage is that relaxation strains are small and steady state is not always be reached. This is a problem when investigating a material whose steady state rheology depends on attaining a steady state microstructure. It is thus a significant problem under conditions favouring dislocation flow mechanisms, where relatively large strains are needed to establish a steady state dislocation or dynamically recrystallised microstructure. In the present experiments, work-hardening-induced during crystal plastic flow of our samples, in the pre-compaction stage, means that dislocation-related flow during stress relaxation will certainly not represent steady state flow

Table 1. List of relaxation experiments on pre-compacted granular salt (sodium chloride).

Exp.	Grain size (μm)	Pore fluid	Porosity (%)	Range of stress (MPa)
CP1	412 ± 12	Lab air	30–29.9	19–12.7
			15–14.8	44–35
			10–9.56	57–37
CP3	412 ± 12	Decane	30–29.97	13–11
			15–14.88	38–32
			10–9.58	48–29
			8–7.6	38–21
CP4	412 ± 12	Argon	30–29.97	26–24
			10–9.9	65–61.5
CP5	412 ± 12	Solution	10–8.7	61–4.6
			5–3.6	61–4
			1–0.5	155–7
CP6	70 ± 20	Argon	15–14.9	47–42
			10–9.86	64.5–58
			5–4.68	94–81
			1–0.65	130–117
CP8	70 ± 20	Solution	10–8.6	62–0.5
			5–3.6	59–2.4
			1	108–8
CP9	412 ± 12	Lab air	3–2.7	125–75
			1	118–98
CP10	137 ± 12	Solution	25–24.74	18–1.3
			20–19.6	22.5–1.7
			15–14.29	36–0.2
			10–9.2	37.5–3
			5.3–3.5	84–5.44
CP12	137 ± 12	Lab air	5–4.16	105–71
Anl3	560 ± 20	Solution	5–3.26	95–25
Anl13	137 ± 12	Solution	10–8.89	50–0.1
			4–2.5	85–5
Anl17	<50	Solution	10–9.7	12–0
			5–3.66	70–1.6
Anl19	<50	Solution	5–3.5	62–1.5

(Schulze, 1984). Fitting of a conventional power law flow equation to relaxation data, when dislocation mechanisms dominate, will accordingly yield power law parameters (n-values) that describe the data but cannot be interpreted as steady state values. In contrast, power law parameters obtained during relaxation by diffusion creep processes, such as pressure solution, will represent near-steady state values, as only very small strains are needed to attain steady state in this case.

3 RESULTS

The relaxation experiments carried out are given in Table 1. The results of relaxation experiments can be plotted as axial stress vs. time. Figure 2 shows the relaxation curves of samples filled with different pore fluids, namely dry argon gas, lab air, decane or NaCl-saturated solution. It is clear from Figure 2 that moisture/water can significantly weaken the salt samples. Figure 3 shows the relaxation curves of samples flooded with saturated solution. Here, the effects of porosity and grain size are clearly seen. Under otherwise the identical conditions, the stress relaxes faster in finer grained samples with higher porosity.

The stress relaxation data can be converted into rate data using equation (1). Plotting the rate data vs. stress in log-log space, the slopes give directly the creep rate dependence on the stress for the samples tested under various conditions. Figures 4-8 show the rate data.

4 DISCUSSION

Recognising that the relaxation creep rate data will not represent steady state flow for a dislocation dominated deformation mechanism at low temperatures, a power law of the form (Bechthould et al., 2004; Carter & Hansen, 1983; Carter et al., 1993; Spiers & Carter, 1998)

$$\dot{\varepsilon} = A_c \sigma^n \frac{EXP\left(\frac{-Q}{RT}\right)}{d^m}\left[f(\phi)\right] \qquad (2)$$

can nonetheless be used to describe creep behaviour occurring at during relaxation. Here, $\dot{\varepsilon}$ is the compaction strain rate, σ is the applied effective stress, n is the (apparent) stress exponent, Q is the activation energy, and d and ϕ are the grain size and porosity respectively. For steady state flow, m takes the value of 3 or 0 depending on whether creep is due to grain size sensitive diffusional or grain size insensitive dislocation mechanisms. The steady state values of n and Q also depend on the creep mechanism, with n taking values of 1 for pressure solution or 3–5 for dislocation creep. As already indicated, steady state flow may be approximated in stress relaxation tests when flow is dominated by pressure solution or diffusion creep, whereas when dislocation mechanisms dominate the n value obtained is often higher than at steady state (Schulze, 1984).

The most striking features of our stress relaxation results on pre-compacted salt are the significant effects of moisture/water. The strain rate vs. stress data for argon dry, lab air and solution-flooded samples are distinct (Figures 4, 5, 6).

In the argon dry samples, the strain rates are very sensitive to stress. The average apparent n value for the argon dry samples is about 20. Porosity (in the range of 30–1%) and grain size have hardly any effects on the slopes or n values (Figure 4).

Moisture in the lab air clearly weakens lab dry samples compared to the argon dry ones. The decane-flooded samples (filled with lab air before injecting

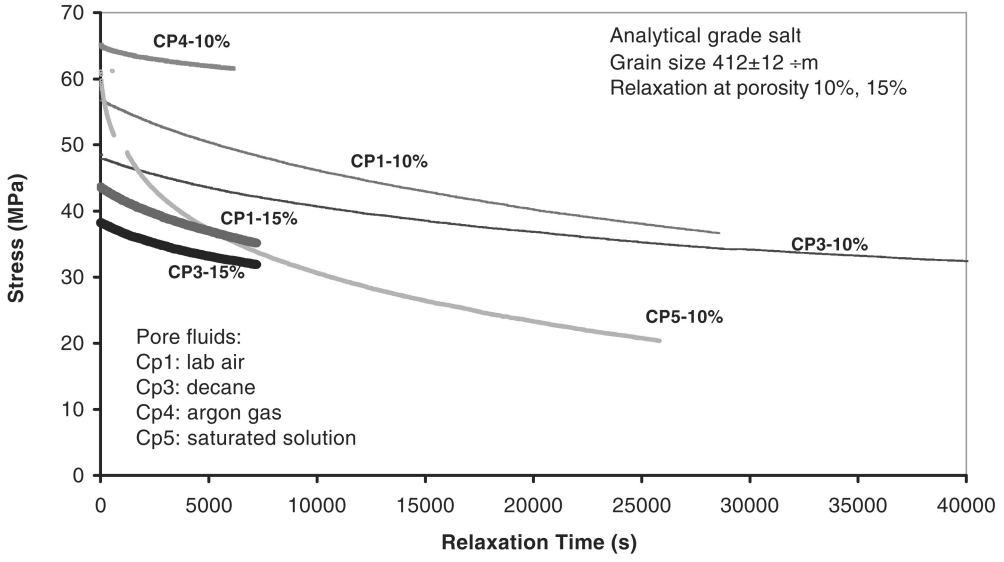

Figure 2. Stress relaxation curves for samples filled with different pore fluids. Note the similarity of lab air filled and decane filled sample. The sample flushed with dry argon gas is strong and the sample flooded with saturated solution is weak. The porosity of the samples during the relaxation test is indicated in %.

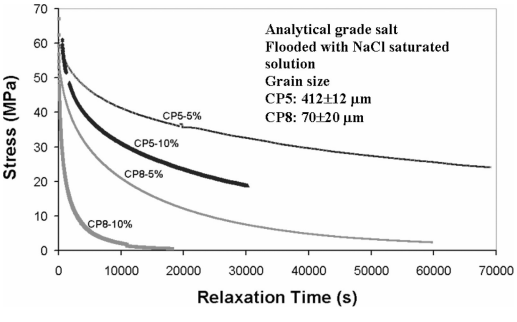

Figure 3. Stress relaxation curves of two samples with different grain size (μm) at porosity 10% and 5%. Note that the slopes are steeper in samples with higher porosity and finer grain size.

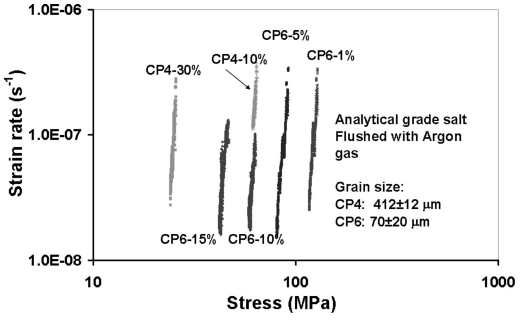

Figure 4. Strain rate vs. stress obtained from relaxation experiments of samples flushed with argon gas. Note the slopes of the curves are independent on the grain size (μm) and porosity (%).

decane) show similar behaviour to the lab air filled samples. The average n value of the lab air and decane filled samples is 5.1 (Figure 5). It is not clear if creep in lab air filled salt samples is sensitive to grain size. We have not done well-controlled experiments at the same porosity for samples with different grain size.

In the saturated solution flooded samples, the n values are nearly exactly 1, at stresses less than 15 to 20 MPa (Figure 6). In the higher stress region (>15–20 MPa), higher n values are evident (>1–6) (Figure 6). The rates are sensitive to grain size d for samples flooded with saturated solution in all stress regions tested.

High n values were obtained in the literature by several authors for rapid deformation of dry rock-salt. For dry compaction creep, Holcomb and Zeuch obtained n value of 18.5, Spiers et al. (1986) report values >20. Deformation of single crystals at high stresses normally gives high n values. Wanten et al. (1996) got an average n value of 11 from deformation experiments on single crystal at room temperature. Skvortsova et al., (2003) obtained n value of about 12 at stresses >30 MPa from their indentation experiments on flat single crystals at room temperature. Several authors infer that the mechanism in the high n value region is dislocation glide (Wanten et al., 1996;

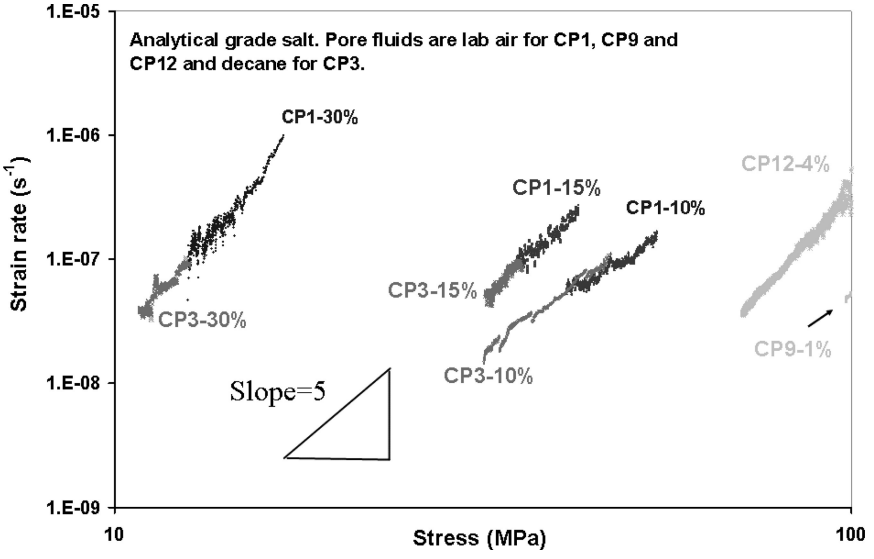

Figure 5. Strain rate vs. stress obtained from relaxation experiments on samples filled with lab air and decane. Grain size: 412 ± 12 μm for CP1, CP3, CP9; 137 ± 12 μm for CP12. Porosity indicated in %.

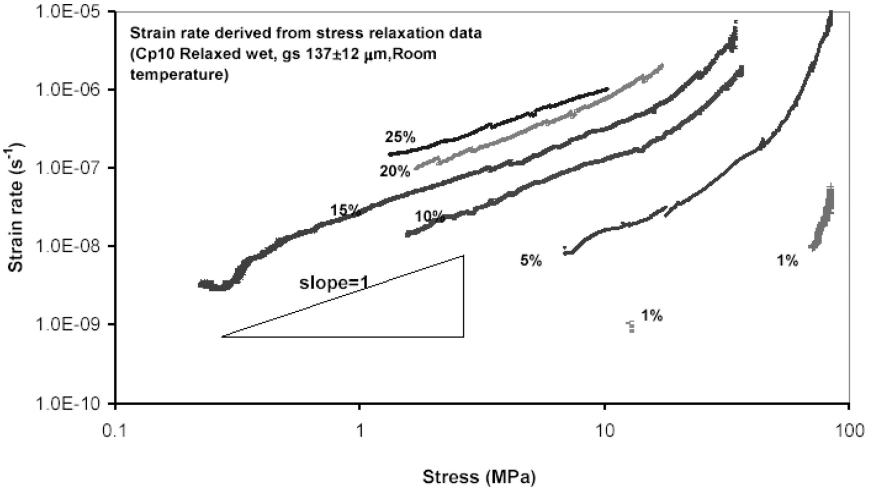

Figure 6. Strain rate vs. stress obtained from relaxation experiments on sample CP10 at different porosity (%). Sample CP10 was flooded with saturated solution.

Skvortsova et al., 2003). Very high values of n (>15) in rapidly compacted porous aggregates probably result from work hardening at grain contacts and/or a contribution of near time- independent grain rearrangement, especially at high porosity (Zhang, 1996).

Many studies on crushed rocksalt and dense rocksalt conclude that the steady state flow laws have a stress exponent of about 5. For example, the BGR rate law based on the compaction experiments of Korthaus (1996) incorporates an n value of 5, usually associated with dislocation creep. Carter & Hansen (1983) and Carter et al. (1993) obtained an value of 5.3 in the high stress region for dense rocksalt. These experiments were all carried out at nominally dry conditions.

It is well established that intact dense rocksalt normally contains 0.05–0.5wt% water, and that experiments on salt without special humidity control will always adsorb moisture from the air. The similarity of n values of our lab air samples with experiments done on dense and crushed rocksalt may suggest that

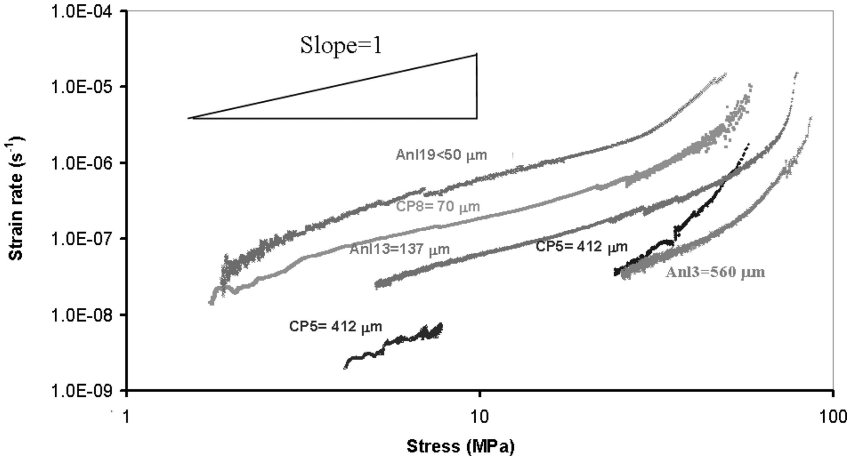

Figure 7. Strain rate vs. stress obtained from relaxation experiments of samples flooded with saturated solution at 5% porosity. Strain rates increase with decreasing grain size (μm).

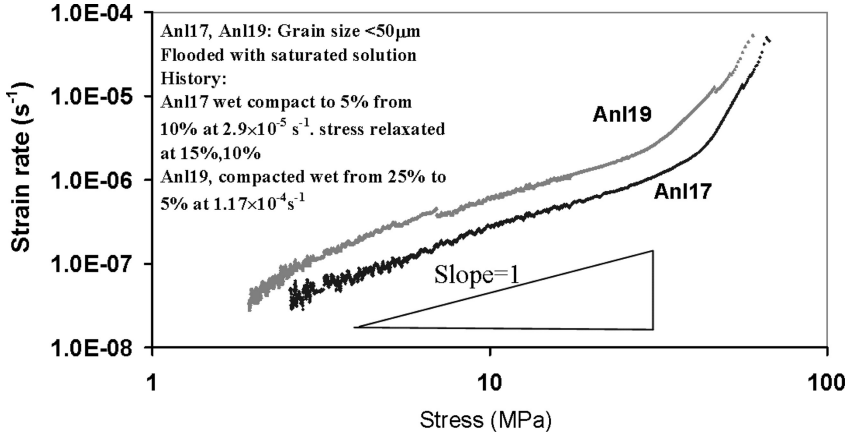

Figure 8. The effect of deformation history on the compaction creep of brine-flooded salt samples by pressure solution. Sample Anl 19 creeps faster than Anl 17 under the identical experimental conditions. The complex deformation history of Anl17 may cause grain growth prior to creep by pressure solution.

moisture or traces of brine play a similar role, though caution is needed here as steady state is not attained in relaxation.

The microstructural studies of our lab air filled sample show extensive recrystallization by grain boundary migration. The highly deformed grains with high dislocation density were replaced by recrystallized strain-free grains. The strain-free grains had subeuhedral shape and grew into the old deformed grains (Pennock et al., 2007). A non-steady state process of dislocation-dominated flow plus recrystallization by grain boundary migration, leading to $n = 5$ during relaxation, therefore seems likely.

The deformation mechanism in the saturated solution flooded samples at lower stresses (<15–20 MPa), is probably pressure solution, as evidenced by the n value of 1 and microstructural observations of solution transfer (Zhang & Grupa, 2007). In the range of porosity 25–5%, the n values are almost independent on porosity. However, when getting down to very low porosity (<5%), the n values slightly increase (Figure 6). At high stress, the n values from samples flooded with solution increase from 1 to 6. See-through experiments on single crystals immersed in saturated solution at high stress clearly showed that plasticity-coupled undercutting of grain contacts occurs under these conditions (Spiers & Brzsesowsky, 1993; Zhang & Grupa, 2007). Karcz et al. (2006) observed similar undercutting dissolution phenomena.

Although the stress sensitivity for our wet samples is in good in agreement with pressure solution, there is a difference between the grain size dependence seen in our stress relaxation experiments and conventional pressure solution compaction at lower stresses (<8 MPa) (Spiers et al., 1990; Spiers & Brzesowky, 1993). Pressure solution theory predicts an inverse grain size dependence to the power of 3 ($m = 3$) in the case of flow controlled by the grain boundary diffusion as the rate limiting step (Rutter et al., 1978). Compaction experiments on wet salt by Spiers et al. (1990) obtained m values close to 3. The m values we have obtained from our stress relaxation experiments are between 1.4 and 1.7. This discrepancy can be explained by the different deformation history. In our experiments, our samples experienced a complex deformation history, i.e. multi-step relaxations and higher stresses. The microstructure was probably modified by dislocation-coupled recrystallization or contact undercutting processes. We have compared a multi-relaxation test with a single relaxation test. The results show that the sample subjected to multistep relaxation crept slower than the single relaxation experiment. A possible explanation is that grains grow during multistep relaxation tests (Figure 8).

5 CONCLUSIONS

Our experiments show that water/moisture plays a large role in controlling the rheological properties of compacting rocksalt. In argon dry samples (no moisture) the stress exponent describing flow during relaxation is about 20, while this value drops to 5.1 if lab air is allowed to access the samples. In the argon dry samples, the creep mechanism is probably dislocation glide, with the high n-value reflecting work hardening during the pre-compaction stage. In the solution-flooded samples, the stress exponent is almost exactly 1 in the lower stress region (<20–15 MPa). These samples recrystallize by (fluid assisted) grain boundary migration, and pressure solution is the dominant deformation mechanism. In the lab air filled samples, the deformation mechanism is not easily interpreted in terms of a single mechanism. Dislocation glide coupled with contact undercutting and recrystallization by fluid assisted grain boundary migration likely control relaxation.

REFERENCES

Bechthold, W., E. Smailos, S. Heusermann, W. Bollingerfehr, Bazargan Sabet, T. Rothfuchs, P. Kamlot, J. Grupa, S. Olivella & F. D. Hansen 2004. *Backfilling and sealing of underground repositories for radioactive waste in salt (BAMBUS II project)*, Final report.

Carter, N. L., F. D. Hansen 1983. "Creep of rocksalt." *Tectonophysics*, 92, 275–333.

Carter, N. L., Horseman, S. T., Russell, J. E., and Handin, J., 1993, Rheology of rocksalt, *Journal of Structural Geology*, 15, 1257–1271.

De Bresser, J.H.P., J.H.Ter Heege and C.J. Spiers 2001. "Grain size reduction by dynamic recrystallization: Can it result in major rheological weakening?" I*nternational Journal of Earth Sciences*, 90, 28–45.

De Meer, S., C. J. Spiers & S. Nakashima 2005. "Structure and diffusive properties of fluid-filled grain boundaries: An in-situ study using infrared (micro) spectroscopy." *Earth and Planetary Science Letters* 232(3–4): 403.

Drury, M. R. and J. L. Urai 1990. "Deformation-related recrystallization processes." *Tectonophysics* 172, 235-253.

Karcz, Z., E. Aharonov, D. Ertas, R. Polizzotti & C.H. Scholz 2006. "Stability of a sodium chloride indenter contact undergoing pressure solution." *Geology* 34: 61–63; doi: 10.1130/G21772.1.

Korthaus, E. 1998. "Consolidation and deviatoric behaviour of dry crushed salt at temperatures up to 150°C." *The mechanical behaviour of salt, Proceedings of the fourth conference*, Trans Tech Publications, 365–377.

Guillopé, M. & J. P. Poirier 1979. "Dynamic recrystallization during creep of single crystalline halite: an experimental study." *Journal of Geophysical Research* 84: 5557–5567.

Holcomb, D. J., and D. H. Zeuch 1990. "Modeling the consolidation of a porous aggregate of dry salt as isostatic hot pressing." *Journal of Geophysical Research*, 95, 15, 611–15,622.

Hunsche, U. and O. Schulze 1996. "Effect of humidity & confining pressure on creep of rocksalt." in *The Mechanics Behaviour of Salt. Proceedings of the Third Conference*, Palaiseau, 1993, Trans Tech Publications, 237–248.

Hunsche, U. and O. Schulze 2002. Effect of humidity & confining pressure on creep of rocksalt, in The Mechanics Behaviour of Salt. Proceedings of the Third Conference, Palaiseau, 1993, Trans Tech Publications, 237–248.

Peach, C. J., C. J. Spiers & P. W. Trimby 2001. "Effect of confining pressure on dilatation, recrystallisation and flow of rocksalt at 150°C." *Journal of Geophysical Research* 106(B7): 13315–13328.

Rutter, E. H., Atkinson, B. K., and D. H. Mainprice 1978. "On the use of stress relaxation testing method in studies of the mechanical behaviour of geological materials." *Geophys. J, R., astr. Soc*, 55, 155–170.

Schulze, O., 1984. "Thermomechanical properties of irradiated rocksalt." *Nuclear Instruments and Methods in Physics Research*, B1: 542–548.

Shenk, O. & J. L. Urai 2004. "Microstructural evolution and grain boundary structure during static recrystallization in synthetic polycrystals of sodium chloride containing brine." *Contributions to Mineral Petrology* 146: 671–682.

Skvortsova, Z. N., I. V. Kas'yanova & V.Yu. Traskine 2003. "Indentation study of adsorption plastification of sodium chloride single crystals." *Colloid Journal* 65, 399–402.

Spiers, C. J., J. Urai, G. S. Lister, J. N. Boland & H. J. Zwart 1986. "The influence of fluid rock interaction on the rheology of salt rock and on ionic transport in the salt." University of Utrecht, 132pp.

Spiers, C. J., P. M. T. M. Schutjens, R. H. Brzesowsky, C. J. Peach, J. L. Liezenberg & H. J. Zwart, Eds. 1990. "Experimental determination of constitutive parameters governing creep of rocksalt by pressure solution." *Deformation*

Mechanisms, Rheology and Tectonics, The Geology Society, London.

Spiers, C. J and R. H. Brzesowky 1993. "Densification behaviour of wet granular salt: Theory versus experiments." *Seventh Symposium on salt*, Elsevier Science Publishers, Amsterdam. Vol. I, 83–92.

Spiers, C. J. & N. L. Carter 1998. "Microphysics of rocksalt flow in nature." *Proceedings of the Fourth Conference on the Mechanical Behaviour of Salt*, Trans Tech Publications.

Ter Heege J.H., J.H.P. De Bresser and C.J. Spiers 2005. "Rheological behaviour of synthetic rocksalt: the interplay between water, dynamic recrystallization and deformation mechanisms." *Journal of Structural Geology,* 27, 948–963.

Urai, J. L. 1983. "Water assisted dynamic recrystallization and weakening in polycrystalline bischovite." *Tectonophysics* 96: 125–157.

Urai, J. L., C. J. Spiers, C. J. Peach, R. C. M. W. Franssen & J. L. Liezenberg 1987. "Deformation mechanisms operating in naturally deformed halite rocks as deduced from microstructural investigations." *Geologie en Mijnbouw* 66: 165–176.

Urai, J. L., C. J. Spiers, H. J. Zwart & G. S. Lister 1986. "Weakening of rocksalt by water during long-term creep." *Nature* 324: 554–557.

Wanten, P. H., C. J. Spiers, and C. J. Peach 1996. "Deformation of NaCl single crystal at 0.27Tm<T<0.44 Tm, in The Mechanics Behaviour of Salt." Proceedings of the Third Conference, Palaiseau, 1993, Trans Tech Publications, 117–128.

Zhang, X. & J. Grupa 2007. "Compaction behaviour and permeability of low porosity compacted salt grit (dry and wet)." *NRG report*, 21146/06.77412/P, Petten, The Netherland.

The Mechanical Behavior of Salt – Understanding of THMC Processes in Salt –
Wallner, Lux, Minkley & Hardy, Jr. (eds)
© 2007 Taylor & Francis Group, London, ISBN 978-0-415-44398-2

Deformation mechanisms and rheology of Pre-cambrian rocksalt from the South Oman Salt Basin

J. Schoenherr, Z. Schléder*, J.L. Urai
Geologie – Endogene Dynamik, RWTH Aachen University, Germany
*(*now Midland Valley Exploration Ltd., United Kingdom)*

P.A. Fokker
Shell International Exploration and Production B.V. Rijswijk, The Netherlands

O. Schulze
Bundesanstalt für Geowissenschaften und Rohstoffe, Hannover, Germany

ABSTRACT: The Neoproterozoic to Early Cambrian Ara Salt from the South Oman Salt Basin has been investigated for creep behavior and microstructure. The salt behavior is of relevance for oil production out of intra-salt carbonate "stringers". Test and in-situ conditions are about $T = 100°C$ and $p_c = 70$ MPa. Strain rate stepping and temperature stepping tests have been performed, with creep rates varying from 5 10^{-8} to 10^{-5} s^{-1}. All tests were run to a total strain of 25–30%. Both secondary and primary creep parameters have been determined. Secondary creep is basically reached only at rates of 10^{-7} s^{-1} or lower (15 MPa differential stress or lower), still orders of magnitude faster than expected in-situ rates, except perhaps borehole closure related creep during drilling. Microstructural observations revealed that the main deformation mechanism during the tests was dislocation creep associated with grain boundary migration recrystallization. This is evidenced by subgrain size reduction, the development of slip lines and the formation of new strain-free grains growing at the expense of subgrain-rich grains. Comparing literature data, the Ara Salt appears to be quite common (average), both under the microscope as in creep behavior.

1 INTRODUCTION

1.1 *Experimental deformation of halite*

The vast amount of experimental creep data on halite shows that there is a significant factor of 100–1000 variation in creep rate for different types of natural halite deformed under same stresses and temperatures, due to differences in chemistry, water content, secondary phases and deformation history. By comparing dry versus wet (Ter Heege et al., 2005), pure versus doped (Heard and Ryerson, 1986), second phase free versus dirty (Hunsche et al., 2003) and annealed versus deformed samples (Ter Heege et al., 2005) we gained a first order approximation of the influence of these parameters on creep rate of halite and also on the physics behind the individual processes. However, when more variables are simultaneously present, it is still poorly known, how these processes interact and what their exact influence on rheology is. It is still impossible to predict creep rate parameters with any accuracy from chemical analysis and microscope studies. Lab creep testing will hence still be required.

The draw back of creep tests is that true simulation of relevant in-situ creep rates (10^{-9} to 10^{-13} s^{-1} for mining and oil-gas extraction related creep deformation) would require very long lasting experiments, since the creep rate must be maintained for several percents of strain to reach a steady state strain rate. This problem is normally solved by extrapolation from experiments done at higher than natural strain rate, stress or temperature. However, such an extrapolation is only valid, if the deformation mechanisms remain the same in the experiment and in nature.

Microstructure analyses provide insights into the correct, mechanism-based deformation processes. The constitutive models (including recrystallization processes) have to be used to verify the validity of extrapolation of laboratory data to natural conditions.

Although both, microstructure study and experiments on synthethic salts help to predict the rheology, the only way to derive this for a specific salt type is to carry out a set of triaxial tests, which establishes required parameters for describing rheology. This was performed for the Infra-Cambrian Ara Salt,

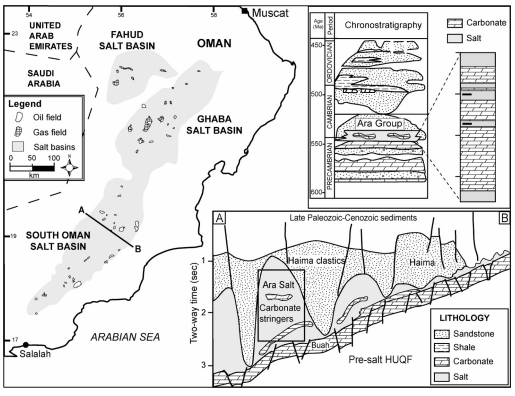

Figure 1. Overview map of salt basins in the deep subsurface of interior Oman (grey) and associated oil and gas fields. The simplified cross section illustrates Ara Salt diapirs, which enclose isolated Ara carbonate "stringer" reservoirs; frame highlights Ara Group (compiled from Peters et al., 2003 and Qobi et al., 2001) and inset upper right, showing the chronostratigraphy of the SOSB and the position of Infra-Cambrian Ara Group. Thick black horizontal lines in the lithological section mark salt cores investigated for this study; note that tick marks represent 50 m intervals.

which forms a number of large salt diapirs in the South Oman Salt Basin (SOSB) at a depth of 3 to 5 km. It encases highly over-pressured carbonate reservoirs (the so-called "stringers") for oil and gas (Fig. 1).

Previous studies of the Ara Salt have shown that it once lost its seal capacity in the direct vicinity ($\sim$ 10 m of vertical distance) of the stringer reservoirs, which is evidenced by the presence of solid bitumen at grain boundaries and microcracks (Schoenherr et al., submitted). At the same time, this salt shows widespread evidence for intracrystalline plastic deformation by the presence of subgrains. Using subgrain size piezometry and the well established correlation between subgrain size and remaining in-situ stress (Carter et al., 1993), the calculated maximum past differential stress for the Ara Salt around the stringer reservoirs is less than 2 MPa.

The mechanical and transport properties of this salt are of relevance in predicting seal capacity, flow of salt around boreholes and in geomechanical modeling of the salt loading (compression) of the "stringer" reservoirs during production. Thus, the aim of our deformation experiments was to obtain as much as possible information on the rheological properties of Ara Salt under in-situ conditions and low strain rates, corresponding to deformations around a producing carbonate stringer reservoir over decades.

1.2 *Deformation mechanisms in halite*

Based on laboratory experiments, deformation of halite at high (or medium) confining pressures is dominated by different deformation mechanisms: dislocation cross-slip (CS), dislocation climb (CL) and pressure solution (PS). Several studies on natural halite indicate that at geological strain rates salt is in the transition regime where both dislocation creep and solution-precipitation creep mechanisms operate (e.g. Ter Heege et al., 2005). Assuming that dislocation creep processes and pressure solution act in parallel and in absence of microcracking, the steady-state flow of natural halite can be approximated by the following equation (Spiers and Carter, 1998):

$$\dot{\varepsilon} = \dot{\varepsilon}_{CS} + \dot{\varepsilon}_{CL} + \dot{\varepsilon}_{PS} \tag{1}$$

where $\dot{\varepsilon}$ is the total strain rate in s^{-1}, $\dot{\varepsilon}_{CS}$ and $\dot{\varepsilon}_{CL}$ are strain rates from dislocation creep processes, and $\dot{\varepsilon}_{PS}$ is the strain rate from pressure solution.

Dislocation creep behavior is characteristic in experiments using natural samples with grain sizes over 2 mm. The deformation mechanism is a combination of dislocation climb and dislocation cross-slip (Carter et al., 1993), in wet halite usually accompanied with dynamic recrystallization by fluid-assisted grain boundary migration. The combined creep mechanism is usually treated as a single combined creep mechanism for practical reasons. For halite, the strain rate ($\dot{\varepsilon}$) can be related to the flow stress (σ) using a power law creep equation:

$$\dot{\varepsilon} = A_1 \, exp\left(\frac{-Q_1}{RT}\right)(\sigma_1 - \sigma_3)^n \tag{2}$$

where the pre-exponential constant A is expressed in $MPa^{-n}\,s^{-1}$, Q is the apparent activation energy for creep in $J\,mol^{-1}$, the gas constant R is in $J\,mol^{-1}K^{-1}$, the temperature T is in K, the differential stress $(\sigma_1 - \sigma_3)$ is in MPa and n is the dimensionless stress exponent. A somewhat more scientific notation would be:

$$\dot{\varepsilon} = A_1 \exp\left(\frac{-Q_1}{RT}\right)\left(\frac{\sigma}{\sigma_\#}\right)^n \tag{2a}$$

where A_1 is in s^{-1}, σ is the *Von Mises* stress in MPa ($=\sigma_1 - \sigma_3$ for triaxial loading) and $\sigma_\#$ is a unifying constant of 1 MPa.

2 METHODS

2.1 *Triaxial creep tests*

The triaxial creep tests were carried out at the laboratories of the Bundesanstalt für Geowissenschaften und Rohstoffe (BGR), in Hannover, Germany. The creep tests were performed on cylindrical 50 × 100 mm samples and designed to best represent the in-situ conditions at a depth of $\sim$5 km in the Ara Salt interval.

For all experiments sample preparation was the same, which involves adding 50 or 20 ml brine (∼35 drops) in between the jacket and the sample to restore the small amounts of water, which is always present in natural salt rocks (Roedder, 1984; Urai et al., 1986) but may have been lost during storage. The sample was put into the creep machine together with a thin Teflon foil between the ends of the sample and driving the pistons to minimize friction and barreling. The starting (confining) pressures were $p_c = 3.5$–4 MPa with a starting stress of $\sigma_1 = 4.5$ MPa and 6 MPa. After this, the sample was heated up to the required temperature (80, 100, 120°C) with <30°C/h. The pressure was then increased hydrostatically with ∼1 MPa/min until $p_c = 70$ MPa and $\sigma_1 = 72$ MPa. During the experiments the p_c was kept at ∼70 MPa. The samples were dismantled and machined down (de-barreling) at 10% and 20% or at 15% depending on the test sequence.

2.2 *Microstructure analysis*

From the original halite cores we cut a 1 cm thick slab parallel to the long axis of the core, using a diamond saw cooled by water to avoid microcracking of the sample. This slab is used as an undeformed reference material. From the remaining material cylindrical samples were machined down for the creep tests. After the creep tests, 1 cm thick slabs were cut from the deformed cores parallel to the deformation axis. Following the conventional method at the institute of *Geologie–Endogene Dynamik, RWTH Aachen*, from both slabs, the experimentally undeformed material and the experimentally deformed material double polished and etched thick sections (∼1.5 mm) were prepared.

Note that, for the sake of simplicity, we introduced short laboratory sample names to refer to the Ara Salt samples (AS) and experiments, respectively (e.g. AS 1). For similar reasons, we use the term of "undeformed" for denoting the naturally deformed samples and the term "deformed" for experimentally deformed samples.

3 RESULTS AND DISCUSSION

3.1 *Triaxial creep tests*

In this paragraph we describe some of the six deformation tests, which is followed by a characterization of the corresponding microstructures. Six creep tests were performed and corrected for measured piston friction (1.5 MPa). All but one are strain rate stepping tests performed at 100°C.

The stress-strain curve of experiment AS 4 shows three steps, which correspond to a temperature decrease from 120°C (0–10%), to 100°C (10%–20%) to 80°C at 20%–30% strain (Fig. 2c). Each temperature step of this test is characterized by an increase

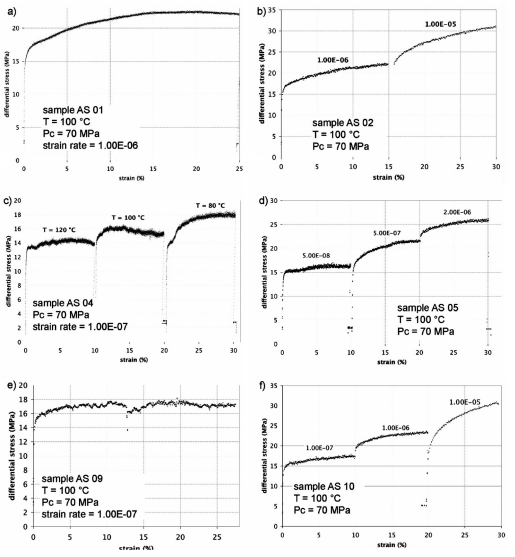

Figure 2. Stress–strain curves for Ara Salt creep experiments; test parameters are indicated by insets. a) Creep test AS 1 shows primary creep until a strain of ∼17%, followed by steady state creep. b) Each strain rate step of test AS 2 shows continuous strain hardening. The gap at 15% strain is due to interruption of the test during machining down the sample. c) Stress-strain curve for the AS 4 experiment at a strain rate of 10^{-7} s^{-1} and three temperature steps. d) Creep test AS 5 has three strain rate steps. True steady state conditions were only reached between 8–10% strain in the 5×10^{-8} s^{-1} strain rate step, while the other steps still show signs of strain hardening. e) The creep curve of sample AS 9 shows steady state from a strain of ∼8%. Small oscillations may be a result of competing processes of strain hardening and strain softening. f) Creep curve of test AS 10 shows three strain rate steps from 10^{-7} to 10^{-5} s^{-1}. The 10^{-6} s^{-1} step appears to approach steady state in the last few percents of strain.

of ∼2 MPa in differential stress due to the decreasing temperature. Steady state flow occurred in all temperature steps. This test was designed to estimate the activation energy Q for the secondary creep law.

The AS 9 test was performed at a constant strain rate of 10^{-7} s^{-1} to a total strain of about 27% (Fig. 2e). The resulting microstructures of both processes, i.e. subgrains and lobate grain boundaries were observed in this sample (Figs. 5a and 5c).

The differential stress and steady state strain rate data were plotted in order to determine the relative position of the Ara Salt rheology to other reported halites (Fig. 3). The reason for the lack of the steady-state conditions in some experiments (AS 2 and partially AS 10) results from the relatively high strain rate. Only the rates at or below 10^{-7} s^{-1} displayed steady state within 10–15% of strain. Figure 3 shows that Ara Salt rheology is comparable with the most common halite (e.g. Asse, Gorleben) for which an extensive

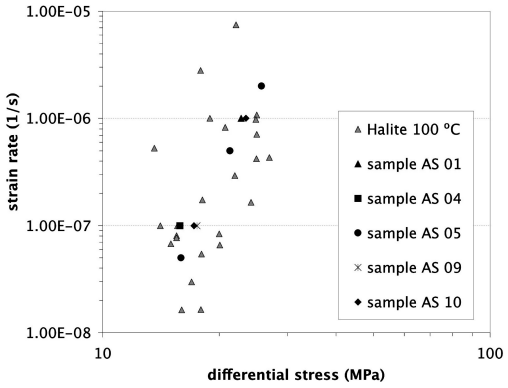

Figure 3. Experimental creep data from the Ara Salt tests (black symbols). For comparison the test results are plotted with halite from various sources (gray triangles), which has been deformed under similar conditions, i.e. at 100°C (Hansen and Carter, 1984; Senseny, 1988; Horseman and Handin, 1990; Hunsche et al., 2003; Ter Heege et al., 2005).

dataset is available (Table 1). As a result of the limited range in strain rates at which steady state creep occurred, it is impossible to pinpoint the exact power n. With some assumptions on the primary creep mechanism, we can limit the range to about 4–6. We assume that in-situ, the Ara Salt has the most commonly used stress exponent n for halite, which is ∼5.

In the literature, many flow laws were published for different types of halite (Table 1). These flow laws differ in A, Q and n values. If we assume the $n = 5$ value discussed above, we are able to deduce the minimum activation energy Q from the stepped temperature experiment AS 4 by plotting 1/T versus ln (differential stress). Then, Q is 32400 J mole^{-1} and the pre-exponential A is 1.82×10^{-9} (MPa^{-n}) s^{-1} (Table 1 and Eq. 2 and 2a).

3.2 *Microstructural evolution*

3.2.1 *Undeformed samples*

The starting (undeformed) material consists of almost pure colorless halite with 2–3% impurities of fine-grained idiomorphic anhydrite crystals and minor fine-grained carbonate grains. Grain size analysis revealed a grain size distribution between 0.5–7 mm with a mean equivalent circular diameter (ECD) of 2 mm.

In all samples, some anhedral grains contain cube-shaped fluid inclusions in its centre, which are aligned in more or less parallel bands alternating with fluid inclusion-poor bands (Fig. 4a). Analyses of homogenization temperature of similar fluid inclusions microstructures suggest that one pair of a fluid inclusion-rich and a fluid inclusion-poor band reflect daily temperature variations of the brine, from which the crystal precipitated (Benison and Goldstein, 1999). Thus, such grains are considered to be of primary (syn-depositional) origin (Roedder, 1984). Grain boundaries generally contain abundant isolated and amoeboid fluid inclusions under transmitted light (Fig. 4b), which probably derive from the liberation of the primary fluid inclusions due to grain boundary migration recrystallization (GBMR) (Schléder and Urai, 2005). When the (Schléder and Urai, 2005). When the migrating grain boundary reaches the fluid inclusion, its content is collected and redistributed at the grain boundary (Schenk and Urai, 2005). Under reflected light, GBMR is also indicated by strain-free crystals, which show lobate grain boundaries related to substructure-rich grains (Fig. 4c). Fluid inclusions trails, which are aligned parallel to the lobate grain boundaries and terminations of small isolated fluid inclusions at the grain boundary, indicate that GBMR was fluid-assisted. Other less substructured grains show elongated subgrains with an orientation perpendicular to grain boundaries (Fig. 4d). This points to the operation of dislocation creep processes due to GBMR.

The experimentally undeformed samples are (incompletely) dynamically recrystallized as shown by anhedral primary grains (Fig. 4a). Grain boundary migration processes are indicated by substructure-free

Table 1. Literature creep data for various halite types and data from this study.

Source	Halite type	A (MPa-n s^{-1})	Q (J mol^{-1})	n
Wawersik and Zeuch (1986)	Salado	8.82E−06	50160	4.9
	Salado	2.71E−03	69180	5.1
	Asse	7.26E−06	53920	5.0
	West Hackbr.	3.15E−05	54840	4.7
	Bryan mound	8.93E−05	63290	4.5
	Bryan mound	7.78E−03	74530	5.2
	Bayou Choctaw	3.94E−06	49450	4.1
Spiers et al. (1990)	Synthetic	4.70E−04	24530	3.0
Carter et al. (1993)	Avery Island	1.60E−04	68100	5.3
	Avery Island	8.10E−05	51600	3.4
Ter Heege et al. (2005)	Synthetic wet salt	2.75E−02	80000	5.6
This study	Ara Salt	1.82E−09	32400	5.0

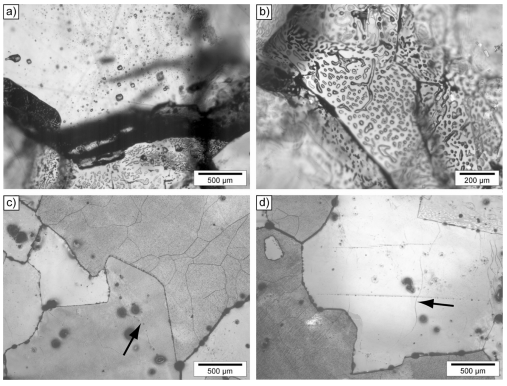

Figure 4. Microstructures of undeformed samples. a) Transmitted light micrograph shows relicts of a primary crystal with numerous fluid inclusion bands and fluid-filled tubes and bubbles at grain boundary in lower part of micrograph (sample AS 1). b) Transmitted light micrograph of sample AS 9 shows arrays of fluid-filled tubes and isolated fluid inclusions at grain boundaries. c) Reflected light micrograph shows <200 µm-sized subgrains in crystal upper right and strain-free crystals below. Note array of fluid inclusions (arrow) indicating position of a grain boundary before migration (sample AS 1). d) Reflected light micrograph shows less substructured grain with elongated subgrains (arrow). Grain boundary is interpreted to have migrated to lower left. Note small (new) strain-free crystal in large (old) subgrain-rich crystal at upper left (sample AS 1).

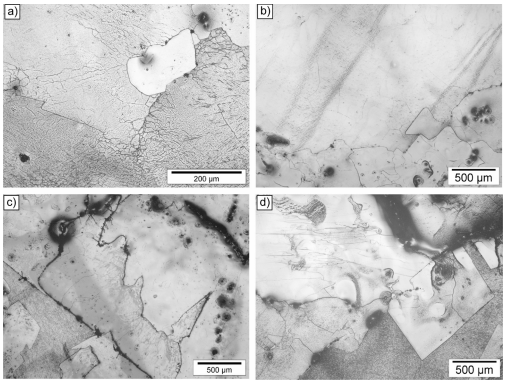

Figure 5. Reflected light micrographs of deformed samples. a) Sample AS 9 shows grains with much smaller subgrain size as in corresponding undeformed sample (compare with fig. 4b). Note development of new strain free grain between old dislocation-rich grains. b) Micrograph shows linear to wavy slip lines, running from upper right to lower left. The slip lines abruptly end at grain boundaries lower left and centre right, which is probably the result of later replacement by GBMR (sample AS 1). c) Highly serrated grain boundary between "new" strain-free grain (upper right) and substructured "old" grain. d) Micrograph shows complex structure in sample AS 1: "old" grain lower left (with <200 µm-sized subgrains) is partly replaced by "new" grain at lower right (with <20 µm-sized subgrains). Large grain at the upper part of image showing elongated subgrains replaced "old" and "new" grain. Finally, the subidiomorphic grain at the right grew at the expense of all grains.

Table 2. Maximum in-situ differential paleo-stress of undeformed Ara Salt cores calculated from subgrain size.

Sample	No. of subgrains	Subgrain diameter (μm)	Differential stress (MPa)
AS 3	106	222	0.96
AS 9	76	208	1.01

grains, which show a lobate-shaped geometry with respect to the substructured ones. Under reflected light, most grains show 150–300 µm-sized subgrains (Fig. 4c), which indicate a maximum past differential stress of ~ 1 MPa (subgrain size piezometry using data of Carter et al., (1993) and Franssen (1993); for results see Table 2).

3.2.2 *Deformed samples*

The final microstructure (after 25–30% strain) of the deformed Ara Salt shows that grain size slightly decreased (average grain size is ~ 1.5 mm). Most grains exhibit internal substructure such as ~30 µm-sized subgrains (Fig. 5a) and linear to wavy slip lines (Fig. 5b), the latter probably indicating cross slip of screw dislocations (Carter et al., 1993). The substructured grains are, in places consumed by new strain-free grains (Figs. 5a and 5c–d) by grain boundary migration, which is shown by highly serrated grain boundaries (Fig. 5c). Those grain boundaries show less fluid inclusions than grain boundaries in the undeformed samples.

The most significant differences between microstructures of the starting and deformed material are:

- subgrain size reduction from 150–200 µm to 10–50 µm
- no crystals with (primary) fluid inclusion bands were observed in the deformed samples
- presence of slip lines in the deformed samples
- replacement of grains with 150–200 µm-sized subgrains by almost strain-free grains in deformed samples

We interpret these differences due to dynamic recrystallization of the halite during the experiments, which produces some obvious changes in the microstructure. This is shown for instance by the absence of primary fluid inclusion bands, which have been consumed by GBMR. It has been shown that dislocation creep processes were active during the experiments, which are responsible for the continuous strain hardening at the higher strain rates. This is

indicated by reduced subgrain size and the presence of slip lines. During deformation with the very low strain rates GBMR most likely operated in the later stage of the experiments (probably due to strain softening) as suggested by new strain-free grains grown at the expense of grains exhibiting 10–50 μm-sized subgrains. GBMR most likely removed the primary fluid inclusions, which were then liberated during fluid-assisted grain boundary migration.

3.3 *Primary versus secondary creep*

The test results were fitted with a combined hardening and softening law, the hardening (primary creep) law being derived from Fokker (1995), which can be translated to a *Lemaître* type of creep equation. The primary creep mechanism is not important for halite response on reservoir rocks (given the slow loading during decades) but might be of importance for bore hole closure during drilling. Unraveling the mechanism gives some clues on the applicable mechanisms.

Equation 3 shows the applied hardening and softening law. The total (vertical) strain is denoted by ε, the strain softening by secondary creep (calculated via Equation 2a) is denoted as ε_s and a correction strain is denoted by ε_{corr}.

$$\dot{\varepsilon} = A_p \exp\left(\frac{-Q_p}{RT}\right)\left(\frac{\sigma}{\sigma_0(\varepsilon - \varepsilon_s - \varepsilon_{corr})^{\beta}}\right)^m \qquad (3)$$

The correction strain is some strain hardening or strain softening effect due to the coring, machining or annealing, when no strain rate is applied on the sample. It is likely that during the build-out, build-in procedure for machining down the sample, some "strain softening" or annealing occurs, evidenced by repeated strain hardening effects at unchanged rates. Since the strain rate stepping was only performed at constant temperatures, we presumed an activation energy equal to the secondary creep mechanism ($Q_p = Q_s$), a hypothesis which was not tested.

The best fitting set of parameters for all creep tests appears to be: $m = 10$; $\beta = 0.18$; $\sigma_0 = 22$ MPa; $A_p = 0.00354\ s^{-1}$. Note that σ_0 is interdependent with A_p and m. The primary creep law hence only requires 3 parameters to fit for constant temperature tests.

Figure 6 shows the resulting stress-strain simulation for the test on sample AS 5. The best fit could be obtained by assuming a negative (hardening) strain correction of 4% at the beginning of the test and positive strain (softening) of 4% and 1.5% during the (dis)mounting and machining of the samples.

3.4 *Test procedures*

The applied test temperature of 100°C is simply too low to obtain steady state creep at strain rates that differ an order of magnitude and are within the strain rate potential of the applied test apparatus. If similar tests should be repeated, it should be considered to run constant stress test for the lower strain rates or to modify the machines to be able to handle slower strain rates ($10^{-8}\ s^{-1}$).

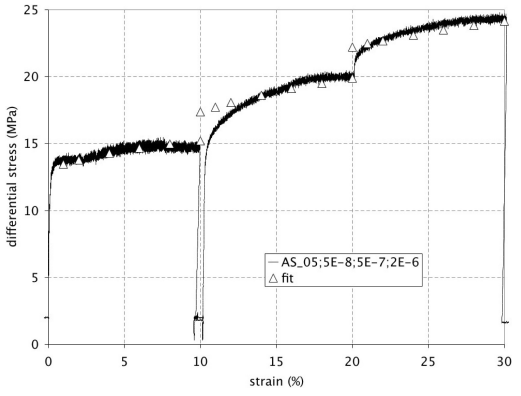

Figure 6. Creep rate fit for sample AS 5 with increasing creep rates of $5 \times 10^{-8}\ s^{-1}$, $5 \times 10^{-7}\ s^{-1}$ and $2 \times 10^{-6}\ s^{-1}$. The triangles represent the fit.

When halite samples are strained to 20–30%, they require machining down to prevent excessive barreling and sleeve failure. Advantage of using the same sample for 2–3 tests is that one is sure that there is no sample-to-sample variation. The high achieved strains do not enhance the reaching of steady state though, since healing effects are operating in the period that the sample is reworked, part of the period being at or near the test temperature. For the derivation of steady state parameters it is hence important to obtain steady state within 10–15% of strain, hence applying low strain rates or high(er) test temperatures.

4 CONCLUSIONS

The Ara Salt is comparable with the most common halite rocks for which an extensive dataset is available (e.g. Hunsche et al., 2003).

The basic results and conclusions are summarized:

1. The steady state mechanical data for the Ara Salt can be described by a power law equation with $n = 5$, $Q = 32400\ J\ mole^{-1}$ and $A = 1.82 \times 10^{-9}\ s^{-1}$. Separate primary creep parameters have been derived.
2. Microstructure analysis has shown that dislocation creep processes led to the reduction in subgrain size and the formation of (wavy) slip lines. In addition, fluid-assisted grain boundary migration recrystallization triggered growth of new strain-free grains, which replaced grains with a high dislocation density.

3. Test procedures for "deep salt" should be focused on obtaining steady state creep within 10–15% of strain with at least one order of magnitude in strain rates. Tests in the twilight zone of primary and secondary creep are more difficult to analyze.

ACKNOWLEDGMENTS

The authors thank the Ministry of Oil and Gas in the Sultanate of Oman for permission to publish these results and Petroleum Development Oman for providing the salt cores.

REFERENCES

Benison, K.C. and Goldstein, R.H. 1999. Permian paleoclimate data from fluid inclusions in halite. Chemical Geology, 154: 113–132.

Carter, N.L., Handin, J., Russell, J.E. and Horseman, S.T. 1993. Rheology of rocksalt. Journal of Structural Geology, 15(9/10): 1257–1271.

Fokker, P.A. 1995. The behaviour of salt and salt caverns. PhD Thesis, Delft University.

Franssen, R.C.M.W. 1993. Rheology of synthetic rocksalt with emphasis on the influence of deformation history and geometry on the flow behaviour. PhD Thesis, Rijksuniversiteit Utrecht.

Hansen, F.D. and Carter, N.L. (1984) Creep of Avery Island rocksalt. Proceedings of the first Conference on mechanical Behavior of Salt, Clausthal-Zellerfeld, Germany, Trans. Tech. Publications: 53–69.

Heard, H.C. and Ryerson, F.J. 1986. Effect of cation impurities on steady-state flow of salt. In: B.E. Hobbs and H.C. Heard (Editors), Mineral and rock deformation: laboratory studies. AGU Geophysical Monograph. American Geophysical Union, 36: 99–115.

Horseman, S.T. and Handin, J. 1990. Triaxial compression tests on rocksalt at temperatures from 50°C to 200°C and strain rates from 10^{-4} to 10^{-9} 1/s. In: A.G. Duba, W.B. Durham, J.W. Handin and H.F. Wang (Editors), The brittle-ductile transition in rocks. American Geophysical Union, 56: 103–110.

Hunsche, U., Schulze, O., Walter, F. and Plischke, I. 2003. Projekt Gorleben. Thermomechanisches Verhalten von Salzgestein. 9G2138110000, BGR, Hannover.

Peters, J.M., Filbrandt, J.B., Grotzinger, J.P., Newall, M.J., Shuster, M.W., Al-Siyabi, H.A. 2003. Surface-piercing salt domes of interior North Oman, and their significance for the Ara carbonate "stringer" hydrocarbon play. GeoArabia, 8(2): 231–270.

Qobi, L., de Kuijper, A., Ming Tang, X. and Strauss, J. 2001. Permeability determination from stoneley waves in the Ara Group carbonates, Oman. GeoArabia, 6(4): 649–666.

Roedder, E., 1984. The fluids in salt. American Mineralogist, 69: 413–439.

Schenk, O. and Urai, J.L. 2005. The migration of fluid-filled grain boundaries in recrystallizing synthetic bischofite: first results of in-situ high-pressure, high-temperature deformation experiments in transmitted light. Journal of metamorphic Geology: 695–709.

Schléder, Z. and Urai, J.L. 2005. Microstructural evolution of deformation-modified primary halite from the Middle Triassic Röt Formation at Hengelo, the Netherlands. International Journal of Earth Sciences, 94(5–6): 941–955.

Schoenherr, J., Urai, J.L., Kukla, P.A., Littke, R., Schléder, Z., Larroque, J.M., Newall, M.J., Al-Abry, N., Al-Siyabi, H.A., Rawahi, Z. submitted. Limits to the sealing capacity of halite: A case study of the Infra-Cambrian Ara Salt from the South Oman Salt Basin.

Senseny, P.E. (1988) Creep properties of four salt rocks. Proceedings of the Second Conference on mechanical Behavior of Salt, Clausthal-Zellerfeld, Germany, Trans. Tech. Publications: 431–444.

Spiers, C.J., Schujtens, P.M.T.M., Brezowski, R.H., Peach, C., Liezenberg, J.L., Zwart, H.J. 1990. Experimental determination of constitutive parameters governing creep of rocksalt by pressure solution. In: R.J. Knipe and E.H. Rutter (Editors), Deformation mechanisms, rheology and tectonics. Geological Society of London Special Publications, 54: 215–227.

Spiers, C.J. and Carter, N.L. (1998) Microphysics of rocksalt flow in nature. Fourth Conference on the Mechanical behaviour of Salt, The Pennsylvania State University, June 17 and June 18, 1996, Trans Tech Publication Series on Rock and Soil Mechanics, 22: 115–128.

Ter Heege, J.H., De Bresser, J.H.P. and Spiers, C.J. 2005. Rheological behaviour of synthetic rocksalt: the interplay between water, dynamic recrystallization and deformation mechanisms. Journal of Structural Geology, 27(6): 948–963.

Urai, J.L., Spiers, C.J., Zwart, H.J. and Lister, G.S. 1986. Weakening of rocksalt by water during long-term creep. Nature, 324: 554–557.

Taylor & Francis
Taylor & Francis Group
http://taylorandfrancis.com

The Mechanical Behavior of Salt – Understanding of THMC Processes in Salt –
Wallner, Lux, Minkley & Hardy, Jr. (eds)
© 2007 Taylor & Francis Group, London, ISBN 978-0-415-44398-2

Evolution of a young salt giant: The example of the Messinian evaporites in the Levantine Basin

C. Hübscher & G.L. Netzeband
Institute for Geophysics, Center for Marine and Atmospheric Sciences, University of Hamburg, Germany

ABSTRACT: Recently published academic and industrial 2D- and 3D-seismic data elucidate early stages of the evolution of the Messinian evaporites in the Levantine Basin/eastern Mediterranean. The tabular evaporites within the basin represent a salt giant which was deposited in a deep basin-shallow water environment. Six evaporitic sequences have been identified within the entire basin. Four units are interpreted as massive halite units and two of them as alternating successions of clastic sediments and/or evaporitic facies. Individual deformation of the intra-evaporitic sequences like folding and thrusting strongly suggests tectonic shortening during the depositional phase. A second thin-skinned tectonic phase started at the upper Pliocene when the prograding shelves and slopes squeezed the evaporites basinward. There is a clear line of evidence for fluid flow through and out of the evaporites.

1 INTRODUCTION

Owing to its special rheology, salt is capable of decoupling deep rooted tectonics from the supra-salt response. Salt tectonics controls the formation of complex traps for hydrocarbon or metals. Lateral salt flow may cause subaerial or submarine land slides. Salt diapirs are potential waste repositories. The interaction of fluids and salt may cause subrosion and subsequent surface collapses with a potential impact on civil infrastructures. Owing to their impermeability evaporites control fluid dynamics and hydrocarbon distribution. The thorough understanding and prediction of salt tectonics and fluid dynamics is therefore fundamental in frontier research and it is crucial to develop ways to optimise exploitation and risk assessment. However, in spite of their general importance within the earth system there is a significant lack of knowledge about the early evolution of juvenile salt giants and their controlling factors.

The Levantine Basin in the south-eastern Mediterranean Sea is a world class site for studying the early evolution of such a salt giant, since the Messinian evaporites (ME) are comparatively young, the sediment load varies along the basin margin, they are little tectonically overprinted, and the geometry of the basin and the overburden is well-defined. On the regional scale, the high interest in the analysis of the ME is based on the fact that the so called Messinian Salinity Crisis (MSC) represented the most significant environmental change in the Mediterranean realm. The reconstruction models are based on the analysis of evaporites in the marginal basin, which led partly to contradictory models (see Rouchy & Caruso 2006 and the references therein).

During the last few years, new attempts were made to unravel the structural evolution of the ME in Levantine Basin and associated fluid dynamics. Since 2004 several studies were published in which the evolution of the Levantine basin is discussed by means of academic seismic data. (Loncke et al. 2004, Gradmann et al. 2005, Loncke et al. 2006, Netzeband et al. 2006a, b). The release and subsequent publication of industrial 2D and 3D-seismic data led to a giant step forward in the understanding of salt tectonic related processes (Frey-Martinez et al. 2005, Bertoni & Cartwright 2005, 2006, in press a, b, Gardosh & Druckmann in press). In this paper we will summarise the recent achievements in understanding salt dynamics in the Levantine Basin and will point out the ongoing debates.

2 GEOLOGICAL FRAMEWORK

The Levantine Basin in the south-eastern Mediterranean Sea is bounded to the south by the Egyptian and to the east by Levantine coast (Fig. 1). The Eratosthenes Seamount in the north-west of the basin is considered to be a continental fragment of the African plate (Makris et al. 1983). Between the Eratosthenes

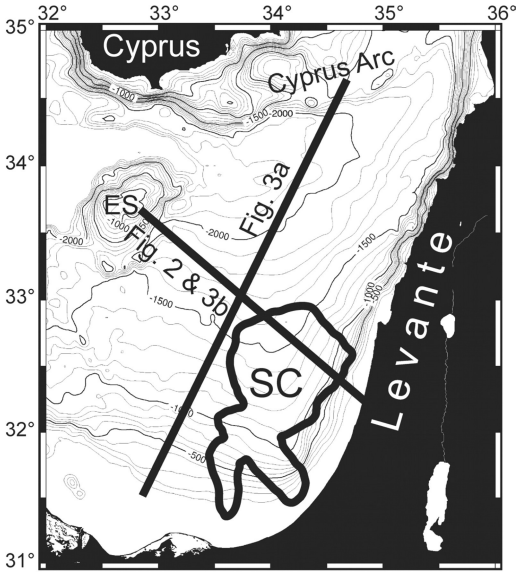

Figure 1. Map of the Levantine Basin. Black lines show locations of cross-section in Fig. 3. ES: Eratosthenes seamount; SC: slump complex (after Frey-Martinez 2005).

Seamount and the Egyptian coast there is the gateway to the Herodotus Basin to the west. The Levantine Basin includes the northward moving African plate, the postulated Sinai sub-plate (Almagor 1993, Mascle et al. 2000), the N–NW moving Arabian plate, and the westward moving Anatolian plate. The Cyprus Arc, which results from the collision between the African and Eurasian plate represents the northern boundary (e.g., Robertson et al. 1998; Vidal et al. 2000a).

Recent studies suggest that the underlying crust of the Levantine Basin is of continental origin (Vidal et al. 2000b, Gardosh and Druckman 2006, Netzeband et al. 2006b). The basin-fill deposits have a thickness of 14–16 km (Netzeband et al. 2006b, Gardosh and Druckmann, 2006, Fig. 2). The basin is considered to be a relic of the Mesozoic Neo-Tethys Ocean (Robertson and Dixon 1984, Garfunkel 2004). The initial rifting occurred in the Middle Triassic in a northwest-southeast direction (Garfunkel 1998, Robertson 1998). Inversion and hence contraction pulses started in the Upper Cretaceous and ended in the Miocene. The folding was associated with the closing of the Neo-Tethyan ocean, the so-called Syrian Arc inversion and contraction (Gardosh & Druckmann 2006). A number of smaller fault zones were interpreted in the Levantine Basin, which were associated with the rifting and contraction phase. Several SW–NE striking shear zones converge towards the north, e.g., the Pelusium Line, the Hinge Line and the Damietta-Latakia Line (Neev 1975, 1977, Neev et al. 1976, Abdel Aal et al. 2000). There is some evidence that these faults are still

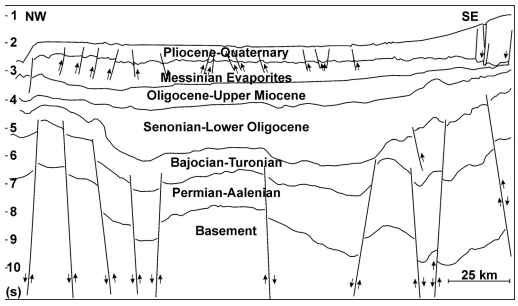

Figure 2. Line-drawing of a seismic time section between the central Levantine coast and the Eratosthenes seamount (after Gardosh & Druckmann in press).

active (Gradmann et al. 2005, Netzeband et al. 2006a), however, as shown by Gardosh & Druckmann (2006, Fig. 2), these faults do not significantly overprint the Miocene to recent succession in the central basin.

In Late Miocene (5.9 Ma ago) the combination of tectonic uplift, sea level changes and climatic conditions caused a narrowing of the western connection to the Atlantic Ocean and initiated the Messinian Salinity Crisis (Hsü et al. 1973; 1978). The water shortage and the high evaporation rates in the Mediterranean climate resulted in a significant sea level drop and an increase in the salt concentration finally lead to precipitation. The first reported increase in salinity took place in Sicily at 6.26 Ma (Blanc-Valleron et al. 2002). The deposition of the widely exposed ME started at 5.96 Ma (Gautier et al. 1994; Krijgsman et al. 1999). Hilgen & Langereis (1993) dated the end of the salinity crisis to 5.33 Ma. The lowered base of erosion during the MSC caused the drainage channels to incise canyons and valleys into the continental shelf (Garfunkel et al. 1979; Almagor & Garfunkel, 1979). The eastern limit of the evaporite deposition is the elevated and uplifted Syrian Arc fold belt.

The Plio-Quaternary deposits overlie the ME unconformably (Almagor 1984) and consist mainly of Nile derived sediments (Ross & Uchupi 1977). South of Haifa the continental shelf and slope are formed by the easternmost part of the Nile fan and a broad and smooth shelf (Almagor 1984).

3 STRUCTURAL EVOLUTION OF THE MESSINIAN EVAPORITES

3.1 *Overall structure*

The evaporites in the Levantine Basin reach a maximum thickness of about 2 km. Two cross-sections elucidate the overall structure of Late Miocene to recent deposits (Fig. 3). In the east, a series of anticlines of the Syrian Arc foldbelt acted as a structural barrier

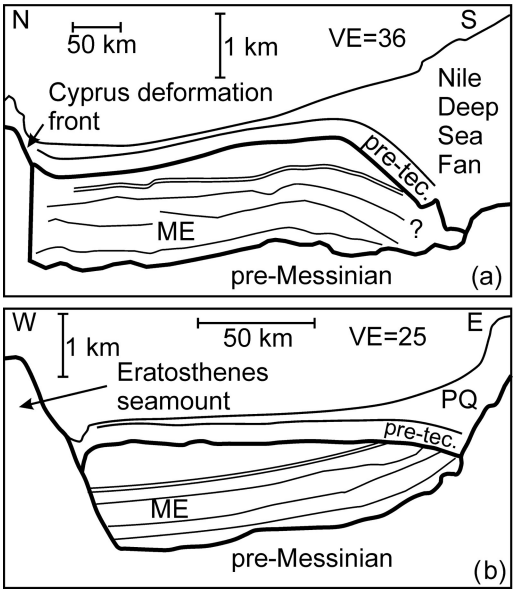

Figure 3. Simplified line-drawings of pre-stack depth migrated seismic sections across the entire Levantine Basin (after Netzeband et al. 2006a). For location see Fig. 1.

indirectly governing the overall landward extension of the evaporites (Bertoni & Cartwright 2006a, Gardosh & Druckmann 2006). The load of the Nile Deep Sea Fan (NDSF) pushes the entire evaporites in a NNE direction and parallel to the bathymetric gradient. In front of the lower NDSF, the evaporites are thickened due to forebulging (Fig. 3a). In the bottleneck between the Eratosthenes Seamount and the Levantine slope the evaporites are squeezed. In the north, the Cyprus Arc acts as a backstop, where compressional folds strike parallel to the arc as it is revealed in bathymetric data (Benkhelil et al. 2005).

The top of the evaporites declines beneath the Nile Cone in the south and beneath the sediment prism off the Levantine margin not only because of the lateral displacement (Netzeband et al. 2006a). The differential load of the basinward prograding overburden also causes the evaporites to creep towards the basin. The load of the basinward prograding sediment causes differential subsidence which is highest beneath the thickest part of the sediment prism. The resulting down-warping at the basin margins pretends rollback folding and thin-skinned extension, respectively, also in areas where no or very little thin-skinned extension occurred.

3.2 *Stratigraphy of Messinian evaporites*

Six Messinian sequences labelled ME-I – ME-VI can be traced across the entire Levantine basin (Figs. 3, 4).

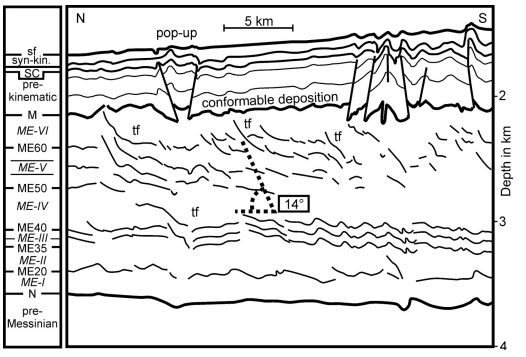

Figure 4. Line-drawing of pre-stack depth migrated seismic section showing intra-evaporitic sequences labelled ME-I-VI (after Netzeband et al. 2006a). Horizon labels according to Bertoni & Cartwrigh (2006 in press b). tf: thrust fault.

Sequences ME-I, II, IV and VI are seismically transparent and sequences ME-III and ME-V reveal several internal reflections. Since the entire succession of the ME has never been drilled, the interpretation of the sequences has to rely on seismic data. The absence of seismic reflections is typical of salt bodies (Mitchum et al. 1977) and so is the interval velocity of ca. 4 km/s (Netzeband et al. 2006a). Consequently, we suggest to interpret sequences ME-I, II, IV and VI as halite deposits. The interpretation of the layered sequences is more uncertain. Some authors consider them as evaporites with intercalated (and presumably overpressurized) clastics Garfunkel (1979) and Gradmann et al. (2005). However, 3D-seismic data analysis proved a high lateral continuity of seismic reflection characters and identified polarity changes which are more indicative of chemical sedimentation processes (Bertoni & Cartwright in press b). In this case the acoustic impedance contrasts could result from alternating halite, anhydrite, limestone and shale/marl facies.

Chemical depositional processes do not necessarily produce reflection horizons which represent isochrones. But e.g., a laterally prograding overburden could cause a temporal and lateral increase in overburden thickness and pressure, respectively, which could have resulted in gypsum-anhydrite conversion and, consequently, in acoustic impedance contrasts. In this case internal reflections would represent diachrons.

Submarine canyons represented preferential sites of erosion and deposition of evaporites at the basin margin during the MSC. Seismic geomorphological analysis of 3D seismic data strongly suggests the occurrence of clastic bodies within the basal part of the ME (Bertoni & Cartwright in press a). They are composed of two closely spaced channel-mouth lobe deposits and are presumably correlated with a long-lived system of canyons (i.e. the El Arish and Afiq Canyons).

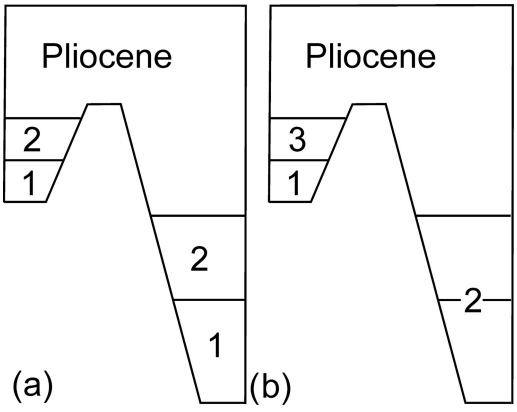

Figure 5. Endmember models elucidating the ongoing debate regarding the relationship between marginal and basinal evaporite stratigraphy (simplified after Rouchy & Caruso 2006). The sequences may have developed contemporaneously (a) or alternating (b).

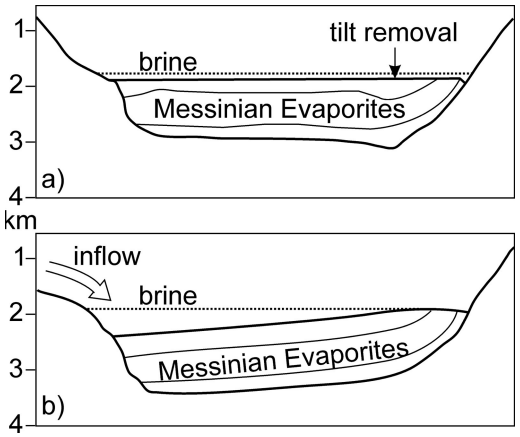

Figure 6. Endmember models elucidating the growth pattern of the Messinian evaporites. a) Evaporites aggradation in an untilted basin. b) Progradation and lateral facies change owing to dipping basin floor and water inflow, which cause a lateral salinity gradient.

The temporal and stratigraphical relation between marginal and basinal evaporites is still a matter of debate. The same age for the onset of evaporite deposition in the marginal basins and in the deep basin and therefore a correlated stratigraphy is considered by some research groups (Krijgsman et al. 1999, Fig. 5a). Other authors assume diachronic deposition (e.g., Clauzon et al. 1996, Cornée et al. 2002, Butler et al. 1995, Riding et al. 1998, Fig. 5b). Rouchy & Caruso (2006) suggested a progressive but fast deposition of evaporites from the margin to the deep central basin. It is noteworthy that the vast reconstructions of the Messinian paleo-environment are based on the descriptive and analytical work on the succession preserved in the marginal basins only. The climate archive represented by about 95% of the ME within the deep basins has not been opened yet.

3.3 *Deposition and erosion pattern*

Outside the main part of the NDSF the internal reflections dip towards northwest. Both the eastern and northern dip component is seen in Fig. 3a and b. Different models apply to explain an isochronic deposition of each sequence.

Each sequence aggraded within the central basin almost symmetrically in a deep basin – shallow water environment if a hinge zone is assumed 40 km west of the eastern termination point (Netzeband et al. 2006a, Fig. 6a). The northwestern tilt of the basin after the deposition of sequence ME-V could have been the consequence of the collision between the Eratosthenes Seamount and Cyprus or, alternatively, of the increasing load due to evaporite deposition.

If no tilting is assumed, the evaporites in the northwest were deposited in a much deeper water depth than those in the southeast (Fig. 6b). Marine water inflow from the Herodotus basin through the gateway between Eratosthenes Seamount and Cyprus Arc would have caused laterally varying salinity and, consequently, laterally varying deposition rates and facies.

Towards the east and south the reflections and sequences, respectively, terminate updip against the M-reflection in different distances to the pinch-out line of the ME (Fig. 3a.) e.g., the termination distance of sequence ME-VI is 40–60 km (Bertoni & Cartwright 2006a). Beneath the NDSF only ME-VI could be clearly identified, it also toplaps the M-reflection (Fig. 3b). The similar depth levels of the toplap location indicate a simultaneous erosion of the marginal parts of the sequences, e.g., owing to subaerial exposure at the end of the MSC. The abrupt up-dip termination and absence of asymptotic tapering rules out the interpretation of M as a nondepositional surface. The geometry of the eroded evaporites at the basin margin remains uncertain.

3.4 *Syn-depositional deformation*

The intra-evaporitic sequences are highly deformed by folds and faults (Fig. 4). Fold forms are oftenly associated with the propagation of thrust faults. In many regions, the lower Pliocene deposits overly M concordantly, even if the intra-evaporite sequences are deformed. The time of deformation obviously predates the erosional truncation of the uppermost evaporites. Consequently, Netzeband et al. (2006a) suggested the first time that thin-skinned salt tectonics occurred

during the deposition phase. Bertoni & Cartwright (in press b) discussed this intra-evaporite deformation pattern by means of 3D-seismic data. The strongest deformation has been observed in published 2D- and 3D-seismic data for ME-III and ME-V. In Fig. 4 the thrust fault planes dip with up to 14°, maximum values of 30° have been observed in the 3D-data.

The most likely driving forces for the syn-depositional deformation are plate-tectonics or gravity gliding. 3D-data analysis showed that the vergence of the intra-evaporitic folds is oblique to the regional stress field, which makes a plate-tectonic cause unlikely. According to the thin-skinned tectonic concept, the slope of a margin or simply the differential load of a seaward prograding shelf causes the overburden to move basinward leaving extensional structures such as listric normal faults and rotated blocks along the slope. A submarine Nile fan of unknown dimensions emerged presumably in the Messinian (Barber 1981, Griffin 2002). Such a fan squeezing the evaporites basinward during the precipitation phase should laterally interfinger with the ME. The post-Messinian pre-tectonic sequence has a thickness of some 100 meters (s. next chapter), a similar thickness should be assumed for the syn-depositional fan. However, industrial seismic data give no evidence for this (Abdel Aal et al. 2000). Therefore we suggest that the basinward creep and thrusting of the individual evaporitic sequences during the deposition phase was driven by gravitation but without significant sediment load. The lateral displacement was presumably comparable with modern salt glaciers, e.g., in Iran. Owing to the onload of the deposited ME the basin-floor tilted towards the basin center which may have acted also as a trigger mechanism. Further, the internal shear strength of the entire salt body was reduced since sequence boundaries have acted as detachment layers.

3.5 *Post-depositional deformation*

There is a clear line of evidence that a 2nd phase of thin-skinned extension started in the later Pliocene (Garfunkel et al. 1979, Almagor 1984, Gradmann 2005). Extensional faults in the overburden include typically listric and antithetic growth faults, turtle back structures and crestal grabens (Humphris 1978, Martin 1978). Some faults pierce the seafloor proving that this phase is still active (Gradmann et al. 2005). Salt rollers emerged in the extensional domain (Fig. 7). A pre- and syn-tectonic unit can be clearly identified. The pre-tectonic unit is about 300–400 ms TWT or 250–400 m thick and it is characterized by parallel horizons. The syn-tectonic unit includes the sediment prism off the western shelf and reveals divergent horizons above the salt rollers.

The pre- and syn-tectonic sequences are separated by a huge late-Pliocene slump complex off the southern Levantine slope (Frey-Martinez et al. 2005). The

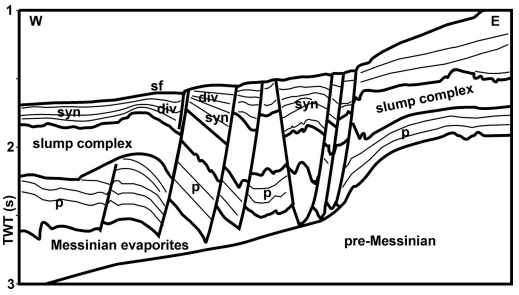

Figure 7. Thin-skinned salt tectonic in the extensional domain. Pre- and syn-tectonic deposits are separated by a slump complex. p: parallel. div: divergent; syn: syn-tectonic; sf: sea floor.

slump complex has been mapped by means of 3D-seismic data and the volume was estimated to ca. 1000 km^3. Several trigger mechanisms are possible, e.g., oversteepening, seismicity, gas migration and initial salt tectonic. A time correlated sequence of low seismic reflectivity can be traced all over the basin separating pre- and syn-tectonic sequences also in the compressional domain (Netzeband et al. 2006a, Fig. 4).

3.6 *Migration of fluids and volatiles*

Fluid escape structures have been reported from the southern and eastern basin margin. Possible fluid resources are located beneath and within the ME (Fig. 8a). Several factors combine to control fluid release locations. E.g., the ME were considered as a sealing sequence and syn-tectonic faults as conduits (Loncke et al. 2004, Fig. 8b). However, a mud volcano is located at the lower NDSF and above almost undisturbed and 1.5 km thick ME without any evidence for lateral fluid flow (Netzeband et al. 2006a). A cone-like feature at the top of the ME directly beneath the mud volcano was interpreted as salt that precipitated from fluids escaping out of the ME (Fig. 8b). This fluids remobilized sediments within the overburden that feed the mud volcano.

Buried circular collapse structures above the tabular ME are recorded by 3D-seismic data on the eastern basin margin (Bertoni & Cartwright 2005). The structures formed during the Pliocene as the buried ME underwent extensive dissolution in a submarine, deep-water setting. The authors propose that focused vertical fluid flow at the base of the evaporitic series dissoluted the more soluble evaporites within the entire ME succession (Fig. 8c). Fluid through and outflow from the ME has been also reported. Near vertical faults represent the conduits from the top of the ME to the seafloor, where muddy fluids escape. Possible fluid reservoirs within the ME are intercalated sediments or water that was released from gypsum-anhydrite conversion.

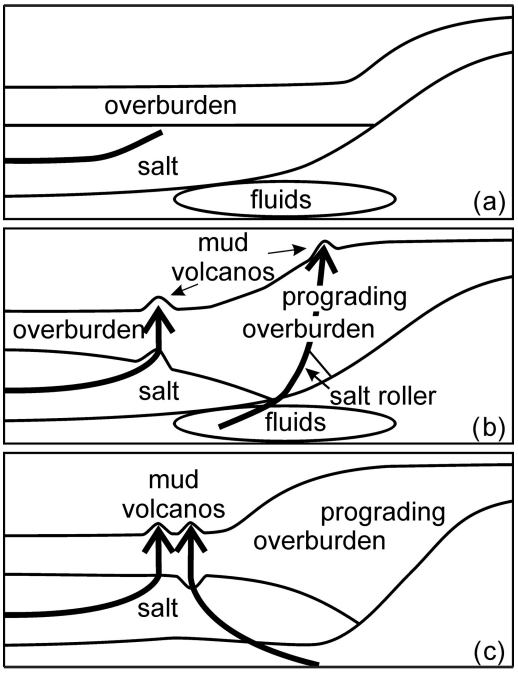

Figure 8. Endmember models for salt tectonic related fluid dynamics. a) Fluids are present within the evaporites and beneath. b) The differential load of the prograding marginal sequences initiates basinward salt creeping. Extensional faults act as conduits for fluids which migrate upwards where salt has vanished. Fluids escape from the salt and feed mud volcanoes. Precipitated salt form salt cones on top of the main salt body. c) The differential sediment load causes differential subsidence which squeezes fluid through and out of the evaporites.

The fluid escape structures at the eastern basin margin are located at the lower slope. It can be concluded that the prograding slope caused differential sediment load on the basin margin and differential subsidence, respectively (Fig. 8c). The fluids trapped within the ME and beneath were overpressurized and started to migrate upwards.

4 SUMMARY

The basinal ME have a thickness of up to 2 km. Downwarping of the ME at southern and eastern basin margin results from both thin-skinned extension and laterally differential subsidence. Six evaporitic units can be traced throughout the basin. Four units are interpreted as massive halite units and two of them as alternating successions of clastic sediments and evaporitic facies. The relationship between these basinal and the marginal sequences is unclear. The particular units were deposited in a basinward prograding pattern, which was a consequence of a basinward tilt of the basin floor and/or a water inflow from the gateway between Cyprus and the Eratosthenes Seamount. The intra-evaporitic reflections show a clear line of evidence of folding and thrusting occurring prior to the reflooding of the basin and during the evaporite depositional phase. The causative processes are unexplored. A second thin-skinned salt tectonic event started in the late Pliocene when a slump complex was deposited on the rim of the basinal ME. The consequences of a multi-layered rheology on salt tectonic need future research. The basinward prograding overburden overpressurized fluid within and beneath the evaporites from where they escape. The tabular ME do not necessarily represent a sealing sequence, the origin of intra-evaporitic conduits remains unclear.

REFERENCES

Abdel Aal, A., El Barkooky, A., Gerrits, M., Meyer, H., Schwander, M., Zaki, H. 2000. Tectonic Evolution of the Eastern Mediterranean Basin and its significance for hydrocarbon prospectivity in the ultradeepwater of the Nile Delta. *The Leading Edge* 19: 1086–1102.

Almagor, G., Garfunkel, Z. 1979. Submarine slumping in the continental margin of Israel and northern Sinai. *American Association Petroleum Geology Bulletin* 63: 324–340.

Almagor, G., 1984. Salt controlled slumping on the Mediterranean slope of central Israel. *Marine Geophysical Researches* 6: 227–243.

Almagor, G. 1993. Continental slope processes off northern Israel and southernmost Lebanon and their relation to onshore tectonics. *Marine Geol*ogy 112: 151–169.

Barber, P.M. 1981. Messinian subaerial erosion of the proto-Nile delta. *Marine Geol*ogy 44: 253–272.

Benkhelil, J., Bayerly, M., Branchoux, S., Courp, T., Gonthier, E., Hübscher, C., Maillard A., Tahchi, E. 2005. La branche orientale de l'Arc de Chypre: Aspects morphostructuraux d'une frontière de plaques d'après la campagne BLAC (2003). *Comptes Rendus Geoscience* 337: 1075–1083.

Bertoni, C., Cartwright, J.A. 2005. 3D seismic analysis of circular evaporite dissolution structures, Eastern Mediterranean. *Journal of the Geological Society* 162: 909–926.

Bertoni, C., Cartwright, J.A. 2006a. Controls on the basinwide architecture of late Miocene (Messinian) evaporites on the Levant margin (Eastern Mediterranean). *Sedimentary Geology* 188–189: 93–114.

Bertoni, C., Cartwright, J.A. in press, a. Clastic depositional systems at the base of the Messinian (late Miocene) evaporitic series of the Eastern Mediterranean: Evidence from 3D seismic data. *Geological Society Special Publication*.

Bertoni, C., Cartwright, J.A. in press b. Major erosion at the end of the Messinian Salinity Crisis: evidence from the Levant Basin, Eastern Mediterranean. *Basin Research*.

Blanc-Valleron M.-M., Pierre C., Caulet J.-P., Caruso A., Rouchy J.-M., Gespuglio G., Sprovieri R., Pestrea S., Di Stefano E. 2002. Sedimentary, stable isotope and micropaleontological records of paleoceanographic change in the

Messinian Tripoli Formation (Sicily, Italy). *Palaeogeography, Palaeoclimatology, Palaeoecology* 185: 255–286.

Buchbinder, B., Zilberman, E. 1997. Sequence stratigraphy of Miocene–Pliocene carbonate–siliciclastic shelf deposits in the Eastern Mediterranean Margin (Israel): effects of eustasy and tectonics. *Sedimentary Geology* 112: 7–32.

Butler, R.W.H., Lickorish, W.H., Grasso, M., Pedley, H.M., Ramberti, L., 1995. Tectonics and sequence stratigraphy in Messinian basins, Sicily: Constraints on the initiation and termination of the Mediterranean salinity crisis. *Geological Society American Bulletin* 107: 425–439.

Clauzon, G., Suc, J.-P., Gautier, F., Berger, A., Loutre, M.-F. 1996. Alternate interpretation of the Messinian salinity crisis: Controversy resolved? *Geology* 24(4): 363–366.

Cornée, J.J., Roger, S., Münch, P., Saint-Martin, J.P., Féraud, G., Conesa, G., Pestrea, S. 2002. Messinian events : new constraints from sedimentological investigations and new 40Ar/39Ar ages in the Melilla-Nador Basin (Morocco). *Sedimentary Geology* 151: 127148.

Frey-Martinez, J., Cartwright, J., Hall, B. 2005. 3D seismic interpretation of slump complexes: examples from the continental margin of Israel. Basin *Research* 17: 83–108.

Gardosh, M., Druckmann, Y., 2006. Stratigraphy and tectonic evolution of the Levantine Basin, offshore Israel. In: A. Robertson (Ed), Tectonic Development of the Eastern Mediterranean Region, *Geological Society Special Publication* (in press).

Garfunkel, Z., Arad, A., Almagor, G. 1979. The Palmahim Disturbance and its regional setting. *Geological Survey of Israel Bulletin* 72: 56.

Garfunkel, Z. 1998. Constraints on the origin and history of the Eastern Mediterranean basin. *Tectonophysics* 298: 5–35.

Garfunkel, Z. 2004. Origin of the Eastern Mediterranean basin: a reevaluation. *Tectonophysics* 391, 11–34.

Gautier, F., Clauzon, G., Suc, J.-P., Cravatte, J. Violanti, D., 1994. Age et durée de la crise de salinité messinienne. *Comptes Rendus de l'Académie des Sciences Paris, ser. 2*, 318: 1103–1109.

Gradmann, S., Hübscher, C., Ben-Avraham, Z., Gajewski, D., Netzeband, G. L. 2005. Salt tectonics off northern Israel. *Marine and Petroleum Geology* 22: 597–611.

Griffin, D.L. (2002) Aridity and humidity: two aspects of the late Miocene climate of North Africa and the Mediterranean. *Palaeogeography, Palaeoclimatology, Palaeoecology* 182: 65–91.

Hilgen, F.J., Langereis, C.G. 1993. A critical re-evaluation of the Miocene/Pliocene boundary as defined in the Mediterranean. *Earth Planetary Science Letters* 118: 167–179.

Hsü, K.J., Cita, M.B., Ryan, W.B.F., 1973. The origin of the Mediterranean Evaporites, in: Ryan, W.B.F., Hsü, K.J. (Eds.), *Initial Reptorts DSDP, Leg 13*. U.S. Govt. Printing Office, Washington D.C.: 1203–1232.

Hsü, K.J., Monadert, L., Bernoulli, D., Cita, B.C., Erickson, A., Garrison, R.E. 1978. History of the Mediterranean Salinity Crisis, in: Hsü, K.J., Montadert, L. (Eds.), *Initial Reptorts DSDP, Leg 42.I*. U.S. Govt. Printing Office, Washington D.C.: 1053–1078.

Humphris Jr., C.C. 1978. Salt movements on continental slope, Northern Gulf of Mexico. *American Association of Petroleum Geologists Studies in Geology* 7: 69–85.

Krijgsman, W., Hilgen, F.J., Raffi, I., Sierro, F.J., Wilson, D.S., 1999. Chronology, causes and progression of the Messinian salinity crisis. *Nature* 400: 652–655.

Loncke, L., Mascle, J., FANIL Scientific Party 2004. Mud volcanoes, gas chimneys, pockmarks and mounds in the Nile deep-sea fan (Eastern Mediterranean): geological evidences. *Marine and Petroleum Geology* 21: 669–689.

Loncke, L., Gaullier, V., Mascle, J., Vendeville, B., Camera, L. 2006. The Nile deep-sea fan: An example of interacting sedimentation, salt tectonics, and inherited subsalt paleotopographic features. *Marine Petroleum Geology* 23(3): 297–315.

Makris, J., Ben-Avraham, Z., Behle, A., Ginzburg, A., Giese, P., Steinmetz, L. 1983. Seismic reflection profiles between Cyprus and Israel and their interpretation. *Geophysical Journal of the Royal Astronomical Society* 75: 575–591.

Martin, R.G. 1978. Northern and Eastern gulf of Mexico continental margin: stratigraphic and structural framework Framework, facies, and oil trapping characteristics of the upper continental margin. *American Association of Petroleum Geologists Studies in Geology* 7: 21–42.

Mascle, J., Benkhelil, J., Bellaiche, G., Zitter, T., Woodside, J., Loncke, L., PRISMED II Scientific Party 2000. Marine geologic evidence for a Levantine-Sinai plate, a new piece of the Mediterranean puzzle. *Geology* 28: 779–782

Mitchum, R.M., Vail, J.R., Sangree, J.B. 1977. Seismic stratigraphy and global changes of sea-level, part 6: seismic stratigraphic interpretation procedure. In: *Seismic Stratigraphy – applications to Hydrocarbon exploration* (ed. C.E. Payton), *American Association of Petroleum Geologists Memoirs* 26: 117–134.

Neev, D. 1975. Tectonic evolution of the Middle East and the Levantine basin (easternmost Mediterranean). *Geology* 3: 683–686.

Neev, D. 1977. The Pelusium Line – a major transcontinental shear. *Tectonophysics* 38: T1–T8.

Neev, D., Almagor, G., Arad, A., Ginzburg, A., Hall, J.K. 1976. The geology of the Southeastern Mediterranean Sea. *Geological Survey of Israel Bulletin* 68: 1–51.

Netzeband, G., Gohl, K., Hübscher, C., Ben-Avraham, Z., Dehghani, A., Gajewski, D., Liersch, P. 2006a. The Levantine Basin – crustal structure and origin. *Tectonophysics* 418: 178–188.

Netzeband, G., Hübscher, C., Gajewski, D. 2006b. The structural evolution of the Messinian Evaporites in the Levantine Basin. *Marine Geology* 230, 249–273.

Riding, R., Braga, J.C., Martín, J.M. & Sánchez-Almazo, I.M. 1998. Mediterranean Messinian Salinity Crisis: constraints from a coeval marginal basin. Sorbas, SE Spain. *Marine Geology* 146: 1–20.

Robertson, A.H.F., Dixon, J. E., 1984. Introduction: Aspects of the geological evolution of the Eastern Mediterranean. In: Dixon, J. E., and Robertson, A.H.F. (Eds.), *Geological Evolution of the Eastern Mediterranean*. Geological Society Special Publication 17: 1–74,

Robertson, A.H.F. 1998. Mesozoic–Tertiary tectonic evolution of the easternmost Mediterranean area: Integration of marine and land evidence. In: Robertson, A.H.F., Emeis, K.-C., Richter, C., Camerlenghi, A. (Eds.), *Proceedings of ODP, Science Results, 160*. Ocean Drilling Program, College Station, TX, 723–782.

Rouchy J.-M., Caruso A. 2006. The Messinian salinity crisis in the Mediterranean basin: A reassessment of the data and an integrated scenario. *Sedimentary Geology* 188–189: 35–67.

Ross, D.A., Uchupi, E., 1977. Structure and sedimentary history of the Southeastern Mediterranean Sea-Nile cone area. *American Association of Petroleum Geologists Bulletin 61 (6)*: 872–902.

Vidal, N., Klaeschen, D., Kopf, A., Docherty, C., Von Huene, R., Krasheninnikov, V. A. 2000a. Seismic images at the convergence zone from south of Cyprus to the Syrian coast, eastern Mediterranean. *Tectonophysics* 329: 157–170.

Vidal, N., Alvarez-Marrón, J., Klaeschen, D. 2000b. Internal configuration of the Levantine Basin from seismic reflection data (Eastern Mediterranean). *Earth and Planetary Science Letters* 180: 77–89.

Part 4. THM-processes in crushed salt backfill of final repositories – observations at laboratory and in-situ scales, modeling

Taylor & Francis
Taylor & Francis Group
http://taylorandfrancis.com

The Mechanical Behavior of Salt – Understanding of THMC Processes in Salt –
Wallner, Lux, Minkley & Hardy, Jr. (eds)
© 2007 Taylor & Francis Group, London, ISBN 978-0-415-44398-2

Thermomechanical modelling of the behaviour of drifts in rock salt

S. Olivella & A. Gens
Department of Geotechnical Engineering and Geosciences, UPC

ABSTRACT: This paper presents analyses of problems related to radioactive waste disposal in salt formations including crushed salt backfills. The large in situ test performed in ASSE mine which simulates an emplacement of a heat emitting waste in a drift has been modeled in 3D. The drift was backfilled with crushed salt, and the model includes also observation drifts. The second part of the paper, shows analyses that attempt to predict the permeability variations induced in the EDZ zone induced both by cavity excavation and by thermal loading.

1 INTRODUCTION

Saline geological formations are considered as one of the rocks suitable to dispose nuclear waste. Rock salt and highly compressed crushed salt are characterised by very low permeability. As crushed salt consolidates, its behaviour resembles the behaviour of rock salt. Two geometrical concepts about waste storage in salt rock have been developed and experimentally investigated: the borehole emplacement concept and the drift emplacement concept.

The borehole concept was developed firstly and it consisted in the waste storage within the rock using vertical holes. The borehole concept was studied in the framework of DEBORA I and DEBORA II in situ experiments (Bechthold et al, 1999; Bechthold and Bollingerfehr, 2001; Rothfucs et al, 1996). In contrast, the drift emplacement considers a direct disposal in horizontal openings, backfilled and sealed subsequently. The drift emplacement was investigated through the in situ TSDE experiment. Both concepts, borehole emplacement and drift emplacement, use exclusively saline materials as barriers differing from other multi-barrier systems, which for instance use swelling bentonite as backfill and concrete as seal. Thus, salt rock (host rock), crushed salt (backfill) and compacted crushed salt will form a multi-barrier system.

The drift emplacement concept is based on a generalised compaction of the granular material due to the convergence of the drift walls and enhanced by temperature and, eventually, moisture. The crushed salt will be transformed then into a material highly non-permeable (important to guarantee the long-term waste isolation). Salt flow is enhanced if heat is applied and therefore the backfill has to be placed as soon as possible. On the other hand, salt rock could be altered in the drift walls (enhancing the disturbance around the drifts). In the multi-barrier concept, the backfill is an important component because of its supporting and sealing functions but also due to its ability to conduct the decaying heat from the waste into the host rock. Porosity and permeability decrease continuously and tends to values similar to the ones in the solid rock.

The long-time investigation of radiological multi-barrier systems needs of numerical tools able to predict the future behaviour of a repository. To reach this end some constitutive laws and numerical programs are needed. The TSDE experiment was studied within the framework of two European Community funded projects known as BAMBUS I (Bechthold et al, 1999) and BAMBUS II (Bechthold and Bollingerfehr, 2001). In these projects numerical efforts devoted to modelling several laboratory and in situ tests were significant. The main objective was to obtain comprehensive models able to describe the coupled thermo-mechanical response of crushed salt and host rock.

ANSALT, ANTEMP, FLAC, ADINA, ANTIC, GEOMEC, MARC and CODE_BRIGHT were the FEM codes used by the different research teams working in the BAMBUS projects. Several models based on the TSDE experimental characteristics were made and used to simulate the thermal and mechanical behaviour of salt (modelling review in Olivella et al, 2001)[vi]. As the drift concept uses horizontal openings for waste storage, the mentioned models were based on a 2D representation, assuming plane-strain ($\varepsilon_z = 0$).

1.1 *The thermal simulation of drift emplacement (TSDE) in situ test*

The TSDE test was the first long-term in situ test performed to understand the feasibility of multi-barrier repositories in rock salt. The main objective was to

demonstrate the feasibility of waste storage in horizontal openings (drift emplacement concept). The TSDE experiment was carried out in the Asse salt mine (north of Germany). Evaporitic rocks constitute the geological context. The geological formation belongs to the Strassfurt Series that was emplaced during the Permian Age (225–230 millions of years ago). The test is described in Droste et al (1996).

The TSDE experiment was designed making use of the underground facilities of the Asse mine. Experimental framework involves measurement of temperature (evolution and distribution), porosity variations and other mechanical reactions (as cavern closure or salt compaction). Experimental work was mainly concentrated in the study of crushed salt.

The test started on September 25, 1990 and shut down took place on February 1, 1999. In a post-test investigation phase following from August 2000 until April 2003, one test drift was uncovered to perform a validation program. Backfill removal and post-test investigations are part of the project BAMBUS II.

The experimental field (Figure 1.1) is constituted by a set of sub-horizontal and parallel galleries constructed on two underground levels (750 m and 800 m in depth). Two drifts were opened on the 800 m level and several heaters were placed on (simulating the heat generation by the radioactive waste). Such heaters are based on the Pollux cask characteristics (each radiological cask is used storing 8 PWR Westinghouse elements, with uranium enrichment of 4.1%). The maximal thermal power of heaters is 10 kW (6.4 kW of design power). These heaters are designed with a safety factor of 2 (thought to support vertical stresses of 18 MPa).

Additionally, two drifts were excavated on the 750 m level with the axial plane coincident to the axial plane (in vertical) of the 800 m caverns. Some instrumentation specially designed for the TSDE was installed in this level, following the experimental work (including TV monitoring). In addition to the data analysis performed on the 750-m level a number of instrumentation probes and core loggings served at studying the problem evolution. Boreholes of different diameter and length were excavated and instrumented within rock and backfill. Several cross-sections were selected in both the heated zone and the non-heated zone.

In situ monitoring related to this work, consisted in temperature, stress-state and deformational measurements. Temperature was registered by means of 80 thermometers, located on the heaters surface, backfill and rock. Within the backfill the temperature was checked for the heaters surface (as mentioned), on the floor, at 1.1 and 2.2 m respect to floor and in the upper part of backfill. Within the rock, measurements were done at several distances from the drift walls.

Drift closure was measured by telescopic steel tubs with an extensometer and it was checked manually and

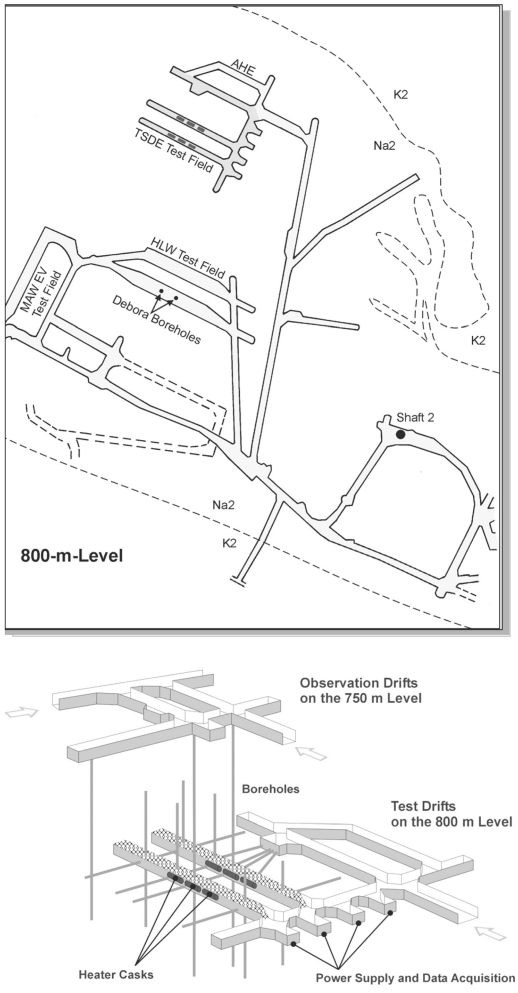

Figure 1.1. a) Plan view of the 800 m level at Asse mine (Germany) with the Debora and TSDE test fields. b) Schematic representation of the TSDE in situ test.

automatically in the 750 m level. Sections B^{+1}, $D1^{-1}$, G1 and G2 were the selected sections for measurement in the heated area whereas in the non-heated area were sections $E1^{-1}$ and E2 were considered (super-index expresses distance in meters from the section). The accuracy was of about 400 mm at 200°C.

Axial and radial displacements were measured by inclinometers and extensometers. Multiple extensometers of glass fibre were used in A and D1 heated sections and E1 and E2 cooler sections (its accuracy was length-dependent: 0.02 mm to 20 m, 0.1 mm to 50 m and 0.3 mm to 100 m). The backfill settlement was measured for three levels, using several metallic plates coupled to a steel plate directly connected to the drift floor (each level agree well with one third of

the backfill). The roof-plate distances were registered through electric transducers.

The stress measurement was done using hydraulic pressure cells, located on the drift walls, between the backfill and the rock. The vertical and the three horizontal stress components were measured: orthogonal, parallel, and 45° inclined respect to the axial direction. Additionally, some sub-vertical components were measured: 45° inclined, parallel and perpendicular to the galleries axe. In all cases the accuracy was of about 0.02 MPa. The measurement was done in the heated sections B, D1, D2 and G1, and in the cold section E1. Porosity was calculated from convergence measurements. Initially, the backfill porosity was of 35%, decreasing to about 20% at the end of the experiment.

When an underground opening is excavated there exist some stress field readjustments affecting the near-field of the excavation. Rock movement towards the opening from the surrounding drift walls is therefore expected. These movements are very critical for the repository safety because they induce instabilities that are difficult to quantify. Material downfall and dilation processes can be produced in the near-field (Excavation Disturbed Zone = EDZ). To reduce the development of the EDZ the openings will have to be filled as soon as possible by means of special methods. Otherwise material flow is initiated (salt is a material highly viscous and it flows easily under an increase of temperature) and continues in movement under the stress field produced by the lithostatic pressure.

Initially, salt response is elastic, however, if external actions are maintained, the salt behaviour becomes viscoplastic and irreversible. Time is then a key factor. In most of cases, plastic deformation is highly ductile, however if stress concentration is increased other processes such as fracturing may appear. This behaviour is generally found near the drift floor or in the upper part of the drift walls (depending on the geometry of the opening). Ductile/viscous deformation is known as creep.

Creep controls salt deformation in nature. This process is time-dependent, thus creep is produced as consequence of a stress-state which keeps constant during a period of time. In a natural rock creep is produced due to the crystalline net imperfections (dislocations) that the material uses to move itself. Creep is common for all crystalline materials and it can be explained through dislocation theory. In rock salt we refer to this mechanism as Dislocation Creep (DC). In fact, it is produced as a consequence of different associated mechanisms of dislocation: dislocation glide (sliding deformation) and dislocation climb (climbing movement) are the most common deformational types associated to DC.

Not all deformations are related to the crystalline net features, there are deformation induced by the presence of brine (in pores). In these cases and under some thermodynamic conditions several processes of diffusion may act. Diffusion mechanisms consist in a transport of saline material from and to some selected zones within the natural media. The main process is called FADT (Fluid Assisted Diffusion Transfer) otherwise also called Pressure Solution Creep.

In the framework of the TSDE experiment a dry material was considered. In the BAMBUS I and II projects water was not considered and only thermo-mechanical analysis were performed. In the numerical model presented in this work, the presence of water will therefore be discarded.

1.2 *Constitutive model for salt*

A general constitutive model for crushed salt has been developed and the final form has been presented in Olivella and Gens (2002) where calibrated parameters for the model were also obtained. The model was implemented in the numerical code CODE_BRIGHT (Coupled Deformation BRIne Gas and Heat Transport problems) which is a finite element code prepared for solving THM problems in geological media (Olivella et al 1996).

2 THERMO-MECHANICAL MODELLING OF TSDE TEST

2.1 *Introduction*

This analysis corresponds to a further effort of Thermo-Mechanical modelling of TSDE in situ test. In the context of BAMBUS-I various calculations were also performed. UPC team included two calculations in BAMBUS-I. The first one was 2-D thermo-mechanical analysis that was performed in a relatively small domain (6 to 7 times the drift size). The boundary at such short distance was demonstrated to be insufficient both for temperatures and for field stresses, although it permitted to control stress to a lower constant value compared to the actual lithostatic stress.

The long term duration of the test (10 years) requires a larger domain for the thermal problem to be solved, requires three dimensions and the incorporation of other ventilated drifts. The first model incorporated a thermal conductivity of the backfill dependent on porosity only. However, since the temperature has an important effect on salt thermal conductivity, dependence on temperature is also necessary. Plane strain models over predict temperatures, convergences and stresses because a 2-D approach is equivalent to an infinite drift with a continuous heater. And the test has a length of 15 m which is certainly a limited length that does not permit to assume plane strain and plane heat flow conditions.

A fully coupled 3-D model simulating TSDE is presented. This model was subsequently improved

from two previous geometries also in 3-D that are not described in the paper. The final model is based on a domain of $100 \times 125 \times 25\,m^3$ and incorporates 2 observation drifts parallel to the heated drifts.

2.2 *Model description and results obtained*

The 3D model presented here consists in a domain with three horizontal drifts located on two underground levels (750-m and 800-m). Two symmetric planes have been considered (YZ and XZ) and therefore sixt drifts are represented in the mesh. On the 800-m level there are three parallel drifts, two backfilled with crushed salt and one empty. On the 750-m level there are also two empty drifts. Drifts on the 750-m level and backfilled drifts on the 800-m level are located in the same vertical plane.

Within two drifts of the 800-m level six heaters were emplaced (three in each one). Due to symmetry, only one and a half heaters will be represented. The thermal properties of these heaters are based on the thermal characteristics of Pollux radiological casks.

The 3D mesh (figure 2.1) used is formed by linear hexahedrons of 8 nodes that use selective integration in order to avoid numerical problems related to the incompressibility of the rock salt under creep. The mesh is regular except that it has been refined a little bit in the vicinity of the heated drifts. The total mesh is composed by 65954 nodes and 59072 elements. Considering four degrees of freedom per node (temperature and three displacements) a total of 250000 degrees of freedom have been calculated per time step.

Salt rock, crushed salt and steel (canisters) are the three materials considered in the model presented here. These materials are characterised by some mechanical (porosity, Young module, Poisson coefficient) and thermal parameters (thermal conductivity and specific heat) that are summarised in Table 2.1. Boundary conditions of different types have been used in the model boundaries. Porosity was zero in the rock and 0.35 in the backfill. Temperature in the observation drifts was imposed to 36°C, and this was crucial for temperature predictions in the model. Heat flow rate was fixed for each heater to $Q = 1280$ J/s. The initial temperature was considered of 36°C for the whole domain. Initial stress (all directions) was assumed to be 12 MPa before drifts excavation and a period of stress relaxation was considered before heating started.

Heat flow and salt deformation were simulated by means of this 3D thermo-mechanical analysis. Temperature (distribution and time evolution) was measured within the rock (at several distances from the drifts walls) and backfill. Stresses were calculated for several points in the backfill (floor, roof and drift walls). Drift closure was calculated in horizontal and vertical directions (in the TSDE experiment closure measurements were of importance since they served calculating the backfill porosity by means of differential displacements). Calculation of backfill porosities was performed directly from deformations at each point.

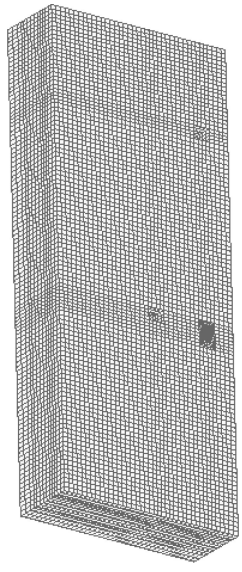

Figure 2.1. Finite element mesh considered in the calculations.

Table 2.1. Material properties.

	Units	Rock salt	Backfill
Elastic deformation			
Young module	MPa	25000	20
$dE/d\phi$	MPa	0	−80000
Poisson ratio	–	0.27	0.27
Creep deformation			
Pre-exp. Parameter	–	2.08e−06	2.08e−06
Activation energy	J/mol	54000	54000
Stress exponent	–	5	5
e_{max} (maximum void ratio)	–	–	0.75
e_{nat} (natural void ratio)	–	–	0.538
Thermal behaviour			
Thermal expansion coefficient	$°C^{-1}$	4.2e−5	4.2e−5
Thermal conductivity	W/°C/m	5.73	5.73
Temp dependence	$W/°C^2/m$	−1.838e−2	−1.838e−2
Temp dependence	$W/°C^3/m$	2.860e−5	2.860e−5
Temp dependence	$W/°C^4/m$	−1.510e−8	−1.510e−8
Porosity dependence, α	–	2.91	2.91
Specific heat solid phase	J/kg	855	855
	J/kg/°C	0.177	0.177

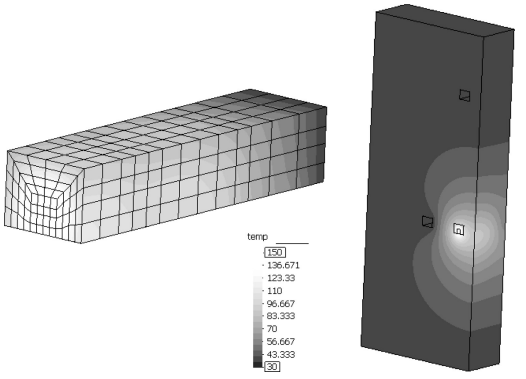

Figure 2.2. Heated domain and detail of the heated backfill after 9 years of heating.

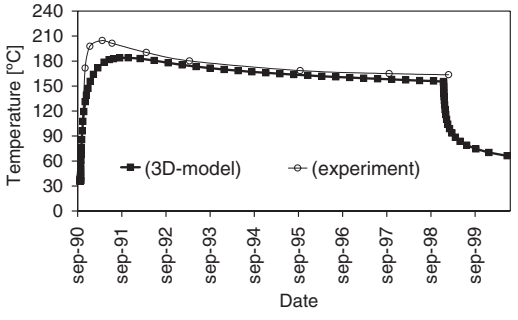

Figure 2.3. Temperature on the heater.

Drift closure was calculated in horizontal and vertical directions as the difference of horizontal and vertical displacements. Displacement was updated for every time-step during the simulation. Convergences were obtained as:

$$\Delta u_{horiz} = u_x^{pillar} - \left(-u_x^{drift\ wall}\right)$$
$$\Delta u_{vert} = u_z^{floor} - \left(-u_z^{roof}\right) \quad (2.1)$$

Temperature was registered in several points within the backfill (roof, pillar wall, floor and at 1.1 and 2.2 m above this later). In the rock, measurement was done for several depths (reaching a maximum of 30 m depth). Temperature calculation was obtained through the 3D model presented here at similar locations within the backfill (Figures 2.2, 2.3, 2.4).

Stresses were measured for the backfill-rock contact and at several locations within the rock. Calculation of stress was done only in the backfill-rock interface, because the main objective was to study the backfill properties (porosity and compaction) since this material controls the effectiveness of the multi-barrier system.

Backfill temperature evolution in other points (figure 2.4) shows an initial increase and a steady-state

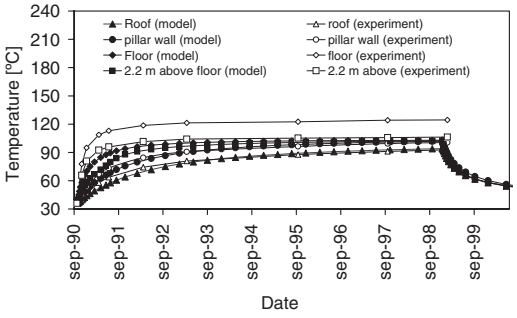

Figure 2.4. Temperature in the backfill.

reached in about two-three years, but the pic is not shown. Subsequently temperature is maintained for a narrow band between 80 and 100°C. For the drift floor the temperature increase is higher than in the other points (reaching values of 100°C). Minimum temperatures were calculated in the roof; here, 90°C were never overcome. In the pillar between cavities and the drift walls the calculated temperatures were very approximate, however, higher values were obtained for the pillar (because it was heated from both sides).

Increase of temperature was very high in all considered points (heater surface, drift walls, drift floor and inner part of backfill). Obviously this increase was higher near the heaters (190°C approximately on heater surface) after six months of heating (figure 2.3). Temperature decreases later, during a period of 2–4 years due to increased thermal conductivity of the backfill caused by porosity reduction. In the backfill-heater contact steady-state was reached during 1995, with temperature of 150°C. Temperature decreased strongly at shut down of the heaters which was initiated in 1999 (February, 1).

However, in the backfill-heater contact temperature is underpredicted slightly with differences of the order of 5°C. Probably mesh refinement would be required in this zone. In the pillar wall and also in the roof the differences were smaller. The maximum differences are for the temperature on the floor, in this case the calculated temperature is 20°C lower than the measurement.

In the host rock, temperature was measured at several distances from the drift wall: 0.3, 1.2 and 5 m below drifts (Figure 2.5); 2, 4 and 8 m above drifts (Figure 2.6); 1.2, 2.5 and 5 m within the pillar (figure 2.7) and drift wall (pillar between heated and non-heated drifts) (figure 2.8).

The maximum temperature was calculated at 0.3 m below the drift floor, reaching values near 160°C. Calculated temperatures were higher to measured values during the first months of heating. Differences decrease as long as calculation advances. At 1.2 m beneath the drift floor maximum temperatures of about

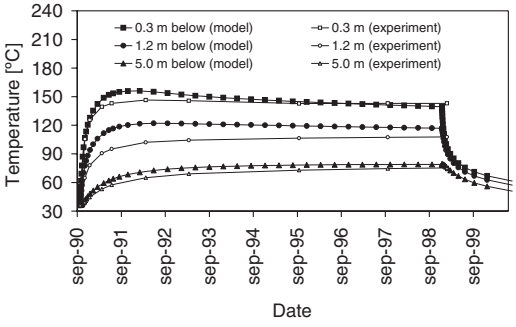

Figure 2.5. Rock temperature below the heated drifts.

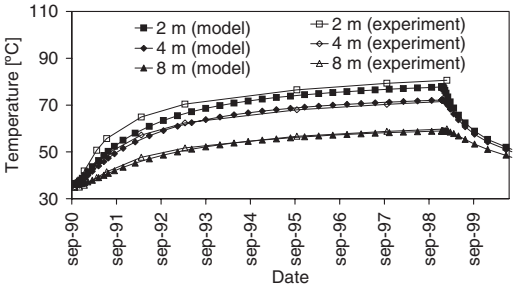

Figure 2.6. Rock temperature above the heated drifts.

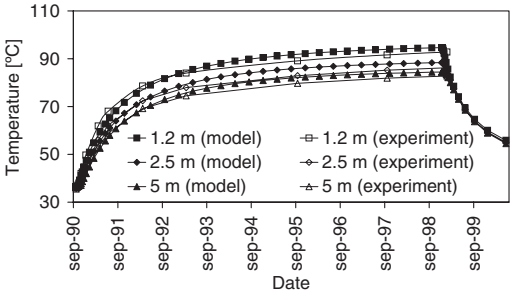

Figure 2.7. Rock temperature between the heated drifts.

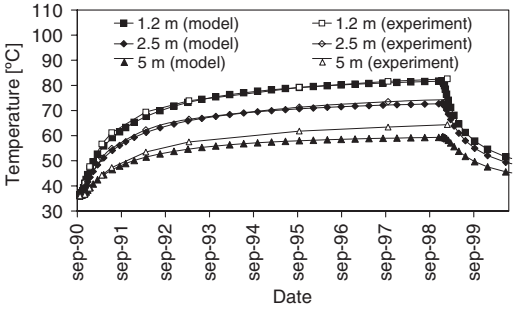

Figure 2.8. Rock temperatures beside the heated drifts.

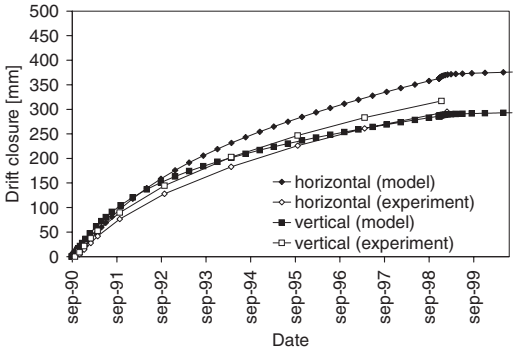

Figure 2.9. Drift closure in the heated area.

100°C are reached, calculated values are lower than the measurements (reaching 120°C).

Calculated values increase smoothly during all the analysis performed. At 5 m in depth calculations and measurements are very similar. Steady-state is not achieved and a continuous temperature increase is obtained. Some differences may be due to a poor mesh refinement.

Temperatures were measured at 2, 4 and 8 m above the drift roof (orthogonal to it) (figure 2.6). For 2 m the maximum calculated temperature was about 80°C (at the end of heating) decreasing to 60°C at 8 m. Above the drift roof temperature is not constant, even when cooling starts. Calculated values are very accurate in this case. Measurements and calculations are coincident for 4 m and 8 m above the heated drifts.

Within the pillar the maximum temperature was calculated for a distance of 1.2 m from drift wall (figure 2.7). As before, the steady-state is not reached and the maximum temperature is about 95°C. Temperature differences are small (less than 10°C). Beside the heated drifts, the maximum temperature was measured at 1.2 m and it was about 80°C (figure 2.8).

As mentioned, a period of 1.5 years had passed between the excavation of openings and the TSDE experiment starting. During this period of stress relaxation, some closure was registered (closure rate was accelerated later by the heating). Modelling the relaxation of stresses before heating was crucial for obtaining accurate results in terms of convergences and stresses. It should be noticed that heating of the rock causes a thermal expansion induced stresses which are responsible for creep deformation. This process is highly sensitive to the initial stress state.

In the non-heated area drift closures were satisfactorily calculated as shown in Figure 2.9. Vertical drift closure was very well calculated, with values that differed between 20 and 50 mm in relation to the experimentally registered (up to 300 mm). Horizontal closure differed more than 50 mm. However,

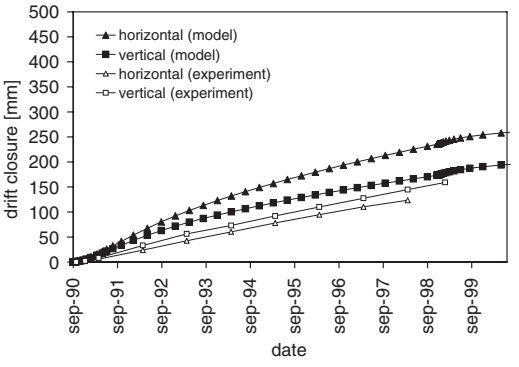

Figure 2.10. Drift closure in the non-heated area.

the calculated values are by far much better than the predictions in 2D which showed errors up to 50% in convergences.

In the non heated section (figure 2.10) the calculated closure was not as satisfactory as for the heated section. Measured and calculated values differed, especially for the horizontal convergence.

2.3 *Discussion of results*

The model presented here is the first attempt to perform an implicit fully coupled Thermo-Mechanical analysis of TSDE in situ test in three dimensions with CODE_BRIGHT. Plane strain used in former models, i.e. assuming an infinite drift with a continuous heater, showed overprediction of temperatures and convergences. Improvements of this model are: it includes explicitly two observation drifts, which affect both temperatures and stresses, and models the stress relaxation before heating start up. These are crucial for temperature and convergence predictions. The crushed salt constitutive model was calibrated in the context of BAMBUS I with respect to a comprehensive data set and remained unchanged during the improvements mentioned above.

3 EDZ MODELLING IN ROCK SALT

3.1 *Introduction*

Investigation of the Excavation Disturbed Zone (EDZ) around underground openings is important since the EDZ can increase its permeability, change its stiffness and, consequently, affect the repository behaviour. Changes in permeability have to be taken into account in further studies of fluid and contaminant transport. Changes in stiffness are important for the calculation of convergences in these openings. Dilation takes place in the EDZ due to the high shear stress and low confining stress which develop in this zone. The rock salt behaviour of salt is time-dependent and viscous

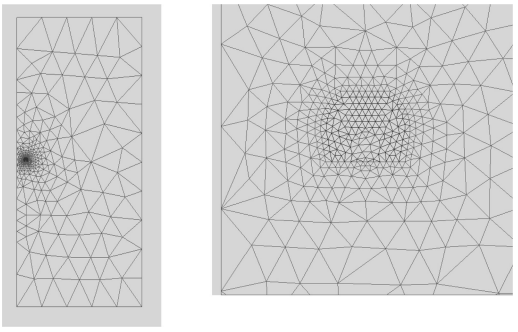

Figure 3.1. View of the finite element mesh used in the analyses and detail of the drift area (all elements are quadratic triangles, i.e. 6 nodes).

deformations have to be considered. Some basic models of rock salt creep ignore dilatancy. A constitutive model was developed (Olivella and Gens, 2002) which couples creep deformation and viscoplasticity. Originally, the model was established to describe the creep deformations in crushed salt, i.e transition from a loose aggregate to a compacted salt material. Later, a viscoplastic contribution was added in order to represent other deformation mechanisms such as grain reorganisation, grain crushing and dilatancy. In this section the model, including its viscoplastic component, is used to describe the mechanical deformations suffered by the rock under dilatancy conditions.

3.2 *Model description*

The main objective of the calculations included in this section has been to simulate the dilatancy properties of the rock. This has permitted to use a relation between porosity and permeabilities which is based on values measured ‘in situ’ in these areas (experimental values of the Asse salt mine). The calculations include creep deformation of the rock and backfill and the viscoplastic deformation in transient and non-isothermal conditions.

At this level of investigation a two-dimensional model is considered and it has been built by triangular quadratic elements (1033 elements and 2108 nodes) (figure 3.1). We are aware of the limitations of the 2D representation and they have been mentioned above; however, with this 2D model it was possible to use an optimum mesh refinement near the drift wall. Three materials have been considered: rock salt, backfill, and steel (canister). The main properties of these materials are summarised in Table 3.1. A constant stress of 12 MPa and a temperature of 36.4°C have been fixed in the upper and right boundaries, whereas in the bottom and left boundaries the displacements have been imposed to zero. A heat input of 19.61 J/s has been considered in the canister.

Table 3.1. Parameters for mechanical and thermal behaviour.

	Units	Rock salt	Backfill
Elastic deformation			
Young module	MPa	25000	200
$dE/d\phi$	MPa	0	−5000
Poisson ratio	–	0.27	0.27
Creep deformation			
Pre-exp. Parameter	–	2.08e−06	2.08e−06
Activation energy	J/mol	54000	54000
Stress exponent	–	5	5
Viscoplastic deformation			
Fluidity parameter	1/s	0.005	0.05
Activation energy	J/mol	54000	54000
n power term	–	3	3
m power term	–	4	4
a coefficient	–	3400	3400
Max. Void ratio	–	0.45	0.74
slope of critical line	–	0.95	1
P_0	MPa	15	0.001
Thermal behaviour			
Thermal expansion coefficient	$°C^{-1}$	4.2e−5	4.2e−5
Thermal conductivity	W/°C/m	5.73	5.73
Temp dependence,	$W/°C^2/m$	−1.838e−2	−1.838e−2
Temp dependence	$W/°C^3/m$	2.860e−5	2.860e−5
Temp dependence	$W/°C^4/m$	−1.510e−8	−1.510e−8
Porosity dependence, α	–	2.91	2.91
Specific heat solid phase	J/kg	855	855
	J/kg/°C	0.177	0.177

The initial conditions are the following:

	Rock salt	Backfill	Canisters
Initial stress (σ_0)	−12 MPa	−0.01 MPa	−0.01
Initial temperature (T_0)	36.4 °C	36.4 °C	36.4 °C
Initial porosity (ϕ_0)	0.001	0.31	0.0

and the duration of the simulation is 3645 days, i.e.10 years.

Initially, the porosity value in the rock was considered to be very low. In fact a residual porosity of 0.001 is normally present in the unconnected voids. When the analysis begins, porosity increases due to shear stress induced dilatancy, especially around the cavity and for short distances. The highest values were registered in the walls, close to the roof of the drifts. The maxim porosity, a bit higher than 0.025, was measured in the upper part of the pillar wall between cavities, approximately for 600 days of simulation. Later, due to the progressive drift closure and backfill pressure increase, porosity values decreased in all points as shown by the smooth slopes of curves in figure 3.2. After 3500 days, the values reached range in the interval of 0.005 and 0.015 (figure 3.3).

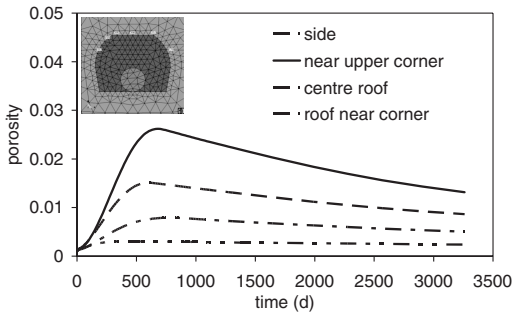

Figure 3.2. Time evolution of porosity in the rock around the opening. (EDZ TSDE TEST case).

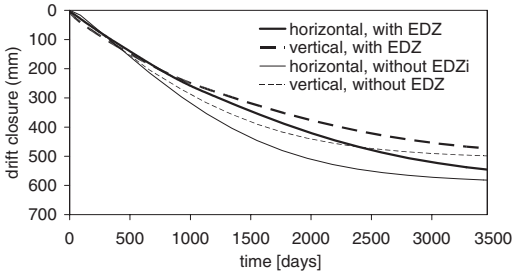

Figure 3.3. Time evolution of closures with and without EDZ considered in the host rock. It is shown that dilatancy induced by shear stress reduces convergence. (EDZ TSDE TEST case).

In order to see the influence of dilatancy on the overall behaviour of the cavity, drift closures are plotted for the analyses that consider and do not consider dilatancy. Figure 3.3 shows that convergence is reduced by the presence of dilatancy in the model. The differences decrease as the simulation progresses.

Figure 3.4 shows the time evolution of porosity in the rock for the area (upper part of cavity walls) which present the higher dilatancy close to the drift. Figure 3.2 has a scale up to 0.07 (7%). In contrast, figure 3.4 contains not only the points in the EDZ region but also the variation of porosity in points in the backfill. It can be observed that for these points the initial porosity is 0.31 (31%). The effect of dilatancy can be observed in the period from 0 to 1000 days. It can be observed also that porosity in the backfill is always higher than in the rock and this is a compatibility consequence of using the same mechanical model practically (only the viscoplastic potential parameters and the fluidity are somewhat different).

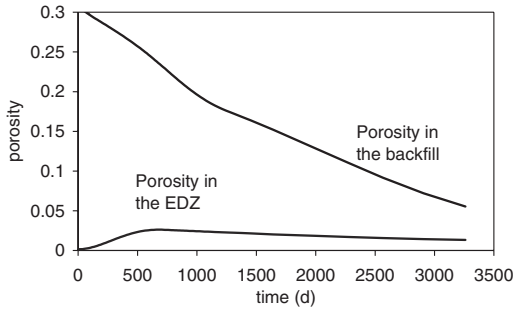

Figure 3.4. Porosity evolution in the EDZ and in the backfill (EDZ TSDE TEST case). It can be observed that porosity development in the EDZ (induced by dilatancy) produces a distortion of the porosity evolution in the backfill.

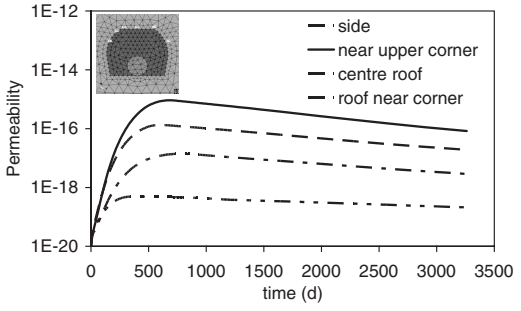

Figure 3.5. Permeability evolution for points in the EDZ (TSDE TEST case).

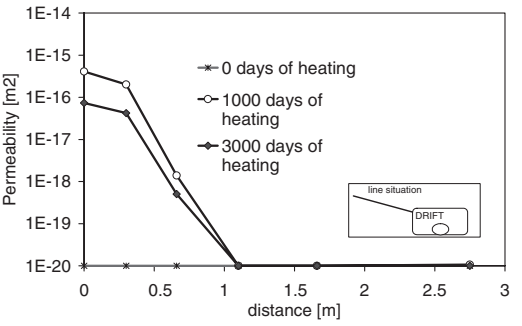

Figure 3.6. Evolution of permeability into the rock for some times (EDZ TSDE TEST case).

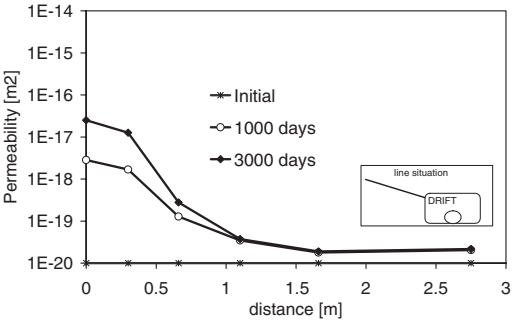

Figure 3.7. Permeability evolution in the rock near the drift walls (EDZ OPEN DRIFT case). Permeability monotonously increases.

One of the objectives of the investigation of the EDZ consists in predicting its permeability. In order to achieve this objective a power law has been used. This law expresses permeability as a function of the initial permeability, initial porosity, and the current porosity of the rock. This law neglects anisotropy effect which could be incorporated later. The mathematical expression is as follows:

$$k = k_0 \frac{\phi^n}{\phi_0^n};\ k = 10^{-21} \frac{\phi^{3.5}}{0.001^{3.5}} = 3.2 \times 10^{-11} \phi^{3.5} \qquad (3.1)$$

where k is intrinsic permeability, ϕ is porosity, and n is the power of porosity, were some values are proposed based on permeability measurements in rock salt.

Permeability in the EDZ has been calculated using this law and is plotted in Figure 3.5. For a porosity of 0.027 a value of 10^{-15} m^2 is obtained. These values of permeability are in agreement with those obtained in the Asse mine through gas flow tests. Figure 3.6 shows permeability as a function of distance.

The permeability and porosity evolutions with respect to the drift wall have been studied in the rock for several distances. Figure 3.7 shows permeability values respectively. The plots correspond to a line which starts in the upper part of the drift wall and goes through the rock in the direction where the most important dilation is expected. The results are presented for 0, 1000 and 3000 days of simulation.

The highest permeability was reached between 500 and 1000 days of heating approximately. Later, permeabilities decrease and the values were (next to the drift wall) of about 10^{-16}–10^{-17} m^2. The initial situation was not recovered after 10 years of simulation. The dilation effects on permeability were not important for distances greater than 1.5 metres.

Dilatancy has been also investigated for non-heated sections, this is referred as the EDZ OPEN DRIFT case. This was done in order to obtain results for a reference case (non-heated open drift), which has more information from in situ measurements. Dilatancy may be present during the excavation of the drifts, before backfilling. Dilatancy may act also in the near-field of instrumentation boreholes or around open drifts excavated for other purposes.

The geometry considered is the same as was used for the TSDE test case. The relationship proposed above

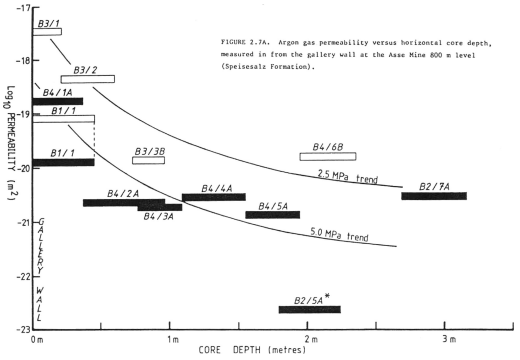

Figure 3.8. Permeability values obtained trough Argon gas injection in a rock salt sample coming from the Asse mine.

has been used to calculate the permeability values also in this case (Figure 3.7). The permeability results reflect correctly the spatial evolution of permeabilities near the drift walls if one compares them with the experimental results shown in Figure 3.8 measured in Asse mine by Peach et al (1987).

Both, the order of magnitude and the spatial variation are reasonably well captured by the model.

Stress paths provide an explanation of the response observed in the test. They permit to see the different regimes of stress response. First there is an elastic response due to the presence of the drift and the assumption of isotropic initial stress (12 MPa in all directions). Afterwards there is a stress relaxation caused by the viscous components of the model. Then a dilatant deformation takes place due to the shape of the yield function. Finally, there is a decrease in the deviatoric stress and increase in the mean stress which implies that the dilatant conditions vanish. Dilatancy disappears when deviatoric stress falls below 7 MPa, approx. This would correspond to a time before 1000 days. For the EDZ OPEN DRIFT case, it can be observed that the dilatant regime remains due to the absence of confinement (no backfill in this case).

4 CONCLUSIONS

A three-dimensional coupled thermo-mechanical analysis contributes to the understanding of an in situ test simulating a repository in rock salt. The main features of the calculations are: (1) Full coupling between mechanical and thermal problem, (2) Performed in three dimensions, (3) Incorporates the updated version of the creep model for crushed salt, (4) Includes observation drifts with appropriate boundary conditions, (5) A relaxation of stresses before heating is considered, (6) Actual lithostatic stress of 12 MPa is considered.

The comparison of calculated temperatures, convergences and stresses with the corresponding measurements shows a good agreement. The most important discrepancies appear in the cold section. Former calculations in two-dimensions were leading to overestimation of temperatures and stresses, and consequently, of convergences.

Another modelling effort related to the behaviour of the EDZ (Excavation Disturbed Zone) has been conducted. The analysis consists in allowing dilatancy induced by shear stress to develop. As dilatancy develops,
rock porosity and thus rock permeability increase in the vicinity of the drift wall. A reference case of an open drift is also used for comparison with the TSDE test. It happens, as well, that the calculated permeabilities for the open drift case are very consistent with measured values in the salt mines.

ACKNOWLEDGMENTS

The authors acknowledge the funding of the European Community through the contracts of BAMBUS I and BAMBUS II projects.

REFERENCES

Bechthold, W., T. Rothfuchs, A. Poley, M. Ghoreychi, S. Heusermann, A. Gens, S. Olivella (1999): Backfilling And Sealing Of Underground Repositories For Radioactive Waste In Salt (Bambus Project), EUR 19124 EN, CEC.

Bechthold, W. and W. Bollingerfehr (2001): Backfilling and Sealing of Underground Repositories for Radioactive Waste in Salt, Phase Ii, (Bambus Project), Proc. Cluster URL Seminar Mol.

Droste, J., H.K. Feddersen, T. Rothfuchs and U. Zimmer (1996): The TSS Project: Thermal Simulation of Drift Emplacement, GRS.

Olivella, S., A. Gens, J. Carrera, E.E. Alonso (1996): Numerical Formulation for a Simulator (CODE_BRIGHT) for the Coupled Analysis of Saline Media Engineering Computations, Vol 13, No 7 87–112.

Olivella S., A. Pudewills, A. Gens, U. Heemann, (2001): Review of TSDE In Situ Test Thermo-Mechanical Modelling. CLUSTER Seminar, organised by CEE, Mol, EUR 19954, pp 103–118.

Olivella S. and A. Gens (2002): A constitutive model for crushed salt, Int. J. Numer. Anal. Meth. Geomech., 26:719–746.

Peach, C.J., C.J. Spiers, A.J. Tankink, H.J. Zwart (1987): Fluid and ionic transport properties of deformed salt rock, Nuclear Science and Technology, CEC, vol EUR 10926 EN.

Rothfuchs, T., J. Prij, K.-P. Kröhn, B.A. Van den Horn, K. Wieczorek (1996): The DEBORA – Project Phase I. Development of Borehole Seals for High-Level Radioactive Waste Repositories in Salt Formations, Final Report, EUR 16928 EN, CEC, Brussels.

The Mechanical Behavior of Salt – Understanding of THMC Processes in Salt –
Wallner, Lux, Minkley & Hardy, Jr. (eds)
© 2007 Taylor & Francis Group, London, ISBN 978-0-415-44398-2

Modeling of hydro-mechanical behavior of rock salt in the near field of repository excavations

A. Pudewills
Forschungszentrum Karlsruhe GmbH, Institut für Nukleare Entsorgung, Karlsruhe, Germany

ABSTRACT: In this paper, the development of the Excavation Disturbed Zone (EDZ) in the rock salt around a disposal drift and the consolidation behaviour of backfill material are presented. In order to perform this analysis, finite element codes containing a set of time- and temperature-dependent constitutive models have been used. A new viscoplastic constitutive model for rock salt that can describe the damage of the rock is proposed. The results of the simulations show that under expected repository conditions the volume closure and the compaction of the backfill are mainly determined by the temperature increase and the lithostatic pressure. Furthermore, the numerical results demonstrate the importance of the increasing compaction pressure in the backfill on the evolution of the EDZ.

1 INTRODUCTION

Repository concepts for disposal of heat generating radioactive waste are based on multiple barriers for protection of the environment against the radioactive nuclides. According to one of these concepts, the containers with the radioactive waste will be placed in vertical boreholes or long parallel drifts at a depth of about 800 to 1000 m below the surface in a rock salt formation (Bechthold 1993). The remaining space between the containers and host rock will be filled with dry crushed salt. It is expected that in response to the thermally induced creep closure of the excavations the backfill material will compact sufficiently to serve as an efficient seal for the radioactive waste. The performance assessment of such nuclear waste repositories in rock salt requires laboratory tests, field experiments, and the use of adequate numerical models to predict the long-term thermomechanical effects in the near and far fields of the repository. The numerical reliability of the calculations and the predictive capabilities were recently demonstrated in benchmark activities and also by comparison with results of the in situ heater tests (Bechthold 1999, Pudewills 2003).

Construction of deep underground structures leads to the perturbation of the initial lithostatic stress state in the rock mass around the openings, creating micro-cracks and degrading the hydro-mechanical rock properties. The evolution of the EDZ and the hydro-mechanical behavior of this zone represents important issues with respect to the integrity of the geological and technical barriers.

The aim of numerical modeling is to predict the development and evolution of the EDZ under different conditions and its interaction with the backfill material. To investigate the processes, numerical models with adequate constitutive laws are under development.

A new material model for rock salt that can describe the damage of the rock has been implemented in the available finite-element codes. According to this model, the total strain rate is given as the sum of elastic and viscoplastic strain rates. The viscoplastic strain rate is decomposed into a part without volume changes of the material and a second one taking into account the volume changes due to the damage. In this case, the viscoplastic flow function depends on mean stress, deviatoric stress, and volumetric strain. The rock damage was judged by criteria for shear and tensile fracture and by the dilation criterion. A preliminary relationship between permeability and the volumetric strain is employed to calculate the hydraulic properties of the EDZ.

The FAST-BEST code, based on the coarse mesh method (Ploumen 1979) and secifically developed for studying the drift disposal, was used to predict the temperatures. For the thermomechanical analyses the general-purpose code ADINA (Adina R&D Inc. 2004) was used. This code was extended to investigate the creep compaction of backfill material.

2 CONSTITUTIVE MODEL FOR ROCK SALT

The constitutive model proposed is based on the assumption of small strains, where the total strain rate is split into elastic and viscoplastic parts as follows:

$$\dot{\varepsilon}_{tot} = \dot{\varepsilon}_{el} + \dot{\varepsilon}_{vp} \tag{1}$$

where:
$\dot{\varepsilon}_{el}$ – elastic strain rate tensor,
$\dot{\varepsilon}_{vp}$ – viscoplastic strain rate tensor.
The elastic behavior is assumed to be time-independent. Furthermore, the viscoplastic strain rate tensor is decomposed into a viscoplastic strain rate tensor by constant volume and a viscoplastic strain rate tensor due to damage that considers the volume change, such as dilatancy or compaction of the material:

$$\dot{\varepsilon}_{vp} = \dot{\varepsilon}^{c}_{vp} + \dot{\varepsilon}^{d}_{vp} \tag{2}$$

where:
$\dot{\varepsilon}^{c}_{vp}$ – viscoplastic strain rate without volume change,
$\dot{\varepsilon}^{d}_{vp}$ – viscoplastic strain rate due to damage which describes a volumetric strain.

For each viscoplastic strain rate, an associated flow rule is used (Owen 1985):

$$\dot{\varepsilon}^{vp}_{ij} = \gamma \langle \Phi(F(\sigma)) \rangle \frac{\partial Q}{\partial \sigma_{ij}} \tag{3}$$

where:
$\gamma = a_1 \cdot e^{-\frac{a_2}{T}}$ – the fluidity parameter,
a_1, a_2 – material constants,
T – temperature.

The term $\langle \Phi(F) \rangle$ denotes a monotonic function of the yield function (F). The meaning of the brackets $\langle . \rangle$ is as follows:

$$\begin{cases} \langle \Phi(F) \rangle = 0 & \text{if } F \le 0 \\ \langle \Phi(F) \rangle = \Phi(F) & \text{if } F > 0 \end{cases} \tag{4}$$

The function Φ (F) is defined as:

$$\Phi(F) = (F - F_0)^m \tag{5}$$

in which (m) is an arbitrary constant and (F_0) is the uniaxial yield stress and set to zero for instance. For our viscoplastic model, the functions (F^c) and (F^d) are as follows:

$$F^c = q^2 \qquad \text{(without volume change)} \tag{6}$$

$$F^d = n_1 \cdot p^2 + n_2 \cdot q^2 \tag{7}$$

Table 1. Material constants and parameters used in the numerical analysis.

Thermoelastic properties	$E = 36$ GPa; $\nu = 0.27$; $\alpha = 4.2E-05$ 1/K
Viscoplasticity, equations (3), (5)	$a_1 = 2.08E-05$ 1/s; $a_2 = 6520\,K^{-1}$; $m = 2$; $T = 293$ K
Dilatancy equations (8), (9)	$c_1 = 0.7$, $c_2 = 500$, $c_3 = 1$
Permeability equation (10)	$A = 3.2\,E-11$; $B = 3.5$ (Bechthold, 2004)

where: p – the mean normal stress,
q – the standard stress deviator;
n_1, n_2 – material functions of the volumetric strain, ε_{vol}, and expressed as:

$$n_1 = c_1 \cdot \left(\frac{q^2}{p^2} - c_2 \cdot \frac{\eta_0 + \varepsilon_{vol}}{1 + \varepsilon_{vol}} \right) \tag{8}$$

$$n_2 = 1 - c_3 \cdot n_1 \cdot \frac{p^2}{q^2} \tag{9}$$

with c_1, c_2, c_3 being material constants to be evaluated by laboratory tests. In the present approach η_0 is the initial porosity of the undisturbed rock salt.

The viscoplastic material model for damage is based on the mathematical formulation proposed by (Hein 1991) for granular materials, such as crushed salt, and was implemented in the finite-element code ADINA. A detailed description of the finite-element algorithm is presented in (Pudewills 1999). This algorithm was also used to implement the current damage model in both programs. Furthermore, separate criteria are available for shear and tensile fracture and a compression-dilation criterion (Hunsche 1993) to judge the damage of rock salt (i.e. microcracks or fractures).

A preliminary relation between permeability and the volumetric strain given in the references Pfeifle (1998) and Bechthold (2004) is used to calculate the permeability of the rock salt:

$$k = A \cdot \varepsilon_{vol}{}^{B} \tag{10}$$

where (k) is permeability of rock salt and A and B are material parameters.

3 CONSTITUTIVE MODEL FOR BACKFILL

The constitutive relation of crushed salt as backfill material is based on a viscoplastic formulation

Table 2. Parameter for the constitutive model of backfill material.

Eq. (11)	Eqs. (12) und (13)
$A = 5.45 \cdot 10^{-7}\ MPa^{-5}s^{-1}$	$a = 0.0165$
$Q/(R/T) = 6520\ K^{-1}$	$b = 0.9$
	$c = 0.1$
	$m = 2.25$
	$d = 0.0003$
	$\eta_0 = 0.36$

and considers both volumetric and deviatoric strain rates under hydrostatic and deviatoric stress conditions (Hein 1991).

$$\dot{\boldsymbol{\varepsilon}}_{cs} = A \cdot e^{-Q/R/T} \cdot (h_1 \cdot p^2 + h_2 \cdot q^2)^2 \cdot (h_1 \cdot p / 3 \cdot \mathbf{1} + h_2 \cdot \mathbf{S}ij) \quad (11)$$

with h_1 and h_2 functions of the backfill porosity:

$$h_1(\eta) = a / (((\eta_0/\eta)^c - 1) / \eta_0^c + d)^m \quad (12)$$

$$h_2(\eta) = b \cdot h_1(\eta) + 1 \quad (13)$$

where $\dot{\boldsymbol{\varepsilon}}_{cs}$: tensor of the strain rate
p: mean normal stress
1: unit tensor
q: deviatoric stress invariant
Sij: tensor of the deviatoric stress
η: porosity
η_0: initial porosity
T: absolute temperature
Q: activation energy
R: universal gas constant
a, b, c, d and m are material parameters

The material parameter values and the functions h_1 and h_2 are derived from extensive triaxial tests performed by Korthaus (1996).

4 ANALYSIS OF A DISPOSAL DRIFT

Taking into account the periodic pattern and symmetry of the disposal field, it was also assumed that all disposal drifts in the emplacement panel were excavated at time zero and filled with POLLUX casks and crushed salt instantaneously after 0.7 years. A three dimensional model of a representative portion of the disposal drift were defined for the thermal analysis. Details of thermal calculations are given in reference Pudewills (1997).

In further two-dimensional thermomechanical calculations the temperatures are interpolated from a vertical section passing through the centre of the model geometry. A plane strain finite element model was used for this investigation. The vertical section right through the center of a POLLUX cask represents only one half of the disposal drift and of the pillar between adjacent drifts (Fig. 1). Symmetry conditions are assumed on the left and the right border. The upper boundary of the model was loaded with 18 MPa (i.e. the lithostatic pressure at the depth of the emplacement level).

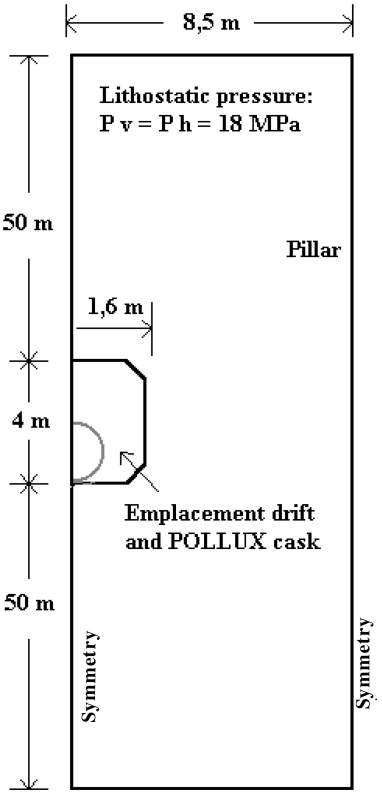

Figure 1. Geometry and boundary conditions of the model.

The numerical simulation started with the calculation of the isothermal drift closure and the stress distribution around the disposal drift prior to the emplacement of the POLLUX casks. After about 200 days, the temperature development and the backfill material in the drift were taken into account. The thermomechanical analyses were continued over a period of 50 years.

For the illustration, in Figure 2 the distribution of the deviatoric stress and the volumetric strain (void volume) in the vicinity of the disposal drift 10, 250 days after excavation and about 1.75 years after casks and backfill emplacement are presented. The region in the pillar next to the drift shows highest effective stress during this phase. The calculated permeability of the rock salt around the test drift are in the order of magnitude with few in situ measurements (Bechthold 2004).

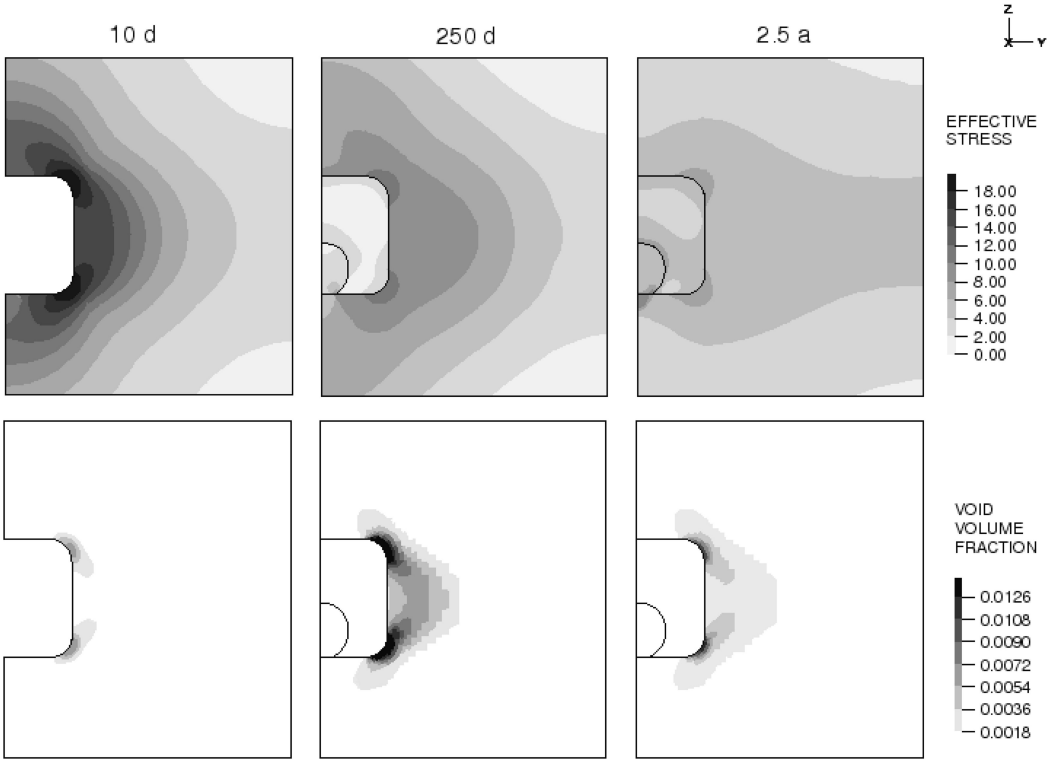

Figure 2. Distribution of the effective stress and the void volume fraction in the vicinity of a disposal drift 10, 250 days and 2.5 years after excavation.

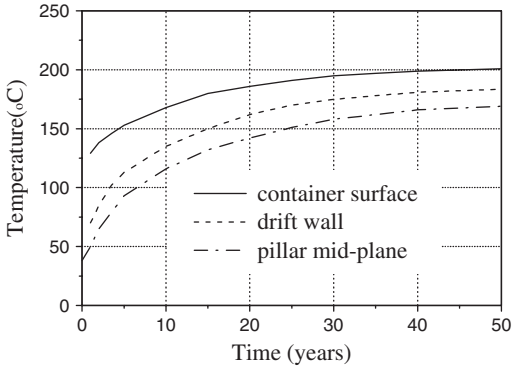

Figure 3. Calculated temperature at three different positions.

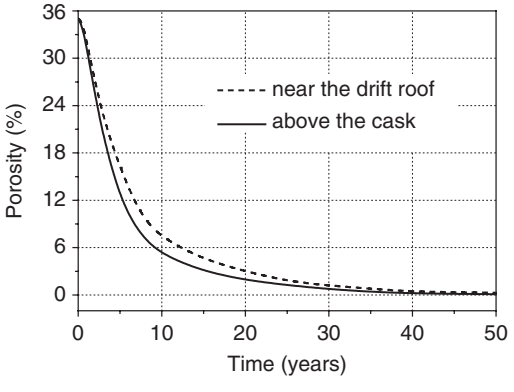

Figure 4. Development of the backfill porosity.

The compression-dilation boundary near the drift surface has almost been reached and the extension of this disturbed zone is about 2 m.

After emplacement of the casks and backfill in the disposal drift, the volume closure and, hence, the compaction of the backfill material are mainly determined by the temperature development and the thermomechanical behavior of the crushed salt.

The histories of the calculated temperatures at three characteristic points are presented in Figure 3. The development of the backfill porosity at two positions in the drift and the stresses in the backfill material are shown in Figures 4 and 5.

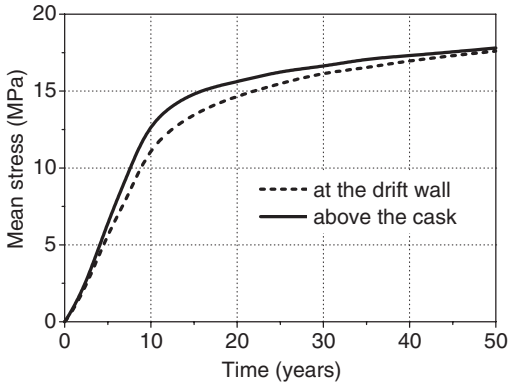

Figure 5. Development of mean stress into backfill.

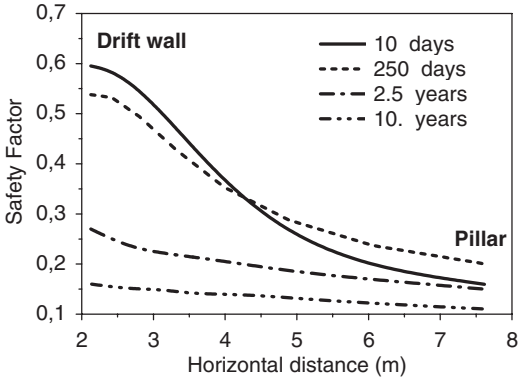

Figure 6. Development of the safety factor in the pillar for different times.

These results show that in a repository at a depth of about 870 m the creep rates of the rock salt and the closure rates will be significantly higher than observed in the in situ test drifts (Bechthold 2004) and that the backfill will be compacted to a porosity of about 2% after about 20 years of heating. The region in the pillar next to the drift shows highest shear stress during the operational phase.

Over time, the compaction pressure in the crushed salt increases and becomes large enough to support substantially the rock salt around the drift and a relaxation and redistribution of the stresses in the pillar take place during the first 10 years after the emplacement of the casks. Considering the strength criterion given by Hunsche (1993), a safety factor was defined as the ratio of the current value of the octaedric shear stress to the predicted octaeder shear stress upon failure (i.e. $FS = \tau_o/\tau_{o,f}$). The failure of the rock salt due to compressive stress will occur when $FS > 1$. The distribution of the calculated safety factor in the pillar at the different time points is shown in Figure 6. It should be pointed out that the safety factor at the drift wall decreases relatively fast from values of about 0.55 at the start of heating to the values less than 0.1 after 10 years. Due to this fact there are no cracks to be expected according to the failure criterion applied.

5 CONCLUSIONS

- A new viscoplastic model that describes the damage of the rock salt was used to study the evolution of the EDZ. After excavation, the EDZ moves rapidly outwards from the opening. Then the expansion rate decreases due to the increasing support of the backfill material
- The numerical results show that already after 20 years of heating the porosity in the backfill has become greatly reduced.
- Over time, the compaction pressure in the backfill increases and therefore it supports the rock salt around the drift. A relaxation and redistribution of the stress in the pillar takes place. However, the assumed safety factor remains everywhere less than unity, i.e., no fractures or micro-cracks are expected.
- The calculation results demonstrate that the crushed salt behavior is a key factor in the long-term stability of the disposal drifts in salt formations.
- Nevertheless more complex material laws taking into account the damage and also the healing of rock salt have to be considered.

REFERENCES

Adina R & D Inc. 2004. ADINA (Automatic Dynamic Incremental Nonlinear Analysis), Report ARD 01-9, Watertown, MA, USA.

Bechthold, W., Closs, K.D., Knapp, U. & Papp, R. 1993. System analysis for a dual-purpose repository, Final Report, EUR 14595 EN, Brussels.

Bechthold, W. et al. 1999. Backfill and Material Behaviour in Underground Repositories for Radioactive Waste in Salt (BAMBUS Project), Final Report, EUR-19124 EN, Brussels.

Bechthold, W. et al. 2004. Backfilling and sealing of underground repositories for radioactive waste in salt, (Bambus-II project), Final report, EUR-20621-EN, Brussels.

Hein, H. J. 1991. Ein Stoffgesetz zur Beschreibung des thermomechanischen Verhaltens von Salzgranulat, Dissertation, RWTH Aachen.

Hunsche, U. 1993. Strength of rock salt at low mean stress, *Geotechnik-Sonderheft*, *Glückauf*, Essen, pp. 160–163.

Korthaus, E., 1996. Consolidation and Deviatoric Deformation Behaviour of Dry Crushed Salt, Proc. of 4th Conf. on the Mechanical Behavior of Salt, Montreal, Canada, pp. 365–377.

Owen, D. R. J. & Hinton, E. 1980. Finite elements in plasticity: theory and practice, Pineridge Press, Swansee.

Pfeifle, T. W. et al. 1998. Experimental Determination of the Relationship between Permeability and Microfracture-Induced Damage in Bedded Salt, *Int. J. of Rock Mech. &*

Min. Sci., (35): 4–5, Paper No. 42 Conference Ref.: USA-324-1.

Ploumen, P. Strickmann, G. & Winske, P. 1979. Untersuchungen zur Temperaturentwicklung bei der Endlagerung hochradioaktiver Abfälle, Teil I: Berechnung der zeit- und ortsabhängigen Temperaturfelder, ATW, (2): 85–91.

Pudewills, A. 1997. Thermal simulation of drift emplacement: temperature analyses, FZKA 5955, Forschungszentrum Karlsruhe GmbH.

Pudewills, A. & Krauss, M. 1999. Implementation of a viscoplastic model for crushed salt in the ADINA program, *Computers and Structures*, (72): 293–299.

Pudewills, A. & Droste, J. 2003. Numerical modelling of the thermomechanical behaviour of a large-scale underground experiment, *Computers and Structures*, (81): 911–918.

The Mechanical Behavior of Salt – Understanding of THMC Processes in Salt –
Wallner, Lux, Minkley & Hardy, Jr. (eds)
© 2007 Taylor & Francis Group, London, ISBN 978-0-415-44398-2

Simulation of long term thermal, hydraulic and mechanical interaction between buffer and salt host rock

Wenqing Wang & Robert Walsh
GeoSystemsResearch, Center for Applied Geoscience, University of Tübingen

Hua Shao
Federal Institute for Geosciences and Natural Resources (BGR), Hannover

Mingliang Xie
INTERA – Environmental Consultants, Ottawa, Canada

Olaf Kolditz
Environmental Informatics, Helmholtz-Center for Environmental Research (UFZ), Leipzig / TU Dresden

ABSTRACT: This work is focused on the numerical analysis of thermo-hydro-mechanical (THM) coupled processes in a hypothetical nuclear waste repository hosted in salt rock. Creep behavior of the salt rock is an important aspect of the present study. A temperature dependent quasi-stationary creep model, based on the BGR model, is utilized to represent time dependent deformation effects in salt rock induced by mechanical and thermal processes. The finite element method is employed for modeling the resulting THM coupled problem. Two comparative case studies (accounting to and neglecting creep effects) are carried out for a two-dimensional model of a nuclear waste repository scenario undergoing THM coupled processes. The importance of the creep processes in salt rock and crushed salt buffer materials is highlighted by comparing the results of the two scenario simulations.

1 INTRODUCTION

Radioactive nuclear waste will generate a large amount of heat for a long period of time. This will significantly influence thermal, hydraulic, mechanical as well as chemical processes in the near field rock of nuclear waste repositories (Tsang 1987). As a result, material properties of rock and buffer materials can alterate considerably at a long term scale. Such phenomenona are of interest in order to assess the long term safety of nuclear repositories. Salt rock in the deep underground is a candidate as host rock for the deposition of high-level nuclear waste, due to the appropriate thermo-physical properties of high thermal conductivity, low permeability and porosity, and creep behavior (Yaramanci 1994, Korthaus 1998, Pudewills 2001, Hou & Lux 2004). Among these properties, in particular the creep behavior, which causes irreversible deformation over time, supports the sealing of open repositories in a relative short time span. Therefore, thermal and creep effects are important processes influencing the disposal of the nuclear waste.

The subject of the present study is the numerical analysis of THM coupled processes in salt rock including creep effects. To this purpose the finite element method (Lewis & Schrefler 1998, Kolditz 2002, Wang et al. 2005, Wang & Kolditz 2007) is used in order to solve the heat transport, fluid mass balance and momentum balance equations for salt rock and crushed salt buffer materials. The implementation of creep processes was conducted in the framework of the numerical simulator GeoSys/RockFlow (Kolditz et al. 2006).

The presented numerical scheme is applied to a two dimensional model of the near field of a hypotheticcal nuclear waste repository with crushed salt as buffer material. The numerical modeling covers the excavation phase as well as the closure phase. The interaction between the buffer material and the host rock occurs during the closure phase. This is the time period after the waste canister and crushed salt are installed in the excavated drift. To investigate the changes of temperature and creep in the near field of the repository and the buffer material, we consider a million year period of THM coupled processes. A quasi-stationary temperature dependent creep model (BGRa model, Cristescu & Hunsche 1997), is used to represent creep behavior in salt rock.

The paper is organized as follows: (1) description of the governing equations and constitutive equations, (2) definition of the two-dimensional numerical model for the near field of a nuclear waste repository, and (3) presentation, discussion and comparison of simulation results.

2 GOVERNING EQUATIONS

2.1 *Non-isothermal flow in porous media*

We consider non-isothermal fluid flow in a deformable porous medium including vapor diffusion effects. The Richards approximation is used for unsaturated flow behavior as only few water is contained in the system. The Richards approximation neglects the gas phase dynamics. If gas pressure effects become important two-phase flow models have to be involved into the THM concept. The corresponding fluid mass balance equation for the liquid phase is given by

$$\begin{aligned} & n\left[\frac{\rho_w-\rho_v}{\rho_w}\frac{\partial S}{\partial p}+S\beta_p+(1-S)\frac{\rho_v}{\rho_w^2 RT_{abs}}\right]\frac{\partial p}{\partial t} \\ & \quad +\nabla\cdot\left(\mathbf{q}_w+\mathbf{q}_v\right)/\rho_w+S\frac{\partial}{\partial t}(\nabla\cdot\mathbf{u}) \\ & \quad n\frac{1-S}{\rho_w}\left(h\frac{\partial\rho_{vS}}{\partial T}+\frac{\rho_v p}{RT_{abs}^2}\right)\frac{\partial T}{\partial t}=0 \end{aligned} \tag{1}$$

where β_p is the storativity. The unknown field functions of eqn. (1) are saturation of the liquid phase S and liquid pressure p. Additionally, coupling terms resulting from temperature T changes and displacements $\mathbf{u}$ have to be considered. The third terms addresses temporal porosity changes due to consolidation processes.

With the classical Darcy law, liquid flow q_w driven by pressure and gravity forces is defined as

$$\mathbf{q}_w=-nS\left(\rho_w\frac{k_{rel}}{\mu}(\nabla p-\rho\mathbf{g})\right) \tag{2}$$

where, ρ is the density, n is the effective porosity of the media, μ is the viscosity of the fluid, k_{rel} is the relative permeability, and g is the gravitational acceleration. Additionally, we have to consider vapor flow in variably saturated pores due to molecular diffusion and to temperature gradients. Vapor flow is given by (Rutqvist et al. 2005)

$$\mathbf{q}_v=-D_{pv}\nabla p-f_{Tv}D_{Tv}\nabla T \tag{3}$$

where f_Tv is a thermal diffusion enhancement factor, which is equal to 1.0 in the present simulation, and D_{pv} and D_{Tv} are diffusion coefficients defined by the following expressions

$$\begin{aligned} D_{pv} &= \frac{D_v\rho_v}{\rho_w RT_{abs}} \\ D_{Tv} &= D_v\left(h\frac{\partial\rho_{vS}}{\partial T}-\frac{\rho_v p}{\rho_w RT_{abs}^2}\right) \end{aligned} \tag{4}$$

with T_{abs} the temperature in Kelvin and h the relative humidity according to

$$h=e^{P/\rho_w RT_{abs}} \tag{5}$$

where $R=461.6$ J/kgK [notation] is the specific gas constant for water vapor, and ρ_{vS} is the saturated vapor density given by (Rutqvist et al. 1999),

$$\rho_{vS}=10^{-3}\,e^{19.891-4975/T_{abs}} \tag{6}$$

and vapor density $\rho_v=h\rho_{vS}$.

The boundary conditions for the flow problem are Neumann type as

$$\mathbf{q}_w\cdot\mathbf{n}=q_\Gamma,\forall\,\boldsymbol{x}\in\partial\Omega \tag{7}$$

or Dirichlet type as

$$p=p_\Gamma,\quad S=S_\Gamma,\forall\,\boldsymbol{x}\in\partial\Omega \tag{8}$$

This initial-boundary-value-problem can be solved after specifying the initial conditions of the unknowns.

2.2 *Deformation with time effect*

The total strain increment $\Delta\epsilon$ can be decomposed into the components of reversible (elastic) strain, temperature induced strain, and irreversible time dependent strain (creep) in the following manner

$$\Delta\boldsymbol{\epsilon}=\Delta\boldsymbol{\epsilon}^e+\alpha\,\Delta T\mathbf{I}+\Delta\boldsymbol{\epsilon}^c \tag{9}$$

where $\mathbf{I}$ is the identity tensor. For the time dependent strain increment, we consider a quasi-stationary creep model (BGRa model by Cristescu & Hunsche 1997), which defines the uniaxial creep strain increment as

$$\Delta\epsilon^c=Ae^{-Q/R_uT}\left(\frac{\sigma}{\sigma^f}\right)^m\Delta t \tag{10}$$

where A, m and Q are parameters determined by experiments, Q[J/mol] is the empirically derived activation energy, $R_u=8.314472$ J/(K_{mol}) [notation] is the universal gas constant, and $\sigma_f=1$ MPa is a stress scaling

factor. For multi-axial deformation, a creep potential can be derived based on the BGRa model (10) as

$$g^c = Ae^{-Q/R_uT}\left(\frac{\sigma}{\sigma^f}\right)^m \tag{11}$$

where $\sigma = ||s||$ is the norm of deviatoric stress s tensor. Furthermore, the portion of the total strain tensor contributed by creep can be obtained by

$$\Delta\boldsymbol{\epsilon}^c = \frac{\partial g^c}{\partial \boldsymbol{\sigma}}\Delta\boldsymbol{\sigma}\Delta t \tag{12}$$

With the generalized Hooke's law, the effective stress with the influence of time effects can be expressed as

$$\Delta\boldsymbol{\sigma} = \mathbb{C}(\Delta\boldsymbol{\epsilon} - \alpha\,\Delta T\mathbf{I} - \Delta\boldsymbol{\epsilon}^c) \tag{13}$$

where $\mathbb{C}$ is the elastic constitutive tensor. Incorporating the stress defined for THM coupled processes in eqn.(13), deformations in porous media can be described by the momentum balance equation as

$$\nabla\cdot(\boldsymbol{\sigma}^k + \mathbb{C}(\Delta\boldsymbol{\epsilon} - \alpha\,\Delta T\mathbf{I} - \Delta\boldsymbol{\epsilon}^c) - Sp\mathbf{I}) + \rho\mathbf{g} = 0 \tag{14}$$

where σ^k is the stress state of the preceding time step k.

2.3 *Heat transport*

For the heat transport problem, we consider convective and diffusive transport. There are two basic kinds of convection recognized as *forced convection* and *free convection*. In the first, the velocity of convective motion is not influenced by temperature dependent fluid properties and the heat energy transport is controlled by the extant pressure field and the resulting flow field. In the latter, flow velocities are driven solely by buoyancy effects in the fluid, which are related to temperature change through the coefficient of thermal expansion. In real hydrogeological systems, there is a mixture of both types of convection. The expression of heat flux in forced convection is given by

$$\mathbf{q}_\mathrm{T} = -(1-n)K_e\nabla T + n\sum_{\gamma}^{phase}(\rho^\gamma C_p^\gamma)T\mathbf{v} \tag{15}$$

where K_e is the heat conductivity, $\Sigma_\gamma^{phase}(\rho_\gamma C_p^\gamma)$ is the flux of heat transported by fluid phases. This flux is reduced by the effective porosity. With the definition of heat flux in (15), the governing equation of the convective heat transport can be derived as

$$\sum_{\gamma}^{phase}(\rho^\gamma C_p^\gamma)\frac{\partial T}{\partial t} - \nabla\mathbf{q}_\mathrm{T} + Q_\mathrm{T} = 0 \tag{16}$$

with the boundary condition

$$\mathbf{q}_\mathrm{T}\cdot\mathbf{n} = q_\mathrm{T}|_\Gamma,\ \text{or}\quad T = T_\Gamma,\ \forall\,\boldsymbol{x}\in\partial\Omega \tag{17}$$

and the initial condition

$$T(\boldsymbol{x}) = T_0(\boldsymbol{x}),\ \forall\,\boldsymbol{x}\in\Omega \tag{18}$$

3 NUMERICAL APPROACH

The method of weighted residuals is applied to derive the weak formulation for all governing equations given in section 2. Assume $\omega\in H^1_\Gamma(\Omega)$ is the test function. The corresponding weak forms are:

- for fluid mass balance equation (1)

$$\begin{aligned}&\int_\Omega n\left[(\rho_w-\rho_v)\frac{\partial S}{\partial p} + S\beta_p\rho_w + (1-S)\frac{\rho_v}{\rho_w RT_{abs}}\right]\frac{\partial p}{\partial t}\omega\,\mathrm{d}\Omega\\ &\quad -\int_\Omega \mathbf{q}_w\cdot\nabla\omega\,\mathrm{d}\Omega + \int_\Gamma \mathbf{q}_w\mathbf{n}\,\omega\,\mathrm{d}\Gamma\\ &\quad +\int_\Omega \nabla\mathbf{q}_v\omega\,\mathrm{d}\Omega + \int_\Omega S\rho_w\frac{\partial}{\partial t}(\nabla\cdot\mathbf{u})\omega\,\mathrm{d}\Omega\\ &\quad +\int_\Omega n(1-S)\left(h\frac{\partial\rho_{vS}}{\partial T} + \frac{\rho_v p}{RT^2_{abs}}\right)\frac{\partial T}{\partial t}\omega\,\mathrm{d}\Omega = 0\end{aligned}, \tag{19}$$

- for heat balance equation (16)

$$\begin{aligned}&\int_\Omega(\rho C_p)\frac{\partial T}{\partial t}\omega\,\mathrm{d}\Omega - \int_\Omega \mathbf{q}_\mathrm{T}\cdot\nabla\omega\,\mathrm{d}\Omega\\ &\quad +\int_\Gamma \mathbf{q}_\mathrm{T}\cdot\mathbf{n}\,\omega\,\mathrm{d}\Gamma - \int_\Omega Q_\mathrm{T}\omega\,\mathrm{d}\Omega = 0\end{aligned}, \tag{20}$$

- for the momentum balance equation (14)

$$\begin{aligned}&\int_\Omega\frac{1}{2}(\boldsymbol{\sigma} - Sp\mathbf{I}) : (\nabla\boldsymbol{\omega} + (\nabla\boldsymbol{\omega})^\mathrm{T})\,\mathrm{d}\Omega - \int_\Omega \boldsymbol{\omega}^\mathrm{T}\cdot\rho\mathbf{g}\,\mathrm{d}\Omega\\ &\quad -\int_\Gamma \boldsymbol{\omega}^\mathrm{T}\cdot\mathbf{t}\,\mathrm{d}\Gamma = 0\end{aligned} \tag{21}$$

Using the Galerkin finite element method, and discretizing the three weak forms in the finite element space leads to three coupled algebraic equations with primary variables p, T and $\boldsymbol{u}$. The coupled equations are solved in the staggered manner.

4 REPOSITORY MODEL

In this work, we consider a hypothetical repository model based on Task D of the DECOVALEX project (Barr et al. 2004), which is adapted to salt rock. Cylindrical drifts with a radius of 1.12 m are excavated at a depth of 800 m in salt rock. Waster canisters

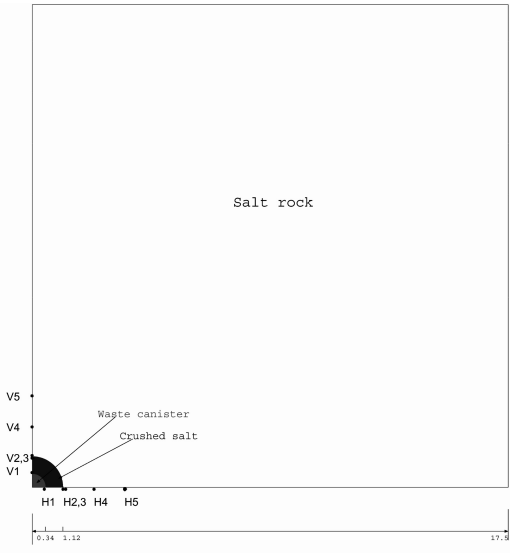

Figure 1. Schematic model of the near field. V1–V5 and H1–H5 are the observation points.

with radius of 0.45 m are installed into to the drifts, which are sealed with crushed salt. Fig. 1 illustrates a schematic near field model. The observation points for comparison are H1-H5 and V1-V5, respectively. H2 and V2 are on the border between the buffer material and the salt rock, and H3 and V3 are located in the salt rock at a distance of 0.01m from the border. The thermal energy generated by the canister is determined by the rate of radionuclide decay and the thermal conductivity of the canister material. Based on this the heat flux from the canister q_T can be calculated. The variation of heat flux with time, which is depicted in Fig. *2*, can be approximated by a function $q_{\mathrm{T}}^{0} e^{\lambda t}$ (Setrada-Gasca & Cobble, 1987).

5 THM MODELING

The modeling is conducted in a domain with vertical dimension of 300 m, which is large enough to represent the near field of the repository in salt rock. Fig. 3 shows the finite element mesh used for the numerical simulations.

Prior to THM modeling for the operational phase, an excavation simulation is performed with a given initial stress field defined by

$$\begin{aligned} \sigma_{xx} &= -(0.055h + 4.6)\ [\mathrm{MPa}], \\ \sigma_{yy} &= -(0.02h + 0.6)\ [\mathrm{MPa}], \\ \sigma zz &= -g\rho h \end{aligned} \tag{22}$$

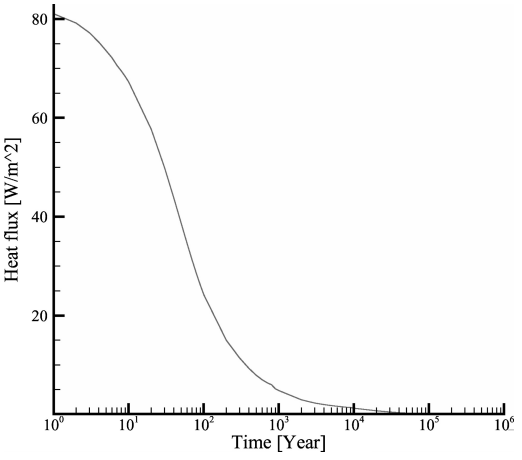

Figure 2. Heat flux from the canister.

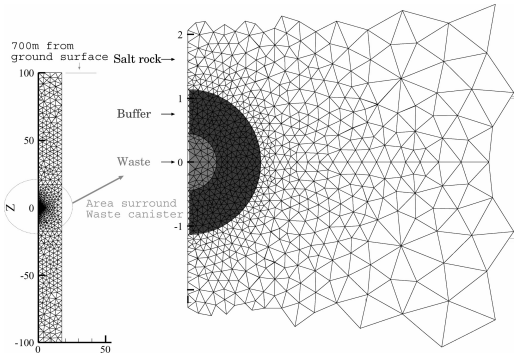

Figure 3. Finite element mesh for modeling.

Equation (22) presents the initial stress definition for the simulation of the operational phase. These formulas are directly taken from the DECOVALEX task D definition. where h is the depth from the ground surface. The initial temperature in the salt body and crushed salt buffer is 30°C. Water saturation is assumed to be 0.4 in the buffer and 0.2 in salt rock. Creep parameters and thermal conductivity as given by Pudewills (2001) are used in the present study for both crushed and salt rock. The values of material properties used for modeling are listed in Table 1. The temperature dependent thermal conductivities of salt rock and crushed salt are depicted in Fig. 4.

In order to demonstrate the influence of creep effects simulations have been performed with and without creep. The simulations are carried out under the assumption of elastic compaction of crushed salt. Both of the simulations give similar results for saturation and temperature under the present boundary and initial conditions. As shown in Fig. 5a,b, temperatures

Table 1. Properties of crushed salt and salt rock.

Parameter	Unit	Value of crushed salt	Value of salt rock
Density	kg/m^3	2200	2200
Young's modulus	MPa	8000	24000
Poisson ratio	–	0.25	27
Thermal expansion coefficient	–	4.2×10^{-5}	4.2×10^{-5}
A of BGRa	year^{-1}	34.37424	65.7
m of BGRa	–	5	4
Activation energy	J mol^{-1}	54.2	54
Thermal conductivity	W/mK	Fig. 4	Fig. 4
Thermal capacity	J/kgK	642	890
Saturated permeability	m^2	1.0×10^{-20}	1.0×10^{-21}

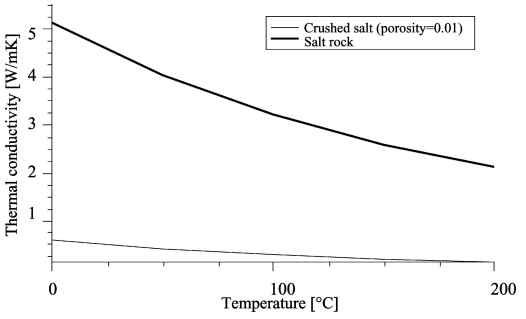

Figure 4. Thermal conductivity as temperature function.

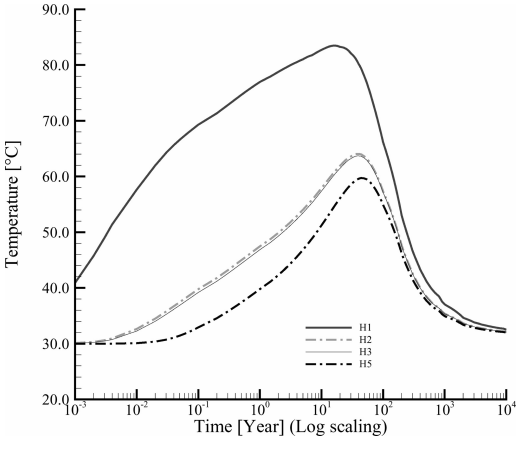

Figure 5a. Temperature evolution at observation points along a horizontal line.

at observation points V1 and H1 reach their maximum value after approximately 16 years.

Fig. 6 a depicts the evolution of saturation at observation points V1, V2 and V3, respectively. As there is only few water in the system, the liquid saturation

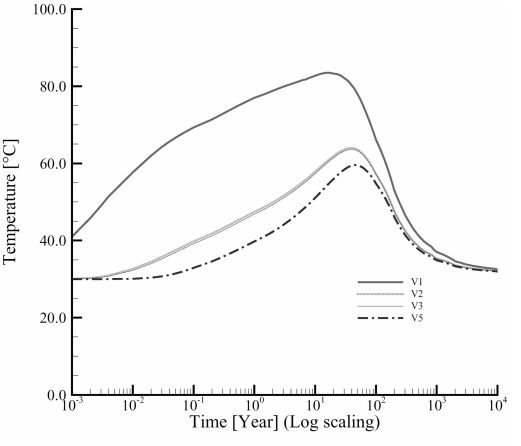

Figure 5b. Temperature evolution at observation points along a vertical line.

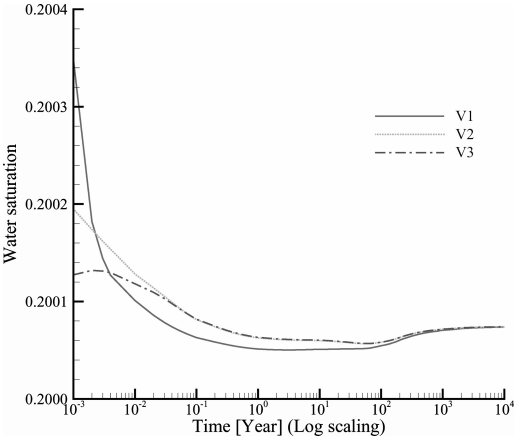

Figure 6a. Saturation evolution at observation points (V1,V2,V3) along a vertical line.

changes are very small. Recalling the temperature evolution at observation points V1 and V3 shown in Fig. 5b, one can observe that the water saturation at these points decreases slightly along with increasing temperature. This is due to the vaporization process of liquid water, which is considered in the present simulation. The water transport in the system in terms of water saturation is presented in Fig. 6a.

Fig. 7a and Fig. 7b give a comparison of stress evolution with and without creep effects. If creep is ignored, the stress evolutions follow the behavior of temperature development. The stress increases or decreases when the temperature increases or decreases, correspondingly. The stress reaches the maximum value when the temperature evolution curve

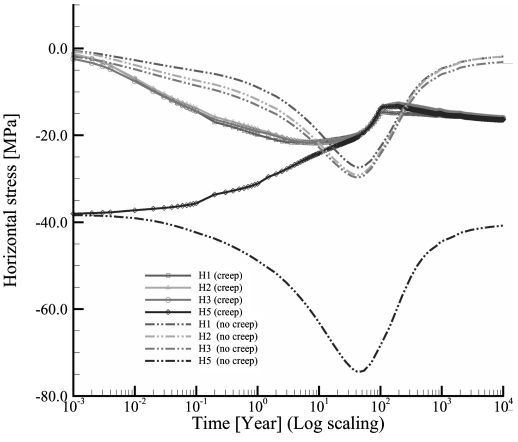

Figure 6b. Horizontal stress evolution at observation points (H1,H2,H3,H5) along a horizontal line.

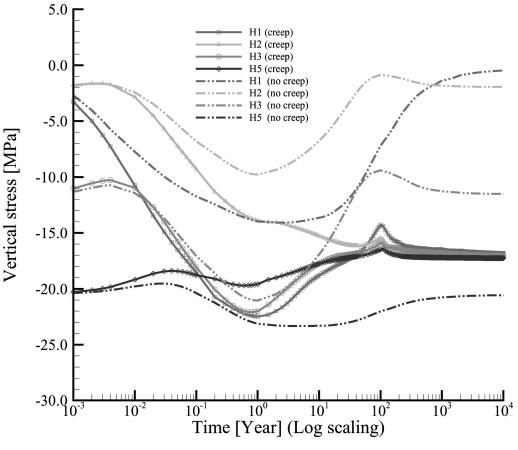

Figure 7a. Vertical stress at specific points on the horizontal line.

arrives at the peak point. In the contrast to this behavior, one can find in Fig. 7a and Fig. 7b that creep relaxes the stress changes, which are induced by temperature changes. Moreover, it is also clear that stresses in the buffer of crushed salt and in the near field salt rock become to be almost identical when the thermal power of the canister decays as the time elapses. Recalling that observation points H1, H2, V1, and V2 are in the buffer zone of crushed salt and observation points H3, H5, V3, and V5 are in the salt rock.

Porosity changes in the crushed salt due to deformation processes are important to hydraulic parameters such as permeability. Based on experimental results on crushed salt by Stührenberg (2004) (Fig. 8), we developed an empirical function of the stress and porosity relationship (Fig. 8). Fig. 9 presents the results for the porosity calculation at observation point H1. Recalling

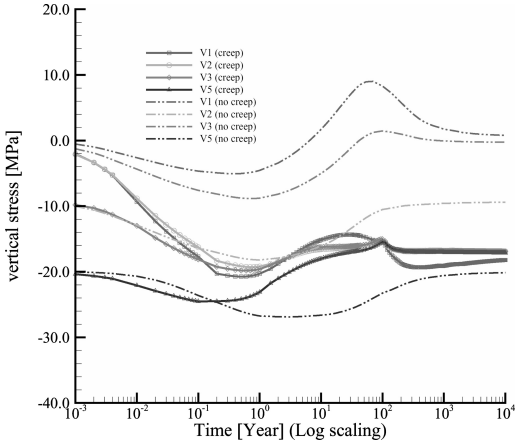

Figure 7b. Vertical stress at specific points on the vertical line.

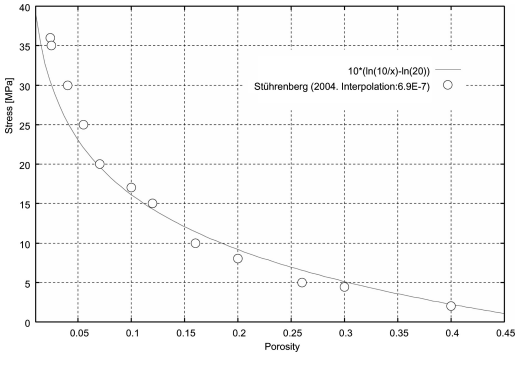

Figure 8. Functional relationship between stress and porosity of crushed salt based on measurements by Stührenberg (2004).

the stress evolution given in Fig. 7a and Fig. 7b, we find that the porosity is reduced when stress is increased.

The porosity is calculated according to the experimentally derived results by Stührenberg (2004), which is directly related to stress measurements (i.e. first stress invariance, Fig. 8). Therefore, the temporal evolution of local porosities as shown in Fig. 9 is directly related to the stress development (Fig. 7a,b).

6 CONCLUSIONS AND FUTURE WORK

In the present study a thermo-hydro-mechanical numerical model is presented for salt rock with crushed salt as buffer material for nuclear waste isolation. This poro-visco-thermo-elastic model includes pressure, creep, and temperature coupling effects. The problem is analysed by THM coupled differential

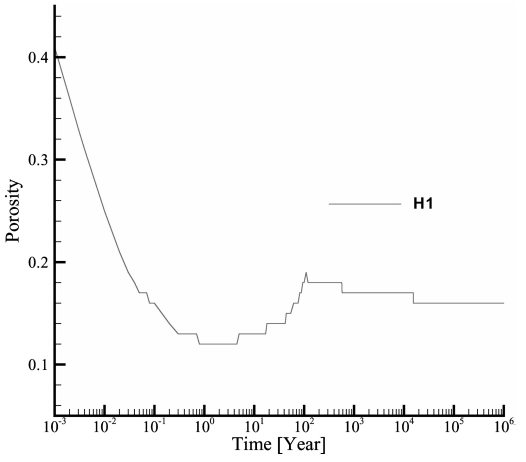

Figure 9. Porosity versus time at observation point H1.

equations, which were solved using the finite element method. A quasi-stationary creep model (BGRa model) is employed to represent time dependent deformation effects in salt rock. The numerical scheme for time-dependent deformation effects is based on an explicit integration of the creep strain rate.

The THM coupled simulations are carried out for a two-dimensional benchmark test originally presented in the DECOVALEX project for bentonite buffers. Some experimentally determined material parameters for salt rock and crushed salt are directly used for the simulation. When creep is taken into consideration in the model, the stress results show that creep can considerably influence the evolving mechanical parameters of the buffer material and the near-field rock. The importance of the creep behavior is highlighted by comparing the results of simulations with and without the consideration of creep. The results show that creep behavior relaxes the effect of temperature on stress. Moreover, the salt rock and the crushed salt buffer have almost the same stress level when a steady state is achieved although their mechanical properties are different and are assumed to be constant in the present study.

The presented poro-visco-thermo-elastic model is the first implementation of this type of coupled THM model in the framework of RockFlow software and it uses a number of simplifications for applications in salt rock. The visco-elastic model itself is verified against several test examples, e.g. Norton's creep model and Balley's analytical solution (Kolditz et al. 2006). A non-isothermal Richards model including vapor flow is used for unsaturated flow in the buffer/host rock system. The Richards model has certain limitations, in particular, if the dynamics of the gaseous phase becomes important. However, several studies have shown, that the Richards model provides a satisfactory approximation even for low-permeable porous media (Kolditz & de Jonge 2004, Rutqvist et al. 2006). In the present case study only few water is in the system and the water is transported mainly as vapor according to the extended Darcy equation (3). Only few studies are available concerning multi-phase flows of brine-gas systems in salt rocks, in particular if the hydro-mechanical coupling becomes important. Therefore, the validity of simplified approaches such as the Richards model has to be verified carefully and improved in future works. In particular, multiphase flow effects have to be considered in brine-gas systems in salt rocks.

ACKNOWLEDGEMENTS

This research work was partially supported by the BMBF under grant No. 02C1114. The authors are grateful of Chris McDermott for his helpful comments of this paper. Also, the authors would like to thank Manfred Wallner for his scientific, technical and logistic support to our research.

REFERENCES

Barr, J. et al. 2004. Draft description for DECOVALEX-THMC task D: Long-term permeability/porosity changes in EDZ and near field, due to THM and THC processes in volcanic and crystalline-bentonite systems. Technical report, Earth Sciences Division, Lawrence Berkeley National Laboratory, USA.

Cristescu, N.D. & Hunsche, U. 1997. *Time Effects in Rock Mechanics*. Wiley.

Hou Z & Lux K.-H. (2004) A new coupling concept for the hydro-mechanical interaction of clay stone and rock salt in underground waste repositories, International Journal of Rock Mechanics and Mining Sciences, Volume 41, Supplement 1, May 2004, Pages 708–713, Proceedings of the ISRM SINOROCK 2004 Symposium.

Korthaus, E. 1998. Experiments on crushed salt consolidation with true triaxial testing device as a contribution to an EC benchmark exercise. Technical report, Institut für Nukleare Entsorgungstechnik, Forschungszentrum Karlsruhe GmbH, Germany.

Kolditz, O. 2002. *Computational Methods in Environmental Fluid Mechanics*. Springer, Berlin.

Kolditz O & de Jonge J (2004): Non-isothermal two-phase flow in low-permeable porous media. Computational Mechanics, DOI 10.1007/soo466-003-0537-0, vol 33, no 5, 345–364.

Kolditz, O. et al. 2005. A process-oriented approach to compute THM problems in porous media. In T. Schanz, editor, *Unsaturated Soils: Numerical and Theoretical Approaches*, pages 53–66, Springer Proceedings in Physics 94.

Kolditz, O. et al. 2006. GeoSys/RockFlow benchmarks, Tech. Report, Centre of Applied Geosciences, University of Tübingen.

Lewis, R.W. & Schrefler, B.A. 1998. *The Finite Element Method in the Static and Dynamic Deformation and Consolidation of Porous Media (Second Edition)*. Wiley.

Pudewills, A. 2001. Numerical analysis of long-term thermo-mechanical behavior of repository structures. In *Transaction SMiRT*.

Rutqvist, J. et al. 1999. Coupled thermo-hydro-mechanical analysis of a heater test in unsaturated clay and fractured rock at Kamaishi mine. LBNL-44203.

Rutqvist, J. 2005. Coupling thermal-hydrological-mechanical analysis within the framework of DECOVALEX-THMC, Task D_THM, step 1: Model inception. Technical report, Earth Sciences Division, Lawrence Berkeley National Laboratory, USA.

Rutqvist, J., J.T. Birkholzer, M. Chijimatsu, O. Kolditz, Q. Liu, Y. Oda, W. Wang, C. Zhang, 2006. Results from an International Simulation Study on Coupled Thermal, Hydrological, and Mechanical (THM) Processes near Geological Nuclear Waste Repositories, Proc. International High-Level Radioactive Waste Management Conference, Las Vegas, April 30 to May 4, 2006.

Setrada-Gasca, C.A. & Cobble, M.H. 1987. Theoretical approximation to transient heat conduction in nuclear waste repositories. *Journal of Engineering Mathematics*, 21:287–293.

Stührenberg, D. 2004. Compaction and permeability behavior of crushed salt and mixtures of crushed salt and bentonite, *DisTec* 2004 in Berlin.

Tsang, C.-F. (editor) 1987. *Coupled processes Associated with Nuclear Waste Repositories*, Academic Press, New York.

Wang, W. et al. 2005. Progress on THM analysis, an inception report for DECOVALEX-THMC task D. Technical report, Center for Applied Geosciences, University of Tübingen, Germany.

Wang, W. & Kolditz. 2007. O. Object-oriented finite element analysis of thermo-hydro-mechanical (THM) problems in porous media. *International Journal for Numerical Methods in Engineering*, 69:162–201.

Yaramanci, U. 1994. Relation of *in situ* resistivity to water content in salt rock. *Geophysical Prospecting*, 41: 229–239.

The Mechanical Behavior of Salt – Understanding of THMC Processes in Salt –
Wallner, Lux, Minkley & Hardy, Jr. (eds)
© 2007 Taylor & Francis Group, London, ISBN 978-0-415-44398-2

Post-tests on thermo-mechanically compacted salt backfill

Chun-Liang Zhang, Tilmann Rothfuchs & Johannes Droste
Gesellschaft für Anlagen- und Reaktorsicherheit (GRS)
Theodor-Heuss-Strasse, Braunschweig, Germany

ABSTRACT: To examine the geotechnical properties of salt backfill which had been compacted for more than 8 years at high temperatures of 90°C to 170°C in the TSDE test drifts in the Asse salt mine, post-tests were carried out on drilled cores. The triaxial compression behavior of the backfill was investigated on large samples of 280 mm diameter and 510 mm to 710 mm lengths. The bulk modulus increased with decreasing porosity. The strength measured on the pre-consolidated samples is comparable to that obtained on the same material but without pre-compaction. Coupled to the mechanical tests, permeability measurements by nitrogen gas were conducted at different porosities. The permeability decreases exponentially from $1 \cdot 10^{-12}$ m^2 at a porosity of 26% to $1 \cdot 10^{-13}$ m^2 at a porosity of 7%. The post-test results confirm the *in-situ* measurements and the constitutive models used for the prediction of the backfill behavior.

1 INTRODUCTION

The *in-situ* experiment of Thermal Simulation of Drift Emplacement (TSDE) was performed in the Asse salt mine in order to verify constitutive models for predicting the compaction behavior of crushed-salt backfill in high-level radioactive waste (HLW) repositories in rock salt. The test field consisted of two 3.5-m-high and 4.5-m-wide and 70-m-long backfilled drifts. In each test drift, three simulated and electrically heated Pollux casks of 1.5 m diameter and 5.5 m length were deposited. Heating was started in September 1990. After five months, the maximum temperature of 210°C was reached at the cask surfaces. Subsequently, the temperatures decreased to ∼170°C and remained in that range over the whole heating period of more than 8 years. Thermally-accelerated drift closure led to a reduction of backfill porosity from initially 35% to 20% in the heated area and to 31% in the non-heated area. The pressure build-up in the heated backfill ranged between 2 and 4 MPa. The coupled thermo-hydro-mechanical processes in the salt backfill and the surrounding rock salt were numerically simulated by modeling teams in the frame of BAMBUS project (Bechthold et al. 1999; Droste et al. 2001). In order to verify the constitutive models used in the numerical calculations, post-test analyses of the thermo-mechanically compacted backfill were conducted after uncovering of the test field in the years 2000 and 2001. The post-tests performed at the GRS geotechnical laboratory focused on the hydro-mechanical behavior of the backfill and are presented in this paper.

2 SAMPLES

For post-test analyses in the laboratory, samples of the compacted backfill were taken from different cross sections in the heated and the non-heated area. Figure 1 shows the layout of the test drifts and cross section I1 of the heated drift B with the locations of the cored boreholes in the backfill.

From the boreholes K4, K5 and K6, six large samples were prepared to sizes of 280 mm diameter and 510 to 710 mm lengths for triaxial compression tests. Three samples are shown exemplarily in Figure 2. The sample characteristics are given in Table 1. The porosities are very similar ranging between $\phi = 25.5\%$ and 26.4%, except for sample K5-4 where $\phi = 28.9\%$. More than 80 other samples which were taken from borehole K3 (D = 100 mm, L = 19.3 m) and from 6 cross sections in the heated and non-heated area of drift B were used for the determination of porosity and permeability of the compacted backfill.

The crushed salt had been emplaced in the drifts by means of the slinger technique. Because the coarser grains had been falling faster than the fine grains, the grain size distribution over the drift cross section was not homogeneous as can be clearly seen from Figure 3. The grain size varied over a wide range increasing from $d_{50} = 1$ mm in the top region to $d_{50} = 6$ mm in the bottom region (d_{50} is the grain size at 50% passage). The

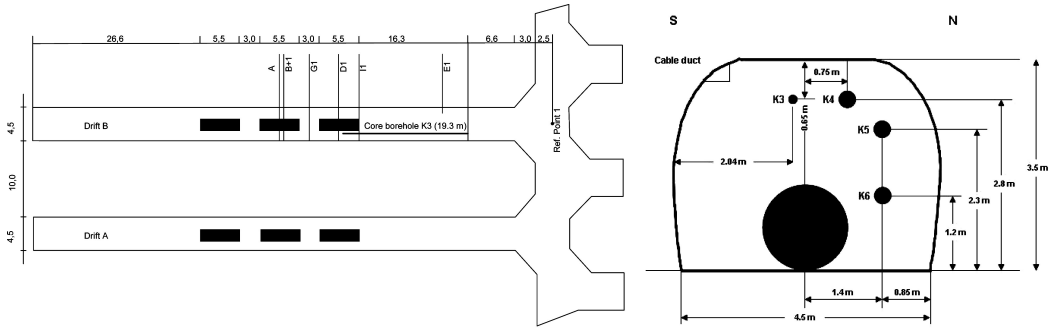

Figure 1. a: Layout of the TSDE test drifts. b: Locations of the cored boreholes in cross section I1 (drift B).

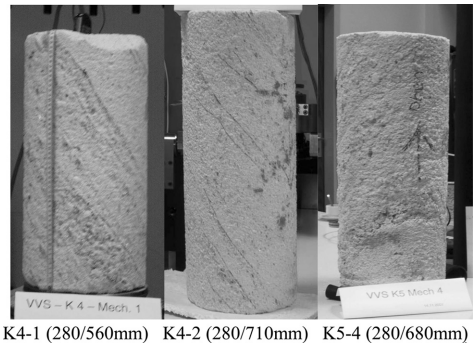

K4-1 (280/560mm) K4-2 (280/710mm) K5-4 (280/680mm)

Figure 2. Large samples drilled from the partially compacted salt backfill.

Table 1. Characters of large samples from the TSDE backfill.

Sample	Sampling position	Diameter (mm)	Length (mm)	Density (g/cm^3)	Porosity (%)
K4-1	K4/27.2–28.4 m	280	561	1.609	25.6
K4-2	K4/29.4–30.4 m	280	712	1.630	25.5
K5-1	K5/27.2–28.0 m	280	509	1.611	26.4
K5-2	K5/28.0–29.0 m	280	579	1.643	26.0
K5-4	K5/29.0–30.0 m	280	679	1.557	28.9
K6-3	K6/31.5–32.5 m	280	585	1.525	26.0

maximum grain size was 31 mm. The grain density was determined by 2.18 g/cm^3.

3 POROSITY

The porosity distribution in the backfill was determined on about 90 samples from four cross sections and borehole K3 in the heated and non-heated area of drift B. The porosity ϕ was calculated using the grain density ρ_g and the bulk density ρ_b of the sample by:

$$\phi = 1 - \frac{\rho_b}{\rho_g} \tag{1}$$

The bulk density was determined from the sample mass and volume.

Figure 4 shows the distribution of backfill porosity at cross section B^{+1} in the central heater area along a vertical and a horizontal profile. Though the variations are significant it can be seen that the porosity decreases generally toward the roof (Fig. 4a) and from the pillar toward the opposite drift wall (Fig. 4b). Actually, the porosity is lowest in the centre of the test field with average porosity values of 21% (vertical profile) and 19% (horizontal profile). These values agree well with the value of 20% derived from drift closure measurements.

It is interesting to compare the post-test results with model predictions. Exemplarily, Figure 5 shows the comparison of the 2D-calculations by Pudewills (Bechthold et al. 1999) with the results of *in-situ* and post-test measurements. The good agreement confirms the constitutive models used.

4 PERMEABILITY

Nitrogen gas was used as the flow medium in the permeability tests. The gas injection pressure was adjusted in the range of 0.1 to 1.0 bar and the gas flow rate was measured with thermal mass flow sensors. The gas permeability was calculated according to Darcy's law:

$$k = \frac{2 \cdot q \cdot \mu \cdot l \cdot p_0}{A \cdot \left(p_1^2 - p_0^2\right)} \tag{2}$$

with k = gas permeability, q = flow rate, μ = viscosity of the gas, l = sample length, A = cross section area of the sample, p_1 = injection pressure, and p_0 = atmospheric pressure.

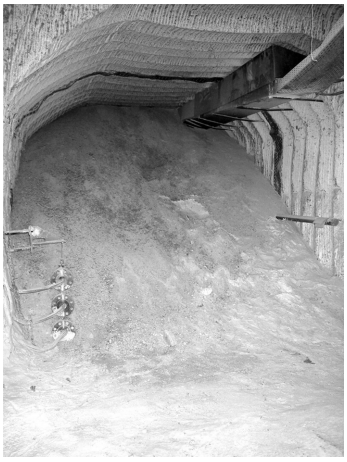

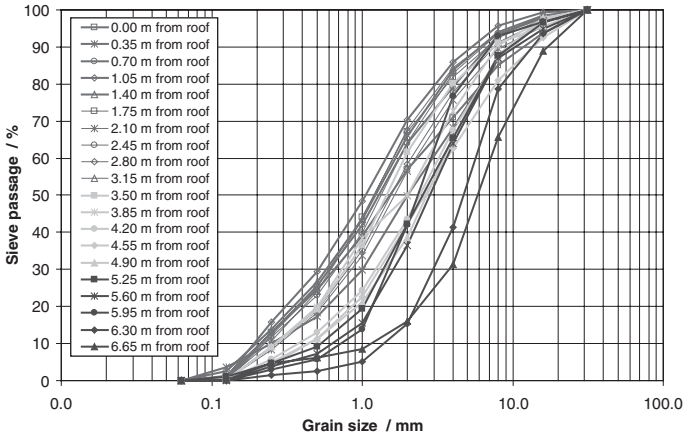

Figure 3. a: Backfill slope at the drift entrance. b: Grain size distribution of 20 backfill samples from the top to the bottom of the backfill slope at the entrance of drift A.

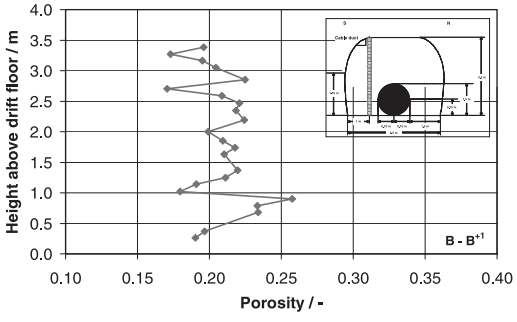

a: Vertical porosity distribution

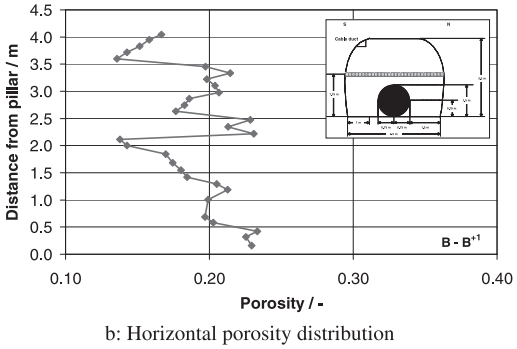

b: Horizontal porosity distribution

Figure 4. Porosity distribution in cross section B^{+1} in the central heater area.

Figure 6 shows the vertical distribution of porosity and permeability measured in cross section D1 at the middle of heater 1. The porosity increases from the floor to the roof what can be explained by faster

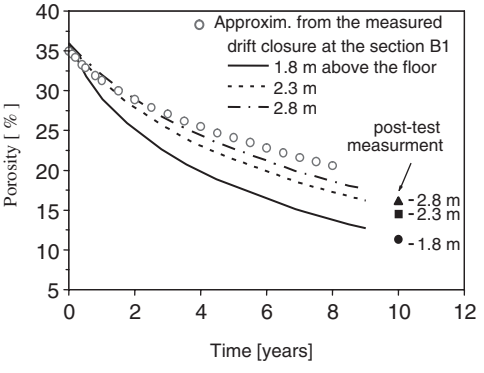

Figure 5. Comparison between model predictions (Bechthold et al. 1999) and the backfill porosity evolution determined *in-situ*.

compaction of the backfill at the higher temperatures near the heater. But in the more compacted area near the floor, the permeability is slightly higher. This might be caused by the larger grains in the bottom region (Fig. 3) giving larger pore sizes and connectivity. The permeability values range between $5 \cdot 10^{-12}$ and $1 \cdot 10^{-11}$ m^2.

In Figure 7, the permeability values from the different cross sections are shown in comparison with the *in-situ* measurements and the results of previous GRS tests on coarse grained crushed salt ($d < 30$ mm) (Bechthold et al. 1999; Rothfuchs et al. 1999; Droste et al. 2001). The permeability values determined in the post-tests are in the same range as the *in-situ* measurements of about $1 \cdot 10^{-11}$ m^2. The permeability of fine grained crushed salt ($d < 8$ mm) is lower than that of coarse grained material. When extrapolating the test data to very low porosities less than 1%,

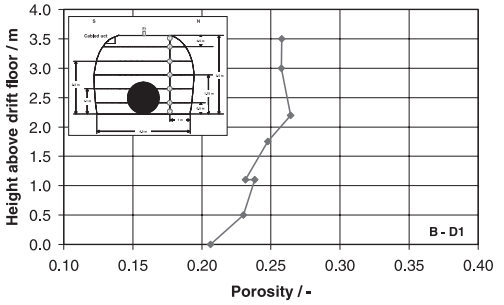

a: Porosity

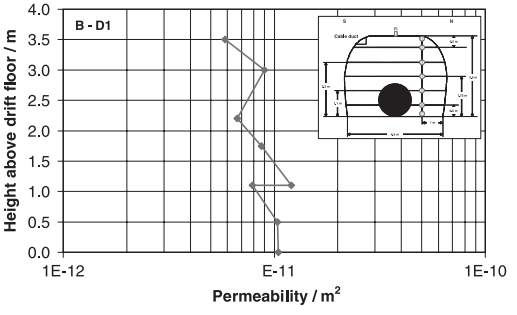

b: Permeability

Figure 6. Distribution of porosity and permeability in cross section D1.

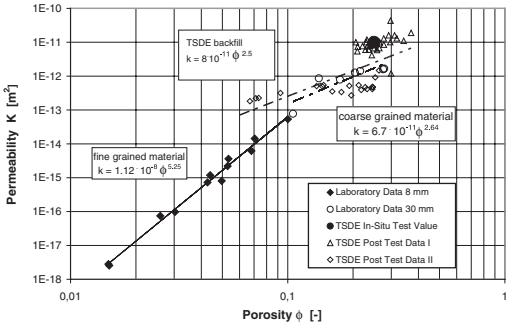

Figure 7. Gas permeability of salt backfill in dependence on porosity and grain size.

which correspond to intact rock salt, the permeability of fine grained backfill would reach the same values of $k < 10^{-20}$ to 10^{-21} m^2 as the intact rock salt. The coarse grained backfill material, however, would not reach these permeability values.

5 COMPACTION

The compaction behavior of the pre-consolidated backfill was investigated on six large samples (Table 1)

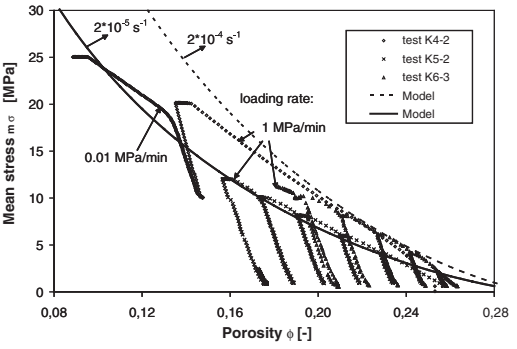

Figure 8. Hydrostatic compaction behavior.

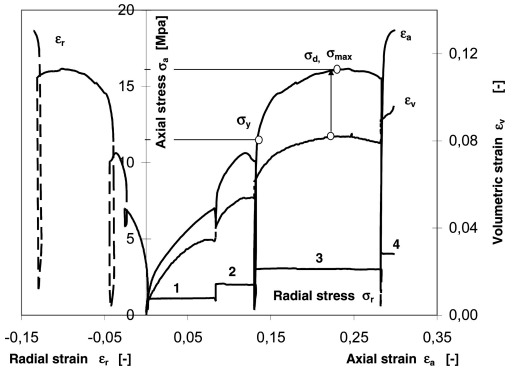

Figure 9. Deviatoric compression behavior.

in a big servo-controlled triaxial apparatus which allows a maximum sample size of 280 mm diameter and 720 mm length. The tests were done at ambient temperature of 24 ± 1°C. Two samples were compressed hydrostatically and the other four under deviatoric loading conditions by loading rates of 0.01 – 1 MPa/min.

Figure 8 presents the results of the hydrostatic compression tests. At ambient temperature and high compaction rates, a pre-consolidation pressure of 4.0 MPa to 4.5 MPa was determined from the first linear elastic limit of the compaction curve. This value is slightly higher than the backfill pressure of 2 MPa to 4 MPa which was measured *in-situ*. Further compaction beyond the pre-consolidation pressure is non-linear, following the normal compaction curve of the material. A low loading rate induces more compaction at the same stress. In the unloading paths, bulk moduli were measured at different porosities. The bulk modulus increases rapidly from 300 MPa to 600 MPa in the porosity range of $\phi = 26\%$ to 22% and then keeps almost constant up to a porosity of $\phi = 16\%$.

Figure 9 shows a typical test under multi-failure loading conditions on sample K4-1. On the plotted

K4-1 σ_a/σ_r=18.7/4 MPa shear damage | K5-1 σ_a/σ_r=20/4 MPa shear damage | K6-3 σ_a/σ_r=58.4/10 MPa no shear damage

Figure 10. Backfill samples after deviatoric compression.

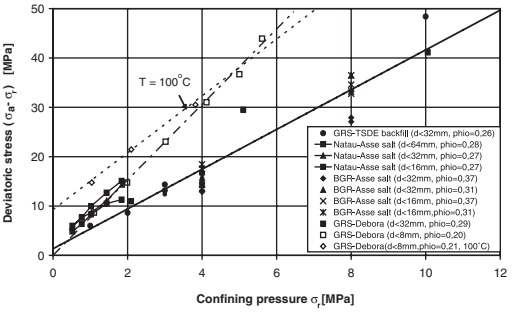

Figure 11. Strength of the salt backfill.

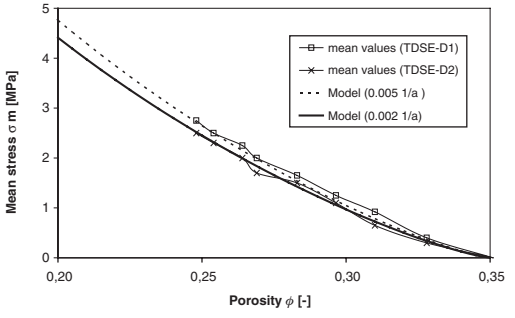

Figure 12. Comparison between measured and calculated backfill pressure as a function of porosity for the average TSDE *in-situ* conditions.

stress – strain curves, axial yield stress σ_y, onset of dilatancy σ_d, and peak failure strength σ_{max} are marked. The stress – strain curves indicate very large deformations even after the peak strength and without sharp rupture. The major component of the deformation is plastic. Each increase of confining pressure after reaching peak strength causes further compaction, higher stiffness, and higher strength of the samples. Increase of the volume initiated at high deviatoric stresses is not significant. In the unloading paths, the elastic parameters were determined: Young's modulus $E = 710$ MPa and Poisson's ratio $\nu = 0.34$ (for $\phi = 22\%$) and $E = 11{,}450$ MPa and $\nu = 0.28$ (for $\phi = 1\%$).

Figure 10 shows three samples after testing. At a lateral stress of 4 MPa, shear damage took place by increasing axial stress to 19 MPa and 20 MPa, whereas at high lateral stress of 10 MPa, the sample was only more compacted and no shear damage occurred even at a very high axial stress of 58 MPa.

The strength values determined in the multistage tests on pre-compacted backfill are summarized in Figure 11 and compared to the results from the same backfill material which was not pre-compacted (Diekmann & Schnier 1989; Natau & Keller 1991; Rothfuchs et al. 1999; Droste et al. 2001). For coarse grained material with a maximum grain size over 16 mm, the strength values are not significantly different. Fine grains seem to increase the strength. The lower the initial porosity, the higher is the strength. The cohesion of the salt backfill is less than 0.6 MPa and the friction angle varies in the range of 43° to 53°. Increasing temperature results in an increase of cohesion between salt grains.

Based on the compression tests, the parameters of Zhang's model (Bechthold et al. 1999; Droste et al. 2001) were established:

$$\dot{\varepsilon}_v = A \exp\left(\frac{-Q}{RT}\right)\left(\frac{\sigma_m}{\sigma_o}\right)^n \left[\ln\left(\frac{\phi_o(1-\phi)}{\phi(1-\phi_o)}\right)\right]^{-m} \qquad (3)$$

where $\dot{\varepsilon}_v$ = compaction rate, T = absolute temperature, Q = activation energy, R = gas constant, σ_m = mean stress, $\sigma_o = 1$ MPa, ϕ = porosity, ϕ_o = initial porosity, A, n, m = material parameters. Assuming $\phi_o = 30\%$, $\dot{\varepsilon}_v = 2 \cdot 10^{-5}$ and $2 \cdot 10^{-4}$ 1/s, the associated compaction parameters were determined by fitting the test data (Fig. 8): $A = 6 \cdot 10^8$ 1/s, $Q = 156$ kJ/mole, $n = 12$, $m = 15$. Using these parameters, the average compaction behavior of the TSDE backfill was predicted for the average conditions of $T = 100$°C, $\dot{\varepsilon}_v = 2 \cdot 10^{-3} - 5 \cdot 10^{-3}$ 1/a, and $\phi_o = 35\%$ (Bechthold et al. 1999; Droste et al. 2001). As can be seen from Figure 12, the calculation results coincide quite well with the *in-situ* measurements.

6 CONCLUSIONS

Generally, the *in-situ* measurements of porosity and permeability of the salt backfill in the TSDE test drifts are validated by the post-test analyses. Previous experimental results of the compaction and permeability behavior of crushed salt are well reproduced by the post-tests on the pre-consolidated backfill samples. The good agreement between model predictions and field observations confirm the constitutive models and parameters for the backfill material.

ACKNOWLEDGMENTS

The authors gratefully acknowledge the funding of the post-test investigations within the TSDE project by the German Federal Ministry of Economics and Technology (BMWi) and the Commission of the European Communities.

REFERENCES

Bechthold, W., Rothfuchs, T., Poley, A., Ghoreychi, M., Heusermann, S., Gens, A., Olivella, S. 1999. Backfilling and Sealing of Underground Repositories for Radioactive Waste in Salt (BAMBUS Project), Final Report. *EUR 19124 EN*.

Droste, J., Feddersen, H.-K., Rothfuchs, T. 2001. Experimental Investigations on the Backfill Behavior in Disposal Drifts in Rock Salt). *GRS – 173*.

Rothfuchs, T., Feddersen, H.-K., Kroehn, K.-P., Miehe, R., Wieczorek, K. 1999. The DEBORA-Project: Development of Borehole Seals for High-Level Radioactive Waste – Phase II. *GRS – 161*.

Diekmann, N. & Schnier, H. 1989. Geotechnische Erkundung und Standsicherheitskriterien Bergwerk Gorleben. *BGR-Abschlußbericht*.

Natau, O. & Keller, S. 1991. Grundlagenuntersuchungen zu Salzhaufwerk mit Korndurchmessern bis 65 mm in Abhängigkeit von der Lagerungsdichte und des Spannungsniveaus. *Forschungsbericht 02E80401*.

The Mechanical Behavior of Salt – Understanding of THMC Processes in Salt –
Wallner, Lux, Minkley & Hardy, Jr. (eds)
© 2007 Taylor & Francis Group, London, ISBN 978-0-415-44398-2

In-situ measurements and 3-D model calculations of backfill compaction and EDZ development in waste disposal drifts in salt rock

S. Heusermann & U. Heemann
Federal Institute for Geosciences and Natural Resources (BGR), Hannover, Germany

ABSTRACT: To improve methods and tools for the prediction of the long-term thermomechanical behaviour of a repository for radioactive waste in salt, experimental and theoretical studies were performed in the framework of two R&D projects at the Asse mine regarding the behaviour of disposal drifts, backfill material and host rock. Experimental studies included the long-term measurement of thermally induced stress change as well as permeability tests in the host rock and the excavation damaged zone (EDZ) around the test drifts. Theoretical investigation comprised the 3-D modelling of the in-situ experiment using the JIFE finite-element code. Results of calculations show that dilatancy and porosity occur in the near vicinity of the emplacement drifts. Calculated permeability increases in the vicinity of the test drifts and decreases to negligible values within a short distance. The experimental data are compared to the results of model calculations.

1 INTRODUCTION

Salt rock is the basic component of the multi-barrier system regarded in repository concepts for the disposal of heat generating radioactive wastes in deep salt structures. Referring to those concepts an important achievement was the development of the concept of direct disposal of spent nuclear fuel elements in conjunction with an ambitious R&D programme. One programme part covered the theoretical and experimental investigation of the disposal of self-shielding Pollux casks in parallel running drifts. Initially, the test was started as a German project in 1985 within the TSDE project (Thermal Simulation of Drift Emplacement) and was continued as an international project from 1999 to 2004 within the BAMBUS I and II projects (Backfill and Material Behaviour in Underground Salt Repositories). The BAMBUS project was undertaken as a joint project of several European groups from France, Germany, Netherlands, and Spain (FZK, BGR, DBE, G.3S, GRS, IfG, NRG, and UPC) and one US group (DOE/CBFO) and was funded by the European Commission and the national governments and authorities. The objective was to enlarge the basis for optimising the repository design and for predicting the long-term performance of the host rock barrier and backfill of the disposal drifts. The project work was divided into in-situ investigations, laboratory testing, modelling, and desk studies (Bechthold et al. 2004).

In-situ investigations were carried out at the Asse salt mine at the 800-m level. Two parallel test drifts

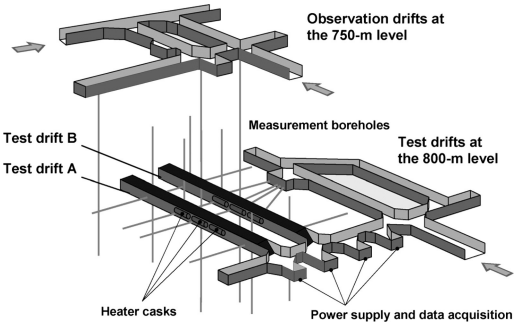

Figure 1. Schematic view of the TSDE test field.

A and B were excavated to emplace the heater casks. Following, the drifts were backfilled with crushed salt and the casks were electrically heated over more than eight years (Bechthold et al. 1999). Figure 1 shows a schematic view of the TSDE test field including both test drifts at the 800-m level each with three heater casks as well as several observation and access drifts at the 750-m and 800-m level. The main issues to be investigated were the thermomechanical response of the host rock, the compaction of the backfill caused by heating and rock stress, the decrease of porosity and permeability of the backfill with time, and the evolution of the excavation damaged zone (EDZ) around the drifts.

Three-dimensional finite-element calculations with the JIFE code were made to analyse the results of

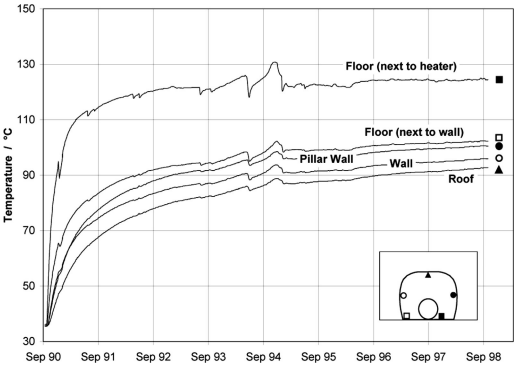

Figure 2. Temperature measured in the backfill (Bechthold et al. 1999).

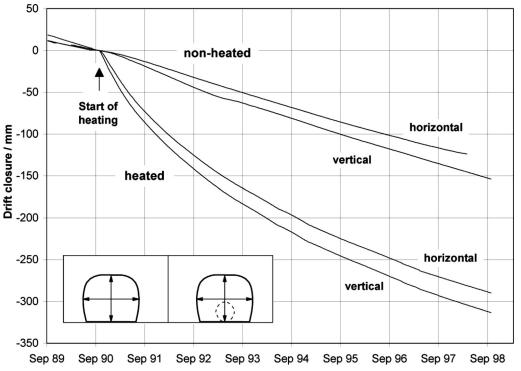

Figure 3. Measured drift closure (Bechthold et al. 1999).

measurements and to predict the thermomechanical behaviour of the host rock and the backfill.

2 EXPERIMENTAL INVESTIGATIONS

The in-situ investigations included the measurement of temperature, rock deformation, drift closure, and stress change in the host rock, the observation of the backfill compaction regarding porosity and pressure, and the detection of the EDZ around the test drifts referring to the permeability. A minor part of the measurements in the salt rock was started in 1988 before excavating the drifts. The major part was carried out during the heating period from September 1990 to February 1999 and during the following cooling stage up to the end of 2002.

Heat conduction through compacting backfill is influenced by two processes: (1) Backfill conductivity increases with decreasing porosity, (2) the conductivity of the salt grains decreases with increasing temperature. Thus, temperature gradients in the backfill can be still measured after eight years of heating (Fig. 2). Five years after start of heating the temperatures in the backfill near to the heater casks had reached steady state conditions, whereas in the backfill near to the walls and roof the temperatures were still rising. Heating of the pillar between the test drifts from both sides resulted in higher temperatures compared to the temperatures measured at the opposite wall.

The measurement of drift closure started immediately after drift excavation. During this time period, closure rates averaged 0.25 %/year in horizontal direction and 0.3 %/year in vertical direction. With the start-up of heating, the closure rates accelerated up to twelve times the rates observed before heating (Fig. 3). Until the end of 1998, the closure rates were reduced by the compaction and increasing mechanical support of the backfill. At the end of 1998, the rates were

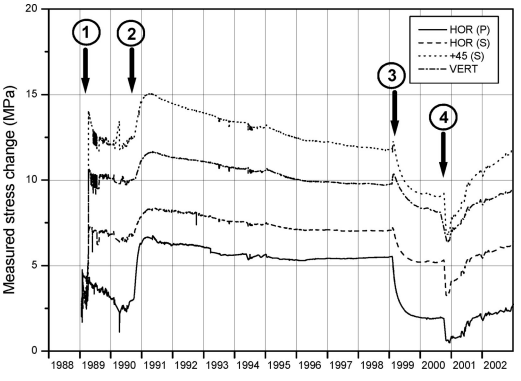

Figure 4. Stress change measured in the salt rock.

0.4 %/year in horizontal direction and 0.5 %/year in vertical direction.

Drift closure measurements were used to determine the backfill porosity. After eight years of heating, the initial backfill porosity of about 35 % had been reduced to between 24 and 25.5 % in the heated zone and to between 30.5 % and 32 % in the non-heated zone.

The experimental work of BGR concentrated on the long-term measurement of thermally induced change of stress in the rock salt as well as on the determination of the permeability of the rock salt around the test drifts.

To measure long-term stress changes in the host rock induced by drift excavation, by heating, and by subsequent cooling, numerous stress monitoring probes were equipped with Glötzl type hydraulic pressure cells with different set-ups and orientations and were installed in several boreholes. The most frequent configuration, i.e. four-component probes, measured the vertical component, the horizontal components perpendicular and parallel to the drift axis, and a subvertical component with an inclination of 45°.

The monitoring probes were located in the roof, walls, and floor of the drifts, as well as in the pillar between the test drifts at different distances to the heater casks. To enable the measurement of excavation-induced stress change, a major part of the probes was installed prior to excavation of the test drifts.

Measurements of stress change started in early 1989. Figure 4 depicts a selection of measured data from a 4-component probe during the period early 1989 through end of 2002. This probe was located in the pillar in a distance of 1 m to the wall of drift B. A rapid and distinct increase in stress could be observed as a result of stress redistribution caused by excavation of the test drifts (Fig. 4, point 1). With the start-up of heating in September 1990 (Fig. 4, point 2) the stresses increased again reaching a maximum after some weeks. Different developments of stress change occurred depending upon the distance to the heater casks and direction of measurement. While the input of heat showed only minor increases of vertical stress directly at the drift wall, distinct increases of vertical stress could be observed in the axis of the pillar, where the maximum increase was measured. The heating was stopped in February 1999 (Fig. 4, point 3) causing a significant and continuous stress decrease at all observation points in the pillar for several months. At the end of 2000, the re-excavation of test drift B passed the position of the monitoring probes (Fig. 4, point 4). Due to the remove of the backfilling the backfill pressure at the drift wall dropped to zero and the monitoring probes measured distinct stress decreases of 1.5 MPa to 2.5 MPa. This was followed by a continuous stress increase again.

The major part of the stress monitoring probes installed in the pillar has at least worked for more than 14 years. The obtained measurement results show all significant effects of drift excavation, heating, cooling, and removing of the backfilling.

To determine the extent of the EDZ around the test drifts and the hydraulic conditions in the host rock, permeability measurements were carried out in the pillar between both drifts in early 2002. To that aim, several horizontal or inclined boreholes were drilled from the re-opened test drift B to drift A. The inclined borehole has a distance to the floor of drift A of approx. 0.5 m at one corner to 1.5 m at the opposite one of the floor.

The pulse injection method was used for measurements at various borehole depths in the EDZ of drift B, in the middle of the pillar between the drifts, and in the EDZ below drift A. The test intervals with a length of about 0.3 m were sealed off by a double-packer probe and were pressurized up to a level of 5 bar. Pressure and temperature in the borehole section as well as the reference atmospheric pressure and reference temperature in the test drift and their variation with time were recorded and sampled with a computer-based data acquisition system.

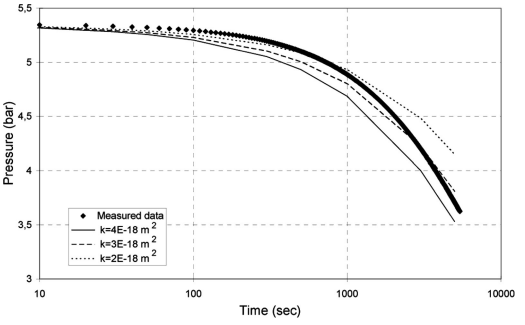

Figure 5. Permeability determined by injection pressure tests in the centre of the pillar between the test drifts.

Evaluation and interpretation of the measurements were made by comparing the measured variation of injection pressure to characteristic pressure curves obtained by theoretical models (Fig. 5). Each set of experimental data was fitted by several master curves such that the best match served a range of permeability for the investigated borehole section.

At a borehole depth of up to 0.5 m, a medium to high permeability of $k = 1 \cdot 10^{-6}$ to $1 \cdot 10^{-15} m^2$ occurs. This is obviously caused by dilatancy and microcracking of the EDZ in the near vicinity of drift B. Medium to high values could be detected too below drift A at borehole depths from about 10 to 12.5 m caused by a relatively far extension of the EDZ beneath the floor of drift A. A major part of the tests yielded a low permeability of $k = 2 \cdot 10^{-18}$ to $4 \cdot 10^{-18} m^2$. Comparing these results to permeability values of rock salt at other test locations ($k \leq 1 \cdot 10^{-21}$ m^2), the values indicate a general increase of permeability in the test field. This may be caused by the long-term thermomechanical loading of the rock around the test drifts.

3 MODEL CALCULATIONS

Several theoretical studies of the thermomechanical evolution of the TSDE test were made by the participating groups in the BAMBUS project. Different codes and models were used to prove their predictive capabilities referring to a complex TM modelling associated with long-term repository predictions. The computational studies and their comparison helped to improve codes and refine models based on the results of in-situ and laboratory investigations (Bechthold et al. 2004).

3.1 *Finite-element code JIFE*

Model calculations of the BGR were made using the new JIFE code developed in a cooperation between SRD company, Berlin, and BGR (Heemann et al. 2003). Particular effort has been spent to this

development to provide an interactive object-oriented and fast tool for considering coupled THMC processes. The specific constitutive models, e.g. composite model for transient and steady-state creep (Hunsche & Schulze 2003), dilatancy model (Hunsche & Schulze 2003), and crushed-salt model (Heemann et al. 1999), needed for modelling the thermomechanical behaviour of rock salt have been implemented into the JIFE code. To enable the calculation of large 3-D models with hundred thousands of degrees of freedom different iterative solvers are available.

3.2 *Constitutive models*

According to Hunsche & Schulze (1994), the effective steady-state creep rate can be calculated using the common Norton-type formulation:

$$\dot{\varepsilon}_{eff}^{cr} = A_{cr} \cdot e^{-\frac{Q}{RT}} \cdot \left(\frac{\sigma_{dev}}{\sigma^*} \right)^n \tag{1}$$

with $R =$ universal gas constant ($8.3143 \cdot 10^{-3}$ kJ/mol · K), $T =$ temperature (K), $\sigma_{dev} =$ deviatoric stress (MPa), $\sigma^* =$ reference stress (1.0 MPa) and the material parameters $A_{cr} =$ structural factor (0.18/d), $n =$ stress exponent (5.0), $Q =$ activation energy (54.0 kJ/mol).

To describe dilatancy of the rock salt, a new model based on extensive lab test series on rock salt has been considered according to Hunsche & Schulze (2003). The volumetric rate of dilatancy $\dot{\varepsilon}_{dil,vol}$ is correlated to the deviatoric creep rate, $\dot{\varepsilon}_{cr.dev}$ via an empirical relation using r_v (depending on σ_{dev} and hydrostatic stress σ_{hyd}):

$$\dot{\varepsilon}_{dil,vol} = r_v \cdot \dot{\varepsilon}_{cr,dev} \tag{2}$$

If the octahedral shear stress τ_{oct} (equivalent to the deviatoric stress) exceeds the dilatancy boundary τ_D, the factor r_v is positive and dilatancy will occur:

$$r_v = \sqrt{3} \left| \frac{(\tau_{oct} - \tau_D)}{\sigma_{hyd}} \right|^{1/m} \quad (if\ \tau_{oct} > \tau_D) \tag{3}$$

$$\tau_D = a \cdot \sigma_{hyd} + b \cdot \sigma_{hyd}^2 + c \cdot \sigma_{hyd}^3 \tag{4a}$$

$$\tau_{oct} = \frac{\sqrt{2}}{3} \sigma_{dev} \tag{4b}$$

where $m = 0.625$, $a = 0.90785$, $b = -0.0056\ \mathrm{MPa}^{-1}$, and $c = -3.676\mathrm{E}^{-5}\ \mathrm{MPa}^{-2}$.

The permeability of the rock salt is assumed to be a function of the porosity caused by dilatancy and includes two regimes (Popp 2002, 2007). In the first regime of low dilatant volume the change of permeability with porosity is rather strong and nonlinear. Beyond a certain boundary permeability increases more or less linear with porosity. The two regimes have been combined in one equation (Heemann & Heusermann 2004).

The constitutive equations for crushed salt include two conceptual models. First, the compaction of crushed salt with a distinct void ratio e can be described by a geometric idealization of a grain (inner cube with pyramidal corners on the six sides) according to Heemann (2006, unpubl.). Contact to neighbouring grains is given at the flattening peaks of the pyramidal corners. During compaction the area of the contact zone grows linearly. This is assumed to be typical for small cubic-like particles of crushed salt. The stress concentration in these contact areas governs the local creep rates and thus global stresses. Compaction and deviatoric deformation can be described in a very similar way because they are based on the same geometry and the creep model of rock salt. Secondly, when the void ratio e decreases to very low values, further compaction is better described by the closure of voids in rock salt. Both models can be combined in a simple and nearly ideal way:

$$\dot{\varepsilon}_{vol} = -2A \exp\left(\frac{-Q}{RT}\right) \left(\left(\frac{\sigma_{hyd}}{U'} \right)^2 + b \left(\frac{\sigma_{dev}}{U'^{\beta}} \right)^2 \right)^{\frac{n-1}{2}} \cdot \ldots$$

$$\ldots \cdot \cot(\alpha) \sqrt{U} \left(\frac{\sigma_{hyd}}{U'} \right) \frac{\frac{1}{k} + e}{1+e}\, e \tag{5}$$

$$\dot{\varepsilon}_{dev} = 2A \exp\left(\frac{-Q}{RT}\right) \left(\left(\frac{\sigma_{hyd}}{U'} \right)^2 + b \left(\frac{\sigma_{dev}}{U'^{\beta}} \right)^2 \right)^{\frac{n-1}{2}} \cdot \ldots$$

$$\ldots \cdot \cot(\alpha) \sqrt{Uc} \left(\frac{\sigma_{dev}}{U'^{\beta}} \right) \frac{\frac{1}{k} + e}{1+e}\, e + A \exp\left(\frac{-Q}{RT}\right) \sigma_{dev}^n \tag{6}$$

$$U = \left(\frac{3}{2} \tan(\alpha) \right)^2 \left(\left(\frac{1 + k e_0}{1 + k e} \right)^{\frac{1}{3}} - 1 \right)^2 \tag{7a}$$

$$U' = \left(\frac{1}{\kappa U} \right)^{\gamma} \tag{7b}$$

$$\cot(\alpha) = \sqrt{1 + k e_0} - 1 \tag{7c}$$

where $A = 0.18$ MPa/d, $e_0 = 0.45$, $\kappa = 1.151$, $\gamma = 0.896$, $\beta = 0.755$, $b = 3.075$, $c = 0.855$, and $k = 3.0$. In Equations 5–7 parameter k was introduced to account for the grain size distribution by defining the ratio of large particles which minimally affect the compaction

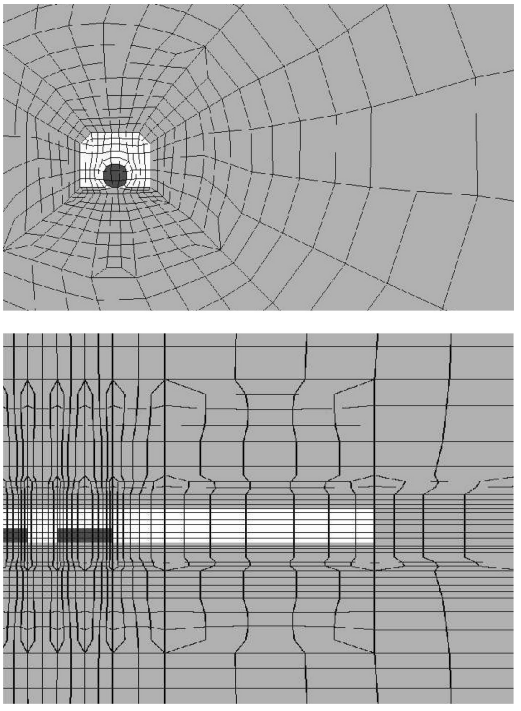

Figure 6. Part of the 3-D finite-element mesh of the TSDE test field (top: front view, bottom: side view).

process. The angle α is complementary to the inclination angle of the pyramidal corners of a grain and has to be determined from k and initial void ratio e_0 using Equation 7c. The resultant model can sufficiently describe the behaviour of natural crushed salt.

3.3 *Finite-element modelling*

The discretisation of the three-dimensional FE-model is shown in Figure 6. The TSDE test field included two 75 m long drifts backfilled with crushed salt after emplacement of three heater casks in each of them. The test field was modelled with a half-cylindrical shape of 200 m radius and 50 m depth. The front side of the model is a vertical plane of symmetry perpendicular to the drift axis and running through the centre of the middle heaters. A second vertical plane of symmetry runs along the axis of the pillar between the two drifts. The model includes 20396 linear 3-D solid elements with 62,358 DOF and additional 21,498 DOF for the thermal calculations. The drifts were assumed to be excavated instantaneously. After 1.5 years, the heaters and the crushed salt were taken to be emplaced instantaneously and the heaters were switched on with an electrical power of 6.6 kW per cask. Heating was continued for further 8.5 years. The total calculation time was set to 11 years. The model calculations served to

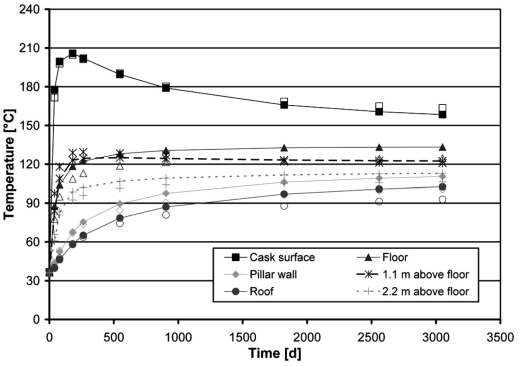

Figure 7. Measured (symbols only) and calculated (symbols with lines) temperature in the backfill (heated drift section).

predict temperatures, deformations, and stresses in the salt rock and the backfill as well as dilatancy, porosity and permeability in the EDZ and to compare those values to experimental results.

4 RESULTS

To compare calculated values to measured data a reduced data set was exemplarily used here. The following values and measurement points were selected: temperature in the backfill (five points at the cask, floor, pillar, and roof), temperature in the salt pillar between the test drifts (three points with different distance to the drifts), drift closure in the heated and non-heated drift sections (horizontal and vertical directions), backfill porosity (two points), backfill pressure (four points at the floor, pillar, wall, and roof), rock stress change (one point in the pillar, vertical and horizontal direction), and permeability in the salt rock (several points along the axis of an inclined borehole drilled from the wall of drift B towards the area beneath the floor of drift A).

The calculated temperatures agree sufficiently to the measured values (Fig. 7, 8). Calculated values tend to be slightly higher than measured values, especially in the salt rock.

Drift closure was measured in the heated and non-heated sections of the test drifts. The prediction of the closure in the non-heated section agrees sufficiently with the experimental data. Calculating the drift closure in the heated section a significant overestimation can be recognized (Fig. 9). Analogous deviations of calculated and measured porosity of the backfill material in the heated sections occur since the porosity is determined from the observed drift closure (Fig. 10). Figure 11 depicts the measured and calculated variation of the pressure in the backfill material (heated section). Generally, the experimental values

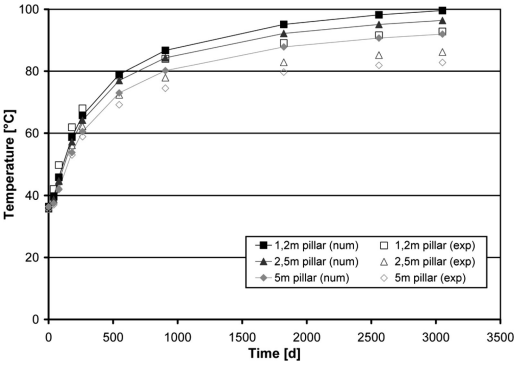

Figure 8. Measured and calculated temperature in the rock salt pillar between the test drifts.

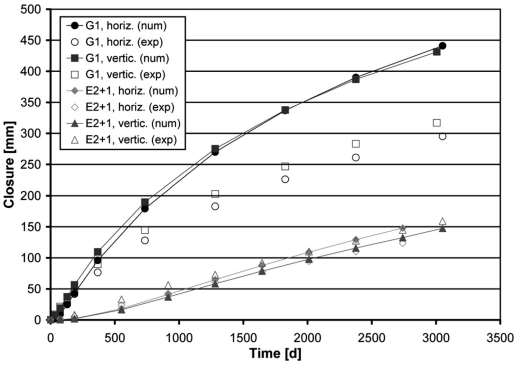

Figure 9. Measured and calculated drift closure.

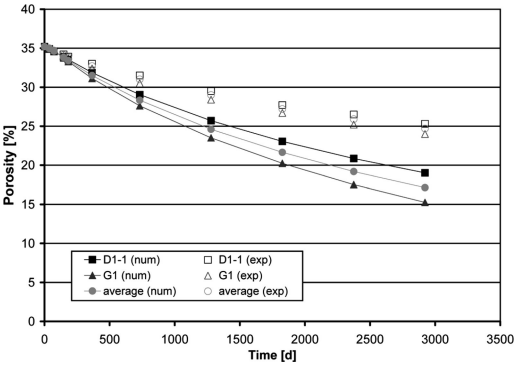

Figure 10. Measured and calculated porosity of the backfill material (heated drift section).

are under-estimated. Slight differences occur regarding the measuring points at the floor, wall and pillar. Significant differences occur for the point at the roof.

In Figure 12, the measured and calculated change of rock stress in the axis of the pillar between the drifts

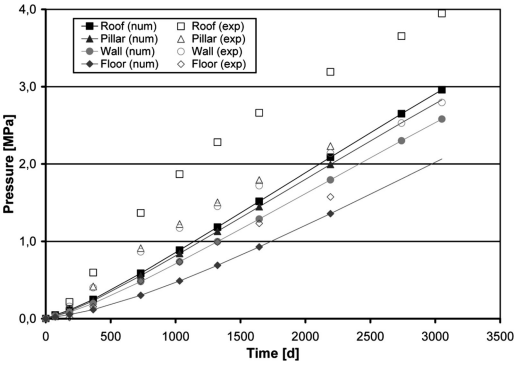

Figure 11. Measured and calculated backfill pressure (heated drift section).

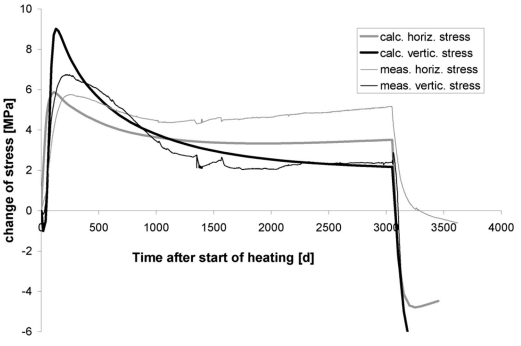

Figure 12. Measured and calculated stress change during heating in the rock salt pillar between the test drifts.

is plotted. Both vertical and horizontal (perpendicular to the drift axis) stress components are plotted for the entire heating phase (about 3100 days) and the subsequent cooling phase. Comparing experimental and theoretical stress change values, a satisfactory agreement can be assessed; all measured effects, e.g. distinct stress increase at the beginning of heating or distinct stress reduction during the cooling phase, can be described by means of the three-dimensional finite-element modelling.

Special attention was paid to the calculation of the EDZ around the test drifts in terms of dilatancy, porosity, and permeability. The evolution of dilatancy within the "cold" period prior to heating is rather slow and maximum porosity values of about 0.11% occur after 1.5 years near the bottom corners of the drifts. Further 1.5 years later, with increasing dilatancy, porosity reaches maximum values of 1.54% and after a total of 10 years 3.3% in maximum due to the heating and thermally enforced creep. That is a factor of 30 within 8.5 years.

While the highest values of dilatancy occur around the drift corners and for a minor part at the basis of

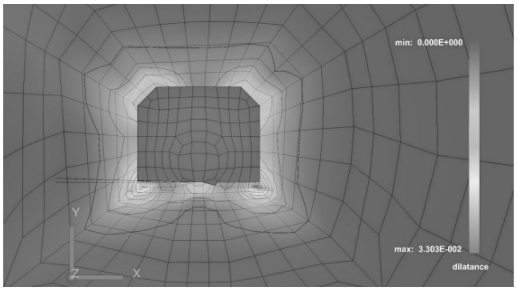

Figure 13. Calculated dilatancy around the test drifts after 8.5 years of heating.

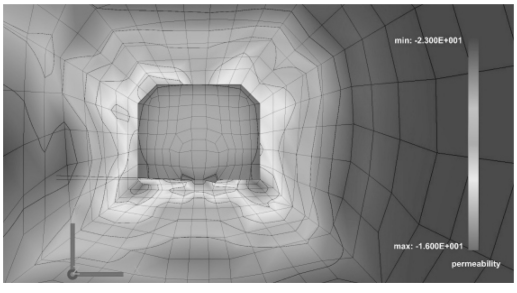

Figure 14. Calculated permeability around the test drifts after 8.5 years of heating.

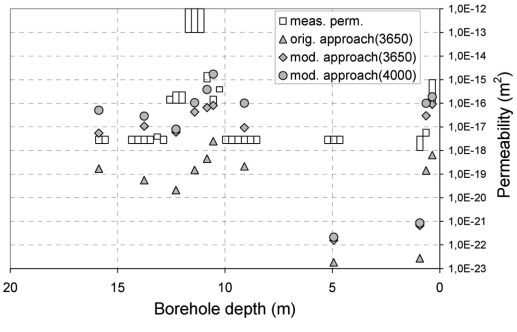

Figure 15. Measured and calculated permeability in the rock salt pillar between the test drifts.

the heater casks (Fig. 13), permeability is distributed rather homogenously around the whole shape of the test drifts. At the end of the "cold" period prior to heating, permeability does not exceed 10^{-20} m^2. It increases to 10^{-17} m^2 after 1.5 years of heating and to about 10^{-16} m^2 at the end of heating (Fig. 14). In the middle of the drift walls permeability reached values of 10^{-18} m^2. In the "cold" area permeability keeps to about 10^{-20} m^2.

The calculated permeability values were compared to the experimental data obtained in the inclined measurement borehole about three years after the end of heating. In Figure 15, the measured data are plotted and compared to the theoretical values calculated for different approaches of the permeability-porosity dependency at the end of heating (3650 and 4000 days after excavation of the drifts). For the original approach referring to Popp (2002) at the end of the heating period, the theoretical values are low compared to the experimental data. For the modified approach referring to Heemann & Heusermann (2004) the agreement is much better and may be more suitable to take into account the stress and porosity changes in the cooling phase of the TSDE test. Obviously, the influence of cooling on permeability is surprisingly small. The very high values of permeability measured near to the corner of drift A are apparently induced by cracks with a high hydraulic conductivity which are not considered in the FE model. The permeability values measured in the undisturbed rock mass (e.g., in the centre of the pillar) show a more or less constant distribution and are some magnitudes higher than the calculated values.

5 CONCLUSIONS

To improve methods and tools for the prediction of the long-term thermomechanical behaviour of a repository for radioactive waste in salt, experimental and theoretical studies were performed in the framework of the BAMBUS project. In-situ investigations were carried out in the TSDE test field at the Asse salt mine and included the measurement of temperature, rock deformation, drift closure, backfill porosity and pressure, rock stress change and permeability. The experimental work of BGR concentrated on long-term measurement of thermally induced rock stress change and the determination of the permeability in the EDZ around the TSDE test drifts. Theoretical studies included the improvement of constitutive equations describing the thermomechanical behaviour of crushed salt. These equations were implemented into the new finite-element code JIFE and used for the three-dimensional modelling of the TSDE test.

The results of stress change measurement show all significant effects of drift excavation, heating and cooling of the host rock, and removing of the backfilling from one test drift. The major part of stress monitoring probes has successfully worked for more than 14 years. To determine experimentally the extent of the EDZ in the host rock around the test drifts and the permeability of the EDZ, the common pulse test method was proven to be useful.

Modelling of the TSDE test using the JIFE code produced results that compared rather favourably with TSDE measurement data (temperatures, deformations, drift closure, backfill pressure, rock stress changes, permeability in the EDZ). As an example, the agreement of calculated and measured stress changes and

permeability of the host rock is demonstrated. Incorporating the three-dimensional full-coupled thermomechanical modelling of the TSDE test, the calculation results show a distinct improvement compared to the previous experience in the former BAMBUS I project.

The new FE code JIFE is a fast and efficient tool to calculate the thermal and thermomechanical response of the host rock and the backfilling in the TSDE test. The code makes it possible to take into account all necessary features of modelling the TSDE test (e.g. full 3-D calculation, full thermo-mechanical coupling, geometrically non-linear calculation, state-of-the-art constitutive models for creep, dilatancy, permeability of rock salt, and compaction of crushed salt). It is a tool with a high predictive capability for repository design calculations and repository performance assessments. Recent code developments are referred to take into account the main THMC processes to be considered in a waste repository in rock salt.

REFERENCES

Bechthold, W., Rothfuchs, T., Poley, A., Ghoreychi, M., Heusermann, S., Gens, A. & Olivella, S. 1999. Backfilling and sealing of underground repositories for radioactive waste in salt (BAMBUS Project), Report EUR 19124 EN, CEC, Brussels.

Bechthold, W., Smailos, E., Heusermann, S., Bollingerfehr, W., Bazargan Sabet, B., Roth-fuchs, T., Kamlot, P., Grupa, J., Olivella, S. & Hansen, F.D. 2004. Backfilling and sealing of underground repositories for radioactive waste in salt (BAMBUS II Project), Report EUR 20621 EN, CEC, Brussels.

Heemann, U. 2006. Idealized salt grain model and its application to dry crushed salt (unpubl.).

Heemann, U. & Heusermann, S. 2004. Theoretical and experimental investigation on stresses and permeability in the BAMBUS project. *DisTec 2004, Int. Conf. on Radioactive Waste Disposal, April 26–28,* Berlin.

Heemann, U., Heusermann, S., Sarfeld, W. & Faust, B. 1999. Numerical modelling of the compaction behaviour of crushed salt. *Numerical Models in Geomechanics (Eds.: G.N. Pande, S. Pietruszczak & H.F. Schweiger), 627–632,* Rotterdam: Balkema.

Heemann, U., Sarfeld, W. & Faust, B. 2003. 3D-calculation of dilatancy and permeability. *European Commission CLUSTER Conference on the Impact of EDZ on the Performance of Radioactive Waste Geological Repositories, Nov. 3–5, 2003,* Luxembourg.

Hunsche, U. & Schulze, O. 1994. Das Kriechverhalten von Steinsalz. *Kali und Steinsalz*, 11(8/9), 238–255.

Hunsche, U. & Schulze, O. 2003. The dilatancy concept – a basis for the modelling of coupled TMH processes in rock salt. *European Commission CLUSTER Conference on the Impact of EDZ on the Performance of Radioactive Waste Geological Repositories, Nov. 3–5, 2003,* Luxembourg.

Popp, T. 2002. Transporteigenschaften von Steinsalz – Modellierung der Permeabilitäts-Porositäts-Beziehung. *Meyiana 54*, 113–129, Kiel.

Popp, T., Wiedermann, M., Kansy, A. & Pusch, G. 2007. Gas transport in dry rock salt – implications from laboratory investigations and field studies. *6th Conf. on the Mech. Behavior of Salt. May 22–25,* Hannover, Germany.

The Mechanical Behavior of Salt – Understanding of THMC Processes in Salt –
Wallner, Lux, Minkley & Hardy, Jr. (eds)
© 2007 Taylor & Francis Group, London, ISBN 978-0-415-44398-2

Long-term laboratory investigation on backfill

D. Stührenberg
Federal Institute for Geosciences and Natural Resources (BGR), Stilleweg, Hannover, Germany

ABSTRACT: Crushed salt is the preferred backfill material for a technical barrier in a final repository of radioactive waste in salt formations because it will have the same properties as the host rock after full compaction. However, it must be compacted by the convergence of the host rock to stabilize the underground openings and to reduce sufficiently the permeability in the EDZ and the backfill. High temperatures close to the waste containers favour the compaction process of pure crushed salt quite well. At lower temperatures, addition of bentonite supports the compaction process and favourably reduces the permeability. On basis of our laboratory test results we recommend a mixture of 85% crushed salt and 15% Ca-bentonite as a backfill barrier component in the lower temperature range.

1 INTRODUCTION AND OBJECTIVE

Crushed salt is the preferred backfill material in a final repository of radioactive waste in salt formations. The compatibility with the host rock and the initial gas permeability of the porous material, which can impede an unacceptable high pressure due to cask corrosion, are well desired features. The intended long-term barrier effect of crushed salt, however, is only achieved after it has been compacted by the convergence of the host rock and the permeability has been sufficiently reduced. The anyway slow convergence will be reduced moreover by the resistance of the compacting backfill, which increases with increasing density. In order to shorten the very long time that is needed for compaction in situ, the backfill resistance must be as low as possible. The objective is to obtain a convenient backfill material with a predictable behavior used as a technical barrier in a repository.

2 COMPACTION BEHAVIOR OF THE BACKFILL MATERIAL "CRUSHED SALT"

A large number of compaction and permeability tests on crushed salt and on mixtures of crushed salt and bentonite have been carried out in the BGR laboratories in the last 17 years. The results were published in several papers (Zhang & Stührenberg 1997, Stührenberg & Walter 2000, Stührenberg & Heusermann 2004, Stührenberg 2004). A main advantage of the test series is that the tests are executed with the same test equipments and mostly under the same conditions. This induces a large confidence in the comparison of test results from different material.

Figure 1. Heatable Oedometer test equipment.

The principal compaction behavior is obtained by laboratory tests in an oedometer – the standard test equipment used for granular rock. Figure 1 shows the main part of the heatable test equipment. Its function is illustrated in Figure 2.

At the BGR, constant compaction rates are selected to load the specimen with a diameter of 30 cm, analogous to a constant room or drift convergence rate. The test result is the "backfill resistance" σ_1 which is defined in Figure 2. This stress definition

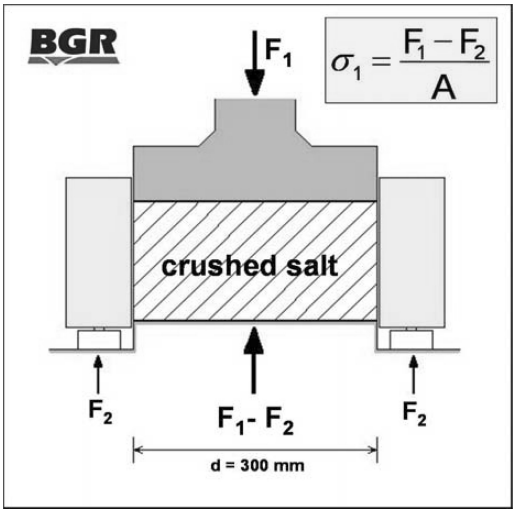

Figure 2. Principal sketch of the Oedometer.

allows comparing the behavior of different oedometer samples.

In oedometer tests the confining stress component is unknown. Bechthold (1999) has given a logarithmic expression to calculate this component approximately as a function of the axial stress and the porosity.

Low compaction rates in the order of magnitude observed in situ ($\leq 10^{-10}$ s^{-1}) cannot be used in the laboratory for an entire experiment because no significant compaction is achieved within a reasonable period of time. Nevertheless low rates are important to determine the in situ behavior, because the compaction rate has a considerable influence on the backfill resistance. The results from tests with applied constant compaction rates between 10^{-7} and 10^{-10} s^{-1} allow comparison of the behavior of different samples. In a stress-porosity (void ratio) plot like in Figure 3 it is possible to obtain results by interpolating and extrapolating the data and curves. The void ratio is the ratio between the pore volume and the solid matter volume of the porous material. The density of the dry solid crushed salt (rock salt) sample is 2.16 g/cm^3.

Figure 3 shows the results of an oedometer test with crushed salt ("Reference material" from the Asse Salt mine) at a temperature of 200°C. The grain-size distribution of the material is discussed in Stührenberg & Walter (2000), Fig. 3, and in Zhang & Stührenberg (1997), Fig. 1, curve 1. It corresponds largely to the material obtained using a part-face header. The backfill resistance in Figure 3 is shown as a function of the void ratio e. The interpolation lines represent the evolution of the backfill resistance in dependence of the applied compaction rate. It increases with increasing density of the material, but it decreases with decreasing compaction velocities. With a compaction rate of

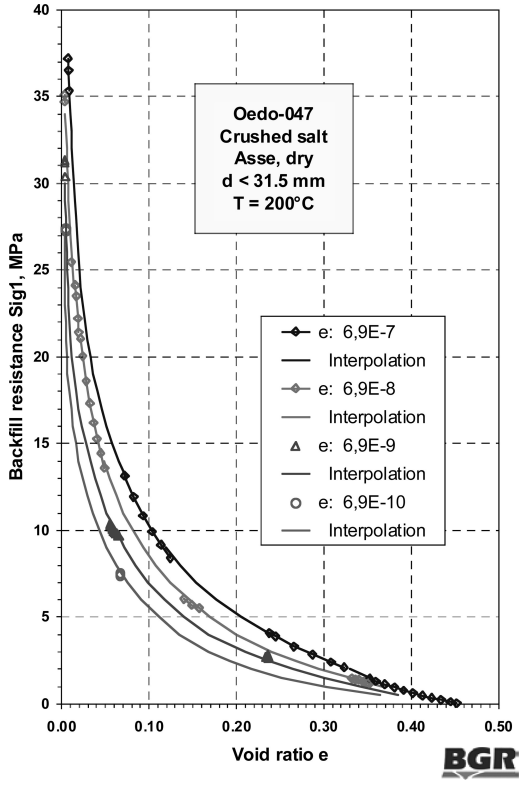

Figure 3. Oedometer test results of pure crushed salt with different compaction rates, T = 200°C.

$6.9 \cdot 10^{-7}$ s^{-1} a backfill resistance of about 10 MPa is measured at a void ratio of e = 0.1. A backfill resistance of only 5.5 MPa is to expect under the small compaction rate of $6.9 \cdot 10^{-10}$ s^{-1} at the same density. Caused by the high temperature of 200°C the specimen was nearly completely compacted at the end of the test after 65 days to the density of natural rock salt ($e \approx 0.01$).

As outlined in Stührenberg (2004) the backfill resistance decreases with increasing temperature and also with small amounts of moisture (tests with 0.6 or 1.2 weight% were performed). A sudden influx of brine to an incompletely compacted crushed salt sample results in a sudden drop in its backfill resistance. The compaction behavior of material from different locations with the same mineralogical composition is similar: The results for material from the Zechstein z2 in the Asse salt mine ("Älteres Steinsalz") are nearly the same as those for the Zechstein z2HS ("Hauptsalz") in the Gorleben mine.

High convergence rates in backfilled cavities of a repository in salt formations will occur at high temperatures, i.e. close to the heat generating waste. Under this condition high densities of the crushed salt

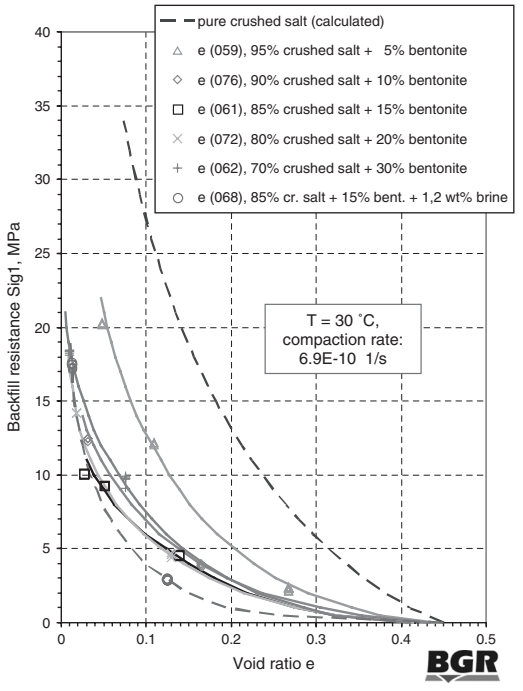

Figure 4. Compaction behaviour of different mixtures of crushed salt and bentonite at room temperature.

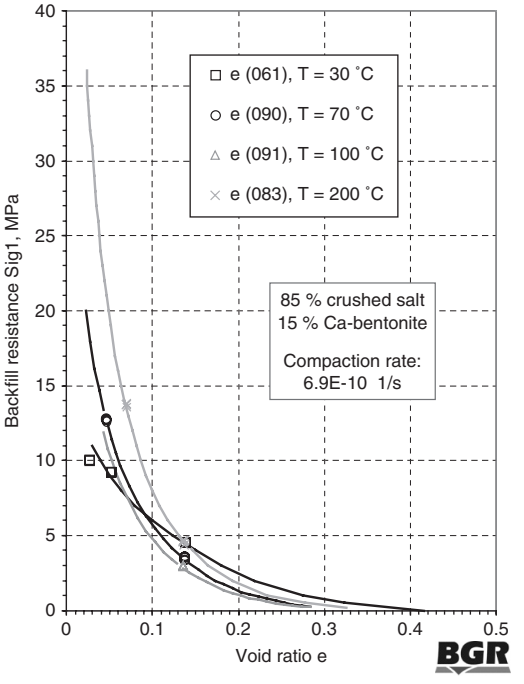

Figure 5. Compaction behaviour of 85/15-mixtures of rushed salt/bentonite at different temperatures.

backfill can be expected because the achieved backfill resistance is much smaller than the level of overburden pressure of about 16 to 18 MPa. However, in repository sections with a smaller temperature level and a lower compaction rate it is advantageous to use a backfill with a smaller resistance against its own compaction.

3 COMPACTION BEHAVIOR OF CRUSHED SALT AND BENTONITE

The investigations in the last years were focused on laboratory tests on mixtures of crushed salt and bentonite, because added bentonite can reduce the permeability of the backfill considerably – at least at room temperature. Additionally the backfill resistance of those mixtures is reduced at room temperature, too. At higher temperatures, however, the moisture content of the bentonite may be reduced which is expected to influence the compaction behavior unfavourable. Although the controlling processes of these phenomena have not been clarified until now, several interesting laboratory results are available. The recent investigations were done within the EU research project NF-PRO. The material used excluded was Ca-bentonite "Deponit-Ca". To ensure the comparability with the pure crushed salt, the density of the compacted dry bentonite sample was chosen to 2.00 g/cm^3, instead of the grain density of about 2.7 g/cm^3. This solid sample density was verified by a Proctor test. With the rock salt density of 2.16 g/cm^3 a mixed density is calculated and used to determine the void ratio.

Figure 4 shows the oedometer test results on several mixtures of crushed salt and Ca-bentonite under the compaction rate of $6.9 \cdot 10^{-10}$ s^{-1} at room temperature (data and interpolated lines as demonstrated in Fig. 3). For comparison the curve of pure crushed salt is plotted, too. At a void ratio of $e = 0.1$, for example, its backfill resistance is more than 25 MPa. With an addition of 10 to 20% Ca-bentonite the backfill resistance can be reduced to values between 6 and 8 MPa. A furthermore decrease to less than 4 MPa is attained with a small amount of brine in the sample. This mixture shows the smallest backfill resistance in comparison to those without added brine until a void ratio of $e \approx 0.05$ is achieved. Further compaction results in similar backfill resistance values for all of the tested mixtures.

Figure 5 shows the test series on mixtures of 85% crushed salt and 15% bentonite at different temperatures. The curve of the test at $T = 30°C$ represents the result with a backfill resistance at the lower side of the lines in Figure 4. The results of the tests at $T = 70$, 100 and 200°C are congruent. In contrast to the compaction

behavior observed at pure crushed salt the backfill resistance at T = 200°C is much higher than those of 70 and 100°C. The slope of the elevated temperature curves is smoother in the test stage up to a void ratio of about 0.2. But at smaller void ratios the compaction behavior is characterized by an important increase in backfill resistance values which becomes even steeper with increasing temperature.

The trend in the temperature dependence of the compaction behavior shown in Figure 5 is confirmed by three test results on 90/10 mixtures that are plotted in Figure 6. The backfill resistance curves of the tests at 70 and 100°C, respectively, are close to each other. At smaller void ratios, i. e. less than about 0.16, their backfill resistance is higher than that at room temperature. Nevertheless, the backfill resistance of the test at T = 100°C remains well smaller than that of the compaction test which was carried out with pure crushed salt at T = 100°C (dashed curve in Fig. 6).

The observed behavior of the crushed salt/bentonite mixtures at higher temperatures could be caused by the reduction in water content and mineralogical composition of the bentonite. In bentonite the three types of water can be differentiated: The pore water, interlayer water and structural or constitutional water (Hammer et al. 2002). Although the exact behavior is subject of ongoing investigations and discussion some general guidelines can be exposed: The pore water can be removed easily upon air drying. The interlayer water is desorbed mainly between 80 and 150°C. The structural water is irreversibly desorbed mainly between 500 and 700°C. Very important for the elapsing processes are not only the temperature values but also the time period. This must be taken into account at the assessment of the long term behavior of bentonite backfill.

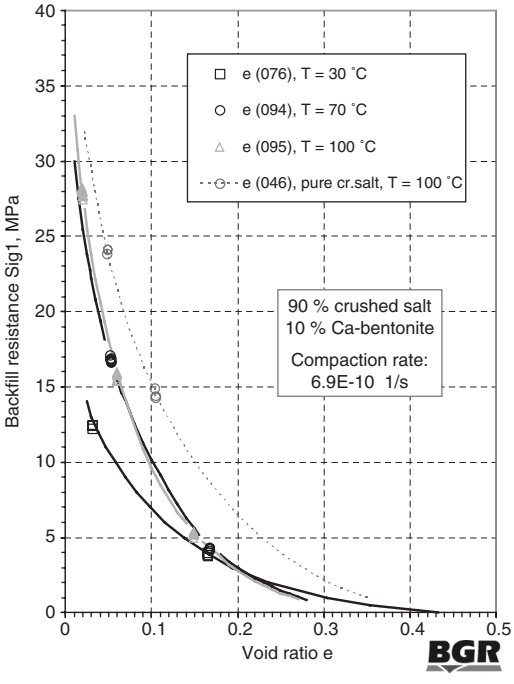

Figure 6. Compaction behaviour of 90/10-mixtures of crushed salt/bentonite at different temperatures.

The test periods of the crushed salt/bentonite tests shown in the Figures 4 to 6 were between 41 and 147 days. A time dependence on the results due to different compaction rates cannot be identified.

The Ca-bentonite "Deponit-Ca" used in the BGR tests is stored in an air-conditioned room with a relative air humidity of 35 to 40%. Proved by drying in a hot cabinet at 105°C its water content is in the range of 12 to 14% measured already after few hours. Further investigation will focus on the question whether the bentonite itself or only the water content is chiefly responsible for the observed temperature dependence of the bentonite mixture.

4 PERMEABILITY TESTS ON CRUSHED SALT AND BENTONITE MIXTURES

Permeability tests are performed in a combined compaction-permeability apparatus with a fixed diameter of d = 10 cm (Uniaxialpermeameter). It is mounted in the load frame of the triaxial test equipment. The porous sample in the permeameter is compacted stepwise by a strain controlled axial load. At a constant porosity saturated brine is pressed from the lower end face through the specimen. Several intervals (test stages) per porosity status are performed at different fluid pressures up to 10 bars. The pressure is adapted to the present sample density. The emitted liquid is measured in a graduated cylinder and weighed. Figure 7 shows a part of the loading frame, the permeameter and in front the liquid measuring device and the fluid feed line.

The procedure of a permeability test is explained in Figure 8 by three time history curves. The sample was a mixture of 80% crushed salt with a maximum grain diameter of 16 mm and 20% Ca-bentonite. The test temperature was about 32°C. The scattered curve is the axial stress Sig1 which results from the strain controlled mechanical loading. It is calculated from the main piston force and the cross sectional area of the sample. Like in an oedometer test, the stress increases in the loading phases and decreases to a nearly constant level when the compaction is stopped (stress relaxation). The bold curve (secondary axis) shows the void ratio of the sample. The grey thin line represents the fluid pressure which is applied in the permeability phases or which is resulting as internal pressure built

up in the compaction phases. It is measured in the fluid feed line close to the test cylinder.

In summary, 9 compaction phases and 9 permeability test phases with 29 different flow stages were performed in this test. The initial compaction rate of 0.1 mm/h ($1.5 \cdot 10^{-7}$ s^{-1}) was reduced to at last 0.0083 mm/h ($1.6 \cdot 10^{-8}$ s^{-1}), because the internal fluid pressure increased to more than 10 bars. The required stress to compact the wet material remained on a low level. In the last compaction phase, where the void ratio of the sample approached to less than 0.1 (porosity $\Phi = 9\%$), a maximum stress of 3.7 MPa was registered. This is a very small value in relation to the backfill resistance of dry material.

Figure 7. Equipment for permeability tests.

Figure 9 shows two photos of the 80/20 mixture specimen after compaction and fluid pressure tests. The left photo shows the whole specimen with the fused disks after removing the rubber jacket, the right one the cut specimen.

An example for the brine outflow results is shown in Figure 10. The brine flow phase III with 4 stages (Fig. 8, no. 12 to 15) was conducted at void ratio of 0.235. All primary fluid pressure levels were held below 1 bar. The regression of an outflow curve as shown in Figure 10 result in the volumetric flow rate Q that is used to calculate the permeability K after Darcy's law. All results of one brine flow phase are summarized to a mean value concerning the void ratio (porosity) stage. At smaller void ratios of the specimen, the brine flow becomes smaller, although the fluid pressure is elevated.

The permeability results of several tests with different material mixtures are shown in Figure 11 as a function of the void ratio e in a log-log diagram. The values of each test sample are fitted using a power law regression $k = e^x$. This fit yields a straight line in

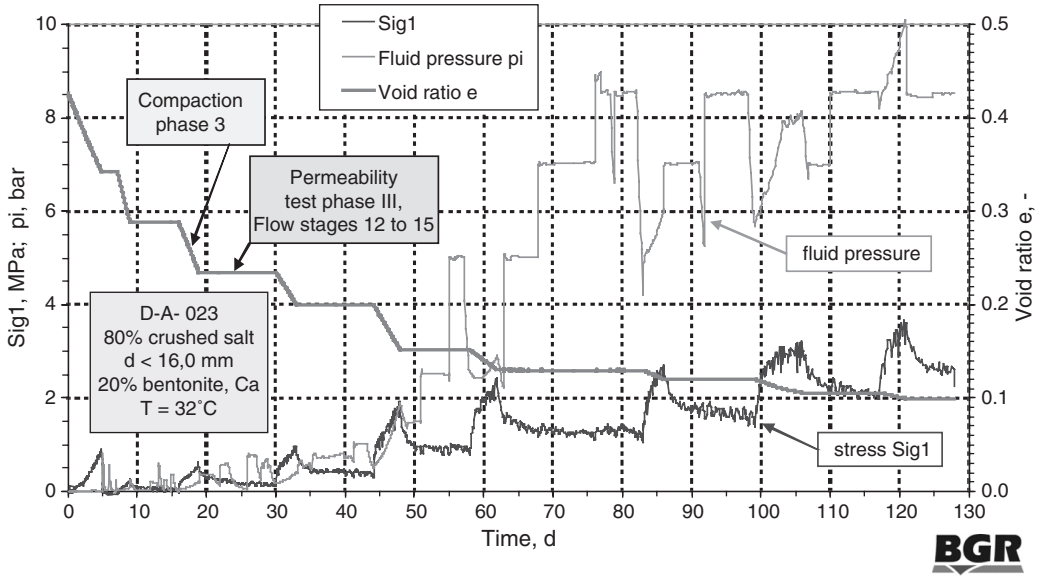

Figure 8. Permeability test with brine on an 80/20 crushed salt/bentonite mixture: axial stress, fluid pressure and void ratio.

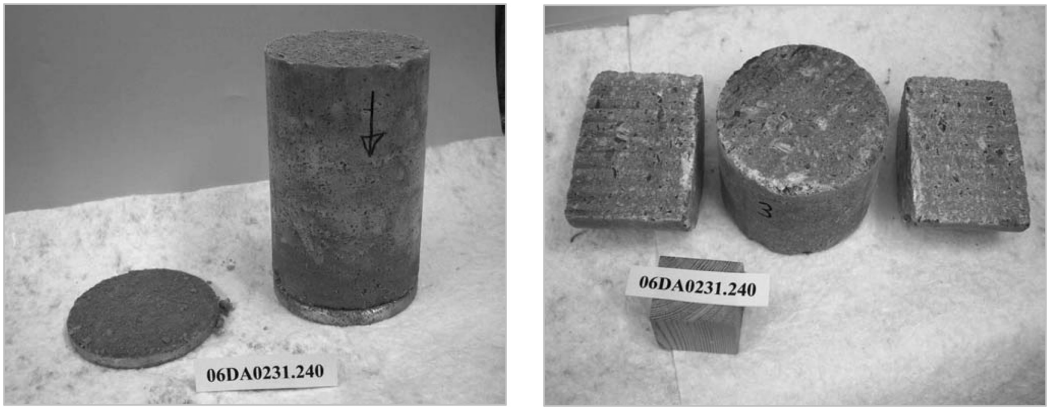

Figure 9. 80/20 specimen after compaction and permeability test.

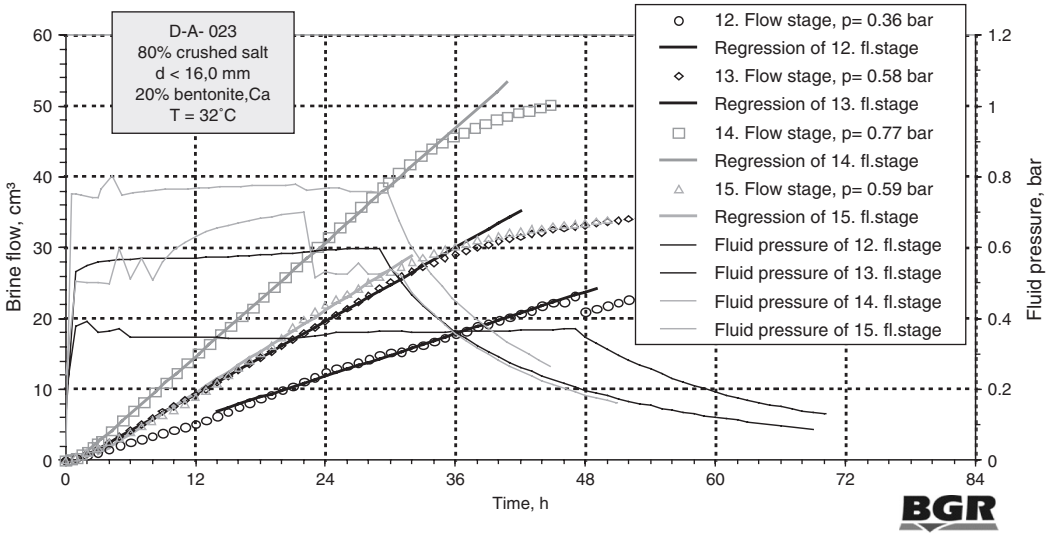

Figure 10. Permeability test with different fluid pressures: Brine flow phase III, e = 0.2351 = const.

the log-log plot and is well suitable to compare the results.

The mixture with only 5% Ca-bentonite nearly coincides with the permeability behavior of the pure crushed salt. At an amount of about 10 % Ca-bentonite the permeability of crushed salt is reduced by about 2 orders of magnitude. The barrier effect is increased furthermore by 2 orders of magnitude with an addition of 15 or 20% Ca-bentonite. However, the difference between the results of tests with 15% and 20% is small. This result recommends that the optimum in permeability reduction can be obtained with about 15% Ca-bentonite – at least at room temperature. Tests at elevated temperatures are needed to investigate the effect of desaturation.

5 SUMMARY AND CONCLUSIONS

Crushed salt used as backfill can be compacted well by the drift convergence at high temperature (150–200°C) as it occurs in repositories of high radioactive waste close to the waste containers. For lower temperature it is advantageous to improve the material behavior, i. e. to reduce the backfill resistance against its own compaction and/or to reduce the permeability against brine in relation to its porosity. Mixtures of crushed salt and bentonite have been found as suitable to achieve this objective. The backfill resistance of the crushed salt is considerably reduced with additives of 10 to 20% Ca-bentonite in case of room temperature. Oedometer tests at elevated temperatures of 70°C and higher,

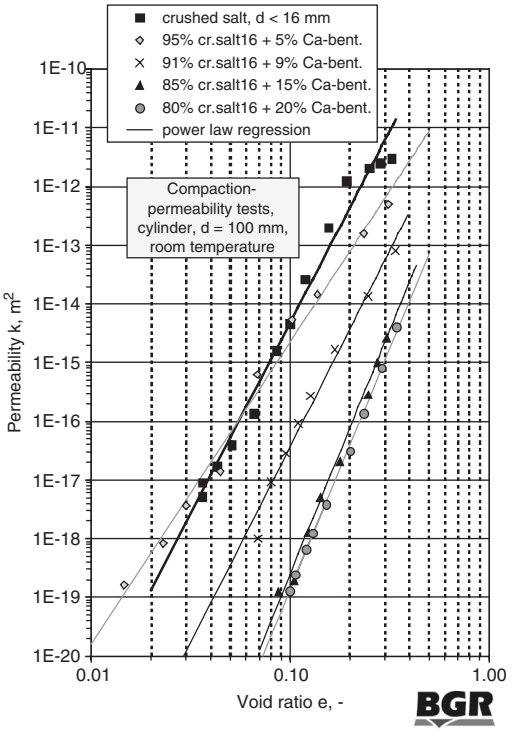

Figure 11. Permeability of crushed salt and mixtures of crushed salt and Ca-bentonite with brine.

however, showed an increased backfill resistance, in contrast to the behavior of pure crushed salt which becomes softer. Nevertheless, at room temperature these backfill resistance values are smaller than those of the pure crushed salt. The permeability of 80/20 or 85/15 mixtures of crushed salt and bentonite is reduced up to four orders of magnitude for equal void ratios. Hence, this mixture can be recommended as a backfill barrier component in a repository of radioactive waste in a salt dome.

However permeability tests at elevated temperature are needed to investigate the impact of desaturation in combination with sound investigations on the mechanism which control the compaction behavior of crushed salt and bentonite mixtures.

REFERENCES

Hammer, J. & Kleeberg, R. Gehlken, P.-L. Kasbohm, J. & Böttcher, G. 2002. Bestimmung der mineralogischen Zusammensetzung von Sedimenten. In: Hammer, J. (Hrsg.): *Quartäre Sedimente als Geologische Barrieren. Handbuch zur Erkundung des Untergrundes von Deponien und Altlasten, Bd. 9. 227–264,* Berlin: Springer.

Stührenberg, D. & Walter, F. 2000. Compaction and Permeability of Crushed Salt, Experimental Results. *Proc. "DisTec 2000", Intern. Conference on Radioactive Waste Disposal, Sept. 4–6, 2000*, Berlin.

Stührenberg, D. & Heusermann, S. 2004. Laboratory Investigations on Backfill and Rock Salt within the BAMBUS II Project. *European Commission, EURADWASTE '04, Radioactive Waste Management Community Policy and Research Initiatives*, Luxembourg, March 2004.

Stührenberg, D. 2004. Compaction and Permeability Behavior of Crushed Salt an Mixtures of Crushed Salt and Bentonite. *Conference Proceedings of DisTec2004, International Conference on Radioactive Waste Disposal*, Berlin, April 2004.

Bechthold, W. et al. 1999. Backfilling and Sealing of Underground Repositories for Radioactive Waste in Salt (BAMBUS Project). *European Commission, EUR 19124 EN, CEC.*

Zhang, C.L. & Stührenberg, D. 1997. Compaction and its Effect on the Permeability of Crushed Salt with Added Brine or Bentonite. *Proc. of the Sixth International Conference on Radioactive Waste Management and Environmental Remediation (ICEM' 97),* Singapore.

Taylor & Francis
Taylor & Francis Group
http://taylorandfrancis.com

The Mechanical Behavior of Salt – Understanding of THMC Processes in Salt –
Wallner, Lux, Minkley & Hardy, Jr. (eds)
© 2007 Taylor & Francis Group, London, ISBN 978-0-415-44398-2

Microstructural study of reconsolidated salt

G.M. Pennock, X. Zhang, C.J. Peach & C.J. Spiers
Faculty of Geosciences, Utrecht University, Utrecht, The Netherlands

ABSTRACT: In this study we examine the microstructures of reconsolidated rock salt after rapid pre-compaction to a porosity of 5%, followed by stress relaxation testing. Synthetic NaCl powder was used for the deformation experiments. Nominally dry material was exposed to laboratory air during stress relaxation at a nominal porosity of about 5%. The relaxation behaviour of this material could be described by a power law with an (apparent) n value of ∼5. The microstructure of polished and lightly etched material was characterized using scanning electron microscopy (SEM) and electron back scattered diffraction (EBSD). A large number of grains were strain free, although some extensively deformed grains were also present. Intra- and intergranular porosity, grain indentations, and channel-island grain boundary microstructures, were also observed. These microstructural features confirm that, in addition to crystal plastic flow, several other mechanisms were operating during reconsolidation. In particular, extensive recrystallization by fluid activated grain boundary migration had occurred. When recrystallization occurs, the strained material is reset to an undeformed state. In view of this, and the drastic work hardening flow that must have occurred during pre-compaction, stress relaxation did not involve steady state deformation. Other mechanisms such as pressure solution may also have operated.

1 INTRODUCTION

Salt rock formations, such as domes and pillows, are widely considered as a suitable host for a geological repository of nuclear waste, in which crushed rock-salt is used to backfill and seal the repository. The closure and sealing of the repository is achieved by compaction and presumed "healing" of the crushed salt. The lithostatic pressure at the repository depth, together with the plasticity of the rock salt, leads to convergence creep of the rocksalt and the compaction of salt plugs and/or backfill. However, limited knowledge exists regarding the sealing/healing process that converts permeable salt grit backfill into an impermeable backfill with properties similar to those of natural rock salt. Reliable assessment of salt grit backfill and seal behaviour depends on better quantification of the compaction and permeability reduction processes operating in granular salt in the low porosity range ($<$10%).

In this study, we examine the microstructures of reconsolidated rocksalt after rapid compaction to low porosity (∼5%) and subsequent stress relaxation, to investigate the active deformation mechanisms and microstructural processes.

2 EXPERIMENTAL

The compaction creep behaviour of pre-compacted, granular salt was investigated in the presence of laboratory air using stress relaxation tests (Rutter & Mainprice 1978; Zhang & Grupa 2006). Synthetic polycrystalline NaCl powder was sieved into grain sizes ranging from 100 to 600 μm and stored in an oven at 50°C for 2–3 days before use. The powders were then rapidly compacted at room temperature in an oedometer to different lengths, i.e. porosities. This pre-compaction was carried out at fast rates of $10^{-5}-10^{-6}$ s^{-1}. Powders were flushed with laboratory air during compaction and subsequent relaxation at room temperature. The stress relaxation behaviour was then determined as a function of time. The microstructure of one representative sample (CP12) is presented here. The initial grain size was 137 ± 12 μm and porosity was about 5% after pre-compaction in lab. air (Zhang & Grupa 2006).

After relaxation, samples were quickly dried, impregnated with low viscosity resin, cut, and impregnated a second time, before polishing in a dry room (Urai et al. 1987). Samples were lightly etched for 3–5 seconds using a 95% saturated NaCl solution

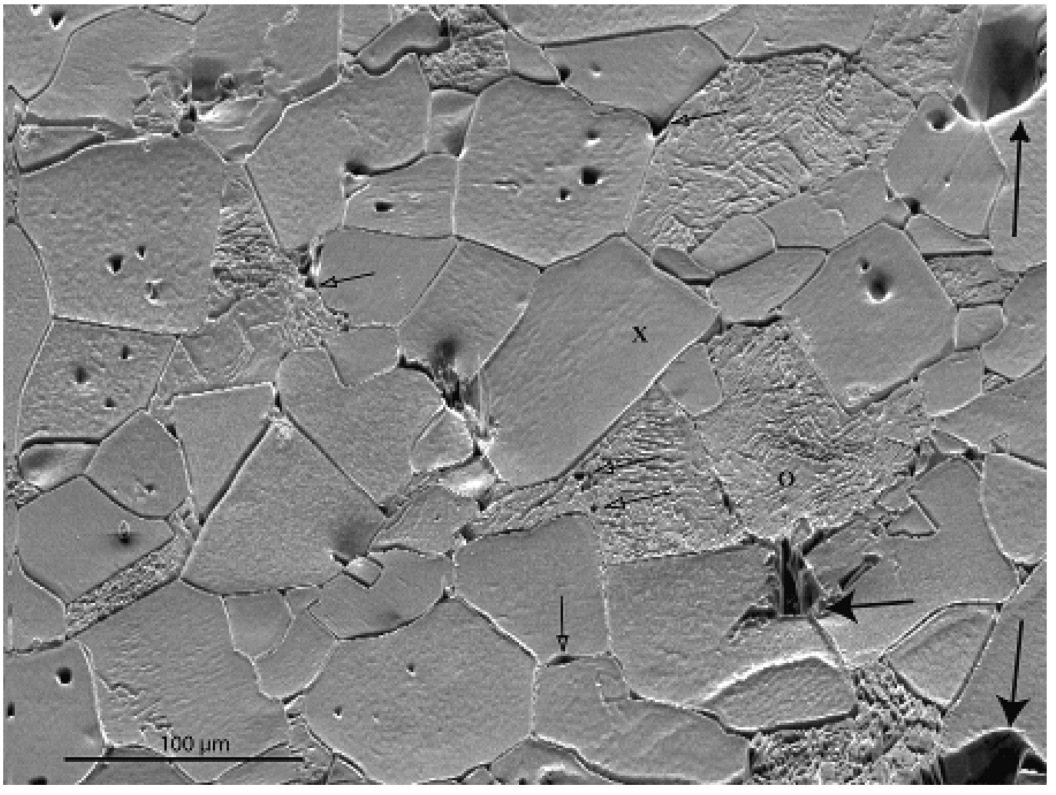

Figure 1. SEM secondary electron image of a compacted NaCl sample (CP12) after polishing and etching. Structured **(O)** and unstructured **(X)** grains, a few large pores (large arrows) and small pores are present. Several intergranular pores are shown with open arrows. (Remnants of resin, which is not removed by the etching process, protrude from a few of the large pores). Compression axis is horizontal in all images.

containing $FeCl_3$ and lightly carbon coated. Microstructures were characterized using an XL30 SFEG scanning electron microscope (SEM) operating at about 19 kV and 2 nA beam current.

All microstructures presented were analysed at a stage tilt of 70°; electronic correction for tilt foreshortening was made. Orientations of grains were mapped using a step size of 1 µm with electron backscattered diffraction (EBSD) (Randle 1993). This technique has been used to estimate the strain in NaCl caused by dislocation creep and pressure solution (Pennock et al. 2005; Pennock et al. 2006a). The angular misorientation resolution of EBSD maps presented in this work is about 0.5°.

3 RESULTS

The mechanical data obtained from the stress relaxation tests could be described in terms of a power law behaviour with an apparent (non-steady state) n-value of ∼5 (Zhang & Grupa 2006; Zhang et al. 2007). Bearing in mind the initial rapid pre-compaction stage, this n-value cannot be interpreted in terms of any steady state mechanism (Schulze 1984). The microstructure showed a mixture of structured and unstructured grains and pores. (Figure 1). The structured grains contained a considerable amount of heavily etched dislocation substructure whereas unstructured grains were relatively substructure free, showing only a very small amount of etch topography. Pores, some of which appear to have a 'negative crystal' shape (square and triangle cross-section), were located predominantly within unstructured grains. Many irregular shaped pores were also located along grain boundaries. In some places the pattern of the intragranular pores appeared to outline the earlier location of the trace of a grain boundary (dotted white line, Figure 2). EBSD mapped images (Figure 3) showed that the more structured grains were highly deformed, showing considerable lattice bending across the grain, whereas the unstructured grains showed very little lattice bending (Figure 3c). The grain boundary traces of both deformed and recrystallized grains were

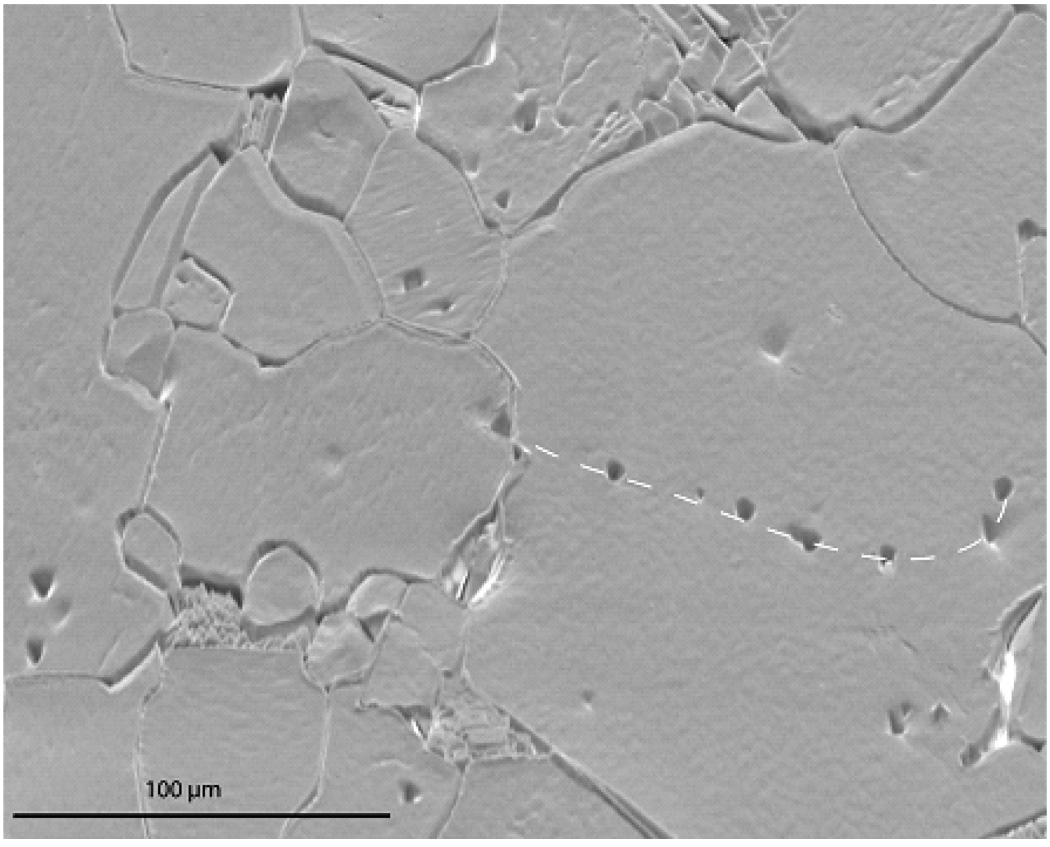

Figure 2. SEM secondary electron image showing pores in the unstructured (recrystallized) grains have a negative crystal shape. The white line outlines an array of pores which probably shows the earlier location of a grain boundary.

generally straight and many grains had a square trace (cube shape) in which the grain boundary traces were close to {100} planes (Figure 3d). Several unstructured grains showed interpenetrating contact between neighbouring grains, both unstructured and structured, (Figures 1–4). EBSD showed that the area close to the penetrated, unstructured grains sometimes contained evidence of deformation in the form of lattice bending (Figure 4a, b) but not always (Figure 4c–e). Etching of the grain boundaries mostly resulted in deep grooves but some of the grain boundary contacts, of both structured and non-structured grains, showed ridge features (boxed region, Figure 3a).

4 DISCUSSION

The absence, or limited presence of, lattice bending observed in EBSD maps of unstructured grains, and the presence of intragranular porosity, suggests that these grains have recrystallized. The structured grains on the other hand are heavily deformed and this probably occurred, for the most part, during the rapid compaction stage, as the strain during stress relaxation was small.

Many of the recrystallized grain surfaces do show topographic etch features at a very fine scale. As the density of these features does not vary with lattice bending (e.g. compare the central grain in Figure 4a and b) they are probably caused by variations in etch behaviour of the different crystallographic faces in the polished section (Trimby et al. 2000), and are not necessarily associated with etching of individual dislocations.

The contrast at the indenting ridge of the cube shaped grain shown in Figures 4e is also thought to be topographic in origin, caused by differential etching of a grain boundary surface that is inclined to the exposed specimen surface. This contrast is similar in origin to that observed at grain boundaries in many other grains (e.g., Figures 2 and 3). The contrast is not caused by an orientation difference, at least, within the scale shown in the key.

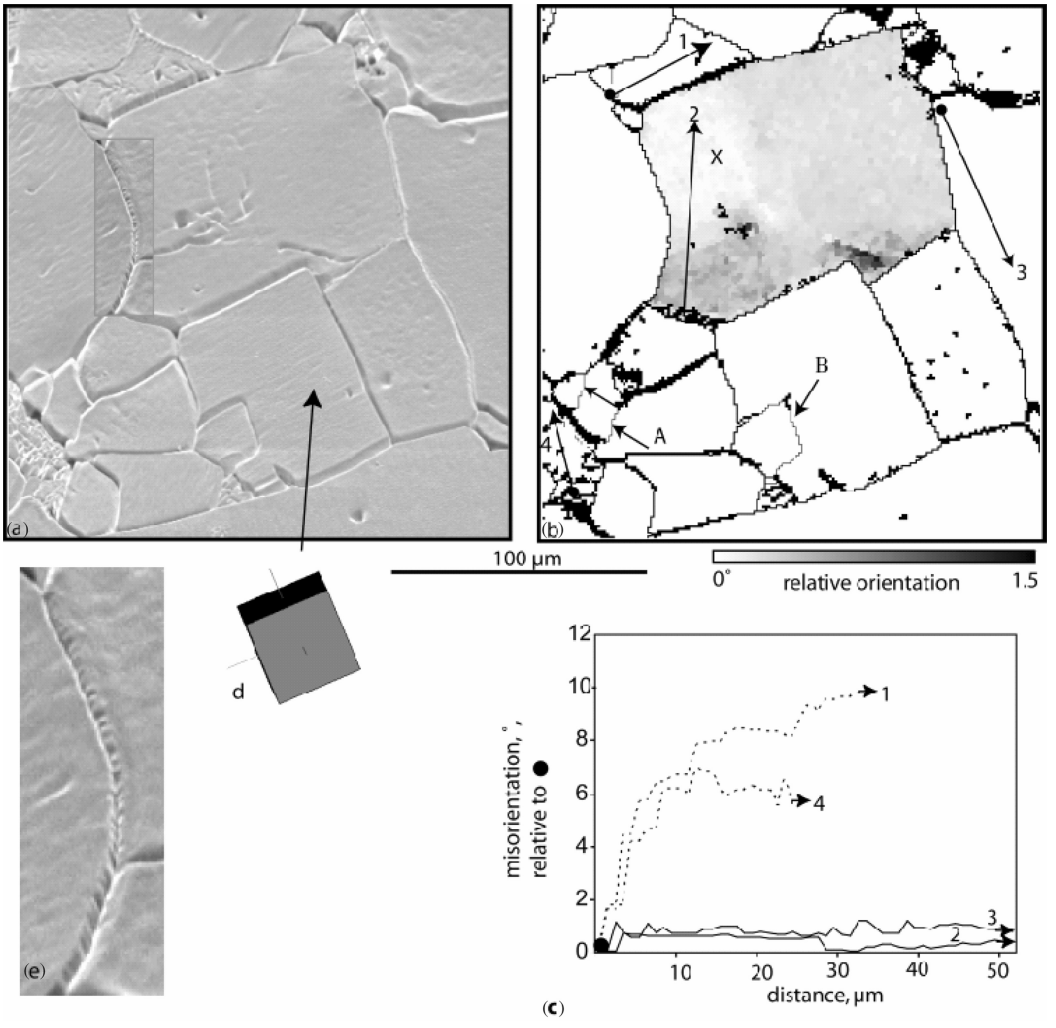

Figure 3. SEM secondary electron image showing location of (b) EBSD map, step size 1 µm. The mapped image shows grain boundaries (thick black lines) and subgrain boundaries (thin black lines, with misorientations >3°); orientation analysis was not possible in the black regions. The grey, shaded grain shows the relative orientation difference within the grain from the location marked with an 'X'; the orientation difference is less than 1.5° over the whole of the grain, with the upper left hand corner of the grain having a slightly different orientation to the rest of the grain. The cumulative misorientations, relative to points marked ●, across four grains are shown in (c): clearly the structured grains 1 and 4 show a large misorientation difference of up to 9°, whereas the unstructured grains 2 and 3 show only small differences of about 1°. Grains A and B contain subgrains (arrowed) which have misorientations greater than 3°. (d) The orientation of the arrowed grain is shown schematically as a cube. The grain boundary traces are approximately parallel to the {100} cube faces. (e) The boxed region in (a) shows detail of ridges along adjacent grain boundaries.

Recrystallization at room temperature must have involved water assisted grain boundary migration (Urai et al. 1986), which, in the absence of water, does not occur until temperatures above about 450°C (Guillopé & Poirier 1979; Franssen 1993). This process must have occurred during the relatively long period of stress relaxation, as the precompaction stage was very rapid. This implies that the small amount of water vapour present in the laboratory air used to flush the samples was clearly sufficient to mobilize the boundaries.

Other evidence that water played a role in grain boundary migration is clearly seen by the formation of the negative crystal shaped pores. In many cases, these pores were distributed in linear arrays within the unstructured recrystallized grains (Figure 2),

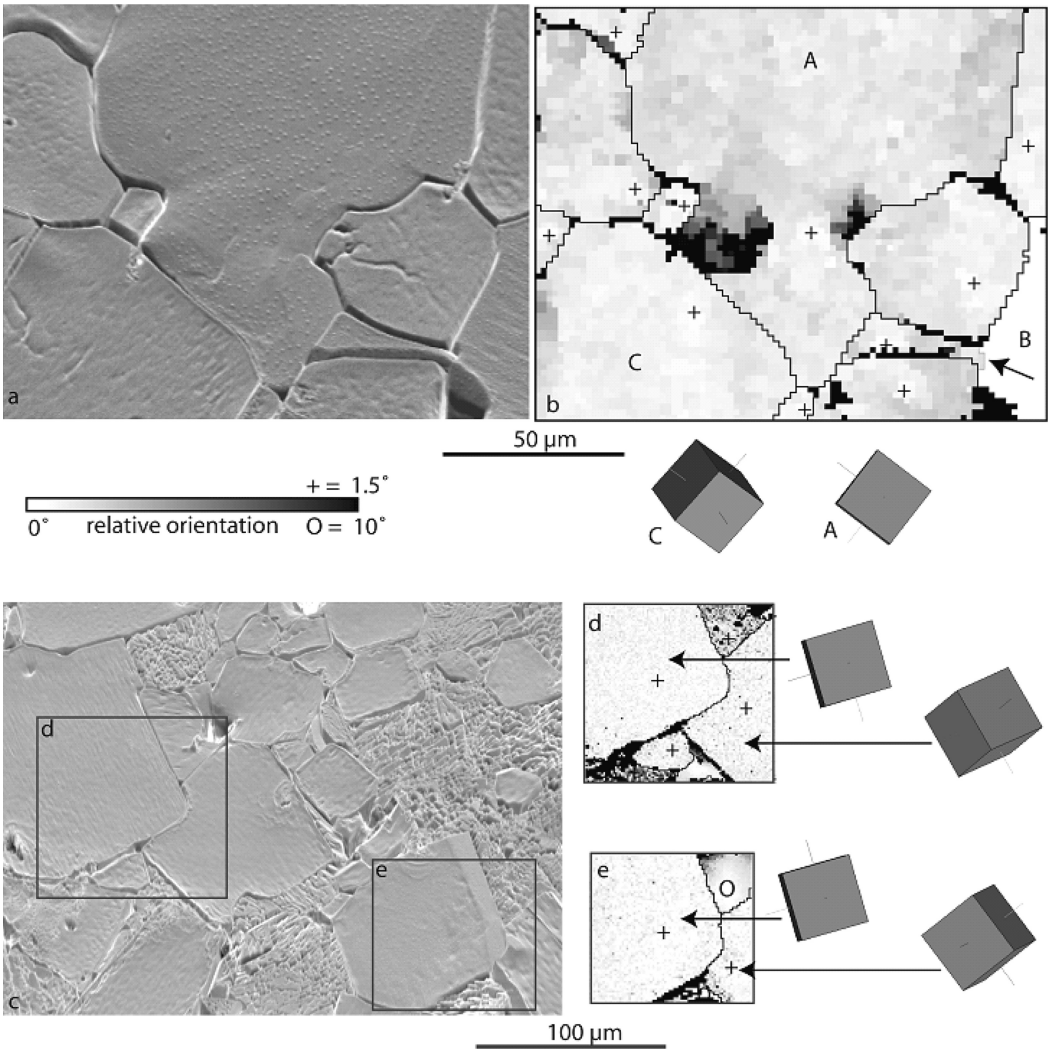

Figure 4. SEM secondary electron images showing indented contacts between unstructured grains with (a) irregular and (c) cube shapes. (b, d and e) are the corresponding EBSD maps, step size 1 µ m. In (b) grain A shows slight lattice bending in contact regions near to grain indentation, whereas in (d) and (e) there is no evidence of lattice bending. The relative orientation from locations marked as either '+' or **'O'** are shaded in grey: grains marked as + show very little variation in orientation across the grain (<1.5°) whereas the more structured grains marked **O** show larger variations (up to 10°). The orientation of several unstructured grains with straight boundaries is also shown schematically as cubes: the grain boundary traces are all close to {100}. The unstructured grain 'B' in (b) extends between two neighbouring grains and forms a low angle subgrain boundary, with a misorientation of about 2° (arrow).

suggesting that the pores were originally intergranular and not intragranular. The pores remained isolated within the recrystallized grains, after being swept by water assisted grain boundary migration. Their negative crystal shape is consistent with the presence of water, as this equilibrium shape is unlikely to have developed at room temperature unless water was present to assist mass transport.

The source of the water is expected to be intergranular water, originating from the laboratory air. Cube-shaped negative crystal pores are occasionally observed as inclusions in the powder material used to make the samples (Spiers & Schutjens 1990; Schutjens 1991). However, as argon flushed control samples showed very little stress relaxation under identical conditions (Zhang & Grupa 2006), we believe that the

water assisting grain boundary migration did indeed originate from the laboratory air.

The ridge structure observed at grain boundaries between recrystallized grains is consistent with the channel and island microstructure reported for wetted grain boundaries (Urai 1983; Spiers et al. 1990; Shenk & Urai 2004; De Meer et al. 2005). The migration of the grain boundaries was most likely driven by differences in strain energy, although anisotropic grain boundary energies or diffusivities, (De Meer et al. 2005; Pennock et al. 2006a) are likely to have been important and are consistent with the development of many cube shaped grains with boundary traces parallel to {100} faces (Pennock et al. 2006b).

Although recrystallization by water assisted grain boundary migration is apparent, some crystal plastic deformation probably occurred during stress relaxation, as supported by the slight lattice bending in some of the recrystallized grains. However, the presence of low angle subgrain boundaries need not necessarily be taken as evidence for plastic deformation. Subgrains, like those shown in grain A, Figure 3, for instance, are likely to have originated from cataclasis during rapid compaction. The absence of lattice bending in other recrystallized grains suggests that these grains recrystallized at a later stage of stress relaxation, when the stresses and strain rates were much lower, although the possibility that static recrystallization occurred cannot be ruled out (Shenk & Urai 2004).

Another water assisted mechanism that may have contributed to the strain during stress relaxation is pressure solution (Spiers & Carter 1998). The grain indentations that occur between two 'unstructured' grains are consistent with pressure solution, although the extent of indentation is too large for the small strains experienced during stress relaxation. Strain induced and anisotropy related grain boundary migration could both give similar microstructures. Distinguishing which mechanism is operating is difficult.

These microstructural features confirm that, in addition to crystal plastic deformation, several other mechanisms were operating during stress relaxation. In particular, extensive recrystallization had occurred by fluid assisted grain boundary migration. When recrystallization occurs, the strained material is reset to an undeformed state and the material can no longer be considered in terms of steady state deformation conditions. Other mechanisms such as pressure solution, strain induced grain boundary migration and plasticity induced solution transfer may also influence the relaxation behaviour.

Relaxation by fluid assisted grain boundary migration has such an influence on the microstructure of crushed salt that it must also influence the evolution of fluid transport properties during the long term healing processes. It is likely that these processes will enable the crushed salt to attain almost identical microstructures and properties to those found in undisturbed natural salt on a relatively short time scale.

5 CONCLUSIONS

Microstructures of reconsolidated crushed salt, after rapid compaction to 5% porosity and stress relaxation to about 1% porosity in the presence of lab. air have been examined. Stress relaxation, due to flow with an apparent n value of 5, occurred via multiple mechanisms, including crystal plastic flow and water assisted boundary mechanisms, including grain boundary migration.

REFERENCES

De Meer, S., C. J. Spiers & S. Nakashima, 2005, "Structure and diffusive properties of fluid-filled grain boundaries: An in-situ study using infrared (micro) spectroscopy," *Earth and Planetary Science Letters,* 232 (3–4): 403.

Franssen, R. C. M. W., 1993, "Rheology of synthetic rocksalt." PhD, Nr. 113, Utrecht University, Utrecht, pp 221.

Guillopé, M. & J. P. Poirier, 1979, "Dynamic recrystallization during creep of single crystalline halite: an experimental study," *Journal of Geophysical Research,* 84: 5557–5567.

Pennock, G. M., M. R. Drury, C. J. Peach & C. J. Spiers, 2006a, "The influence of water on deformation microstructures and textures in synthetic NaCl measured using EBSD," *Journal of Structural Geology,* 28 (4): 588–601.

Pennock, G. M., M. R. Drury & C. J. Spiers, 2005, "The development of subgrain misorientations with strain in dry synthetic NaCl measured using EBSD.," *Journal of Structural Geology,* 27 (12): 2159–2170.

Pennock, G. M., M. R. Drury & C. J. Spiers, 2006b, "Grain boundary populations in wet and dry NaCl," *Materials Science and Technology,* 22 (11): 1307.

Randle, V., 1993, "*The Measurement of Grain Boundary Geometry.*" Bristol and Philadelphia, Institute of Physics Publishing.

Rutter, E. H. & D. H. Mainprice, 1978, "The effect of water on stress relaxation of faulted and unfaulted sandstone," *Pure and Applied Geophysics,* 116: 634–654.

Schulze, O., 1984, "Thermomechanical properties of irradiated rock salt.," *Nuclear Instruments and Methods in Physics Research,* B1: 542–548.

Schutjens, P. M. T. M., 1991, "Intergranular pressure solution in halite aggregates and quartz sands: an experimental investigation." PhD, Utrecht University, Utrecht, 233.

Shenk, O. & J. L. Urai, 2004, "Microstructural evolution and grain boundary structure during static recrystallization in synthetic polycrystals of sodium chloride containing brine," *Contributions to Mineral Petrology,* 146: 671–682.

Spiers, C. J. & N. L. Carter, 1998, "Microphysics of rocksalt flow in nature." *Proceedings of the Fourth Conference on the Mechanical Behaviour of Salt*, Trans Tech Publications.

Spiers, C. J. & M. T. M. Schutjens, 1990, "Densification of crystalline aggregates by fluid-phase diffusional creep."

Deformation Processes in Minerals, Ceramics and Rocks. D. J. Barber and P. G. Meredith, Unwin-Hyman: 334–353.

Spiers, C. J., P. M. T. M. Schutjens, R. H. Brzesowsky, C. J. Peach, J. L. Liezenberg & H. J. Zwart, Eds 1990, Experimental determination of constitutive parameters governing creep of rocksalt by pressure solution. *Deformation Mechanisms, Rheology and Tectonics*, The Geology Society, London.

Trimby, P. W., M. R. Drury & C. J. Spiers, 2000, "Misorientations across etched boundaries in deformed rocksalt: a study using electron backscattered diffraction," *Journal of Structural Geology,* 22: 81–89.

Urai, J. L., 1983, "Water assisted dynamic recrystallization and weakening in polycrystalline bischovite," *Tectonophysics,* 96: 125–157.

Urai, J. L., C. J. Spiers, C. J. Peach, R. C. M. W. Franssen & J. L. Liezenberg, 1987, "Deformation mechanisms operating in naturally deformed halite rocks as deduced from microstructural investigations," *Geologie en Mijnbouw,* 66: 165–176.

Urai, J. L., C. J. Spiers, H. J. Zwart & G. S. Lister, 1986, "Weakening of rock salt by water during long-term creep," *Nature,* 324: 554–557.

Zhang, X. & J. Grupa, 2006, "Compaction behaviour and permeability of low porosity compacted salt grit (dry and wet)," European Commission Community Research, NF-Pro project, public deliverable D3.5.7, 21146/06 77412/P, pp. 107, (also NRG report number 21146/06.77412/P).

Zhang, X., J. Grupa, C. J. Spiers & C. J. Peach, 2007, "Stress relaxation experiments on compacted polycrystalline salt." *6th Conference on the mechanical behavior of salt; Understanding of THMC processes in salt rocks*, Hannover, Germany, Taylor and Francis.

Taylor & Francis
Taylor & Francis Group
http://taylorandfrancis.com

The Mechanical Behavior of Salt – Understanding of THMC Processes in Salt –
Wallner, Lux, Minkley & Hardy, Jr. (eds)
© 2007 Taylor & Francis Group, London, ISBN 978-0-415-44398-2

Mechanical and permeability properties of highly pre-compacted granular salt bricks

K. Salzer, T. Popp & H. Böhnel
Institut für Gebirgsmechanik GmbH, Leipzig, Germany

ABSTRACT: In the salt concept for the disposal of high level radioactive waste in deep geological rock formations granular salt is the favorite for backfilling of remaining openings because of its advantageous physical properties. However, its initial sealing capacity is low due to the high porosity. Besides others, the usage of pre-compacted blocks of crushed salt offers an alternative sealing concept. Our investigations are aiming to investigate both the mechanical compaction behavior and the evolution of transport properties in salt bricks (artificial pressed granular salt with a porosity of ∼8%), as a prerequisite to develop mechanism-based constitutive models describing these processes in the low porosity region (10–1%). A key factor is the role of water, since it affects in a complex manner the coupled hydraulical/mechanical properties of granular salt.

1 INTRODUCTION

The storage of radioactive waste in deep geological rock formations is the only accepted concept for a save long-term disposal to exclude a threat to actual and future generations. Besides clay and crystalline rock formations salt deposits are internationally evaluated as host rocks, e.g. by the USA, the Netherlands and Germany.

To ensure containment and long-term retardation of radionuclide releases various storage concepts for radioactive waste have been developed based on a complex system of geological and technical barriers (so-called multi-barrier system) (NEA-EC 2003). Backfill and seals are an important part of the engineered barrier system (EBS) representing man-made engineered materials placed within a repository, in addition to the waste form/ waste canisters. In the salt concept crushed salt was selected as the most suitable backfill material because (1) it has good compacting properties, (2) its thermal and mechanical properties after compaction are similar to the surrounding rock salt, and (3) it is easy available.

During the time-dependent closure of drifts and boreholes caused by thermo-mechanical creep of the surrounding salt rock the crushed salt will be compacted and its initial porosity and permeability will decrease as demonstrated in large scale in situ-experiments, e.g. in the Amelie mine (Kazan & Ghoreychi 1996) and the Asse salt mine (Bechthold et al. 1999, 2004). Over long time periods, the crushed salt is expected to gradually reconsolidate into a material comparable to virgin rock salt.

However, a limiting factor for the use of saliferous granulates as backfill is their initially high porosity and permeability, resulting in a low sealing capacity and mechanical integrity just after emplacement. Besides adding bentonite to enhance compaction and to reduce permeability, an alternative concept for sealing is the use of pre-compacted salt elements, e.g. bricks, which are characterized by porosities below 10% resp. low permeability and high uniaxial strength (Stockmann 1994).

Depending on whether granular salt or pre-compacted salt bricks are used reliable descriptions of both, the mechanical long term behavior and fluid transport properties of both salt and backfill system, are therefore of urgent need for final performance assessment. Whereas the creep (e.g. Hunsche & Schulze 1994; Spiers & Carter 1998) and transport behavior of natural rock salt (e.g. Stormont & Daemon 1992; Popp et al. 2001; Popp et al. this volume) and of crushed rock salt with porosities above 10–15% (e.g. Bechthold et al. 2004) have been thoroughly studied only limited knowledge exists regarding the processes that convert permeable salt backfill materials (porosity $<10\%$) into an impermeable backfill with properties similar to those of natural salt rock. Furthermore, there is a fundamental demand in research and development regarding the understanding and adequate description of the mechanical behavior of the contact between the highly compacted granular salt and the host rock as well as between blocks made of highly compacted granular salt among themselves and the host rock.

Our laboratory investigations are aiming at a comprehensive data basis regarding compaction and

hydraulical behavior of the pre-compacted salt bricks (initial porosity <10%) with respect to the numerical description of their long-term behavior if they are used as sealing elements. Special account is given to humidity effects, affecting both, mechanical and hydraulical properties. The investigations are focusing on the following issues:

(1) Triaxial compression and permeability tests at different confining pressures on highly precompacted crushed salt samples.
(2) Gas injection tests on fluid saturated salt bricks with respect to 2-phase properties (e.g. permeability and threshold pressure).
(3) Long term hydrostatic compaction tests with and without added brine, respectively.
(4) Shear-tests at increasing normal pressure between highly pre-compacted crushed salt blocks and host rock (rock salt) including wetting with brine.

2 EXPERIMENTAL CONDITIONS

2.1 *Sample characteristics and preparation*

A salt brick used in our investigations is a cold pressed ($p \geq 130$ MPa in some few seconds) artificial rectangular solid (240 mm × 115 mm × 71 mm; ±1%) of highly compacted crushed salt composed of nearly pure sodium chloride (≥95% NaCl) with grain sizes between <0.16 mm and 0.5 mm. Such specimens of salt bricks have been produced in large series by the company K + S in 1990 in advance of the planned in situtest dam construction in the Asse salt mine. The fabrication of the salt bricks is already described in detail in Stockmann (1994). A summary of their petrophysical properties is given in Table 1.

Cylindrical test specimen were drilled from a salt brick and then trimmed with a turning lathe to its final dimensions (depending on the test type). The masses of the samples were qualified with a precision balance (±0.01 g) and their dimension (diameter and height) were measured with a digital sliding caliper (±0.1 mm). The specimen density is calculated from the weight and volume of the test sample.

Impregnation of so called "wet" samples was performed with saturated NaCl-brine (density: $\rho = 1.205$ g/cm^3 at 21°C; source: Asse-mine, Germany) storing them in a brine filled container which was evacuated for 5 minutes up to 1 mbar. It has to be mentioned that despite the always equal procedure the amount of brine absorbed by the various specimens is different and significantly lower than it was estimated on the basis of the initial porosity of around 8%. There is only a correlative dependency between the porosity/density and the absorbed volume of brine, which varies between 0.85 and 1.3 Vol.-%. Therefore, it can be concluded that only a partial pore space is accessible for brine and most of pore space is composed of isolated pores.

Table 1. Standard salt brick properties.

Parameter	Value
Dimensions	240 × 115 × 71 mm (±1%)
Density	1950 ± 20 kg/m^3
Porosity	9 ± 1%
H_2O-content	0.20 ± 0.02%
Vp	4.13 ± 0.02 km/s
Vs	2.35 ± 0.01 km/s
Shear modulus	11.0 ± 0.1 GPa
Young's modulus	27.75 ± 0.22 GPa
Uni-axial strength	59.8 ± 1 MPa
Bulk modulus	19.4 ± 0.2 GPa

2.2 *Rock mechanical procedures*

The strength testing experiments were performed in a standard Karman-cell in the servo-hydraulic testing machine (RBA 2500, Schenk/Trebel Germany). The cylindrical samples (144 mm height and 72 mm diameter) are sealed with rubber tubes and oil is used as confining medium. Outside the vessel three LVDT transducers are mounted between the piston and the load frame near the sample for the measurement of the axial strain. The axial load is determined from an external load cell. Deformation induced volume changes ΔV of the specimens are determined by a volume balance of the oil volume changes as measured via the pressure intensifier and the axial piston displacement in the cell.

During the tests permeability can be measured simultaneously parallel to the sample cylinder axis using the stationary flow method (e.g. Popp et al., 2001). To maintain access of the gas to the sample, a central hole exists in the pistons whereby the specimens are additionally prepared with small boreholes on their axial ends (diameter 5 mm, length 35 mm) to minimize end effects during straining.

Triaxial creep tests at constant deviatoric stresses and compaction tests at quasi-hydrostatic conditions respectively were performed on smaller specimens (80 mm height and 40 mm diameter) in a creep-test rig equipped with Karman-cells. The axial stress comes from a mechanical load device, which can be used in a range up to 200 kN, while the confining pressure (up to 30 MPa) results from a hydraulic system kept constant by an accumulator. The axial load is determined by a calibrated load cell before each experiment. Axial stress and confining pressure are kept constant with an accuracy of ±1% during the tests. All test parameters like axial deformation (three dial gauges), confining pressure and temperature were manually checked and recorded daily.

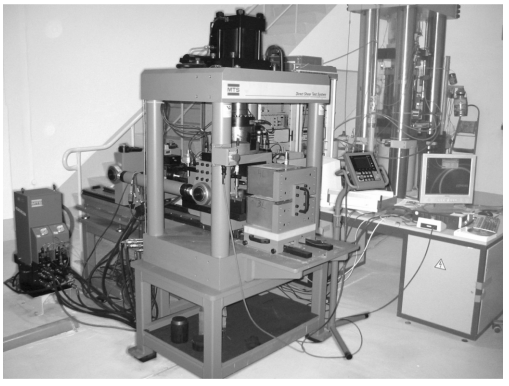

Figure 1. Direct shear system (MTS model 816) in the lab of the IfG Leipzig.

To determine the contact properties between the salt bricks itself and the salt contour, we used the shear testing equipment (MTS Systems Corporation model 816) installed at the IfG (Figure 1). As main advantage, it allows new types of testing procedures for direct shear tests with different boundary conditions (for experimental details see Blümel, 2000).

3 LABORATORY INVESTIGATIONS

3.1 *Strength and creep properties of dry material*

In advance of the usage of salt bricks as a dry masonry abutment for a dam construction various specimens were tested regarding their strength behavior. Stress-deformation curves (in strain control) were recorded for a constant deformation rate of $\dot{\varepsilon}_1 = 2.5 \cdot 10^{-5}$ s^{-1} at room temperature (23°C). Constant confining pressures were applied in stages of $\sigma_3 = 0$, 2, 5, 10 and 20 MPa.

As summarized in Figure 2, the stress-strain curves exhibit strain hardening in the pre-failure range, whereas the evolution of dilatancy occurs only at uniaxial stress resp. at higher axial deformation. The dominating effect of sample compaction, in accordance to confining pressure, is still visible. Due to the sample compaction it has to be mentioned that the axial stresses need to be corrected referred to the actual sample diameter. However, although such a correction can be done based on the relationship between measured axial and volumetric strains only the non-corrected values are shown in a conservative manner in Figure 2.

Remarkably, the load bearing capacity and dilatancy behavior of the crushed rock salt test specimens differ from the behavior of the compact natural rock salt due to reachable larger deformations, relatively high load bearing capacities and the reduction

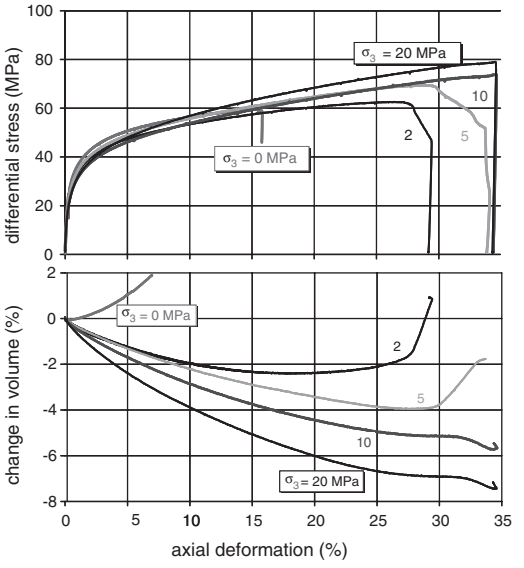

Figure 2. Summary of triaxial strength tests on salt bricks at 23°C. (above) stress-strain curves, (below) dilatancy as a function of axial strain.

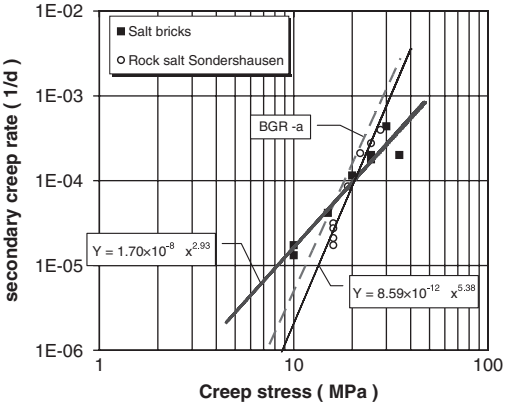

Figure 3. Measured steady-state creep rates in salt bricks compared to natural rock salt samples from the salt mine Sondershausen (Na2) and the BGRa-creep-law.

of the dilatancy due to the decrease of pore space. Most important, dilatant deformation resp. shear failures occur only in a low peripheral pressure range ($\sigma_3 \geq 5$ MPa). At higher pressures ($\sigma_3 \geq 10$ MPa) no failure is observed. The general deformation style corresponds to the macroscopic appearance of deformed specimens (Figure 4).

However, it is important that the strength of the salt bricks is drastically reduced if brine is present. Although this effect was not systematically investigated, one experiment performed with a wet sample

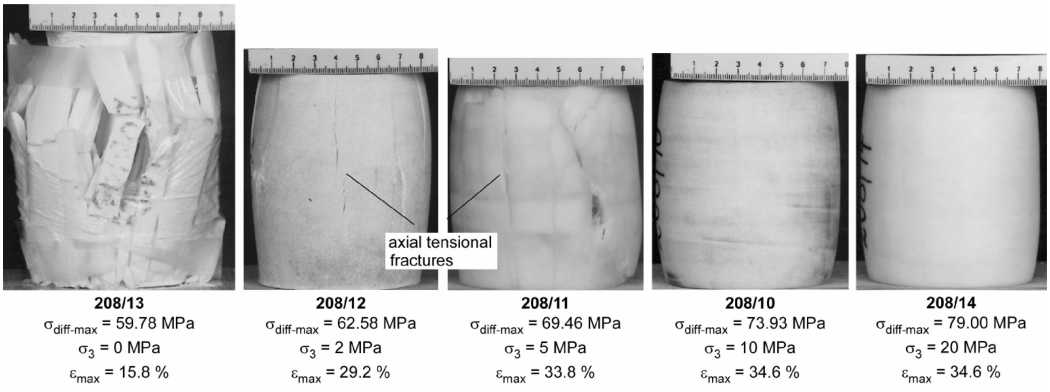

Figure 4. Axially deformed cylindrical salt bricks specimens after testing at various confining pressures and at constant strain rate of 2.5×10^{-5} 1/s. Note the change of the deformation style from brittle to ductile due to the increasing confining pressure.

(at $\sigma_3 = 10$ MPa) showed a systematically lowered strength behavior (around 15 MPa) compared to the reference sample at dry conditions.

As a supplementary test, specimen 27 was compressed with a lateral to vertical stress ratio of $\sigma_3 = 0.33 \cdot \sigma_1$ aiming on a nearly constant cross section during axial deformation (with $\Delta\varepsilon_V \approx \Delta\varepsilon_1$) corresponding to a quasi-oedometer test. However, the test showed, that a factor of 0.33 is too small to avoid bulging of the test specimen (compare Table 2). Probably the ratio is in the order of $\sigma_3 \approx 0.4 \cdot \sigma_1$.

With respect to long-term properties laboratory creep tests on cylindrical salt brick samples (l = 80 mm, d = 40 mm) were carried out to validate the material parameters used for modelling. An evaluation of the creep rates after the NORTON's law (e.g. Hunsche and Schulze 1994)

$$\dot{\varepsilon}_{Krs} = K \cdot (\sigma_1 - \sigma_3)^n \quad (1)$$

gives the relatively low stress exponent n = 2.55. This implies that besides dislocation glide/creep in the halite crystals further mechanisms contribute to the overall deformations. Presumptively, solution-precipitation creep or "pressure solution" (e.g. Spiers & Carter 1998, Bechthold et al 2004) plays an important role as a quasi-viscose part.

A comparison of the creep parameters of the investigated salt bricks with the creep law BGR-a and creep parameters of Staßfurt rock salt from Sondershausen (Anhydrite region) shows clearly the faster creep of crushed rock salt in the range of small $\sigma_{diff} < 15$ MPa than the reference curves (Figure 3).

3.2 *Long term creep tests on wet and dry samples*

For a better understanding of the humidity effects on the long-term properties hydrostatic compaction tests (three wet and two dry) with an overall duration of at least more than one year were performed in the creep rigs at $\sigma_{hyd} = 3$, 10 and 20 MPa respectively. In addition, in the dry experiments the temperature was varied to estimate the activation energy.

Table 2. Sample parameters of the long term compaction experiments.

No.	σ_{hyd} (MPa)	ρ (g/cm^3)	w (wt.-%)	ε_1 (%)	ε_V (%)	$\varnothing_E$ (%)
208/36	3	1.992	0.42	3.10	6.32	2.18
208/38	10	1.975	0.65	3.44	6.77	2.08
208/39	20	1.973	0.46	3.33	7.91	1.12
208/40	10	1.974	0.07	0.43	0.98	8.25
208/37	20	1.975	0.06	1.26	3.09	6.24

Abbreviations: ρ = density; w = water content; $\varnothing_E$ = final porosity.

Because information on the volumetric strain is unreliable in granular salt precise shape measurements of the samples (once during and after the test) regarding sample length, diameter and volume were made which facilitate an estimate of the volumetric strain only based on the continuous measurement of ε_1. The sample parameters and experimental conditions are summarized in Table 2. The time dependent compaction behavior compared to the respective sample porosities is shown in Figure 5.

Comparing the various curves it can be clearly seen that besides the loading conditions the water content is obviously the key factor for the compaction behavior. But the efficiency of the compaction process changes with progressive compaction.

Referring to the non-moisturized samples (i.e. "dry"), it is documented by the test results that they do not reach a significant compaction (e.g. in the order of several %) within the whole test period. An

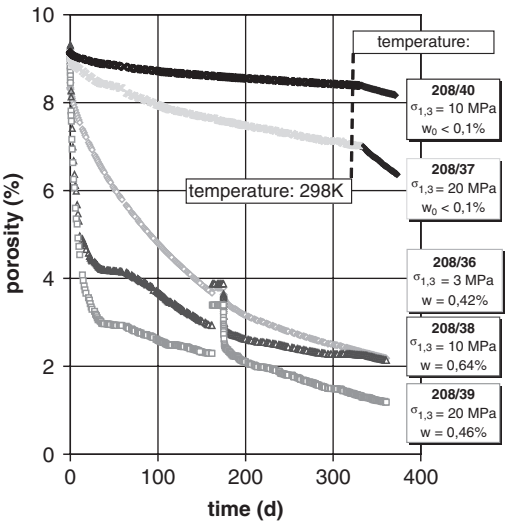

Figure 5. Results of hydrostatic compaction creep tests on cylindrical samples of pre-compacted salt brick material. Note effect of added water content (w). After 162 days the experiments were interrupted and the wet samples were built out to evaluate the shape parameters for the calibration of the volumetric strain approximation (as described before).

approximation of the time dependent compaction curves via a power function leads to an estimate of the necessary time for reaching significant compaction. In the non-moistened samples the necessary time for reaching a reference state of approx. 6% porosity would be around 8–9 years (for 20 MPa) and around 180 years (for 10 MPa) respectively. In contrast, the necessary time periods in moistened salt brick samples are only 9 days at $\sigma_{hyd} = 20$ MPa, 14 days at $\sigma_{hyd} = 10$ MPa, and around 90 days at $\sigma_{hyd} = 3$ MPa, respectively, indicating very rapid porosity reduction also at low stress conditions.

With progressive compaction, in both wet samples deformed at $\sigma_{hyd} = 10$ MPa resp. 20 MPa, the initial compaction proceeds very fast until after around 50 days a saturation state at a remaining porosity level of $Ø \leq 4\%$ is reached. Then the compaction is progressively impeded. In contrast, the time dependence of the sample 208/36 ($\sigma_{hyd} = 3$ MPa) is characterized by transient behavior over about 200 days until the final phase of nearly stationary deformation is achieved corresponding to those at higher stresses.

Additionally in the dry experiments the temperature were varied (from 25°C to 55°C) which allows an estimate of the activation energy which was found to be in the order of Q = 39 kJ/mol (0.4 eV) Such value is typical for material transport in rock salt by diffusion (e.g. Hunsche & Schulze 1990).

Table 3. Experimental conditions for strength tests with stepwise permeability measurements.

Specimen No.	σ_3 (MPa)	ε_{max} (%)	$\varepsilon_{Vol(end)}$ (%)
26	2	22.88	+1.67
25	5	29.98	−6.68
28	10	39.91	−8.37
28*)	3 (=$\sigma_{3\text{-eff}}$)	41.64	−7.60
27	0.33·σ_1	4.00	−2.58

*) Deformation during continuous application of a gas pressure $p_p = 7$ MPa resulting in the onset of dilatancy.

3.3 *Permeability tests on dry samples*

In addition to the overall compaction behavior knowledge about changes of transport properties in highly compacted granular salt undergoing deformation is of utmost importance regarding their sealing efficiency. In supplement of the strength tests (see chapter 3.1) three triaxial deformation tests at 2, 5 and 10 MPa confining pressure with stepwise permeability measurements were performed. Specific sample parameters are summarized in Table 3.

The general deformation characteristics in these tests correspond to the behavior observed in the standard tests. Whereas in the low confining pressure experiment (sample 26, $\sigma_3 = 2$ MPa) a minimum in the volumetric strain occurs (at $\varepsilon_1 = 2.4\%$ with $\varepsilon_V = -0.6\%$, $\sigma_{diff} = 34$ MPa), followed by subsequent dilatancy, in both other samples deformed at $\sigma_3 = 5$ resp. 10 MPa the overall deformation is associated with compaction down to 1–2% remaining porosity.

Remarkably, in the last step sample 28 was deformed during application of a gas pressure ($p_1 = 7$ MPa, $\sigma_3 = 10$ MPa). The pore pressure effect lowered the horizontal stress to $\sigma_{3;eff} \approx 3$ MPa and resulted in a rapid change of deformation style from compaction to dilatancy associated with a volume increase of around 0.8% (Table 3). In addition, after the experiment the sample displays clear indication of the development of shear failure resulting in two distinct fracture sets, which emphasizes the importance of the effective stress concept in porous granular salt.

During the constant rate deformations test the experiments were interrupted (in steps of two to three percent axial deformation) and the stationary gas-permeability k was measured with N_2 at each deformation step (including the initial value $\varepsilon_1 = 0\%$). In summary, nearly 40 measurements were recorded. The respective porosity Ø values were determined on the basis of the initial porosity, as estimated from the sample density and the volumetric strain. The results of the various tests are depicted in Figure 6 as a double logarithmic diagram of k vs. Ø.

Although the data show some scattering, the general permeability-porosity dependency obtained

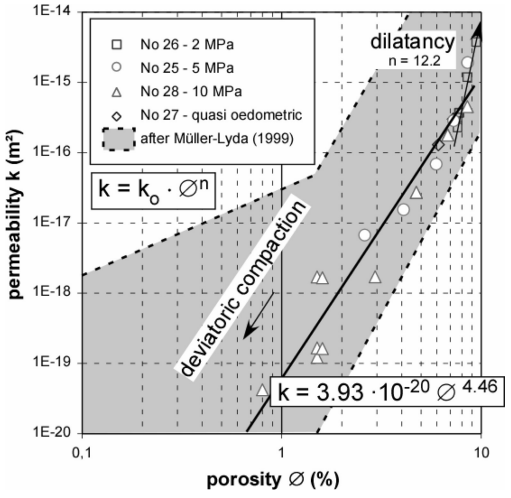

Figure 6. Porosity-permeability data for dry salt brick material deformed in compression under triaxial loading conditions at room temperature. In addition, the ranges of the datasets of Müller-Lyda (1999) are schematically indicated.

during the deviatoric compaction corresponds to former results and falls into the variation field, reported by Müller-Lyda (1999). In detail, two opposite trends for the porosity/permeability relationship can be distinguished. Whereas in the low pressure range ($\sigma_3 = 2$ MPa) where dilatant deformation proceeds a steep increase of both, permeability and porosity occurs (n = 12.2), the opposite trend is observed at higher pressures ($\sigma_3 \geq 5$ MPa) but with smaller slope. Using a simple power-law ($k = k_0 \cdot \varnothing^n$) relation the compaction behavior can be expressed with:

$$k = 5.7 \cdot 10^{-20} \cdot \varnothing^{4.31} \quad (2)$$

The observed exponent n for compaction agrees very well with the mean value of 4.5 obtained by Müller-Lyda (1999). However, the last author mentioned that in wet granular salt n is significantly higher (up to 5.5) but that generally at porosities lower than ~0.5% and in a permeability range of around 10^{-20} m^2 n becomes significantly smaller than 4.

3.4 *Capillary threshold effects in a wet sample*

If water is present at the grain boundaries and gas will penetrate into the rock matrix of the salt bricks two-phase flow will occur which is associated with capillary effects. Fluid transport is then controlled by

- the interfacial tension of the fluids involved,
- the wettability of the solid surface (wetting angle) with respect to the fluids, and
- the structure of the pore system.

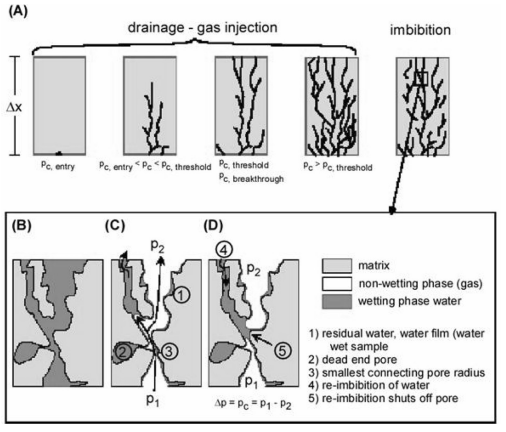

Figure 7. Two phase flow in porous media. (a) Stages of capillary gas breakthrough (drainage) and re-imbibition process in fine-grained rocks (schematic); (b) initially water-saturated sample; (c) gas breakthrough, (d) re-imbibition (modified after Hildenbrand 2003).

According to the Washburn equation (Washburn 1921) intrusion of a non-wetting fluid into a cylindrical capillary of radius r only occurs if the capillary pressure p_c (i.e. the pressure difference between the two immiscible fluids with p_1 and p_2) within a pore is exceeded:

$$p_c = p_2 - p_1 = -\frac{2 \cdot \gamma \cdot \cos\theta}{r} \quad (3)$$

Here γ is the interfacial tension (N/m), and θ the wetting angle (degrees) and r is the radius (m) of the ideal cylindrical pores.

As schematically depicted in Figure 7 the capillary sealing efficiency of a porous medium with a heterogeneous pore system (i.e. a given pore-size distribution) is characterised by the "break through" or "threshold pressure" (p_T). This term refers to the excess pressure in the non-wetting phase at which the wetting phase is displaced to an extent that the percolation threshold is exceeded and continuous flowpaths of non-wetting phase develop across the pore system. These flowpaths will comprise the largest interconnected pores, which offer the least resistance to capillary displacement. At this stage the flow of the non-wetting phase will be focused and restricted to a small portion of the interconnected pore system. If the excess pressure increases further, additional fluid flow pathways will develop across the porous medium, thus increasing the effective permeability to the non-wetting phase and the non-wetting phase saturation.

The coupled transport and mechanical properties of highly compacted and moistened granular salt were investigated in a multi-stage deformation experiment, similar to those described before, but using a wet salt

brick sample (no. 208/41). Its internal humidity content was estimated to be in the order of 1.3 wt.-% corresponding to the other data, resulting in a partially or, referring to the accessible pore space, nearly saturated pore space.

The gas-injection experiment consists of several stages of hydrostatic compaction and controlled axial deformation, respectively, which here can not described in detail. Threshold pressure was determined in relaxation phases ($\varepsilon_1 = \text{const.}$) directly by incrementally increasing the pressure of gas in contact with the end of a fully saturated core sample and observing the pressure at which gas first penetrates through the core (the minimum resolution of the used flow meter is 0.2 ml/min) (Figure 8). This approach gives the pressure required for the incipient development of interconnected gas flow paths through the pore network. After reaching a stable gas flow through the sample the gas permeability is measured as reference for the later comparisons (here described as intrinsic permeability). Because after this step the sample is further compacted resulting in a porosity decrease the effects of partial water loss during the gas injection test can be neglected.

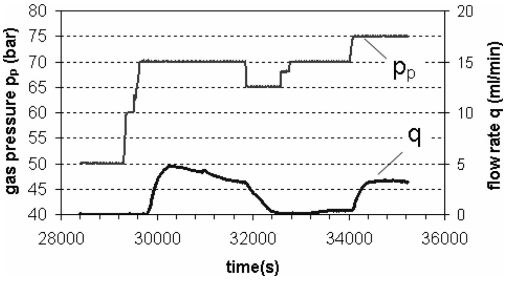

Figure 8. Examples for the determination of the capillary gas threshold pressure. Stepwise increase of the injection pressure with concomitant gas flow measurements ($\varepsilon_1 = 11.3\%$, $\varepsilon_{vol} = 5.5\%$). Note, that the steep increase of gas flow occurs in the gas injection pressure step to 70 bar (1. cycle) resp. shifted to 75 bar in the 2. cycle indicating time-dependent compaction.

The results from at least 9 gas injection tests on the salt brick sample 208/41 undergoing deformation are shown in Figure 9 in relation to literature results from different lithologies, i.e. sedimentary rocks.

As concluded by various authors (e.g. Marshal et al. 2005) a clear trend between threshold pressure and so-called intrinsic permeability is seen for the different lithologies, but the spread of the data is enormous. For comparison, we indicated the ranges of threshold pressure correlated with permeability for various lithological salt portions as estimated by Davies (1990). It has to be mentioned that these estimates are only based on the overall relationship for sedimentary rocks and

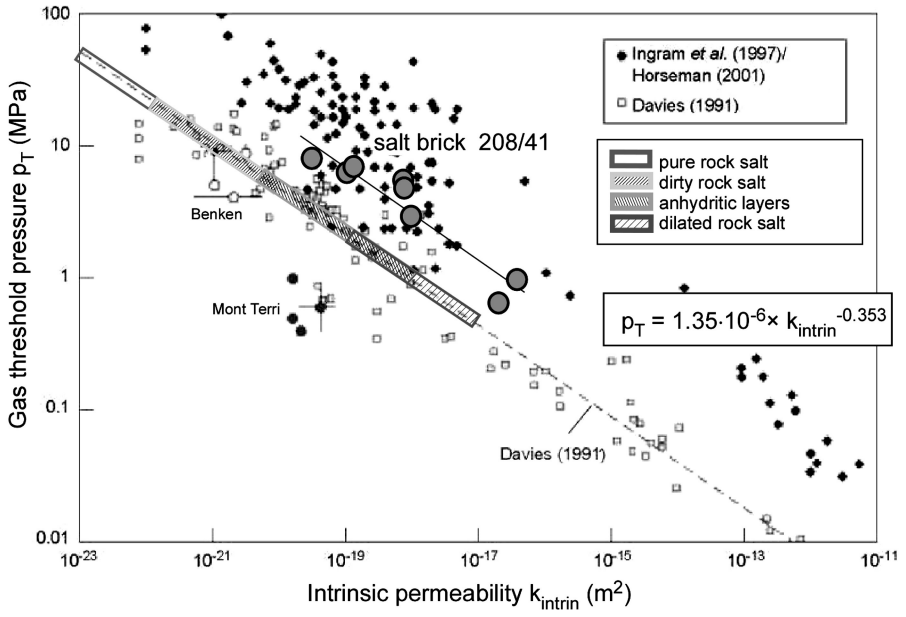

Figure 9. Relationship between gas threshold pressure and intrinsic permeability for various low permeability rock formations (claystones, shales, sandstone) (modified after Marshal et al., 2005 – for the various references see the later authors). In addition, the ranges of threshold pressure correlated with permeability for various lithological salt portions are indicated (as estimated by Davies 1990). The results obtained here are shown by big black-rendered grey circles.

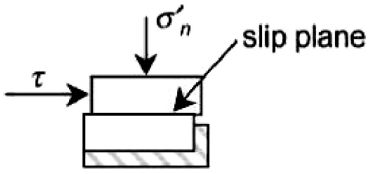

Figure 10. Loading geometry in direct shear test.

the known permeability ranges of various salt types resp. salt with different disturbance state.

In a first approximation, the relationship between permeability (k_{intrin}) and gas threshold pressure (p_T) for the moistened salt brick corresponds in a double-logarithmic diagram to a linear trend which is slightly higher than the prognosis postulated by Davies (1991) as presented in Figure 8:

$$p_T = 1.35 \cdot 10^{-6} \cdot k_{intrin}^{-0.35} \quad (4)$$

Because our experiments are short term tests, the test duration during the various injection tests may not be sufficient to detect the gas-breakthrough already in the investigated time interval which would result in an overestimation. However, taking this in mind our results representing synthetic and highly compacted granular salt correspond reasonably well to the published data.

3.5 *Shear-tests between dry or wet salt-brick surfaces*

For a performance assessment of the long-term sealing or buffer system build up by salt bricks under investigation it is also necessary to determine the contact properties between these bricks and between the bricks and host rock, i.e. rock salt. Such discontinuities can act as mechanical weakness zone or preferred pathways. For the mechanical behavior of interfaces the relevant variables are stress traction vector with one normal component (σ_n) and one tangential in a simple 2-dimensional stress field, i.e. τ (or two tangential in 3D), and the conjugate "strain" variables are the corresponding relative displacements, as shown schematically in Figure 10.

However, such stress conditions can be only realized in direct shear tests, which are therefore of urgent need to reproduce slip between various materials. For realization of required shear tests a modern MTS-shear test system is available at the IfG (Figure 1). It is a high-response servo-hydraulic system with digital control technology, strain measurement equipment mounted onto the specimen and programmable control modes, enabling new types of test procedures to be performed.

To investigate the shear strength between the various contacts, halved salt bricks were stacked one on the top of the other and covered with a plastic foil to protect them against dissolution by the wet concrete that fixes the samples in the shear boxes. So, the contact planes between the two bricks are exactly perpendicular to the shear direction in the centre of the shear box. Samples for the second test row were similarly prepared. Instead of two salt bricks (or salt brick halves) a salt brick was arranged on a rough contact plane of a host rock block (i.e. medium-grained rock salt).

On both contact types two series of multiple-step shear tests were performed aiming on the properties of the dry and wet interfaces:

(1) *Properties of dry interfaces:* Determination of shear strength with a multiple-step shear test by cyclical shearing of one sample half (forward/backward) with several normal stresses ($\sigma_n = 0.5$, 1, 2, 4, and 6 MPa).
(2) *Effect of wetting:* Realization of shear tests between samples with moistened surfaces at various loading times and normal stresses. – Investigation of efficiency of healing processes.

In appraisement of the various results presented in Figure 11 it is obvious that in each experiment the stress-depended strength of discontinuity plane can be described by the MOHR-COLOUMB criterion. As result the shear resistance at critical stress conditions (shear failure) is expressed by a linear dependency of cohesion (c) and angle of friction (φ):

$$\tau_f = c + \sigma_f \cdot \tan \varphi \quad (5)$$

The respective results are given in Table 4.

Most important, under the influence of normal stresses, but only in wet samples interfacial cohesion forces and/or other strengthening effects are activated depending on the loading time and the moisture content of the contact. In contrast, on dry surfaces only a small healing or strengthening effect is recognizable, whereby the magnitude depends on loading time.

4 SUMMARY AND CONCLUSIONS

Our investigations on artificial saltbricks cover a wide field of relevant rock-mechanical and hydraulical properties. Remarkably, the load bearing capacity and dilatancy behavior of the saltbricks ("dry" state) differ significantly from the behavior of the compact natural rock salt due to reachable larger deformations and relatively high load bearing capacities whereby local dilatancy is overlapped by the decrease of porosity during loading. Creep tests clearly show the faster creep of crushed salt in the range of small $\sigma_{diff} < 15$ MPa than natural rock salt.

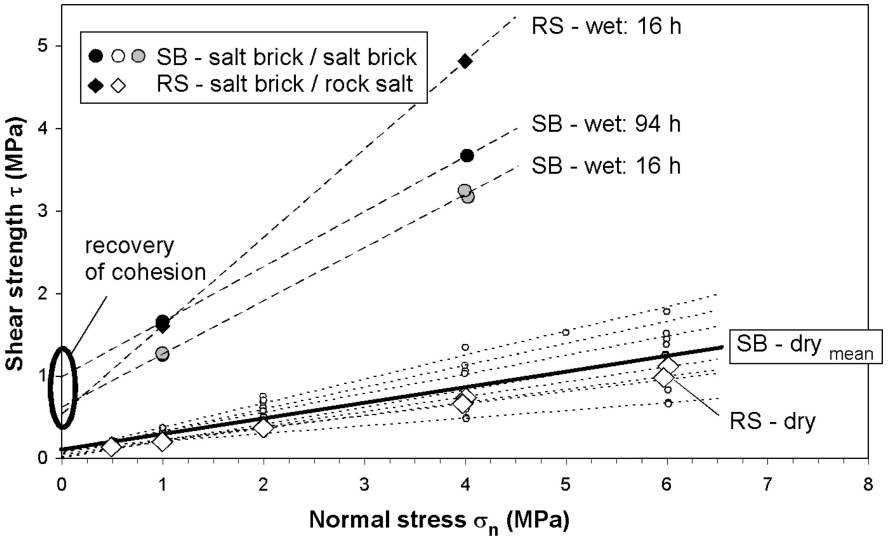

Figure 11. Shear strength characteristics of lab-dry and moistened brick-brick and brick-rock salt contacts. Healing effects are promoted by the presence of moisture and increase systematically with stationary ageing over 16, 70 and 94 hours at fixed normal stress (multiple step tests at constant normal stress).

Table 4. MOHR-COULOMB-parameters from shear tests for various interfaces.

Interface	humidity state	c (MPa)	φ (°)
Saltbrick/saltbrick*)	dry	0.08 ±0.04	11 ±4
Saltbrick/saltbrick**):		wet – 16 h	0.6333
Saltbrick/saltbrick**):		wet – 94 h	1.0034
Saltbrick/rock salt**):	dry	–	~10
Saltbrick/rock salt**):	wet – 16 h	0.54	47

*) Tested in multi-stage shear tests with cyclical shearing (mean value of 6 exp.); **)Single shear experiment at each σ_n-stage.

However, it is important to note that the strength of the salt bricks is drastically reduced when moisture is present. Hydrostatic compaction experiments clearly demonstrate that besides the loading conditions the water content is the key factor for the compaction processes. After one year only in the wet samples a final porosity in the order of 2% was reached. The efficiency of the compaction depends on the stress but in each case the compaction rates are decreasing when a saturation state at around 4% remaining porosity is passed.

During the stress induced compaction permeability decreases whereby the observed permeability-porosity relationship fits very well in the generally observed variation field for the compaction of granular salt. If water is present at the grain boundaries two-phase flow will occur associated with capillary effects. Threshold pressures determined for wet salt brick are slightly higher than the relationship estimated by Davies (1991), which may be due to the not sufficient test duration resulting in an overestimation of the threshold pressure. However taking the overall data scatter in the literature into account it can be argued that due to the difficulties of gas threshold measurements associated with lithological rock differences a unique relationship for describing capillary pressure effects seems not to be realistic.

Shear tests were performed to investigate contact properties between saltbrick surfaces and the rock salt. Whereas at dry conditions only some friction occurs, significant strengthening is observed when moisture is present because of activation of cohesion. This is in agreement with previous data reported for simulated faults in salt (Bos et al. 2000) and offers a direct proof of healing in salt rocks.

Summarizing our experimental results we can conclude that the principal challenges remaining in relation to the salt backfill materials are

(1) Understanding of physical processes which control the efficiency of granular salt compaction especially with respect to humidity effects.
(2) Development of generally agreed constitutive models for compaction in granular salt that can be reliably extrapolated to in-situ conditions.

ACKNOWLEDGEMENTS

The studies presented in this paper have been funded as part of the integrated project NF-PRO jointly by the

European Commission under the Euratom Research and Training Programme on Nuclear Energy within the Sixth Framework Programme (2002–2006), and the German Federal Ministry of Research and Education under contract 02 E 9904.

We thank the colleagues of WP 3.5 for fruitful cooperation. Especially, C.J. Spiers advices valuable hints. One anonymous reviewer gave constructive comments which helped to clarify some statements, especially referring to the gas breakthrough measurements.

REFERENCES

Bechthold, W., Rothfuchs, T, Poley, A., Ghoreychi, M., Heusermann, S., Gens, A. & Olivella, S. 1999. "Backfilling and Sealing of Underground Repositories for Radioactive Waste in Salt, (BAMBUS Project)", EUR 19124 EN, CEC.

Bechthold, W., Smailos, E., Heusermann, S., Bollingerfehr, W., Bazargan Sabet, B., Rothfuchs, T., Kamlot, P., Grupa, J. Olivella & Hansen, F.D. 2004. Backfilling and Sealing of Underground Repositories for Radioactive Waste in Salt (BAMBUS-II Project), EUR 20621 EN, CEC.

Blümel, M. 2000. Improved procedures for laboratory rock testing. Proc. ISRM Symposium EUROCK 2000, Aachen, 573–578.

Bos, B., Peach, C.J. & Spiers, C.J. 2000. Slip behavior of simulated, gouge-bearing faults under conditions favouring pressure solution, Journal of Geophysical Research 105, 16699–16717.

Davies, P.B. 1991. Evaluation of the role of threshold pressure in controlling flow of waste-generated gas into bedded salt at the Waste Isolation Pilot Plant (WIPP). Sandia Rep. SAND 90–3246.

Kazan, Y & Ghoreychi, M. 1996. Essais In situ CPPS – Etude Thermomécanique du Champ Proche d'un Puits de Stockage de Déchets Radioactifs dans le Sel, Rapport de la Commission Européenne EUR 16946 Fr, CEC.

Hildenbrand, A. 2003. Fluid Transport Process in Mudstones. PhD TH Aachen, ISBN: 3-86130-087-7.

Hunsche, U. & Schulze, O. 1994. Das Kriechverhalten von Steinsalz.- Kali und Steinsalz, 11 (8/9), 238–255.

Marschall, P., Horseman, S. & Gimmi, T. 2005. Characterisation of Gas Transport Properties of the Opalinus Clay, a Potential Host Rock Formation for Radioactive Waste Disposal. Oil & Gas Science and Technology – Rev. IFP, Vol. 60, No. 1, 121–139.

NEA-EC 2003. Engineered Barrier Systems and the Safety of Deep Geological Repositories, State-of-the-art Report, EUR 19964 EN. CEC.

Popp, T., Kern, H. & Schulze, O. 2001. The evolution of dilatancy and permeability in rock salt during hydrostatic compaction and triaxial deformation.- J. Geophys. Res. 106, No. B3, 4061–4078.

Spiers, C.J. & Carter, N.L. 1998. Microphysics of rocksalt flow in nature. In: M. Aubertin (Ed.), The Mechanical Behavior of Salt: Proceedings of the Fourth Conference. Trans. Tech. Publ. Series on Rock and Soil Mechanics, 22, 115–128.

Stockmann, N. (ed.) 1994. Dammbau im Salzgebirge, Abschlussbericht Projektphase II, Berichtszeitraum vom 01.07.1989–31.12.1992, GSF-Bericht 18/94.

Stormont, J.C. & Daemen, J.J.K. 1992. Laboratory study of gas permeability changes in rock salt during deformation, Int. J. Rock Mech. Min. Sci. Geomech. Abstr., 29, 325–342.

Washburn, E.W. 1921. Note on a method of determining the distribution of pore sizes in a porous material, Proceedings of the National Acadamy of Science, 115–116. Bulletin, 63, 723–760.

Part 5. THMC-processes in backfill materials – laboratory observations and modeling

Taylor & Francis
Taylor & Francis Group
http://taylorandfrancis.com

The Mechanical Behavior of Salt – Understanding of THMC Processes in Salt –
Wallner, Lux, Minkley & Hardy, Jr. (eds)
© 2007 Taylor & Francis Group, London, ISBN 978-0-415-44398-2

The mechanical behavior of building materials based on the hydration of evaporite minerals

Th. Leusmann & H.-J. Engelhardt
DBE Technology GmbH, Peine, Germany

ABSTRACT: In Germany, radioactive and many types of chemotoxic waste must be disposed in deep mines. Among others, a suitable host rock for the ultimate disposal of the hazardous waste is salt. With respect to safety analyses a contact of the building materials used for backfilling and sealing measures with solutions must be considered. However, many conventional materials deteriorate in the saline milieu and/or their long-term behavior is difficult to describe. Moreover, questions exist concerning the reaction of these materials with gases. For this reason, a new family of building materials was developed. All recipes have in common the mixing of Mg-bearing salts with salt solutions. They harden as a result of salt hydrate crystallisation. After an initial contraction during the liquid phase several systems show a considerable swelling. Measurements have been carried out to quantify the increase in volume (open system) and the resulting crystallisation pressures in closed vessels. A constitutive law describing Young's modulus and creeping in the early age of the material enables the calculation of crystallisation pressure from swelling strain. The parameters of the constitutive equation for creeping were fit to results of the laboratory experiments.

1 INTRODUCTION

Technical barriers are essential elements of multi-barrier closure concepts of repositories for radioactive and chemotoxic waste in deep geological formations. For the construction of barriers and for the backfilling of openings in salt deposits a new family of building materials was developed, comprising of salt mixtures, whose long-term behavior can be determined easily by geochemical calculations and natural analogue studies.

In order to demonstrate the integrity of technical barriers it is necessary in the course of safety analyses to carry out thermo-mechanical computations. For the realistic calculation of stress distribution and the proof of integrity so-called material models or constitutive laws are implemented in the numerical codes to provide a proper idealization of strength, Young's modulus, and heat evolution. The generation of hydration heat, as well as the evolution of uniaxial compressive strength, tensile strength, and Young's modulus can be described by constitutive laws used for concretes (Engelhardt et al. 2003, Polster et. al. 2006, Onken & Rostásy 1995, Gutsch 1999). For these material properties the new family of building materials show values comparable to natural rock salt, kieseritic hard salt or carnallitite.

In addition to thermal influences, shrinkage as a result of free water fixation in the crystal structure of the hardening products causes stresses in the constructions, whereas swelling may compensate tensile stresses due to thermal contraction. Consequently, a constitutive law was implemented in a specially developed one-dimensional numerical model considering the shrinkage and swelling behavior of the building materials. In analogy to shrinkage the swelling induced by hardening is here called autogenous swelling according to Grube (2003) and Lura et al. (2003) which is defined as the result of crystal growth enclosing voids into the microstructure of the salt mixtures.

The constitutive laws were developed for a reference recipe consisting of the raw materials kieserite ($MgSO_4 \cdot H_2O$) as binder component, halite (NaCl) as aggregate, small amounts of silica fume according to EN 13263, and a saturated NaCl-solution. Figure 1 shows a thin section of the reference recipe. The kieserite (ESTA kieserite "fine"), rock salt aggregate, and the silica fume are commercially available in large amounts. Finally the constitutive laws were implemented in the finite difference program FLAC to calculate the stress evolution of a permeation barrier and to proof its integrity during different states of construction.

2 EXPERIMENTAL PROCEDURES

Besides the investigation of rheological parameters of the fresh materials, comprehensive measurements

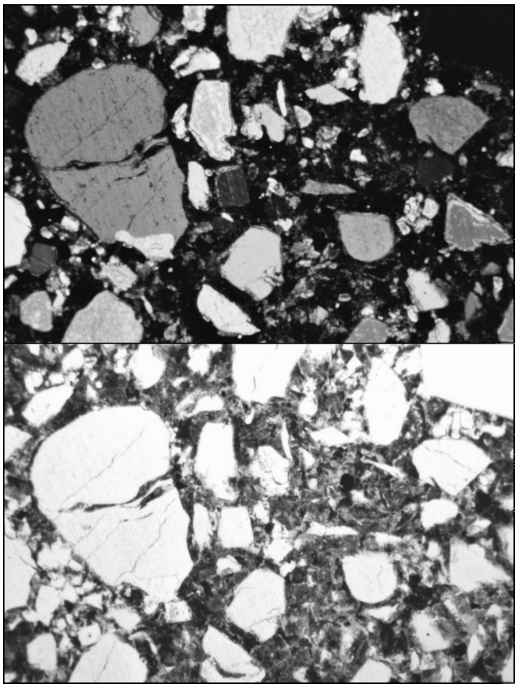

Figure 1. Transmitted light thin section photographs of the reference recipe after 56-d-storage at room temperature (above cross and below plane polarized light). According to chemical calculations the sample contain the major components hexahydrite ($MgSO_4 \cdot 6H_2O$, ~41 vol.-%), kieserite (~22 vol.-%), halite (~31 vol.-%), and silica fume (~6.0 vol.-%). In the cross polarized light kieserite (grain size <2 mm) shows different shades of grey and sometimes fissures. Halite is black (see upper right corner of the photographs). In the plane polarized light both minerals are white. Silica fume reduces the transparency of the fine grained matrix containing the reaction products.

were performed to describe the evolution of strength, Young's modulus, hydration heat, autogenous swelling and the crystallisation pressure in dependence of time and temperature.

The procedures were selected according to the state-of-the-art of concrete technology. Thus, the uniaxial compressive and tensile strength and the Young's Modulus in compressive mode were determined according to EN 12390-3 and DIN 1048-5. Measurements in an adiabatic calorimeter were carried out to quantify the hydration heat and the progress of the hydration. Below, the experimental procedures for the measurement of autogenous swelling and crystallisation pressure are described in detail.

All mixtures are homogenized in conventional laboratory concrete mixers. The raw materials were put into the batch mixer in the sequence, NaCl-solution, silica fume, aggregate, and finally kieserite. The mixtures were filled in special moulds to enable a volume expansion during the swelling measurements or stiff steel moulds for crystallisation pressure tests. All tested mixtures were slightly consolidated according to EN 12390-2 (DIN 1048-5) on a vibrating table or in the case of small samples on a sieving machine before the experiments were started to remove bigger air-bubbles. With an increasing air void content a decrease of crystallisation pressure can be expected.

2.1 *Autogenous swelling*

For the measurement of the shrinkage and/or swelling of cementicious materials many procedures are described in the literature (Alawieh 2006) as well as industrial standards (e.g. DIN 52450, EN 680, EN 12617-4, EN 1170-7, EN 445).

Many of the methods described in the literature cited above are used to measure the volume or length change due to variations or humidity or do not consider the material characteristics of the salt mixtures.

Thus, the autogenous swelling of the mixture was determined using three different methods described below.

A sensitive method indicating the shrinkage or swelling of building materials during the hardening process is to place plastic bottles containing an uptake tube into fresh test specimens. The bottles were filled with a non-evaporating solution (oil) ranging into the uptake tube with a defined diameter. Then, the volume variations were monitored at room temperature by simply observing the meniscus of the oil level in the capillary tube with time (Geiker 1983).

A simple method to quantify the increase of volume is to measure the edge length of test specimens before and after hardening of the building materials. The test specimens were produced in styrofoam moulds which allow an almost free expansion of the material. The moulds were weighed before and subsequent to the filling for the calculation of density variations. To avoid water uptake due to the hygroscopicity of the salts or a loss of pore water, which would affect the measurement results, thin plastic layers were attached at the walls of the moulds and the surfaces of the samples were covered with plastic sheets. Furthermore, the closed moulds were sealed with air-tight plastic foil. Figure 2 shows unfilled and filled cubic moulds each having a volume of approximately 3.4 l. To get an information on the temperature dependence of the swelling process, the filled moulds were stored in a climatic chamber at a temperature of 37°C. An important requirement for the applicability of this method is that the mixtures show an negligible amount of bleed solution.

To get a full history of the volume increase another method is needed. An alternative test is the measurement of swelling with a strain sensor. The strain sensor

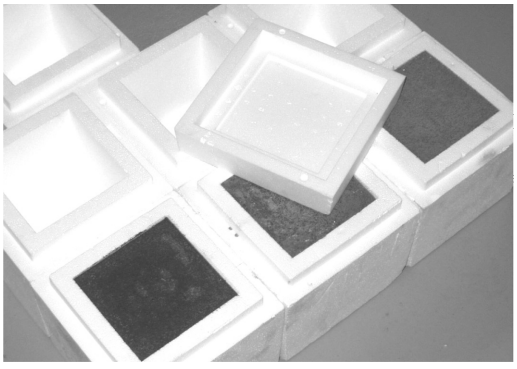

Figure 2. Preparation of cubic test specimens (edge length approx.15 cm) in styrofoam moulds used for volume increase measurements of the building materials.

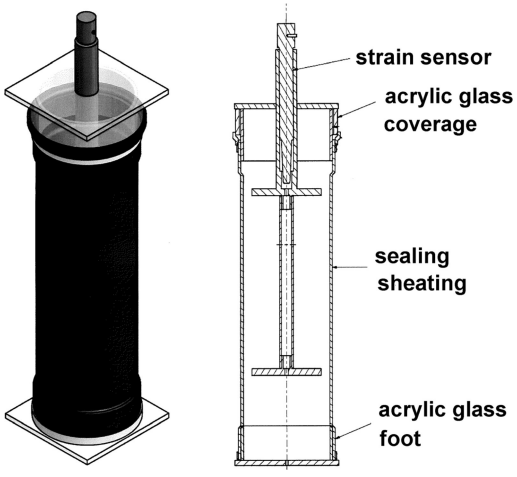

Figure 3. Setup for the determination of the autogenous swelling induced strain. On the left side an isometric view and a longitudinal cross section on the right side.

has a defined length of 100 mm. Figure 3 shows the experimental setup with a diameter of about 50 mm. The setup was placed in a water quench with a volume of about 300 litres for guaranteeing isothermal conditions during the measurement (20°C). A detailed description of the procedure is given by Leusmann (2005) and Krüger (2006).

2.2 *Crystallisation pressure*

In analogy to the measurement of the swelling process two methods were used for the determination of the crystallisation pressure. Both methods have in common that the suspension is filled in a thick-walled stainless steel cylinder. The most important differences are the positions of the pressure and temperature

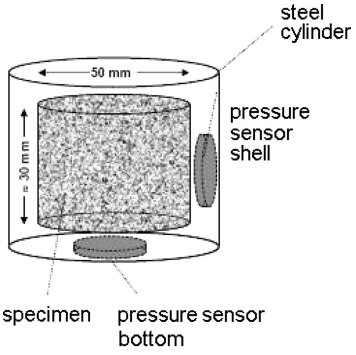

Figure 4. Experimental setup for crystallisation pressure measurements, according to GRS, Braunschweig (see GRS 2005).

sensors inside the cylinder, the technique of the pressure measurement, and the size of the sample.

Figure 4 shows the experimental setup of the GRS, Braunschweig which uses two pressure sensors at the shell and the bottom of the cylinder. In this case the samples volume is about 59 cm^3 and in comparison to the grain sizes of the mixtures the dimensions of the cell are relatively small, however, the requirements on the ratio of maximum grain size to the shortest dimension of the test specimen according to regulations of concrete technology are fulfilled. The suspensions were vibrated slightly on a laboratory sieving machine because the high energy of a vibrating table could lead to a loss of material.

The second test method developed by DBE TECHNOLOGY is based on fiber optic technique and records the pressure and temperature inside the specimen. The pressure cylinder has an inside diameter of 15 cm, a height of 30 cm, and a volume of approx. 5.3 l comparable to the size of cylindrical test specimens which are used for the determination of concrete strength, Young's modulus or Poisson's ratio, Figure 5 shows the cap of the cylinder containing the sensors and the valves needed for the venting prior to the start of the measurements. The suspension was covered with a thin layer of oil which flows through the vent valves when the steel cap is fixed on the cylinder.

In order to prevent the impact of thermal effects on the measurement results, both devices are stored prior to and during the measurement in climatic chambers.

3 EXPERIMENTAL RESULTS

To provide some information on the general properties of the developed material a few important parameters are given for the reference recipe with kieserite as binder component. The test specimen reached a compressive strength of 35.2 MPa, a tensile strength

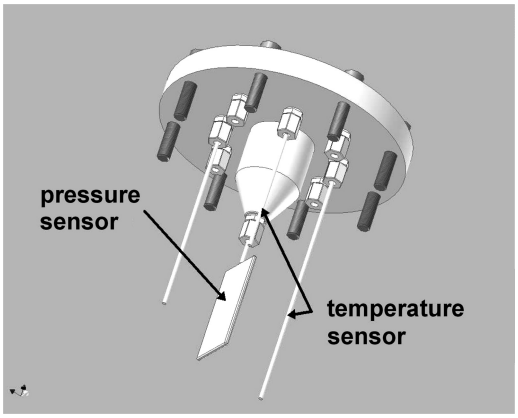

Figure 5. Steel cap of the measurement device developed by DBE TECHNOLOGY (diameter approx. 18 cm) containing the pressure sensor, the temperature sensors, and the valves for venting.

of 1.8 MPa and a Young's Modulus of 22,900 MPa as maximum values (see DBE TECHNOLOGY 2007).

The results for autogenous shrinkage and crystallisation pressure lead to constitutive laws describing the viscoelastic material behaviour of the salt mixtures in the early stage of hardening.

Subsequent to the end of the measurements the test specimens were inspected with regard to homogeneity and integrity as far as the experimental set-up allowed a non-destructive removal of the equipment. The specimens showed a homogeneous distribution of the grains and no cracks or fissures were observed.

3.1 *Results of swelling measurements*

The measurements of the specimens produced in the flexible styrofoam moulds yielded a volumetric increase of 1.0–1.5 vol-% after 28 days of hardening at a temperature of 37°C. The measurements corresponds to values of 1.1–2.1 vol-% calculated from the change in density determined according to DIN 1048-5.

The investigated recipe is characterized by a high fluidity enabling a transport through pipes over long distances. This fluidity bases on a low solid-solution ratio limiting the contacts between the suspended particles. During the hardening process the proportion of the solids increases due to the fixation of water of the pore solution in the crystal structure of magnesium sulphates and the crystallisation of halite. This process lead to a development of a crystal network containing the reaction products and the inert phases of the mixture. As long as the contacts between the solids are limited the volume should decrease because of the dominance of chemical shrinkage. Following this period crystal growth superimposes the chemical

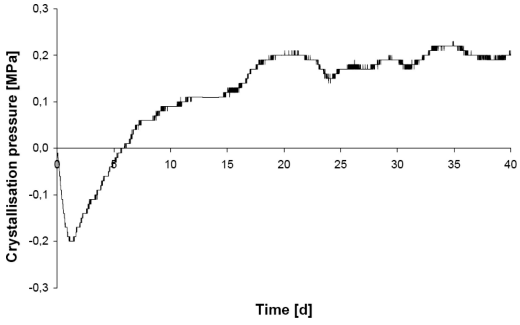

Figure 6. Crystallisation pressure detected at the boundary of a specimen (see GRS 2005).

influence and builds up a crystal network including voids which could lead to the autogenous swelling.

Supplementary performed measurements of pore size distribution by mercury intrusion according to DIN 66133 shows that the samples dried at 105 degrees Celsius are dominated of pores with a size of 1 to 70 μm. It is assumed that this dominance of macropores and mesopores are caused by the high content of coarse raw materials as well as the influence of swelling.

The observations made during the "plastic bottle tests" confirmed these theoretical considerations qualitatively. Furthermore, the records with the strain sensor delivering the full history of volume development also showed a short period of shrinking in the early phase of hardening.

In comparison to cement-based materials the tested salt mixture shows the opposite swelling progression. Cement based materials show a short phase of swelling before shrinking starts and the initial "sulphate expansion" is related to an oriented growth of ettringite. For the salt mixtures the opposite progression was detected. The test with a strain sensor delivered the full history of swelling. In the early phase of hardening a short period of shrinking was detected. After that the material started to swell and reached a strain of 3.3‰ after 21 days when the measurement was stopped.

3.2 *Results of crystallisation measurements*

Fundamentals of the development of pressure as a result of crystal growth are described by Winkler (1975) and Klöcker (1979). According to these information the pressure depends on the temperature, decreases with the molar volume of the mineral, and increases with the degree of oversaturation.

The measured history of crystallisation pressure at the boundary of a specimen is shown in Figure 6.

Similar to the progress of swelling strain the crystallisation pressure shows a short period of tensile and an ensuing period of compressive stress. After 20 d- hardening the increase of the pressure seems

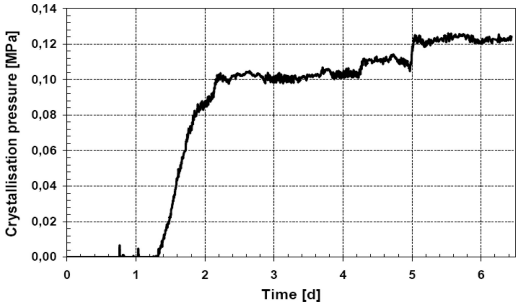

Figure 7. Crystallisation pressure detected inside the specimen with the measurement device shown in Figure 5 in relation to . The DBE TECHNOLOGY-device enables only the registration of values ≥0.0 MPa.

to stop at a value of 0.2 MPa. Although the material has reached a significant Young's modulus and the swelling strain continues to increase, the increase of pressure stops. A crystallisation pressure of 0.2 MPa is low considering the significant swelling strain.

Figure 7 shows the results of the measurement inside the specimen. The maximum pressure of 0.12 MPa reached after six days of hardening is also low. The pressure sensor inside the specimen was not able to detect tensile stress.

Figures 6 and 7 show that the crystallisation pressure has an uneven progress. Short relieves with following increases in pressure in the microstructure may be a reason for the unsteady development (see Renard et al. (2001), Schutjens & Spiers (1998)). The point in time the development of crystallisation pressure starts differs comparing Figure 6 from 7. The generation of crystallisation pressure detected by the DBE TECHNOLOGY device (Figure 7) starts earlier. A reason for this could be the better consolidation and/or the longer mixing period compared to the experiment carried out at the GRS. Four experiments were carried out on the reference material including kieserite as binder component. They all show maximum values of 0.12–0.20 MPa for crystallisation pressure.

4 MATERIAL MODEL FOR AUTOGENOUS SWELLING

A mathematical description for the relation of autogenous shrinkage, temperature and hardening is given by Gutsch (1999).

$$\varepsilon_{as}(t_e, t_{e1}, T(t)) = \varepsilon_{as0} \cdot \left[\frac{t_e - t_{e1}}{t_{as} + t_e - t_{e1}}\right]^{0.5} \quad (1)$$

ε_{as0} ultimate value of autogenous shrinkage
t_{as} time parameter
t_{e1} effective concrete age at the moment the swelling process starts

The constitutive law described by Equation 1 was developed to specify the behaviour of concrete and is transferable to swelling of magnesia binders (Krüger 2006). Equation 1 uses the effective concrete age t_e to include the dependence on temperature variation T(t).

$$t_e(T(t)) = \int_0^t e^{\frac{E_a}{R}\left[\frac{1}{293} - \frac{1}{273+T(t)}\right]} dt \quad (2)$$

T(t) material temperature [K]
R ideal or universal gas constant [8.31443 J/(mol·K)]
E_A Arrhenius activation energy [J/mol]

The activation energy depends above all on the mineralogy of the binder system and the chemical composition of the pore solution. It is determined by measurements of the adiabatic temperature rise and/or results to the development of strength or Young's modulus at different temperatures.

The exponential term of Equation 2 converts increments of curing time at the actual material temperature T to equivalent increments at the reference temperature of 293 K. Thus, the equivalent age can be defined as the age of the material cured at a constant temperature that yields the same relative strength evolution as under the actual temperature history. At a temperature of 293 K the setting time is identical to the equivalent age.

The effective concrete age can be eliminated by using Equation 3 which specifies the relationship between the degree of hydration α and the effective concrete age t_e. The degree of hydration is introduced as the ratio of the reacted binder constituents to the total amount of binder constituents, which can react, or because of the coupling of the reaction rate with heat production, as the ratio of the amount of heat generated by the hydration reactions to the total amount of heat production.

$$\alpha = e^{-\left[\ln\left(1+\frac{t_e}{t_1}\right)\right]^b} \quad (3)$$

The degree of hydration is the central parameter in the other constitutive laws describing the generation of hydration heat, as well as the evolution of uniaxial compressive strength, tensile strength, and Young's modulus. It ranges from the value 0.0 to 1.0, in contrast to the actual time and the equivalent age which can reach infinite values. The final value of 1.0 corresponds to a thermodynamic affinity of 0.0 showing that there is no driving force for chemical reactions. The abbreviations t_1 [h] and b [–] denote the so-called

Jonasson parameters of the model. For the reference recipe with kieserite the parameters were determined to $t_1 = 203$ h and $b = -0.215$.

Using Equation 3 in Equation 1 the swelling strain is also describable as a function of the degree of hydration α given by Equation 4.

$$\varepsilon_{as}(\alpha, \alpha_0) = \varepsilon_{as\infty} \cdot \left(\frac{e^{(-\ln \alpha)^{\frac{1}{b}}} - e^{(-\ln \alpha_0)^{\frac{1}{b}}}}{e^{(-\ln \alpha)^{\frac{1}{b}}} - e^{(-\ln \alpha_0)^{\frac{1}{b}}} + \frac{t_{as}}{t_1}} \right)^{0.5} \quad (4)$$

The minimum degree of hydration α_0 included in Equation 4 marks the moment of the hydration process since solid-state properties of the mixture become effective and strength as well as Young's modulus start to grow. In concrete technology it is often compared to the so-called final set time.

For the reference recipe a minimum degree of hydration α_0 of 0.29 was obtained, corresponding to an effective age t_e of 91 h.

5 CALCULATION OF CRYSTALLISATION PRESSURE FROM SWELLING STRAIN

According to physical analyses, the driving force of autogenous shrinkage of concrete is the change in the capillary pressure induced by self-desiccation in its cement matrix. Self-desiccation is caused by the balance between the absolute volume reduction (chemical shrinkage) and the building up of the capillary network.

For an estimation of the chemical shrinkage that would occur as a result of the chemical reaction of kieserite with the NaCl-solution chemical calculations were performed with the program EQ3/6. On the basis of the recipe, the amount of product minerals and consumed kieserite, as well as the densities of the components of the recipe it was possible to derive Equation 5 which describes the amount of chemical shrinkage (ε_{CS}) in relation to the temperature.

$$e_{CS} = 0.048\ [\text{vol-\%/°C}] \cdot T\ [\text{°C}] + 2.18\ [\text{vol-\%}] \quad (5)$$

Equation 5 results in a value of 3.86 vol-% at a tem-perature of 35°C. Owing to the coupling of the chemical reaction with heat generation and the degree of hydration it is possible to deduce Equation 6 which is valid for a temperature of 35°C and results in a value of approx. 1.12 vol.-% at the minimum degree of hydration.

$$\varepsilon_{CS}(\alpha) = \alpha \cdot 3.86\ [\text{vol.-\%}] \quad (6)$$

The amount of shrinkage shall rise with the proportion of salt solution as the recipe contains an excess of kieserite and shall decrease with the content of inert components. The internally appearing chemical shrinkage represents the upper limit for the external measurable autogenous shrinkage.

The relative humidity inside the pores of the mixtures can be estimated on the basis of the calculated water activity. It decreases during the hardening from about 0.76 (NaCl-solution) to approx. 0.63 (NaCl-$MgSO_4$-solution) at the end of the reaction. These values corresponds to a relative humidity of 76% and 63%, respectively.

The material model describing the viscoelastic behaviour of concrete (Gutsch 1999) in combination with the constitutive law describing the propagation of Young's modulus enables the calculation of crystallisation pressure from swelling strain. The mentioned creep function (Equation 7) used in Hooke's Law allows the calculation of strain increments from stress increments and vice versa using the method of finite differences.

$$\varphi(t_{e,cr}(T(t)), t_{e,cr1}(T(t), \alpha_1) = \frac{\varepsilon_c(t, t_1, \alpha_1, T(t, t_1))}{\varepsilon_{el}(t_1)} = P_{1c}(\alpha_1) \cdot \left[\frac{t_{e,cr} - t_{e,cr1}}{t_c} \right]^{P_{2c}(\alpha_1)} \quad (7)$$

Equation 7 describes the proportion between viscous ε_c and elastic strain ε_{el}. The dependence of viscous strain from temperature is considered by using an effective creep age $t_{e,cr}$ which is calculated from the temperature history T(t) using Equation 2. The dependence from hardening is taken into account by using creep parameters p_{1c}, p_{2c} addicted to the degree of hydration α.

Figure 8 shows the calculated crystallisation pressure from swelling strain using Equation 4 and 7 in Hooke's Law. The crystallisation pressure is calculated in an one-dimensional numerical model under a rigid restraint.

The calculated pressure reaches values unequal to zero when a minimum degree of hydration α_0 is

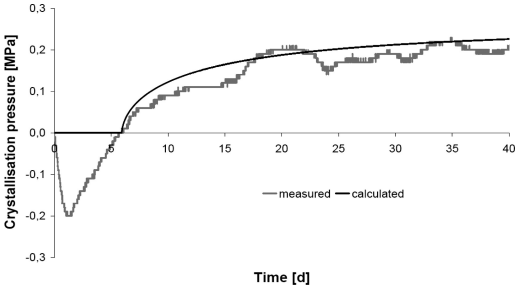

Figure 8. Measured and calculated evolution of crystallisation pressure during the first 40 days of the hardening process at a temperature of 37°C (see Figure 6).

reached. Before this limit is reached a calculation of swelling strain and crystallisation pressure leads to invalid values. The value for the minimum degree of hydration α_0 of 0.29 was taken over from the other constitutive law. The parameter fitting leads to an ultimate swelling value $\varepsilon_{as,\infty}$ of 6.0‰ (see Equation 4).

6 SUMMARY

High swelling deformations of hydrating evaporite minerals should cause a high degree of restraint. Measurements of the crystallisation pressure disprove this statement. The relaxation of the tested material lowers the further increase of crystallisation pressure. Compared to other loadings acting on an underground barrier the crystallisation pressure detected at the reference recipe is very small. Therefore the positive effect of prestressing the surrounding rock should be neglected. The use of the reference recipe as building material would merely lead to a better connection between the constructional element an the surrounding rock.

A parameter fitting to a single measurement of swelling strain and a single measurement of crystallisation pressure shows that the connection between those is describable by the viscoelastic material model given by the so-called creep function and a constitutive law for autogenous shrinkage. The parameters of the viscoelastic model were fitted to the experimental results and a calculation of crystallisation pressure from swelling strain in a simple one dimensional model shows a good correlation between calculated results and the results for the chosen measurements.

Whether this connection between crystallisation pressure and swelling strain is valid in general has to be verified by additional measurements.

ACKNOWLEDGEMENTS

The authors thank the Federal Ministry for Education and Research for financing the research project (AISKRISTALL) and the GRS Braunschweig for the execution of the crystallisation pressure measurements and their cooperation within the project. Finally, we thank Dr. habil. H.-J. Herbert of the GRS Braunschweig and Dr. O. Schulze of the Federal Institute for Geosciences and Natural Resources (BGR) for the helpful remarks on this article.

REFERENCES

Alawieh, H. (2006) Zur experimentellen Bestimmung der Schwindverformungen von Zementstein. Thesis Ruhr-Universität Bochum.

DBE TECHNOLOGY (2007) Abdichtung von Wegsamkeiten in Salzformationen mit kristallisierenden Evaporitmineralen (AISKRISTALL). Final Report, PTKA-WTE, Förderkennzeichen 02S8112.

DIN 1048-5 (1991) Testing concrete; testing of hardened concrete (specimens prepared in mould).

DIN 52450 (1985) Testing of inorganic non-metallic building materials; determination of shrinkage and expansion on small specimens.

DIN 66133 (1993) Determination of pore volume distribution and specific surface area of solids by mercury intrusion.

EN 1170-7 (1997) Precast concrete products – Test method for glass-fibre reinforced cement – Part 7: Measurement of extremes of dimensional variations due to moisture content.

EN 12390-2 (2000) Testing hardened concrete – Part 2: Making and curing specimens for strength tests.

EN 12390-3 (2001) Testing hardened concrete – Part 3: Compressive strength of test specimens.

EN 12617-4 (2002) Products and systems for the protection and repair of concrete structures – Test methods – Part 4: Determination of shrinkage and expansion.

EN 13263 (2005) Silica fume for concrete – Part 1: Definitions, requirements and conformity criteria.

EN 445 (1996) Grout for prestressing tendons – Test methods.

EN 680 (2005) Determination of the drying shrinkage of autoclaved aerated concrete.

Engelhardt, H.-J., Kreienmeyer, M., Lerch, C., Müller-Hoeppe, N., Köster, R., Eilers, G. & Preuss, J. (2003) A Constitutive Law of Salt Concrete Used for Closure of a LILW-Repository. Proc. ICEM03, 9th Int. Conf. on Radioactive Waste Management and Environmental Remediation, Oxford (England), ICEM03-4570.

Geiker, M. (1983) Studies of Portland Cement Hydration: Measurements of Chemical Shrinkage and a Systematic Evaluation of Hydration Curves by Means of the Dispersion Model. Ph. D. Thesis, Technical University of Denmark, Lyngby, Denmark.

GRS (2005) Abdichtung von Wegsamkeiten in Salzformationen mit kristallisierenden Evaporitmineralen (AISKRISTALL) GRS-Untersuchungen „Geochemische und geotechnische Arbeiten zur Auswahl und Charakterisierung von geeigneten Salzmischungen“ Final Report, Förderkennzeichen 02S8112.

Grube, H. (2003) Betontechnologie. Die Schwindverformungen des Betons, Definition der Schwindarten, Ursachen, Größe der Verformungen und baupraktische Bedeutung. Beton, 12/2003: 598–603.

Gutsch, A.-W. (1999) Stoffeigenschaften jungen Betons – Versuche und Modelle, DAfStb. Heft 495; Berlin.

Klöcker, H.S. (1979) Hydratationskinetik und Kristallisationsdruck im System $CaSO_4$-H_2O. Diss., TH Aachen, Fak. Bergbau- u. Hüttenwesen.

Krüger, S. (2006) Makroskopisches Modell für autogenes Quellen und Schwinden. Diplomarbeit, iBMB, TU Braunschweig.

Leusmann, Th. (2005) Temperaturuntersuchung an erhärtendem Zementstein. Seminarvortrag, iBMB, TU Braunschweig.

Lura, P., Jensen, O.M. & van Breugel, K. (2003) Autogenous shrinkage in high-performance cement paste: Evaluation of basic mechanisms. Cem. Concr. Res., 33: 223–232.

Onken, P. & Rostásy, F.S. (1995) Wirksame Betonzugfestigkeit bei früh einsetzendem Temperaturzwang. Deutscher Ausschuss für Stahlbeton (DAfStb), Heft 449.

Polster, M., Engelhardt, H.-J. & Heydorn, M. (2006) Entwicklung eines Materialmodells für Magnesiabinder. Proc. Ibausil, 16th Int. Conf. of Building Materials, Vol. 1, Bauhaus-Universität Weimar: S0925–S0932.

Renard, F., Dysthe, D.K., Feder, J., Bjørlykke, K., Jamtveit, B. (2001) Enhanced pressure solution creep rates induced by clay particles: experimental evidence from salt aggregate. Geophysical Research Letters, 28: 1295–1298.

Schutjens, P.M.T. & Spiers, C.J. (1998) Intergranular pressure solution in NaCl: grain-to-grain contact experiments under optical microscope. Oil & Gas Technology, 54: 729–750.

Tazawa, Ei-Ichi (1999) Autogenous Shrinkage of Concrete. Proc. Int. Workshop on Autogenous Shrinkage of Concrete (AUTOSHRINK '98), Hiroshima, Japan, June 1998, deriving from work carried out by a technical committee of the Japan Concrete Institute (JCI).

Winkler, E.M. (1975) Stone – Properties, durability in man's environment. Springer-Verlag, New York.

Zhutovsky, S. (2003) Modeling of autogenous shrinkage. In: A. Bentur (ed.), Early Age Cracking in Cementitious Systems. Report RILEM Technical Committee 181-EAS, RILEM Publications SARL, p. 169–178.

The Mechanical Behavior of Salt – Understanding of THMC Processes in Salt –
Wallner, Lux, Minkley & Hardy, Jr. (eds)
© 2007 Taylor & Francis Group, London, ISBN 978-0-415-44398-2

Self sealing backfill (SVV) – A salt based material for constructing seals in salt mines

H.-J. Herbert
GRS – Gesellschaft für Anlagen- und Reaktorsicherheit mbH, Braunschweig, Germany

ABSTRACT: A self-sealing salt backfill (SVV) based on anhydrous magnesium sulphate has been developed. Fine grained dry initial material (SVV) can be emplaced pneumatically. Artificial flooding of the pore space with brine initiates a reaction that leads to the formation of a brine tight seal. The reaction consumes the brine completely and forms an impermeable plug with a new mineralogy and greater volume of solids. The initial high porosity is reduced to 2–5 vol.-% of isolated pores. Mineralogical assemblages obtained in the experiments and measured by X-ray diffraction agree well with results of geochemical modelling with EQ3/6. The geochemical modelling allows the quantification of the short- and long-term volume changes in the system and demonstrates that in the long run stable mineral assemblages will be obtained. The volume increase leads to a considerable crystallization pressure. The porosity/permeability relationship resembles that of highly compacted crushed rock salt backfill. The mechanical properties are comparable with the values of undisturbed rock salt. These results indicate that SVV is a self-sealing long-term stable and to wide extend predictable predictable material.

1 INTRODUCTION

Different backfilling and sealing concepts for radioactive and hazardous chemical waste repositories in salt formations have been developed or are under discussion in Germany. The host rock – salt – is the main barrier against radionuclide release and the release of toxic components into the biosphere. Engineered barrier systems (EBS) are required to ensure repository stabilization and sealing against brine intrusion.

The German concepts for radioactive waste disposal in salt formations consider crushed salt as the main backfill and EBS material. This material can stabilize open voids. However, the initial porosity of about 50 vol.-% represents no barrier against intruding brines. Therefore the search was extended towards other salt materials that can meet both requirements, mechanical stabilization and low permeabilities. GRS started in 2000 the development of such a salt based sealing material. It was called SVV, in German "Selbstverheilender Versatz". SVV is a self-sealing salt backfill based on anhydrous magnesium sulphate.

2 REQUISITE PROPERTIES FOR A SEAL

Ideal properties of a sealing material for EBS barriers in salt formations are:

- Stable mineralogical composition in chemical equilibrium with the host rock,
- low permeability, $<10^{-18}$ m^2, of the system seal/EDZ (Excavation Damaged Zone),
- geomechanical properties similar to those of the host rock,
- simple and technically feasible construction procedures.

3 GENERAL SVV PROPERTIES

The general properties of SVV will be described only briefly in this paper as they have been discussed extensively in several previous publications (Sander & Herbert 2000, Sander & Herbert 2002, Herbert & Kull 2004 and Herbert et al. 2006)

The backfill consists mainly of fine grained anhydrous $MgSO_4$ with a grain density of 2.63 g/cm^3. Other salt minerals such as halite and sylvite may be added in varying proportions according to the desired hydraulic and geochemical parameters. The dry material can be emplaced pneumatically and reaches a bulk density between 1.35 and 1.40 g/cm^3. The initial high pore volume of about 50 vol.-% can be filled with brine. The artificial flooding of the pore space with brine triggers a fast exothermic reaction, which leads to the formation of new hydrated salt minerals. Free water in the brine is consumed, the brine becomes oversaturated, and additional minerals are precipitated. At the end of the reaction, after 20–50 days, all free water in the brine is consumed, the pores are filled with solid material

and an almost dry and brine tight seal has been formed. The original large pore space of 50 vol.-% is reduced to 2–5 vol.-%. The remaining pores are isolated, and the corresponding permeability is low, between 10^{-18} and 10^{-20} m^2.

The mineral assemblage of the new seal has a higher volume than the combined volume of the initial material and brine. The volume increase due to the SVV/brine reaction leads to a considerable crystallization pressure, between a few bars up to 100 bars. The crystallization pressure depends on several factors (see below) and can be adapted to a certain extend the requirements.

The water uptake capacity of the anhydrous $MgSO_4$is higher than the water content of the brine in the original pore space. Thus, at the end of the reaction and the total consumption of free water in the brine the anhydrous magnesium sulphate is not completely consumed. The remaining unreacted $MgSO_4$ guarantees the continuing integrity of the seal in the case of additional brine intrusion. SVV maintains its capacity of self-sealing as long as unreacted (anhydrous) $MgSO_4$ is left.

4 BOUNDARY CONDITIONS AND SVV PROPERTIES

Boundary conditions, such as initial materials, solid/solution ratio, flooding regime (slow or fast flooding) and fluid pressure, have a considerable influence on chemical stability as well as on hydraulic and mechanical properties of the resulting sealing material. These parameters must be optimized in order to obtain the desired low permeabilities, mechanical properties and crystallization pressures. Whereas anhydrous $MgSO_4$ can be used in all salt and potash rocks with different mineralogical composition, the brine must be adapted to the mineralogy of the host rock. The chemical composition of the solution should be in equilibrium with the surrounding mineralogy. The solid/solution ratio is responsible for the amount of $MgSO_4$ that participates in the reaction. The more $MgSO_4$ reacts with brine, the lower is the resulting permeability and the higher the crystallization pressure. That means that the properties of the seal can be influenced by the amount of brine introduced into the system. The highest possible amount of brine should be introduced into the pore space as rapidly as possible in order to obtain homogeneous conditions in the entire seal. A slow brine inflow into the pore space leads to a clogging of the pathways in the vicinity of the brine inflow and prevents parts of the pore space from being flooded. In order to introduce the brine as quickly as possible a high fluid pressure and a sufficient high pump rate is required.

In laboratory experiments extremely high fluid pressures can be applied. For technical reasons, however, the fluid pressure is not allowed to exceed 30–35 bars. From a technical point of view it is possible to build abutments which can withstand brine pressures of 35 bars. Abutments for higher brine pressures are much more expensive. Abutments are required for maintaining a constant volume during the $MgSO_4$/brine reaction. After the end of the reaction they are not needed any more. Therefore the costs for these barriers can be kept low.

5 EXPERIMENTAL

The experiments were designed in a way to provide the data needed for performance assessment of an SVV seal under *in-situ* conditions. The experiments were conducted on three different scales to limit the possibility that no unexpected scale effects arise when real size SVV dams are built. The experimental set up was similar in all experiments. SVV was filled into the confined volume of a pressure vessel and flooded with brine. Masses of intruded and percolated brine were continually determined with a balance. The brine was pumped into the pressure vessel with an hplc pump. Temperature, brine pressure, and total pressure (the combined brine pressure and crystallization pressure) were recorded.

Twenty six experiments were conducted in small pressure cells (Figures 1 and 2). Three experiments were performed on a larger scale in pressure tubes of 1 m length and 40 cm diameter (Figure 3). Two experiments took place *in-situ* in the Asse mine at the 850 m level in boreholes of 15 m length and 50 cm diameter in a rock salt formation (Figure 4). The flooding time, 1 hour – 2 days, was depended on the size of the experiment. The curing time 40–60 days, was mainly a function of the solid/solution ratio and the brine composition.

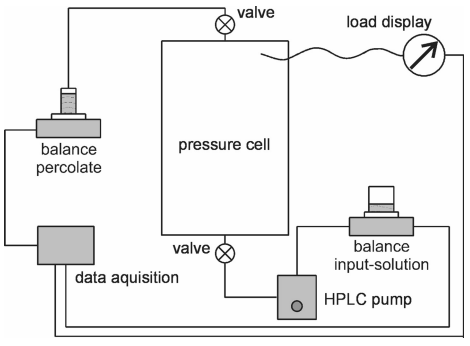

Figure 1. Schematic experimental setup for the measurement of crystallization pressure and fluid permeability.

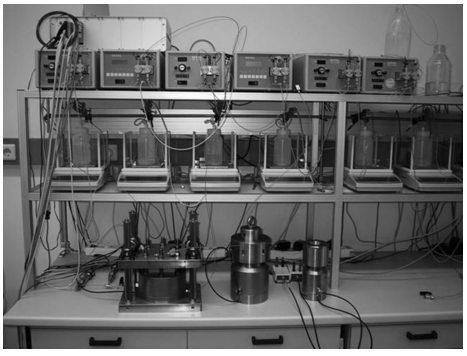

Figure 2. Photograph of the experimental setup with data acquisition, HPLC pumps, scales and three pressure cells of different size and geometry.

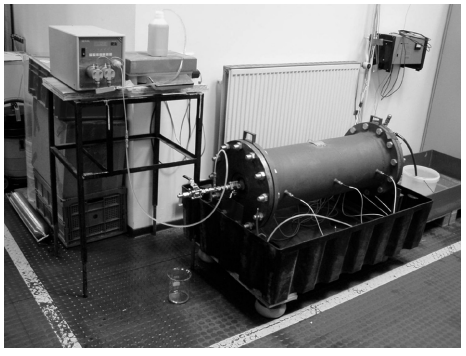

Figure 3. Experimental setup of large scale crystallization pressure measurements in a pressure tube of 1 m length and 20 cm diameter.

Figure 4. SVV experiments in boreholes (15 m long, 50 cm diameter) in rock salt in the Asse salt mine.

6 MATERIALS

The initial materials used guarantee the chemical and mineralogical stability of the sealing material. Adequate recipes have been developed for salt formations with different mineralogies.

Most experiments were performed with pure anhydrous $MgSO_4$ purchased from K + S AG Kassel in 50 kg bags. Grain sizes range from 0.1 to 1 mm. The pure anhydrous $MgSO_4$ can be used in all salt formations regardless of their specific mineralogical composition. In some experiments, however, a mixture of 80 wt-% anhydrous $MgSO_4$ + 10 wt.-% halite + 10 wt.-% sylvite was used in order to determine whether formation of preferential pathways observed in the reaction of anhydrous $MgSO_4$ with NaCl solution can be avoided. The experiments were conducted with three different brines which are in chemical equilibrium with different salt mineralogies. The NaCl-saturated solution and the $MgCl_2$-rich IP21 solution are naturally encountered brines in salt formations. They result from the reaction of water with the German Zechstein salt formations, rock salt and carnallitite. Carnallitite is a carnallite ($MgKCl_3 \cdot 6H_20$) and kieserite ($MgSO_4 \cdot H_2O$) bearing potash rock. The third solution, the $CaCl_2$-rich tachhydrite solution, is an artificial brine. It was used in a series of experiments in order to find out whether SVV seals can be constructed also in the extremely soluble potash rocks with tachhydrite ($Mg_2CaCl_6 \cdot 12H_2O$) and without dissolving the tachhydrite in the contact zone. The chemical composition of the three solutions and their saturation state are given in Table 1 and Table 2, respectively.

7 MINERALOGY

The mineralogical composition of the SVV sealing material after completion of the reaction SVV/brine depends mainly on the mineralogical composition of the initial SVV material and the composition of the initial solution. Figures 5 and 6 show the large variety of mineralogical compositions which can be obtained by using pure anhydrous $MgSO_4$ or mixtures with halite + sylvite and different brines. A close view at the X-ray diagrams reveals that in all cases higher amounts of higher hydrated minerals were formed close to the inflow of brine. This is due to the fact that close to the inflow the solution has the highest water content.

Table 1. Composition of the solutions in SVV experiments.

Solution	Density [g/ml]	Na [g/l]	K	Ca	Mg	Cl	SO_4
NaCl solution	1.2000	140.4				216.4	
IP21 solution	1.2894	9.1	19.15	0.02	86.4	267.3	23.0
Tachhydrite solution	1.4784	1.42	2.46	207.6	347.5	471.0	0.0

Table 2. Saturation state of the solutions in SVV experiments.

Mineral, formula	Solution [kcal]		
	NaCl	IP21	Tachhydrite
Anhydrite, $CaSO_4$		0.754	
Antarcticite, $CaCl_2 \cdot 6H_2O$			−0.132
Bischofite, $MgCl_2 \cdot 6H_2O$		−1.621	−0.394
$CaCl_2 \cdot 4H_2O$			0.128
Carnallite, $KMgCl_3 \cdot 6H_2O$		−0.304	0.306
Halite, NaCl	0.001	−0.167	1.354
Kainite, $KMgCl_3SO_4$		−0.307	
Pentahydrite, $MgCl_2 \cdot 5H_2O$		−0.502	
Sylvite, KCl		−0.081	
Tachhydrite, $Mg_2CaCl_6 \cdot 12H_2O$			0.391

The further the solution moves through the SVV, the more water is consumed. This illustrates the desirability of obtaining an almost instantaneous flooding of the entire initial pore space.

8 GEOCHEMICAL MODELLING

Figure 7 shows an example of the modelling of the reaction of IP21 solution with anhydrous $MgSO_4$ and additions of halite and sylvite. The comparison of the actually observed minerals (Figure 7) with the minerals calculated for the metastable reaction path (Figure 8, upper left diagram) shows very good agreement. With only one exception all observed minerals appear. The exception is hexahydrite ($MgSO_4 \cdot 6H_2O$). Instead of hexahydrite, pentahydrite ($MgSO_4 \cdot 5H_2O$) was identified in the samples. This excellent agreement between calculations and observed mineralogical composition was obtained in all investigated reactions. This indicates the applicability of both Gibbs Excess parameters and solubility constants for aqueous species and mineral phases involved in the reactions (HMW data from Harvie et al. 1984). It also shows, the reliability of the volume calculations, which are in accordance with the observations. The volume of the system after reaction is greater than the volume at the start of the reaction. This volume increase is responsible for the observed crystallization pressure. The modelling allows detailed insight into the mineralogical and volume changes along the entire reaction path. A detailed quantitative reaction equation can be written for each reaction step. This information is valuable for correctly interpretating the experimental results and for the optimization of the seal properties. Furthermore, data can be derived which are needed for the coupled hydro-mechanical-chemical model calculations. From each sample of every single experiment, all data needed for the description of coupled processes can be derived: mineralogical composition, consumed mass of initial SVV material, consumed mass of brine and water, single volume of all consumed and precipitated mineralogical phases, the resulting filled and open pore volume, and last, but not least, the permeability. The data needed for accurately deriving the relationship between porosity and permeability can be obtained by combining geochemical modelling data and experimental measurements. The system volume can be calculated and verified by direct measurement of the free pore water content and the weight of percolated brine.

Geochemical modelling has the additional advantage of allowing predictions concerning the long-term chemical stability of the seal. Such information can not be derived directly from experiments. The experiments show that the reactions follow the metastable reaction path. A distinction between metastable and stable reaction path can be done along the following considerations.

Thermodynamically the system is fully defined by the molar masses of its constituting endmembers. Mixing anhydrous $MgSO_4$ with an increasing mass of free water therefore leads to the formation of mixtures of $MgSO_4$/Kieserite, Kieserite/Starkeyte, Starkeyte/Pentahydrite, Pentahydrite/Epsomite, and finally Epsomite/brine. As long as the number of mols of water is lower than the number of mols of $MgSO_4$, any occurrence of higher hydrated $MgSO_4$-sulphates than kieserite may be considered as metastable. Metastable phases, however, may persist for a long time for kinetic reasons, and because transport of water molecules inside the system is slow because no interconnected network of free pores exist. Over geologic time scales, however, and with little water in rock salt formations, only kieserite persists, as evidenced consistently by geologic experience and thermodynamic equilibrium calculation.

Thus geochemical modelling gives a detailed quantitative insight into the short- and long-term development of the system. In Figure 7 results are given for the calculated metastable and stable reaction paths. The metastable reaction products ($MgSO_4$ hydrates), starkeite, pentahydrite, epsomite and hexahydrite do not appear in the calculations of the stable reaction path. Instead of these water rich minerals the water poor kieserite ($MgSO_4 \cdot H_2O$) appears. Kieserite is the stable $MgSO_4$ mineral in all German Zechstein potash formations. The thermodynamic calculations showthat metastable mineral assemblages are transformed into stable minerals by losing water of crystallization. This water remains in the system and reacts further forming new metastable minerals which eventually are all transformed into stable minerals, as well. In the example given in Figure 7, the stable mineral assemblage is kieserite and kainite $KMgCl_3 \cdot 3H_2O$). We have many

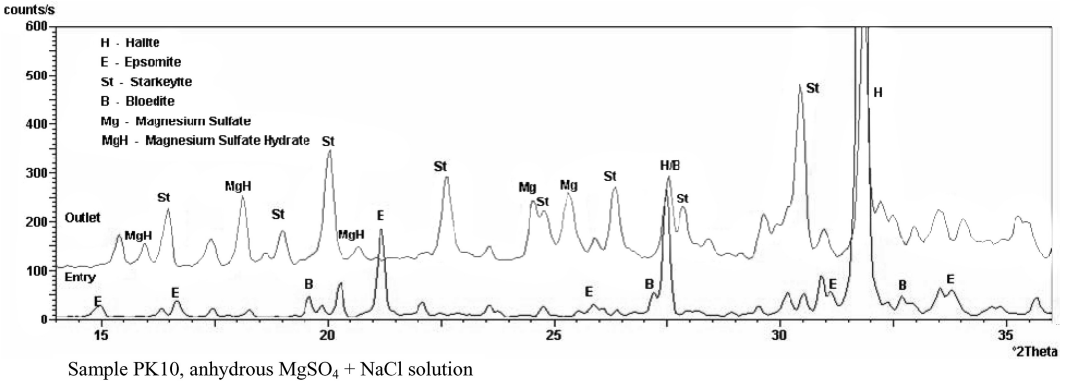

Sample PK10, anhydrous $MgSO_4$ + NaCl solution

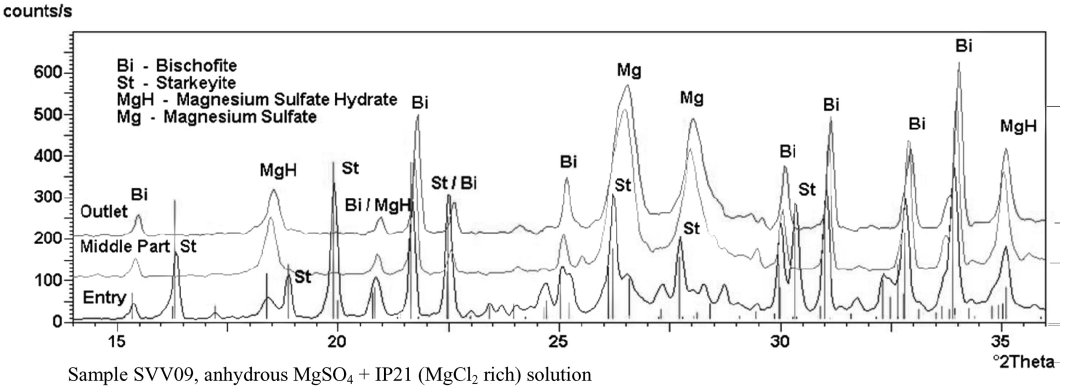

Sample SVV09, anhydrous $MgSO_4$ + IP21 ($MgCl_2$ rich) solution

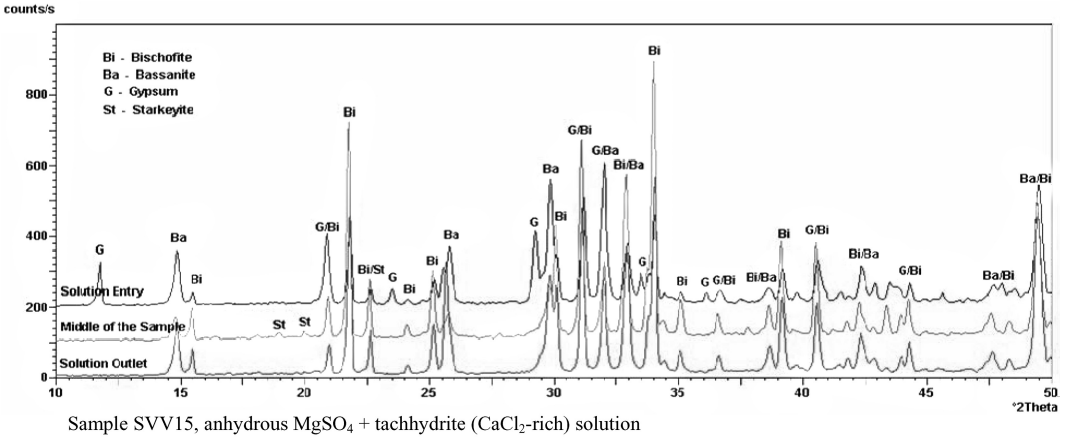

Sample SVV15, anhydrous $MgSO_4$ + tachhydrite ($CaCl_2$-rich) solution

Figure 5. XRD diagrams of SVV ($MgSO_4$ anhydrous) after reaction with NaCl solution (top), IP21 ($MgCl_2$ rich) solution (centre), and tachhydrite ($CaCl_2$-rich) solution (bottom) at different distances from the brine inflow.

examples for the existence of such stable mineral parageneses in nature. We, therefore, can reliably predict that the short-term metastable minerals in the SVV seal will be transformed into stable parageneses.

The calculation of the stable reaction path shows that the new stable paragenesis also has a greater volume than the original volume of the SVV at the start of the reaction. That means that the low permeability and

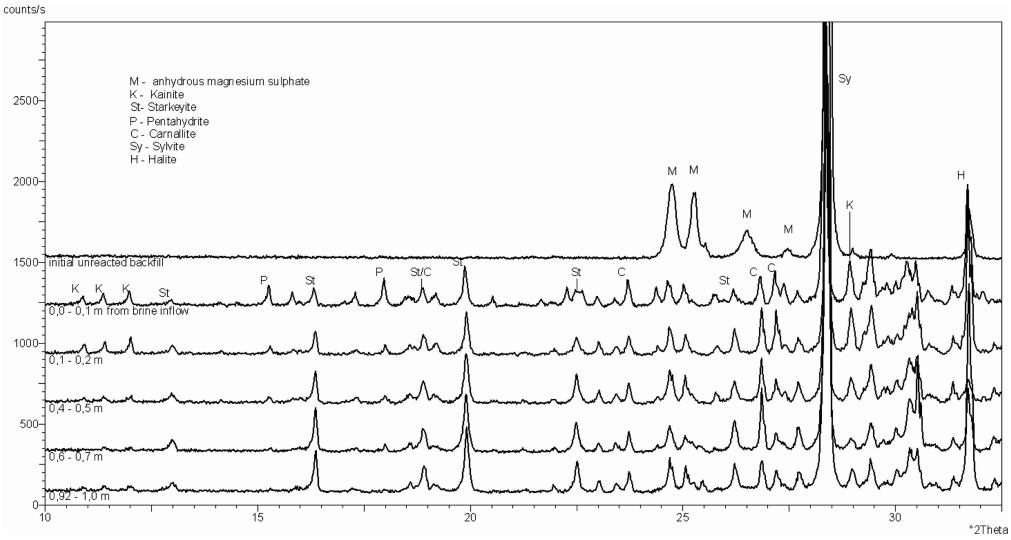

Figure 6. XRD diagrams of SVV (80 wt,-% $MgSO_4$ anhydrous + 10 wt.-% halite + 10 wt.-% sylvite) after reaction with IP21 ($MgCl_2$-rich) solution in a 1-m-long tube, at different distances from brine inflow.

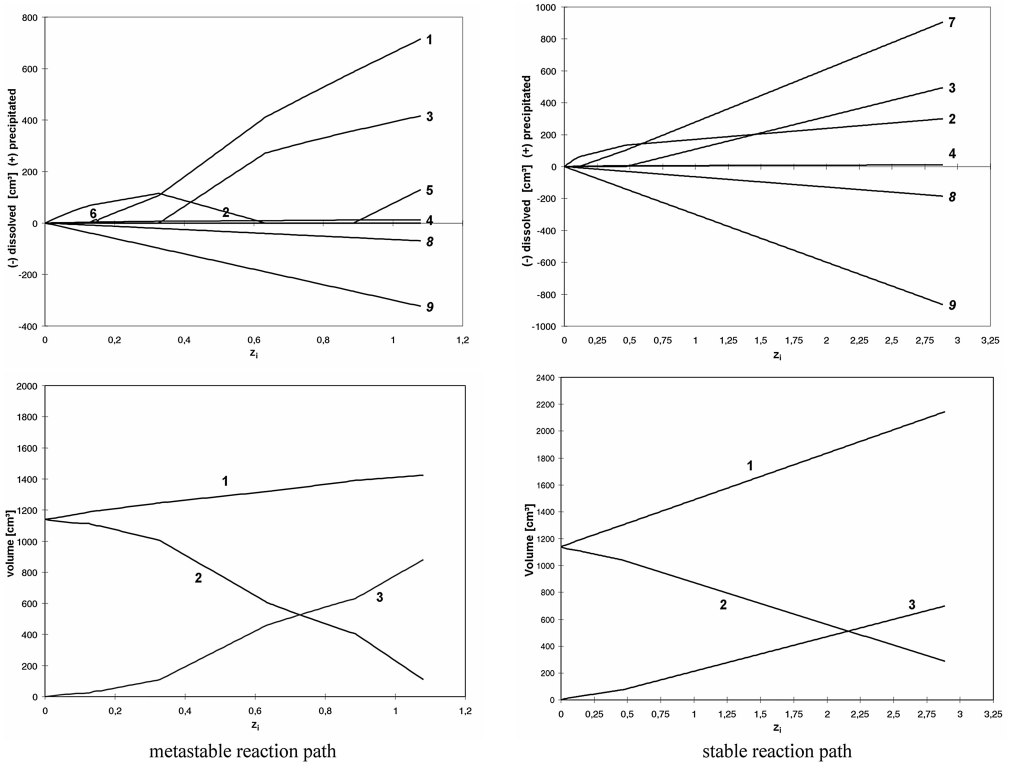

metastable reaction path stable reaction path

Above 1 = starkeyite 2 = kainite 3 = carnallite 4 = halite 5 = bischofite 6 = hexahydrite 7 = kieserite 8 = sylvite 9 = anhydrous magnesium sulphate

Below 1 = volume of the system (difference between the sum of solution and consumed anhydrous magnesium sulphate and the sum of precipitated minerals) 2 = volume of the solution 3 = volume of precipitated minerals

Figure 7. Calculated reaction path of self-sealing backfill (80 wt-% $MgSO_4$ anhydrous + 10 wt.-% halite + 10 wt.-% sylvite) with a halite-carnallite-cainite-polyhalite- sylvite saturated solution ("IP21 solution").

the crystallization pressure observed in the short-term reaction are preserved even during the slow change towards stable mineral assemblages.

9 CRYSTALLIZATION PRESSURES

9.1 *General evolution*

Figure 8 illustrates a typical development of important parameters during a swelling pressure experiment. Brine is pumped into the pressure cell which is filled with fine grained loose and dry SVV material. The pump is volume-regulated, i.e., it pumps a constant volume per minute. The maximum pump pressure is set at 35 bars. At the beginning, the brine enters the large pore space (50% of the total volume) without encountering resistance. The valve at the outlet of the pressure cell is open in order to let the air escape from the system. The initial fluid pressure is very low. Open pore spaces are successively filled as the brine pressure rises. At higher brine pressure, new pores become accessible and are flooded resulting in a temporarily falling brine pressure. This process recurs several times until the maximum brine pressure is reached. When the first brine starts to exit from the pressure cell the valve is closed in order to keep the brine in the system. The compressed air is released by opening the outlet valve several times for a short time. The brine trapped in the system is recorded by weighing the injected and the percolated mass of solution.

The reaction starts immediately after the first inflow of brine. Important processes are hydration of the $MgSO_4$, and oversaturation of the brine with ensuing mineral precipitation. A crystallization pressure develops and is superimposed on brine pressure. In the pressure cell the pressure is recorded by a pressure gauge. This total pressure consists of both, brine and crystallization pressure. At the beginning, the pressure is mainly brine pressure. At the end of the reaction, the brine is consumed and the recorded pressure is practically the crystallization pressure. The final crystallization pressure can be either lower or higher than the brine pressure according to the boundary conditions of the reaction (original materials, solid/fluid ratio, homogeneity of brine distribution in the system). In order to obtain the highest possible crystallization pressure (which guarantees the lowest permeability) the highest possible amount of brine must be introduced into the system. The maximum input brine pressure (35 bars) is maintained until no more brine enters the pressure cell at which time the pump is switched off. The total pressure registered in the cell falls but later starts to rise again as the reaction proceeds and new minerals increase the crystallization pressure. The experiment is finished when a maximum pressure is reached and stays constant for an extended time.

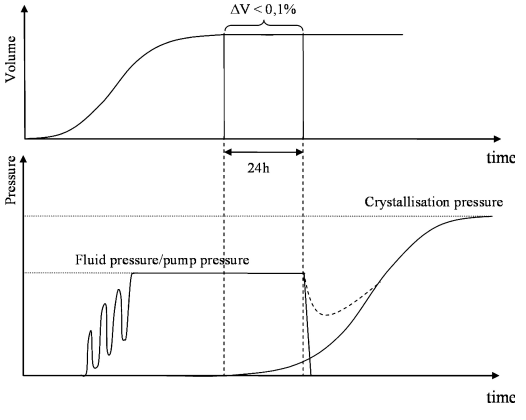

Figure 8. Schematic view of the evolution of fluid pressure, crystallization pressure and volume change of the SVV material during brine inflow.

9.2 *Results*

The Figures 9–11 show examples of crystallization pressure measurements of anhydrous $MgSO_4$ with the three different brines. The samples PK and SVV were measured in small pressure cells and the "Tube" samples in 1-m-long and 40-cm-diameter pressure tubes. In the small pressure cells, mean pressures of about 40 bars were obtained with NaCl and IP21 solution and about 60 bars with tachhydrite solution. Repeated measurements, however, showed that the reproducibility of the crystallization pressures was rather low and the standard deviation high (Table 3).

With regard to the low reproducibility of crystallization pressure it must be kept in mind, however, that its value reflects the state at a very small point in the system. It is not an integral property of the sample, as are other properties like permeability. It is hypothesized that its absolute value is strongly influenced by

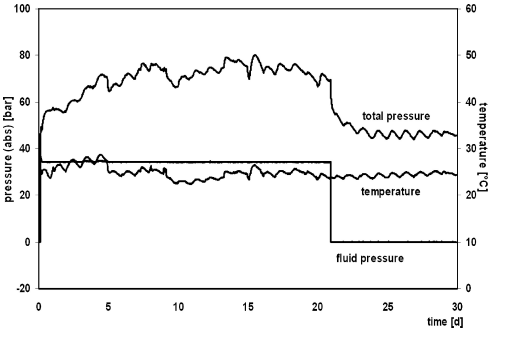

Figure 9. Sample PK10 – Example of a crystallization pressure measurement of SVV (pure anhydrous $MgSO_4$) during the reaction with saturated NaCl solution in the small pressure cell.

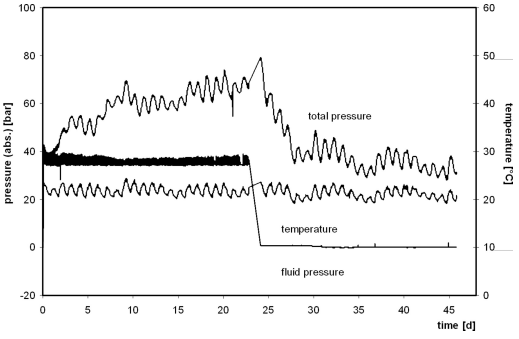

Figure 10. Sample SVV 09 – Example of a crystallization pressure measurement of SVV (pure anhydrous $MgSO_4$) during the reaction with IP21 ($MgCl_2$-rich) solution in the small pressure cell.

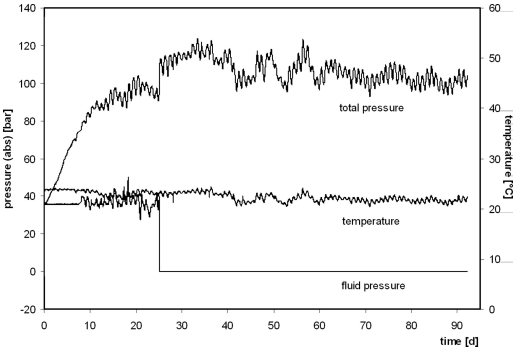

Figure 11. Sample SVV 15 09 – Example of a crystallization pressure measurement of SVV (pure anhydrous $MgSO_4$) during the reaction with tachhydrite ($CaCl_2$-rich) solution in the small pressure cell.

inhomogeneities in the system, which are significant for the comparatively small pressure gauge, but are not significant for a description of integral properties of the entire system. Therefore, no clear relationship between crystallization pressure and the solid/liquid ratio could be established.

This hypothesis is supported by findings in the large-scale tube experiments (Figures 12 and 13). In spite of the fast flooding no truly uniform distribution of the brine occurred in the samples. The proportion of brine differed from place to place in the samples, leading to differences in the amount of hydrated and precipitated minerals and thus to differences in the local crystallization pressure. In the tube experiments the crystallization pressures and temperatures were measured at 15 cm, 50 cm and 85 cm from the point of brine inflow. At each pressure gauge the registered pressure was different.

The challenge for future work will be to obtain a more uniform brine distribution in the initial pore

Table 3. Crystallization pressures p_c [bar] of anhydrous MgSO4 with three different brines.

Sample NaCl sol.	pc [bar]	Sample IP21 sol	pc [bar]	Sample Tachydr. sol	p_c
PK1	37	SVV05	44	SVV02	37
PK2	33	SVV06	31	SVV03	28
PK3	31	SVV07	70	SVV04	35
PK4	40	SVV09	69	SVV08	71
PK5	35	SVV10	39	SVV11	89
PK6	7	SVV12	17	Tube3.1	59
PK7	26	SVV13	65	Tube3.2	15
PK8	96	Tube 1	25	Tube3.3	15
PK9	14	Tube 2	30		
PK10	46	Tube 4.1	38		
PK11	87	Tube 4.2	32		
		Tube 4.3	10		

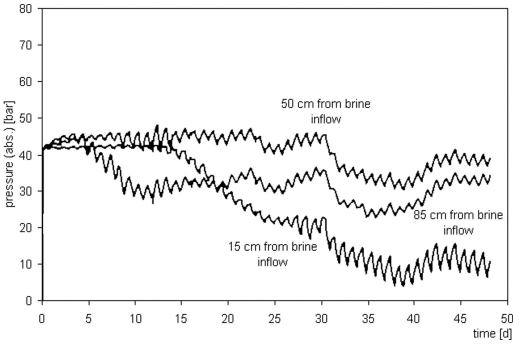

Figure 12. Sample "Tube 4" Development of total pressure during the reaction of SVV (pure anhydrous $MgCl_2$) with IP21 ($MgCl_2$-rich) solution, at different locations (15, 50 and 85 cm from the inflow of brine.

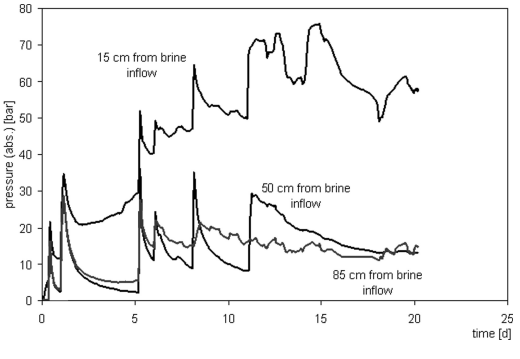

Figure 13. Sample "Tube 3" Development of total pressure during the reaction of SVV (pure anhydrous $MgCl_2$) with tachhydrite ($CaCl_2$-rich) solution, at different locations (15, 50 and 85 cm from the inflow of brine).

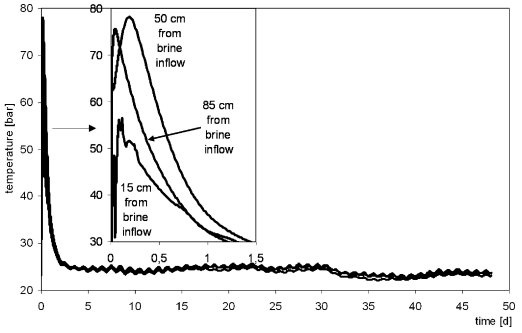

Figure 14. Sample "Tube 4" Temperature development during the reaction of SVV (pure anhydrous $MgCl_2$) with IP21 ($MgCl_2$-rich) solution, at different locations (15, 50 and 85 cm from the inflow of brine).

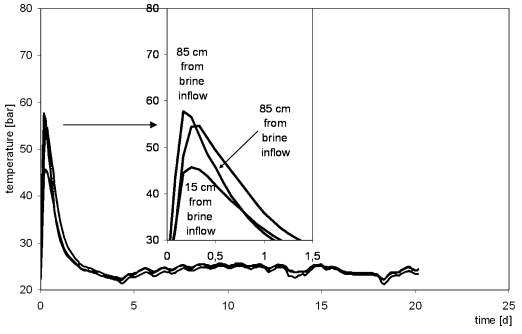

Figure 15. Sample "Tube 3" Temperature development during the reaction of SVV (pure anhydrous $MgCl_2$) with tachhydrite ($CaCl_2$-rich) solution, at different locations (15, 50 and 85 cm from the inflow of brine).

space. Maybe this can be obtained by using pumps with a higher flow rate. From a modelling point of view another approach could be to adapt scaling of finite elements to the scaling of unavoidable heterogeneities.

10 TEMPERATURES

The temperature development during the exothermic reaction of anhydrous $MgSO_4$ with IP21 and tachhydrite solution is shown in Figures 14 and 15. With the first brine inflow into the system a sharp temperature increase was observed. In IP21 solution tube experiments maximum temperature of 78°C was reached. In the tachhydrite solution experiment only 58°C were recorded. Subsequently the temperatures decreased again immediately to ambient values. The measured peak temperatures agree well with calorimetric measurements and calculations for the respective systems and are not problematical for the construction of SVV seals.

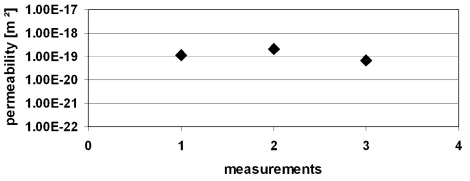

Sample SVV 13, anhydrous $MgSO_4$ + IP21 ($MgCl_2$-rich) solution, fluid pressure 30 bars

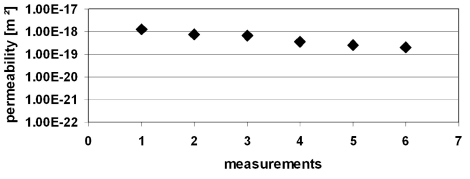

Sample "Tube 3", anhydrous $MgSO_4$ + tachhydrite ($CaCl_2$-rich) solution, fluid pressure 70 bars

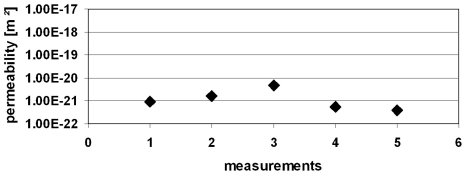

Sample "Tube 3", anhydrous $MgSO_4$ + tachhydrite ($CaCl_2$-rich) solution, fluid pressure 80 bars

Figure 16. Flow through permeability measurements on SVV samples after reaction with brines.

11 PERMEABILITIES

Permeability measurements were performed with the pulse injection method and the flow-through injection method. Generally the brine permeability was measured. Darcy's low was used for the calculation of permeability. In Figure 16 examples of permeability measurements are shown which were obtained in small-cell and large-tube experiments with IP21 and tachhydrite brine. The most important conclusion from these measurements is that very low mean permeabilities can be obtained in all investigated reactions at all scales. Figure 17 illustrates the relationship between permeability and residual porosity of the SVV material after reaction with IP21 solution. Similar results were obtained for tachhydrite brine. These results are in agreement with experimental results for crushed highly compacted dry and wet rock salt backfill (Fein et al. 1996) (Figure 17).

12 GEOMECHANICAL PROPERTIES OF SVV

Figure 18 shows results of uniaxial and triaxial compression tests on different samples and different scales.

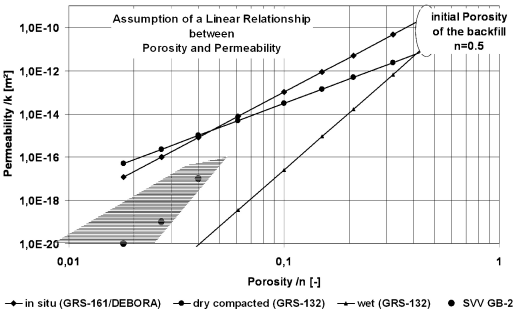

Figure 17. Porosity/permeability relationship of SVV samples after reaction with IP21 solution in comparison with data from wet and dry compacted crushed rock salt backfill.

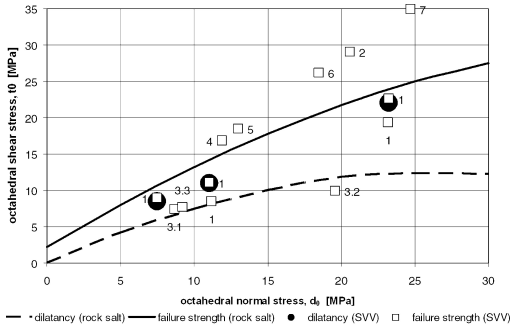

1 = *in-situ* experiment in 15 m borehole: 80 wt.-% anhydrous $MgSO_4$ + 10 wt.-% Halite + 10 wt.-% sylvite + NaCl-saturated solution
2 = small pressure cell sample SVV 09: 100 wt.-% anhydrous $MgSO_4$ + IP21 ($MgCl_2$-rich) solution
3 = large-scale sample "Tube 2": 100 wt.-% anhydrous $MgSO_4$ + IP21 ($MgCl_2$-rich) solution
4 = small pressure cell sample SVV 02: 100 wt.-% anhydrous $MgSO_4$ + tachhydrite ($CaCl_2$-rich) solution
5 = small pressure cell sample SVV 03: 100 wt.-% anhydrous $MgSO_4$ + tachhydrite ($CaCl_2$-rich) solution
6 = small pressure cell sample SVV 08: 100 wt.-% anhydrous $MgSO_4$ + IP21 ($MgCl_2$-rich) solution
7 = small pressure cell sample SVV 15: 100 wt.-% anhydrous $MgSO_4$ + tachhydrite ($CaCl_2$-rich) solution

Figure 18. Failure strength and dilatancy boundary of SVV samples after reaction with different brines in comparison with data from undisturbed rock salt.

All SVV failure strength values obtained from triaxial compression tests are located between the curves of failure strength and the dilatancy boundary determined for rock salt (Schulze et al. 2001). The values above the rock salt failure strength curve were calculated from uniaxial compression tests. These values may be too high because of the non-ideal sample geometry. As a conclusion from these measurements we can state that the rock mechanical behaviour of SVV after reaction with brine resembles that of rock salt.

13 CONCLUSIONS

All results indicate that SVV is a self-sealing, long-term stable material with similar mineralogical, chemical, hydraulical and mechanical properties than rock salt. The physico-chemical processes during the reaction SVV/brine are well understood. Coupled THMC models for SVV are under development and make fast progress. It can be stated that SVV is a well suited predictable material for seal constructions in salt formations.

ACKNOWLEDGEMENT

The results presented in this paper were obtained in the frame of the projects 02C1335 and 02C1285 financed by the German ministry for Education and Research (BMBF). The author thanks his colleagues Lothar Meyer, Uwe Hertes, Lothar Hartwig, Karsten Hellwald, Jürgen Dittrich, Christian Reichelt and Helge Moog for their valuable contributions.

REFERENCES

Fein, E.; Müller-Lyda, I. & Storck, R. (1996): Ableitung einer Permeabilitäts-Porositätsbeziehung für Salzgrus und Dammbaumaterialien – GRS Report GRS – 132: 99p.

Herbert, H.-J. & Kull, H. (2004): A new self sealing and self healing backfill material for repositories in salt formations – *Proceedings of the Solution Mining Research Institute Fall 2004 Conference, 3–6 October 2006, Berlin, 239–264.*

Herbert, H.-J.; Kull, H. & Müller-Lyda, I. (2006): Weiterentwicklung eines Selbst Verheilenden Versatzes (SVV) als Komponente im Barrieresystem Salinar – *GRS-Report, GRS-220, 65 p.*

Harvie, D.E.; Moller, N. & Weare, J. H. (1984): The prediction of mineral solubilities in natural waters: the Na-K-Mg-Ca-H-Cl-SO_4-OH-HCO_3-CO_3-CO_2-H_2O system to high ionic strength at 25°C. – *Geochimica et Cosmochimica Acta, v. 48, 723–751.*

Sander, W. & Herbert, H.-J. (2000): A new hydraulic barrier – Performance of a self-sealing salt backfill material. In *Proceedings DisTec 2000, Disposal Technologies and Conceps 2000,* Kontec Gesellschaft für technische Kommunikation mbH, Hamburg. ISBN 3-9806415-3-8.

Sander, W. & Herbert, H.-J. (2002): Wirksamkeit der Abdichtung von Versatzmaterialien – Geochemische Untersuchungen zum Langzeitverhalten von Salzversatz mit Zuschlagstoffen – *GRS-Report, GRS-180, ISBN 3-931995-48-8, 266p.*

Schulze, O.; Popp, T. & Kern, H. (2001): Development of damage and permeability in deforming rock salt – Engineering Geology 61, 163–180. Elsevier, Amsterdam (special Issue on Geosciences and Nuclear Waste Disposal. Eds.: Ch. Talbot & M. Langer.

The Mechanical Behavior of Salt – Understanding of THMC Processes in Salt –
Wallner, Lux, Minkley & Hardy, Jr. (eds)
© 2007 Taylor & Francis Group, London, ISBN 978-0-415-44398-2

Coupled modelling of the C: HM behaviour of self healing salt based backfill

F. Werunsky & Z. Hou*
Professorship for Waste Disposal and Geomechanics, Clausthal University of Technology, Clausthal-Zellerfeld, Germany
**now with: Institute of Petroleum Engineering, Clausthal University of Technology, Clausthal-Zellerfeld, Germany*

H.C. Moog
GRS – Gesellschaft für Anlagen – und Reaktorsicherheit mbH, Braunschweig, Germany

ABSTRACT: Through underground sealing systems direct influx of brine or water in disposal cavities of underground waste repositories is initially ruled out. Therefore dam materials with restraint systems, in case of a water or brine intrusion, are a good choice. To simulate the behaviour of such a material with a chemical based restraint system, CHM coupling is essential. This paper deals with a numerical model which describes the coupled C: HM behaviour of a self healing salt based backfill "SVV". Therefore with implemented thermodynamic equilibrium calculations the phase composition and solid phase integral volume can be predicted and thus the curing process during the injection of solution described. Concurrent samples of SVV have been produced and thereby measured data has been compared to the results of simulations. Afterwards the samples were disassembled and investigated with respect to their mechanical behaviour and composition in terms of mineral phases for further comparisons between simulation and experiment.

1 INTRODUCTION

Disposal of radioactive waste in deep geological formations is considered the best method to isolate long-living radionuclides from the biosphere on a long-term scale. A key feature for the feasibility of radioactive waste disposal is the closure of remaining cavities, boreholes and drifts to prevent intrusion of aqueous solution. Under the ambient conditions of temperature and pressure rock salt features plasticity which eventually leads to a complete sealing of pathways for aqueous solution. It is therefore considered one of favourable host rock formations for deep geological disposal of waste.

The material to seal the mentioned pathways should be thermodynamically stable in the saline environment and be able to close remaining porosities upon contact with aqueous solution. It is the long-term thermodynamic stability which makes anhydrous $MgSO_4$, also referred to as "SVV", a favourite candidate material for this purpose (e.g. Herbert 2007).

"SVV" is the abbreviation for the German expression "Selbstverheilender Salzversatz" and means self healing backfill. SVV removes water from aqueous solutions by binding it as crystal water. In this reaction the volume of the stowage is growing and the infiltrating water is exhausted. After the reaction the stowage is almost impermeable. This is because the growth in volume results in a smaller porosity, a smaller permeability and the evolution of a crystallisation pressure. Therefore, SVV is theoretical able to close existing cracks in a dam structure automatically.

In last 30 years a great knowledge about the mechanical behaviour of rock salt has been acquired and applied. At present time there are many constitutive models for rock salt, even a few with damage, dilatancy and healing, compaction behaviour, like Hou/Lux (Hou 1997, 2002 and Hou & Lux 1998). Known are also relations between porosity, stress and permeability of damaged rock salt (e.g. Hou 2002). There are a few constitutive models for crushed salt (e.g. Zhang 1993, Stührenberg and Zhang 1996, Sjaardema and Krieg 1987, Pfeifle 1990, Hein 1991 and Korthaus 1998) and several porosity – permeability relations (e.g. Fein et al. 1996, Müller – Lyda & Fein 1999, Brodsky et al. 1998, Pfeifle 1990). But none of these models can be used to describe the mechanical behaviour of SVV because the hydration process is not included.

SVV has been investigated earlier in terms of geochemical reactions which it undergoes after contact with brines, or separately in terms of some final hydraulic and mechanical properties. Within the framework of a running joined project GRS Braunschweig, TUC (Clausthal University of Technology) and ZAG (Centre for Applied Geosciences at the University of Tübingen) strive to combine efforts to integrate computer codes for the coupled modelling of the C (chemical), H (hydraulic), and M (mechanical) behaviour of Bentonite and SVV ("CHM-project").

First results of mechanical experiments will be presented in this paper. And first results of numerical simulations with the rock mechanical and hydraulic programme MISES III coupled with thermodynamic equilibrium calculation will be shown.

2 EXPERIMENTS/METHODS

2.1 *Producing of SVV samples*

Samples were produced within a cell previously designed for the measurement of swelling pressures of saturated bentonite (Herbert & Moog, 2002). The general scheme of the used cell is shown in Figure 1.

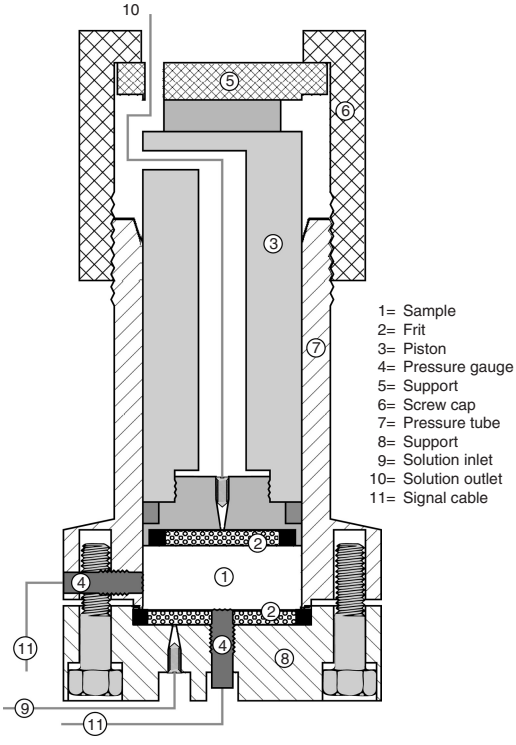

Figure 1. Construction scheme of the cell used to measure the swelling pressures of saturated bentonite.

First the sensors are checked by closing the cell and applying water pressure. Then the cell is dried and filled with $MgSO_4$ with a starting porosity of 50%.

There are two different types of SVV samples produced. The first type has a diameter of 50 mm, a length of 100 mm and is made out of 262 g of anhydrous $MgSO_4$. The second type is 70 mm in diameter, 140 mm in height and needs 720 g anhydrous $MgSO_4$.

The cell is closed by the piston, which is pushed in manually till a closed linkage is attained with the magnesium sulphate. In this position the piston is fixed with the screw cap. The inlet valve is connected to a bottle of NaCl – solution. Solution is delivered with a HPLC pump.

The cell is flooded with NaCl-saturated brine from the bottom to the top of the cell with a fluid pressure of 35 bars and a delivery rate of 1 ml/min and 2.7 ml/min for type 1 and type 2, respectively. During the flooding and curing the following data are measured: fluid pressure in the pump, total pressure in the cell, room temperature and mass of the brine pumped into the cell. The valve at the outlet is open till the first drop of brine leaves the cell, and is then closed. Thus, almost all air can escape from the cell. Now slowly the crystallisation pressure is built up by creation of $MgSO_4$ hydrates, which is an exothermic reaction. The cell is left for 21 days under the fluid pressure and the total pressure can rise up till three times of the adjusted fluid pressure (compare Fig. 2).

After 21 days of reaction time the cell is separated from the HPLC pump and both valves are opened. For about three days brine is allowed to leak from the inlet and the outlet valve. This brine is collected and weighed and its mass subtracted from the total mass of solution delivered by the HPLC pump for volume balancing.

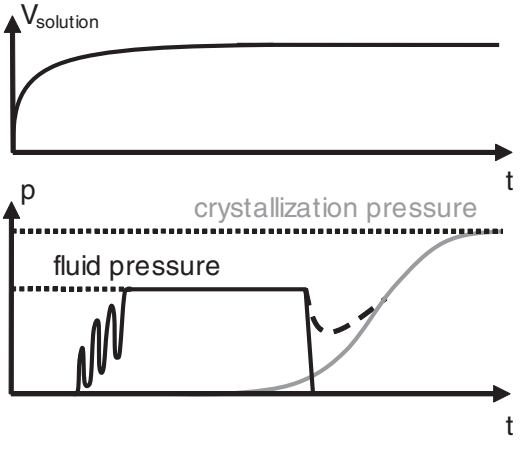

Figure 2. Schematic diagram of injected brine and crystallisation pressure.

After two weeks of curing the emerged crystallisation pressure can be determined by subtracting the used fluid pressure from the measured total pressure in the cell (both are mean values over the last 24 hours, to minimize the influence of temperature changes). After that the sample is pressed out of the cell, for what a compressive force up to 200 kN can be necessary because of high crystallisation pressures.

2.2 *Triaxial compression tests*

A confining pressure of 3.5 MPa, similar to the measured crystallisation pressure, was chosen as test condition for triaxial compression tests with SVV samples. During triaxial compression tests the following items are measured: confining pressure σ_c, axial pressure σ_1, axial strain ε_1, volume strain ε_{vol} and ultrasonic p-wave velocity v_p. First results showed a much smaller deformability than rock salt, so a much smaller deformation rate of 0.025%/min was used. Because of NaCl precipitation and solving, there is a soft area around the inlet (compare Fig. 3), which had to be removed before the tests. Therefore the samples didn't have a ratio 2:1 between height and diameter. The resulting ratio was only about 1.5:1, so that the measured strength should be higher, supposable about 20%.

2.3 *Numeric simulations*

The programme used for the mechanical and hydraulic simulations is the FEM programme MISES III. For the chemical coupling, EQLINK, an interface to the thermochemical library CHEMAPP (Eriksson und Hack 1990, Eriksson et al. 1994, Eriksson et al. 1995) is integrated in MISES III. This way, thermodynamic equilibrium calculations, and hence precipitation and dissolution processes can be described quantitatively at run time. The thermodynamic database used was a subset of a parameter file prepared within the frame of the Yucca Mountain Project in the USA (Mariner 2005). It allows for calculations of saturated solutions of oceanic salts between 298 and 573 K. From the calculated balance of volumes it is possible to calculate changes of permeability, strain and crystallisation pressure of the SVV sample. These effects lead to the changes in strain, structure damage, healing, volume dilatancy and permeability in the surrounding rock salt mass.

To make MISES III ready for the CHM – coupling, EQLINK/CHEMAPP had to be integrated and implemented in the FEM programme MISES III. Then a sub programme for the initialization of the chemical system and for the starting values in the zones needed to be implemented. As initial condition the zones were filled with the same amount of SVV per volume like in the experiments. Then a new constitutive model had to be added to MISES III to calculate the effects of the changes in chemistry on the mechanical and hydraulic properties of SVV.

In the first step, two extreme cases of lab experiments are simulated. The first case assumes that the saturation is much faster than the chemical reactions. So all brine put in by one step, is spread equally among all zones of SVV body (instantaneous flooding). Therefore the model used in this case is a plane strain model with only one square zone of 1 m × 1 m and a total volume of 1 m^3.

The second case assumes that the chemical reactions take place before the brine passes through a zone. To keep the system straightforward a plane strain model with 20 square zones of 1 m × 1 m in a row with a total volume of 20 m^3 is used (Fig. 4). All brine is put step by step into the first zone. Every step the equilibrium in a zone is calculated and then the liquid phase passed to the next zone. In this way all 20 zones are processed for each time step (compare Fig. 4). So the hydration process is highly inhomogeneous because through the first zone flows all brine while the last zone gets the first water when all other zones are flooded.

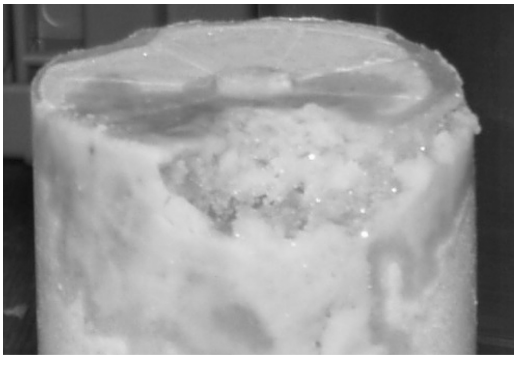

Figure 3. Photo of a sample zoomed on the area of the inlet.

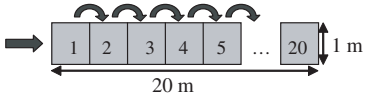

Figure 4. Schematic diagram of the second model to show how brine passes from one to another zone.

3 RESULTS

3.1 *Principal reactions*

Upon contact with aqueous NaCl solution anhydrous $MgSO_4$ dissolves and other mineral phases are precipitated. Figure 5 gives an overview.

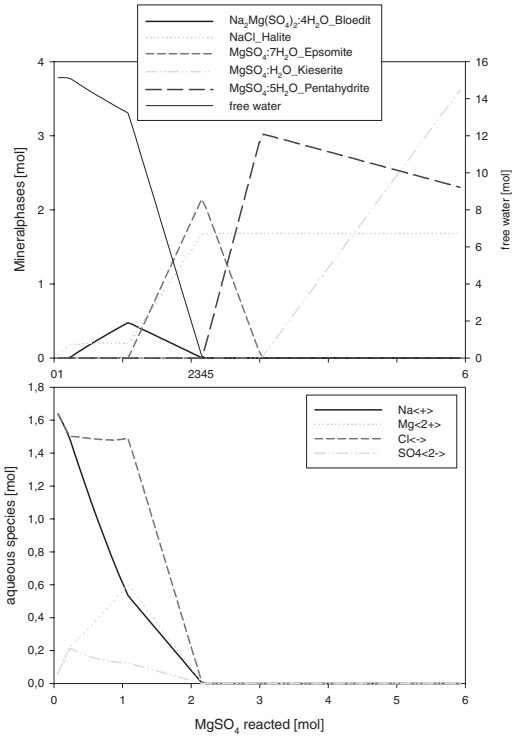

Figure 5. Development of mineral phases and solution composition depending on the reacted amount of $MgSO_4$.

To give an impression of chemical reactions within the sample, a model calculation was performed. It was assumed that a fixed mass of saturated NaCl solution is reacted with an increasing mass of anhydrous $MgSO_4$. This calculation was performed with the same database as those for reactive transport modelling with MISES III.

At the beginning anhydrous $MgSO_4$ dissolves, giving rise to NaCl precipitation. The dissolution of $MgSO_4$ can be observed from a visual inspection of the samples. The dissolved mass of Mg increases and leads to the saturation of bloedite. It is only with the beginning of bloedite precipitation that free water is removed from solution.

With the beginning of bloedite precipitation, Na as well is removed from solution. Any mol of sulphate introduced leads to the removal of 2 mol sulphate as bloedite. Therefore, in this phase, mass of sulphate in solution decreases in spite of continuous addition of $MgSO_4$. To the contrary Mg increases as for any two mol Mg only one Mol is removed from solution as bloedite.

Eventually, Mg content in solution attains a value where $MgSO_4$ heptahydrate (epsomite) is saturated. With the beginning of epsomite precipitation bloedite dissolves, releasing Na to the solution. This in turn leads to simultaneous precipitation of halite (NaCl). Furthermore, free water is being removed more rapidly from solution.

Accepting the experimental values for saturated NaCl solution having reacted with anhydrous $MgSO_4$, about 2 Mol anhydrous $MgSO_4$ are necessary to remove free water from the system altogether. As the hydrates of $MgSO_4$ exhibit a higher specific volume as anhydrous $MgSO_4$ the reaction volume is positive giving rise to a decrease of porosity and a crystallisation pressure.

This calculation does not give an exact image of the processes taking place within the sample. While epsomite precipitation is possible in principle, other hydrates with less crystal water dominate because anhydrous $MgSO_4$ in relation to the available pore volume of saturated NaCl – solution is in excess. The various hydrates form according to local equilibrium conditions, e.g. in a single pore, which might not reflect a hypothetical overall state of equilibrium which would evolve when the entire sample could react with the solution instantaneous. In reality, however, transport processes within the sample will be such as to draw near to an overall state of equilibrium, which under the given conditions of temperature and pressure is defined by the masses of NaCl, $MgSO_4$ and H_2O which constitute the sample. It is therefore hypothesized that, upon curing, water is still being transported within the sample, converting unreacted $MgSO_4$ to various hydrates. This hypothesis is supported by a recent publication where experiments are reported which document the exchange of water between different $MgSO_4$-hydrates through the gas phase (Chipera & Vaniman 2007).

Another point to be kept in mind is reaction kinetics. Locally, Mg chlorides instead of Mg sulphates might form giving rise to Na_2SO_4 (thenardite) – formation elsewhere, which is not predicted by thermodynamic equilibrium modelling. It is further known that pentahydrite forms more rapidly as does kieserite leading to metastable conditions where pentahydrite prevails while kieserite should actually be stable.

3.2 *Triaxial compression tests*

Exemplarily, the result of a short time compression test is shown in Figure 6 . The dilatancy boundary is about 25 MPa and the failure strength about 82 MPa. Compared with rock salt these values are much higher. The deformability instead is below 1% before failure much smaller than that of rock salt.

In Figure 7 the changes of normalised ultrasonic p-wave velocities through the sample are shown. The subsequent dilatancy boundary with a value about 60 MPa differs quite from the value about 25 MPa, determined by the volumetric strain. One possible

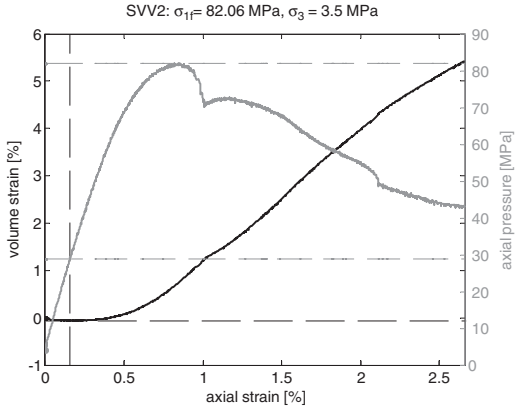

Figure 6. Results of a triaxial strength test of SSV ($\sigma_c = 3.5$ MPa): Stress and volumetric strain curves vs. axial strain (Note that the values for the dilatancy onset and failure strength are indicated).

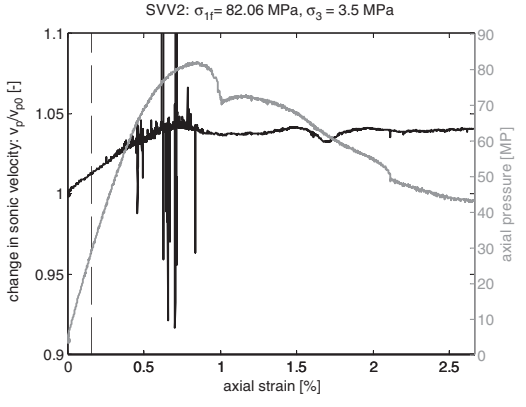

Figure 7. Stress–strain curve of the same test in Figure 6 and changes of normalized p-wave velocities vs. axial strain.

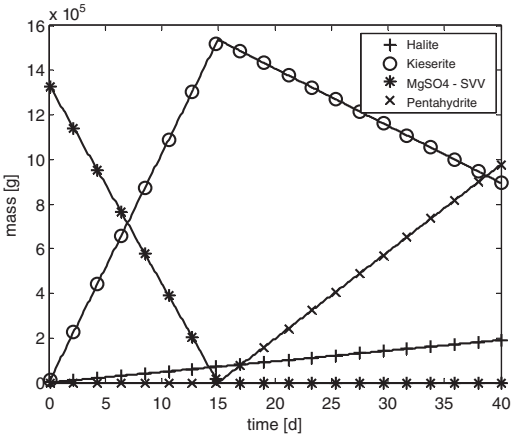

Figure 8. Development of mineral phases during the cure process (Case 1).

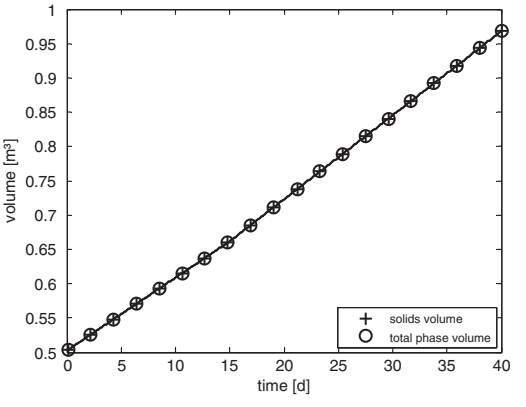

Figure 9. Volume of the different phases during the flooding (Case 1: model volume of 1 m^3 and an initial porosity of 50%).

reason could be material damages caused by the high compressive force to press the SVV samples out of the cell before triaxial tests. Consequently, further research works should be done to explain why the measured dilatancy boundaries are so different using different methods.

3.3 *Simulation results*

The numerical models describe the curing process during the injection of solution. The resulting phase composition during the flooding of model 1 can be seen in Figure 8. Because of clarity not all considered phases are displayed but only those which are actually formed during the calculation. So there are only four different phases existing: halite (NaCl), SVV ($MgSO_4$), kieserite ($MgSO_4 \cdot H_2O$) and pentahydrite ($MgSO_4 \cdot 5H_2O$). The total water is, as expected, being converted into crystal water, first into kieserite, then into pentahydrite. Because of the water being absorbed, NaCl is precipitating. The result is an increase of solid phase volume from 0.5 m^3 at the beginning, corresponding to the model volume of 1 m^3 and a starting porosity of 50%, to 0.97 m^3, as displayed in Figure 9. But the solid phase volume doesn't exceed the total volume of 1 m^3, so the porosity is being reduced from 50% to about 3% and there is no crystallisation pressure.

A view on Figure 10 shows that the phase composition, calculated in case 2 for the first zone, is quite different from the one calculated in case 1.

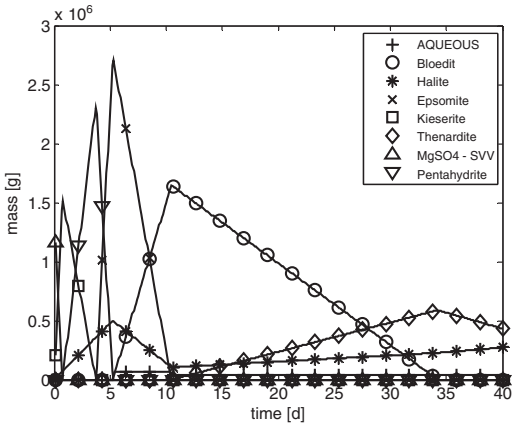

Figure 10. Development of the different phases during the flooding in the first element (Case 2).

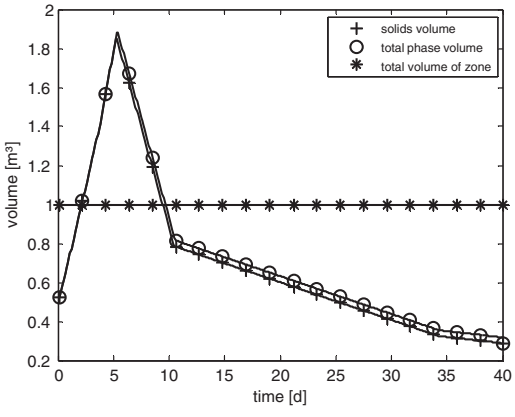

Figure 11. Volume development of the first zone of the 20 zones over 40 days (Case 2).

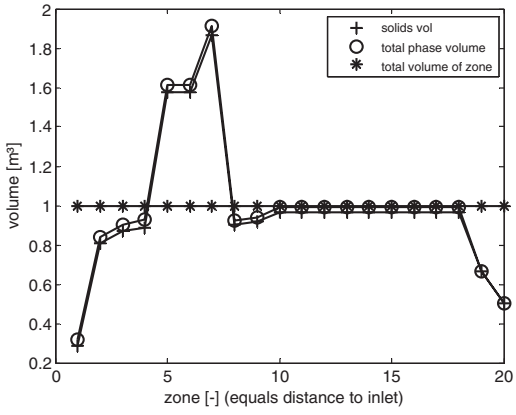

Figure 12. Final volumes of the 20 zones after the cure process (Case 2).

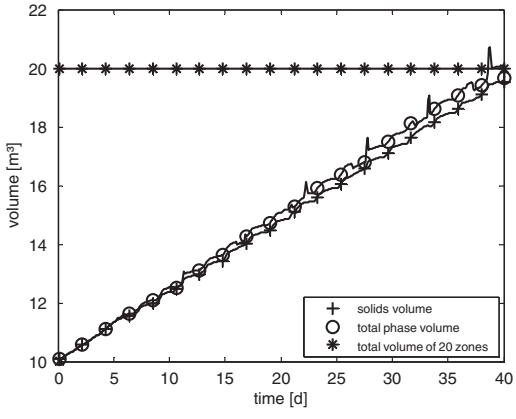

Figure 13. Development of the added volume of all 20 zones (Case 2).

First the water is bound by SVV to form kieserite, then to pentahydrite and then to heptahydrate. When all SVV material is transformed to heptahydrate, the maximum amount of water, which can be bound, is reached. From this point on no more water can be bound and, therefore, a free fluid phase exists. After this point further phases are occurring, like bloedite or thenardite and the precipitated NaCl is also declining, because of dissolving and being transported to the next zone.

From the phase masses shown in Figure 10 the trend of the volume in the first zone, displayed in Figure 11 can be seen. Till day five the volume increases constantly up to 1.88 m^3. This is the point, where all $MgSO_4$ has bound seven water molecules. From then on the volume decreases rapidly to about 0.8 m^3 and then slower till 0.29 m^3. At the end of 40 d the volume of the first element is even smaller than the primary volume at the beginning of lab experiments. But this is only the first zone. Figure 12 shows the end volume after 40 d of all 20 zones. The increasing volume differs quite between the different zones. The first four and the last two zones have quite small volumes, the zone eight till 18 have almost 1 m^3 volume and only the zones five, six and seven have a much bigger volume than 1 m^3. So the final volume between the different zones differs quite a lot, and is strong inhomogeneous. But interesting is especially the total volume of all elements. Its development can be seen in Figure 13. After 40 days it slightly exceeds 20 m^3 marginal with 1%. The different volume of the zones depends on their different phase composition. A picture with the different phases is Figure 14. The first part consists of bloedit,

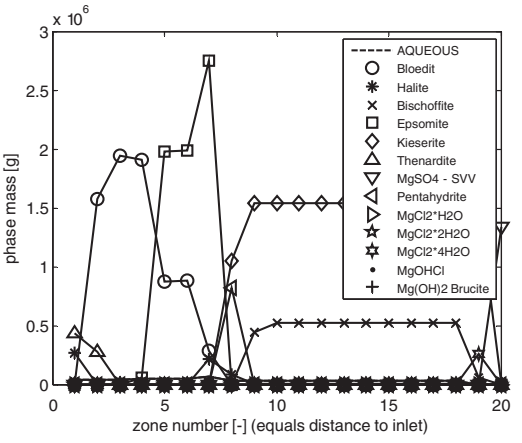

Figure 14. Phase arrangement after the cure process in the different zones (Case 2).

followed by epsomite. The second half is dominated by kieserite and minor contributions of bischoffite and anhydrous $MgSO_4$ in the last zone.

4 CONCLUSIONS

The mechanical properties of SVV with a high stiffness and low deformability, show promise for a suitable sealing material.

Both numerical simulation cases represent two extreme situations and rely to an ideal mixture of brine and SVV. The real situation must be between the simulated two cases. Nevertheless several observations from the tests can be simulated by case 2. In the experiments there is a soft area around the inlet (compare Fig. 3). This coincides with the simulated volume distribution of the different zones (compare Fig. 12). The allocation of the phase composition in the different zones agrees somehow with measurements, too. E.g. bloedite was measured only near the inlet, but never at the outlet (compare Fig. 14). These results from case 2 are much more promising than the ones of case 1. So in future the main aspects will be on simulations similar to case 2. The final numerical model will be able to proof the safety case and functionality of a dam system in underground repositories with SVV as sealing material and the interactions between the excavations damaged zone and dam.

ACKNOWLEDGEMENT

The results presented in this paper were obtained in the frame of the running joined project 02C1275/02C1285 financed by the German ministry for Education and Research (BMBF).

REFERENCES

Chipera, S.J. & Vaniman, D.T. 2007. Experimental stability of magnesium sulfate hydrates that may be present on Mars. *Geochim. Cosmochim. Acta* (71), No. 1: 241–250.

Eriksson, G. & Hack, K. 1990. ChemSage – A Computer Program for the Calculation of Complex Chemical Equilibria. *Metallurgical Transactions B* (21B): 1013.

Eriksson, G. & Sippola, H. & Sundman, B. 1994. A Proposal for a General Thermodynamic Software Interface. *In A. Jokilaakso, Proceedings of the Colloquium on Process Simulation*: 67–103, Report TKK-V-B99.174.

Eriksson, G. & Spencer, P.J. & Sippola, H. 1995. A General Thermodynamic Software Interface. *In A. Jokilaakso, Proceedings of the 2nd Colloquium on Process Simulation:* 113, Report TKK-V-B104.

Fein, E. et al. 1996. Ableitung einer Permeabilitäts – Porositätsbeziehung für Salzgrus und Dammbaumaterialien. *GRS – Bericht 132*.

Hein, H.-J. 1991. Ein Stoffgesetz zur Beschreibung des thermomechanischen Verhaltens von Salzgranulat, *Dissertation an der RWTH Aachen.*

Herbert, H.-J. 2007. Self Sealing Backfill (SVV) – A salt based material for sealing constructions in salt mining. In K.-H. Lux, W. Minkley, M. Wallner & H.R. Hardy, Jr. (ed.), *Basic and Applied Salt Mechanics; Proc. of the Sixth Conf. on the Mechanical Behavior of Salt (MECASALT VI)*, Hannover, May 2007. Rotterdam: Balkema.

H.-J. Herbert & H.C. Moog, 2002. *Untersuchungen zur Quellung von Bentoniten in hochsalinaren Lösungen, Gesellschaft für Anlagen – und Reaktorsicherheit mbH.* Abschlußbericht zum Vorhaben 02 E 8986 5. ISBN 3-931995-47-X.

Hou, Z. 1997. *Untersuchungen zum Nachweis der Standsicherheit für Untertagedeponien im Salzgebirge. Dissertation an der TU-Clausthal.* Clausthal – Zellerfeld: Papierflieger Verlag.

Hou, Z. 2002. *Geomechanische Planungskonzepte für untertägige Tragwerke mit besonderer Berücksichtigung von Gefügeschädigung, Verheilung und hydrome – chanischer Kopplung. Habilitationsschrift an der TU Clausthal.* Clausthal – Zellerfeld: Papierflieger Verlag.

Hou, Z. & Lux, K.-H. 1998. Ein neues Stoffmodell für duktile Salzgesteine mit Einbeziehung von Gefügeschädigung und tertiärem Kriechen auf der Grundlage der Continuum – Damage – Mechanik. *Geotechnik* (21) Nr. 3.

Korthaus, E. 1998. Experiments on Crushed Salt Consolidation with True Triaxial Testing Device as a Contribution to an EC – Benchmark Exercise (FZKA 6181). Forschungszentrum Karlsruhe.

Mariner, P. 2005. In-Drift Precipitates/Salt Model ANL-EBS-MD-000045 REV 02. At the time of preparing this document, this source was available under *http://www.osti.gov/bridge/servlets/purl/840433-C0aewk/native/840433.pdf.*

Müller – Lyda, I. & Fein, E. 1999. Zusammenhang von Permeabilität und Porosität von Salzgrus. *Workshop des Bundesamtes für Strahlenschutz und des Projektträgers*

Entsorgung über „Eigenschaften von Salzgrus als Versatzmaterial im Wirtsgestein Salz“, 18. und 19. Mai 1999 im BfS, Salzgitter.

Pfeifle 1990. Consolidation, Permeability and Strength of Salt/Bentonite Mixtures with Application to the WIPP. *SAND 90 – 7009*. Sandia National Laboratories.

Sjaardema, G.D. & Krieg, R.D. 1987. A Constitutive Model for the Consolidation of WIPP Crushed Salt and Its Use in Analyses of Backfilled Shaft and Drift Configurations. *SAND87 – 1977*UC – 70*. Sandia National Laboratories.

Stührenberg, D. & Zhang, C. 1996. Kompaktionsverhalten von trockenem Salzgrus, BGR Hannover. *Kali und Steinsalz*, Band 12 (Heft 3).

Zhang, C. & Schmidt, M.W. & Staupendahl, G. & Heemann, U. 1993. Entwicklung eines Stoffansatzes zur Beschreibung des Kompaktionsverhaltens von Salzgrus. *Bericht Nr. 93 – 73 des Instituts für Statik der Technischen Universität Braunschweig, gemeinsame Veröffentlichung mit dem GSF – Institut für Tieflagerung Braunschweig.*

The Mechanical Behavior of Salt – Understanding of THMC Processes in Salt –
Wallner, Lux, Minkley & Hardy, Jr. (eds)
© 2007 Taylor & Francis Group, London, ISBN 978-0-415-44398-2

Reactive transport modelling in salt material based on Gibbs energy minimization

Mingliang Xie[1], Helge C. Moog[2], Wenqing Wang[1], Horst-Jürgen Herbert[2],
Hua Shao[3] & Olaf Kolditz[1]
[1] *GeoSystemsResearch, ZAG, University of Tübingen, Tübingen, Germany*
[2] *GRS, Theodor Heuss Str: 4, Braunschweig, Germany*
[3] *BGR, Germany*

ABSTRACT: The German concept for the geological disposal of high level radioactive waste (HLW) considers salt formations as a suitable host rock for underground repositories. To prevent aqueous solution from accessing waste containments, these need to be sealed off with a material compatible to the host rock. One candidate material for this purpose is anhydrous salt which upon contact with aqueous solution forms hydrates with higher specific volumes thereby closing flow paths. This paper presents a new model to deal with reactive transport in a high-saline environment. It covers conditions where all accessible pores are filled with solution as well as conditions where no aqueous solution is present at all. This paper reports about the conceptual model and provides demonstration test cases.

1 INTRODUCTION

Salt rock is considered to be one of the potential bed rock for high level radioactive waste (HLW) repositories. This is because of the fact that salt rocks are isolated from fresh water system and thus indicates stable and isolated geological and hydrogeological conditions. The permeability of salt rock is very low. The plastic-viscoplastic properties enables the salt rock to self-seal EDZ. Such effect can be enhanced owing to the heat generation of the HLW-canisters.

The free water content in salt rock is very low. Crystal water, however, can exist to some extent. During excavation, e.g. construction of the room and draft system, and during emplacement of the waste (i.e. operation period), and even after the enclosed period, water/vapor can be released to the EDZ and absorbed by salt and exist as crystal water. Heat generated by nuclear waste canister can even dehydrate the salt rock in the pore system and transport the vapor into the surrounding rock. Hydration or crystallization can change the volume of the minerals and consequently the pore system and/or pressure under constrained condition.

Consider progress has been made in the past decade in modelling reactive transport in nature systems (Noorishad et al. 1987), (Yeh and Tripathi 1991), (Lichtner 1988), (Steefel and MacQuarrie 1996), (Parkhurst and Appelo 1999), (Xuand Pruess 2001), (Hummel et al. 2002), (Xie et al. 2006). Numerically, three major approaches have been used to couple multi-species transport and geochemical reactions: global implicit approach, sequential non-iterative approach (SNIA) and sequential iterative approach (SIA). Two major approaches have been achieved in chemistry, chemical engineering and geochemistry: the law of mass action and the free energy minimization technics (GEM). The geochemical reactions of most reactive transport approaches are based on the law of mass action for groundwater system, which is difficult for the simulation of complex geochemical reactions like redox reactions. This is owing to the fact that most of the equations of geochemical reactions which appear in equilibrium systems are nonlinear. Free energy minimization technics (GEM) is a more robust numerical method, which is widely developed in chemistry, chemical engineering (Steefel and MacQuarrie 1996). However, GEM is rarely used in reactive transport codes.

This paper provides a new reactive transport model that coupled a chemical simulator ChemApp (Eriksson et al. 1996) based on GEM into the transport code GeoSys/RockFlow. It is verified against the coupling of GeoSys/RockFlow with PHREEQC based on the law of mass action and applied to simulate the complex coupled thermo-hydro-chemical (THC) processes for HLW repositories in salt rock.

2 CONCEPTUAL MODEL

The new reactive transport model is developed for fully or partially saturated porous media where the aqueous and/or gaseous phases are considered mobile, while the solid phases are considered immobile.

2.1 *General equations for flow process*

The general mass balance equation of fluid phase in undeformable porous media can be derived:

$$\frac{\partial(nS^\gamma\rho^\gamma)}{\partial t} + \nabla \cdot \mathbf{q}_f^\gamma = Q_f^\gamma \tag{1}$$

where n is the effective porosity, γ specifies gaseous or aqueous phase, S^γ and ρ^γ are the saturation and density of phase γ respectively, Q_f^γ denotes source/sink terms, $\mathbf{q}_f^\gamma$ is the fluid flux defined with the classic Darcy's law as:

$$\mathbf{q}_f^\gamma = -nS^\gamma[\frac{k_{rel}^\gamma \mathbf{k}}{\mu^\gamma}(\nabla p^\gamma - \rho^\gamma \mathbf{g})] \tag{2}$$

where $\mathbf{k}$ is the intrinsic permeability tensor, k_{rel}^γ is the relative permeability, and μ is the fluid viscosity.

If it is fully saturated, $S^\gamma = 1$ and $k_{rel}^\gamma = 1$.

2.2 *Equations for heat transport process*

The general governing equation for heat transport is:

$$\sum_{\gamma=1}^{phases} (\rho^\gamma C_p^\gamma)\frac{\partial T}{\partial t} - \nabla \mathbf{q}_\mathrm{T} = Q_\mathrm{T} \tag{3}$$

where C_p^γ is the specific heat capacity of fluid phase γ, T is temperature, Q_T is the heat source term, $\mathbf{q}_\mathrm{T}$ is the heat flux derived by:

$$\mathbf{q}_\mathrm{T} = -\lambda \nabla T + n \sum_{\gamma=1}^{phases} (\rho^\gamma C_p^\gamma) T \mathbf{v}^\gamma \tag{4}$$

where λ is the heat conductivity, $\mathbf{v}^\gamma$ is fluid phase velocity.

2.3 *Multicomponent transport*

The balance equation for multicomponent mass transport in porous media is given by e.g. (Bear 88):

$$\begin{aligned} nS^\gamma \frac{\partial C_i^\gamma}{\partial t} &= -v^\gamma \nabla C_i^\gamma + \nabla(nS^\gamma D_i^\gamma \nabla C_i^\gamma) \\ &+ nS^\gamma Q_i^\gamma + nS^\gamma \Gamma_i^\gamma (C_1^\gamma ... C_m^\gamma) \end{aligned} \tag{5}$$

where C_i^γ is the concentration of the i-th species of a m multi-species system in phase γ, v^γ is the Darcy velocity of phase γ, D_i^γ is the diffusion – dispersion coefficient of component i in phase γ, Q_i^γ is the source/sink term and $\Gamma_i^\gamma(C_1^\gamma \ldots C_m^\gamma)$ is the source/sink term of species i in phase γ due to temperature dependent equilibrium chemical reactions with all other species in the same phase.

2.4 *Gibbs energy minimization*

The Gibbs energy minimization methods use mass balance as a constraint and adjust the amount of each species of a system to reach the minimal total Gibbs free energy of the defined system:

$$dG_{T,p} = 0 \tag{6}$$

$$G_{T,p} = \sum_{i=1}^{N_{tot}} \mu_i n_i \tag{7}$$

ChemApp is a programmer's library based on the Gibbs free energy minimization technique developed by (Eriksson et al. 1996). It consists of a rich set of subroutines, which provides almost all the necessary tools for the calculation of complex multicomponent, multiphase chemical equilibria and the determination of the associated energy balances.

2.5 *Coupling scheme*

The object-oriented program GeoSys/RockFlow was adopted to solve the system of coupled processes. The coupling processes are schematically described in Figure 1. Time is discretized using Euler scheme, spatial discretization is by the Finite Element Method (FEM). For each timestep, flow and heat transport are calculated. Because these two processes are strongly coupled, the program iterates between them. Reactive mass transport is separated using an operator splitting technique and a two-step non-iterative sequential approach. In the first step, conservative transport is calculated for all chemical components based on the phase velocities calculated for two-phase flow, while in the second step the geochemical reactions are simulated. In this work, transport and reactions are calculated only in the liquid phase. For the reaction step, the geochemical simulator ChemApp (Eriksson et al 1996) is employed, which calculates the geochemical reactions accounting for the temperature dependence of the reaction coefficients. The GeoSys/RockFlow simulator is designed using object-oriented and process-oriented methods, which allows the coupling of two-phase flow, heat transport, mass transport, chemical reactions and deformation in an efficient way (Wang and Kolditz 2006).

2.6 *Numerical method*

The Galerkin finite element method was applied to solve the weak forms of all the governing equations

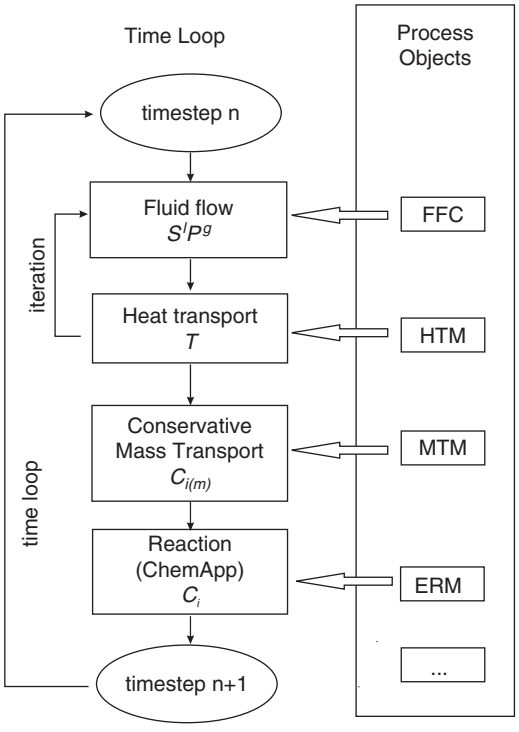

Figure 1. Schematic representation of the coupling concept used in GeoSys/RockFlow.

described above in this section. Owing to the fact that similar types of partial differential equations (PDEs) for diverse physical problems differ only in material coefficients, element class and objects were developed by (Wang and Kolditz 2006) and applied to deal with the local element matrices and vectors arising from the finite element discretization of the PDEs. These element functions are thus able to deal with different element types (lines, triangles, quadrilaterals, tetrahedra, prims, hexahedra) by automatically choosing the related element interpolation functions. Therefore, the new reactive transport model can be used for 1D, 2D and 3D problems.

3 EXAMPLES

Two examples are provided in the following sections. The first example is a 1D benchmark test in the literature for the verification of the new reactive transport model. The second example is a 2D test example based on a planned laboratory experiment to demonstrate the capability of the model. This first calculation concentrates on the reactive transport process and serves as experiment design and shows the capability for simulate geochemical reactions with little or even no water conditions. The coupling effect of chemical process on the transport is currently under code development.

3.1 *1D benchmark test*

A 1D Transport and calcite dissolution case was adopted to verify the coupling. This test example was proposed by (Engesgaard and Kipp 1992) for a model verification of their MST1D code against the CHEMTRNS model by (Noorishad et al. 1987). It was later on used by (Prommer 2002) to verify PHT3D. The one-dimensional model domain was 0.5 m long and composed of porous media with porosity of 0.32, bulk density 1800 kg/m^3. The pore water was initially in equilibrium with calcite ($2.176 \times 10^{-5}\, mol/kg$ of soil). This sample was successively flushed by 0.001 M $MgCl_2$ solution from one end, leading to multiple precipitation/dissolution fronts. Dolomite was not present initially but formed temporally. Thermodynamic database used is based on the NAGRA/PSI database (Hummel et al. 2002).

The simulated results are shown in Figures 2–4. The results agree well with each other. The simulated pH values differ slightly with that by PHT3D. However, by comparison with the results presented in (Engesgaard and Kipp 1992), the results obtained by GeoSys/RockFlow+CHEMAPP are closer.

3.2 *2D column test*

3.2.1 *Test description*

To isolate hazardous waste in salt rock formations a sealing material is needed which is geochemically stable on long-term time scale and which upon contact with aqueous solution, which under the given conditions is bound to be saturated with NaCl, reacts such as to form a low-permeable barrier. To study this, granular anhydrous $MgSO_4$ was placed inside a cylindrically shaped containment and percolated with saturated, dyed NaCl-solution. After saturation the containments are closed and the samples are allowed to equilibrate for several weeks. Afterwards, samples were partitioned and each part characterized both visually and by X-Ray diffractometry.

3.2.2 *Geochemical reactions*

Chemical reactions within a sample of percolated $MgSO_4$ have been investigated both experimentally and theoretically with reactive transport modelling. They are identical to those described in another paper submitted to this proceedings (Werunsky et al. 2007). The possible mineral/water interactions in the system are briefly described in the equations (9–14). The molar volumes of each minerals are listed in Table 1. It is clear to see that the molar volume of each mineral increases with the number of the crystal water molecules in the mineral. The molar volume

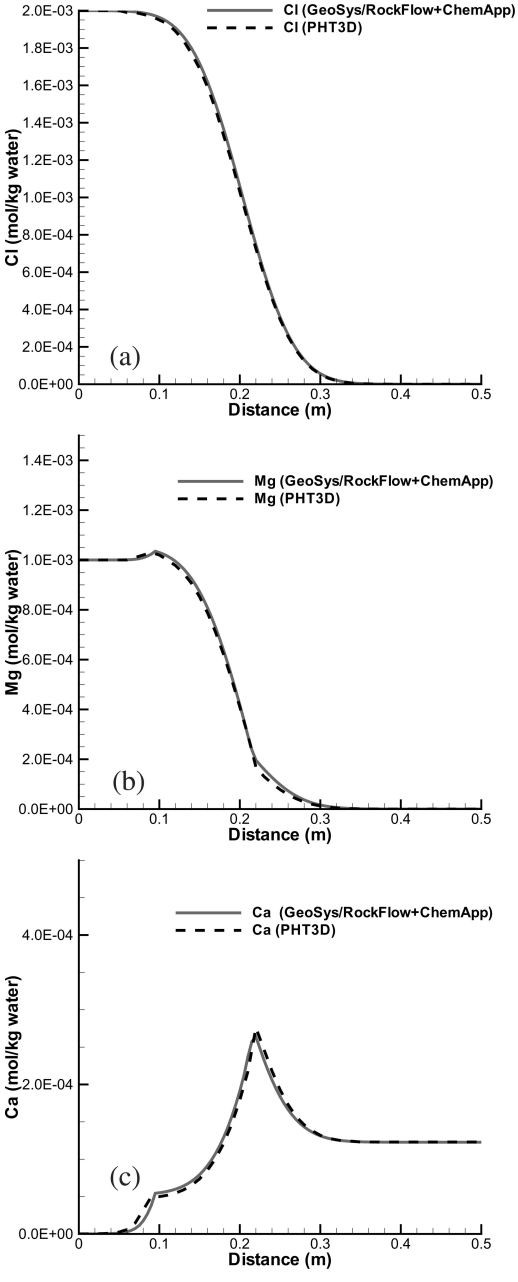

Figure 2. Comparison of simulated ionic concentrations.

of Epsomite is over 3 times of that of $MgSO_4$_OW. With the intrusion of *NaCl* saturated solution, $MgSO_4$ powder starts to react with water and is converted into minerals with higher molar volume such as Kieserite, Pentahydrite and Epsomite. Therefore, the volume of solid material increases. Water in the *NaCl* solution is consummated and Halite precipitates. Under

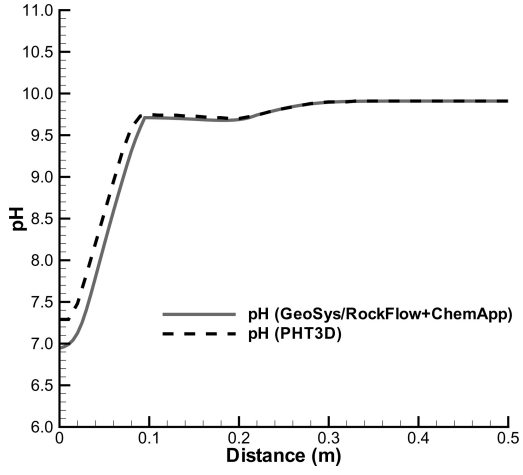

Figure 3. Comparison of simulated pH value.

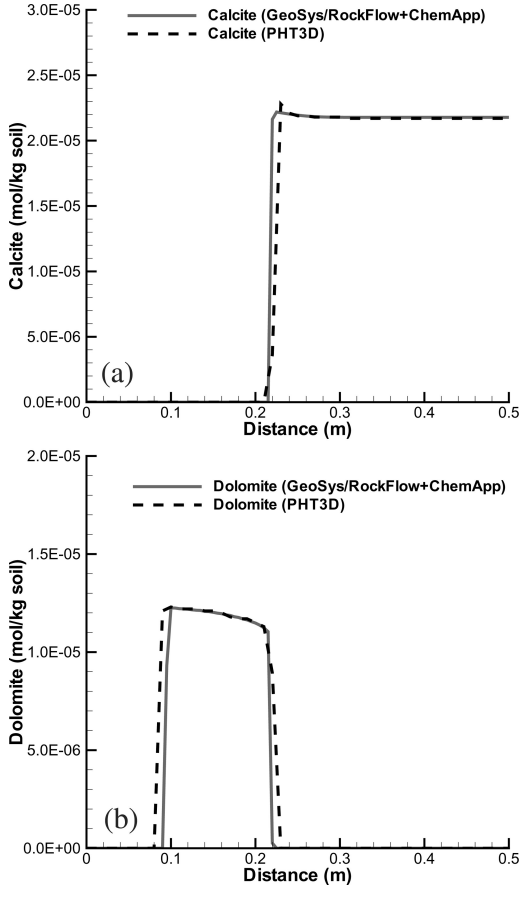

Figure 4. Comparison of simulated minerals Calcite and Dolomite.

Table 1. Molar volume of minerals.

Mineral	Chemical formulae	Molar vol. (cm^3/mol)
Bloedit	$Na_2Mg(SO_4)_2 : 4H_2O$	149.98
$MgSO_4$_OW	$MgSO_4$	45.25
Kieserite	$MgSO_4 : H_2O$	56.60
Pentahydrite	$MgSO_4 : 5H_2O$	110.76
Epsomite	$MgSO_4 : 7H_2O$	146.80
Halite	$NaCl$	27.02
Thenardite	Na_2SO_4	53.33

constrained conditions, the porosity of the sample decreases and permeability decreases.

Thermodyamic equilibrium between mineral phases and aqueous solution in the system $NaCl - MgSO_4 - H_2O$ were calculated using the Pitzer model (Pitzer 1973), (Pitzer and Kim 1974), (Pitzer 1975), (Pitzer 1991). The respective Pitzer parameters were taken from Mariner (Mariner 2005). Hence, solid phase composition and composition of aqueous solution can be calculated for arbitrary system compositions in terms of $Na^+, Cl^-, Mg^{2+}, SO_4^{2-}$, and H_2O. Density of solution and specific volumes of all mineral phases evaluated. While the data allow for calculations at temperatures up to 200°C, the presented test case was calculated for the standard temperature 25°C only.

$$Na_2Mg(SO_4)_2 : 4H_2O \longrightarrow Mg^{2+} + 2Na^+ + 2{SO_4}^{2-} + 4H_2O \quad (8)$$

$$MgSO_4 \longrightarrow Mg^{2+} + {SO_4}^{2-} \quad (9)$$

$$MgSO_4 : H_2O \longrightarrow Mg^{2+} + {SO_4}^{2-} + H_2O \quad (10)$$

$$MgSO_4 : 5H_2O \longrightarrow Mg^{2+} + {SO_4}^{2-} + 5H_2O \quad (11)$$

$$MgSO_4 : 7H_2O \longrightarrow Mg^{2+} + {SO_4}^{2-} + 7H_2O \quad (12)$$

$$NaCl \longrightarrow Na^+ + Cl^- \quad (13)$$

$$Na_2SO_4 \longrightarrow 2Na^+ + {SO_4}^{2-} \quad (14)$$

3.2.3 *Model setup*

The simplified 2D model setup for the numerical simulation of the reactive transport processes is shown in Figure 5. Standard temperature and pressure are assumed to be unchanged during the simulation. Owing to the fact that the sample is very porous, the porosity is 0.502 and permeability (initial permeability is given as $1.0 \times 10^{-10}\ m^2$) is very high at the beginning, salt water is thus very easy to flow through the sample even under very low liquid pressure. Therefore, saturated condition was given for first step for

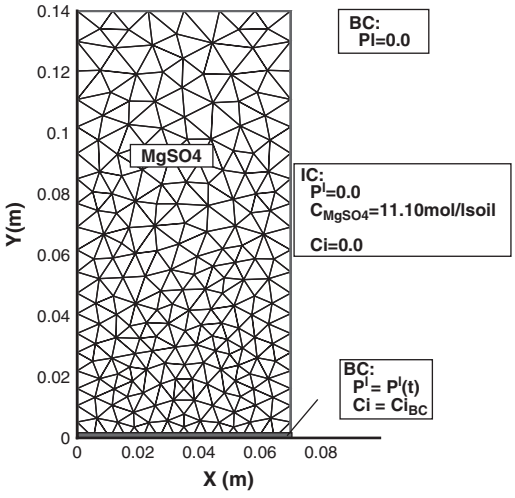

Figure 5. Geometry and model setup.

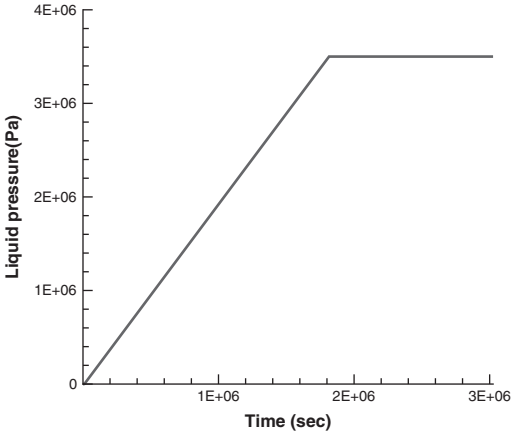

Figure 6. Time curve of liquid pressure on the bottom.

the simulation. The initial conditions (IC) are: liquid pressure (P^l) is equal to 0.0 for the whole sample, the mineral abundance of $MgSO_4$_OW is 11.10 mol/l soil, all of the other chemical species are set to be 0.0. Saturated $NaCl$ solution (Na^+ and Cl^- in 6.1672 M, H^+ and OH^- in 5.07×10^{-8} M) is injected from the bottom with an increasing liquid pressure over time (Figure 6) and given as boundary conditions (BC).

3.2.4 *Simulated results*

At the beginning anhydrous $MgSO_4$ dissolves, giving rise to NaCl-precipitation. The dissolution of $MgSO_4$ can be observed from a visual inspection of the samples. Mineral phases formed during penetration of anhydrous $MgSO_4$ with saturated NaCl-solution are $Na_2Mg(SO_4)2*4H_2O$ (Bloedite), $MgSO_4*4H_2O$

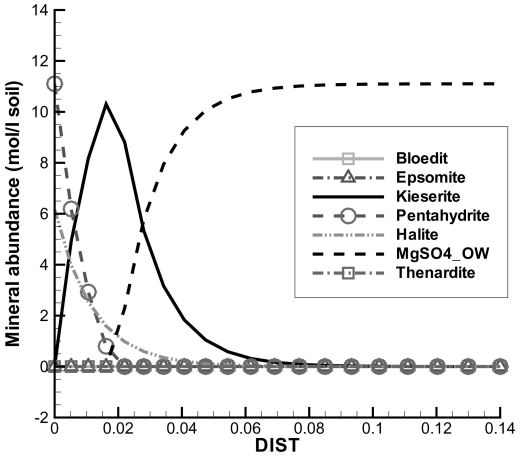

Figure 7. Simulated results of mineral abundances at 5.4×10^2 sec.

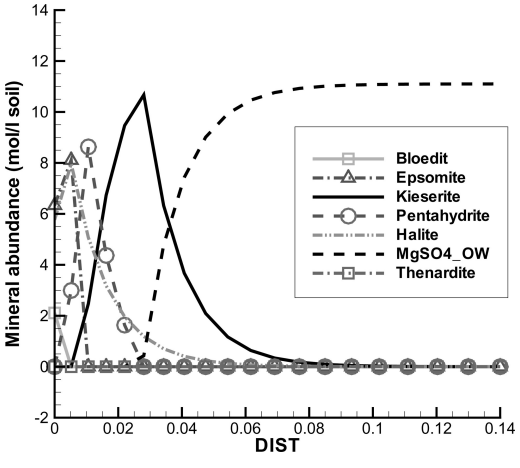

Figure 8. Simulated results of mineral abundances at 1.1×10^3 sec.

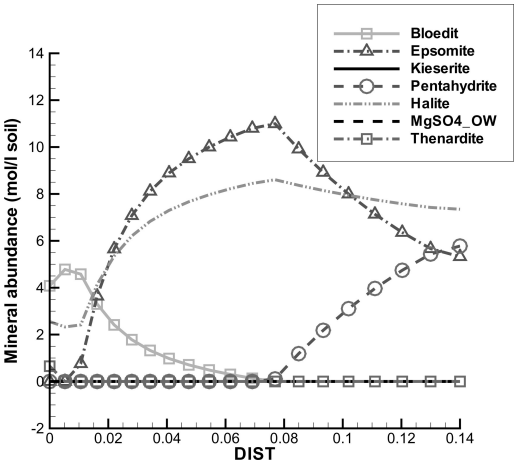

Figure 9. Simulated results of mineral abundances at 1.1×10^4 sec.

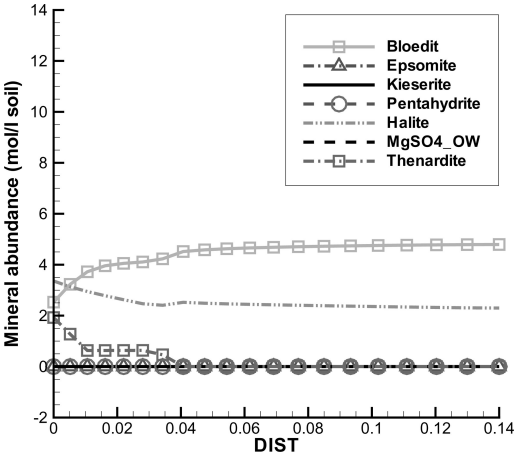

Figure 10. Simulated results of mineral abundances at 1.1×10^6 sec.

(Starkeyite), and $MgSO_4$*$5H_2O$ (Pentahydrite). Unreacted anhydrous $MgSO_4$ as well as NaCl (Halite) are also observed. After a curing time of several weeks, a quasi homogenous distribution of all these phases within the sample is attained. However, preferential pathways evolve along which pure NaCl is encountered.

The simulated results of the 2D simplified example are shown by a cross section along the vertical axis in Figures 7–10. At the initial conditions, there was only $MgSO_4$ powder. After the intrusion of *NaCl* saturated solution, $MgSO_4$_OW was converted into Kieserite ($MgSO_4 : H_2O$) and later on into Pentahydrite($MgSO_4 : 5H_2O$) after 540 second. These reactions result in the decrease of water in the solution and thus halite precipitates (Figure 7).

With the further intrusion of NaCl saturated solutions, the above reactions continue. Further minerals like Epsomite ($MgSO_4 : 7H_2O$) and Bloedit ($Na_2Mg(SO_4)_2 : 4H_2O$) appear after the simulation time at 1.1×10^3 sec. $MgSO_4$_OW ($MgSO_4$) disappeared (Figure 8).

After the simulation time at 1.1×10^4 sec, mineral Kieserite disappeared also from the system and converted into Pentahydrite, Epsomite and Bloedit (Figure 9). The dominant minerals are thus Epsomite and Halite. Thenardite starts to appear from the bottom (left side in the figure) and increases with

further solution intrusion (Figure 10). As a consequence, the total volume of the solid minerals increases and the effective porosity as well as permeability decreases.

It is important to point out that the decreasing porosity and permeability reduces the flux. However, it is not considered in this calculations yet. Therefore, the simulated flux is much higher than experimental value, which will be considered in the next phase. Nevertheless, this calculation provides the possible reactions in such geochemical system, which gives instructions for the design of further experiments.

4 CONCLUSIONS AND OUTLOOK

A new reactive transport model is developed by coupling the thermodynamic chemical simulator ChemApp into the OOP software GeoSys/RockFlow. ChemApp is based on the Gibbs energy minimization technique and thus is quite suitable for geochemical reaction calculation under extreme conditions such as high salinity, no water, high pressure and high temperature conditions etc.

The model is verified by a 1D benchmark test example and shows good agreement with other codes based on the law of mass action. This indicates that codes based on thermodynamical geochemistry or law of mass action can reach the same result if the database are properly constructed.

Another example to demonstrate the capability of the model is conducted to simulate on-going experiments on salt material. Qualitatively, the reactions with no water at the initial condition and later on with the intrusion of *NaCl* saturated solutions are reasonable. Upon reaction of saturated NaCl-solution $MgSO_4$-hydrates are formed whose molar volumes are higher than that of anhydrous $MgSO_4$. This leads to a closure of pore space and eventually to low permeability and crystallization pressure. This renders the investigated material as potentially suited for the safe isolation of hazardous waste boreholes located in salt rock formations. Further work is to include the coupled effect of the reaction induced porosity and permeability changes and later on to the crystallization pressure simulation.

ACKNOWLEDGEMENT

The work is supported by German Federal Ministry of Education and Research (BMBF) under grant 02C1295 and 02C1285. The authors would like also to acknowledge DECOVALEX team especially Jens Birkholzer and Eric Sonnenthal (Lawrence Berkeley National Laboratory), PSI team (Dmitrii Kulik, Georg Kosakowski) for providing suggestions and very useful discussions to this research. Thanks also extend to Lothar Meyer (GRS), Zhengming HUO and Lei ZHOU (Technical University Clausthal). We thank Dr. Pitterich (FZK) for his support of this research work.

REFERENCES

Bear, J. (1988). *Dynamics of fluids in porous media* (2nd edition ed.). New York: Dover Publications Inc.

Engesgaard, P. and K. Kipp (1992). A geochemical transport model for redox-controlled movement of mineral fronts in groundwater flow systems: A case of nitrate removal by oxidation of pyrite. *Water Resour. Res. 28*, 2829–2843.

Eriksson, G., K. Hack, and S. Petersen (1996). ChemApp – A programmable thermodynamic calculation interface. In J.Hirsch (Ed.), *Werkstoff Woche '96, Symposium 8, Simulation, Modellierung, Informationssysteme.* DGM: Informationsgesellschaft-Verlag.

Hummel, W., U. Berner, E. Curti, F. Pearson. and T. Thoenen (2002). *NAGRA/PSI Thermochemical database 01/01.* Universal Publisher/uPublish.com.

Lichtner, P. (1988). The quasi-stationary state approximation to coupled mass transport and fluid-rock interaction in a porous medium. *Geochimica et Cosmochimica Acta 52*, 143–165.

Mariner, P. (2005, November). In-drift precipitates/salt model. Report ANL-EBS-MD-000045 REV 02, Bechtel SAIC Company, Las Vegas, Nevada. Prepared for: U.S. Department of Energy Office of Civilian Radioactive Waste Management Office of Repository Development.

Noorishad, J., C. Carnahan. and L. Benson (1987). Development of the non-equilibrium reactive chemical transport code CHEMTRNS. Report LBL-22361, Lawrence Berkeley Laboratory, University of California.

Parkhurst, D. and C. Appelo (1999). User's guide to PHREEQC (Version 2) - A computer program for speciation, batch-reaction, onedimensional transport, and inverse geochemical calculations. Report 99–4259, U.S. Geological Survey, Denver, Colorado.

Pitzer, K. (1973). Thermodynamics of electrolytes. 1. Theoretical basis and general equations. *Journal Physical Chemistry 77,* 268–277.

Pitzer, K. (1975). Thermodynamics of electrolytes. 5. Effects of higher-order electrostatic terms. *Journal Solution Chemistry 4,* 249–265.

Pitzer, K. (1991). *Activity Coefficients in Electrolyte Solutions* (2nd ed.). CRC Press.

Pitzer, K. and J. Kim (1974). Thermodynamics of electrolytes. 4. Activity and osmotic coefficients for mixed electrolytes. *Journal American Chemical Society 96,* 5701–5707.

Prommer, H. (2002). A reactive multicomponent transport model for saturated porous media. Draft of users manual version 1.0. Report, Contaminated land assessment and remediation research centre, the university of Edinburgh.

Steefel, C. and K. T. B. MacQuarrie (1996). Approches to modelling reactive transport in porous media. In P. C. Lichtner, C. I. Steefel, and E. H. Oelkers (Eds.), *Reactive transport in porous media,* Volume 34 of *Reviews in Mineralogy,* pp. 83–129. Mineralogical Society of America.

Wang, W. and O. Kolditz (2006). Object-oriented finite element analysis of thermo-hydromechanical (THM) problems in porous media. *International Journal for Numerical Methods in Engineering.*. DOI 10.1002/nme.1770.

Werunsky, F., Z. Hou. and H. C. Moog (2007). Coupled modelling of the C:HM behaviour of self healing salt based backfill. This issue. BGR: Balkema.

Xie, M., S. Bauer, O. Kolditz, T. Nowak. and H. Shao (2006). Numerical simulation of reactive processes in an experiment with partially saturated bentonite. *Journal of Contaminant Hydrology 83,* 122–147.

Xu, T. and K. Pruess (2001, January). Modeling multiphase non-isothermal fluid flow and reactive geochemical transport in variably saturated fractured rocks: 1. methodology. *American Journal of Science 301,* 16–33.

Yeh, G. and V. Tripathi (1991). A model for simulating transport of reactive multispecies components: model development and demonstration. *Water Resources Research 27*(12), 3075–3094.

The Mechanical Behavior of Salt – Understanding of THMC Processes in Salt –
Wallner, Lux, Minkley & Hardy, Jr. (eds)
© 2007 Taylor & Francis Group, London, ISBN 978-0-415-44398-2

Coupled modelling of physical/chemical retardation and transport of CO_2/CH_4 for a backfilled salt rock repository

H. Alkan & W. Müller
ISTec, Institut für Sicherheitstechnologie, Cologne, Germany

ABSTRACT: A numerical study on the retardation/retention and transport of the gases generated in a backfilled salt rock repository system is performed using the reactive flow simulator TOUGHREACT and the results are presented. The basic retardation/retention mechanisms are investigated as the dissolution of the gases, the precipitation of carbonates and compressibility of the gas phase. The solubility of CO_2 in brines is higher than other generated gases. Its dependency on ionic strength as well as on electrolyte type is found to be considerable. If the thermodynamical and chemical conditions dominating in the emplacement caverns are favorable the carbonation may be an important retention mechanism. The buffering of pH lowering effect of dissolved CO_2 with suitable backfill materials contributes to the precipitation of carbonates which in turn decreases the porosity and permeability. If the thermodynamical conditions results in the formation of gas phase, the higher compressibility and density of CO_2 compared with other gases appears as another advantage for its retardation on the way to geosphere. The capillary trapping and self sealing due to precipitation in the flow paths can also give some minor contributions to the retardation even to the retention of the gases.

1 INTRODUCTION

In geological disposal of radioactive-toxic wastes, gases are generated mainly due to corrosion (mainly H_2) and microbial degradation (CO_2 or CH_4) of the wastes, and this may affect the safe enclosure of the underground repositories. Therefore, the generation and transport of the gases in geological repositories is one of the most investigated themes. Significant efforts have been made and continue to be expended in numerous projects to understand the potential and impacts of the gas generation and transport.

Although the movement of the gas in the repository is basically conceptualized as "gas transport" or "gas migration" this is clearly due to the fact that gas is the source term. Gas transport from a repository has two important aspects, the first one is the pathway it follows and the second is the phase behaviour determining the basic mechanisms and parameters. The transport is realized as one phase, liquid or in some cases as two-phase depending on the dominating phase behaviour. Advection is the main transport mechanism and is evaluated basically by the Darcy or Hagen-Poiseuille Laws depending on the flow paths. Dispersion and diffusion are the main secondary transport mechanisms contributing to the movement of the gas. Other mechanisms such as sorption are cited for the minor contribution depending on the events and features occurring in the repository and near-far field of the repository. Another very important aspect of the transport is the retardation and/or retention mechanisms which are responsible from the delay of the gas transport to the geosphere.

For a realistic evaluation of the gas generation and its transport through the emplacement caverns and in the rest of the repository system with its near-far field some simplifying assumptions are required. The fist assumption is that the emplacement caverns are all completely filled with a protection liquid. With this assumption the presence of irreducible and in-situ gas saturation is neglected. From a petrophysical point of view this is not realistic; after the flooding of the caverns with the protection fluid, the remaining gas saturation may reach up to 20–30%. Initially this irreducible and/or remaining gas consists of mainly air. Gas being generated from the wastes will be mixed with in-situ gas at first and at the same time due to the possible higher diffusion characteristics, it will diffuse into the liquid. If the thermodynamics state the presence of the free gas phase, the free gas will expand and due to its lower density and higher compressibility (its degree depending on the type of the gas) will be stored preferentially in upper parts of the caverns or begin to flow with the liquid phase.

From thermodynamical and chemical points of view and as a ranking order, it is assumed that at the

beginning of the gas generation the gas saturation in the system is zero. The second assumption is that the diffusion rate is high enough so that the gas being generated diffuses instantaneously in the liquid phase. This assumption is acceptable taking the low generation rates and dissolution properties of the gases into account.

With these assumptions the transport of the gas is determined based on the following retardation /retention mechanism:

- Dissolution in liquid phase
- Precipitation as solid phase
- Compression of the gas phase

The extent and magnitude of these mechanisms are determined under the control of the thermodynamical and chemical equilibrium conditions dominating in the repository. The main objective of this study is to contribute to the understanding of the retardation/retention processes by investigating each mechanism numerically. Another objective is to state the actual knowledge on the coupling of the reactive flow to the numerical modelling of the THMC behaviour of the backfilled salt rock repositories.

2 NUMERICAL APPLICATION

The reactive flow simulator TOUGHREACT/ECO_2 was used for numerical modelling of gas generation, and retardation/retention processes during the transport in a repository system. TOUGHREACT is a numerical tool for coupled modelling of subsurface fluid and heat flow, solute transport, and chemical reactions (Xu et al., 2004). It is used to assess mineral and solution alteration in hydrothermal systems, water disposal sites, underground radioactive waste disposal, contaminant transport, and monitoring of groundwater quality. TOUGHREACT is applicable to one-, two-, or three-dimensional geologic domains with physical and chemical heterogeneity. In TOUGHREACT, the phase behaviour and physical properties of the phases are calculated using incorporated equation of state (EOS) modules that can be activated according to the modelling cases. In this study, ECO_2 is applied as an EOS module (Pruess et al., 2005). ECO_2 is used to model non-isothermal multiphase flow in the system H_2O–NaCl–CO_2. It represents fluids as consisting of two phases: a water-rich aqueous phase, herein often referred to as "liquid," and a CO_2-rich phase, referred to as "gas." The partitioning of H_2O and CO_2 between liquid and gas phases is modeled as a function of temperature, pressure, and salinity (Pruess, 2005).

For modelling study, input data is chosen typical for a salt mine. A simple irregular 2D grid model was built using the mesh-maker facility of TOUGHREACT. An emplacement cavern (chamber) at approximately 750 m depth is modelled, with dimensions of 25×8 m. A total volume of 200 m^3 was assigned for backfill material, and four source terms were located in the model chamber. For the determination of the source term, the model assumed a waste volume of 400 m^3, based on a volume ratio of 0,66 for waste to total excavated volume. The gas generation rate was approximated from previous studies to be 4×10^{-11} kg/(s.m^3 waste), assuming a transformation of the organic carbon to CO_2 (Bracke et al., 2004).

In the model, mineral composition of the rock salt was set to 99% halite and 1% anhydrite. Two different compositions of backfill materials were applied. The first one represented standard backfill material used with waste disposal in rock salt (Backfill C, C = Cement), consisting mainly of halite (40%) and portlandite (50%). The second one is brucite-based backfill material, also called Mg-Depot (Backfill B, B=Brucite). In previous studies, it was concluded that this backfill material has advantages for setting up a robust geochemical environment and hydraulics (Metz et al., 2004). A small amount of iron was included in each composition to simulate steel waste drums. Secondary phases, likely to exist in the backfill, were also added to the composition. Mineral grain radius and surface area were set to 1 mm and 10 cm^2/g, respectively, for all minerals. More details on the model applied can be found in Alkan et al., 2006.

One limitation of TOUGHREACT was encountered when modelling the composition of the $MgCl_2$-based brines. It is reported that the activity coefficients of aqueous species is calculated according to the Debye-Hückel theory, with parameters derived by Helgeson et al.(Xu et al., 2004). The major assumption of the Debye-Hückel theory is that the dominant cation and anion in solution are sodium and chloride, respectively, indicating that the applicability of this method depends strongly on the dominant presence of NaCl. Consequently, use of an $MgCl_2$-based brine as the aqueous phase in TOUGHREACT is somewhat restricted. Since ionic strengths smaller than 3–4 are proposed as a practical limit for application of the Debye-Hückel theory, the concentration of the $MgCl_2$ was limited to 2 M in the modelling.

3 DISSOLUTION IN LIQUID PHASE

The assessment of dissolution of the gases in liquid is due to the complex thermodynamics of the gas-brine-minerals system. Gas solubility is dependent on temperature, pressure, and detailed chemical composition of both the gas and the brine. Considering a species i likely to exist in both the gaseous and the aqueous phases, its activity in the aqueous phase ($a_{i,aq}$) is related to its activity in the gaseous phase ($a_{i,gas}$)

according to the general law of mass equilibrium equation:

$$\frac{a_{i,aq}}{a_{i,gas}} = K_i(p,T) \quad (1)$$

where K_i is the thermodynamic equilibrium constant of the reaction $i_{aq} \leftrightarrow i_{gas}$, p is the pressure (bar), and T is the absolute temperature (K). The activity of the gases at real conditions can be defined from the fugacity which is a function of the pressure, the temperature and the molar fraction of the specie in gas phase. Similarly, the activity of an aqueous species depends on the pressure, the temperature, and the solution composition. Combining the activity of aqueous species with the activity of gases leads to the following general formulation of gas solubility in a complex brine (Kervevan et al., 2005):

$$m_{i,aq} = \frac{K_i \Phi_{i,gas} x_{i,gas} p}{\gamma_{i,aq}} \quad (2)$$

where $\Phi_{i,gas}$, $x_{i,gas}$, and $\gamma_{i,aq}$ are, respectively, the fugacity coefficient (dimensionless), the molar fraction (dimensionless) of the species *i*in the gaseous phase, and the activity coefficient (dimensionless). Compared to other gases (CH_4, air) the solubility of CO_2 in solution is app 8–10 times higher, therefore CO_2 is the most important gas component in terms of retardation/retention by solubility.

Estimating the activity of aqueous species requires the calculation of their activity coefficient integrating the effect of salinity, temperature, and pressure. For low salinity solutions, activity coefficients can be easily calculated by ion association approaches such as Debye-Hückel's, or Davies. These approaches, implemented in most of the geochemical codes such as EQ3/6 of TOUGHREACT are mathematically simple and well parameterised. However, for higher salinities, the calculated results diverge from observations, even in the case of NaCl solutions. In these cases, the use of a more specific interaction model such as Pitzer's model (Pitzer, 1973) is necessary. Pitzer's model, has been specifically designed to reproduce experimental data at high ionic strength.

Compared to ion association models, Pitzer's formalism is mathematically more complex and relies on many parameters. Some semi-empirical attempts were also made to calculate the solubility of CO_2 in solutions of high ionic strength. These studies are mainly conducted in the framework of understanding the mechanisms of geological CO_2 sequestration and give reliable predictions. In a recent study for calculating the solubility of CO_2 in the solutions of various ionic type and strength the following equation is proposed (Duan et al., 2006).

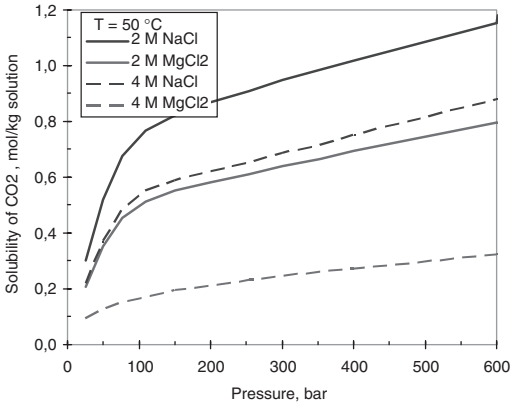

Figure 1. Effect of the salt type, concentration and pressure on the solubility of CO_2 in saline waters, calculated after Duan et al.2006.

$$\ln(m_{CO_2}) = \ln y_{CO_2}\phi_{CO_2}p - \mu_{CO_2}/RT - 2\lambda_{CO_2-Na}(m_{Na}+m_K+2m_{Ca}+2m_{Mg}) \quad (3)$$
$$-\zeta_{CO_2-Na-Cl}m_{Cl}(m_{Na}+m_K+m_{Mg}+m_{Ca}) + 0.07m_{SO_4}$$

where T is absolute temperature in Kelvin, p represents the total pressure of the system in bar, R is the universal gas constant, m is the molality of components dissolved in water, y_{CO_2} is the mole fraction of CO_2 in vapour phase, Φ_{CO_2} is the fugacity coefficient of CO_2, μ_{CO_2} is the standard chemical potential of CO_2 in liquid phase, λ_{CO_2-Na} is the interaction parameter between CO_2 and Na^+, and $\zeta_{CO_2-Na-Cl}$ is the interaction parameter between CO_2 and Na^+, Cl^-. The fugacity coefficient of CO_2, Φ_{CO_2}, is calculated as a function of temperature and pressure, as proposed in the same study.

The dependence of the CO_2 solubility on the pressure, temperature, ionic strength and on the electrolyte type provides important information on the retardation and on the retention of CO_2. The effect of temperature on the liquid-gas equilibrium is more significant than the effect of the pressure which is not considered in many of the studies. The effect of the ionic strength is also pronounced. Due to the individual activity coefficients of the components the effect of the electrolyte type is also expected. Figure 1 illustrates the CO_2 solubility as function of pressure and ionic strength (molarity) for two NaCl and $MgCl_2$ solutions. Figure 2, on the other hand, shows the solubility of CO_2 directly as function of the ionic strength for NaCl equivalent solution salinity at 1 bar. If it is considered that the liquid phase in the emplacement caverns consist of saturated solutions, the dissolved CO_2 ratio should not exceed 0,01 as mass ratio to the solution.

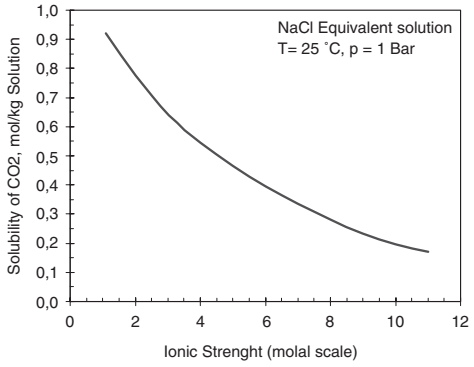

Figure 2. Solubility of CO_2 in salt solutions as function of ionic strength (Kervevan et al., 2005).

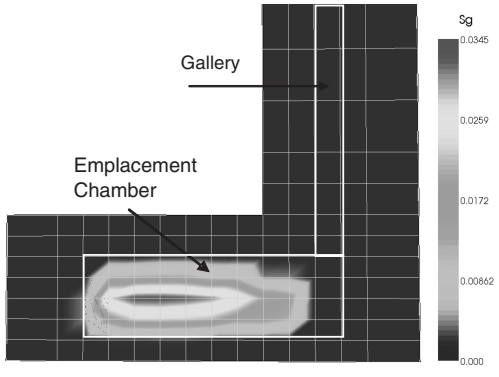

Figure 3. Calculated distribution of gas saturation in the emplacement chamber after 5000 years of gas generation.

Figure 3 shows the CO_2 (gas) saturation distribution calculated with the basic model used for this study after 5000 years of gas generation. After 5000 years app. 3000 kg CO_2 is generated; one third of this amount is released to gas phase and the rest remains dissolved in the liquid phase. It should be noted that in this calculation the maximum allowable salinity is given as 0,26 NaCl equivalent mass ratio. For higher salinity systems a more rapid exsolution thus a more rapid transition to the two-phase state might be expected. In all calculations it is assumed that no dissolved CO_2 has been spent for the solid-liquid equilibrium.

4 PRECIPITATION AS SOLID PHASE

In terms of reactive transport, CO_2 is the only meaningful gas component. The dissolved CO_2 in solution may results in the precipitation or the dissolution of the saturated-under saturated mineral species. The dissolution of CO_2 in water can be represented with the following chemical reaction:

$$CO_2(g) + H_2O \rightarrow H_2CO_3(aq) \tag{4}$$

According to Henry's Law, the concentration of H_2CO_3(aq) is proportional to the CO_2 partial pressure (p_{CO2}). With increasing partial pressure of CO_2 or dissolved CO_2 amount, the concentration of H_2CO_3(aq) will be higher. H_2CO_3 dissociates according to the following reaction:

$$H_2CO_3(aq) \leftrightarrow H^+ + HCO_3^- \tag{5}$$

HCO_3^- dissociates further as follows:

$$HCO_3^- \leftrightarrow H^+ + CO_3^{2-} \tag{6}$$

These equations indicate that increased CO_2 pressure (dissolved CO_2 ratio) lowers pH, and this would increase the solubility of the minerals as well as the solubility of the released radioactive components such as actinides. On the other hand increasing CO_2 pressure also increases [HCO_3^-] and thus [CO_3^-] which may be reacting with free cations such as Ca^{2+} and Mg^{2+} to precipitate as carbonates (e.g. calcium and magnesium carbonate). The solubility product of calcium carbonate is app. one order of magnitude smaller than the solubility product of magnesium carbonate. This means that for magnesium carbonate to precipitate, the product of the concentration of magnesium ions and carbonic ions must be an order of magnitude higher than the product of the concentration of calcium and carbonic ions. However the solubility product constant for magnesite, $MgCO_3$ is also very low and therefore favours its precipitation:

$$MgCO_3 \leftrightarrow Mg^{2+} + CO_3^{2-} \tag{7}$$

Obviously, the retardation with precipitation is considered without kinetics and nucleation which can play significant roles in forming the mineral particles. Calcite is assumed to precipitate in local thermodynamic equilibrium although the precipitation of magnesite is due to the kinetics. The incorporation of the kinetics to the mineral dissolution/precipitation is modelled generally due to Transition State Theory for which the effective reaction rate V (mol.s^{-1}) is expressed with the following equation (Kervevan et al., 2005):

$$V = k.S.f_r(a_{H+})^n(1-\frac{Q}{K}) \tag{8}$$

where k is a kinetic constant in $\mathrm{mol \cdot cm^{-2} \cdot s^{-1}}$, S is the total surface area (cm^2) assumed to be a constant term when precipitation occurs and proportional to the remaining mineral mass in the case of dissolution, f_r is the fraction of the total surface area

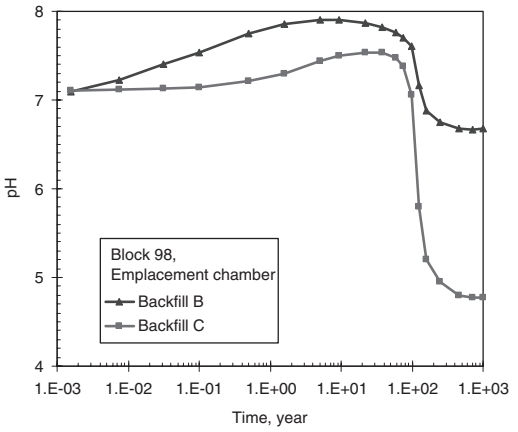

Figure 4. Calculated pH development with time for the cases Backfill B and Backfill C.

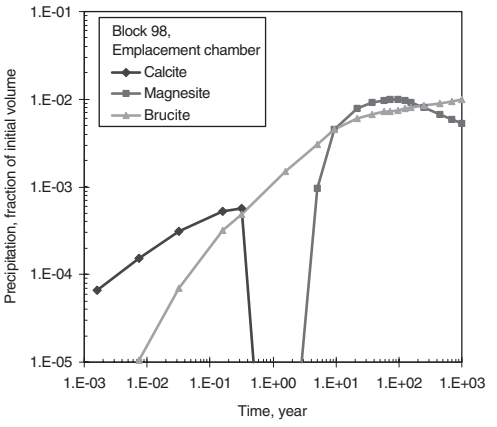

Figure 5. Precipitation of relevant minerals, Case backfill B.

effectively reactive, a_{H+} is the H^+ activity term, Q is the ionic activity product, and $K$is the thermodynamic equilibrium constant of the considered precipitation/dissolution reaction. The kinetic constant k is for each mineral species experimentally determined or calculated as function of temperature based on activation energy. The reactive surface area is difficult to characterize and can be assumed with the aid of some theoretical porous media models. The difference in mass of the mineral species should be calculated as the effect on the porosity and thus on the permeability using available porosity-permeability models such as Kozeny-Carman model or the following cubic law approach:

$$k = k_i \left(\frac{\phi}{\phi_i} \right)^3 \qquad (9)$$

where k_i and ϕ_i are the initial permeability and porosity.

The results of the modelling study performed using two different types of backfill materials showed interesting results on the dissolution and precipitation behaviour in a repository. The precipitation of the dissolved inorganic carbon (DIC) is obviously a preferred processed for reducing the dissolved amount of CO_2 which in turn may increase the pressure and the solubility in the liquid phase. Figure 4 shows the variation of pH in the cases of using conventional material (Backfill C, portlandite based) and brucite (Backfill B, $Mg(OH)_2$) based material as backfill. The decrease in pH after the beginning of CO_2 generation is remarkable. The drop in pH is more pronounced for the case C for which the conventional backfill material is used. Figure 5 shows on the other side, the precipitation of the relevant minerals in the case of brucite based backfill material. As expected from the

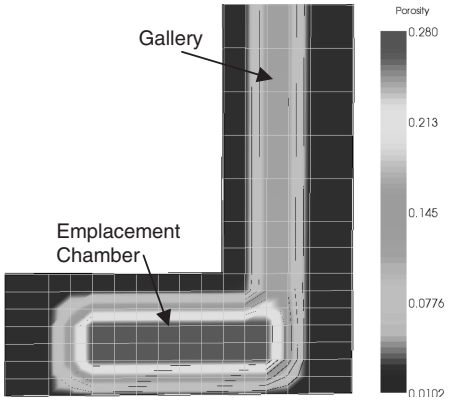

Figure 6. Calculated porosity distribution after 5000 years of gas generation.

equilibrium conditions calcite precipitates rapidly. The precipitations of magnesite as well as of brucite are significant. If the dissolution of halite present in mineral composition is excluded, the effect of the precipitation can play a significant role on reducing the porosity thus permeability. Figure 6 shows the resulting porosity in the emplacement chamber as well as in the gallery after 5000 years of gas generation for case B. It can be concluded that the original porosity of 0,30 of the emplacement chamber reduces up to 0,28 indicating a decrease of app. 7% in 5000 years. For the cases studied the precipitated carbonate amount respectively magnesite is far from spending all dissolved CO_2. This is concluded from the calculated continuous increase in HCO_3^- concentration in the solution. This is probably due to the insufficient feeding of Mg^+ cations by the protection fluid for which the modelled molality is limited due to the use of Debye-Hückel activity model in TOUGHREACT.

From the literature it is known that for all the pH values (1–14), the $MgCO_3$ has lower solubility than the brucite, $Mg(OH)_2$ and therefore, will precipitate preferentially. However, $Mg(OH)_2$ might also precipitate very readily due to its low solubility product constant:

$$Mg(OH)_2 \leftrightarrow Mg^{2+} + 2OH^- \quad (10)$$

From theoretical and experimental studies under similar thermochemical conditions, it is known thatthe $Mg(OH)_2$ reacts with CO_2 in solution in an exothermic reaction under very mild conditions as (Pokrovsky et al., 1999):

$$Mg(OH)_2 + CO_2 \leftrightarrow MgCO_3 + H_2O \quad (11)$$

Previous studies have reported that carbonation of $Mg(OH)_2$ has conversions (due to precipitation) as high as 90% at low temperatures and pressures forming a precipitate that is mainly $MgCO_3{*}3H_2O$. Therefore, the use of $Mg(OH)_2$ is a very interesting alternative as backfill material because of the inherent low carbonation processing conditions of $Mg(OH)_2$ compared to other processes and the reaction being exothermic. Studies on the use of brucite as backfill show a complete limitation of the dissolved CO_2 concentration by very low values (Metz et al. 2004). The resulting buffering of the pH is also an indication for lower solubilities of the actinides.

The above given discussion of the modelling efforts concludes that at conditions where the precipitation of carbonates is favoured with suitable thermodynamical and chemical conditioning considerable amount of dissolved CO_2 in the solution can be retarded by conversion to carbonate precipitation. This in turn retards the forming of free gas phase thus the transition to the phase flow conditions in the whole of the system.

5 COMPRESSION OF THE GAS PHASE

As discussed in previous sections, the exsolution of the gas is strictly dependent on the thermodynamical and chemical equilibrium state of the CO_2-brine-solid phases. Once the free gas phase is appeared, the two-phase flow dominates the transport. This is controlled by the relative permeability concept and capillary forces. The mobility of the gas phase is higher than the liquid phase thus it is expected that gas overrides the liquid phase tending to migrate vertically to the top of the geologic structure. Modelling of two-phase flow in porous media requires the specification of the functional relationship between capillary pressure, relative permeability and saturation. Together capillary pressure, relative permeability control the way the liquid, brine (wetting phase) and gas, e.g. CO_2 (non-wetting) phases interact.

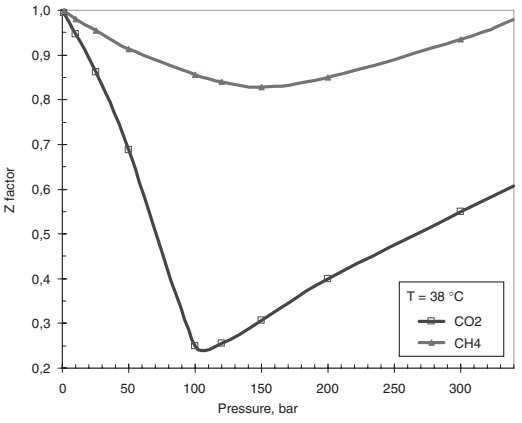

Figure 7. The compressibility (z) factor of CO_2 and CH_4 as function of pressure.

The retardation and/or retention of the gas phase in two-phase flow conditions may be considered in two basic mechanisms. The first one is the possible trapping of the gas because of the capillary forces dominating in pore spaces. A minor amount of gas which is conventionally non-wetting phase in salt rock or in confining rocks can be trapped in small capillaries or fractures.

The second mechanism is the major consideration and can be determined by the phase properties of the gases. The compressibility and density of CO_2 is much higher than other gases which may be generated in the repository. A comparison of the compressibility factors of CO_2 and CH_4 is illustrated in Figure 7. The meaning of this behaviour is that for the same pressure and temperature approximately four times more CO_2 can be retained in a same emplacement volume. The much greater density of CO_2 compared to other gases contributes to this retention.

Another retardation factor in two phases is related to the precipitation of the minerals causing a probable self sealing effect. If CO_2 exsolves from the solution due to the dominating thermodynamics, the liquid phase becomes supersaturated to the dissolved minerals which in turns precipitate. Calcite and magnesite with their low solubility products are two potential candidates for this mechanism. The precipitation of the minerals in small capillaries and fractures can play important role in trapping the released gas in the geological system.

6 CONCLUSION

The retardation/retention of the gases being generated and transported is one of the main considerations for the safe closure of the geological repositories.

Although many studies were recently conducted on gas transport under various disciplines, some aspects of this title are yet open. This includes especially the numerical evaluation of retardation/retention of the generated gases and their incorporation to the THMC coupled modelling.

An attempt for reactive modelling of the retardation/retention mechanisms in a backfilled emplacement cavern in rock salt provided preliminary numerical evaluation. The retardation/retention of CO_2 is significant due to its thermophysical and chemical characteristics. Its solubility in water is higher than other gases. It is more compressible and denser. The carbonation is another retardation/retention advantage of CO_2 which can be favoured based on the well studied, selected emplacement conditions.

Numerical modelling of these mechanisms is possible by the application of the reactive flow simulators such as TOUGHREACT. Some modifications and improvements on these simulators are required however due to the marginal solution and mineral properties of the salt repositories. A validated hydro-chemical simulator is an important contribution towards a universal numerical coupling of the THMC processes.

REFERENCES

Xu T., Sonnenthal E., Spycher N., Pruess K., TOUGHREACT User's Guide: A Simulation Program for Nonisothermal Multiphase Reactive Geochemical Transport in Variably Saturated Geologic Media", Earth Sciences Division, Lawrence Berkeley National Laboratory University of California, Berkeley, CA 94720. May 2004.

Pruess K., "ECO2N: A TOUGH2 Fluid Property Module for Mixtures of Water, NaCl, and CO2", Earth Sciences Division, Lawrence Berkeley National Laboratory University of California, Berkeley, CA 94720 August 2005.

Bracke G., Müller W., Kugel K., "Derivation of Gas Generation Rates for the Morsleben Radioactive Waste Repository (ERAM)", International Conference on Radioactive Waste Disposal, April 26–28, Proceedings, 322–328, 2004.

Alkan H., Müller W., Bracke G. Toughreact/ECO2 On Reactive Transport Modelling Of CO2 In A Geological Repository, Nuclear Technology, 2006 (submitted).

Kervévan C., Azaroual M., Durst P., Improvement of the Calculation Accuracyof Acid Gas Solubility in Deep Reservoir Brines: Application to the Geological Storage of CO2, Oil & Gas Science and Technology – Rev. IFP, Vol. 60 (2005), No. 2, pp. 357–379.

Duan Z., Sun R., Zhu C., Chou I-M., An Improved Model for the Calculation of CO_2 Solubility in Aqueous Solutions Containing Na^+, K^+, Ca^{2+}, Mg^{2+}, Cl^-, and SO_4^{2-}, Marine Chemistry, 98, 131–139, 2006.

Pokrovsky O.S., Schott J., Thomas F., Process at the Magnesium-Bearing Carbonates/Solution Interface, I. a Surface Speciation Model for Magnesite, Geochemica et Cosmochimica Acta, Vol. 63, No. 6, pp. 863–88.

Pitzer, K. S., Thermodynamics of electrolytes, 1, Theoretical basis and general equations, J.Phys.Chem., 77, 268–277, 1973.

Metz V., Schüßler W., Kienzler B., Fanghängel Th., Geochemically Derived Non-Gaseous Radionuclide Source Term for Asse Salt Mine-Assessment for the Use of a Mg(OH)2-Based Backfill Material, Radiochim. Acta 92, 819–825, 2004.

Pruess K., ECO2N: A TOUGH2 Fluid Property Module for Mixtures of Water, NaCl, and CO2, Earth Sciences Division, Lawrence Berkeley National Laboratory University of California, Berkeley, CA 94720 August 2005.

Taylor & Francis
Taylor & Francis Group
http://taylorandfrancis.com

Part 6. Studies of mining and mine abandonment

Taylor & Francis
Taylor & Francis Group
http://taylorandfrancis.com

The Mechanical Behavior of Salt – Understanding of THMC Processes in Salt –
Wallner, Lux, Minkley & Hardy, Jr. (eds)
© 2007 Taylor & Francis Group, London, ISBN 978-0-415-44398-2

Dynamic processes in salt rocks – a general approach for softening processes within the rock matrix and along bedding planes

W. Minkley & J. Mühlbauer
Institut für Gebirgsmechanik GmbH, Leipzig, Germany

G. Storch
K + S Kali GmbH, Germany

ABSTRACT: Understanding of the relevant failure processes is a prerequisite for dimensioning of underground mining openings. Investigation of brittle failure processes in potash mining and their simulation by rock mechanical modelling clearly demonstrate that the fracture mechanisms of slender and compact pillars are quite different. The collapse of a compact pillar is only possible if besides an overall softening of the rock coevally an accessory loss of cohesion occurs at pronounced weakness planes, particularly along the bedding planes towards the hanging and the underlying layers of the pillars. For the description of the different dynamic processes specialised constitutive models are available, which were verified with various case studies. Exemplarily, the dynamic failure event that actually occurred at the mined top of a domal carnallitite structure has been recalculated. The pronounced seismological s-wave signal which had been recorded during the event has been convincingly referred to development of a shear fracture as the relevant failure mechanism.

1 INTRODUCTION

During the history of potash mining which lasts more than 150 years several rock bursts occurred. In analysis of these dynamic failure events it can be concluded that generally insufficient knowledge about the softening of salt rocks was responsible for such disasters. Additionally, the mechanical behaviour of bedding planes and discontinuities acting as pronounced weakness planes in the salt mass has been mostly neglected.

Dynamic processes in the salt rock mass can occur when either the salt rock or the bedding planes abruptly soften. It is well known that some salt rocks such as carnallitite are characterized by an intensive destrengthening and liability to brittle fracture (Fig. 1). In contrast, in rock salt, sylvinite and hard salt a gradual transition to the region of residual strength is observed as soon as the maximum load bearing capacity is exceeded. The higher the halite content the more ductile is the deformation of the salt rock in the post-failure state.

In retrospect of carnallitite mining, totally 10 rock bursts with magnitudes up to $M_L = 5.6$ occurred (Minkley 1998, 2004). In the hard salt of the Stassfurt potash seam two field collapses have been reported (Gimm & Pforr 1961). In a trona (a sodium carbonate mineral, i.e. $Na_3(HCO_3)(CO_3)\cdot 2H_2O$) mine in Wyoming a rock burst happened with a magnitude of

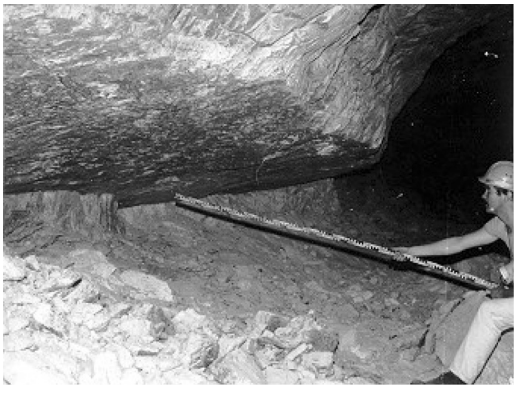

Figure 1. Contour failure at a carnallitite pillar with separation in the contact with the roof rock salt; Seismic event magnitude $M_L = 1.7$.

$M_L = 5.1$ (Swanson & Boler 1995). In the Russian Solikamsk mine where sylvinite is mined whereby carnallitite is exposed in the roof a rock burst with the magnitude of $M_L = 4.8$ took place in 1995, which caused the most abrupt subsidence on the surface ever observed, with amounts up to 4.5 m.

However, even in some rock salt mines dynamically spreading field collapses are reported when the room-and-pillar system with slender pillars is used.

On 10/31/1873, in Varangéville (France) an earthquake-like ground motion occurred when in a depth of 156 m a rock salt field collapsed. The square pillars had a width-to-height ratio W/H = 1.1 and the utilisation factor of the deposit was approx. 82%.

On 03/12/1994, in the Retsof salt mine (USA) a failure event happened which had a magnitude $M_L = 3.6$. This event occurred in a yield-pillar panel at a depth of about 330 m (van Sambeek et al. 2000). The width-to-height ratio of the slender support pillars (yield pillars) was approx. 0.7. Although initially decreasing convergence rates were measured in the yield-pillar test panels, this trend changed dramatically to a rapid and increasing closure rate few weeks before the collapse happened. This indicates tertiary creep failure resulting in the collapse of the slender support pillars. As a consequence of this event the mine is flooded.

Unlike the fracture of slender pillars which can be sufficiently explained by softening of the salt rocks in potash mines the failure process in compact pillars can only be explained in connection with translatory motion and, consequently, a shear process occurring between seam and roof and floor.

As a result of a large number of recalculations (Minkley 2004) and dynamic calculations in advance of a panel collapse (Minkley & Menzel 1999) the mechanism of rock bursts in potash mining is widely conceived. The fracture process is initiated by the local failure of one or more pillars either by dynamic excitation during blasting or spontaneously by a creep failure. Starting from this local instability the fracture process propagates like a chain reaction and, thus, can destroy – within few seconds – complete working panels with thousands of pillars which had not been dimensioned in a manner to provide the necessary structural stability.

To facilitate an adequate mechanical modelling of such dynamic failure processes a new approach is developed based on a combined description of softening phenomena acting as well within the salt rock matrix and at distinct weakness planes in the salt rock mass (for more details about the used models see Minkley & Mühlbauer, this volume). For verification, several modelling results for various case studies at different scales will be presented. Finally, the capability of the combination of visco-elasto-plastic constitutive model and new shear softening model is highlighted with an actual example.

2 FAILURE MECHANISM OF SALT ROCK PILLARS

2.1 *Slender pillars*

The fracture process of a slender pillar shall be illustrated by means of the example of a rock salt pillar having a width-to-height ratio of W/H = 1. In the calculation model for the given longitudinal pillar a comparatively high load of 38 MPa has been applied to initiate a failure of this pillar. The uniaxial strength of the rock salt is 33 MPa as has been determined on cylindrical samples having a diameter-height ratio of 0.5. By analogy with the phenomena observed in-situ as well as in the calculation model the softening of the pillar contour starts adjacent to the roof and the floor (Fig. 2). Already after 13 days a continuous broad shear band has developed within the strength is heavily reduced. The pillar core will be overloaded due to stress redistribution from the contour to the inner zone. After 14 days the softening has seized the whole

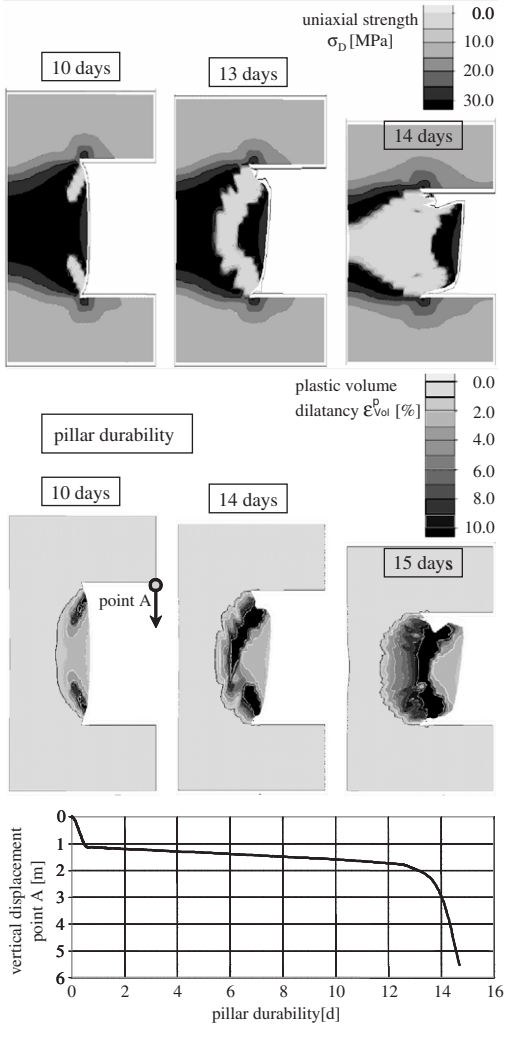

Figure 2. 2D-calculation model for a slender rock salt pillar. Time-depending development of uniaxial strength σ_D and plastic volume dilatancy ε^p_{Vol} until creep failure occurs.

core area and the pillar fails finally by creep failure (Fig. 2).

The still undamaged rock salt shell at the pillar contour which has not been subjected to the softening is shifted further into the working room. This example illustrates that slender pillars can fail without significant shear displacements at the roof and at the floor.

2.2 *Compact pillars*

Generally, in compact pillars the failure mechanism is more complex. Though, failure process here also starts at the pillar contour, a pillar collapse may only develop if at the same time a shear failure between pillar and roof as well as floor occurs (Fig. 3).

For a long time this complex failure mechanism could not be described in a satisfactory manner by rock mechanical models. It was not successful to reproduce in rock mechanical calculations the stability behaviour of compact carnallitite pillars under static and dynamic load conditions by using the conventional Mohr-Coulomb friction approach.

Recently, a series of laboratory shear tests were carried out with respect to the rate-dependent shear behaviour on the bedding planes between carnallitite and rock salt, which significantly improved the understanding of the bedding plane softening at high loading rates. In the case of static loading, frictional and cohesive forces are acting in the relevant contact planes on the top and the bottom of a pillar without comprising a potential for a sudden drop in shear stress (compare Fig. 5). Only under dynamic loading at a high rate of shear motion an additional adhesive friction resistance is activated whose overcoming is associated with a loss of shear stress resulting in an abrupt drop to the level of residual friction. These new results facilitates the development of a specific shear softening model for saliniferous bedding planes (Minkley & Mühlbauer, this volume).

Figure 3. Localisation of shear zones in case of the failure of a compact carnallitite pillar (laboratory test model has been cut after failure).

To verify the practical suitability of the new shear model developed for the description of the saliferous bedding plane behaviour a recalculation with respect to the Voelkershausen rock burst in1989 was carried out (IfG 2005). The rock mechanical structure model which has been used for this purpose is shown in Figure 4.

By analogy with the initiation of the rock burst a blasting carried out in a single pillar was simulated in the dynamic calculation. In this dynamically excited pillar a contour failure occurs. The stresses behind the destrengthened contour reach up to 80 MPa (Fig. 4). The further development of the fracture process depends decisively on the shear behaviour on the bedding planes of the pillar to the roof and to the floor. When assuming that no loss in the cohesive and the additional adhesive friction component occurs then it would not be possible that in a compact pillar such a progressive fracture process would develop which turns into system instability. These interesting facts which have not been known until now yield from the results of the respective dynamic calculations.

However, when on the bedding planes between carnallitite and rock salt, as has been experimentally

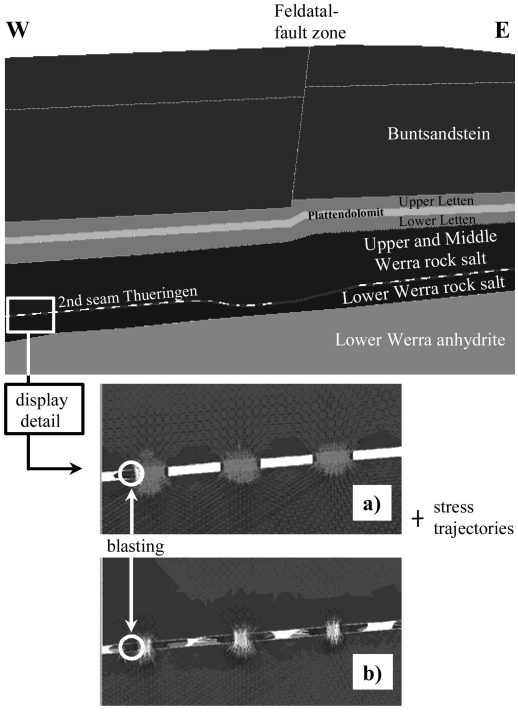

Figure 4. Calculation model with respect to the Voelkershausen rock burst (upper part) and detailed section to illustrate the failure process of the compact carnallitite pillars (lower part). Bedding planes a) without softening, b) with softening phenomena.

proven, softening processes occur after the peak shear strength has been overcome, then a completely different picture will appear. For this purpose, the dynamic calculation was repeated using the same initiation by blasting. However, softening processes on the parting planes are taken into consideration now. Due to the velocity- and displacement-depending softening on the bedding planes between carnallitite and rock salt the constraint of the compact pillars abruptly disappears and the contour regions of the carnallitite pillars are shifted into the working room like during an explosion (Fig. 4-b). Following the loss of load bearing capacity the carnallitite in the pillar cores is briquetted under very high vertical stresses (in the order of magnitude of 100 MPa).

As a result of the calculation, following the dynamic initiation by blasting a progressive developing failure process takes up and spreads over to the neighbouring pillars. This process stops only at the working-free panel in the region of the Feldatal-fault zone (Fig. 4) which corresponds to the real extent of the Voelkershausen rock burst in 1989.

2.3 *The new shear model*

In foregoing recalculations (e.g. Minkley 2004) the shear strength had to be always reduced in comparison to that used in the static calculation phase for initiating a rock burst on the compact carnallitite pillars (ratio of pillar width to pillar height $W/H \geq 4$) within the dynamic calculations. However, with the recently developed shear model and on the basis of the experimentally derived shear parameters for bedding planes between carnallitite and rock salt it became possible to describe the behaviour of bedding planes under static and dynamic loading conditions until rock burst occurs by using a single uniform set of parameters.

The resulting shear resistance for the contact planes of the pillars with the rock salt roof and the rock salt floor constitutes of:

- kinetic friction + cohesion in the case of quasi-static loading $v \ll v_K$ (Fig. 5, left)
- kinetic friction + adhesive friction + cohesion in the case of dynamic loading $v \ll v_K$ (Fig. 5, right)

That means that under dynamic loading the shear resistance is higher due to overcoming the additional peak of adhesive friction.

When using the new shear model the results of the rock mechanical calculations shows both the contour damage of the pillars with the characteristic concave form of the outburst as a sign of the cohesive interconnection as is found before the rock burst occurred, on the one side, and in case of the rock burst simulation the translatory motion of the crushed rock material of the pillars towards the working rooms which reaches the order of magnitude of several metres

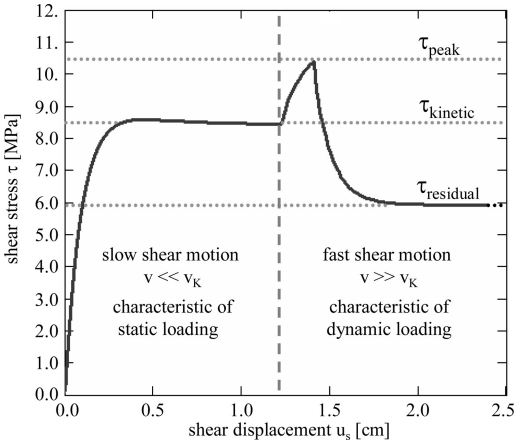

Figure 5. Shear behaviour on saline bedding planes during a sudden change of the displacement rate.

(Fig. 4, lower part). In all panels which had been subject to rock bursts in potash mining, striations on the bedding planes between the rock of the pillars and the surrounding rock have been found as an indication of the intensive development of the shear motion upon the loss of the adhesive friction.

3 DYNAMIC EVENT IN THE CASE OF DOME WORKING

3.1 *Initial situation*

In the Werra potash region thick accumulations of the carnallitic seam Thueringen are mined by applying a specifically developed method (Mocka 1988). According to this so-called dome mining method the development galleries are driven within the subjacent Lower Werra rock salt. Taking the base galleries in the rock salt as starting point the mining of the overlying carnallitic seam is performed by upwards directed boreholes in a fan-like arrangement and by blasting. The opened dome cavities have a trapezoidal cross section with roof spans to the hanging rock salt reaching a maximum of 55 m. The dome cavities which have been driven in the carnallitite of the seam Thueringen reach working heights of up to 90 m (Fig. 6).

The dome working has been accompanied by a mining-induced seismicity which has shown to be usually bound to the working shooting.

So on 09/22/2005 in the Unterbreizbach mine a comparatively strong seismic event was recorded again. The German network of seismic stations has determined a magnitude $M_L = 2.7 \ldots 3.2$. Both, seismic positioning and the found fragmental caved material have quickly shown that a dome under actual mining had been the origin of this event (Fig. 7).

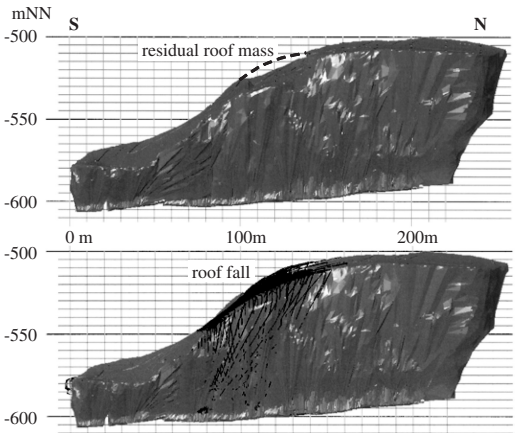

Figure 6. 3D-laser scanning of the dome cavity before (upper part) and after (lower part) the seismic event occurred.

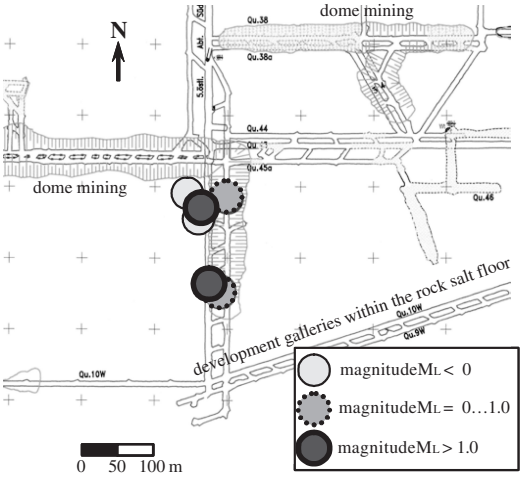

Figure 7. Plan view of the dome mining system indicating the several locations which were seismically determined at the multiple event on 09/22/2005.

The particularity of this event is seen in the fact that this comparatively strong fracture process was triggered without any initiation by blasting. Direct prior the event in the dome and in the closer environment blasting was not carried out at all.

The main event had a pre-phase which has been documented by two energetically weak seismic processes which started to run approx. 0.5 and 0.3 s, respectively, before the energetically strong fracture process.

The main event is characterized by a marked s-wave which identifies the failure process as a shear fracture (Fig. 8). Depending on the wave type the spectrum yields a corner frequency of 8…6 Hz. Accordingly,

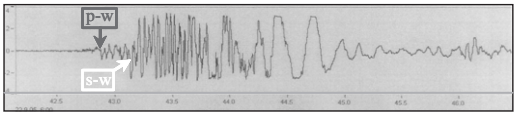

Figure 8. Seismogram of the main event with positions of first arrival of the p- and s-waves.

the Madariaga model yields a fracture plane having a radius nears 100 m (K-UTEC 2005).

3.2 *Rock mechanical modelling*

The mechanical description of the failure mechanism which in the seismogram has been identified as a shear fracture requires as a prerequisite that softening processes on mechanical weakness planes such as bedding planes in the salt massif are simulated in an adequate manner in the calculation model. In view of these needs and under consideration of the complex geological situation the new developed shear model was used for this task. As already mentioned before, this model allows to describe the displacement- and velocity-depending shear behaviour on bedding planes for instance between carnallitite and rock salt.

For simulating the mechanical properties of the solid salt rock the visco-elasto-plastic constitutive model is used which has also been developed by the IfG. Here, the calculations have been carried out using the program *UDEC* (Itasca 2004) in which both above-mentioned constitutive models are available as user-defined models.

The shear parameters used in the calculations are based on laboratory investigations on bedding planes between carnallitite and rock salt (Fig. 9). They are summarised in Table 1.

The entire saliniferous formation has been modelled using this visco-elasto-plastic constitutive model. All material parameters for Werra rock salt and for the carnallitite are shown in Table 2. Here, for representing the potash seam Thueringen the parameter set for carnallitite variety C80 was applied.

Exploratory boreholes along the dome axis and the derived geologic profile section through the dome had revealed that rock salt lenses having a thickness of several metres are embedded in the carnallitic potash seam towards the roof. In the case of the roof fall which has been detected by survey (compare Figure 6) it is possible that a residual bank of the seam consisting of carnallitite and rock salt or exclusively rock salt was concerned.

Under consideration of the complex geological situation the temporal evolution of the roof fall was modelled as depicted in the Figures 10 to 12.

Already when driving the cavity in the thick seam accumulation the carnallitite is subject to softening and in the dome walls shear zones develop.

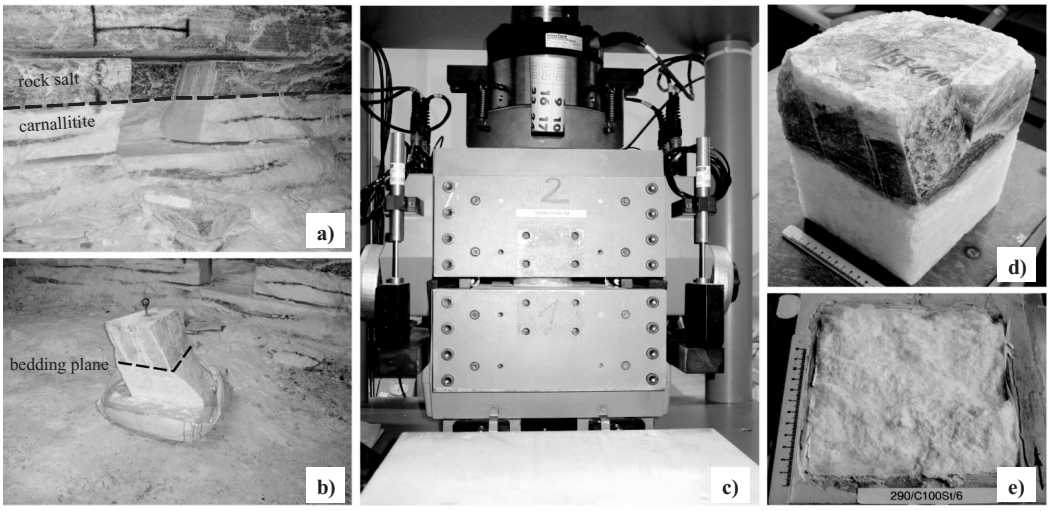

Figure 9. Laboratory studies of bedding planes. a, b) Sampling of a rock block with an evident bedding plane; c) Shear box with embedded specimen; d) Prepared specimen before; e) and sheared specimen after the test (shear plane surface).

Table 1. Shear model parameters for bedding planes between carnallitite C_{100} (carnallite content >90%) and rock salt.

Parameter	Symbol	Value	Unit
Residual friction angle	ϕ_R	27	deg
Upslide angle	i_0	15	deg
Compressive strength contact area	σ_K	10	MPa
Curvature parameter 1	K1	0.8	
Curvature parameter 2	K2	0.4	
Cohesion	c	1	MPa
Maximum adhesive friction coefficient	$\Delta\mu_{MAX}$	0.8	
Softening distance 1	L1	0.003	m
Softening distance 2	L2	0.1 . . . 0.5	m
Distance parameter	r	0.05	
Velocity factor	b_S	1.2	
Critical shear velocity	v_K	0.00001	mm/s
Shear stiffness	k_S	10	GPa/m
Normal stiffness	k_N	10	GPa/m

Table 2. Material parameters of the visco-elasto-plastic constitutive model.

Parameter Symbol	Rock formation: Werra rock salt	Rock formation: seam Thueringen	Unit
G^M	10	6	GPa
K^M	17	10	GPa
η^M	$8{\cdot}10^9$	$5.6{\cdot}10^8$	MPa·d
m	0.33	0.18	MPa^{-1}
G^K	$6.3{\cdot}10^4$	$2.3{\cdot}10^3$	GPa
η^K	$1.7{\cdot}10^5$	$2.3{\cdot}10^3$	MPa·d
σ_D	15*	12.6**	MPa
σ_{MAX}	43*	96**	MPa
σ_ϕ	3.2*	9.6**	MPa

*dilatancy boundary **failure boundary

The shear zones reach a maximum extension of 20…30 m into the loosened wall regions. The rock salt bank located at the roof is viewable limiting the loosening processes in the sideways adjacent areas of the seam. However, above the rock salt bed the softening in the carnallitite advances to on the hanging rock salt.

Whereas in the carnallitite softening processes have been initiated as a response to the creation of the cavity, in the rock salt at first hardening takes place until the failure limit is reached. Therefore, the rock salt bed at the roof is in a critical state and deflects under the load of the overlying carnallitite mass which is no longer

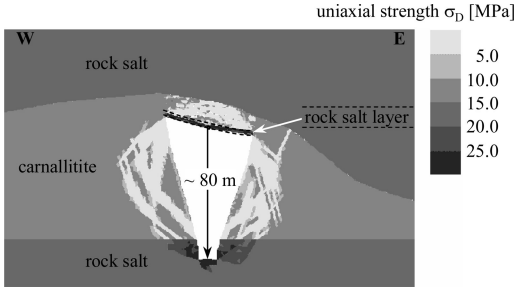

Figure 10. Results of model calculation: Localisation of shear zones in the carnallitite around the dome cavity before the failure of the residual roof mass occurred.

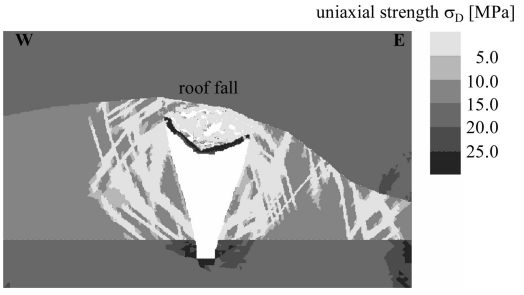

Figure 11. Extension of the softening zones in the carnallitite dome flanks in the case of the failure of the hanging rock mass.

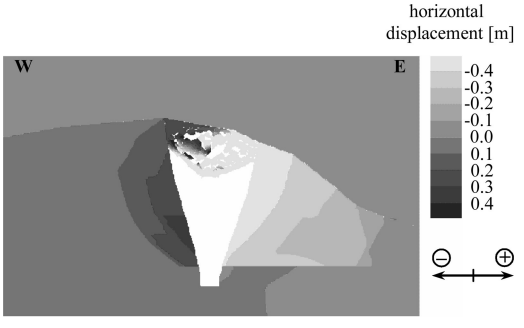

Figure 12. Extent of horizontal shifts of the dome flanks after the hanging residual bank of the seam has failed.

completely constrained and, thus, is no longer self-sustaining. Therefore, the roof region presents itself in an unstable state which is capable to pass spontaneously, i.e. without any exterior excitation, into the failure mode which means that a roof fall will occur.

Following the dynamic calculation the rock mass in the roof which supports the upper parts of the dome flanks falls after 0.3 seconds. Due to the abrupt disappearance of the constraint the eastern dome wall responses by a sudden displacement towards the dome cavity (Fig. 12).

As a consequence of this dynamic loading process a loss in adhesive and cohesive friction resistance, resp., occurs on the inclined bedding plane between the carnallitic seam Thueringen and the hanging Werra rock salt of the eastern dome flank. After the shear displacement has started on the bedding plane between carnallitite and rock salt, i.e. after 0.3 s, in the calculation the main burst occurs.

Both the calculated acceleration in the hanging Werra rock salt and the energy release grow in a jump-like manner. Due to the loss of constraint with the roof the eastern dome pillar is displaced towards the dome cavity and largely subject to damaging (Fig. 11). The displacement of the carnallitic flank of the seam accumulation depends on the softening process of the bedding planes between the potash seam Thueringen and the Werra rock salt. Without this softening behaviour such fracture events would not be able to occur as is evidenced by calculations in which destrengthening were not taken into consideration for the bedding planes. Both the stress drop over a large area on the bedding plane contact between carnallitite and rock salt and the resulting additional softening in the dome flanks are the causes of the considerable energy release which takes place during the event. The calculated energy release in the two-dimensional model allows to calculate approximately the value of the magnitude as is determined on the basis of the seismic records.

The rockmechanical modelling provides a logical explanation of the marked s-wave which is found in the seismogram and is regarded a proof that the decisive failure process is a shear fracture. Due to the shear failure of the steeply inclined bed boundary of the eastern flank of the seam accumulation, the dome wall is shifted for several decimetres towards the dome cavity. The displacement processes occurring at the western dome wall are considerably smaller since they do not occur on the flatly inclined bedding planes towards the hanging and underlying rock salt but on the pre-damaged shear fracture zones in the carnallitite (Fig. 12).

Far-reaching processes of stress redistribution are the consequence of the shear rupture process. The high-pressure belt in the closer environment of the dome, particularly in the roof region, which were present before the failure event occurred are shifted far into the inner flank regions of the carnallitite accumulation. In the eastern flank region having a low bed thickness very high stress loads are focussing.

The rock salt pillars direct below the western dome wall are situated within a de-stressed region. The hydrofrac measurement in the borehole F-UB-26 and the resultant minimum principal stresses σ_3 in the rock salt pillar (Fig. 13) show a good agreement when taking into consideration the differing pillar geometry in-situ and in the 2D-calculation model. Also the measured stresses in the hydrofrac borehole F-UB-25 in the western wall of the parallel drift are in good agreement with the model-calculated minimum stresses.

In the results of the calculations the same crackings which have been found at the pillar ends facing to the dome cavity occurred as well (Fig. 14). These cracks were formed due to the subjection to tension in the contour region of the dome foot standing in rock salt. In the carnallitic dome flanks above the Lower Werra rock salt the tensile cracks have an essentially deeper extension into the walls.

3.3 *Conclusions*

The rock mechanical calculations provide explanation of the cause and of the mechanism of the failure

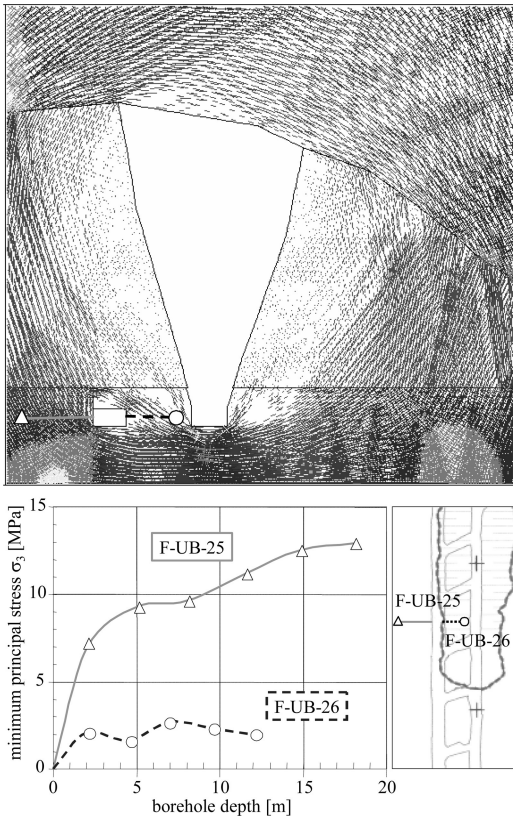

Figure 13. Vectors of the minimum principal stress in the result of the calculation (upper part); and results of hydrofrac measurement within the rock salt floor in-situ (lower part).

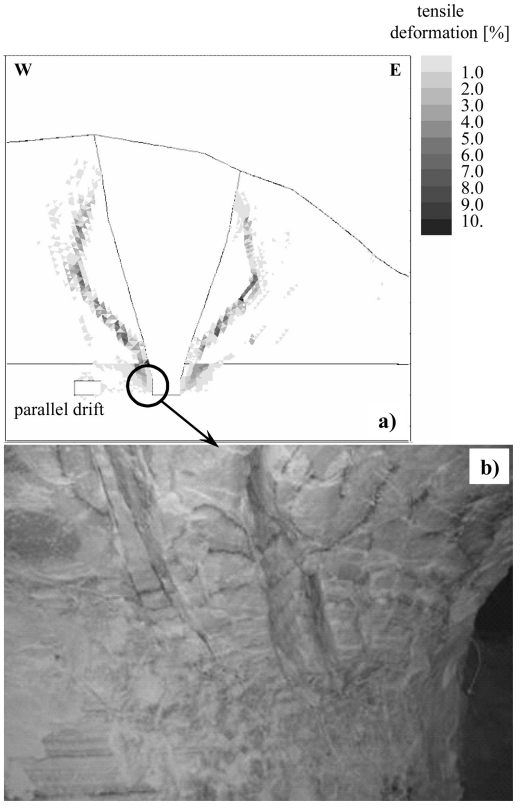

Figure 14. Tensile cracks around the dome cavity. a) Results of model calculation; b) Visible cracks in rock salt in the lower part of the dome cavity.

process which occurred on 09/22/2005 in the mentioned dome mining area. This explanation is furthermore in good agreement with the results of the investigations in the domains of seismology, mine surveying and geotechnics.

Cause and initiator of the failure process was the roof fall of a residual bank of the seam having a thickness of approx. 5…6 m which extended over an area of approx. 40 × 45 metres at a distance of 100 m behind the working edge of the dome.

Due to the abrupt failure of this roof mass which until then had hindered the displacement of the dome walls at the top, within the flanks of the dome shear displacements were activated on the bedding plane contact between the potash seam Thueringen and the Middle Werra rock salt. After the adhesive peak shear strength on the bedding planes had been overcome, a drop in shear stresses has occurred so that the dome walls were abruptly shifted toward the worked cavity. In the seismogram this process appears as a marked s-wave which identifies the main failure process as a shear fracture.

Furthermore, the result of modelling shows that this shear process has occurred mainly on the bedding planes between carnallitite and rock salt of the eastern flank of the seam accumulation. This is due to the steep incline in connection with the local thinning of the seam.

Following the Madariaga model the radius of the seismic focus of the shear fracture area has been assessed to be circa 100 m which lies in the same order of magnitude as the dimension of the bedding plane where in the rock mechanical model intensive shear displacements have occurred.

When dome workings are driven then these kind of spontaneously occurring powerful seismic events can simply be prevented by avoid or blast down all residual masses of the seam in the cavity roof.

4 SUMMARY

The combination of both constitutive models about the mechanical behaviour of salt rocks and bedding

planes offers the possibility of a deeper understanding of the dynamic processes running in the salt rock massif. With respect to several rock bursts which occurred in potash mining in the past until now numerous calculations have been carried out. These examples demonstrate that for a comprehensive explanation of failure processes the softening processes both within the salt rocks and on the bedding planes must be taken into consideration. With this prerequisite, the model simulation of failure processes provides an important increase in knowledge about the limits of system stability of working systems.

In conclusion, only the comprehensive understanding of the rock mechanical causes of failure processes inside mining systems provides a better potential of a safe dimensioning of working sites where the aspects of mining with regard to economy and safety are taken into account.

REFERENCES

Gimm, W. & Pforr, H. 1961. *Gebirgsschläge im Kalibergbau unter Berücksichtigung von Erfahrungen des Kohle- und Erzbergbaus.* Freiberger Forschungshefte A 173. Berlin: Akademie.

IfG 2005. *Prognose der dynamischen Langzeitstabilität von Grubengebäuden im Salinar unter Berücksichtigung von Diskontinuitäts- und Schichtflächen*. Final report for Forschungszentrum Karlsruhe, FKZ 02C0892. Leipzig: Institut für Gebirgsmechanik.

Itasca 2004. *UDEC – Universal Distinct Element Code, Vers. 4.0*. Minneapolis: Itasca Consulting Group Inc.

K-UTEC 2005. *Auswertung der seismischen Vorgänge am 22.09.2005 in der Zeit von 06.00 bis 08.07 MESZ im Kaliwerk Werra der Grube Unterbreizbach der K+S KALI GmbH*. Report from Kali-Umwelttechnik GmbH Sondershausen, unpubl.

Mocka, N. 1988. *Beitrag zur technologischen und geomechanischen Beherrschung des Abbaus von Lagerstättenanstauungen im Carnallitit im VEB Kalibetrieb "Werra"*. Dissertation, Bergakademie Freiberg.

Minkley, W. 1998. Zum Herdmechanismus von großen seismischen Ereignissen im Kalibergbau. In G. Leydecker (ed.), *Geologisches Jahrbuch* E 55: 69–84. Stuttgart: Schweizerbart.

Minkley, W. & Menzel, W. 1999. Vorausberechnung des Kollapses eines Grubenfeldes – Gebirgsschlag Teutschenthal 11. September 1996. In R.M. Geertman (ed.), *Proc. 9th Int. Congress on Rock Mechanics, Paris, 25–28 August 1999*, *Vol. 2*: 1115–1118. Rotterdam: Balkema.

Minkley, W. 2004. *Gebirgsmechanische Beschreibung von Entfestigung und Sprödbrucherscheinungen im Carnallitit*. Aachen: Shaker.

Minkley, W. & Mühlbauer, J. 2007. Constitutive models to describe the mechanical behaviour of salt rocks and the imbedded weakness planes. *In Proc. 6th Conference on the Mechanical Behaviour of Salt, Hannover, 22–25 May 2007*, in press. Rotterdam: Balkema.

Swanson, P.L. & Boler, F.M. 1995. *The magnitude 5.3 seismic event and collapse of the Solvay Trona Mine: Analysis of pillar/floor failure stability.* U.S. Bureau of Mines, Open File Rept.: 86–95.

van Sambeek, L.L., Gowan, S.W., Payment, K.A. 2000. Loss of the retsof rock salt mine. In R.M. Geertman (ed.), *Proc. 8th World Salt Symposium, The Hague, 7–11 May 2000, Vol. 1*: 411–416. Amsterdam: Elsevier.

Taylor & Francis
Taylor & Francis Group
http://taylorandfrancis.com

The Mechanical Behavior of Salt – Understanding of THMC Processes in Salt –
Wallner, Lux, Minkley & Hardy, Jr. (eds)
© 2007 Taylor & Francis Group, London, ISBN 978-0-415-44398-2

Performance of a mining panel over tachyhydrite in Taquari-Vassouras potash mine

Leo Rothenburg
University of Waterloo, Canada

Afonso L.P. Carvalho Jr.
CVRD, Brazil

Maurice B. Dusseault
University of Waterloo, Canada

ABSTRACT: Taquari-Vassouras is an underground potash mine in northeastern of Brazil operated by Companhia Vale Do Rio Doce. Sylvinite is mined at depths ranging from 430 to 640 m where room and pillar panels are excavated using continuous mining equipment. The stratiform ore deposit consists of a lower and upper sylvinite layers separated by a barren halite interval. The underlying evaporites include a massive tachyhydrite layer separated from the lower sylvinite by a halite layer that in some areas is very thin or non-existent. Tachyhydrite is highly hygroscopic, weak, and creeps two orders of magnitude faster than the surrounding salts under similar conditions. One of the mine panels was successfully excavated in the area where tachyhydrite is in direct contact with sylvinite. An extensive array of convergence stations was installed in the panel and the panel was closely monitored. A series of room-and-pillar scale and panel-scale numerical analyses were carried out with the objective to establish the mechanism of tachyhydrite influence on the panel performance. It was established that despite operating difficulties related to floor heave, the presence of tachyhydrite has a positive influence on the stability of the roof.

1 INTRODUCTION

The potash deposit in the Taquari-Vassouras region of northeastern Brazil is found within evaporites of the Ibura Member in the Sergipe/Alagoas sedimentary basin. Sylvinites of the Ibura Member are mined at a depth of about 500 meters in an underground mine located near the city of Aracaju. Production started in 1985. The mine is currently owned and operated by Companhia Vale do Rio Doce (CVRD). It produces about 1% of the world's potash. The history of the mine and some production data can be found at the company's web site (www.cvrd.com.br).

The evaporite sequence of Sergipe is only a marginal bay of the South Atlantic evaporite basin formed during the Middle Cretaceous split of South America from Africa (Szatmari et al, 1979). A potash mine on the African side of the South Atlantic evaporite basin, the Holle potash mine in Congo Basin flooded in 1977 (Ruiter, 1979; Feuga et al, 2005). This fact has always been a source of caution in the development of the Taquari-Vassouras deposit.

The geologic history of the Ibura Member involves nine sedimentary cycles defined by Szatmari, 1974. The basal parts of the evaporite sequence of Sergipe consists of calcareous muds and halites overlying the basal shales (Cycle I), passing to carnallites and tachyhydrites (Cycles III to VI), and then back to sylvinites and halite of Cycle VII at the top of salt. The two sylvinite beds mined at Taquari-Vassouras are interdispersed between the halites of Cycle VII. The total thickness of Cycle VII is about 40 m and the sylvinite beds form irregularly distributed and discontinuous layers with about 5 m average ore thickness. This is reflected in a rather irregular pattern of mining panels scattered over the mine area as shown in Figure 1. Depths of panels vary from about 400 m to over 600 m, with sylvinite beds dipping locally by as much as 15°C. High geothermal gradients in the area maintain the virgin rock at temperatures in excess of 38°C. Mining is carried out by the room and pillar method using continuous Marietta mining machines. Several vertical passes are used when the ore is sufficiently thick. Excavation heights average about 5 m.

Although both sylvinite beds are present in most parts of the deposit, only one bed is mined at any particular location as the other bed is frequently too thin or discontinuous in the same area. The lower sylvinite bed

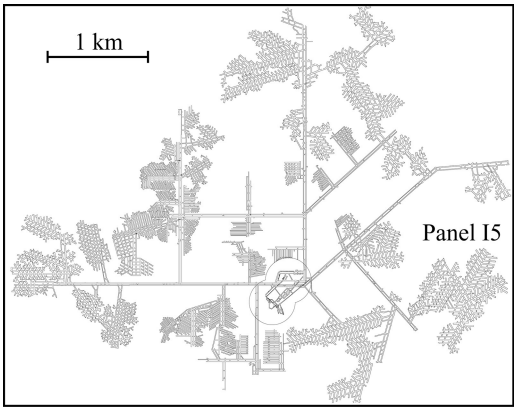

Figure 1. 2002 layout of the Taqari-Vassouras mine.

overlies the tachyhydrite layers with thickness ranging from 1 m to 80 m. As a result, most panels were excavated in the upper sylvinite. Prior to excavating Panel I5, several small test panels were excavated in the lower sylvinite.

Mining the lower sylvinite bed is complicated by the presence of a generally massive tachyhydrite layer underlining the lower sylvinite. Some halite or carnallite in between these layers are very thin or non-existent in many parts of the mine. Pure tachyhydrite [$CaMg_2C_{16}\cdot12(H_2O)$] is highly hygroscopic, weak, and creeps two orders of magnitude faster than the surrounding salts under similar conditions. Although the tachyhydrite found in the mine area contains carnallite and halite as secondary components, its macroscopic mechanical behavior is clearly controlled by tachyhydrite. To minimize its intrusion into openings, a protective sylvinite or halite slab in the floor is desirable to control floor heave.

Due to bed thickness restrictions, one of the mine panels in the Taquari-Vassouras mine, Panel I5, has been successfully excavated with a minimal protective slab in the area where tachyhydrite is in direct contact with sylvinite. The location of Panel I5 in the mine is shown in Figure 1. The Panel was closely monitored during excavation and for several years after, by measuring convergence in a dozen key locations. A series of room-and-pillar scale and panel-scale numerical analyses was carried out to establish the mechanism of tachyhydrite influence on the panel performance. The paper presents the results of this unique study as well as other CVRD data relevant to mining over tachyhydrite.

2 PANEL I5 LAYOUT AND STRATIGRAPHY

Excavation of Panel I5 started in late 1996 and took about 3 years to complete, with some 1.64 million tons

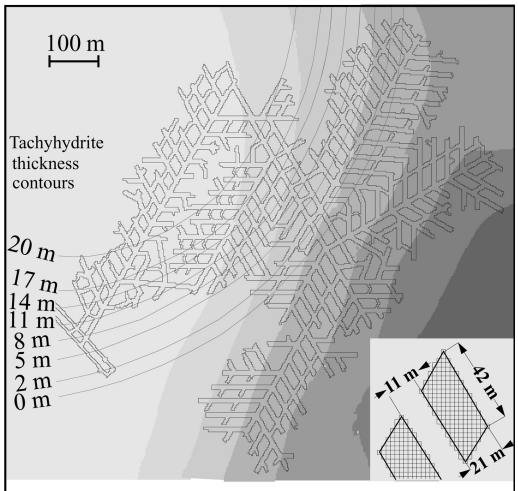

Figure 2. Layout, depth and tachyhydrite contours of Panel I5.

of ore excavated. The layout of the panel, depths of excavations and tachyhydrite contours in the panel area are illustrated in Figure 2. In areas where the tachyhydrite thickness is about 20 m, excavations are at a shallow depth of some 450 m. The sylvinite ore thickness varies across the panel significantly, allowing one vertical excavation pass (2.74 m) in most tachyhydrite areas, and typically two vertical passes (5.28 m) where tachyhydrite is not present. Main entries of the panel and most rooms are 10.9 m wide and excavated using horizontal Marietta passes. At this room width, the mining machine can conveniently negotiate 60° turns in the direction of excavation, resulting in parallelepiped-shaped pillars. Their minimum dimension is about 21 m. The typical room-pillar geometry is illustrated on the insert in Figure 2, where pillars are shown discretized for purposes of numerical analyses. The illustrated configuration corresponds to an extraction ratio of 49%. Cuts into the abutments increase the overall panel extraction ratio to 55%.

The composite stratigraphic sequence in the Panel I5 area is shown in Figure 3 where several prominent markers delineating main strata are indicated. In particular, the upper boundary of the Cycle VII at its contact with Breccia corresponds to Marker 38. The lower boundary of Cycle VII is in a discordant contact with tachyhydrites of the preceding Cycle VI. The two sylvinite beds are found above and below Marker MVII-10. In general, the zone in which sylvinite is found starts below fine-grained halite, at a

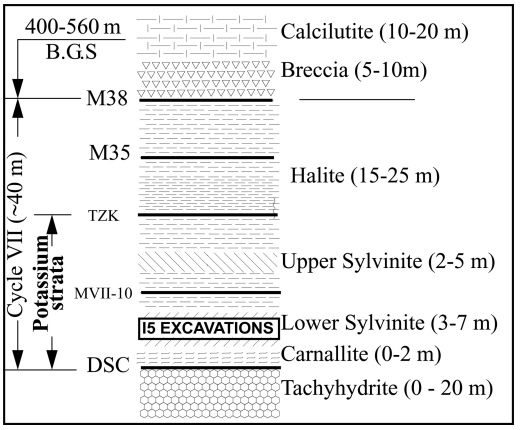

Figure 3. Layout and depth of Panel I5.

level marked TZK (top of the potassiferous zone) in Figure 3. The salt thickness in the roof of excavations above Panel I5 is in excess of 20 m.

3 POTENTIAL AQUIFER AND IMPLICATIONS

During excavation of mine shafts in 1981, a thin (6–8 m), poorly-consolidated sandstone aquifer was encountered above the mining level. Intensive injections were necessary to stop the inflow into shafts (Soubrouillard and Lourdel, 1984). Although the aquifer has been found about 80 m above the mine level, the possibility of it being much closer to the mine in some locations is considered likely as a result of a survey using Time Domain Electromagnetic Method (Chouteau et al, 1997).

Even if an aquifer is present near the Panel I5, it is generally expected, (e.g. Berest, 2003), that the salt back thickness of over 20 m should provide adequate protection from inflow. However, unexpected flooding at the Holle Mine, Republic of Congo (Ruiter, 1979), under a similarly thick salt cover but on the African side of the Taquari-Vassouras deposit, contributed to extreme caution in the way the CVRD mine was designed and is being operated. Mine panels are designed in such a way that stresses at the top of the salt remain above the potential aquifer pressure over the lifetime of the mine. The logic behind this design reflects the notion that natural or deformation-induced microfractures in salt promote the opening of microscopic pathways through salt when fluid pressure exceeds confining stress. The pathways may enlarge with time, eventually leading to an inflow. Concerns about the reduction of confining stress in the overburden below the aquifer pressure were expressed by Van Sambeek (1993) in connection with the inflow

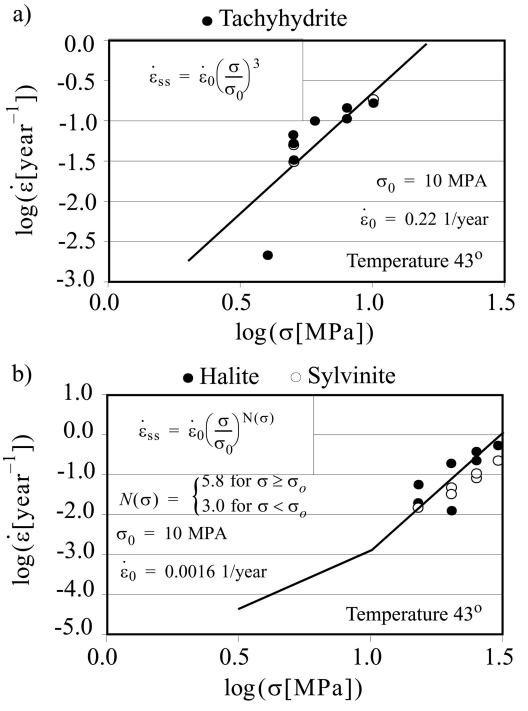

Figure 4. Summary of creep tests.

at K2 mine, as well as Mraz and Genzwill (1986), in connection with the same event.

In order to implement the stated design approach, various numerical tools and laboratory data in conjunction with field observations are necessary. These elements of design and analysis are described below.

4 CREEP PROPERTIES OF SALTS

Mechanical properties of Taquari-Vassouras evaporites from the mine were determined combining laboratory tests with calibration of a numerical model using convergence measurements in an isolated test room with tachyhydrite in the floor. The procedure has been described by Mraz et al (1996) and is briefly summarized below.

Samples of halite, sylvinite and tachyhydrite were tested at the University of Waterloo in 1995–96 at a temperature of 43°C. Tests on tachyhydrite were carried out in the range of shear stress between 4 MPa and 10 MPa and in the range of confining stresses expected in-situ. Steady-state creep rates from laboratory data in Figure 4a were approximated using the Norton creep law with the exponent 3. It should be noted that an unconstrained regression of laboratory data gives an exponent of 3.22. As the number of tests is relatively small, 11 in total, the exponent determined

from the unconstrained regression changes somewhat when one point is eliminated from the full regression set. In such conditions, it is appropriate to choose the Norton Law with the exponent of 3 as having general significance corresponding to a physically distinct creep mechanism.

Due to slow creep of halite and sylvinite under shear stresses expected in-situ, samples of these materials were tested at elevated shear stresses ranging from 15 MPa to 30 MPa in order to complete tests within a reasonable time period. The data are illustrated in Figure 4b, also showing the Norton Law approximation with an exponent of 5.8 in the range of stresses where tests were carried out. Although separate analyses of halite and sylvinite data give somewhat different Norton Law approximations, distinctions are not warranted, particularly when the intended application is to study the effects of tachyhydrite that creeps orders of magnitude faster than both salts. In addition, boundaries of sylvinite and halite are not always confidently known to utilize in a model. Far more important is the fact that due to limitations of testing, the information on creep behavior in the low range of shear stress must come from in-situ data.

If the creep law with a high exponent of 5.8 is extended into the range of low shear stress, convergence measurements in the test room intended for calibration/verification of parameters would have been impossible to match. The test room (C1D1) was excavated in lower sylvinite in 1988 in such a way that a variable thickness of sylvinite (and carnallite) remained in the floor at different sections of a 100 m long room. The distance to tachyhydrite in the floor varied from 3.5 m to 1.2 m. The test room was excavated to have a 4 m square section and was monitored for about 7 years, with both horizontal and vertical convergence rates remaining steady. Although vertical convergence rates, strongly influenced by tachyhydrite, can be matched with the single exponent Norton Law, matching horizontal rates requires a multi-exponent creep law illustrated in Figure 4b. With the lower exponent assumed to be 3, the transition stress, σ_o, was determined by regression of computed rates on measured rates, and σ_o rounded off to 10.0 MPa was obtained. The details of monitoring data and calibration results can be found in Mraz et al (1996). Computations were carried out using the FEM code VISCOT in plane strain mode. Unfortunately, similar computations are not feasible on the scale of a panel as large as Panel I5.

5 TECHNIQUES OF PANEL-SCALE ANALYSES

A large-scale numerical analysis of a system like Panel I5 is clearly not feasible using techniques requiring full 3D discretization. To appreciate the issue, note that the discretization of Panel I5, occupying more that 1 sq km area, involves some 150,000 plane square elements reasonably representing the layout of rooms and pillars on the mining plane, Figure 2. Discretization of the overburden and underburden would require at least 20 million brick zones to use in a finite difference code like FLAC3D. This makes computations not feasible even with the most modern computers. On the other hand, numerical techniques that require no 3D discretization, such as the Boundary Element or its Displacement Discontinuity version, are practically limited to elastic rocks surrounding excavations (Solomon, 1963). More complex material behavior of pillars can be accommodated in the Displacement Discontinuity (DD) method by modeling pillars as non-linear springs and dashpots with equivalent properties. In the Displacement Discontinuity implementation used for analysis of Panel I5, equivalent properties were determined from FLAC3D analyses of individual pillars.

Apart from computational challenges related to the panel-scale analysis, description of the mechanical behavior of overburden rocks on a scale of several kilometers is a difficult issue in its own right. The Taquari-Vassouras overburden model that was developed from the interpretation of convergence measurements in other panels of the mine is described further and discussed in connection with convergence observations in Panel I5.

6 SINGLE PILLAR BLOCK BEHAVIOR

Just as the creep rate of a laboratory sample stabilizes under constant stress, a salt pillar is expected to compress at a steady rate if the gross pillar load remains constant. The steady-state is reached after some short transient period when stress redistribution within the pillar is completed. Since the horizontal confining stress increases from zero at the surface to some maximum value in the interior, creep rates are nonuniform throughout the pillar.

Despite the complexity of stresses and deformations within a salt pillar, a rather simple pattern emerges if compression of the entire salt stratum between non-salt layers is considered. Because of the rigidity of the strata above and below salt layers, deformations of the pillar block are practically identical over the pillar and over surrounding rooms. This is shown in Figure 5 that summarizes convergence rates along the centerline of a circular pillar, as well as along a section through the center of the surrounding circular room. A 3D view of the geometry analyzed using FLAC3D is shown in Figure 6b. The pillar block is analyzed under the tributary load corresponding to lithostatic stress at 500 m depth. The extraction ratio of the block is

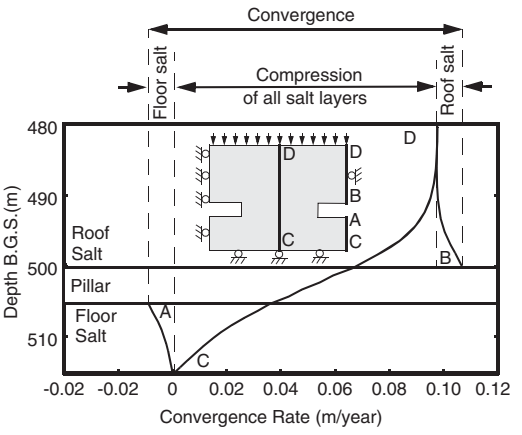

Figure 5. Components of convergence rates.

50% and the pillar diameter as well as the room width are typical of Panel I5. The steady-state compression rate of all salt layers is about 0.10 m/year while the computed convergence rate is 0.12 m/year. The difference between the two relates to the intrusion of salt from the roof and from the floor into the opening. Both rates are practically identical and each contribute about 0.01 m/year into convergence despite the fact that the salt thickness in the roof is 20 m while the salt thickness in the floor is 10 m. The excavation height is 5 m. Identical salt properties are assigned to all layers. It should be noted that the computed convergence rate is on the high side of measured rates at 500 m depth. This example will be now compared to the case when tachyhydrite is present in the floor.

In order to ascertain the influence of tachyhydrite on floor heave, creep constants in all other salt layers were set to zero in the analyses illustrated in Figure 6. In the two cases analyzed, essentially rigid circular and 60° parallelepiped pillars were allowed to sink into tachyhydrite under lithostatic load. The computed sinking rates are 0.33 m/year and 0.40 m/year for circular and parallelepiped pillars respectively, Figure 6a. Also, Figure 6c illustrates displacement rate contours in tachyhydrite indicating floor heave of 0.51 m/year for the circular pillar. The corresponding convergence is $0.33 + 0.51 = 0.84$ m/year. The computed average convergence for the parallelepiped- shaped pillar is over 1 m/year. These steady state rates are excessive compared to the rates that were actually observed is Panel I5. This suggests that the actual load on pillars is less than tributary based on lithostatic stress.

Extensive parametric analyses utilizing VISCOT in axisymmetric mode resulted in the following relationship for the steady-state rate of penetration into tachyhydrite of thickness D of a pillar with diameter B, surrounded by a room of width W, with the pillar

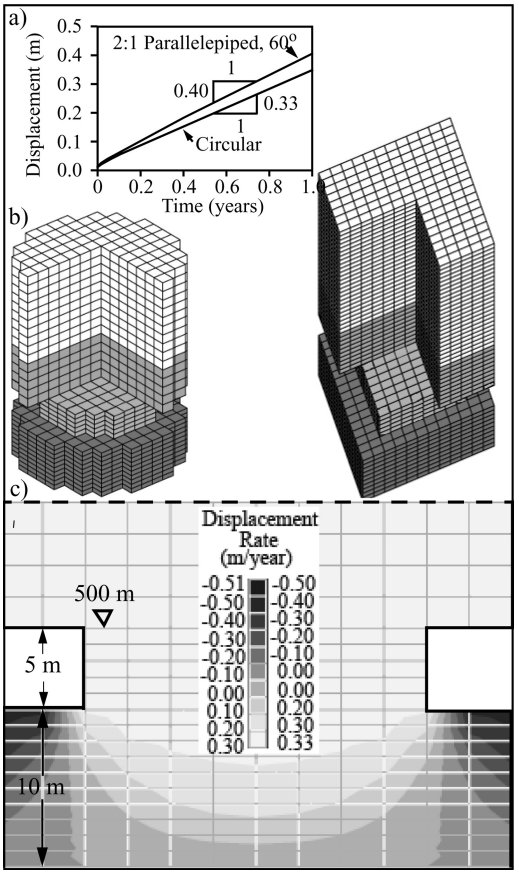

Figure 6. Pillar block analyses.

being under average vertical stress σ_z:

$$\dot{\delta} = BK_D\left(\frac{D}{B}\right)K_W\left(\frac{B}{W}\right)\dot{\varepsilon}_o\left(\frac{\sigma_z}{\sigma_o}\right)^3,$$

where functions K_D and K_W have the following analytical approximations:

$$K_D = 0.0285\frac{25\tilde{D}^2}{1 + 25\tilde{D}^2(1 - \exp(-4\tilde{D}^2)) + 20\exp(-4\tilde{D}^2)}$$

$$K_W = \frac{\tilde{W}}{1.345 + \tilde{W}(1 - Exp(-0.333\,\tilde{W}))}.$$

The previous formulae are in terms of non-dimensional $\tilde{D} = D/B$ and $\tilde{W} = W/B$ Both functions are illustrated in Figure 7. It should be noted that the numerically derived solution is applicable to any power-law material with exponent 3. Limited studies suggest that the influence functions K_D and K_W are slightly dependent on the power law exponent. For the circular pillar in

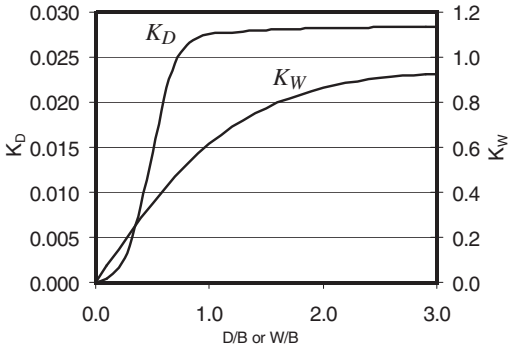

Figure 7. Coefficients for calculating pillar penetration rate.

Figure 6, the outlined solution gives the penetration rate of 0.29 m/year as compared to 0.33 m/year computed using FLAC3D. The difference is likely due to the coarse mesh used in the FLAC3D analyses while very fine VISCOT mesh was used in computations leading to and K_D and K_W.

The shape of the function K_D is such that the tachyhydrite depth in excess of the pillar width does not influence the rate of pillar penetration. However, the sensitivity of pillar penetration to the room width is apparent over a wider range of room widths.

7 PILLAR INTERACTIONS – FEM ANALYSES

The pillar block analyses described in the previous section reflect the situation when displacements along vertical boundaries of the block create no shear resistance. Such "roller" boundary conditions essentially confine the gross load within the analyzed area. This type of situation can only occur in an infinite system where each element is a mirror image of it's neighbor across the roller plane. Abutments would necessarily break any symmetry that may exist in the mining panel, thus forcing load sharing between pillars and abutments.

In any realistic situation, pillars in a panel interact with each other and share lithostatic load with abutments depending on deformation characteristics of pillars and properties of rocks surrounding the panel. Apart from complete symmetry, the limiting case when each pillar carries full lithostatic load from its tributary area implies soft overburden with no ability to develop shear stress for load transfer. On the other hand, an infinitely stiff overburden can span from abutment to abutment with no need for pillar support. This limiting case corresponds to zero pillar load. The tributary load corresponds to the upper limit.

The presence of soft tachyhydrite in the vicinity of excavations creates a peculiar situation when the overburden behaves as "stiff" while the underburden

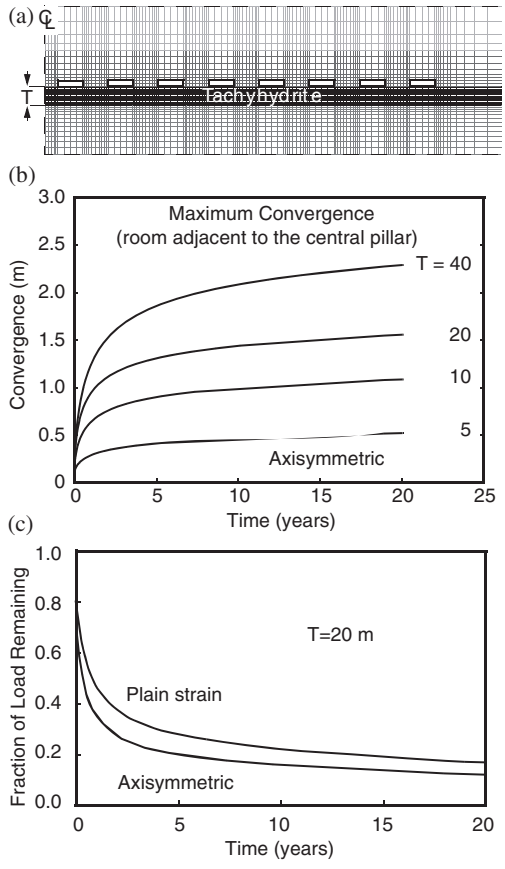

Figure 8. Panel-scale analyses using FEM.

is "soft". The behavior of this system is unusual in a number of ways and is analyzed further using a combination of modeling and observations.

In order to investigate the influence of tachyhydrite on a panel performance, a series of plane strain and axisymmetric VISCOT runs were carried out on layouts that reflect Panel I5 in terms of extraction ratio and the overall panel size. A fragment of the FEM mesh used in these analyses is illustrated in Figure 8a. The mesh involves a layout with 16 rooms in the 750 m wide area and 1000 m abutments. The axisymmetric layout corresponds to a series of concentric rooms and circular pillars. The plane strain layout represent infinitely long rooms. Both plane and axisymmetric analyses were carried out for a range of tachyhydrite thicknesses.

The computed convergence versus time curves feature strong dependence on the tachyhydrite thickness shown in Figure 8b. Rapid slowdown of convergence rates with time indicates load transfer away from pillars in the panel. This is confirmed by calculations

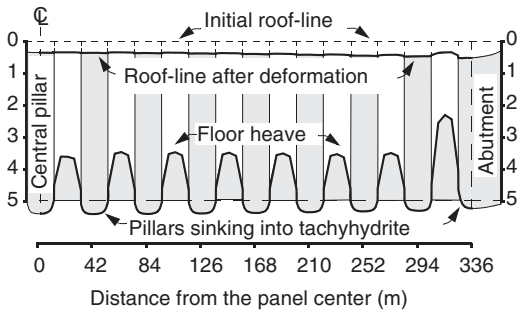

Figure 9. Floor heave and roof line deformations.

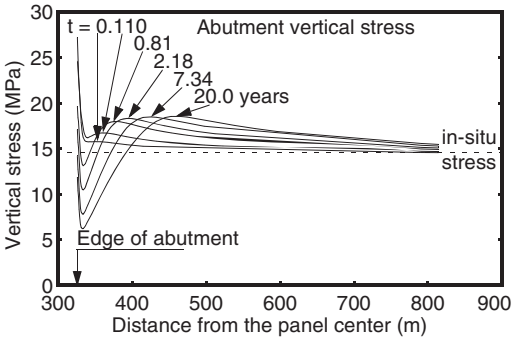

Figure 10. Transfer of abutment load into the interior.

illustrated in Figure 8c where the average load on pillars is shown as a fraction of tributary load. The load lost by pillars is transferred to abutments. The total load on pillars and abutments is maintained with high accuracy.

Perhaps the most important feature of the analysis is illustrated in Figure 9 showing computed displacements of the roof line and deformations at the floor level. The latter includes floor heave and sinking of pillars. The uniform movement of the roof across the panel is a highly positive feature of the panel performance, as differential movements in the roof are the primary cause of roof falls. The stiff roof/pillar system pushed pillars into soft tachyhydrite without developing differential movements in the roof.

It is interesting to note that the volume of salt flowing into openings is clearly greater than the volume of tachyhydrite displaced by pillars, Figure 9. Careful investigation traced this to the elastic modulus of tachyhydrite, which, from laboratory tests, is about 2 GPa, or 1/10 of the sylvinite modulus. Unloading of the panel leads to reduction of stresses in tachyhydrite and its expansion. This creates a peculiar situation where swelling of tachyhydrite results in additional support to pillars, thus reducing their rate of sinking into the tachyhydrite. This effect is not present when the tachyhydrite modulus is taken equal to the modulus of sylvinite. It can also be noted from Figure 9 that the floor heave in the room adjacent to the abutment is considerably higher than in other rooms. This is because load transfer to abutments results in an additional stress that squeezes tachyhydrite from underneath the abutment into the adjacent room. Higher floor heave near abutments is invariably observed.

Tachyhydrite under abutments makes the latter more compliant as a result of tachyhydrite extrusion. As this process is taking place, the peak pillar stress migrates outward, Figure 10. Although this behavior is common even without tachyhydrite, the latter considerably enhances the load migration rates thus unloading the abutment near the edge.

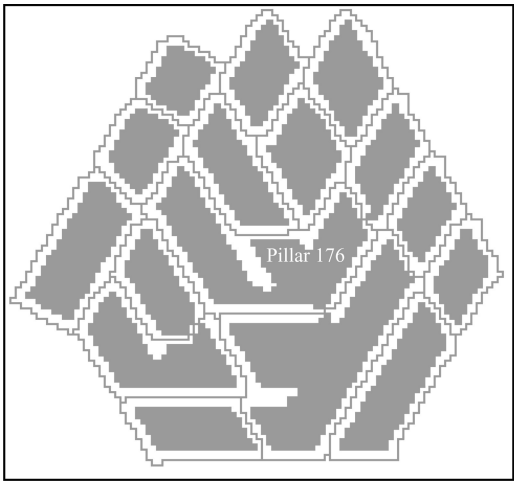

Figure 11. Tributary areas of pillars.

8 PANEL-SCALE ANALYSES

Even when pillars interact with each other and abutments, their behavior can be considered quasi-independent within their tributary areas identified on a fragment of Panel I5 in Figure 11. This is because displacements along vertical tributary boundaries in the middle of rooms are primarily vertical, as if a "roller" boundary condition is prescribed on such a boundary. This property of vertical tributary boundaries can be observed in the multi-room VISCOT solutions described above. Each pillar then can be discretized and analyzed independently to determine it's performance under the full range of possible loads, with the tributary lithostatic load being the upper limit. Analyses using FLAC 3D of individual pillars, such as the one in Figure 12, can be used to establish pillar block models to use in a displacement discontinuity code such as VELMINA (Rothenburg, 1992). Because

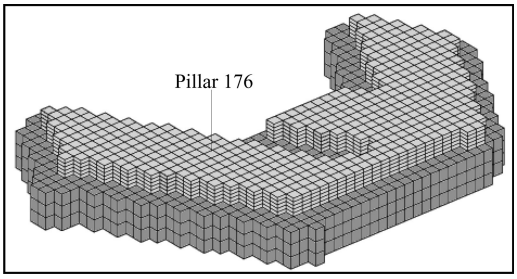

Figure 12. FLAC3D discretization of a pillar for VELMINA analysis.

a typical mining panel normally includes many geometrically identical pillars, the computational task is not difficult when discretization is automatic based on the plane layout. This procedure is now implemented in the VELMINA code to determine actual loads on interacting pillars.

9 PANEL I5 CONVERGENCE MEASUREMENTS

Both VISCOT and VELMINA codes give comparable convergence result that qualitatively differ from field observations in Panel I5. Examples of comparing convergence measurements and modeling results are illustrated in Figure 13.

All measurements in Panel I5 indicate that convergence rates stabilize after some initial time period, typically several months. This performance is similar in other panels of the Taquari-Vassouras mine. On the other hand, numerical models used indicate continuously diminishing convergence rates due to various load transfers. The key element of both VISCOT and VELMINA codes leading to unlimited transfer of loads to abutments is the elastic overburden.

10 A VISCO-ELASTIC OVERBURDEN MODEL

The issue of a physically appropriate constitutive model for rocks surrounding the salt strata in the Taquari-Vassouras mine and in many other instances of large scale analyses is a difficult one. Observations clearly point to the limited ability of the overburden to transfer loads from pillar to pillar and to abutments. On the other hand, shear stresses induced in the overburden, particularly in the case of thick roof salts overlaying tachyhydrites, are too small to expect "plastic deformations" associated with strength-limited behavior. Still, from the modeling point of view, only plastic deformations in the overburden can limit load transfer

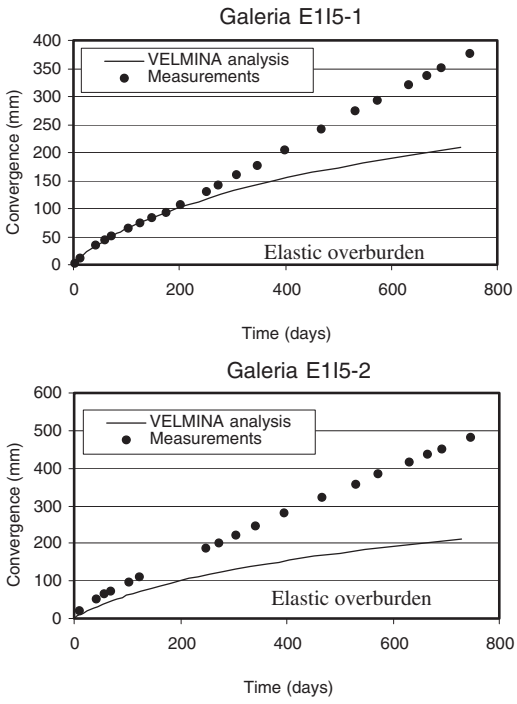

Figure 13. Convergence measurements and VELMINA/ elastic model.

and stabilize pillar loads so that steady state is reached, as observed.

The simplest 1-parameter model that can be easily implemented in the displacement discontinuity setting of the VELMINA code involves linearly viscous behavior where plastic strains are volume-preserving and proportional to shear stress. The proportionality coefficient can be in a form of Young's modulus but with the dimensionality GPA/year. The value found by modeling non-tachyhydrite panels was rounded to $\overline{E} = 10$ GPa/year. To appreciate the numerical sense of this value, note that a stress change of 10 MPa would generate 0.1% strain if a uniaxial load is maintained for one year. A 1 m cube of rock will then deform by 1 mm. It is not difficult to imagine rock joints that will lead to such deformations.

The value $\overline{E}$ of used for re-analysis of Panel I5 corrects the problem illustrated in Figure 13 and gives a response consistent with the steady state, as illustrated in Figure 14.

The model also represents average convergence rates very well, as illustrated in Figure 15, which compares average convergence measurements and average computed convergence. Computations were carried out respecting the sequence of panel excavations.

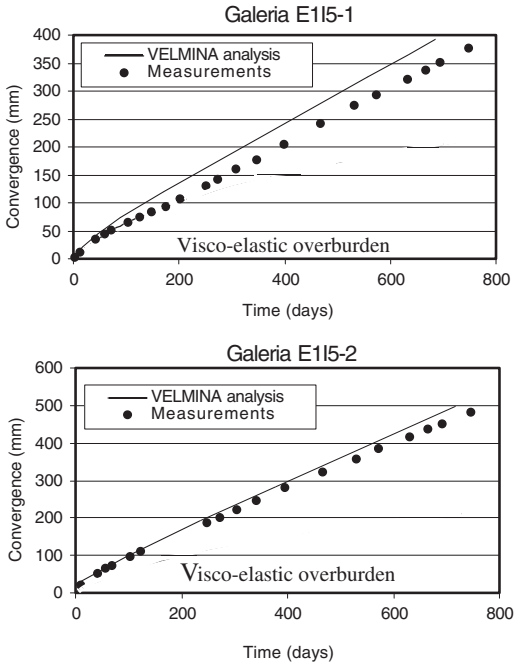

Figure 14. Convergence measurements and VELMINA/ plastic model.

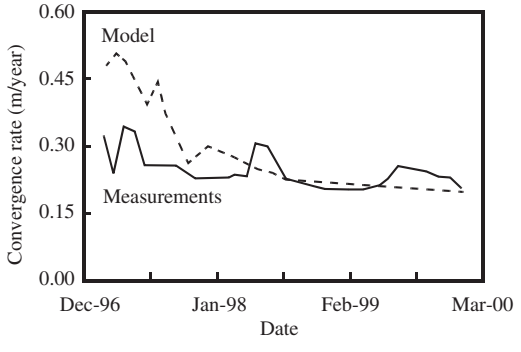

Figure 15. Measured and computed average convergence rates.

The model overestimates transient convergence rates during the excavation period.

The map of convergence rates is shown in Figure 16, while the vertical stress distribution is shown in Figure 17. It is important to note that tachyhydrite areas of Panel I5 are under reduced stress. However, stress computations at the top of salt give values above the potential aquifer pressure.

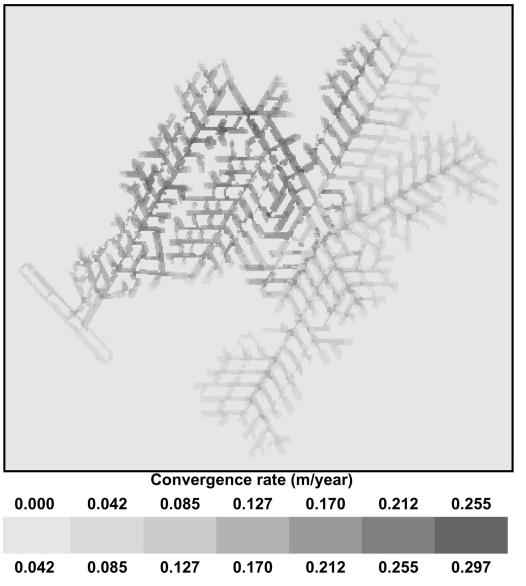

Figure 16. Steady state convergence rate distribution.

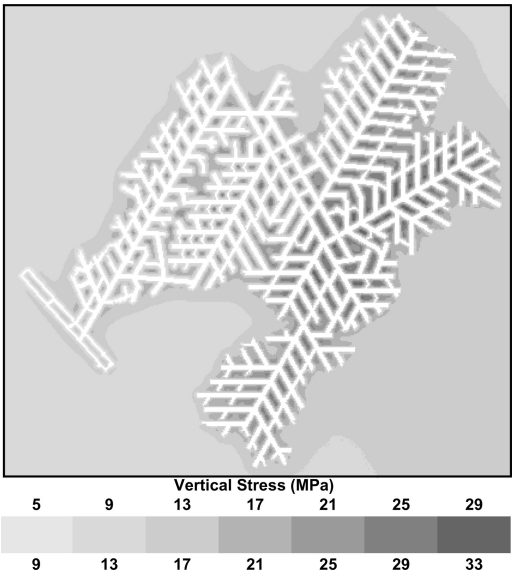

Figure 17. Steady state vertical stress distribution.

11 CONCLUSIONS

Despite considerable operational difficulties of mining in conditions of severe floor heave, Panel I5 was successfully excavated. Extensive analyses indicate that the roof stability is improved due to exposed tachyhydrite in the floor and "soft" behavior of abutments.

Visual observations in Panel I5 confirm this conclusions. A numerical model of Panel I5 has been developed by supplementing the displacement discontinuity method with FLAC3D analyses of individual pillar blocks. Physically realistic and accurate panel-scale analysis requires accounting for plastic properties of overburden rocks.

REFERENCES

Berest, P., Brouard, B., and Feuga, B., 2003. Dry Mine Abandonment, *SMRI Fall Meeting*, Chester, UK.

Chouteau, M., Phillips, G., and Prugger, A., 1997. Mapping and Monitoring Softrock Mining, *Proc. of Exploration 97*, Prosp. and Dev. Assoc. of Canada, Sept. 14–18. Toronto.

Feuga, B., Schlund, J-M., and Wasmer, B., Geoderis, M.F., 2005. The Flooding of the Holle Potash Mine, *SMRI Fall Meeting*, Nancy, France.

Mraz, D.Z, Rothenburg, L., Valente, A. A. and Frank R., 1996. Evaluation of a mining panel in Taquari-Vassouras potash mine. In: F. Hassani & H. Mitri (eds). *Rock Mechanics Tools and Techniques*. Balkema.

Maraz, D.Z. and Genzwill, D., 1986. Evaluation of Subsidence over a Deep Saskatchewan Potash Mine", *2nd Workshop on Surface Subsidence Due to Underground Mining*, June, Morgantown, West Virginia.

Rothenburg, L., Frane, M.A., and Mraz, D.Z., 1992. Calibration of two and three dimensional models for intact saltrock, Proc, Int. Cong. on Mine Design, Aug. 26–29, Queen's U.

Ruiter, P.A.C., 1979. The Gabon and Congo Basins Salt deposits. Economic Geology, 74, pp. 419–431.

Salamon, M.D.G., 1963. Elastic analysis of displacements and stresses induced by the mining of seam or reef deposits, *J. S. Afr. Inst. Min. Metall*., 64, 128–149.

Soubrouillard, G. and Lourdel, Y., 1984. L'ingénierie Minière integer: example du project Potasse Sergipe au Brésil: Industries Minérale, Les techniques, 3–84, 246–255.

Szatmari, P., Carvalho, R.S. de Simoes, I.A. Tibana, P. and Leite, D.C., 1974. Evaporitos de Sergipe, v. 1, Projeto Evaporitos, SEM Ba / SEPES, Aracajú, p. 159.

Szatmari, P., Carvalho, R.S. de, Simoes, I.A., 1979. A Comparison of Evaporite Facies in the late Paleozoic Amazon and Middle Cretaceous South Atlantic South Basins. Economic Geology, 74, pp. 432–447

Van Sambeek L.L., 1993. The IMC K2 Mine Flooding. *SMRI Fall Meeting*, LaFayette, LA.

The Mechanical Behavior of Salt – Understanding of THMC Processes in Salt –
Wallner, Lux, Minkley & Hardy, Jr. (eds)
© 2007 Taylor & Francis Group, London, ISBN 978-0-415-44398-2

Monitoring of roof stability in salt mines

J.-P. Schleinig & V. Lukas
K+S Aktiengesellschaft, Kassel, Germany

ABSTRACT: Understanding the mechanical behavior of salt related to roof stability of drifts is of crucial importance for the safety of workers and installations in mines. In its potash and rock salt mines K+S uses different measures and instruments to collect geomechanical data and to monitor roof stability. Examples of the various methods to monitor the roof behavior are discussed for the potash mine Werra and the rock salt mine Borth. This monitoring supplies quantitative data for further geomechanical interpretation and is the base for a prognosis of the development of roof stability.

1 INTRODUCTION

The roof stability of drifts is a fundamental precondition for a safe mining process. Therefore many methods are used to measure the mechanical behavior of roof and hanging walls of drifts, which have to kept open for a long period of time for infrastructural reasons e.g. ventilation, transport and conveyor belts. Because of the special behavior of salt rock general measuring and interpretation methods have to be specified.

K+S uses different measures and instruments to collect geomechanical data and to monitor roof stability in its potash and rock salt mines. Example from two mines, the potash mine Werra and the rock salt mine Borth, with the application of various methods and the interpretation of their results are presented in the paper. These results are the basis for the deduction of roof stabilizing measures as scaling or additional bolting.

2 MEASURING METHODS

The measuring methods to collect geomechanical data, which are used for interpretation of roof behavior, can in general be distinguished between movement- and stress-measuring methods. This paper deals with the methods and results of movement measurements. The targets of movement measurement are mainly the subsidence of the roofs, the rock bolt deformation and the development of cracks in the roof.

Measurements methods to observe the subsidence of the roof contour and the hanging wall are mainly leveling and extensometer measurements. Leveling needs marked points at the roof, i.e. rock bolts or special measuring points, and supply absolute values of subsidence. Extensometers consist of a wire or rod, which is fixed in one or more horizons in the borehole and is free at the borehole mouth. Measured values are relative movements between the fixed points in the borehole and the borehole mouth.

Further methods to observe the behavior of drift roofs and hanging walls are ultra sonic measurement of rock bolts, high frequency georadar and borehole television measurements.

The ultra sonic measurements of rock bolts are used to observe the linear expansion of the bolts. The technique is described in Zapp et al. (2005). The principle of this measurement is the propagation and reflection of ultra sonic waves in rock bolts. The ultra sonic wave runs through the rock bolt and is reflected at its ending. The running time of the wave is used to evaluate the effective rock bolt length. The measuring is done by contacting a sensor at the rock bolts end. This sensor contains the transmitter and receiver. Figure 1 shows two sensors and the recorder. The quality of the reflected signal depends on the rock bolt steel quality and the rock bolt loading. Figure 2 shows a measuring result displayed at the recorder with a clear reflection. The first peak (green marked) of the reflection is used to measure the running time to calculate the actual rock bolt length. The calculated rock bolt length is shown at the top of the display (orange marked) with in this case 1.252 mm.

The investigation starts with the measuring of the rock bolt before and after its installation. Experiences show, that the installation procedure needs about 4 mm rock bolt deformation, depending on the applied initial load. The following measurements show the development of rock bolt deformation and are compared with rock bolt deformation capacity.

Figure 1. Recorder and two sensors of the ultra sonic tool.

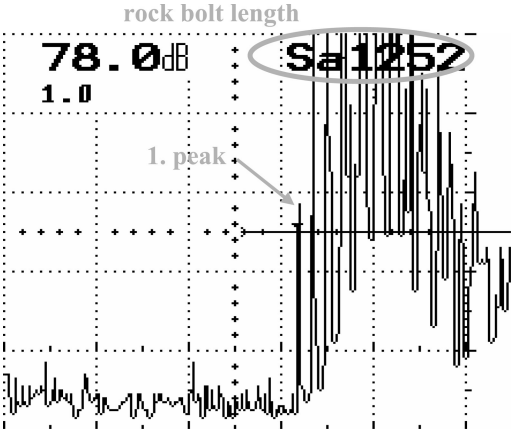

Figure 2. Measuring result with a clear reflection.

The georadar technique is based on the propagation and reflection of high frequency electromagnetic waves (20 MHz−2 GHz). The technique is widely described in Daniels (1996). The radar method provides images of non-conductive media at shallow depths. The reflections are due to a contrast in the dielectric permittivity and conductivity, e.g. salt versus an open fracture. The radar pulse has a large frequency bandwidth to achieve a high resolution. The penetration, which can reach several hundreds of meters in resistive environments, decreases when the used frequency increases. A higher frequency provides on the other hand a better resolution. The quality of the profiles is well improved by using processing techniques like filtering, automatic gain control, background removal and migration. A planar reflector

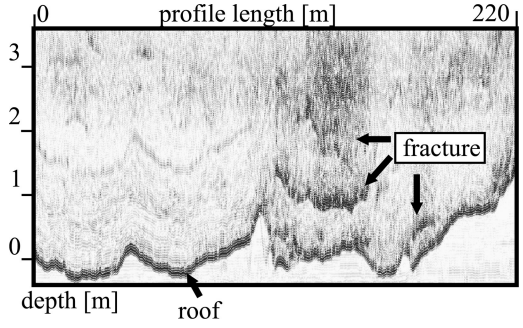

Figure 3. Radar profile carried out in the salt mine.

results in a planar event on the radar profile. Heterogenities (e.g. a hole) with very small dimensions compared to the wavelength result in a hyperbolic event on the radar profile.

Because of his high resistivity, the salt rock is a good medium for the propagation of radar waves. GPR and borehole radar have been successfully used in potash and salt mines in order to map stratigraphic features or to determine the extension of the deposit [e.g. Beer, 1990; Käding & Lukas, 1997; Zeibig & Wendzel, 2000].

An example of a radar profile carried out in a potash mine is given on Figure 3.

The first reflection after the direct wave corresponds to the reflection on the roof. This reflection is energetic because of the large permittivity contrast between air and salt. The arrival time changes along the profile because of the irregularity of the roof. The other reflections correspond to open fractures. The polarity of these reflections is opposite to the polarity of the reflection of the roof because it corresponds to a contrast in permittivity from salt to air. As the velocity of electromagnetic waves is known, the position of the fractures in salt can be easily determined.

The georadar technology is used to map a large number of drifts in a fast and economic way. The results show the lateral extend of cracks along the profiles and the distance of the cracks in the hanging wall.

The method of borehole television measurements are used to observe the occurrence and development of cracks in the roof and further to explain unclear measurement results of alternative monitoring methods. A borehole camera with cable drum is presented in Figure 4.

The small mirror at the camera allows to monitor the borehole contour perpendicular to the borehole axis. A typical picture of borehole television observation is shown in Figure 5.

The results of these different movement measurements can be used directly to describe the development of roof stability or as input parameters for numerical simulations.

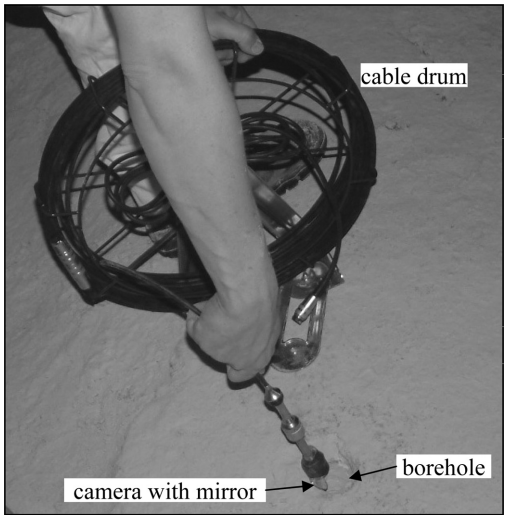

Figure 4. Borehole camera with cable drum.

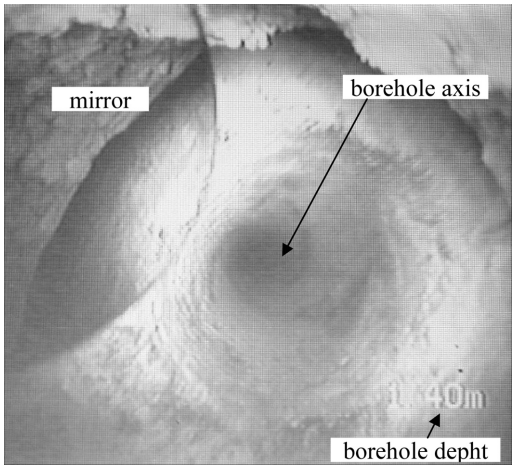

Figure 5. Typical borehole picture.

3 MEASUREMENTS IN THE POTASH MINE OF WERRA

3.1 *Deposit and mine*

The potash mine Werra of K+S Kali GmbH is located in the middle of Germany between the towns Bad Hersfeld and Bad Salzungen. In depths between 400 m and 1.000 m the potash ore is extracted at two levels with a vertical distance of approx. 50 m. The thickness of the potash layers varies between 2 m and 7 m. The potash ore is mined by the room and pillar method.

Two measurements systems ensuring roof stability are described as follows. The first system deals with ensuring roof stability in infrastructural drifts. The second system describes the behavior of roof and hanging wall in an infrastructural drift in the upper horizon influenced by active mining in the lower horizon.

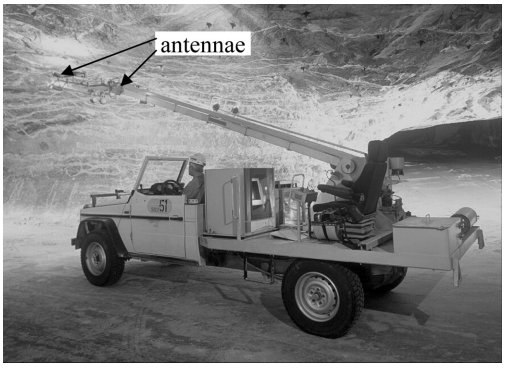

Figure 6. Measuring car with two antennas.

3.2 *Ensuring roof stability by a high frequency georadar system*

The Werra mine has reached a lateral extent comparable to the city of Munich. Therefore a large number of drifts connecting shaft and active mining areas for transportation, ventilation, conveys etc. have to be kept open and safe for a long period of time. The length of these drifts totals to several hundreds of kilometers. Therefore a special system had to be developed controlling the roof stability in these drifts regularly. The special requirements objectives were the distinction between fractures and geological reflections on the radar profiles and the need to carry out extensive surveys in a relatively short time period because of the total length of the drifts.

After some successful initial tests using different radar equipments, a car was equipped with a control unit and a hydraulic arm to lift a maximum of 4 antennae near the roof of the drift. At the moment two 900 MHz antennae are installed. The survey speed of this two channels application is approx. 15 km/h. Tests have shown that a direct coupling of the antenna to the salt is not necessary. A working distance of 0.5 to 1 m to the roof gives a satisfactory signal quality. Figure 6 shows the equipment used for the investigation of fractures in the roof of the drift.

This radar technique has proved to be efficient for mapping fractures in the roof of drifts and is daily carried out in the Werra mine. The measurements show that the dynamic acquisition at the speed of 15 km/h does not affect the quality of the data.

The lateral extends and the distances of the cracks are mapped and measures to restore roof stability are deduced. A special focus is related to cracks near the

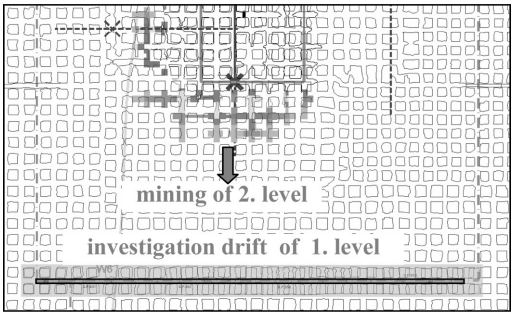

Figure 7. Principle situation of the first and second level in a ground view.

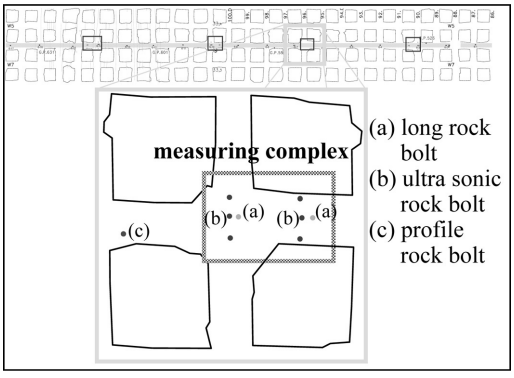

Figure 8. Investigation area at the first level with a measuring complex.

upper end of rock bolts as they result in destabilizing the rock bolt itself.

3.3 *Investigation of roof stability by various methods*

Geomechanical observations and roof falls in the past document the geomechanical interference of the lower mining level if approaching existing drifts in the upper level. In preparation of a planned crossing between an infrastructural drift in a mined area of the upper horizon and active mining in the lower horizon various methods are applied to monitor the roof behavior. Figure 7 shows the principle situation in a ground view. The small rectangles are pillars at the existing first level. The shaded area marks the drift at the first level, where the investigations are carried out. From the upper part of the figure the second level mining area approaches the investigation drift at the first level. The vertical distance between both levels averages 50 m.

In Figure 8 the investigation area at the first level is shown in detail. By the time of approach and undercutting of the investigation area at the first level by mining at the second level for the observation of roof stability the following measuring methods are applied:

- Leveling a profile of rock bolts along the drift axis as well as of long rock bolts (6 m long) and ultra sonic rock bolts in the measuring complex,
- ultra sonic measurements of rock bolts,
- high frequency georadar measurements along the drift axis.

The leveling of profile and ultra sonic rock bolts supply the subsidence of the roof, which can be compared with the subsidence of the hanging wall measured by leveling of long rock bolts. By comparing the results an impression about loosening in the roof and about the subsidence of hanging wall without loosening near the roof is generated. The ultra sonic measurements of rock bolts show the rock bolt strain of the lining. The high frequency georadar measurements along the drift axis allow identifying cracks near the roof as well as their development.

The results of these measurements can be concluded as followed:

- First very small roof subsidence can be observed with a horizontal distance of about 400 m between the mining area (2. level) and the investigation area (1. level).
- From a horizontal distance of about 80 m between the mining area (2. level) and the investigation area (1. level) a significantly subsidence of the roof can be observed.
- The subsidence of the roof and the hanging wall are widely consistent. The ultra sonic measurements attest the small strain of roof and rock bolts.
- The high frequency georadar measurements show, that
  - the roof and hanging wall are in general not cracked,
  - during undercutting by mining area (2. level) the existing cracks increase partly in lateral extend,
  - during undercutting by mining area (2. level) only small cracks are formed.

4 MEASUREMENTS IN THE ROCK SALT MINE OF BORTH

4.1 *Deposit and mine*

The rock salt mine of the esco, european salt company, in Borth is located in the north-western part of Germany. In depths of 800 to 1.000 m rock salt of the Zechstein formation is mined by a modified method of long pillar mining system. The rock salt has a purity of more than 98% of NaCl and the thickness of the mined horizon is 20 m.

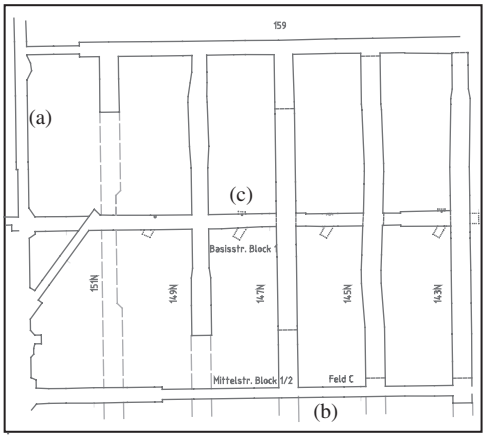

Figure 9. Ground view of a mining block.

Figure 9 shows a principle ground view of a mining block. The mining consists of the following steps. Starting from the extraction drift (a) the mining block will be prepared by two ventilation drifts in the upper area of mining horizon (b) and by two central drifts (c), which are located one upon the other with a horizontal pillar of about 10 m. The mining goes from the right to the left side and is carried out in two phases. In the first phase a hanging drift with a width of 20 m and a height of 5 m is mined to connect the upper central drift with the ventilation drift. In the second phase the cavity is opened to a height of about 20 m with the same width as the hanging drift. The length of each mined cavities is 165 m.

This mining system was applied about three years. A measuring system was necessary to evaluate the roof stability in the central upper und lower drifts, which were used in the whole time of mining in the block.

4.2 *Measuring methods and results*

The main methods to observe the subsiding of the drifts roof and the hanging wall were the leveling of rock bolts combined with extensometer measuring. The leveling of rock bolts supplied the absolute subsidence of the drifts roof. In a distance of about 1 m to the leveled rock bolt a wire extensometer was installed in a borehole. In the upper central drift the extensometer showed the relative movement between the hanging wall in distances of 2 m and 6 m above the roof and the roof contour. The combination of both methods allowed to estimate the absolutely subsidence of the drift roof and of two horizons (2 m and 6 m) above the roof. Figure 10 shows a measuring profile in the upper central drift.

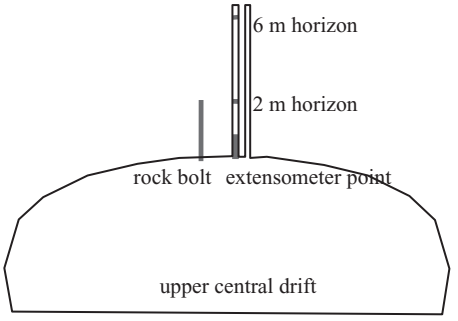

Figure 10. Cross section of the upper central drift.

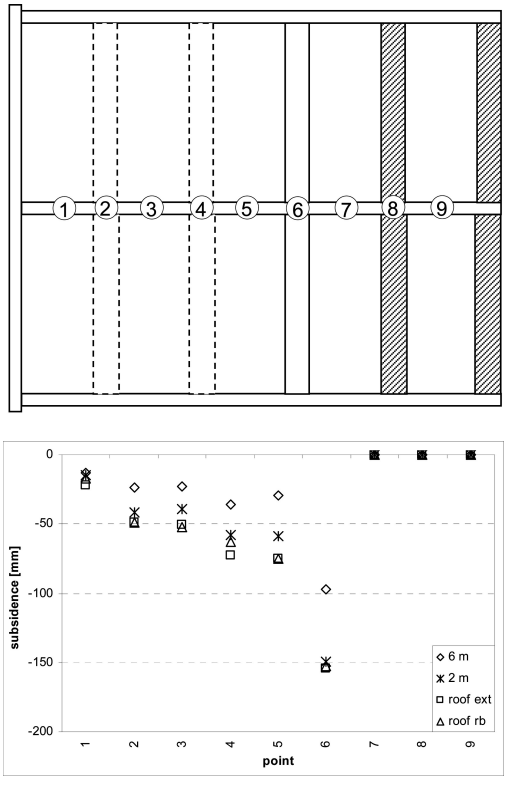

Figure 11. Principal ground view and measuring results.

A second borehole was drilled in the case, that a borehole television inspection was necessary to explain unclear measuring results.

In the lower central drift a similar system was installed. The extensometer shows here the movement of the horizontal pillar between the upper and lower central drifts.

Typical results of subsidence measuring in the upper central drift are shown in Figure 11. In the upper part

the principal ground view to a special time of mining process is shown. Further on the location of the measuring points (1 to 9), the mined cavities (hatched areas), the realized hanging drifts and the planned cavities (dashed areas) are given. The measuring point locations are the same in the upper and lower central drift. The diagram below gives the measuring results. The vertical axis is the absolute subsidence of all measured horizons: roof rock bolt (roof rb), roof extensometer (roof ext), horizons 2 m and 6 m above the roof in the hanging wall. The horizontal axis shows the number of measuring points.

The results can be interpreted as followed:

- The mining of the four stopes on in the right hand side is finished. Therefore measuring points 7, 8 and 9 are no longer accessible due to drift closing, which is necessary to ensure ventilation.
- The measuring point 6 is out of order. It showed unrealistic subsidence during the whole measuring time. This was checked by borehole television in an adjacent borehole and by high frequency georadar measurements. There were no debondings in the roof or hanging wall.
- The measuring points 1 to 5 represent the subsidence caused by mining. The subsidence increases in the direction to the actively mined stopes in the block.
- The measuring point 4 shows an interesting fact. There is a subsidence difference between the roof rock bolt and the roof extensometer point. Therefore the roof extensometer point seems to be fixed at a local loose part of the roof.
- The difference between the roof points and the 2 m horizon of extensometer reached 20 mm in maximum. Therefore the current rock bolt deformation is about 20% of the maximum rock bolt deformation capacity.

The measurements of upper and lower central drifts can be summarized as followed:

- There is more roof subsidence in the lower than in the upper central drift.
- The subsidence between the roof rock bolt and the roof extensometer point is not as uniform as in the upper central drift.
- The roof strain is bigger than in the upper central drift, which is verified by borehole television measurements.
- The roof stability and the rock bolt function are ensured in the upper central drift. In the lower central drift measuring results show, that further roof stabilizing measures as scaling or additional bolting are necessary.

5 CONCLUSIONS

Monitoring of the roof behavior supplies quantitative data for further geomechanical interpretation and is the basis to forecast the development of roof stability. In mines of the K+S group various observation methods for roof stability are used to ensure the safety of workers and installations. The used methods and the interpretation of their results allow to evaluate the development of the roof and the hanging wall. If it necessary, further roofing stabilizing methods as scaling or additional bolting can be deduced.

REFERENCES

Beer, W. 1990. Elektromagnetische Reflexionsmessungen. Zwölf Jahre praktische Anwendungen und Ergebnisse. *Kali und Steinsalz 10*, H 7/8, pp. 226–232.

Daniels, D.J. 1996. Surface penetrating radar. *The institution of Electrical Engineers.* United Kingdom.

Käding, K.-C. & Lukas, V. 1997. Untertageradar (EMR) als Planungsinstrument im Salzbergbau. *Kali und Steinsalz 12*, H 5, S. 151–157.

Zapp, J., Wittenberg, D. & Wüllenweber, A. 2005. Entwicklung und Einführung der Ultraschallprüftechnik für eingebaute Spreizhülsenanker im Kali und Steinsalzbergbau. *Kali und Steinsalz* 2/2005, pp. 26–33

Zeibig, S. & Wendzel, J. 2000. Exploration of anhydrite wall and klippe structures for an optimized extraction of rock salt in the K+S mine Bernburg (Northern Germany). *Proceedings 8th World Salt Symposium, The Hague*. Published by Elsevier. Vol. 1: 193–198.

The Mechanical Behavior of Salt – Understanding of THMC Processes in Salt –
Wallner, Lux, Minkley & Hardy, Jr. (eds)
© 2007 Taylor & Francis Group, London, ISBN 978-0-415-44398-2

Determination of mechanical homogeneous areas in the rock salt mass using creep properties for a classification scheme

Ingo Plischke
Federal Institute for Geosciences and Natural Resources, Hanover, Germany

ABSTRACT: The knowledge of the mechanical behavior of rock salt, especially the creep behavior, is important for the dimensioning and the long-term safety analysis of underground openings. The multiple internal configuration of the salt structures has to be taken into account in the corresponding model calculations. A mapping and characterization procedure based on laboratory creep tests is outlined. The results demonstrate the suitability and the efficiency of the method in which the classification of the rock mass is performed by the identification of areas of similar creep ductility. It provides the basis for the derivation of a site specific geo-mechanical model. The method was used for the site characterization of the Morsleben salt structure and the Gorleben salt dome. For the Morsleben site an example is given concerning the influence of several geological-mineralogical parameters on the creep behavior.

1 INTRODUCTION

For reliable model calculations of underground openings in rock salt formations the mechanical properties of the host rock must be investigated, because particularly its creep behavior varies considerably. Therefore, the rock has to be characterized appropriately and classified. Then, the same material law and the specific set of parameters of a certain part of the host rock with similar mechanical behavior can be reliable used.

A salt structure can have a rather complicated geology. In addition to general geological information, the site specific underground investigation is needed which delivers data to identify the stratigraphic strata and to develop the geological model.

Halitic, carnallitic and anhydritic rocks which are the main types of salt rocks in salt formation differ considerably in their mechanical behavior. This can be a special challenge for the construction of a mine or cavern, although such construction is primarily done in the halitic rock, i.e. rock salt. However, the mechanical behavior of the halitic rocks can also vary considerably, depending on its chemical and mineralogical composition. Tectonical and petrographic characteristics can also have an influence.

Therefore, the creep behavior of the rock salt in all parts of the mine of importance has to be examined and analyzed. It cannot be taken for granted that the variation of the creep behavior is only correlated with the stratigraphic strata in the halite. Therefore, the geological – mineralogical parameters have to be analyzed in more detail (Albrecht et al. 1990 & 1993) and (Hunsche et al. 1996).

2 METHODOLOGY

The results of creep tests are compiled for the determination and mapping of comprehensive, i.e. homogenous areas in a salt rock formation. A homogenous area distinguishes itself as an area with nearly identical creep behavior. By definition such areas differ from each other by a factor of 2 in the steady state creep rate where the laws BGRa or BGRb deliver the reference. With respect to a geological model a mechanical model may be elaborated by this method which gives the basis for numerical model calculation.

Mapped homogeneous areas are often correlated with geological sections. But it has to be stressed that attributes resulting from tectonical site history may superimpose the geologic situation.

The comparison with geological and petrographic attributes and the well determined correlations (see Figure 4) approve statements about mapped areas from which petrography and stratigraphic assignments are known, but could not be inspected, for instance by drilling. In this context, the evaluation of correlations between geological, petrographical and mechanical properties is essential for the prediction of the spatial and time dependent evolution of stress and strain in the formation.

In this paper, the determination of homogeneous areas in the ERAM (Endlager für radioaktive

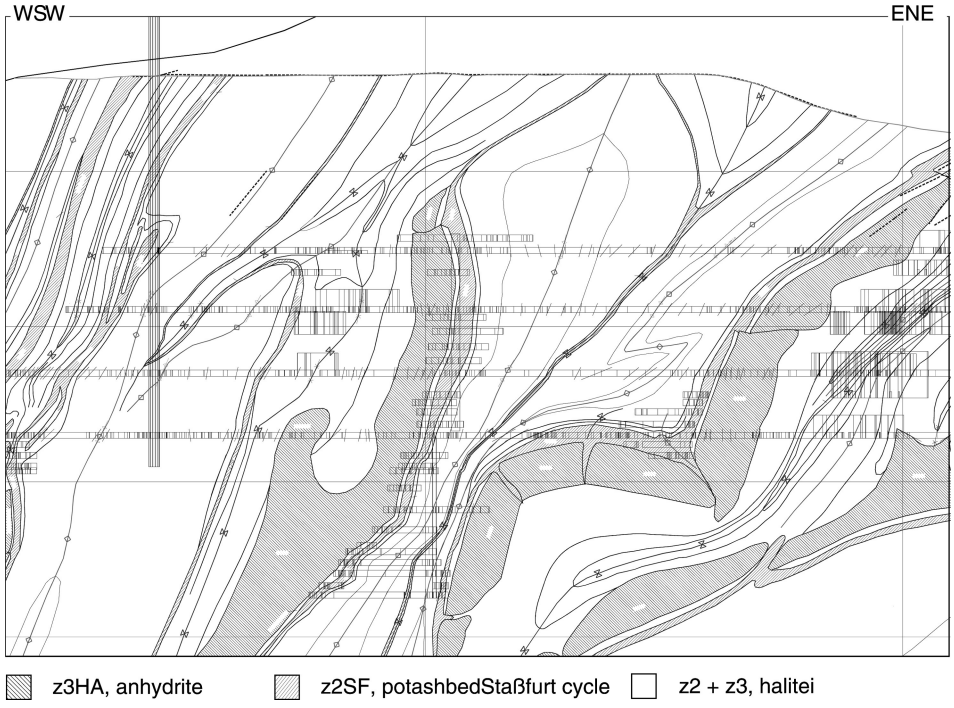

Figure 1. Modified geological cross section, 3.1 ERA Morsleben after Behlau. & Mingerzahn (2001).

Abfallstoffe Morsleben) is elucidated. The geological model is the prerequisite. Figure 1 shows a vertical geological cut through the ERAM.

The steady state creep behavior of rock salt from various rock zones is determined by uniaxial and triaxial creep testing. Figure 2 shows results (deformation versus time) of some creep test performed with some creep test performed with specimens from different strata of the ERAM.

By comparing the experimentally determined steady state creep rates with the steady state creep laws BGRa or BGRb (equation 1 and 2), respectively, it is possible to calculate the creep class K or determine that in accordance to Figure 3.

Equation (1) and Equation (2) describe the dependence of the steady state creep rate on temperature T and stress σ. Q is the activation energy for creep dominated by dislocation mechanisms.

Grading of creep classes for uniaxial creep tests at room temperature is based on creep law BGRa. For tests at higher temperatures (more than 30°C), when samples can dry out, and for triaxial tests where humidity assisted creep is suppressed, creep law BGRb delivers the basis. In case of uniaxial creep tests, a pre-factor for the humidity affected creep has to be mentioned, if the relative humidity deviates from 45% r.h. during the test.

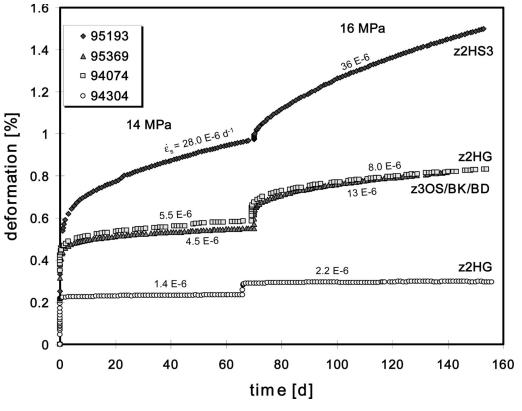

Figure 2. Creep tests on rock salt from different stratigraphic horizons, ERA Morsleben. Numbers indicate steady state creep rate (1 per day).

Reference creep law BGRa

$$\dot{\varepsilon}_s = V \cdot A \cdot \exp\left(\frac{-Q}{R \cdot T}\right) \cdot \left(\frac{\sigma}{\sigma^*}\right)^n \qquad (1)$$

$A = 0.18\,\mathrm{d}^{-1}$ $\quad n = 5$ $\quad \sigma^* = 1$ MPa (normalization)
$Q = 54$ kJ/mol $\quad R = 8.314 \cdot 10^{-3}$ kJ/(mol·K)

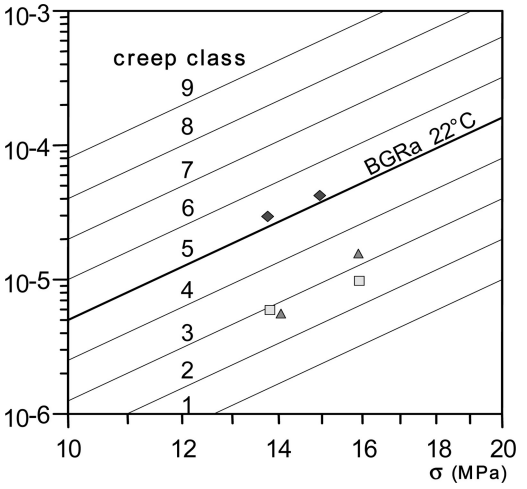

Figure 3. Definition of creep classes, the creep law BGRa gives the reference for class "5". Each next class represents the two-fold higher or lower creep ductility.

Table 1. Relation between pre-factor and creep classes.

Creep class K	−1	0	1	2	3	4	5	6	7	8	9
Pre-factor V	1/64	1/32	1/16	1/8	1/4	1/2	1	2	4	8	16

Reference creep law BGRb

$$\varepsilon_s = V\left[A_1 \cdot \exp\left(\frac{-Q_1}{R \cdot T}\right) + A_2 \cdot \exp\left(\frac{-Q_2}{R \cdot T}\right)\right] \cdot \left(\frac{\sigma}{\sigma^*}\right)^n \tag{2}$$

$A_1 = 2.3 \cdot 10^{-4} \cdot d^{-1}$; $A_2 = 2.1 \cdot 10^{6} \cdot d^{-1}$
$Q_1 = 42\ kJ \cdot mol^{-1}$; $Q_2 = 113\ kJ \cdot mol^{-1}$

$$V = \frac{2^K}{32} \tag{3}$$

The exponent K indicates the creep class of a homogenous area. In the creep laws BGRa and BGRb the pre-factor has to be $V = 1$ where $V = 2^K/32 = 1$ requires the creep class $K = 5$.

The application of this method, where a whole salt formation is subdivided and assembled into homogeneous parts with nearly the same creep capability, makes the characterization of this whole formation manageable. Table 1 shows the relation of the creep classes K with pre-factor V.

3 RESULTS

3.1 *Creep class determination and mapping*

For different locations and stratigraphic layers of the Stassfurt cycle (z2) and the Leine cycle (z3) in the ERAM Table 2 shows the recommended pre-factor V, which has to be applied in numerical model calculations, where the creep equation BGRa is used for the prediction of the long-term evolution of stress and strain. The limits of variation are also shown. To display possible dependencies and trends, the mean value of the crystallinity and content of impurities (especially anhydrite) are additionally specified. As mentioned, these correlations deliver the basis to determine creep classes of non sampled rock areas with respect to its geological position.

The frequency distributions of the evaluated creep classes were used to determine the "recommended creep class" and its "limits of deviation" for particular stratigraphic units. In general the "recommended creep class" was picked at the maximum of a histogram. "Limits of deviation" of homogeneous areas was determined on the base of the evaluated maximal and minimal creep classes. In most cases extreme results were ignored, because closer inspection showed non-representative behavior.

3.2 *Correlation*

It was often found that a stratigraphic unit includes different homogeneous areas, on the other hand it is also possible that different stratigraphic layers can be collected to one homogeneous area. The results of the creep tests on rock salt and potash salt give the basis for a systematic analysis. Nearly 300 creep tests from the ERAM were analyzed with respect to the influence of the following parameters: stratigraphy, crystallinity, bedding (dip), impurity content, density, tectonical history, state of preservation of the specimen.

Except "stratigraphy" and "state of preservation of the specimen" these are all primary parameters, where each of them can have a separate influence. In a sedimentation cycle of rock salt (z2 or z3) we can generally recognize following dependencies:

- Within a cycle of sedimentation younger strata are creeping slower than elder ones, in general.
- Strata which were intensively pressed together by a tectonic impact creep faster than those which were rolled or folded.
- Rock salt with dispersively distributed impurities creeps slower than other types of rock salt.
- Coarse grained rock salt creeps faster than fine grained material.

Grain size can not have directly an influence on creep behavior. If coarse grained rock salt is generated

Table 2. Recommended pre-factor for the creep equation BGRa and limits of deviation for different locations and stratigaphic layers of the Stassfurt cycle (z2) and Leine cycle (z3) from the ERAM.

Location	Stratigraphy	Pre-factor V	Limits of deviation + (factor) – (factor)	
Ostfeld, Zentralteil u. Gorleben	z2SF/ct	BGR-Carnallitit	10	1/10
Westfeld, RB354	z2SF/ki	1/32 · BGRa	2	1/2
Westfeld, RB328	z2SF (Hartsalz)	1/2 · BGRa	2	1/4
Ostfeld, RB012	z2HG und z2UE	1/8 · BGRa	4	1/2
Westfeld, RB325,RB326,RB354, Zentralteil, RB323	z2HG – z2UE	1/32 · BGRa	2	1/2
Ostfeld, RB012,RB301	z2HS	1/2 · BGRa	8	1/4
Westfeld, RB328	z2HS3	1 · BGRa	2	1/2
Zentralteil, RB323	z2HS3	1/16 · BGRa	4	1
Marie, RB345	z2HS3	1/4 · BGRa	4	1/2
Südfeld, RB330	z3BS	1/16 · BGRa	2	1
Ostfeld, RB012, Zentralteil, RB320,RB321	z3LS	1 · BGRa	2	1/8
Ostfeld, RB302, Südostfeld, RB317	z3OS	1/2 · BGRa	4	1/4
Südfeld, MoRB331	z3(LS+OS)	1 · BGRa	2	1/2
Südostfeld, RB318	z3OS/BK/BD	1/4 · BGRa	2	1
Nordstrecke, RB303	z3OS/BK/BD	1/16 · BGRa	2	1/4
Ostfeld, RB382,RB383	z3BK/BD	1 · BGRa	2	1/2
Westfeld, RB328, Südfeld, RB330, Zentralteil, RB353,RB322, Marie, RB304,	z3AM	1/32 · BGRa	1	1/2
Nordstrecke, RB303,RB312, Südostfeld, RB318, Ostfeld, RB324	z3AM	1/16 · BGRa	4	1/2
Nordstrecke, RB303	z3SS	1/8 · BGRa	2	1/4
Westfeld, RB328, Südfeld, RB330	z3SS	1/32 · BGRa	1	1/2
Südfeld, RB330	z4	1/8 · BGRa	4	1/2

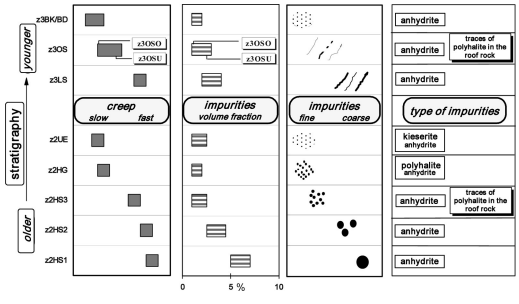

Figure 4. Correlations between creep behavior and structure.

by recrystallization, the causal particle displacements are increased by particle coagulation. Therefore grain size is only an oblique advice for the creep behavior (see also Figure 4).

With help of the former specified results it is possible to create a geomechanical model. In Figure 5 the mapping of the homogeneous areas of the ERAM are demonstrated. Thus it is possible to model the long time behavior of the rock zone.

4 SUMMARY

Nearly 300 creep tests on rock salt from different locations and stratigraphic strata of the Stassfurt cycle (z2) and Leine cycle (z3) from the ERAM have shown that structural attributes strongly affect the creep behavior of rock salt.

The stationary creep rate is taken as the most important measure for the characterization of the mechanical behavior of rock salt. The creep rate can vary by a factor of more than 100 for different types of rock salt.

The evaluated stationary creep rates of all the tests have been classified with help of a creep rate vs. stress-diagram to define “creep classes” which differ by a factor of 2.

Creep is significantly influenced even by small amounts of impurity particles which act as obstacles for the transcrystalline movement of dislocations.

The elaborated correlations between petrographics and geomechanics yields the basis for the prognosis of geomechanical properties of such parts in the salt formation which have not been investigated in detail or which belong to the barrier system where drilling or mining is prohibited.

Figure 5. Homogeneous areas in cut 3.1 ERA Morsleben.

The comparison between the geological and the geomechanical model shows that it is possible on one hand to integrate two or more stratigraphic layers to one homogeneous geomechanical area, otherwise one stratigraphic layer can belong in different positions in a salt formation to two or more different homogeneous areas. In any case, the mapping yields the geomechanical model for the rock salt which is used for the numerical model calculation and long-term prediction of temporary and spatial evolution of stress and strain in the formation. This was realized for example at the backfilling of the northern field of the ERAM (Preuss et al. 2004) as well as for safety computations for the geomechanical stability and integrity of the mine (Büttner & Heusermann 2004).

REFERENCES

Albrecht, H., Hunsche, U., Plischke, I. & Schulze, O. 1990. Mapping of the mechanical properties of a salt dome. In D.G. Price (ed) *Proceedings of the 6th Congress of the International Association of Engineering Geology (IAEG), Amsterdam (Netherlands) 1990; Vol.I: 23–29.* Rotterdam: Balkema.

Albrecht, H., Hunsche, U. & Schulze, O. 1993. Results from the application of the laboratory test program for mapping homogeneous parts in the Gorleben salt dome. *Geotechnik-Sonderheft 1993; 155–158.* Essen: Glückauf.

Büttner, K. & Heusermann, S. 2004. Geomechanical stability and integrity of the salt barrier in the central part of the Morsleben repository. *Proceedings of DisTec2004, Berlin (Germany), 26–28 April, 2004: 329–336.* Hamburg: Kontec.

Behlau, J. & Mingerzahn, G. 2001. Geological and tectonic investigations in the former Morsleben salt mine (Germany) as a basis for the safety assessment of a radioactive waste repository. *Engineering Geology* 61: 83–97 Amsterdam: Elsevier.

Hunsche, U., Mingerzahn, G. & Schulze. O. 1996. The influence of textural parameters and mineralogy cal composition on the creep behavior of rock salt. In M. Ghoreychi, P. Berest, H. Hardy, Jr. & M. Langer (eds), *The Mechanical Behavior of Salt III; Proc. Third Conf., Palaiseau (France),14–16 September, 1993:143–151.* Clausthal: Trans Tech Publications.

Preuss, J., Lerch, C., Amelung, P. & Polster, M. 2004. Closure of the Morsleben Repository – 3-D Numerical Modelling of the Northern Field. *Proceedings of DisTec2004, Berlin (Germany), 26–28 April, 2004: 349–355.* Hamburg: Kontec.

Taylor & Francis
Taylor & Francis Group
http://taylorandfrancis.com

The Mechanical Behavior of Salt – Understanding of THMC Processes in Salt –
Wallner, Lux, Minkley & Hardy, Jr. (eds)
© 2007 Taylor & Francis Group, London, ISBN 978-0-415-44398-2

Modeling of strain softening and dilatancy in the mining system of the southern flank of the Asse II salt mine

P. Kamlot & R.-M. Günther
Institut für Gebirgsmechanik GmbH, Leipzig, Germany

N. Stockmann & G. Gärtner
GSF – Forschungszentrum für Umwelt und Gesundheit GmbH, FB Asse, Remlingen, Germany

ABSTRACT: In the Asse II salt mine's southern flank an array with relatively small pillars and stopes was excavated between 1916 and 1964 in the course of halite extraction. Most of the volume of the chambers (in total approx. 3.5 Mio. m^3) was exposed to free convergence until 1995, when a backfilling campaign by pneumatic transportation of a granular salt material started, which lasted until 2003. The barrier to the overburden rocks is formed by rock salt with a minimal thickness of only 15 m in the upper part. The flank dips by approx. 70° in a SW direction. The rock mechanical evolution has been monitored for decades by displacement observations, stress and strain measurements in the pillars, and recording of the backfill pressure built-up in the chambers. Furthermore, microseismic activity in the mine and the adjacent overburden has been recorded. Softening and damaging in the pillars and stopes of the mining horizon have led to stress redistributions into the overburden rocks, where fracturing processes were generated as well. Hence, because of the small dimensions of the bearing elements on the southern flank and the close distance to the overburden, far reaching geomechanical interactions exist. The purpose of the project was the modeling of mining history and of observed rock mechanical behavior aiming at the stability proof and prediction until the end of operating phase. For that a time-dependent elasto-visco-plastic constitutive law was used which describes softening, dilation, and creep. The material parameters were found in special laboratory experiments determining the residual strength after exceeding the peak of the stress-strain curves in the domain of dilatancy. In the 3D-modeling course all calculated stresses, deformations, and geomechanical reactions could be confirmed as measured in situ. Therefore, the model can be considered as validated and qualified for prediction.

1 INTRODUCTION

The Asse II mine which is located in Lower Saxony in a steep inclined structure in a salt ridge is probably a unique rock mechanical situation due to its long and changeable history (1) as a commercially used salt mine and (2) as a R&D facility (research and development work) on the final disposal of radioactive waste in salt formations.

IfG Leipzig has been involved in the geomechanical assessment of the Asse mine for about 10 years. During this time different modeling concepts and constitutive laws were developed to simulate the geomechanical behavior of the pillars and stopes as observed in the mine. In an early working phase, using a stationary creep law, coupled with elasto-plasticity as long-term strength boundary, the extensive displacements on the southern flank could be simulated. They are characterized by creep in the saliniferous layers and plastic deformation in the bearing elements (pillars, stopes) and adjacent overburden rocks. In the non-saliniferous overburden a high degree of separation and low rock strength had to be presupposed.

However, for stability proof in detail and prediction of geomechanical behavior until the end of operation it was fundamental to simulate dilatancy, strain softening and rupturing. For that, a time dependent elasto-visco-plastic constitutive law was used which describes softening, dilation and creep. The adoption on the site conditions of the Asse mine and the validation on basis of the underground measurements will be presented in the following.

The article is divided into the topics:

(1) Description of the site conditions.
(2) Interpretation of the measurements and observations of mine surveying.
(3) Explanation of the constitutive law, parameter determination, and confirmation, using lab tests.

Figure 1. Cross section in the middle of the E-W extension of the mine. The frame envelops the mining fields on the southern flank, in the core of the anticline and on the northern flank (see Figure 2).

(4) Description of the 3D-model, of calculated results and validation using mine surveying observations.
(5) Discussion of consequences on stability and closing measures.

2 DESCRIPTION OF THE SITE CONDITIONS

The Asse mine is situated in an 8-km long ridge, striking from NW to SE. Its core consists of a Zechstein salt anticline which was formed during the Late Cretaceous (see Figure 1). The N-S cross section in the middle of E-W extension of the mine shows that the southern flank has a steep dip. The overburden rocks of the northern flank are older than those at the southern flank because the anticline has been affected by a strike fault downthrown to the south. The oldest rock cropping out on the south side of the anticline is Lower Muschelkalk and on the north side it is Lower Buntsandstein.

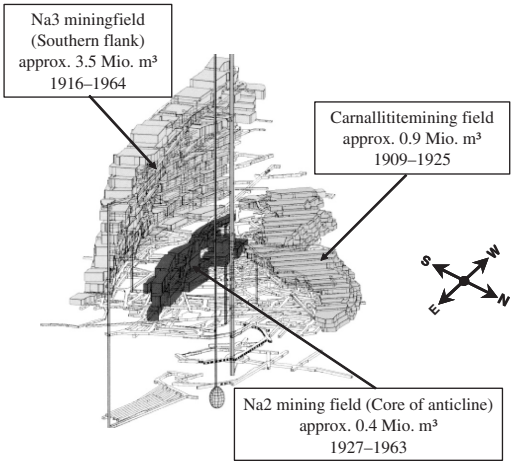

Figure 2. Mining fields to be evaluated in the Asse II mine. The geological structure is depicted in Figure 1.

The overburden rocks are separated tectonically and are partly highly stressed. The Zechstein rocks consist mainly of rock salt of the Stassfurt (Na2) and Leine (Na3) formations. The carnallitite K2 is part of the Stassfurt series.

Due to the close distance of the openings in the upper part of the mine to the overburden and the long operation time without backfill a loss of the integrity of the rock salt barrier to the southern overburden took place. An inflow of brine from the overlaying layers was first observed in 1988 and is now on the order of 12 m^3 per day. The brine is penetrating through discrete flow pathways in the geological halite barrier and is saturated with NaCl and $CaSO_4$, but not with $MgCl_2$.

As described in Figure 2, the Leine rock salt in the southern flank was mined from 1916 to 1964. About 130 rooms were excavated on 13 levels. In general there are 9 rooms next to each other at one level in the strike direction of the deposit. A standard chamber on the southern flank is 60 m long (E-W direction), 40 m wide (N-S direction) and 15 m high. Between adjacent chambers there are 12 m thick pillars (except for the pillar between the mining rows 4 and 5 with a thickness of 20 m, see Figure 3). Between chambers arranged one above the other there are 6 m thick stopes. The total cavity volume is about 3.5 Mio. m^3.

The mining field of Stassfurt rock salt with a cavity volume of about 0.4 Mio. m^3 is located in the core of the anticline. It was excavated from 1927 to 1963. The Carnallitite mining field on the northern flank was excavated from 1909 to 1925 and has a cavity volume of about 0.9 Mio. m^3.

The mining fields cover a depth range between 490 and 775 m. The cavities left from the potash mining were almost completely backfilled during mining. The chambers in halite were only partially backfilled

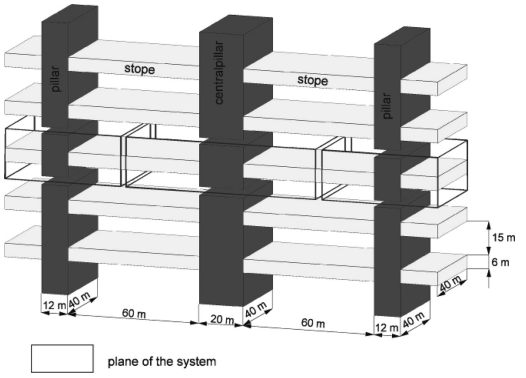

Figure 3. Detail of the Na_3 mining field on the southern flank with central pillar between mining rows 4 and 5. For evaluation of the geometrical loading conditions different planes of the pillar-chamber systems were used.

during the R&D phase using crushed salt from excavation of single drifts in the deeper areas of the anticline. The mostly open chambers were exposed to free convergence until 1995, when a backfilling campaign by pneumatic transportation using a compatible granular salt material started, which lasted until 2003.

The geomechanical behavior of the Na_3 mining field on the southern flank is of the utmost importance for the mine because of its volume, extension and the close distance to the overburden. The barrier to the overburden is formed by rock salt with a minimal thickness of 15 m in the upper part. The flank dips by approx. 70° in a SW direction. Therefore, the overburden pressure at the southern flank is mainly subhorizontal.

Low- and intermediate-level radioactive waste is embedded in chambers in the Na_3 and Na_2 in the 750, 725, and 511 m levels.

The investigations discussed here refer mainly to the Na_3 field. Comparable evaluations took place regarding to the Na_2 and the carnallitite field.

3 RESULTS OF MINE SURVEYING

The Asse mine is monitored during several decades by geotechnical, geophysical and hydrogeological measuring programmes. The stress monitoring stations in the backfill show until now a stress increase up to a range between 0.2 and 0.6 MPa. Despite this comparatively low value, a reinforcement impact against the pillar cross-extension is detectable. As Figure 4 shows, due to the backfilling measures the pillar deformation rates became stabilized and reveal recently a declining trend.

The pillar stabilization is confirmed by the drop of the microseismic activity in the mining field on the southern flank; however, a growing activity in the

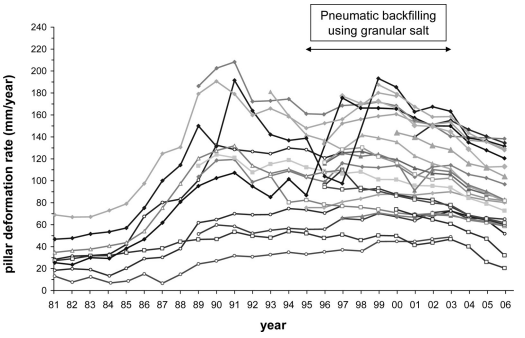

Figure 4. Decrease of pillar deformation rates in the Na_3 mining field due to backfilling. There are depicted different pillars at levels from 490 to 700 m. The deformation rate is valid for a thickness of 40 m.

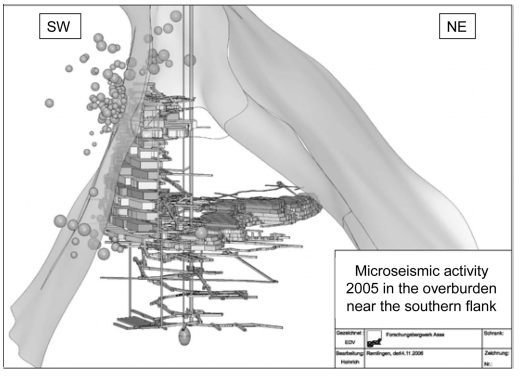

Figure 5. In the overburden rocks 2005 measured microseismic activity. The symbols represent magnitudes from −3 to −1.

adjacent overburden rocks is detectable (see Figure 5). This documents stress redistribution from the mine to the overlaying rocks, which leads to fissuring there. As long as the overburden displacement continues, these geomechanical interactions will also continue.

Remarkably, the inflow rate of overburden brine has not changed in the last years.

Due to the geometry of the chamber arrangement on the southern flank, with small pillars and stopes, the bearing assembly is a pliable system, which is meanwhile (after decades of operation time) characterized by creep fracturing, strong plastic deformation, and rupturing. A significant broken contour zone of a pillar in the upper levels is shown exemplarily in Figure 6. This situation corresponds to the general experiences from conventional mining in rock salt and potash mines with comparable geometry. Although the location was recently backfilled, the deformation and damaging processes will continue in the future, as long as the displacements of the overburden continue.

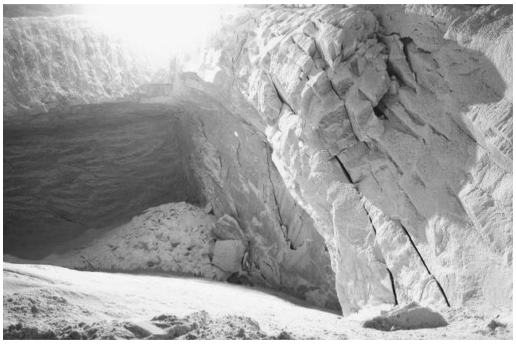

Figure 6. Pillar with broken contour zone in the upper part of Na_3 mining field.

In summary, with respect to the planned model calculations, the current geomechanical situation can be described in accordance with Stockmann & Hensel (2003) as following:

- Because of not sufficient dimensioning, the bearing system of pillars and stopes was to weak to withstand the overburden pressure.
- In consequence, strain-softening (in combination with creep), dilatancy and fracturing took place.
- The pillars are partly split and most stopes have collapsed.
- After decades of free convergence the chambers were backfilled and a slight stabilization effect is detectable.
- The loss of bearing capacity of the pillars led to higher stresses in the adjacent overburden rocks, implying fissuring as well.
- A far-reaching geomechanical interaction is detectable and has to be modeled.

4 LABORATORY INVESTIGATIONS ON CREEP, SOFTENING, DILATANCY AND RESIDUAL STRENGTH

Due to poor knowledge about the strength and creep behavior of highly stressed rock salt in the dilatant domain the experimental investigations were aimed at the determination of the residual strength after exceeding the peak strength of the stress-strain curves. It had to be clarified whether a residual strength plateau exists (if so, in what deformation range) or complete strength loss occurs immediately. Furthermore, the creep behavior of dilatant deformed rock salt samples had to be studied.

In Figure 7, selected strength curves of differential stress vs. axial deformation and the corresponding volumetric strain vs. axial deformation under different confining pressures from 0.2 to 10 MPa are depicted. The differential stress is the difference between axial

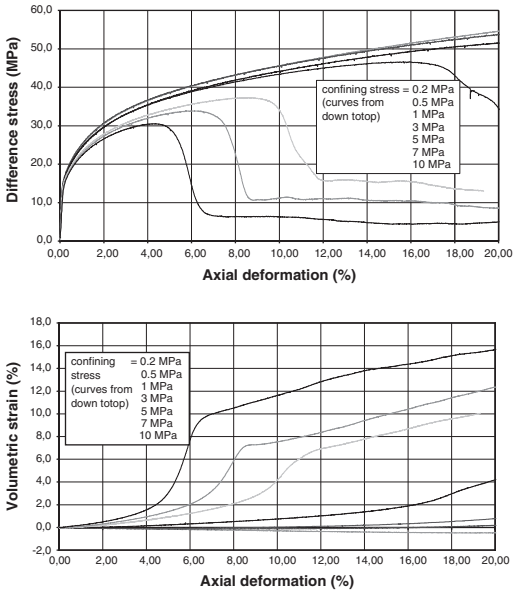

Figure 7. Strength and corresponding volumetric strain under different confining pressures in strain controlled tests. The deformation rate was $\dot{\varepsilon}_1 = 5 \cdot 10^{-6}\,\mathrm{s}^{-1}$.

stress σ_1 and confining pressure σ_3. The tests were driven at a deformation rate of $\dot{\varepsilon}_1 = 5 \cdot 10^{-6}\,\mathrm{S}^{-1}$. The sample dimensions were diameter = 98 mm and length = 196 mm. The curves show typical strain hardening until failure occurs. After exceeding the maximal stress under low confining pressures up to 3 MPa, a strain softening, accompanied by a remarkable dilatancy, is visible. At the shear failure the dilatancy curves rise steepest in the domain of the most weakening (strongest damaging). A geomechanically positive conclusion it can be drawn that a residual strength with a more or less constant value up to deformations of 20% exists in which the volumetric deformation increases with approximately constant slope. It means, damaging in the specimen proceeds, but is concentrated in a fracture plane.

Such a residual strength in the established deformation range is decisive for the bearing capacity of the pillars and is presupposed in the constitutive law used in the model calculations. Its validity has been proven by determination of minimal stresses in the pillars by hydrofracturing and stress monitoring (pressuring cells) with magnitudes from 0 to 4 MPa.

The evaluation of creep test series of pre-damaged and dilated rock salt samples demonstrated a creep behavior significantly different from that of intact material. Creep rates equivalent to those of intact samples were obtained at significantly lower stress levels (see Figure 8). The secondary creep rates of intact samples matched well the reference creep law BGRa for

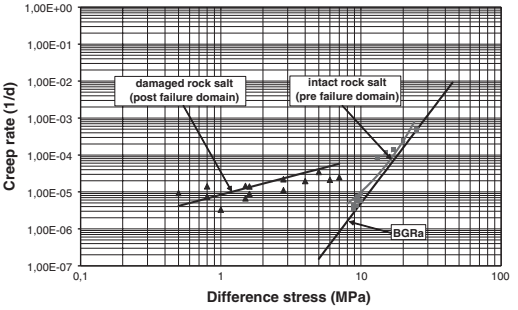

Figure 8. Stationary creep rates of intact and damaged rock salt.

rock salt with a stress exponent of 5. The stress dependence of pre-damaged rock salt was significantly lower, in a range of about 1.

The evaluation of laboratory test series facilitates the determination of the parameters necessary for the MINKLEY model (Minkley et al., 2001). This constitutive law is implemented as DLL-file in the program code FLAC^{3D} (Itasca, 2002).

Further investigations on undamaged rock salt samples in comparison with pre-damaged specimens, respectively, for wet and dry conditions aiming at the planned closing measures in the Asse mine by controlled flooding with brine, are presented in Kamlot et al. (2006). They are outside the scope discussed here.

5 VISCO-ELASTO-PLASTIC CONSTITUTIVE LAW FOR ROCK SALT

5.1 *Explanation of the constitutive law*

In the used constitutive model the plastic behavior implying softening and dilatancy is described by a modified non-linear MOHR-COULOMB yield or failure criterion connected with a non-associated flow rule. The MOHR-COULOMB fracture hypothesis depends on the minimum principal stress σ_3 and, if the failure envelope is reached, on the plastic deformation. The dilatancy function depends on σ_3 and plastic deformation as well. Besides the elasto-plastic characteristic, most salt rocks show viscous behavior. Therefore, the elasto-plastic softening model with dilatancy has been combined with the Burgers creep model. The primary creep phase is modeled by the Kelvin model, and the secondary creep is controlled by the Maxwell model. The tertiary creep is governed by a dilation softening mechanism. In the constitutive model the short-time and the long-time strengths are taken into consideration by a yield limit which depends on the deformation rate. In Figure 9 the concept of the constitutive law is illustrated as an interacting system of mechanical standard models.

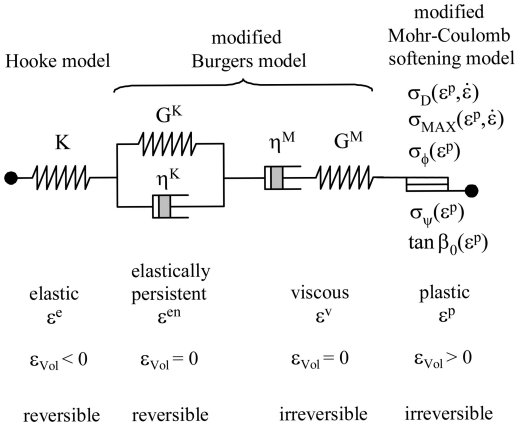

Figure 9. Visco-elasto-plastic model concept.

Below the dilatancy boundary the deformation is composed of the following components:

$$\varepsilon = \varepsilon^{e} + \varepsilon^{en} + \varepsilon^{v} \quad (1)$$

Above the dilatancy limit the total deformation is given by:

$$\varepsilon = \varepsilon^{e} + \varepsilon^{en} + \varepsilon^{v} + \varepsilon^{p} \quad (2)$$

Both the elastic deformation component ε^e and the component of the elastic persistence ε^{en} are reversible quantities, whereas both the viscous ε^v and the plastic portions of deformation ε^p are irreversible quantities. The elastic and the plastic deformation components are time-independent, whereas the components of elastic persistence and the viscous components are time-dependent quantities.

More detailed information about the physical background of the constitutive law and its application in practice is given in Minkley & Mühlbauer (2006).

5.2 *Validation using laboratory tests*

As a prerequisite for the later geomechanical evaluation of a complex in-situ situation it is important to validate the constitutive law with the laboratory tests. This was done using recalculations of strain controlled tests under different deformation rates (Figure 10) and of a creep test until creep failure (Figure 11).

In Figure 10 the good agreement between the stress-strain curves obtained in laboratory tests on Asse rock salt under a confining pressure of 1 MPa and the results of the corresponding numerical recalculations is depicted. As can be seen, the stress-strain curves depend on the deformation rate. The higher the rate, the higher the peak strength. Because the in-situ deformation rates are some orders of magnitudes lower than in laboratory, it is essential for modeling that the

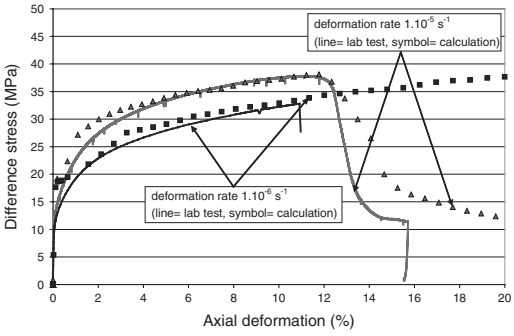

Figure 10. Recalculation of strain-controlled tests on rock salt. The deformation rates were $1 \cdot 10^{-5}\,s^{-1}$ (triangles) and $1 \cdot 10^{-6}\,s^{-1}$ (squares). As confining pressure 1 MPa was applied.

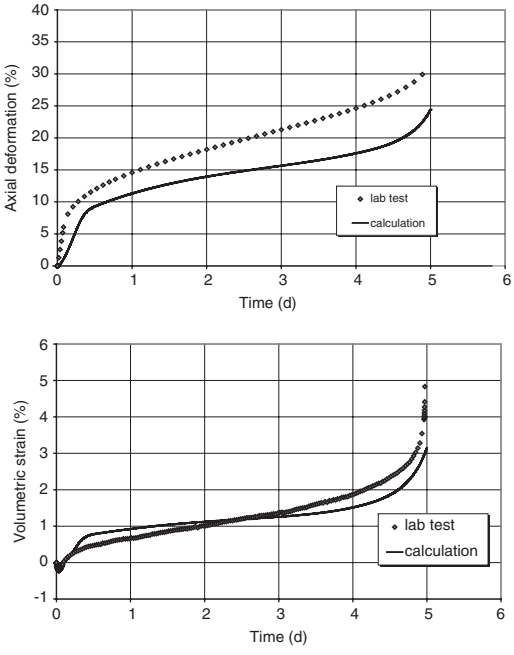

Figure 11. Recalculation of a creep test on a rock salt specimen: axial stress $\sigma_1 = 41$ MPa and confining pressure $\sigma_3 = 3$ MPa. Time-dependent axial deformation (above) and volumetric strain (below).

constitutive law is able to simulate different strain rates in a correct manner.

The constitutive model is able to describe the viscous behavior of salt rock until creep failure, too. The recalculation of a creep test carried out on Asse rock salt is shown in Figure 11. It can be concluded that the material law is suitable for modeling the geomechanically most relevant characteristics for the southern flank of the Asse mine.

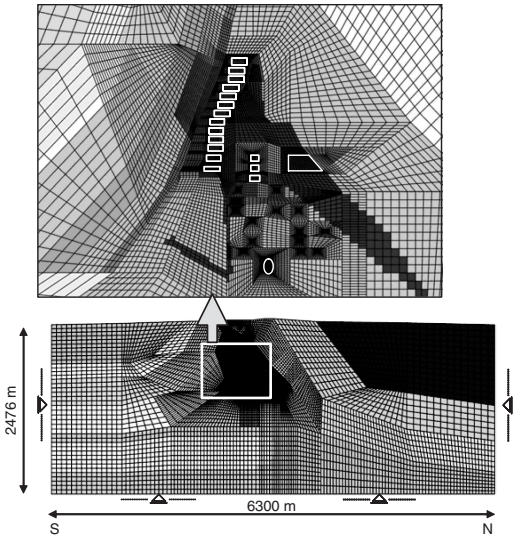

Figure 12. 3D-calculation model in total (below) and in detail (above, analogous to Figure 1). It is located in the middle of the E-W extension of the mine (see Figure 1). The dimension perpendicular to the sketch is 36 m.

6 3D-MODELING OF THE MINING HISTORY AND GEOMECHANICAL EVALUATION

6.1 *Model description and modeling course*

For the analysis of the temporal evolution of the Asse II mine during the initial mining and the operational phase a 3D-model was constituted based on the program code FLAC^{3D} (Itasca, 2002), which is a three-dimensional explicit difference element program that is capable of solving a wide range of complex problems in continuum mechanics.

The model (Figure 12) comprises a vertical section through the salt ridge of around 2.5 km height and 6.3 km width incorporating shape, dimension, depth and geological/tectonic situation of the Asse anticline and surrounding rocks. The large dimensions of the model are necessary to allow stress redistributions between southern flank and overburden which have to be expected because of the mining parameters (degree of excavation). The vertical boundaries and the basis are fixed perpendicular to the edge, and the top is free. The primary stresses in the model follow the density, depth, and material parameters.

The non-salt overburden rocks consist of a complex sequence of the Triassic Buntsandstein, Muschelkalk and Keuper rocks, followed by Jurassic (Jura) and Cretaceous (Kreide) rocks. Geological engineering observations of cores from the overburden revealed that there is a strong geo-tectonic fracturing with a locally high degree of separation in the layers of indurated clay, marl and limestone. Such weakening

planes are described by discrete tectonic joint faces and a ubiquitous joint material model. The ubiquitous joint model in FLAC^{3D} is a MOHR-COULOMB plastic solid with an embedded penetrative weak plane (ubiquitous joint) of specific orientation.

In the salt formations carnallitite was distinguished from rock salt, whereas the latter is not differentiated between the different stratigraphical sequences of the Staßfurt (Na_2) and Leine (Na_3) series. Further stratigraphic subdivisions are the carnallitite K2 and the cap rock.

The contours of the chambers in halite are visible in the vertical cross section as rectangles. Furthermore, the envelope of the carnallitite field and of the cavern in the deepest levels of the mine is sketched.

The halite and carnallitite in the vicinity of the underground openings are represented by the MINKLEY model. For the rock salt far from the mined excavations the temperature dependent BGRa creep law is used. The stress-dependent compaction behavior of the backfill is simulated by a law developed for crushed salt.

Modeling followed these steps:

- Calculation of the initial (primary) stress conditions before mining.
- Modeling of temporal evolution of the mining activities by subsequent creation of underground openings.
- Simulation of the backfilling in the rock salt chambers since 1995.

6.2 *Modeling of far-reaching geomechanical interaction between southern flank and overburden*

The model calculations conducted in the recent years aimed at the best-possible integration of all available in-situ measurements (displacements, stress monitoring, microseismic) and geomechanical observations (rupturing). Based on these analyses it can be stated that two processes have to be considered: (1) Due to post-failure regime in the pillars and stopes on the southern flank a softening takes place and (2) in the adjacent overburden rocks damage is generated as well.

Approximately 80% of the deformation in the horizontal cross-cutting direction results from displacements from the south. This observation can be explained only by strong plastic deformation in the adjacent overlaying strata. Using the model of a stiff and undamaged overburden, the horizontal cross-cutting displacements from the north, generated due to halite creep in the saddle core, would produce the highest value. Furthermore, to account for the measured displacements of southern overburden, the assumption of a reduced strength caused by hydraulic pore pressures in the overburden rocks is necessary. The magnitude of the hydraulic pressure of the overburden brine is influenced by the plastic shear deformation (damaging) and the consequent increase in the degree of separation. This assumption of coupled hydro-mechanical interactions is well-established by geo-hydraulic investigations.

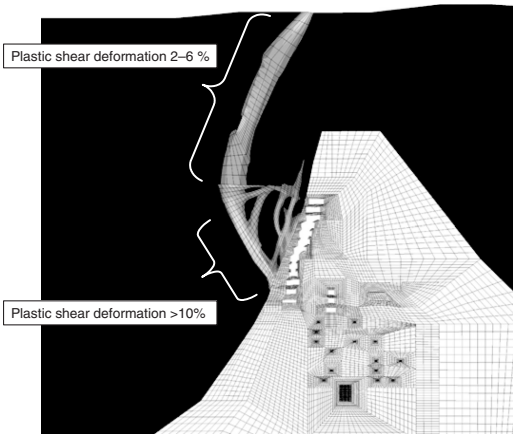

Figure 13. Calculated plastic shear deformation in the overburden rocks at the present time.

In Figure 13 the relatively high plastic shear deformations, valid for the present, are depicted. Remarkably, the location of the shear bands is not significantly influenced by the large tectonic joint faces. Rather, the orientation of the shear bands is caused by the displacements toward the chambers on the southern flank.

Only by modeling such damaging processes the measured mobility of the southern overburden can be simulated.

The location of the shear bands in the adjacent overburden corresponds very well to the zones of increased microseismic activity (Figure 5).

The calculated high plastic shear deformation in the halite barrier (minimal thickness 15 m) corresponds to the plastic volumetric deformation in the same area. This displays damaging and dilatancy, which may suggest a loss of the barrier integrity. In fact, in the depth interval between 511 and 553 m the intrusion of overburden brine takes place.

In Figure 14 the correspondence of measured and calculated displacements of the southern overburden in two levels (553 and 700 m) is demonstrated. This alone is an exemplary proof of the model validity.

6.3 *Modeling of the geomechanical situation in the mining system on the southern flank*

The aim of the modeling discussed here was to investigate in detail the geomechanical situation and the

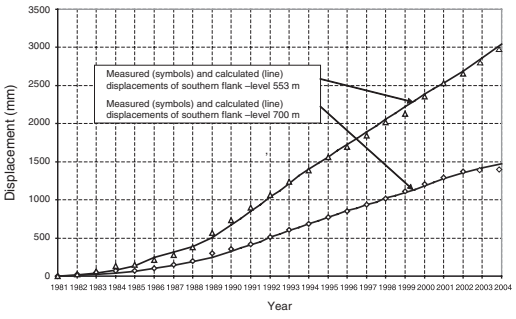

Figure 14. Comparison of calculated (line) and measured (symbols) displacements of southern overburden in 2 levels.

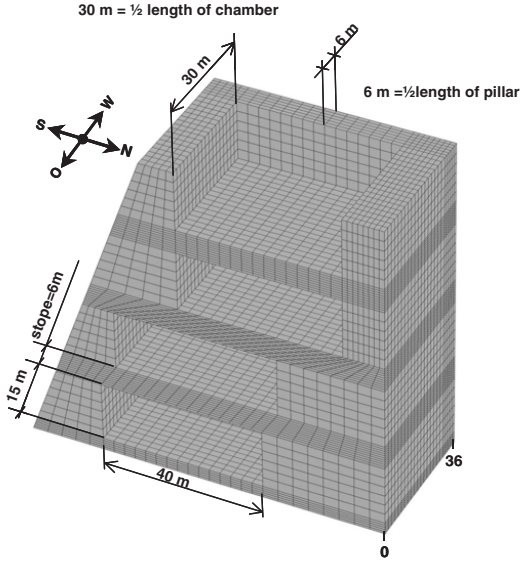

Figure 15. Detail of 3D-calculation model of the upper levels 511 m to 574 m of the southern flank.

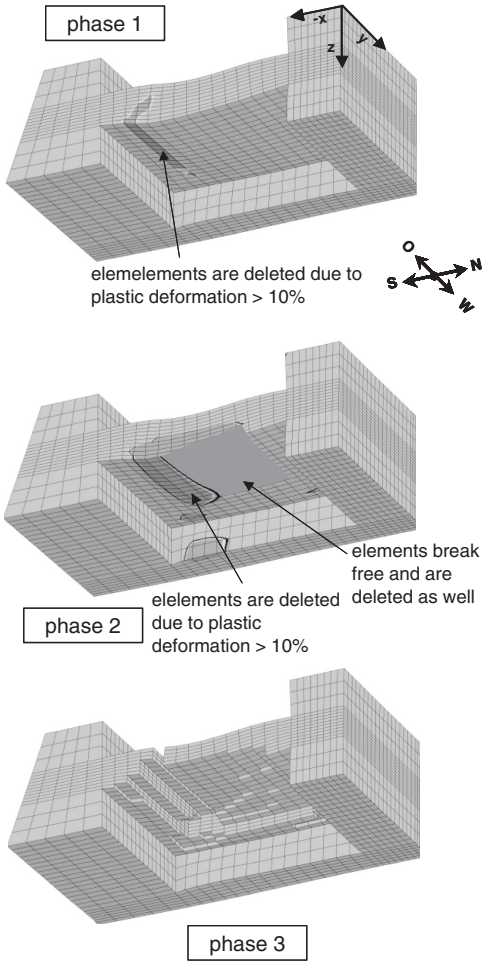

Figure 16. Calculation of different phases of a stope failure.

interactions between pillars and stopes in the mining system. The boundary condition to the southern overburden results from the displacement rates as calculated in agreement with the measured rates (see Figure 14).

In Figure 15, a detail of the mining system of the southern flank depicted in Figure 12, the chambers of the 511 m to 574 m levels are shown. The detail represents a view into the chambers in south-west direction. Half a chamber (total length 60 m) and half a pillar (total length 12 m) is created. The depth interval is between 496 m (roof of chamber 511 m level) and 577 m (half height of stope between the 574 m and 595 m levels). In this interval the geomechanical exposure of the halite barrier is critical. The height of the chambers is 15 m and the thickness of the stopes is 6 m. The cross-cutting width of the model depends on the flank dip, and the dimension along strike follows by 36 m.

In Figure 16 the modeled failure of a stope, as observed in situ in the last decades, is sketched. After a plastic shear deformation of 10% (confining pressure $\approx$ 0 MPa) the elements are assessed as broken and are deleted. This is in accordance with the results of the laboratory tests. In a uniaxial stress state, a residual strength cannot be presupposed. Furthermore, in the course of modeling it has to be considered that elements which are broken free have to be deleted as well.

The gradual failure in the stopes is consistent with in-situ observations and leads to stress redistributions into the pillars with increasing plastic shear deformation and strain softening. Figure 17 gives an impression of the actual plastic shear deformation and the strength

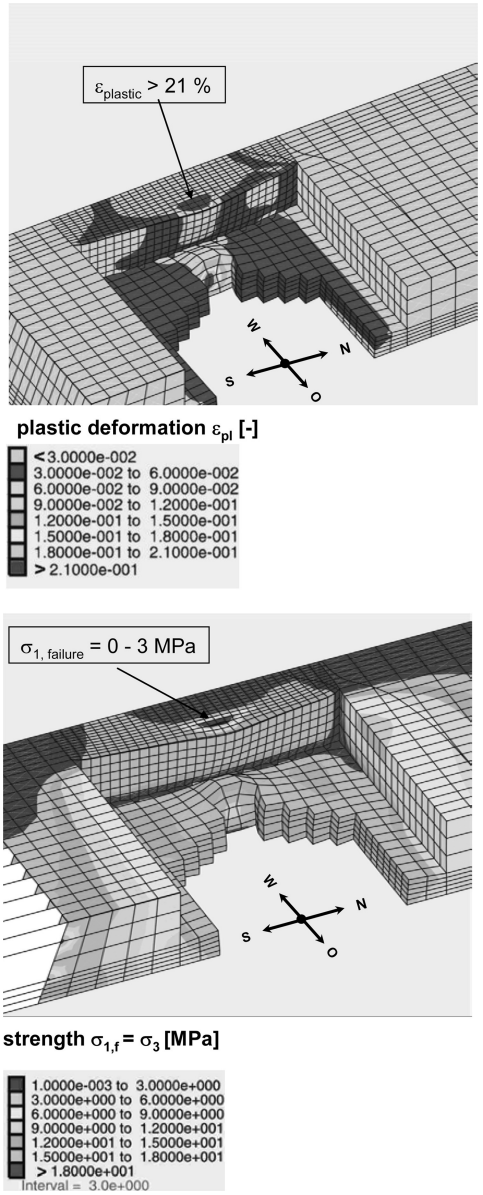

Figure 17. Actual plastic shear deformation (above) and actual strength (below). The surface is a horizontal cut in half height of a chamber in level 574 m.

state in a typical pillar-stope location on the southern flank. The view is in a north-west direction. The model section is limited at the surface by the half-chamber height and at the ground by the half-stope height at the 574 m level. The chambers in this level have been backfilled. The elements of the stope core were replaced due to complete strain softening. This is equivalent to the in-situ situation in most chambers on the southern

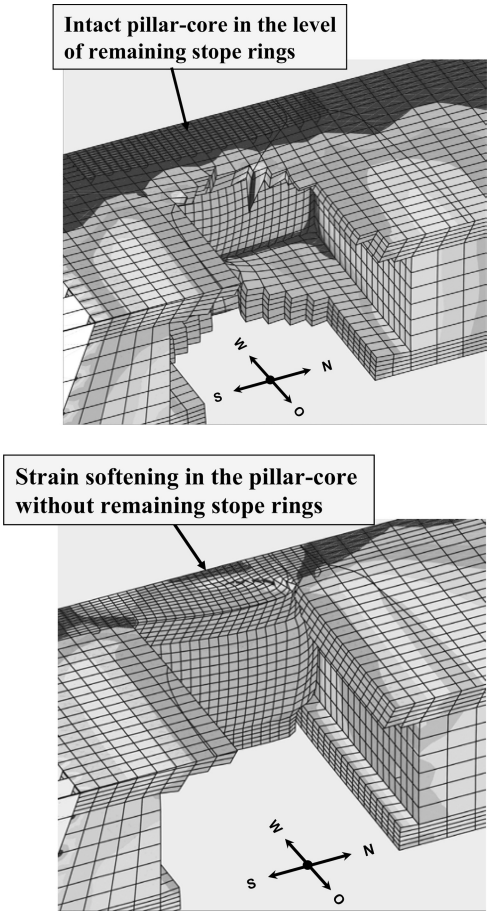

Figure 18. Comparison of strength with (above) and without (below) remaining stope rings. The surface is a horizontal cut in half height of the stope between level 574 m and 553 m. The legend is equivalent to Figure 17 (below).

flank where only the remaining rings are visible after failure of the central parts of the stopes. An evident shear band is generated in the half-chamber height in cross-cutting direction (upper part of Figure 17), accompanied by a zone of complete strain softening (lower part). The in-situ borehole observations validate these calculation results. It must be emphasized that such shear bands were detected in the majority of the pillars.

The calculated strength states in Figure 18 reveal the geomechanical importance of the remaining rings of the stopes. With remaining rings, a stable pillar core in this depth is detectable, whereas without the rings strong strain softening takes place.

It can be concluded, that, as long as the displacement rates on the southern flank will not increase and as long as the pillars are embedded in the backfill, the

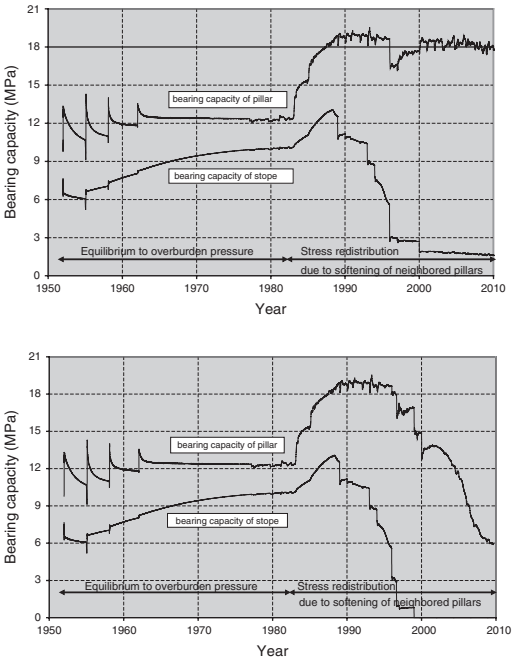

Figure 19. Bearing capacity of system 553 m level with (above) and without (below) remaining ring after stope failure.

load bearing capacity will stay stable on the level of the residual strength (upper part of Figure 19). The stress built up between 1983 and 1990 is in accordance with the acceleration of the pillar deformation rates (see Figure 4). The reason was identified in strength exceeding in pillars and mainly stopes on the southern flank. Thus, the geomechanical interaction between failure of the stopes in the mining system and the load redistribution to the adjacent overburden layers can be proven. As Figure 19 shows, the overall stability depends on the remaining rings of the broken stopes. If they will fail completely, a drop of the load bearing capacity cannot be excluded (lower part of Figure 19). This marks the high sensitivity of the system. There are no load bearing reserves detectable.

Summarizing, the 3D-model is in good agreement with the in-situ measurements and observations. Thus, it can be appraised as validated and can be used for prediction until the end of the operating phase (Kamlot et al. 2006).

7 SUMMARY AND CONCLUSIONS

Because the owner of the Asse mine, the GSF (Forschungszentrum für Umwelt und Gesundheit), has no further research requirements, the mine is now being prepared for closure according to the regulations of the Federal Mining Law (Bundesberggesetz). Due to the long operation period during which excavations were kept open, it has to be recognized that the pillars and stopes in the excavation fields are characterized by creep deformation, strain softening, and rupturing. For geomechanical evaluation and prediction until the end of operation, IfG Leipzig performed comprehensive rock mechanical studies based on laboratory investigations, in-situ tests, and modeling calculations. These investigations considered the specific site conditions with a weakened and damaged load bearing system.

The following assessment can be drawn:

- In the load bearing system on the southern flank and the adjacent overburden, damage and softening processes take place. Despite the supporting impact of the backfill it has to be concluded that the deformation and damage processes will continue in the future depending on the overburden displacements.
- In special laboratory tests a residual strength was found which is decisive for prognosis the bearing capacity of the pillars until the end of operation.
- For modeling, a time-dependent elasto-visco-plastic constitutive law was used that describes softening, dilation, and creep. The constitutive law was validated on the basis of laboratory tests.
- The validity of the performed modeling is confirmed by the in-situ measurements. Accompanying the future closing measures, the models will be checked and improved regarding their quality for prediction.

REFERENCES

Kamlot, P., Stockmann, N. & Teichmann, L., 2006. Stability proof of the Asse salt mine and geomechanical assessment of the planned closing measures. Proceedings SMRI Spring Meeting, Brussels.

Minkley, W., Menzel, W., Konietzky, H. & te Kamp, L., 2001. A visco-elasto-plastic softening model and it's application for solving static and dynamic problems in potash mining. Proceedings of the 2nd International Flac Symposium, Lyon, 21–27, Balkema, Lisse.

Itasca Consulting Group Inc., 2002. Fast Lagrangian Analysis of Continua in 3 Dimensions, Manual FLAC^{3D} 2.1, Minneapolis, Minnesota.

Minkley, W. & Mühlbauer, J., 2006. Constitutive models to describe the mechanical behavior of salt rocks and the imbedded weakness planes. Presentation 6th Conference on the Mechanical Behavior of Salt, in preparation.

Stockmann, N. & Hensel, G. 2003. Geotechnisches Kontroll- und Überwachungssystem zur Gewährleistung der Sicherheit der Schachtanlage Asse. Schriftenreihe des Instituts für Markscheidewesen der Bergakademie Freiberg, 4. Geokinematischer Tag, Heft 1.

The Mechanical Behavior of Salt – Understanding of THMC Processes in Salt –
Wallner, Lux, Minkley & Hardy, Jr. (eds)
© 2007 Taylor & Francis Group, London, ISBN 978-0-415-44398-2

Three-dimensional geomechanical modelling of old mining rooms in the central part of the Bartensleben salt mine

S. Fahland, S. Heusermann, R. Eickemeier & H.-K. Nipp
Federal Institute for Geosciences and Natural Resources (BGR), Hannover, Germany

J. Preuss
Bundesamt für Strahlenschutz, Salzgitter, Germany

ABSTRACT: Finite-element calculations have been made to analyse the stability of large old mining rooms and the integrity of the salt barrier in the Bartensleben salt mine. The recent state of stress and deformation around the rooms as well as dilatancy in the salt rock has been investigated. Several finite-element codes and two- and three-dimensional models were used taking two different dilatancy models into account. Roofs and pillars of the rooms are subjected to high creep deformations and partly to tensile stresses. Extended zones of dilatancy occur in the vicinity of the rooms and in the salt rock between rooms and anhydrite layers. As expected, the 3-D modelling yields lower stresses and deformations as well as reduced dilatant salt rock zones compared to the 2-D models.

1 INTRODUCTION

The Morsleben repository was used from 1972 until 1998 for the disposal of low- and medium-level radioactive wastes. The repository was established in the old Bartensleben mine, a former salt and potash mine consisting of several mining parts, e.g. the southern, the western, and the eastern part as well as the central part (Fig. 1). The last one has the most considerable degree of excavation and numerous large old mining rooms. Thus, from a geomechanical point of view, the central part which is not used as a repository is the most critical and important part of the mine.

To analyse the geomechanical stability of the underground structure as well as the integrity of the salt barrier in the central part of the Bartensleben mine a geotechnical safety analysis is required. Such an

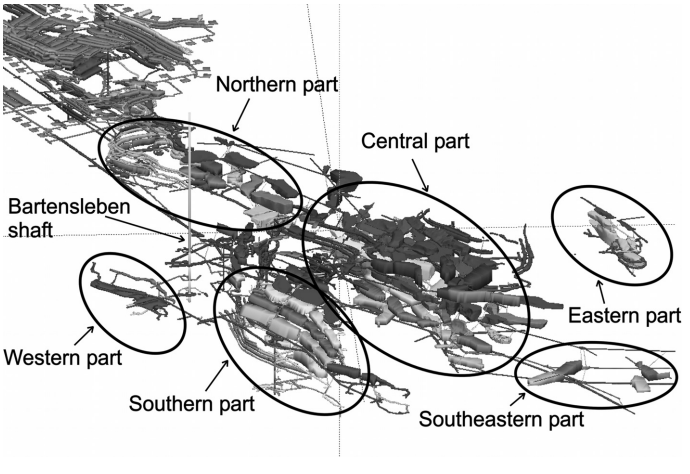

Figure 1. 3-D sketch of the Bartensleben salt mine generated with ERAM-SIS (Heller et al. 2004).

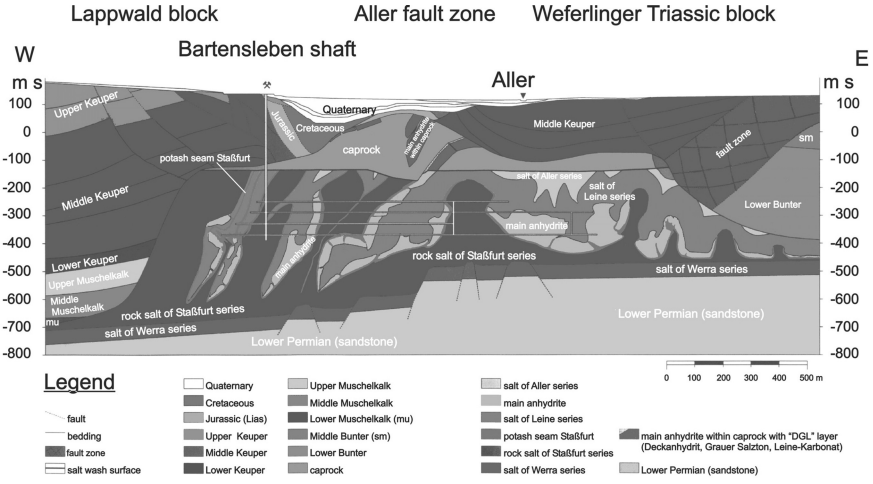

Figure 2. Geological structure of the Bartensleben salt mine (adopted from BfS).

analysis is based on geological and engineering-geological studies of the site, on laboratory tests and in-situ measurements, and on geomechanical model calculations. Model calculations are the most important part of the geotechnical safety assessment and comprise the geomechanical modelling of the host rock to simulate as closely as possible the conditions of the site and the behaviour of the rock, e.g. geology, repository or mine geometry, initial rock stress, as well as constitutive models and parameters (Langer 1999).

The paper comprises the results of numerical modelling to analyse the stability of the old mining rooms and integrity of the salt barrier in the southern central part of the Bartensleben mine with the most unfavourable mining situation. Different finite-element codes and models have been used including two-dimensional calculations on a characteristic cross section as well as three-dimensional calculations of a typical configuration of rooms in the southern central part.

2 GEOLOGICAL MODEL

The Bartensleben mine is located in the fault structure "Allertalzone" (Fig. 2). The top of the salt structure is at approximately 140 m below mean sea level, respectively about 270 m below ground surface. The thickness of the salt structure varies between 380 m and 500 m. The exploration and modelling of the geological structure of the salt rock and the overburden in several characteristic cross sections of the central part of the Bartensleben mine is based on the geological mapping of drifts, rooms, and numerous drillcores of the site as well as on ground-penetrating radar measurements (Behlau & Mingerzahn 2001).

The salt rock is characterised by a distinct folding of the salt layers and a high amount of main anhydrite layers (z3HA) of the Leine-sequence. The structure of the salt rock in the central part includes the main stratigraphic units of the Zechstein strata (salt layers z2HS, z2SF, z3LS, z3OS, z3BK/BD, z3AM/SS, and anhydrite layers z3HA). The structure of the overburden and country rock includes the caprock, Bunter, Muschelkalk, Keuper, Jurassic, Cretaceous, and Quaternary layers.

3 GEOMECHANICAL MODEL

3.1 *Idealized geological structure and mining configuration*

The idealization of the geological structure of the salt rock and the overburden of the southern central part in the Bartensleben mine is based on a characteristic geological cross section perpendicular to the axis of the structure and the mining rooms.

The main units of the Zechstein strata (salt layers z2HS, z2SF, z3LS, z3OS, z3BK/BD, z3AM/SS, and anhydrite layers z3HA) and, if necessary, composites of the main units (z3OS/BK/BD) are considered. The Hauptsalz z2HS was separated into two several parts (z2HSW and z2HSO), due to different creep behaviour. The structure of the overburden was idealized taken into account the main layers caprock cr, DGL layer (including layers of Deckanhydrit, Grauer Salzton, and Leinekarbonat) within the caprock, Keuper k, Jurassic-Cretaceous j-kr, and Quaternary q (Fig. 3).

The characteristic cross section used for geomechanical modelling comprises several old mining

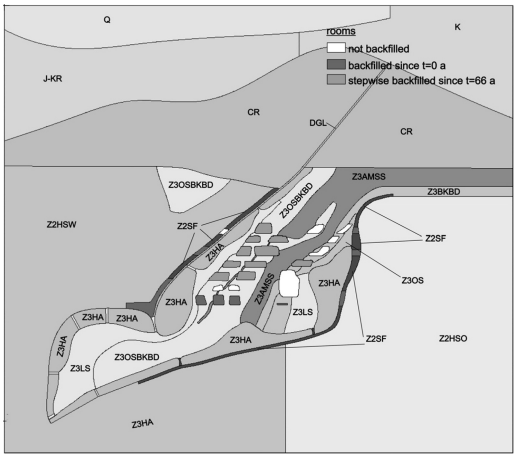

Figure 3. Idealized geological structure.

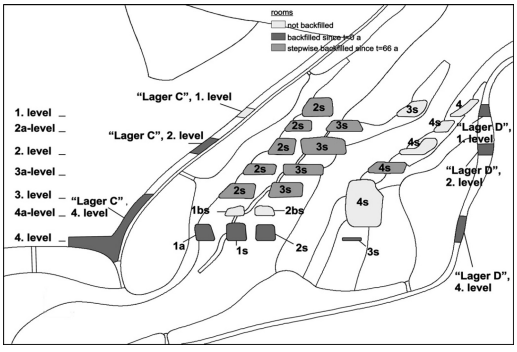

Figure 4. Configuration of old mining rooms.

rooms excavated a couple of decades ago and located at different levels of the mine. According to the strong inclination of the salt layers the excavation rows are arranged in a steep configuration forming several pillars and roofs. The rooms as well as the pillars and roofs show different sizes and shapes determined on the basis of the mapping of the mine and by scanning the room contour. Figure 4 depicts a schematic view of the rooms which were considered in the geomechanical model. A minor part of the rooms was backfilled (at time $t = 0$) with crushed salt after excavating the potash or rock salt, while the major part has been left open since excavation. For purposes of stabilisation, backfilling of a number of selected rooms with saltcrete has been started (at time $t = 66$ years after excavation).

3.2 *Constitutive models*

The idealized geological layers were classified with regard to their material behaviour. For reasons of simplification, the anhydrite layers and the overburden were assumed to be solely elastic. The ductile rock salt layers were classified with respect to the steady-state creep behaviour. For the anhydrite layers, the modulus of elasticity was determined to 30 GPa in laboratory tests taking the post-failure stage into account with respect to the jointed anhydrite blocks. The deformation behaviour of the ductile rock salt layers was described by a constitutive equation including both elastic and steady-state creep deformations. According to Hunsche & Schulze (1994), the effective steady-state creep rate can be calculated using:

$$\varepsilon_{eff}^{cr} = A_{cr} \cdot e^{-\frac{Q}{RT}} \cdot \left(\frac{\sigma_{dev}}{\sigma^*} \right)^n \tag{1}$$

with R = universal gas constant ($8.3143 \cdot 10^{-3}$ kJ/mol·K), T = temperature (K), σ_{dev} = deviatoric stress (MPa), σ^* = reference stress (1.0 MPa) and the material parameters A_{cr} = structural factor (1/d), n = stress exponent (−), Q = activation energy (54.0 kJ/mol). The several types of rock salt layers mainly differ with respect to the structural factor A_{cr}. Thus, the creep capability of the layers can be taken into account using a factor A^* related to the reference value $A_0 = 0.18$ 1/d:

$$A_{cr} = A^* \cdot A_0 \tag{2}$$

Different values of A^* were determined in laboratory creep tests on samples taken from the several salt layers of the mine.

In addition, the dilatant behaviour of rock salt was considered using two different models. First, a viscoplastic model was used to consider viscoplastic flow if the stress state exceeds the dilatancy boundary. Here, the dilatancy boundary is assumed to coincide with the yield function F which is described by a Drucker-Prager criterion:

$$F = \alpha \cdot J_1 + \sqrt{J_2^D} - k \tag{3}$$

with $J_1 = 1.$ invariant of stress tensor (MPa), $J_2^D = 2.$ invariant of stress deviator (MPa^2), α = fictive angle of friction (−), k = fictive cohesion (MPa). The parameters α and k were determined to $\alpha = 0.2887$ and $k = 0$. The viscoplastic model includes the common usage of an associated flow rule.

Secondly, a new dilatancy concept based on extensive lab test series on rock salt has been considered according to Hunsche & Schulze (2003). The volumetric rate of dilatancy $\dot{\varepsilon}_{dil,vol}$ is correlated to the deviatoric creep rate, $\dot{\varepsilon}_{cr,dev}$ via an empirical relation using r_v (depending on σ_{dev} and hydrostatic stress σ_{hyd}):

$$\dot{\varepsilon}_{dil,vol} = r_v \cdot \dot{\varepsilon}_{cr,dev} \tag{4}$$

If the octahedral shear stress τ_{oct} (equivalent to the deviatoric stress) exceeds a boundary stress τ_D, the factor r_v is positive and dilatancy will occur:

$$r_v = \sqrt{3}\left|\frac{(\tau_{oct} - \tau_D)}{\sigma_{hyd}}\right|^{1/m} \quad (if\ \tau_{oct} > \tau_D) \tag{5}$$

$$\tau_D = b \cdot (-\sigma_{hyd})^c \tag{6a}$$

$$\tau_{oct} = \frac{\sqrt{2}}{3}\sigma_{dev} \tag{6b}$$

with empirical parameters m = 0.5, b = 0.7071, and c = 1.0. Taking these parameters into account Eq. 3 and Eq. 6a describe the same dilatancy boundary. Thus, both models can be directly compared.

Both backfilling materials, crushed salt and saltcrete, were assumed to show solely elastic behaviour. For crushed salt which was used to backfill a few rooms directly after mining, the modulus of elasticity was taken to E = 17.5 MPa. For saltcrete which is actually used for the backfilling of selected rooms, E was taken to 3500 MPa.

4 NUMERICAL CALCULATIONS

The main objectives of the calculations were to determine stresses, strains, and displacements as well as dilatancy in the salt rock of the southern central part of the Bartensleben mine as basic values for the analysis of the stability of the old mining rooms and the integrity of the salt barrier. Additionally, the following items were considered:

- Use of two finite-element codes for purposes of comparison and quality control,
- comparison of two different constitutive models describing the dilatancy of rock salt,
- effects of three-dimensional modelling of the mine on the calculated results and comparison to 2-D modelling.

Calculations were made using the well proven and released finite-element code ANSALT developed by BGR (Nipp 1991) and the new JIFE code for THMC processes developed in a cooperation between SRD company, Berlin, and BGR (Heemann et al. 2003). Pre- and post processing of the data was done with the INCA/PATRAN tool.

4.1 *Finite-element modelling*

Finite-element modelling of the southern central part of the Bartensleben mine took the idealized structure of the geological layers (Fig. 3) and the geometry of the old mining rooms (Fig. 4) into account. In a first step, a two-dimensional plane-strain model was used representing a characteristic cross section of the structure. This is valid to a certain degree since the rooms have a considerable length in the normal direction and the stress and deformation state calculated in a 2-D model is more unfavourable compared to the real 3-D mechanical behaviour and more conservative with regard to the assessment of stability and integrity of the structure. In a second step, this model was extended to a three-dimensional model considering half of the length of the rooms and of the pillar at the head of the rooms for reasons of symmetry.

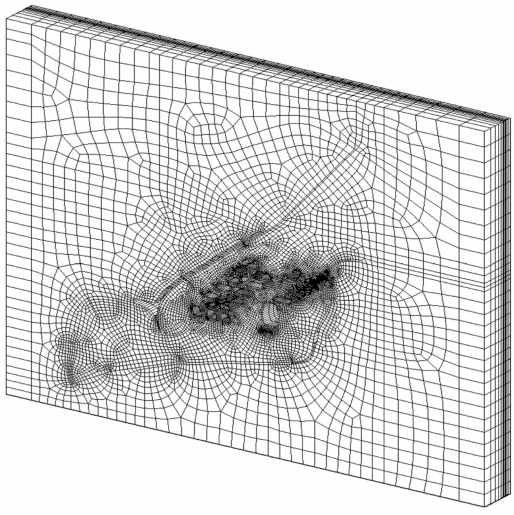

Figure 5. 3-D finite-element mesh.

Figure 5 shows a plot of the entire 3-D model, 750 m in height, 850 m wide and 75 m in length, comprising about 120,000 nodal points and 120,000 isoparametric 8-node elements. It was assumed that the rooms were instantaneously excavated in the year 1940. Thus, up to now a time elapse of about 66 years must be regarded to analyse the recent stress and deformation state. The total time elapse considered in the model amounted 100 years up to the year 2040. A minor part of the rooms (Fig. 4, dark-grey coloured) was backfilled with crushed salt directly after extracting the potash or salt. Backfilling of selected rooms of the central part with saltcrete was considered in the model for the present time $t = 66$ years after excavation (Fig. 3).

4.2 *Model variations*

Several model variations were studied:

- Reference model ZB-S4-ANS-2D: This two-dimensional plane-strain model was calculated with the ANSALT code taking the dilatancy boundary referring to Eq. 3 into account.

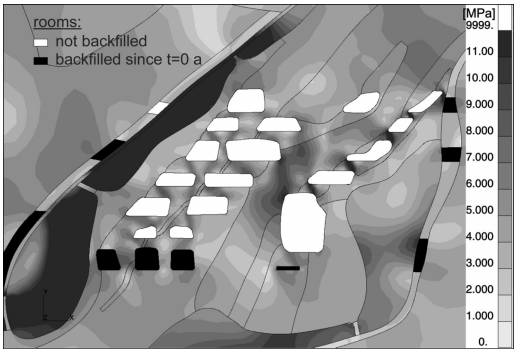

Figure 6. Deviatoric stresses at time $t = 66$ years after excavation calculated with 2-D models (ZB-S4-ANS-2D and ZB-S4-JIFE-2D).

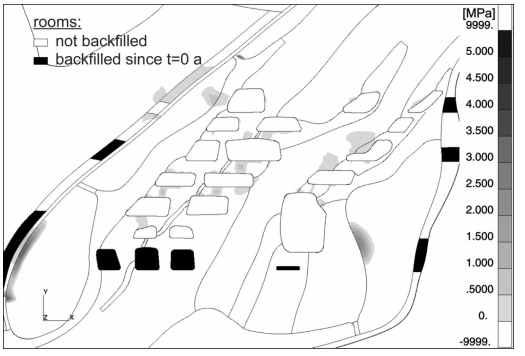

Figure 7. Calculated tensile stresses, 66 years after excavation.

- Model variation 1 (ZB-S4-JIFE-2D): This two-dimensional plane-strain model was calculated with the JIFE code regarding the new dilatancy concept (Eqs. 4 to 6).
- Model variation 2 (ZB-S4-JIFE-3D): This is an extended version of model variation 1 and served to consider the three-dimensional structural behaviour of the mine including the pillars at the head of the rooms.

4.3 *Results*

To analyse the stability and integrity of the structure the required data were calculated, e.g. principal stresses, deviatoric stresses, tensile stresses, effective strains, and displacements as well as dilatant zones in the salt rock. Figure 6 shows the distribution of deviatoric stresses around the mine at time $t = 66$ years after excavation (model ZB-S4-ANS-2D). High deviatoric stress values occur especially in the roofs of the eastern excavation row (with rooms no. 4 s at levels 1, 2a, 2, 3a, and 4a, see Fig. 4) as well as in wide parts of the anhydrite layers caused by creep of the salt structure, stress redistribution and subsequent accumulation of stress in the anhydrite.

Due to the pronounced unfavourable spatial arrangement and shape of the rooms, numerous roofs of the mine are partly subjected to tensile stress (Fig. 7). Considering the very low tensile strength of rock salt of about 0.5 to 1.0 MPa, these values indicate an unfavourable loading and stress state of the roofs.

Comparing the stress values calculated with ANSALT in model ZB-S4-ANS-2D to the data calculated with JIFE in model ZB-S4-JIFE-2D, very similar results can be obtained approving the reliability of both codes.

To analyse the local and zonal stability of the rooms the calculated tensile stresses, dilatant salt rock and effective strains were considered. Especially, the increase of effective strain with time in the roofs of the rooms was evaluated and compared to the maximum allowable strain determined in short-term tests at several strain rate levels in the laboratory.

To analyse the integrity of the salt rock barrier from a geomechanical point of view, two criteria were considered regarding a hydraulic and a dilatancy criterion (Langer & Heusermann 2001). Regarding the hydraulic criterion, the geomechanical integrity of the barrier is guaranteed if the hydrostatic pressure of an assumed column of brine extending to the surface does not exceed the minimum principal rock stress at the given location. Comparing the hypothetical brine pressure to the minimum principal stress calculated here with the different models, the results are very similar to former results presented by Heusermann & Fahland (2005). If the dilatancy boundary referring to Eq. 3 or Eqs. 4 to 6 is exceeded micro-cracks will form and cause damage and permeability. The dilatant rock zones calculated with the reference model ZB-S4-ANS-2D for a time elapse of 66 years after excavation are plotted in Figure 8. For reasons of comparison, the corresponding results of model ZB-S4-JIFE-2D are shown in Figure 9.

Excavation of the rooms and creep of the salt rock cause the development of dilatancy around the rooms. The major part of the roofs and pillars as well as larger rock zones between rooms and the anhydrite layers (Figs. 8–10, grey coloured) are subjected to dilatancy. Thus, the integrity of the barrier is not guaranteed since migration of brine from the caprock via the jointed anhydrite layers and the dilatant salt rock into the mining rooms cannot be excluded.

Comparing the results of the two-dimensional models ZB-S4-ANS-2D (ANSALT code with dilatancy boundary referring to Eq. 3) and ZB-S4-JIFE-2D (JIFE code with dilatancy boundary referring to Eqs. 4–6), more or less the same dilatant rock zones could be obtained (Figs. 8, 9). The results obtained for the southern central part correspond well

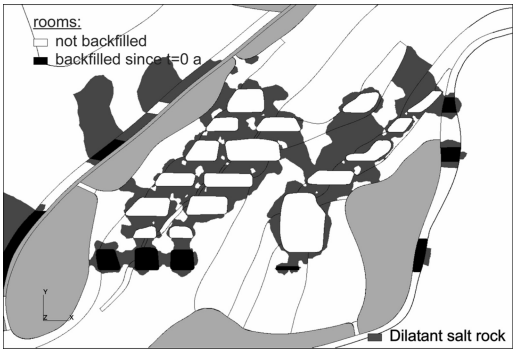

Figure 8. Calculated dilatant zones in the salt rock (model ZB-S4-ANS-2D).

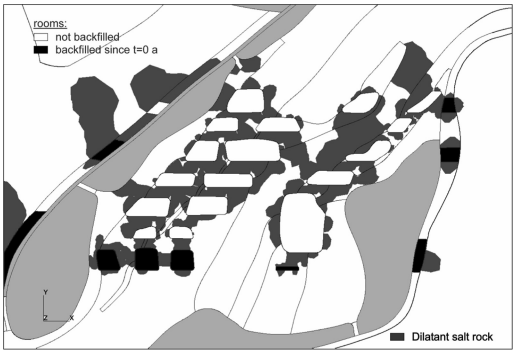

Figure 9. Calculated dilatant zones in the salt rock (model ZB-S4-JIFE-2D).

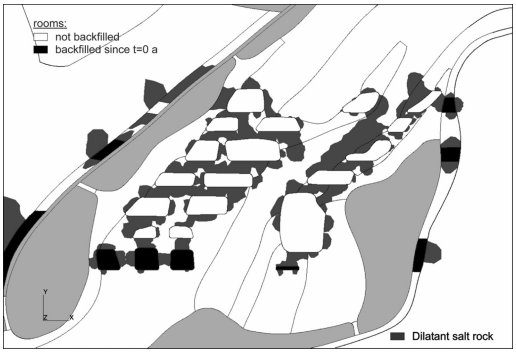

Figure 10. Dilatant zones in the salt rock calculated with the three-dimensional model ZB-S4-JIFE-3D.

to the results of former two-dimensional calculations regarding the northern central part which has a comparable geological structure and degree of excavation (Heusermann & Preuss 2002).

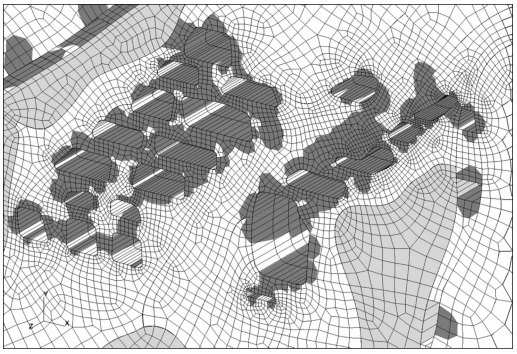

Figure 11. Spatial distribution of dilatant zones in the salt rock after 66 years (model ZB-S4-JIFE-3D).

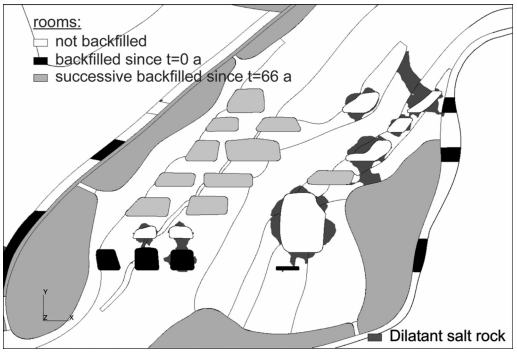

Figure 12. Dilatant zones after backfilling of selected rooms (model ZB-S4-ANS-2D).

If the three-dimensional stress and deformation state is considered in model ZB-S4-JIFE-3D, a certain reduction of dilatancy in the salt rock compared to two-dimensional modelling can be determined (Figs. 10, 11). This is caused by the more favourable three-dimensional structural behaviour and the related lower amount of deviatoric stresses in the considered cross section of the mine.

The long-term stability of the mining rooms and integrity of the salt barrier can be significantly improved by backfilling the rooms with a suitable material. With respect to the actual backfilling concept (Preuss et al. 2002), a selected number of rooms (at levels 1 to 3a, see Fig. 3) were assumed to be backfilled with saltcrete in the model. The stiffness of the saltcrete was taken to E = 3500 MPa. In the model calculations the backfilling was assumed to take place at present (66 years after excavation). Results were obtained for a time elapse of up to 34 years starting from now (or 100 years starting from the time of room excavation).

As an example, Figure 12 shows the zones of dilatant salt rock calculated for a time elapse of $t = 100$

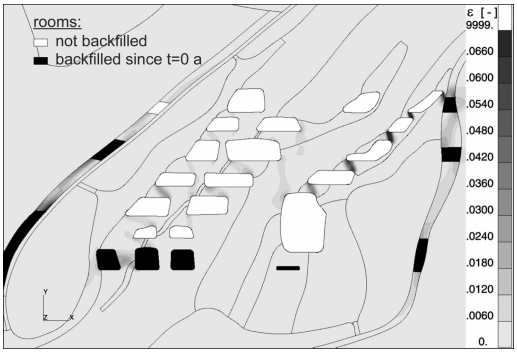

Figure 13. Calculated effective strains (model ZB-S4-JIFE-2D, 66 years after excavation).

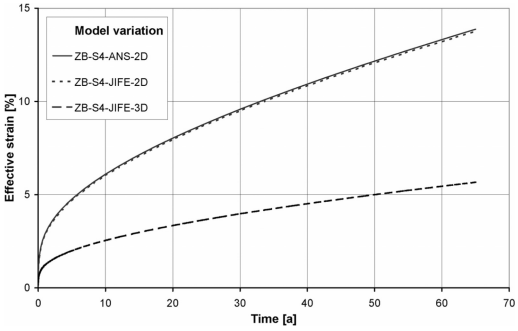

Figure 14. Effective strains over time in the roof of room 4 s, 2nd level, calculated with 2-D and 3-D models.

years after excavation (corresponding to 34 years after starting of backfilling). Comparing these results to the state before backfilling (Fig. 8), it can be seen that the dilatant zones are distinctly reduced. Most of the previous dilatant zones are disappeared, especially around the backfilled rooms. Dilatancy appears only locally in the vicinity of the open rooms as well as between some backfilled rooms and the anhydrite blocks, and in some upper parts of the salt barrier.

To analyse the stability of the mine at a small and medium scale, the stress and deformation state in roofs and pillars was considered. Especially, the effective strains determined with the several two- and three-dimensional models were compared to the maximum allowable strain measured in the laboratory at certain strain rates and extrapolated to the lower strain rates occurring in situ (Heusermann & Fahland 2005). In Figure 13, the calculated effective strains at time $t = 66$ years are plotted.

The more or less diagonal configuration of the rooms and the resulting characteristic asymmetric deformation of the roofs between the rooms cause a significant shear and bending zone reaching diagonally from the left corner in the floor of the upper room to the right corner in the roof of the lower room. The related strain values in the roofs increase with time due to the creep of the salt rock. Comparing the deviatoric strains to the maximum allowable strain determined in the laboratory it must be stated that the values calculated with the two-dimensional models have reached or exceeded more or less the ultimate values. For the long term, creep and dilatant deformation of the roofs will cause micro-cracks or, in case of accumulated micro-cracks, a single or a few macro-cracks. These results are confirmed by recent observations of fractures in several roofs of the central part of the Bartensleben mine.

To analyse the effects of 2-D and 3-D modelling on the calculated deformation state, the development of effective strain over time in the roof of room 4 s, 2nd level, was considered. This is the roof with the most unfavourable stresses and strains. Figure 14 depicts the variation of effective strain over time in the mid-plane of the roof. Regarding 2-D modelling with the ANSALT and JIFE code, very similar results could be obtained indicating again the correctness and reliability of both codes. After a time elapse of 66 years after excavation, a maximum strain value of about 14% could be determined. This value is assessed to exceed the maximum allowable strain determined in the laboratory.

If the 3-D structural behaviour is considered using model ZB-S4-JIFE-3D, an obvious reduction of the calculated strains could be achieved. Thus, 66 years after excavation, a maximum strain value of about 6% could be obtained. This significant difference between the results of 2-D and 3-D modelling is caused by the consideration of the pillars at the head of the mining rooms and the more favourable and realistic stress and deformation state in the 3-D model. It indicates that the stresses, strains and extension of dilatant zones in the salt rock obtained by 2-D modelling must be assessed as very conservative values.

5 CONCLUSIONS

To assess the stability of old mining rooms and the integrity of the salt barrier in the southern central part of the Bartensleben mine of the Morsleben repository, geomechanical model calculations have been carried out. In a first step, a two-dimensional model of a characteristic cross section of the mine was used based on an idealized model of the geological structure. In a second step, this model was extended to a three-dimensional model considering half of the length of the rooms and of the pillar at the head of the rooms for reasons of symmetry. The calculations comprised the analysis of the recent state of the rooms and the salt barrier as well as the evaluation of stability and integrity.

The following results could be obtained by means of finite-element modelling:

- The analysis of the recent status of the southern central part of the mine shows that the local and medium-scale stability of the mine is strongly influenced by an unfavourable shape of the rooms and steep configuration of excavation rows. Thus, tensile stresses, high deviatoric strains and dilatancy occur especially in the roofs between the mining rooms. Fractures in the roofs with subsequent roof fall cannot be excluded in such cases. Recent observations of several fractures in numerous roofs of the mine are in good agreement with the results of numerical modelling. However, this local phenomenon does not considerably affect the present large-scale stability and integrity.
- The integrity of the salt barrier is given for most parts of the salt rock, especially at the top of the salt structure. However, significant zones of dilatancy occur around the rooms and between the rooms and the anhydrite layers. Thus, potential migration of brine from the caprock into the mining rooms via the anhydrite layers and the dilatant salt rock cannot be excluded. This makes it necessary to backfill the rooms with a suitable material to reestablish a favourable stress state around the rooms and to reduce the dilatant rock zones.
- If a number of selected rooms in the mine are backfilled with a suitable material, a distinct reduction of dilatant rock zones will occur within a couple of years or a few decades depending mainly on the stiffness of the backfill material.
- Additionally, two several finite-element codes and two different models describing the dilatancy evolution were used for reasons of comparison. Both codes, the well proven ANSALT code and the new JIFE code, yielded the same results in terms of stresses, strains, and displacements indicating their correctness and reliability. Using two different equations to describe the dilatancy boundary of rock salt, a more or less sufficient agreement of the calculated extension of the dilatant rock zones was obtained.
- The effect of three-dimensional modelling of the mine on calculated stresses, strains and dilatant rock zones was studied with the JIFE code and the results were compared to the data obtained in 2-D models. As expected, deviatoric stress and effective strain values as well as the extension of dilatant zones in the salt rock are distinctly reduced in the 3-D model. This is caused by the consideration of the pillars at the head of the mining rooms in the 3-D model and the related stress and deformation state which is more favourable compared to the 2-D models. Thus, stresses, strains and extension of dilatant zones obtained by 2-D modelling must be assessed as very conservative results.

REFERENCES

Behlau, J. & Mingerzahn, G. 2001. Geological and tectonic investigations in the former Morsleben salt mine (Germany) as a basis for the safety assessment of a radioactive waste repository. *Eng. Geol.*, 61, 83–97.

Heemann, U., Sarfeld, W. & Faust, B. 2003. 3D-calculation of dilatancy and permeability. *European Commission CLUSTER Conference on the Impact of EDZ on the Performance of Radioactive Waste Geological Repositories, Nov. 3–5, 2003,* Luxembourg.

Heller, M., Mauke, R., Mohlfeld, M. & Skrzyppek, J. 2004. ERAM-SIS: A spatial information system for visualization and management of geotechnical data. *Proc. DisTec 2004, Int. Conf. on Radioactive Waste Disposal, April 26–28,* 130–136, Berlin.

Heusermann, S. & Fahland, S. 2005. Long-term geomechanical stability and integrity of the salt barrier in the central part of the Bartensleben mine. *Post-Mining 2005, Nov. 16–17,* Nancy, France.

Heusermann, S. & Preuss, J. 2002: Geomechanische Modellberechnungen zur Beurteilung der Integrität der Salzbarriere im Zentralteil der Schachtanlage Bartensleben. *Z. Angew. Geol*., Heft 2/2002, 23–29, Hannover.

Hunsche, U. & Schulze, O. 1994. Das Kriechverhalten von Steinsalz. *Kali und Steinsalz*, 11(8/9), 238–255.

Hunsche, U. & Schulze, O. 2003. The dilatancy concept – a basis for the modelling of coupled TMH processes in rock salt. *European Commission CLUSTER Conference on the Impact of EDZ on the Performance of Radioactive Waste Geological Repositories, Nov. 3–5, 2003*, Luxembourg.

Langer, M. 1999. Principles of geomechanical safety assessment for radioactive waste disposal in salt structures. *Eng. Geol.*, 52, 257–269.

Langer, M. & Heusermann, S. 2001. Geomechanical stability and integrity of waste disposal mines in salt structures. *Eng. Geol.*, 61, 155–161.

Nipp, H.-K. 1991. Testbericht und Freigabemitteilung für das Programmsystem ANSALT I (Release 1991–1). Bericht, Archiv-Nr. 108586, BGR, Hannover.

Preuss, J., Eilers, G., Mauke, R., Müller-Hoeppe, N., Engelhardt, H.-J., Kreienmeyer, M., Lerch, C. & Schrimpf, C. 2002. Post Closure Safety of the Morsleben Repository. *Waste Management Conference '02, February 24–28, 2002,* Tucson, Arizona, USA.

The Mechanical Behavior of Salt – Understanding of THMC Processes in Salt –
Wallner, Lux, Minkley & Hardy, Jr. (eds)
© 2007 Taylor & Francis Group, London, ISBN 978-0-415-44398-2

Geotechnical control of critical construction elements during the backfilling activities of the ERAM – Experience gained in using the observation method

R. Mauke
Federal Office for Radiation Protection (BfS), Salzgitter, Germany

B. Stielow & M. Mohlfeld
Zerna, Köpper & Partner, Bochum, Germany

ABSTRACT: In the Morsleben Radioactive Waste Repository (ERAM) 22 huge salt mine caverns have been backfilled with a hydraulic transportable salt concrete since October 2003. These backfilling activities are necessary to maintain the mine in a stable condition and to keep the salt barrier intact. The rock behaviour before, during and after the stabilising activities is systematically registered by an extensive geotechnical measurement and monitoring system. It was designed on the basis of preliminary calculations to predict the probable behaviour of the rock salt. The TM (thermal, mechanical) calculations should be calibrated by the measurement results to guarantee the operational safety during backfilling activities.

1 INTRODUCTION

The Morsleben repository (ERAM) is a twin mine, consisting of the sections Bartensleben and Marie. The central part of the Bartensleben mine is a highly excavated zone with large cavities (see Figure 1). Mechanical calculations show that this part of the mine has to be stabilized to preserve the integrity of the salt barrier (Hund et al. 2004). The "salt barrier" represents the impermeable layer between the mine openings and the lower boundary of the overburden which protects the mine from potential water or brine inflow. This stabilization should be realized by a number of cavities which will be backfilled with a salt concrete. The backfilling material and the surrounding rock salt act together as a system of arches and pillars supporting the overburden and minimizing deformations of the main anhydrite, which tends to show brittle failure and may act as a future pathway for the transport of brine and radionuclides.

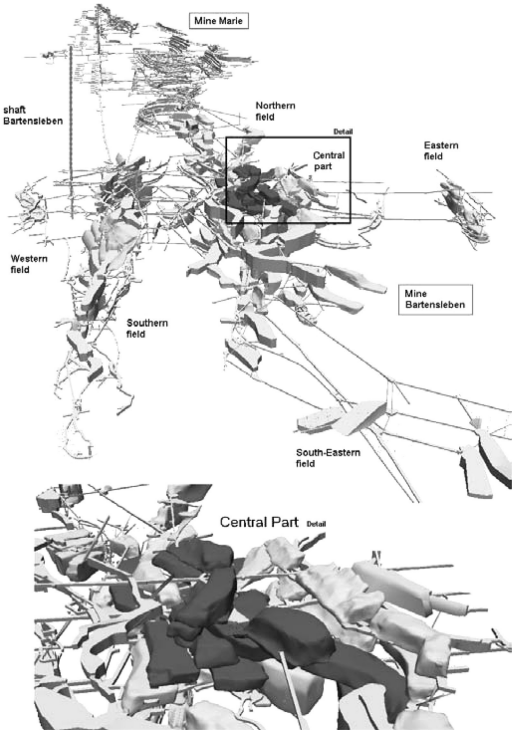

Figure 1. Mine openings of the ERAM (backfilled caverns in dark color).

2 PROOF METHOD

In accordance with the geotechnical regulations of the European Standard, Eurocode 7, a geotechnical monitoring program has been developed to observe the surrounding rock behaviour and the influences of the backfilling activities. The EC 7 provides the observation method in addition to suitable calculations

and a precautionary concept how to deal with cavities whose stability is not sufficient. The observation method covers:

- Visual inspection
- Prognosis and defined tolerance limits
- Measurements of the construction
- A sufficient reaction time for the introduction and implementation of corrective measures when significant deviations of deformations occur.

3 FIRST CALCULATIONS

Prior to backfilling activities some prognosis thermo-mechanical calculations (using the FDM code FLAC 3D 2.20) assessed the areas with the highest stresses in the rock salt (Hund et al. 2004). By taking the planned backfilling into account it can be shown that global improvement of the geomechanical situation can be realized by backfilling the cavities extensively with a stabilizing material.

On the basis of the thermo-mechanical calculations and by considering the influence of hydration an appropriate order of backfilling has been developed. This backfilling concept had to take into account that some pillars and roofs are already disturbed due to loading and convergence.

In general the states of construction are not critical but even in spite of comprehensive system reflections there are nevertheless some construction phases for which the local stability cannot be proved.

4 MEASUREMENT CONCEPT

For proving measure efficiency and observing rock situations before, during and after backfilling activities an extensive measurement program has been developed. Especially the rock behaviour in geomechanically exposed supporting structures will be monitored by the measurement equipment. Measuring displacements, rock stresses and temperatures provide the basic information for

- The collection of data for the validation of extrapolations (Chapter 6)
- The adaptation of extrapolated values (within bandwidths) on the basis of validated calculations
- The definition of limiting values for loadings and strains on supporting elements
- Agreement of a precautionary concept
- The continuous comparison of the predicted with the measured values to observe that limits are kept (Chapter 7)
- The control of the backfilling progress and the realization of precautionary measures as required.

Of special interest is a sufficient reaction time for relevant measures and the progressive extrapolation of the expected behaviour. In reality a violation of expected planning values may often occur. In most cases other assessment elements will, however, be available, which lead to an acceptable safety level. Therefore instruments have to be provided which offer the possibility to revise the expected behaviour by changing the input data when required. Direct measurements of strains, calibrated extrapolations, new ground evaluations and the statistical evaluation of available measurement results are able to serve this purpose. By consequently using this procedure the actual safety level can also be raised significantly during the completion of a complex geotechnical construction as the formally correct and sufficient proof of safety can be achieved.

The measuring program consists of various instrument types are listed in figure 2.

Because of the requirement to intervene in the backfilling progress or to introduce necessary measures if limit values are exceeded, most measuring systems work automatically. For quality assurance of the results regular control measurements will be carried out with calibrated test sensors. For each measuring location a separate limit value is programmed. In the event that limit values are exceeded an alarm signal is sent to the

Displacement measuring	**Extensometer measuring (20):** deformation (strain) in geomechanically exposed supporting elements such as roofs and pillars
	Convergence indicator (17): convergence measuring the surface displacements in representative cross sections
	Crack observation (2): measuring the displacements of existing fractures
	Inclination measuring (4): inclination and the axial translation by an inclinometer probe and an incremental extensometer probe in some pillars
Rock stress measuring	**Hydro fracturing measurements (13):** determine the minimum principal stress in representative supporting areas
	Stress monitoring stations SMS (13): record the modification of rock stresses and temperatures in representative bearing areas
	Load cells (ca. 60): vertical and horizontal supporting stress in the contact zone between rock and backfilling material
Temperature measurements: Temperature in the backfilling material and the rock	

Figure 2. Measuring systems (Weidenbach et al. 2004).

central observation station from where measures are initiated.

Micro-acoustic and seismic measurements in a wide rock area around the backfilling activities complete the monitoring (Eilers et al. 2007).

5 OCCURRENCE OF DIFFICULTIES DURING OPERATION

5.1 *Load cells*

With load cells it should be possible to register the stress evaluation between rock and backfilling material. In general the load cells are embedded in mortar with screwed chipboards. In addition to the standard load cell construction, two special load cell constructions were tested at the first cavern to be filled (see Figure 3).

At the first special construction, the horizontal and the vertical load cell are placed in a metal frame. With this structure the installation can be accomplished very quickly and expensive safety work for the ridges can be avoided.

The aim of the second solution is to harmonize the loading on the cell by placing it under a Styrofoam plate. This construction has already been used successfully at a foundation of a bridge (Jung & Kügler, 2002).

Figure 4 shows the comparison of the measurement results. Differences in results are obvious but explicable. Measured loadings of the special constructions are all on a lower level than the ones of standard load cells. At the first construction the massive frame has led to load redistributions. At the other one the choice of a wrong Young's modulus of the Styrofoam plate is probably the reason for incomparable results. Nevertheless both solutions have been rejected.

5.2 *Humidity protection*

Because of the salt concrete composition no exceeding brine was expected. But during the filling of the first cavern some brines occurred in the lower parts of the mine. Since there was no possibility to predict the brine appearance the measuring systems had to be fitted against humidity. For example water resistant sensors were installed, cable boxes were filled with epoxy resin or data stations were dislocated. Besides the composition of the salt concrete has been optimized.

5.3 *Post injection*

In some boreholes stress monitor stations (SMS) have been installed to observe the stress evaluation during and after filling the caverns. These SMS consist of 6 load cells with different orientations. After installation the borehole is filled with a special mortar under pressure. As expected the first measurements showed that there was no contact between mortar and load cell. Therefore a special post injection system had been designed. About 3 months after the post injections the peak values have decreased to predicted levels and the measurements can be taken into account for ongoing geomechanical calculations.

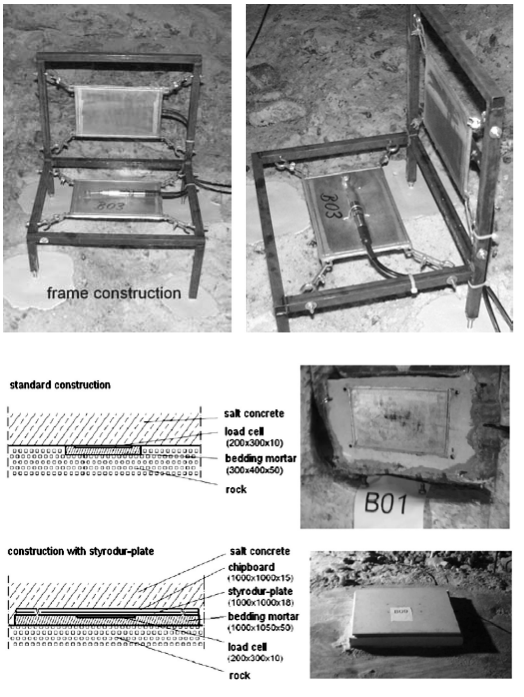

Figure 3. Load cell constructions.

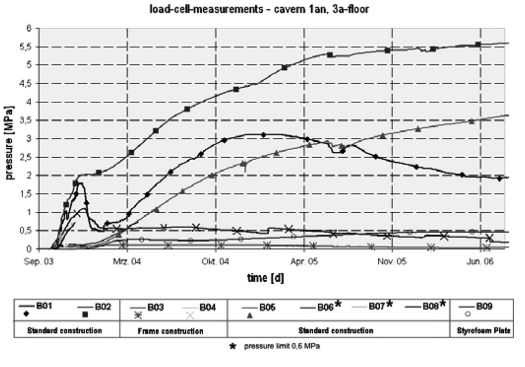

Figure 4. Load cell measurements.

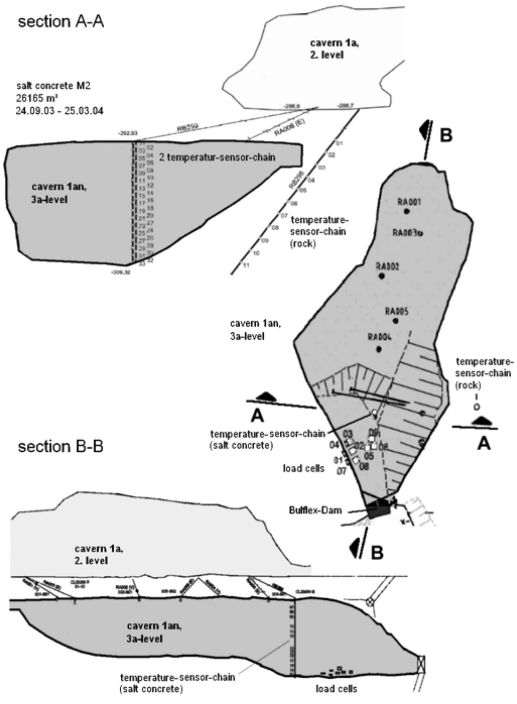

Figure 5. Measuring systems.

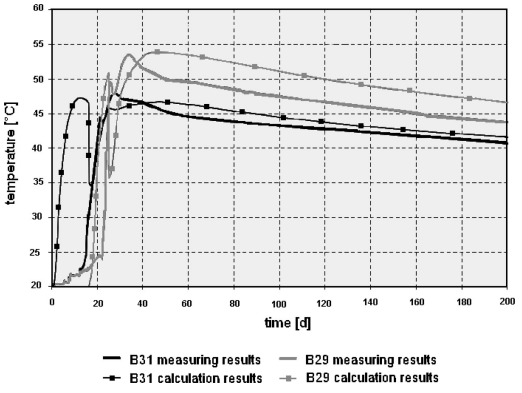

Figure 6. Temperature measurements/calculations (Düsterloh et al. 2005).

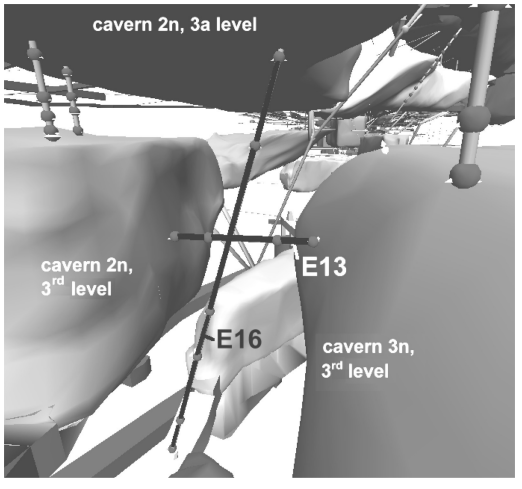

Figure 7. Pillar.

6 VALIDATION OF CALCULATIONS

6.1 *Load cell calculations*

The measured stresses in the first filled cavern reached very high values (about 5.0 MPa) unexpectedly quickly. Previous calculations for dimensioning the load cells could not give any explanation for this effect. In addition some calculations on a 2d model should demonstrate possible influences which could lead to such stresses. Thermal expansion during hydration of concrete and geometric factors are possible reasons but final explanations have not been found yet. Maybe further measurements will illuminate this issue.

6.2 *Temperature calibration*

In the first backfilled cavern the calculation model should be calibrated. To this end the backfilling progress and the temperature evolution were determined. The temperature was measured in the cavern by two temperature lines of 66 sensors and in the surrounding rock by a temperature line of 11 sensors (see Figure 5). The backfilling progress was analyzed by balancing the quantity, the height of backfilled material and measuring the temperature at the filler opening itself. To calibrate the different backfilling periods, material heights and layers were taken into account. Additional investigations were carried out so that the concrete temperature while placing it could be included as well.

Even considering the real backfilling progress the measured temperatures are in good agreement with the calculated temperatures (Figure 6).

Additional adjustments relative to the modeling of temperatures are not necessary.

6.3 *Vertical pillars*

Some pillars need to be assessed or evaluated because of their essential stabilizing function in the backfilling concept. Especially pillars with the potential hazard of continuing damages are controlled by deformation measurements (extensometer: E13, E16). With this method accelerating displacements which can be the forerunner of a stability failure will be recognized and precautions can be realized (see Figure 7, here the

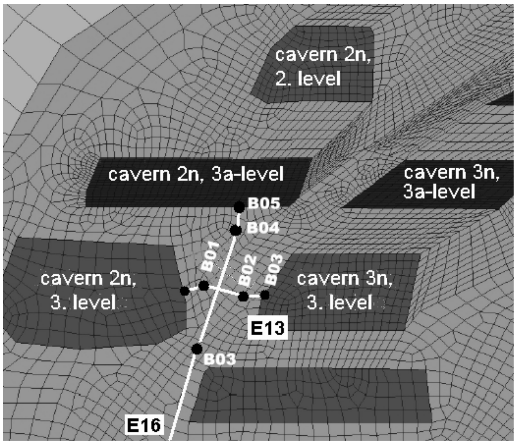

Figure 8. Model of the pillar (DBE. 2006).

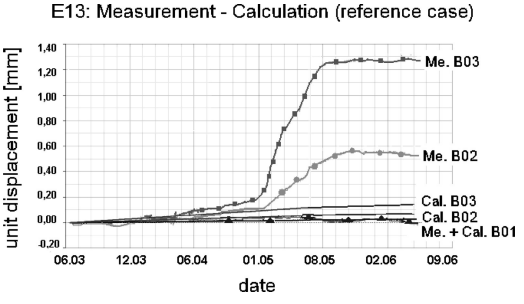

Figure 9a. Calibration calculation – reference case (DBE. 2006).

caverns at the 3rd level remain unfilled whereas the caverns at the 3a level are backfilled).

Calculations have been carried out to predict the deformations for the installed extensometers. For this prognosis the experiences from the preliminary measurements and the thermal calibrated calculation models were taken into account.

By taking different creeping classes of the rock salt, humidity creeping, plastic material behaviour etc. into consideration the preliminary measurements are calibrated for the unfilled system. It can be seen that the measured displacements are rising more steeply than those calculated in the reference case (see Figure 9a). The drastic increase of the measured displacements in the first week of May is affected by mining processes because the backfilling started later.

With the usage of a higher creeping class the calculated results fit much better to the measured displacements (see Figure 9b). The handling of plastic material properties lead to calculated displacements which are too high (see Figure 9c).

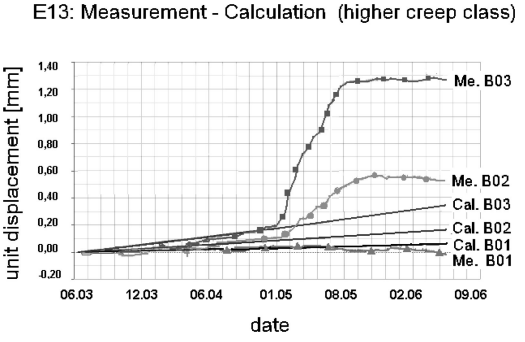

Figure 9b. Calibration calculation – higher creeping class (DBE. 2006).

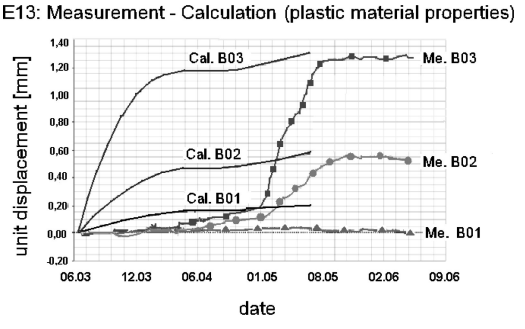

Figure 9c. Calibration calculation – plastic material properties (DBE. 2006).

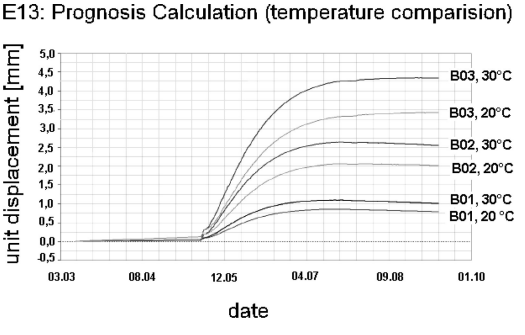

Figure 10. Prognosis calculations (DBE. 2006).

First prognoses have been carried out with the best estimate variant of the calibration of the unfilled system. Further parameter analyses (backfilling velocity, material temperature (for example Figure 10)) increase the certainty of the results.

Backfilling activities in the upper caverns are obviously shown by the steep rise of the displacement evolutions. The deformations before and after the backfilling progress can be identified by a slow and

continuous gradient. The prognosed horizontal displacements of the pillar reach values of 1 to 2 cm during the backfill period. However, since the pillar tolerates axial deformations of about one decimeter there are no damages expected.

7 COMPARISON OF MEASUREMENTS WITH CALCULATIONS

The monitoring data were daily provided to the responsible department of the BfS and other experts by transfer via internet. All significant results were reported by the contractor in weekly and monthly written bulletins. The powerful databank system ERAM SIS (Heller et al. 2004) allows a permanent comparison of the measured data with the predicted displacements. In general these comparisons show a good agreement but nevertheless there will always be some measurement results which cannot be explained by calculations.

Particularly geomechanically exposed supporting structures will be observed at shorter intervals during backfilling than safer areas. If deformation limits (first alarm limits) are exceeded a geotechnical evaluation takes place and the backfill management will be informed. Suitable and effective measures will then be taken, which are described in a special precautionary concept (e.g. temporary stop of backfill up to new planning of backfill measures).

8 EXPERIENCE GAINED IN USING THE OBSERVATION METHOD

The geotechnical observation method has been developed to control rock behaviour before, during and after backfilling activities in the areas of geomechanically exposed supporting elements. Thereby the

- Data for model calculations are determined (stresses, displacements, temperatures)
- Limit values for loading of supporting elements corresponding to Eurocode 7 are established
- Prognosis behaviour can be reviewed
- Keeping of the limit values is observed and the backfilling progress is managed.

All in all the mine stability will be successfully proved.

The application of the observation method to the ERAM requires some adaptations. E.g. new information during the years of backfilling leads to changes of utilization for some caverns. And this leads to modifications in the backfill and the measurement conception, too.

For ambitious projects like the described backfill measures in Morsleben it should be common practice that a part of the project costs is used for measurements and safeguards methods.

Except for this the need of a permanent evaluation of the measures exists on the part of the responsible applicant BfS and the relevant authorizing bodies. The monitoring system serves this purpose.

REFERENCES

DBE. 2006. bGZ – Schwellenwerte für die zulässigen Beanspruchungen für Schweben und Pfeiler während der Verfüllung der Abbaue 2n und 3n auf der 3a-Sohle, Peine (unpublished report)

Düsterloh, U., Lux, K.-H. & Roussev, P. 2005. Validierung numerischer Berechnungsmodelle zur Abbildung des thermo-mechanischen Tragverhaltens von Abbau 1an (13YEA21/R003), Clausthal-Zellerfeld (unpublished report)

Eilers, G., Friedrich, C. & Klippel, O. 2007. Seismic underground monitoring of the Morsleben mine closure. 6th Conference on the Mechanical Behavior of Salt: Understanding of the THMC Processes in Salt Rocks, Hannover

Heller, M., Mauke, R., Mohlfeld, M. & Skryppek, J. 2004. ERAM-SIS: A Spatial Information System For Visualization And Management Of Geotechnical Data. International Conference on Radioactive Waste Disposal (DISTEC2004), Berlin

Hund, W., Laumert, G., Preuss, J.; Eilers, G., Mauke, R., Köster, R., Fischer, H., Oppitz, J., C. Schrimpf, C., Kreienmeyer, M., Müller-Hoeppe, N. 2004. Stabilization Of The Central Part Of The Morsleben Repository (bGZ). WM Konferenz, Tucson

Jung, R. & Kügler, M. 2002. Die Spundwandplattengründung im Großbrückenbau am Beispiel der neuen Elbebrücke Tangermünde. Conference “Messen in der Geotechnik 2002”, Braunschweig, 419–430.

Weidenbach, J., Fischle, W., Mauke, R., Rathke, C. 2004. Central Part Of The Morsleben Repository – Geotechnical Monitoring Programme. International Conference on Radioactive Waste Disposal (DISTEC2004), Berlin

Part 7. Cavern design for gas storage and solution mining

Taylor & Francis
Taylor & Francis Group
http://taylorandfrancis.com

The Mechanical Behavior of Salt – Understanding of THMC Processes in Salt –
Wallner, Lux, Minkley & Hardy, Jr. (eds)
© 2007 Taylor & Francis Group, London, ISBN 978-0-415-44398-2

Effects of cavern shapes on cavern and well integrity for the strategic petroleum reserve

S.R. Sobolik & B.L. Ehgartner
Sandia National Laboratories, Albuquerque, New Mexico, USA

ABSTRACT: This report presents computational analyses to determine the structural integrity of different salt cavern shapes. Three simple characteristic shapes (caverns with enlarged tops, bottoms, and mid-sections) are evaluated for increasing cavern volumes and compared to the baseline shape of a cylindrical cavern. The intent of these calculations is to develop some guidelines to predict cavern performance and damage in salt, utilizing the three-dimensional modeling capabilities of high-performance analytical codes and sophisticated material models.

1 INTRODUCTION

The U.S. Strategic Petroleum Reserve (SPR) stores crude oil in 62 caverns located at four different sites in Texas (Bryan Mound and Big Hill) and Louisiana (Bayou Choctaw and West Hackberry). The petroleum is stored in solution-mined caverns in salt dome formations. Each cavern is constructed and then operated using hanging strings inserted through well bores that are lined with cemented steel casings from the surface to the top of the cavern.

The SPR sites, as well as most other oil and natural gas storage sites in salt domes along the Gulf Coast, are varied in terms of cavern structure and layout. Some sites, such as the Big Hill site, are characterized by a cavern field of reasonably uniform cavern dimensions (radius, height, shape, and depth) and spacing. Other sites, such as Bayou Choctaw, are characterized by diverse cavern characteristics. Most cavern field designs are based on a pillar-to-diameter (P/D) ratio and assumed cylindrical cavern shapes; this criterion has served cavern designers well. However, this criterion does not take into account the unusual cavern shapes created either by design, variability in salt properties, or by happenstance. In general, caverns in the SPR are intentionally shaped with larger tops to accommodate future oil drawdowns where the bottom portions of the caverns are preferentially leached, and hence the overall cavern shape becomes more cylindrical, as raw water is injected at depth to remove the oil. In practice, the future shapes of caverns will depend upon the drawdown and refill scenarios. As a result, caverns shapes with enlarged bottoms and mid-sections are possible. Salt composition also results in unpredictable cavern shapes as the insoluble content or dissolution rates of salt can vary spatially. This explains some of the asymmetries found in the cavern shapes. As a result a wide variety of cavern shapes exist for the SPR and the relative advantages and disadvantages of the shapes are not clear. The analyses described in this report are designed to examine the effect on cavern stability with variations in cavern shapes and sizes. The results will be useful in evaluating current and future shapes of existing caverns, and will provide insight for designing future expansion caverns. The analyses employ a stratigraphy and material properties corresponding to the Big Hill site, but evaluate different cavern shape geometries.

Several three-dimensional models using a close-packed arrangement of 19 caverns have been built and analyzed using a simplified symmetry involving a 30-degree wedge portion of the model. The caverns are modeled without wells and casing to simplify the calculations. These calculations utilized the power law creep model. The four cavern shapes were evaluated at several different cavern radii against four design factors. These factors included the dilatant damage safety factor in salt, the cavern volume closure, axial well strain in the caprock, and surface subsidence. The relative performance of each of the cavern shapes varies for the different design factors, although it is apparent that the enlarged bottom design provides the worst overall performance. The results of the calculations are put in the context of the history of cavern analyses assuming cylindrical caverns, and how these results affect previous understanding of cavern behavior in a salt dome.

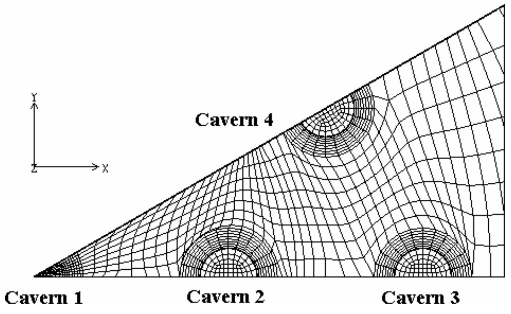

Figure 1. Finite element mesh with cross-section through caverns (plan view).

2 ANALYTICAL MODEL

The analytical model simulates caverns that were leached to full size over a one year period, filled with oil, and then permitted to creep for an additional 45 years. The standard pressure condition applied to the cavern was based on an average wellhead pressure of 6.52 MPa (945 psi). This pressure was held constant throughout the 45-year simulation except for workover periods, during which the wellhead pressure was dropped to 0 MPa. These workover periods typically last for three months in duration, and occur once every 5 years. Previous analyses have shown that this abrupt pressure drop will induce the greatest potential for damage. The duration of the simulated workover may be slightly longer than is typically encountered in the field, but is chosen to provide an adverse condition and closely simulate actual subsidence measurements.

The analysis utilized the finite element code JAS3D (Blanford et al., 2001), which is ideal for simulations of processes occurring over many years; the power law creep model for salt; and a three-dimensional, 30-degree wedge capable of modeling a 19-cavern field because of geometrical symmetry. JAS3D was designed to solve large quasi-static nonlinear mechanics problems. The continuum mechanics modeled by JAS3D are based on two fundamental governing equations. The kinematics are based on the conservation of momentum equation, which can be solved either for quasi-static or dynamic conditions (a quasi-static procedure was used for these analyses). The stress-strain relationships are posed in terms of the conventional Cauchy stress. The mesh for this wedge is illustrated in Figure 1. Cavern 1 represents one cavern, at the center of the 19-cavern field, and Caverns 2, 3, and 4 each represent 6 caverns in the field due to model symmetry. Four material blocks are used in the model to describe the stratigraphic layers: the overburden, two layers of caprock, and the salt dome. The overburden is made of sand, the upper caprock layer is made of gypsum or limestone, and the lower caprock layer is made of anhydrite. This stratigraphic material closely matches

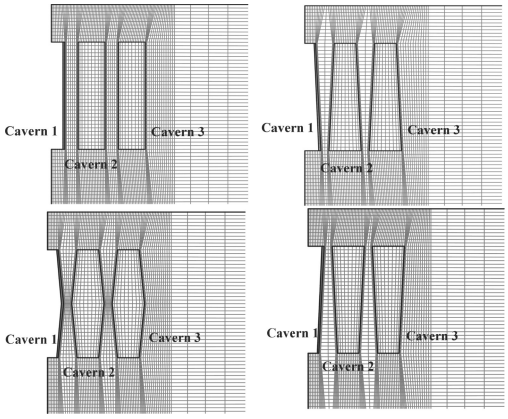

Figure 2. Cavern shapes: cylinder, expanded bottoms, middles, and tops.

that used for Big Hill (Park et al., 2005). For simplifying the mesh, the stratigraphic layers of the cavern field are extended horizontally throughout the mesh, rather than trying to model the rocks surrounding the salt dome.

Four standard cavern shapes are considered in these analyses: cylindrical, enlarged top, enlarged middle, and enlarged bottom. These shapes are illustrated in detail in Figure 2. There are 17 cases in all, each case with a specified cavern shape and base radius which is representative of current conditions based on existing sonar data for SPR sites. Table 1 lists the 17 cases that were considered in this analysis; caverns of different shapes for a given base radius are approximately equal in volume to the cylindrical cavern with the same base radius. Most current caverns at the SPR sites have radii in the range of 30–46 m (100–150 feet). All cases were simulated to 45 years of operation except the four cases for which the base radius was 76 meters (250 feet); these were run out to 100 years to determine if there were any continuing trends not observed in the first 45 years. Minimum and average pillar to diameter (P/D) ratios and cavern volumes (in MMB = millions of barrels) are calculated for each case. The intent is to see if there is any advantage to the use of one or the other in developing criteria to evaluate caverns. All simulated caverns are 576 m (2000 feet) in height, and begin at a depth of 701 m (2300 feet).

The power law creep model has been used for Waste Isolation Pilot Plan (WIPP) and SPR simulations for many years. Values for the creep constant, the stress exponent, and the thermal activation energy constant for the power law creep model have been obtained for hard and soft salts through mechanical property testing of salt cores collected from boreholes (Wawersik & Zeuch, 1984; Munson, 1998). These properties have been further modified by matching site subsidence and cavern volume loss data (Ehgartner & Sobolik, 2002;

Table 1. Cavern shape case summary.

Cavern shape case		Radius at heights (all lengths in feet)					
Name	Base radius	0	1000	2000	Volume, MMB	Min. P/D	Avg. P/D
Cylindrical caverns							
cyl100	100	100	100	100	11.19	2.75	2.75
cyl150	150	150	150	150	25.18	1.5	1.5
cyl200	200	200	200	200	44.76	0.875	0.875
cyl250	250	250	250	250	69.94	0.5	0.5
cyl300	300	300	300	300	100.72	0.25	0.25
Caverns with enlarged bottom diameter							
bot100	100	150	100	50	12.12	1.5	3.12
bot150	150	200	150	100	26.11	0.875	1.60
bot200	200	250	200	150	45.70	0.5	0.92
bot250	250	300	250	200	70.88	0.25	0.52
Caverns with enlarged middle diameter							
mid100	100	50	150	50	12.12	1.5	3.12
mid150	150	100	200	100	26.11	0.875	1.60
mid200	200	150	250	150	45.70	0.5	0.92
mid250	250	200	300	200	70.88	0.25	0.52
Caverns with enlarged top diameter							
top100	100	50	100	150	12.12	1.5	3.12
top150	150	100	150	200	26.11	0.875	1.60
top200	200	150	200	250	45.70	0.5	0.92
top250	250	200	250	300	70.88	0.25	0.52

Table 2. Power law creep mechanical properties used for big hill salt (Park et al., 2005).

Property	Value
Density, kg/m^3	2300
Elastic modulus, GPa	2.48
Bulk modulus, GPa	1.65
Shear modulus, GPa	0.992
Poisson's ratio	0.25
Creep Constant A, 1/(Pa^n-sec)	8.69×10^{-36}
Exponent n	4.9
Thermal constant Q/R, K	6034

Table 3. Material properties of overburden and caprock layers.

Property	Lower Caprock (anhydrite)	Upper caprock (limestone)	Over-burden
Material Model	Soil/foam	Elastic	Elastic
Density, kg/m^3	2300	2500	1874
Elastic Modulus, GPa	75.1	7.0	0.1
Poisson's Ratio	0.35	0.29	0.33
Bulk Modulus, GPa	83.4		
Shear Modulus, GPa	27.8		
Constant A_0, MPa	2338		
Constant A_1	2.338		
Constant A_2	0		

Park et al., 2005). The creep constitutive model considered only secondary or steady-state creep. The creep steady state strain rate is determined from the effective stress as follows:

$$\dot{\varepsilon} = A_2\left(\frac{\sigma}{\mu}\right)^n \exp\left(-\frac{Q}{RT}\right) = A\sigma^n \exp\left(-\frac{Q}{RT}\right), \qquad A = \frac{A_2}{\mu^n} \tag{1}$$

where,

$\dot{\varepsilon}$ = creep strain rate,
σ = effective or von Mises stress,
μ = shear modulus, E/2(1 + ν), E = Young's modulus, ν = Poisson's ratio),
T = absolute temperature,
A_2, A, n = constants determined from fitting the model to creep data,
Q = effective activation energy, and
R = universal gas constant.

The properties assume a homogeneous material, and are generally obtained from laboratory measurements. In order to obtain agreement with the measured closure of underground drifts at the WIPP, a reduced modulus is used to simulate the transient response of salt (Morgan & Krieg, 1990). The elastic modulus reduction factor (RF) is known to vary for salts (Munson, 1998). The Big Hill salt is identified in Munson (1998) as a "soft" salt, as opposed to "hard" salts at Bayou Choctaw and Bryan Mound. These analyses were designed to consider the greater potential for deformation of the soft salts. For the Big Hill site, a value for RF of 12.5 was determined by calibrating to best match the measured closure and subsidence rates at those sites through back-fitting analysis. For these analyses, the same reduction factor will be used for the moduli. The salt properties used for these analyses are listed in Table 2.

Mechanical properties of each of the other geologic materials used in this analysis are listed in Table 3. The surface overburden layer, which mostly comprises sand and sandstone, is considered isotropic and elastic, and has no assumed failure criteria. The upper caprock layer, consisting of gypsum and limestone, is also assumed to be elastic. Their properties are assumed to be the same as those used for previous West Hackberry analyses (Ehgartner & Sobolik, 2002). The anhydrite as simulated in the lower caprock layer is expected to experience inelastic material behavior. The anhydrite layer is considered isotropic and elastic until yield occurs (Butcher, 1997). Once the yield stress is

reached, plastic strain begins to accumulate. Yield is assumed to be governed by Drucker-Prager criteria, and the corresponding material model in JAS3D is a soils and crushable foams model (a more detailed discussion of this model is included in Sobolik & Ehgartner, 2006).

3 RESULTS

There are many performance measures used by storage cavern designers to evaluate a cavern field. Depending on the function of the storage site, the local geological and geographical features, and the economics risks being undertaken, certain design factors of the site may take precedence over others. For example, subsidence may be a more important factor for cavern fields located near sea level, if the predicted safety factors for each shape under consideration are acceptable. At some sites, well failures in the caprock are problematic and well strains may become the dominant factor. The importance of cavern shapes will be examined by the use of four separate design factors: safety factors based on the hydrostatic pressure and deviatoric stress, cavern volume closure, axial well strain in the caprock, and surface subsidence. These measures are compared to both minimum and average P/D ratios, as well as cavern volumes, for different cavern radii. The cavern shapes will be ranked on the basis of each design factor, and an overall evaluation will be discussed in the conclusions section.

3.1 *Safety factors in salt surrounding the caverns*

The safety factor used in this study is identified by a dilatant damage criteria defined by a linear function relating shear stress to hydrostatic pressure. Dilatancy is considered the onset of damage to rock resulting in significant increases in permeability. Dilatant damage in salt typically occurs at the point at which microfracturing initiates, resulting in volume increase. Dilatant criteria typically relate two stress invariants: the first invariant of the Cauchy stress tensor I_1 (equal to three times the mean stress) and the square root of the second invariant of stress deviator J_2, or $\sqrt{J_2}$ (a measure of the overall deviatoric or shear stress). One dilatant criterion is the equation typically used from Van Sambeek et al. (1993),

$$\sqrt{J_2} = 0.27 I_1 . \tag{2}$$

This damage criterion defines a linear relationship between I_1 and $\sqrt{J_2}$, and such linear relationships have been established from many suites of lab tests on WIPP, SPR, and other salt samples. This criterion was applied during post-processing of the analyses. A safety factor index was defined for this criterion (SF_{VS}) by normalizing $\sqrt{J_2}$ from Equation 2 by $\sqrt{J_2'}$ yielding:

$$SF_{VS} = \frac{0.27 I_1}{\sqrt{J_2'}}, \tag{3}$$

where J_2' is the value of the second invariant of the stress deviator tensor predicted from the simulation at every point in the mesh. Several earlier publications define that the Van Sambeek safety factor SF_{VS} indicates damage when $SF_{VS} = 1$, and failure when $SF_{VS} \leq 0.6$. This report will use these damage thresholds.

The minimum safety factors typically occur during the workover periods, when the pressure at the wellhead is reduced to 0 psi. When the minimum safety factor in the salt is plotted as a function of time, observations can be made regarding the change in safety factor as the initial cavern radius is increased, and also as a function of time. The minimum safety factors decrease, both at operating and at workover pressures, as the radius increases. The safety factors during standard operations and pressures range between 3 and 6, and the workover safety factors range between 1 and 2. Figures 3–6 present the minimum safety factor in salt for the workover periods only for varying cavern radius for the four cavern types – cylindrical, enlarged bottom, enlarged middle, and enlarged top, respectively. The results in Figure 3 for the cylindrical caverns show a slight increase during the 45-year period, and a slight decrease in later years. The results are similar in Figures 5 and 6 for the enlarged middle and enlarged top caverns during the first 45 years, and remaining steady in the later years. In Figure 4, the enlarged bottom caverns show a different behavior, as the workover safety factors decrease over time. This is especially noticeable in the time period after 45 years. For all these calculations, no safety factor was calculated to be in the failure range (<0.6), and only the 91-m (300-ft) radius cylindrical cavern had any safety factors in the damage range (<1) during the first 45 years of operation.

Figures 3–6 indicate that the enlarged middle caverns have the highest overall safety factors. To further investigate this trend, the minimum safety factor for each shape can be plotted as a function of an indicator of size. Figure 7 plots the minimum safety factor as a function of initial cavern volume within the 45-year operation period. The enlarged middle caverns clearly have the highest safety factor regardless of volume. The significant drop in safety factor for the cylindrical caverns occurs for the 90-m (300-ft) base radius case. Figure 8 plots the minimum safety factor as a function of average P/D. The behavior according to average P/D compares more closely with the initial cavern volume than according to the minimum P/D. The results shown in Figures 7 and 8 indicate that

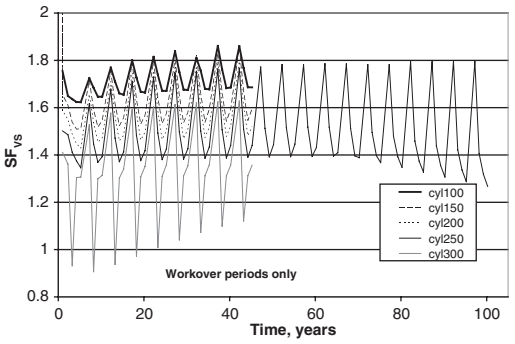

Figure 3. Minimum safety factor, cylindrical caverns (workovers only).

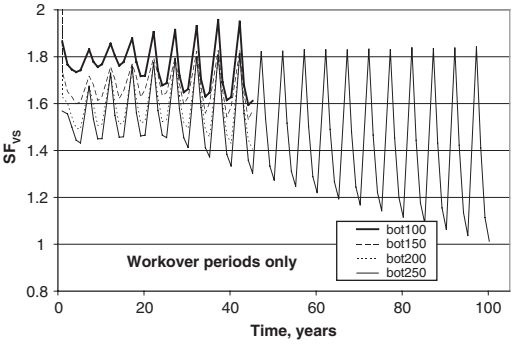

Figure 4. Minimum safety factor, enlarged-bottom caverns.

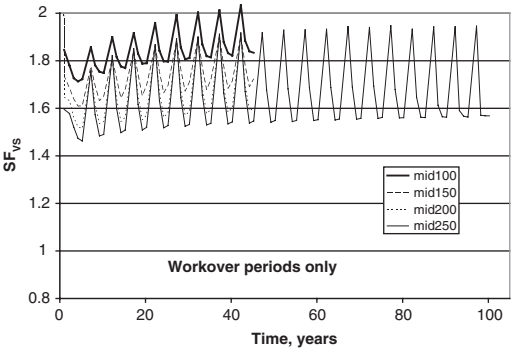

Figure 5. Minimum safety factor, enlarged-middle caverns.

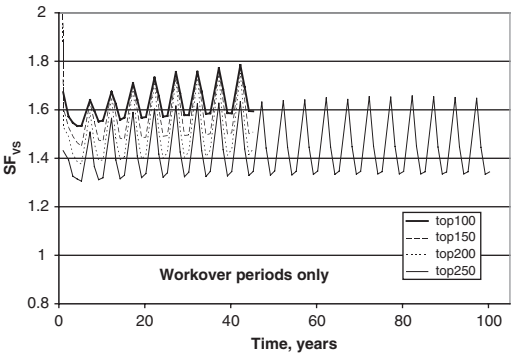

Figure 6. Minimum safety factor, enlarged-top caverns.

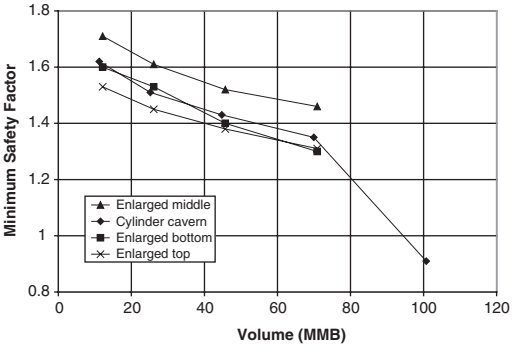

Figure 7. Minimum safety factor as a function of initial cavern volume.

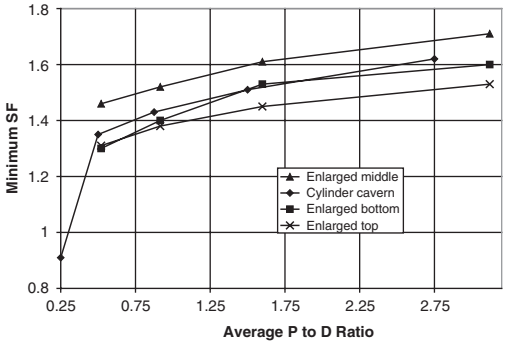

Figure 8. Minimum safety factor as a function of average P/D.

there may exist either a critical threshold value for either volume or average P/D for which the safety factor precipitously changes, and these thresholds may be related. The enlarged-top caverns tend to have the lowest safety factors of the four designs during the 45-year simulation period. Although the enlarged-bottom caverns appear to perform better than the cylindrical caverns during the 45-year simulations, the 100-year simulations indicate that the safety factors for the enlarged bottom caverns eventually become the lowest. From a design perspective, caverns with enlarged middles can have up to three times the volume as enlarged-top caverns, or twice that of cylindrical caverns, and still have equivalent minimum safety factors, while allowing for a smaller P/D ratio. A rank order,

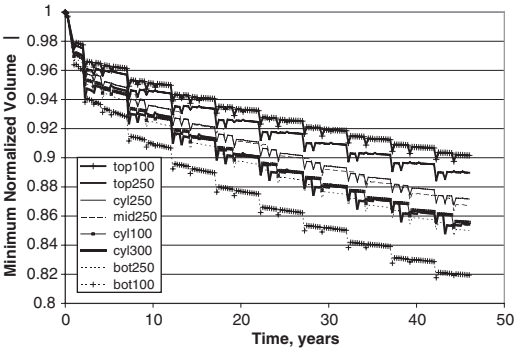

Figure 9. Minimum normalized volume history for selected cases.

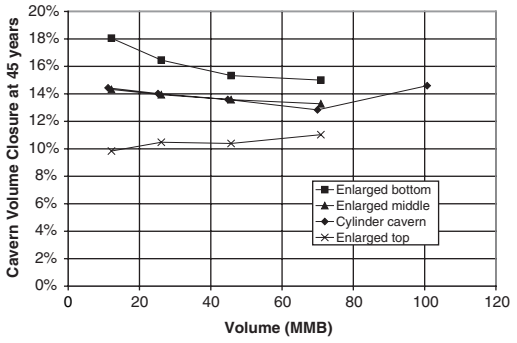

Figure 10. Cavern volume closure as a function of initial cavern volume.

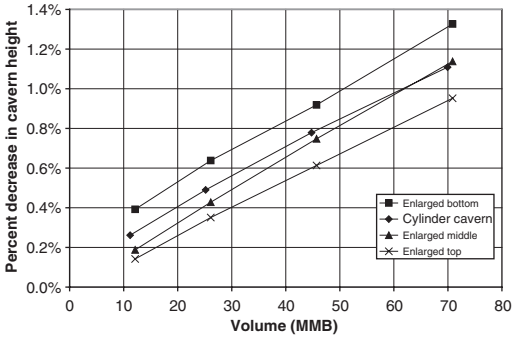

Figure 11. Decrease in cavern height as a function of initial cavern volume.

from best performance to worst, based on safety factors would be: 1) enlarged middle; 2) cylinder; 3) enlarged bottom; and 4) enlarged top.

3.2 *Cavern volume closure*

The volume of the caverns decreases (i.e., cavern closure increases) as the salt creeps. Figure 9 shows a history of the decrease in normalized volume for selected cases. The normalized volume is the volume at a given time divided by the initial volume of each case before standard operations. The enlarged-top caverns clearly exhibit the least cavern closure, and the enlarged-bottom caverns clearly exhibit the greatest closure. An interesting observation that can be made is that the normalized cavern closure increases for the enlarged top case as the radius increases, but decreases for the other cases with increasing radius, with the exception that the closure suddenly increases from the 76-m (250-ft) to the 91-m (300-ft) radius cylindrical caverns. This change for the cylindrical caverns at 91-m (300-ft) radius indicates that the stress field around a cavern is no longer effectively independent, but is interacting with the stress field of the adjacent cavern. Remember that most of the intercavern web is much thicker than implied by the P/D ratio. Additional calculations suggest the distance at which the cavern interaction causes accelerated closure. This effect of cavern shape and radius on closure is better illustrated in Figure 10, where the percent closure after 45 years of operation is plotted in terms of initial cavern volume. The enlarged top caverns have the least amount of cavern closure because both the downward displacement of the cavern ceiling and the upward displacement of the cavern floor are the least for the four design shapes. Similarly, the corresponding displacements for the enlarged bottom caverns are the greatest. The percent decrease in height for each cavern shape is shown in Figure 11. It seems counterintuitive that the enlarged top caverns would have the smallest downward ceiling displacement, as they have the largest area of oil pressure at the ceiling. However, the ΔP between oil pressure and in situ hydrostatic pressure at the top of the caverns is approximately 7.6 MPa (1100 psi), whereas the ΔP at the bottom of the caverns is about 20 MPa (2900 psi). Therefore, having the larger area at the bottom of the cavern allows the greater pressure difference there to dominate the overall redistribution of stress and deformation of the salt, thus producing in the cavern closure results shown here. A rank order, from best performance to worst, based on cavern volume closure would be: 1) enlarged-top; 2 & 3) enlarged-middle and cylinder; and 4) enlarged-bottom.

3.3 *Axial well strain in the caprock*

The physical presence of wells and surface structures are not included in the finite element model, but the potential for ground deformation to damage these structures can be conservatively estimated by assuming that they will deform according to the predicted ground strains. At well locations, subsidence will primarily induce elongation of the axis of the well. Under these conditions, the cemented annulus of the wells may crack forming a horizontal tensile fracture that may extend around the wellbore. This may not

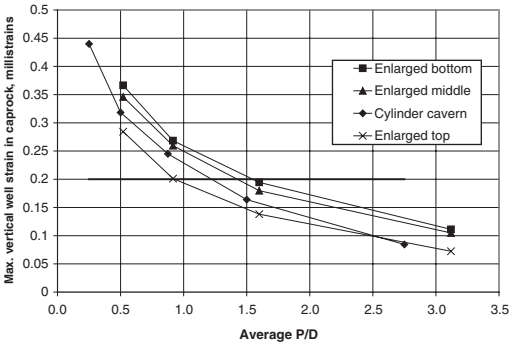

Figure 12. Maximum vertical well strain in caprock as a function of average P/D ratio.

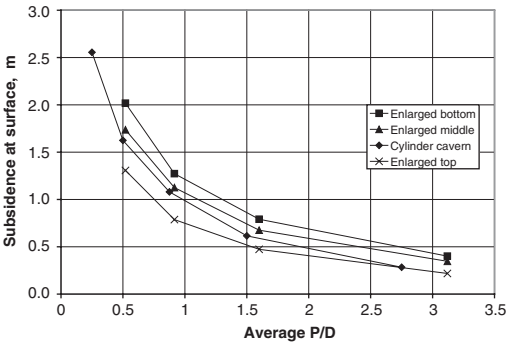

Figure 13. Maximum surface subsidence as a function of average P/D ratio.

result in vertical fluid migration along the casing, but could permit horizontal infiltration into ground waters. This may be a vulnerability, especially in the caprock, where acidic ground waters may gain access to the steel casing and corrode it. More extensive damage could heavily fracture the cement which could result in a loss of well integrity in that leakage could occur from the cavern along the outside of the casing. Such leakage could result in flow to the surrounding environment, resulting in loss of product. The allowable axial strain for purposes of this report is assumed to be 0.2 millistrains in tension. This would be typical of cement with a compressive strength in the range from 17 to 34 MPa (Thorton & Lew, 1983). It should also be noted that vertical well strain reduces the collapse resistance of the steel casings. For a typical SPR well located in the caprock, negligible casing collapse resistance is predicted at 1.6 millistrains.

A comparison of the predicted maximum axial strain of the well in the caprock after 45 years of operation for the 17 cases is shown in Figure 12. Note that the enlarged top caverns have the least axial well strain of the four shapes, due in large part to the lesser amount of downward displacement of the ceiling of the caverns discussed in the previous section. Similarly, the enlarged bottom caverns produce the greatest axial strains. A rank order, from best performance to worst, based on axial well strain in the caprock would be: 1) enlarged top; 2) cylinder; 3) enlarged middle; and 4) enlarged bottom.

Figure 12 indicates that all cavern shapes will eventually cause well strains over 0.2 millstrains as the initial cavern (cavern volume) radius increases. Note that factors other than cavern shape, including depth of wellbore, thickness of the various geological layers, and cohesion of the steel and cement to the surrounding sand, salt, and rocks, also influence the axial strain imparted to the well casings. Therefore, the plot in Figure 12 is meant as a comparison between cavern shapes.

3.4 *Surface subsidence*

The issue of surface subsidence is an important design and operations factor for surface facilities, especially for those located in flood prone areas, but subsidence also results in horizontal ground strains that can damage buildings, pipelines, and other infrastructure. Expected subsidence during the 100-year life of a facility on the order of up to three meters is not uncommon. Therefore, the performance of a cavern shape design can be defined by the expected subsidence. Figure 13 compares the predicted surface subsidence of the 17 cases as a function of average P/D ratio. Because of the lesser amount of cavern deformation predicted for the enlarged top design, the surface subsidence for that case is also predicted to be the least. The enlarged bottom caverns are predicted to produce 60–70% more surface subsidence than the enlarged top caverns. The enlarged middle and cylindrical designs produce similar results to each other. A rank order, from best performance to worst, based on surface subsidence would be: 1) enlarged top; 2) cylinder; 3) enlarged middle; and 4) enlarged bottom.

Structural damage on the surface is typically caused by large accumulated surface strains caused by surface subsidence. These strains can cause distortion, damage, and failure of buildings, pipelines, roads, bridges, and other infrastructure. Surface strains will accumulate in structures over time, which increases the possibility of damage in older facilities. Typically, subsidence strains tend to be compressive in the central portion of the subsided area and become tensile in nature for areas farther removed. Some guidance and solutions are available to evaluate the predicted surface strains. Some examples of allowable strains are presented by Peng (1985). For purposes of this paper, the allowable strain is taken to be 1 millistrain for both compression and tension. Criteria for shear strains have not been found, perhaps because they are less important. In practice, allowable strain limits for a

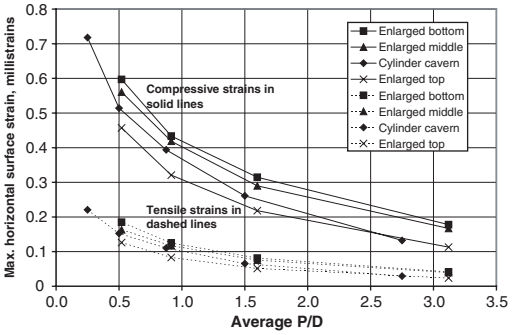

Figure 14. Predicted maximum compressive and tensile ground strains at surface.

structure are design specific and should be examined on a case-by-case basis.

The horizontal surface strains are related to the subsidence above the caverns. Typically, the region above the caverns undergo compressive horizontal stresses at the surface as the geologic units sag, but at some distance away from the cavern field the horizontal strains become tensile at the periphery of the subsidence trough or depression. Figure 14 shows the predicted maximum horizontal compressive and tensile ground strains for the 17 cases. Note the similarity of these curves to those for surface subsidence showing the enlarged bottom case as the worse condition. The maximum compressive strain occurs directly over the center cavern (Cavern 1), whereas the maximum tensile strain occurs at a radius ranging from 1450–2000 m from the center cavern, with this distance increasing as the cavern radii increase. In all cases, the predicted maximum strains are below the threshold 1 millistrain, but as discussed above the predicted ground strains will vary by site due to the geology and specifics of the cavern field.

3.5 *Summary of cavern shape rankings*

Table 4 provides a summary of the rankings of the performance of the four cavern shapes based on the four design factors. The enlarged top caverns appear to produce the least amount of geological deformation, as measured by cavern volume closure, axial well strain, and surface subsidence. This minimal amount of deformation is likely due to the fact that the enlarged top (and therefore, tapered bottom) has less cavern surface area in the region of highest pressure differential between oil pressure and in situ hydrostatic pressure, at the bottom of the caverns, decreasing upward vertical displacement of the floor. Also, the angle of the slope of the cavern walls allow for an effective uplift force, decreasing downward vertical displacement of the ceiling. However, this decrease in deformation comes at the price of higher deviatoric stresses, making the possibility of dilatant damage and fracturing greater in the roof than for the other cases. The enlarged bottom caverns appear to have the least overall desired features, and the enlarged middle caverns have some of the advantages of the enlarged top caverns with lesser deviatoric stresses.

Table 4. Summary of cavern shape rankings.

Design Factor	1st	2nd	3rd	4th
Safety factor in salt	enlarged middle	cylinder	enlarged bottom	enlarged top
Cavern volume closure	enlarged top	enlarged middle, cylinder		enlarged bottom
Axial well strain in caprock	enlarged top	cylinder	enlarged middle	enlarged bottom
Surface subsidence	enlarged top	cylinder	enlarged middle	enlarged bottom

4 CONCLUSIONS

These analyses evaluated the effect of cavern shape on the performance and stability of underground reservoirs in salt domes. Four cavern shapes – cylindrical, enlarged top, enlarged middle, and enlarged bottom – were evaluated against four design factors. These factors included the dilatant damage safety factor in salt, the cavern volume closure, axial well strain in the caprock, and surface subsidence. The following conclusions were obtained from the results of the analyses:

- The enlarged top caverns had the best performance when evaluated against the design factor of cavern volume closure, axial well strain in the caprock, and surface subsidence. This performance comes at the expense of the greater possibility for dilatant or shear damage, for which the enlarged top caverns performed the worst.
- The enlarged middle design has the highest safety factors of the four designs, and was in the middle of the group for the other three design factors.
- The enlarged bottom caverns had generally the worst performance of the four designs.
- The average P/D ratio provides a more robust comparison parameter for the different cavern shapes than the minimum P/D ratio.

The results of this study are applicable to existing cavern geometries and are also useful in evaluating behavior of future cavern shapes due to leaching associated with oil drawdowns and cavern shapes under consideration for expansion of the SPR. For example, the probability of dilatant damage to salt will increase with increasing cavern volumes by leaching. However, the results of this analysis suggest that a cylindrical cavern may be preferentially leached to a

cavern with an enlarged middle and maintain the safety factor of the original cavern. The results also show the sensitivity of important cavern performance measures as caverns deviate from the commonly simulated or assumed cylindrical cavern shape. The findings of this study are cast in terms of cavern volume for application in designing new cavern fields, and in terms of the pillar to diameter ratio which is commonly used to evaluate stability of existing caverns. Future analyses could examine the impact of the geology, particularly the caprock, on the performance metrics and consider even greater distortions in cavern shape, particularly with respect to the enlarged mid-section which was shown to provide a favorable cavern shape and the enlarged roof caverns. Further analyses of those cavern shapes could define optimal cavern shapes.

The results of these analyses may also be used for SPR cavern and site expansions. The Energy Policy Act of 2005 calls for expansion of the U.S. Strategic Petroleum Reserve from ~700 million to its full authorized storage capacity of one billion barrels. Expansion of existing caverns, additional construction of caverns at the current sites, and development of at least one new salt dome site will need to be performed. Additionally, the Department of Energy (DOE) has mandated that the P/D ratio of each cavern developed since 1983 at the Strategic Petroleum Reserve sites must be greater than 1.78 after five complete oil draw down cycles (DOE, 2001). Analyses such as this cavern shape integrity assessment can be used for the design of new or expanded caverns or sites, and also potentially for technical justification of the relaxation of the P/D criterion so existing caverns might be enlarged.

ACKNOWLEDGEMENT

Sandia is a multiprogram laboratory operated by Sandia Corporation, a Lockheed Martin Company, for the United States Department of Energy's National Nuclear Security Administration under Contract DE-AC04-94AL85000.

REFERENCES

Blanford, M.L., M.W. Heinstein, & S.W. Key, 2001. *JAS3D. A Multi-Strategy Iterative Code for Solid Mechanics Analysis.* ***User's Instructions,*** *Release 2.0*. SEACAS Library, JAS3D Manuals, Computational Solid Mechanics/Structural Dynamics, Sandia National Laboratories, Albuquerque, NM.

Butcher, B.M., 1997. *A Summary of the Sources of Input Parameter Values for the WIPP Final Porosity Surface Calculations*, SAND97-0796 Sandia National Laboratories, Albuquerque, NM.

DOE (Department of Energy), 2001. Design Criteria-Level III, *US Department of Energy, Strategic Petroleum Reserve*. New Orleans, LA, November, 2001.

Ehgartner, B.L. & S.R. Sobolik, 2002. *3-D Cavern Enlargement Analyses*, SAND2002-0526, Sandia National Laboratories, Albuquerque, NM.

Morgan, H.S. & R.D. Krieg, 1990. *Investigation of an Empirical Creep Law for Rock Salt that Uses Reduced Elastic Moduli*, SAND89-2322C, presented at the 31st U.S. Symposium on Rock Mechanics held in the CO School of Mines in June 18–20, 1990, Sandia National Laboratories, Albuquerque, NM.

Munson, D.E., 1998. *Analysis of Multistage and Other Creep Data for Domal Salts*, SAND98-2276, Sandia National Laboratories, Albuquerque, NM.

Park, B.Y., B.L. Ehgartner, M.Y. Lee, & S.R. Sobolik, 2005. *Three Dimensional Simulation for Big Hill Strategic Petroleum Reserve (SPR)*, SAND2005-3216, Sandia National Laboratories, Albuquerque, NM.

Peng, S.S., 1985. Coal Mine Ground Control. 2nd Ed., John Wiley and Sons, New York NY.

Sobolik, S.R. & B.L. Ehgartner, 2006. *Analysis of Cavern Shapes for the Strategic Petroleum Reserve*, SAND2006-3002, Sandia National Laboratories, Albuquerque, New Mexico.

Thorton, C.H & I.P. Lew, 1983. *Concrete and Design Construction. Standard Handbook for Civil Engineers*, Chapter 8, 3rd ed., F.S. Merritt, editor, McGraw-Hill, New York, NY.

Van Sambeek, L.L., J.L. Ratigan, & F.D. Hansen, 1993. *Dilatancy of Rock Salt in Laboratory Tests*, Int. J. Rock Mech. Min. Sci. & Geomech. Abstr. Vol. 30, No. 7, pp 735–738.

Wawersik, W.R. & D.H. Zeuch, 1984. *Creep and Creep Modeling of Three Domal Salts – A Comprehensive Update*, SAND84-0568, Sandia National Laboratories, Albuquerque, NM.

Taylor & Francis
Taylor & Francis Group
http://taylorandfrancis.com

The Mechanical Behavior of Salt – Understanding of THMC Processes in Salt –
Wallner, Lux, Minkley & Hardy, Jr. (eds)
© 2007 Taylor & Francis Group, London, ISBN 978-0-415-44398-2

Influence of effective stress on strain rate around the gas storing cavern

J. Ślizowski
Polish Academy of Sciences, Mineral and Energy Economy Research Institute, Cracow, Poland

K.M. Urbańczyk
Research and Development Centre for Mining of Raw Chemical Materials – Chemkop, Cracow, Poland

ABSTRACT: Mogilno salt dome has very complicated geological structure, thus natural gas storage caverns had to be placed at various depths, in rock salt of different strength and creep properties. Creeping law parameters given by laboratory testing of core samples can be inadequate. The paper presents selected results of the sensitivity study on influence of exponent in Norton law and boundary conditions on strain and stress state of rock formation around the storage cavern and its convergence. It was found that, in several cases, lower exponent and thus lower creeping rate leads to greater strains on the cavern wall and higher cavern convergence. This behavior can be caused by greater influence of effective stress reduction than that of strain rate resulting from the creeping law. It means that caverns in rock salt of smaller creeping rate reaction on effective stress change can be less stable than in case of greater creeping.

1 INTRODUCTION

The first Polish natural gas storage plant in salt caverns – KPMG Mogilno owned by Polish Oil and Gas Company PGNiG and operated by Investgas is located in Mogilno salt dome in central Poland and now 10 caverns are in operation.

Geological structure of Mogilno salt dome is not so favorable for the purpose as e.g. several salt domes in Germany. It is caused by great deep of primary Zechstein ledge (5–6 km b.g.l.) and its impurity by clay minerals. As a result, the salt layers have very steep inclination, even overhanging, large zone of pure and homogeneous salt are hardly met. K+Mg salts and salt-mudstone occur in the Mogilno dome as well. Because of that it was impossible to locate all caverns at similar depth and shapes of caverns in several cases differ from the designed (cf. Fig. 1). Even the kinds of rock salt, where the caverns are located differs each other in mechanical properties. Rock salt met in a cavern borehole can be not representative for cavern wall. Thus creeping law parameters given by laboratory testing of core samples can be inadequate for predicting the cavern behavior. For this reason, sensitivity study was made using Norton creeping law with different parameters to know how one may rely on cavern stability analysis using data from laboratory tests.

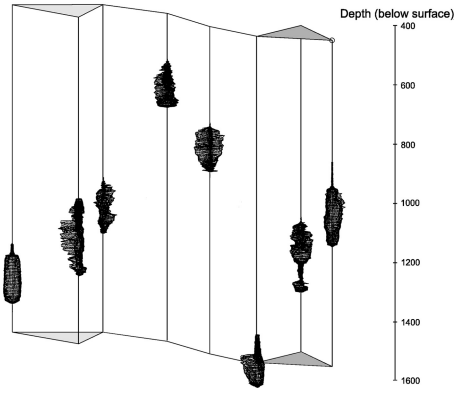

Figure 1. Location depth and shape of KPMG Mogilno caverns – situation at the end of the first project stage.

2 MODEL OF ROCK SALT BODY

Norton creep law, most commonly used, was applied in the analysis:

$$\varepsilon_{ef} = A\mathrm{e}^{-\frac{Q}{RT}}\sigma_{ef}^{n} \tag{1}$$

Table 1. Norton law coefficients used in the calculations.

Set	A [d^{-1}]	n	Q/R [°K]
1	1.9155	2.75	5750
2	0.10772	4.0	5750
3	$1.915 \cdot 10^{-2}$	4.75	5750
4	$3.41 \cdot 10^{-3}$	5.5	5750

$$d\varepsilon_{ij} = \tfrac{3}{2}\varepsilon_{ef}\frac{s_{ij}}{\sigma_{ef}}dt \tag{2}$$

$$\sigma_{ef} = \frac{1}{\sqrt{2}}\sqrt{(\sigma_1-\sigma_2)^2+(\sigma_2-\sigma_3)^2+(\sigma_3-\sigma_1)^2}$$

- effective stress,

$$\varepsilon_{ef} = \frac{\sqrt{2}}{3}\sqrt{(\varepsilon_1-\varepsilon_2)^2+(\varepsilon_2-\varepsilon_3)^2+(\varepsilon_3-\varepsilon_1)^2}$$

- effective strain,

s_{ij} - stress deviator components,

This law is sufficient for designing safe storage field. With different values of law parameters, various solutions can be obtained and the less safe possibilities analyzed. Simplicity of Norton law allows to make sensitivity analysis more easily, than in case of more complicated creeping law. One can observe effects which could be difficult to find and analyze in the case of more complex creeping law. E.g. reduction of extreme stresses and decrease of creep rate connected with it, will be more difficult to assess if one applies formula which includes primary creep.

In case of stress distribution analysis around the cavern placed at fixed definite, the most significant is influence of exponent n.

The aim of calculations presented here was mainly analysis, how value of this exponent influences stress and strain distribution and cavern convergence. Four values of n were used in the calculations.

The same value of 5750°K was taken for coefficient Q/R in all calculated variants. Parameter A was adopted in such a way, to obtain for every n the same creep rate – 0.02%/d at effective stress $\sigma_{ef} = 10$ MPa and temperature T = 50°C (323°K). It is relatively high rate, but a little bit smaller than given by BGRa law and much bigger than from BGRb law. Table 1. contains sets of all Norton law coefficients used in the calculations.

Strain rates corresponding to creep law variants used in the calculation are shown in Figure 2.

Values of exponent n adopted here cover the whole range of values determined after laboratory tests for rock salt specimens from Mogilno salt dome. (Ślizowski, Urbańczyk 2004). It agrees with range of n known from the literature (e.g. Hardy et al 1985) with

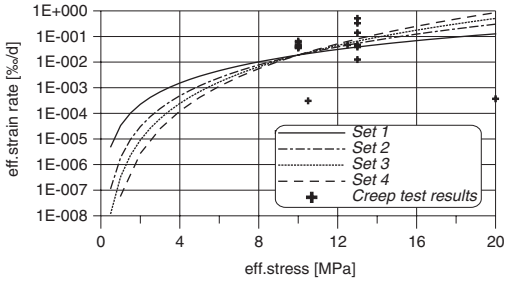

Figure 2. Rate of stationary creep at temperature of 50°C according to creep law variants used in the calculations.

one exception (Hunsche, Hampel 1999), where value of exponent n was assessed being equal to 7.0.

Shape of the cavern for which the calculations were done is presented on Figure 3. It is an idealized shape and being such it does not correspond precisely to anyone of KPMG Mogilno caverns, nevertheless it is close to the shape of biggest caverns in KPMG Mogilno.

The cavern is a cylinder with diameter of 70 m, ended by spherical dome at the roof and similar at the bottom. Cavern roof is located 1000 m deep, the bottom −1250 m.

Two variants of boundary condition were taken into calculations:

Variant A – corresponds to an isolated single cavern, i.e. with no interaction of other caverns. The boundary of the model is 150 m distant from the cavern wall (185 m from the cavern axis). Natural lithostatic pressures are assumed at the boundary.

Variant B – corresponds to a cavern influenced by six neighboring caverns placed in triangular net of module 250 m. The boundary of the model is 125 m distant of the cavern axis. No radial displacement is assumed at the boundary.

In case of KPMG Mogilno, influence of neighboring caverns is not so great as in variant B, because of differences in location depth.

Similarly to the different radial extent of the model, different extent in depth is taken in the variants, as it is shown in Figure 3.

Variant A was approximated using 1160 finite elements (1239 nodes), variant B using 928 elements (1003 nodes). Concentration of elements was similar in both cases.

Two kind of cavern loading scenario were simulated:

– scenario for theoretical purposes, aimed to determine internal cavern pressure influence on distribution of σ_{ef} and $\dot{\varepsilon}^{v}_{ef}$ around the cavern in stationary conditions,
– scenario similar to typical storage cavern operation, aimed to verify the results of previous calculations and assess the cavern convergence.

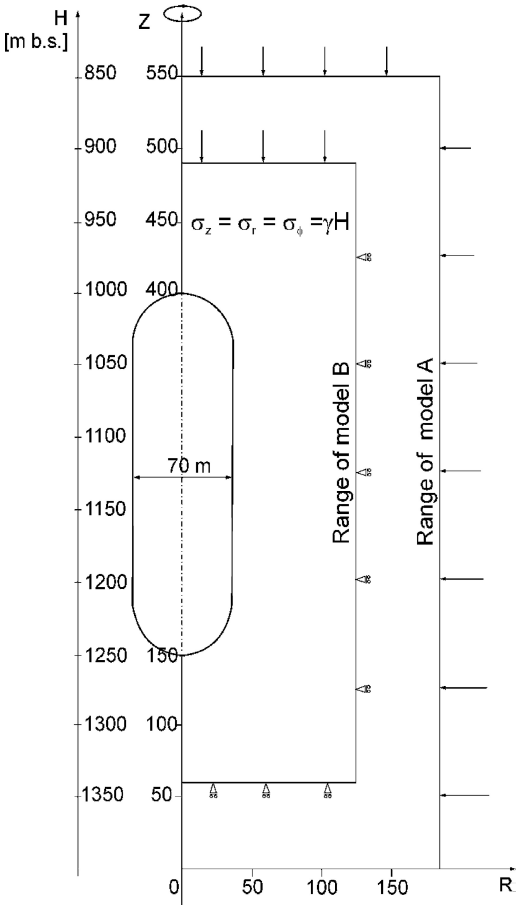

Figure 3. Cavern shape used in the calculations and variants of the model extent and boundary conditions.

The first scenario consisted of eleven 2-years-long stages of constant internal cavern pressure. Stress and strain state was determined first for the cavern filled with brine. Brine density and the cavern depth gave brine pressure of 11.8 MPa at the cavern roof and 14.7 MPa at the bottom. Then internal pressure was diminished in 4 stages (successively 7 MPa, 4 MPa, 2 MPa, 0 MPa). Then the pressure was increased in 6 stages (successively 2 MPa, 4 MPa, 7 MPa, 10 MPa, 14 MPa, 18 MPa) to the maximum allowable cavern pressure obtained using gradient of 18,44 kPa/m, as it was applied for the most of KMPG Mogilno caverns.

The second scenario divided yearly cycle of the cavern operation into 4 stages (cf. Ślizowski, Urbańczyk 2003)

– 30 days of gas withdrawal,
– 150 days of idle with minimum operational pressure,
– 30 days of gas injection,
– 200 days of idle with maximum operational pressure.

5-yearly cycles of cavern operation were proceeded by 4-years long period of cavern filled with brine.

Finally, the range of the calculations consisted of 12 models referenced below by the symbol:

Model Xm.n

where:

X – number of model extent and boundary conditions (A or B),
m – number of creeping low parameters set (1–4 cf. Table 1),
n – number of scenario (1 or 2).

Actually, for scenario 1, calculations for border values of exponent *n* were performed providing 4 models referenced as A1.1, A4.1, B1.1 and B4.1.

For scenario 2, calculations for all possible variants combinations were performed providing 8 models referenced as A1.2, A2.2, A3.2, A4.2, and B1.2, B2.2, B3.2, B4.2.

Finite element method and GEOSOLK specialized software package was used for the calculations (Ślizowski, Urbańczyk 2003).

3 EFFECTIVE STRESS AND EFFECTIVE STRAIN RATE

Values of effective stress and effective strain rate at the cavern wall obtained in simulation of scenario 1, are presented in Figures 4. and 5.

Stages for which internal cavern pressure was the same (2, 4, 7 MPa) are drawn together, to easily compare them.

Qualitatively all distributions at the cavern bottom and cavern wall are similar. Stages, where internal cavern pressure was decreased, both effective stresses and effective strain rates decrease in time and effect diminish with pressure. Opposite effect is observed in the case of increased internal pressure. Both analyzed quantities increase with time, and stress increase each stage is bigger.

Next important feature of obtained distributions is the fact, that for given internal cavern pressure, analyzed quantities stabilize at the same values independently whether pressure was increased or decreased. E.g. for 4 MPa, asymptotic value of effective stress is 14.8 MPa for model A1.1 in both cases.

From quantitative point of view, the situation is more complicated and depends which quantity is taken into account.

In case of effective stress, one can observe, that stresses at the cavern wall have smaller value for set 4 of creep parameters (the highest *n*). It concerns both

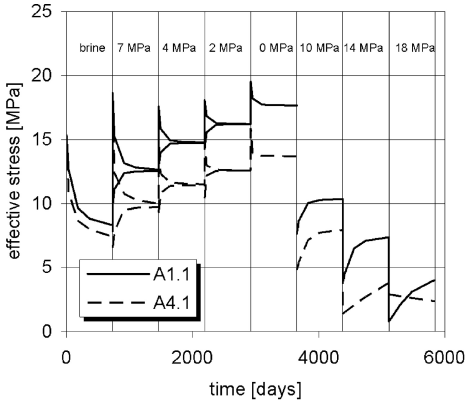

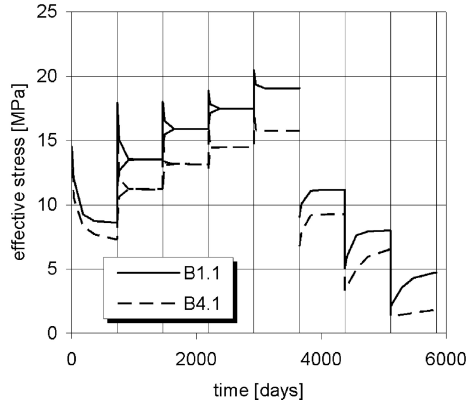

Figure 4. Effective stress at the cavern wall, scenario 1.

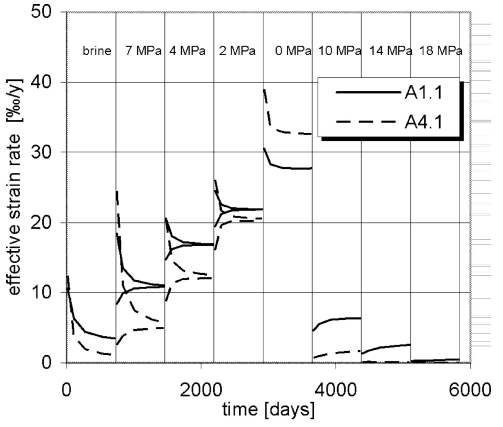

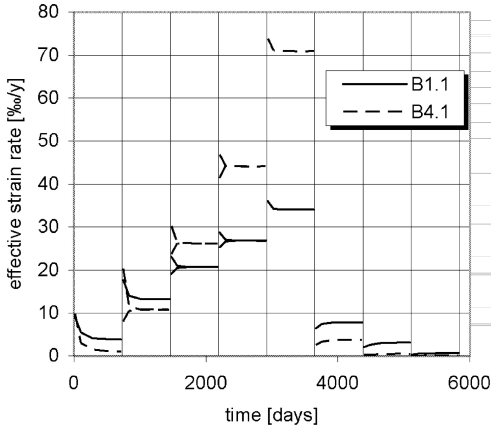

Figure 5. Effective strain rate at the cavern wall, scenario 1.

model A and B. Such effect can be expected, the higher value of *n*, the better ability to reduce the extreme stresses. Interesting is the fact, that the above relation is observed even for high values of internal cavern pressure, when effective stresses are below 10 MPa and creep rate for set 4 of creep parameters is smaller than for set 1.

In the case of strains, one could expect opposite effect, i.e. that strain rate is higher for parameters set giving higher value of creep rate. It is not generally valid in every case. E.g. for internal pressure of 7 MPa, higher value of strain rate is obtained in case of set 1. It means, that sometimes effect of stress reduction is stronger than differences between creep rates of analyzed creep laws.

For scenario 2, in case of idle periods under the minimum internal pressure, effective stress values at the cavern wall are lower for higher values of exponent *n*, similarly as for scenario 1 (Fig. 6). But in case of idle periods under the maximum internal pressure, the relation is opposite, i.e. the higher value of *n*, the higher values of effective stresses.

Values of effective strains at the cavern wall during the whole modeled period are presented in the Figure 7.

Values of effective strain rate at the cavern wall during the last year of modeled cavern operation (5th year) are presented in Figure 8.

In case of models A, effective strain rate values decrease when value of exponent *n* is increased, but in case of model B – increase. This leads to change in relations between total effective strains. One can see in Figure 6. that strains in model B3.2 after some time became equal to total strains in model B4.2.

4 CAVERN CONVERGENCE

Values of effective strain rate influence the convergence behavior of the cavern.

Values of relative convergence obtained from simulation of scenario 2. are presented in the Figure 9. Yearly convergence per mille for successive operation years are presented in the Table 2.

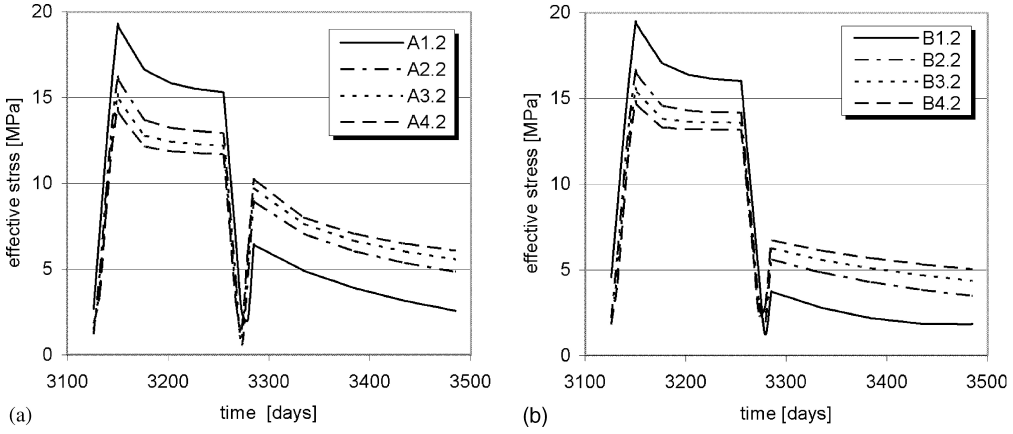

Figure 6. Effective stress at the cavern wall, scenario 2 during 5th year of operation.

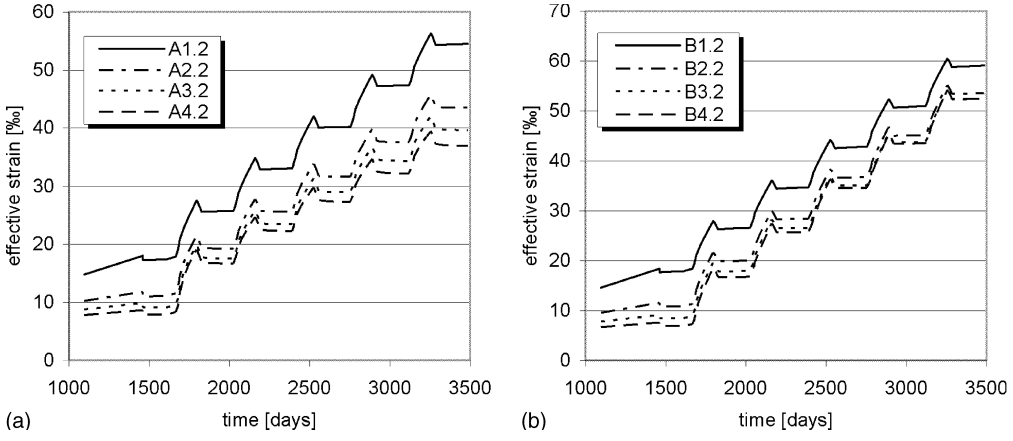

Figure 7. Effective strains at the cavern wall, scenario 2.

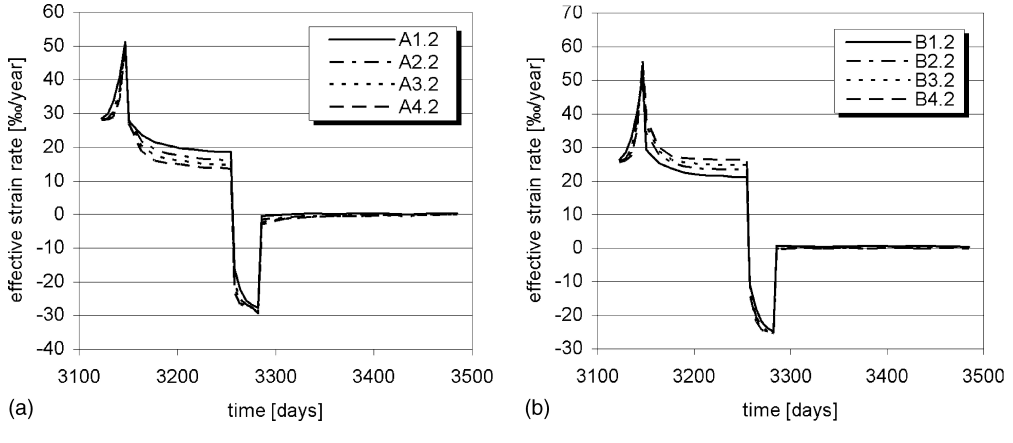

Figure 8. Effective strain rate at the cavern wall, scenario 2, during 5th year of operation.

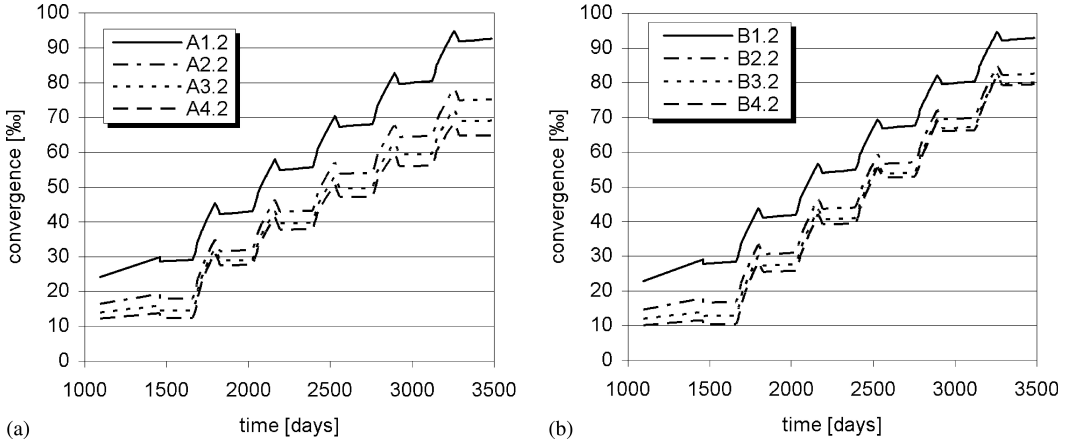

Figure 9. Cavern convergence, scenario 2.

As in case of effective stress, a relationship occurs between cavern convergence and creep law. As one can see in Figure 9., the higher value of exponent *n*, the lower value of convergence. This is valid for models of kind A.

For models of kind B, where higher values of convergence are obtained, the situation is opposite.

The effect must be connected with the fact, that convergence is the sum of strains from the whole rock mass if in the model extent, both from zone of effective stress lower than 10 MPa and from zone of values higher (for 10 MPa creep rate is the same for all parameters set taken into account).

Table 2. Yearly cavern convergences for scenario 2 of the cavern operation.

	Relative convergence yearly [‰]				
Years	1	2	3	4	5
Model A1.2	13,8	12,7	12,4	12,3	12,2
Model A2.2	13,9	11,3	10,8	10,6	10,5
Model A3.2	14,4	10,7	10	9,7	9,6
Model A4.2	15,2	10,2	9,3	8,9	8,7
Model B1.2	13,5	12,9	12,8	12,7	12,6
Model B2.2	14,2	13,1	12,9	12,8	12,7
Model B3.2	14,7	13,3	13,1	13	12,9
Model B4.2	15,4	13,6	13,5	13,3	13,2

5 CONCLUSIONS

Designing and assessing the long-term cavern stability, one should take into account the possible most adverse values of parameters in the constitutive equation of rock salt.

In case of Norton law, for the cavern located at definite depth, the exponent *n* have the most significant influence on the stress and strain state around the cavern.

It is known effect that for higher values of *n*, the values of effective stress at the cavern wall diminish, but similar effect can be observed for effective strain rates and for the cavern convergence.

In literature one can observe a tendency to use high values of exponent *n* (ca 5). Our calculations show, that such choice cannot be treated as the most safe. Often smaller value of the exponent can provide more conservative assessment of long term cavern stability.

REFERENCES

Hardy Jr., H. R., Chabannes C. R., Mrugala M., 1985: Laboratory and Theoretical Studies Relative to the Design of Salt Caverns for the Storage of Natural Gas. *Sixth International Symposium on Salt,* Toronto: Salt Institute Inc., Alexandria, Virginia. vol. 1. 385–415.

Hunshe U., Hampel A., 1999: Rock-salt – the mechanical properties of the host rock material for a radioactive waste repository. *Engineering Geology* 52, 271–291.

Ślizowski J., Urbańczyk K. 2003: Prognozowanie konwergencji względnej komory magazynowej gazu ziemnego przy zastosowaniu zaktualizowanego modelu górotworu solnego. *Gospodarka Surowcami Mineralnymi*. 19, z.2. 43–56.

Ślizowski J., Urbańczyk K., 2004: *Influence of depth on rock salt around the single chambe*r. Cracow: IGSMiE,.

The Mechanical Behavior of Salt – Understanding of THMC Processes in Salt –
Wallner, Lux, Minkley & Hardy, Jr. (eds)
© 2007 Taylor & Francis Group, London, ISBN 978-0-415-44398-2

Pillar deformation-induced surface subsidence in the Hengelo brine field, the Netherlands

R.F. Bekendam
GeoControl, Maastricht, The Netherlands

J.L. Urai
GeoStructures, Maastricht, The Netherlands

ABSTRACT: In the Hengelo area, East Netherlands, solution mining of rock salt is carried out by Akzo-Nobel from a 50 m thick salt deposit of Triassic age, located at about 350 m depth. Until recently surface subsidence was mainly ascribed to upward migration (stoping) above overmined caverns. However, in the oldest part of the brine field the extraction ratio is so high, that also deformation of the remaining salt pillars has to be taken into account. The effect of pillar creep on surface subsidence was investigated by the construction of a series of subsidence rate maps, per year from 1947 to 2003, and the analysis of the relationship of the pattern of these subsidence rates and the most likely cavern and pillar outlines.

This study not only confirmed the existence of several subsidence areas as a result of stoping, but also revealed evidence of a pillar deformation-induced subsidence area. The stress state in this pillar proved to be such that significant dilatancy must be considered. It was concluded that in the dilatant pillar solution-precipitation creep can contribute to the total deformation at the same amount as dislocation processes. It is recommended to incorporate solution-precipitation processes in future geomechanical models of pillar creep, even under non-dilatant conditions.

1 INTRODUCTION

Akzo-Nobel has mined salt since 1933 near the cities of Hengelo and Enschede. Until now about 300 mainly multiple-well caverns were created using more than 500 wells. Cavern diameters generally range from 50 to 150 m. The salt is produced from a 50 m thick, near-horizontal bedded salt-deposit of Upper Triassic age, situated at about 300 to 500 m depth. The salt layer is directly overlain by a relatively tough anhydritic layer of 20 m thickness, and then by 200 to 400 m of mainly friable claystones. In the south-western part of the brine field the upper part of the claystones contain limestone and dolomite layers. The Mesozoic rock formations do not continue up to the surface but are covered by about 70 to 140 m of clayey Tertiary and Quaternary soil units.

Due to inadequate mining methods in the past a number of areas have subsided and will continue to subside for several decades. More areas of surface subsidence may evolve in the future. At present six subsidence areas of significant trough subsidence have formed as a result of stoping, which is upward cavern migration due to subsequent failure and collapse of roof layers (Fig. 1). The troughs measure 150 to 300 m diameter and presently 1 to 3.5 m depth. In two cases the trough subsidence was preceded by sinkhole formation. The largest sinkhole measured 35 m diameter and 3.5 m depth. Additionally, in the oldest part of the brine field, where the above mentioned troughs and sinkholes also developed, deformation of the salt pillars in between the caverns could play a role as well. In the research project (Bekendam & Urai 2006, Urai & Bekendam 2006), described in this paper, it was investigated if creep deformation of pillars contributes to surface subsidence and, if so, which microphysical processes apply.

First the various types of ground movements in the subsurface and their expression of surface subsidence are outlined below.

2 TYPES OF SUBSIDENCE IN THE BRINE FIELD

2.1 *Phase I subsidence*

Phase I subsidence occurs as a result of convergence of the salt towards the intact cavern, situated completely within the salt formation (Fig. 1a). Surface subsidence is hardly detectable in this case (0.5 mm/year at most).

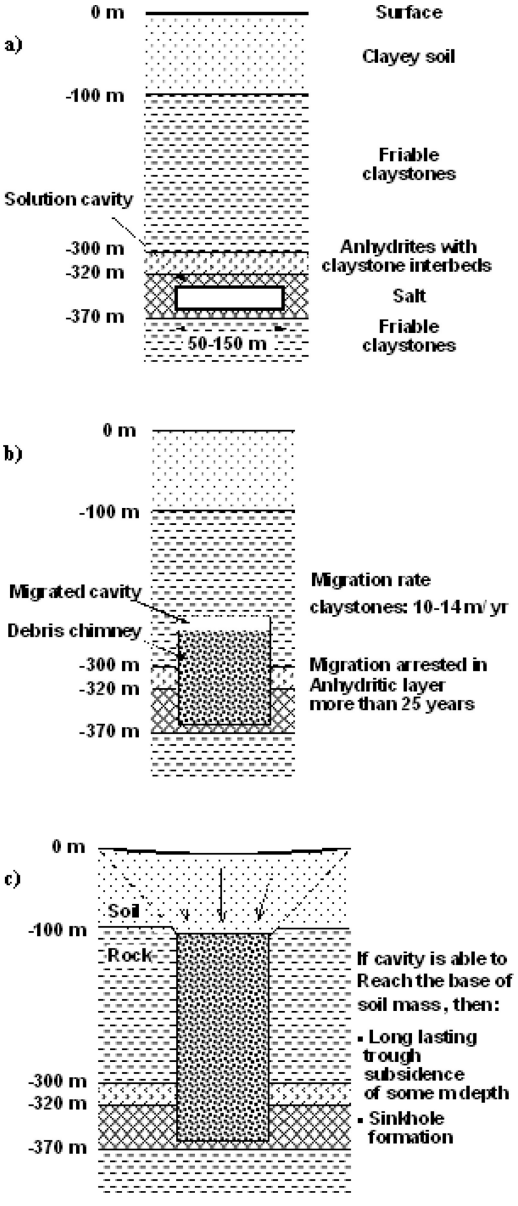

Figure 1. Three phases of stoping-induced subsidence: Phase I (a), Phase II (b), and Phase III (c).

2.2 *Phase II subsidence*

This subsidence mechanism can only develop when the uppermost salt layers have collapsed or were dissolved due to overmining. Additionally, the cavern must be able to break through the anhydritic layer. At several caverns the roof migrated inside the anhydritic layer tens of years ago, but has remained there at the same level until now. Whether these caverns will migrate further, and if so when, is difficult to predict.

If the cavern breaks through the anhydritic layer, upward migration through the overlying claystones occurs at a more or less constant rate of 10–14 m/year (Bekendam 1997). During the process the roof debris is deposited at the bottom of the cavern, and a debris-filled chimney is formed, which steadily increases in height (Fig. 1b). This process is denoted as Phase II subsidence. Due to the bulking effect (broken rock occupies a greater volume than intact rock) the height of the cavern continuously decreases. Thus, caverns of relatively small initial height cannot reach the base of the Tertiary soils because they become completely filled with debris at a lower elevation. Analysis of a limited number of field cases revealed a bulking factor of 1.11 for the overburden rocks of the Hengelo brine field (Bekendam 2005).

On account of numerical experiments an increasing subsidence at the surface is to be expected during cavern migration due to the increasing deflection of the rock mass over the cavern roof and the increasing convergence of the walls of the debris chimney. However, Phase II surface subsidence is difficult to detect because its rates are small and often dominated or obscured by the much higher rates of nearby Phase III subsidence areas.

2.3 *Phase III subsidence*

If a cavity is capable of migrating up to near the base of the Tertiary, significant subsidence starts (Phase III), which exceeds Phase I and Phase II surface subsidence by far. Phase IIIA concerns the movements of the soil layer into the migrated opening (Fig. 1c) and is characterised by a sudden acceleration of surface subsidence (Fig. 2). Phase IIIB applies to long-lasting compaction of the debris chimney by the weight of the soil mass, accompanied by a continuous deceleration of surface subsidence (Bekendam 2000, 2005). In four of the six cases mentioned above the ductile soil mass of a relatively low stiffness gradually subsided over the migrated opening during Phase IIIA and a subsidence bowl developed at an angle of draw of about 45° from the rock-soil interface. In the other two cases a sinkhole developed during Phase IIIA, probably due to the relatively large height of the migrated cavern. For the largest sinkhole some influence of a nearby tectonic fault possibly existed. Phase IIIB always develops as trough subsidence, causing either a further deepening of the Phase IIIA trough or the formation of a new trough centered at the sinkhole. Phase IIIB subsidence proceeds for a long time, at least for several decades, because compaction of a generally more than 200 m high chimney of roof debris is involved.

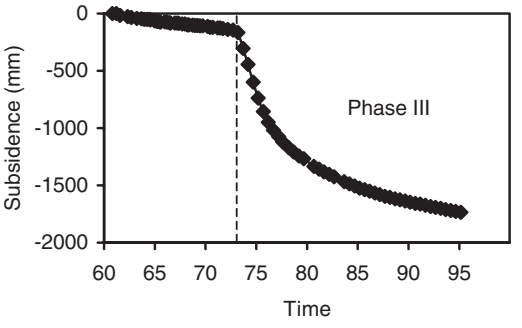

Figure 2a. A typical Phase III stoping-induced subsidence vs. time curve at point H near the centre of the subsidence area over well 4.

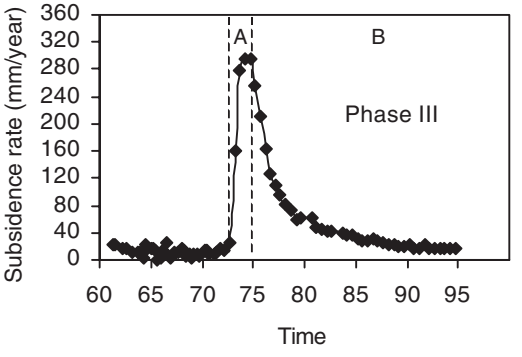

Figure 2b. The corresponding Phase III subsidence rate vs. time curve at point H.

2.4 *Pillar deformation-induced subsidence*

At some locations the horizontal extent of caverns and the distance between them is such that a relatively small pillar-like area of undissolved salt remains. The stability was analysed for elongated pillars, in between rows of caverns, by means of numerical models (e.g. Eickemeier & Heusermann 2004), and for pillars between three or more caverns, arranged in a cluster, using a modified tributary area method (Van Sambeek 1996, 2004). On the basis of these analyses mining was stopped in a number of caverns. Surface subsidence due to pillar deformation could not be detected at the locations investigated, because levelling points were not installed in between wells and the subsidence is probably too small to be measured at the levelling points near the wells.

However, the area of the oldest caverns (approximately wells 1–50) was not included in these studies. Generally, with the exception of the well 15, no sonar measurements exist of these caverns, and their boundaries can only be roughly estimated on the basis of production figures. Even such estimation is difficult because most caverns are interconnected and it is not known how much salt has been dissolved at each particular well. However, the cavern interconnections are known and the centres of the caverns are probably indicated correctly as well.

Until recently all surface subsidence was considered to be the result of stoping above overmined caverns. However, deformation of the salt pillars in between the caverns should be taken into account as well, especially in the oldest part of the brine field with the highest extraction ratio. The possible effect of pillar creep on surface subsidence was investigated by the construction of a series of subsidence rate maps and the analysis of the relationship of the pattern of these subsidence rates and the cavern and pillar outlines. Additionally, subsidence and subsidence rate vs. time graphs were analysed for much more levelling points than had been done previously. Contrary to the more modern part of the brine field, a much more dense net of levelling points exists here fortunately, partly because of the vicinity of the salt production plant and other buildings.

3 APPROACH TO THE STUDY

It is not possible to derive subsidence maps directly from the levelling data, because different levelling points were measured at different time intervals. To circumvent this problem subsidence rates were mapped instead of subsidence. The levelling data were processed to create XYZ- data files for each year, where X and Y represent the coordinates and Z the subsidence rate in mm/year, as a basis for contour maps. Observations of uplift of 10 mm/year or more and extra levelling points with the same coordinates were eliminated. After the creation of contour maps for each year, inconsistent subsidence rates were removed from the data files, followed by the production of upgraded contour maps:

a) inconsistency in space: e.g. a rate of hundreds of mm/year amidst a further consistent and gradual pattern of rates of a few tens of mm/year at most.
b) inconsistency in time: e.g. a sudden rate of several tens or even hundreds of mm/year in a given year, where the rate is one order of magnitude less in the preceding and following years.
c) subsidence rates due to a waste dump near wells 60–62 and 86–89.

Then a statistical analysis of the residuals was performed. A residual is a quantitative measure of the degree of fit and equals the difference per data point between the actual subsidence rate in the XYZ-data files and the interpolated subsidence rate on the contour surface for a given year (Figs 3, 4). On the basis of this analysis only contour values of less

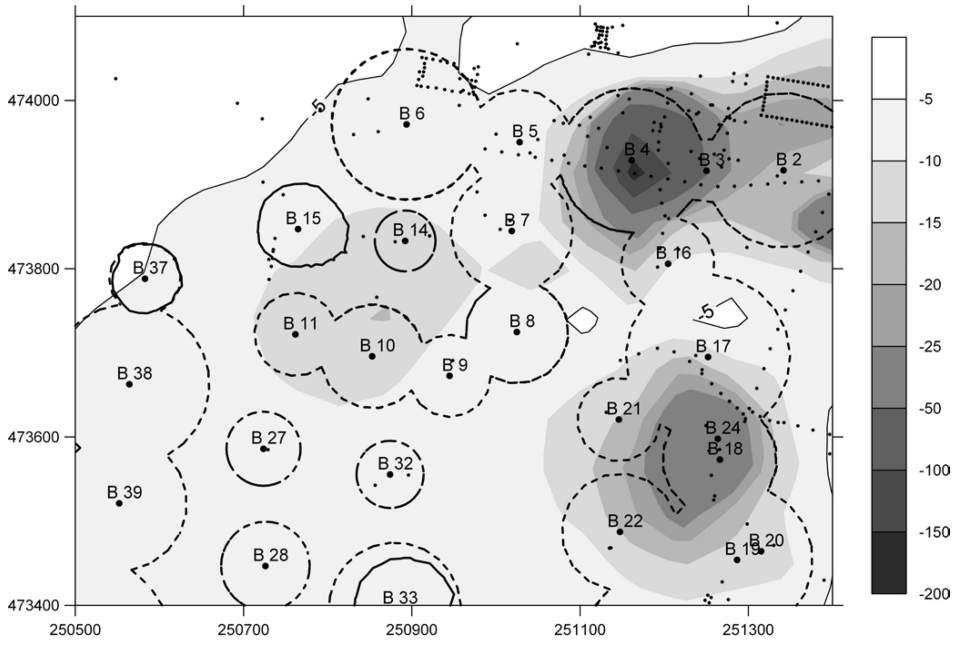

Figure 3. Contour map of the subsidence rate in October 1976 for an old part of the Hengelo brine field, with well numbers and levelling points (small dots). Cavern outlines, measured by sonar, are indicated by continuous lines. Dashed lines mark approximate boundaries of caverns, not determined by sonar.

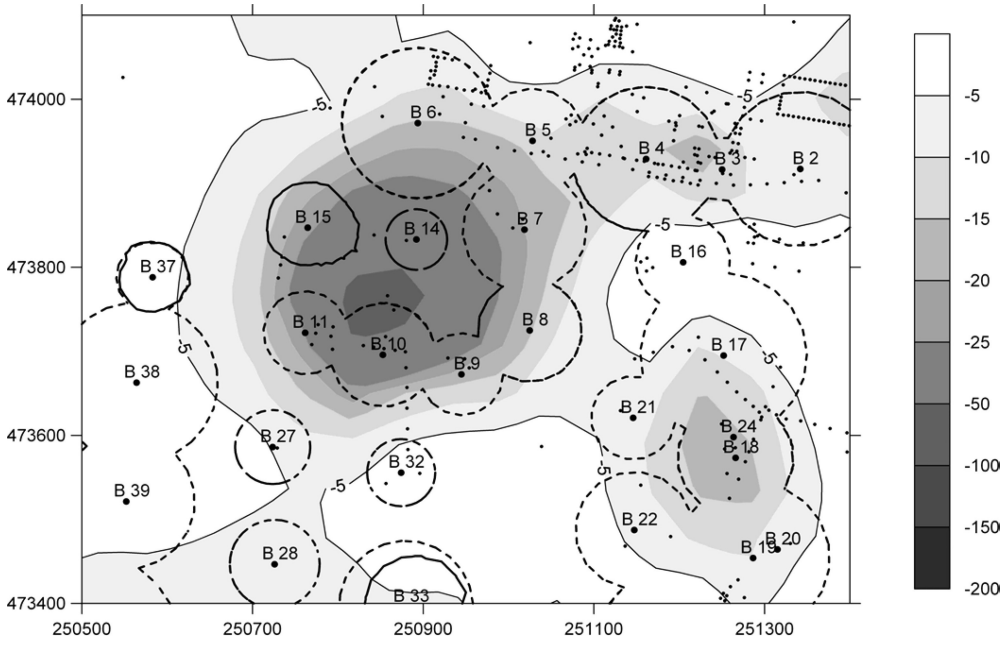

Figure 4. Contour map of the subsidence rate in October 1995 for an old part of the Hengelo brine field, with well numbers and levelling points (small dots). Cavern outlines, measured by sonar, are indicated by continuous lines. Dashed lines mark approximate boundaries of caverns, not determined by sonar.

than −5 mm/year and more than + 5 mm/year can be considered relevant.

For each year the relationship between the pattern of subsidence rate contours and the cavern and pillar outlines were analysed, in order to identify a component of surface subsidence due to pillar creep deformation. Special attention was paid to:

a) areas which are not located on a salt pillar and where stoping occurs.
b) areas which are located on a salt pillar, outside the influence of stoping induced subsidence.
c) areas which are located on a salt pillar, where stoping induced subsidence has either not evolved yet or has decreased to a relatively low rate.

4 RESULTS OF THE ANALYSIS

4.1 *Evidence of Phase III stoping-induced subsidence*

As expected, the areas of Phase III subsidence could be well distinguished in the contour maps. For example in Fig. 3, which shows subsidence rates in October 1976, two stoping-induced subsidence areas, at wells 4 and wells 18–24, are prominent. Subsidence at well 4 had just started in 1972, attaining a maximum rate of about 300 mm/year in the centre of the trough in 1974 (Fig. 2). In October 1976 this rate had diminished to 200 mm/year. In 1995 (Fig. 4) the rate was less than 10 mm/year and the subsidence area can hardly be recognised on the contour map.

The Phase III subsidence area, centred at wells 18–24, had already developed in 1963, with an initial maximum rate of 1500 mm/year. This is the first and also deepest subsidence trough of the brine field. Subsidence had decelerated to 45 mm/year in 1976, and then to 15–20 mm/year in 1995. The present rate is just 10–15 mm/year.

Throughout the years, both subsidence troughs are characterised by a consistent pattern of rates, which gradually increase towards its centre. For all levelling points within these areas the subsidence- and subsidence rate vs. time curves show the shape, which is typical for Phase III stoping-induced subsidence: a rapid acceleration in the first 1–2 years, followed by a gradual long-lasting deceleration (Fig. 2). This consistency also applies to the later Phase III subsidence areas near wells 30–31, 33–36 and 70, which started to develop in 1977, 1983 and 1989 respectively.

4.2 *Evidence of pillar deformation-induced subsidence*

The subsidence area at well 10, formerly considered as Phase III, proved to be based only on one levelling point, mounted at the well 10 itself. A rapid acceleration in 1975 seemed to occur only at this

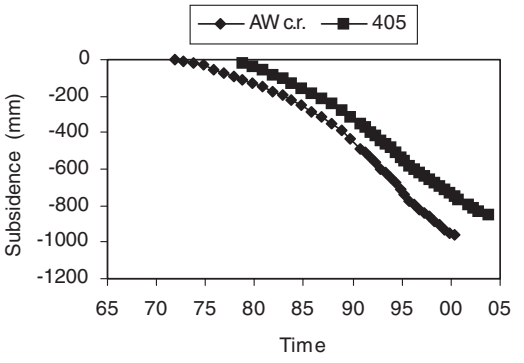

Figure 5a. Subsidence vs time at points AW c.r. and 405, near the centre of the pillar deformation/induced subsidence bowl.

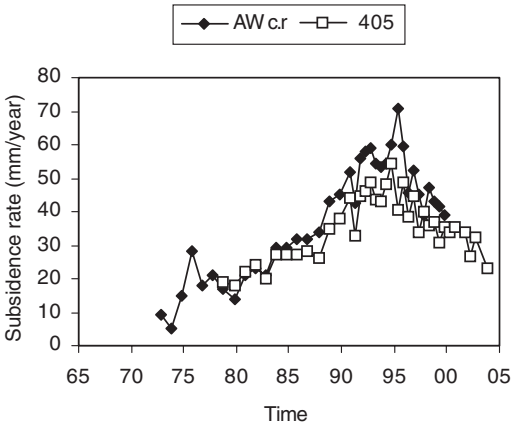

Figure 5b. Subsidence rate vs time at points AW c.r. and 405, near the centre of the pillar deformation/induced subsidence bowl. Note the gradual acceleration till 1995, followed by a gradual deceleration.

location, and did not develop at any of the other levelling points in its direct vicinity. Instead, all other levelling points in the area showed a subsidence development which completely differs from that of Phase III subsidence (Fig. 5). Subsidence did not accelerate within 1–2 years, but its rate gradually increased during a much longer period, from the early sixties to 1995. At that time a maximum rate of about 70 mm/year was attained in the centre of the trough. Then the rate decreased until today. Additionally, the centre of the area where levelling points show this development of ground movements is located over a pillar. Therefore this subsidence area cannot be ascribed to Phase III. The observed ground movements can neither be considered to be completely due to Phase II phenomena, because rates of up to 70 mm/year are beyond the range of possible rates for

this type of subsidence.The only possible explanation is deformation of the narrow, undissolved ring-shaped "pillar" salt, which surrounds well 14 (Figs. 3, 4). As explained in Section 2.4, the cavern outlines are approximate, but there is no doubt that the most intensive salt extraction occurred in this part of the brine field. Therefore, it is to be expected that the maximum pillar creep rates result at this location.

By means of the analytical calculation methods by Van Sambeek (1996, 2004) pillar shortening rates of the order of 50 mm/year were estimated for just a small part of the pillar-area, the circular area enclosed by caverns 10,11,14 and 15. This corresponds to a vertical strain rate of 10^{-10} to 10^{-11} s^{-1} and a subsidence rate of about 15 mm/year, using a Litwiniszyn influence function with $n = 4$ (Bekendam et al, 2000). Subsidence rates due to creep of the complete pillar area can attain the observed 50–70 mm/year.

5 DEFORMATION MECHANISMS IN THE SALT PILLARS

According to the criteria for long-term stability (Hunsche et al. 2004), the pillar proved to be unstable, i.e. it could have entered a stress state under which plastic deformation was accompanied by significant dilatancy. However, it is important to consider that the stresses even in the dilatant pillar are far from the dry failure envelopes for the Hengelo salt, presented by Langer (1984). Dilatancy means that the porosity created in the pillar is filled by saturated brine.

In dilatant pillars the grainsize of halite can be modified in comparison with the conditions before mining by two processes, dynamic recrystallization and intragranular microcracking. A decrease in the initial grainsize of 5 to 25 mm means an increased component of solution-precipitation creep. Therefore the actual creep- and subsidence rates may exceed the values estimated above, which are based on dislocation creep as the only microphysical process.

To estimate the importance of different deformation mechanisms under these conditions, a diagram is presented extrapolating the two deformation mechanisms to low strain rates, for different values of the grain size (Fig. 6). For the dislocation creep law commonly used parameters are taken, based on the creep parameters for the Hengelo halite reported by Hunsche et al. (2004), but noting that in these experiments a direct measurement of the stress exponent n has not been done, and therefore extrapolation to lower strain rates is somewhat uncertain.

Under the stress conditions in the pillar, the dynamically recrystallized grainsize is between 3 and 10 mm (Ter Heege et al. 2005). Therefore this process does not lead to significant grainsize reduction, except perhaps in the most coarse-grained layers.

Microcracking can occur along grain boundaries (intergranular) with no decrease in grain size, and in the grains (intragranular) which causes a significant decrease in grainsize. Unfortunately, there are no published data on the microstructure of halite deformed under dilatant conditions in the presence of brine. Therefore it is not possible to estimate the effective grainsize in dilated pillars. However, it seems reasonable that at the relatively low total strains in this pillar, the effective grainsize will not be reduced by more than a factor of two (each grain broken in half).

On the basis of Fig. 6 we can now estimate the contribution of solution-precipitation creep to the total strain rate of dilatant pillars. Accurate calculations are difficult because dry dilatant halite tends to creep faster than non-dilatant halite under otherwise the same conditions, the different halite layers have slightly different dislocation creep properties, clay may be present at grain boundaries in parts of the section, the effects of pore pressure in the dilated pillars are difficult to take into account accurately, and the possibility that part of the pillar was(is) in contact with a not 100% saturated solution. Keeping in mind these uncertainties, from Fig. 6 it can be seen that solution-precipitation creep in the dilatant pillar is a significant process. Its contribution to the total deformation can be of the same order as dislocation processes, although details of the process are difficult to quantify due to the lack of relevant data.

Creep rates in pillars which are considered stable (non-dilatant) and are loaded at deviatoric stresses lower than those in the dilatant pillars, are much lower (Fig. 6). Although no measurements are available for very slow pillar deformation in areas with stable pillars, we can predict that (even without grainsize reduction) at this lower strain rate solution-precipitation creep may be dominant in the fine grained sections, and less important in the very coarse grained sections, activated by the small amount of brine present in grain boundaries of the Hengelo halite (Hunsche et al. 2004).

6 ANALYSIS OF THE INCREASE AND DECREASE OF THE PILLAR DEFORMATION-INDUCED SUBSIDENCE RATE

6.1 *Acceleration of subsidence rate*

The increase of the subsidence rate between 1960 and 1995 cannot be explained by an increase in pillar stresses due to decreasing pillar widths, because the wells 5–11 and 14 were already taken out of production in 1960, and the single well 15 in 1968. Possible explanations are:

a) increasing dilatancy and increasing solution-precipitation creep rates.

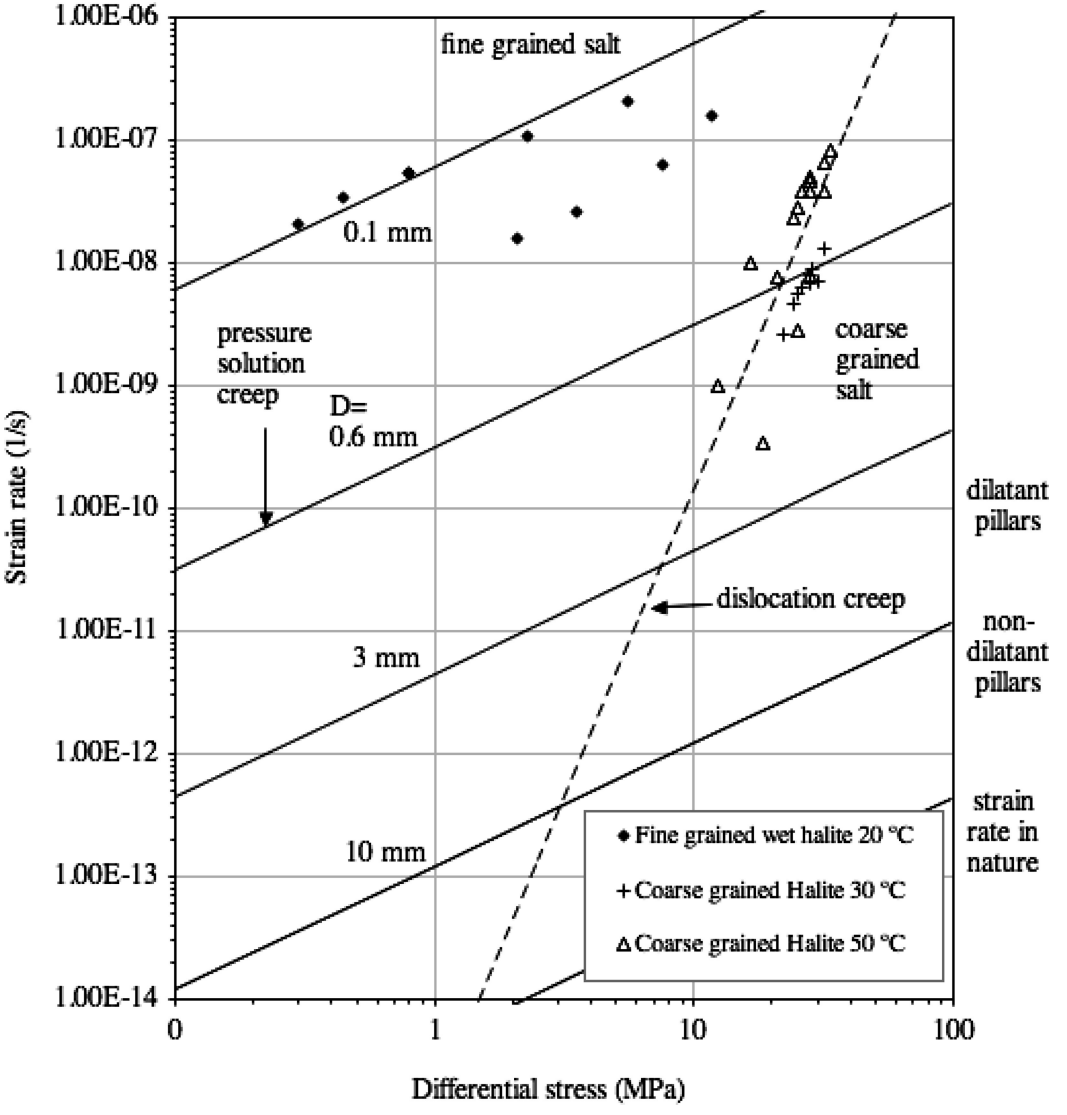

Figure 6. Differential stress – strain rate diagram summarizing laboratory data for a wide range of salts, from experiments by Sandia, BGR, Utrecht university and other Laboratories. Application of these data to conditions of long-term pillar creep requires extrapolation. Broken line is extrapolation of the (grainsize insensitive) dislocation creep law, taking $n = 5$ (BGR creep law). Solid line is the room temperature solution-precipitation creep law for different grainsizes. It can be seen that for a pillar containing brine at grain boundaries, and a grainsize of 3 mm the two mechanisms contribute equally to the deformation at a strain rate around 10^{-11} s^{-1} which corresponds to a deformation rate of 10 mm/year for a 30 m high pillar. After Schleder and Urai (2005).

b) dissipation of the pressure arches over the pillar areas. Cavern migration up to 50 m below the rock-soil boundary is known for well 15. Probably migration also started at several of the other wells 6–11 and 14 (Figs. 3, 4), possibly at different times. Due to the resulting debris chimneys the pressure arches over the pillar areas were (partly) destroyed and the vertical pillar load increased significantly. On the other hand, the debris material within the tributary area of the pillar does not load the pillar anymore. However, this effect is considered less important than the increase of vertical load due to

the breakdown of the pressure arch. In this regard it should also be noted that stoping did not proceed up to the Tertiary for most caverns concerned, and, accordingly, the pillar is still loaded by the soil overburden and an important part of the rock overburden.

c) a component of Phase II surface subsidence, as a direct result of the stoping process.

6.2 *Deceleration of subsidence rate*

The decrease of the subsidence rate could be attributed to:

a) an increase in cross sectional area of the pillar as a result of the creep deformation.
b) lateral support to the pillar, when the widening pillar comes into contact with the debris piles produced by the upward migration of adjacent caverns.
c) friction between the debris material and the chimney walls, resulting in a partial transfer of the vertical pillar stress onto the debris piles.

ACKNOWLEDGEMENTS

We would like to thank Akzo Nobel Salt BV for permission to publish the results of our study in this paper.

REFERENCES

Bekendam, R.F. 1997. Stoping in weak rock over salt solution cavities in the Hengelo Field, The Netherlands, and its expression in terms of surface subsidence. *Proc. SMRI Meeting Cracow, 1997*: 1–25.

Bekendam, R.F. 2005. Compaction of rock debris combined with the bulking effect, and the assessment of final subsidence in relation to initial cavern dimensions. GeoControl report (Akzo-Nobel contract nr. 51/60000190).

Bekendam, R.F., Oldenziel, C. & Paar, W. 2000. Prediction of time-dependent subsidence, tilt and horizontal strain over upwards migrated salt solution cavities. In R.M. Geertman (ed), *Proc. 8th world salt symposium, May 2000, The Hague*, Vol 1: 221–227.

Bekendam, R.F. & Urai, J.L. 2006. Pillar deformation-induced subsidence, Stage 1. GeoControl Report S00605.

Eickemeier, R. & Heusermann, S. 2004. Geomechanische Berechnungen zur Standsicherheit und Integrität von Inline-Pfeilern in paralellen Kavernenreihen. BGR Report 10527/04.

Hunsche, U., Naumann, M. & Plischke, I. 2004. Kavernenfeld Hengelo , Bohrung 480, Arbeitspaket 2, Durchführung von Versuchen an Steinsalzproben aus dem Röt. Abschlussbericht BGR.

Langer, M. 1984. Geotechnische Laboruntersuchungen an Bohrkernen des Kavernenfeldes Hengelo, BGR Report.

Sambeek, L.L.van. 1996. Salt pillar design equation. In: *Proc. Fourth Conf. On the Mech. Beh. of salt*: 1–14.

Sambeek, L.L.van. 2004. Stability analysis of inactive cavern clusters: Hengelo brinefield. Respec topical report RSI-1793, Revision 2.

Schleder, Z. & Urai, J.L. 2005. Microstructural evolution of deformation- modified primary halite from Hengelo, the Netherlands. *International Journal of Earth Sciences* 94(5–6): 941–956.

Ter Heege, J.H.P., De Bresser, J.H.P. & Spiers, C.J. 2005. Dynamic recrystallization of wet synthetic polycrystalline halite: dependence of grain size distribution on flow stress, temperature and strain. *Tectonophysics* 396: 35–57.

Urai J.L. & Bekendam, R.F. 2006. Pillar deformation-induced subsidence, Stage 2. GeoControl Report S00612.

The Mechanical Behavior of Salt – Understanding of THMC Processes in Salt –
Wallner, Lux, Minkley & Hardy, Jr. (eds)
© 2007 Taylor & Francis Group, London, ISBN 978-0-415-44398-2

Execution and analysis of sonar surveys to support rock-mechanical evaluations

A. Reitze, H. von Tryller & F. Hasselkus
SOCON Sonar Control Kavernenvermessung GmbH

ABSTRACT: The echometric surveillance of caverns is especially important with regards to their safe and effective operation. As opposed to brine production caverns, storage caverns are generally subject only to convergence and do not undergo large and irregular changes of shape under normal conditions. Echometric surveillance is therefore primarily employed to obtain proof of the cavern stability and convergence.

Applying the state-of-the-art tool technology it is possible during an echometric survey to measure and process besides the geometry all relevant parameters such as speed of sound, pressure and temperature with a single tool run. Only when considering the physical parameters it is possible to achieve high-accurate results from sonar surveys.

To support rock-mechanical evaluations it is sometimes advantageous to make measurements for specific regions of a cavern with a higher density of measuring points. So-called spiral measurements as well as surveys with an extremely high measuring point density can provide very accurate and detailed information.

In the first instance of the presentation the techniques used for surveying caverns as well as the survey procedure are described in general. Subsequently some interesting results of sonar surveys in regard to rock-mechanical evaluations and questions are presented.

1 GENERAL INSTRUCTIONS

1.1 *Basic measurement principle of sonar surveys*

Geometric surveying of caverns is made using sonic tools on the basis of travel time measurements. In this method the time taken by an acoustic pulse to travel from the measuring tool to the cavern wall and back is determined, i.e. the measured travel time corresponds to the two-fold distance. To convert the travel time into distance it is necessary to know the acoustic velocity in the medium. This means that the accuracy and reliability of the measured cavern geometry depends directly also on the quality of the acoustic velocity determination.

Sonic measurements in caverns must be made in widely differing media. The range of media extends from saturated brine to liquid hydrocarbons and natural gas and even to air at atmospheric conditions. The physical conditions in a cavern depend in the first place on the actual medium, which itself is affected by any previous cavern operations as well as by the surrounding rock.

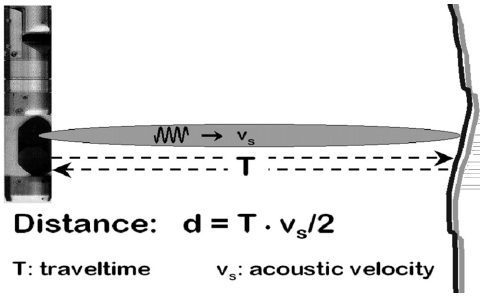

Figure 1. Distance determination using travel time measurements.

1.2 *Physical conditions in caverns*

The physical conditions in a cavern, however, are often not sufficiently appreciated with regard to carrying out sonic surveys. And if the parameters are not considered or are only roughly estimated, in particular the acoustic velocity and the temperature, then the results obtained may be inaccurate or even distorted. Indeed, precise measurement results can be obtained only if the physical conditions in a cavern are appropriately considered not only during the actual survey, but also in the interpretation of the results.

The acoustic velocity needed to convert the measured travel times into distances is subject to complex

physical relationships but depends essentially on the temperature and density of the medium. Figure 3 shows the typical ranges of acoustic velocity that can be expected when carrying out cavern surveys in different types of media.

Some of these distinct variations in a specific medium cannot be explained solely by changes in temperature and pressure. In the case of brine the acoustic velocity is strongly dependent on the salinity and the chemical composition. An occurrence of potassium and magnesium in the brine, for instance, tends to make the acoustic velocity higher.

In liquid hydrocarbons the viscosity plays an important part. The acoustic velocity in gaseous hydrocarbons is affected not only by the pressure and temperature, but also by the moisture content and composition of the gas.

Insofar as the medium in a cavern is homogenous and not affected by external influences, a uniform gradient exists with the temperature increasing with the depth. In practice, however, the temperature during a survey is greatly affected by any previous activities that have been carried out in the cavern. In brine caverns the vertical temperature distribution in a cavern depends especially on the position of the brine casing string and the temperature of the fresh water used for leaching. As a result this can lead to considerable temperature differences and large gradients in a cavern (Fig. 3).

Medium	Acoustic velocity [m/s]
Saturated Brine	1790–1900
Water	1450–1550
Oil and products	1200–1500
Natural gas	390–540
Air	330–375

Figure 2. Acoustic velocities in different media.

2 EXECUTION OF CAVERN SURVEYS

2.1 *Survey procedure*

In order to be able to perform optimal cavern surveying it is essential to find out the physical conditions in the cavern before the actual sonar survey is carried out. The variation of the individual parameters in the vertical survey axis should be measured by running an advance log. So as to be able to properly control the survey procedure and the subsequent interpretation of

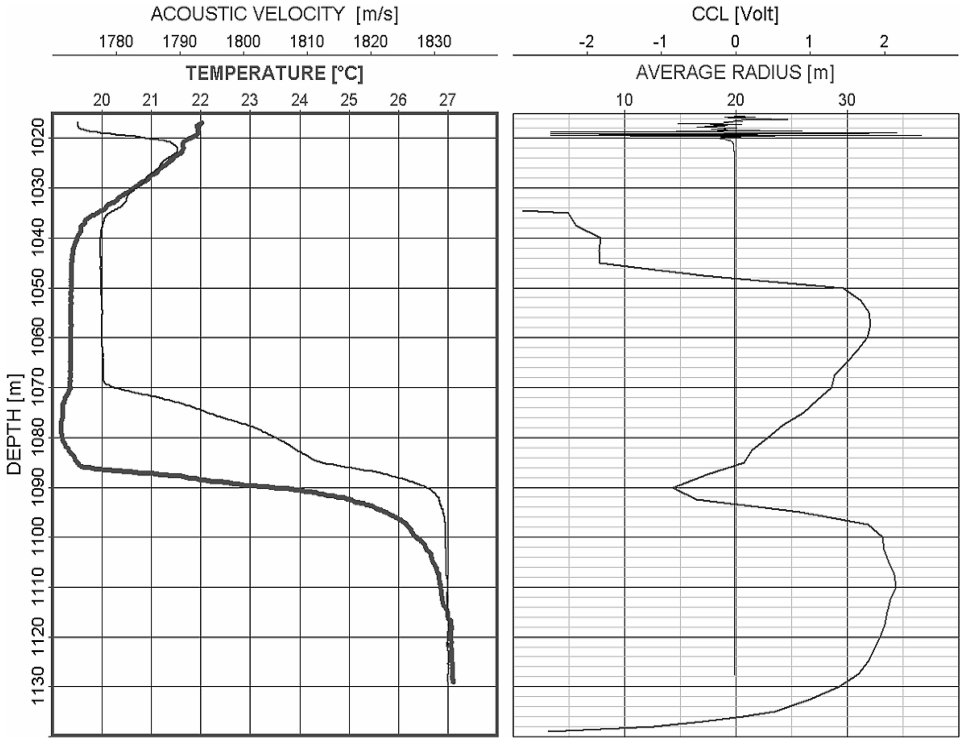

Figure 3. Log of temperature, acoustic velocity and CCL in a brine cavern.

results, it is extremely important that the data are measured continuously over the entire depth range of a cavern. Information obtained at isolated points cannot provide adequate clarification of the true physical conditions.

To convert the measured travel times into distances it is necessary primarily to know the acoustic velocity over the entire vertical extension of the cavern. In addition, the temperature distribution should also be recorded as it can be used for a plausibility check of the acoustic velocity distribution. Temperature recording must be made in particular with a view to cavern sections which have large temperature gradients or horizontal layering, because such zones must specifically be taken into account in order to achieve optimum results.

If, for example, the temperature gradient is not recorded and the measurements with transducers are performed through a zone in which the temperature greatly varies, the ensuing refraction of the sonic beam would lead to an incorrect determination of the shape and volume of the cavern.

After the initial logging the cavern shape will be surveyed by a multitude of horizontal sections over the entire cavern depth as well as sections with titled sonar head to measure bottom, roof or any other irregularities of a cavern. The surveying principle of SOCON is based on a point by point sampling of the cavern wall. The measuring head is first positioned in the required direction with the required inclination and is maintained there until the point has been measured and all the necessary correlations and plausibility checks have been carried out. It is then moved to the next measuring position. Such a step by step rotation normally causes vibrations which make it impossible to measure. However, this procedure is possible with SOCON tools as they are equipped with gyro stabilizers which stop tool vibration. The following figure gives an overview on the whole survey procedure.

2.2 *Tool technology*

All echo tools have been developed by SOCON and represent the culmination of 40 years of experience in carrying out ultrasonic cavern surveying. The modular tool design (Fig. 5) contains subsystems for recording all the relevant parameters in a single survey run. Each functional unit, such as transmitter-receiver section, compass, rotation-tilt control, acoustic velocity measurement or CCL/Multiple-CCL, is equipped with its own processor and is controlled from the main computer at the surface via a digital bus. The advantage of the modular design is that future modifications no longer affect the whole tool but instead just individual modules.

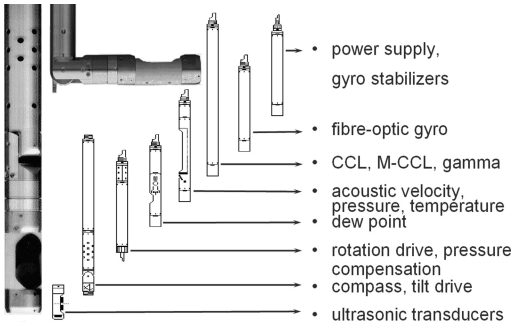

Figure 5. Modular design of the SOCON echo tools type BSE/BSFII.

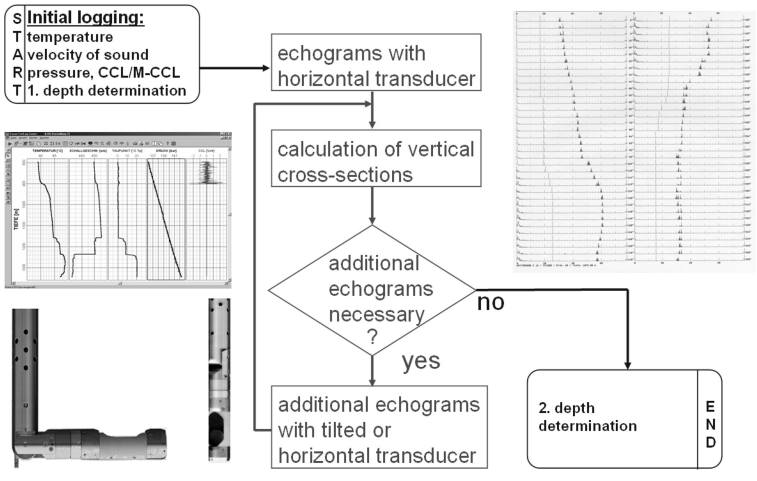

Figure 4. Survey procedure.

Such a flexible arrangement as well as the large dynamic range of the transmitter-receiver electronics make it possible to adjust the tool quickly to the prevailing survey conditions. The crucial factor in selecting the proper wavelength for carrying out a survey is the medium in the cavern with its specific sonic wave propagation characteristics. The wavelength in turn affects the size of the angle of beam spread of the sonic lobe and depends on the acoustic velocity in the medium as well as on the measuring frequency.

Moreover, the modular design allows extra modules, for instance for dew-point measurements, to be easily added to the system. Each module represents an individual pressure resistant unit separated from the other modules by bulkheads so as to improve the operating safety and protect the sensitive components.

The tool is equipped with gyro stabilizers to suppress circular motion during surveying that would otherwise occur as a result of the stepwise rotational advance. The acoustic velocity is determined over three different reference lengths.

Rotation and tilting of the tool head can be effected in steps of one degree (1°), which enables irregularities of the cavern wall to be detected with high resolution.

A four-conductor cable is required to operate the echo tool, which can used at temperatures between 0°C and 75°C and at pressures of up to 300 bar.

3 SURVEY EXAMPLES

3.1 *Full measurement of storage caverns*

The echometric survey of a storage cavern serves the combined purposes of identifying any changes in shape and also determining the actual cavern volume. The cavern convergence can be determined by comparing volumes surveyed in successive measurements.

The shape of a cavern can be more or less regular depending upon the geological situation and the specific implementation of individual leaching steps. The spectrum of possible shapes ranges from smooth regular cylindrical and pear-shaped caverns through to highly irregular Christmas tree shapes. Figure 6 illustrates the roof section of a storage cavern having a very regular shape, determined using two full surveys. As can clearly be seen, no significant changes in shape took place during the observation period. Only uniform convergence has occurred.

Irregularly shaped caverns often have projections protruding from the wall into the cavern. Zones of this kind are obviously subject to relatively high rock stresses because they are only supported by the medium stored in the cavern. In the case of gas storage caverns in particular, where operational requirements often result in very low internal cavern pressures, this support is accordingly also minimal. The fall of such a projection often leaves behind a smoother cavern wall.

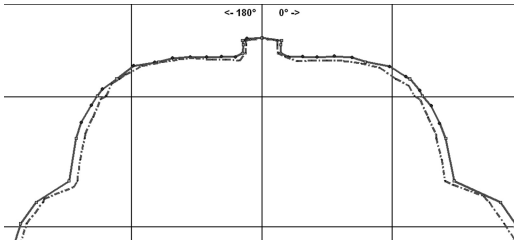

Figure 6. Convergence in the roof zone of a cavern.

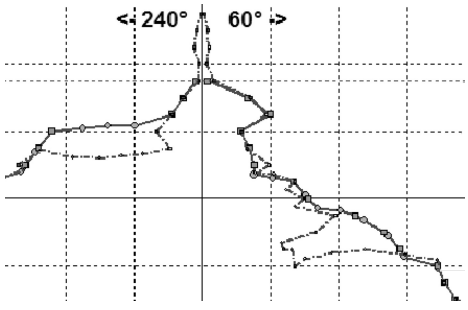

Figure 7. Changes in a cavern roof zone (previous sonar shown as a broken line).

Figure 7 illustrates a cavern with a somewhat irregular shape, in which spalling has taken place in the roof zone in the period between two full surveys.

This example demonstrates the importance of observing and analysing roof developments during the operating phase of a storage cavern. Bearing in mind that even minor changes may be crucial, the demands made on echometric surveillance are correspondingly high.

3.2 *Spiral measurement*

To increase the survey point density cavern surveys can be carried out as spiral measurements. Whereas the standard method is based on a point-by-point procedure these measurements are made while raising the echo tool and simultaneously slowly rotating it. As a result the cavity is sampled with such a high survey point density that even fine structures on the cavity wall can be resolved.

Very accurate echometric calliper measurements can be achieved in the cavity neck with this method, which, as opposed to the relatively coarse conventional calliper, allows detailed analysis. This is especially important in the critical zone of the cavity neck because here free passage must always be guaranteed. Changes in shape in this zone must be followed very closely so that if necessary appropriate measures can be initiated in good time.

Figure 8. View of a cavity roof as revealed by spiral measurements.

The transducer head is tilted upwards at a fixed angle during spiral measurements of the roof. This enables pockets in the roof structure to be detected, which is of great importance when the integrity of a cavern roof has to be proofed.

3.3 *High resolution measurements*

Another method of enhancing the density of survey points in addition to that of spiral measurement is for example to reduce the vertical separation between two measurement horizons. Depending upon the size of the cavern, the distance can be between two and 10 metres. Reducing this to just a few decimetres provides a much more detailed scan of the cavern wall. The resolution can be further raised by reducing the angular steps between individual measurement sections.

Both of these procedures result in a very large number of individual scan sections such that detailed investigations of this kind are only justified in certain cavern zones.

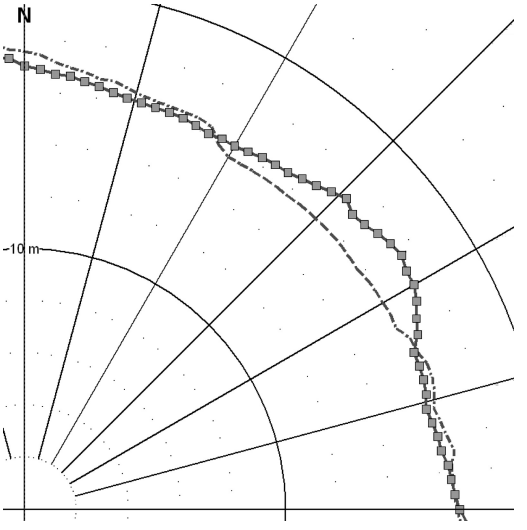

Figure 9. Identification of spalling and convergence from the cavern wall between two high resolution sonar surveys (previous sonar shown as a broken line).

Figure 9 shows a square of a horizontal section of a cavern surveyed with a vertical measurement horizon separation of only 0.2 metres and with angular steps of 2 degrees.

The sonic signals acquired were then further enhanced by employing quadruple correlation together with five-fold recording of each horizontal section. Consequently zones of spalling and convergence could clearly be identified.

Taylor & Francis
Taylor & Francis Group
http://taylorandfrancis.com

The Mechanical Behavior of Salt – Understanding of THMC Processes in Salt –
Wallner, Lux, Minkley & Hardy, Jr. (eds)
© 2007 Taylor & Francis Group, London, ISBN 978-0-415-44398-2

Some aspects of the transient behavior of salt caverns

M. Karimi-Jafari & P. Bérest
LMS, Ecole Polytechnique, Palaiseau, France

B. Brouard
Brouard Consulting, Paris, France

ABSTRACT: The effects of transient creep in salt caverns are discussed. Salt behavior is viscoplastic: following a change in cavern pressure, a slow redistribution of stress takes place. This explains the long duration of any transient phase in a cavern. Stress redistribution also makes fracturing easier when cavern pressure is kept low for a long period of time. "Reverse" creep, a transient mechanical phenomenon that can be observed in the laboratory, also exists in salt caverns and may lead to misinterpretation of Mechanical Integrity Tests.

1 INTRODUCTION

The transient mechanical behavior of *salt samples* has been discussed by several authors (*e.g.*, Lux & Heuserman 1983; Munson & Dawson 1984; Aubertin 1996; Cristescu & Hunsche 1998). When submitted to a rapid applied-load increase, samples experience a period lasting several weeks (or months) during which the strain rate gradually decreases to reach the steady-state rate. Conversely, when submitted to a rapid load decrease (stress drop), samples sometimes experience "reverse creep", or increase in sample height, over a couple of weeks or more (Fig. 1).

Less attention has been paid to the transient behavior of *salt caverns – i.e.*, the change in cavern volume or (closed) cavern pressure following a rapid change in cavern fluid pressure. *In situ* "transient" tests are difficult to perform, as measuring small changes in cavern volume or shape is not easy (Bérest *et al.* 2006), and only a small number of such tests have been described in the literature. A few definitions are useful at this step. Cavern pressure is said to be "halmostatic" when the central string is filled with saturated brine and zero pressure is applied on that central string at the wellhead. In a brine well, or in a liquid- or liquefied-storage cavern, cavern pressure most often is close to halmostatic. In a natural-gas storage cavern, cavern pressure is lower than halmostatic (and faster volume loss rates can be expected) when the gas stock is smaller. Cavern pressure is said to be "oleostatic" when the well is filled with a light liquid hydrocarbon, a situation sometimes encountered during *in situ* tests.

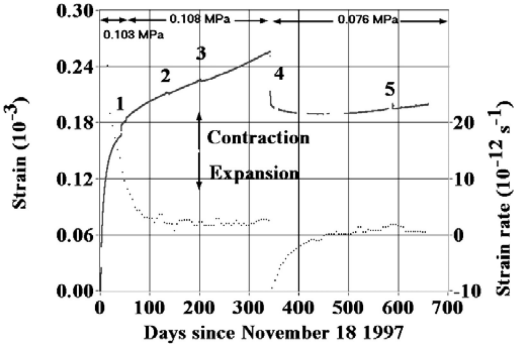

Figure 1. Strain and strain rate as functions of time during a creep test. Reverse creep appears when the applied stress drops from 0.108 MPa to 0.076 MPa (Bérest *et al.* 2005).

The general outline for the mechanical behavior of caverns is similar to that for a rock sample when, instead of sample strain-rate, $\dot{\varepsilon}$, one considers the cavern volume loss (or increase) rate, $\dot{V}/V$, and, instead of the mechanical load applied to a rock sample, σ, one considers the difference between the overburden (or geostatic) pressure and the cavern pressure, $P_\infty - P_i$.

A few differences must be noted, however: (1) in a cavern (resp., in a sample), the mechanical loading is more severe when cavern pressure is *lower* (resp., when applied stress is *higher*), (2) any pressure change in a cavern triggers several transient phenomena, of which transient creep is only one, and (3) transient creep in a cavern lasts much longer than in a rock sample.

In this paper, we discuss several aspects of cavern transient mechanical behavior.

2 CAVERN BEHAVIOR FOLLOWING A PRESSURE DROP (GEOMETRICAL VERSUS RHEOLOGICAL TRANSIENT CREEP)

The transient mechanical behavior of a cavern is more complex than the transient mechanical behavior of a sample. In fact, one must distinguish between the "rheological" transient behavior (as observed during a laboratory test) and the "geometrical" transient behavior of a cavern–when cavern pressure changes, the non-uniform stress field around the cavern slowly changes from its initial distribution to its final steady-state distribution, an effect that does not exist when a triaxial test is performed on a cylindrical rock sample. These two transient effects combine in a cavern: the geometrical transient behavior is responsible for the long duration of the transient phase in a cavern. This is illustrated in Figure 2. Computation begins when the cavern is leached out. In the 800-m deep cavern presented in Figure 2, during cavern creation, pressure rapidly decreases from geostatic (the pressure prevailing before the cavern is created) to halmostatic. Later, the cavern pressure is kept constant and equal to halmostatic (a situation approximately met in a liquid-hydrocarbon storage facility or brine-production cavern) and $P_\infty - P_i = 8$ MPa. Two constitutive laws are considered: (a) the Norton Hoff law, in which only steady-state constitutive behavior is taken into account; and (b) the Munson-Dawson (modified) law, in which, in addition to steady-state rheological behavior, transient rheological behavior is taken into account. Parameter values are the same as those defined below in Section 3.3. The volume-loss-rate versus time curve is shown in Figure 2. Note that even when no rheological behavior is taken into account (Norton-Hoff law), a transient period lasting several decades can be observed before steady-state cavern behavior is reached. (In fact, it is not reached before 100 years. In general, the transient period is longer when the *n*-exponent in the Norton-Hoff law is larger.) This is in sharp contrast to the behavior of a cylindrical rock sample submitted to a constant mechanical load (see Fig. 2; the applied stress is 8 MPa). Taking into account the transient rheological behavior (Munson-Dawson law) makes volume loss rate slightly slower, but the geometrical transient behavior is by far the most significant effect. In most cases, "steady-state" cavern-volume loss rate underestimates the actual rate.

3 CAVERN TRANSIENT EXPANSION

The following sections describe "reverse creep" as it affects salt caverns. Several *in situ* tests are described (Section 3.1). These tests are difficult to interpret (Section 3.2); the Manosque test was selected to fit constitutive laws against field data (Section 3.3).

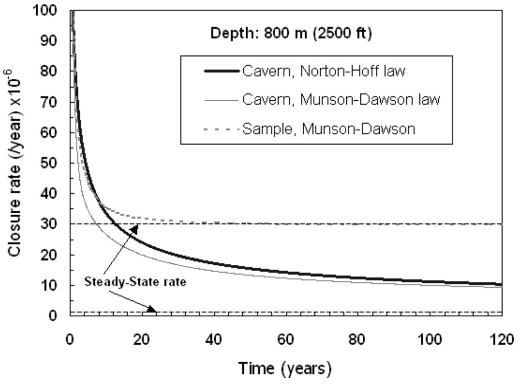

Figure 2. Closure rate as a function of time in a brine production cavern.

3.1 *Outflow measurement test*

Before an *in situ* test is conducted, cavern pressure is kept halmostatic, and the brine outflow rate from the cavern is measured. At the beginning of the test, cavern pressure is lowered to oleostatic: the well is filled with a light liquid hydrocarbon and opened at ground level, and the hydrocarbon outflow rate is measured over several weeks. (In some cases, the well is shut, and the flow rate of the liquid that must be injected or withdrawn to keep wellhead pressure constant is measured.) At the end of the test, the halmostatic pressure is restored, and the brine outflow rate is measured again. Such tests have been performed by Hugout at Etrez (1988–a re-interpretation of this test can be found in van Sambeek *et al.*, 2005), by Brouard *et al.* (2004) and by Clerc-Renaud & Dubois (1980), who performed a test in a cavern at the Manosque site (Southeastern France), operated by Géostock. This cavern was 569- to 864-m deep with a volume of 235,000 m^3. The cavern was filled partly with oil (oil volume of 185,000 m^3). The wellhead oil pressure was 550 psi before the test, and the wellhead brine pressure was zero. Slowly decreasing brine outflow was observed (Fig. 3); it was generated by the warming of cavern oil and brine and, to a lesser extent, by cavern creep closure. The wellhead oil pressure was released (PQ on Fig. 3) by opening a valve that isolated the annular space from the central string. Oil outflow then was measured for 2000 hours (QR on Fig. 3), after which brine was injected in the central tube to increase the wellhead oil pressure by 550 psi (RS on Fig. 3). Brine outflow then was measured for 2000 hours (ST on Fig. 3). Fast convergence rates following a pressure decrease (phase QR) and "reverse" convergence rates following a pressure increase (phase ST) were observed.

It should be noted that, in addition to these three "outflow measurement" tests, hundreds of *in situ* tests

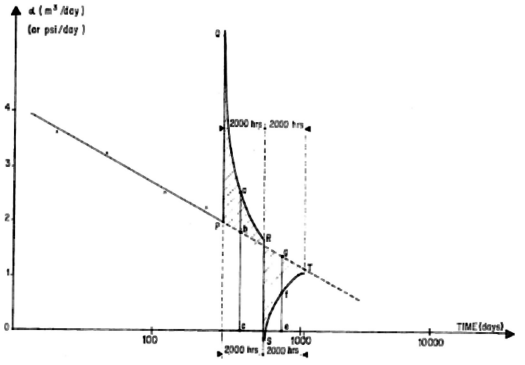

Figure 3. Oil outflow test (Clerc-Renaud & Dubois 1980).

that triggered reverse creep were performed worldwide: any Mechanical Integrity Test (MIT), which involves a rapid pressure build-up followed by an observation period lasting several days can be considered as a "reverse creep" test.

3.2 *Difficulties in interpretation of in situ tests*

During the *in situ* tests described above, transient creep apparently was observed, as the fluid outflow rate experienced a drastic change after pressure decreased or increased. However, precise interpretation is difficult as, together with transient mechanical behavior, any rapid pressure change triggers several other transient phenomena. According to the Le Chatelier (or Braun) principle, these test-triggered phenomena tend to restore the pre-existing pressure in a closed cavern and may lead to an overestimation of the effects of creep. The three main such phenomena (other than transient creep) are (1) additional dissolution (Any change in cavern pressure leads to a change in brine saturation: following a rapid pressure build-up, salt is dissolved, more room is available for cavern brine, and cavern pressure drops accordingly.), (2) transient brine permeation (The permeability of salt is exceedingly small; however, a rapid pressure increase generates fast transient permeation over a couple of days.), and (3) adiabatic pressure build-up (A rapid pressure increase results in a small increase in brine or oil temperature that is followed by cooling and contraction of the liquid and, ultimately, by pressure decrease). They are described in more detail in Van Sambeek *et al.* (2005). These must be taken into account, as their effects are identical to those of transient creep. Most often, however, they especially are active for 2–3 days immediately following the change in cavern pressure. While they are significant during an MIT, they often can be neglected when a test lasting several weeks is considered.

3.3 *Constitutive behavior*

Two constitutive laws were considered: (1) the Munson-Dawson modified (M-D) law, and (2) the Lemaitre-Menzel-Schreiner (L-M-S) law. They do not include "reverse" creep [Munson *et al.* (1996) proposed an advanced version of the M-D law that does take reverse creep into account; this version is not considered here.]. These two laws are described below.

The *Lemaitre-Menzel-Schreiner (L-M-S)* law is used widely in France and can be described as follows:

$$\dot{\varepsilon}_{ij}^{vp} = \frac{\partial}{\partial t}(\zeta)^{\alpha}\frac{\partial}{\partial \sigma^{ij}}\left(\sqrt{3J_2}\right) \tag{1}$$

$$\dot{\zeta} = \left(\frac{\sqrt{3J_2}}{K}\right)^{\frac{\beta}{\alpha}} \tag{2}$$

The (modified) *Munson-Dawson* (*M-D*) law is a generalization of the Norton-Hoff law that takes into account the transient behavior of rock salt. The Norton-Hoff law captures the main features of steady-state salt behavior in the range of stresses and temperatures commonly encountered in salt caverns:

$$\dot{\varepsilon}^{ij} = \dot{\varepsilon}_e^{ij} + \dot{\varepsilon}_{ss}^{ij} \tag{3}$$

$$\dot{\varepsilon}_{ss}^{ij} = A\,exp\left(-\frac{Q}{RT}\right)\frac{1}{n+1}\frac{\partial}{\partial \sigma_{ij}}\left[\left(\sqrt{3J_2}\right)^{n+1}\right] \tag{4}$$

$$\dot{\varepsilon}_e^{ij} = \frac{1+\nu}{E}\dot{\sigma}^{ij} - \frac{\nu}{E}\dot{\sigma}^{kk}\delta^{ij} \tag{5}$$

Munson and Dawson introduced a multiplier (F) and an internal variable (ζ) to describe salt transient behavior:

$$\dot{\varepsilon}^{ij} = \dot{\varepsilon}_e^{ij} + F\dot{\varepsilon}_{ss}^{ij} \qquad \begin{array}{ll} F = e^{\Delta\left(1-\zeta/\varepsilon_t^*\right)^2} & \text{when } \zeta \le \varepsilon_t^* \\ F = e^{-\delta\left(1-\zeta/\varepsilon_t^*\right)^2} & \text{when } \zeta \ge \varepsilon_t^* \end{array} \tag{6}$$

$$\dot{\zeta} = (F-1)\dot{\varepsilon}_{ss}, \quad \dot{\varepsilon}_{ss} = A\,exp\left(-\frac{Q}{RT}\right)\left(\sqrt{3J_2}\right)^n \tag{7}$$

$$\varepsilon_t^* = K_0 e^{cT}\sigma^m \text{ and } \Delta = \alpha_w + \beta_w Log_{10}(\sigma/\mu) \tag{8}$$

$$\delta = \delta_o, \ \mu = E/2(1+\nu), \ \sigma = \sqrt{3J_2} \tag{9}$$

Parameters of these two constitutive laws first were fitted against the as-observed oil outflow during the 2000-hour long QR phase of the Manosque test (day 485 to day 585). An excellent fit (see Fig. 4) was

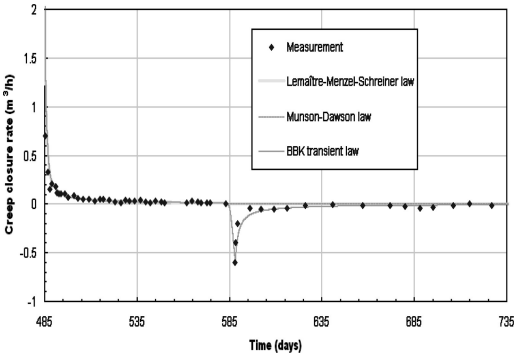

Figure 4. Three constitutive laws are fitted against as-observed oil flow during the days 485 to 585 to predict brine flow during days 585 to 735. (The M-D and L-M-S curves are identical.)

obtained when the following values of the parameters were selected:

$$\beta = 3.3,\ \alpha = 0.13,\ K = 1.5 \text{ MPa} \quad \text{(L-M-S law)};$$

$$A\exp\left(-Q/RT\right) = 2\cdot 10^{-11} \text{ MPa}^4\text{/day},$$

$$n = 4,\ K_o = 1.2\cdot 10^{-10},\ c = 0.0315 \text{ /K},\ m = 3,$$

$$\alpha_w = 15,\ \beta_w = 0,\ \delta = 0.58 \quad \text{(M-D law)}.$$

Note that the Lemaitre and Munson-Dawson laws give similar results: the two curves are identical. The two set of parameters then were used to "predict" the flow rate during the ST phase, when brine was injected into or withdrawn from the central tubing to keep the wellhead pressure as constant as possible. The L-M-S and M-D laws were not able to capture the effect of the pressure increase on day 585. This is no surprise, as those two laws do not include "reverse" creep.

In order to better take into account "reverse" creep, the Munson-Dawson law was modified slightly to become the BBK Transient law, as follows:

$$F = 1 - \left(1 - \varsigma/\varepsilon_t^*\right)^p / \left(1-k\right)^p \text{ when } \varsigma > \varepsilon_t^* \qquad (10)$$

Note that reverse creep appears when $\varsigma > k\varepsilon_t^*$, or $F < 0$.

A good fit was reached against the measured flow during ST phase (Fig. 4) when the following values of the parameters were selected: $p = 2.4$, $k = 1.1$.

3.4 *Conclusion*

Interpretation of the Manosque test proves, as did interpretation of the Etrez test (Van Sambeek *et al.* 2005), that, following a rapid increase in cavern pressure, "reverse" creep takes place in a closed cavern. This effect must be taken into account to interpret a Mechanical Integrity Test precisely, as reverse creep makes apparent leaks greater than actual leaks. Examples can be found in Karimi *et al.* (2005).

4 HYDRO-FRACTURING

Here, we discuss the effects of a pressure build-up large enough to lead to rock fracturing (or a drastic increase in salt permeability). The elastic case is considered first (Sections 4.1 and 4.2). New features appear when the viscoplastic case is considered (Section 4.3). The case of a full-size cavern and field evidence are discussed in Section 4.4 and 4.5.

4.1 *Introduction*

Hydro-fracturing tests may be performed in wells, before washing-out takes place, to assess *in situ* stresses. This is especially helpful when the cavern is used later to store natural gas, whose maximum operating pressure must be kept lower than the minimum *in situ* stress. It generally is accepted that fracturing at a borehole well is reached when the fluid pressure, P, is larger than the least compressive stress, σ_m (Compressive stresses are negative.), by an amount that is related to the "tensile strength" of the rock mass ["a complex material parameter, certainly not an intrinsic material property" (Rummel *et al.* 1996)], or $P + \sigma_m > T$. The fracturing pressure often is called the breakdown pressure, P_c. The shut-in pressure, P_{si}, is the fluid pressure reached a certain period of time after the well was shut-in; it is smaller than the breakdown pressure and generally is considered as being more representative of the minimum *in situ* stress. For a rock-salt mass, it often is assumed that the natural state of stress at depth is spherical–*i.e.*, the three main stresses are equal, $S_h = S_H = S_v = -P_\infty$ (However, anomalous stress distribution can be found, for example, at the fringe of a salt dome.) In such a case, the least compressive stress at the borehole wall during a fracturing test is the tangential stress, $\sigma_m = \sigma_{\theta\theta}$. Several cases must be distinguished according to the period during which fracturing is performed.

4.2 *Elastic behavior*

When elastic behavior is considered (an assumption which is correct only during a short period of time after the well is drilled), stress distribution in the rock mass is:

$$\sigma_{rr} + P_\infty = \left(P_\infty - P\right)\left(a/r\right)^2 \qquad (11)$$

$$\sigma_{\theta\theta} + P_\infty = (P_\infty - P)(a/r)^2 \quad (12)$$

$$\sigma_{zz} + P_\infty = 0 \quad (13)$$

where a is the borehole radius. When $P > P_\infty$, the least compressive stress is $\sigma_{\theta\theta}$, and fracturing is reached when:

$$P > P_c = P_\infty + T/2 \quad (14)$$

Hydro-fracturing tests in a salt formation most often are interpreted according to this simple formula (see Rummel *et al.* 1996; Schmidt1993; Staudtmeister & Schmidt 2000; Doe & Osnes 2006). However, as stated by Rummel *et al.* (1996), the shut-in pressure profile (a measure for the minimum principal stress) is "derived from the final refrac cycle to guarantee fractures had propagated away from the borehole and had adjusted to the far field stress" (p.1), a comment whose significance is highlighted in the following paragraphs.

4.3 *The effect of stress distribution at the borehole wall*

In the case of rock salt, as was pointed out first by Wawersik & Stone (1989), the state of stress in the vicinity of a borehole may be complex, making test interpretation more difficult. When a borehole is kept open for a long time (say, several years), the brine pressure remains halmostatic, $P = P_h$, and stress redistribution, from the initial "elastic" distribution to the final "steady-state creep" distribution, takes place slowly. In this process, the tangential stress becomes significantly larger (Compressive stresses are negative.) than it had been when the stress distribution was "elastic". When pressure is increased rapidly in a well (as it is during a hydro-fracturing test), the incremental stress increase is elastic, and the tangential stress often becomes smaller than brine pressure before the brine pressure becomes geostatic, in sharp contrast with what occurs during a standard hydro-fracturing test in an elastic medium. A simple analysis can be performed when Norton-Hoff constitutive behavior is adopted. Assume that the brine pressure in the well was kept halmostatic, $P = P_h$, during a period long enough to reach mechanical steady-state, or

$$\sigma_{rr} + P_\infty = (P_\infty - P_h)(a/r)^{2/n} \quad (15)$$

$$\sigma_{\theta\theta} + P_\infty = (P_\infty - P_h)(1-2/n)(a/r)^{2/n} \quad (16)$$

$$\sigma_{zz} + P_\infty = (P_\infty - P_h)(1-1/n)(a/r)^{2/n} \quad (17)$$

Now, pressure in the well is increased rapidly. The additional stresses generated by a pressure increase of $(P - P_h)$ can be computed using the elastic solution and

$$\sigma_{\theta\theta} + P_\infty = (P_\infty - P_h)\left(1-\frac{2}{n}\right)\left(\frac{a}{r}\right)^{2/n} + (P - P_h)\left(\frac{a}{r}\right)^2 \quad (18)$$

and fracturing will be reached at the borehole wall ($r = a$) when $\sigma_{\theta\theta} + P > T$, or

$$P > P_\infty + T/2 - (P_\infty - P_h)(1-1/n) \quad (19)$$

In other words, *fracturing pressure is significantly smaller when a test is performed long after a borehole is opened.* In fact, in some cases, fracturing will be reached even when the pressure is smaller than geostatic.

4.4 *Hydro-fracturing in salt caverns*

We now consider the somewhat more complex case of a cavern whose pressure was kept constant (say, halmostatic) over many years. At the end of this period, pressure is increased to reach fracturing. Several differences with the borehole case are noted. On one hand, cavern shape is not as simple as borehole shape. (It is not a perfect cylinder.) On the other hand, the pressure build-up rate often is much slower in a cavern. For instance, when a cavern is sealed and abandoned, brine pressure slowly increases due to several phenomena, including cavern creep closure and brine thermal expansion; this process may take years before fracturing pressure is reached. In other words, in sharp contrast with the case of borehole fracturing, stresses are given time to redistribute before fracturing is reached.

A 1000-m deep, 200-m high cavern is considered (see Fig. 5). The cavern was kept idle for 20 years to allow stresses to redistribute.

Then, the pressure is increased slowly, and various pressure build-up rates are considered. (The pressure build-up phase lasts from 1 day to 27 years). Computations stopped when "fracturing" occurred – *i.e.*, when the least principal stress at the cavern wall, σ_m (Compressive stresses are negative.), is such that $\sigma_m + P > 0$. (For simplicity, no tensile strength is taken into account.) The corresponding values of the fracturing gradient are plotted on Figure 5. They are smaller than the geostatic gradient, which is 0.022 MPa/m.

4.5 *Field evidence*

Rokhar *et al.* (2000) describe a test performed in 1990 in the Etzel K102 cavern, a 230,000-m^3 cavern in the cavern field located in the Etzel salt dome. The cavern roof is 850 m deep, and its height is 662 m. The objective of the test was to induce a fracture at slow pressurization rates. It was hoped that such

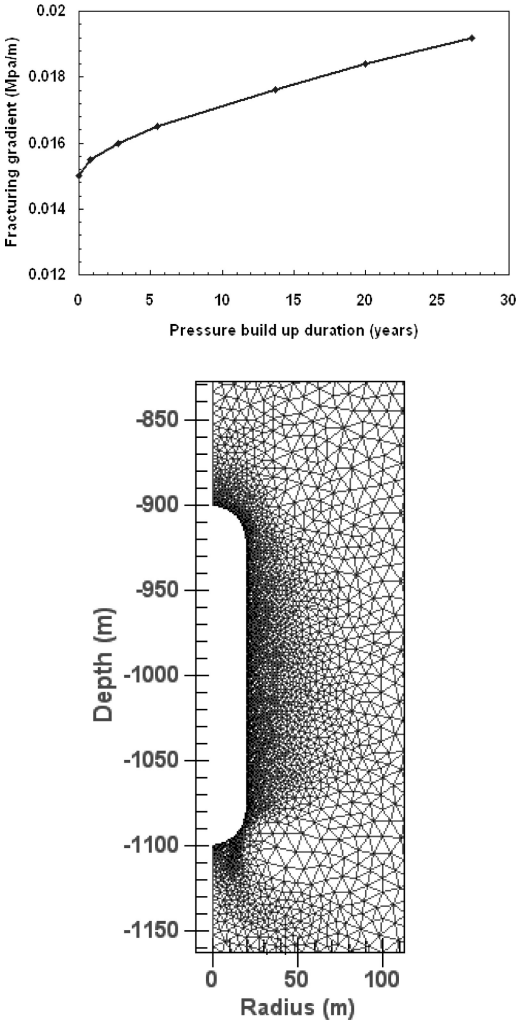

Figure 5. Fracturing gradient (no tensile strength) as a function of pressure build-up duration. (The cavern had been kept idle for 20 years before sealing.).

slow rates would induce a fracture (*i.e.*, breakdown) gradient significantly higher than the fracture gradient reached during standard hydro-fracturing tests. A systematic procedure was used during the test: each pressure build-up phase was followed by an observation period lasting several weeks. During the third step, at which a gradient of 0.0219 MPa/m was to be reached, the ratio of the injected-volume rate versus the pressure build-up rate began to increase, clear proof of the onset of a fracture (or of increased, or "secondary", salt permeability). When injection stopped, the pressure began to drop; after a two-month observation period, extrapolation to a final pressure level of 0.0217 MPa/m appeared plausible. It is noted that the geostatic pressure gradient derived from borehole investigations was 0.0241 MPa/m–*i.e.*, far larger than the gradient reached during the third step. In hindsight, this early estimate was considered too high; additional investigations have proven that the geostatic pressure gradient ranges between 0.0204 MPa/m and 0.0211 MPa/m (*i.e.*, slightly smaller than the cavern breakdown pressure.) It is suggested here that redistribution of stress in the rock mass, as explained above, may have been influential in the early onset of fracture (or of increased salt permeability).

Durup (1990) performed an SMRI-supported tightness test on the 1000-m deep Ez58 well six years after the well was drilled. (A partial stress redistribution is thought to have had enough time to take place.) The 200-m high open hole was subjected to a series of stepwise increasing pressures. One objective of the test was to determine the pressure gradient corresponding to the beginning of loss of tightness. This gradient was reached after a pressure build-up of one-year; it was slightly less than 0.024 MPa/m. In this case, the effects of stress redistribution seem to be less significant than in the Etzel case, as fracturing pressure was significantly higher (by 2 MPa) than geostatic pressure. This difference may be explained by: (a) a shorter "waiting" period, (b) a larger rock tensile strength, and/or (c) a larger overburden density.

4.6 *Conclusions*

Strong mechanical and mathematical arguments yield the conclusion that fracturing in a well or cavern that has been kept idle for a long period of time is reached at a pressure level much smaller than the figure obtained during a hydro-fracturing test performed soon after the well was drilled. This conclusion may have important consequences, especially when cavern abandonment is considered.

However, field data are somewhat equivocal. It must be kept in mind that several uncertainties make the interpretation of *in situ* test results difficult. For example, if the above-mentioned formula for the onset of fracturing is accepted,

$$P > P_\infty + T/2 - \left(P_\infty - P_h\right)\left(1 - 1/n\right) \tag{20}$$

It is clear that large uncertainties may affect the value of the geostatic pressure (P_∞), as mentioned by Rokhar *et al.* (2000), as well as the value of the tensile strength (T), making any validation of this formula difficult.

5 CONCLUSIONS

The transient mechanical behavior of a cavern has been discussed. It has been proven that: (1) transient

behavior lasts much longer in a cavern than in a sample, (2) when submitted to a rapid pressure increase, a cavern experiences "reverse" creep, an effect that can lead to overestimation of the actual leak during an MIT, and (3) when a cavern (or a borehole) is kept idle for a long period of time, a slow redistribution of stresses takes place in the rock mass, and a relatively low pressure increase may lead to fracturing. However, field data remain scarce, and interpretation is difficult. Further investigations are needed, as the consequences of the mechanical behavior of caverns possibly are significant.

REFERENCES

Aubertin, M. 1996. On the physical origin and modeling of kinematic and isotropic hardening of salt. In *Proc. 3rd Conf. Mech. Beh. of Salt*: 3–17. Clausthal-Zellerfeld, Germany: Trans. Tech. Pub.

Bérest, P., Blum, P.A., Charpentier, J.P., Gharbi, H. & Valès, F. 2005. Very slow creep tests on rock samples. *Int. J. Rock Mech. & Min. Sc*. 42: 569–576.

Bérest, P., Brouard, B., Karimi, M. & Bazargan, B. 2006. *In situ* mechanical tests in salt caverns. In *Proc. SMRI Spring Meeting*, *Brussels*: 92–130.

Brouard, B., Bérest, P., Héas, J.Y., Fourmaintraux, D., de Laguérie, P. & You, Th. 2004. An *in situ* creep test in advance of abandoning a salt cavern. In *Proc. SMRI Fall Meeting, Berlin*: 46–64.

Clerc-Renaud, A. & Dubois, D. 1980. Long-term operation of underground storage in salt. In A. H. Coogan & L. Hauber (eds), *Proc.5th Symp. on Salt:* Vol. II, 3–10. Cleveland: The Northern Ohio Geological Society.

Cristescu, N.D. & Hunsche, U. 1998. *Time Effects in Rock Mechanics.* West Sussex, England: John Wiley & Sons.

Doe, Th. & Osnes, J. 2006. *In situ* stress and permeability tests in the Hutchinson salt and the overlaying shale, Kansas. In *Proc. SMRI Fall Meeting, Rapid City*: 181–213.

Durup, G. 1990. Field tests in Well EZ 58. *SMRI Project Report n° 90-00002-S*.

Hugout, B. 1988. Mechanical behavior of salt cavities – *in situ* tests – model for calculating the cavity volume evolution. In *Proc. 2nd Conf. Mech. Beh. of Salt*: 291-310. Clausthal-Zellerfeld, Germany" Trans. Tech. Pub.

Karimi-Jafari M., Bérest, P., Van Sambeek, L. Brouard, B. & Bazargan, B. 2005 Interpretation of Mechanical Integrity Tests In *Proc. SMRI Fall Meeting, Nancy*: 153–173.

Lux, K.H. & Heusermann, S. 1983. Creep tests on rock salt with changing load as a basis for the verification of theoretical material laws. In *Proc. 6th Int. Symp. on Salt*: Vol. I, 417–435. Alexandria, Virginia: The Salt Institute.

Munson, D.E. & Dawson, P.R. 1984. Salt constitutive modeling using mechanism maps. In *Proc. 1st Conf. Mech. Beh. of Salt*: 717–737. Clausthal-Zellerfeld, Germany: Trans. Tech. Pub.

Munson, D.E., De Vries, K.L., Fossum, A.F. & Callahan, G.D. 1996. Extension of the Munson-Dawson model for treating stress drops in salt. In *Proc. 3rd Conf. Mech. Beh. of Salt*: 31–44. Clausthal-Zellerfeld, Germany: Trans. Tech. Pub.

Rokhar, R.B., Hauck, R., Staudtmeister, K. & Zander-Schiebenhöfer D. 2000. The results of the pressure build-up test in the brine filled cavern Etzel K102. In *Proc. SMRI Fall Meeting, San Antonio*: 89–103.

Rummel, F., Benke, K. & Denzau, H. 1996. Hydraulic fracturing stress measurements in the Krummhörn gas storage field, Northwestern Germany. In, *Proc. SMRI Spring Meeting, Houston.*

Schmidt, T. 1993. Fracture tests for determining primary stress conditions in salt deposits provide clues to the rock mechanics of salt caverns. In *Proc. 7th Symp. on Salt*: 135–140. Amsterdam: Elsevier.

Staudtmeister, K. & Schmidt, T. 2000. Comparison of different methods for the estimation of primary stresses in rock salt mass with respect to cavern design. In *Proc. 8th World Salt Symposium*: Vol. I, 331–335. Amsterdam: Elsevier.

Van Sambeek, L.L., Bérest, P. & Brouard, B. 2005. Improvements in Mechanical Integrity Tests for solution-mined caverns used for mineral production or liquid-product storage. *SMRI Research Project Report 2005-1*,142 pages.

Wawersik, W. & Stone, C.M. 1989. A characterization of pressure records in inelastic rock demonstrated by hydraulic fracturing measurements in salt. *Int. J. Rock Mech. Min. Sci. & Geomech. Abstr*. 613–627.

Taylor & Francis
Taylor & Francis Group
http://taylorandfrancis.com

The Mechanical Behavior of Salt – Understanding of THMC Processes in Salt –
Wallner, Lux, Minkley & Hardy, Jr. (eds)
© 2007 Taylor & Francis Group, London, ISBN 978-0-415-44398-2

THMC numerical simulation and a solution mining method for thin salt deposits

W.G. Liang & Y.S. Zhao
Mining Technology Institute, Taiyuan University of Technology, Taiyuan, Shanxi Province, China

C.H. Yang
Rock and Soil Mechanics Institute, Chinese Academy of Sciences, Wuhan, Hubei Province, China

M.B. Dusseault
Earth Sciences Department, University of Waterloo, Waterloo, Ontario, Canada

ABSTRACT: Thin salt deposits present different solution mining issues than thick ones. For thin salts, traditional single-well plus annular casings solution mining methods are neither feasible nor economic. Here, we propose and model the hydraulic coalescence solution mining method for thin salt deposits, based on circulation between wells linked through hydraulic fracturing, using the non-salt interfaces to constrain fracture propagation. Solution mining of salt is a chemico-thermal process, and the salt deposit will deform viscously under the combined effects of cavity growth and gravity-induced stresses during the mining process. This is clearly a THMC process (Thermal, Hydrological, Mechanical, Chemical process). In this paper, the coupled THMC process is addressed theoretically, then a set of numerical simulations are carried out.

1 INTRODUCTION

The shape of salt deposits depends on the specific conditions of its emplacement in the geological environment (Jeremic 1994). According to the classification of Jeremic (1994), there are four types of salt deposit shapes resulted from different geological environments: blanket, flexural, dome and vein-like geometries. For flexural and vein-like salt deposits, dry methods or solution mining methods are adopted according to the specific geological disposition of the deposit and economical analysis. However, for salt deposits in blanket or dome geometries, the solution mining method is often preferred because of its high efficiency and excellent economics.

Salt deposits in blanket form are the typical sedimentary deposits which have not experienced significant tectonic movement and deformation, although they may be recrystallized. Such deposits are often horizontally extended over a large area and lateral changes of deposit thickness over distances of a kilometer or less are generally modest. It is thus technologically easy and economically feasible to mine the salt with either a dry mining method for competent, shallow deposits, or a solution mining method for deeper or geomechanically difficult deposits. In dry mining, rooms and pillars are arranged regularly and roof stability guaranteed by proper pillar sizing (long pillars are preferred to square pillars); sufficient salt is left in place to support overburden loads for the operating life of the mining panels. Flanking barrier pillars between mining panels provide large-scale overburden support, and pillars within the mining panels provide roof integrity.

However, different methods will have different economic conditions in blanket salt deposits with different geology and geometry (especially thickness). Unless a particular seam is targeted, such as KCl-rich seams in a thick NaCl sequence, as in Saskatchewan potash mines, it is generally the case that solution mining is the most economic and efficient method, especially for thick (tens to hundreds meters) and deeply buried (>1000 m) salt deposits.

Here, we focus on thin, shallow blanket salt deposits, the thickness of which is less than 10 meters. This type of salt deposit is generally of late Tertiary or Quaternary age, hence the sedimentary history of the deposit is relatively short and the burial depth is generally shallow, from tens to hundreds of meters. For example, a mirabilite deposit in the Yuncheng salt lake area, Shanxi Province, China, is $\sim$6 m thick and is buried $\sim$80 m underground. A glauberite deposit

in Meishan, Sichuan Province, China, is ~9 m thick and is buried ~260 m underground. For these thin salt deposits, mineral exploitation is the sole object, in contrast to the use of the salt bed for storage caverns, which is confined to thick bedded salt deposits or salt domes. For thin, shallow beds, a single-well solution mining method is not feasible economically, and there are technical difficulties as well when the solution cavern diameter grows to several times the deposit thickness. A multi-well hydraulic coalescence and controlled solution mining method has been successfully performed in the above two salt deposits in China.

In this paper, the multi-well hydraulic coalescence and controlled solution mining method will be analyzed theoretically, then THMC coupling aspects in the solution mining of the salt deposit are delineated, and a set of numerical simulations presented. The numerical simulation results are intended to guide field practice so as to improve efficiency and control the process. The method is technologically feasible and economical in practice, and has now been used in several salt solution mines.

2 HYDRAULIC COALESCENCE AND CONTROLLED SOLUTION MINING METHOD

2.1 *Hydraulic fracturing*

Hydraulic fracturing is a widely used technology, originally developed in the oil industry to stimulate oil production, and now used in *in situ* stress measurement and water well stimulation. It is also applied in underground disposal of liquid toxic wastes, in the placement of solid wastes in the form of a slurry, and in geothermal energy exploitation. Because of the large value associated with oil production enhancement with hydraulic fracturing, initiation, geometry and propagation of hydraulic fractures have been intensively investigated (Adachiand & Detournay 2002, Hossain *et al*. 2000, Savitski & Detournay 2002). This rich literature will not be summarized here, but it is necessary to delineate the basic principles of the technology.

Rock is unable to bear extensional strains without evidencing tensile fracture, one of its adverse properties. Experiments demonstrate that the uniaxial tensile strength of rock samples is no more than 1/10 ~ 1/8 of its uniaxial compressive strength, even somewhat less for typical salt rocks. In a porous rock sample loaded both externally with a confining stress σ_n and with an internal pressure p, the sample will break through an induced hydraulic fracture when the inner pore pressure significantly exceeds the external pressure by an amount equal to the tensile strength (σ_t) of the rock.

$$p \geq \sigma_n + \sigma_t \quad (1)$$

In fact, if there are sharp-tipped flaws pervading the rock specimen, the pressure required to propagate a hydraulic fracture will be significantly less than this, and in the limit, when a long, sharp-tipped fracture exists, the propagation pressure can approach a value only slightly higher than σ_n.

Equation (1) is a theoretical expression for the initiation of hydraulic fracturing, where the value σ_t is understood to be an *in situ* value related to the fracture toughness under the specific loading conditions. During hydraulic fracturing, when the pumped water pressure at a point is greater than the local minimum stress (either horizontal or vertical) plus some measure of the tensile resistance of the material, the material will crack perpendicular to the minimum stress direction in the absence of strong anisotropic fabric.

2.2 *Interfaces in bedded salt deposits*

For the deposition of evaporites, there are hypotheses for their formation such as the bar-basin theory, ring theory, fractional sedimentation theory and cyclic sedimentation theory, as well as others (Jeremic 1994). All hypotheses agree on one point: the evaporite is deposited in a particular sequence according to the species concentration in the brine. Experimental evaporation of sea water demonstrates that iron hydroxide is precipitated first, followed in order by calcium carbonate (limestone), calcium sulfate (in the form of anhydrite or gypsum), sodium chloride (common salt), magnesium salts, and lastly potassium and other sodium salts, these last occurring at the top of the deposit. Beds of salts deposited in this manner are known as classic evaporite sequences. In nature, the process of evaporation is subject to many influences and conditions, and erosion, clastic sedimentation and repeated dissolution can take place; hence, salt beds seldom occur in an ideal sequence. Often there are interbeds of gypsum, limestone, dolomite, and shale in rock salt deposits; and moreover potassium and magnesium salts are seldom present in quantity, due either to non-deposition or removal by solution after deposition (Crockford 1949). What is more, the impurities (soil or mud grains are often intermixed in the sequence) and the gravity effect on high density grains affect matters. Soil or mud grains are often deposited prior to salt grains before the crystallization during that cycle, and usually form the bottom of the salt deposit, or are found disseminated between salt crystals. The mudstone at the base becomes the interface between different salt deposits, or sometimes it occurs as a division in the same deposit, which can be observed in many rock cores (e.g. Figure 1, which we obtained during drilling).

Such interfaces can be easily broken while hydraulic fracture is executed around the location because of the effect of a sharp-tipped fracture, combined with the inherent weakness of these interface

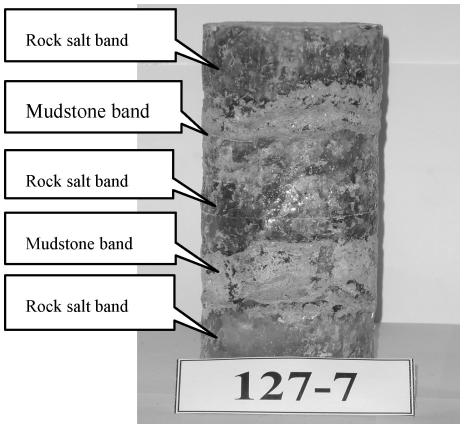

Figure 1. Bedded salt & mudstone composite rock core.

zones. According to equation (1), the interface will be opened as long as the hydraulic pressure is larger than the compressive stress in the mudstone, plus a small effect of tensile strength.

2.3 *Hydraulic coalescence*

Hydraulic coalescence arises as the result of fracture propagation. According to the theory of fracture mechanics (Hubbert & Willis 1957, Shen 1996), a vertical fracture resulting from hydraulic pressurization is generally a wing-type fracture (or an elliptical fracture), and fracture propagation is through a brittle fracture-tip process. It is shown from experiments that the stress intensity coefficient K_I increases with the stress level in the rock mass, and when K_I increases to the critical value K_{IC}, the fracture development is at a critical state of transformation from stability to instability (propagation). Fracture development is probably best described by the condition of fracture extension and brittle fracturing of the rock, expressed as

$$K_I \geq K_{IC} \tag{2}$$

where K_I is the stress intensity coefficient and K_{IC} is the critical stress intensity coefficient of the rock mass, which is in some way also related to its tensile resistance and to the length (scale) of the fracture.

Eqn (2) is the breaking condition for the intact rock under hydraulically-induced fracturing. For a natural weak interface in a blanket salt deposit, the hydraulic fracturing expression in Eqn (1) is also a fracture propagation expression: the water pressure p is related to the stress intensity coefficient K_I, and the effects of σ_n and σ_t are included in the critical stress intensity coefficient K_{IC}. As long as the water pressure is greater than the local vertical stress, which in our case is presumed to be the minimum stress (σ_3) at shallow depth, plus a minor tensile stress effect, the fracture will propagate

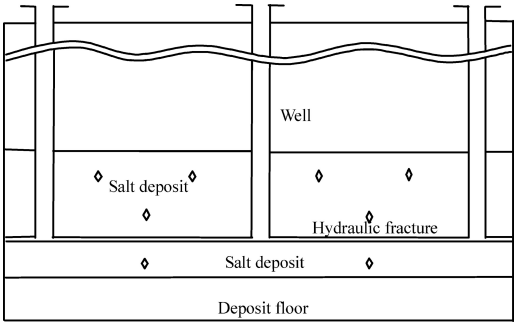

Figure 2. A section plan of multi-well hydraulic fracturing in bedded salt deposit.

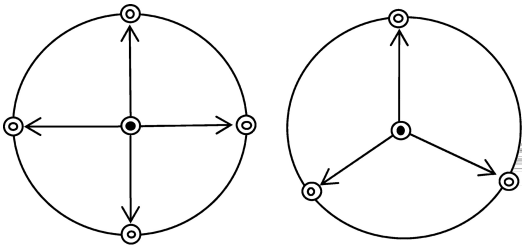

Figure 3. Layout of the multi-wells.

until the critical condition can not be satisfied. Thus, a set of wells can be coalesced through fracturing along the interface of the deposits as shown in Figure 2.

We note that for such salt deposits, an isotropic stress state in the salt with all stresses being approximately equal is most likely because of the creep behavior of salt and the lack of tectonic effects.

2.4 *Controlled solution mining*

After coalescence among the wells (two or more) with the hydraulic fracture propagating along the interface in the deposit, controlled solution mining can be executed. In order to control the shape and size of the solution cavity, a carefully designed scientific production program and solution control plan is important. Here, we take a multi-well plan as an example: at least four wells are drilled, and the layout of the wells is generally in the form of a cross or a star, with one well in the center, as shown in Figure 3.

As all the wells have been coalesced through the fracture along the interface, solution mining can be performed with fresh water pumped into the central well and the brine flowing out of the other surrounding wells. The salt solutioning is controlled on the surface by periodically changing the flowing path of the liquids in the cavity according to the measured operational indicators of the individual wells. The operational

indicators mainly include the flux, the brine concentration and the water pressure for each wells. In this way, the dissolution of the salt deposit is controlled and the solution cavity can be developed close to the designed shape and size. Compared with other approaches that have less control, the multi-well hydraulic fracturing and controlled solution mining approach can significantly improve the recovery ratio of the mineral and minimize the production costs in thin salt deposits. In other words, careful well spacing and control can lead to a high recovery ratio for the salt before well collapse, roof impairment, or other factors arise.

3 THMC COUPLING OF SOLUTION MINING

Mineral dissolution is a physical chemical process during which the solid mineral molecules change to ions dissolved in water which then can migrate from high concentration to low concentration regions under advective forces related to density effects, combined with thermal effects. In the liquid phase itself, we presume that pure Fickian diffusion is inconsequential; the mass transfer process is advectively dominated. However, Fickian diffusion is vital for the dissolution of the salt itself.

The dissolution of the mineral involves energy absorption and release. For example, dissolution of halite or mirabilite absorbs heat, which lowers the solvent (water) temperature and abates the mineral dissolution rate in water, whereas the dissolution of thenardite releases heat, which increases the solvent temperature and facilitates mineral solution until the solute saturation point is reached. Hence, heat transfer exists during the process of mineral solution or solution mining, and it is intimately related with the dissolved mineral quantity. The more mineral dissolved in water, the more heat exchange involved, either being absorbed or released, which in turn affects the mineral solution rate because of the thermal activation effect associated with Fickian processes. This is a Thermal and Chemical (TC) coupling process.

After hydraulic fracture coalescence occurs between drilled wells in a certain area, the crack made by hydraulic fracturing will deform with dual effects of salt dissolution and the stress (including the water pressure and the *in situ* stress). The water pressure will advectively facilitate the contact of water molecules with the salt deposit, hence mineral dissolution is facilitated, and this will widen the fracture aperture. On the other hand, the aperture of the fracture is also affected by the effective stress, which is equal to the *in situ* stress minus the water pressure in the crack, and under the effect of the overburden stress this tends to reduce the aperture, providing that $p < \sigma_v$. The time-dependent deformation of the crack is thus a comprehensive effect of solution and effective stress, even ignoring any possible effects of creep deformation. This is a Hydrological and Mechanical (HM) coupling process.

The process of hydraulic fracturing coalescence and controlled solution mining of salt is a fully THMC process (Thermal, Hydrological, Mechanical, Chemical process). The theory of the respective processes involved is relatively mature and will not be elaborated, but the basic equations will be listed as they form the basis of the numerical simulations.

3.1 *The equation of fracture seepage*

As the fracture aperture is very narrow, liquid flow in the fracture can be considered as laminar seepage. According to the Darcy Law for fluid seepage (Bear 1972),

$$q = KJ \tag{3}$$

where q is fluid flux, K is seepage coefficient and J is hydraulic gradient. In the state of two dimensions in a fracture, the constitutive equation for seepage along the plane of fracture extension can be denoted as follows:

$$\begin{aligned} q_1 &= k_f \frac{\partial p}{\partial s_1} \\ q_2 &= k_f \frac{\partial p}{\partial s_2} \\ k_f &= \frac{w^3}{12\,\mu} \end{aligned} \tag{4}$$

here, q_i is flux, k_f is the fracture seepage coefficient, and w is aperture.

According to the mass conservation, and taking advantage of Gauss' formula, we can write a differential mass balance equation (source-sink) expressing fluid continuity using density ρ and the void index of the fracture, n,

$$\frac{\partial(\rho n)}{\partial t} + \nabla \bullet (\rho V) = I \tag{5}$$

In hydraulic fracture in a salt rock deposit, the fracturing fluid (water is the solute) volume is almost unchanged even though there exists dissolution of salt, so the inner source term I can be considered to be zero in every element, and velocity V can be substituted with flux q, so the liquids seepage motion in the fracture can be described as:

$$div\ (\rho q) = \frac{\partial (n \rho)}{\partial t} \tag{6}$$

As the salt rock deposit is generally tight in texture and the porosity is quite low, the void index n can

be replaced by the fracture aperture w. According to the relation of the fluid compressibility and the fluid density, $\beta = \frac{1}{\rho}\frac{d\rho}{dp}$ (the compressibility β is equal to 1 when the water suffering lower pressure), therefore the right side of Eqn. (6) can be denoted as follows:

$$\frac{\partial(n\rho)}{\partial t} = \rho\frac{\partial n}{\partial t} + n\frac{\partial \rho}{\partial t} = \rho\frac{\partial w}{\partial t} + w\rho\frac{\partial p}{\partial t} \tag{7}$$

Thus, we have the final fracture seepage equation,

$$k_f\frac{\partial^2 p}{\partial s_1^2} + k_f\frac{\partial^2 p}{\partial s_2^2} = \rho\frac{\partial w}{\partial t} + w\rho\frac{\partial p}{\partial t} \tag{8}$$

where p is the fluid pressure in the fracture, w is the fracture aperture, k_f is the fracture seepage coefficient, n is the void index of the fracture, and s_1, s_2 are natural coordinates of the fracture in transverse directions.

3.2 *The equations of rock mass and fracture deformations*

In the initial stage of solution mining, the deformation of the rock mass and the fracture are considered separately. The rock mass is considered as a continuum and the stress equilibrium equation denoted by displacement is (Zhao, 1994)

$$(\lambda + \mu)u_{j,ij} + \mu u_{i,jj} + F_i = 0 \tag{9}$$

The equation of the fracture deformation resulting from hydraulic fracture is

$$\begin{aligned} \sigma_n' &= K_n\varepsilon_n \\ \sigma_n' &= \sigma_n - p \end{aligned} \tag{10}$$

In these equations, λ and μ are the Lamé elastic deformation constants, u is the displacement of the rock mass, and F_i is the bulk force.

What needs to be clarified is that the salt rock is assumed to be elastic in this case; the deformation from creep effects in the salt rock is omitted in this analysis because the strong solubility of salt rock leads to mass fluxes which overwhelm creep deformation during conditions of active dissolution. Furthermore, from a practical point of view, the cases we are dealing with are relatively shallow and low temperature, therefore the magnitude of creep deformation is likely to be negligible in comparison to other effects.

3.3 *Mass transfer equation of the solute*

After hydraulic fracturing and coalescence along the interface, the salt around the fracture will be dissolved into the water and the original fresh water gradually turns into a brine of some concentration which approaches equilibrium by means of the two types of mass-transfer: diffusion and convection. According to the theory of mass transfer (Luikov 1961, Wang 1998), the relation between diffusive flux and concentration of the liquid can be described by Fick's diffusive law,

$$J_i = -D_{ij}\frac{\partial C}{\partial x_j} \tag{11}$$

where J_i is the component of diffusive flux, C is the concentration of fluid changing with location and time, and D_{ij} is the tensor of the diffusivity coefficient. On the basis of the diffusive law and conservation of mass, the equation of diffusion and convection of a dissolving fluid in a salt rock deposit can be derived,

$$\frac{\partial C}{\partial t} = \frac{\partial}{\partial x_i}(D_{ij}\frac{\partial C}{\partial x_j}) - \frac{\partial}{\partial x_i}(CV_i) + I \tag{12}$$

The first term on the right-hand side of Eqn. (12) denotes the transfer of chemical liquid caused by diffusion; the second term denotes the transfer caused by fluid convection between locations of different concentration (pressure-driven because the aperture is small and the vertical height minimal therefore density effects are minimal), t denotes time, and I denotes the term of sources and sinks of concentration which is a function of the solubility of salt mineral, the concentration and the temperature of the fluid. Empirically, it has been observed that: $I = \alpha(-logC) \times T \times t$, based on laboratory results.

3.4 *Heat transfer equation in the solution space*

According to the theory of heat transfer, there are three types of heat exchange, conduction, convection and radiation. There exist heat conduction and convection simultaneously in the dissolution region of a salt deposit being exploited. This can be described by

$$\frac{\partial(\rho_w c_{vw} T_w)}{\partial t} = \lambda_w\nabla^2 T_w - (\rho_w c_{pw} T_w k_{fi} p_{,i}) + Q(x,y,\eta) \tag{13}$$

where ρ_w is the density of the chemical liquid, C_{vw} and C_{pw} are the specific heat coefficients for a unit volume and a unit pressure respectively, λ_w is the heat transfer coefficient, and T_w is the liquid temperature. The first item on the right side of the equation is heat conduction, the second item is heat convection and the third item is a source-sink term for heat, which reflects the heat absorbed or released per unit salt dissolution (exothermic or endothermic), obtained through experimentation.

4 NUMERICAL SIMULATION

4.1 *Method and initial assumptions*

A finite element numerical solution and the methods of coupling and iterative approach were applied to the above THMC coupling model. The initial conditions of water pressure, temperature, and concentration are given; then, the solid deformation and stress field, which initially are functions of water pressure and the local *in situ* stress, are calculated at the initial time t_i, and the fracture aperture can be calculated. Taking these results into the liquid seepage equation, the flow velocity and the distribution of water pressure in the fracture can be obtained. Then we take the calculated results as input to the mass transfer equation, whereby the solution concentration can be obtained. With the obtained solution concentration, a dissolved mass of the mineral and heat emission (adsorption) can be acquired, and a new liquid temperature obtained. At the same time, a new fracture aperture resulting from the coupled interaction of the hydraulic fracture and salt dissolution can be acquired. Substituting the water pressure and dissolved thickness as new data into the equation of solid deformation, the fracture aperture can be obtained for the next calculation circle. Such calculations are continued repeatedly and an assessment of fracture characteristics and the dissolving of the rock salt during the solution mining can be finally obtained.

The boundary or initial conditions of the simulation (Figures 4 and 5) are as follows: for the solid, the load on upper side is evenly distributed, $\sigma = \sigma_o$, for the fluid in the fracture, the flux is given in the injection well as $q = q_0$. The concentration and the temperature of the solution are stipulated in the vicinity of the injection well, $C = 0\ \mathrm{g/cm^3}$, $T = 100°\mathrm{C}$.

According to experimental results (Liang *et al*. 2003, Xu *et al*. 2005), a heat quantity of 241.96 KJ is needed to dissolve 1 kg of the salt mineral mirabilite. The empirical relationship of the mineral solution velocity (V_s) to the temperature (T) and concentration (C) of the liquid solution is expressed as: $V_S = -10(\ln C) \times (0.005T)\ (\mathrm{g/dm^2/h})$.

The numerical results for these simple simulations are shown in Figures 6 to 10.

4.2 *Results and discussion*

Figure 6 is the pressure distribution along the plane section during the initial solution period. The pressure decreases gradually with a particular gradient simply from flow resistance, but this gradient will also decrease with an increase in fracture aperture because of dissolution.

Along the path from the injection to the production well, the solution concentration will increase due to the gradual dissolution of the salt mineral (Figure 7). The concentration around the injection well is the lowest, while the aqueous solution is close to saturation near the production well.

During the progress of mineral solution, the solution temperature decreases rapidly due to the effect

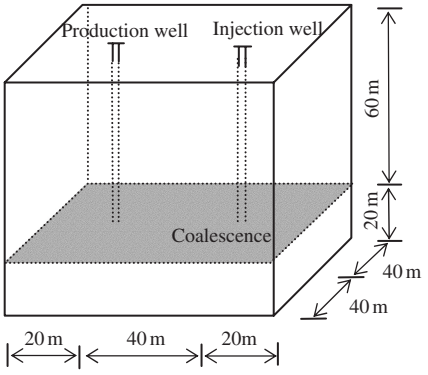

Figure 4. The physical model for double-well convection solution mining.

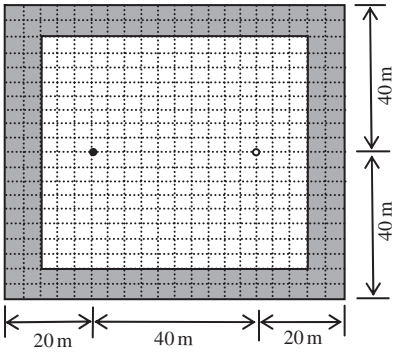

Figure 5. Plane section along the coalesced fracture.

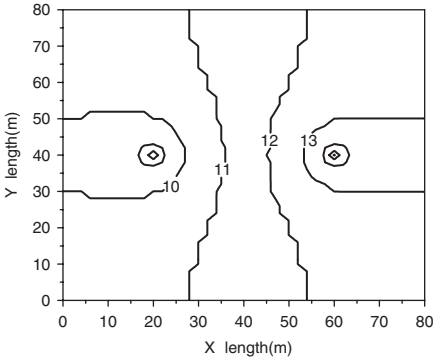

Figure 6. Isobars for water pressure in the solution mined cavity (51 h).

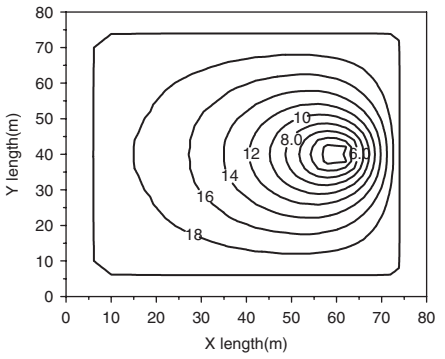

Figure 7. Isolines of solution concentration in the solution mined cavity (51 h).

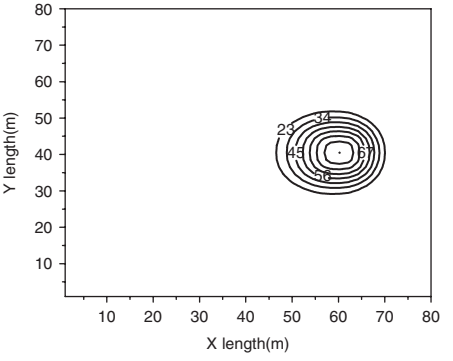

Figure 8. Isotherms of solution temperature in the solution mined cavity (51 h).

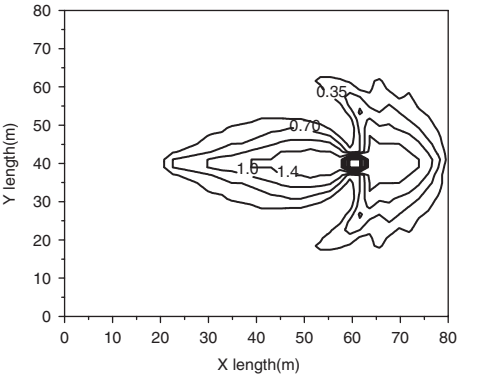

Figure 9. Isolines of mineral solution speed in the solution mined cavity (51 h).

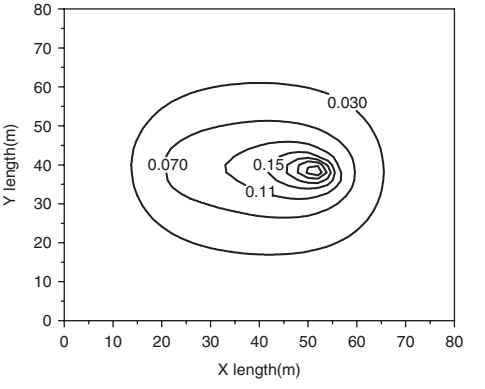

Figure 10. Isopach of the dissolutioned thickness (51 h).

of heat consumption for endothermic thenardite mineral solution (Figure 8). At the same time, the mineral dissolution velocity also decreases, and trends toward zero when the temperature of the solution is lower than 5°C.

The numerical simulation results demonstrate that the dissolution velocity of the mineral around the injection well is much higher than that around the production well (Figure 9), with the combined effect of solution concentration and temperature. With the coupling effect of temperature, concentration and convection of the solution, the dissolved height of the open conduit around the injection well and production well is 0.3 m and 0.1 m respectively. This dissolved height is gradually less along the direction from the injection well to the production well (Figure 10).

All of these results are logical, and the rates and knowledge of the coupled effects can be used to help optimize the process in practice, using numerical simulation to assess the effects of different flux rates, which are induced by pressure differences, which are in turn affected by the dissolution behavior and the field stresses.

5 CONCLUSIONS

For thin salt deposits (less than 10 m), finding a profitable mining method is very important. In this article, the method of hydraulic coalescence solution mining method is presented. It takes advantage of the existence of a non-salt interface in a shallow salt deposit to constrain fracture propagation and fluid flux path.

This method has been successfully used in thenardite deposit mining in Yuncheng, Shanxi Province, China (Liang and Zhao, 2002) and glauberite deposit mining in Pengshan, Sichuan Province, China.

The numerical simulation results are consistent with the monitoring data collected during the solution mining of the thenardite deposit in Yuncheng, the site where it was first demonstrated that the method is viable for the mining of thin, shallow salt deposits.

The numerical model is predicated by the principles of THMC coupling, based on the physics of the process, subject to some simplifications.

Of course, the solution mining process for a mixed salt deposit is a highly complicated process because of inhomogeneities, non-constant stresses that arise because of stress redistribution, different dissolution rates for different minerals, and so on. Although these scientific problems need to be investigated deeply, the model seems sufficiently robust to serve as a practical guide for solution mining in these cases.

ACKNOWLEDGMENTS

This research has been financed by the National Natural Science Foundation of China (No.50174040, 50304011, 50434050) and the Youth Science Foundation of Shanxi Province (No.20041020).

REFERENCES

Adachi, J. I. & Detournay, E. 2002. Self-similar solution of a plane-strain fracture driven by a power-law fluid. *International Journal for Numerical and Analytical Methods in Geomechanics* 26(6):579–604.

Crockford, M.B.B. 1949. Occurrences of Common Salt in Alberta:1–10. Research Council of Alberta, University of Alberta, Edmonton, Alberta.

Hossain, M.M., Rahman, M.K., & Rahman, S.S. 2000. Hydraulic fracture and propagation roles of wellbore trajectory, perforation and stress regimes, Journal of Petroleum and Engineering 27:129–149.

Hubbert, M.K. & Willis, D.G. 1957. Mechanics of Hydraulic Fracturing: 153 ~ 166. Trans. AIME.

Jeremic, M.L. 1994. Rock Mechanics in Salt Mining. A.A.Balkema, Rotterdam, Netherlands.

Liang, W., Li, Z., & Zhao, Y. 2003. Experimental study on solution mining of salt deposit. Journal of Liaoning Technical University (Natural Science Edition). 22(1):54–57 (in Chinese).

Liang, W. & Zhao, Y. 2002. Theory and practice of multi-well hydraulic fracturing in salt deposit. Chinese Journal of Rock Mechanics and Engineering 21(suppl):2579–2582 (in Chinese).

Savitski, A.A. & Detournay, E. 2002. Propagation of a penny-shaped fluid-driven fracture in an impermeable rock: asymptotic solution. International Journal of Solids and Structures 39(26):6311–6337.

Shen, C.K. 1996. Fracture Mechanics. Shanghai: Tongji University Publishing Company.

Xu, S., Liang, W. & Zhao, Y. 2005. Experimental study on dissolution characteristic of glauberite rock salt. Journal of Liaoning Technical University (Natural Science Edition) 24(1):5–7 (in Chinese).

The Mechanical Behavior of Salt – Understanding of THMC Processes in Salt –
Wallner, Lux, Minkley & Hardy, Jr. (eds)
© 2007 Taylor & Francis Group, London, ISBN 978-0-415-44398-2

Usability evaluation of the existing solution-mined caverns for gas storage

C.H. Yang & Y.P. Li
Institute of Rock and Soil Mechanics, Chinese Academy of Sciences, Wuhan, P.R. China

Q.H. Qian
Engineering Institute of Engineering Corps, PLA University of Science & Technology, Nanjing, P.R. China

D.H. Wei
West-east Pipeline Company, PetroChina Company Limited, Beijing, P.R. China

F. Chen & X.Y. Yin
Institute of Rock and Soil Mechanics, Chinese Academy of Sciences, Wuhan, P.R. China

ABSTRACT: Salt rocks are commonly used as the ideal geologic host rocks for storage of gas and crude oil, and are being considered for the disposal of radioactive waste. However, the sediment characteristics of salt rocks in China are greatly different with that in the many other countries. According to the requirement of the West-East Gas Transmission Pipeline Project in China, the existing salt caverns in Jintan Salt Mine, Jiangsu province, were selected to be natural gas storages after appropriate reconstruction. In this paper, the feasibility studies of the gas storage for the construction of Jintan gas storage project were introduced. The geological investigation of the host salt rock formation, the experimental analysis on the mechanical and creep characteristics of salt rocks and mud rocks, numerical study on deformation and stability of these caverns, and in-situ test in brine-filled cavern tests for two salt caverns were presented, respectively. It was concluded that the six salt caverns, Xi-1, Xi-2, Dong-1, Dong-2, Gang-1 and Gang-2 caverns, were suitable to be utilized as gas storages. The conclusions about usability and some suggestion for the old cavern reconstruction and running were as follows:

1. The mechanical and creep test showed that the creep characteristics of rock salt and rock salt containing mudstone were similar. Under differential stress 15.0 MPa, the steady creep strain rate of salt rocks was $(2.5\sim5.0)\times10^{-5}$/h, that of salt rocks containing mudstone was $(1.9\sim3.8)\times10^{-5}$/h, and that of mud rocks containing salt was $(0.5\sim1.0)\times10^{-5}$/h. The steady creep strain rates of the three rocks were in the same order, so the cavern cap rocks would not have to suffer incompatible creep deformations.
2. The breakthrough pressures of the cavern roof rocks were between 6.68∼21.25 MPa, which provided the caverns a good sealability. The six caverns were far from the faults, so, these faults would not affect the stability and sealability of gas storage.
3. The numerical analysis results of cavern stability and deformation showed that, with the increase of internal pressure, the maximum displacement and the volume reduction of salt caverns decrease gradually. Increasing internal pressure could restrain obviously the cavern volume reduction, so, in order to prolong the service life of gas storage, it was strongly recommended that the running time under low internal pressure should be reduced as soon as possible.
4. Allowable operational pressure difference between the adjacent caverns depended on the design service life and the minimum operational pressure. The results showed that the cavern stability could be guaranteed if the operational pressure was between 6 to 14.5 MPa. For safety, it was suggested that the operational pressure difference between two adjacent caverns should not exceed 3.0 MPa.
5. Based on the data of volume reduction rates of each cavern under different pressure reduction rate, a volume reduction rate of 0.015%/day was suggested to be the ultimate limit during a gas extraction phase. The maximum pressure reduction rate should not exceed 0.55 MPa/day during gas extraction phases.

6. The results of brine pressure and discharge tests of Xi-1 cavern and Xi-2 cavern showed that the two caverns were sealed well, and they could withstand the maximum internal pressure up to 15.43 MPa. Under differential stress of 5∼10 MPa, the creep rate of rock salt 2.36×10^{-5}/h obtained from laboratory tests agreed well with the result 2×10^{-5}/h by inversion analysis of the cavern pressure test. Therefore, from the numerical simulation of a former gas storage running process, it was reasonable to adopt the above-mentioned creep parameters of the salt rocks from the Jintan Salt Mine.

ACKNOWLEDGMENTS

The authors acknowledge the financial support from National Natural Science Foundation of China (50374064, 50334060) and the Project of National Basic Research Program of China (2002CB412704).

The Mechanical Behavior of Salt – Understanding of THMC Processes in Salt –
Wallner, Lux, Minkley & Hardy, Jr. (eds)
© 2007 Taylor & Francis Group, London, ISBN 978-0-415-44398-2

The engineering thermal analysis for natural gas storage in deep salt formation

J.W. Chen, C.H. Yang, Y.P. Li & X.Y. Yin
Institute of Rock & Soil Mechanics, Chinese Academy of Sciences, Wuhan, P.R. China

ABSTRACT: Engineering thermal analysis for natural gas storage in deep salt formation is one of the bases of stability evaluation and running control. The presented analysis, in which the actual cavern shape and the thermal field were considered, is based on the variable mass system thermodynamics and it is performed on the FLAC^{3D}. The numerical analysis results show that: the pressures of wellbore top and gas (in cavern) increase linearly during injection process and decrease linearly during production process; the change of temperature of gas and cavern wall obey parabola law during injection process; during production process, the temperature decreases firstly, then the decrease tendency slows down, and the temperature even increases a few at last; the temperature of wellbore bottom and top changes as that of gas does during the whole cycle but the former change magnitude is smaller than the later one. Though the influence range of temperature field during the performance is only 7–15 m around the cavern, the temperature gradient is very greater comparatively. This high gradient of temperature may affect the stability of the cavern.

1 INTRODUCTION

The salt caverns are utilized widely as gas storage for its little environment effect, high safety and low expenditure in industry application. The first application of storage cavern for natural gas in solution mined salt caverns in China (Jintan city, Jiangsu province) will come to be reality soon.

The pressure and temperature in and around the caverns will change during the natural gas injection and production process. In this case, analysis of temperature and pressure of gas (in cavern) and simulation of temperature and stress field of the wall rock are very important work for stability analysis of the storage caverns.

However, reports of engineering thermal analysis for gas storage are not many (Hagoort, 1997, Tan et al., 2000, Wang & Bu, 2001, Tan et al., 2004). Because of the complicated mathematical model, most scholars assumed cavern shape to be cylinder or sphere (e.g. Tan et al., 2000., 2004), some scholars also proposed simple method based on the variable mass system thermodynamics for the rigid container (Wang & Bu, 2001).

In this paper, the mathematical model was established based on the variable mass system thermodynamics (Wu & Ma, 1983), and the proposed method was applied to predict the temperature and stress (pressure of gas) of Jintan cavern during gas injection and production.

2 MATHEMATICAL MODELING

2.1 *Continuity equation*

Assuming temperature and pressure to be homogenous in the cavern, and the change of the volume V of the cavern to be negligible, we could get:

$$\frac{P_r V}{RZ_r T_r} = \frac{P_i V}{RZ_i T_i} \pm \frac{\rho_{SC} \Delta G d\tau}{M_g} \tag{1}$$

Where i denotes the initial condition (at timeτ); r denotes the finally condition (at time$\tau + d\tau$); ΔG is the volume of gas injection per time(negative denotes gas production); Z is the compressibility factor; T is absolute temperature; R is gas constant; P is pressure of natural gas; M_g is molecular weight of natural gas; $d\tau$is time-step; and ρ_{SC} is density of natural gas in standard condition.

2.2 *Energy equation*

According to variable mass system thermodynamics (Wu & Ma, 1983):

$$\delta Q = dU + h_e \delta m_e - h_i \delta m_i + \delta W_{CV} \tag{2-a}$$

during the gas injection, $\delta m_i = G_{in}\rho_{SC}$, $\delta m_e = 0$ and the shaft power is negligible ($\delta W_{CV} = 0$), thus:

$$um = u_i m_i + \Delta m h + Q \tag{2-b}$$

Where i denotes the injection; e denotes the production; U is internal energy, $U = H - PV$; Q is quantity of heat change of external boundary; m is mass of natural gas, and $m = \rho_{SC} G_{SC}$; H is enthalpy, then the thermodynamics can be written as (Chen Guitang, 1998):

$$dH = C_P dT - \left[V - T\left(\frac{\partial V}{\partial T}\right)_P \right] dP \tag{3}$$

Based on Berthelot's equation of gas state, the compressibility factor can be described as:

$$Z = 1 - \frac{9P}{128P_c}\frac{T_c}{T}\left(\frac{6T_c^2}{T^2} - 1\right) \tag{4}$$

where subscript c denotes the critical state of gas.

Considering the gas injection or production to be continuing, and the heat capacity $C_P \approx const$, the equation of enthalpy from equation 3 and 4 can be written as follows:

$$\begin{aligned} H &= \int_0^{T_R} C_P dT + \int_0^{P_R} \frac{9RT_c}{128P_c}\left(\frac{18T_c^2}{T^2} - 1\right) dP \\ &= C_p T_R + \frac{9RT_c}{128P_c}\left(\frac{18T_c^2}{T^2} - 1\right) P_R \end{aligned} \tag{5}$$

$$\begin{aligned} U_R &= H_R - P_R V_R \\ &= (C_p - R)T_R + \frac{9RT_c}{128P_c}\left(\frac{24T_c^2}{T_R^2} - 2\right) P_R \end{aligned} \tag{6}$$

Thus, we obtain the energy equation as follows (ΔG is negative if gas production):

$$\begin{aligned} &\rho_{sc}(G_i + \Delta G d\tau)\left[(C_P - R)T_r + \frac{9RT_C}{128P_C}\left((\frac{24T_C^2}{T_r^2} - 2)P_r \right) \right] \\ &= \rho_{sc} G_i \left[(C_P - R)T_i + \frac{9RT_C}{128P_C}\left(\frac{24T_C^2}{T_i^2} - 2)P_i \right) \right] + \\ &\rho_{sc}(\Delta G d\tau)\left[C_P T_r + \frac{9RT_C}{128P_C}\left((\frac{18T_C^2}{T_g^2} - 1)P_g \right) \right] + Q \end{aligned} \tag{7}$$

Where T_g denotes temperature of natural gas ($T_g \neq T_i$ during injection, while $T_g \approx T_i$ during production); P_g denotes pressure of natural gas ($P_g = P_i$).

2.3 *Heat change equation*

The non-steady heat conduction between natural gas and wall rock, and the heat convection on the interface between gas and cavern are both considered, but thermal radiation is negligible.

The equation of non-steady heat conduction is:

$$\frac{\partial T}{\partial \tau} = a\left(\frac{\partial^2 T}{\partial x^2} + \frac{\partial^2 T}{\partial y^2} + \frac{\partial^2 T}{\partial z^2}\right) + \frac{q_{in}}{C\rho} \tag{8}$$

Where a is temperature conductivity; ρ is density of salt rock; q_{in} is heat-generation, and $q_{in} = 0$.

The boundary conditions are:

initial temperature field: $T|_{\tau=\tau_0} = T_0(x, y, z)$;

on the interface: $-\lambda \frac{\partial T}{\partial n} = h(T_{cave} - T_r)$

then the total quantity of heat change is as follows:

$$Q = h(T_{cave} - T_r)\sum S \cdot d\tau \tag{9}$$

Where h is convection heat-transfer coefficient; $\sum S$ is total area of convection heat-transfer; T_{cave} is temperature of interface between gas and cavern.

2.4 *Equation of gas flowing in wellbore*

Assuming no power exporting from wellbore, y-direction to be down and the position of wellbore top to be $y = 0$, we could get:

$$\frac{dP}{\rho} - g\cos\alpha dL + udu + \frac{2fu^2 dL}{2d} = 0 \tag{10-a}$$

$$u = \frac{w}{\rho A} = Z\frac{m}{24\times 3600}\times\frac{T}{293}\times\frac{1.01325\times 10^5}{P}\times\frac{4}{\pi d^2} \tag{10-b}$$

$$\rho = \frac{MP}{ZRT} = \frac{28.97\gamma_g P}{ZRT} = \frac{28.97\gamma_g P}{8314.413ZT} \tag{10-c}$$

Natural gas flowing in wellbore is turbulent flow, according to Wood's experimental expression, the fanning's friction coefficient is written as follows:

$$f = \alpha + \beta \mathrm{Re}^{-\gamma} \tag{11}$$

Parameters of the expression are:

$$\alpha = 0.026(\varepsilon/d)^{0.225} + 0.133(\varepsilon/d) \qquad \beta = 22(\varepsilon/d)^{0.44}$$
$$\gamma = 1.62(\varepsilon/d)^{0.134}$$

the Renold's number is: $\mathrm{Re} = (wd)/(A\mu)$

where g is gravity acceleration; L is length of wellbore; f is friction coefficient; u is velocity of natural gas; d is hydraulic diameter, defined as $d = 4A/S$; A is area of cross section of wellbore; S is perimeter of cross section of wellbore; w is the flux of mass; ε is

roughness of wellbore; μ is viscous coefficient; V is kinematic viscosity coefficient; α is declining angle of wellbore.

From the assumption that 1) the wellbore is vertical; 2) change of velocity along wellbore is negligible; 3) gradient of temperature is constant along wellbore; 4) friction coefficient is constant, the equation 10-a can be written as:

$$\frac{dP}{\rho} - gdL + \frac{2fu^2 dL}{2d} = 0 \tag{12}$$

Thus, we could get the pressure of wellbore bottom P_{wh} as follows (Lingen P. L. 1974):

$$P_{wh} = P_{bh}\left\{\begin{array}{l}\left(1-\dfrac{\Delta T}{T_{bh}}\right)^{2N_{gp}T_{bh}/\Delta T} \\ +\dfrac{N_{fg}}{2(N_{gp}-\Delta T/T_{bh})}\left(1-\dfrac{\Delta T}{T_{bh}}\right)^2 \\ \times\left[\left(1-\dfrac{\Delta T}{T_{bh}}\right)^{2(N_{gp}T_{bh}/\Delta T-1)} -1\right]\end{array}\right\}^{1/2} \tag{13}$$

Where subscript bh denotes the position being $y=0$, wh denotes the position being $y=L$, and av means average; $\Delta T = T|_{y=0} - T|_{y=L}$ is the difference of temperature between top and bottom of the wellbore.

During production, assume the bottom of wellbore is $y=0$ and y-direction is up, thus (Hagoort 1992):

$$\frac{dP}{\rho} + gdL + \frac{2fu^2 dL}{2d} = 0 \tag{14}$$

For solution of equation 14, we set $N_{gp} = -N_{gp}$ and we can get the solution according to equation 13.

2.5 *The relation of temperature and pressure between wellbore top and bottom*

Because of very high velocity of gas flowing along wellbore, we can premise entropy to be constant, so the temperature and pressure of top and bottom of wellbore could be connected with each other:

$$P_{bh}^{(k-1)/k} T_{bh}^{-1} = P_{wh}^{(k-1)/k} T_{wh}^{-1} \tag{15}$$

where k is the specific heat capacity ratio.

3 DISCUSSION OF THE SOLUTION

During the gas injection and production, initial condition and some parameters are different, so the method of the solution, especially of the gas flowing equation and the energy equation, may be different.

3.1 *Solution of gas flowing equation*

During the gas production, natural gas flux is known, pressure and temperature of wellbore bottom are equal to those of gas in cavern (the known parameters are the temperature and pressure of wellbore bottom).

For case of gas injection, temperature of the wellbore top is constant, pressure of the wellbore bottom is equal to that of gas(in cacvern), but temperature of wellbore bottom and gas are different(the known parameters are the temperature of wellbore top and the pressure of wellbore bottom).

The equations of gas flowing along wellbore are little different between those in the case of gas production and injection, but the solution is quite different. However, we can choose appropriate coordinate to obtain the similar solution of the equation.

3.2 *Quantity of heat exchange*

We could get temperature of the cavern wall T_{cave} and the quantity of heat Q from the equation 8 and 9, but it's very difficult to get the analytic formula of T_{cave} for any cavern shape, therefore, some scholars supposed the cavern shape to be cylinder or sphere, so the aimed is to solve the equation group comprised of equations 1, 7, 8, 9, 13 and 15(Tan Yufei et al., 2000, 2004).

4 METHOD OF SOLUTION

We propose to solve the mathematical model based on the well established FLAC^{3D} software of the ITASCA company with some assumption. With this method, any cavern shape and three dimension temperature field could be taken into account.

4.1 *Hypothesis and solution*

From these hypothesis: 1) in the cavern, temperature and pressure of gas is homogenous; 2) the average temperature of different monitor sites(about 10 sites) on the cavern wall is the temperature of cavern wall(T_{cave}), the formula 1 and 4 could be inverted as $P_r = f(P_i, T_i, T_g, T_r)$, and the energy equation could be written into $g(P_i, T_i, T_g, T_r) = 0$. Based on Newton's method, when:

$$|g(P_i, T_i, T_g, T_r)| \le \varepsilon \tag{16}$$

the iteration is convergent and we could get T_r.

The flow chart of the solution for injection process is shown as figure 1. The flow chart for production process is similar to that for injection process except for not substituting T_g to Equation 7 and gas flow calculation in wellbore.

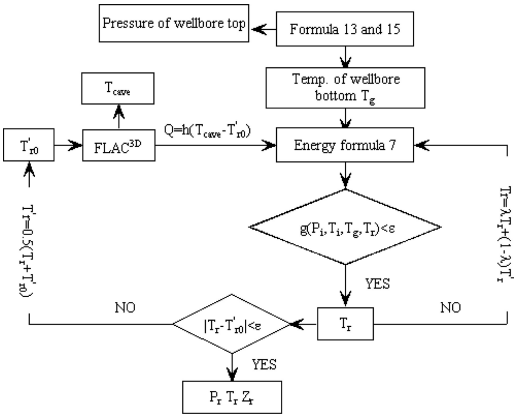

Figure 1. The flow chart of the analysis during gas injection process.

4.2 *Modeling and initial condition*

According to the designed cavern shape of Jintan, vertical direction is z-axes, the model range of $z \geq 0$ is $\frac{z^2}{100^2} + \frac{x^2+y^2}{35^2} \leq 1$, the range of $z \leq 0$ is $x^2 + y^2 + z^2 \leq 35^2$, depth of $z = 0.0$ is 1350.0 m, the range of the entire model is:

$$0.0 \leq x \leq 210.0;\ 0.0 \leq y \leq 210.0\ ;\ -210.0 \leq z \leq 600.0$$

The model comprises of 7088 nodes and 6090 zones, the zones are all hexahedron.

Temperature at the top of the model ($z = 600$ m) is 33.8°C, at the bottom ($z = -210$ m) is 51.944°C (the gradient of temperature is 2.24°C/100 m, temperature of the earth surface is 17°C), $x = 0.0$ and $y = 0.0$ are adiabatic planes. The initial temperature of gas in the cavern is 45°C during production and 30°C during gas injection.

4.3 *Parameters*

Of salt, density is 2200 kgm^{-3}; Specific heat is 859 $Jkg^{-1}K^{-1}$; Thermal conductivity is 4.8 $Wm^{-1}K^{-1}$, Convective heat-transfer coefficient is 100 $Wm^{-2}K^{-1}$.

Of cavern, Max/min pressure is 14.5/6.5 MPa; Max/min temperature is 318/303 K.

Of wellbore, length is 1250 m; Inner diameter of wellbore is 0.224 m; Roughness is 3.0×10^{-4} m, Temperature of wellbore top during injection is 298 K.

Of natural gas, Critical pressure is 4.5 MPa; Critical temperature is 185 K, density ratio is 0.5192; Specific heat is 38 $Jmol^{-1}K^{-1}$ and Specific heat ratio is 1.345.

Capacity of cavern is obtained from the following formula:

$$G = \frac{VM_g}{R\rho_{SC}}\left(\frac{P_{\max}}{Z_{\max}T_{\max}} - \frac{P_{\min}}{Z_{\min}T_{\min}}\right) \tag{17}$$

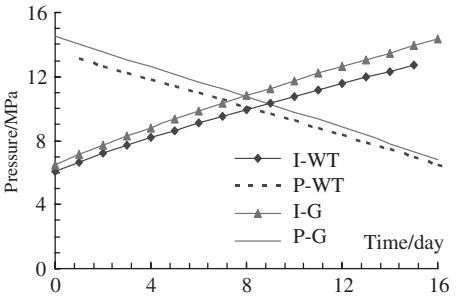

Figure 2. Pressure of wellbore top and gas(in the cave) during production and injection process(I denotes gas injection, P denotes gas production, WT denote wellbore top and G denote gas).

Where G is capacity of the cavern; V is the volume of the cavern (0.34636×10^6 m^3).

From Equation 17, G_{max} is 49.247×10^6 m^3, G_{min} is 21.688×10^6 m^3 and flux ΔG is 19.936 m^3s^{-1} (in the standard condition and the total time is 16 days during injection or production performance).

5 NUMERICAL SIMULATION

The time-step is one day for this numerical simulation, we predicted pressure and temperature of gas (in the cavern), temperature of cavern wall, temperature and pressure of wellbore top and bottom, compressibility factor of nature gas (showed as figure 2–6) and thermal field around the cavern (figure 9 is the temperature filed on the 16th day in the case of gas production).

Numerical simulation result shows that, pressure of gas (in the cavern) and wellbore top both change linearly during injection and production process; Pressure of gas increases more rapidly than that of wellbore top during gas injection, but decreases more slowly during gas production (shown as figure 2).

Temperature of cavern wall and gas decrease rapidly at beginning, while increases at last during gas production process. The trend of temperature variation is similar to some scholar's works (Tan et al., 2000, 2004). But during gas injection, the temperature increases at beginning, then decreases slowly at last (see figure 4). The influence range of temperature field is only about 13 m along x-axes (horizon) and about 15 m in the z-axes direction(vertical) during gas injection process(see figure 7), while x-axes about 7 m and z-axes about 10 m during production process (see figure 8). Range of temperature influenced is small compared with the cavern size, but the temperature gradient is high comparatively near the cavern, which may affect the stability of the cavern.

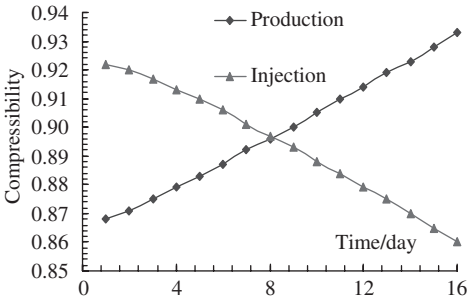

Figure 3. Compressibility factor of gas during production and injection process.

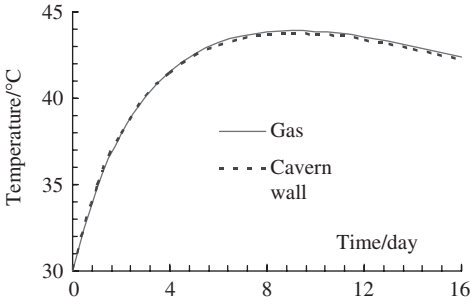

Figure 4. Temperature of gas and cavern wall during injection process.

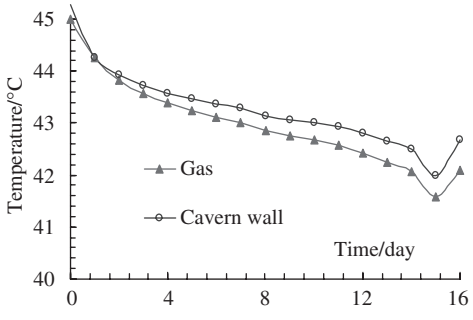

Figure 5. Temperature of gas and cavern wall during production process.

Temperature tendency of wellbore top and bottom is similar to that of the cavern, but the magnitude is smaller (show as figure 6).

6 CONCLUSION

Engineering thermal analysis for gas storage in deep salt formation is one of the bases of stability evaluation and running control for the cavern. The actual cavern shape and three dimension temperature filed can be taken into account in the presented method. We have also applied the proposed method to simulate temperature and pressure of gas and cavern based on Jintan designed cavern. The numerical predictions will be useful for the management and evaluation of stability of the caverns.

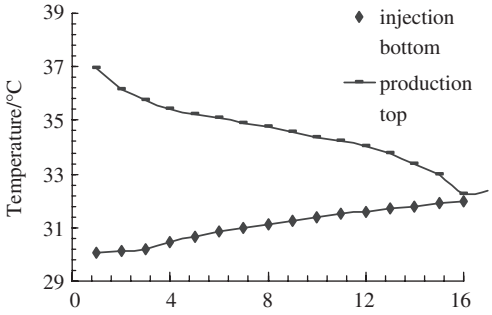

Figure 6. Temperature of wellbore bottom during injection and of wellbore top during production process.

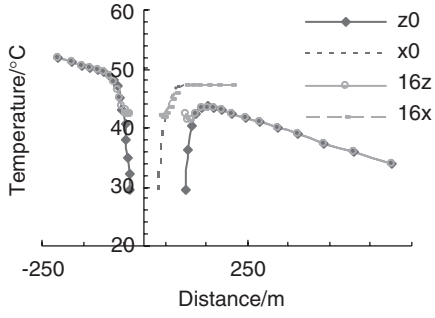

Figure 7. The influence range of temperature field along x-axes and z-axes during gas injection process(0 denotes the first day and 16 denotes the 16th day).

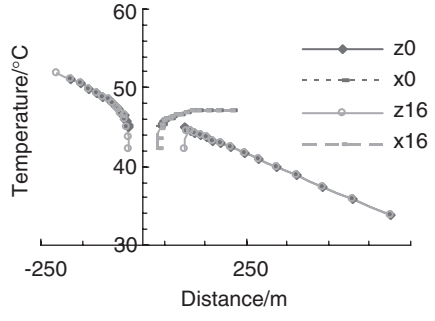

Figure 8. The influence range of temperature field along x-axes and z-axes during gas production process(0 denotes the first day and 16 denotes the 16th day).

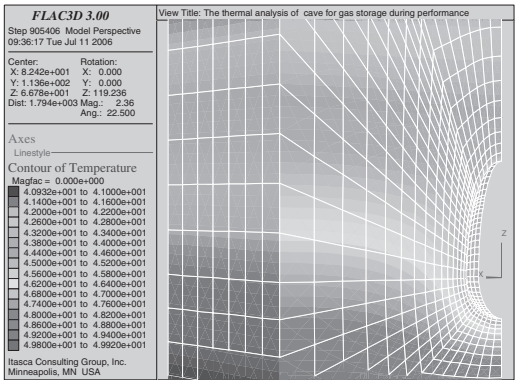

Figure 9. The temperature contour of the wall rock on the 16th day during gas process.

ACKNOWLEDGMENTS

The authors acknowledge the financial support from National Natural Science Foundation of China (50434350, 50334060) and the Project of National Basic Research Program of China (2002CB412704).

REFERENCES

Chen Guitang. 1998. Thermodynamics of Engineering. Beijing Institute of Technology press: Beijing, China.

Hagoort J. 1992. Principle of gas resource engineering. Petroleum Industry Press: Beijing, China.

Jacques Hagoort. 1997. Simulation of production and injection performance of gas storage caverns in salt formations. SPE Reservoir Engineering11: 279–281.

Lingen P. L. 1974. Description of Groningen Gas Well performance suitable for medium and long range planning. SPE paper 4816 presented at the SPE European Spring Meeting(1974 of the Society of Petroleum Engineers.)The Netherland, May: 29–30.

Tan Yufei, Lian Leming, Yan Mingqing 2000. Dynamic model and its application for simulation of gas storage in salt formation. Journal of coal gas & heat energy20(2): 91–94[in Chinese]

Tan Yufei, Chen Jiaxin, Xiao Xiangjun. 2004. The parameters of engineering thermal dynamics during production and injection performance of gas storage in salt[J]. Storage of Gas 23(5): 16–18 [in Chinese].

Wang Li & Bu Cong. 2001. Estimation of the pressure and temperature of salt formations for gas storage during production and injection performance. Petroleum layout and design12(2): 32–33[in Chinese].

Wu Peiyi & Ma Yuan. 1983. Variable mass system thermodynamics and its application. Beijing, China: High Education Press.

The Mechanical Behavior of Salt – Understanding of THMC Processes in Salt –
Wallner, Lux, Minkley & Hardy, Jr. (eds)
© 2007 Taylor & Francis Group, London, ISBN 978-0-415-44398-2

Investigation on the long-term stability of gas storage in Jintan Salt Mine

X.Y. Yin, C.H. Yang, Y.P. Li & J.W. Chen
Institute of Rock & Soil Mechanics, Chinese Academy of Sciences, Wuhan, P.R. China

ABSTRACT: The solution-mined salt caverns can be utilized to store the natural gas and also the high-radioactive waste, so it is important to analyze the long-term stability of salt caverns. A user-defined creep constitutive model is compiled as a dynamic link library (DLL) file that can be loaded whenever it is needed and implemented into the software FLAC^{3D}. The stability after excavation and the law of the long-term volume convergence ratios of salt caverns selected in Jintan Salt Mine have been studied by the numerical method. The computation parameters are obtained from previous experimental results. The results show that the higher internal pressure will benefit the stability of salt caverns. The volume convergence ratios of salt caverns are below 22 percent as the running internal pressure of gas storage varies from 6 to 14.5 MPa. Based on the results of the numerical analysis, some useful advice has been provided for the construction and management of the gas storage in Jintan Salt Mine.

1 INTRODUCTION

Underground gas storage is one of the effective approaches to solve the seasonal variation of gas consumption. Rock salt is a unique medium with many merits, such as its excellent physical properties, compact fabric, very low permeability and porosity, good creep behavior, simple hydrogeologic condition and so on. In addition, it can adapt well to the variation of the gas pressure in a cavern due to its steady mechanical behavior. It is well known that the solution-mined salt caverns can be utilized to store natural gas. As early as during the Second World War, Canada began firstly to store liquid or gaseous energy. Hereafter, during "Suez Crises" England took the lead to start the crude oil storage (Thoms & Gehle 2000). Ten years later the natural gas storage also started in US and Canada. So far more and more underground storages have been built in solution-mined salt caverns in some developed countries. Numerous researches on the reconstruction of solution mined salt caverns and the mechanical behavior of rock salt have been carried out. Schulze et al. (2001) studied the permeability and damage expansion of rock salt in detail. The thermodynamic property of rock salt was investigated by Pudewills & Krauss (1999) using numerical methods. Now some progresses have been made in the solution mining technology of rock salt, in maintaining the stability of salt caverns, and in the well logging technology. However, considering that the sediment characteristics of rock salt in China are greatly different from many other countries, the assessment of the long-term stability of salt caverns still needs further research.

According to the requirement of Gas Transmitting from West to East Project in China, two pre-existing salt caverns in Jintan Salt Mine are selected to store natural gas. The stability after excavation and the law of the long-term volume convergence ratios of the two preferred salt caverns 1 and 2 in Jintan Salt Mine are studied by the finite difference software FLAC^{3D}.

2 THE COMPUTATION MODEL

2.1 *The geologic conditions of Jintan Salt Mine*

According to the borehole data, the rock salt distribution of Jintan Salt Mine is comparatively steady and gentle. As a whole the rock salt layer inclines to north- west and the dip angle is less than 10°. The rock salt body occupies an area of 12 km in the long axis and 5.6 km in the short axis. Its thickness varies from 67.85 m to 230.95 m. The central part of the rock salt body is thicker than the outer. The depth of the top surface of rock salt layers is 850 m to 1100 m. The longitudinal section configuration is relatively simple. From bottom to top, the rock salt bed is composed of three main salt mine layers, layer I, layer II and layer III. The average thickness of layer I is 58 m. The second rock salt layer distributes uniformly with a thickness between 50 m and 80 m (the average thickness is 64 m).

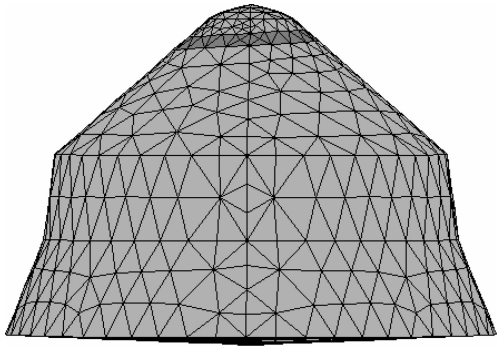

Figure 1. Computation model of salt cavern 1.

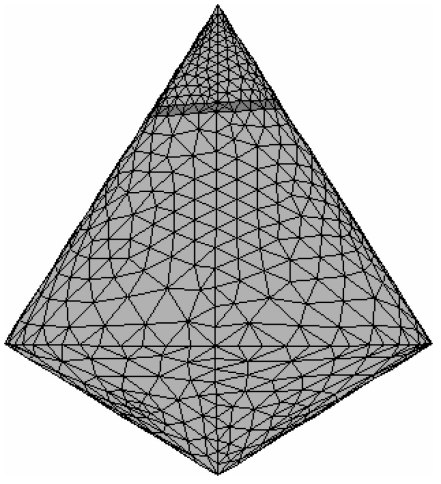

Figure 2. Computation model of salt cavern 2.

The thickness of the third rock salt layer is only 30 m to 50 m. It should be noted that there are two obvious mud rock interlayers: one between layer I and layer II, and the other between layer II and layer III. The thickness of the interlayer between layer I and layer II varies from 0.6 m to 4.9 m (the mean thickness is 3 m), and the thickness of the other interlayer varies from 0.3 m to 4.8 m (the mean thickness is 2.5 m). The rock layers above and below the rock salt layer are mainly composed of mudstone containing rock salt and mudstone.

2.2 *The model of salt caverns as gas storage*

According to the sonar measurement data of the caverns, the model parameters of two caverns are as follows:

The two salt caverns are both pyramidal. Their maximum radii are 52.6 m and 44.4 m respectively, and the thicknesses of the salt rock roofs are 26.5 m and 11.9 m, respectively. The computation models of the two salt caverns are shown in Figure 1 and Figure 2.

2.3 *The overall computation model*

The numerical model needs to be simplified appropriately before analyzing the stability of salt caverns. These simplifications include: the rock layers are assumed to be isotropic homogeneous continuum; the interfaces between rock layers bond perfectly, that is to say, the displacement of each bonded rock layer is continuous. In practical numerical computation, the three-dimensional model is established by the software FLAC^{3D} according to the geological conditions in Jintan Salt Mine and also their plan position. The computation domain is a cube, whose total height (including three rock salt layers, two mud rock interlayers, and, in addition, two mud rock layers) is 900 m. The average total thickness of all the rock salt layers and mud rock interlayers is 146.67 m. In addition, the area of the bottom surface is 800 m × 800 m. In the model, the x-z plane is horizontal and the y-axis is in the vertical direction. The meshes around the salt caverns are fine, while the meshes away from the salt caverns become gradually coarser. The vertical section of computation model is shown in Figure 3.

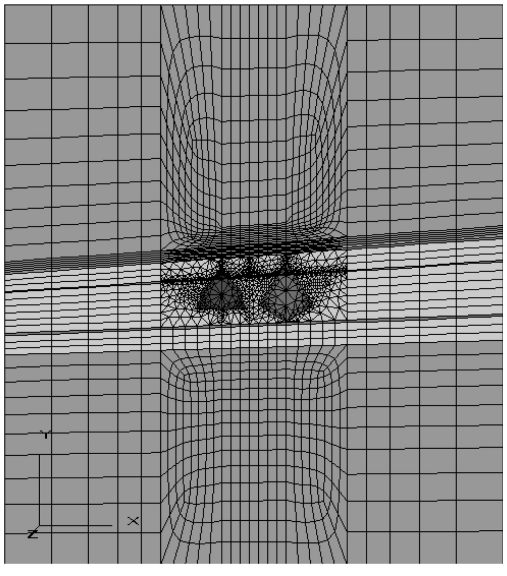

Figure 3. Schematic diagram of computation model's vertical section plane. The rock salt layers and the interlayers are indicated by the finer mesh.

3 CALCULATION CONDITIONS

3.1 *Initial stresses*

According to the geological data in Jintan Salt Mine, the rock layer is approximately horizontal, so the geological tectonic stress is small. The thickness of the overburden rock is 525.5 m. The vertical component of the initial stress can be derived from the depth and the average density of stratum. The magnitude of the stress gradient along depth direction is the bulk density of each rock stratum. Because the center of salt cavern 1 and cavern 2 is in about 1000 meter depth and the depth domain of calculation model is 525.5 m to 1425.5 m, the coefficient of lateral stress $\lambda^* = \sigma_{\text{vertical}}/\sigma_{\text{horizontal}}$ is set to $\lambda^* = 1.0$, i.e. the state of stresses is assumed to be generally isotropic. In addition, to investigate the effect of the lateral stress coefficients λ^* on the long-term volume loss of salt caverns, the effect of different lateral stress coefficients is also studied in the numerical simulations.

3.2 *Boundary conditions*

Considering the effect of these caverns on the state of stresses in the rock, this will be weak enough in a distance of 250 m (five times away from cavern radius) to be neglected. Therefore, the boundary conditions of the numerical model are taken as follows: the top surface of the model has a free stress border, and the magnitude of the vertical uniform stress is 12.09 MPa; the bottom surface and the other four surfaces are fixed in their own normal directions, i.e. no lateral deformation is allowed at the vertical border surfaces of the model.

4 THE NUMERICAL SIMULATION OF STABILITY OF SALT CAVERNS

4.1 *The stability after excavation*

In computation, Mohr-Coulomb elasto-plastic model in software FLAC^{3D} has been used to analyze the stability of salt caverns after excavation. The computation parameters, shown in Table 1, are obtained by a series of mechanical experiments.

The excavation in FLAC^{3D} can be simulated through a null zone that is used to represent the removed or excavated material. Two calculation cases are adopted to analyze the effect of different internal pressures on the stability of salt caverns after excavation. Case 1: the internal pressure is 6 MPa; Case2: the internal pressure is 11 MPa. The plastic zone around the salt caverns, the displacement vector, and the contour of vertical stresses are shown in Figure 4, Figure 5 and Figure 6.

Table 1. Computation parameters.

Rock layer	Elastic module (MPa)	Friction angle (°)	Density (kg/m^3)
Mudstone	10000	35	2650
Rock salt	18000	30	2300
Mudstone interlayer	4000	30	2650
	Cohesion (MPa)	Tensile strength (MPa)	Poisson
Mudstone	1.0	1	0.27
Rock salt	1.0	1	0.27
Mudstone interlayer	0.5	0.5	0.3

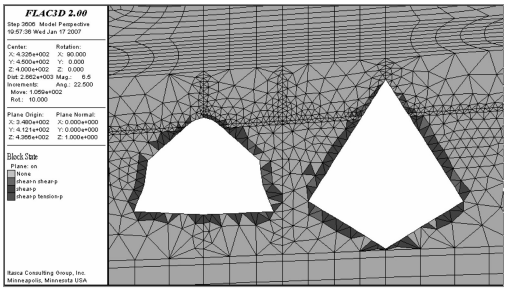

(a)

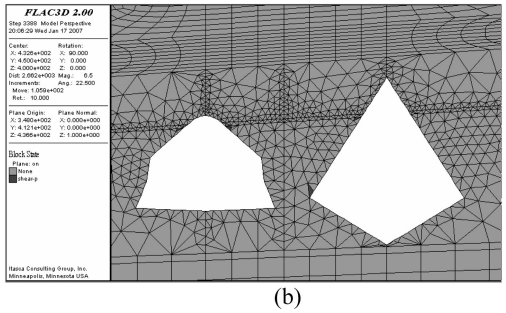

(b)

Figure 4. Plastic zone after excavation;(a) The internal pressure at 6 MPa; (b) The internal pressure at 11 MPa.

From the calculation results, it is obvious that the plastic zones around the caverns are broader in the first case than those in the second case (Figure 4). This indicates that the amount of the internal pressure influences directly the stability of salt caverns. In both cases, the displacements focus on the excavation faces of caverns in the normal direction. The displacement becomes smaller with increasing distance from the excavation faces. In both cases the maximum of the displacement occurs at the bottom of salt cavern. At cavern 1 it is 4.95 cm in case one (6 MPa internal pressure) and 3.5 cm in case two (11 MPa internal

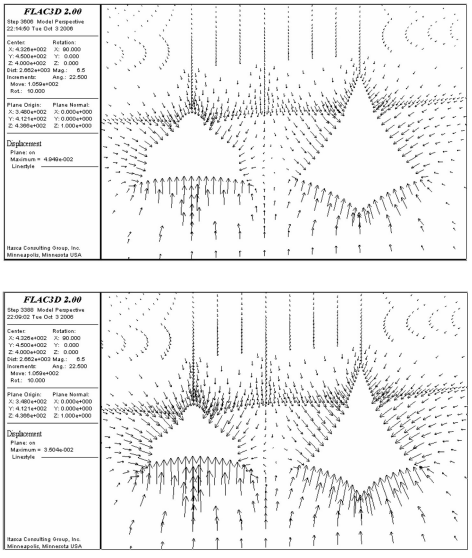

(a)

(b)

Figure 5. Displacement Vector diagram after excavation; (a) The internal pressure at 6 MPa; (b) The internal pressure at 11 MPa.

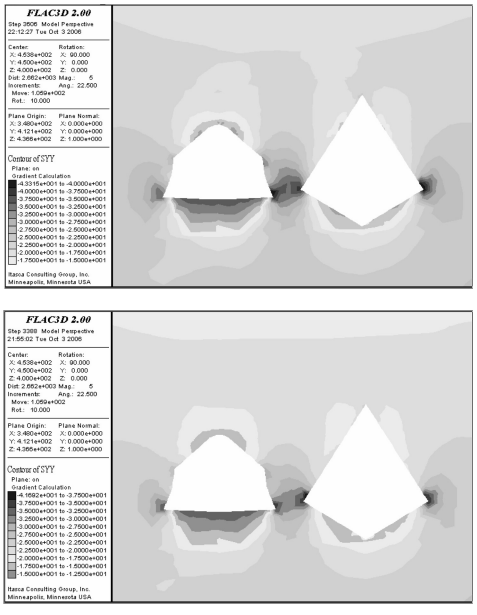

(a)

(b)

Figure 6. Contour map of vertical stresses after excavation; (a) The internal pressure at 6 MPa; (b) The internal pressure at 11 MPa.

pressure). In case one, the vertical displacements at the top of salt cavern 1 and salt cavern 2 are 1.82 cm and 0.82 cm, respectively, and those at the bottom are 4.95 cm and 3.66 cm, respectively. In case two the vertical displacements at the top of salt cavern 1 and cavern 2 are 1.17 cm and 0.52 cm respectively, and those at the bottom are 3.5 cm and 2.65 cm respectively. It is shown in Figure 6 that stress concentrations occur in the interlayers as well as at the top, at the bottom and in the elements at about the maximum radius of a salt cavern.

4.2 *Creep calculation*

So far, a lot of research work (Langer 1993, Peach 1996, Munson 1997, Yang et al. 1999, Yang et al. 2000, Han et al. 2001, He et al. 2002, Yang et al. 2002, Yan et al. 2003) on rock salt has been carried out owing to its complex mechanical behavior. Based on the creep test of rock salt, nearly all the domestic and foreign scholars believed that rock salt has a creep character as follows: rock salt behaves like liquid fluid medium even at very small axial stress difference, and its creep velocity depends on a higher-order nonlinear function of axial stress difference and also temperature. As a result, as long as a stress difference occurs around a salt cavern, the volume loss is unavoidable.

4.2.1 *The constitutive creep law for rock salt*

The creep behavior of rock salt is important for the evaluation of the maintenance of underground gas storage and the determination of the parameters in engineering construction and management.

Many researches indicate that creep of rock salt is related to the material properties, the load, the natural environment (temperature, humidity, confining pressure). When the stress level is not too high, the creep curve of rock salt can be divided into two stages: one is the primary creep stage; the other is the steady creep stage. By summarizing the test data of rock salt and mudstone in Jintan, the total creep strain can be expressed as:

$$\varepsilon = \varepsilon_p + \varepsilon_s \tag{1}$$

where ε_p and ε_s are the primary creep strain and the steady creep strain, respectively. They can be derived from the following equations:

$$\varepsilon_p = A(1 - e^{-\alpha t}) \tag{2}$$

$$\varepsilon_s = \beta q^n t \tag{3}$$

where α, β, A, n are material parameters which can be determined by the creep experiments; $q = \sqrt{3/2\sigma_{ij}^d \sigma_{ij}^d}$; σ_{ij}^d is deviatoric stress; t is time.

Taking the time derivative into account, Equation (2) and Equation (3) can be expressed as:

$$\dot{\varepsilon}_p = \alpha A e^{-\alpha t} \tag{4}$$

$$\dot{\varepsilon}_s = \beta q^n \tag{5}$$

So, the total creep strain rate can be expressed as:

$$\dot{\varepsilon} = A\alpha e^{-\alpha t} + \beta q^n \tag{6}$$

It is indicated from Equation (4) and Equation (5) that the primary creep rate becomes smaller with the increase of time. The steady creep rate is proportional to the power of the Mises equivalent stress at constant temperature. According to the research results of Yang et al. (2000), the steady creep rate of rock salt varies a little, if the confining pressure is greater than a certain level (i.e. $\sigma_{\min} > 3$ MPa). So Equation (1) can reflect the creep behavior of rock salt in three dimensional stress conditions. Because of its elementary formulation the Equation (1) is conveniently used in our numerical computations.

4.2.2 *The implementation of the constitutive creep model into FLAC^{3D}*

The user-defined constitutive model can be written in C++, and compiled as a DLL file that can be loaded whenever it is needed (Itasca Consulting Group Inc. 2002). The main function of the model is to return the calculated new stresses, which result from strain increments. In the C++ language, the emphasis is directed on an object-oriented program structure, using classes to represent objects. In this paper, the creep constitutive model, Equation (1) is implemented into the finite difference software FLAC^{3D}.

For the computations, viscoplasticity has been modeled by combining the before-mentioned creep model with the Drucker-Prager plasticity model, because both models are formulated in terms of the second invariant of the deviatoric stress tensor. When both creep and plastic flow occur, the associated strain rate can be expressed as

$$\dot{\varepsilon}_{ij}^{d} = \dot{\varepsilon}_{ij}^{de} + \dot{\varepsilon}_{ij}^{dv} + \dot{\varepsilon}_{ij}^{dp} \tag{7}$$

where $\dot{\varepsilon}_{ij}^{de}$, $\dot{\varepsilon}_{ij}^{dv}$ and $\dot{\varepsilon}_{ij}^{dp}$ represent elastic, viscous and plastic deviatoric strain rate, respectively. The viscous part of the deviatoric strain rate is coaxial with the deviatoric stress tensor, and is given by

$$\dot{\varepsilon}_{ij}^{dv} = \frac{3}{2}\left(\frac{\sigma_{ij}^{d}}{q}\right)(\dot{\varepsilon}_p + \dot{\varepsilon}_s) = \frac{3}{2}\left(\frac{\sigma_{ij}^{d}}{q}\right)(A\alpha e^{-\alpha t} + \beta q^n) \tag{8}$$

where σ_{ij}^{d} is the deviatoric stress, q is the stress magnitude:

$$q = \sqrt{\frac{3\sigma_{ij}^{d}\sigma_{ij}^{d}}{2}} \tag{9}$$

When the shear yield function of the Drucker-Prager model is met, the plastic strain rate can be expressed as:

$$\dot{\varepsilon}_{ij}^{dp} = \sqrt{3}\cdot d\lambda \frac{\sigma_{ij}^{d}}{2q}, \quad \dot{\varepsilon}_{vol}^{p} = d\lambda \cdot q_{\psi} \tag{10}$$

where $d\lambda$ is a multiplier determined from the requirement that the final stress tensor must satisfy the yield condition, $\dot{\varepsilon}_{vol}^{p}$ is the plastic volume strain rate, q_{ψ} is a constant.

Similarly, the plastic strain rate for tensile yield is:

$$\dot{\varepsilon}_{ij}^{dp} = 0, \quad \dot{\varepsilon}_{vol}^{p} = d\lambda \tag{11}$$

We define the so-called first guess of the stresses $\sigma_{ij}^{d^I}$ and σ_0^I during visco-elastic deformation as follows

$$\sigma_{ij}^{d^I} = \sigma_{ij}^{d^0} + 2G\Delta t(\dot{\varepsilon}_{ij}^{d} - \dot{\varepsilon}_{ij}^{dv}) \tag{12}$$

$$\sigma_0^{I} = \sigma_0^{0} + \dot{\varepsilon}_{vol} K \Delta t \tag{13}$$

where $\sigma_{ij}^{d^0}$, σ_0^0 represent the deviatoric stress and mean normal stress at time t, and G, K represent bulk modulus and shear modulus.

The new stress at $t + \Delta t$, if plastic flow occurred, can be calculated in the following way

$$\sigma_{ij}^{d^N} = \sigma_{ij}^{d^I} - 2G\Delta t\dot{\varepsilon}_{ij}^{dp} \tag{14}$$

$$\sigma_0^{N} = \sigma_0^{I} - K\Delta t \cdot \dot{\varepsilon}_{vol}^{p} \tag{15}$$

Otherwise, the new stress is equal to the visco-elastic guess stress. The main flow chart of the user-defined model is shown in Figure 7.

4.2.3 *The creep simulation at a constant internal pressure*

In order to study the effect of different gas pressures during operation on the volume creep (i.e. convergence), the long term stability of the salt caverns 1 and cavern 2 under constant pressures has been simulated by FLAC^{3D}. In the computations, six different constant internal pressures, 6 MPa, 7 MPa, 9 MPa, 11 MPa, 13 MPa and 14.5 MPa, have been applied in the salt cavern 1 and cavern 2 simultaneously.

Under a constant internal pressure, the volume convergence ratios, i.e. the relative volume change by convergence $\Delta V/V_0$, of the two salt caverns increase with time. A reduction of the internal pressure will also increase the rate of convergence. It is shown in Figure 8 that the volume convergence ratio increases rapidly in the first 5 years, and then the tendency slows down gradually. In addition, after half a year of simulated time, the volume convergence ratios of salt caverns 1

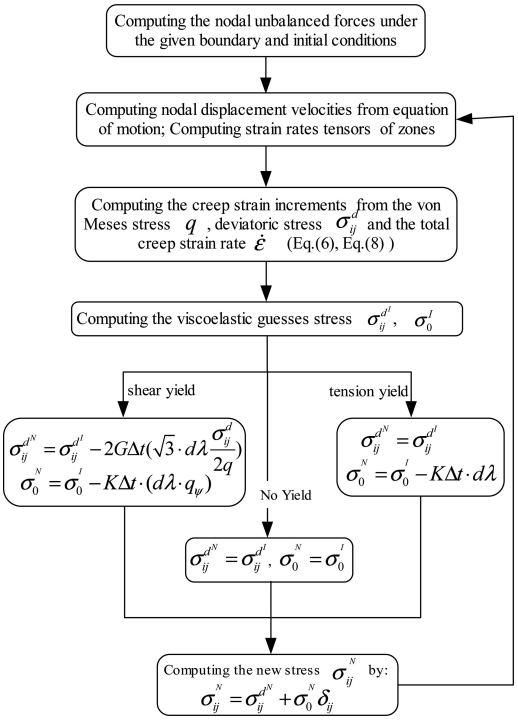

Figure 7. The main flow chart of the model.

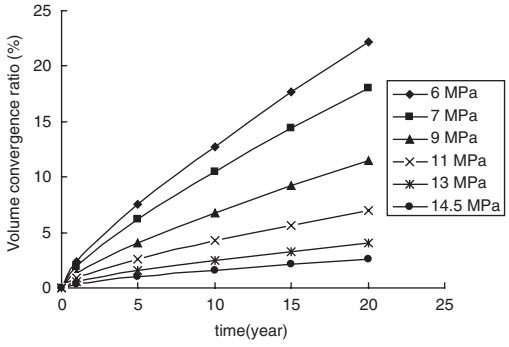

Figure 8. Volume convergence ratio $\Delta V/V_0$ of salt cavern 1 under different internal pressures vs. time.

and 2 are 1.45% and 0.93%, respectively, under 6 MPa internal pressure. They are about 6.11 and 5.89 times larger than those under 14.5 MPa internal pressure. After 20-year simulated time, the maximum of the displacement occurs at the bottom of salt cavern 1, which is 4.6 m, and the volume convergence ratios of salt cavern 1 and cavern 2 are 22.2% and 14.3%, respectively, at 6 MPa internal pressure. They are about 8.74 and 8.57 times larger than those under 14.5 MPa internal pressure. After 20 years, the volume convergence

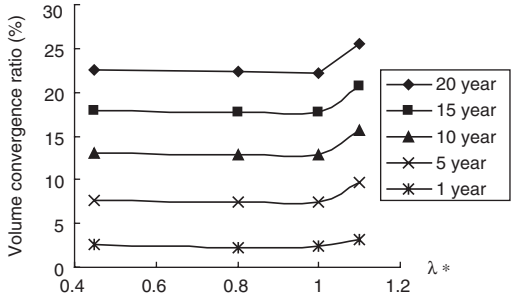

Figure 9. Volume convergence ratio of salt cavern 1 at 6 MPa internal pressure and different periods of operation vs. different lateral stress coefficients.

ratio under 6 MPa internal pressure is about fifteen times larger than that after half a year, while under 14.5 MPa internal pressure it is only about ten times. These results indicate that the increase of the internal pressure can reduce the volume loss of salt caverns distinctly. So, it is recommended strongly that the periods of time, where the gas storage is performed at a low internal pressure, should be as short as possible in order to preserve the service life of salt caverns as long as possible.

To investigate the effect of the coefficient of lateral stress $\lambda^* = \sigma_{\text{vertical}}/\sigma_{\text{horizontal}}$, the volume loss of the salt caverns at four different coefficients of lateral stress, $\lambda^* = 0.45, 0.8, 1.0, 1.1$, respectively, have been simulated under 6 MPa internal pressure. The results show that, when λ^* is smaller than 1, the volume convergence rate increases hardly with the variation of the coefficient of lateral stress. However, when λ^* is larger than 1, the volume convergence rate increases obviously with the increase of the lateral stress coefficients.

5 CONCLUSIONS

From the numerical analysis of the stability of salt caverns some conclusions can be drawn:

(1) After excavation, there is no tension stress around the salt caverns in the two calculation cases. In the case of 6 MPa constant internal pressure, the maximum displacement at the bottom of the salt cavern 1 will be 4.95 cm if only the elasto-plastic deformation behavior is taken into the computation, but will achieve 4.6 m after 20 years if convergence by creep is taken into account.

(2) The creep of a salt cavern during operation can result in volume loss. After 20 years the volume convergence ratio of salt cavern 1 will be 22.2% in case of an internal pressure of 6 MPa and 2.5% in case of 14.5 MPa. For cavern 2 it will be 14.3%

in case of 6 MPa and 1.7% in case of 14.5 MPa, respectively. In addition, the volume convergence ratio decreases greatly with the increase of the internal pressure. This indicates that the internal pressure can affect directly the service life of salt caverns, so it is very necessary to maintain a gas pressure during the operation of a cavern which is related to the stress in the surrounding rock.

(3) When lateral stress coefficient λ^* is smaller than 1, the volume convergence rate increases hardly with the variation of the coefficient of lateral stress. However, when λ^* is larger than 1, the volume convergence rate increases obviously with the increase of the lateral stress coefficient.

(4) Based on the computing results, if the operation pressure of the two salt caverns is not smaller than 6 MPa, it can be guaranteed that the volume convergence ratio is smaller than 22% after twenty years of service life.

ACKNOWLEDGMENTS

The authors acknowledge the financial support from National Natural Science Foundation of China (50434050, 50374064) and the Project of National Basic Research Program of China (2002CB412704).

REFERENCES

Han, J.Z., Shi, T.H. & He, K.P. 2001. On-site evaluation method for the inversion analysis of salt formation creep parameters. *Journal of Southwest Petroleum Institute* 23(3): 26–29.

He, K.P., Zhang, L.W. & Zhang, Z.L. 2002. Viscous and elastic flow model for gypseous salt creep and finite element analyses. *Acta Petrolei Sinica* 23(3): 102–106.

Itasca Consulting Group Inc. 2002. FLAC3D (Version 2.1) users manual. USA: *Itasca Consulting Group Inc*.

Langer, M. 1993. Use of solution-mined caverns in salt for oil and gas storage and toxic waste disposal in Germany. *Engineering Geology* 35(2): 183–193.

Munson, D.E. 1997. Constitutive model of creep in rock salt applied to underground room closure. *Int. J. Rock Mech. Min. Sci. and Geomech. Abstr* 34(3): 233–247.

Peach, C.J. 1996. Deformation dilatancy and permeability development in halite/anhydrite Composites. In Ghoreychi, M., Berest, P., Hardy, H.R. Jr. (ed.), *Proc. of the 3rd Conf. on the Mechanical Behavior of Salt*. Clausthal-Zellerfeld, Trans. Tech. Publ.

Pudewills, A. & Krauss, M. 1999. Implementation of a viscoplastic model for crushed salt in the ADINA program. *Computers and Structures* 72(1–3): 293–299.

Ren, S. & Jiang, D.Y. & Liu, X.R. 2003. Analysis on ground stress of rock salt cavern's surrounding rock with 3D-Sigma. *Underground Space* 23(4): 414–416.

Schulze, O., Popp, T. & Kern, H. 2001. Development of damage and permeability in deforming rock salt. In Ch. Talbot & M. Langer (eds.) *Special Issue on Geosciences and Nuclear Waste Disposal. Engineering Geology* 61: 163–180. Amsterdam: Elsevier.

Thoms, R.L. & Gehle, R.M. 2000. A brief history of salt cavern use, In: Proc. 8th World Salt Symposium, Vol.1: 207–214. Amsterdam: Elsevier.

Yan, X.Z., Yang, H.L. & Yang, X.J. 2003. The reason analysis of mudstone creep on casing damage. *Drilling & Production technology* 26(3): 65–68.

Yang, C.H., Bai, S.W. & Wu, Y.M. 2000. Stress level and loading path effect on time dependent properties of salt rock. *Chinese Journal of Rock Mechanics and Engineering* 19(3): 270–275.

Yang, C.H., Yin, J.H. & He, K.P. 1999. The investigation of stress relaxation of salt rock. *Chinese Journal of Rock Mechanics and Engineering* 18(3): 262–265.

Yang, C.H., Zeng, Y.J. & Wu, W. 2002. Constitutive relationship of deep salt rock and its application to petroleum drilling engineering. *Chinese Journal of Rock Mechanics and Engineering* 23(3): 102–106.

Taylor & Francis
Taylor & Francis Group
http://taylorandfrancis.com

Part 8. Abandonment of caverns

Taylor & Francis
Taylor & Francis Group
http://taylorandfrancis.com

The Mechanical Behavior of Salt – Understanding of THMC Processes in Salt –
Wallner, Lux, Minkley & Hardy, Jr. (eds)
© 2007 Taylor & Francis Group, London, ISBN 978-0-415-44398-2

The Bernburg test cavern – in situ investigations and model studies on cavern abandonment

D. Brückner, A. Lindert & M. Wiedemann
Institut für Gebirgsmechanik GmbH, Leipzig, Germany (IfG)

ABSTRACT: This paper summarizes test results obtained during the so-called "Test Cavern" project performed in the salt mine Bernburg (Saxony-Anhalt, D) aiming on the long term behaviour of a sealed brine filled cavern. Because its evolution depends on the system's geomechanical and hydraulic properties and their interactions, an extensive research program were done comprising in-situ tests in a brine filled model cavern and bore holes, rock mechanical investigations and modelling. Only for the purpose of well defined test conditions and for facilitating a latter direct inspection of the brine pressure affected rock wall a model cavern with a total volume of around 22 m^3 was leached of at an underground level of around 420 m. Major part of the research program were the pressure build up tests performed as well in the test cavern and as well in boreholes for over a duration of 2.5 years allowing an estimate regarding scale effects. With respect of interpreting the in situ results an accompanying rock mechanical investigation program was carried out to prove the deformation behaviour of the surrounding rock mass, the stress state in the solid by hydro-fracturing and the rock mechanical behaviour of rock salt samples from the surrounding rock mass. Finally, the observed time dependent coupled processes were numerical modelled using a modified FLAC-Code allowing the quantitative simulation of pressure dependent brine permeation in into the wall.

1 INTRODUCTION

Understanding the complex coupling of hydro-mechanical parameters for rock salt is of vital importance for planning of solution mining activities, e.g. the dimensioning of the single cavern, the cavern field and, particularly, the determination of the optimal storage pressure. Therefore, a lot of work has been done in the past how these parameters can be optimised to increase the working gas capacity (Lux et al., 2001; DeVriess et al., 2002; Lu et al., 2002). However, the caverns need to be abandoned some day by sealing the access bore hole.

In consequence, subsequent to its closure, the following scenario is generally feared: Due to the convergence of the surrounding salt masses and brine thermal expansion the pressure will rapidly increase and in the worst case exceed the lithostatic pressure to a level that causes seal failure or cracks (e.g. Ehgartner and Linn, 1994; Wallner and Paar, 1997). In assessing the risk of loss of mechanical stability and hydraulic integrity in abandoned caverns recent investigations have demonstrated, that the pressure increase is limited because of the rock salt formations become permeable if the fluid pressure exceeds the stress in the salt (e.g. Berest et al., 2001). Coevally the internal pressure will reach an equilibrium balanced by creep closure and brine outflow whereby the leakages rates of fluids from the top of the cavern may be small due to the compressibility of the system salt – fluid. Nevertheless, the nature of the cavern fluid transport from the cavern into the salt formation may be the most significant and technically controversial issue in cavern sealing and abandonment (Ratigan, 2001). The knowledge about details of the pressurization of sealed caverns and estimations on the final equilibrium pressure are of urgent importance e.g. for licensing a closure concept by responsible authorities.

As demonstrated in the literature (e.g. Berest et al., 1995) the long-term evolution of a sealed and abandoned brine-filled cavern depends on the system's geomechanical (cavern closure by creep) and hydraulic characteristics (brine permeation into the salt wall). Focusing on these interactions, an extensive research program comprising in-situ tests, rock mechanical investigations and modelling has been performed in the Bernburg salt mine in close cooperation between the mine operator esco and the IfG. The main purpose of the research were site specific investigations of the coupling between the relevant rock mechanical and hydraulical processes in rock

salt which may occur during cavern abandonment. The main work topics are as follows:

(1) Because the amount of over-pressurization is obviously a function of cavern size (e.g. Berest and Brouard, 1995) the major part of the in-situ investigation program consists of pressure build up tests in two different scales over duration of 2.5 years: in boreholes ($V \approx 20.000\ cm^3$) and the test cavern ($V \approx 22\ m^3$). For an estimate of in situ stress conditions and rock mass deformations supplementary, hydrofrac tests and long term convergence measurements were done before and during the test period.
(2) For interpretation and as a reliable basis for numerical modelling, an extensive rock mechanical testing program was performed to determine relations and parameters for the description of the material behaviour affected by pore fluid pressures.
(3) Finally, the observed time dependent processes were numerical modelled using a modified FLAC-Code with mutual checking of calculated and measured data. In addition, the pressure dependent brine permeation processes were recalculated.

2 TEST PROGRAM

2.1 *Laboratory tests*

The comprehensive rock mechanical and geotechnical investigation program was composed of triaxial and uniaxial tests on rock salt samples collected from the test area to describe the rock mechanical behaviour (strength, dilatancy and creep) and the porosity and permeability relationship simulating in situ conditions with or without increased pore fluid pressures.

Additionally, the compaction behavior of the elastomer packer material and the amount of friction between the packer and the borehole wall were determined to ensure its usability as sealing medium for the packers system in the access bore hole of the test cavern.

2.2 *In-situ investigations*

The test area is situated in a depth of about 420 m within in a very homogenous part of the older rock salt (Staßfurt-salt) in the central region of the so called Bernburg shaft anticline (Figure 1). Corresponding to the lithological structure the test cavern is characterized by the steep inclined bedding of the rock salt interlayered by anhydrite bands (compare Figure 4).

As a prerequisite for the in situ tests a 11 m long test chamber in the profile 8 m × 8 m has been drifted from an existing access and a model cavern (volume ≈ 22 m³) has been leached of around 30 m below the chamber floor. An ultrasonic survey confirms its nearly ideal cylindrical shape which offers

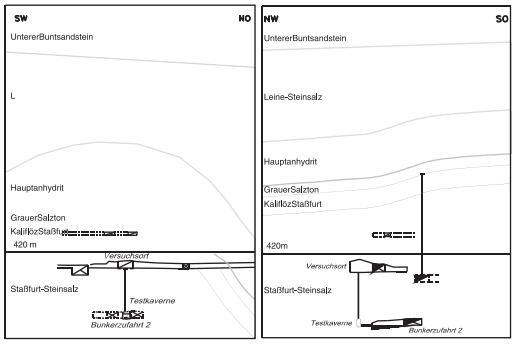

Figure 1. Geological situation at the test site in the center of the so-called Bernburg shaft anticline, depicted in two perpendicular oriented geological cross-sections.

optimal test conditions. In the test chamber different boreholes were drilled in the NW-wall parallel to the anticline axis.

The in-situ program is based on the following work topics:

(1) Firstly, in preparation of the leaching process of the test cavern a nearly vertical borehole was drilled in two steps down to 38 m below the chamber floor by a core drill machine. The first 28 m have been realized with a diameter of 124 mm and the lowest 10 m with 76 mm diameter, reaching the later cavern level. After documentation, the drilled core samples were used for mineralogical investigations and for preparing samples for rock mechanical testing.

In the upper 28 m with 124 mm diameter the casing system for adapting the later packer seat was installed consisting of an elastomer packer system with a total length of 1.8 m. Before beginning with the leaching process the sealing efficiency of the packer system installed in the access bore hole of the test cavern was proved with nitrogen, i.e. to ensure that there is no leakage through the casing-shoe and the packer.

The leaching-out of the cavern took place in the direct leaching procedure (water pipe route in deep position, high-hanging brine tubing route). The process, however, was intermittent, due to the daily exchange of developed brine by fresh water. As blanket nitrogen was used.

Then, after finishing the leaching, as main part of investigation various pressure build up tests were performed in the brine filled cavern. However, to avoid technical problems which usually occur if brine is used the technical pressurization was done by injecting hydraulic oil as pressure transmitting medium, i.e. acting as blanket. Both test methods, i.e. stepwise pressure variations (pulse tests) and stationary tests with

application of constant flow rates between 1 to 175 l/h were applied for determination of the brine permeability whereby the stationary test regimes facilitate also the determination of the modulus of compression for the cavern – brine system.

(2) Furthermore, for evaluating scale effects, additional pressure build up tests were performed in two neighbored and weakly inclined brine-filled boreholes drilled horizontally in the test chamber. Generally, the same test regimes were realized as in the test cavern but at shorter time intervals. Again, the pressurization was done using an oil blanket.

(3) As a prerequisite for interpreting the test results, geotechnical in-situ investigations were performed in the various test horizons, e.g. at the test chamber level and in the level of the test cavern around 30 meters below, i.e. monitoring the overall convergence by extensometers and determining of the minimum stress distribution with hydraulic fracturing.

(4) Because it was an important task to estimate the penetration depth of brine in the pressurized salt wall an access gallery was mined for direct inspection of the penetrated zone as well as for the cavern itself after finishing the hydraulic permeation tests in the test cavern. For a better visualization of the fluid pressure affected zone the brine was coloured with a tracer.

2.3 *Numerical modeling*

The numerical modeling comprised the development of a two-dimensional model on the basis of FEM calculations using the program code FLAC-2D. The model includes the test chamber, the test cavern and the surrounding rock mass to estimate the initial stress field resulting from the overburden in comparison to the data sets obtained by hydrofrac and extensometer measurements.

The rotationally symmetrical model of the test cavern and its surrounding served to simulate the several test steps from the in-situ tests, i.e. the primary stress state, the leaching process, the pressure build up tests, the convergence and creep behavior and the process of brine penetration as a function of pore fluid pressure, permeability and porosity. The verification of the penetration process around the boreholes and the test cavern on the basis of analytical recalculations of the pressure tests assuming Darcy's law.

3 GEOTECHNICAL IN-SITU RESULTS

The knowledge about the primary stress field and the mechanical behaviour of the surrounding salt rock is a prerequisite for each further evaluation of the observed

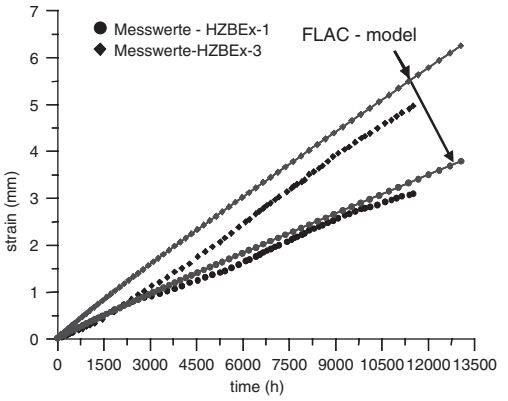

Figure 2. Comparison between in situ measured and calculated geotechnical data sets – convergence as function of time.

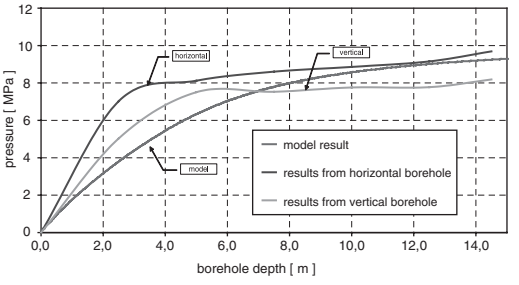

Figure 3. In situ measured hydrofrac data compared to numerical mode.

pressure behaviour of sealed underground openings. The convergence measurements were done in the test chamber in two neighboured and weakly inclined bore holes. Surface markers were connected with two fixed points located in 3 and 20 m borehole depth, respectively, for measuring the horizontal movements in the wall.

The convergence rates are small and with 2.3 mm/a and 4.2 mm/a nearly constant (Figure 2).

The obtained deformation curves could be nicely recalculated by the combined creep law consisting a deformation-hardening function and life time dependent recovery proposed by Salzer et al. (2002).

The minimum stress distribution in the wall between 1 and 20 m has been measured with the hydraulic fracturing method in various bore holes. The results confirm nearly isotropic stress conditions (only 10% fluctuation) and correspond fairly to the estimated lithostatic pressure (see Figure 3).

Therefore, we did the conclusion that the region seems not to be influenced by the underground openings that had been excavated during the operation of the salt production mine.

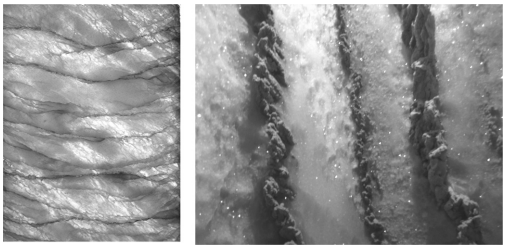

Figure 4. Lithological appearance of rock salt at the Bernburg site. (left) Photograph of a rock salt slide from a core sample of the cavern drill hole showing the characteristic features of homogenous medium grained rock salt with diffuse anhydrite intercalations. (right) view inside the cavern showing the pronounced internally folded anhydrite layers separating the salt layers (picture width approx. 1 m).

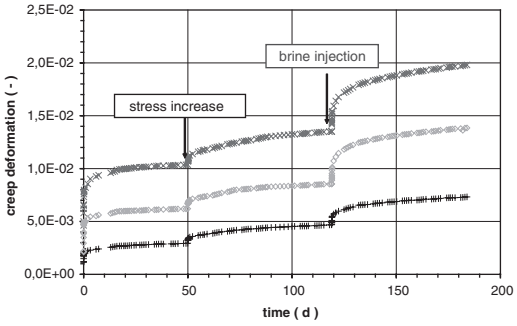

Figure 5. Creep curves of various rock salt samples from the Bernburg area with two stress levels of 8 and 10 MPa and a subsequent wetting of the sample with brine.

4 LABORATORY INVESTIGATIONS

4.1 *Strength properties of rock salt*

For the rock mechanical investigations core samples were taken directly of the cavern drill hole and horizontal holes near the test chamber.

As shown in Fig. 4 the samples are mainly composed of halite (around 90%) and subordinately of anhydrite (up to 10%). The Staßfurt rock salt at the test cavern site is typically characterized by alternating layers (distance between around 10 cm to several decimetres) of medium to coarse grained rock salt from white into grey indicating sedimentary bedding with intercalated anhydrite bands. These are up to several cm thick and are internally complex folded.

Triaxial strength tests, only at room temperature, have been performed, preferably at low ($p_c = 1$ MPa) and high pressure ($p_c = 10$ MPa) simulating the stress decrease in the cavern contour during leaching and, respectively, the in situ conditions of the undisturbed rock salt at 500 m depth. During the constant deformation rate tests relaxation phases were intercalated where the deformation was held constant over more than 20 hours allowing a direct transfer of the measured deformation rates to in situ creep rates of several cm per year (for details, see Salzer et al., 2002). However, in summary test results nicely confirm earlier observations obtained on medium to coarse grained rock salt from the Bernburg area (e.g. Arnold et al., 2002).

4.2 *Creep properties of rock salt*

Because humidity may affect creep of the surrounding salt constant stress tests with creep phases without and with added brine to the samples have been performed (Figure 5). Generally it was observed that the brine effect leads to an increase of creep rates of around 3 times in the wet samples compared to dry material.

With respect to the subsequent performed modelling, it has to be mentioned that the combined creep law of Salzer et al. (2002) provides a good description of both, the measured stress-strain curves under triaxial compression as well as the transient and stationary creep.

4.3 *Permeation properties of rock salt*

Additional work was done to investigate the tightness of the rock salt under application of pore fluid pressures. Initial permeability testing proofs an effective porosity of 0.2% and permeability in the order of 10^{-21} to 10^{-20} m^2, which correspond to undisturbed rock salt (e.g. Popp et al., 2002).

Using such samples, measurements of fluid permeation are performed by applying fluid pressure via pipes through the axial loading pistons at the ends of the hydrostatically loaded sample.

It should be stressed that during increasing the fluid pressure no remarkable changes in permeability was observed. Only until the pressure passes the confining pressure an increase in permeability and porosity (indirectly measured by the sample volume change) occurs which qualitatively corresponds to the observations made by Fokker (1995).

5 BORE HOLE PRESSURE BUILD UP TESTS

In advance of investigations performed in the test cavern additional pressure build up tests were done in two inclined 25 m long bore holes with a diameter of 44 mm. Both were sealed between 9 to 10 m behind the borehole front using a hydro-mechanical packer system. After realizing stable packer conditions, the bore holes had been filled with brine. Finally, approx. two litres hydraulic oil have been injected to drive out all air inclusions and to act as blanket at the top of the hole. The overall volume filled into the boreholes was 22 and 24 litres.

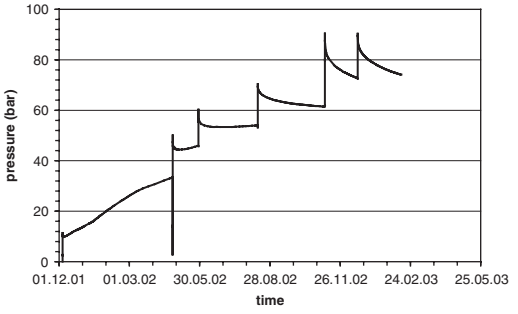

Figure 6. Results of pulse tests with various pressure steps in a brine filled bore hole fluid pressure vs. time.

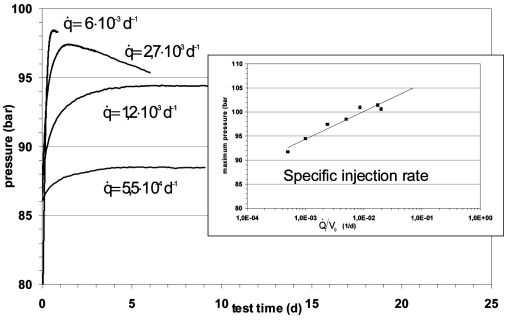

Figure 7. Results of stationary tests with various inflow rates into a brine filled bore hole. Fluid pressure vs. time. The inset shows the general trend between maximum pressure and pump rate.

The intrinsic modulus of compression for the brine filled borehole was determined by rapidly loading and unloading the pressure with measuring the injected and expelled oil volume. The volume pressure balance gives a value of about 1.7 GPa.

The further test program which was going on for a period of two years consists of two types of tests. The first type of tests requiring most of the test period was the so called pulse test (Figure 6), i.e. starting from a desired pressure level the objective and observing precisely the temporary pressure decay due to subsequent brine permeation into the wall. The second test type was the stationary test, where a constant pump rate was applied focusing on appearance of pressure equilibrium due to a balance between the injected fluid volume and the brine outflow into the surrounding rock salt mass.

Beginning with the pulse tests, multi-stage pressure stepping tests were performed whereby each pressure step has been done in periods of 8 to 10 weeks. The whole course of pressure evolution is depicted in Fig. 6. Remarkable, the transitional behaviour of the first step shows a reversal from pressure decrease to an increase which is qualitatively repeated in the next two steps, started at 50 and 60 bar, respectively. However, it has to note, that the pressure build up rates are progressively reduced, from 0.1 bar/d to 0.01 bar/d. This behaviour was referred to convergence effects overlapping the brine permeation into the rock. In the subsequent steps permeation becomes the dominating effect as documented in a transient behaviour of pressure decay achieving a constant rate which is directly related to the pressure level.

In the final stage, two years after beginning the borehole tests, a maximum pressure of 90 bar had been reached, which is approx. 80% of the estimated lithostatic pressure in the gallery. Higher pressures were not realized to avoid hydro-fracturing.

In the second test period the boreholes were loaded with constant fluid injection rates over several days. The used injection rates vary between 0.5 and 40 ccm/h which were recalculated to convergence rates referred to the volume of the bore holes to allow a comparison with the test cavern results. As indicated in Fig. 7 depending on the pump rate the pressure rises up and reaches a maximum which is subsequently followed by a weak decrease. Importantly, as summarized in the inset in Fig. 7 we have found indications that a rate depended pressure maximum exists.

Based on the observed pressure decay respectively the constant rate tests the permeability of the rock salt surrounding the boreholes was calculated. Importantly it varies between 10^{-22} and 10^{-20} m^2 depending on the difference between the minor principal stress of the rock salt mass and the fluid pressure.

6 INVESTIGATIONS IN THE TEST CAVERN

Basically the tests in the cavern have the same conception as being realized in the borehole tests covering both, pulse and stationary tests. To ensure that no technical leakage may occur the tightness of the packer equipment and the casing has been tested before and after leaching of the test cavern. The check has been done with nitrogen by pressurizing the cavern roof and the casing with a gas pressure of about 20 bar. The requirements for technical thickness were found to be fulfilled by observing a well-head pressure drop with a rate lower than 0.05 bar/d (Figure 8), which could be confirmed after a test duration of two weeks.

Starting in January 2002, in the first step, the cavern has been weakly pressurized up to 10 bar well-head pressure (Figure 9) with injection of 8.8 litres hydraulic oil. Based on the volume pressure balance, which was proved in the various pumping up cycles the modulus of compression for the system brine-cavern could be determined to be in the range of 2.7 MPa, which is higher than in the bore holes. This value is combined with well-head pressure decay rates according

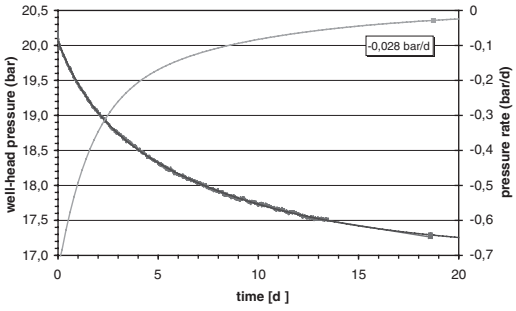

Figure 8. Initial tightness test with nitrogen against the brine filled cavern.

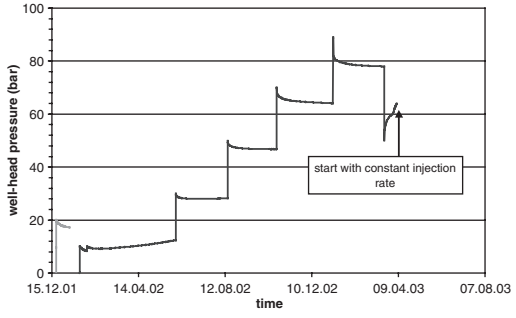

Figure 9. Pressure evolution during pulse tests performed in the brine filled test cavern (around 22 m^3) with stepwise increase of the initial pressure.

to convergence rates between 0.03 and 0.06% per year. Generally, while manually pumping up the pressure increase in the cavern is directly proportional to the amount of oil injection resulting in a gradient of 1.22 bar/l.

After sealing the well at 10 bar we expected a slight pressure build up due to cavern convergence. First a slight pressure decrease was observed comparable to the experiments in the bore holes. A transitional phase with a minimum of 9.1 bar was reached after 3 weeks. Afterwards, the well head pressure had started to increase with a progressive tendency. 4 months later the well-head pressure has reached 12.3 bar, whereby from march with initially 26 mbar/d to may with finally 43 mbar/d the pressure build up rate became nearly doubled.

In the next step the pressure was pumped up to 30 bar by injecting 14.2 l hydraulic oil. An initial rapid pressure decay was observed which is followed by a transient phase until it became a minimum at around 28 bar. Then during a 6 weeks phase a slight increase up to 28.2 bar occurs. The resulting pressure build up rate was approx. 4 mbar/d.

In the third step at an initial pressure of 50 bar a rapid pressure decrease has been observed which

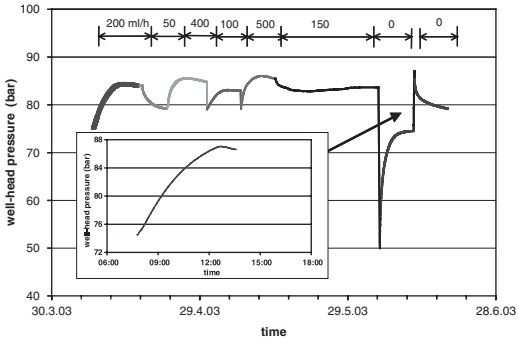

Figure 10. Pressure evolution during stationary tests performed in the brine filled test cavern (around 22 m^3) with variations of the pump rate. Note, that in the last two pressure steps has been manually set to 50, and 85 bar respectively, to observe the pressure recovery.

has been followed by a phase with a degressive trend until a plateau of nearly constant pressure has been established after two month. During the next pressurisation 20.77 litres hydraulic oil were injected leading to a well-head pressure of 70 bar. After ten weeks the pressure has dropped down to 64.2 bar. The rate was degressive again and reached 12 mbar/d at the end of the period.

In the fifth step the well-head pressure was increased up to 89 bar and the system became more and more week Whereas in the lower pressure steps ($<$80 bar) a nearly linear relationship between injected volume and pressure is observed, the necessary oil injection to reach higher pressures rises nearly exponentially up.

After the cavern was tightly closed, the pressure dropped down to 82 bar only one day later. After a period of 3 month a well-head pressure of 78 bar has reached. At the end of the test the pressure decrease rate was 11 mbar/d.

The following stage of the test started with active depressurisation of the well-head pressure down to 50 bar. Importantly, after sealing again the pressure risen up to 60 bar, which is obviously to the reverse inflow of the fluid penetrated into the cavern wall under higher pressures.

After finishing the pulse tests a series of stationary tests followed, with constant injection rates between 50 and 500 ml/h according to specific rates of about $5 \cdot 10^{-5}\ d^{-1}$ to $5 \cdot 10^{-4}\ d^{-1}$ (Figure 10).

The constant injection rate test started at around 75 bar with a pump phase of 200 ml/h resulting in a parabolic shape until a maximum at around 85 bar. It was followed by a phase of weak decrease. Lowering the pump rate to 50 ml/h induces pressure rise down with a degressive trend and approaching equilibrium at around 76 bar. This behaviour has been verified in several steps with different pump rates.

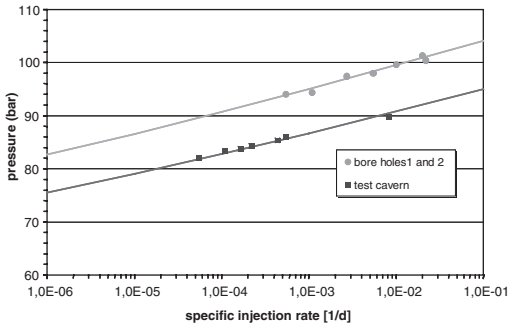

Figure 11. Comparison of the results of stationary tests performed at the boreholes and the test cavern (Note, the well head pressure is used in the case of test cavern). A scale effect can be observed.

The achievement of stable pressure equilibrium in the cavern has been proved by lowering the pressure to 50 bar and monitoring the rise up of pressure after sealing the cavern. The wellhead pressure tends to receive a constant value in the order 75 bar after one week. Repeating the experiment but starting at 85 bar led to a pressure decay with a trend which could be extrapolated to the equilibrium pressure observed before.

Summarizing the tests with flow rate variations a rate dependent maximum pressure was found which is followed by a pressure recovery with slight decrease. The trend is expressed by a relationship between specific injection rate and maximum pressure as depicted in Fig. 11.

Considering realistic convergence rate resulting in a pressure increase the results of the injection tests led to the conclusion, that the anticipated pressure build up in the tightly closed cavern will not achieve the lithostatic pressure, or somewhat more general, the minor principal stress of the covering rock mass. This is a consequence of the observed balance between brine pressure, i.e. that it is a function of rock mass convergence and thermal effects, and the related permeation of brine into the salt. As quantified in the laboratory tests, it can be anticipated that if the pressure difference between the fluid pressure in the cavern and the confining (lithostatic) pressure becomes smaller, permeability k (and subordinately porosity Φ) of the salt will increase favouring permeation processes.

7 DIRECT PROBING OF THE CAVERN CONTOUR

An important goal of investigation was the documentation of solution effects on the salt surface and a determination of the extent of the brine penetrated zone. After depressurisation and brine withdrawal an access to the cavern was opened by traditional mining, which is depicted in Fig. 1.

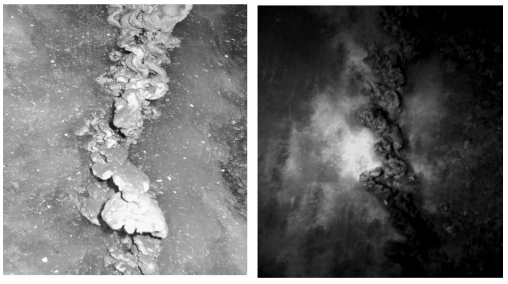

Figure 12. Photographs of the cavern interior and of the contour for visualization of permeation phenomena a: normal light and b: UV-light.

Although the salt was expected to show no preconditions for solution transport the most impressing feature, after entering the inner part, is the occurrence of nearly vertical inclined anhydrite layers up to 10 cm thickness. They appear, as well as transections or as cover mainly on the wall surfaces in the north and south direction. The salt itself is visible free of disturbed zones or fractures and looks wet without local leakage (Figure 12).

Focusing on the anhydrite structures, most of the insoluble material is found as detrital accumulation in the mud. The residual parts of anhydrite are forming internally complex folded skeletons rising up to 20 cm into the opening. Because the layers are internally broken and jointed they are obviously not impeding the solution process as indicated by a nearly ideally cylinder geometry of the cavern.

However, most important, visual inspection with UV-light gives indications that the permeation into the wall is preferentially concentrated on layers with anhydrite structures. Carefully inspection of the contour indicates, at least, three zones of fluid permeation into the wall:

- Up to 30 cm: pervasive solution front
- Up to 60 cm: inhomogeneous fluid distribution with local spots and rims
- Up to 100 cm: local 2D-spreading along anhydrite layers

In summary, our observations confirm that permeation processes in undisturbed salt are possible but they can be locally enhanced by internal anhydrite layers as major path ways. The extent of the observed permeation front corresponds very well to the results obtained by numerical modelling.

8 NUMERICAL MODELLING

As preliminary remark it has to be noted that the obtained data sets, comprising the results of the various pressure test in relation to the known rock mechanical

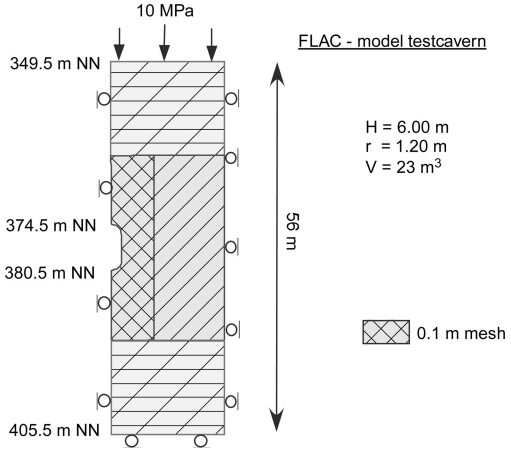

Figure 13. Rock mechanical model of the test cavern. The domain and the boundary conditions for the numerical formulation as well as the finite element mesh used for the numerical analyses are indicated.

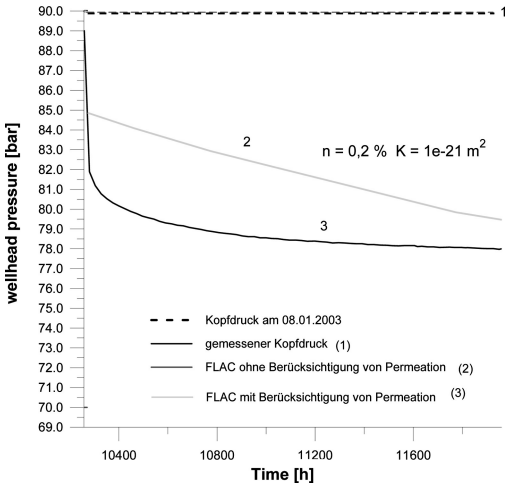

Figure 14. Rock mechanical model calculation for the 90 bar fluid pressure step, with stepwise consideration of the various influence processes. Note that a sufficient description of the pressure decay is only possible if permeation is considered.

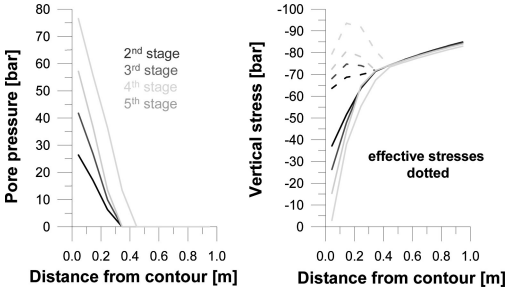

Figure 15. Rock mechanical model calculation simulating various steps of brine pressure increase – stress distribution around the cavern in a selected horizontal cross section at half cavern height.

parameters are representing a unique base for verifying numerical simulation of pressure dependent brine permeation processes in salt caverns.

In order to demonstrate the suitability of the used numerical tools for a long term prognosis of the cavern abandonment a rotationally symmetrical model with the Finite Difference codeFLAC^{3D} was constructed. It comprises a rock transection of 56 m height (depth range: −340.5 m NN up to 405.5 m NN) and 15 m radius in the salt. Hereby, it is considered that the primary stress depends on the depth at which the test area is located. The load on the model surface has been estimated by the dead weight of discrete elements according to lithostatic pressure gradient:

- Above the salt: 23.6 kPa;
- of the rocksalt 21.5 kPa

The modelled test cavern is idealized as a 6 m high cylinder with semi sphere end caps and 1.2 m radius and with a volume of around 23 m^3. The simulation of the leaching process was implemented into the model by stepwise (5 times) erasing the equivalent elements. The FE model (Figure 13) includes around 20000 elements with varying sizes from 0.1 m in the contour to maximum 0.3 m at the random. As already mentioned, the combined creep law was used with a deformation-hardening function and life time dependent recovery proposed by Salzer et al. (2002):

$$\varepsilon = \varepsilon_{\mathrm{E}} + \varepsilon_{\mathrm{CR}}$$

where ε_{E} and $\varepsilon_{\mathrm{CR}}$ are the elastic and creep portion of the strain

With the model the observed pressure variations in the various pressurisation steps (an example is given in Figure 14) could be nicely recalculated, whereby, both, convergence and permeation processes were found to be in balance if the fluid flow into the salt varies as a function of fluid pressure.

In the primary tightness test and the first pressure cycle the observed nearly constancy (or only weak pressure increase) corresponds to the initial rock properties with an effective porosity of 0.2% and a permeability in the order 10^{-21} to 10^{-20} m^2. However, simulating the pressure behaviour at higher pressure steps requires higher outflow rates into the wall, resp. an increase of permeability and porosity in the contour.

Importantly, as demonstrated by the the modelled stress states surrounding the cavern (Figure 15) the total stresses σ_{xx} nearby the contour increase while

the wellhead pressure growths from stage to stage, whereas the effective stresses σ_{xx}^{eff} acting inside the rock matrix are nearly constant. Furthermore, the total vertical stresses σ_{yy} growth in the total brine saturated zones with each pressure stage but they are fluid pressure independent in the not saturated zones of the cavern contour. As well as the total and the effective tangential stresses decreases from on stage to the next. During the 5th stage the effective tangential stresses σ_{zz}^{eff} approaching the tensile stresses due to the high pore pressure. When the pore pressure exceeds the acting confinement of the rock matrix, an increase of both, permeability and porosity is the consequence.

However, a stable equilibrium is reached at brine pressures in the order of 90 bars, which demonstrated that both, convergence processes and spatial grow of the permeation front are stopped. If the cavern out flow is set to constant values equivalent to the tested values which correspond to realistic convergence rates a stable pressure plateau will be reached at around 85 bar.

In summary, the used computer code with consideration of varying permeability and storage capacity (i.e. porosity) of the surrounding salt was found to be a powerful tool for application to complex pressure build up scenarios in salt formations (e.g. abandonment brine filled caverns, flooded salt mines). It is important to mention that during all computations with a wide spectrum of load conditions the integrity of the cavern contour has never been violated.

9 SUMMARY AND CONCLUSIONS

The main focus of this project was the investigation of coupled hydraulical-mechanical processes in rock salt associated with the pressure build up in a abundant and sealed brine filled cavern to deliver a comprehensive database for numerical modeling.

Because of the competing effects of salt convergence, pressure build up and brine outflow due to permeation processes, many factors have to be considered for a prognosis. The pressure increase is mainly caused by convergence processes and contrary influenced by permeation. Importantly, the temporary pressure rise up is limited and reaches a plateau below the minor principal stress component acting in the covering rock mass.

An extensive investigation program with in situ measurements, rock mechanical laboratory testing and model computations had been undertaken in the Bernburg salt work. Rock mechanical experience was gained for abandonment of brined filled and sealed caverns particularly with regard to a better understanding of time depending fluid pressure build up and the attainment of balance between fluid outflows into the wall, i.e. permeation, and internal pressure.

It can be stated, that the pressure build-up correlates with the compressibility of the coupled brine volume-salt system which is a function of the size of the underground opening. The pressure limiting parameter is the fluid outflow to the salt which depends on properties of the salt matrix but as well as on the appearance of anhydrite or clay layers acting as predominant path ways.

The use of 3D-modelling results in a better understanding of the permeation processes around salt caverns and permits, therefore, a reliable prognosis about the pressure behaviour of abandoned caverns.

ACKNOWLEDGEMENTS

The studies presented here were done in close cooperation between the K+S Aktiengesellschaft, the european salt company (esco) and the IfG. The mining experiences of the esco staff (Bernburg) were a prerequisite for successfully performing the ambitious in situ operations coordinated by A. Hiltscher and H. Zwätz (both esco). The research benefited from the fruitful cooperation and discussions with many colleagues from various institutions, in particular with F. Farkas, R. Kriesche, A. Wendzel (all esco) and J.-P. Schleinig (K+S).

LITERATURE

Arnold, C., Lischka, J., Heinrich, C., Schreiner, W. & Lux, K.H., 2002. Postleaching of caverns at natural gas storage Bernburg Germany, Saxony-Anhalt. Proc. SMRI Fall Meeting 2002, Bad Ischl, Austria.

Berest, P. & Brouard, B., 1995. Behaviour of sealed solution-mined caverns. *Proc. SMRI Spring Meeting 1995*, New Orleans.

Berest, P., Berges, J. & Brouard, B., 2001. A salt-cavern abandonment test. Int. J. Rock Mech. & Mining Sci., 38, 357–368.

DeVries, K.L., Mellegard, K.D. & Callahan, G.D., 2002. Prof-of-concept research on a salt damage criterion for cavern design: a project status report. *Proc. SMRI Spring Meeting 2002,* Banff, Alberta, Canada.

Ehgartner, B.L. & Linn, J.K., 1994. Mechanical behaviour of sealed SPR Caverns, *Proc. SMRI Fall Meeting*, Houston, USA.

Fokker, P.A., 1995. The behaviour of salt and salt caverns. Proefschrift, Technische Universität Delft, 143 pp.

Lu, M., Broch, E., Heinrich, F., Hausdorf, A., Schreiner, W. & Lindert, A., 2002. Feasibility study of large volume gas storage in rock salt caverns by numerical method. In: The *Mechanical Behavior of Salt V; Proc. of the Fifth Conf., (MECASALT V)*, Editors: N.D. Cristescu, H.R. Hardy, Jr., R.O. Simionescu, Bucharest 1999, Balkema, Lisse, 317–328.

Lux, K.H., Düsterloh, U. & Hou, Z., (2001). Increasing the profitability of storage cavities by improvement of the

dimensioning concept including CDM. *Proc. SMRI Fall Meeting*, Albuquerque, New Mexico.

Popp, T., Kern, H. & Schulze, O., (2002): Permeation and development of dilatancy and permeability in rock salt.- In: *The Mechanical Behavior of Salt V; Proc. of the Fifth Conf., (MECASALT V),* Editors: N.D. Cristescu, H.R. Hardy, Jr., R.O.Simionescu, Bucharest 1999, Balkema, Lisse, 95–124.

Ratigan, J., 2001. A status report on the solution mining research institute cavern sealing and abandonment program. *SMRI-Report*.

Salzer, K., Schreiner, W. & Günther, R.-M., 2002: Creep law to decribe the transient, stationary and accelerating phases. In: *The Mechanical Behavior of Salt V; Proc. of the Fifth Conf., (MECASALT V)*, Editors: N.D. Cristescu, H.R. Hardy, Jr., R.O. Simionescu, Bucharest 1999, Balkema, Lisse, 177–190.

Wallner, M. & Paar, W.A., 1997. Risk of progressive pressure build up in a sealed cavity, *Proc. SMRI Fall Meeting*, El Paso, 177–188.

The Mechanical Behavior of Salt – Understanding of THMC Processes in Salt –
Wallner, Lux, Minkley & Hardy, Jr. (eds)
© 2007 Taylor & Francis Group, London, ISBN 978-0-415-44398-2

Deep salt cavern abandonment: A pilot experiment

G. Hévin, C. Caligaris, J.G. Durup, O. Pichayrou & C. Rolin
Gaz de France, Direction des Grandes Infrastructure, Saint-Ouen, France

ABSTRACT: Sealing a solution-mined cavern in a salt formation that has been used for mineral production, hydrocarbon storage, or waste disposal has been a contemporary topic for many years. As a result of knowledge gained from a series of succinct sealed well and cavern field tests performed in the late 1980s and early 1990s by Gaz de France, issues related to the abandonment of salt caverns became more focused. The main difficulty of the abandonment problematic is linked to fluid pressure increase in the cavern after sealing. This phenomenon is the result of different factors that interact with each other: creep, heat transfer, dissolution, percolation, for instance. All these factors must be taken into account for designing the abandonment process. This paper will discuss these factors and will highlight their practical impacts on a deep salt cavern abandonment experiment (1500 meters deep). First measurements will be also presented.

1 INTRODUCTION

Underground salt cavern for storages are largely developed all over the world. One of the most beneficial characteristics of these underground caverns is their ability to store large quantities of hydrocarbon products. Salt caverns are essentially impermeable, meaning no fluid or gas can escape through the surrounding rock salt. This makes them ideal for storing high-pressure hydrocarbon products ranging from LPG's (Liquefied Petroleum Gasses) to Natural Gas (methane). But the storage of gaseous hydrocarbons remains the main use of salt caverns today.

The question of long term sealing or plugging of such a solution-mined cavern in a salt formation has been a contemporary topic for many years. Gaz de France performed in the late 1980s and early 1990s a series of succinct sealed well and cavern field tests (Durup 1991) in cooperation with Ecole Polytechnique (France) and were partially funded by the Solution Mining Research Institute Inc. (USA). These tests improved the knowledge of issues related to this problematic (Bérest et al. 1998) and allowed to recommend strategies/procedures for cavern abandonment. In 2002, Gaz de France decided to perform a pilot experiment on a deep salt cavern to validate this and to improve the present expert knowledge.

This paper introduce the issues and the factors to take into account in this problem range: salt creep, heat transfer between salt formation and cavern fluid, salt dissolution, fluid cavern percolation through the salt, for instance. The practical impacts of these factors are then highlighted with the test currently being performed on a cavern in a depth of 1500 meters. This cavern is on the natural gas storage site of Tersanne (south east of France) operated for over 35 years. The first results, particularly in term of temperature, are presented and compared to the simulation in the last part of the paper.

2 OVERVIEW OF THE MAIN ISSUE IN THE SALT CAVERN SEALING

2.1 *Salt creep*

When the underground rock salt formation is subjected to a stress difference, the salt deforms continuously. This visco-plastic deformation is termed "salt creep". The magnitude of the creep rate (or deformation rate) of salt depends on (a) the physical properties of the salt, (b) the magnitude of the stress differences existing in the salt, and (c) the temperature of the salt formation.

When a cavern is created in a salt formation, stress differences develop and the salt surrounding the cavern begins to creep (or flow) into the opening. Creep will continue until the cavern volume vanishes. Salt creep into a cavern will indeed continue indefinitely unless the isostatic stress state is reestablish. This could only achieved if a material with the same physical properties and temperature is placed into the cavern. But for practical and economical reasons, the filling material is generally saturated brine.

As the salt surrounding the cavern flows towards and into the cavern, the fluid in a sealed cavern is compressed. Since the rate at which the salt flows

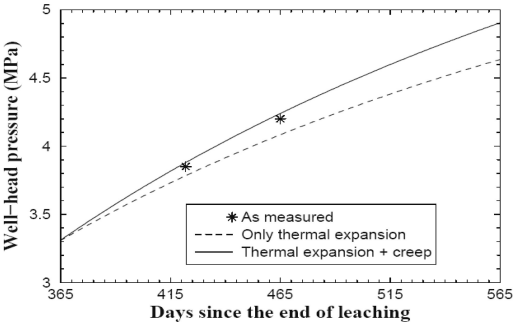

Figure 1. Pressure rise computations for Etrez cavern field, France.

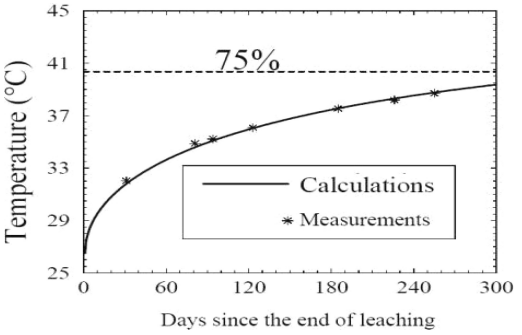

Figure 2. Brine warming computations for Etrez cavern field, France.

or creeps into the cavern depends on the difference between the cavern fluid pressure and a measure of the salt stress, the rate of convergence by creep slows as the cavern fluid pressure increases. Stationary creep can be described by Norton-Hoff's constitutive law (more details in chapter 3.6), whose uniaxial formulation is:

$$\dot{\varepsilon} = A\exp\left(-\frac{Q}{RT}\right)\sigma^n \tag{1}$$

In the case of a spherical cavern (the exact shape of a cavern is not spherical, but this approximation holds for rough estimations) the stationary volume loss rate can be written :

$$\dot{V}/V = -A\exp\left(-\frac{Q}{RT_\infty}\right)\frac{3}{2}\left[\frac{3}{2n}(P\infty - P_c)\right]^n \tag{2}$$

Where P_∞ is the lithostatic pressure, P_c is the fluid pressure in the cavern and T_∞ the geothermal temperature in the cavern average depth.

Figure 1 shows computations of a typical cavern fluid pressure response after a cavern is merely shut-in for instance after a leaching phase, (or sealed). Of course, the pressure rise observed in an actual shut-in cavern well is the result not just of salt creep, but also of the other factors described below. Pressure rise measurements on the field correspond essentially to the added effects of thermal expansion and creep (computed forecast in full line in the figure). This specific diagram shows two field measurements (down-hole pressure logs) matching quite satisfactorily with a pressure forecast curve; other cases with more frequent field points also confirm this statement.

2.2 *Salt massif/cavern fluid heat transfer*

Solution mining of a salt cavern results in a significant disruption of the thermal environment in the salt formation. The raw water injected into the formation to leach out a cavern is always much cooler than the salt formation. Continual leaching of a cavern to its final shape can result in a significant cooling of the salt formation surrounding the cavern, particularly near the cavern boundary. Unless a cavern has been inactive for a long period of time (several years), the fluid in the cavern will be at a much lower temperature than the "pre-cavern" temperature of the rock salt. The time required for the fluid in a salt cavern to reach a "steady-state" (far field) temperature depends of course on the temperature difference, but also to a large extent on the dimensions of the cavern.

Figure 2 illustrates a typical temperature increase of the brine in an inactive salt cavern. Here almost 75% of initial geothermal temperature is reached in a small 8000 m^3 cavern after one year. Temperature monitoring on the field (temperature logs) show that a good match can be obtained between measurements and computations.

Thus, when the cavern is sealed, heat will flow from the salt formation to the cavern fluid and the cavern fluid temperature will rise. The temperature rise in the fluid will result in an expansion of the fluid and if the cavern is sealed, the cavern fluid pressure will increase. This temperature rise is perhaps the most significant factor in producing an increase in the sealed cavern fluid pressure.

Thermal expansion effects can then easily be computed; if $\dot{T}$ is the temperature increase rate, then the contribution of thermal expansion to pressure build up rate is:

$$\dot{P} = \frac{\alpha}{\beta}\dot{T} \tag{3}$$

where the parameters are approximately $\alpha = 4.4 \times 10^{-4}\ K^{-1}$ and $\beta = 4 \times 10^{-4}\ MPa^{-1}$ for a spherical cavern. Hence, a 1 K temperature increase in a closed cavern leads to a 1.1 MPa pressure build up.

2.3 *Salt dissolution*

Again, unless a cavern has been idle for a long time, the cavern fluid will not be 100% saturated with sodium chloride. After the cavern is sealed, dissolution will continue as the saturation approaches 100% and as the temperature of the cavern fluid rises. Salt dissolution results in an increase in the cavern volume, which will decrease the cavern fluid pressure. For example, if fresh water is injected in a salt cavern, the cavern volume will eventually increase by about 15% beyond the volume of injected fresh water as the water becomes saturated. This cavern volume increase will consequently produce an associated pressure decrease.

Furthermore, the salt dissolution process itself is an endothermic chemical reaction. This endothermic reaction will reduce the temperature of the cavern fluid (brine), which further decreases the cavern fluid (brine) pressure.

2.4 *Brine transport from the cavern into the salt formation*

Any brine permeating from the cavern into the surrounding salt formation will decrease the volume of fluid in the cavern, and thus, the pressure in the cavern fluid. The nature of the cavern fluid transport from the cavern to the salt formation is perhaps the most significant issue in cavern sealing and abandonment. It is difficult to comprehend fluid pressures within the salt matrix when we normally think of salt as an impermeable matter. But, penetration of cavern brine into the salt formation will result in fluid pressures in the salt matrix which will in turn affect the salt matrix stresses, the creep of the salt, the salt micro-permeability, and in turn, the cavern fluid pressure. This complex situation has been a major challenge in the SMRI Cavern Sealing & Abandonment Research Program (Ratigan 2003).

As the cavern fluid pressure increases in a cavern, eventually a fluid pressure distribution will be approached in which the cavern fluid pressure in the upper part of the cavern exceeds the maximum (least-compressive) stress in the salt behind the cavern wall. Similarly, in the lower part of the cavern, the brine pressure will be less than the maximum (least-compressive) principal stress in the salt surrounding the cavern behind the cavern wall. This condition will necessarily occur simply caused by the density contrast between salt and the cavern fluid. The vertical pressure gradient in the brine must be consistent with the brine density, which is markedly less than (about one-half) the density of salt. Thus, a pressure difference will always exist (at least over a portion of the cavern surface) between the cavern fluid and the salt formation.

Some cavern fluid will always permeate into the salt in the cavern wall both before and after cavern sealing

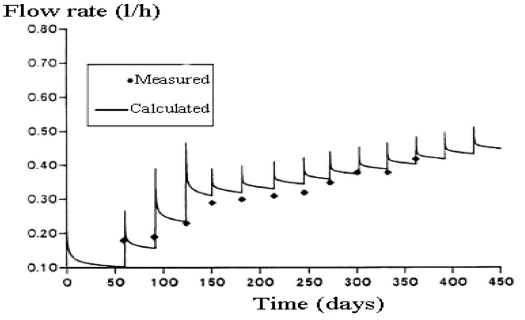

Figure 3. Brine percolation in a salt formation (Durup 1994).

(unless the cavern fluid pressure is less than the pore pressure in the surrounding salt). Before the cavern is sealed, the amount of cavern fluid that permeates into the salt cavern walls is negligible. After the cavern is sealed and the cavern fluid pressure increases, the amount of cavern fluid permeating the cavern wall increases both because the pressure gradient (driving the fluid transport) increases and because the salt permeability may increase. This "secondary" permeability observed in different laboratory experiments could be linked to a micro-fracturation (Fokker 1995). This micro-fracturation is different from a classical crack creation, which would be the ultimate result of rock damage because the other features of the rock salt stay unchanged .

Figure 3 illustrates increasing amounts of cavern fluid (brine flow-rate) permeating into the salt formation as a function of imposed increasing pressure gradients in the cavern. This relationship between the pressures and the flow-rates has served to evaluate a "global micro-permeability" K for this specific rock-salt massif.

Brine percolation across the cavern wall can be evaluated by supposing that the cavern behaves like a spherical cavern, of radius R such that $V = 4\pi R^3/3$, that is in a porous medium and that percolation globally obeys Darcy's law. During steady state, the brine flow rate across the cavern wall can be expressed as :

$$\dot{\varepsilon}_{perc} = \frac{Q}{V} = -3K\frac{P_c - P_0}{\eta R^2} \tag{4}$$

where K is salt global micro-permeability (typically between 10^{-22} m^2 and 10^{-19} m^2), P_c the brine pressure in the cavern, P_0 the natural pore pressure in the salt massif, R the cavern radius, and η the cinematic viscosity of the brine (typically 1.2×10^{-3} Pa.s at 45°C, which is decreasing with increasing temperature). P_0 corresponds to the halmostatic pressure which supposes that there is no brine flow through the cavern wall when the later is open to the atmosphere

at the surface; this has been observed on the field (Durup, 1994).

If the cavern fluid pressure cannot be reduced sufficiently through the permeation described above, it is conceptually possible that a salt fracture or fractures could develop, which in turn, would reduce the cavern fluid pressure. Whether or not a fracture or fractures develop depends on the rate of cavern fluid pressurization. Low pressurization rates are not expected to result in fracturing of the salt, some brine permeating the salt will limit the eventual brine pressure rise in the cavern. On the contrary, very high rates of pressurization might well produce a fracture. High rates of fluid pressure increases are generally the result of cavern fluid thermal expansion in a sealed cavern. Thus, if the cavern fluid thermal expansion can be mitigated, for example by a waiting a certain space of time before sealing, where the cavern temperature is allowed to approach equilibrium, then the risk of salt fracture will be either significantly reduced or completely avoided.

2.5 *Brine transport from the cavern at the casing shoe*

Cavern fluid pressure decrease, which results from cavern fluid transport out of the cavern at the sealing plug/casing shoe, is similar to a cavern fluid pressure decrease resulting from cavern fluid transport into the walls of the cavern.

Permeation can occur through the sealing cement plug and the cement between the salt borehole wall and the deepest casing. Additionally, pressure decrease can conceptually occur from fluid transport that produces and results from fracturing of the salt/cement or the cement/casing interfaces.

2.6 *Coupled processes*

The processes discussed above are interconnected or "coupled." Some of the couplings are "one-way couplings" while others are "two-way couplings."

For example, brine temperature change results in brine pressure change. However, brine pressure change does not cause significant brine temperature change. This is a one-way coupling.

On the other hand, salt creep causes brine pressure change and brine pressure change affects salt creep. This is a two-way coupling. Because of this complex coupling, a comprehensive understanding of the sealed cavern stress states and potential fluid (brine) transport is only possible through sophisticated numerical modeling.

On this basis, Gaz de France financed the development (together with Brouard Consulting) of the specific modeling tool LOSAC® dedicated for the abandonment of salt caverns. This is the code used to interpret and predict down-hole cavern behaviour in the TE02 pilot abandonment experiment.

3 THE TE02 PILOT EXPERIMENT

3.1 *Brief description of the Tersanne cavern gas storage and the cavern TE02*

Tersanne is a cavern gas storage situated in south-east of France. It is the first cavern storage facility of Gaz de France. It is composed of 14 caverns developed from 1968 to 1986. All these caverns were in operation until 2004. The salt caverns were developed in a 200 meter thick halite layer between 1350 to 1550 meters below the surface. The salt is pure with only a few percent of dispersed clayey and anhydrite insolubles. The last casing shoe is typically 25 meters below top of salt, cavern neck is about 15 meters high and the cavern itself about 100 meters high. The average cavern spacing of about 300 meters integrates topographical constraints, but gives a globally hexagonal cavern network. Except for TE01 and TE02, each Tersanne cavern had an average initial cavern storage space of 200,000 m^3.

Cavern TE02 is the very first cavern developed by Gaz de France for natural gas storage, leached from 1968 to 1970. It was also the smallest cavern: it's initial geometrical volume was 100,000 m^3. After 35 years of gas operation, about 60% of this volume was lost by salt creeping. The cavern initial diameter was 56 m. The top of the salt layer is 1372 meter deep for a last cemented casing shoe at 1392 m. The cavern roof is cone-shaped for mechanical stability. It starts at 1406 m which correspond to a cavern neck of 13 meter.

3.2 *The concept followed for the experiment*

A largely accepted salt cavern abandonment concept has been proposed to the industry through the SMRI (Brouard et al. 2001). Basically, this concept states that provided (a) the salt formation has adequate permeability properties, and (b) that cavern brine thermal expansion is mitigated by a waiting time allowing cavern temperature to approach equilibrium, then cavern brine pressure will reach an equilibrium pressure reflecting the equalizing effects of brine permeation and salt creep. The primary objective of the TE02 pilot abandonment project is to verify this concept for a relatively deep gas cavern (about 1500 meters deep) where thermal and mechanical conditions are very specific. Indeed, even if similar tests have been initiated, all have up to now addressed relatively shallow salt caverns (less than 500 meters deep). This is the first case where the concept is experimented on a deep natural gas storage cavern.

Figure 5 shows an example of forecast of the very long term (300 years) pressure evolution after (1) temperature effects are mitigated, and (2) the salt cavern is sealed. Pressure is calculated at well head for practical experimental reasons, but the real permanent sealing, will be ensured by realizing cement plugs at the casing

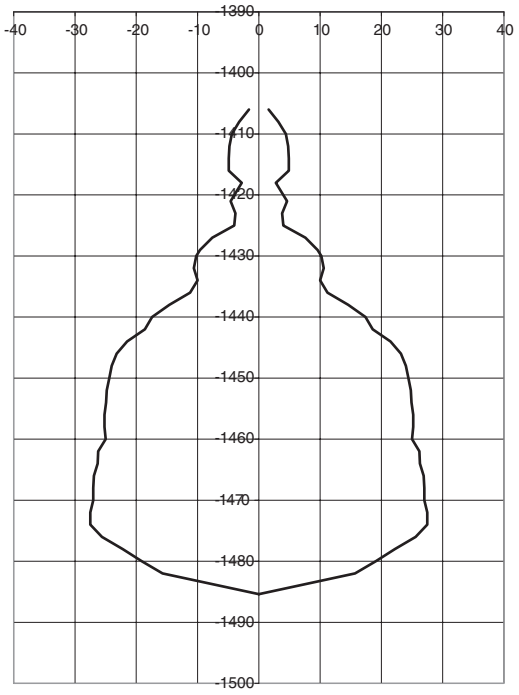

Figure 4. Initial TE02 cavern shape from 1970 sonar survey.

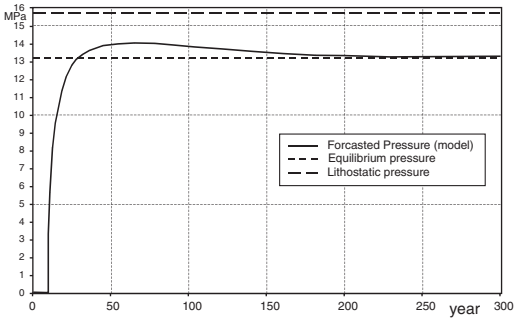

Figure 5. Preliminary forcast of the long term pressure evolution after sealing TE02 cavern.

shoe and at different depth intervals in the well. Consequently, the anticipated well head pressure will be nil.

The curve anticipates long term equilibrium pressure to be over 2 MPa below lithostatic pressure, hence clearly highlighting that any risk of fracturation is well avoided. The slight pressure rise above equilibrium pressure over the first hundred years corresponds to residual temperature effects.

The principal objective of the TE02 experiment will be to collect sufficient data over several years in order to improve the reliability of the final forecast.

3.3 *Re-brining and salt dissolution concerns*

The very first task performed in this pilot test was to remove the natural gas from the cavern and to have it refilled with saturated brine ("re-brining"). This operation started in April 2005 with the replacement of the natural gas pushed out of the cavern by fresh water injected at the bottom of the cavern. Approximately 40,000 m^3 of water were needed to re-fill TE02 cavern, confirming that about 60% of the initial cavern volume has been lost by salt creep over the past 35 years of operation (1970–2005). From past experience, this value of almost 2% volume loss per year is quite typical of Tersanne caverns.

This removal operation lasted 35 days. Less than two months later, by end of June, the water had naturally turned into saturated brine (about 320 g/litre) and this saturation process was carefully monitored by regularly sampling brine from the cavern (7 samples over the re-brining period), and measuring its density.

This saturation process implied some salt dissolution at the cavern walls, increasing the cavern volume by about 15% and subsequently modifying the cavern shape. The water was injected at the bottom of the cavern through a brine tubing and Gaz de France calculated precisely this dissolution process with a specific in-house software called RESAUM. This software determines in real time the depth of the gas/brine interface, which was deliberately maintained below the last casing shoe as long as complete saturation of the brine was not reached, in order to reduce any potential risk of uncontrolled dissolution at the casing shoe. Ultimately however, the last casing shoe was also drowned, all the remaining gas was removed, and the bore-hole was completely filled up with brine all up to the surface (July 2005).

The gas completion will be removed by the end of 2006 and a sonar survey will be run for detailed data on the cavern shape (and volume). Additionally, the last casing and its cementation will be controlled (Corrosion and Cement Bond logs). The cavern will be equipped with a permanent logging cable for continuous temperature profile and down-hole pressure monitoring; these are crucial input parameters for the LOSAC software. Well-head pressures will be also continuously monitored and any withdrawing of brine to reduce cavern pressure is being precisely measured and interpreted in terms of creep and compressibility.

3.4 *TE02 cavern compressibility*

A standard value of the cavern intrinsic compressibility factor for Tersanne caverns (see Equation (3)) is $\beta = 4 \times 10^{-4}\,\mathrm{MPa}^{-1}$. Very first estimations of the apparent compressibility β' of TE02 were performed during early stage withdrawing of brine (September 2005) from the cavern, and this parameter, which is

just a ratio $\beta' \sim dV/dP$, was found to be approximately 50 m^3 per MPa of pressure decompression. β' is linked to the intrinsic compressibility factor by the relation $\beta' = \beta V$ where V is the cavern volume. So β can be expressed by $\beta = \beta'/V = dV/(V.dP)$.

From TE02 cavern volume of $V \approx 40{,}000\ m^3$ can be derived $\beta = 12,5 \times 10^{-4}\ MPa^{-1}$ which is clearly over three times the standard value. Such discrepancies have already been observed either when cavern shape is flat (or "penny-shaped") or when the cavern shows wall surfaces with "pockets" liable to trap gas during the re-brining (Brouard et al. 2001). Figure 4 shows that TE02 cavern shape has neither of these particularities. Our opinion is that these preliminary measurements were performed at such an early stage after the re-brining process that there was still substantial dissolved natural gas in the brine. In time and with subsequent withdrawing and evacuation of dissolved gas, TE02 cavern compressibility values are expected to decrease and approach standard values.

Regular cavern compressibility measurements are scheduled in the future test program.

3.5 *Temperature effects*

Immediately after TE02 was re-filled with brine, the most active factor in the salt cavern was brine warming (creep and brine percolation can be neglected at this early stage). This temperature rise induces a brine thermal expansion

$$\dot{\varepsilon} = \alpha \dot{T} \tag{5}$$

(T_i being the brine temperature). If TE02 was at this stage permanently closed at the well-head, the expansion would be prevented and consequently brine pressure would increase

$$\dot{\varepsilon} = \beta \dot{P} \tag{6}$$

which means that

$$\dot{P} = (\alpha/\beta)\dot{T} \tag{7}$$

For a thermal expansion coefficient of saturated brine of $\alpha = 4.4 \times 10^{-4}\ K^{-1}$, and a standard intrinsic compressibility factor $\beta = 4 \times 10^{-4}\ MPa^{-1}$, this means that a increase of 1 K in temperature generates about 1 MPa increase in pressure. Now this clearly highlights the need to have precise evaluations of two factors:

- the temperature evolution inside TE02 cavern
- the compressibility factor for TE02 cavern

Temperature effects in TE02 was first evaluated for an average reference cavern depth of 1468 m. At this depth, and considering an average geothermal gradient at Tersanne of A = 0.0363 K/m, the initial salt massif temperature is 68°C. But since the water used to re-fill TE02 was only at about 15°C, the temperature gap was potentially 53°C. Cavern temperature is relatively uniform with depth due to brine mixing by thermo-convection. Therefore, there existed a potential pressure increase of 53 MPa if the cavern was permanently sealed right away. Added to the cavern brine pressure (halmostatic pressure) of 18 MPa at the reference depth, the total cavern pressure of 71 MPa would largely exceed the fracturing pressure at the cavern walls, especially at the weakest point, which is at casing shoe (1392 m). There the lithostatic pressure is only about 30 MPa. To avoid this situation, it has been chosen to allow the brine temperature to rise naturally without shut the well.

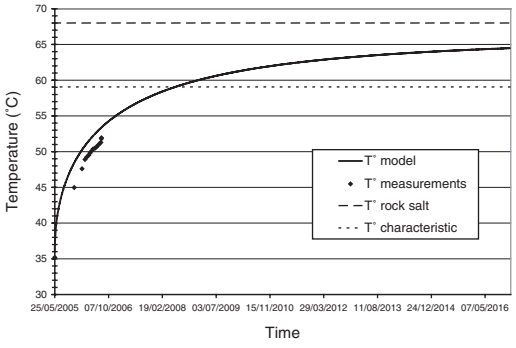

Figure 6. TE02 temperature evolution.

Practically that means a waiting phase of several years will be needed until the cavern temperature has "sufficiently" approached equilibrium with the rock massif. During this observation phase, measurements will include cavern temperature profiles, creep evolution (pressure increase data), and compressibility values (pressure relief data). These data will serve as input in Gaz de France's specific cavern abandonment tool LOSAC to forecast a reliable date for the final cavern sealing.

Figure 6 shows the first measurements of the cavern temperature compared to the preliminary computations. The computations forecast that the brine steady state temperature of about 68°C will only be reached after several decades. However, over 75% of this final temperature (T° characteristic on the Figure 6) can be reached in about 4 years.

While the injected water temperature at well-head was only 15°C (April 2005), in-situ measurements indicated that the temperature was already 35°C by June 2005 and reaches 52°C by August 2006. From the end of the re-brining process (July 2005) and the anticipated date of removal of the gas completion (end of 2006), the cavern brine is therefore essentially in its transient thermal expansion phase.

The measurements show also that the model overestimates slightly the temperature, that could signify that the time to reach the T° characteristic is underestimated. If the first measurements were confirmed with the optical fibre logging system scheduled after the removal of the gas completion, it would be possible to re-evaluate input parameters of the model and get a better fitting.

At present, the cavern is not permanently open to allow operations of preparation of the completion removal on the plateform. The brine production rate seems to be relatively unstable and difficult to analyse. After the removal of the completion, the cavern will stay in a steady state for long time. Reliable data could get in term of brine production, compressibility, rise of temperature, for instance.

3.6 *Available data to evaluate salt creep and permeation in TE02 cavern*

The salt creep described in chapter 2.1 needs to be determined for TE02, essentially because it is one of the major component which makes the cavern pressure rising (if the well-head is temporarily shut, as planned for later more stabilized periods). For its creep rate computations, the LOSAC software requires the mechanical parameters of a steady-state behaviour law, sometimes called the Norton-Hoff constitutive (or power) law:

$$\dot{\varepsilon} = A \exp(-\frac{Q}{RT})\sigma^n \tag{8}$$

Where A, n and Q are the well-known parameters, σ is the applied stress, and T is the (absolute) rock-salt temperature. Fitting of Tersanne rock-salt laboratory data to this constitutive law yielded an exponent n close to 3, and Q/R values ranging from 4100 to 6600 K which are all quite typical values.

This creep law for rock salt is characterized by a constant strain rate which is generated by a constant stress (after a transient phase), with a highly non-linear influence of the stress on the strain rate. Additionally, in this steady-state creep law there is no visco-plastic stress threshold nor any strain hardening. But, this law is well adapted for salt cavern abandonment, because the issue is the very long term behaviour (maybe centuries) of a salt cavern submitted to a relatively simple pressure scenario of the cavern brine pressure (either slightly increasing or at equilibrium if the abandonment concept is verified). In fact, during salt creep tests under uniform stress, experience shows that after only some months, strain rates clearly stabilize.

If there is very little brine percolation out of the cavern, cavern pressure will rapidly approach equilibrium with the geostatic pressure and the application of this law will efficiently express this kinetic. On the other hand, if percolation is more active, the application of this law will tend to indicate an unchanged equilibrium pressure as long as cavern volume has not decreased substantially, which is a slight drawback. In fact, the mechanical behavior of rock-salt under extremely low stresses (as will be the case on the long term in a closed abandoned cavern) remains difficult to study, even in laboratory.

In terms of permeation, Gaz de France has regularly performed brine tightness tests on all the Tersanne wells (1968–1980), just after the drilling of each well, when there was only the borehole (simple geometry and small volume) i.e. before leaching begins. The basic principle of these tests is to apply a constant brine pressure level on the rock salt and to measure the corresponding steady-state brine percolation rates in the rock-salt massif. The value of the brine percolation rate validates (or occasionally do not validate) the tightness of the rock-salt massif and the cementation of the last casing shoe at the corresponding pressure level.

The results of these Tersanne tightness tests have been interpreted in terms of global in-situ micropermeability of the rock salt (Brouard et al. 2001). The interpretation was carried out in two steps. Firstly, the measured "apparent percolation rates" were corrected by taking into account such effects as transient permeation, temperature, transient creep, salt dissolution, compressibility, for instance. Secondly, the "corrected" steady-state percolation rate was back-calculated using assumptions on porosity, pore compressibility, and an "equivalent" global micropermeability K. The average K value for Tersanne rock salt is 2×10^{-21} m^2.

4 CONCLUSION

This paper provides an overview of the conceptual approach which Gaz de France intends to apply for the long term abandonment of its deep salt caverns (currently operated as compressed natural gas storages). It involves a complex combination of several physical processes and further research effort is required to improve the understanding of their effects on a specific cavern site. Consequently, Gaz de France has initiated a real-scale pilot abandonment test on TE02, the oldest cavern at the Tersanne gas storage facility.

In 2006, preparatory work for the test is ongoing: the cavern has been re-brined in 2005, gas completion removal is scheduled by the end of 2006, and the cavern will be equipped with down-hole monitoring devices (pressure and temperature). The cavern will remain several years under observation allowing sufficient temperature build-up of the brine.

The first results confirm that the transient thermal expansion phase of the re-filled brine is most important for the conditions in the cavern . It seems also that the rate of temperature is slightly smaller than forecasted but this observation must be validated. All the data collected will serve as input for LOSAC, an in-house software specifically developed for salt cavern long term abandonment computations.

The basic objective of this test is to demonstrate that pressure build-up in a closed Tersanne salt cavern does not reach geostatic values at the top of the cavern and the casing (i.e. no fracturing), but due to the combined effects of salt creep and salt (micro-) permeability, the pressure build-up will surely vanish, because a steady-state value of cavern pressure, significantly lower than geostatic pressure, will be reached.

Determining the appropriate and reliable date for the safe, environmentally friendly and definitive long-term closure of this specific salt cavern well will be the major result of the experiment.

REFERENCES

Berest, P., Bergues, J., Brouard, B., DeGreef, V., Le Bras, Y., Durup, J.G. & Guerber, B. 1998. Long-Term Evolution of a Sealed Cavern; SMRI Research Project No. 98-0004, prepared for the Solution Mining Research Institute by LMS – Ecole Polytechnique & Gaz de France, France.

Brouard, B., Bérest, P. & Durup, J.G. 2001. In-situ salt permeability testing. Proc. of the Solution Mining Research Institute, Fall Meeting 2001, Albuquerque.

Durup, J.G. 1991. Long-term Permeability Field-test in Rock salt; Proc. International Congress on Rock Mechanics, Aachen.

Durup, J.G. 1994. Long-term tests for Tightness Evaluations with Brine and Gas in Salt; Proc. of the Solution Mining Research Institute, Fall Meeting 1994, Hannover.

Fokker, P.A. 1995. The Behavior of Salt and Salt caverns. Thesis dissertation, Delft University of Technology, The Netherlands.

Ratigan, J., 2003. The Solution Mining Research Institute Cavern Sealing and Abandonment Program 1996–2002; Proc. SMRI Spring Meeting 2003, Houston.

The Mechanical Behavior of Salt – Understanding of THMC Processes in Salt –
Wallner, Lux, Minkley & Hardy, Jr. (eds)
© 2007 Taylor & Francis Group, London, ISBN 978-0-415-44398-2

Long-term behaviour of sealed brine-filled cavities in rock salt mass – A new approach for physical modelling and numerical simulation

K.-H. Lux
Professorship for Waste Disposal and Geomechanics, Clausthal University of Technology, Clausthal-Zellerfeld, Germany

ABSTRACT: The load-bearing behaviour of caverns constructed in salt formations to extract minerals or to store energy has been the focus of scientific research for many decades. This research previously concentrated on confirming the stability and safety of the caverns during construction and operation. During the past 10 years, the focus has also partially fallen on the questions involving the abandonment of caverns and their long-term behaviour. Various options are available for abandoning caverns: the preferred option in most cases is filling the caverns with water/brine and sealing the access borehole. The load-bearing behaviour of fluid-filled closed caverns has therefore been the focus of technical and scientific investigations. This paper presents a new approach to the analysis of the load-bearing behaviour of sealed fluid-filled salt caverns. This primarily concerns the process of brine infiltration into the originally impermeable salt rock, and the physical modelling and numerical simulation of this process.

1 INTRODUCTION

Salt caverns have been constructed in many countries around the world for several decades. These salt caverns may be a by-product of the solution mining of halite or specifically planned for the storage of hydrocarbons such as oil and natural gas. The load-bearing behaviour of salt caverns during the construction and operation phases has also been the focus of scientific and technical investigations at a national and international level for many decades, e.g. Lux (2006) and the references contained in this paper. In the case of waste disposal caverns in Germany, recommendations have already been elaborated concerning the stipulated confirmation of stability, tightness and environmental protection, especially long-term safety. This excludes the disposal of liquid waste in salt caverns, because investigations carried out at the time were unable to rule out fluid-pressure related failure of the rock mass formation.

The scientific and technical investigations concentrate on further developing the principles for physically modelling the geomechanical and geohydraulic processes (improving the understanding of the processes) and the computer simulation (improving reliability of the load-bearing structural analysis). The ultimate aim of this work is to improve the precision of the confirmation required to guarantee static stability and tightness, as well as economic optimisation (e.g. increasing cavern size or extending the operating parameters and operating procedures) by reducing uncertainties or lowering conservative assumptions and safety margins.

Another question which was raised at around the start of the 80s was how to deal with the salt caverns after shutting down leaching operations once the authorised final configuration had been reached (brine extraction) or after shutting down storage operations (oil/natural gas storage). At a national and international level, experts came to the conclusion over the course of time that salt caverns scheduled for abandonment should be filled with water/brine, plugged after a certain undetermined time (dedicated to temperature equalization between fluid and rock mass) with a long-term fluid-tight seal in the borehole, and then left to their own devices. The aspect that requires clarification for the official abandonment operating planning procedure is how a sealed brine-filled cavern behaves in the long-term, e.g. with respect to pressure build-up as a result of rock mass convergence, and the capacity of the salt rock to withstand fluid pressure, especially at levels higher than the rock mass stresses of the surrounding salt rock mass.

2 STATE OF THE ART

In Germany the long-term behaviour of sealed brine-filled caverns has been the subject of scientific investigations for many years (a list of references is

given in Lux (2006)). The basic question looked at by the theoretical studies during the 80s was the size of the hydraulic pressure built up in a sealed cavern as a result of formation convergence, and whether the fluid pressure causes fracturing in the cavern roof zone. Another question concerned the actual size of the frac pressure involved. Some investigations indicated that the rock would frac when the minimum formation pressure was reached. On the other hand, other investigations also indicated that because of the hydraulic tensile strength of the salt frac-failure only occurred when much higher hydraulic pressures were reached.

To provide a final and convincing answer to these controversial theses which have been the subject of discussions for many years, a consortium of cavern operators decided to supplement the theoretical studies by conducting a large-scale field test from 1991 to 1994 in a representatively selected and properly technically equipped cavern in Germany. This was carried out at the Etzel K102 cavern (Consortium 'Druckaufbautest' 1994). The aim of this test was to determine the fluid pressure level at which the formation would start to fail and whether this failure involved macrofracing analogous to the fracturing of the rock during a hydraulic fracturing operation, or whether the loss of formation integrity was due to a different failure mechanism. Other field tests were conducted in France and Germany (see Lux (2006) for a reference list). A summary of the state of developments at the end of the last decade, and the discussions on the abandonment of salt caverns is reported in Crotogino & Schmidt (1999).

The latest field experiments dealing with this topic involved carrying out a pressure build-up test in a cavern-like cavity specially excavated in a salt mine in Germany for this purpose. The cavity had a volume of approx. 22 m^3. At the end of the experiment a gallery was driven into the cavern to enable direct visual inspection of the penetration of the tracered brine into the rock immediately surrounding the cavity.

3 PRESSURE-DRIVEN INFILTRATION AS THE PROCESS MECHANISM

According to the current level of understanding, liquid and gas tight halite formations under primary formation pressure become permeable under low to negligible pressure build-up rates with brine as a pressure fluid when a fluid pressure level is reached that approximately corresponds to the minimum formation pressure of homogenous and texturally uniform halite. This is a result of the progressive infiltration of brine through the micro migration paths formed as a result of this fluid pressure build-up. The following hypothesis can be formulated for the physical modelling and numerical simulation of this infiltration process when supplementing the SMRI-model that is based on an approach which assumes already slightly permeable halite a priori:

- The undisturbed halite formation is liquid tight and gas tight under primary rock mass pressure conditions.
- Secondary migration paths are formed at a micro and meso level along the grain boundary surfaces in the grain fabric of the salt rock under a specific constellation of conditions (still to be determined in more detail) involving brine pressure and the minimum formation stress.
- The volume-related intensity (= secondary porosity) and propagation rate (= microfrac formation rate) of the secondary migration paths are dependent on the rock type and the stress state, and can be estimated, in an integral way at least, from laboratory tests.
- The mean (integral) fracture propagation in the rock mass follows the rules of hydrofrac theory with respect to their general direction when considered at a macroscopic level. The local stress field and the rock fabric have the most significant influence on the main direction of fracture propagation.
- Dispersive fracture propagation is ignored in the first modelling step but should be integrated within the theory at a later date.
- The main parameters determining the progression of the brine front in the salt rock at isothermal conditions are salt rock mass convergence (dependent on the creep behaviour of the salt rock, the depth of the cavern and the cavern geometry as well as the formation stress), brine compressibility, secondary porosity, and the difference between the minimum formation stress and fluid pressure at the fracture propagation front.

This physical model approach has two main advantages compared to the concept described in SMRI (2002):

- The basic assumption that the halite rock in an undisturbed state is fluid tight and gas tight under the influence of formation pressure does not have to be abandoned for modelling reasons by specifying an interlinked fluid-filled fabric of pore spaces with primary permeability.
- The secondary more permeable formation zone is not derived from a stress-state-related condition, and its 3-dimensional development is also not only restricted to the immediate periphery of the cavern. Instead, its development in time and space is individually determined as a result of the physical modelling/numerical simulation by the secondary migration paths induced by the brine infiltration in the rock. This involves estimating the secondary permeability from the secondary porosity, which is then used to characterise the hydraulic properties of the infiltrated part of the rock.

4 BASICS OF PHYSICAL MODELLING AND NUMERICAL SIMULATION

4.1 *The computer code INFIL*

A computer code for the numerical simulation of the infiltration process was developed based on the observations from laboratory tests (fluid infiltration in halite specimens) and the still only verbally formulated approaches presented here on the start of infiltration and the propagation of microfractures as the basis for the physical modelling. This software called INFIL does not just include the program to implement the physical model of a time and stress/fluid pressure controlled infiltration process in a primarily impermeable continuum. It is also the central control program of a software package for the numerical simulation of the geomechanical processes taking place prior to cavern sealing, and particularly, the geomechanical/(geo)hydraulic coupled processes taking place after cavern sealing, via pressure build-up, and infiltration all the way through to the ultimate flow through the secondary migration paths induced by the infiltration process, which can be subdivided into a pressure build-up phase, an infiltration phase and a flow phase.

4.2 *Pressure build-up phase*

The pressure build-up phase means a simulation of the past history, and then after sealing, a simulation with the MISES3 simulator (FEM-software) of the cavern convergence and brine temperature change related pressure build-up in the brine-filled sealed cavern. If the brine heats up in relation to a temperature gradient between the formation and the brine, the mechanical-hydraulic simulation is superimposed by an independent thermodynamic simulation which quantifies the time-dependent changes in brine temperature and the associated brine expansion and resulting change in brine pressure.

4.3 *Infiltration phase*

Physical modelling and numerical simulation of the infiltration process give rise to specific approaches concerning the start of infiltration, the direction of infiltration, the infiltration rate and the infiltration paths, as well as the infiltration intensity and infiltration propagation.

4.3.1 *Start of infiltration*

Brine infiltration into the salt rock mass begins when the fluid pressure exceeds the minimum principal stress in a directly fluid-pressurised rock mass element:

$$p_{Fl} > \min \sigma . \tag{1}$$

If the fluid pressure is lower than the minimum principal stress, there is no infiltration.

4.3.2 *Direction of infiltration*

The infiltration direction is derived from the direction in which the secondary migration paths are induced. Applying the hydrofracturing theory to a material with an isotropic fabric implies that fracture propagation takes place normal to the smallest principal stress and therefore vice versa in the direction of the largest principal stress. More complex relationships exist in anisotropic rock fabrics where empirically the migration paths develop preferentially along the bedding or cleavage planes. Additional assumptions must be incorporated in the model in such cases.

4.3.3 *Infiltration rate*

The infiltration rate is lithology-dependent and must be determined in the laboratory. Laboratory investigations reveal the dependence of infiltration rates on the hydromechanically effective fluid pressure (stress difference between fluid pressure and minimum formation stress), which is termed $\Delta\sigma_p$. The empirically selected approach is

$$\bar{v}_{\text{inf}} = a \cdot \exp\left(b \cdot \Delta\sigma_p\right) \tag{2}$$

where a and b are dependent on the infiltrated rock mass material and the infiltration medium (e.g. tracer fluid, brine or gas).

4.3.4 *Infiltration path*

The physical model assumes constant conditions/states for time increment Δt. The infiltration path derived from equation (2) is therefore:

$$\Delta u_{\text{inf}} = \bar{v}_{\text{inf}} \cdot \Delta t \tag{3}$$

4.3.5 *Infiltration intensity*

The infiltration intensity describes the fluid volume accommodated i.e. stored in the secondary induced pore space within a rock element. The secondary induced pore space is determined in the laboratory and characterised by the secondary porosity ϕ^s. The infiltration volume (storage volume) for a rock element and a time increment Δt is defined as

$$\Delta V_{\text{inf}} = \phi^s \cdot \Delta V_0 = \left(m \cdot \Delta\sigma_p + c\right) \cdot \Delta V_0 \tag{4}$$

4.3.6 *Infiltration propagation*

When infiltration has begun, infiltration continues into the neighbouring rock when the complete infiltration (saturation) of the observed rock element has taken place after a period of time and when, taking into account the changed fluid pressure conditions (infiltration-related decompression, creep and temperature-related compression) as well as the changed formation stress field (creep-related stress relocations), the conditions have been fulfilled for further infiltration into the next rock element adjacent to the originally observed rock element (infiltration conditions).

4.4 *Flow phase*

If the infiltration front reaches a permeable salt solution or groundwater bearing horizon, the infiltration process changes to a flow process. The flow here follows the secondary migration paths formed during the infiltration phase. The salt rock mass continues to be impermeable away from the infiltration zone.

When modelling the flow process, it is assumed that lamina flow takes place in the brine-saturated interlinked secondary migration paths in the infiltration zone in accordance with the Darcy flow model

$$v_f = k_f \cdot i. \tag{5}$$

The hydraulic conductivity is derived here from the secondary permeability which itself is related to the secondary porosity and the secondary stress field via PoroPerm-Model. Various PoroPerm-Models are known from the literature (a reference list is given in Lux (2006)).

If looked at in more detail, the infiltration zone can be considered as a porous water-saturated medium that mechanically – via the (disturbed) mineral grain fabric – as well as hydraulically – via the pore water pressure – has a supporting effect on the surrounding impermeable rock, and vice versa is accordingly placed under stress as a result of the damage to the grain fabric caused by the creation of secondary migration paths and the pore water pressure. However, it does not have the same mechanical properties as the neighbouring non-infiltrated rock. This change to the stress conditions and material properties of the rock in the infiltration zone (brine-infiltrated halite) needs to be taken into consideration when analysing the load-bearing behaviour, or determined by carrying out suitable laboratory tests.

5 SOME RESULTS OF LABORATORY INVESTIGATIONS

Laboratory investigations on relatively large specimens measuring $l/d = 30/15\,\text{cm}$ were carried out in test apparatus specially designed and constructed for these tests to determine the infiltration behaviour of halite. The testing principle involves placing the specimens under triaxial stress and simultaneously applying an axial fluid pressure. The fluid pressure is the technical test variable and can be adjusted to lie above or below the lateral (minimal) mechanical stress. The axial stress is usually higher than the fluid pressure. This test constellation leads in theory (in isotropic fabrics) to an axially-aligned propagation of the infiltration front with respect to the specimens. The horizontal stresses occurring at the end of the specimen at the boundary to the pressure piston of the test apparatus, arising from the blocked lateral

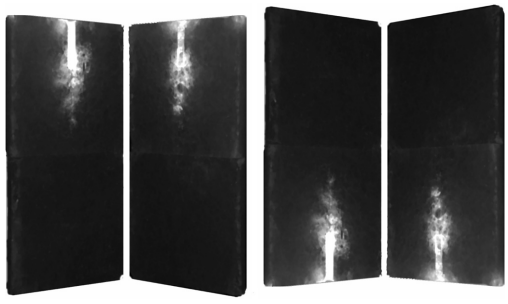

Figure 1. Formation of the infiltration zone in a sample (laboratory tet, left figure) and according to the circumstances in a cavern (right figure).

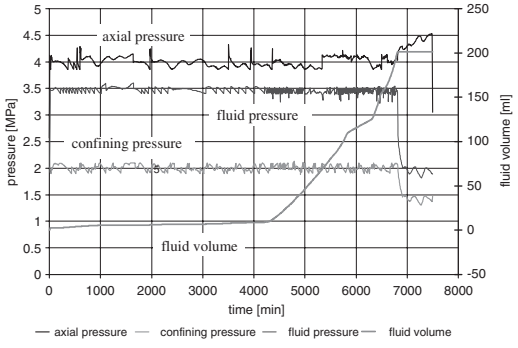

Figure 2. Measurement data of an infiltration test.

extension in addition to the externally applied lateral stresses, are estimated to be minor. Fluid infiltration takes place via an artificially created slot or small drill-hole a few centimetres long to simulate an imperfection in the fabric of the fluid-pressure stressed rock surface. The mechanical stresses, i.e. the axial pressure σ_1 and the lateral pressure $\sigma_{2,3}(\equiv \min\sigma)$ as well as the fluid pressure p_{Fl}, are measured during the test. The fluid pressure p_{Fl} is kept constant by adding pressure liquid if infiltration takes place. The associated fluid volume V_{inf}, which corresponds to the infiltration volume, is also measured.

The test finishes at the end of a defined test or infiltration time, or if a fluid breakthrough and an approximately stationary flow has been reached. The specimen is dissected at the end of the test. Because the pressure fluid contains a tracer, the infiltrated zones can be visualised under UV-light. Figure 1 shows a typical infiltration test result.

Representative measurement data of an infiltration test are shown in Figure 2. The diagram shows the mechanical and hydraulic pressures adjusted to remain constant, as well as the amount of fluid injected into the specimen to maintain a constant fluid pressure. This fluid volume therefore corresponds to the volume of

fluid infiltrated into the specimen and therefore also corresponds to the infiltration volume.

The tests reveal that the injection or infiltration volume plotted against time can be divided into two periods characterised by approximately constant but very different infiltration (= injection) rates. In the interpretation, the first part of the curve with the much lower rate is seen as corresponding to the actual infiltration process: driven by the pressure which is adjusted to remain constant, the fluid creates inter-granular migration paths in the crystal grain fabric when it reaches an adequately high pressure level compared to the lateral mechanical (minimum) stress. The fluid penetrates the inter-granular migration paths which are then propagated as the fluid moves forward. This gives rise to an interlinked fabric of microfractures whose main propagation direction corresponds to the direction of the largest main stress. The microfracture fabric also propagates laterally at the same time although to a subordinate degree. This phase of the test is called the infiltration phase.

The infiltration phase ends relatively abruptly – clearly shown in the measurement data by the almost instant significant rise in injection rate at a specific point in time. This time is interpreted to correspond to the hydraulic breakthrough of the fluid and the creation of a hydraulic connection between two reservoirs with different fluid pressures. The second part of the curve with the higher injection rate is therefore interpreted as corresponding to the flow process. The flow paths are the secondary migration paths created during the infiltration process. Because this flow process continues in principle at a constant flow rate and under otherwise constant conditions, it can be assumed that no new migration paths are created during this period despite the change in pore pressure conditions corresponding to the hydraulic potential field.

6 FIRST BASIC NUMERICAL SIMULATIONS AND RESULTS

Based on the proposed physical model a computer program has been developed for numerical simulation of cavern behaviour. Different phases have to be considered: pressure build-up phase, infiltration phase and flow phase. This computer code called INFIL is described in detail in Wolters (2005).

In one of the first numerical simulations, a typical salt cavern from a larger cavern field is considered which has a cavern roof at a depth $z_D = -1115$ m, a cavern sump at a depth $z_S = -1315$ m and therefore a cavern height of $h = 200$ m, as well as a cavern diameter of $d = 80$ m. Top salt lies at a depth of $z = -715$ m. Top salt is overlain by a porous water-saturated formation.

To model and simulate the load-bearing behaviour of the shutdown cavern, it is initially assumed that sufficient time has elapsed for temperature equalisation to take place between the rock and the brine between the flooding of the cavern with water/brine and the installation of the cavern seal – making it possible initially to ignore the thermally-related increases in pressure. For the numerical simulation, the pressure build-up in this case starts after installation of the fluid-tight cavern seal under isothermal conditions and a hydrostatic internal pressure level ($\gamma_{Fl} = 0.012$ MN/m^3. The influence of thermally-induced pressure increases in the context of the modelling approach presented here is discussed in Lux (2006).

The analysis at first looks at the geohydraulic/geomechanical processes taking place, and the load-bearing behaviour of the rock, taking into consideration a variable rock stress state during the infiltration process reflecting internal cavern pressure and time. The point in time at which infiltration begins arises automatically from the first fulfilment of the infiltration conditions in the calculation zone in accordance with equation (1).

For the defined rock model with a homogenous structure and isotropic material properties, it can be assumed empirically that the infiltration process in principle follows the line of decreasing lithostatic depth pressure, and spreads upwards from the cavern roof through the overlying salt in the direction of top salt.

Pursuant to the modelling approach, the infiltration process changes to a flow process after reaching a permeable horizon. As a consequence, analysis of the infiltration process is followed by analysis of the subsequent flow process – modelled in a simplified form as laminar and stationary Darcy flow over the defined time increment.

The following figures show some selected typical results of the numerical simulation:

- Figure 3 firstly shows that around 30 years pass in this example until the internal pressure in the cavern has built up to the necessary level required to initiate the infiltration process. This internal pressure is then maintained at a fairly constant high level for a relatively long period of around 100 years with respect to the duration of the infiltration process of around 125 years in total. Figure 3 also shows the volume of brine infiltrated into the rock salt during this process. The strong rise in the last two decades prior to hydraulic breakthrough is attributable to the increasing infiltration rate. This is itself a reflection of the decreasing depth pressure.
- Figure 4 shows the corresponding calculated propagation of the infiltration zone at different times during the infiltration process. This reveals that the infiltration front only develops very slowly at the beginning in the zone close to the cavern but then spreads relatively fast later on in the more distal

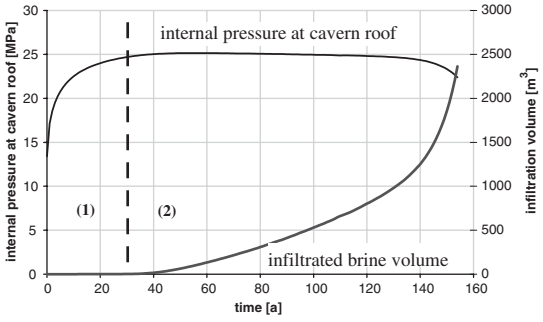

Figure 3. Time-dependent development of internal pressure at cavern roof and of infiltrated brine volume with (1) pressure increasing phase and (2) infiltration phase unitl hydraulic break-through.

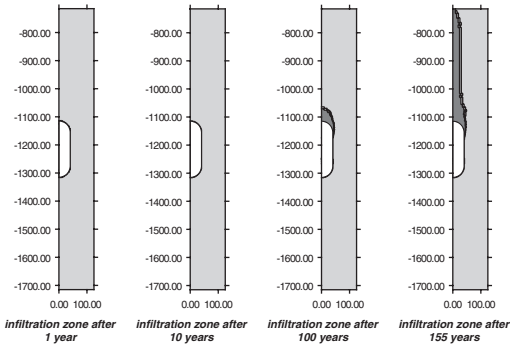

Figure 4. Propagation of the infiltration front at different points in time.

locations from the cavern. The continuously high internal pressure during the infiltration phase gives rise to a period of only 125 years from the start of infiltration to hydraulic breakthrough. Assuming adequately reliable modelling/simulation, this reveals that the time period during which the load-bearing system of the sealed cavern and the surrounding halite formation could be sustainably altered by the infiltration process, and its transformation to a flow process along the secondary migration paths created by infiltration, are of an order of magnitude suitable for engineering treatment. Indeed several factors could enlarge this time spans significantly: lower creep rates than modelled at low deviatoric stresses, a creep limit, capillary forces between fluid and salt rock crystal surfaces in the micro-pathways.

– Following hydraulic breakthrough into a porous water-saturated formation a stationary Darcy flow takes place after the infiltration process in this simulation example, the volume flow of the brine extruded as a result of rock convergence is $Q \approx 48\ \mathrm{m^3/a}$ corresponding to a convergence rate of $\dot{K} \approx 0.005\%/\mathrm{a}$. The convergence of a sealed cavern after breakthrough and hydraulic connection is significantly dependent on the transmissivity of the infiltration zone and the creep behaviour of the surrounding salt under the relevant stress conditions. It is important to point out again here the key influence of the location-specific rock mass convergence – i.e. convergence under the conditions affecting the sealed cavern and therefore the very low deviator stresses – on the long-term load-bearing behaviour of the cavern, and the effects on the surrounding geology and the ground surface.

In the long term context, the final flow phase is of crucial importance to the load-bearing behaviour of the load-bearing system formed by the salt rock mass and the sealed fluid-filled cavern, as well as its effects at the ground surface.

To demonstrate the general capability of the INFIL-code, the so-called Etzel Field Test has been re-analysed.

7 ETZEL FIELD TEST AND BACK-ANALYSIS

7.1 *Test procedure and basic results*

The Etzel field test refers to a pressure build-up test carried out between 1991 and 1994 at cavern K102 in the Etzel cavern field. This test is used here as the first validation of the INFIL software. Figure 5 shows the cavern position and the geometry of the cavern. The test cavern is a relatively slim but extremely high cavern with a height of $h = 662$ m. The pressure build-up test was carried out to determine whether, and if yes, how, and at which pressure level the rock salt surrounding the cavern loses its integrity, i.e. its fluid tightness, during a slow increase in internal pressure. The conditions during the pressure build-up test, and in particular the time involved, were therefore to correspond as closely as possible to the behaviour of a sealed cavern (low pressure build-up rate, long test duration) also taking into consideration economic factors.

Figure 6 shows the test data and specifically the change in internal pressure against time (brine-side head pressure). The pressure build-up phase and the pressure reduction phase are marked by sections in which the fluid pressure changes as a result of brine injection and brine extraction, and other sections where the fluid pressure remains roughly constant when no brine is injected or extracted, so the test can be subdivided into injection and extraction phases as well as observation phases.

Based on the understanding at the time (planning for the test began around the middle of the 80s), two different types of potential failure were looked at, namely

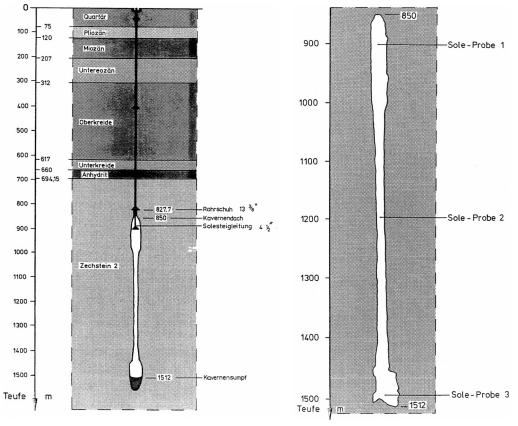

Figure 5. Cavern Etzel K102.

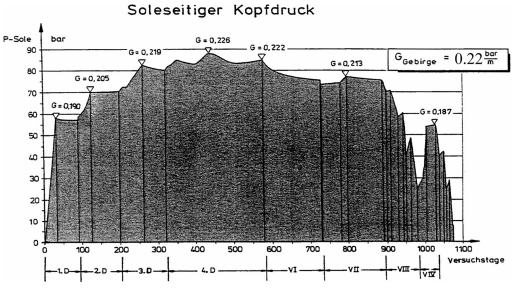

Figure 6. Time-dependent development of fluid pressure.

– the loss of formation integrity (tightness) as a result of the formation of macrofracs at fluid pressure gradients considerably higher than the primary formation pressure gradient (an additional liner was installed to ensure that the system was technically capable of testing this condition) or alternatively
– the loss of formation integrity as a result of gradual microfissure creation at fluid pressure gradients at around the same level as the primary formation pressure gradients.

The test curve in Figure 6 (time-dependent fluid pressure) shows that during the first three test phases (pressure build-up and observation phases) up to the achievement of fluid pressure gradients of $p'_{Fl} = 0.219$ bar/m at the pre-defined brine injection rate, although the pressure build-up intensity decreases there are still overall clear increases in brine pressure. The first significant drop in pressure occurred during the observation phase after stopping brine injection during the third test phase. This indicates brine infiltration of the rock. During the subsequent fourth test phase, it was still possible to achieve another increase in pressure to a gradient of $p'_{Fl} = 0.226$ bar/m only by doubling the injection rate for a much longer injection

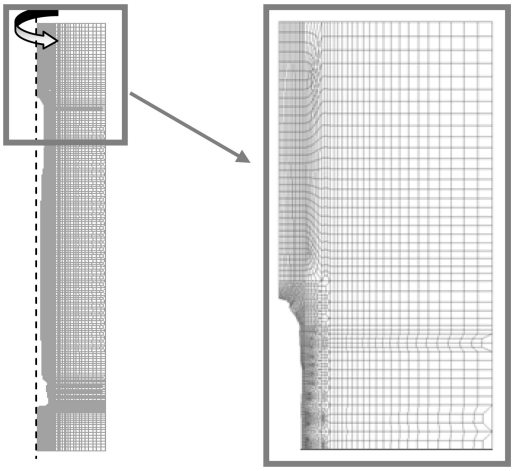

Figure 7. FEM-model of cavern K102.

time and therefore at a significantly lower pressure build-up rate. After this point, the fluid pressure drops to a gradient of $p'_{Fl} = 0.222$ bar/m despite continuing injection. During the subsequent observation phase, the pressure continued to drop continuously. This was taken as clear evidence that the fluid pressure strength level of the rock had been reached or clearly exceeded during this test. However, with respect to the type of failure, instead of the formation of singular macrofracs (also not excluded a priori) the failure took the form of fluid-pressure-induced zonal secondary migration paths consisting of microfissures.

The key findings of the field experiment were therefore:

– The failure of the rock (loss of integrity) during a slow increase in pressure does not take place as a result of spontaneously formed local macrofractures but rather as a result of gradual zonal infiltration in fluid-pressure-induced microfissures (= formation of a linked secondary micro migration path system).
– The fluid pressure level during failure corresponds roughly to the primary pressure depth level.
– 1257.2 m^3 of injected brine remained in the formation after returning the pressure to the initial level.

7.2 *Comments on modelling and numerical simulation*

The calculation model with the discretisation of the cavern K102 is shown in Figure 7. This reveals that the calculation model corresponds relatively closely to the cavern roof zone as well as the other cavern configuration. The salt formation is modelled as being homogenous and isotropic. The Lubby2 elastic-viscous constitutive model is used to model the creep

behaviour. The material parameters correspond to the parameters for the salt deposit derived from laboratory tests. When modelling/simulating the infiltration process, the material parameters are set as in the preceding calculation example because of the absence of location-specific data.

The numerical simulation of the field test covers a period of 723 days. As shown in Figure 6, the fourth observation phase ends at the end of this period. The pressure is then reduced in several stages, but the process of pressure reduction is not part of the simulations made here.

7.3 *Calculation results*

The start and/or continuation of infiltration is decided as part of the infiltration model used here with the help of the criterion equation (1).

A detailed look at the way the internal pressure builds up during the first two pressure build-up phases actually shows that the first pressure build-up phase takes place at a constant pressure build-up rate under constant injection rate conditions (linear pressure build-up). During the first observation phase, the pressure level already reached may decline marginally, but basically remains constant (microfissures at cavern wall?). The second pressure build-up phase with a lower injection rate initially shows a correspondingly smaller pressure build-up rate. By the end of the second pressure build-up phase however the pressure build-up rate grows much more strongly even though the injection rate remains constant. During the subsequent observation phase, the fluid pressure remains constant over a period of approx. 75 days until the start of the third pressure build-up phase.

This development of fluid pressure build-up is not proportional to the externally applied injection rate but appears to be irregular, and can only be explained when incorporating the secondary stress field combined with the development of the infiltration front and possibly also to an inhomogeneous and anisotropic rock fabric.

14 parameter variations were calculated to perform a sensitivity analysis. The sensitivity analysis procedure involved varying only one parameter at a time in each case to determine its precise effect on the pressure build-up, infiltration volume and infiltration zone parameters. Note that assumed dependencies were sometimes confirmed by the numerical simulation but sometimes also refuted. Renewed analysis of the reaction of the load-bearing system to the variation in parameters then provided new information and a better understanding of the process.

Regarding the calculation result which produced the best match between the calculation data and the measurement data, it can therefore be concluded that given the extent of abstraction, the approximate nature of the model approach, and the numerous parameters (and in

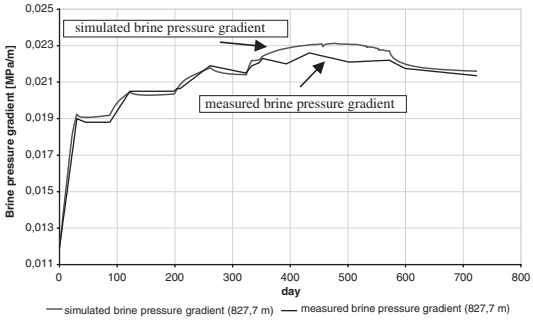

Figure 8. Time-dependent development of brine pressure gradient (measured and simulated).

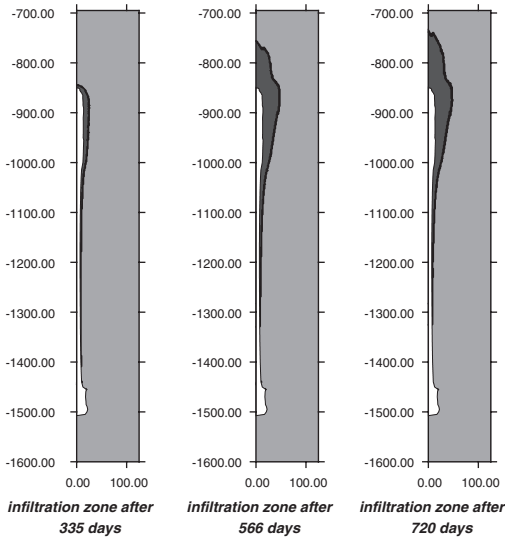

Figure 9. Propagation of infiltration front in time and space.

particular when also considering the parameters not varied but treated instead as determined) the surprisingly good match between the calculation data and the measurement data according to Figure 8 was achieved at an unexpectedly high level of quality and sensitivity in its response to the changes in the test conditions (injection rate).

Figure 9 shows that at calculation time $t = 566$ d the infiltration front has expanded considerably further into the rock mass both in the direction of top salt as well as laterally at the depth of the lower cavern roof zone: however, at the end of the pressure build-up test it only reaches a depth of $z = -760$ m and therefore extends around 90 m from the cavern into the overlying rock, and is therefore still approx. 60 m below top salt. The subsequent observation phase only leads to a further small extension of the infiltration front in the direction of top salt because in the absence of brine

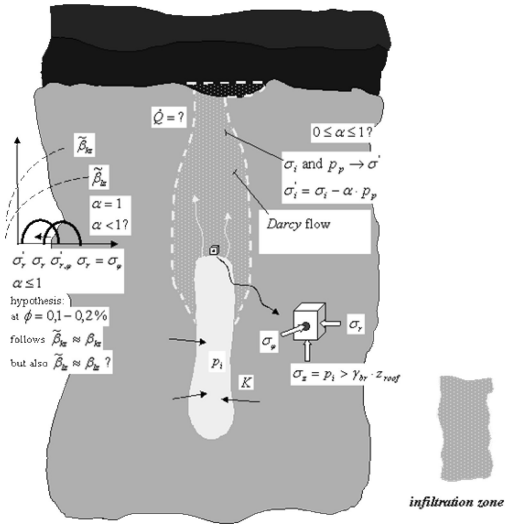

Figure 10. Questions concerning the long-term behaviour of sealed liquid-filled salt cavities, especially after breakthrough of fluid into the non-saline cap rock.

injection, the progression of the infiltration front leads to a reduction in fluid pressure and thus a lowering of the effective fluid pressure.

8 CONSEQUENCES FROM THE ANALYSIS OF THE LOAD-BEARING BEHAVIOUR OF SEALED FLUID-FILLED SALT CAVERNS WITH RESPECT TO ABANDONMENT FEASIBILITY

The numerical simulations of the long-term load-bearing behaviour of fluid-filled sealed salt caverns on the basis of the modelling approach in line with the infiltration hypothesis presented here graphically show

- the time-dependent course of fluid infiltration within the rock, whereby
- the lateral propagation of the infiltration zone and the development of secondary permeability are spatially restricted to a narrowing zone of salt rock mass extending from the cavern roof in the direction of top salt and
- the salt rock mass lying outside of this infiltration zone still retains its primary permeability and can therefore be considered to be impermeable.

The numerical simulations also enable further quantification of the mechanical and hydraulic variables used to analyse and evaluate the load-bearing behaviour of the rock taking into consideration stability, integrity and third party protection (surface protection, environmental protection).

Figure 10 provides an initial summary of the questions which arise from the identified load-bearing behaviour of the rock mass under the influence of hydromechanically coupled processes. In this context, the focus is less on the specific numerical values of each of the variables, but on the resulting proof or observation aspects.

The following questions were identified concerning proof aspects within the context of the post-operational abandonment of a fluid-filled and sealed cavern in creepable salt rock taking into consideration stability, integrity and third-party protection. The questions include specification of the location-specific conditions in each case but do not necessarily include all of the potential questions:

- Does an infiltration zone develop which propagates progressively until it reaches a permeable formation?
- Do all rock salt facies behave more or less the same or are there significant principle differences regarding the process of fluid infiltration?
- How much time does the infiltration process take until hydraulic breakthrough?
- How do the mechanical properties of the rock change in the infiltration zone?
- Which long-term hydraulic situation establishes itself after hydraulic breakthrough (pore pressure, internal cavern pressure)?
- Does more pressure-induced fracturing of the rock take place after hydraulic breakthrough?
- Is the load-bearing capacity of the infiltrated salt rock mass above the roof of the cavern/infiltration zone guaranteed in the long-term (pore pressure level and internal pressure level, mechanically-effective pore pressure, mechanical stress) or is there a risk of progressive collapse of the roof of the cavern with a tendency to develop a collapse cone?
- Can the released cavern fluid (brine, storage medium residues) be discharged in an environmentally compatible way into the (deep) groundwater?
- Do the results have an influence on the specifications for the construction of the borehole plug?
- How long does it take before final convergence is reached?
- Is the surface subsidence rate and the final amount of surface subsidence acceptable?
- Is there a long-term risk of collapse up to the ground surface?

With respect to cavern abandonment, this clearly shows that in addition to the construction of the borehole plug, there are still some scientific and technical aspects which require clarification from a rock-mechanical point of view. Work on these aspects is to be carried out in the near future. It also clearly shows that after shutting down operations, an observation phase of some years should first be planned in prior to sealing the cavern.

REFERENCES

Consortium 'Druckaufbautest' 1994. *Druckaufbautest in der Kaverne K102.* Research Project Report (unpublished).

Crotogino, F. & Schmidt, U. 1999. *Endverwahrung von Salzkavernen – Stand der Entwicklung.* Forschung, Technik und Innovation, Preussag – Interne Veröffentlichungen, H. 23.

Lux, K.-H. 2006. *Zum langfristigen Tragverhalten von verschlossenen solegefüllten Salzkavernen – ein neuer Ansatz zu physikalischer Modellierung und numerischer Simulation.* Clausthal: TU Clausthal, Professur für Deponietechnik und Geomechanik, Schriftenreihe Heft 15.

Lux, K.-H., Rokahr, R.B. & Kiersten, P. 1986. *Gebirgsmechanische Anforderungen an die untertägige Deponierung von Sonderabfällen im Salzgebirge.* Köln: Forschung und Praxis U-Verkehr und unterirdisches Bauen, STUVA.

SMRI – Rokahr, R.B., Crotogino, F. & Rolfs, O. 2002. *High Pressure Cavern Analysis.* Solution Mining Research Institute, Research Project Report (unpublished).

Wolters, R. 2005. *INFIL – Ein EDV-Programm zur numerischen Simulation des Infiltrationsprozesses von fluiden Phasen in impermeable Salzgesteinsformationen.* Handbook, TU Clausthal, Professur für Deponietechnik und Geomechanik (unpublished).

The Mechanical Behavior of Salt – Understanding of THMC Processes in Salt –
Wallner, Lux, Minkley & Hardy, Jr. (eds)
© 2007 Taylor & Francis Group, London, ISBN 978-0-415-44398-2

Deep salt-cavern abandonment

B. Brouard
Brouard Consulting, Paris, France

P. Bérest & M. Karimi-Jafari
LMS, Ecole Polytechnique, Palaiseau, France

ABSTRACT: When a salt cavern is sealed and abandoned, its pressure slowly changes due to various mechanical, hydraulic, thermal and chemical effects. These effects are described in this paper. Several of them can be predicted accurately. It is suggested that an abandonment test be performed before sealing a cavern in order to assess each effect separately, a prerequisite for credible long-term prediction.

1 INTRODUCTION

Over the past several years, there has been growing concern about the long-term behavior of deep underground salt caverns after they have been sealed and abandoned. By "deep", we mean caverns whose depths range between 400 and 2000 m and whose horizontal dimensions are much smaller than their depth. (There is no risk of a collapse leading to the creation of a sinkhole in such caverns.) Many authors have contributed to this topic; several of them are referenced in the following. The Solution Mining Research Institute (SMRI), which represents companies, consultants and research centers involved in the solution-mining industry, has set this problem at the center of its research program (Ratigan, 2003).

Prior to abandoning a storage cavern, hydrocarbons are withdrawn from it, and it afterward is filled with brine. (Brine production caverns obviously are filled with brine.) Cavern pressure at that point is halmostatic – i.e. it results from the weight of the brine column filling the well from the surface to the cavern, or P_h (MPa) $= 0.012\,H$ (m), where H is the cavern depth. A special steel plug is set above or below the casing seat, and cement is poured into the well, isolating a brine "bubble" whose long-term evolution must be predicted. Many "shut-in pressure" tests performed on closed caverns have proven that brine pressure increases in sealed caverns (see, for instance, Fokker 1995; Bérest *et al.* 2000). Typical initial build-up rates are 3 to 10 MPa/year, but much faster rates can be observed in very deep (say, deeper than 2000 m) caverns. The final value of cavern brine pressure is of utmost importance. In salt formations, the natural state of stress resulting from overburden weight generally is assumed to be isotropic – i.e. the geostatic pressure is P_∞ (MPa) $= 0.022\,H$ (m). (This assumption, however, must be verified on a case-by-case basis.) When the cavern pressure is larger than geostatic, hydrofracturing is likely: brine may flow upward through fractures to shallow water-bearing strata, leading to water pollution, the consequences of which must be assessed for each site-specific situation.

2 FACTORS CONTRIBUTING TO PRESSURE EVOLUTION

2.1 *Introduction*

The behavior of a sealed cavern is governed by four main phenomena: (1) brine thermal expansion; (2) salt mass creep; (3) brine permeation through the cavern walls; and (4) leaks through the casing or casing shoe. These lead to cavern volume or brine volume changes:

$$\dot{V}_c/V_c = \beta_c \dot{P} - \alpha_c \dot{\overline{T}}_R - Q_{creep}/V_c \tag{1}$$

$$\dot{V}_b/V_b = -\beta_b \dot{P} + \alpha_b \dot{T} - Q_{leak}/V_b - Q_{perm}/V_b \tag{2}$$

where V_c is the cavern volume, V_b is the cavern brine volume, P is cavern brine pressure, T is cavern brine temperature, $\overline{T}_R$ is the average rock temperature change (more precisely defined in Section 2.5), Q_{creep} is the viscoplastic cavern volume change rate, Q_{leak} is the leak rate through the casing or casing shoe, Q_{perm} is the brine seepage rate through the rock mass; and $\alpha_b, \beta_b, \alpha_c, \beta_c$ are thermo-elastic coefficients that will be discussed later.

Other phenomena play a minor role. For instance, the amount of salt that can be dissolved in a given mass of water is an increasing function of pressure and temperature: an increase in P or T leads to additional dissolution. Salt dissolution is an endothermic reaction, and the volume of saturated brine is smaller than the sum of the volumes of its components (salt and water). From this, any increase in P or T is followed by a slightly delayed decrease (by a few percent of the initial change; precise figures are discussed in Van Sambeek *et al.* 2005). In other words, the "instantaneous" thermoelastic coefficients ($\alpha_b, \beta_b, \alpha_c, \beta_c$) must be modified accordingly when slow processes are considered.

In a closed cavern, $V_b = V_c = V$ and Equations (1) and (2) result in

$$(\beta_c + \beta_b)\dot{P} = \alpha_b \dot{T} + \alpha_c \dot{\bar{T}}_R + \left(Q_{creep} - Q_{leak} - Q_{perm}\right)/V \qquad (3)$$

In the long term (several centuries) $\dot{T}$, $\dot{T}_R$ and $\dot{P}$ vanish to zero and there exists an "equilibrium pressure" such that $Q_{creep} = Q_{leak} + Q_{perm}$ (Q_{leak} is likely to be small). One aim of an in situ test is to predict "equilibrium pressure" value. For this reason the various terms in (3) must be assessed; they are discussed in the following paragraphs.

2.2 *Cavern compressibility*

Cavern compressibility, $\beta V = (\beta_c + \beta_b)V$, is proportional to the cavern (or brine) volume. Compressibility factor β is the sum of the brine compressibility factor ($\beta_b = 2.57 \times 10^{-4}\,\mathrm{MPa}^{-1}$ holds for a rapid injection; the "long-term" figure is $\beta_b = 2.7 \times 10^{-4}\,\mathrm{MPa}^{-1}$, see above) and the cavern compressibility factor, or β_c, which depends upon both rock-salt elastic properties and cavern shape. A typical value of the cavern compressibility factor is $\beta_c = 1.3 \times 10^{-4}\,\mathrm{MPa}^{-1}$, which makes $\beta = 4 \times 10^{-4}\,\mathrm{MPa}^{-1}$; however, larger values are sometimes encountered – for instance, when the cavern is somewhat flat (Bérest *et al.* 1999).

Cavern compressibility can be measured simply when injecting brine and measuring the resulting brine pressure build-up. Cavern compressibility is the slope of the curve (injected brine *vs* brine pressure). However, mistakes can be made easily: when injecting (or withdrawing) fluids into (or from) a cavern, one may modify the composition or temperature of the fluids in the well. The relation between wellhead pressure and cavern pressure is modified accordingly, leading to possible misinterpretation.

2.3 *Leaks*

As will be seen later, the permeability of rock salt is exceedingly small in most cases. The real problem is usually the "piping" – that is, the cemented well that connects the cavern to the ground surface. Although correct and robust well designs prevent most leakages, full-scale testing is necessary to ensure that acceptable tightness exists. Tightness tests are performed before commissioning a cavern (and from time to time during cavern operation). It often is considered that the maximum allowable leak rate during such a test is $Q_{leak} = 160\,m^3$/year (Thiel 1993). Smaller apparent-leak rates often are measured during actual tests and Van Sambeek *et al.* (2005) proved that actual tests often overestimate the actual leak. It can be assumed that such a leak, which is effective when a cavern is in operation, will be made much smaller – or even nil – had the casing been plugged and filled with cement before cavern abandonment. For this reason, it is important to measure accurately leaks that occur during an abandonment test. The leak detection system is based on the density difference between brine and oil densities. ("Green" oil often is used during *in situ* tests). The system is similar to that described by Diamond *et al.* (1993) for brine production wells. The annular space is filled with oil to down below the last casing shoe; the central tubing also contains a small amount of oil (see Fig. 1). Let Q be a cavern or *brine* volume change rate; it generates the same pressure drop (when $Q < 0$) or build-up ($Q > 0$) rates in the cavern ($\dot{P}_c$), as well as in both the tubing ($\dot{P}^{wh}_{tub}$) and the annular space ($\dot{P}^{wh}_{ann}$) at the wellhead:

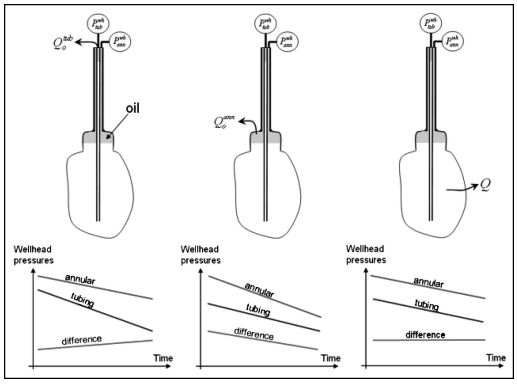

Figure 1. Principle of the oil-leak detection system.

$$\dot{P}^{wh}_{tub} = \dot{P}^{wh}_{ann} = \dot{P}_c = Q/\beta V \qquad (4)$$

The two curves (annular-space pressure *vs* time) and (central-tubing pressure *vs* time) are perfectly parallel (right-hand picture in Fig. 1).

A green oil leak from the central tubing (Q^{tub}_o) through the wellhead produces the same pressure drop both in the central tubing and in cavern – i.e. $\dot{P}^{wh}_{ann} = \dot{P}_c = -Q^{tub}_o/\beta V$. However, brine density ($\rho_b \approx 1200\,\mathrm{kg/m^3}$) is larger than the density of green oil ($\rho_o \approx 810\,\mathrm{kg/m^3}$): thus, a green oil leak yields to

both an upward vertical displacement of the oil/brine interface and an additional pressure drop in the central tubing, $\dot{P}^{wh}_{tub} = \dot{P}^{wh}_{ann} - (\rho_b - \rho_o)\, g Q^{tub}_0 / S_{tub}$, where S_{tub} is the cross-sectional area of the central tubing.

A green oil leak from the annular space (Q^{ann}_o) through the casing, casing shoe or at the wellhead acts in the reverse: the pressure drop rate in the tubing is simply $\dot{P}^{wh}_{tub} = \dot{P}_c = -Q^{ann}_o / \beta V$; in the annular space, it is $\dot{P}^{wh}_{ann} = \dot{P}_{tub} - (\rho_b - \rho_o) g Q^{ann}_o Q^{ann}_o / S_{ann}$.

This system has proven to be extremely effective. It can detect leak rates smaller than 0.1 l/day, and even smaller leaks (0.01 l/day) when the pressure-difference evolutions are corrected from the effects of daily and annual ground-temperature fluctuations (Brouard Consulting *et al.* 2006).

2.4 *Brine thermal expansion*

In many cases, brine thermal expansion is by far the preeminent factor explaining brine pressure build-up in a closed cavern. Its effects slowly reduce with time, although, they can be effective during several decades in a large cavern.

The pristine temperature of rock increases with depth, a typical value being $T^{\infty}_R(H) = 45°\mathrm{C}$ at a depth of $H = 1000$ m, but caverns are leached out using soft water pumped from a river, lake or shallow aquifers that have cooler temperatures. Brine temperature at the end of leaching, T^0, is close to the soft-water temperature and significantly lower than the rock temperature, which is $T_R(\underline{x}, t) < T^{\infty}_R$. When the cavern remains idle after leaching is completed, the initial temperature difference slowly resorbs with time, due to heat conduction in the rock mass and heat convection in the cavern. However, the injections and withdrawals of fluids during the operational life of a cavern yield additional temperature changes. The average brine temperature in a cavern, T, is almost uniform, as has been proven by temperature logs: thermal convection stirs brine cavern effectively. Appropriate heat-transfer equations can be written as follows:

$$\partial T_R / \partial t = k^{th}_{salt} \Delta T_R \tag{5}$$

$$\left[\rho_b C_b \dot{T} - \alpha_b T \dot{P}\right] V = \int_{\partial\Omega} K^{th}_{salt}\, \partial T_R / \partial n \cdot da \tag{6}$$

$$T(t) = T_R\,(\text{wall}) \tag{7}$$

$$T_R\left(\underline{x}, t = 0\right) = T^0_R(\underline{x}) \text{ and } T\left(t = 0\right) = T^0 \tag{8}$$

The first equation holds inside the rock salt mass (k^{th}_{salt} is the thermal diffusivity of salt, $k^{th}_{salt} \approx 3 \times 10^{-6}\ \mathrm{m^2/s}$);the second equation is the boundary condition at the cavern wall ($K^{th}_{salt} = k^{th}_{salt} \rho_{salt} C_{salt}$ is the thermal conductivity of rock-salt: $K^{th}_{salt} = 6\ \mathrm{W/m/°C}$ is typical, and $\rho_b C_b = 4.8 \times 10^6\ \mathrm{J/m^3/°C}$ is the volumetric heat capacity of brine). The term $\alpha_b T \dot{P}$ is small and can be disregarded, as $\dot{P}/\dot{T} \approx \alpha_b / \beta$ and $\alpha^2_b T / \beta \rho_b C_b \approx 0.03$ (This term is significant only when short-term thermal effects of a rapid pressure build-up are considered.) The third equation stipulates that the rock temperature at the cavern wall, T_{wall}, is equal to the brine temperature. The last equation describes the temperature distribution in the cavern and in the rock formation when cavern sealing is performed ($t = 0$). In most cases, this quantity is poorly known, as the thermal history of the rock during the cavern's operational life often is complex. Brouard Consulting *et al.* (2006) suggest measuring cavern temperature to assess both cavern temperature and the rate of temperature increase. Temperature evolution can be measured by a temperature gauge set in the cavern for several weeks (However in a large cavern, brine warming is an exceedingly slow process and measuring temperature evolution may prove to be very difficult; in most cases a resolution as small one thousands of a degree Celsius and no gauge drift are needed.) This allows back-calculation of an "equivalent" thermal history – i.e. fictitious initial instant $t_0 < 0$ and initial temperature $T^0_R(\underline{x}, t_0) = T^0_R$ (T^0_R is *uniform* throughout the entire rock mass.) are computed; they are such that the temperature and temperature rate at $t = 0$ are the same as the measured figures. This procedure provides good predictions of later temperature evolutions.

2.5 *Cavern thermal expansion/contraction*

In sharp contrast to brine expansion, cavern expansion cannot be described simply by a relation between rock temperature change and cavern volume change. For a given cavern shape, the following thermo-elastic problem must be solved: no body forces; no traction applied at the cavern wall; and thermal strain distributed in the rock mass, $\varepsilon_{th} = \alpha_{salt}(T_R - T^{\infty}_R)$, where $\alpha_{salt} = 4 \times 10^{-5°}\mathrm{C}^{-1}$. In the case of an idealized spherical or cylindrical cavern, the resulting coefficient $\alpha_c$is zero (see, for instance, Boley & Weiner 1997).

2.6 *Salt mass creep*

All solution-mined caverns converge as they gradually, and quite slowly, shrink. The driving force is the difference between the geostatic pressure, P_{∞}, and cavity internal pressure, P. At this step, a few comments on the mechanical behavior of salt are helpful.

1 In the long term, rock salt flows even under very small deviatoric stresses.
2 Creep rate is a highly non-linear function of applied deviatoric stress and temperature.

3 Steady-state creep is reached after several weeks or months when a constant load is applied to a sample; it is characterized by a constant creep rate.
4 Transient creep is triggered by any change in the state of stress; it is characterized by high initial rates (following a deviatoric stress increase) that slowly reduce to reach steady-state creep.
5 When deviatoric stress is large (compared to the mean stress), salt may experience damage and dilatancy, and its permeability drastically increases. The same occurs when salt is in contact with brine which has pressure that is higher than the minimum principal stress (Fokker 1995).

The main features of steady-state creep are captured by the following simple model (Norton-Hoff power law):

$$\dot{\varepsilon}^{ij} = \dot{\varepsilon}_e^{ij} + \dot{\varepsilon}_{ss}^{ij} \tag{9}$$

$$\dot{\varepsilon}_{ss}^{ij} = A\exp\left(\frac{-Q}{RT}\right)\frac{1}{n+1}\frac{\partial}{\partial\sigma_{ij}}\left[\left(\sqrt{3J_2}\right)^{n+1}\right] \tag{10}$$

$$E\dot{\varepsilon}_e^{ij} = (1+\nu)\dot{\sigma}_{ij} - \nu\dot{\sigma}_{kk}\delta_{ij} + \alpha_{salt}\dot{T}\delta_{ij} \tag{11}$$

where J_2 is the second invariant of the deviatoric stress tensor; $E, \nu, \alpha_{salt}, A, n, Q/R$ are model parameters.

Several authors suggest constitutive laws that take into account transient creep. A complete set of equations can write:

$$\dot{\varepsilon}^{ij} = \dot{\varepsilon}_e^{ij} + F\dot{\varepsilon}_{ss}^{ij} \tag{12}$$

$$\dot{\sigma}_{ij,j} = 0 \tag{13}$$

$$\sigma_{ij}(\underline{x} = \infty, t)n_j = -P_\infty n_j \tag{14}$$

$$\sigma_{ij}\left(\text{wall}, t\right)n_j = -P\left(t\right)n_j \tag{15}$$

where F is a multiplying factor (introduced by Munson & Dawson (1986) to account for transient creep). The second relation is the equilibrium condition, and (14) and (15) are the boundary conditions. Numerical computation allows cavern convergence (i.e. loss of volume) to be assessed as a function of time and cavern pressure history.

Values of the parameters A, n, Q/R (as measured during laboratory experiments) were collected by Brouard & Bérest (1998): for 12 different salts, constant n is in the range $n = 3$–6, illustrating the highly non-linear effect of applied stress on the strain rate, and Q/R ranges from 4000 to 10,000 K. It must be noted, however, that, especially in the case of bedded salt formations containing a fair amount of insolubles, laboratory test results often are scattered.

2.7 *Salt permeability*

For every standard engineering purpose, rock salt can be considered as an impermeable rock. Its matrix hydraulic conductivity is small, and no fractures exist in a massive salt formation. The generally low permeability numbers resulting from laboratory tests are scattered ($K_{salt}^{hyd} = 10^{-21}\,\text{m}^2$ to $10^{-18}\,\text{m}^2$.) Some authors believe that *in situ* (virgin) permeability is null (Lux *et al.* 2006). *In situ* tests were performed in bedded salt formations. A 1-year-long test performed in a well at Etrez site and supported by the SMRI (Durup 1994) gave $K_{salt}^{hyd} = 6 \times 10^{-20}\,\text{m}^2$. Another SMRI-supported abandonment test at the same site, (Bérest *et al.* 2001) gave $K_{salt}^{hyd} = 2 \times 10^{-19}\,\text{m}^2$. Such figures are extremely low. From the perspective of product confinement, when short-term use is considered, salt caverns are extremely safe. However, when very long-term behavior is considered, the general picture changes. When brine warming becomes negligible, due to high cavern stiffness, even tiny fluid loss, can lessen the effect of cavern creep significantly and prevent cavern pressure from reaching high levels. The set of equations relevant to the hydro-mechanical behavior of salt can be written as

$$\frac{1}{M}\frac{\partial p}{\partial t} + btr\dot{\varepsilon} = \frac{K_{salt}^{hyd}}{\mu_b}\Delta p \tag{16}$$

$$p\left(\text{wall}, t\right) = P\left(\text{wall}, t\right) \tag{17}$$

$$p\left(\underline{x} = \infty, t\right) = p^0 \tag{18}$$

where M is the Biot's modulus, p is pore pressure, b is the Biot's coefficient, μ_b is dynamic viscosity of brine ($\mu_b = 1.4 \times 10^{-3}\,\text{Pa}\cdot\text{s}$ is typical), p^0 is the initial pore pressure (The existence of a uniform brine pore pressure throughout the rock salt mass is arguable, as salt porosity, or ϕ, is low – often lower than 1% – and pore connectivity is likely to be poor. However, the (few) *in situ* tests performed in salt mines or salt caverns have proven that the notion of a pore pressure is consistent with test results. It often is assumed that pore pressure is equal to halmostatic pressure, but tests performed at the WIPP site have proven that pore pressure is higher than expected (Dale & Hurtado 1997). More recently, several observations made at a storage site (de Laguérie *et al*. 2004) strongly suggest that pore pressure in this specific site was lower than halmostatic.) In fact, all these assertions are controversial, as the applicability of the notions elaborated in the context of reservoir engineering to almost impermeable rocks is questionable. Biot's modulus is defined by $1/M = \phi/K^{fl} + (b-\phi)/K^s$ where $\phi = 10^{-2}$, $1/K^{fl} = \beta_b = 2.7 \times 10^{-4}\,\text{MPa}^{-1}$ and $K^s = 25\,\text{GPa}$ are typical. Cosenza *et al.* (1999), following McTigue (1986) suggest $b = 0.1$, leading to

$1/M = 6.3 \times 10^{-6}\,\mathrm{MPa}^{-1}$. It often is assumed that, in (16), $btr\dot{\varepsilon}$ can be disregarded, making the hydraulic problem uncoupled. In fact, there are many reasons to believe that coupling is strong because salt permeability is influenced by the state of stress (Lux 2006; Rokhar *et al*. 2003).

Parameters of the hydraulic behavior of rock salt are difficult to measure in the laboratory; furthermore, scale effects are suspected to be significant, and *in situ* tests are preferred. It is much simpler to measure salt permeability (and diffusivity) in a borehole than in a full-size cavern, where multiple effects intermingle (In a borehole, the ratio of surface to volume is larger than it is in a cavern by two orders of magnitude, and the effect of permeation on pressure evolution is made larger accordingly. Examples of this are discussed in Brouard *et al.* (2001) or Doe & Osnes (2006).

3 ASSESSING THE VALUE OF LONG-TERM PREDICTIONS

Our goal is to predict the long-term evolution of a sealed and abandoned cavern. We assume in the following that we want to be able to make accurate quantitative predictions for a period of about 3 centuries and to make qualitative predictions when longer periods of time are considered. The quality of assumptions made above – all contributing to the pressure history in a closed cavern – must be assessed.

Cavern compressibility was measured in dozens of caverns (It is a fundamental pre-requisite for interpreting cavern tightness tests, a mandatory test for most caverns), and values of $\beta = 4$ to $5 \times 10^{-4}\,\mathrm{MPa}^{-1}$ are reported generally. No lower figures have been found. (The value for brine compressibility is a lower bound for cavern compressibility.) It has been said that "long-term" cavern compressibility is slightly higher than "short-term" cavern compressibility, but the difference is small. Larger figures are encountered in flat caverns, or when the cavern contains a small amount of gas, which is much more compressible than brine (Bérest *et al.* 1999). However, larger compressibility values make the pressure build-up rate slower, a significant advantage in the context of cavern abandonment (Bérest *et al.* 2006a).

Brine thermal expansion is a well-described phenomenon: the various constants (e.g. $\alpha_b, K_{salt}^{th}, k_{salt}^{th}$) are well known, and their range of variation from one site to another is small. The system of equations (5) to (8) is robust, leading to excellent temperature evolution prediction because conduction is the only heat transfer process in an impermeable rock, and because thermal convection, which stirs brine and makes its temperature uniform throughout the cavern, is generated by the natural geothermal gradient, a perennial driving force. Furthermore, the rate of brine expansion slowly vanishes to zero; in the very long term, its influence is small. The coefficient of cavern thermal expansion, α_c, is null in an idealized, perfectly spherical or cylindrical cavern; it can be computed easily for any cavern shape.

Leaks can be assessed accurately during an *in situ* test when a system such as that described above is used. In tests performed to this date (Bérest *et al.* 2001; Brouard Consulting *et al.* 2006), these leaks were exceedingly small; they are expected to be smaller still after the cavern is sealed.

Salt creep has been studied extensively: see, for example, the proceedings of the five conferences on the Mechanical Behavior of Salt. Dedicated numerical models, able to accommodate sophisticated constitutive laws, have been written to predict the behavior of underground caverns. However, actual cavern convergence data are rough, scarce, and somewhat inaccurate (Bérest *et al.* 2006b), making validation of sophisticated models uncertain. It was noted previously that the constants in mechanical constitutive laws vary to a large extent from one site to another, in sharp contrast to the constants in the thermal model, for example. Laboratory experiments generally have been performed on rock samples submitted to relatively large deviatoric stresses. It has been argued (Bérest *et al.* 2005; Pennock *et al*. 2006) that the constitutive laws inferred from these tests do not apply to the much smaller deviatoric stresses to be encountered at large distance of the cavern or even in the vicinity of an abandoned cavern that experiences high cavern brine pressure. (Creep rates should be much faster than those extrapolated from standard laboratory results).

Salt permeability is by far the most uncertain factor in long-term cavern behavior. The concept of a homogeneous isotropic permeability (i.e. a uniform value of K_{salt}^{hyd} throughout the entire salt mass) is probably incorrect. Bedded salt contains a fair amount of impurities, and it is suspected that its permeability is much higher than the permeability of pure salt. Salt permeability is strongly influenced by the state of stress, and several authors believe that most of the (small) permeability observed during *in situ* tests in salt caverns is induced by cavern creation and operation (more precisely, either by tensile or high deviatoric stresses developed at the cavern wall when the cavern fluid pressure is very high or very low, respectively.) For instance, Doe & Osnes (2006) performed tests in Kansas wells, where they found that the wells exhibited composite behavior in which the material near the well had a higher permeability than the material farther away, possibly reflecting a borehole damage zone.

Uncertainties remain, and the present state of knowledge does not allow for blind predictions (i.e. predictions based on laboratory measurements). *In situ* tests must be performed before decommissioning a cavern. Note that, as far as possible, *in situ* tests must

not be used to back-calculate model parameters, but, rather, to check that model parameters, which are to be determined independently, were assessed accurately before the test. In fact, cavern compressibility, brine thermal expansion and brine leaks can be measured accurately, but the same cannot be said of the rate of cavern creep closure and rock permeability. Orders of magnitude are known (e.g. K_{salt}^{hyd} belongs *a priori* to the range 10^{-22} m^2 to 10^{-18} m^2; the rate of cavern creep closure in an (opened) 1000-m deep cavern typically is 3×10^{-4} year^{-1}, and the actual figure can be faster or lower by one order of magnitude).

4 INTERPRETING ABANDONMENT TESTS

For the reasons explained above, one must try to assess separately the four effects that explain pressure build-up during an abandonment test. Pressure evolution must be observed for a sufficiently long "observation period". The objective of the test is to prove that an accurate prediction can be made. It was said that pressure increase (or decrease) rate, effects of thermal expansion and leaks can be measured accurately or predicted. They simply provide an estimation of the difference between brine permeation effects and cavern-creep closure effects:

$$Q_{creep} - Q_{perm} = (\beta_c + \beta_b) V\dot{P} - (\alpha_c + \alpha_b) V\dot{T} + Q_{leak} \qquad (19)$$

Assessing each of these two effects (Q_{creep} and Q_{perm}) *separately* is more difficult, and assumptions must be made. It generally is assumed that salt permeation is governed by the steady-state Darcy law and that cavern creep closure is governed by steady-state creep – two assumptions that are somewhat arguable. Salt formation permeability and Norton-Hoff parameters then can be back-calculated through an optimization process (Section 5).

However, transient effects also play a significant role and make test interpretation trickier. The test often consists of a trial-and-error process to assess the various effects that take place when the cavern is submitted to different brine pressure levels: the cavern pressure is changed periodically through injection or withdrawal of a liquid [It is important to check that such movements do not result in a change in well fluids density, because the relation between well pressures (which can be measured easily) and cavern pressure (which must be assessed correctly) must be known.] One important drawback of this testing strategy (which allows cavern response to various pressure conditions to be explored) is that any rapid pressure change triggers transient effects that blur the general picture for a time. (For example, after an increase in pressure, "reverse" salt creep seems to take place and cavern volume increases for a time, making cavern convergence negative (Karimi *et al.* 2007). For this reason, the transient evolution of cavern pressure must be computed. In Brouard Consulting *et al.* (2006), a dedicated software program (*LOCAS*, Brouard *et al.*, 2006) is described that takes into account the various transient effects that affect a closed cavern whose pressure is subject to rapid changes.

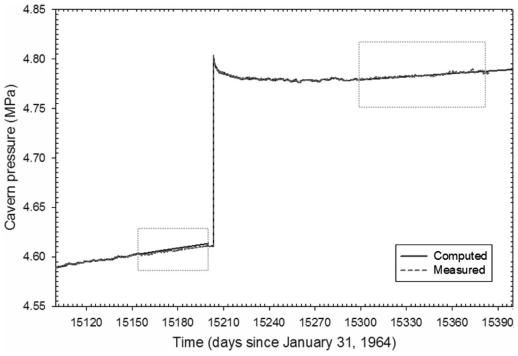

Figure 2. Cavern pressure evolution fitted against Darcy's law and Norton-Hoff's law during two fitting periods.

Fortunately, from the perspective of cavern abandonment, exact assessment is not always necessary. If it can be proven that in the range of cavern pressure experienced during the test, the brine permeation rate is faster than the creep closure rate (i.e. when combined, and when the effect of brine thermal expansion is subtracted, they lead to a pressure drop), it is clear that the cavern equilibrium pressure (achieved after a very long period of time, when the rate of brine permeation exactly balances the rate of cavern creep closure) is smaller than any cavern pressure experienced during the course of testing.

5 OPTIMIZATION PROCESS

Finite-element computations allow fitting mechanical and hydraulic parameters through an iterative comparison between computed cavern pressure and measured cavern pressure. The average pressure difference (in hPa) between computed and measured pressures can be plotted in contour plots as a function of the fitting parameters. In fact, three parameters are considered for optimization: salt permeability, or K_{salt}^{hyd} (Steady-state flow is assumed.); and the two parameters of the Norton-Hoff steady-state law, n and $A^* = A \exp(-Q/RT)$. (Q/R and A cannot be assessed separately, as temperature changes are too small during the test). Optimization allows K_{salt}^{hyd} to be determined fairly accurately. It proves more difficult to determine A^* and n. [Several (A^*, n) couples provide good fits.]

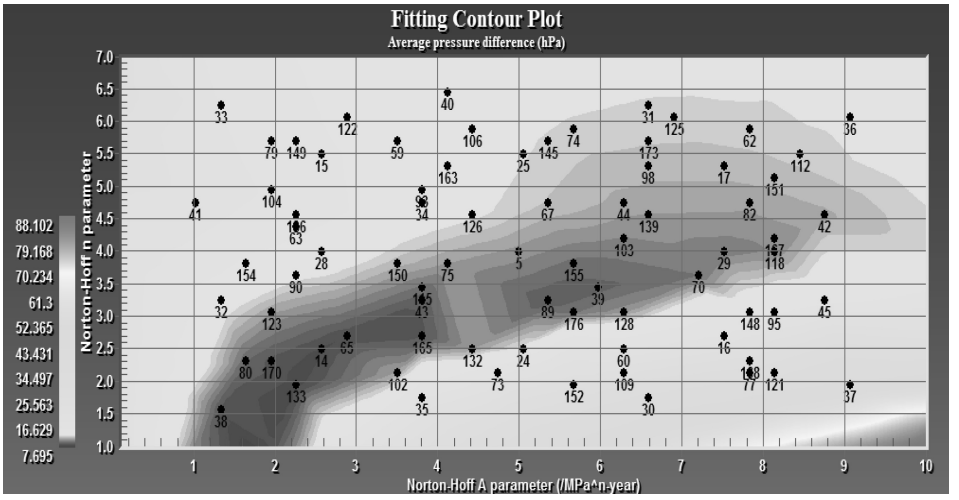

Figure 3. Fitting map in the case of salt permeability of $K_{salt}^{hyd} = 4 \times 10^{-20}$ m^2.

The reason for this is that during an abandonment test, cavern pressure experiences relatively small changes. The following example is from Brouard Consulting *et al.* (2006). An *in situ* test (supported by the SMRI) was performed in a small cavern of the propane storage facility operated by Total at Carresse, France. Pressure evolution during a part of this test is drawn on Figure 2. Note that the range of cavern pressures experienced during the test is small ($P =$ 4.6 to 4.8 MPa). Optimization was performed for two intervals of time (intervals beginning several months after any large pressure change in order to allow transient effects to dissipate). First, a best fit for salt permeability was sought, and a value of $K_{salt}^{hyd} \approx 4 \times 10^{-20}$ m^2 was found. Assuming that this estimation is correct, the mechanical parameters A^* and n were searched for with a Monte Carlo procedure.

Figure 3 shows the fitting map. Precise determination of A^* and n appears to be difficult (Several couples provide a fairly good fit.), but long-term (one-century) predictions are not deeply affected by the values of A^* and n selected for the computations.

6 CONCLUSIONS

In a sealed cavern, brine pressure evolution is governed by cavern compressibility, brine thermal expansion, leaks, cavern convergence due to salt creep, and brine permeation through the cavern wall. The three first phenomena can be assessed accurately. As far as creep closure and brine permeation are concerned, uncertainties remain. *In situ* testing must be performed for a sufficiently long observation period to allow calibration of the various parameters and to credible long-term predictions.

REFERENCES

Bérest, P., Bergues, J. & Brouard, B. 1999. Review of static and dynamic compressibility issues relating to deep underground caverns. *Int. J. Rock Mech. Min. Sci.* 36(8): 1031–1049.

Bérest, P., Brouard, B. & Durup, G. 2000. Shut-in pressure tests – Case studies. In. *Proc. SMRI Fall Meeting, San Antonio*: 105–126.

Bérest, P., Bergues, J., Brouard, B., Durup, J.G. & Guerber, B. 2001. A salt cavern abandonment test. *Int. J. Rock Mech. Min. Sci.* 38: 357–368.

Bérest, P., Blum, P.A., Charpentier, J.P., Gharbi, H. & Valès, F. 2005. Very slow creep tests on rock samples. *Int. J. Rock Mech. & Min. Sci* 42: 569–576.

Bérest, P., Karimi-Jafari, M., Brouard, B. & Durup, G. 2006a. Brine warming in a sealed cavern: What can be done?" In *Proc. SMRI Fall Meeting, Rapid City*: 61–80.

Bérest, P., Karimi-Jafari, M., Brouard, B. & Bazargan, B. 2006b. *In situ* mechanical tests in salt caverns. In *Proc. Technical Class, SMRI Spring Meeting, Brussels*: 91–130.

Boley, B.A. & Weiner, J.H. 1997. *Theory of Thermal Stresses*. Mineola, New York: Dover.

Brouard, B. & Bérest, P. 1998. A classification of salt according to their creep properties.In *Proc. SMRI Spring Meeting, New Orleans:* 18–38.

Brouard, B., Bérest, P. & Durup, G. 2001. *In-situ* salt permeability testing. In *Proc. SMRI Fall Meeting, Albuquerque*: 139–157.

Brouard, B., Karimi-Jafari, M., Bérest, P. & Frangi, A. Using LOCAS Software to Better Understand the Behavior of Salt Caverns. In *Proc. SMRI Spring Meeting*, *Brussels*: 273–288.

Brouard Consulting, Institute für Unterirdisches Bauen (IUB), Ecole Polytechnique, Total E&P France & Géostock. 2006. Salt-cavern abandonment field test in Carresse. *SMRI RFP 2003-2-B, Final Report* (available to non-SMRI members in May 2007).

Cosenza, Ph., Ghoreychi, M., Bazargan, B. & de Marsily, G. 1999. *In situ* rock salt permeability measurement for long term safety assessment of storage. *Int. J. Rock Mech. & Min. Sci.* 36: 509–526.

Dale, T. & Hurtado, L.D. 1997. WIPP air-intake shaft disturbed-rock zone study. In *Proc. 4th Conf. Mech. Beh. of Salt, Montréal, June 1996*: 525–535. Clausthal-Zellerfeld, Germany: Trans. Tech. Pub.

De Laguérie, P., Héas, J.Y., Fourmaintraux, D., You, Th., Brouard, B. & Bérest, P. 2004. Decommissioning and abandonment procedure of LPG caverns at Carresse (France). In *Proc. SMRI Fall Meeting, Berlin*: 27–44.

Diamond, H.W., Bertram, B.M., French, P.S., Petrick, G.D., Schumacher, M.J. & Smith, J.B. 1993. Detecting very small casing leaks using the water-brine interface method. In *Proc. 7th Symp. on Salt, Amsterdam*: Vol. 1, 363–368. Amsterdam: Elsevier Science.

Doe, Th. & Osnes, J. 2006. *In situ* stress and permeability tests in the Hutchinson salt and the overlaying shale, Kansas. In *Proc. SMRI Fall Meeting, Rapid City*: 181–213.

Durup, J.G. 1994. Long term tests for tightness evaluations with brine and gas in salt. In *Proc. SMRI Fall Meeting*, *Hannover*.

Fokker, P.A. 1995. The behavior of salt and salt caverns. Thesis Dissertation, Delft University of Technology, The Netherlands.

Karimi-Jafari, M., Bérest, P. & Brouard, B. 2007. Some aspects of the transient behavior of salt caverns. In *Proc. 6th Conf. Mech. Beh. Salt, Hannover* (to be published).

Lux, K.H., Düsterloh, U. & Wolters, R. 2006. Long-term behaviour of sealed brine-filled cavities in rock salt mass – A new approach for physical modeling and numerical simulation. In *Proc. SMRI Fall Meeting, Rapid City*: 105–133.

McTigue, D.F. 1986. Thermoelastic response of fluid-saturated porous rock. *J. Geophys. Res.* 91: 9533–9542.

Munson, D.E. & Dawson, P.R. 1986. Salt constitutive modelling using mechanism maps. In *Proc. 1st Conf. Mech. Beh. of Salt*: 717–737. Clausthal-Zellerfeld, Germany: Trans. Tech. Pub.

Pennock, G.M., Drury, M.R., Peach, C.J. & Spiers, C.J. 2006. The influence of water on deformation microstructures and textures in synthetic NaCl measured using EBSD. *J. Struct. Geol.* 28: 588–601.

Ratigan, J. 2003. The Solution Mining Research Institute cavern sealing and abandonment program 1996 through 2002. In *Proc. SMRI Spring Meeting, Houston*: 141–164.

Rokhar, R., Staudtmeister, K., Zander-Schiebenhöfer, D. 2003. High pressure cavern analysis. In *Proc. SMRI Spring Meeting, Houston*: 88–113.

Thiel, W.R. 1993. Precision methods for testing the integrity of solution mined underground storage caverns. In *Proc. 7th Symp. on Salt*: Vol. 1, 377–383. Amsterdam: Elsevier Science.

Van Sambeek, L., Bérest, P. & Brouard, B. 2005. Improvements in Mechanical Integrity Tests for solution-mined caverns used for mineral production or liquid-product storage. *Topical Report RSI-1799, prepared for the Solution Mining Research Institute*.

Proceedings of the "SMRI Meetings" are available at SMRI-105, Apple Valley Circle, Clarks Summit, PA 18411, USA. These Proceedings have been edited as separate volumes since the Fall 1996 Meeting.

The Mechanical Behavior of Salt – Understanding of THMC Processes in Salt –
Wallner, Lux, Minkley & Hardy, Jr. (eds)
© 2007 Taylor & Francis Group, London, ISBN 978-0-415-44398-2

Author index

Alkan, H. 285

Bekendam, R.F. 369
Bérest, P. 383, 445
Böhnel, H. 239
Bornemann, O. 63
Brouard, B. 383, 445
Brückner, D. 417

Caligaris, C. 427
Callahan, G.D. 9
Carvalho, Jr., A.L.P. 305
Chen, F. 399
Chen, J.W. 401, 407

DeVries, K.L. 9
Droste, J. 209
Durup, J.G. 427
Dusseault, M.B. 305, 391
Düsterloh, U. 3

Eberth, S. 129
Ehgartner, B.L. 353
Eickemeier, R. 337
Engelhardt, H.-J. 251

Fahland, S. 337
Faust, B. 139
Fokker, P.A. 167

Gärtner, G. 327
Gens, A. 185
Grupa, J. 159
Günther, R.-M. 77, 89, 109, 327

Hampel, A. 77, 89, 99
Hasselkus, F. 377
Heemann, U. 77, 89, 139, 215
Herbert, H.-J. 259, 277
Hesser, J. 45
Heusermann, S. 215, 337
Hévin, G. 427
Hillmann, C. 139
Hou, Z. 77, 89, 269
Hübscher, C. 175

Jockwer, N. 27

Kamlot, P. 327
Kansy, A. 17
Karimi-Jafari, M. 383, 445
Kolditz, O. 201, 277

Leusmann, Th. 251
Li, Y.P. 69, 399, 401, 407
Liang, W.G. 391
Lindert, A. 417
Lukas, V. 315
Lux, K.-H. 3, 129, 435

Mauke, R. 345
Mellegard, K.D. 9
Minkley, W. 77, 89, 119, 295
Mohlfeld, M. 345
Moog, H.C. 269, 277
Mühlbauer, J. 119, 295
Müller, W. 285

Netzeband, G.L. 175
Nipp, H.-K. 337

Olivella, S. 185

Peach, C.J. 159, 231
Pennock, G.M. 231
Pichayrou, O. 427
Plischke, I. 321
Popp, T. 17, 53, 239
Preuss, J. 337
Pudewills, A. 77, 89, 195
Pusch, G. 17

Qian, Q.H. 69, 399
Qu, D.A. 69

Reitze, A. 377
Rokahr, R. 77, 89
Rolin, C. 427
Rothenburg, L. 305
Rothfuchs, T. 209

Salzer, K. 53, 77, 89, 109, 239
Sarfeld, W. 139
Schléder, Z. 167
Schleinig, J.-P. 315
Schoenherr, J. 167
Schulze, O. 33, 77, 89, 99, 167
Shao, H. 201, 277
Ślizowski, J. 363
Sobolik, S.R. 353
Spiers, C.J. 149, 159, 231
Spies, T. 45
Stielow, B. 345
Stockmann, N. 327
Storch, G. 295
Stührenberg, D. 223

von Tryller, H. 377

Urai, J.L. 149, 167, 369
Urbańczyk, K.M. 363

Voigt, H.-D. 53

Walsh, R. 201
Wang, W.Q. 201, 277
Wei, D.H. 69, 399
Werunsky, F. 269
Wieczorek, K. 27
Wiedemann, M. 17, 53, 417
Wilsnack, T. 53
Wolters, R. 77, 89

Xie, M.L. 201, 277

Yang, C.H. 69, 391, 399, 401, 407
Yin, X.Y. 399, 401, 407

Zapf, D. 77, 89
Zetsche, F. 77, 89
Zhang, C.-L. 209
Zhang, X. 159, 231
Zhao, Y.S. 391
Zulauf, G. 63
Zulauf, J. 63